ASTROPHYSICS AND SPACE SCIENCE LIBRARY 357

Werner Becker
Editor

Neutron Stars and Pulsars

ASSL

Springer

Neutron Stars and Pulsars

Astrophysics and Space Science Library

Neutron Stars and Pulsars

by

Werner Becker (Ed.)

Springer

Werner Becker
Max-Planck-Institut fur Extraterrestische Physik
Giessenbachstrasse 1
85741 Garching
Germany

Cover Image: Artist's view on a pulsar magnetosphere with emission beams.
© by W. Becker

ISBN: 978-3-540-76964-4 e-ISBN: 978-3-540-76965-1
DOI: 10.1007/978-3-540-76965-1

Library of Congress Control Number: 2008935631

Cover design: eStudio Calamar S.L.

Printed on acid-free paper

springer.com

Preface

When the existence of neutron stars was confirmed by the discovery of radio pulsars in August 1967, there was general optimism that it should not be too difficult to explore and understand the physical properties of a rotating magnetised compact star with $\sim$10 km radius. Forty years and more than 13 PhD student-generations later, everybody involved in the $\gg$neutron star business$\ll$ has lost this illusion, meanwhile learning how complex neutron stars are and how difficult it is to understand their physical properties.

Neutron stars form in supernova explosions and/or by an accretion induced collapse of a white dwarf. At the time of their discovery – and for many years later – it was generally accepted that neutron stars can only be observed as pulsars. According to the source of energy they were split into two classes, i.e. being powered by either rotation or accretion. Today, the neutron star world is much more intrincate than it was fourty decades ago. In addition to the accretion powered pulsars, which are predominantly bright X-ray sources, and the rotation-powered pulsars which are observed throughout the electromagnetic spectrum, there are now X-ray Dim Isolated Neutron Stars (XDINs), "radio-quiet neutron stars", Compact Central Objects (CCOs) in supernova remnants, Soft Gamma-ray Repeaters (SGRs) and Anomalous X-ray Pulsars (AXPs).

Accordingly, neutron stars manifest themselves in many different ways. They become visible by high-energy processes occurring on their surface or surrounding region. In most of these objects, ultra-strong magnetic fields are a crucial element in the radio, optical, X-ray and gamma-ray emission processes which dominate the observed spectrum.

Observationally, neutron star research is advancing steadily. A great array of space instruments (the Hubble Space Telescope, ROSAT, ASCA, BeppoSAX, RXTE and the Compton Gamma-Ray Observatory), launched in the last decade of the twentieth century have opened new windows on neutron star research with high quality data in energy bands from the optical to gamma-rays. With the more recently launched satellite X-ray observatories Chandra and XMM-Newton, the H.E.S.S. Array of Imaging Atmospheric Cherenkov Telescopes, upgraded radio observatories and ground based optical telescopes a number of questions which

remained unanswered for many years could be addressed and have led to new and exciting findings which have changed the earlier picture of neutron star evolution substantially.

However, even in view of these great observational capabilities and the intense research over a period of more than 40 years, there are fundamental questions which still have not been answered. How are the different manifestations of neutron stars related to each other? What are the physical parameters which differentiate AXPs/SGRs/CCOs/XDINs and rotation-powered pulsars? What is the maximal upper bound for the neutron star mass and what is the range of possible neutron star radii? Is there any exotic matter in neutron stars? Do strange stars exist? And what are the physical processes responsible for the pulsars' broad band emission observed from the infrared to the gamma-ray band? These are just a few of the long standing open questions.

To adequately address these questions, it requires a wide range of scientific disciplines, including nuclear and condensed matter physics of very dense matter in neutron star interiors, plasma physics and quantum electrodynamics of the magnetospheres, relativistic magnetohydrodynamics of electron-positron pulsar winds interacting with some ambient medium. Not to forget the role of a test bed neutron stars provide for general relativity theories as well as being sources of gravitational waves. It is this variety of disciplines which, among others, makes the neutron star research so fascinating and attractive, not only for those who have been working in the field for many years but also for students and young scientists.

Especially students and young scientists often have the problem of finding a comprehensive reference with up-to-date information on multi-wavelength studies from neutron stars and pulsars and the various theoretical models. We have created this book to give them a reference at hand, which not only reviews the progress made since the early days of pulsar astronomy but focuses especially on questions such as (1) what have we learned about the subject and how did we learn it? (2) what are the most important open questions in this area? And (3) what new tools, telescopes, observations, calculations are needed to answer these questions?

Many of the authors who have contributed to this book have devoted a significant part of their scientific career on exploring the nature of neutron stars and understanding pulsars. Every one of us has paid special attention to write an educational comprehensive review article keeping beginners, students and young scientists as potential readers in mind. I am confident that this book will be a valuable source of information for them.

I am very thankful to all the authors for their contributions and to the referees for the time they have spent in getting the quality of the book to its final level.

Garching, *Werner Becker*
July 2008

Contents

Contributors

J. Arons Departments of Astronomy and of Physics, and Theoretical Astrophysics Center University of California, Berkeley, USA and Kavli Institute of Particle Astrophysics and Cosmology, Stanford University, USA, *arons@astro.berkeley.edu*

W. Becker Max-Planck Institut für extraterr. Physik, Giessenbachstrasse 1, 85741 Garching, Germany, *web@mpe.mpg.de*

S. Bogdanov Harvard-Smithsonian Center for Astrophysics, 60 Garden St., Cambridge, MA 02138, USA, *sbogdano@cfa.harvard.edu*

K.S. Cheng Department of Physics, University of Hong Kong, *hrspksc@hkucc.hku.hk*

O.C. de Jager Unit for Space Physics, North-West University, Potchefstroom 2520, South Africa, *fskocdj@puk.ac.za*

A. Djannati-Ataï CNRS, Universite Paris 7, Denis Diderot, 75005 Paris, France

R.F. Elsner NASA Marshall Space Flight Center, VP62 Huntsville, AL 35812, USA, *ron.elsner@nasa.gov*

U. Geppert German Aerospace Center, Institute of Space Systems, System Conditioning, Rutherfordstr. 9, 12489 Berlin, Germany, *ulrich.geppert@dlr.de*

J. Grindlay Harvard-Smithsonian Center for Astrophysics, 60 Garden St., Cambridge, MA 02138, USA, *josh@cfa.harvard.edu*

D. Hanna McGill University Physics Department, Rutherford Physics Building, 3600 University St., Montreal, QC, Canada H3A 2T8, *hanna@physics.mcgill.ca*

A.K. Harding Astrophysics Science Division, NASA Goddard Space Flight Center, *harding@twinkie.gsfc.nasa.gov*

K. Hurley U.C. Berkeley Space Sciences Laboratory, 7 Gauss Way, Berkeley, CA 94720-7450, USA, *khurley@ssl.berkeley.edu*

V.M. Kaspi McGill University Physics Department, Rutherford Physics Building, 3600 University St., Montreal, QC, Canada H3A 2T8, *vkaspi@hep.physics.mcgill.ca*

J.G. Kirk Max-Planck-Institut für Kernphysik, Postfach 10 39 80, 69029 Heidelberg, Germany, *John.Kirk@mpi-hd.mpg.de*

M. Kramer Jodrell Bank Centre for Astrophysics, University of Manchester, Alan-Turing Building, Oxford Road, Manchester M13 9PL, UK, *Michael.Kramer@manchester.ac.uk*

J.M.E. Kuijpers Department of Astrophysics, IMAPP, Radboud University Nijmegen, The Netherlands, *kuijpers@astro.ru.nl*

D.R. Lorimer Department of Physics, West Virginia University, Morgantown, WV 26506, USA, *Duncan.Lorimer@mail.wvu.edu*

A.G. Lyne University of Manchester, Jodrell Bank Observatory, Macclesfield, SK11 9DL, UK, *andrew.lyne@manchester.ac.uk*

Y. Lyubarsky Department of Physics, Ben Gurion University, P.O. Box 653, Beer-Sheva 84105, Israel, *lyub@bgu.ac.il*

R.N. Manchester Australia Telescope National Facility, CSIRO, P.O. Box 76, Epping, NSW 1710, Australia, *dick.manchester@csiro.au*

M.A. McLaughlin Department of Physics, West Virginia University, Morgantown, WV 26506, USA, *maura.mclaughlin@mail.wvu.edu*

R. Negreiros Department of Physics, San Diego State University, 5500 Campanile Drive, San Diego, CA 92182-1233, USA, *negreiro@sciences.sdsu.edu*

S.L. O'Dell NASA Marshall Space Flight Center, VP62, Huntsville, AL 35812, USA, *Steve.O'Dell@nasa.gov*

D. Page Departamento de Astrofísica Teórica, Instituto de Astronomía, Universidad Nacional Autónoma de México, México D.F 04510, México, *page@astroscu.unam.mx*

G.G. Pavlov Penn State University, Department of Astronomy and Astrophysics, 525 Davey Laboratory, University Park, PA 16802, USA, *pavlov@astro.psu.edu*

J. Pétri Max-Planck-Institut für Kernphysik, Postfach 10 39 80, 69029 Heidelberg, Germany, *Jerome.Petri@mpi-hd.mpg.de*

R. Prix Max-Planck-Institut für Gravitationsphysik, Albert-Einstein-Institut, Callinstr. 38, 30167 Hannover, Germany, *Reinhard.Prix@aei.mpg.de*

B.D. Ramsey NASA Marshall Space Flight Center, VP62, Huntsville, AL 35812, USA, *Brian.Ramsey@nasa.gov*

P. Rosenfield Department of Physics, San Diego State University, 5500 Campanile Drive, San Diego, CA 92182-1233, USA, *philrose@sciences.sdsu.edu*

M. Ruderman Department of Physics and Columbia Astrophysics Laboratory, Columbia University, New York, NY, USA, *mar@phys.columbia.edu*

D.A. Smith Centre d'études nucléaires de Bordeaux Gradignan – CENBG UMR 5797, CNRS/IN2P3 – Université Bordeaux 1, Chemin du Solarium – BP120 33175, Gradignan Cedex, France, *smith@cenbg.in2p3.fr*

D.J. Thompson Astrophysics Science Division, NASA Goddard Space Flight Center, Greenbelt, MD 20721, USA, *David.J.Thompson@nasa.gov*

S. Tsuruta Department of Physics, Montana State University Bozeman, MT 59717, USA, *uphst@gemini.msu.montana.edu*

R. Turolla Department of Physics, University of Padova, Italy, *turolla@pd.infn.it*

F. Weber Department of Physics, San Diego State University, 5500 Campanile Drive, San Diego, CA 92182-1233, USA, *fweber@sciences.sdsu.edu*

M.C. Weisskopf NASA Marshall Space Flight Center, VP62, Huntsville, AL 35812, USA, *martin@smoker.msfc.nasa.gov*

V.E. Zavlin Space Science Laboratory, NASA Marshall Space Flight Center, SD59 Huntsville, AL 35805, USA, *vyacheslav.zavlin@msfc.nasa.gov*

Chapter 1
Radio Pulsar Statistics

Duncan R. Lorimer

1.1 Introduction

Forty years after the discovery of radio pulsars by Jocelyn Bell and Antony Hewish at Cambridge in 1967 [22], the observed population presently exceeds 1,700 objects with spin periods in the range 1.4 ms to 8.5 s. Pulsar astronomy is currently enjoying a golden era, with over half of these discoveries in the past 7 years due largely to the phenomenal success of the Parkes multi beam survey [46]. From the sky distribution in Galactic coordinates shown in Fig. 1.1, it is immediately apparent that pulsars are concentrated strongly along the Galactic plane. This is particularly striking for the youngest pulsars known to be associated with supernova remnants. Also shown in Fig. 1.1 are the millisecond pulsars which have spin periods in the range 1.5–30 ms. The more isotropic sky distribution of the millisecond pulsars does not necessarily imply that they have a different spatial distribution; the difference simply reflects the observational bias against detecting short-period pulsars with increasing distance from the Sun. This is one of many selection effects that pervades the observed sample.

From such a violent birth in supernovae, it is perhaps not surprising to learn that pulsars are high-velocity objects. The right-hand panel of Fig. 1.1 shows pulsar proper motions on the plane of the sky taken from a recent study by [23]. The mean transverse speed of the current sample of 233 pulsars is $246 \pm 22\,\mathrm{km\,s^{-1}}$. From a sample of proper motions for pulsars younger than 3 Myr, Hobbs et al. find the mean 3-D velocity of pulsars to be $400 \pm 40\,\mathrm{km\,s^{-1}}$. The origin of these high velocities most likely lies in a combination of pre-supernova binary orbital motion (e.g. [24]) and/or impulsive kicks due to small asymmetries in the supernova explosions (e.g. [25]). Millisecond pulsars have significantly lower space velocities; their mean transverse speed is only $87 \pm 13\,\mathrm{km\,s^{-1}}$, while a study by Lyne et al. [44] showed the mean 3-D speed to be $130 \pm 30\,\mathrm{km\,s^{-1}}$. Despite these differences,

D.R. Lorimer
Department of Physics, West Virginia University, Morgantown, WV 26506, USA
e-mail: Duncan.Lorimer@mail.wvu.edu

W. Becker (ed.), *Neutron Stars and Pulsars,* Astrophysics and Space Science Library 357,

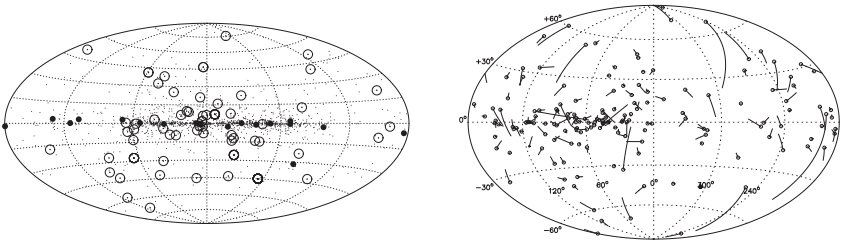

Fig. 1.1 *Left*: the distribution of pulsars in Galactic coordinates. Pulsar–supernova remnant associations and millisecond pulsars are shown by the *filled and open circles* respectively. *Right*: pulsar proper motions in Galactic coordinates (after [23]). The *solid lines* show the proper motion (neglecting the unknown radial velocity) over the last million years

population syntheses indicate that the two populations are consistent with the idea that all neutron stars share the same velocity distribution. The millisecond pulsars represent those binary systems which have survived and have necessarily smaller space velocities as a result [62].

The observed emission from radio pulsars takes place at the expense of the rotational kinetic energy of the neutron star. As a result, in addition to observing the pulsar's spin period, P, we also observe the corresponding rate of spin-down, $\dot{P}$. Such measurements give us unique insights into the spin evolution of neutron stars and are summarized on the P–$\dot{P}$ diagram shown in Fig. 1.2. The diagram contrasts the normal pulsars ($P \sim 0.5\,\mathrm{s}$ and $\dot{P} \sim 10^{-15}\,\mathrm{s\,s^{-1}}$ which populate the "island" of points) and the millisecond pulsars ($P \sim 3\,\mathrm{ms}$ and $\dot{P} \sim 10^{-20}\,\mathrm{s\,s^{-1}}$ which occupy the lower left part of the diagram).

The differences in P and $\dot{P}$ imply fundamentally different ages and magnetic field strengths for the two populations. Assuming the spin evolution of the neutron star to be a due to magnetic dipole radiation, we can make rough estimates of the inferred age $\tau \propto P/\dot{P}$ and magnetic field strength $B \propto (P\dot{P})^{1/2}$. Lines of constant B and τ are drawn on Fig. 1.2 from which we infer typical magnetic fields and ages of 10^{12} G and 10^7 yr for the normal pulsars, and 10^8 G and 10^9 yr for the millisecond pulsars. The rate of loss of rotational kinetic energy $\dot{E} \propto \dot{P}/P^3$ (also known as the "spin-down luminosity") is also indicated. As expected, these are highest for the young and millisecond pulsars.

In addition to spin behaviour, a very important additional difference between normal and millisecond pulsars is binarity. Orbiting companions are observed around about 80% of all millisecond pulsars but less than 1% of all normal pulsars. The companions are either white dwarfs, main sequence stars, or other neutron stars. Pulsars with low-mass companions ($<0.5\,\mathrm{M}_\odot$ – predominantly white dwarfs) usually have millisecond spin periods and essentially circular orbits with orbital eccentricities in the range $10^{-5} < e < 10^{-1}$. Measurements of white-dwarf "cooling ages" (see [65]) agree generally with millisecond pulsar characteristic ages and support the idea that these binary systems have typical ages of a few Gyr. Binary pulsars with high-mass companions ($>1\,\mathrm{M}_\odot$ – neutron stars or main sequence stars) have larger spin periods ($>20\,\mathrm{ms}$) and are in more eccentric orbits: $0.1 < e < 0.9$.

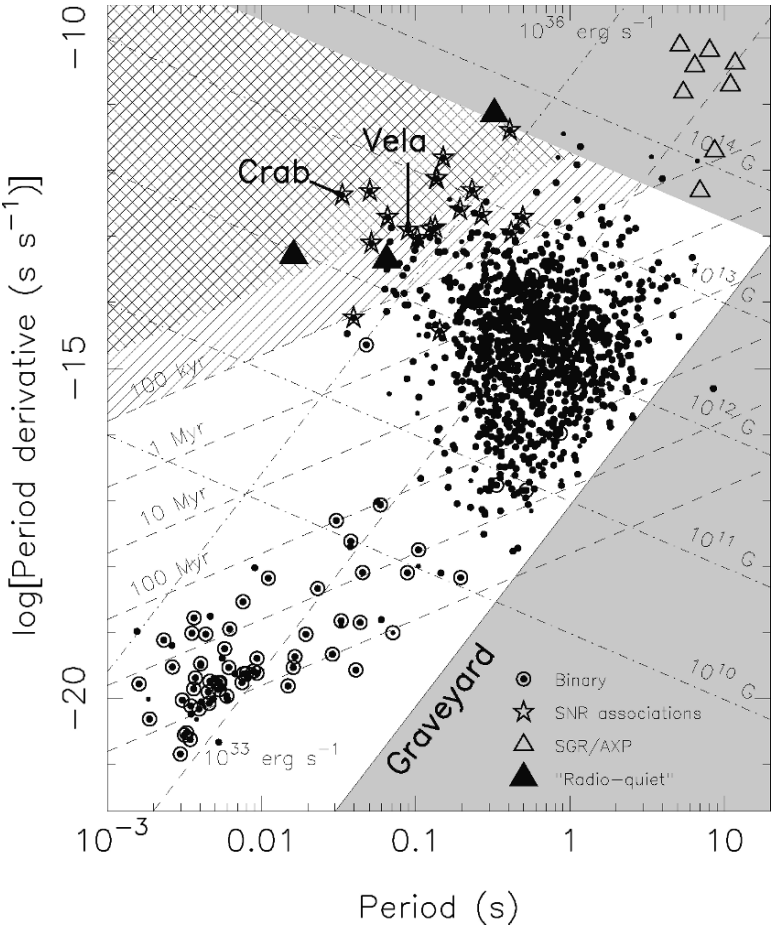

Fig. 1.2 The ubiquitous P–$\dot{P}$ diagram showing isolated and binary radio pulsars, "radio-quiet" pulsars, soft-gamma repeaters (SGRs) and anomalous X-ray pulsars (AXPs). Figure kindly provided by Michael Kramer

The existence of binary pulsars can be understood by a simple evolutionary scenario which starts with two main-sequence stars (see [8]). The initially more massive (primary) star evolves first and eventually explodes in a supernova to form a neutron star. The high velocity imparted to the neutron star at birth and dramatic mass loss during the supernova usually is sufficient to disrupt most (90% or more) binary systems [54]. Those neutron stars remaining bound to their companions spin down as normal pulsars for the next 10^{6-7} yr. Later on, the remaining (secondary) star comes to the end of its main sequence lifetime and begins a red giant phase. For favourable orbital parameters, the strong gravitational field of the neutron star attracts matter from the red giant and forms an accretion disk. As a result, the system becomes visible as an X-ray binary.

The accretion of matter transfers orbital angular momentum to the neutron star, spinning it up to short periods and dramatically reducing its magnetic field [10]. A limiting spin period is reached due to equilibrium between the magnetic pressure of the accreting neutron star and the ram pressure of the in-falling matter [1, 19, 32]. Such "spun-up" neutron stars are often referred to in the literature as *recycled pulsars*. Unlike the young pulsars with high spin-down rates, the now weakly-magnetized recycled pulsars appear in the lower-left hand part of the P–$\dot{P}$ diagram and spin down much more gradually and over a longer timescale.

The ultimate fate of the binary system depends on the mass of the secondary star. The two main outcomes are double neutron star binaries, for secondaries massive enough to explode as a supernova, and neutron star-white dwarf binaries for less massive secondaries. Very recently, the first double neutron star system has been found, PSR J0737–3039, in which both stars are observed as pulsars: a 22.7-ms pulsar "A" [11] and a 2.7-s pulsar "B" [45]. In the framework of the above model, we identify A as the first-born neutron star with a short spin period and low inferred magnetic field, while B is the younger, second-born, neutron star with a higher magnetic field.

1.2 The Observed Pulsar Spatial Distribution

Pulsar astronomers are extremely fortunate in that they have a reasonably accurate means of estimating distances to their objects from measurements of pulse dispersion caused by free electrons in the interstellar medium (see [70]). In Fig. 1.3, the most recent Galactic electron density model [15] is used to project the current sample of pulsars in the ATNF catalog (`www.atnf.csiro.au/research/pulsar/psrcat`) onto the Galactic plane. Two main features can be seen in this

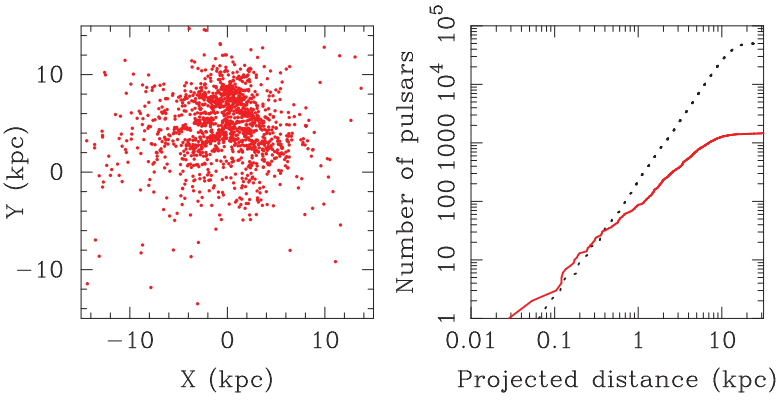

Fig. 1.3 *Left*: the currently known pulsar population projected onto the Galactic plane. The Galactic center is at the origin and the Sun is at (0.0,8.5) kpc. *Right*: cumulative distribution as a function of projected distance from the Sun. The *solid line* is the observed sample while the *dashed line* is the expected distribution of a simulated population free from selection effects

diagram: (a) pulsar positions trace the spiral-arm structure of our Galaxy (though this is somewhat incestuous, since spiral arms are now incorporated into the electron density model); (b) rather than being distributed about the Galactic center, the majority of pulsars are clearly biased towards the bright/nearby objects.

To get an idea of how biased the sample is, the right panel of Fig. 1.3 shows the cumulative distribution of pulsars as a function of distance from the Sun projected onto the Galactic plane. Also shown is the expected distribution for a simulated population in which there are no selection effects. As can be seen, the two samples are closely matched only out to a kpc or so before the selection effects become significant. From these curves, we deduce that *less than 10% of the potentially observable population in the Galaxy is currently detectable.*

The number of potentially observable pulsars in the Galaxy can be estimated very crudely by the source counting method (see, e.g. [31]) where one uses the cumulative distribution and counts sources out to a distance where the sample is thought to be more or less complete. By assuming some underlying spatial distribution function, this number can be extrapolated to get the total number of pulsars in the Galaxy. Based on Fig. 1.3, we count 100 objects out to 1 kpc, i.e. a mean surface density of $100/(\pi \times 1\mathrm{kpc}^2) \simeq 30\,\mathrm{kpc}^{-2}$. If pulsars have a radial distribution similar to that of other stellar populations, the corresponding local-to-Galactic scale factor is $1{,}000 \pm 250\,\mathrm{kpc}^2$ [55]. With this factor, we estimate there to be of order 30,000 potentially observable pulsars in the Galaxy.

1.3 Selection Effects in Radio Pulsar Surveys

The inverse square law. Like all astronomical sources, observed pulsars of a given luminosity L are strongly selected by their apparent flux density, S. For a pulsar at a distance d from the Earth which beams to a certain fraction f of 4π sr, $S = L/(4\pi d^2 f)$. Since all pulsar surveys have some limiting flux density, only those objects bright or close enough will be detectable. Note that in the absence of prior knowledge about beaming, geometrical factors are usually ignored and the resulting "pseudo-luminosity" is quoted at some standard observing frequency; e.g., at 1,400 MHz, $L_{1400} \equiv S_{1400} d^2$.

The radio sky background. A fundamental sensitivity limit is the system noise temperature, T_{sys}. While every effort is made to minimize this at the telescope, synchrotron radiating electrons in the Galactic magnetic field contribute significantly with a "sky background" component, T_{sky}. At observing frequencies $\nu \sim 0.4$ GHz, T_{sky} dominates T_{sys} along the Galactic plane. Fortunately, $T_{\mathrm{sky}} \propto \nu^{-2.8}$ so this effect is significantly reduced when $\nu > 0.4$ GHz.

Propagation effects in the interstellar medium. Dispersion and scatter-broadening of the pulses in the interstellar medium hamper detection of short period and/or distant objects. The effects of scattering are shown in Fig. 1.4. Fortunately, like T_{sky}, the scatter-broadening time τ_{scatt} has a strong frequency dependence, scaling roughly

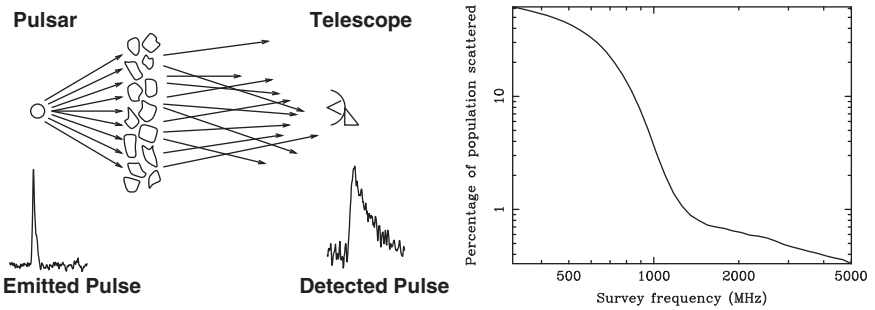

Fig. 1.4 *Left*: pulse scattering by irregularities in the interstellar medium shown here as an idealized "thin screen" of material lying midway between the pulsar and the observer. *Right*: a simulation showing the fraction of pulsars undetectable due to scattering as a function of observing frequency

as ν^{-4}. Figure 1.4 shows that for survey frequencies below 1 GHz, scattering "hides" a large fraction of the population. Additionally, scintillation, the diffractive and refractive modulation of apparent flux densities by turbulences in the interstellar medium [56] affects pulsar detection. For example, two northern sky surveys carried out 20 years apart with comparable sensitivity [17, 59] detected a number of pulsars above and below the nominal search thresholds of one experiment but not the other. Surveying the sky multiple times minimizes the effects of scintillation and enhances the detection of faint pulsars through favourable scintillation.

Finite size of the emission beam. The fact that pulsars do not beam to 4π sr means that we see only a fraction f of the total active population. For a circular beam, Gunn and Ostriker [21] estimated $f \sim 1/6$. A consensus on the precise shape of the emission beam has yet to be reached. Narayan and Vivekanand [50] argued that the beams are elongated in the meridional direction. Lyne and Manchester [41], on the other hand, favour a circular beam. Using the same database, Biggs [9] presented evidence in favour of meridional compression! All these studies do agree that the beam size is period dependent, with shorter period pulsars having larger beaming fractions. Tauris and Manchester [64] found that $f = 0.09\,[\log(P/\mathrm{s}) - 1]^2 + 0.03$, where P is the period. A complete model for f needs to account for other factors, such as evolution of the inclination angle between the spin and magnetic axes.

Pulse nulling. The abrupt cessation of the pulsed emission for many pulse periods, was first identified by [3]. Ritchings [57] presented evidence that the incidence of nulling became more frequent in older long-period pulsars, suggesting that it signified the onset of the final stages of the neutron star's life as an active radio pulsar. Since most pulsar surveys have short (<few minutes) integration times, there is an obvious selection effect against nulling objects. Means of overcoming this effect are to look for individual pulses in search data [51], survey the sky many times, or use longer integrations. Indeed, 35-min pointings in the Parkes multi-beam survey have been particularly successful in this regard, discovering a number of nulling pulsars [69].

Radio intermittency. Recently, a new class of "sometimes pulsars" has been found. These provide unique and new insights into neutron star physics and populations [28]. The prototype, PSR B1931+24, shows a quasi-periodic on/off cycle in which the spin-down rate increases by ∼50% when the pulsar is in its on state compared to the off state! While the behaviour of this pulsar appears to be linked to the increase in magnetospheric currents when it is on, there is no satisfactory explanation for this effect. Since PSR B1931+24 is only visible for 20% of the time, we can readily estimate that there should be at least five times as many similar objects. We believe this number may be severely underestimated. It is important to establish how many similar objects exist, and what the related timescales of their non-emitting state are. An even more extreme class of intermittent neutron stars are the so-called rotating radio transients (RRATs; [47]) which are reviewed by Mclaughlin in this volume.

1.4 Techniques to Account for Observational Selection

Although the source-counting trick mentioned in Sect. 1.2 gives us an idea of the size of the underlying population, to make further inroads, we really need to make full use of all available data. From an observationally-biased sample, we seek to characterize the underlying population accounting for the aforementioned selection effects. For a given survey of integration time, τ, and bandwidth, $\Delta\nu$, the quantity

$$S_{\rm min} \sim \frac{T_{\rm sys}}{G}\sqrt{\frac{W/P}{\Delta\nu\tau}} \tag{1.1}$$

is the limiting sensitivity to pulsars of a certain period, P, and post-detection pulse width, W, given an antenna with gain, G, and system temperature, $T_{\rm sys}$. In practice, survey thresholds vary as a function of sky position and pulsar parameters. The problem is best tackled using a Monte Carlo approach which attempts to model these subtleties. Below we outline two contrasting techniques to make inferences about the underlying population.

1.4.1 Population Inversion Techniques

The first method, originally developed by Large [33], is of particular interest to determine the spatial distribution of the parent population. Given the observed distribution $N(P,z,R,L)$ in terms of period, P, distance from the Galactic plane, z, Galactocentric radius, R, and luminosity, L, we may write

$$\mathrm{d}N(P,z,R,L) = V(P,z,R,L)\,\rho(P,z,R,L)\,\mathrm{d}P\,\mathrm{d}z\,\mathrm{d}R\,\mathrm{d}L, \tag{1.2}$$

where V is the volume of the Galaxy effectively searched and ρ is the underlying (true) distribution of the population. Since we know N and can estimate V on the

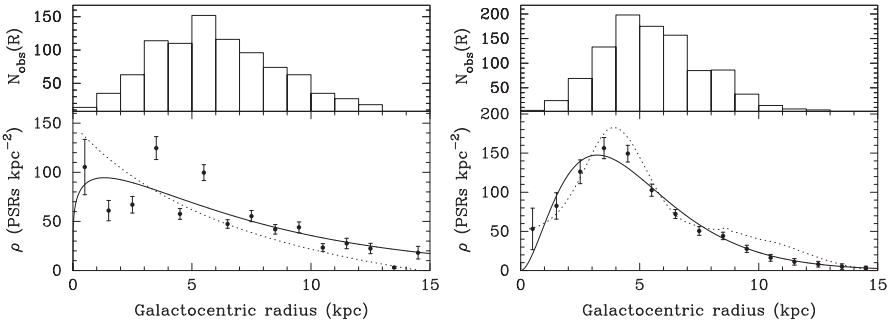

Fig. 1.5 *Left*: the observed radial distribution (*top panel*) and corrected Galactic radial density function $\rho(R)$ (*lower panel*) derived using the electron density model derived by Lyne, Manchester and Taylor [42]. *Right*: the observed and corrected density functions derived using the [15] model. In both cases, the *dotted curves* show the assumed form of the radial distribution used, while the *solid lines* shows a fit to the corrected distribution (after [38])

basis of pulsar survey sensitivities,[1] we can invert (1.2) to solve for ρ. The only simplification required to do this is to assume that P, z, R and L are independent quantities. Fortunately, apart from a very weak coupling between P and z, there are no significant relationships between any of these parameters. The problem then reduces to four equations which can be solved for the underlying distributions: $\rho_P(P)$, $\rho_z(z)$, $\rho_R(R)$ and $\rho_L(L)$.

Of particular interest is ρ_R, the underlying radial pulsar density. For many years, the standard reference for ρ_R was Lyne, Manchester and Taylor [42]. Their results were approximated in most subsequent work using a Gaussian distribution for ρ_R (e.g. [49]). However, as can bee seen from Fig. 4 of their paper, the form of ρ_R at small R is poorly constrained [6] and there is no reason to prefer a Gaussian over a function which tends to zero at small R. Using the results of the Parkes multi-beam survey, which has discovered many more pulsars in the inner Galaxy, [38] revisited this question and their results are shown in Fig. 1.5. They found that the underlying form of any radial distribution derived from the current sample is closely coupled to the assumed distribution free electrons assumed to calculate pulsar distances. Further progress on the radial density distribution of pulsars requires independent distance estimates for more pulsars in the inner Galactic quadrants. Another possibility worth exploring would be to treat the electron density distribution as a free parameter in future studies.

1.4.2 Monte Carlo Population Synthesis

The above technique can be regarded as a "snap-shot" approach to the problem. It makes no attempt to incorporate time-dependent effects such as period and

[1] For any given pulsar with luminosity L and survey with sensitivity $S_{\rm min}$ defined in equation (1), $V = (L/S_{\rm min})^{3/2}$. This needs to be computed over the whole sky for various survey thresholds using a Monte Carlo simulation.

luminosity evolution, which may be significant. By far the most common means to investigate the pulsar population has been via full-blown population syntheses which attempt to follow the birth, life and death of pulsars and the survey detection thresholds. The main problem with this approach is in reconciling the many assumptions necessary in such a simulation. Indeed, many of the details of the model (e.g. magnetic field evolution) are virtually a matter of personal taste and different authors have different preferences on what principles to adopt. In one of the most recent approaches of this type, [18] have detailed a comprehensive approach to this problem and describe a model which appears to mimic many of the observed population characteristics.

Following an earlier review of pulsar statistics [48], we can summarize the essential ingredients of a population synthesis by the following pseudocode. For each model pulsar, we need to:

1. Generate an initial position in the model galaxy based on some assumed R and z distributions and assuming either axisymmetry or spiral arm structure
2. Generate an initial 3-D velocity with respect to the local standard of rest
3. Generate an age from a flat distribution out to some maximum time, $T_{\max}$
4. Generate a birth spin period and magnetic field from some preferred distribution functions
5. Solve the equation of motion in a model for the galactic gravitational potential to compute the current position and velocity
6. Solve a model for the pulsar spin evolution to compute the current period and period derivative
7. Generate a pulse width from some radiation beam model and determine whether the pulsar is observable from the Earth
8. If the pulsar is observable, generate a luminosity using some simple model $\left(\text{e.g. } L \propto f(P,\dot{P})\right)$ and hence compute the flux observed from the Earth
9. Decide, based on models for major pulsar surveys, whether this pulsar is detectable

This sequence would then be carried out for N_{model} model pulsars, where the resulting model birth rate is $N_{\text{model}}/T_{\max}$. By comparing the resulting model detectable pulsars with the observed sample, it is possible to optimize the model parameters and investigate the results of different assumptions. For further discussion on the philosophy of this approach, the interested reader is referred to [18].

1.5 Outstanding Problems

In view of the difficulties in correcting for these selection effects, and the inherent problem of small-number statistics, many controversies have pervaded pulsar statistics over the years. I review here a personal selection of some of the many unsolved topics. My apologies to those who have, to their satisfaction, already solved these problems!

1.5.1 Population Size and Birth Rate

How many radio-active pulsars are in our Galaxy and its globular cluster systems? What is the birth rate of normal and millisecond pulsars? How do they compare to their proposed progenitor populations? What fraction of neutron stars are born as radio pulsars? These are perhaps the most fundamental of all questions in this field, yet a satisfactory answer to them is still not known. A combination of small-number statistics, uncertain assumptions about the beaming fraction and errors in the pulsar distance scale (which carry over to the luminosity function) have conspired to produce a wide range of estimates ranging by four orders of magnitude from 10 pulsars per century (e.g. [63]) to 0.001 pulsars per century [2] for the normal population.[2]

A recent birth rate calculation was carried out by [68] using a sample of 815 normal pulsars from the Parkes multi-beam survey. By analysing the flow or "current" of pulsars across the P–$\dot{P}$ diagram [52, 67], the total birthrate of the population was found to lie between 1–2 pulsars per century for 1,400-MHz luminosities above 1 mJy kpc^2. Dividing the population into groups according to magnetic field strength, Vranesevic et al. found that over half of the total birthrate is contributed by pulsars with fields $>2.5 \times 10^{12}$ G. This is in spite of the fact that such pulsars make up less than 30% of the observed sample and, based on their scale factors, only about 5–10% of the total population.

The main problem with birth rates determined from pulsar current analyses is that they are inherently lower limits, since they do not account for pulsars with luminosities below the sample limit (1 mJy kpc^2 in the above case). The all-encompassing nature of the Monte Carlo approach is not subject to such limits and provides an estimate of the true birth rate of the population. The most recent analysis of this kind [18] finds the birth rate in their optimal model to be 2.8 ± 0.1 pulsars per century. However, as noted by these authors, the true uncertainty in this number is likely to be larger by a factor of 5 when accounting for the various model assumptions and plausible input parameter ranges.

While the birth rate of millisecond pulsars is significantly smaller than for normal pulsars (e.g. [44]), it is not clear whether their proposed progenitors, the low-mass X-ray binaries, can account for the whole population. This latter issue is the well publicized "millisecond pulsar birth rate problem" [29]. More recent studies, using a larger sample of objects, have shown that the discrepancy was most likely due to small-number statistics. The current consensus, for the Galactic disk population, is that the millisecond pulsar population is consistent with the low-mass X-ray binaries [44].

[2] I have taken extreme values from the literature to make the point here. See the caveats made in both the cited papers before taking these numbers too literally!

1.5.2 The Birth Spin Periods of Pulsars

The initial spin period distribution of pulsars has been the topic of much debate. Although earlier studies found the data to be consistent with all pulsars being born with short periods ($\sim$20 ms; e.g. [42]), other authors find evidence for a broader distribution (e.g. [67]). The latter authors used a pulsar current analysis and found evidence for a step function at $P = 0.5$ s in their distribution of pulsar current. This was claimed as evidence for an "injection" of pulsars into the population with $P \sim 0.5$ s. Subsequent studies have either confirmed (e.g. [49]) or refuted these claims (e.g. [35]). In the recent pulsar current analysis of [68], the observed distribution of pulsar current is consistent with up to 40% of all pulsars being born with periods in the range 0.1–0.5 s. Similar results were found by [38] using a slightly larger sample.

1.5.3 Period Evolution and Field Decay of Isolated Pulsars

The classic model for spin-down of an isolated pulsar is to write the braking torque as a generalized power law. For an angular velocity $\Omega = 2\pi/P$, the equation of motion is given by $\dot{\Omega} = K\Omega^n$, where K is proportional to the braking torque and n is the so-called braking index. For a constant value of K and pure magnetic dipole braking $n = 3$, the equation of motion on the P–$\dot{P}$ diagram is such that pulsars follow a slope of -1 in a log–log plot like Fig. 1.2, i.e. along the lines of constant dipole magnetic field.

The dipolar braking hypothesis can be tested for a handful of young pulsars, where timing measurements provide n. So far, all six measured values of n are consistent with a flat distribution in the range 1.4–2.9. In other words, all of the pulsars with measured values of n are moving along lines with slopes greater than -1 on the P–$\dot{P}$ diagram. When these vectors are plotted (see, for example [40]) one sees that the directions these young pulsars are moving would place them above the pulsar island! So the conundrum is, either the pulsars in the island have a different set of progenitors than the young objects, or there is some evolution in the braking index as a function of time.

The evolution in braking index can either be provided by integrating the equation of motion assuming that n is genuinely a function of time, or that K decays with time. In all simulations of the P–$\dot{P}$ plane that I am aware of to date, the shape of the diagram is reproduced by modeling the evolution of K with time. Excellent fits to the observed diagrams (see, for example, Fig. 8 in [20] can be obtained by decay laws of the form $K(t) \propto \exp(-t/t_D)$ for decay times t_D of a few million years. This is usually interpreted as exponential decay of the magnetic moment of the neutron star on a timescale of a few million years. While earlier versions of these simulations were criticized [66] as not taking into account period dependent beaming, the work of [20] does, I believe, account for this effect and still prefers a short magnetic field decay time. Recently, [14] have proposed a new model for pulsar spin-down

where the inclination angle between the spin and magnetic axes of the neutron star are taken into account. This model seems to explain the P–$\dot{P}$ distribution and the observed braking indices and appears to be very promising. Further investigation of this model are required.

Despite the good agreement on the P–$\dot{P}$ plane, there are a number of vexing issues: (a) spontaneous decay of the magnetic field on such short timescales is inconsistent with the observations of millisecond pulsars which have Gyr ages and yet field strengths at the level of 10^8 G; (b) the exponential model is inconsistent with all braking index measurements, since it always predicts an effective $n \geq 3$; (c) in principle, the same behaviour could be reproduced by modeling the evolution of n rather than field decay; (d) what is the ultimate fate of low-braking-index pulsars? For example, the Vela pulsar has $n = 1.4$ [43] and is moving towards the magnetars on the P–$\dot{P}$ diagram, rather than the pulsar island. Lyne [40] proposed that such objects might be the progenitors of the magnetars. This idea requires further investigation.

1.5.4 Statistical Puzzles in the Millisecond Pulsar Population

Twenty-five years after the discovery of the first millisecond pulsar [4], the sample of these objects currently known is now close to 200, with the majority being found in searches of globular clusters (for a review, see [12]). While searches in clusters are far from straightforward, finding millisecond pulsars in the Galactic disk is a difficult endeavor due to the dispersive and scattering effects of the interstellar medium which hamper their detection. Indeed, only 55 out of roughly 1,500 pulsars (4%) currently known in the Galactic disk are millisecond pulsars. Despite this low fraction, the numbers are now at the level where statistically significant trends can be identified in the sample and inferences made about the underlying population.

One such example is the apparent difference in luminosities between isolated and binary millisecond pulsars, first noted by Bailes et al. [7] from 430-MHz observations, in which isolated millisecond pulsars were on average fainter than their binary counterparts; this trend was also seen by [27] in 1,400-MHz data. More recently [34] revisited this issue from a different perspective. They found that, while the velocity distribution of the isolated millisecond pulsars is compatible with that of binary systems, there appears to be a difference in the distribution of heights above the Galactic plane for the two populations, with solitary millisecond pulsars being more tightly clustered than the binary systems. As discussed by Lommen et al., given identical velocity dispersions, the only way to explain the different scale heights would be if the isolated millisecond pulsars are truly fainter on average and therefore easier to detect closer to the Earth and hence closer to the Galactic plane. If the luminosity difference is a real effect, then it represents an important clue to the origin of millisecond pulsars.

Lorimer et al. [39] have recently revisited this issue using an updated sample of millisecond pulsars. While they confirm the effect seen by Bailes et al. [7] from

samples of pulsars selected by 430-MHz surveys, the same trend is not apparent in surveys carried out at 1,400 MHz. There are two possible explanations as to why the luminosity difference is not seen in both the 430-MHz and 1,400-MHz samples. The first possibility is that the high-frequency sample does not probe the luminosity function as deeply as the low-frequency sample. From the current data, it remains a tantalizing possibility that the effect is only seen in the 430-MHz sample which is more sensitive to the low end of the luminosity function than at 1,400 MHz.

A second possibility is that the difference is due to a selection effect. It is well established [44] that 430-MHz surveys probe only the local population of millisecond pulsars out to a distance of 2–3 kpc at most due to propagation effects in the interstellar medium. As a result, samples of pulsars from these surveys tend to be stacked in favour of nearby low-luminosity objects. For any reasonable luminosity function, the high-luminosity pulsars are rarer objects. If isolated millisecond pulsars are simply less numerous than their binary counterparts, small-number statistics will therefore bias the sample in favour of low luminosity objects as there is a greater chance of having a low-luminosity pulsar in the sample compared to a higher luminosity one.

Through simulations, Lorimer et al. [39] confirm that this effect could play a significant role in the observed sample. When averaged over many simulations, the median 430-MHz luminosity of the sample with 10 pulsars was 20% lower than the larger sample. Based on the currently available data, they conclude that there is no requirement for the isolated pulsars to have different spatial, kinematic or luminosity distributions than binary millisecond pulsars. It remains a mystery, however, as to whether isolated millisecond pulsars formed through a different underlying process.

A related issue concerns the origin of the 6.2-ms pulsar B1257+12, the only pulsar planetary system known in the Galactic disk [71] and is something of an anomaly among the millisecond pulsar population. The three planets (A, B and C) in the system known so far have orbital periods of 25, 67 and 98 days with masses of 0.02, 4.3 and 3.9 Earth masses respectively [26]. The one other planetary system known, PSR B1620–26, in the globular cluster M4 could have formed through exchange interactions in the cluster [60]. However, such interactions are not expected in the Galactic disk. Did the planets in the form from a debris disk of circum-pulsar material? Why are planets not seen around other Galactic millisecond pulsars? Although small planets such as A in the 1257 system could be undetectable in some millisecond pulsar timing (e.g. [39]), the signals from higher mass planets such as B and C would be unmistakable in timing residuals. Based on the current sample, the fraction of millisecond pulsars with planets appears to be less than $1/55 \sim 2\%$.

1.5.5 Where Are All the Isolated "Recycled" Pulsars?

The discovery of new pulsars often sheds light on previously unseen areas of the neutron star "zoo" which likely represent quite rare evolutionary processes. One example is the discovery of two isolated pulsars J2235+1506 [13] and J0609+2130

[36] with spin properties similar to the double neutron star binaries. Camilo et al. suggested that J2235+1506 might be the remains of a high-mass binary system that disrupted during the second supernova explosion.

Is this hypothesis consistent with the observations? One way to test this is to consider the fraction, η, of binary systems that remain bound after the second supernova explosion. Numerous authors have followed the orbital evolution of a wide variety of binary systems containing neutron stars using detailed Monte Carlo simulations. For example, [53] find $\eta \sim 4\%$. We therefore expect for each double neutron star system we observe to find of order 20 systems which disrupted. Currently we know of eight double neutron star binaries. Why, then, do we not see of order 160 pulsars like J0609+2130 or J2235+1506? [5] suggests that this could be reconciled if the kick velocities to the neutron stars in these systems are not as high as the bulk of the population. This currently outstanding problem may indicate a different evolutionary scenario for these objects and warrants further study.

1.5.6 How Much Do We Understand About Globular Cluster Pulsars?

Following the early globular cluster discoveries, a detailed analysis by [30] characterized the population properties of globular cluster pulsars and found their total active population to be $\sim 10^4$. Such a large population appeared to be far higher than could be explained by low-mass X-ray binaries alone and suggested that there is an even greater birthrate problem in cluster millisecond pulsars than in the Galactic disk. Unlike the disk population, the problem has so far not been resolved; this may be a selection effect – to my knowledge, the work of Kulkarni et al. has not been superceded.

With the recent renaissance in globular cluster discoveries reviewed [12], the population of pulsars known in clusters has undergone a four-fold increase. Although some care will be necessary to model the effects of interstellar scintillation and Doppler smearing due to rapid orbital motion, two selection effects which are very important in globular cluster surveys, there is clearly now much to be learned from a systematic study of the latest results. Some key questions are: what is the number and birth rate of cluster pulsars? what conditions (if any) are necessary for pulsar production in clusters? how many relativistic binaries are there in clusters, and what impact do these systems have on the cosmic rate of binary inspiral?

1.6 Concluding Remarks

Pulsar astronomy is currently enjoying the most productive phase of its history, with applications providing a wealth of new information about compact-object astrophysics, general relativity, the Galactic magnetic field, the interstellar medium,

binary evolution, planetary physics and even cosmology. Our understanding of the Galactic pulsar population has improved dramatically thanks largely to the success of the Parkes multi-beam survey [46]. Astronomers are currently active in a number of new surveys which will bring significant advances in sensitivity.

At Parkes, a multi-beam survey at 6 GHz is currently underway covering the inner Galaxy for highly dispersed and scattered pulsars. A 1.4-GHz multi-beam survey now underway at Arecibo should discover over 300 normal pulsars [38]. To date, around 40 pulsars have been found [16] with the most exciting object so far being the highly relativistic binary PSR J1906+0746 [37]. The superior period sensitivity of ALFA over other surveys at Parkes suggest that a substantial number of millisecond pulsars will also be found. Searches with the 100-m Green Bank telescope (GBT) are currently focusing on globular clusters, where 56 pulsars have so far been found – about half of all currently known cluster pulsars! Plans are also afoot, however, to survey the sky at 350 MHz with the GBT. Following earlier pilot studies (Hessels, Ransom et al., private communication) which discovered several new pulsars, drift-scan surveys will commence in summer 2007 with the aim of covering much of the sky in the coming 5 yr. Simulations we have carried out suggest that of order 100 millisecond pulsars could be discovered by the GBT.

In the Netherlands, a 328-MHz pulsar survey is being carried out in a "grating array" mode using the Westerborg synthesis radio telescope [58] in which multiple sub-beams are formed within the large primary beam of the array. So far a number of pulsars have been found and under investigation. The multi-beaming concept is likely to be technology used here is likely to be exploited further with the planned Low Frequency Array (LOFAR; `lofar.org`) which is expected to find of order 1,500 pulsars in surveys carried out at frequencies at or below 200 MHz [61]. LOFAR would be a fantastic probe of the local pulsar population and provide vital new constraints on the low end of the shape of the luminosity function.

These and other up and coming surveys are only a precursor for what might be possible with the Square Kilometer Array (SKA), an ambitious world-wide collaboration currently planned for the year 2020 (see `skatelescope.org`). Simulations for pulsar surveys with this instrument demonstrate that the increase in sensitivity of the SKA (around two orders of magnitude over current radio telescopes!) would mean that essentially every Galactic pulsar beaming towards us (of order 30,000 objects!) could be detectable. Perhaps by the year 2030, the sample of radio pulsars will be finally free of selection effects.

An Open Approach to Pulsar Population Syntheses

The Monte Carlo techniques used in Sect. 1.4 have been implemented by a number of authors over the years. As mentioned in Sect. 1.5, there are examples of similar modeling treatments reaching different conclusions. Indeed, Andy Fruchter once applied Benjamin Disrali's famous quote to this field, saying that "there are lies, damned lies and pulsar statistics". Although perhaps a little facetious,

the point here is that, when trying to make sense of the pulsar population, it is sometimes hard to know who/what to believe! In an attempt to clarify this issue, I have placed my population modeling software, `psrpop` in the public domain (`psrpop.sourceforge.net`) and strongly encourage others to do so. The current version of `psrpop` can be used to carry out a population inversion analysis and search pulsar populations for arbitrary survey parameters. A full-blown Monte Carlo model of pulsar evolution a la [18] is now under development.

References

1. Arzoumanian, Z., Cordes, J. M. & Wasserman, I., 1999, ApJ, 520, 696
2. Arzoumanian, Z., Chernoff, D. F. & Cordes, J. M., 2002, ApJ, 568, 289
3. Backer D. C., 1970, Nature, 228, 42
4. Backer D. C. et al., 1982, Nature, 300, 615
5. Bailes M., astro-ph/0702698
6. Bailes M. & Kniffen, D. A., 1992, ApJ, 391, 659
7. Bailes M. et al., 1997, ApJ, 481, 386
8. Bhattacharya, D. & van den Heuvel, E. P. J., 1991, Phys. Rep., 203, 1
9. Biggs J. D., 1990, MNRAS, 245, 514
10. Bisnovatyi-Kogan, G. S. & Komberg, B. V., 1974, Sov. Astron., 18, 217
11. Burgay, M. et al., 2003, Nature, 426, 531
12. Camilo, F. & Rasio, F., 2005, In: Rasio & Stairs (eds) Binary and millisecond pulsars, ASP Conference Series, Vol. 328, 147
13. Camilo, F. et al., 1993, ApJ, 412, 37L
14. Contopoulos, I. & Spitkovsky, A., 2006, ApJ, 643, 1139
15. Cordes, J. M. & Lazio, T. J. W., 2002, astro-ph/0207156
16. Cordes, J. M. et al., 2006, ApJ, 637, 446
17. Damashek, M., Taylor, J. H. & Hulse, R. A., 1978, MNRAS, 225, L31
18. Faucher-Giguère, C. A. & Kaspi, V. M., 2006, ApJ, 643, 332
19. Ghosh, P. & Lamb, F. K., 1979, ApJ, 234, 296
20. Gonthier, P. L., Van Guilder, R. & Harding, A. K., 2004, ApJ, 604, 775
21. Gunn, J. E. & Ostriker, J. P., 1970, ApJ, 160, 979
22. Hewish, A. et al., 1968, Nature, 217, 709
23. Hobbs, G. et al., 2006, MNRAS, 360, 974
24. Iben, I. J. & Tutukov, A. V., 1996, ApJ, 456, 738
25. Janka, H.-T., Scheck, L., Kifonidis, K., Müller, E. & Plewa, T., 2005, ASP Conf. Ser. 332: The Fate of the Most Massive Stars, 332, 363
26. Konacki, M. & Wolszczan, A., 2003, ApJ, 591, 147
27. Kramer, M. et al., 1998, ApJ, 501, 270
28. Kramer, M. et al., 2006, Science, 312, 549
29. Kulkarni, S. R. & Narayan, R., 1988, ApJ, 335, 755
30. Kulkarni, S. R. et al., 1990, ApJ, 356, 174
31. Kundt, W., 1992, In: Hankins, Rankin & Gil (eds) IAU Colloquium 128. Pedagogical University Press, Zielona Gora, Poland, p. 86
32. Lamb, F. K. & Yu, W., 2005, In: Rasio & Stairs (eds) Binary and millisecond pulsars, ASP Conference Series, Vol. 328, 299
33. Large, M. I., 1971, IAU Symp. No. 46, Dordrecht, Reidel, p. 165
34. Lommen, A. N. et al., 2006, ApJ, 642, 1012
35. Lorimer, D. R., 1993, MNRAS, 263, 403
36. Lorimer, D. R. et al., 2004, MNRAS, 347, L21

37. Lorimer, D. R. et al., 2006, ApJ, 640, 428
38. Lorimer, D. R. et al., 2006, MNRAS, 372, 777
39. Lorimer, D. R. et al., 2007, MNRAS, 375, 282
40. Lyne, A. G., 2004, In: Camilo & Gaensler (eds) IAU Symp. 218, PASP, 257
41. Lyne, A. G. & Manchester, R. N., 1988, MNRAS, 234, 477
42. Lyne, A. G., Manchester, R. N. & Taylor J. H., 1985, MNRAS, 213, 613
43. Lyne, A. G. et al., 1996, Nature, 381, 497
44. Lyne, A. G. et al., 1998, MNRAS, 295, 743
45. Lyne, A. G. et al., 2004, Science, 381, 303
46. Manchester, R. N. et al., 2001, MNRAS, 328, 17
47. McLaughlin, M. A. et al., 2006, Nature, 439, 817
48. Michel, F. C., 1991, Theory of neutron star magnetospheres, University of Chicago Press, Chicago
49. Narayan, R., 1987, ApJ, 319, 162
50. Narayan, R. & Vivekanand, M., 1983, A&A, 122, 45
51. Nice, D. J., 1999, ApJ, 513, 927
52. Phinney, E. S. & Blandford, R. D., 1981, MNRAS, 194, 137
53. Portegies Zwart, S. F., Yungelson, L. R., 1998, A&A, 332, 173
54. Radhakrishnan, V. & Shukre, C. S., 1985, In: Srinivasan, G. & Radhakrishnan, V. (eds) Supernovae, their progenitors and remnants, p. 155, Indian Academy of Sciences, Bangalore
55. Ratnatunga, K. U. & van den Bergh, S., 1989, ApJ, 343, 713
56. Rickett, B. J., 1970, MNRAS, 150, 67
57. Ritchings, R. T., 1976, MNRAS, 176, 249
58. Rubio-Herrera, E. et al., 2006, In: Becker & Huang (eds) Proceedings of the 363 WE-Heraeus Seminar on “Neutron stars and pulsars”, 56 (astro-ph/0701183)
59. Sayer, R. W., Nice, D. J. & Taylor J. H., 1997, ApJ, 474, 426
60. Sigurdsson, S. et al., 2003, Science, 301, 193
61. Stappers, B. W. et al., 2006, In: Becker & Huang (eds) Proceedings of the 363 WE-Heraeus Seminar on “Neutron stars and pulsars”, 100 (astro-ph/0701229)
62. Tauris, T. M. & Bailes M., 1996, A&A, 315, 432
63. Taylor, J. H. & Manchester, R. N., 1977, ApJ, 215, 885
64. Tauris, T. M. & Manchester, R. N., 1998, MNRAS, 298, 625
65. van Kerkwijk, M. H., 1996, In: Johnston, Walker & Bailes (eds) IAU Colloquium 160, p. 489
66. van Leeuwen, J., 2004, PhD Thesis, Utrecht University
67. Vivekanand, M. & Narayan, R., 1981, JA&A, 2, 315
68. Vranesevic, N. et al., 2004, ApJ, 617, L139
69. Wang, N., Manchester, R. N. & Johnston, S., 2007, MNRAS, (astro-ph/0703241)
70. Weisberg, J. M., 1996, In: Johnston, Walker & Bailes (eds) IAU Colloquium 160, p. 47
71. Wolszczan, A. & Frail, D. A., 1992, Nature, 355, 145

Chapter 2
Radio Emission Properties of Pulsars

Richard N. Manchester

2.1 Introduction

Pulsars are fascinating objects with a wide range of applications in physics and astronomy. Characterised observationally by a highly periodic pulse train with periodicities typically in the range a few milliseconds to several seconds, they are generally identified with highly magnetised and rapidly rotating neutron stars formed in supernova explosions. Rotation of the star causes beamed emission, probably emanating from open field lines associated with the magnetic poles, to sweep across the sky generating one observed pulse per rotation period. A total of 1,765 pulsars are now known and almost all of these lie within our Galaxy.[1] As Fig. 2.1 illustrates, pulsars come in two main classes, those with periods in the millisecond range and the so-called "normal" pulsars with periods of order 1 s. Most millisecond pulsars (MSPs) are binary, that is, in an orbit with another star, whereas only a few percent of normal pulsars are binary. MSPs, which comprise about 10% of the known population, are believed to be relatively old pulsars which have been spun up or "recycled" by accretion from a binary companion [3]. Because of exchange interactions occurring in their dense cores, globular clusters are a fertile breeding ground for MSPs [10] and about three-quarters of the known MSPs are associated with these clusters.

Pulsar periods are extremely stable but they are not constant. All pulsars are slowing down because of loss of rotational kinetic energy to some combination of magnetic-dipole radiation (electro-magnetic waves at the pulsar spin frequency) and relativistic particle outflow. The spin-down rate can be expressed as

$$\dot{\nu} = -K\nu^n \,, \tag{2.1}$$

R.N. Manchester
Australia Telescope National Facility, CSIRO, P.O. Box 76, Epping, NSW 1710, Australia
e-mail: dick.manchester@csiro.au

[1] Pulsar parameters used in this paper have been obtained from the ATNF Pulsar Catalogue, Version 1.29, http://www.atnf.csiro.au/research/pulsar/psrcat [44].

W. Becker (ed.), *Neutron Stars and Pulsars,* Astrophysics and Space Science Library 357,

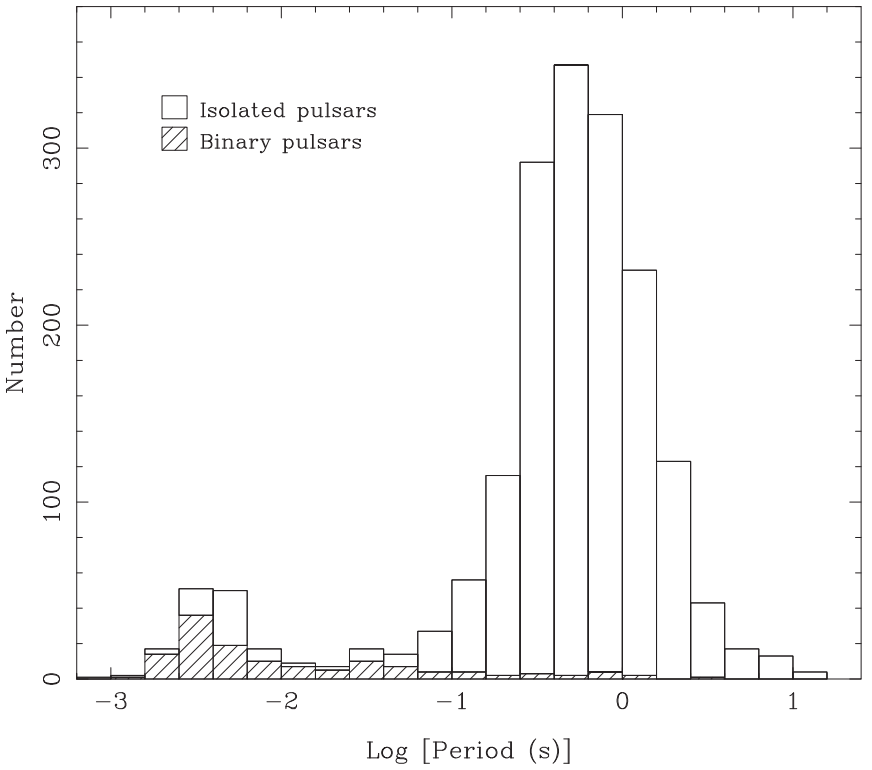

Fig. 2.1 Histogram of observed pulsar periods. Pulsars which are members of a binary system are identified

where K depends on the magnetic field strength at the stellar surface, B_s, and the neutron-star moment of inertia, I, and n is the braking index. For pure magnetic-dipole braking, $n = 3$ and

$$K = \frac{8\pi^2 B_s^2 R^6 \sin^2\alpha}{3Ic^3}\,, \tag{2.2}$$

where α is the inclination angle of the dipole magnetic axis relative to the spin axis.

We can define a "characteristic age" for the pulsar $\tau_c = P/(2\dot{P})$, where $P = 1/\nu$ is the pulsar period and $\dot{P}$ is its first time derivative. If the pulsar was born with a period much less than the present value and its spin-down is characterized by a braking index close to 3.0, then the characteristic age is a good indicator of the true age. We can also estimate the strength of the dipole field at the neutron-star surface, $B_s = 3.2 \times 10^{19}(P\dot{P})^{1/2}$ G, where $n = 3$, $I = 10^{45}$ g cm^2 and $\alpha = 90^\circ$ have been assumed.

Figure 2.2 shows the observed distribution of pulsars on the P–$\dot{P}$ plane. MSPs have very low spin-down rates and hence relatively weak magnetic fields compared to normal pulsars. In contrast, Anomalous X-ray Pulsars (AXPs)[2] lie in the upper

[2] Soft Gamma-ray Repeaters (SGRs) with coherent pulsations are included in the AXP classification.

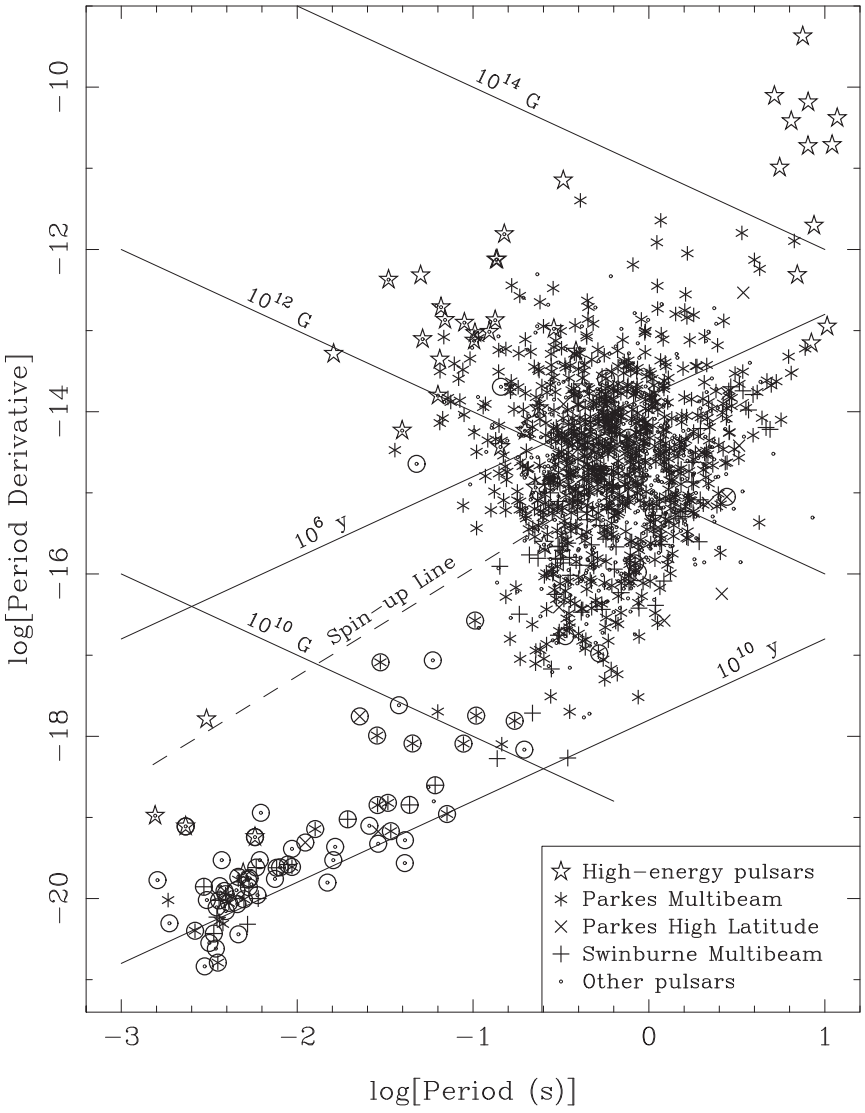

Fig. 2.2 Distribution of pulsars versus pulse period and period derivative. Pulsars which have detectable pulsed emission at high energies (optical, X-ray and γ-ray), including the so-called Anomalous X-ray Pulsars (AXPs), are indicated. Lines of constant characteristic age and surface dipole magnetic field are shown, along with the "spin-up line", the minimum period attainable through accretion from a binary companion. Pulsars discovered in the principal recent pulsar surveys are indicated

right corner of the P–$\dot{P}$ diagram with periods in the range 5–12 s and very strong implied magnetic fields in the range 10^{14}–10^{15} G. Despite their rapid spin-down, the X-ray luminosity of these "magnetars" is too great to be powered by the rotational energy loss; decay of the super-strong magnetic fields is believed to be the energy

source [11]. Young pulsars lie predominantly in the upper left part of the diagram with magnetic fields of order 10^{12} G. For $n = 3$, these pulsars will evolve along lines of constant magnetic field into the region occupied by the bulk of the known pulsar population. Lying between the MSPs and the tail of the normal pulsar distribution, there is an important group of group of binary pulsars. These systems are characterized by relatively massive companions and include all of the known double-neutron-star systems. Because of the rapid evolution of the binary companion, the recycling phase was relatively short-lived in these systems and so these pulsars typically have intermediate periods in the range 20–100 ms.

More than half of the known pulsars have been discovered in the past few years, most notably using the 20-cm multi-beam receiver on the Parkes 64-m radio telescope in NSW, Australia. The main surveys undertaken with this system are described in Sect. 2.2 and other recent surveys using the 300-m Arecibo radio telescope and the 100-m Green Bank Telescope are described in Sect. 2.3. In the remainder of the review, some interesting recent results related to the pulsar emission mechanism are described – no claim to completeness is made. Recent results on pulse nulling and mode changing are described in Sect. 2.4. Recent results on pulse-to-pulse modulations and subpulse drifting are discussed in Sects. 2.5 and 2.6 describes recent observations of "giant" pulses and their implications. The extraordinary detection of transient radio emission from the magnetar XTE J1810-197 (PSR J1809−1943) is described in Sect. 2.7. Some recent results on the polarisation of young pulsars are described in Sect. 2.8. Some concluding remarks are given in Sect. 2.9.

2.2 Parkes Multi-Beam Pulsar Surveys

The Parkes 20-cm multi-beam receiver has 13 beams arranged in a double hexagon around a central beam and operates at a central frequency of 1,374 MHz [59]. The beams are spaced by two beam-widths on the sky but, by combining sets of four pointings, a given region of sky can be completely covered with beams overlapping at the half-power points. Each beam has two probes receiving orthogonal linear polarizations and, after amplification and down-conversion, each of the 26 signals is fed to a 96×3 MHz filterbank giving a total bandwidth of 288 MHz. Signals from corresponding polarizations are then detected, summed, high-pass filtered, one-bit digitized and recorded to magnetic tape for subsequent analysis.

A number of very successful pulsar surveys have been undertaken with this instrument. The most prolific is the Parkes Multibeam Pulsar Survey [45] which covered a 10°-wide strip along the southern Galactic plane from $l = 260°$ to $l = 50°$ using a sampling interval of 250 μs. The observation time per pointing was relatively long, 35 min, and so the survey was quite sensitive with a limiting flux density of approximately 0.2 mJy for longer-period pulsars unaffected by dispersion smearing within a filter channel. A total of 3,080 pointings was required to cover the survey area. Survey observations commenced in mid-1997 and were completed in 2003.

The data were processed on work-station clusters at ATNF, Jodrell Bank Observatory and McGill University resulting in the detection of 1,015 pulsars of which 760 were new discoveries. Following confirmation of each pulsar, at least 18 months of timing observations were carried out in order to obtain accurate astrometric and timing parameters (cf. Fig. 2.2). A series of papers [16, 23, 34, 38, 45, 49] gives details of all of the pulsars detected and discusses various implications of the results. For example, Kramer et al. [34] discuss the properties of young pulsars and show that about 20 of the known pulsar population are likely to be associated with currently unidentified gamma-ray sources.

The Parkes Multibeam Pulsar Survey database was also searched for isolated dispersed pulses, leading to the discovery of an apparently new class of pulsars, the so-called Rotating Radio Transients or RRATs. McLaughlin et al. [46] detected eleven of these objects which emit an individual strong pulse at intervals ranging from minutes to hours. Careful analysis of the pulse arrival times led to the identification of underlying periodicities in the range 0.4–6 s and, in three cases, to a full timing solution showing the steady period increase typical of pulsars. There is little doubt that RRATs are rotating neutron stars but considerable doubt as to whether they are normal, albeit highly modulated, pulsars near the end of their active life [68] or a distinct population with different birth properties.

A companion survey to the Parkes Multibeam Pulsar Survey, the Parkes High-Latitude Pulsar Survey, was carried out by the same group [5]. This survey covered the region $|b| < 60°$, $220° < l < 260°$ with a shorter sampling interval, 125 μs, and observation time, 4 min, to optimize sensitivity to MSPs and binary pulsars. Data processing for this survey was carried out on clusters at Bologna Astronomical Observatory, Cagliari Astronomical Observatory and Jodrell Bank Observatory. A total of 42 pulsars was detected and 18 of these were new discoveries. Four of the new discoveries are MSPs and three of these four are binary. They include the famous "double pulsar" PSR J0737−3039A/B, the first-known binary pulsar in which both stars are detectable as pulsars [4, 40].

Lorimer et al. [38] discuss the properties of the Galactic population of pulsars based on the results of these two surveys. Figure 2.3 shows the observed and derived distributions in Galactocentric radius and Galactic z-distance, and the derived luminosity function and initial period distribution along with fitted functions to these distributions for two different assumed distributions for the free electrons in the Galaxy – see Lorimer et al. [38] for details of the procedures and the fitted functions.

It is clear that the derived radial distributions (Fig. 2.3a) are strongly dependent on the assumed distribution of free electrons. In particular, the existence of a deficit in the population near the Galactic Centre is quite uncertain, depending entirely on the poorly known electron distribution in the central region. Integration of the derived radial distributions gives a total Galactic population of about 30,000 potentially detectable pulsars with luminosity above 0.1 mJy kpc^2. Assuming that pulsar emission is beamed according to the function derived by Tauris and Manchester [62], the total number of pulsars in the Galaxy with luminosity above 0.1 mJy kpc^2 is derived to be $148,000 \pm 6,000$ for the azimuthally symmetric Model S [41] and $155,000 \pm 6,000$ for the "clumpy" Model C [8].

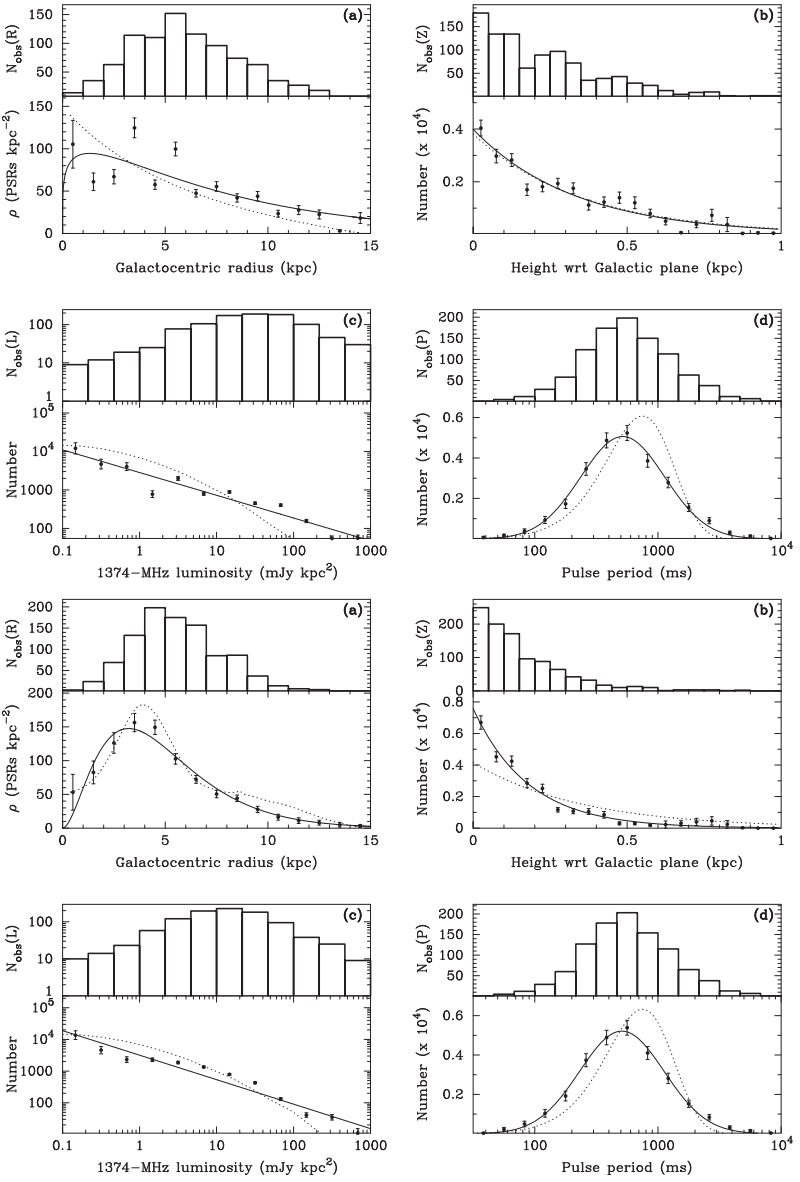

Fig. 2.3 Observed distributions in Galactocentric radius (**a**) and Galactic z-distance (**b**) from the Parkes Multibeam Pulsar Survey data (*upper panels*) and derived distributions for the Galactic pulsar population taking into account survey selection effects (*lower panels*). The *solid lines* are a fit of suitable functions to the derived distributions. The observed and derived luminosity functions are shown in plot (**c**) and the distributions of initial (birth) spin period are given in plot (**d**). Two models for the Galactic free electron distribution are considered, the azimuthally symmetric model of Lyne, Manchester and Taylor [41] (Model S, upper group of four plots) and that of Cordes and Lazio [8] (Model C, lower group of four plots). The *dotted curves* show (**a**) the assumed free electron distribution, (**b**) an exponential distribution of scale height 350 pc, (**c**) the log-normal luminosity function derived by Faucher-Giguère and Kaspi [15] and (**d**) an initial-period distribution used by Kolonko et al. [32]

The derived z distributions are also very dependent on the assumed electron density distributions, with a scale height of about 330 pc for Model S and 180 pc for Model C. Independent studies of the z distribution [47] and the observed distribution of pulsars detected in the Parkes High-Latitude Pulsar Survey [5] are more consistent with the larger scale height.

The derived luminosity function is well fitted by a simple power law but its slope of -0.6 (Model S) or -0.8 (Model C) is flatter than that obtained from earlier studies. The derived initial period distribution is well fitted by a log-normal distribution peaking at about 500 ms. A pulsar current analysis gives a birthrate of 0.34 ± 0.05 per century for potentially detectable pulsars with luminosity greater than 0.1 mJy kpc^2 in the Galaxy. With beaming taken into account, the derived birthrate is approximately 1.3 pulsars per century, depending on the beaming model assumed.

A group based at Swinburne University of Technology used the Parkes multibeam system to search Galactic latitudes between 5° and 30° with the same longitude range as the Parkes Multibeam Pulsar Survey. Like the Parkes High-Latitude Pulsar Survey, the Swinburne survey used a faster sampling interval and shorter observation time to give improved sensitivity for millisecond and binary pulsars [13,25]. The survey detected 230 pulsars of which 95 were new discoveries. Notable amongst them was PSR J1909−3744 , a 2.5-ms pulsar in a 1.5-day orbit with a very narrow pulse, only 42 μs wide at the half-power point [26]. This leads to very precise pulse timing which has enabled an accurate parallax measurement (implied distance 1.14 ± 0.04 kpc) and an accurate measurement of the Shapiro delay, leading to a value for the pulsar mass of 1.438 ± 0.024 M$_\odot$ [27].

Another recent survey undertaken with the Parkes multi-beam receiver is a deep search for pulsars in the Magellanic Clouds [43]. Observation times were 2.3 h per pointing giving a limiting mean flux density for isolated or long-period binary pulsars of 0.12 mJy. The survey required 73 pointings for the Small Magellanic Cloud and 136 pointings for the Large Magellanic Cloud. A total of 14 pulsars was discovered, 12 of which are believed to lie in the Magellanic Clouds. These discoveries bring the total number of pulsars known in the Clouds to 20. Only the high end of the luminosity function is sampled, but the derived values are consistent with the luminosity function for Galactic pulsars. Although the sample is relatively small, there was no evidence for a significant dependence of radio luminosity on either pulsar period or characteristic age.

2.3 Other Recent Surveys

Initial results from a pulsar survey using the Arecibo L-band Feed Array (ALFA) system have been reported by Cordes et al. [7]. The ALFA system has seven beams with a bandwidth of 300 MHz centred on 1,375 MHz. Currently the Pulsar ALFA (PALFA) survey is using signal processors of bandwidth 100 MHz but ultimately the full 300 MHz bandwidth will be used. The PALFA survey plans to

cover $|b| < 5^\circ$ for the two regions of the Galactic plane accessible to the Arecibo telescope, $40^\circ < l < 75^\circ$ and $170^\circ < l < 210^\circ$, but the current observations are restricted to $|b| < 1^\circ$. The observation time per pointing is 134 s for the first region, giving a limiting flux density for long-period, low-DM pulsars of about 0.07 mJy, and 67 s for the anti-centre region with a correspondingly reduced sensitivity. From a preliminary analysis of the data, 11 previously unknown pulsars have been discovered and 29 previously known pulsars detected. One of the new discoveries, PSR J1906+0746, is a relatively young pulsar with a pulse period of 144 ms in a mildly eccentric ($e = 0.085$) 3.98-h orbit [39]. Relativistic perturbations to the orbit are detectable; specifically a periastron advance of $7^\circ.57 \pm 0^\circ.03\,\mathrm{yr}^{-1}$ has been observed, implying a total system mass of $2.61 \pm 0.02\,\mathrm{M}_\odot$. It is not clear if the companion is a heavy white dwarf (with the system having a similar evolutionary history to PSR J1141−6545) or a second neutron star. Another of the new discoveries, PSR J0628+09, is an extremely sporadic emitter with a period of 1.2 s that was discovered in a single-pulse search but not detected in the standard periodicity search. Cordes et al. [7] predict that the PALFA survey will ultimately discover about 1,000 pulsars, but Lorimer et al. [38] suggest a smaller number, about 375 new discoveries.

An outstandingly successful search for pulsars in the globular cluster Terzan 5 using the 100-m Green Bank Telescope has been undertaken by Ransom et al. [53]. Observations during 2004 using a receiving system with 600 MHz of bandwidth centred on 1,950 MHz with a sampling interval of about 80 μs were analysed to reveal a total of 21 previously unknown pulsars in the cluster, bringing the total known to 24 (Fig. 2.4). All of the new pulsars appear to be recycled, but their

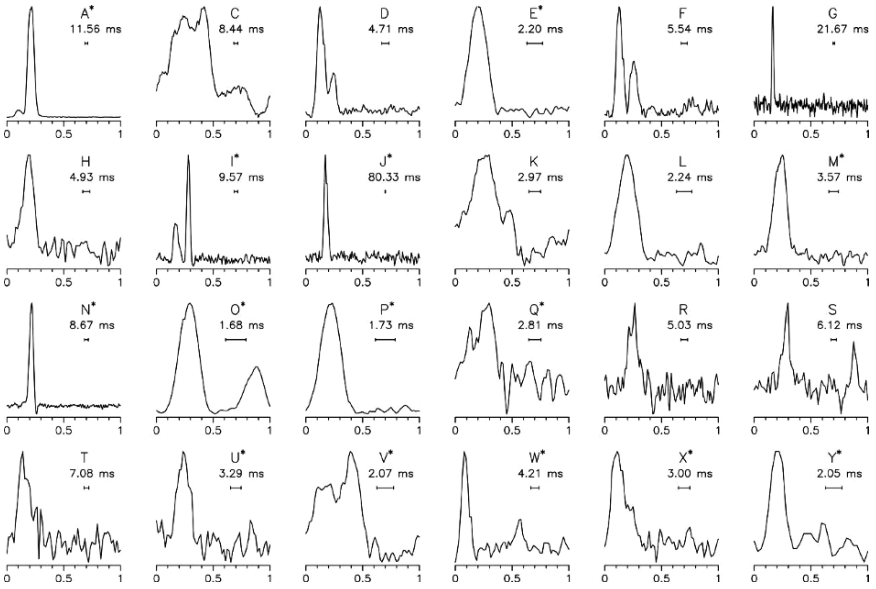

Fig. 2.4 Pulse profiles recorded at the Green Bank Telescope for 24 pulsars in the globular cluster Terzan 5 [53]. The central observing frequency was 1,950 MHz. For each profile the pulsar period and extent of profile smearing (∼0.3 ms) are indicated. An *asterisk* indicates that the pulsar is a member of a binary system

periods cover a larger range, 1.6–80 ms, than the pulsars associated with 47 Tucanae. Thirteen of the new pulsars are binary, with orbital periods in the range 0.25–60 days and near-circular orbits except for two, PSR J1748−2446I and PSRJ 1748−2446J. These two systems respectively have orbital periods of 1.3 and 1.1 days, eccentricities of 0.43 and 0.35 and companion masses greater than 0.24 $M_\odot$ and 0.38 $M_\odot$. With these parameters, relativistic orbit perturbations are detectable. The observed periastron advance leads to total masses of close to $2.2M_\odot$ for both systems, implying most probable pulsar masses of about $1.7M_\odot$, much higher than accurately measured pulsar masses in other pulsar binary systems.

Continued observations and data analysis have led to the discovery of even more pulsars in this cluster. Although details of these further results (with one exception) are not yet formally published, the compilation by Paulo Freire at http://www.naic.edu/ pfreire/GCpsr.html lists a total of 33 pulsars associated with Terzan 5. This one cluster therefore contains about 25% of the total known cluster pulsar population and nearly 20% of all known MSPs! Most notable of the recent discoveries is PSR J1748−2446ad which has the shortest period of any known pulsar, 1.396 ms, corresponding to a spin frequency of 716 Hz [21]. The pulsar is binary in a circular orbit of period 1.04 days and with a companion of minimum mass 0.14 $M_\odot$. As with several other pulsars in short-period binary systems in the cluster, the pulsar is eclipsed for about 40% of the orbit, presumably by an ablated wind from the companion. The mean pulse profile has a weak interpulse approximately midway between the main pulses and its mean flux density at 1,950 MHz is only 80 μJy.

2.4 Pulsar Nulling and Mode Changing

Pulsar nulling is a phenomenon observed mostly in longer-period pulsars in which the pulsed emission abruptly turns off for intervals which range from a few pulse periods to many weeks in different pulsars and then just as abruptly turns on. Mode changing is an apparently related phenomenon in which the mean pulse profile abruptly changes to a different form and then, typically a few minutes later, reverts to the original form. Other pulse properties such as polarisation, subpulse drifting and pulse microstructure are affected by these transitions, showing that they represent a fundamental change in the emission process.

With its relatively long observation time per pointing, the Parkes Multibeam Pulsar Survey provided an excellent database for studies of these phenomena. Wang et al. [65] studied 23 pulsars for which the survey observations showed evidence for nulling behaviour. Figure 2.5 shows a selection of these illustrating the range of "null fraction", i.e., fraction of time that a pulsar spends in the null state. Seven of the 23 pulsars have null fractions in excess of 40% and, with just one short burst during a 2-h observation, PSR J1717−4054 has the largest observed null fraction, $>95\%$.

The close relationship between nulling and mode changing is illustrated by the fascinating behaviour of PSR J1326−6700 shown in Fig. 2.6. The normal emission

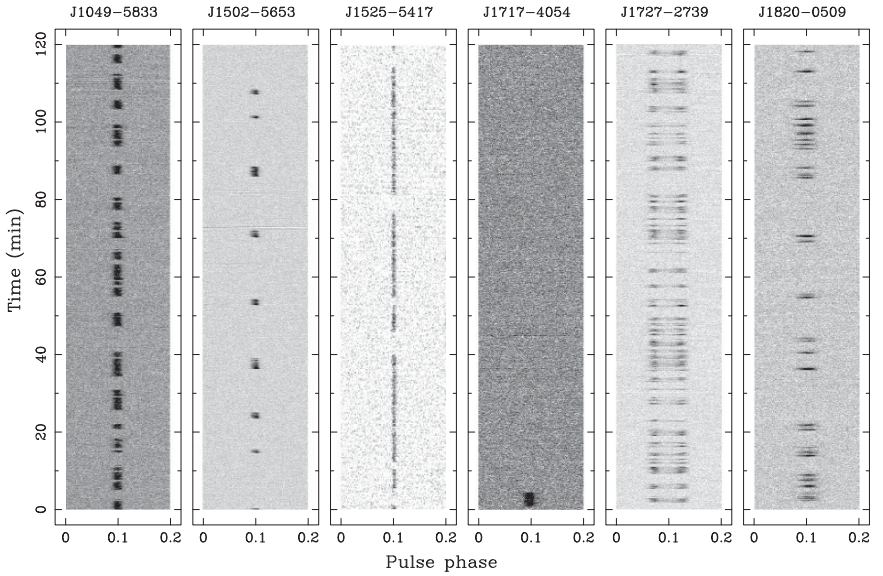

Fig. 2.5 Phase–time plots for six pulsars showing nulling behaviour [65]. A wide range on null fractions and timescales is represented by these examples

from this pulsar has a broad pulse profile with three main components. Every few minutes it switches to a different mode in which essentially all of the normal emission ceases and a new pulse component appears at the leading edge of the normal-mode profile. Another demonstration of the close relationship between nulling and mode changing is provided by PSR B0826−34. This long-period (1.848 s) pulsar is characterized by a very wide pulse profile covering essentially the whole pulse period, complicated drifting subpulse behaviour and very extended null intervals [12]. The null fraction is at least 70% and observed null intervals range in length from a few pulse periods to many hours. Recent observations using the Parkes radio telescope at 1,374 MHz by Esamdin et al. [14] show that the pulsar does not turn off completely in the "null" intervals. Integration of the "null" data show a weak pulse of mean flux density about 2% of that in the "on" phase. As shown in Fig. 2.7, the mean pulse profile in the "null" phase is quite different to that in the "on" phase, showing that the apparent nulls are actually mode changes. Nulls are just an absence of detectable emission and the limits on emission in the null intervals vary, but are at best about 1% of the on-phase flux density. It is possible that, with sufficient sensitivity, pulsed emission would always be found in so-called null intervals. It is clear that both nulls and mode changes result from a large-scale and persistent changes in the magnetospheric current distribution which result in a dramatic change in the radiated beam. Whether it is called a null or a mode change just depends on whether or not a significant part of the modified beam crosses the Earth.

Another interesting recent result which has implications for the interpretation of pulse nulling is the detection of a change in the rate of spin-down during the

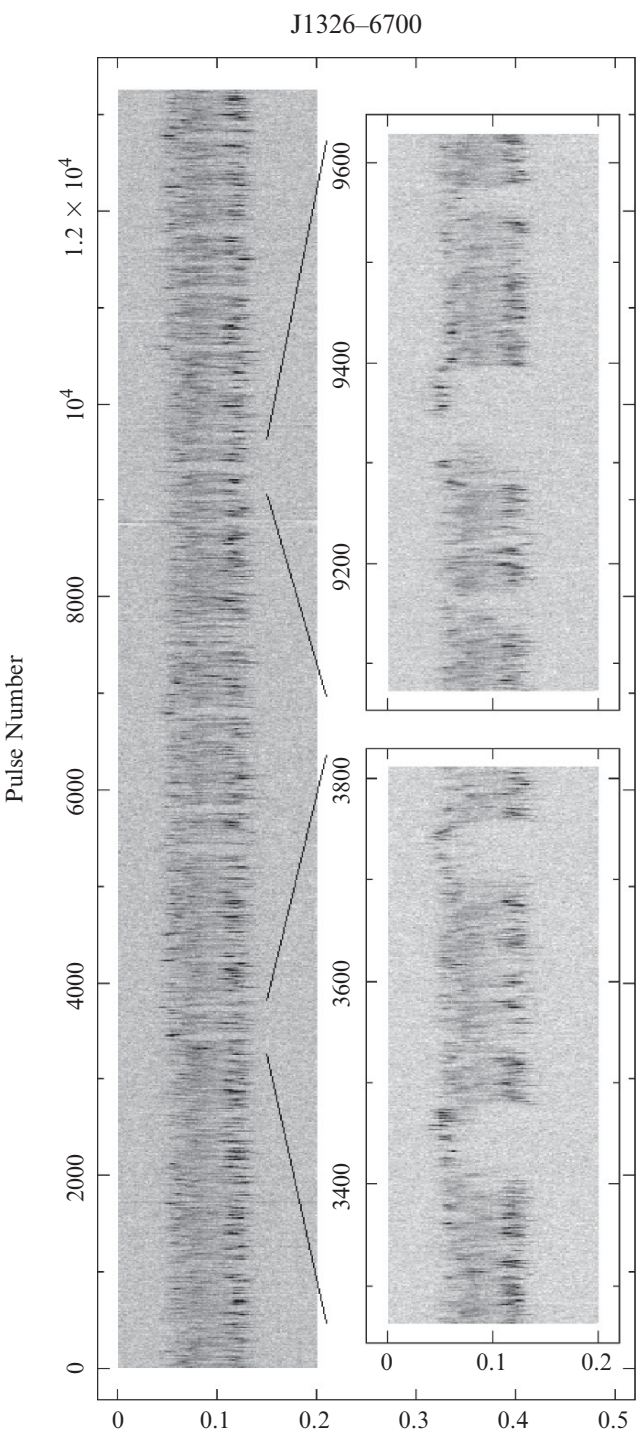

Fig. 2.6 Phase–time plot for individual pulses from PSR J1326−6700. The total data span is a little over 2 h. The *insets* show two portions of the dataset with an expanded scale [65]

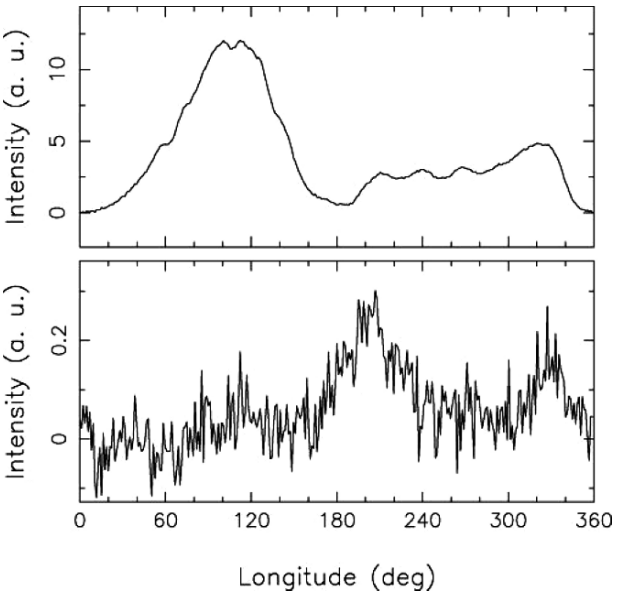

Fig. 2.7 Mean pulse profiles for PSR B0826−34 in its "on" phase (*upper*) and "off" phase (*lower*) [14]

null phase for PSR B1931+24 [35]. This pulsar has a quasi-periodic modulation in which the pulsar is on for 5–10 days and then undetectable for 25–35 days. Because of this long timescale it is possible to measure $\dot{\nu}$ for each "on" phase and compare that with the long-term $\dot{\nu}$. Figure 2.8 illustrates the fascinating result that when the pulsar is on, the spin-down rate $\dot{\nu} = (-16.3 \pm 0.4) \times 10^{-15}\,\mathrm{Hz\,s^{-1}}$, about 50% greater than the value in the off state, $(-10.8 \pm 0.2) \times 10^{-15}\,\mathrm{Hz\,s^{-1}}$, derived from a fit to the timing residuals. This result clearly demonstrates that the magnetospheric currents responsible for the emission of the radio beam also contribute to the pulsar braking. Remarkably, if it is assumed that the braking in the null state is solely due to magnetic-dipole radiation and that the magnetospheric currents are zero in this state, then the magnetospheric charge density in the on state required to generate the additional braking is almost exactly equal to the Goldreich–Julian value [17].

The implication that magnetospheric currents completely switch off in the null state appears somewhat at odds with our previous conclusion that nulls are basically mode changes where the radio beam is either much weaker than in the on state or is redirected so that it doesn't sweep over the Earth as the pulsar rotates. However, it is quite possible that in a null-like mode change either the magnitude of the current or its effectiveness in braking the pulsar is significantly reduced, but not necessarily zero. This leaves open the fractional contribution of magnetic-dipole radiation to the braking and implies magnetospheric charge densities greater than the Goldreich–Julian value, at least in the on state.

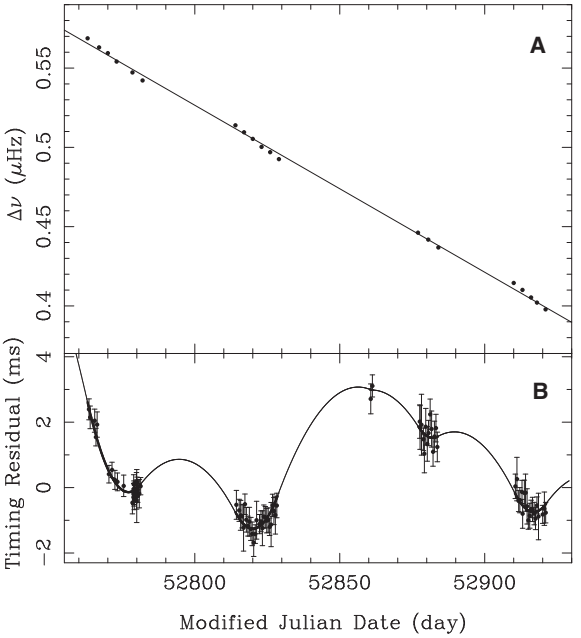

Fig. 2.8 Long-term timing behaviour of the nulling pulsar PSR B1931+24. *Panel-A* gives the time variation of pulse frequency, showing that the spin-down rate is larger than average when the pulsar is on and, by implication, less than average when the pulsar is off. *Panel-B* shows a fit of a simple model with different values of $\dot{\nu}$ for the on and off states to the timing phase residuals [35]

2.5 Pulse Modulation and Drifting

Pulsars exhibit a variety of pulse modulation phenomena which are different to, but never-the-less related to, pulse nulling and mode changing. The power spectrum of pulse-to-pulse fluctuations in pulse energy often shows quasi-periodic components which are usually confined to the outer or conal parts of the pulse profile [2]. Subpulse drifting is a closely related phenomenon in which the pulse phase or longitude of subpulses varies systematically in successive pulses, see for example [63]. The properties of the drifting subpulses, for example, the rate at which they drift across the profile or even their existence, are often affected by nulls and mode changes, illustrating the close connection between these various phenomena [28, 54].

Clear drifting subpulses are only observed in a handful of pulsars. However, a systematic study of 1.4 GHz Westerbork data for 187 pulsars by Weltevrede, Edwards and Stappers [67] has shown evidence for subpulse drifting in 68 pulsars, more than a third of the sample. Taking into account signal/noise limitations, this indicates that more than half of all pulsars have some drifting behaviour. Figure 2.9 illustrates the analysis procedures used. Drifting behaviour is indicated by a concentration of power away from the vertical zero-frequency axis in the 2-dimensional power spectra. Two types of drifting are identified: “coherent” in which the feature

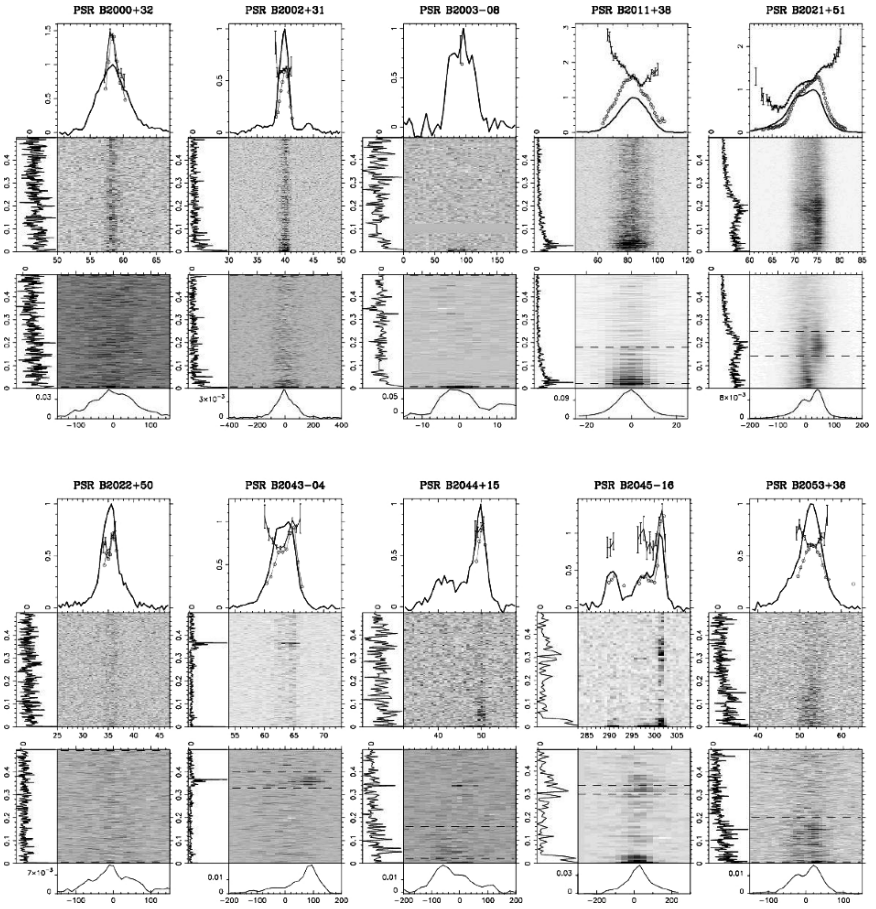

Fig. 2.9 Results of pulse modulation analyses using Westerbork 1.4-GHz data for selected pulsars [67]. In the *upper panel* for each pulsar the mean pulse profile (*solid line*), the variance of the pulse-to-pulse fluctuations (*open circles*) and the corresponding modulation index (points with error bars) are shown as a function of pulse longitude (in degrees). The *middle panels* contain the longitude-resolved fluctuation spectra, i.e., the spectra of time sequences of power in individual longitude bins and the lower panels give the 2-dimensional power spectra of the observed longitude-time variations. The 1-dimensional spectra at the side and bottom are the power integrated across the 2-dimensional plots

in the fluctuation spectrum is narrow (less than 0.05 cycles/period) and "diffuse" in which a wider feature is observed. Examples of the two types given in Fig. 2.9 are PSR B2043−04 (coherent) and PSR B2021+51 (diffuse). Although some pulse modulation indices are larger than 1.0, they are generally smaller, with ∼0.5 being the most common value. There is little correlation of modulation index with the presence or absence of drifting subpulses. However, there is a significant correlation of drifting behaviour with pulsar characteristic age, with older pulsars more likely to show drifting behaviour, especially coherent drifting.

2.6 Giant and Not-So-Giant Pulses

Giant pulses are, by convention, defined to be intense narrow pulses which typically have a pulse energy much greater than that of the average pulse. They are characterized by a power-law distribution of pulse energies and a close association with high-energy (X-ray or γ-ray) pulse emission. They are observed in two classes of pulsars, young energetic pulsars such as the Crab pulsar, which was indeed discovered through its giant pulse emission [58], and MSPs, which also have a high value of spin-down luminosity $\dot{E} = 4\pi^2 I \dot{P} P^{-3}$.

The highest time-resolution observations to date have been published by Hankins et al. [19]. Arecibo observations of the Crab pulsar at 5.5 GHz with a bandwidth of 500 MHz were recorded with a baseband system and coherently de-dispersed to give a maximal time resolution of 2 ns. Figure 2.10 shows that a single giant pulse consists of a series of "nanopulses" with timescales of a few nanoseconds. The extremely short timescale of the nanopulses implies scale sizes for the emitting regions of order 1 m and brightness temperatures of order 10^{37} K. It is likely that these nanopulses are the fundamental units of emission from the coherent process. Their short timescale appears inconsistent with either coherent curvature radiation from electron bunches or maser processes, leaving collapse of wave packets generated by small-scale plasma turbulence as the most likely candidate.

Other recent observations of Crab giant pulses include those of Popov et al. [52] and Jessner et al. [29]. Popov et al. used the Kalyzin 64-m radio telescope at 600 MHz and showed that all pulses in the main pulse and interpulse were giant; i.e., in a long-term synchronous average, the integrated intensity of these two pulse components could be entirely accounted for by the giant pulses. In contrast, no giant

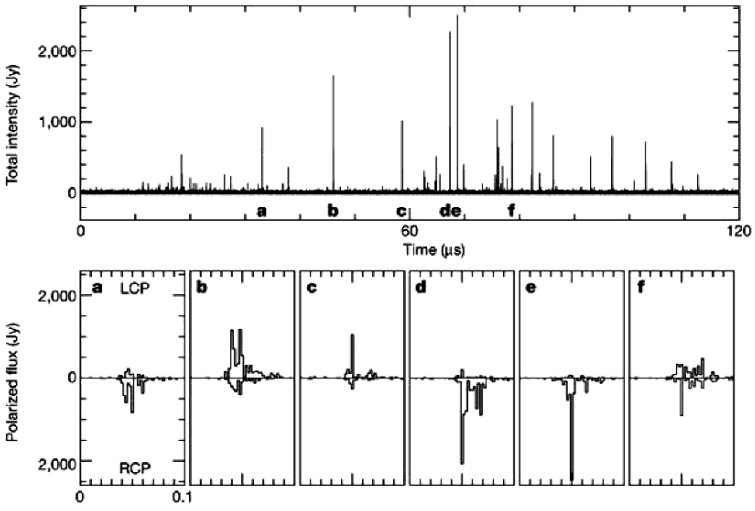

Fig. 2.10 Nanopulses from the Crab pulsar, recorded at 5.5 GHz with the Arecibo radio telescope and coherently de-dispersed to give 2-ns time resolution [19]

pulses were observed from the so-called "precursor" component which precedes the main pulse by about 2 ms, is wider than either the main pulse or the interpulse and is highly linearly polarised.

At high radio frequencies the mean pulse profile has a number of other components which are not seen at lower frequencies (or in X-rays and γ-rays) [48]. Using the Effelsberg 100-m radio telescope at 8.3 GHz, Jessner et al. [29] observed giant pulses, not only from the main pulse and interpulse (at this frequency, the interpulse is much stronger than the main pulse), but also from the two high-frequency components HFC1 and HFC2. A few strong pulses were observed at phases close to the precursor, but it is not clear if they are related to that component.

In the Crab pulsar, the main pulse and interpulse, which as mentioned above are dominated by giant pulses, have precisely the same pulse phase as the peaks of the optical, X-ray and γ-ray pulse components. A similar association of giant pulse emission phases with high-energy pulse components is observed in PSR B1937+21, the original MSP, where both are on the trailing wing of the main radio pulse and interpulse [9]. Recent observations using the 100-m Green Bank telescope at 850 MHz by Knight et al. [31] detected giant pulses from the MSP PSR J0218+4232. As Fig. 2.11 shows, the giant pulses occur at minima in the mean radio

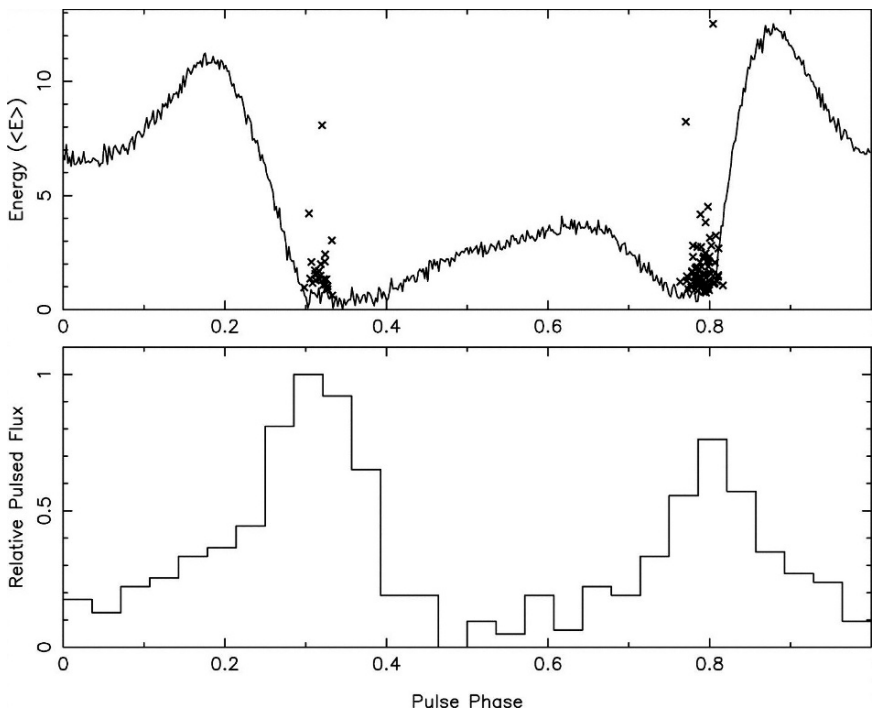

Fig. 2.11 The *top panel* shows the mean pulse profile of PSR J0218+4232 at 850 MHz with the pulse phases and energies of giant pulses marked by crosses. The lower panel shows the *Chandra* 0.1–10 keV X-ray pulse profile phase aligned with the radio profile as emitted from the pulsar (i.e. after correcting for the radio dispersion delay) [31, 36, 55]

profile but are coincident with the phases of the X-ray peaks. These results clearly show that the emission regions for high-energy emission and for giant pulses in both young and millisecond pulsars are closely associated, and that both are distinct from the emission region(s) for the "normal" radio emission.

Very strong individual pulses are observed from more "normal" pulsars. For example, Kuzmin and Ershov [37] observed pulses from PSR B0031−07 at 40 and 111 MHz which were several hundred times as strong as the average pulse. They were confined to a narrower pulse phase range than that covered by the mean pulse profile and were concentrated near the peaks of the mean profile. A very similar phenomenon was observed by Weltevrede et al. [68] at 327 MHz in PSR 0656+14. These results suggest that these are not "giant" pulses in the sense defined at the start of this section. They are much broader, with pulse widths typically several milliseconds, they are related in pulse phase to the normal emission, they do not have a power-law intensity distribution and they are not associated with high-energy emission. Furthermore, these pulsars do not have high values of $\dot{E}$. It seems more likely that these strong pulses reflect extreme examples of normal subpulse modulation. As mentioned in Sect. 2.2 and discussed by Weltevrede et al. [68], it is quite possible that most if not all RRATs are highly modulated pulsars similar to these (but more distant).

2.7 Transient Radio Emission from a Magnetar

Apart from some claimed but unconfirmed detections at low radio frequencies [42, 56], searches for pulsed radio emission from magnetars (AXPs and SGRs) have been unsuccessful. This changed dramatically in March 2006 when strong radio pulses at 1.4 GHz were observed from XTE J1810−197 (PSR J1809−1943) at Parkes [6]. Following a large X-ray flare [24] the AXP was detected as a variable radio continuum source at 1.4 GHz [6, 18]. The Parkes observations revealed strong radio pulses at the 5.54 s period of the AXP which were consistent with the entire radio flux being pulsed. Large day-to-day variations in flux density, which cannot be accounted for by interstellar scintillation, were observed. Observations over a wide range of frequencies using Parkes, the Very Large Array and the Green Bank Telescope showed that, within the uncertainty caused by the flux variations, the pulse spectrum was essentially flat. As Fig. 2.12 shows, strong individual pulses were detected at frequencies as high as 42 GHz, a remarkable and unprecedented result.

This AXP lies within the boundaries of the Parkes Multibeam Pulsar Survey and was observed in 1997 and 1998. No pulsations were detected, showing that the pulsed flux density was less than about 0.2 mJy at that time. This suggests that the strong radio pulsed emission from this object is related to the occurrence of the X-ray flare in early 2003. It is possible that the lack of confirmation of earlier detections of radio emission from magnetars [42,56] results from a similar transient nature of the pulsed emission.

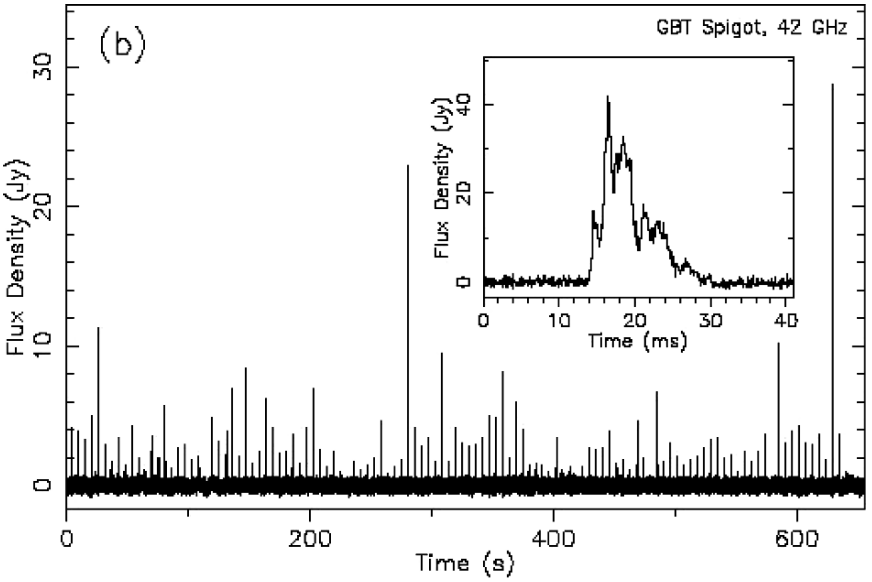

Fig. 2.12 A train of individual pulses from the magnetar PSR J1809−1943 recorded at 42 GHz us ing the Green Bank Telescope. The inset shows the detailed sub-structure of the strongest pulse recorded with 80 μs resolution [6]

2.8 Rotation Axis: Proper Motion Correlation

The relationship between the direction of the pulsar spin axis and the direction of the pulsar space velocity is important in helping us to understand the origin of pulsar velocities. For example Tademaru and Harrison [61] proposed a "photon rocket" mechanism and, more recently, Spruit and Phinney [57] discussed a "slow kick" model, both of which result in an alignment of the pulsar spin and velocity vectors. Early investigations [1] found no correlation between the projected axis of rotation derived from pulsar polarisation observations and the pulsar proper motion vector, suggesting that the pulsar "rocket" mechanism [61] was not effective in accelerating pulsars. However, many of the pulsars in this sample were relatively old, implying a possible decoupling of the orientation of the current proper motion vector and the spin axis direction because of acceleration in the Galactic gravitational field. Furthermore, the interpretation of the observed position angle variations was complicated by the presence of orthogonal polarisation modes [60]. New light was shed on this by remarkable X-ray results showing equatorial tori surrounding the Crab and Vela pulsars [20, 22, 66]. These tori unambiguously define the orientation of the pulsar spin axis and, in both cases, the direction projected on the sky is close to that of the proper motion [20]. Ng and Romani [51] showed that X-ray tori around several other young pulsars were similarly aligned with their proper motion vectors.

Johnston et al. [30] used Parkes observations to improve rotation measures and fitted the rotating-vector model to the observed position angle (PA) variations to

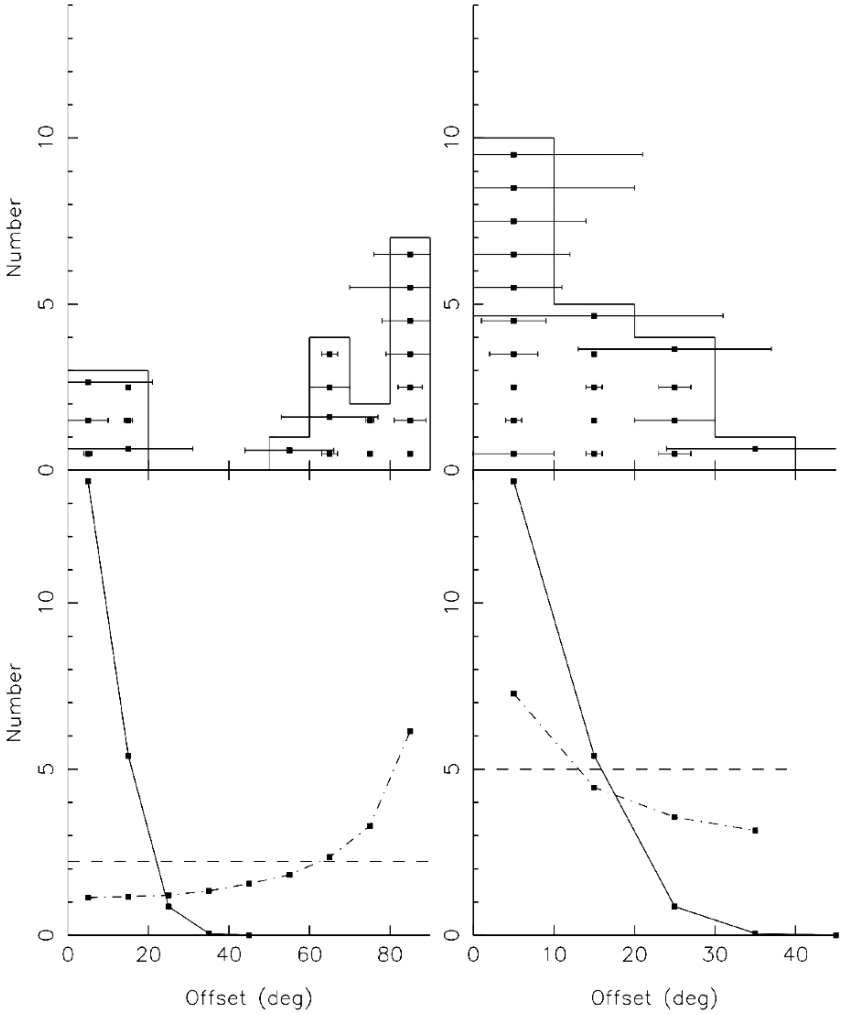

Fig. 2.13 The difference between the position angle of the pulsar rotation axis implied by polarisation observations and the proper motion vector as observed (*top left*) and allowing for the possible presence of orthogonal polarisation modes (*top right*) for 25 pulsars [30]. The *lower panels* show the results of simulations for rotation axes and velocities respectively aligned (*solid line*), orthogonal (*dot-dashed line*) and uncorrelated (*dashed line*)

derive improved estimates of the intrinsic PA of the centre of symmetry of the PA variation across the pulse. The results of comparing these angles with the PA of the proper motion vector are shown in Fig. 2.13. Similar results were obtained by Wang et al. [64] by reanalyzing archival data. Figure 2.13 shows a strong preference for angle differences either close to 0° or to 90° and is inconsistent with a random distribution at the 94% level. If the 90° offsets are attributed to emission in the orthogonal mode (right panel) then the significance improves to 98%. In the case

of three young pulsars, Crab, Vela and PSR B0656+14, this reassignment of the PA difference is confirmed by X-ray and optical observations.

These results strengthen the case for alignment of the rotation and velocity vectors, at least for young pulsars. In the context of the Spruit and Phinney [57] model, they imply that birth kicks effectively act over a time long compared to the birth spin period, so that the components perpendicular to the spin axis average to zero.

2.9 Conclusions

This review has presented a selection, by no means complete, of interesting recent results related to the radio emission from pulsars. Despite the nearly 40 years since their discovery, pulsars remain a highly active and productive field of research. They are distinguished not only by their intrinsic interest, but also by their power and versatility as probes of a wide range of physical and astrophysical problems. Essentially all pulsar observations are sensitivity limited. With new more sensitive facilities such as the Chinese FAST telescope [50] and the Square Kilometer Array [33] being planned, the future of pulsar astronomy is bright.

References

1. Anderson, B. & Lyne, A. G., 1983, Nature, 303, 597
2. Backer, D. C., 1973, ApJ, 182, 245
3. Bhattacharya, D. & van den Heuvel, E. P. J., 1991, Phys. Rep., 203, 1
4. Burgay, M., D'Amico, N., Possenti, A., et al., 2003, Nature, 426, 531
5. Burgay, M., Joshi, B. C., D'Amico, N., et al., 2006, MNRAS, 368, 283
6. Camilo, F., Ransom, S. M., Halpern, J. P., et al., 2006, Nature, 442, 892
7. Cordes, J. M., Freire, P. C. C., Lorimer, D. R., et al., 2006, ApJ, 637, 446
8. Cordes, J. M. & Lazio, T. J. W., 2002, astro-ph/0207156
9. Cusumano, G., Hermsen, W., Kramer, M., et al., 2003, A&A, 410, L9
10. Davies, M. B. & Hansen, B. M. S., 1998, MNRAS, 301, 15
11. Duncan, R. C. & Thompson, C., 1992, ApJ, 392, L9
12. Durdin, J. M., Large, M. I., Little, A. G., et al., 1979, MNRAS, 186, 39P
13. Edwards, R. T., Bailes, M., van Straten, W., et al., 2001, MNRAS, 326, 358
14. Esamdin, A., Lyne, A. G., Graham-Smith, F., et al., 2005, MNRAS, 356, 59
15. Faucher-Giguère, C.-A. & Kaspi, V. M., 2006, ApJ, 643,332
16. Faulkner, A. J., Stairs, I. H., Kramer, M., et al., 2004, MNRAS, 355, 147
17. Goldreich, P. & Julian, W. H., 1969, ApJ, 157, 869
18. Halpern, J. P., Gotthelf, E. V., Becker, R. H., et al., 2005, ApJ, 632, L29
19. Hankins, T. H., Kern, J. S., Weatherall, J. C., et al., 2003, Nature, 422, 141
20. Helfand, D. J., Gotthelf, E. V., & Halpern, J. P., 2001, ApJ, 556, 380
21. Hessels, J. W. T., Ransom, S. M., Stairs, I. H., et al., 2006, Science, 311, 1901
22. Hester, J. J., Scowen, P. A., Sankrit, R., et al., 1995, ApJ, 448, 240
23. Hobbs, G., Faulkner, A., Stairs, I. H., et al., 2004, MNRAS, 352, 1439
24. Ibrahim, A. I., Markwardt, C. B., Swank, J. H., et al., 2004, ApJ, 609, L21
25. Jacoby, B. A., 2004, PhD thesis, Calfornia Institute of Technology
26. Jacoby, B. A., Bailes, M., van Kerkwijk, M. H., et al., 2003, ApJ, 599, L99

27. Jacoby, B. A., Hotan, A., Bailes, M., et al., 2005, ApJ, 629, L113
28. Janssen, G. H. & van Leeuwen, J., 2004, A&A, 425, 255
29. Jessner, A., Słowikowska, A., Klein, B., et al., 2005, Adv. Space Res., 35, 1166
30. Johnston, S., Hobbs, G., Vigeland, S., et al., 2005, MNRAS, 364, 1397
31. Knight, H. S., Bailes, M., Manchester, R. N., et al., 2006, ApJ, 640, 941
32. Kolonko, M., Gil, J., & Maciesiak, K., 2004, A&A, 428, 943
33. Kramer, M., Backer, D. C., Cordes, J. M., et al., 2004, New Astron. Rev., 48, 993
34. Kramer, M., Bell, J. F., Manchester, R. N., et al., 2003, MNRAS, 342, 1299
35. Kramer, M., Lyne, A. G., O'Brien, J. T., et al., 2006, Science, 312, 549
36. Kuiper, L., Hermsen, W., & Stappers, B., 2004, Adv. Space Res., 33, 507
37. Kuzmin, A. D. & Ershov, A. A., 2004, A&A, 427, 575
38. Lorimer, D. R., Faulkner, A. J., Lyne, A. G., et al., 2006, MNRAS, 372, 777
39. Lorimer, D. R., Stairs, I. H., Freire, P. C., et al., 2006, ApJ, 640, 428
40. Lyne, A. G., Burgay, M., Kramer, M., et al., 2004, Science, 303, 1153
41. Lyne, A. G., Manchester, R. N., & Taylor, J. H., 1985, MNRAS, 213, 613
42. Malofeev, V. M., Malov, O. I., & Teplykh, D. A., 2006, Chin. J. Astron. Astrophys., Suppl. 2, 6, 68
43. Manchester, R. N., Fan, G., Lyne, A. G., et al., 2006, ApJ, 649, 235
44. Manchester, R. N., Hobbs, G. B., Teoh, A., et al., 2005, AJ, 129, 1993
45. Manchester, R. N., Lyne, A. G., Camilo, F., et al., 2001, MNRAS, 328, 17
46. McLaughlin, M. A., Lyne, A. G., Lorimer, D. R., et al., 2006, Nature, 439, 817
47. Mdzinarishvili, T. G. & Melikidze, G. I., 2004, A&A, 425, 1009
48. Moffett, D. A. & Hankins, T. H., 1996, ApJ, 468, 779
49. Morris, D. J., Hobbs, G., Lyne, A. G., et al., 2002, MNRAS, 335, 275
50. Nan, R.-D., Wang, Q.-M., Zhu, L.-C., et al., 2006, Chin. J. Astron. Astrophys., Suppl. 2, 6, 304
51. Ng, C.-Y. & Romani, R. W., 2004, ApJ, 601, 479
52. Popov, M., Soglasnov, V., Kondrat'ev, V., et al., 2006, Astron. Lett., 50, 55
53. Ransom, S. M., Hessels, J. W. T., Stairs, I. H., et al., 2005, Science, 307, 892
54. Redman, S. L., Wright, G. A. E., & Rankin, J. M., 2005, MNRAS, 357, 859
55. Rutledge, R. E., Fox, D. W., Kulkarni, S. R., et al., 2004, ApJ, 613, 522
56. Shitov, Y. P., Pugachev, V. D., & Kutuzov, S. M., 2000, In: Pulsar astronomy – 2000 and beyond, IAU Colloquium 177, ed. M. Kramer, N. Wex, & R. Wielebinski (San Francisco: Astronomical Society of the Pacific), 685
57. Spruit, H. & Phinney, E. S., 1998, Nature, 393, 139
58. Staelin, D. H. & Reifenstein, III, E. C., 1968, Science, 162, 1481
59. Staveley-Smith, L., Wilson, W. E., Bird, T. S., et al., 1996, PASA, 13, 243
60. Stinebring, D. R., Cordes, J. M., Rankin, J. M., et al., 1984, ApJS, 55, 247
61. Tademaru, E. & Harrison, E. R., 1975, Nature, 254, 676
62. Tauris, T. M. & Manchester, R. N., 1998, MNRAS, 298, 625
63. Taylor, J. H., Manchester, R. N., & Huguenin, G. R., 1975, ApJ, 195, 513
64. Wang, C., Lai, D., & Han, J. L., 2006, ApJ, 639, 1007
65. Wang, N., Manchester, R. N., & Johnston, S., 2007, MNRAS, 1383
66. Weisskopf, M. C., Hester, J. J., Tennant, A. F., et al., 2000, ApJ, 536, L81
67. Weltevrede, P., Edwards, R. T., & Stappers, B. W., 2006, A&A, 445, 243
68. Weltevrede, P., Stappers, B. W., Rankin, J. M., et al., 2006, ApJ, 645, L149

Chapter 3
Rotating Radio Transients

Maura McLaughlin

3.1 Introduction

Gamma-ray and X-ray telescopes have long been sensitive to transient phenomena, with rich scientific returns resulting from the discovery of sources such as gamma-ray bursts, soft gamma-ray repeaters and anomalous X-ray pulsars. The situation at radio wavelengths, however, is dramatically different. While radio telescopes typically have sensitivity to events with short timescales, they have much narrower fields of view than their high-energy counterparts. Consequently, most transient radio studies have been follow-up observations of events first detected at higher energies. Radio transient studies are important, however, as they can probe explosive and dynamic events which do not necessarily have counterparts at other wavelengths.

Figure 3.1 illustrates the types of objects that we might expect to discover with surveys for short timescale (i.e. durations $\lesssim 1$ day) radio transients. The brightest such sources are radio pulsars, with the "nano-giant" pulses from the Crab pulsar having brightness temperatures up to 10^{38} K [23] and the single pulses of "normal" pulsars having brightness temperatures of 10^{28} K. Well-known weaker sources include planetary radio flares [6], Type I and Type II flares from the Sun and other stars [41], bursts from active stars such as UV Ceti and AD Leo [42], OH maser emission [10], radio flares from brown dwarfs such as BD LP944−20 [3], AGN radio outbursts [1] and intraday variability of GRB afterglows [19] and other extragalactic radio sources due to interstellar scintillation [32].

Are the empty regions of radio transient phase-space in Fig. 3.1 intrinsic or simply due to our poor sampling of the transient radio sky? Several recent discoveries suggest the latter. In 2005, radio bursts of 10 min duration with a 77 min periodicity were detected from the Galactic center, filling in a previously empty region of

M. McLaughlin
Department of Physics, West Virginia University, Morgantown, WV 26506, USA
e-mail: maura.mclaughlin@mail.wvu.edu

W. Becker (ed.), *Neutron Stars and Pulsars,* Astrophysics and Space Science Library 357,

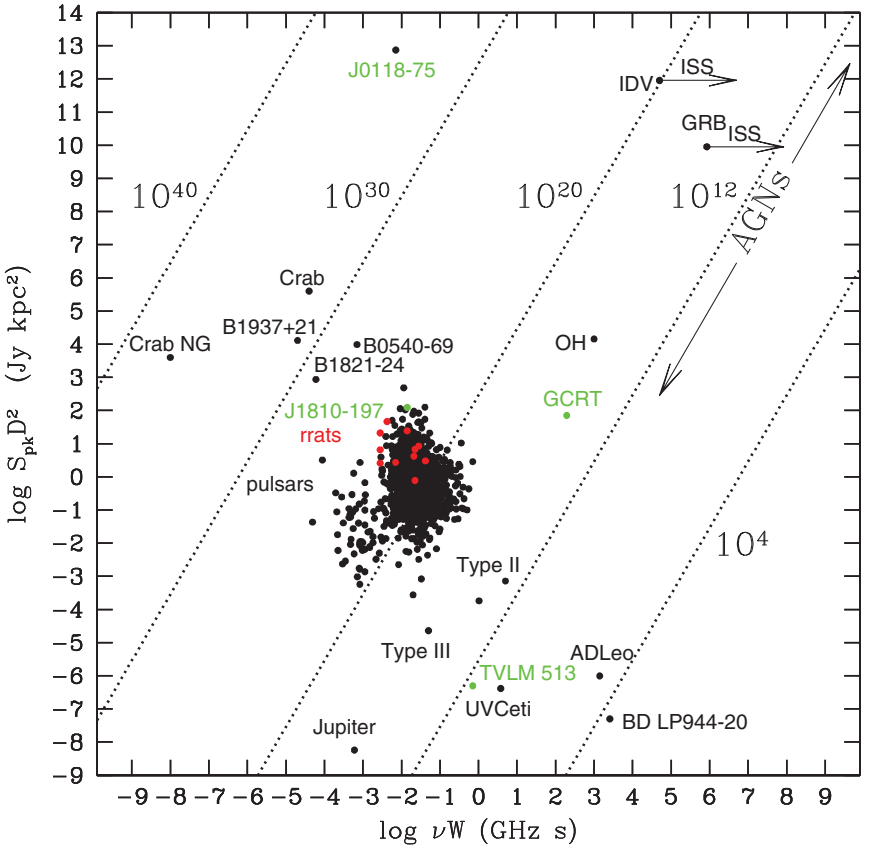

Fig. 3.1 Transient radio sky phase space. A log–log plot of the product of peak flux S in Jy and the square of the distance D in kpc vs. the product of frequency ν in GHz and pulse width W. Lines of constant brightness temperature $T = SD^2/2k(\nu W)^2$ are shown. *Points* are shown for the "nano-giant" pulses detected from the Crab [24], the giant pulses detected from the Crab [14], PSR B1937+21 [9], PSR B1821−24 [55] and B0540−69 [29] and single pulses from the 1,297 pulsars with flux, distance and pulse width listed in the ATNF Pulsar Database [26]. The *red points* indicate the RRATs and the *green points* denote objects discovered since the original publication of this figure in [12]. These new objects include the Galactic Center Radio Transient (GCRT) [27], radio pulses from the anomalous X-ray pulsar XTE J1810−197 [7], an extragalactic radio burst from J0118−75 in a survey of the Small Magellanic Cloud [40] and radio pulsations from the brown dwarf TVLM 513−46546 [22]

transient radio source phase space [27]. Last year, bright individual radio pulses were detected from the transient anomalous X-ray pulsar XTE J1810−197 [7], showing that these "radio-quiet" objects can actually be bright radio sources. Earlier this year, a brown dwarf (TVLM 513−46546) was found to exhibit periodic radio pulsations similar to those seen from radio pulsars [22]. And, very recently, an extremely bright radio burst was detected from J0118−75, in a survey of the Small

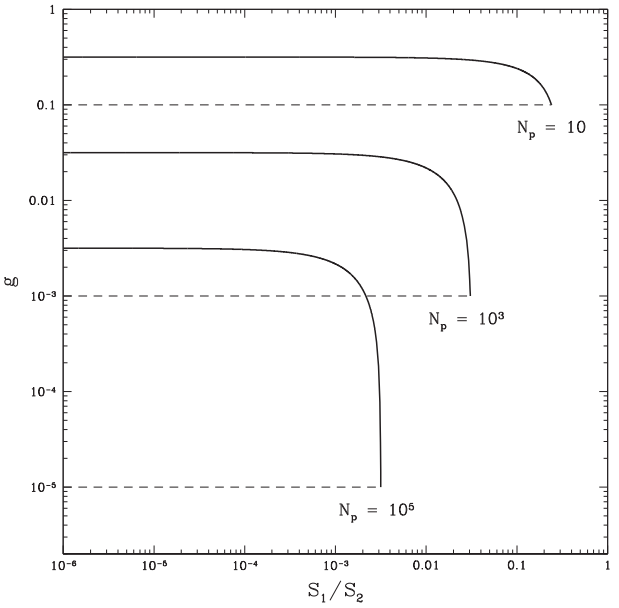

Fig. 3.2 Domain for which a single-pulse search is more sensitive than a periodicity search. The pulse intensity distribution is assumed to be bimodal. S_1 is the intensity of ordinary pulses with probability $1 - g$ and S_2 is the giant-pulse intensity with probability g. The results depend on how many pulse periods, N_p, are analyzed. For each of the three cases shown, a single-pulse search is superior for values 0of g and S_1/S_2 between the *dashed and solid lines*. Figure from [46]

Magellanic Cloud [40]. However, as implied by its anomalous position in Fig. 3.1, its dispersion measure (DM) yields an estimated distance of 500 Mpc; it is therefore thought to be extremely luminous.

Surveys for radio transients are important for detecting new objects such as these, but also for detecting radio pulsars with extreme emission properties. While most pulsars are detected with much higher signal-to-noise ratios in periodicity searches, pulsars with extreme pulse amplitude distributions and pulsars with long periods will sometimes be detected with higher signal-to-noise in searches for isolated dispersed pulses (see Fig. 3.2). This, and of course the possibility of finding new source classes altogether, was the basis for our single-pulse search of the Parkes Multibeam Pulsar Survey data, described in Sect. 3.2, which led to the discovery of the Rotating Radio Transients.

3.2 The Discovery of Rotating Radio Transients

The Parkes Multibeam Pulsar Survey (PMPS) began in August 1997 and was completed in March 2002. This survey operated at a center frequency of 1,374 MHz and used the 13 beam multi-beam receiver at Parkes, with a sampling interval of 250 μs

and 96 frequency channels spanning a 288 MHz bandpass. It is the largest pulsar survey to date, covering the entire Galactic plane visible from Parkes, i.e. $|b| < 5^\circ$ and $l = 260^\circ$ to $l = 50^\circ$, and so far resulting in the discovery of 742 new pulsars [39]. The initial PMPS processing consisted of de-dispersion over a range of trial dispersion measures (DMs) and a search for periodicities using a Fast Fourier Transform (FFT). No search sensitive to single dispersed pulses was included.

In 2002, we began reprocessing the PMPS data using the COBRA cluster at Jodrell Bank Observatory, UK, with a number of new algorithms, including a search for single dispersed pulses. The first step of this search was identical to that for the periodicity search – de-dispersion over a range of trial DMs. These DMs were identical to those used for the FFT search and were chosen to sample the entire expected electron density for the longitude and latitude of the pointing. Trial DMs were spaced more closely at lower values of DM and more coarsely at higher values, due to the already significant smearing across one of our 96 frequency channels. The number of DMs searched ranged from 213 (at high latitudes) to 325 (at low latitudes), corresponding to maximum DM values ranging from 387 to 2,203 pm cm^{-3}.

The second step of the single-pulse search was to search each de-dispersed time series for individual pulses with signal-to-noise ratios above a signal-to-noise threshold of four sigma. This was done by dividing the time series into eight chunks and calculating the mean and rms in each. After the first pass, the mean and rms were recalculated with the brightest pulses removed and the time series were searched again. Each time series was smoothed multiple times by adding adjacent samples and re-searched to heighten sensitivity to broadened pulses. The maximum "smoothing index" (i.e. the number of times adjacent samples were added) used in the search was seven, corresponding to a pulse width of 32 ms. If a pulse was detected with a number of different smoothing indices, only the one resulting in the highest signal-to-noise ratio was saved. Once all DMs were searched in this way, a diagnostic plot like that shown in Fig. 3.3 was created for each pointing. This plot was designed to aid detection of either a number of weak pulses at a non-zero DM (i.e. upper middle plot), or a small number of strong pulses at a non-zero DM (i.e. upper right or lower plot).

Roughly one-quarter of all pulsars detected in the periodicity search were also detected in the single-pulse search. As shown in Fig. 3.4, the ratio of detected signal-to-noise ratios (S/Ns) in the two searches (i.e. brightest single pulse S/N over FFT search S/N) ranged from 0.005 to 1.1, showing that, for most normal pulsars, searches relying on periodicity are indeed most efficient (at least for the parameters of the PMPS).

In addition to the 250 pulsars detected in the single-pulse search that were also detected in the periodicity search, 17 sources of dispersed single bursts with no periodicity-search counterpart were found. These sources were identified through visual inspection of diagnostic plots such as that shown in Fig. 3.5. Comparing results from different beams in the same pointing allowed a discrimination against signals of terrestrial radio frequency interference (RFI). Follow-up observations of these single-pulse detections with Parkes began in August 2003. Several of the detections were found to be normal radio pulsars that were missed in the original

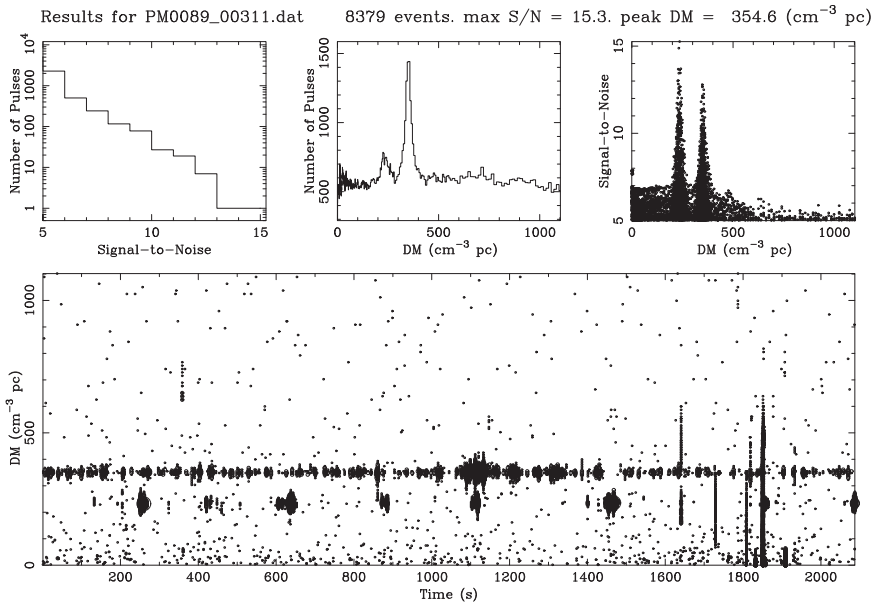

Fig. 3.3 Single-pulse search results for a PMPS beam in which two new pulsars, J1840−0809 with DM of 349 pc cm^{-3} and J1840−0815 with DM of 233 pc cm^{-3}, were detected. While these pulsars have similar periods (956 and 1,096 ms, respectively) their single-pulse amplitude distributions are clearly very different, illustrating the wide range of single pulse properties exhibited by normal pulsars. The plots show (from the *upper left* clockwise): (1) Histogram of S/N for identified pulses with S/N > 5 (*solid line*). Note the logarithmic scale of the *y*-axis. (2) Number of pulses above a 5σ threshold vs. DM. Two broadened peaks at the DMs of the pulsars are obvious. (3) Scatter plot of DM and S/N. (4) All pulses with S/N greater than 5σ plotted vs. DM and time. The size of the circle is linearly proportional to S/N, with the largest circle representing a S/N $\sim$15. The brightest pulses from J1840−0809 and J1840−0815 have S/Ns of 13 and 15, respectively, with the pulsars detected in the FFT search with S/Ns of 101 and 91

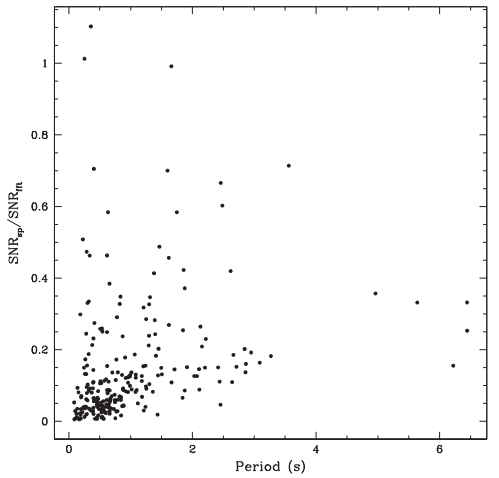

Fig. 3.4 Ratio of single-pulse detection signal-to-noise (i.e. S/N of brightest detected pulse) to FFT detection signal-to-noise vs. period for all known pulsars detected in both searches in the PMPS

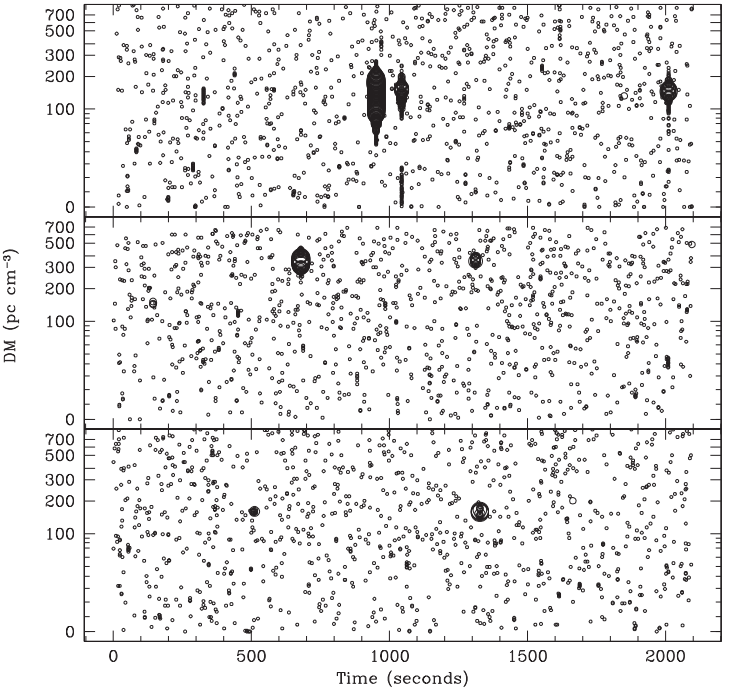

Fig. 3.5 The *lower panel* of the discovery output for (*from top to bottom*) J1317−5759, J1443−60 and J1826−14. All bursts detected with S/N greater than five are shown, with the size of the plotted circle proportional to the S/N of the burst

periodicity search due to RFI masking or human error. One source, J1624−4613, was only detectable in the single-pulse search and has since been found to be detectable roughly 70% of the time with an FFT [39]. This highlights the importance of including single-pulse searches in standard pulsar search analyses. However, 11 of the 20 sources remained completely undetectable in periodicity searches despite multiple follow-up observations. Two types of periodicity searches, the FFT search and a Fast Folding Algorithm (FFA; [56]) were used. In Table 3.1, we list these 11 sources, along with Right Ascension, Declination, longitude, latitude, DM, distance, width at 50% of the burst maximum, peak 1,400 MHz flux density of the strongest burst and average number of bursts detected per hour with the Parkes telescope at 1,400 MHz. Distances listed in Table 3.1 are inferred from the [11] model for Galactic free electron density.

As shown in Table 3.1, the properties of these 11 sources vary widely. The number of bursts detected from objects in the original discovery observations ranged from one (for J1911+00) to nine (for J1819−1458). Discovery DMs ranged from 88 pc cm^{-3} (for J1848−12) to 374 pc cm^{-3} (for J1443−60). The brightest burst, detected from J1819−1458, had S/N of 22, while none of the eight bursts detected from J1839−01 had S/N greater than six. In Fig. 3.5, we show the discovery plots

Table 3.1 Rotating radio transient properties (I)

Name	RA (J2000) h m s	Dec (J2000) ° ′ ″	l °	b °	DM pc cm^{-3}	D kpc	w_{50} ms	S_{1400} mJy	Rate h^{-1}
J0848−43	08:48(1)	−43:16(7)	263.4	0.2	293(19)	5.5	30	100	1.4
J1317−5759	13:17:46.26(5)	−57:59:30.3(6)	306.4	4.7	145.4(3)	3.2	10	1,100	4.5
J1443−60	14:43(1)	−60:32(7)	316.2	−0.6	369(8)	5.5	20	280	0.8
J1754−30	17:54(1)	−30:11(7)	359.9	−2.2	98(6)	2.2	16	160	0.6
J1819−1458	18:19:33.8(3)	−14:58:23(28)	16.0	0.1	196(3)	3.6	3	3,600	18
J1826−14	18:26(1)	−14:27(7)	17.2	−1.0	159(1)	3.3	2	600	1.1
J1839−01	18:39(1)	−01:36(7)	30.1	2.0	307(10)	6.5	15	100	0.6
J1846−02	18:46(1)	−02:56(7)	29.7	−0.1	239(10)	5.2	16	250	1.1
J1848−12	18:48(1)	−12:47(7)	21.1	−5.0	88(2)	2.4	2	450	1.3
J1911+00	19:11(1)	+00:37(7)	35.7	−4.1	100(3)	3.3	5	250	0.3
J1913+1333	19:13:17.69(6)	+13:33:20.1(7)	47.5	1.4	175.8(3)	5.7	2	650	4.7

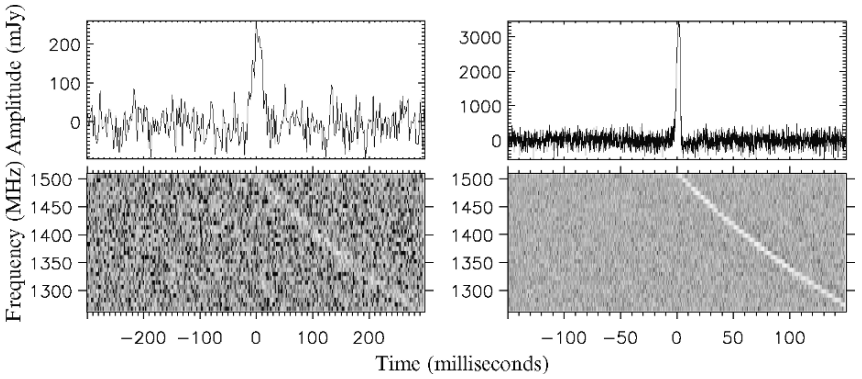

Fig. 3.6 The brightest single dispersed bursts from J1443−60 and J1819−1458. The *lower panel* shows the arrival of the bursts in individual frequency channels. The *upper panel* shows the de-dispersed time series, obtained by summing outputs of the individual receiver channels at the optimum value of the DM

for three sources. In Fig. 3.6, we show frequency-time plots for two of the brightest bursts detected. The expected dispersion sweep is obvious, indicating their astrophysical nature.

The DMs and inferred distances of these sources place them in the Galactic plane, with a concentration towards low latitudes (8 of the 11 sources have $|b| < 2°$). Their space distribution is consistent with that of the normal pulsar distribution. Because of their repeatable nature (i.e. multiple bursts detected at the same value of DM), we first named these sources Repeating Radio Transients (RRATs). We soon realized, however, that we could determine underlying periodicities for some of the RRATs by calculating the greatest common denominator of the differences between the bursts. While there is of course some ambiguity in this approach, for most of the RRATs we have enough detected bursts to determine correct periods. For all sources but J1911+00, the probability that the period we have measured is the correct period

Table 3.2 Rotating radio transient properties (II)

Name	P s	w_{50}/P %	Epoch MJD	$\dot{P}$ 10^{-15} s s^{-1}	B 10^{12} G	τ_c Myr	$\dot{E}$ 10^{31} erg s^{-1}
J0848−43	5.97766(2)	0.50	53,923	–	–	–	–
J1317−5759	2.6421979742(2)	0.38	53,426	12.54(2)	5.826(6)	3.337(6)	2.686(5)
J1443−60	4.758565(5)	0.42	53,410	–	–	–	–
J1754−30	1.32053(4)	1.21	53,928	–	–	–	–
J1819−1458	4.263170456(3)	0.07	53,479	575.0(3)	50.10(1)	0.11747(5)	29.31(1)
J1826−14	0.7706187(3)	0.26	53,587	–	–	–	–
J1839−01	0.93190(1)	1.61	51,038	–	–	–	–
J1846−02	4.476739(3)	0.36	53,492	–	–	–	–
J1848−12	6.7953(5)	0.03	53,158	–	–	–	–
J1911+00	6.94(2)	0.5	53,844	–	–	–	–
J1913+1333	0.9233885242(1)	0.22	53,264	7.87(2)	2.727(4)	1.860(6)	39.4(1)

is greater than 99%. Given the 0.7–7 s range of these periods (see Table 3.2), we inferred that these objects must certainly be rotating neutron stars, and hence termed them Rotating Radio Transients. Period measurements for individual objects will be discussed further in Sect. 3.3.

We are able to time the RRATs by measuring arrival times from individual bursts instead of from integrated profiles. For three of the RRATs (J1317−5759, J1819−1458 and J1913+1333) we can use the pulsar timing profile TEMPO to get phase-connected solutions and measure period derivatives. In Table 3.2 we list period, duty cycle, epoch of period measurement, period derivative, inferred surface dipole magnetic field strength, characteristic age and spin-down luminosity for the 11 sources. The inferred surface dipole magnetic field is calculated as $B \equiv 3.2 \times 10^{19}\sqrt{P\dot{P}}$ G, the characteristic age as $\tau_c \equiv P/2\dot{P}$ and the spin-down luminosity as $\dot{E} \equiv 4\pi^2 I\dot{P}P^{-3}$, where I, the neutron star moment of inertia, is assumed to be 10^{45} g cm^2 (see [38]). The duty cycles are generally smaller than the duty cycles of the cumulative profiles of radio pulsars with similar periods, but may or may not be similar to the duty cycles of single pulses for those pulsars.

3.3 Ongoing Radio Observations of the RRATs

We have been regularly observing all 11 original Parkes RRATs since August 2003 using the Parkes telescope with 1,400 MHz observations at roughly monthly intervals. We have also observed a number of these sources using the more sensitive Arecibo telescope and Green Bank Telescope (GBT). These observations show that the burst amplitude distributions, and perhaps spectral indices, are very different for different RRAT sources. For instance, two objects, J0848−43 and J1754−30, have been shown to be relatively normal pulsars when subjected to higher sensitivity, low frequency observations with the GBT. However, low frequency GBT observations

have not resulted in an increased burst detection rate for several other sources such as J1826−14 and J1846−02. In this section, we describe the results of ongoing radio observations for individual objects.

3.3.1 J0848−43

This RRAT with a 5.98 s spin period had a burst detection rate of one per 40 min when observed with Parkes at 1,400 MHz. However, in a 1-h observation with the Green Bank Telescope (GBT) at 350 MHz in July of 2006 (see Fig. 3.7), we detected one bright (S/N = 14) burst and many weaker (S/N < 8) individual pulses, showing that our Parkes observations were only revealing the tail end (see Fig. 3.8) of a continuous pulse amplitude distribution. We also found that the source is detectable in an FFT or by folding the entire 1-h observation. Three additional epochs confirm

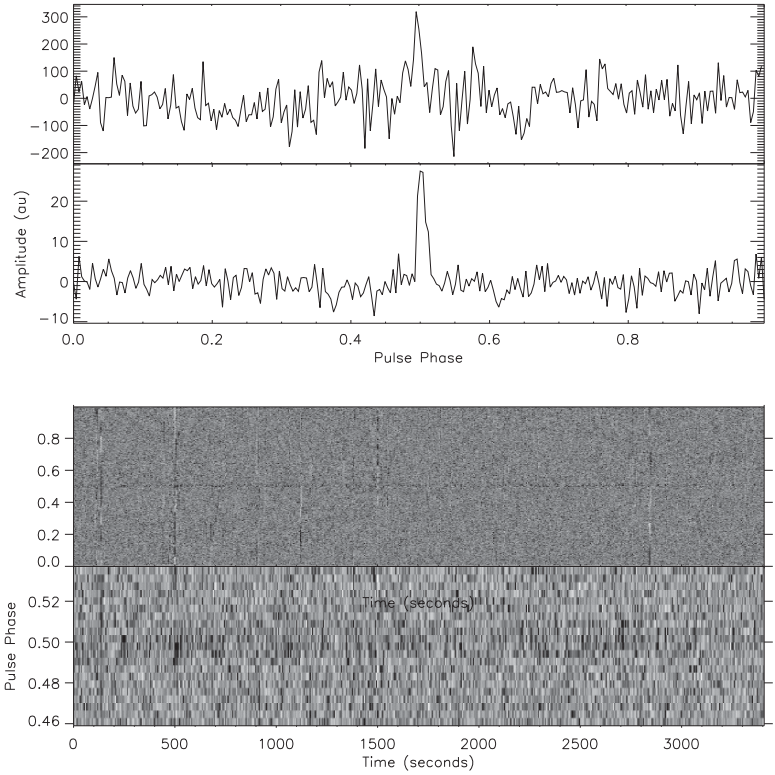

Fig. 3.7 GBT observation at 350 MHz of J0848−43. From *top to bottom*, plots show profile of the brightest individual burst, integrated pulse profile, gray-scale plot of pulse intensity vs. time and same gray-scale but zoomed in on the region of the pulse

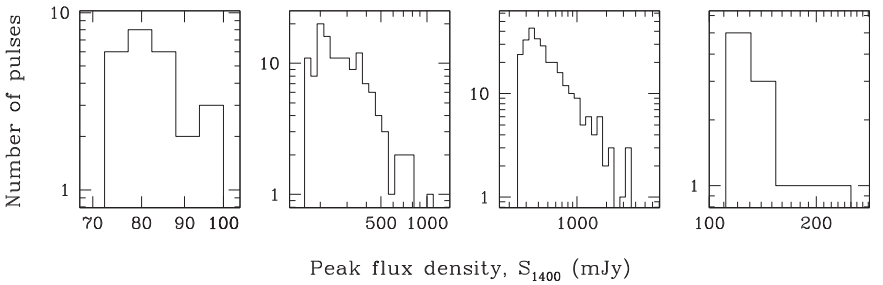

Fig. 3.8 Histograms of the peak flux densities for (*from left to right*) J0848−43, J1317−5759, J1819−1458 and J1846−02 measured with 1,400 MHz Parkes observations. The lower bound of all histograms corresponds to a threshold of 6σ. The minimum detectable flux density varies due to the different burst widths. The burst amplitude distributions are described by power laws of index $\sim$1, less steep than those of giant pulsing pulsars [34]

that the source is always continuously detectable with the higher sensitivity of the GBT and can therefore be timed through standard pulsar timing observations. We expect our GBT observations of this source to yield a period derivative shortly.

3.3.2 J1317−5759

This RRAT with a 2.64 s spin period has a sufficiently high burst rate to enable a period derivative measurement with Parkes, placing its spin-down parameters in the range of the normal pulsar population (see Fig. 3.13). We have ample Parkes data for inferring statistics on its burst rates, which appear to be roughly consistent with Poisson statistics, and amplitude distributions, which are well described by a power-law of index 1.3. Note that giant-pulsing pulsars also show power-law amplitude distributions, but they are typically steeper [34]. This phase-connected solution and hence accurate position of this RRAT has enabled X-ray observations, the result of which will be described in Sect. 3.4.

3.3.3 J1443−60

This RRAT has a spin period of 4.47 s and Parkes 1,400 MHz burst detection rate of only one per 75 min, making it very difficult to measure a period derivative thus far. Our statistics are not sufficient to accurately measure a burst amplitude distribution or infer robust burst rate statistics for this source, but it appears the distribution is roughly flat (i.e. not consistent with being the tail end of a uniform distribution of pulse amplitudes) and there is little evidence for nulling or quasi-periodic on/off states. Unfortunately, the low declination prohibits observations with other radio telescopes.

3.3.4 J1754−30

This RRAT with a 1.32 s period is a fairly sporadic emitter in our Parkes observations. However, like J0848−43, it is detectable as normal pulsar in GBT observations at 350 MHz. We are currently timing this pulsar with the GBT and expect a period derivative measurement shortly.

3.3.5 J1819−1458

The brightness and high bursting rate of this RRAT have allowed a phase-connected timing solution which shows that this 4.26 s period RRAT is relatively young, with a characteristic age of 117 kyr, and has a high inferred surface dipole magnetic field of 5×10^{13} G. X-ray observations of this source are described in Sect. 3.4. We find the burst amplitude distribution to be fit well by a power-law with index of 1.2, again flatter than the indices seen for giant-pulsing pulsars. We can also fit the burst rate distribution of the source extremely well to a Poisson distribution (i.e. the bursts appear to arrive at truly random intervals, with no evidence for clustering or nulling). One puzzling aspect of this source, however, is its spectral index. So far, two observations with the GBT at 350 MHz have failed to detect *any* emission from J1819−1458. We are unsure whether this is due to statistical fluctuations, scattering or if there is indeed something anomalous about its spectral index. We are planning intermediate frequency GBT observations to determine the cause.

3.3.6 J1826−14

Our Parkes observations of this RRAT with a 770 ms period show it to be an extremely sporadic emitter, with evidence for long timescale nulling behavior. In some observations of this source, we detect burst rates as high as one every 100 s. However, we did not detect this source at all in monthly observations from September 2005 until December 2006. There may be some quasi-periodicity to these on-off periods, as seen for intermittent pulsars such as B1931+24 [35] but we require additional data to determine its long timescale. This source was not detected in a half-hour GBT observation at 350 MHz, and only a single burst was detected in a second 1-h observation, showing that is a truly sporadic emitter.

3.3.7 J1839−01

In its original discovery observation, eight bursts with a clear underlying periodicity of 931 ms were detected, with all bursts showing the expected dispersion sweep and

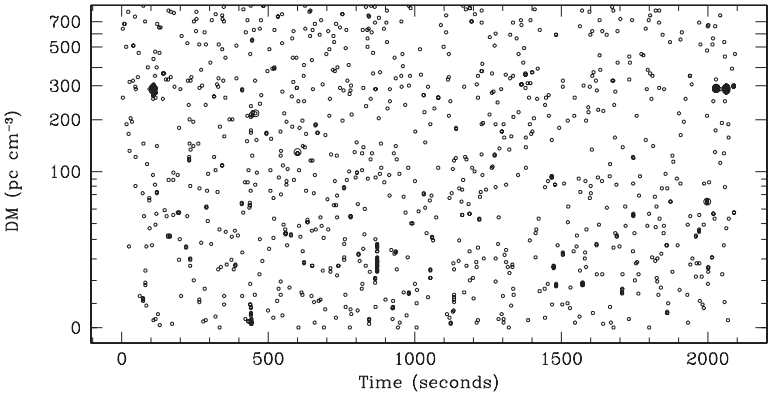

Fig. 3.9 Discovery observation of J1839−01 in the PMPS. Three bursts at ∼100 s and five bursts at ∼2,000 s are detected at a DM of 307 pc cm^{-3}. An underlying periodicity of 931 ms is evident upon inspection of the arrival times of the bursts

having similar pulse profiles. However, this RRAT has not been detected since its original discovery in the PMPS data (taken in 1998). We have also failed to detect this source in two 1-h long integrations with the GBT at 350 MHz. We therefore infer that this is a very long timescale nuller. In Fig. 3.9 we present the original discovery observation of this object. Note that the source shows two on periods, indicating that it also nulls on short timescales.

3.3.8 J1846−02

This source with a 4.47 s period also seems to be a long timescale nuller. While the overall rate of burst detection for this source is only one every 54 min, most of the detected bursts arrive in clusters of several occurring within a few minutes of observation. This source was not detected in two 1-h GBT observations at 350 MHz, likely due to it truly sporadic nature.

3.3.9 J1848−12

Although we see no evidence for any short or long timescale nulling behavior, we detect only roughly one burst every 45 min in 1,400 MHz Parkes observations of this source. In GBT observations of this source, however, we detect bright (S/N $>$ 20) bursts at a rate four times greater than with Parkes. Unlike J0848−43 and J1754−30, we see no evidence for normal pulsar radio emission that can be detected in a time-averaged way. We believe that with regular GBT observations where we measure single-pulse arrival times, we will be able to measure a period derivative for this object.

3.3.10 J1911+00

This source is extremely sporadic, with no more than one burst at any epoch detected with Parkes and an average burst detection rate of only one burst per 3 h. Therefore, a period measurement was not possible from the Parkes data. Arecibo observations of this source at 327 MHz, however, result in a burst detection rate of and have allowed us to measure a tentative period of 6.9 s, though we see no evidence that this object shows normal pulsar-like emission.

3.3.11 J1913+1333

Parkes observations of this fairly prolific RRAT with a 923 ms period allowed us to measure a period derivative, placing this source in a well-populated region of spin-down parameter space (Fig. 3.13). While our Parkes observations revealed only isolated bursts, more sensitive Arecibo observations of this object at 327 MHz have shown that it exhibits distinct on and off states, as shown in Fig. 3.10. During on states, which can last for several minutes, many pulses are observed, while in the off states we can detect no radio emission whatsoever. Our Arecibo observations have allowed us to study the nulling behavior in more depth and have also enabled us to time this source with higher precision, with the position now determined to better than 1 arcsecond. Unfortunately, the rather large age and the high inferred distance, and thus neutral hydrogen column density, are not encouraging for X-ray detection (see Sect. 3.4).

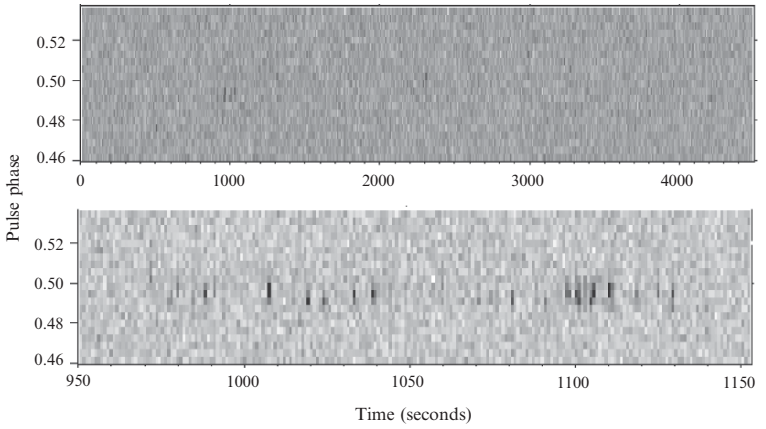

Fig. 3.10 Arecibo observation at 327 MHz of J1913+1333. *Top and bottom* plots show individual bursts throughout the entire observation and during the first on phase at ∼1,050 s

All 11 of the original Parkes RRATs are being continually monitored at radio wavelengths using either the Parkes, Arecibo or Green Bank telescopes. The frequency of monitoring varies from source to source. For instance, we are awaiting an intensive campaign on J0848−43 and J1754−30 with the GBT to yield initial phase-connected solutions, but are only observing J1839−01 once every few months with Parkes, due to its apparent long-period nulling behavior. For all of the RRATs our ultimate goal is to measure period derivatives as this is the only way to connect them with other classes of neutron stars, and to measure more accurate positions that will enable follow-up observations at higher energies. We are also undertaking a campaign to obtain polarization and spectral properties of the single pulses. This should provide useful comparisons with the properties of giant-pulsing and nulling pulsars.

3.4 X-Ray Properties of the RRATs

With periods longer than those of the majority of radio pulsars, the spin-down properties of the RRATs and lack of persistent radio emission suggest a relationship with the X-ray dim isolated neutron stars (XDINS). These seven soft X-ray sources (e.g. [21]) have blackbody spectra with $kT \sim 50$–$120\,\mathrm{eV}$, X-ray periods in the range 3–11 s, and X-ray luminosities $L_X \sim 10^{31}\,\mathrm{ergs\,s^{-1}}$. The high magnetic field and period of J1819−1458 also suggest a relationship with the magnetars, which are characterized by quiescent, bursting, and flaring X-ray emission powered by ultra-strong magnetic fields. They typically have $kT \sim 0.3$–$0.6\,\mathrm{keV}$, non-thermal spectral components with $\Gamma \sim 2$–4 and have high X-ray luminosities $L_X \sim 10^{34}$–$10^{36}\,\mathrm{ergs\,s^{-1}}$ [62]. Of course, normal radio pulsars can also be detected at X-ray energies. The pulsar B0656+14, which [60] have suggested is a nearby RRAT source (see Sect. 3.4), is one of three middle-aged pulsars (i.e. "The Three Musketeers"; [2]) from which pulsed high-energy emission has been detected (e.g. [43]). The spin-down properties of J1819−1458 of course also encourage comparisons with those of high magnetic field pulsars radio pulsars. Four high magnetic field (i.e. $B > 4 \times 10^{13}\,\mathrm{G}$) have been observed at X-ray energies. Two show no X-ray emission, and the other two have kT ranging from 150–200 eV and luminosities of 10^{32}–$10^{33}\,\mathrm{ergs\,s^{-1}}$ [18, 31, 47, 49]. None show any evidence for AXP-like high luminosities or bursting behavior.

Clearly, given the similarities with all of these populations, X-ray observations of the RRATs are crucial for determining their relationship to these other classes of neutron stars. Unfortunately, the positions of most of the RRATs are very poorly constrained to within the $14'$ beam-width of the Parkes telescope at 1,400 MHz. Therefore, only for the three RRATs with phase-connected solutions, and hence accurate timing-derived positions, are X-ray observations possible. We report on X-ray observations of those three objects (J1317−5759, J1819+1458 and J1913+1333) here.

3.4.1 J1317−5759

We obtained a 32 ks observation of J1317−5759 on 16 July 2006 with *XMM-Newton*. The European Photon Imaging Camera (EPIC) PN and MOS instruments were both operated with medium filters and in Small Window mode, providing a time resolution of 6 and 300 ms and effective lifetimes of 71% and 97.5%, respectively. The data were reduced using the *XMM-Newton* Science Analysis System (SAS version 7.0.0) and the most recent calibration files, with a final net exposure time of 30 ks. There is no point source detected at the position of the pulsar. Given the 3 kpc distance, estimated neutral hydrogen column density N_H of 5×10^{21} cm^{-2}, and assuming a blackbody spectrum with $kT = 0.13$ keV, we calculated an upper limit to the absorbed 0.3–5 keV flux of 2.6×10^{-14} ergs s^{-1} cm^2. This translates to an unabsorbed luminosity in the 0.3–5 keV band of 8×10^{32}. This is not very constraining for the nature of the source, as it is lower than the X-ray luminosities of all XDINSs.

We used a 20′ extraction region centered on the source position to create an X-ray lightcurve. No pulsations were detected through an FFT or by folding the data with the radio ephemeris. Likewise, we find no evidence for X-ray bursts or variability on any timescales. Unfortunately, searching for long-term variability is not possible, as there is no detection of a point source at the position of this RRAT in the ROSAT All-Sky Survey [61], and there are no archival observations encompassing this position.

3.4.2 J1819−1458

This RRAT was serendipitously detected by *Chandra* in an observation of the (unrelated) supernova remnant G15.9+0.2 [54]. In this 30 ks ACIS-I observation, we detected a point source at the position of the pulsar with high significance. The spectrum of the source could be well-described by an absorbed blackbody with neutral hydrogen column density $N_H = 7^{+7}_{-4} \times 10^{21}$ cm^{-2} and temperature $kT = 0.12 \pm 0.04$ keV, with an absorbed flux of $\sim 1 \times 10^{-13}$ ergs cm^{-2} s^{-1} between 0.3 and 5 keV. These properties are consistent with emission from a cooling neutron star of age 10^4–10^5 years, broadly in agreement with the 117 kyr characteristic age of PSR J1819−1458. No evidence for bursts or variability was found, and the time resolution of the data was not sufficient for a sensitive search for periodicity.

In order to better characterize the spectrum and search for X-ray pulsations, we obtained a 43 ks *XMM-Newton* observation on 5 April 2006, with observational setup identical to that described in Sect. 3.4.1. We first performed a blind periodicity search, detecting a signal at the expected radio period with high significance. In Fig. 3.11, we show the X-ray data folded with the radio ephemeris; the radio pulse and the X-ray pulsations are aligned within the uncertainties. The X-ray pulsations can be described by a sinusoid and have a pulsed fraction of $34 \pm 6\%$, defined as $(F_{max} - F_{min})/(F_{max} + F_{min})$, where F_{max} and F_{min} are the minimum and

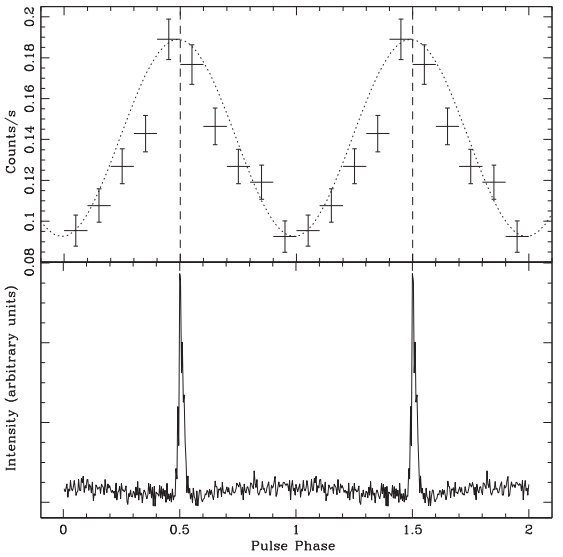

Fig. 3.11 X-ray pulse profile for EPIC-PN, MOS1 and MOS2 data on RRAT J1819−1458. The *dotted line* shows the best-fit sinusoid and the *vertical dashed line* indicates the phase of the peak of the radio bursts. *Bottom*: radio burst profile formed from 114 bursts detected in 6 h of observation at 1.4 GHz with the Parkes telescope

maximum values of the X-ray pulse profile. We also used these data to search for bursts or aperiodic variability. We find no evidence for either on timescales of 6 ms to the duration of the observation and can place the most stringent limit to date of $\leq 3 \times 10^{-9}$ ergs cm^{-2} s^{-1} on the absorbed 0.3–5 keV flux of any bursts.

The spectral analysis of this source was not trivial, as features around 0.5 and 1 keV do not allow a good fit for any single component spectral model. We checked whether these features might be due to calibration issues, to our source and background extraction regions or to residual particle flares and/or particles hitting the detector, and could reliably exclude all of these. We tentatively conclude that the 0.5 keV feature is due to the Oxygen edge (i.e. caused by an overabundance of Oxygen in the direction of the source) and excluded this from the modeling. As shown in Fig. 3.12, we find that we can fit the spectrum well by an absorbed blackbody with $kT = 0.14$ keV with the addition of an absorption feature at 1 keV, with total absorbed flux of 1.5×10^{-13} ergs cm^{-2} s^{-1} (0.3–5 keV). The unabsorbed luminosity in the 0.3–5 keV band is 3.9×10^{33} ergs s^{-1}. This is larger than the RRAT's spin-down luminosity, as for the magnetars, though of course for thermal emission there is no reason why this cannot be so.

Table 3.3 lists all of the models giving satisfactory results (given our limited number of counts). From Monte Carlo simulations [52] we infer the significance of the 1 keV line to be 4σ. We tried to perform pulse phase-resolved spectroscopy, dividing the observation in two phase intervals, but the limited number of counts did not allow us to strongly constrain the spectral variability with pulse phase. Furthermore, we found a hint of an additional non-thermal component with $\Gamma \sim 1$ dominating the

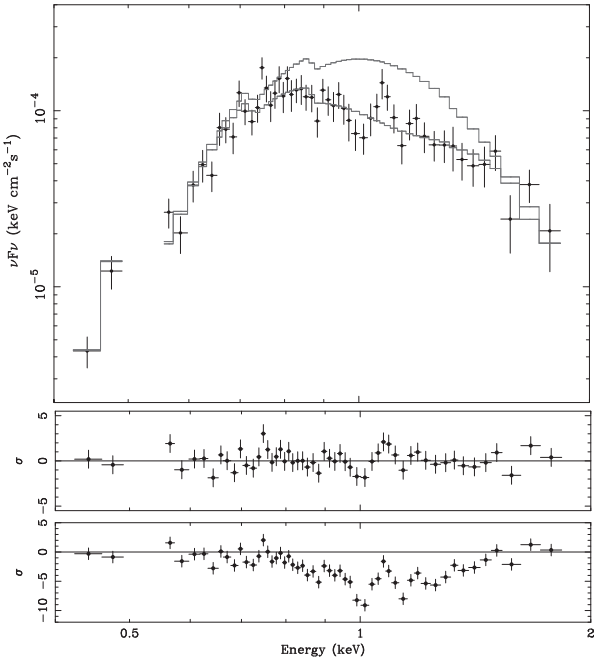

Fig. 3.12 *Top*: *XMM-Newton* EPIC-PN νF_ν spectrum of RRAT J1819−1458, modeled as an absorbed blackbody and Gaussian line (column 2 of Table 3.3). The *points* indicate the data, while the *solid line* shows the corresponding best fit model. *Top line* shows the absorbed blackbody model component of the fit alone. *Middle*: residuals of the absorbed blackbody and Gaussian line model. *Bottom*: residuals of the model without the inclusion of the Gaussian line

Table 3.3 Spectral fits for RRAT J1819−1458 with EPIC-PN. Fluxes are calculated in the 0.3–5 keV energy range, and reported in units of 10^{-13} ergs s^{-1} cm^{-2}. N_H is in units of 10^{22} cm^{-2} and N_{Ne} is in solar units. The values of kT (blackbody temperature), E_G (Gaussian line energy), σ_G (Gaussian line width), E_e (edge threshold energy), E_{cy} (cyclotron line energy) and w_{cy} (cyclotron line width) are in units of keV. The Gaussian line depth τ_G, edge depth τ_e and fundamental cyclotron line depth d_{cy} are dimensionless. Errors are at the 1σ confidence level

Blackbody	(BB) plus Neon	BB plus Gaussian		BB plus edge		BB plus cyclotron	
N_H	$0.59^{+0.06}_{-0.04}$		$0.75^{+0.12}_{-0.09}$		0.57 ± 0.06		$0.81^{+0.09}_{-0.08}$
N_{Ne}	6 ± 1	E_G	$1.11^{+0.04}_{-0.03}$	E_e	$0.92^{+0.03}_{-0.01}$	E_{cy}	$0.99^{+0.03}_{-0.02}$
		σ_G	$0.21^{+0.03}_{-0.06}$			w_{cy}	$0.37^{+0.03}_{-0.06}$
		τ_G	150 ± 60	τ_e	0.67 ± 0.14	d_{cy}	1.2 ± 0.2
kT	$0.144^{+0.008}_{-0.006}$		$0.136^{+0.012}_{-0.008}$		$0.150^{+0.005}_{-0.006}$		$0.144^{+0.008}_{-0.006}$
Abs. Flux	$1.5^{+0.3}_{-0.5}$		$1.5^{+0.6}_{-0.8}$		$1.5^{+0.3}_{-0.6}$		$1.5^{+0.3}_{-0.4}$
χ^2_ν (d.o.f.)	1.20 (50)		1.19 (48)		1.17 (49)		1.13 (48)

spectrum above 1.7 keV. However, the addition of a further component was not statistically significant given our limited number of counts and the high background which dominates the spectrum above 2 keV.

The two main interpretations for the 1 keV line are as an atomic or cyclotron line. An atomic line could be due to the NS atmosphere or, less probably, to a peculiar abundance in the ISM. The structure in the residuals (see Fig. 3.1 middle panel), which in our data is not significant, might be due to a blending of narrow lines which are unresolved due to limited counts. If the feature is due to proton cyclotron resonant scattering, the magnetic field inferred would be 2×10^{14} G, broadly consistent (within the assumptions implicit in timing-derived magnetic fields) with that measured through radio timing of the bursts. In addition, the width and depth of the line are consistent with predictions for proton-cyclotron absorption in highly magnetized neutron stars [63]. It is possible, although unlikely, that the 1 keV feature is the first harmonic, with the 0.5 keV fundamental coincident with the depression in the spectrum that we have interpreted as due to an overabundance of Oxygen. More counts are needed to differentiate between these scenarios. Moreover, phase-resolved spectroscopy is crucial for differentiating between the atomic and cyclotron models, with phase variations expected in the cyclotron hypothesis. If the feature we detect is indeed due to proton-cyclotron absorption, it provides an invaluable means of testing the assumptions implicit in characteristic magnetic fields derived through radio timing and an extremely valuable independent measurement of the magnetic field of an isolated neutron star. Confirming the line and determining its nature is also important for relating this source to other NSs. Cyclotron and atmospheric absorption lines, although strongly predicted by theory, have been observed only for a handful of isolated neutron stars [4, 21, 33], making J1819−1458 a very interesting object.

In summary, the XMM observations of J1819−1458 have confirmed the neutron star nature of J1819−1458 through the detection of X-ray pulsations. They also verify the method used for measuring the radio periods of the RRATs. The X-ray spectrum and luminosity of J1819−1458 are not consistent with magnetar properties, though the soft X-ray spectrum does have a comparable temperature to the quiescent state of XTE J1810−197 ($kT \sim 0.15$–0.18 keV [20, 28]. However, the radio emission characteristics of these two neutron stars are quite different; we only detect roughly one in 50 bursts from J1819−1458, whereas every pulse is detectable with fairly steady flux from XTE J1810−197 [7]. The spectrum, variability and pulse properties are consistent with thermal emission from a cooling neutron star and with the properties of both the XDINSs and the X-ray detected radio pulsars.

3.4.3 J1913+1333

This 5.7 kpc estimated distance to this object makes it an difficult X-ray target. Nonetheless, this RRAT was observed with *Swift*-XRT on 20 November 2005 for an exposure of 9.3 ks (Rea, N., priv. com.). Data was analysed as reported in [53]. No X-ray counterpart was detected, with an upper limit on the *Swift*-XRT count rate of 0.036 counts/s, which translates to an absorbed 0.3–5 keV flux of 7.6×10^{-13} ergs s^{-1} cm^{-2}, assuming an absorption (derived from the DM) of $N_H =$

$8 \times 10^{21}\,\mathrm{cm}^{-2}$ and a blackbody spectrum with $kT = 0.13\,\mathrm{keV}$. This translates to a very unconstraining unabsorbed luminosity limit (0.3–5 keV) of $9.4 \times 10^{34}\,\mathrm{ergs\,s}^{-1}$. Very deep X-ray observations will be required to reach luminosities comparable to those of the XDINSs or of radio pulsars of similar ages.

3.5 What Are They?

As shown in Fig. 3.13, the P and $\dot{P}$ measurements for two RRATs place in the central region of the P–$\dot{P}$ diagram, implying that their spin-down properties cannot be solely responsible for their unusual emission. The third RRAT with measured period derivative, J1819−1458, is in the region of the P–$\dot{P}$ diagram populated by the high

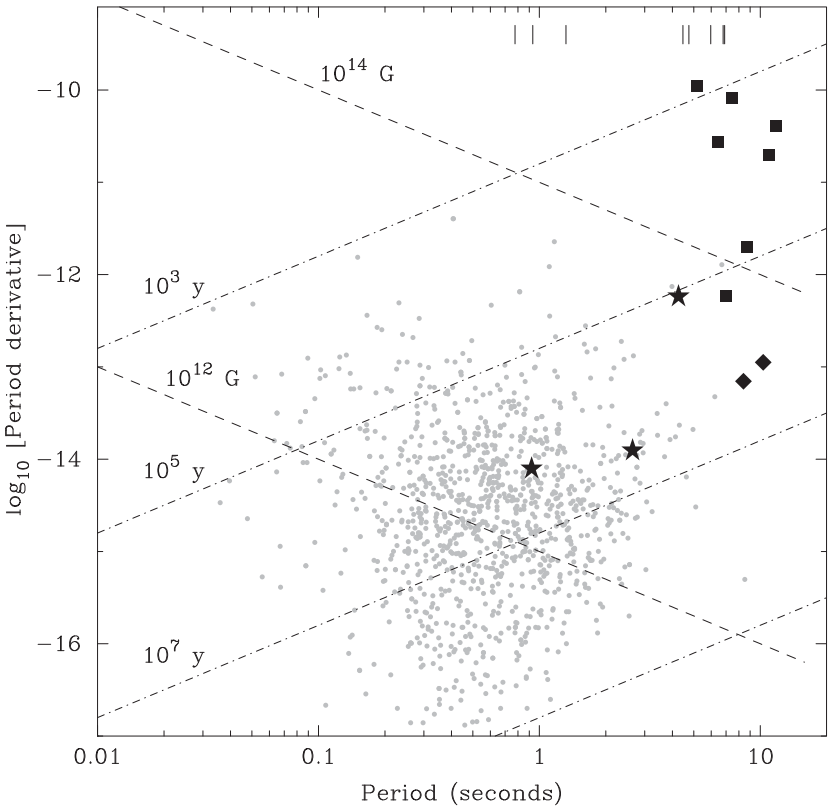

Fig. 3.13 The rotational properties of neutron stars summarized in a P–$\dot{P}$ diagram. The rotational period derivative is plotted against period for pulsars (*dots*), magnetars (*squares* [62]), the isolated neutron stars with measured period and period derivative (*diamonds* [30]), and the three RRATs having measured periods and period derivatives (*stars*). The *vertical lines* at the top of the plot mark the periods of the other eight sources in Table 3.2. *Dashed lines* indicate the loci of constant values of characteristic age and inferred surface dipole magnetic field strength

magnetic field radio pulsars, the XDINSs and the magnetars. Its inferred surface dipole magnetic field of 5×10^{13} G cannot be solely responsible for its bursting emission as other "normal" radio pulsars have higher magnetic fields. For example, PSR J1847−0130 has an inferred surface dipole magnetic field of 9×10^{13} G but shows no evidence for unusual radio emission [47]. As discussed in the previous section, the X-ray properties of this object are consistent with those of the normal radio pulsars and the XDINSs.

What is responsible for the unusual emission of these objects? The RRATs with measured period derivatives do not have high inferred values of magnetic field strength at the light cylinder. Since this is often associated with giant-pulse emission, this may imply that their emission mechanism is different from that responsible for the giant pulses observed from some pulsars (e.g. [34]). The pulse widths of the RRAT pulsars are also much larger than those of giant pulses. Other suggestions are that the RRATs may be neutron stars near the radio "death line" or may be related to "nulling" radio pulsars [64]. However, the period derivatives measured for three RRATs do not place them near canonical pulsar "death lines" (e.g. [8]) and, unlike most nulling pulsars (e.g. [59]), we typically do not see more than one pulse from the RRATs in succession. Another intriguing possibility is that the sporadicity of the RRATs is due to the presence of a circumstellar asteroid belt [13, 37] or a radiation belt such as those seen in planetary magnetospheres [44].

Note that the RRATs are not the first neutron stars which are known to show unusually sporadic emission. The 409 ms pulsar J1752+2359 exhibits strange bursting behavior characterized by 45 s on phases which occur every 3–5 min [36]. Even odder behavior is exhibited by the recently recognized class of intermittent pulsars, the most well-known of which is B1931+24 [35]. This 813 ms pulsar shows radio emission for 5–10 days, and then remains radio quiet for 25–50 days. It may be that the RRATs show similar quasi-periodicity, but that we are simply not sensitive to it on the timescales that we are sampling. Amazingly, the period derivative of B1931+24 is higher in the on state than in the off state, suggesting that a fundamental change in magnetospheric currents happens in the on state. We do not measure such period derivative changes in the RRATs, and their on times appear much shorter, but the physical mechanism responsible for these phenomena may be similar.

We hope to explore all of these ideas further through several avenues. First and foremost, more period derivatives may enable us to further constrain the likelihood that these are related to giant-pulsing pulsars or are pulsars near the P–$\dot{P}$ death line. We are also undertaking polarization observations of several of the RRATs; these are crucial for comparison with the polarization properties of the transient magnetars and of giant-pulsing and nulling pulsars. The idea that the emission of the RRATs, and also of intermittent pulsars and perhaps even moding and nulling pulsars, may be caused by external influences is extremely attractive, but these theories are rather difficult to test. Furthermore, It seems likely that the RRATs themselves are not a homogeneous group. Most likely there are several different reasons for their apparent sporadicity.

3.6 Population Estimates

We detect, on average, one burst for every 3 h of observation for J1911+00. The chance of detection within the single 35 min discovery observation was therefore less than 20%, implying that there should be roughly five times the number of similar sources in the same searched volume. It is easy to see, therefore, that the sporadicity of the RRATs results in substantially increased estimates of the total number of Galactic active radio-emitting neutron stars. Due simply to the bursting timescales of the 11 original Parkes RRATs, we expect there to be twice as many sources as we have detected at a similar sensitivity level and sky coverage. This number is likely a gross underestimate, however. Firstly, it is very difficult to identify such sources in observations which are contaminated with large amounts of impulsive interference. There may be at least twice as many RRATs that were missed due to this effect. Secondly, we are only extrapolating to the area covered by the Parkes survey, and the true distribution of these objects is unknown. In addition, because our sensitivity was diminished for burst durations greater than 32 ms, there may be more sources with longer bursts that fell below our detection threshold. Furthermore, the 11 Parkes RRATs were found from a single observer looking many plots for such signals by eye. It is likely that a second analysis would result in more of these sources being detected (as indeed it has; see Sect. 3.7). It is also important to remember that previous surveys with observations times of a few minutes had little chance of detecting such events and most did not include searches for them.

With these (substantial!) caveats in mind, we carried out a Monte Carlo simulation to provide a first-order estimate of the size of the Galactic RRAT population [48]. The simulation assumes that their spatial distribution follows that derived for the pulsars detected in the Parkes survey, that the burst-duration distribution is similar to that observed in the 11 original Parkes RRATs, and, as measured for the pulsar population [45], that the differential radio luminosity function of an average burst is of the form $d\log N/d\log L = -1$, where N is the number of model sources above a given luminosity $L = Sd^2$, where S is the peak flux density and d is the distance. By calculating the threshold of our survey to model bursts, and generating Monte Carlo realizations, we find the simulations produce a good match to the observations, but are fairly sensitive to the minimum burst peak luminosity $L_{\rm min}$ which could plausibly lie in the range 1–1,000 mJy kpc^2. While an $L_{\rm min}$ of 10 mJy kpc^2 is consistent with the lowest peak luminosities observed for the single pulses of known radio pulsars, this seems inconsistent with the observed luminosity distribution of the original Parkes RRATs (Fig. 3.14). We therefore adopt a minimum luminosity of 100 mJy kpc^2. Higher minimum luminosities are also consistent with the distribution. However, because of recent detections (see Sect. 3.7) of new, weaker RRATs, we believe 100 mJy kpc^2 to be more accurate. Our new simulations (Lorimer D.R., priv. com.) will include all new RRAT detections to set more robust limits.

To be consistent with the detection of 11 Parkes RRATs, the implied size of the Galactic population $N \sim 2\times10^5 (L_{\rm min}/100\,{\rm mJy\,kpc^2})^{-1} \times (0.5/f_{\rm on}) \times (0.5/f_{\rm int}) \times (0.1/f_b)$, where $f_{\rm on}$ is the fraction of sources with bursts visible within our 35 min observation, $f_{\rm int}$ is the fraction of bursts not missed due to interference and f_b is the

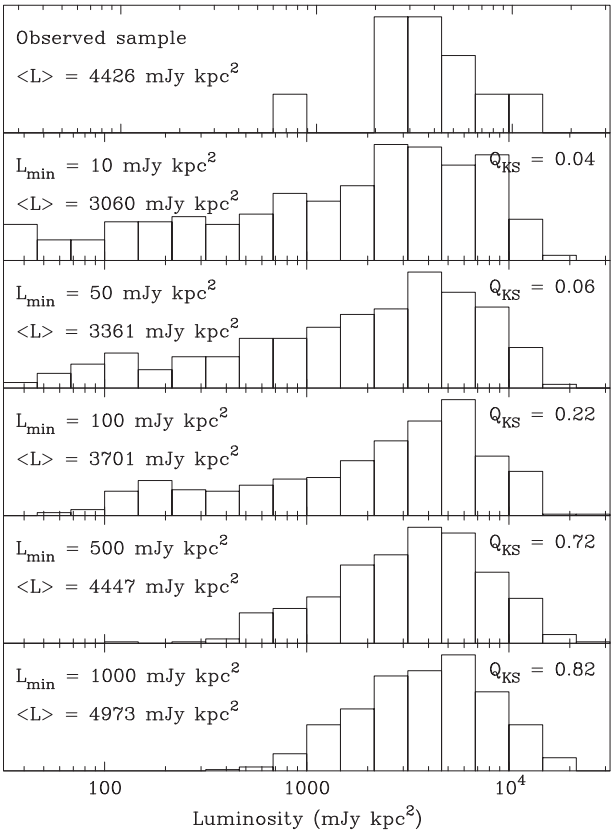

Fig. 3.14 Results of Monte Carlo simulations aimed at constraining the minimum peak luminosity of the RRAT bursts. The *top histogram* shows the minimum luminosity distribution of the Parkes RRATs, and the *bottom plots* show the Monte Carlo distributions for other minimum luminosities. The KS statistic (e.g. [51]) is shown, with low numbers indicating distributions not consistent with the observed

fraction of RRATs whose bursts are beamed towards the Earth. The average beaming fraction for pulsars is roughly 10%, and increases for longer period pulsars [57]. Given the small RRAT duty cycles, our adopted f_b is almost certainly a conservative overestimate. Assuming that the total Galactic population of active radio pulsars is of order 10^5 (e.g. [58]), this discovery increases the current Galactic population estimates by at least several times. This estimate does not account for the other classes of intermittent pulsars like B1931+24, which may boost the radio-emitting Galactic neutron star population even higher. A careful analysis of the birthrates of neutron stars is required to determine if this increased population is consistent with recent supernova rate estimates [16]. This issue was addressed by [50], who concluded that the agreement between the number of observed neutron stars and the supernova rate was comfortable, but this should be revisited.

This work has important implications for ongoing surveys. For instance, they suggest that PALFA surveys should detect roughly five RRATs, and that 10 such sources should be detectable in the 1,400 MHz intermediate and high latitude surveys with Parkes that have been carried out [5, 17]. However, as discussed in Sect. 3.7, recent discoveries suggest that these numbers may be underestimates. The discovery of the RRATs also has important implications for the future of various wide-field radio surveys such as the instruments such as the Extended New Technology Demonstrator (xNTD), the Karoo Array Telescope (KAT), the Low-Frequency Array (LOFAR) and the Square Kilometer Array (SKA). Based on the current design specification for these instruments, from our simulations we expect xNTD and KAT to discover of order 250 of these bursting sources while surveys with LOFAR and the SKA could find 800 and 20,000 of them, respectively.

3.7 Recent Discoveries

Since we first reported the RRATs' discovery, we and others have been applying single-pulse searches to archival data from several surveys and to new search data. This has, not surprisingly, resulted in the discovery of more of these objects.

The single-pulse search output from the Parkes Multibeam Pulsar Survey in which the 11 original RRATs were discovered is in the process of being carefully re-inspected, so far resulting in the discovery of six new RRATs. We have determined periods of 1.2 and 1.6 s for two of these objects from the initial discovery observations. The 1.2-s object lies in the field of view of another pulsar we are timing and so its period has been measured at multiple epochs. For the 1.6-s object, however, there is still a significant chance that the true period is an integer fraction of the measured period. Note the three of the six new objects show just a single non-zero DM burst. The DMs of these sources indicate that they are Galactic sources, unlike the [40] burst.

We also applied the same single-pulse search used in the Parkes Multibeam Pulsar Survey to the Parkes High Latitude Pulsar Survey [5], a 1,400 MHz multi-beam survey of latitudes $|b| < 60^\circ$ and $l = 220$–260°, which resulted in the discovery of 18 new pulsars. We are in the process of analyzing the single-pulse search output and, so far have detected three new sources of single pulses. One of these has been found to be a 1.5 s pulsar which is usually detectable through a standard FFT analysis. The other two sources have too few bursts to allow a period measurement, and await further observations.

We have also incorporated a single-pulse search into the processing of our 1,400 MHz Parkes Deep Multibeam Survey of the Northern Galactic plane, covering $|b| < 1^\circ$ and $l = 50$–60° with 70 min observations.[1] This survey has so far resulted in 13 new pulsars and one object not detectable in the standard periodicity search. This object has a period of 1.9 s, measured from 22 single pulses detected over the course of the observation.

[1] www.as.wvu.edu/~pulsar/dmb.

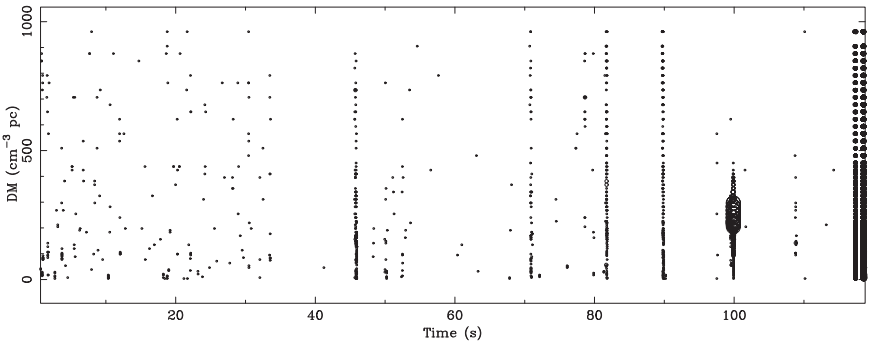

Fig. 3.15 Single pulse search output for J1928+15. We detect three consecutive bursts from this source, separated by 403 ms, around a time of 100 s

Several RRAT-like sources have also been detected in a 350-MHz survey of the Galactic plane with the GBT [25], covering $|b| < 5.5^\circ$ and $l = 75$–165° with 120 s integrations. Of the 33 new pulsars discovered, five were identified through single, dispersed bursts. Three of these appear to have properties consistent with the Parkes RRATs. The rather high rate of single-pulse to standard search detections of this survey may be due to its relatively short integration time (see Fig. 3.12). This survey has also resulted in the discovery of another quasi-periodic nuller like J1752+2359.

The Pulsar Arecibo L-band Feed Array Survey (PALFA) commenced in late 2003 and utilizes a seven-beam, 1,400 MHz receiver on the Arecibo telescope. This survey is expected to cover the entire Galactic plane visible from Arecibo with 268 s pointings, with the multiple beams offering a similar discrimination against RFI as the PMPS. So far, there have been three objects detected in the single-pulse search that were not detectable with the standard search algorithm for which we can measure periods. Two of these are pulsars which are sometimes detectable in standard FFT searches, but that are slightly more "bursty" than normal pulsars. The third object appears to be a long timescale nuller like some of the Parkes RRATs. Three pulses were detected in the original Arecibo observations, separated by 403 ms (see Fig. 3.15), but the source has never been re-detected, despite multiple followup observations. There are several additional candidates from the single-pulse search that await confirmation. The single-pulse analysis of the PALFA data will be reported soon [15]. Note that due to the nature of the RRATs, most of the new objects found in the single-pulse search with Arecibo will *only* be able to be followed up with Arecibo.

3.8 Concluding Remarks

Even 40 years after the discovery of the first radio pulsar, these remarkable objects continue to surprise us with new and varied phenomenology. The mainstream inclusion of single-pulse searches into standard pulsar search pipelines has resulted in

many radio pulsars that are detectable only through their burst emission. The properties of these RRATs are extremely varied. For some sources, we see clear on and of phases and for others we see random isolated bursts. Some objects appear to be very extreme nullers, while others are very similar to normal radio pulsars. Several ideas have been put forth to explain the unusual emission form these sources; it is likely that different explanations apply to different RRATs. The multitude of suggestions highlight our still very poor understanding of the radio pulsar emission mechanism.

Much work remains to be done on the original Parkes RRATs. We are optimistic that period derivatives will be measured soon for some RRATs, allowing comparisons with other neutron stars and facilitating more multi-wavelength observations. We also accept that, for some of the very sporadic sources, period derivatives may simply not be possible. We hope to detect more of the RRATs with measured period derivatives at X-ray energies, for comparison with the X-ray properties of J1819−1458 and other neutron stars. Followup observations on the RRATs detected in other surveys will give us a much better picture of the RRAT population, and also allow more accurate estimates of the number of such sources in the Galaxy. It is clear that the discovery of the RRATs, and other sporadic emitters like the intermittent pulsars, dramatically increase estimates of the radio emitting neutron star population.

These new objects highlight the importance of including searches for transient events in pulsar searches and, along with other recent discoveries in the transient radio sky, hint at the rich variety of transient sources that remain to be discovered by future wide-field instruments such as SKA demonstrators and the SKA itself. In addition to increased sensitivity, these instruments will make multiple passes of the sky, increasing the chances of finding the more intermittent sources. Furthermore, they will have better localization capability, facilitating identifications with sources at other wavelengths.

References

1. Aller, H. D. et al., 1985, ApJS, 59, 513.
2. Becker, W. & Trümper, J., 1997, A&A, 326, 682.
3. Berger, E. et al., 2001, Nature, 410, 338.
4. Bignami, G. F. et al., 2003, Nature, 423, 725.
5. Burgay, M. et al., 2006, MNRAS, 368, 283.
6. Burke, B. F. & Franklin, K. L., 1955, J Geophys Res, 60, 213.
7. Camilo, F. et al., 2006, Nature, 442, 892.
8. Chen, K. & Ruderman, M., 1993, ApJ, 408, 179.
9. Cognard, I. et al., 1996, ApJ, 457, 81.
10. Cohen, R. J. & Brebner, G. C., 1985, MNRAS, 216, 51.
11. Cordes, J. M. & Lazio, T. J. W., 2002, (astro-ph/0207156).
12. Cordes, J. M & McLaughlin, M. A., 2003, ApJ, 596, 1142.
13. Cordes, J. M. & Shannon, R. M., 2006, ApJ, 682, 1152 (astro-ph/0605145).
14. Cordes, J. M. et al., 2004, ApJ, 612, 375.

15. Deneva, J., 2007, in *Proceedings of the 363. WE-Heraeus Seminar on: Neutron Stars and Pulsars*, eds. W. Becker, H. H. Huang, MPE Report 291, pp. 52–55
16. Diehl, R. et al., 2006, Nature, 439, 45.
17. Edwards, R. T. et al., 2001, MNRAS, 326, 358.
18. Gonzalez, M. E. et al., 2005, ApJ, 630, 489.
19. Goodman, J., 1997, New Astron, 2, 449.
20. Gotthelf, E. V. et al., 2004, ApJ, 605, 368.
21. Haberl, F., 2007, A&SS, 308, 181.
22. Hallinan, G. et al., 2007, ApJ, 663, L25.
23. Hankins, T. H. et al., 2003, Nature, 422, 141.
24. Hankins, T. H. et al., 2003, Nature, 422, 141.
25. Hessels, J. W. T. et al., 2007, (astro-ph/0710.1745).
26. Hobbs, G. et al., 2005, AJ, 129, 1993.
27. Hyman, S. D. et al., 2005, Nature, 434, 50.
28. Ibrahim, A. I., et al., 2004, ApJ, 609, L21.
29. Johnston, S. & Romani, R., 2003, ApJ, 590, L95.
30. Kaplan, D. L. & van Kerkwijk, M. H., 2005, ApJ, 628, L45.
31. Kaspi, V. M. & McLaughlin, M. A., 2004, ApJ, 618, L41.
32. Kedziora-Chudczer, L. L. et al., 2001, MNRAS, 325, 1411.
33. van Kerkwijk, M. H. & Kaplan, D. L., 2007, A&SS, 308, 191.
34. Knight, H. S., 2006, Chin J Astron Astrophys Suppl, 6, 41.
35. Kramer, M. et al., 2006, Science, 312, 549.
36. Lewandowski, W. et al., 2004, ApJ, 600, 905.
37. Li, X-D., 2006, ApJ, 646, L139.
38. Lorimer, D. R. & Kramer, M., 2005, Cambridge University Press, 2005.
39. Lorimer, D. R. et al., 2006, MNRAS, 372, 777.
40. Lorimer, D. R., Bailes, M., McLaughlin, M. A., et al., 2007, Science, 318, 777
41. Lovell, A. C. B., 1964, Nature, 201, 1013.
42. Lovell, B, & Solomon, L. H., 1966, The Observatory, 86, 16.
43. De Luca, A. et al., 2005, ApJ, 623, 1051.
44. Luo, Q. & Melrose, D., 2007, MNRAS, 378, 1481.
45. Lyne, A. G. et al., 1998, MNRAS, 295, 743.
46. McLaughlin, M. A. & Cordes, J. M., 2003, ApJ, 596, 982.
47. McLaughlin, M. A. et al., 2003, ApJ, 591, L135.
48. McLaughlin, M. A. et al., 2006, Nature, 439, 817.
49. Pivovaroff, M., Kaspi, V. M. & Camilo, F., 2000, ApJ, 535, 379.
50. Popov, S. B., Turolla, R. & Possenti, A., 2006, MNRAS, 369, L23.
51. Press, W. H. et al., 1986, *Numerical recipes: the art of scientific computing*, Cambridge University Press, Cambridge.
52. Rea, N. et al., 2007, A&SS, 308, 505.
53. Rea, N. et al., 2007, ApJ, 661, L65.
54. Reynolds, S. P. et al., 2006, ApJ, 639, L71.
55. Romani, R. & Johnston, S., 2001, ApJ, 557, L93.
56. Staelin, D. H., 1969, Proc IEEE, 57, 724.
57. Tauris, T. M. & Manchester, R. N., 1998, MNRAS, 298, 625.
58. Vranesevic, N. et al., 2004, ApJ, 617, L139.
59. Wang, N., Manchester, R. N. & Johnston, S., 2007, MNRAS, 377, 1383.
60. Weltevrede, P. et al., 2006, ApJ, 645, L149.
61. White, N. E., Giommi, P. & Angelini, L., 1994, BAAS, 185, 4111.
62. Woods, P. M. & Thompson, C., 2006, in *Compact stellar X-ray sources*, 547.
63. Zane, S. et al., 2001, ApJ, 560, 384.
64. Zhang, B., Gil, J. & Dyks, J., 2007, MNRAS, 374, 1103.

Chapter 4
Intermittent Pulsars

Andrew G. Lyne

4.1 Introduction

Transient phenomena are usually difficult to find and characterise, particularly if much of the time is spent in a null state. This is true of two recently discovered types of transient radio source, namely the Rotating Radio Transient sources (RRATs) and the Intermittent Pulsars. Both spend much of their time invisible in quite different ways, and both have underlying periodicities which are attributable to rotating magnetic neutron stars. In these circumstances, they also represent the small tips of much larger populations which may cause us to revise our views of what "normal" neutron star behaviour is. RRATS are objects which emit occasional single pulses of radio emission, perhaps once every 100–1,000 rotation periods of the neutron star. The phenomenon is described in detail elsewhere in this volume [9]. The intermittent pulsars on the other hand behave like normal regular pulsars for intervals of time measured in days or years, with longer intervals when there is no emission at all. In this paper, we discuss the phenomenon, the search for other instances, the implications for pulsar magnetospheric physics and the galactic population of such objects.

4.2 PSR B1931+24

PSR B1931+24 has been observed for many years in the pulsar timing programme using the 76-m Lovell Telescope at Jodrell Bank. It had been considered to be a seemingly ordinary pulsar, with a spin period of 813 ms [14] and a typical rotational frequency derivative of $\dot{\nu} = -12.2 \times 10^{-15}\,\mathrm{Hz\,s^{-1}}$ (cf. Table 1 in [5]). It was noted

A.G. Lyne
University of Manchester, Jodrell Bank Observatory, Macclesfield, SK11 9DL, UK
e-mail: andrew.lyne@manchester.ac.uk

W. Becker (ed.), *Neutron Stars and Pulsars,* Astrophysics and Space Science Library 357,

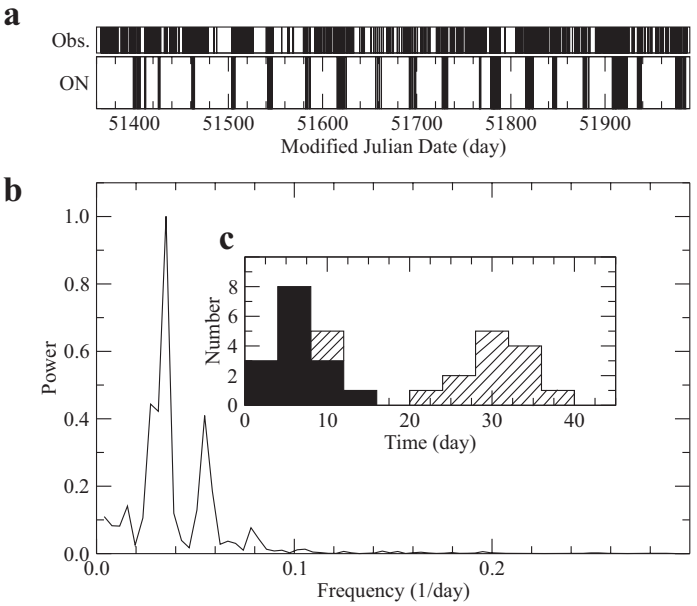

Fig. 4.1 The intermittent nature of the radiation from PSR B1931+24 [7]. (**a**) The *vertical bars* in the *upper diagram* show the location of good observations of the pulsar during a 600-day period. The *lower diagram* shows *vertical bars* for those observations in which the pulsar was detected (ON). (**b**) The spectrum of the time sequence in (**a**), obtained from the Fourier transform of its autocorrelation function. *Inset* are histograms of the lengths of the "ON" (*filled area*) and "OFF" (*hatched area*) intervals

that it exhibits considerable short-term rotational instability, known as timing noise and which is usually thought to be intrinsic to the pulsar, but shows no evidence for the presence of any stellar companion. It became clear a few years ago that the pulsar was not detected in many of the regular observations and that the flux density distribution was bimodal, the pulsar being either ON or OFF [7]. Figure 4.1a shows the best sampled data span which covers a 20-month period between 1999 and 2001 and demonstrates the quasi-periodic fashion of the ON–OFF sequences. The pulsar is typically ON for a week and completely OFF for the following month. The power spectrum of the data (Fig. 4.1b) reveals a strong ∼35-d periodicity with two further harmonics, which reflect the duty-cycle of the switching pattern. Studying a much longer time-series from 1998 to 2005, including some intervals of less densely sampled data, we find that the periodicities are persistent but slowly varying with time in a range from 30 to 40 days. No other known pulsar behaves this way.

Despite the rarity of the switching events, we have been able to observe one switch from an ON state to OFF and found that it occurred within 10 s, the time resolution being limited by the signal-to-noise ratio of the observations.

To investigate the nature of the switching phenomenon, we have examined the rotation rate of the pulsar over a 160-day period during which the sampling of the data was particularly dense (Fig. 4.1, top). The variation is dominated by a

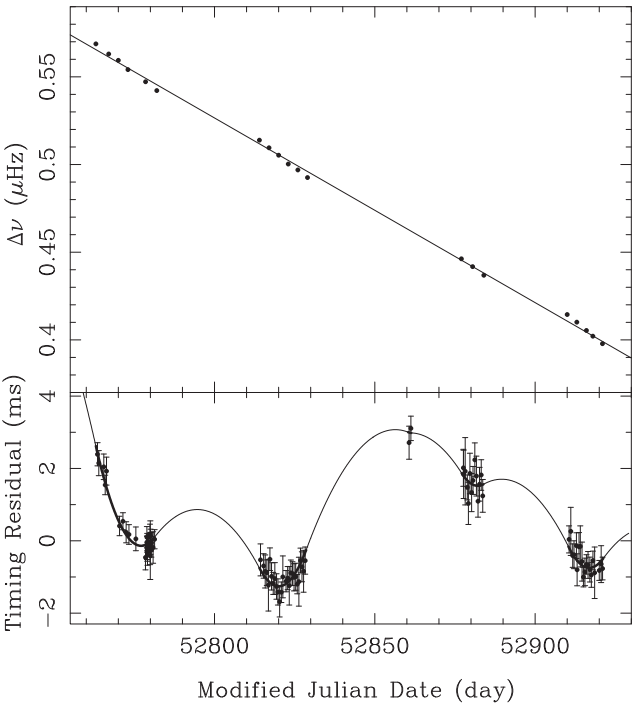

Fig. 4.2 *Top panel*: The variation of the rotational frequency ν of PSR B1931+24 over a period of 160 days [7]. The increase in slope during the "ON" periods compared with the mean slope can be seen clearly, indicating an increase in slowdown rate. *Bottom panel*: Timing residuals relative to a simple slowdown model over the same period. The *line* shows a fitted model which includes a single extra parameter, an increase in frequency derivative during the "ON" phase, and provides an excellent description of the data

decrease in rotational frequency which is typical for pulsars. However, inspection of the longer sequences of the available ON data reveals that the rate of decrease is even more rapid during these phases, indicating greater values of rotational frequency first derivative than the average value (cf. Fig. 4.2). This suggests a simple model in which the frequency derivative has different values during the OFF and ON phases. Such a model accurately describes the short-term timing variations seen relative to a simple long-term slow-down model (Fig. 4.1, bottom). Over the 160-day period shown, the pulsar was monitored almost daily, so that the switching times are well defined, and a model could be fitted to the data with good precision. The addition of a single extra parameter (i.e. two values of frequency derivative rather than one) reduces the timing residuals by a factor of 20 and provides an entirely satisfactory description of the data. A similar fitting procedure has been applied to other well-sampled sections of data and produces consistent model parameters, giving values for the rotational frequency derivatives of $\dot{\nu}_{\rm OFF} = -10.8(2) \times 10^{-15}\,{\rm Hz\,s^{-1}}$ and $\dot{\nu}_{\rm ON} = -16.3(4) \times 10^{-15}\,{\rm Hz\,s^{-1}}$. These values indicate that there is a $\sim$50% increase in spin-down rate of the neutron star when the pulsar is ON.

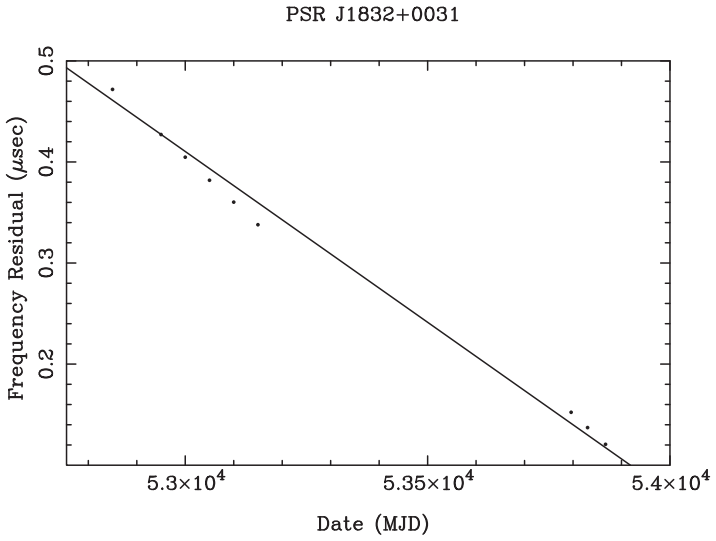

Fig. 4.3 The variation of the rotational frequency ν of PSR J1832+0029 over about 4 years. The pulsar was OFF for the gap of ∼600 days between the two ON periods. Note the increased magnitude of frequency derivative during the "ON" periods

We have searched our databases carefully for other pulsars which may exhibit this phenomenon. Four other candidates have been identified and are being studied now. One of these is PSR J1832+0029 which shows the same basic phenomenon on an even longer timescale. Figure 4.3 shows the variation in its rotational frequency, showing the same increased slow-down rate during the ON periods.

4.3 Discussion

The observed quasi-periodicity in PSR B1931+24's activity and its time-scale have never seen before as a pulsar emission phenomenon and are accompanied by massive changes in the rotational slow-down rate. This raises a number of questions. Why does the emission switch ON and OFF? Why is the activity quasi-periodic? Why is the pulsar spinning down faster when it is ON?

On the shortest, pulse-to-pulse time scales, intrinsic flux density variations are often observed in pulsar radio emission. The most extreme case is displayed by a small group of pulsars, which are known to exhibit nulls in their emission, i.e. the random onset of a sudden obvious lack of pulsar emission, typically for between one and a few dozen pulsar rotation periods [1]. An acceptable explanation for such "nulling", which appears to be the complete failure of the radiation mechanism, is still missing. This nulling represented the longest known time scales for an intrinsic disappearance of pulsar emission. Although the OFF periods in PSR B1931+24

last five orders of magnitude longer than typical nulling and the activity pattern is quasi-periodic, this may well be the same basic phenomenon as nulling.

The approximate 35-day period might be attributed to free precession, although we find no evidence of expected profile changes (e.g. [13]). The sudden change and the quasi-periodicity point toward a relaxation oscillation of unknown nature within the pulsar system, rather than precession.

What can cause the radio emission to cut off so quickly? The energy associated with the radio emission from pulsars accounts for only a very small fraction of the pulsar's slow-down energy which may suggest that the disappearance of radiation is simply due to the failure of the coherence condition in the emission process [10]. However, in this case, the long timescales of millions of pulsar rotations are hard to understand.

An alternative explanation is that there is a more global failure of charged particle currents in the magnetosphere. Intriguingly, the large changes in slow-down rate that accompany the changes in radio emission can also be explained by the presence or absence of a plasma whose current flow provides an additional braking torque on the neutron star. In this model, the open field lines above the magnetic pole become depleted of charged radiating particles during the OFF phases and the rotational slow-down, $\dot{\nu}_{\rm OFF}$, is caused by a torque dominated by magnetic dipole radiation [3, 11]. When the pulsar is ON, the decrease in rotational frequency, $\dot{\nu}_{\rm ON}$, is enhanced by an additional torque provided by the outflowing plasma, $T \sim \frac{2}{3c} I_{pc} B_0 R_{pc}^2$, where B_0 is the dipole magnetic field at the neutron star surface and $I_{pc} \sim \pi R_{pc}^2 \rho c$ which is the electric current along the field lines crossing the polar cap, having radius of by R_{pc} (e.g. [4]).[1] The charge density of the current can be estimated from the difference in loss in rotational energy during the ON and OFF phases. When the pulsar is ON, the observed energy loss, $\dot{E}_{\rm ON} = 4\pi^2 I \nu \dot{\nu}_{\rm ON}$, is the result of the sum of the magnetic dipole braking as seen during the OFF phases, $\dot{E}_{\rm OFF} = 4\pi^2 I \nu \dot{\nu}_{\rm OFF}$, and the energy loss caused by the outflowing current, $\dot{E}_{\rm wind} = 2\pi T \nu$, i.e. $\dot{E}_{\rm ON} = \dot{E}_{\rm OFF} + \dot{E}_{\rm wind}$ where I is the moment of inertia of the neutron star. From the difference in spin-down rates between OFF and ON phases, $\Delta\dot{\nu} = \dot{\nu}_{\rm OFF} - \dot{\nu}_{\rm ON}$, we can therefore calculate the charge density $\rho = 3I\Delta\dot{\nu}/R_{pc}^4 B_0$ by computing the magnetic field $B_0 = 3.2 \times 10^{15} \sqrt{-\dot{\nu}_{\rm OFF}/\nu^3}$ Tesla and the polar cap radius $R_{pc} = \sqrt{2\pi R^3 \nu / c}$ for a neutron star with radius $R = 10$ km and a moment of inertia of $I = 10^{38}\,\mathrm{kg\,m^2}$ [8]. We find that the plasma current that is associated with radio emission carries a charge density of $\rho = 0.034\,\mathrm{C\,m^{-3}}$. This is remarkably close to the charge density $\rho_{\rm GJ} = B_0 \nu / c$ in the Goldreich–Julian model of a pulsar magnetosphere [2], i.e. $\rho_{\rm GJ} = 0.033\,\mathrm{C\,m^{-3}}$.

Such current is sufficient to explain the change in the neutron star torque, but it is not clear what determines the long timescales or what could be responsible for changing the plasma flow in the magnetosphere. In that respect, understanding the cessation of radiation that we see in PSR B1931+24, may ultimately help us to also understand ordinary nulling. Whatever the cause is, it is conceivable that

[1] In order to be consistent with existing literature, such as [4], we quote formulae in cgs-units but refer to numerical values in SI units.

the onset of pulsar emission may be a violent event which may be revealed with high-energy observations. While an archival search for X-ray or γ-ray counterparts for PSR B1931+24 has not been successful, the relatively large distance of the pulsar ($\sim$4.6 kpc) and arbitrary viewing epochs may make such a detection unlikely. The relationship between the presence of pulsar emission via radiating particles and the increased spin-down rate of the neutron star provides strong evidence that a pulsar wind plays a significant role in the pulsar braking mechanism. While this has been suggested in the past (e.g. [12]), direct observational evidence has hitherto been missing. We note that, as a consequence of the wind contribution to the pulsar spin-down, the surface magnetic fields estimated for normal pulsars from their observed spin-down are likely to be overestimated.

The discovery of PSR B1931+24's behaviour suggests that many more such objects exist in the Galaxy but have been overlooked so far because they were not active during either the search or confirmation observations. The periodic transient source serendipitously found recently in the direction of the Galactic centre [6] may turn out to be a short-timescale version of PSR B1931+24 and hence to be a radio pulsar. In general, the timescales involved in the observed activity patterns of these sources pose challenges for observations scheduled with current telescopes. Instead, future telescopes with multi-beaming capabilities, like the Square-Kilometre-Array or the Low Frequency Array, which will provide continuous monitoring of such sources, are needed to probe such timescales which are still almost completely unexplored in most areas of astronomy.

References

1. Backer, D.C., *Nature* 228, 42–43 (1970)
2. Goldreich, P., Julian, W.H., *ApJ* 157, 869–880 (1969)
3. Gunn, J.E., Ostriker, J.P., *Nature* 221, 454 (1969)
4. Harding, A.K., Contopoulos, I., Kazanas, D., *ApJ* 525, L125–L128 (1999)
5. Hobbs, G., Lyne, A.G., Kramer, M., et al., *MNRAS* 353, 1311–1344 (2004)
6. Hyman, S.D., Lazio, T.J.W., Kassim, N.E., et al., *Nature* 434, 50–52 (2005)
7. Kramer, M., Lyne, A.G., O'Brien, J.T., et al., *Science* 312, 549–551 (2006)
8. Lorimer, D.R., Kramer, M., Handbook of pulsar astronomy, Cambridge University Press, Cambridge (2005)
9. McLaughlin, M., This volume
10. Michel, F.C., Theory of neutron star magnetospheres, University of Chicago Press, Chicago (1991)
11. Pacini, F., *Nature* 216, 567–568 (1967)
12. Spitkovsky, A., Electrodynamics of pulsar magnetospheres, in IAU Symposium 218, pp. 357–364, Astro-ph/0310731 (2004)
13. Stairs, I.H., Lyne, A.G., Shemar, S., *Nature* 406, 484–486 (2000)
14. Stokes, G.H., Taylor, J.H., Weisberg, J.M., Dewey, R.J., *Nature* 317, 787–788 (1985)

Chapter 5
The Double Pulsar: A Unique Lab for Relativistic Plasma Physics and Tests of General Relativity

Michael Kramer

5.1 Introduction

Almost a hundred years after Einstein formulated his theory of general relativity (GR), efforts in testing GR and its concepts are still being made by many colleagues around the world, using many different approaches. To date GR has passed all experimental and observational tests with flying colours, but in light of recent progress in observational cosmology in particular, the question of whether alternative theories of gravity need to be considered is as topical as ever.

Many experiments are designed to achieve ever more stringent tests by either increasing the precision of the tests or by testing different, new aspects. Some of the most stringent tests are obtained by satellite experiments in the solar system, providing exciting limits on the validity of GR and alternative theories of gravity like tensor-scalar theories. However, solar-system experiments are made in the gravitational weak-field regime, while deviations from GR may appear only in strong gravitational fields. It happens that nature provides us with an almost perfect laboratory to test the strong-field regime using binary radio pulsars.

While, strictly speaking, the binary pulsars move in the weak gravitational field of a companion, they do provide precision tests of the strong-field regime. This becomes clear when considering strong self-field effects which are predicted by the majority of alternative theories. Such effects would, for instance, clearly affect the pulsars' orbital motion, allowing us to search for these effects and hence providing us with a unique precision strong-field test of gravity.

Pulsars are highly magnetized rotating neutron stars and are unique and versatile objects which can be used to study an extremely wide range of physical and astrophysical problems. Besides testing theories of gravity one can study the Galaxy and the interstellar medium, stars, binary systems and their evolution, plasma physics

M. Kramer
Jodrell Bank Centre for Astrophysics, University of Manchester, Alan-Turing Building, Oxford Road, Manchester M13 9PL, UK
e-mail: Michael.Kramer@manchester.ac.uk

W. Becker (ed.), *Neutron Stars and Pulsars,* Astrophysics and Space Science Library 357,

and solid state physics under extreme conditions. This wide range of applications is exemplified by the first ever discovered double pulsar [3, 16] This unique system allows us to test many aspects of gravitational theories at the same time, representing a truly unique laboratory for relativistic gravity. The experiment is conceptually simple: We observe two clocks attached to point masses which fall in the gravitational potential of their companion. Measuring the ticks of these clocks while they move through space–time allows us to compare our observations with the predictions of various theories of gravity.

5.2 The Double Pulsar

Our team discovered the 22.8-ms pulsar J0737−3039 in April 2003 [3] in an extension to the hugely successful Parkes Multi-beam survey [17]. It was soon found to be a member of the most extreme relativistic binary system ever discovered: its short orbital period ($P_\mathrm{b} = 2.4\,\mathrm{h}$) is combined with a remarkably high value of periastron advance ($\dot{\omega} = 16.9^\circ\,\mathrm{yr}^{-1}$, i.e. four times larger than for the Hulse–Taylor pulsar PSR B1913+16). This large precession of the orbit was measurable after only a few days of observations. The system parameters predict that the two members of the binary system will coalesce on a short time scale of only $\sim$85 Myr. This boosts the hopes for detecting a merger of two neutron stars with first-generation ground-based gravitational wave detectors by a factor of 5–10 compared to previous estimates based on only the double neutron stars B1534+12 and B1913+16 [3, 11].

In October 2003, we detected radio pulses from the second neutron star [16]. The reason why signals from the 2.8-s pulsar companion (now called PSR J0737−3039B, hereafter "B") to the millisecond pulsar (now called PSR J0737−3039A, hereafter "A") had not been found earlier, became clear when it was realized that B was only bright for two short parts of the orbit. For the remainder of the orbit, the pulsar B is extremely weak and only detectable with the most sensitive equipment. The detection of a young companion B around an old millisecond pulsar A and their position in the P–$\dot{P}$-diagram (see Fig. 5.1) confirms the evolution scenario proposed for recycled pulsars (see also Sect. 5.2.3) and provides a truly unique test-bed for relativistic gravity and also plasma physics.

5.2.1 A Laboratory for Plasma Physics

The double pulsar is not only a superb test-bed for relativistic gravity, but it also provides an unprecedented opportunity to probe the workings of pulsars. The pulse emission from B is strongly modulated with orbital phase, most probably as a consequence of the penetration of the A's wind into B's magnetosphere. Figure 5.2 shows the pulse intensity for B as a function of pulse phase and orbital longitude for three radio frequencies. The first burst of strong emission, centred near orbital

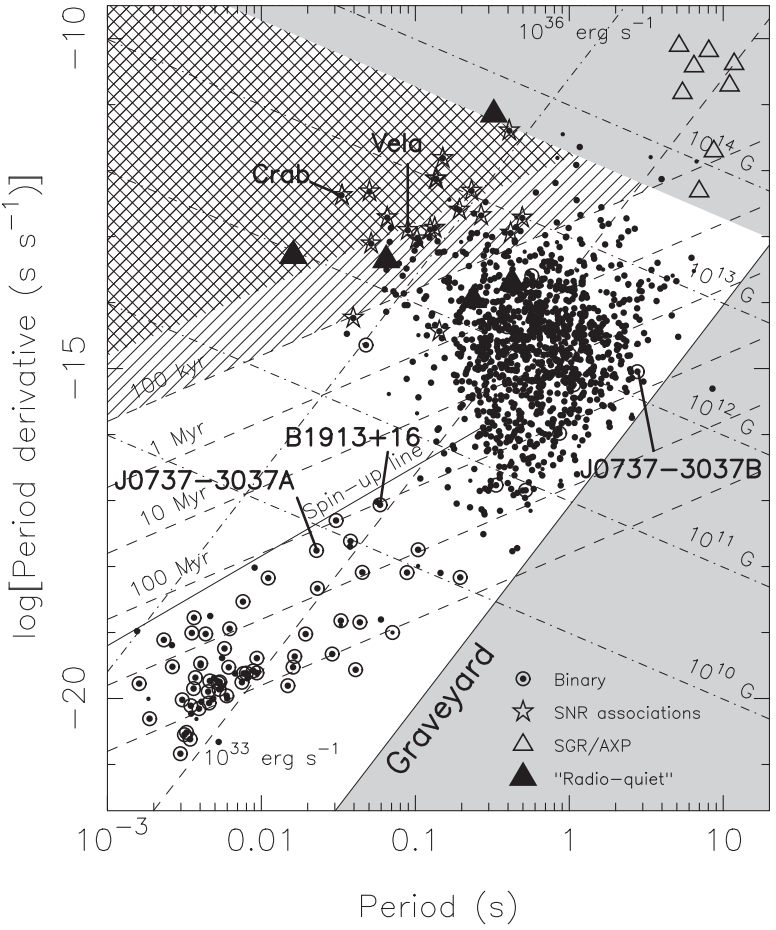

Fig. 5.1 The *P*–*Ṗ*-diagram for the known pulsar population. Lines of constant characteristic age, surface magnetic field and spin-down luminosity are shown. Binary pulsars are marked by a *circle*. The *lower solid line* represents the pulsar "death line" enclosing the "pulsar graveyard" where pulsars are expected to switch off radio emission. The *grey area* in the *top right corner* indicates the region where the surface magnetic field appears to exceed the quantum critical field of 4.4×10^{13} G. For such values, some theories expect the quenching of radio emission in order to explain the radio-quiet "magnetars" (i.e. Soft-gamma ray repeaters, SGRs, and Anomalous X-ray pulsars, AXPs). The *upper solid line* is the "spin-up" line which is derived for the recycling process as the period limit for millisecond pulsars

longitude 210°, covers about 13 min of the orbit, while the second burst, centred near longitude 280°, is shorter and last only for about 8 min. This pattern is stable over successive orbits and obviously frequency independent over the range probed. Deep integrations reveal other orbital phases, where B is visible but much weaker than during the two main burst periods. The figure also shows that not only does the pulse intensity change with orbital phase, but that the pulse shape changes as well. At the start of the first burst the pulse has a strong trailing component and a weaker

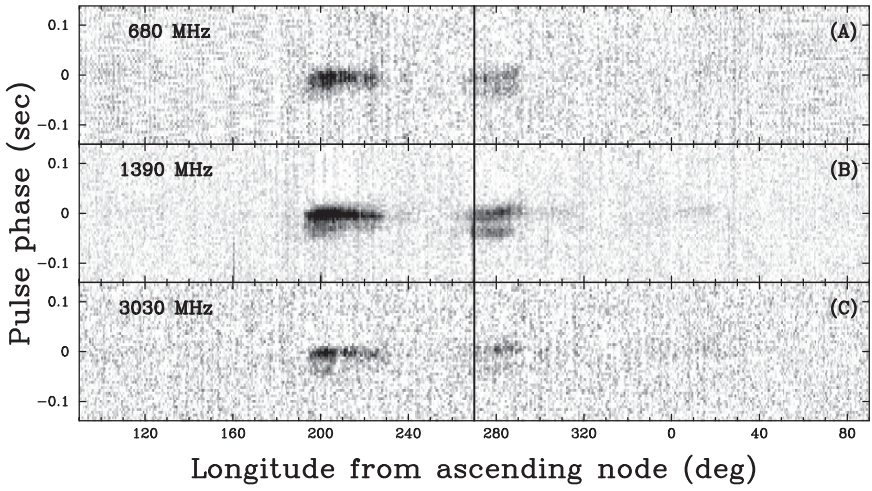

Fig. 5.2 Grey-scale images showing the pulse of PSR J0737−3039B as a function of orbital phase at three observing frequencies [16]

leading component which dies out in the later phases of the burst. In the second burst, there are two components of more equal amplitude. This is the first time that profile changes are observed that clearly depend on orbital phase. Decoding this pattern as the orbit precesses due to relativistic effects and the system is viewed from different directions, offers a unique chance to probe the magnetosphere. Indeed, as discussed later, the "light-curve" of B is changing with time, probably due to the effects of geodetic precession.

It is important to note that by simply seeing B functioning as a radio pulsar, albeit with orbital phases of rather weak emission, confirms our ideas about the location of the origin of radio emission: The fact that B is still emitting, despite the loss of most of its magnetosphere due to A's wind, indicates that the fundamental processes producing radio emission are likely to occur close to the neutron star surface – in accordance with emission heights determined for normal radio pulsars.

The quenching or attenuation of B's radio emission for most of its orbit is only part of the interaction between A and B that is observed. For about 27 s of the orbit, A's emission is eclipsed when A is lined up behind B at superior conjunction (Fig. 5.3). At that moment, the pulses of A pass in about 30,000 km distance to the surface of B. It appears that the magnetospheric transmission for A's emission is modulated during the rotation of B, depending on the relative orientation of the spin-axis of B to A and our line-of-sight. Indeed, a modulation of the light-curve inside the eclipse region consistent with B's (full and half) rotation period is observed [19] (Fig. 5.4).

Perhaps even more exciting is the discovered evidence that A's radiation has some direct impact on the radiation pattern of B. Figure 5.5 shows a blow-up of B's emission at orbital phases where B is strongest. At the right orientation angles, a drifting sub-pulse pattern emerges that coincides with the arrival times of A's pulses at

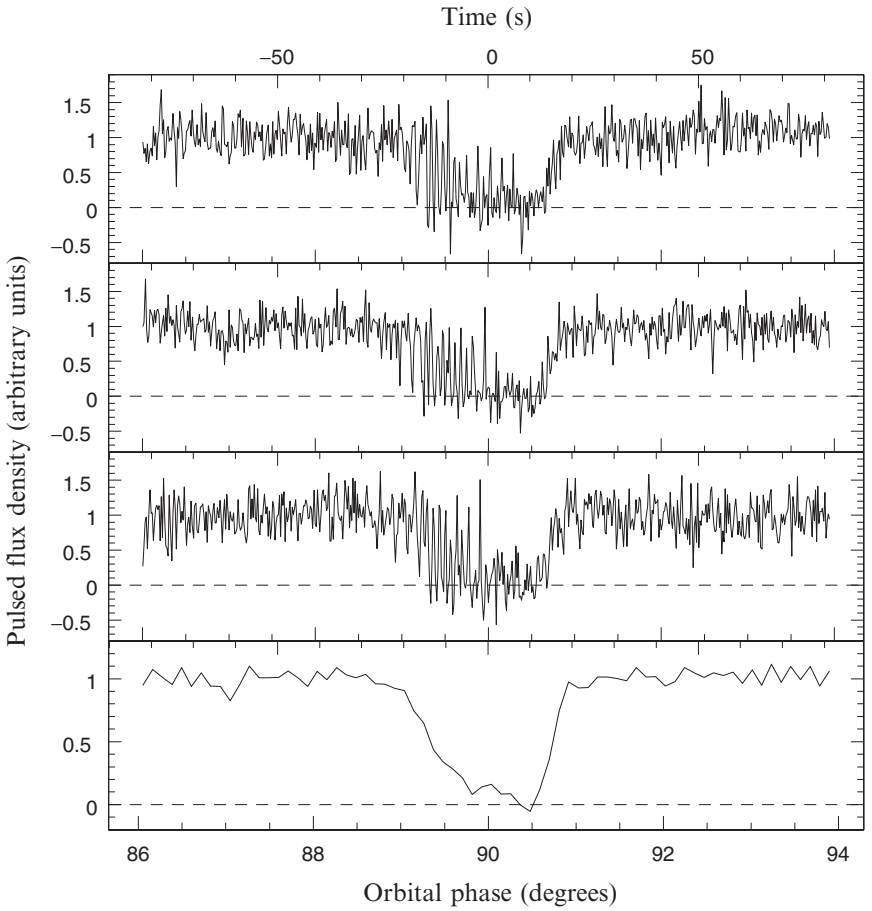

Fig. 5.3 The pulsed flux density of A versus time (with respect to superior conjunction) and orbital phase for (*top three panels*) the three eclipses in the 820-MHz observation and (*bottom panel*) all three eclipses summed [19]. In the individual eclipse light curves, every 12 pulses have been averaged for an effective time resolution of ∼0.27 s. Every 100 pulses have been averaged to create the lower, composite light curve for an effective time resolution of ∼2.3 s. Pulsed flux densities have been normalized such that the pre-eclipse average flux density is unity

B [20]. This is the first time pulsar emission is observed to be triggered by some external force, and it is likely that this will help us to understand the conditions and on-set of pulsar emission in general.

5.2.2 A Laboratory for Strong-Field Gravity

Since neutron stars are very compact massive objects, the double pulsar (and other double neutron star systems) can be considered as almost ideal point sources for

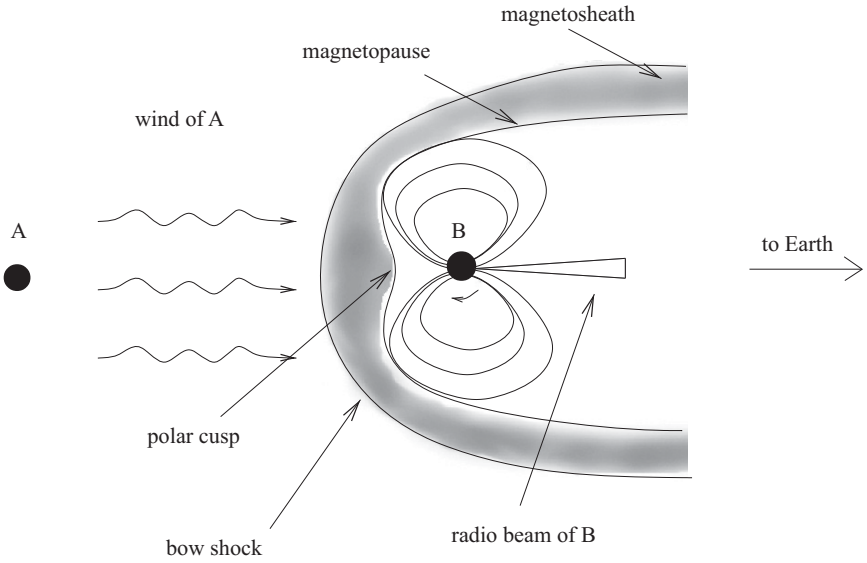

Fig. 5.4 Cartoon (not to scale) showing the interaction between the relativistic wind of A and the magnetosphere of B when the radio beam of B is pointing towards the Earth [20]

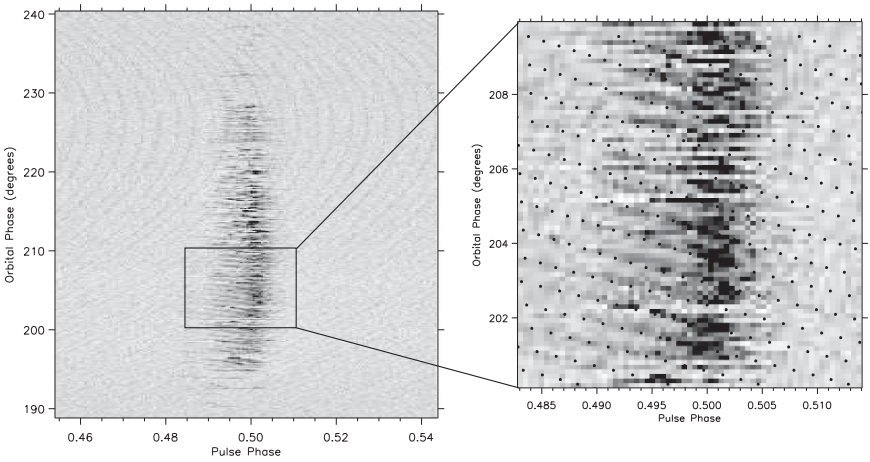

Fig. 5.5 Observations of single pulses of B at 820 MHz for orbital phases 190–240° (only 10% of the pulse period is shown). Drifting features are present through most of these data, but are particularly obvious from orbital phases ∼200–210° which is enlarged on the right. Single pulses of A can be seen in the background of the left figure, where differential Doppler shifts from the orbital motion result in different apparent pulse periods and hence drifting patterns. The expanded view on the right is overlayed with *dots* marking the arrival of pulses of A at the centre of B, coinciding with the observed drift pattern in B [20]

testing theories of gravity in the strong-gravitational-field limit. Timing observations of PSR J0737−3039A/B have been undertaken using the 64-m Parkes radio telescope in New South Wales, the 76-m Lovell radio telescope at Jodrell Bank Observatory, UK, and the 100-m Green Bank Telescope in West Virginia. Because of its narrower and more stable pulse profile, TOAs from A have a much higher precision than those from B and hence are used to determine the position, proper motion and main orbital parameters of the system. For B, the timing model includes only the pulse phase, the pulsar spin frequency, $\nu \equiv 1/P$, its first time-derivative $\dot{\nu}$ and the projected semi-major axis, $x_{\rm B} \equiv (a_{\rm B}/c)\sin i$.

The latest timing results [12] using the DDS timing model [13] resulted in the measurement of five "Post-Keplerian" (PK) parameters. The PK parameters are "corrections" that need to applied to a simple Keplerian orbit in order to describe the observed pulse times-of-arrival (TOAs). It is important to note that the PK parameters are measured as additional parameters in a theory independent and phenomenological way, so that they can be compared with predictions from gravitational theories. One can show [6] that for point masses with negligible spin contributions, the PK parameters should only be functions of the a priori unknown pulsar and companion mass and the easily measurable Keplerian parameters. The actual functions will be different for different theories of gravity, but with the two masses as the only free parameters, an observation of two PK parameters will already determine the masses uniquely in the framework of the given theory. The measurement of a third or more PK parameters then provides a consistency check for the theory to be tested.

The first PK parameter to be measured for the Double Pulsar was $\dot{\omega}$, describing a relativistic advance of periastron. It provides an immediate measurement of the total mass of the system, $(M_A + M_B)$. The second PK parameter γ denotes the amplitude of delays in arrival times caused by the varying effects of the gravitational redshift and time dilation (second order Doppler) as the pulsar moves in its elliptical orbit at varying distances from the companion and with varying speeds.

Two other PK parameters, r and s, are related to the Shapiro delay caused by the gravitational field of the companion. It describes the extra pathlength caused by the curvature of space–time to be traveled by the electromagnetic signal when it passes the companion. Usually, depending on timing precision, a Shapiro delay can only be measured if the orbit is seen nearly edge-on. The short eclipses in A's emission already indicate that we are observing the system almost completely edge-on. Other methods using the variation of the pulsars' intensity due the turbulent interstellar medium are available for an independent measurement of the orbital orientation. Based on such scintillation observations of both pulsars over the short time interval when A is close to superior conjunction, [4] derived a value the orbital inclination angle i that is very close to 90°, i.e. they derive $|i - 90^\circ| = 0^\circ.29 \pm 0^\circ.14$. In general relativity, the parameter s can be identified with $\sin i$ where i is the inclination angle of the orbit. The value of s derived from our timing observations (cf. Table 5.1) corresponds to $i = 88^\circ.69^{+0^\circ.50}_{-0^\circ.76}$. Comparing the two methods, one notes that the scintillation results are based on correlating the scintillation properties of A and B over the short time-span of the orbital motion when they are in conjunction to the

Table 5.1 Parameters for PSR J0737−3039A (A) and PSR J0737−3039B (B) as measured by [13]. The values were derived from pulse timing observations using the DD and DDS models of the timing analysis program TEMPO and the Jet Propulsion Laboratory DE405 planetary ephemeris [24]. Estimated uncertainties, given in parentheses after the values, refer to the least significant digit of the tabulated value and are twice the formal $1-\sigma$ values given by TEMPO. The positional parameters are in the DE405 reference frame which is close to that of the International Celestial Reference System. Pulsar spin frequencies $\nu \equiv 1/P$ are in barycentric dynamical time (TDB) units at the timing epoch quoted in Modified Julian Days. The five Keplerian binary parameters (P_b, e, ω, T_0, and x) are derived for pulsar A. The first four of these (with an offset of 180° added to ω) and the position parameters were assumed when fitting for B's parameters. Five post-Keplerian parameters have now been measured. An independent fit of $\dot{\omega}$ for B yielded a value (shown in square brackets) that is consistent with the much more precise result for A. The value derived for A was adopted in the final analysis. The dispersion-based distance is based on a model for the interstellar electron density [5] and has an uncertainty of order 20%

Timing parameter	PSR J0737−3039A	PSR J0737−3039B
Right Ascension α	$07^{\mathrm{h}}37^{\mathrm{m}}51^{\mathrm{s}}.24927(3)$	–
Declination δ	$-30°39'40''.7195(5)$	–
Proper motion in the RA direction (mas yr^{-1})	−3.3(4)	–
Proper motion in Declination (mas yr^{-1})	2.6(5)	–
Parallax, π (mas)	3(2)	–
Spin frequency ν (Hz)	44.054069392744(2)	0.36056035506(1)
Spin frequency derivative $\dot{\nu}$ (s^{-2})	$-3.4156(1) \times 10^{-15}$	$-0.116(1) \times 10^{-15}$
Timing Epoch (MJD)	53,156.0	53,156.0
Dispersion measure DM (cm^{-3} pc)	48.920(5)	–
Orbital period P_b (day)	0.10225156248(5)	–
Eccentricity e	0.0877775(9)	–
Projected semi-major axis $x = (a/c)\sin i$ (s)	1.415032(1)	1.5161(16)
Longitude of periastron ω (°)	87.0331(8)	87.0331 + 180.0
Epoch of periastron T_0 (MJD)	53,155.9074280(2)	–
Advance of periastron $\dot{\omega}$ (° yr^{-1})	16.89947(68)	[16.96(5)]
Gravitational redshift parameter γ (ms)	0.3856(26)	–
Shapiro delay parameter s	0.99974(−39,+16)	–
Shapiro delay parameter r (μs)	6.21(33)	–
Orbital period derivative $\dot{P}_b$	$-1.252(17) \times 10^{-12}$	–
Timing data span (MJD)	52,760–53,736	52,760–53,736
RMS timing residual σ (μs)	54	2,169
Total proper motion (mas yr^{-1})	4.2(4)	
Distance d(DM) (pc)	∼500	
Distance $d(\pi)$ (pc)	200–1,000	
Transverse velocity ($d = 500$ pc) (km s^{-1})	10(1)	
Orbital inclination angle (°)	88.69(−76,+50)	
Mass function ($M_\odot$)	0.29096571(87)	0.3579(11)
Mass ratio, R	1.0714(11)	
Total system mass ($M_\odot$)	2.58708(16)	
Neutron star mass ($m_\odot$)	1.3381(7)	1.2489(7)

observer. In contrast, the measurement of the inclination angle from timing measurements results from detecting significant harmonic structure in the post-fit residuals after parts of the Shapiro delay are absorbed in the fit for the Römer delay,

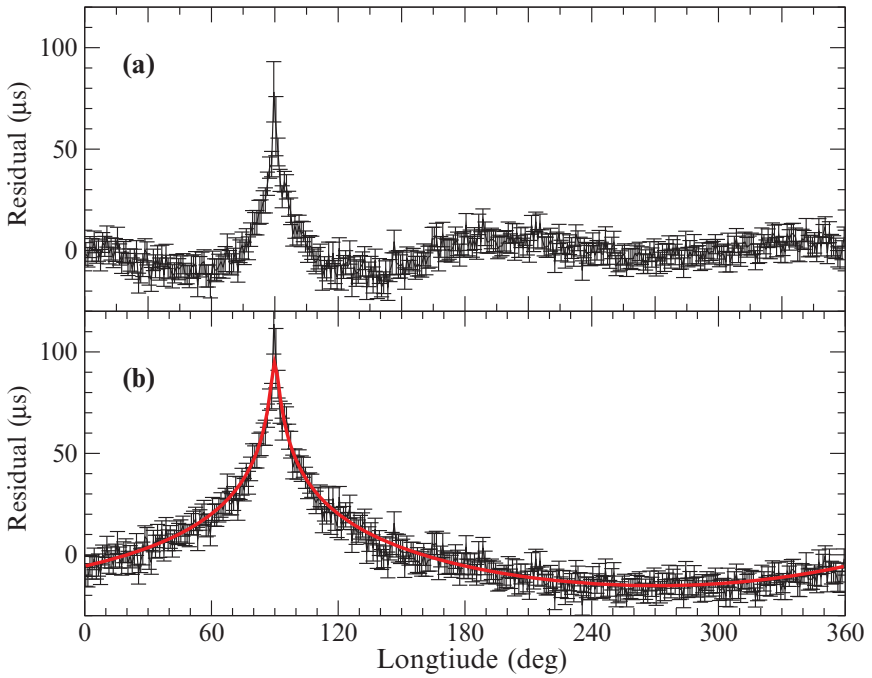

Fig. 5.6 The effect of the Shapiro delay caused by the gravitational potential of B seen in the timing residuals of A. (**a**) Observed timing residuals after a fit of all model parameters given in Table 5.1 *except* the Shapiro-delay terms r and s which were set to zero. (**b**) Residuals illustrating the full Shapiro delay, obtained by holding all parameters to their values given in Table 5.1, except the Shapiro delay terms which were set to zero. The *line* shows the predicted delay at the centre of the data span. In both cases, residuals were averaged in 1° bins of longitude [13]

i.e. the light travel time across the orbit. As shown in Fig. 5.6, these structures are present throughout the whole orbit, so that the results from timing measurements are expected to be more reliable.

After less than 3 years since the Double Pulsar's discovery, we also measured a decay of the orbit due to gravitational wave damping which is expressed by a change in orbital period, $\dot{P}_{\rm b}$. The value of $\dot{P}_{\rm b}$ corresponds to a shrinkage of the orbit at a rate of 7 mm per day.

In addition to tests enabled by the PK parameters, the access to the orbit of both neutron stars – by timing A *and* B – provides yet another constraint on gravitational theories that is qualitatively different from what has been possible with previously known double neutron stars: using Kepler's third law, the measurement of the projected semi-major axes of both orbits yields the mass ratio,

$$R(M_A, M_B) \equiv M_A/M_B = x_B/x_A. \tag{5.1}$$

For every realistic theory of gravity, we can expect R to follow this simple relation [6], at least to 1PN order. Most importantly, the R value is not only

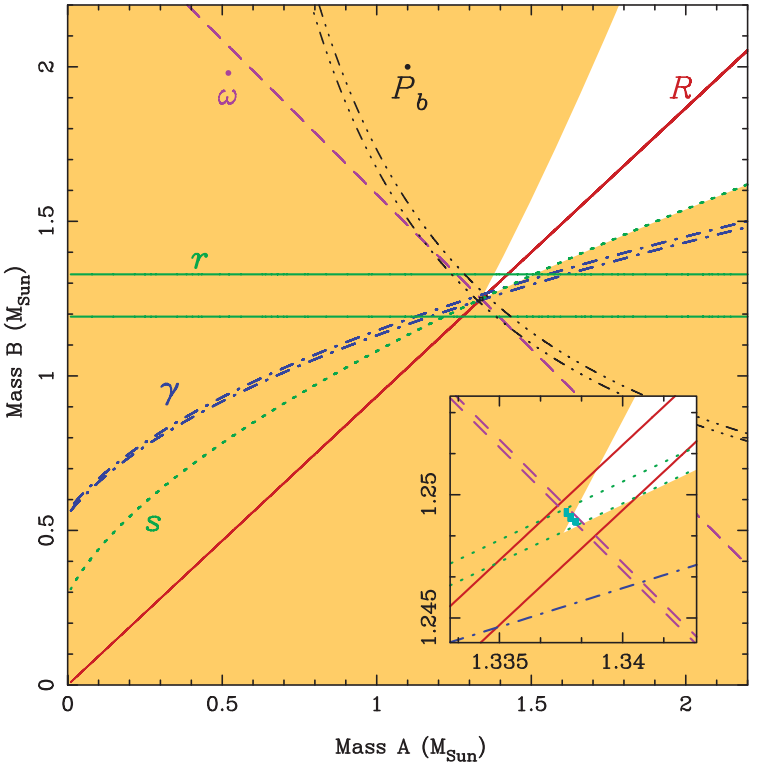

Fig. 5.7 "Mass–mass" diagram showing the observational constraints on the masses of the neutron stars in the double pulsar system J0737−3039 [13]. The *shaded regions* are those that are excluded by the Keplerian mass functions of the two pulsars. Further constraints are shown as pairs of lines enclosing permitted regions as given by the observed mass ratio and PK parameters as predicted by general relativity. *Inset* is an enlarged view of the small square encompassing the intersection of these constraints (see text)

theory-independent, but also independent of strong-field (self-field) effects which is not the case for the PK parameters. In other words, any combination of masses derived from the PK parameters *must* be consistent with the mass ratio. The ability to measure this quantity provides therefore an important and unique constraint. With five PK parameters already available, this additional constraint also makes the double pulsar the most overdetermined system to date where the most relativistic effects can be studied in the strong-field limit.

One can display these tests elegantly in a "mass–mass" diagram as shown in Fig. 5.7. Measurement of the PK parameters gives curves on this diagram that are in general different for different theories of gravity but which should intersect in a single point, i.e., at a pair of mass values, if the theory is valid [6]. Together with the mass ratio R, the PK parameters provide a total of six curves in the mass–mass diagram. Determining an intersection point using a pair of curves, we obtain four independent tests of GR, more than for any other known system.

Table 5.2 Four independent tests of GR provided by the double pulsar as presented by [13]. The second column lists the observed PK parameters obtained by fitting a DDS timing model to the data. The third column lists the values expected from general relativity given the masses determined from the intersection point of the mass ratio R and the periastron advance $\dot{\omega}$. The last column gives the ratio of the observed to expected value for each test. Uncertainties refer to the last quoted digit and were determined using Monte Carlo methods

PK parameter	Observed	GR expectation	Ratio
$\dot{P}_{\rm b}$	1.252(17)	1.24787(13)	1.003(14)
γ (ms)	0.3856(26)	0.38418(22)	1.0036(68)
s	0.99974$(-39,+16)$	0.99987$(-48,+13)$	0.99987(50)
$r(\mu s)$	6.21(33)	6.153(26)	1.009(55)

Figure 5.7 shows that all measured constraints are consistent with GR. The most precisely measured PK parameter currently available is the precession of the longitude of periastron, $\dot{\omega}$. We can combine this with the theory-independent mass ratio R to derive the masses given by the intersection region of their curves: $m_{\rm A} = 1.3381 \pm 0.0007\,{\rm M}_\odot$ and $m_{\rm B} = 1.2489 \pm 0.0007\,{\rm M}_\odot$. Assuming GR and using these masses and the Keplerian parameters, we can predict values for the remaining PK parameters. Table 5.2 lists results for the four independent tests that are currently available. The Shapiro delay (Fig. 5.6) gives the most precise test, with $s_{\rm obs}/s_{\rm pred} = 0.99987 \pm 0.00050$. This is by far the best test of GR in the strong-field limit, having a higher precision than the test based on the observed orbit decay in the PSR B1913+16 system with a 30-year data span [27]. As for the PSR B1534+12 system [22], the PSR J0737−3039A/B Shapiro-delay test is complementary to that of B1913+16 since it is not based on predictions relating to emission of gravitational radiation from the system [25]. Most importantly, the four tests of GR presented here are qualitatively different from all previous tests because they include one constraint (R) that is independent of the assumed theory of gravity at the 1PN order. As a result, for any theory of gravity, the intersection point is expected to lie on the mass ratio line in Fig. 5.7. GR also passes this additional constraint with the best precision so far.

Effects of Geodetic Precession

The measurement of the times-of-arrival (TOAs) are obtained with a standard "template matching" procedure that involves a cross-correlation of the observed pulse profile with high signal-to-noise ratio template [26]. Any change in the pulse profile could lead to systematic variations in the measured TOAs. We performed detailed studies of the profiles of A and B to investigate any possible profile changes with time as such as expected from another effect predicted by GR.

In GR, the proper reference frame of a freely falling object suffers a precession with respect to a distant observer, called geodetic precession. In a binary pulsar system this geodetic precession leads to a relativistic spin–orbit coupling,

analogous to spin–orbit coupling in atomic physics [8]. As a consequence, both pulsar spins precess about the total angular momentum, changing the relative orientation of the pulsars to one another and toward Earth. Since the orbital angular momentum is much larger than the pulsars' angular momenta, the total angular momentum is effectively represented by the orbital angular momentum. The precession rate (e.g. [1]) depends on the period and the eccentricity of the orbit as well as the masses of A and B. With the orbital parameters of the double pulsar, GR predicts precession periods of only 75 yr for A and 71 yr for B.

Geodetic precession has a direct effect on the timing as it causes the polar angles of the spins and hence the effects of aberration to change with time [6]. These changes modify the *observed* orbital parameters, like projected semi-major axis and eccentricity, which differ from the *intrinsic* values by an aberration dependent term, potentially allowing us to infer the system geometry (see Sect. 5.4). Extracting the signature of these effects in the timing data is a goal for the years to come. Other consequences of geodetic precession can be expected to be detected much sooner and are directly relevant for the timing of A and B. These arise from variations in the pulse shape due to changing cuts through the emission beam as the pulsar spin axes precess. Moreover, geodetic precession also leads to a change in the relative alignment of the pulsar magnetospheres, so that the visibility pattern and even the profile of B should vary due to these changes as well.

Indeed, studies of the profile evolution of B [2] reveal a clear evolution of B's emission on orbital and secular time-scales. The light-curves of B (i.e. the visibility of B versus orbital phase) undergo clear changes (Fig. 5.8) while the profile of B as

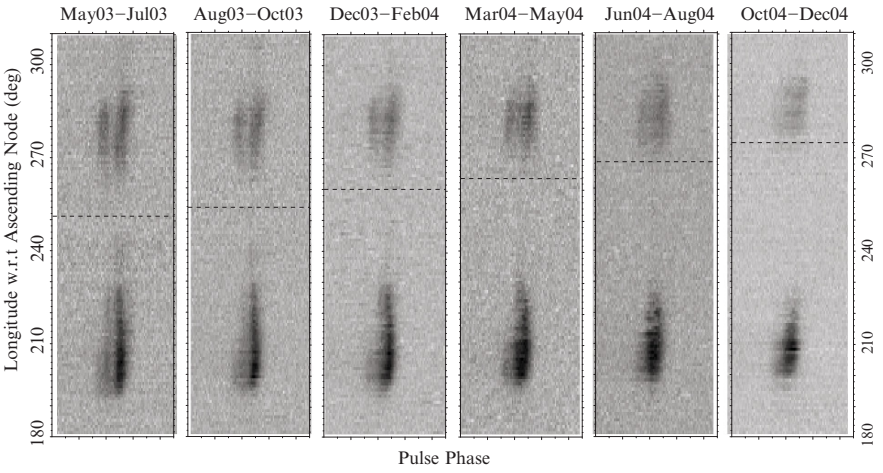

Fig. 5.8 The emission of B at 1,390 MHz as a function of the orbital longitude (vertical axis) and for the pulse phase range 0.18–0.27 (horizontal axis) as in Fig. 5.2. Each panel was obtained by adding all the data in the ∼3-months period indicated at the top of each panel. The *dashed lines* represent the position of the periastron at the given epoch. A change in the visibility pattern of B is clearly visible and most likely caused by geodetic precession [2]

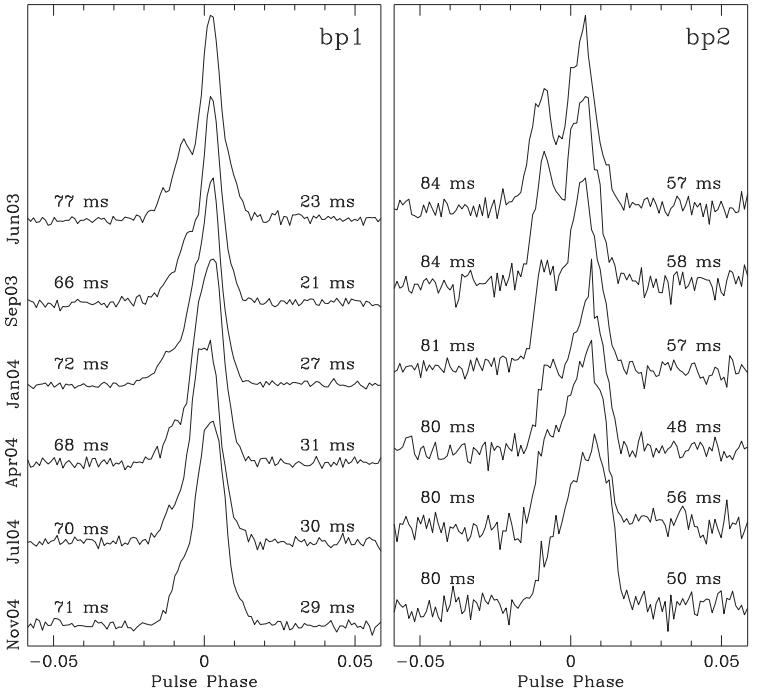

Fig. 5.9 Pulse shapes of B in the two bright phases (see previous figure) as a function of time, again in 3-month intervals. Again, a systematic change in the pulse profile is clearly visible [2]

observed in the bright orbital phases is clearly changing with time also (Fig. 5.9). These phenomena are probably caused by a changing magnetospheric interaction due to geometry variations resulting from geodetic precession. In any case, these changes require sophisticated timing analysis techniques.

For the timing of B, because of the orbital and secular dependence of its pulse profile, different templates were used for different orbital phases and different epochs. A matrix of B templates was constructed, dividing the data set into 3-month intervals in epoch and 5-min intervals in orbital phase. The results for the 29 orbital phase bins were studied, and it was noticed that, while the profile changes dramatically and quickly during the two prominent bright phases, the profile shape is simpler and more stable at orbital phases when the pulsar is weak. In the final timing analysis for pulsar B, we therefore omitted data from the two very bright orbital phases. We also used an unweighted fit to avoid biasing the fit toward remaining brighter orbital phases.

Since the overall precision of our tests of GR is currently limited by our ability to measure x_B and hence the mass ratio $R \equiv m_A/m_B = x_B/x_A$, we adopted the following strategy to obtain the best possible accuracy for this parameter. We used the whole TOA data set for B in order to measure B's spin parameters P and $\dot{P}$, given in Table 5.1. These parameters were then kept fixed for a separate analysis of two

concentrated 5-day observing sessions. On the timescale of the long-term profile evolution of B, each 5-day session represents a single-epoch experiment and hence requires only two sets of profile templates. The value of x_B obtained from a fit of this parameter only to the two 5-day sessions is presented in Table 5.1.

The study of the profile evolution of A [13, 18] did not lead to the detection of any profile change (see Fig. 5.10). This present non-detection greatly simplifies the timing of A but does not exclude the possibility that changes may happen in the future. While the effects of geodetic precession could be small due to a near alignment of pulsar A's spin and the orbital momentum vector, the results could also be explained by observing the system at a particular precession phase. While this case appears to be relatively unlikely, it must not be excluded as such a situation had indeed occurred for PSR B1913+16 [14]. Indeed, a modeling of the results suggests that this present non-detection of profile changes is consistent with a rather

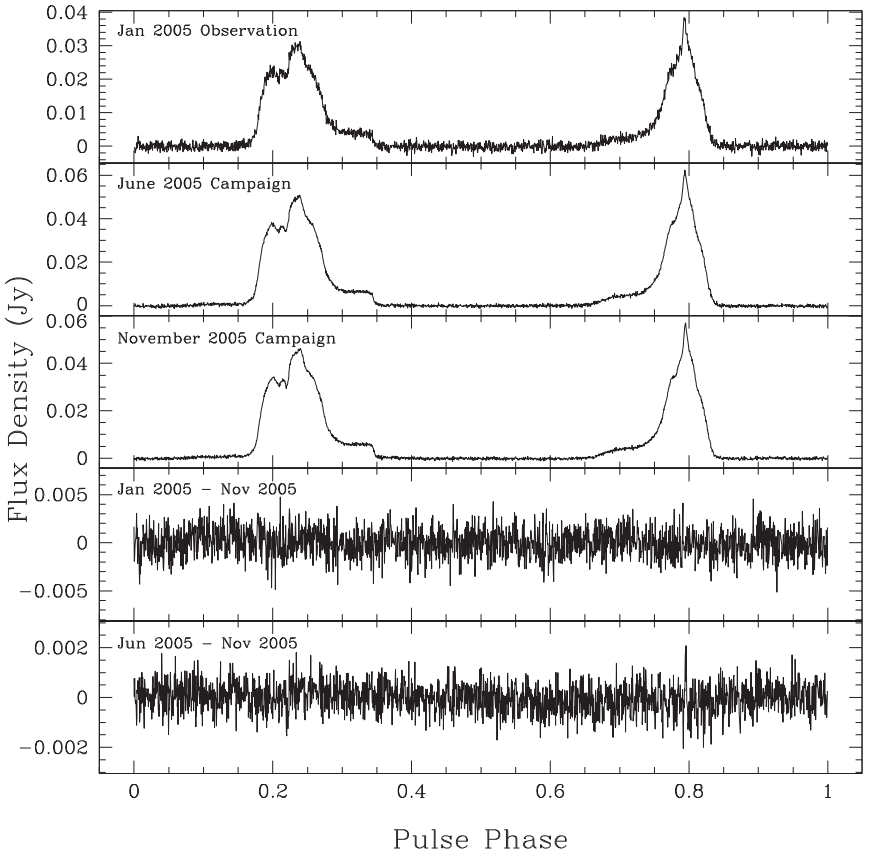

Fig. 5.10 Pulse profiles of A observed at three different epochs. Subtracting one profile from the others does not reveal any significant changes as demonstrated in the two *bottom plots*. Figure provided by Rob Ferdman and Ingrid Stairs

wide range of possible system geometries. One conclusion that can be drawn is that the observations are inconsistent with the large profile changes that had been predicted by some models [10]. Fortunately, independent information is available that suggests that the alignment angle, and hence the impact of geodetic precession, may indeed be very small. This information is derived from a study of the evolution of the system based on the rather small transverse velocity of the double pulsar.

5.2.3 Space-Motion and Evolution of the Double Pulsar

The timing results indicate that the space velocity of the double pulsar system is surprisingly small. Based on the measured dispersion measure and a model for the Galactic electron distribution [5], PSR J0737−3039A/B is estimated to be about 500 pc from the Earth. From the timing data we have measured a marginally significant value for the annual parallax, 3 ± 2 mas, corresponding to a distance of 200–1,000 pc (Table 5.1), which is consistent with the dispersion-based distance that was also used for studies of detection rates in gravitational wave detectors [3] The observed proper motion of the system (Table 5.1) then implies a transverse space velocity of only 10 km s^{-1} with a velocity vector parallel to the Galactic plane. With this information, [23] examined the history and formation of this system, determining estimates of the pre-supernova companion mass, orbital separation, supernova kick and misalignment angle between the pre- and post-supernova orbital planes. One of the surprising results is that the progenitor to the recently formed B was probably less than $2\,M_{\odot}$, lending credence to suggestions that this object may not have formed in a normal core-collapse supernova. They conclude that it therefore must be possible, in at least some cases, for low-mass helium stars to undergo supernova explosions, and that there must be a range of progenitor types that can produce double neutron star systems. The relative frequency of the different types must depend on the initial mass function and ranges of binary orbits. This will have implications for the number of double neutron systems in the Galaxy, the retention of neutron stars in globular clusters and for the apparent dearth of isolated mildly recycled pulsars ejected from unbinding second supernova explosions.

The study of the double pulsar evolution [23] also suggests that the kick velocity was rather small and that the misalignment angle between the spin of pulsar A and the total angular momentum vector (after the second supernova explosion) is probably much less than 10°. In this case, the expected impact of geodetic precession on pulsar A's profile is rather small, consistent with the present observational evidence. This makes us confident that high-precision timing observations of A will continue for quite a while (in contrast to, for instance, the Hulse–Taylor pulsar which may disappear as a radio source at about 2025 [14]. At the same time, the small velocity of the double pulsar system is also extremely good news for tests of alternative theories of gravity where the measurement of the orbital decay is extremely useful.

5.3 Orbital Decay Measurements and Alternative Theories of Gravity

Because the measured uncertainty in $\dot{P}_b$ decreases approximately as $T^{-2.5}$, where T is the data span, we expect to improve our test of the radiative aspect of the system to the 0.1% level or better in about 5 years' time. For the PSR B1913+16 and PSR B1534+12 systems, the precision of the GR test based on the orbit-decay rate is severely limited both by the uncertainty in the differential acceleration of the Sun and the binary system in the Galactic gravitational potential and the uncertainty in pulsar distance [9, 22]. For PSR J0737−3039A/B, both of these corrections are very much smaller than for these other systems. Based on the dispersion measure distance, which is consistent with the marginally significant value for the annual parallax, the observed proper motion of the system (Table 5.1) and differential acceleration in the Galactic potential [15] imply a kinematic correction to $\dot{P}_b$ at the 0.02% level or less. Independent distance estimates also can be expected from measurements of the annual parallax by Very Long Baseline Interferometry (VLBI) observations, allowing a secure compensation for this already small effect. A measurement of $\dot{P}_b$ at the 0.02% level or better will provide stringent tests for alternative theories of gravity as many are, for instance, predicting a significant amount of gravitational *dipole* radiation. Hence, a confirmation that the observations of the double pulsar are consistent with emission of gravitational *quadrupole* radiation to a very high level of precision promises to put limits on some scalar-tensor theories that will surpass even the best current Solar-system tests Damour and Esposito-Farese (Damour & Esposito-Farese, priv. com.).

5.4 Future Tests

In estimating the future improvements in the uncertainty of x_B, and hence R and our current precision for GR tests, we need to consider that geodetic precession will lead to changes to the system geometry and hence to the aberration of the rotating pulsar beam. The effects of aberration on pulsar timing are usually not separately measurable but are absorbed into a redefinition of the Keplerian parameters. As a result, the observed projected sizes of the semi-major axes, $x^{obs}_{A,B}$, differ from the intrinsic sizes, $x^{int}_{A,B}$ by a factor $(1+\varepsilon^{A}_{A,B})$ which depends on the orbital period, the pulse period and on the system geometry [6]. While aberration should eventually become detectable in the timing, allowing the determination of a further PK parameter, at present it leads to an undetermined deviation of x^{obs} from x^{int}, where the latter is the relevant quantity for the mass ratio. The parameter $\varepsilon^{A}_{A,B}$ scales with pulse period and is therefore expected to be two orders of magnitude smaller for A than for B. However, because of the high precision of the A timing parameters, the derived value x^{obs}_A may already be significantly affected by aberration. This has (as yet) no consequences for the mass ratio $R = x^{obs}_B/x^{obs}_A$, as the uncertainty in R is dominated by the much less precise x^{obs}_B. We can explore the likely aberration

corrections to x_B^{obs} for various possible geometries. Using a range of values given by studies of the double pulsar's emission properties [21], we estimate $\varepsilon_A^A \sim 10^{-6}$ and $\varepsilon_B^A \sim 10^{-4}$. The contribution of aberration therefore is at least one order of magnitude smaller than our current timing precision. In the future this effect may become important, possibly limiting the usefulness of R for tests of GR. If the geometry cannot be independently determined, we could use the observed deviations of R from the value expected within GR to determine ε_B^A and hence the geometry of B.

In the near and far future, the precision of the all parameters will increase further, because of the available longer time span and also the employment of better instrumentation. In a few years, we should therefore be able to measure additional PK parameters, including those which arise from a relativistic deformation of the pulsar orbit and those which find their origin in aberration effects and their interplay with geodetic precession (see [6]). On secular time scales we will even achieve a precision that will require us to consider post-Newtonian (PN) terms that go beyond the currently used description of the PK parameters. Indeed, the equations for the PK parameters given earlier are only correct to lowest PN order. However, higher-order corrections are expected to become important if timing precision is sufficiently high. While this has not been the case in the past, the double pulsar system may allow measurements of these effects in the future [16].

One such effect involves the GR prediction that, in contrast to Newtonian physics, the neutron stars' spins affect their orbital motion via spin–orbit coupling. This effect would be visible most clearly as a contribution to the observed $\dot{\omega}$ in a secular (e.g. [1]) and periodic fashion [28]. For the J0737−3039 system, the expected contribution is about an order of magnitude larger than for PSR B1913+16, i.e. $2 \times 10^{-4\circ}\,\mathrm{yr}^{-1}$ (for A, assuming a geometry as determined for PSR B1913+16, [14]). As the exact value depends on the pulsars' moment of inertia, a potential measurement of this effect allows the moment of inertia of a neutron star to be determined for the first time [7]. To be successful requires the measurement of at least two other parameters to a similar accuracy as $\dot{\omega}$. While this is a tough challenge, e.g. due to the expected profile variations caused by geodetic precession, the rewards of such a measurement and its impact on the study of the equation of state of neutron stars make it worth trying.

5.5 Concluding Remarks

With the measurement of five PK parameters and the unique information about the mass ratio, the PSR J0737−3039 system provides a truly unique test-bed for relativistic theories of gravity. So far, GR also passes this test with flying colours. The precision of this test and the nature of the resulting constraints go beyond what has been possible with other systems in the past. The test achieved so far is, however, only the beginning of a study of relativistic phenomena that can be investigated in great detail in this wonderful cosmic laboratory.

References

1. B. M. Barker, R. F. O'Connell, *ApJ* 199, L25 (1975).
2. M. Burgay, A. Possenti, R. N. Manchester, et al., *ApJ* 624, L113–L116 (2005).
3. M. Burgay, N. D'Amico, A. Possenti, et al., *Nature* 426, 531–533 (2003).
4. W. A. Coles, M. A. McLaughlin, B. J. Rickett, et al., *ApJ* 623, 392–397 (2005).
5. J. M. Cordes, T. J. W. Lazio, astro-ph/0207156.
6. T. Damour, J. H. Taylor, *Phys. Rev. D* 45, 1840–1868 (1992).
7. T. Damour, G. Schäfer, *Nuovo Cim.* 101, 127 (1988).
8. T. Damour, R. Ruffini, *C R Acad Sci Paris Sci Math* 279, 971–973 (1974).
9. T. Damour, J. H. Taylor, *ApJ* 366, 501–511 (1991).
10. F. A. Jenet, S. M. Ransom, *Nature* 428, 919–921 (2004).
11. V. Kalogera, C. Kim, D. R. Lorimer, et al., *ApJ* 601, L179–L182 (2004).
12. M. Kramer, I. H. Stairs, R. N. Manchester, et al., *Science* 314, 97–102 (2006).
13. M. Kramer, I. H. Stairs, R. N. Manchester, et al., *Ann Phys* 15, 34–42 (2006).
14. M. Kramer, *ApJ* 509, 856–860 (1998).
15. K. Kuijken, G. Gilmore, *MNRAS* 239, 571 (1989).
16. A. G. Lyne, M. Burgay, M. Kramer, et al., *Science* 303, 1153–1157 (2004).
17. R. N. Manchester, A. G. Lyne, F. Camilo, et al., *MNRAS*, 2001, 328, 17.
18. R. N. Manchester, M. Kramer, A. Possenti, et al., *ApJ* 621, L49–L52 (2005).
19. M. A. McLaughlin, A. G. Lyne, D. R. Lorimer, et al., *ApJ* 616, L131–L134 (2004).
20. M. A. McLaughlin, M. Kramer, A. G. Lyne, et al., *ApJ* 613, L57–L60 (2004).
21. M. Lyutikov, *MNRAS* 362, 1078–1084 (2005).
22. I. H. Stairs, S. E. Thorsett, J. H. Taylor, et al., *ApJ* 581, 501–508 (2002).
23. I. H. Stairs, S. E. Thorsett, R. J. Dewey, et al., *MNRAS* 373, L50–L54 (2006).
24. E. M. Standish, *A&A* 336, 381–384 (1998).
25. J. H. Taylor, A. Wolszczan, T. Damour, et al., *Nature* 355, 132–136 (1992).
26. J. H. Taylor, *Philos Trans R Soc London A* 341, 117–134 (1992).
27. J. M. Weisberg, J. H. Taylor, The relativistic binary pulsar B1913+16, in: F. Rasio, I. H. Stairs (eds.), Binary radio pulsars, Astronomical Society of the Pacific, San Francisco, 2005, pp. 25–31.
28. N. Wex, *Class Quantum Grav* 12, 983 (1995).

Chapter 6
X-Ray Emission from Pulsars and Neutron Stars

Werner Becker

6.1 Introduction

The idea of *neutron stars* can be traced back to the early 1930s, when Subrahmanyan Chandrasekhar discovered that there is no way for a collapsed stellar core with a mass more than 1.4 times the solar mass, $M_\odot$, to hold itself up against gravity once its nuclear fuel is exhausted. This implies that a star left with $M > 1.4\ M_\odot$ (the *Chandrasekhar limit*) would keep collapsing and eventually disappear from view.

After the discovery of the neutron by James Chadwick in 1932 scientists speculated on the possible existence of a *star composed entirely of neutrons*, which would have a radius of the order of $R \sim (\hbar/m_n c)(\hbar c/Gm_n^2)^{1/2} \sim 3 \times 10^5$ cm. In view of the peculiar stellar parameters, Lev Landau called these objects "unheimliche Sterne" (weird stars), expecting that they would never be observed because of their small size and expected low optical luminosity.

Walter Baade and Fritz Zwicky were the first who proposed the idea that neutron stars could be formed in *supernovae*. First models for the structure of neutron stars were worked out in 1939 by Oppenheimer and Volkoff (Oppenheimer–Volkoff limit). Unfortunately, their pioneering work did not predict anything astronomers could actually observe, and the idea of neutron stars was not taken serious by the astronomical community. Neutron stars therefore had remained in the realm of imagination for nearly a quarter of a century, until in the 1960s a series of epochal discoveries were made in high-energy and radio astronomy [20, 73, 148].

X-rays and gamma-rays can only be observed from above the earth's atmosphere,[1] which requires detectors to operate from high flying balloons, rockets or satellites. One of the first X-ray detectors brought to space was launched by Herbert Friedman and his team at the Naval Research Laboratory in order to investigate the

W. Becker
Max-Planck Institut für extraterr. Physik, Giessenbachstrasse 1, 85741 Garching, Germany
e-mail: web@mpe.mpg.de

[1] X-rays are absorbed at altitudes 20–100 km.

W. Becker (ed.), *Neutron Stars and Pulsars,* Astrophysics and Space Science Library 357,

influence of solar activity on the propagation of radio signals in the earth's atmosphere. Using simple proportional counters put on old V-2 (captured in Germany after the World War II) and Aerobee rockets, they were the first who detected X-rays from the very hot gas in the solar corona. However, the intensity of this radiation was found to be a factor 10^6 lower than that measured at optical wavelengths. In the late 1950s, it was therefore widely believed that all other stars, much more distant than the Sun, should be so faint in X-rays that further observations at that energy range would be hopeless.

On the other hand, results from high-energy cosmic ray experiments suggested that there exist celestial objects (e.g., supernova remnants) which produce high-energy cosmic rays in processes which, in turn, may also produce X-rays and gamma-rays [112, 113]. These predictions were confirmed in 1962, when the team led by Bruno Rossi and Riccardo Giacconi accidentally detected X-rays from Sco X-1.

With the aim to search for fluorescent X-ray photons from the Moon,[2] they launched an Aerobee rocket on 12 June 1962 from White Sands (New Mexico) with three Geiger counters as payload, each having a $\sim 100^\circ$ field of view and an effective collecting area of about $10\,\mathrm{cm}^2$ [51]. The experiment detected X-rays not from the Moon but from a source located in the constellation Scorpio, dubbed as Sco X-1, which is now known as the brightest extra-solar X-ray source in the sky. Evidence for a weaker source in the Cygnus region and the first evidence for the existence of a diffuse isotropic X-ray background was also reported from that experiment [52]. Subsequent flights launched to confirm these first results detected Tau X-1, a source in the constellation Taurus which coincided with the Crab supernova remnant [25].

Among the various processes proposed for the generation of the detected X-rays was *thermal radiation from the surface of a hot neutron star* [35], and searching for this radiation has become a strong motivation for further development of X-ray astronomy. However, the X-ray emission from the Crab supernova remnant was found to be of a finite angular size ($\sim$1 arcmin) whereas a neutron star was expected to appear as a point source.

Thus, the early X-ray observations were not sensitive enough to prove the existence of neutron stars. This was done a few years later by radio astronomers.

In 1967, Jocelyn Bell, a graduate student under the supervision of Anthony Hewish at the Cambridge University of England, came across a series of pulsating radio signals while using a radio telescope specially constructed to look for rapid variations in the radio emission of quasars. These radio pulses, 1.32 s apart, with remarkable clock-like regularity, were emitted from an unknown source in the sky at right ascension $19^\mathrm{h}\ 20^\mathrm{m}$ and declination $+23^\circ$. Further observations refined the pulsating period to 1.33730113 s. The extreme precision of the period suggested at first that these signals might be generated by extraterrestrial intelligence. They

[2] The Moon was selected as a target because it was expected that a state-of-the-art detector available at that time would not be sensitive enough to detect X-rays from extra-solar sources. "We felt [...] that it would be very desirable to consider some intermediate target which could yield concrete results while providing a focus for the development of more advanced instrumentation which ultimately would allow us to detect cosmic X-ray sources" [51].

were subsequently dubbed as LGM1, an acronym for "Little Green Man 1" [20]. However, as a few more similar sources had been detected, it became clear that a new kind of celestial objects was discovered. The link between these pulsating radio sources, which were called *pulsars*, and fast spinning neutron stars was provided by Franco Pacini [120, 121] and Thomas Gold [54, 55]. Pacini, then a young postdoc at the Cornell University, had published a paper a few months before the discovery by Bell and Hewish in which he proposed that the *rapid rotation of a highly magnetized neutron star* could be the source of energy in the Crab Nebula. This prediction was based on the pioneering work of Hoyle, Narlikar and Wheeler [74], who had proposed that a magnetic field of 10^{10} G might exist on a neutron star at the center of the Crab Nebula. The most fundamental ideas on the nature of the pulsating radio sources were published by Gold [54, 55] in two seminal *Nature* papers. In these papers Gold introduced the concept of the *rotation-powered pulsar* which radiates at the expense of its rotational energy (pulsar spins down as rotational energy is radiated away) and recognized that the rotational energy is lost via electromagnetic radiation of the rotating magnetic dipole and emission of relativistic particles. The particles are accelerated in the pulsar magnetosphere along the curved magnetic field lines and emit the observed intense curvature and synchrotron radiation.[3]

The discovery of the first radio pulsar was very soon followed by the discovery of the two most famous pulsars, the fast 33-ms pulsar in the Crab Nebula [145] and the 89-ms pulsar in the Vela supernova remnant [95]. The fact that these pulsars are located within supernova remnants provided striking confirmation that neutron stars are born in core collapse supernovae from massive main sequence stars. These exciting radio discoveries triggered subsequent pulsar searches at nearly all wavelengths. Since those early days of pulsar astronomy more than 1,800 radio pulsars have been discovered (see, e.g., the ATNF pulsar database [102] and Chaps. 1 and 2 in this book).

Many radio pulsars had been observed by mid-seventies, and two of them, the Crab and Vela pulsars, had been detected at high photon energies. Although the interpretation of both isolated and accreting pulsars as neutron stars with enormous magnetic fields, $\sim 10^{12}$ G, had been generally accepted, no direct evidence on the existence of such huge fields had been obtained. This evidence came from a remarkable spectral observation of Hercules X-1, an accreting binary pulsar discovered with *Uhuru*. On May 3, 1976, a team of the Max-Planck Institut für extraterrestrische Physik in Garching and the Astronomische Institut of the University of Tübingen, led by Joachim Trümper, launched from Palestine (Texas) a balloon experiment, equipped with a collimated NaI scintillation counter and a NaI–CsI-phoswich detector, sensitive in the range 15–160 keV. They easily detected the 1.24 s pulsations up to 80 keV [93]. However, when Bruno Sacco and Wolfgang Pietsch attempted to fit the observed spectrum with usual continuum spectral models, they found that a one-component continuum model cannot represent the data – all fits gave unacceptably large residuals at $\sim$40–60 keV. Further data analysis confirmed

[3] When a charged relativistic particle moves along a curved magnetic field line, it is accelerated transversely and radiates. This *curvature radiation* is closely related to *synchrotron radiation* caused by gyration of particles around the magnetic field lines.

that the spectral feature was not an artifact (e.g., due to incomplete shielding of the in-flight calibration source ^{241}Am, which emitted a spectral line at $E = 59.5$ keV). It was Joachim Trümper who first recognized that the excess emission at 58 keV (or an absorption feature at 42 keV, depending on interpretation – cf. Fig. 6.1) could be associated with the resonant electron cyclotron emission or absorption in the hot polar plasma of the rotating neutron star. The corresponding magnetic field strength would then be 6×10^{12} or 4×10^{12} G [152]. This observation provided the first direct measurement of a neutron star magnetic field and confirmed the basic theoretical predictions that neutron stars are highly magnetized, fast spinning compact objects.

Particularly important results on isolated neutron stars, among many other X-ray sources, were obtained with *HEAO-2*, widely known as the *Einstein* X-ray observatory. *Einstein* investigated the soft X-ray radiation from the previously known Crab and Vela pulsars and resolved the compact nebula around the Crab pulsar [2]. It discovered pulsed X-ray emission from two more very young pulsars, PSR B0540−69 in the Large Magellanic Cloud and PSR B1509−58, having periods of 50 and 150 ms, respectively. Interestingly, these pulsars were the

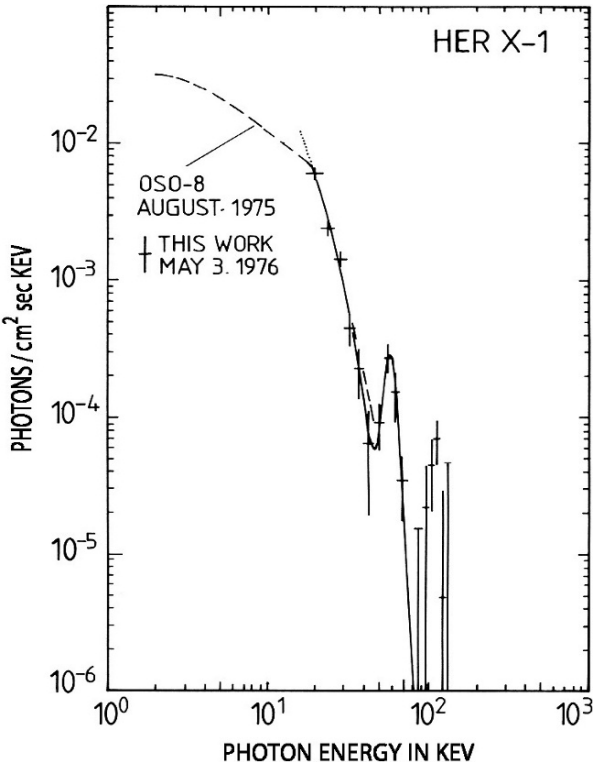

Fig. 6.1 Unfolded X-ray spectrum from Hercules X-1, showing the first measurement of a cyclotron line in a pulsed spectrum of an accreting neutron star. Image from [152]

first ones to be discovered in the X-ray band and only subsequently at radio frequencies. *Einstein* also detected X-rays from three middle-aged radio pulsars, PSR B0656+14, B1055−52, B1951+32 and the X-ray counterparts of two nearby old radio pulsars, PSR B0950+08 and B1929+10. In addition, many supernova remnants were mapped – 47 in our Galaxy and 10 in the Magellanic Clouds and several neutron star candidates were detected as faint, soft point sources close to the center of the supernova remnants RCW 103, PKS 1209−51/52, Puppis-A and Kes 73.

Some additional information on isolated neutron stars was obtained by *EXOSAT* (*European X-ray Observatory Satellite*). In particular, it measured the soft X-ray spectra of the middle-aged pulsar PSR B1055−52 and of a few neutron star candidates in supernova remnants (e.g., PKS 1209−51/52).

The situation improved drastically in the 1990s due to the results from ROSAT, ASCA, EUVE, BeppoSAX and RXTE, as well as Chandra and XMM-Newton launched close to the millennium. The complement to ROSAT, covering the harder X-ray band 1–10 keV, was *ASCA* launched in 1993. The *EUVE* (*Extreme Ultraviolet Explorer*) was launched in 1992 and was sensitive in the range 70–760 RA. It was able to observe several neutron stars at very soft X-rays, 0.07–0.2 keV. The contributions to neutron star research, provided by the instruments aboard *BeppoSAX*, sensitive in the range of 0.1–200 keV, and *RXTE* (*Rossi X-ray Timing Explorer*), both launched in the mid-1990s, were particularly useful for studying X-ray binaries, including accretion-powered pulsars.

At present *Chandra*, with its outstanding sub-arcsecond imaging capability and *XMM-Newton* with its unprecedently high spectral sensitivity and collecting power provide excellent new data.

In the following we will summarize the result on the X-ray emission properties of neutron stars based on observations with these missions. We will browse through the various categories from young Crab-like pulsars to very old radio pulsars, including recycled millisecond pulsars as well as neutron stars showing pure thermal emission. Before doing so, however, we will briefly review the various emission processes discussed to be the source for their observed X-ray emission.

6.2 Physics and Astrophysics of Isolated Neutron Stars

Neutron stars represent unique astrophysical laboratories which allow us to explore the properties of matter under the most extreme conditions observable in nature.[4] Studying neutron stars is therefore an interdisciplinary field, where astronomers and astrophysicists work together with a broad community of physicists. Particle, nuclear and solid-state physicists are strongly interested in the internal structure of neutron stars which is determined by the behavior of matter at densities above the nuclear density $\rho_{\rm nuc} = 2.8 \times 10^{14}$g cm^{-3}. Plasma physicists are modeling the pulsar emission mechanisms using electrodynamics and general relativity. It is beyond the

[4] Although black holes are even more compact than neutron stars, they can only be observed through the interaction with their surroundings.

scope of this article to describe in detail the current status of the theory of neutron star structure or the magnetospheric emission models. We rather refer the reader to the literature [21, 23, 53, 108, 158] and provide only the basic theoretical background relevant to Sect. 6.3 which summarizes the observed high-energy emission properties of rotation-powered pulsars and radio-quiet neutron stars.

6.2.1 Rotation-Powered Pulsars: The Magnetic Braking Model

Following the ideas of Pacini [120,121] and Gold [54,55] the more than 1,800 radio pulsars detected so far can be interpreted as rapidly spinning, strongly magnetized neutron stars radiating at the expense of their rotational energy. This very useful concept allows one to obtain a wealth of information on basic neutron star/pulsar parameters just from measuring the pulsar's period and period derivative. Using the Crab pulsar as an example will make this more clear. A neutron star with a canonical radius of $R = 10\,\mathrm{km}$ and a mass of $M = 1.4\,\mathrm{M}_\odot$ has a moment of inertia $I \approx (2/5)MR^2 \approx 10^{45}\,\mathrm{g\,cm^2}$. The Crab pulsar spins with a period of $P = 33.403\,\mathrm{ms}$. The rotational energy of such a star is $E_{\rm rot} = 2\pi^2\, I\, P^{-2} \approx 2\times10^{49}$ erg. This is comparable with the energy released in thermonuclear burning by a usual star over its entire live. Very soon after the discovery of the first radio pulsars it was noticed that their spin periods increase with time. For the Crab pulsar, the period derivative is $\dot{P} = 4.2\times10^{-13}\,\mathrm{s\,s^{-1}}$, implying a decrease in the star's rotation energy of $\mathrm{d}E_{\rm rot}/\mathrm{d}t \equiv \dot{E}_{\rm rot} = -I\Omega\dot{\Omega} = 4\pi^2 I\dot{P}P^{-3} \approx 4.5\times10^{38}\,\mathrm{erg\,s^{-1}}$. Ostriker and Gunn [117] suggested that the pulsar slow-down is due to the braking torque exerted on the neutron star by its magneto-dipole radiation, that yields $\dot{E}_{\rm brake} = -(32\pi^4/3c^3)\,B_\perp^2\,R^6\,P^{-4}$ for the energy loss of a rotating magnetic dipole, where $B_\perp$ is the component of the equatorial magnetic field perpendicular to the rotation axis. Equating $\dot{E}_{\rm brake}$ with $\dot{E}_{\rm rot}$, we find $B_\perp = 3.2\times10^{19}(P\dot{P})^{1/2}\,\mathrm{G}$. For the Crab pulsar, this yields $B_\perp = 3.8\times10^{12}\,\mathrm{G}$. From $\dot{E}_{\rm rot} = \dot{E}_{\rm brake}$ one further finds that $\dot{P} \propto P^{-1}$, for a given $B_\perp$. This relation can be generalized as $\dot{P} = k\,P^{2-n}$, where k is a constant, and n is the so-called magnetic braking index ($n = 3$ for the magneto-dipole braking). Assuming that the initial rotation period P_0 at the time t_0 of the neutron star formation was much smaller than today, at $t = t_0 + \tau$, we obtain $\tau = P/[(n-1)\dot{P}]$, or $\tau = P/(2\dot{P})$ for $n = 3$. This quantity is called the characteristic spin-down age. It is a measure for the time span required to lose the rotational energy $E_{\rm rot}(t_0) - E_{\rm rot}(t)$ via magneto-dipole radiation. For the Crab pulsar one finds $\tau = 1{,}258\,\mathrm{yrs}$. As the neutron star in the Crab supernova remnant is the only pulsar for which its historical age is known (the Crab supernova was observed by Chinese astronomers in 1054 AD, cf. also Sect. 6.3.1), we see that the spin-down age exceeds the true age by about 25%. Although the spin-down age is just an estimate for the true age of the pulsar, it is the only one available for pulsars other than the Crab, and it is commonly used in evolutionary studies such as, e.g., neutron star cooling (cf. Chaps. 11–12).

A plot of observed periods vs. period derivatives is shown in Fig. 6.2, using the pulsars from the ATNF online pulsar database [102]. Such a P–$\dot{P}$ diagram is

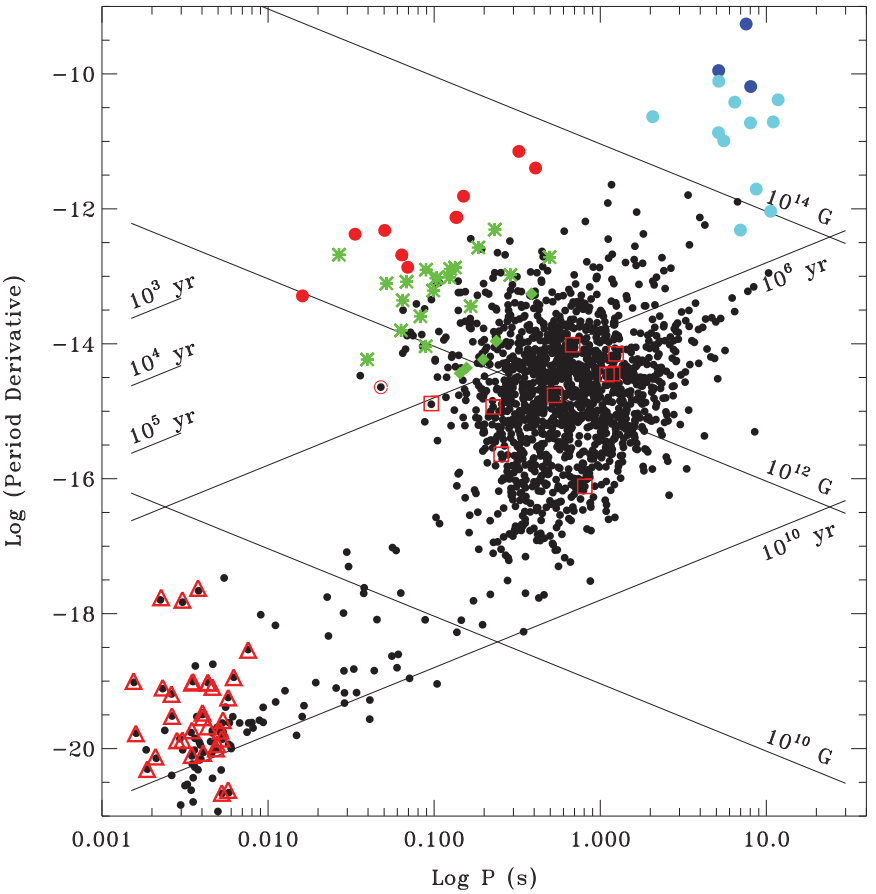

Fig. 6.2 The P–$\dot{P}$ diagram – distribution of rotation-powered pulsars (*small black dots*) over their spin parameters. The *straight lines* correspond to constant ages $\tau = P/(2\dot{P})$ and magnetic field strengths $B_\perp = 3.2 \times 10^{19}(P\dot{P})^{1/2}$ as deduced in the frame of the magnetic braking model. Separate from the majority of ordinary field pulsars are the millisecond pulsars in the lower left corner and the high magnetic field pulsars – soft gamma-ray repeaters (*dark blue*) and anomalous X-ray pulsars *light blue*) – in the *upper right*. Although magnetars and anomalous X-ray pulsars are not rotation-powered, they are included in this plot to visualize their estimated superstrong magnetic fields. X-ray detected pulsars are indicated by colored symbols. *Red filled circles* indicate the Crab-like pulsars. *Green stars* indicate Vela-like pulsars, *green diamonds* the X-ray detected cooling neutron stars, *red squares* million years old pulsars and *red triangles* the X-ray detected millisecond pulsars

extremely useful for classification purposes. The colored symbols represent those pulsars which were detected at X-ray energies by mid 2008. The objects in the upper right corner represent the soft-gamma-ray repeaters (SGRs) and anomalous X-ray pulsars (AXPs) which have been suggested to be magnetars (neutron stars with ultra strong magnetic fields).

Although the magnetic braking model is generally accepted, the *observed* spin-modulated emission, which gave pulsars their name, is found to account only for a small fraction of $\dot{E}$. The efficiencies, $\eta = L/\dot{E}$, observed in the radio and optical bands are typically in the range $\sim 10^{-7}$–10^{-5}, whereas they are about 10^{-4}–10^{-3} and $\sim 10^{-2}$–10^{-1} at X-ray and gamma-ray energies, respectively [15]. It has therefore been a long-standing question how rotation-powered pulsars lose the bulk of their rotational energy.

The fact that the energy loss of rotation-powered pulsars cannot be fully accounted for by the magneto-dipole radiation is known from the investigation of the pulsar braking index, $n = 2 - P\ddot{P}\dot{P}^{-2}$. Pure dipole radiation would imply a braking index $n = 3$, whereas the values observed so far are $n = 2.515 \pm 0.005$ for the Crab, $n = 2.8 \pm 0.2$ for PSR B1509−58, $n = 2.28 \pm 0.02$ for PSR B0540−69, 2.91 ± 0.05 for PSR J1911−6127, 2.65 ± 0.01 for PSR J1846−0258 and $n = 1.4 \pm 0.2$ for the Vela pulsar. The deviation from $n = 3$ is usually taken as evidence that a significant fraction of the pulsar's rotational energy is carried away by a pulsar wind, i.e., a mixture of charged particles and electromagnetic fields, which, if the conditions are appropriate, forms a *pulsar-wind nebula* observable at optical, radio and X-ray energies. Such pulsar-wind nebulae (often called plerions or synchrotron nebulae) are known so far *only* for a few young and powerful (high $\dot{E}$) pulsars and for some center-filled supernova remnants, in which a young neutron star is expected, but only emission from its plerion is detected.

Thus, the popular model of magnetic braking provides plausible estimates for the neutron star magnetic field $B_{\perp}$, its rotational energy loss $\dot{E}$, and the characteristic age τ, but it does not provide detailed information about the physical processes which operate in the pulsar magnetosphere and which are responsible for the broad-band spectrum, from the radio to the X-ray and gamma-ray bands. Forty years after the discovery of pulsars the physical details of their emission mechanisms are still barely known. As a consequence, there exist a number of magnetospheric emission models, but no generally accepted theory.

6.2.2 High-Energy Emission Models

Although rotation-powered pulsars are most widely known for their radio emission, the mechanism of the radio emission is poorly understood. However, it is certainly different from those responsible for the high-energy (infrared through gamma-ray) radiation observed from them with space observatories. It is well known that the radio emission of pulsars is a coherent process, and the coherent curvature radiation has been proposed as the most promising mechanism (see [108] and references therein). On the other hand, the optical, X-ray and gamma-ray emission observed in pulsars must be incoherent. Therefore, the fluxes in these energy bands are directly proportional to the densities of the radiating high-energy electrons in the acceleration regions, no matter which radiation process (synchrotron radiation, curvature radiation or inverse Compton scattering) is at work at a given energy. High-energy

observations thus provide the key for the understanding of the pulsar emission mechanisms. So far, the high-energy radiation detected from rotation-driven pulsars has been attributed to various thermal and non-thermal emission processes including the following:

- Non-thermal emission from charged relativistic particles accelerated in the pulsar magnetosphere (cf. Fig. 6.3). As the energy distribution of these particles follows a power-law, the emission is also characterized by power-law-like spectra in broad energy bands. The emitted radiation can be observed from optical to the gamma-ray band.
- Extended emission from pulsar-driven synchrotron nebulae. Depending on the local conditions (density of the ambient interstellar medium), these nebulae can be observed from radio through hard X-ray energies.
- Photospheric emission from the hot surface of a cooling neutron star. In this case a modified black-body spectrum and smooth, low-amplitude intensity variations with the rotational period are expected, observable from the optical through the soft X-ray range.
- Thermal soft X-ray emission from the neutron star's polar caps which are heated by the bombardment of relativistic particles streaming back to the surface from the pulsar magnetosphere.

In almost all pulsars the observed X-ray emission is due to a mixture of different thermal and non-thermal processes. Often, however, the available data do not allow to fully discriminate between the different emission scenarios. This was true for ROSAT, ASCA and BeppoSAX observations of pulsars and is – at a certain level – still true in Chandra and XMM-Newton data.

In the following subsections we will briefly present the basics on the magnetospheric emission models as well as material relevant to thermal emission from the neutron star surface.

Magnetospheric Emission Models

So far, there is no consensus as to where the pulsar high-energy radiation comes from (see for example [108] and Chaps. 15, 18 and 19). There exist two main types of models – the *polar cap models*, which place the emission zone in the immediate vicinity of the neutron star's polar caps, and the *outer gap models*, in which this zone is assumed to be close to the pulsar's light cylinder[5] to prevent materializing of the photons by the one-photon pair creation in the strong magnetic field, according to $\gamma + B \rightarrow \mathrm{e}^+ + \mathrm{e}^-$ (see Fig. 6.3). The gamma-ray emission in the polar cap models forms a hollow cone centered on the magnetic pole, producing either double-peaked or single-peaked pulse profiles, depending on the observer's line of

[5] The light cylinder is a virtual cylinder whose radius, $R_L = cP/(2\pi)$, is defined by the condition that the azimuthal velocity of the co-rotating magnetic field lines is equal to the speed of light.

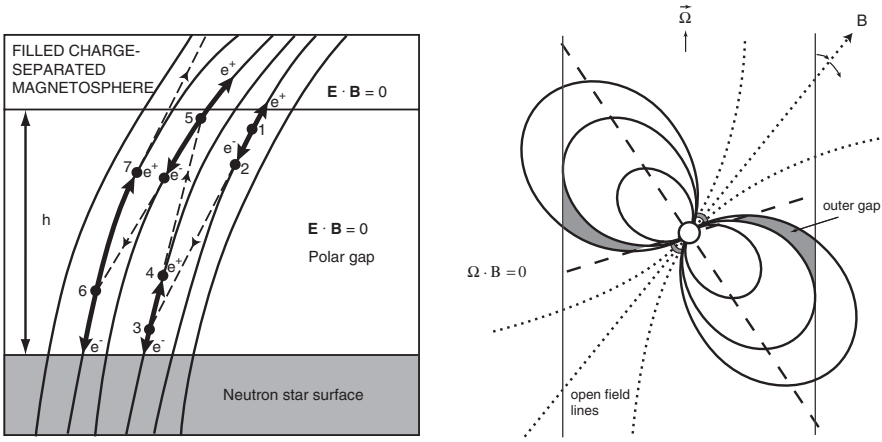

Fig. 6.3 Geometry of the acceleration zones as they are defined in the polar cap model (*left*), according to Ruderman and Sutherland [138], and outer gap model (*right*), according to Cheng, Ho and Ruderman [32, 33]. The polar cap model predicts "pencil" beams emitted by particles accelerated along the curved magnetic field lines. According to the outer gap model, the pulsar radiation is emitted in "fan" beams. Being broader, the latter can easier explain two (and more) pulse components as observed in some X-ray and gamma-ray pulsars

sight. The outer gap model was originally proposed to explain the bright gamma-ray emission from the Crab and Vela pulsars [32, 33] as the efficiency to get high-energy photons out of the high B-field regions close to the surface is rather small. Placing the gamma-ray emission zone at the light cylinder, where the magnetic field strength is reduced to $B_L = B(R/R_L)^3$, provides higher gamma-ray emissivities which are in somewhat better agreement with the observations. In both types of models, the high-energy radiation is emitted by relativistic particles accelerated in the very strong electric field, $\mathcal{E} \sim (R/cP)B$, generated by the magnetic field co-rotating with the neutron star. These particles are generated in cascade (avalanche) processes in charge-free gaps, located either above the magnetic poles or at the light cylinder. The main photon emission mechanisms are synchrotron/curvature radiation and inverse Compton scattering of soft thermal X-ray photons emitted from the hot neutron star surface.

In recent years the polar-cap and outer-gap models have been further developed, incorporating new results on gamma-ray emission from pulsars obtained with the Compton Gamma-Ray Observatory. At the present stage, the observational data can be interpreted with any of the two models, albeit under quite different assumptions on pulsar parameters. The critical observations to distinguish between the two models include, e.g., measuring the relative phases between the peaks of the pulse profiles at different energies. Probably the GLAST gamma-ray observatory (cf. Chap. 23) which is supposed to become operational in summer 2008 will provide valuable information to further constrain both models.

Thermal Evolution of Neutron Stars

Neutron stars are formed at very high temperatures, $\sim 10^{11}$ K, in the imploding cores of supernova explosions. Much of the initial thermal energy is radiated away from the interior of the star by various processes of neutrino emission (mainly, Urca processes and neutrino bremsstrahlung), leaving a one-day-old neutron star with an internal temperature of about 10^9–10^{10} K. After ~ 100 yr (typical time of thermal relaxation), the star's interior (densities $\rho > 10^{10}\,\mathrm{g\,cm^{-3}}$) becomes nearly isothermal, and the energy balance of the cooling neutron star is determined by the following equation:

$$C(T_i)\,\frac{\mathrm{d}\,T_i}{\mathrm{d}\,t} = -L_\nu(T_i) - L_\gamma(T_s) + \sum_k H_k\ ,$$

where T_i and T_s are the internal and surface temperatures, $C(T_i)$ is the heat capacity of the neutron star (cf. Chaps. 11 and 12). Neutron star cooling thus means a decrease of thermal energy, which is mainly stored in the stellar core, due to energy loss by neutrinos from the interior ($L_\nu = \int Q_\nu\,\mathrm{d}V$, Q_ν is the neutrino emissivity) plus energy loss by thermal photons from the surface ($L_\gamma = 4\pi R^2 \sigma T_s^4$). The relationship between T_s and T_i is determined by the thermal insulation of the outer envelope ($\rho < 10^{10}\,\mathrm{g\,cm^{-3}}$), where the temperature gradient is formed. The results of model calculations, assuming that the outer envelope is composed of iron, can be fitted with a simple relation

$$T_s = 3.1\,(g/10^{14}\,\mathrm{cm\,s^{-2}})^{1/4}\,(T_i/10^9\,\mathrm{K})^{0.549} \times 10^6\,\mathrm{K}\ ,$$

where g is the gravitational acceleration at the neutron star surface [64]. The cooling rate might be reduced by heating mechanisms H_k, like frictional heating of superfluid neutrons in the inner neutron star crust or some exothermal nuclear reactions.

Neutrino emission from the neutron star interior is the dominant cooling process for at least the first 10^5 years. After $\sim 10^6$ years, photon emission from the neutron star surface takes over as the main cooling mechanism. The thermal evolution of a neutron star after the age of $\sim$10–100 yr, when the neutron star has cooled down to $T_s = 1.5$–3×10^6 K, can follow two different scenarios, depending on the still poorly known properties of super-dense matter (see Fig. 6.13). According to the so-called *standard cooling scenario*, the temperature decreases gradually, down to ~ 0.3–1×10^6 K, by the end of the neutrino cooling era and then falls down exponentially, becoming lower than $\sim 0.1 \times 10^6$ K in $\sim 10^7$ yr. In this scenario, the main neutrino generation processes are the modified Urca reactions, $\mathrm{n} + N \rightarrow \mathrm{p} + N + \mathrm{e} + \bar{\nu}_e$ and $\mathrm{p} + N + \mathrm{e} \rightarrow \mathrm{n} + N + \nu_e$, where N is a nucleon (neutron or proton) needed to conserve momentum of reacting particles (cf. Table 6.1). In the *accelerated cooling scenarios*, associated with higher central densities (up to $10^{15}\,\mathrm{g\,cm^{-3}}$) and/or exotic interior composition (e.g., pion condensation, quark-gluon plasma), a sharp drop of temperature, down to 0.3–0.5×10^6 K, occurs at an age of $\sim$10–100 yr, followed by a more gradual decrease, down to the same $\sim 0.1 \times 10^6$ K at $\sim 10^7$ yr. The faster cooling is caused by the direct Urca reactions, $\mathrm{n} \rightarrow \mathrm{p} + \mathrm{e} + \bar{\nu}_e$ and $\mathrm{p} + \mathrm{e} \rightarrow \mathrm{n} + \nu_e$, allowed at very high densities.

Table 6.1 Nuclear reactions and their neutrino emissivity as a function of neutron star temperature [123]. T_9 is the temperature in units of 10^9 K. Each particle (n, p, e^-) which takes part in a reaction contributes to the temperature dependence with a T and each neutrino with a T^3. The reactions denoted as direct-Urca, π-condensate, Quark-URCA-process and Kaon condensate are taken into account in the so-called accelerated cooling models. They have an order of magnitude higher neutrino emissivity in comparison with the other nuclear reactions. The higher the neutrino emissivity is the more efficient is the neutron star cooling.

Neutrino emissivity used in neutron star cooling models		
Process	Nuclear reaction	Emissivity (erg/s/cm^3)
Direct URCA-process	$n \rightarrow p + e^- + \bar{\nu}_e$ $p + e^- \rightarrow n + \nu_e$	$\sim 10^{27} \times T_9^6$
π-Condensate	$n + \pi^- \rightarrow n + e^- + \bar{\nu}_e$ $n + e^- \rightarrow n + \pi^- + \nu_e$	$\sim 10^{26} \times T_9^6$
Quark-URCA-process	$d \rightarrow u + e^- + \bar{\nu}_e$ $u + e^- \rightarrow d + \nu_e$	$\sim 10^{26}\ \alpha_c\ T_9^6$
Kaon condensate	$n + K^- \rightarrow n + e^- + \bar{\nu}_e$ $n + e^- \rightarrow n + K^- + \nu_e$	$\sim 10^{25} \times T_9^6$
Modified URCA-process	$n + n \rightarrow n + p + e^- + \bar{\nu}_e$ $n + p + e^- \rightarrow n + n + \nu_e$	$\sim 10^{21} \times T_9^8$
Direct coupled Electron–Neutrino-process	$\gamma + e^- \rightarrow e^- + \nu_e + \bar{\nu}_e$ $\gamma_{plasmon} \rightarrow \nu_e + \bar{\nu}_e$ $e^+ + e^- \rightarrow \nu_e + \bar{\nu}_e$	$\sim 10^{20} \times T_9^8$
Neutron–Neutron and Neutron–Proton-Bremsstrahlung	$n + n \rightarrow n + n + \nu + \bar{\nu}$ $n + p \rightarrow n + p + \nu + \bar{\nu}$	$\sim 10^{19} \times T_9^8$
Electron–Ion–Neutrino-Bremsstrahlung	$e^- + (Z,A) \rightarrow$ $e^- + (Z,A) + \nu_e + \bar{\nu}_e$	$\propto T_9^6$

The neutron star models used in these calculations are based on a *moderate* equation of state which opens the direct Urca process for $M > 1.35\,M_\odot$, the stars with lower M undergo the standard cooling. Recent studies have shown that both the standard and accelerated cooling can be substantially affected by nucleon superfluidity in the stellar interiors (see [122, 153, 163] for comprehensive reviews). In particular, many cooling curves exist intermediate between those of the standard and accelerated scenarios, depending on the properties of nucleon superfluidity, which are also poorly known.

Thus, the thermal evolution of neutron stars is very sensitive to the composition and structure of their interiors, in particular, to the equation of state at supernuclear densities. Therefore, measuring surface temperatures of neutron stars is an important tool to study super-dense matter. Since typical temperatures of such neutron stars correspond to the extreme UV – soft X-ray range, the thermal radiation from cooling neutron stars can be observed with X-ray detectors sufficiently sensitive at $E \lesssim 1$ keV.

6.3 High-Energy Emission Properties of Neutron Stars

As a result of observations with the satellite observatories Einstein, ROSAT, ASCA, BeppoSAX, Chandra and XMM-Newton, 89 rotation-powered pulsars were detected at X-ray energies by mid 2008 (cf. Tables 6.8 and 6.9). Thus, in nearly ten years of operation XMM-Newton and Chandra have almost tripled the number of detected X-ray pulsars compared to what was known at the end of the ROSAT mission in February 1999 [13]. Table 6.2 reflects the progress made in recent years in detecting pulsars of various categories at X-ray energies. This progress clearly goes along with the increase of sensitivity and angular resolution of the available X-ray observatories. While XMM-Newton with its super collecting power allows to obtain timing and spectral information even from faint and millions of years old pulsars, Chandra stands for sub-arcsecond angular resolution which made it possible to detected and study neutron stars located in source confused regions such as supernova remnants and globular clusters.

Fortunately, with the increase in sensitivity of todays observatories a growing number of neutron stars are detected in more than just one waveband (e.g., at radio, optical, EUV, X- and gamma-rays), making it possible for the first time to carry out multi-wavelength studies of the pulsar emission. This is a big advantage as the physical processes which are responsible for the emission in different wavelength bands are obviously related to each other. Multiwavelength studies thus provide a much broader view into the physical processes operating in the neutron star magnetosphere than interpreting emission properties observed in a single wave band only.

6.3.1 Young Neutron Stars in Supernova Remnants

X-ray observations allow us to find both supernova remnants (SNRs) and the compact objects that may reside within them. In fact, neutron stars and neutron star

Table 6.2 Progress in detecting rotation-powered pulsars with X-ray observatories. Status as of July 2008. While EINSTEIN had only the sensitivity to see pulsed X-ray emission from the youngest and brightest pulsars and to detect a few others at the limit of its sensitivity, ROSAT/ASCA and XMM-Newton/Chandra allowed for the first time to study the emission mechanisms of rotation-powered pulsars based on a broader sample and of various categories.

Pulsar age (years)	Pulsar category	Einstein	ROSAT ASCA	XMM-Newton Chandra
$\leq 10^4$	Crab-like	3	5	9
10^4–10^5	Vela-like	1	9	22
10^5–10^6	Cooling NS		5	6
10^6–10^8	Old and nearby	1	3	9
	binary		1	1
$\geq 10^8$	ms-Pulsar		11	42
	Σ detected:	5	33	89

candidates have been found in a small fraction of the 265 known galactic SNRs [61].[6] About 38 of these compact stellar remnants in SNRs are radio pulsars, others are radio-silent (or, at least, radio-quiet) neutron stars which were found as faint point-like X-ray sources near to the geometrical center of their supernova remnant (cf. section "Central Compact Objects in Supernova Remnants").

Being in orbit for more than 80% of their nominal lifetime almost all young radio pulsars have been observed and detected by either XMM-Newton and/or Chandra (cf. Fig. 6.2). The young rotation-powered pulsars can be divided in two groups, Crab-like and Vela-like pulsars, according to somewhat different observational manifestations apparently associated with the evolution of pulsar properties with age. The radio-silent neutron stars include anomalous X-ray pulsars (AXPs), soft gamma-ray repeaters (SGRs), and "quiescent" neutron star candidates in SNRs (called Central Compact Objects, CCOs). Transient radio emission was seen from few AXPs recently [27, 101]. There is growing evidence that AXPs and SGRs are indeed magnetars (see Chap. 21 and [162] for a review). Magnetars are neutron stars with an ultra strong magnetic field ($B \geq 10^{14}$ G) which is supposed to be the source of the detected high energy radiation. A common property of these objects is that their periods are in a narrow range of 5–12 s, substantially exceeding typical periods of radio pulsars. While no gamma-ray emission has been detected from AXPs, SGRs occasionally emit soft gamma-ray bursts of enormous energy (up to 10^{42}–10^{44} erg), a property, which gave this sources their name.

Crab- and Vela-Like Pulsars

On July 4, 1054 AD, Chinese astronomers noted a *guest star* in the constellation Taurus. As we know today, this event marked the arrival of light from the death of a massive main sequence star which underwent a core collapse when its internal thermal energy produced by the nuclear fusion processes was not sufficient anymore to counteract the gravitational force against the star's collapse. The cloud of gas which we observe today at the position of this *guest star* is the Crab supernova remnant. In the optical band the nebula has an extent of 4×6 arcmin, corresponding to $\sim 7 \times 10$ light years for a distance of 2 kpc.

What we observe from the Crab nebula in X-rays is not the thermal emission from the ejecta-driven blast wave of the supernova, though, but the emission from charged particles which emit synchrotron radiation as they move along magnetic field lines. In X-rays the nebula has the form of a torus with jets, wisps and a counter-jet, having an overall extent of 2×2 arcmin in the sky. For the 2 kpc distance the radius of the torus is 0.38 pc, that of the inner ring is 0.14 pc [159]. In a series of Chandra and HST monitoring observations it was found that the nebula near to the pulsar shows temporal variability on time scales of days to weeks and month [72] (cf. also Chaps. 15 and 16). An image showing the Crab nebula and pulsar as observed by Chandra's Low Energy Transmission Grating detector is shown in Fig. 6.4.

[6] http://www.mrao.cam.ac.uk/surveys/snrs/ .

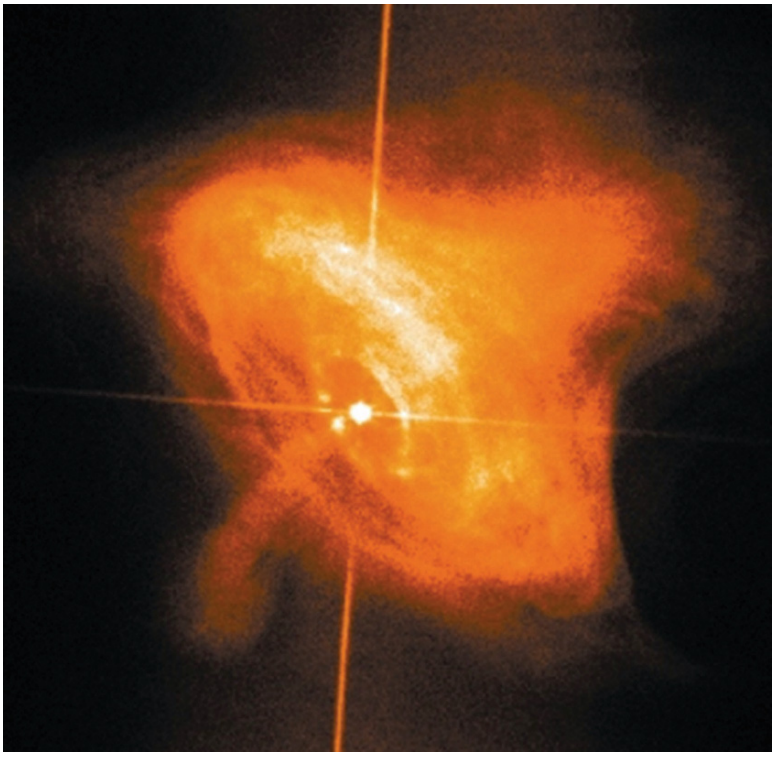

Fig. 6.4 The Crab nebula and its central pulsar as observed by the Chandra LETG detector. The cross-like feature is an artefact from the spectrum dispersed by the LETG fine-support bars

In studying this system it became clear very early that the observed non-thermal emission required a continuous input of energetic charged particles to keep the nebula emitting. It was the question of the Crab nebula's central engine which caused Pacini [120] a few month before the discovery of radio pulsars to propose that a fast spinning and strongly magnetized neutron star could be the required source which supplies the energy into the nebula.

Indeed, the 33-ms pulsar in the Crab supernova remnant, PSR B0531+21, was the first rotation-powered pulsar from which high energy radiation was detected. Being the strongest rotation-powered pulsar with the highest spin-down energy it was considered – until recent years – to be the prototype for all young neutron stars of age 10^3–10^4 years. Because of this and its favorable brightness it was studied in all frequency bands and by almost every observatory suitable to do so. The pulsar's characteristic double peaked pulse profile and its energy spectrum have been measured in detail throughout almost the entire electromagnetic spectrum. A compilation of pulse profiles as observed from the radio to the X-ray bands is shown in Fig. 6.5.

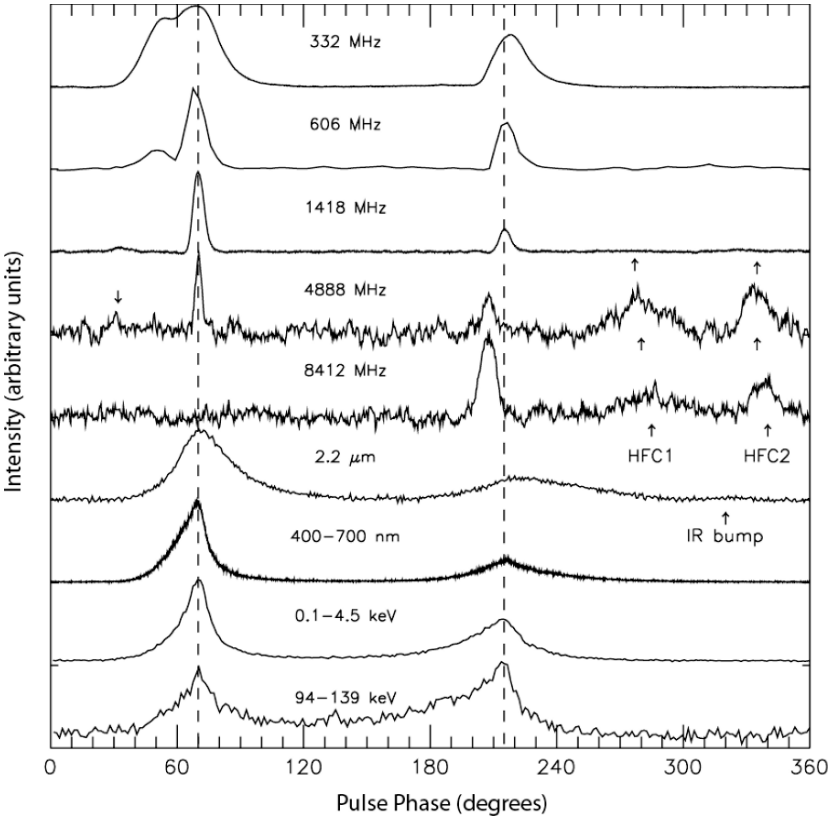

Fig. 6.5 The Crab pulsar's characteristic pulse profiles as observed at various frequency bands (from [111]). The phases of low (LFC) and high frequence (HFC) radio pulse components are indicated. The *dashed lines* indicate the phase of the main pulse component and the interpulse. The profiles have been arbitrarily aligned by the peak of the main pulse

Despite this strong interest and a wealth of data which have been taken from the pulsar since its discovery, it only recently became clear in deep Chandra observations that the X-ray emission from the Crab pulsar is actually 100% pulsed [149] and that the radio, optical and X-ray pulses are not fully phase aligned as suggested by high-energy emission models. Indeed, the X-ray pulses lead the optical pulses by the small amount of $\sim$68 μs and the optical the radio pulses by 236 μs (cf. Fig. 6.6). Mapping these pulse arrival time differences to photon travel-time differences means that for X-ray and optical pulses the arrival time delay can correspond to a difference in emission heights of 50–100 km.

As far as the pulsar's emission mechanisms are concerned, it is very well established that magnetospheric emission from charged particles, accelerated in the neutron star magnetosphere along the curved magnetic field lines, dominates the radiation not only from the Crab pulsar but from almost all young rotation-powered pulsars with ages $\lesssim$5,000 years (cf. Sect. 6.2.2). Accordingly, the radiation

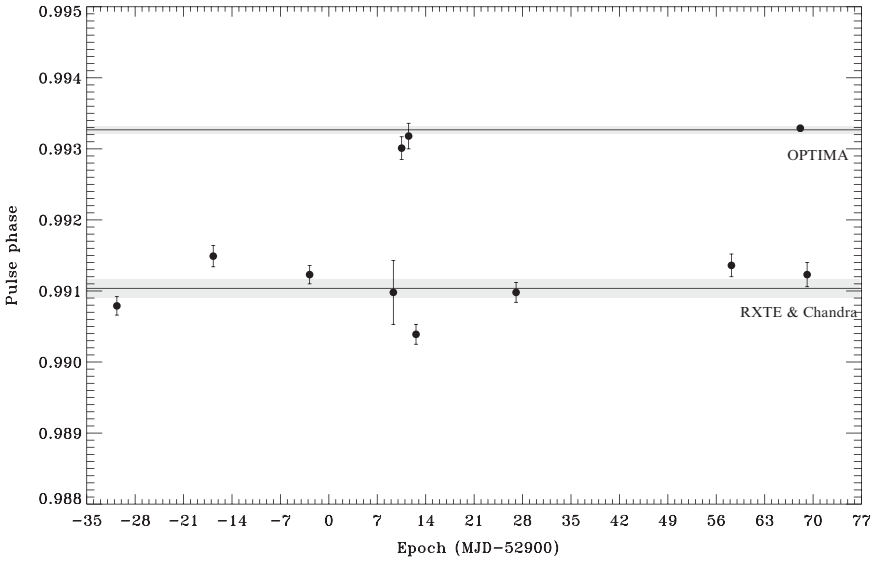

Fig. 6.6 Phase difference of the Crab pulsar's first pulse peak observed at optical and X-ray energies by OPTIMA and RXTE/Chandra. (From [5])

of Crab-like pulsars is characterized by a power-law spectrum, $\mathrm{d}N/\mathrm{d}E \propto E^{-\alpha}$, in which α is called photon-index. This implies that the energy distribution of the charged particles emitting this radiation also follows a power-law in a broad energy range. For the Crab pulsar the slope of its photon energy spectrum slowly increases with photon energy – the photon index varies from $\alpha = 1.6$ at $E \sim 1$ keV to $\alpha = 2.1$ at $E \sim 10^{10}$ eV.

Besides the Crab several other young pulsars have been studied in deep Chandra and XMM-Newton observations. Two pulsars remarkable for their rather hard X-ray spectra are PSR J1617−5055 and PSR J1811−1959 [12, 85]. PSR J1617−5055 is a 69-ms pulsar located about 7 arcmin outside the boundary of the young supernova remnant RCW 103 (cf. Fig. 6.7). The spin-down age of the pulsar is $\tau \sim 8,000$ years (cf. Table 6.8) placing it among the youngest known radio pulsars. An association of the remnant RCW 103 and the pulsar was discussed but found to be unlikely [45,92]. The pulsar distance is not very well constrained. The radio dispersion measure yields a distance of 6.1–6.9 kpc [38] but it was conclude from a comparison between dispersion measure based distances and distances obtained from HI absorption measurements of PSR 1641−45 and PSR 1718−35 – which are both located within 20° of PSR J1617−5055 – that the pulsar could be as close as ∼4.5 kpc [92]. PSR J1617−5055 was discovered by its X-ray pulses in archival GINGA data [151]. XMM-Newton observations classified the pulsar emission as non-thermal [12], with a rather flat photon-index of $\alpha = 1.1$–1.4 (cf. Table 6.6). The pulsar emission turns out to be highly absorbed, prohibiting any measurement of the softer cooling emission from the neutron star surface. Strong pulsed emission up to 15 keV was

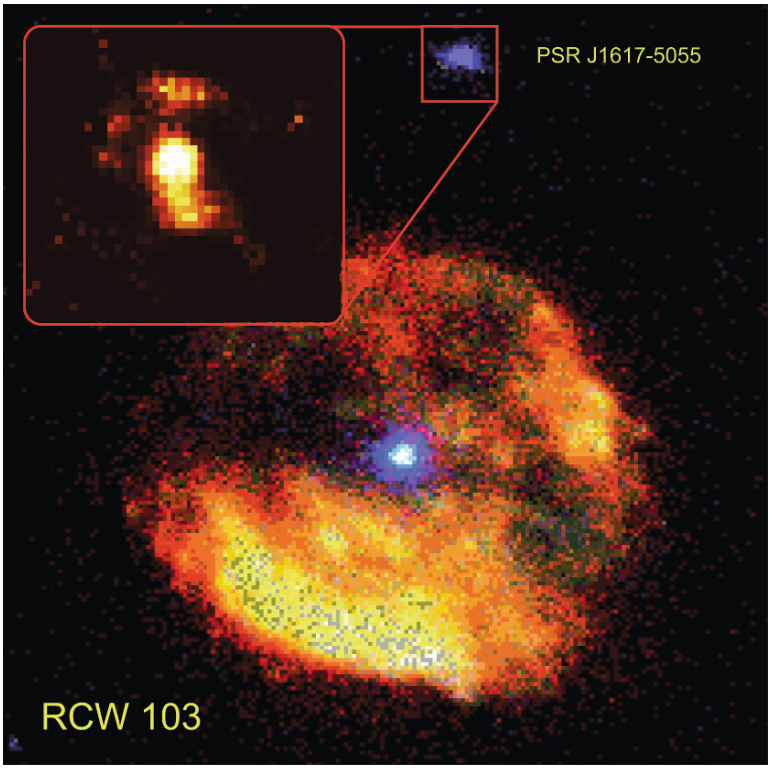

Fig. 6.7 X-ray view of RCW 103 and the young pulsar PSR J1617−5055 as observed by XMM-Newton and Chandra, respectively. The central source in RCW 103 is the CCO 1E 1613−5055. The zoomed in Chandra image on the *upper left* shows the plerion surrounding PSR J1617−5055. (RCW 103 image from [12], PSR J1617−5055 *inset* from [85])

detected by XMM-Newton [12]. The X-ray pulse profile shown in Fig. 6.8 is single peaked and shows a cross similarity to the radio profile. The pulsed fraction is at the level of 50%.

Only recently a pulsar was detected which seems to contradict this empirical evidence of non-thermal dominated emission in young rotation-powered pulsars. PSR J1119−6127, which is located in the SNR G292.2−0.5, has an age of ∼1,600 yrs and a deduced magnetic field strength of $B \sim 4.1 \times 10^{13}$ G. The latter is close to the quantum critical field of $B_{QED} = m_e^2 c^3 / e\hbar = 4.4 \times 10^{13}$ G and close to the magnetar range. There is strong evidence that its spectrum is dominated by thermal radiation corresponding to a temperature of $\sim 2.4 \times 10^6$ K and an emitting radius of ∼2.7 km while its pulsed fraction in the 0.5–2.0 keV band is as high as $\sim 74 \pm 14\%$ [57, 140]. PSR J1119−6127 thus is the youngest pulsar for which thermal emission is detected. It is an interesting question of whether the presence of the strong magnetic field causes the completely different emission scenario than observed in other young and Crab-like pulsars. A synchrotron nebula surrounding

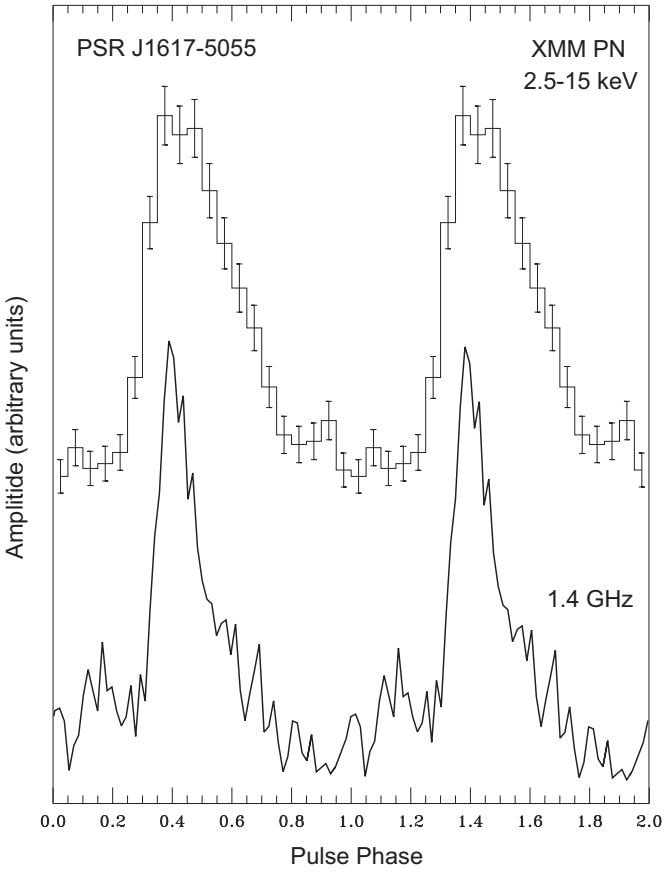

Fig. 6.8 X-ray and radio pulse profiles of PSR J1617−5055 as observed in the 2.5–15 keV band with the XMM-Newton and at 1.4 GHz with the Parkes Radio Telescope. The X-ray pulse has a duty cycle of ∼50% in the 2.5–15 keV band. Two pulse cycles are shown for clarity. Radio pulse profile from [92]

the pulsar has been detected recently above 2 keV and consists of jet-like structures extending to at least 7 arcsec from the pulsar [140]. At least from this point of few the pulsar seems to fit to the emission properties seen in other pulsars of this age.

Pulsars with a spin-down age of $\sim 10^4$–10^5 years are often referred to as Vela-like pulsars, because of their apparent similar emission properties. Among the 22 pulsars of this group which have been detected in X-rays, five of them (the Vela pulsar PSR B0833−45, PSRs J2229+6114, B1706−44, B1046−58 and B1951+32) were detected with the EGRET Gamma-ray observatory, and only the Vela pulsar has been detected in the optical band. In some respects, these objects appear to be different from the Crab-like pulsars. In particular, their optical radiation is very faint compared to that of the very young pulsars, and the overall shape of their high-energy spectra looks different. For instance, the closest ($d \approx 250$ pc) and, hence,

best-investigated Vela pulsar has an optical luminosity four orders of magnitude lower than the Crab pulsar [114], whereas its rotation energy loss is only a factor of 65 lower. Its pulse profile at various wavelength is very complex and difficult to associate with the many possible emission mechanisms [99, 103]. The pulsed fraction in the soft X-ray range, $\approx 7\%$, is much lower than that observed from Crab-like pulsars.

In contrast to the young Crab-like pulsars, the soft X-ray spectrum of the Vela pulsar has a substantial thermal contribution (cf. Table 6.6) with an apparent temperature of $\approx 10^6$ K [103, 119]. On the other hand, the spatial structure of the Vela plerion strongly resembles the inner Crab nebula – it also has a torus-like structure, an inner ring and jets (see Fig. 6.9) and shows temporal intensity variations on time scales of weeks to month [127]. The symmetry axis of the nebula, which can be interpreted as the projection of the pulsar's rotation axis onto the sky plane, is roughly co-aligned with the direction of proper motion. This is similar as observed in the Crab pulsar although the misalignment there is $26 \pm 3°$. The idea of a torus configuration formed by a shock-confined pulsar wind was first introduced by Aschenbach and Brinkmann [2] as a model to explain the shape of the inner Crab

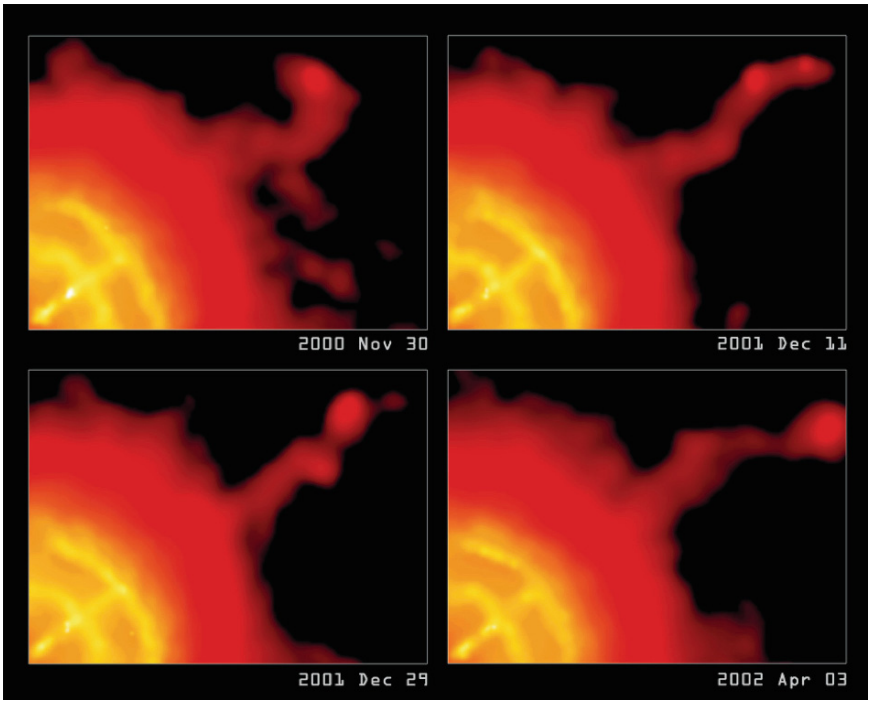

Fig. 6.9 The Vela pulsar and its plerion as observed by the Chandra ACIS-I detector. A torus and jets are seen similar as in the Crab plerionic nebula. The symmetry axis is almost aligned to the pulsar's proper motion direction. The jets are seen to vary in form and intensity on time scales of weeks to month. (Courtesy NASA/CXC/PSU/ [127])

nebula. The discovery of a similar torus-like structure in the Vela synchrotron nebula indicated that this model may be applicable to many young pulsars. According to this model, the torus-like structure and its geometrical orientation with respect to the direction of the pulsar's proper motion arise because the interaction of the post-shock plasma with the ambient medium compresses the plasma and amplifies the magnetic field ahead of the moving pulsar. This, in turn, leads to enhanced synchrotron emission with the observed torus-like shape [143].

Thus, young rotation-powered pulsars are in general surrounded by pulsar-powered nebulae (plerions) and/or supernova ejecta. The pulsar wind nebulae have been seen to show variable emission features on time scales of days to weeks and month [72, 127]. Presumably, the pulsars' magnetospheric emission extends from at least the infrared to gamma-ray energies, with typical photon indices varying between $\alpha \approx 1$–2 (cf. Tables 6.6 and 6.7). As the plerionic emission is synchrotron radiation its spectrum is a power law. In the Crab plerion Willingale et al. [161] found that the shape of the spectrum changes as a function of distance from the pulsar. He fitted the power law slope of the torus ($\alpha = 1.8 \pm 0.006$), the jet ($\alpha = 2.1 \pm 0.013$) and the outer nebula regions ($\alpha = 2.34 \pm 0.006$). Similar results were obtained by Chandra, measuring the hardness ratio distribution throughout the nebula [159]. For the pulsar, a photon spectral index of $\alpha = 1.63 \pm 0.07$ is observed (cf. Tables 6.6 and 6.7). The spectral difference between the jet and the torus is found to be likely due to an intrinsically steeper electron spectrum of the jet. The outer regions of the nebula show the steepest spectrum, which is likely to be due to enhanced synchrotron losses of the electrons during their ride from the pulsar to the outskirts.

Central Compact Objects in Supernova Remnants

For many years, it has been generally believed that all young neutron stars have similar emission properties as those observed in Crab- and Vela-like pulsars, i.e., emitting strongly pulsed radiation caused by non-thermal emission processes in the neutron star's magnetosphere. Several recent observations of compact X-ray sources in supernova remnants, however, suggest that this picture is incomplete and indeed no longer justified: it has been shown that there are other manifestations of young neutron stars, e.g., as anomalous X-ray pulsars, soft gamma-ray repeaters or simply as faint point-like X-ray source in a supernova remnant. Most of these sources were identified by their high X-ray to optical flux ratios, others simply by their locations near to the expansion centers of supernova remnants, strongly suggesting that they are indeed the compact stellar remnants formed in the supernova events. The group of SNRs which are known to host a radio-quiet but X-ray bright central compact object (CCO) is listed in Table 6.3.

Whether this group of CCOs forms a homogenous class of sources such as the rotation-powered pulsars is currently an open question and is actually difficult to answer in view of the small number of known objects. All sources in common is that (1) they are located in supernova remnants of age $\leq 10^4$ yrs, (2) their X-ray luminosi-

Table 6.3 List of X-ray detected radio-quiet and optically dim central compact objects in supernova remnants (status: mid 2008). The X-ray luminosity is computed for the energy band 0.5–10 keV and the specified distances.

CCO	Hosting SNR	Age (kyr)	d (kpc)	P	$\log L_x$ (erg s^{-1})	Ref.
CXO J232327.8+584842	Cas-A	∼0.3	∼3.4	...	∼32.94	[47, 147]
CXO J085201.4−461753	Vela-Jr	∼2?	∼1.0?	...	∼32.40	[3, 88]
RX J0822−4300	Pupis-A	∼2	∼2.2	0.22[a] s	∼33.71	[80, 130]
1E 1207.4−5209	PKS 1209−51/52	∼10	∼2.0	0.424 s	∼33.12	[59, 69]
CXO J185238.6+004020	Kes 79	∼9	∼7.1	0.105 s	∼33.48	[58, 141]
RX J1713.7−3946	G347.3−0.5	∼10	∼1.0	...	∼32.78	[96, 131]
1E 1613−5055	RCW 103	∼2	∼3.3	6.67 h	Variable	[42, 154]

[a]The periodicity of RX J0822−4300 awaits confirmation.

Table 6.4 Spectral parameters from double-blackbody fits to the CCOs in CAS-A (CXOU J232327.8+584842), Vela-Jr (CXOU J085201.4−461753), Puppis-A (RX J0822−4300), PKS 1209−51/52 (1E 1207.4−5209), Kes 79 (CXOU J185238.6+004020), G347.3−0.5 (RX J1713.7−3946) and RCW 103 (1E 1613−5055). Status mid 2008. The unabsorbed X-ray flux is computed for the energy band 0.5–10 keV. The radii of the projected emitting areas are computed for the distances specified in Table 6.3. Errors correspond to a $1-\sigma$ confidence interval.

CCO in SNR	$N_h/10^{21}$ (cm^{-2})	$T_1/10^6$ (K)	R_1 (km)	$T_2/10^6$ (K)	R_2 (km)	$f_x/10^{-12}$ (erg/cm/s)	Ref.
Cas-A	$12.5^{+0.3}_{-0.3}$	$4.89^{+0.07}_{-0.07}$	$0.83^{+0.03}_{-0.03}$			6.30	[67]
Vela-Jr	$3.8^{+0.4}_{-0.3}$	$4.0^{+0.3}_{-0.5}$	$0.36^{+0.05}_{-0.03}$	$6.6^{+3.1}_{-1.2}$	$0.06^{+0.06}_{-0.04}$	2.11	[7]
Pupis-A	$4.5^{+0.5}_{-0.4}$	$2.6^{+0.3}_{-0.3}$	$3.3^{+1.1}_{-0.7}$	$5.1^{+0.3}_{-0.2}$	$0.75^{+0.12}_{-0.15}$	8.94	[80]
PKS 1209−51/52	$1.0^{+0.1}_{-0.1}$	$1.92^{+0.03}_{-0.03}$	$4.5^{+0.1}_{-0.1}$	$3.7^{+0.02}_{-0.02}$	$0.83^{+0.03}_{-0.03}$	2.78	[44]
Kes 79	14^{+3}_{-3}	$5.3^{+0.5}_{-0.5}$	$0.8^{+0.1}_{-0.1}$			0.51	[58]
G347.3−0.5	$4.7^{+0.3}_{-0.4}$	$6.6^{+0.8}_{-0.8}$	$0.6^{+0.9}_{-0.9}$	$3.7^{+0.23}_{-0.23}$	$0.11^{+0.05}_{-0.05}$	5.10	[30]
RCW 103	$16.5^{+1.5}_{-1.5}$	$4.6^{+0.5}_{-0.5}$	$2.3^{+0.7}_{-0.6}$	$9.1^{+0.9}_{-0.9}$	$0.35^{+0.15}_{-0.12}$	Variable	[12]

ties are all in the braked 10^{32}–10^{33} erg s^{-1}, (3) down to an extent of $\leq$1 arcsec none of them has been seen to maintain a plerionic X-ray nebula such as the Crab, Vela or other young pulsars and (4) no radio or optical counterpart could be detected from any CCO by now.

None of these properties is distinctive enough to justify the conclusion that all these sources form an own class of objects (e.g., Geminga is radio-silent as well). Interestingly, though, is that all CCOs share very similar spectral properties and those are markedly different from what is observed in young rotation-powered pulsars. The X-ray spectra of virtually all CCOs are very well modeled by a two component blackbody model with temperatures in the range $T_{bb} = (2\text{–}7) \times 10^6$ K and sizes of the projected emitting areas at the level of $R_{bb} \sim (0.3\text{–}5)$ km (cf. Table 6.4).

The projected emitting radii are in all cases much smaller than a canonical neutron star radius, suggesting that the radiation is emitted from a small part of the neutron star surface. It is, however, by no means clear that the double-blackbody spectral model represents the correct physical description of the emission process, even this model fits the data. An alternative spectral model providing equally good fits than the double-blackbody model does consists of a blackbody plus a power law. The inferred slope of the power law component, though, is ∼4–5 which is steeper than the photon-index $\alpha = 1$–3 observed for other rotation-powered pulsars (cf. Tables 6.6 and 6.7). However, as the true nature of the CCOs and their emission mechanisms are unknown it might not be justified to use the steepness of the power law to reject these models as unphysical. Worth to mention in this context is that the spectra observed from AXPs also require a composite blackbody plus power law model to fit. Spectral parameters obtained from them are similar to what is fitted in CCO spectra [49, 107]. The only CCO for which spectral line features were observed is 1E 1207.4−5209 [44]. A possible interpretation of this spectral features in terms of electron cyclotron absorption at ∼0.7, ∼1.4, ∼2.1 and ∼2.8 keV yields a neutron star magnetic field of $0.6\,(1+z)\times 10^{11} G \sim 8\times 10^{10}$ G [44]. Herein, z is the gravitational redshift which was assumed to be at the level of 25%.

Despite the common spectral emission properties there are distinct differences in the temporal emission properties of some CCOs. For 1E 1613−5055 a strong periodic modulation at 6.67 ± 0.03 h has been found in long XMM-Newton observations along with changes in the X-ray flux by factors 10–100. The latter lends evidence that 1E 1613−5055 is actually in an eccentric orbit with a low-mass star [12, 42]. Flux variability have not been observed in any of the other CCOs. Upper limits obtained by the current observatories are in the 5–10% range.

X-ray pulsations have been observed from CXOU J185238.6+004020 in Kes 79 [58] and 1E 1207.4−5209 in PKS 1209−51 [169]. CXOU J185238.6 and 1E 1207.4−5209 seem to have a very stable rotation period with almost no spin-down over few years [59]. The small spin-down implies that these CCOs may have a rather small magnetic field and that these sources were born with a period close to the one observed today. The latter scenario could mean that CCOs are anti-magnetars rather than magnetars. Clearly, pulsations in more CCOs need to be detected to turn this evidence in a definite conclusion.

It recently became possible to measure the proper motion of a CCO and to confirm that its back projected birth place is in agreement with the remnants explosion center, thus providing the first confirmation that CCOs are indeed the compact remnants formed in the birth event of the hosting supernova remnant. Using two Chandra data sets which span an epoch of 1,952 days Hui and Becker [81] found that the position of RX J0822−4300 in Puppis-A differs by 0.57 ± 0.18 arcsec, implying a proper motion of $\mu = 107 \pm 34$ mas yr^{-1} (cf. Figs. 6.10 and 6.11). For a distance of 2.2 kpc, this proper motion is equivalent to a recoil velocity of 1120 ± 360 km s^{-1}. Both the magnitude and direction of the proper motion are in agreement with the birth place of RX J0822−4300, being near to the optical expansion center of the supernova remnant.

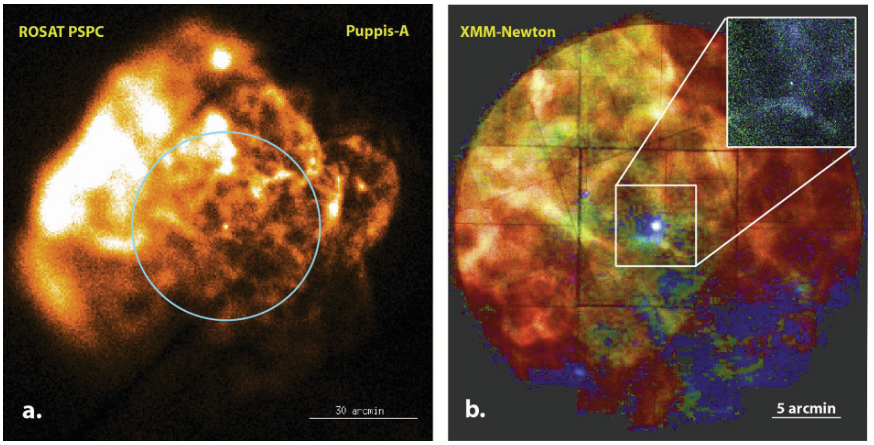

Fig. 6.10 **a** Composite ROSAT HRI image of the Puppis-A supernova remnant. The *blue ring* indicates the 30 arcmin central region which has been observed by XMM-Newton. **b** XMM-Newton MOS1/2 false color image of the central region of Puppis-A (*red*: 0.3–0.75 keV, *green*: 0.75–2 keV and *blue*: 2–10 keV). The central source is the CCO RX J0822−4300. The *inset* shows the squared region as observed by the Chandra HRC-I

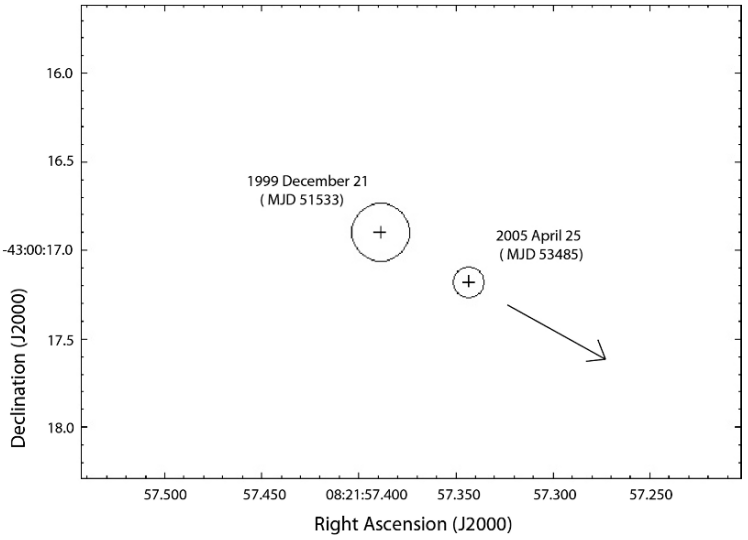

Fig. 6.11 The position (with error circle) of the cental compact object RX J0822−4300 in Puppis-A as observed by Chandra in December 1999 and April 2005. The *arrow* indicates the proper motion direction

It finally is worth to mention that, by now, the relatively small number of discovered members of this class might be to a large fraction due to observational selection effects only. From the observers point of view it is much easier to detect

and identify active pulsars than these quiet compact sources observable only in the soft X-ray band. Also, once a supernova remnant disappears after about 10^5 yrs, it is almost impossible to find and identify its left over CCO. It is therefore very plausible that, in fact, CCOs may be more common than young Crab- and Vela-like radio pulsars.

6.3.2 Cooling Neutron Stars

Thermal radiation from neutron star surfaces was first detected in an unambiguous way from the Vela pulsar, PSR B0656+14, Geminga and PSR B1055−52 [118,119] using ROSAT. ROSAT also discovered seven neutron stars showing pure thermal emission in X-rays (cf. Chap. 7). More sources and many more details on spectra and temporal emission properties of cooling neutron stars were obtained with Chandra and XMM-Newton cf. [11] and Chap. 9). This data have clearly demonstrated that the soft X-ray radiation of rotation-powered pulsars in an age interval of $\sim 10^5$–10^6 yrs is dominated by thermal emission from the neutron star surface. These pulsars are apparently old enough for their magnetospheric emission to become fainter than the thermal surface emission, but they are still young and hot enough to be detectable in the soft X-ray range. As this XMM-Newton and Chandra data have shown, all middle aged pulsars for which the photon statistics is sufficient for a detailed spectral modeling require three spectral components to be modeled. This composite model includes a thermal cooling, a thermal (heated) polar-cap and a non-thermal magnetospheric emission component (cf. Fig. 6.12). The latter component is a power-law (PL) spectrum which prevails in the IR, optical, hard X-ray and gamma-ray ranges. An example fit to the IR-optical-X-ray spectrum of PSR B0656+14 is shown in Fig. 6.12.

Figure 6.13 shows a comparison of observed neutron star temperatures as a function of age compared with the results of standard cooling theory as summarized by Yakovlev and Pethick [163, 164]. For a more detailed comparison of observations and predictions from a variety of cooling models please confer Chaps. 11 and 12. Neutron star surface temperature upper limits for million years old pulsars, like PSR B1929+10, have been obtained for the first time by XMM-Newton. They are summarized in Table 6.5.

6.3.3 Old Nearby Radio Pulsars

Before the start of XMM-Newton, a consistent scenario for the evolution of the X-ray emission properties of aging rotation-powered pulsars was not available. This surprising fact was largely due to the lack of sufficient observational data. Young and middle aged neutron stars, which emit strong pulsed non-thermal and/or surface hot-spot plus cooling emission, were studied reasonably well in the X-ray band. In

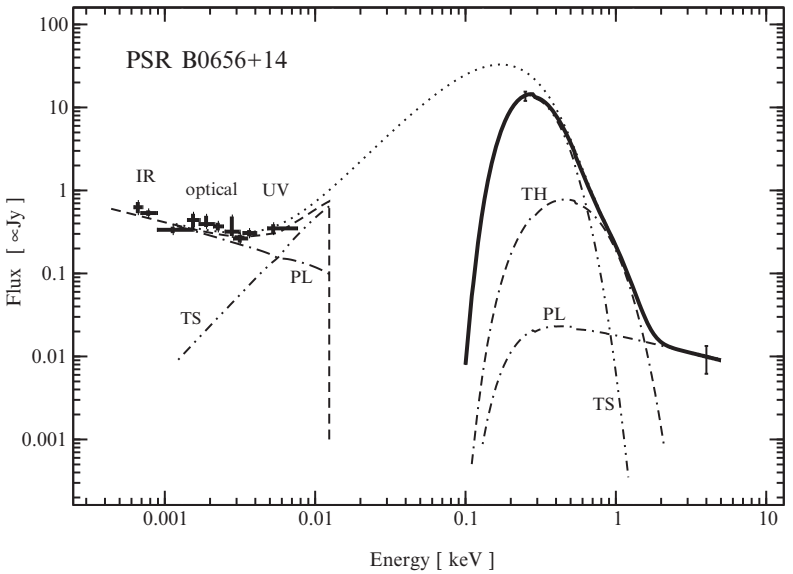

Fig. 6.12 Energy spectrum of PSR B0656+14, a prototype middle-aged cooling neutron star. Shown is the X-ray spectrum fitted with a model consisting of thermal soft (TS), thermal hard (TH) and power-law (PL) components, and IR–optical–UV fluxes measured with the HST and ground-based telescopes. The *dashed and dotted lines* show the continuation of the X-ray spectrum to the optical band with and without allowance for interstellar absorption. Figure from [13]

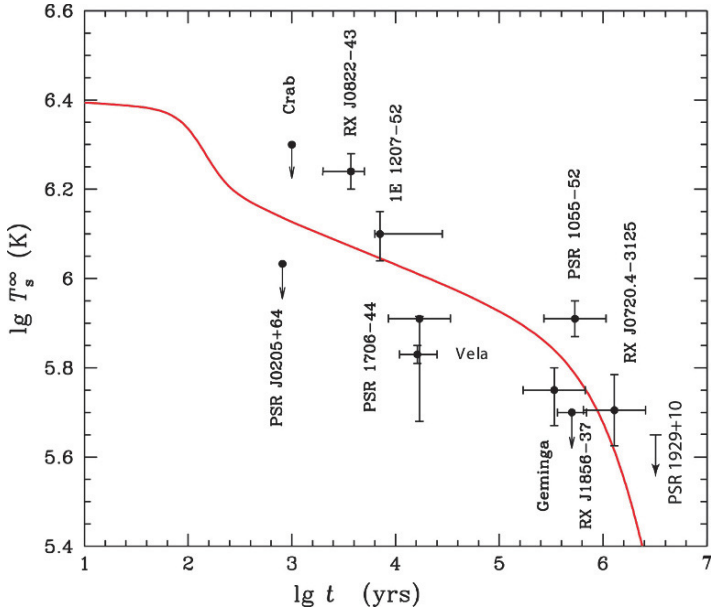

Fig. 6.13 Observations of surface temperatures and upper bounds for several isolated neutron stars. The *solid line* is the basic theoretical cooling curve of a non-superfluid neutron star with $M = 1.3\,\mathrm{M}_\odot$ [163]. The upper limit on the temperature of the old pulsar PSR 1929+10 was added [8]

Table 6.5 3σ-Surface temperature upper limits for old non-recycled pulsars. The upper limits were obtained from adding an additional thermal component (which accounts for blackbody emission from the whole neutron star of radius $R_{NS} = 10$ km) to the best fit power law spectra. See [8–10] for details.

Pulsar	Spin-down age (10^6 years)	$3\sigma\ T_s^\infty$ (10^6 k)
B2224+65	1.12	$\leq$0.68
J2043+2740	1.20	$\leq$0.62
B0628−28	2.75	$\leq$0.53
B1929+10	3.10	$\leq$0.45
B0823+26	4.92	$\leq$0.50
B0950+08	17.5	$\leq$0.48

contrast, most old radio pulsars were too faint for a detailed examination of their X-ray emission. However, especially old rotation-powered non-recycled pulsars are of particular interest for the study of particle acceleration and high energy radiation processes near the neutron star's surface and in its magnetosphere. This is because their ages are intermediate between those of the well-studied young and cooling neutron stars, whose surface may produce copious thermal X-ray photons, and those of very old recycled millisecond pulsars, in which thermal hot-spot and non-thermal magnetospheric X-ray production mechanisms are believed to dominate.

Old, non-recycled pulsars therefore aid in answering questions such as how do the emission properties of the younger pulsars, like Geminga, PSR B0656+14 and PSR B1055−52, change as they age from $\sim 10^5$ to 10^7 years? Will the thermal emission simply fade away due to cooling with increasing age or will the star be kept hot (at about $0.5–1 \times 10^5$ K) over millions of years due to energy dissipation by processes such as internal frictional heating ($\dot{E}_{diss} \sim 10^{28}$–$10^{30}$ erg s^{-1}) and crust cracking, as proposed by vortex creeping and pinning models? What happens to the non-thermal, hard-tail emission seen in the X-ray spectra of the middle-aged field pulsars? Will this emission become the dominant source or will this component also decay with time and will only thermal emission from the hot and heated polar-caps remain?

If one extrapolates the X-ray emission properties of young and cooling neutron stars to this age bracket, one may expect that the cooling emission fades away and thermal emission from heated polar caps dominates the X-rays. Surprisingly, the X-ray emission from old pulsars is largely dominated by non-thermal radiation processes [8–10]. None of the pulsars' X-ray spectra required the inclusion of a thermal component to model the energy spectra (cf. Tables 6.6 and 6.7). Further support for an emission scenario dominated by non-thermal emission mechanisms is given by the observed temporal emission properties. The pulse profiles of PSRs B1929+10, B0950+08 and B0628−28 are not broad and sinusoidal as would have been expected for spin-modulated thermal X-ray emission from heated polar caps, but are double peaked with narrow pulse components and pulsed fractions in the range of ∼30–50% (cf. Fig. 6.14).

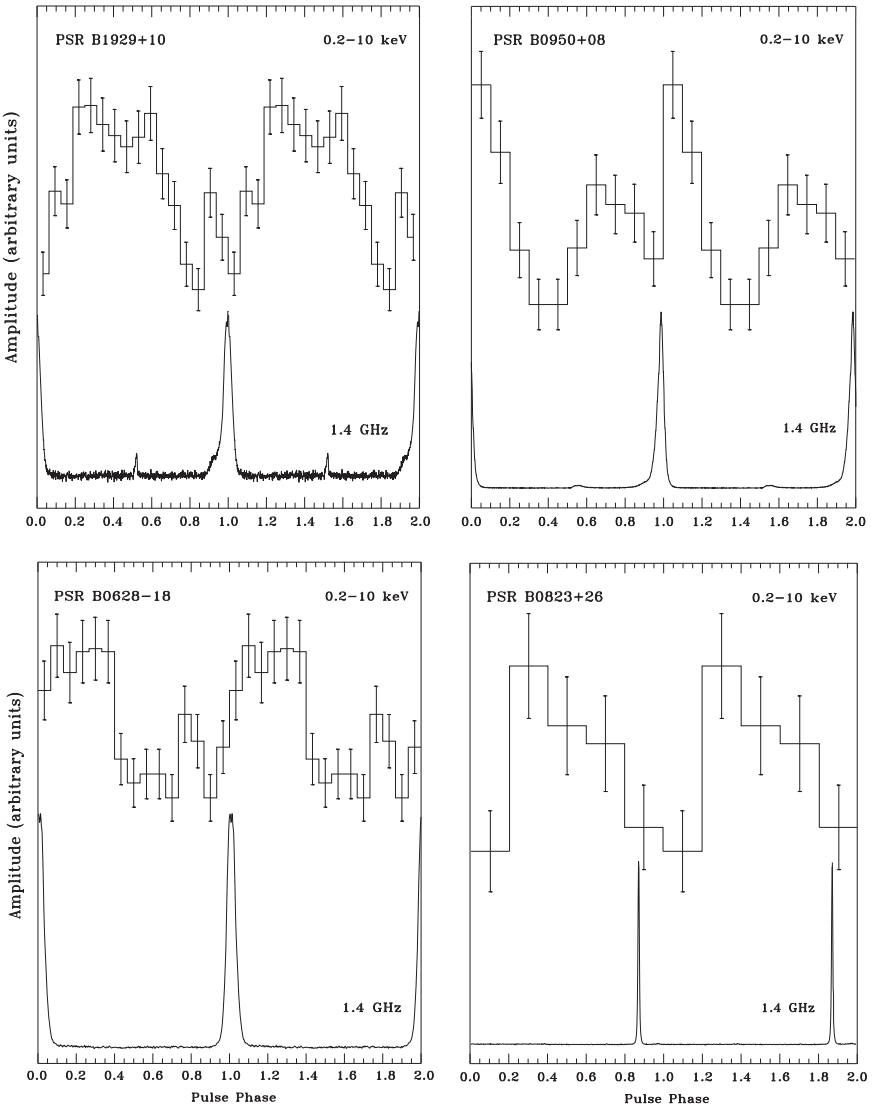

Fig. 6.14 Integrated pulse profiles of the old pulsars PSR B1929+10, B0950+08, B0628−28 and B0823+06 as observed by XMM-Newton (*top*) and at 1.4 GHz with the Effelsberg radio telescope. X-ray and radio profiles are phase aligned. Two cycles are shown for clarity. Small energy dependences in the profiles are observed for B1929+10 and B0950+08

Some models (cf. Chap. 19 and references therein) predict in the framework of the revised space-charge-limited flow model that polar cap heating, as a fraction of the spin-down luminosity, increases with pulsar age and should be most efficient for pulsars of spin-down age $\tau \sim 10^7$ yrs, if they are in fact producing pairs from curvature radiation photons. However, according to [66], PSR B0950+08 and B0823+26

cannot produce pairs from curvature radiation of primary electrons since they both lie below the curvature radiation pair death line in the P–$\dot{P}$ diagram of radio pulsars (cf. [10] for a more detailed discussion). Nevertheless, attempts have been made to fit the spectrum of PSR B0950+08 and PSR B1929+10 by including thermal models (cf. [77, 168]). By statistical means such thermal components are not required to fit the observed spectra. Therefore, contributions from heated polar caps in old pulsars have the character of upper limits rather than detections.

6.3.4 Millisecond Pulsars

In the P–$\dot{P}$ parameter space, millisecond pulsars (ms-pulsars) are distinguished from the majority of ordinary-field pulsars by their short spin periods of $\leq$20 ms and small period derivatives of $\approx 10^{-18}$–10^{-21} (cf. Fig. 6.2). In the frame of the magnetic braking model this corresponds to very old spin-down ages of typically 10^9–10^{10} years and low magnetic field strengths of $\sim 10^8$–10^{10} G. More than $\sim$75% of the known disk ms-pulsars are in binaries, usually with a low-mass white dwarf companion, compared to $\cong$1% binaries among the ordinary pulsars. This gives support to the idea that these neutron stars have been spun-up by angular momentum transfer during a past mass accretion phase [1, 4, 22]. Further evidence for this came from the discovery of seven accreting ms-pulsars which seem to confirm this scenario (see [160] for a review). Presumably, these pulsars were originally among ordinary pulsars which would have turned off because of the loss of their rotational energy if they were not in close binaries (cf. Fig. 6.15). Millisecond pulsars are therefore often called "recycled" pulsars to better distinguish them from fast spinning pulsars seen in young supernova remnants.

By mid of 2008, about 10% of the $\sim$1,800 known radio pulsars fall into the category of ms-pulsars, i.e., are recycled (cf. [102] and Chaps. 1 and 2). The majority of them (almost 137) are located in 25 globular clusters [28] which apparently provide a favorable environment for the recycling scenario. Of these globular cluster ms-pulsars 56 (41%) are solitary, the others are in binaries. Interestingly, the ratio of solitary to binary ms-pulsars is almost identical to the 40% observed in the population of galactic disk ms-pulsars. The formation of solitary recycled pulsars is not well-understood, but it is widely believed that either the pulsar's companion was evaporated (a process which is believed to be at work in the PSR 1957+20 ms-pulsar/binary system) or the system was tidally disrupted after the formation of the ms-pulsar.

Recycled pulsars had been studied exclusively in the radio domain until the 1990s, when ROSAT, ASCA, EUVE, RXTE and BeppoSAX were launched. The first millisecond pulsar discovered as pulsating X-ray source was PSR J0437−4715 [17], a nearby 5.75-ms pulsar which is in a binary orbit with a low-mass white dwarf companion. Further detections followed, which, by mid 2008 sum up to $\sim$47% of all X-ray detected rotation-powered pulsars (cf. Tables 6.8 and 6.9). The data quality available from them, though, is far from being homogenous. While from several

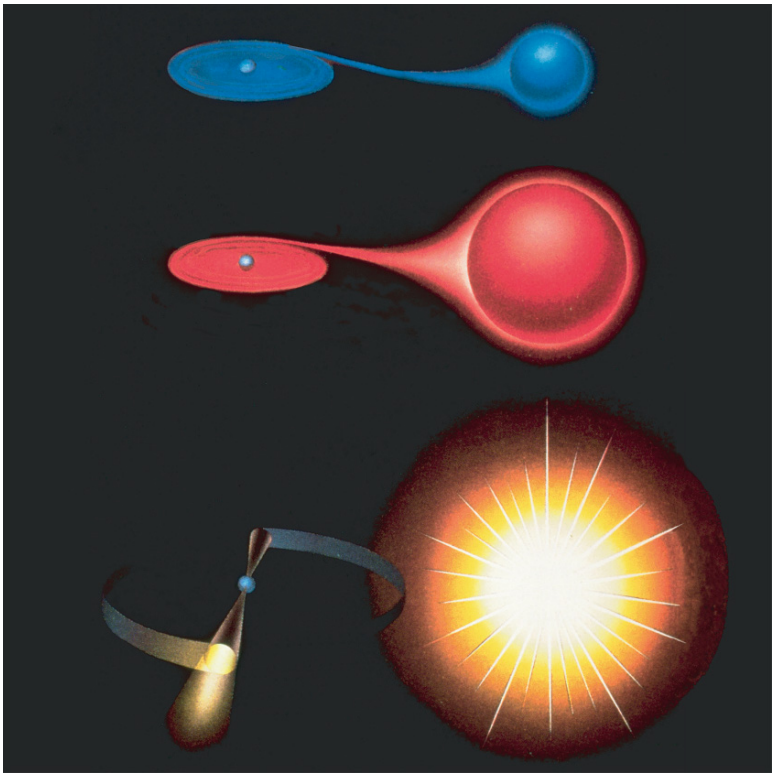

Fig. 6.15 Weakly-magnetized neutron stars that accrete matter from low-mass companion stars form the ∼150 currently known low-mass X-ray binaries (LMXBs). These systems are believed to be the progenitors of "recycled" pulsars. Along with the accretion of matter angular momentum transfer from the companion star takes place which spins-up the neutron star to millisecond periods. As the companion star evolves, a solitary ms-pulsar or a ms-pulsar binary system is left

ms-pulsars high quality spectral, temporal and spatial information is available, many others, especially those on globular clusters, are just detected with a handful of events (cf. also Chap. 8). Nevertheless, the improvements in sensitivity by Chandra and XMM-Newton provided a step forward in classifying the ms-pulsars' X-ray emission properties, indicating that there is a dichotomy between thermal and non-thermal dominated emitters, similar to what is observed from non-recycled pulsars.

X-ray emission observed from ms-pulsars which have a spin-down energy of $\dot{E} \geq 10^{35}\,\mathrm{erg\,s^{-1}}$, i.e., PSR J0218+4232, PSR B1821−24 and PSR B1937+21, is caused by non-thermal radiation processes [11, 94, 115]. This is confirmed by their power law spectra (photon-index α in the range 1.5–2, cf. Table 6.7) and pulse profiles which show narrow peaks and have pulsed fractions of up to ∼90–100% (cf. Fig. 6.16). Common in these pulsars is that all show relatively hard X-ray emission, which made it possible to study some of them already with ASCA, BeppoSAX and RXTE. For example, emission from PSR B1821−24 and PSR B1937+21 is

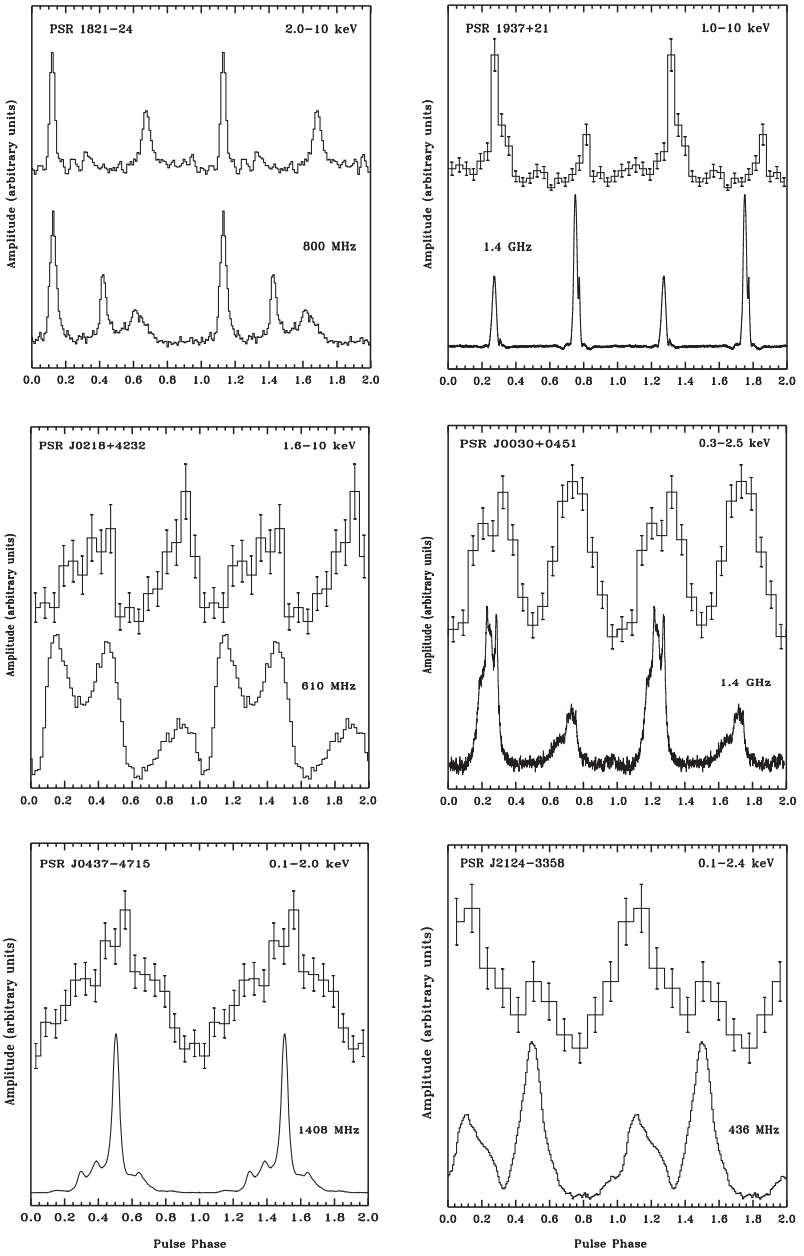

Fig. 6.16 X-ray and radio pulse profiles for the six brightest ms-pulsars. Two full pulse cycles are shown for clarity. The relative phase between the radio and X-ray pulses is only known for PSR 1821−24, B1937+21, 0218+4232 and PSR J0437−4715 with sufficient accuracy. The phase alignment in all other cases is arbitrary

detected by RXTE up to ∼20 keV [110] and PSR J0218+4232 is a candidate for a gamma-ray pulsar [94].

For the remaining ms-pulsars ($P \geq 4$ ms, $\log \dot{E} \sim 33$–34 erg s^{-1}) the X-ray emission is found to be much softer. Their X-ray spectra can be described by compound models consisting of a blackbody plus a power law component (cf. Table 6.7). The latter is required to describe the emission beyond 2–3 keV. For PSR J0437−4715 which is the brightest ms-pulsar detected in X-rays and thus is the one for which the best photon statistics is available, a three component spectral model is required to fit the observed energy spectrum. The model consists of a two temperature blackbody plus a power law model. The X-ray spectrum of PSR J0437−4715 as detected with XMM-Newton is shown in Fig. 6.17.

The relatively small blackbody radii found by these spectral fits suggest that the thermal emission is coming from one or two heated polar-caps whereas the power law component describes the non-thermal radiation emitted from accelerated particles in the co-rotating magnetosphere. The prototypical ms-pulsar of this group, which is still the one for which the best data are available, is the nearest and brightest millisecond pulsar PSR J0437−4715. It was already evident in the ROSAT and ASCA data that its X-ray emission consists of at least two different spectral components [15, 17].

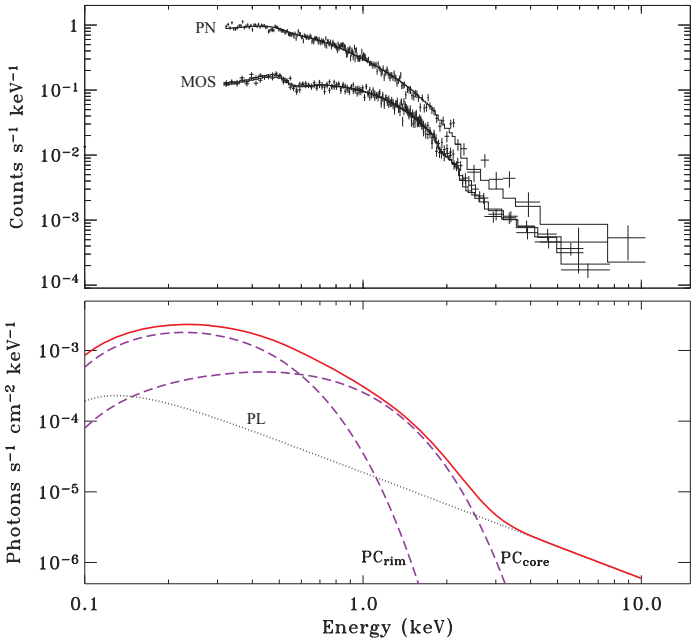

Fig. 6.17 X-ray spectrum of PSR J0437−4715. The *solid curves* show the best fitting model which is the sum of a power law (PL) and a two temperature blackbody model labeled as *core* and *rim*. (From [166])

Chandra and XMM-Newton data have further constrained its emission properties (see [24,166] and Chap. 8). The two thermal components are interpreted as emission from a hot polar cap, having a non-uniform temperature distribution with a hot core ($T_{core} = 1.4 \times 10^6$ K, $R_{core} = 0.4$ km) and a cooler rim ($T_{rim} = 0.5 \times 10^6$ K, $R_{rim} \sim 2.6$ km). The power law component yields a photon index of $\alpha \sim 2.0$. The size of the polar cap is found to be roughly in agreement with the theoretical predictions. Defined as the area of open field lines in which the bombardment by relativistic particles is expected, it is $R_{pc} = R(R\Omega/c)^{1/2}$. Assuming $R = 10$ km for the neutron star radius and taking $\Omega = 1.09 \times 10^3$ for the pulsars angular frequency yields $R_{pc} = 1.9$ km for a polar cap radius of PSR J0437−4715.

Interaction between the relativistic pulsar wind (which carries away the pulsar's rotational energy) and the surrounding interstellar medium is expected to create detectable diffuse emission. If the physical conditions are appropriate this emission takes the form of a pulsar bow-shock nebula as shown in Fig. 6.18.

By now, such diffuse emission is seen in H_α from the black widow pulsar PSR B1957+20 [75,146], from PSR J0437−4715 [19], and from PSR J2124−3358 [50]. Diffuse X-ray emission associated with these bow-shock nebulae could only be detected from PSR B1957+20 [19, 146] and from the solitary ms-pulsar PSR J2124−3358 [82]. For the latter the emission extends from the pulsar to the northwest by ∼0.5 arcmin (cf. Fig. 6.18b). Adopting the pulsar distance of ∼250 pc, the tail has a length of $\sim 1.1 \times 10^{17}$ cm. The spectrum of the diffuse tail emission can be modeled with a power-law of photon index 2.2 ± 0.3, in line with the emission originating from accelerated particles in the post shock flow. Comparable deep observations to those of PSR J2124−3358 and PSR B1957+20 have been performed by XMM-Newton in previous years on almost all X-ray bright ms-pulsars. For PSR J0437−4715, PSR J0030+0451 and PSR J1024−0719, which

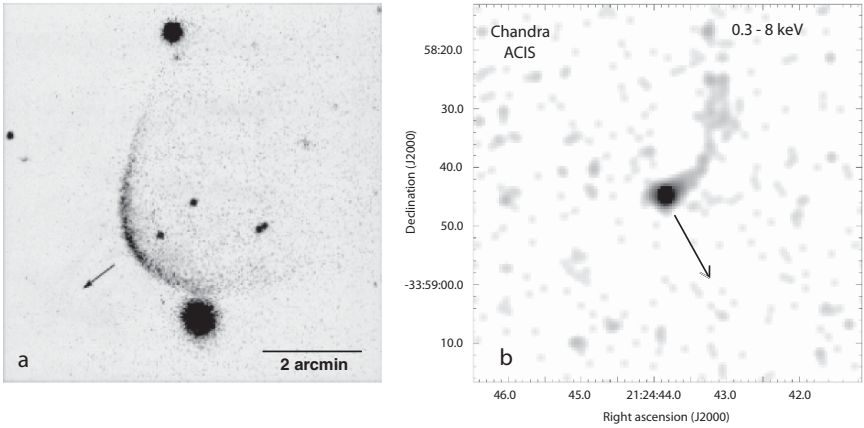

Fig. 6.18 **a** The bow-shock around PSR J0437−4715 as visible in H_α. **b** Chandra image of PSR J2124−3358 and its diffuse, arc-like X-ray emission associated with the pulsar's bow-shock [82]. The pulsars' proper motion directions are indicated

all have spin parameters similar to that of PSR J2124−3358, no diffuse emission was detected down to a $3-\sigma$ limiting flux of $\sim$4–7 $\times\, 10^{-15}$ erg s^{-1} cm^{-2} [82]. The latter suggests that the formation of bow-shocks depends not on the pulsars spin-parameters but might be a function of, e.g., the ISM density and pulsar proper motion.

The majority of the detected ms-pulsars reside in globular clusters. The first millisecond pulsar discovered in a globular cluster was PSR B1821−24A [100] which is located in M28 (NGC 6626). Its inferred pulsar parameters make it the youngest ($P/2\dot{P} = 3.0 \times 10^7$ yrs) and most powerful ($\dot{E} = 2.24 \times 10^{36} I_{45}$ erg s^{-1}) pulsar among all known MSPs (cf. Fig. 6.19 and Table 6.9). Since the *Einstein* era it has been clear that globular clusters contain various populations of X-ray sources of very different luminosities [70]. The stronger sources ($L_x \approx 10^{36}$–10^{38} erg s^{-1}) were seen to exhibit X-ray bursts which led to their identification as low-mass X-ray

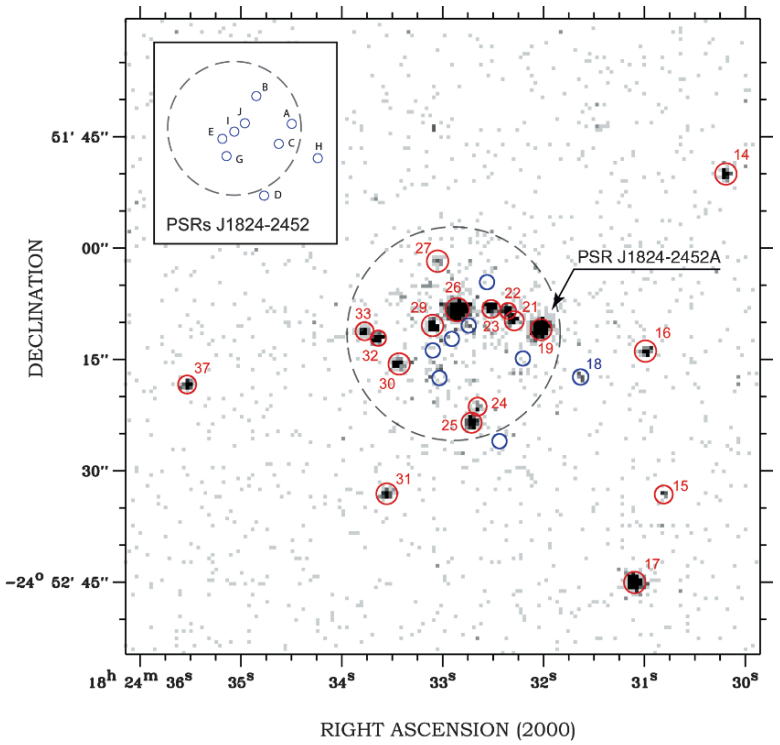

Fig. 6.19 Chandra ACIS image of the central region of the globular cluster M 28. The position of the recently discovered new ms-pulsars are indicated by *blue circles*. Most sources are located within or near to the core-radius (*dashed-circle*). The binary millisecond pulsar PSR J1824−2425H is in agreement with X-ray source #18 [6, 11]. There is faint (only partly resolved) emission near to the center of the cluster. This emission is in agreement with the location of the recently discovered radio pulsars J1824−2425J, J1824−2425I, and J1824−2425E. The *upper left inset* helps to locate the different MSPs. Image from [6]

binaries (LMXBs). The nature of the weaker sources with $L_x \leq 3\times10^{34}$ erg s^{-1} however, was more open to discussion [37,83]. Although many weak X-ray sources were detected in globulars by ROSAT [83, 155], their identification has been difficult due to low photon statistics and strong source confusion in the crowded globular cluster fields, except for a few cases. Of particular interest are the results obtained from Chandra observations of PSR B1821−24A in M28 [11] and on 47 Tuc=NGC 104. From the latter Grindlay [63] reported the detection of 108 sources within a region corresponding to about five times the 47 Tuc core radius. Nineteen of the soft/faint sources (cf. Table 6.9) were found to be coincident with radio-detected millisecond pulsars (MSPs), and Grindlay [62, 63] concluded that more than 50% of all the unidentified sources in 47 Tuc are MSPs. This conclusion is in line with theoretical estimates on the formation scenarios of short-period (binary) pulsars in globular clusters [135]. The application of the Chandra X-Ray Observatory sub-arcsecond angular resolution along with the temporal resolution provided by its HRC-S detector allowed to search for X-ray pulsations from the 47 Tuc millisecond pulsars. This, however, is not just a matter of exposure time. So far, a 830 ksec deep observation found X-ray pulses at a $\sim4\,\sigma$ level from only three 47 Tuc millisecond pulsars [26].

M28 is the globular cluster with the third largest population of known pulsars. Only in Terzan 5 and 47 Tuc more millisecond pulsars have been found by now. Nine new millisecond pulsars were discovered in M28 in a recent radio survey [18]. Inspecting the archival Chandra data to search for possible X-ray emission from these recently discovered radio pulsars allowed to identify the counterpart CXC 182431−245217 of PSR J1824−2425H, while some faint unresolved X-ray emission near to the center of M28 is found to be coincident with the millisecond pulsars PSR J1824−2452G, J1824−2452J, J1824−2452I and J1824−2452E (cf. Fig. 6.19 and [6]). This finding strongly suggests that indeed a large fraction of the unresolved X-ray emission in globular clusters could be from fainter, so far undiscovered millisecond pulsars [11].

6.4 Summary

By mid 2008, emission from 89 rotation-powered pulsars has been detected in the X-ray band. 47 of these sources belong to the group of field pulsars whereas the other 42 sources are recycled millisecond pulsars. Of the latter, 28 reside in globular clusters (cf. Tables 6.8 and 6.9). Spectral information is available from 78 pulsars (cf. Tables 6.6 and 6.7), but the complexity of the tested models and the accuracy of the fitted spectral parameters are strongly inhomogeneous among the detected sources. This is because different pulsars are detected with different photon statistics, which for fainter sources often allow only to discriminate between basic spectral models such as blackbodies and power laws. This is especially true for the million years old field pulsars and the millisecond pulsars which are generally fainter X-ray emitters. The photon statistics is also the limiting factor in detecting X-ray pulses, although here the fraction of pulsed photons and the duty cycle are

important parameters too. By now, X-ray pulses have been detected from 25 field pulsars (e.g., Fig. 6.14) but only from ten millisecond pulsars (e.g., Fig. 6.16 and Table 6.9).

Comparing the emission properties of the 89 detected rotation-powered pulsars gives strong evidence that the observed spectral components and their relative strength vary with the pulsars spin-down age (cf. Fig. 6.20). In young Crab-like pulsars, non-thermal emission dominates. Although these young pulsars should have the highest surface temperature their thermal emission is buried by the even stronger non-thermal magnetospheric emission. However, as the star ages from a few thousand to about hundred thousand years, the non-thermal emission is fading while the star is still hot enough to emit thermal emission from the million degree hot surface. For all middle aged pulsars which are detected with sufficient photon statistics a three component spectral model is required to describe their observed energy spectrum (cf. Fig. 6.20, middle panel). This compound model consist of two thermal components which account for the cooling surface emission and emission from heated polar caps. A third non-thermal component is required to model the emission beyond $\sim$3 keV. In million years old pulsars the star has cooled down to much to show significant cooling emission. Upper limits obtained from the current data, however, are still above the temperatures predicted by thermal evolution models (cf. Fig. 6.13 and Table 6.5). In these million years old pulsars non-thermal radiation takes over again and becomes the dominating emission component (cf. Fig. 6.20, right panel).

Given that the pulsars' emission properties are observed to vary with the spin-down age we checked whether the spectral parameters and/or the pulsars' X-ray efficiency show a spin-down parameter dependence as well. Besides the correction for the interstellar absorption the two parameters which are fitted in power law spectra are the photon-index and the amplitude (usually taken at 1 keV). In Fig. 6.21 the pulse-phase averaged photon-indices of those 54 pulsars which have a non-thermal emission component in their observed X-ray spectrum are plotted as a function of the pulsars' spin-down age. As can be seen from the size of the 1σ error bars the

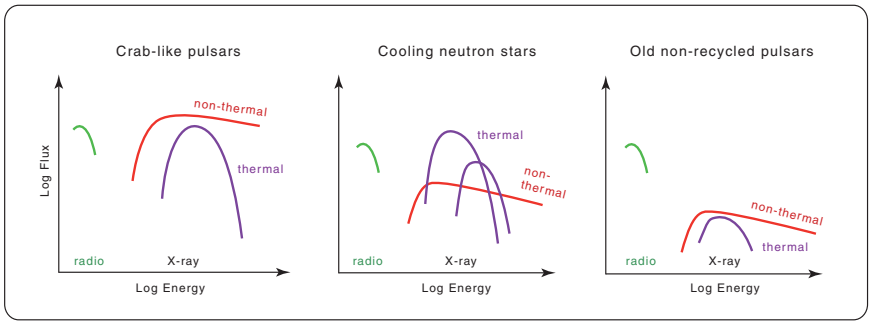

Fig. 6.20 Observed spectral components and their relative strength in rotation-powered pulsars as a function of spin-down age. Non-thermal (*red*) and thermal (*magenta*) spectral components are indicated

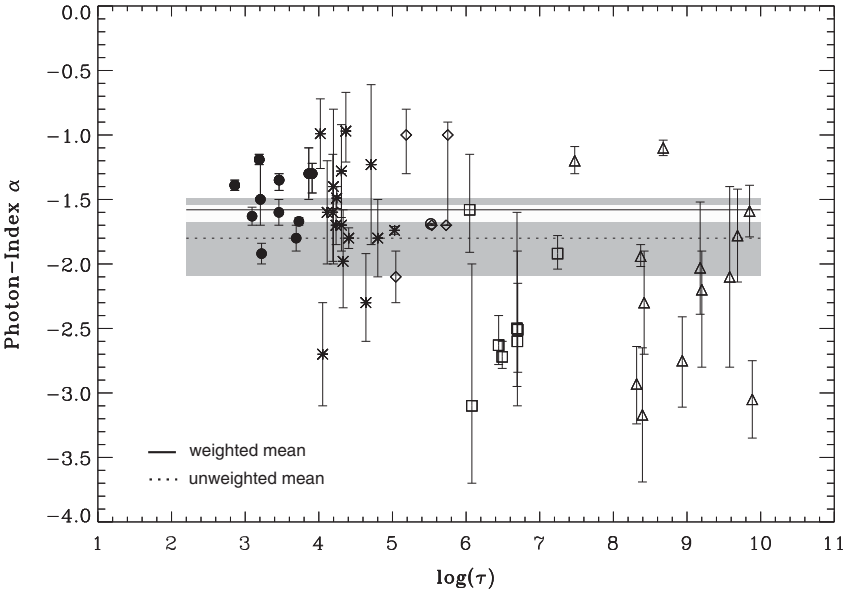

Fig. 6.21 Observed photon-indices as a function of the pulsars' spin-down age. The *solid line* corresponds to the weighted mean, the *dashed line* to the unweighted mean. The *gray shaded/white range* represents the 1σ uncertainty of the unweighted/weighted mean. Symbols are as labeled in Fig. 6.22

data quality varies significantly among those pulsars. Whereas photon-indices from the bright and powerful young pulsars are all measured with relatively high accuracy the uncertainty for most of the older and millisecond pulsars is rather large. Computing the weighted mean (by taking the weight to be the inverse of the size of the error bar) results in an average photon-index of $\alpha = -1.6 \pm 0.07$. This weighted mean, though, is biased by the higher accuracy of the photon-index in younger pulsars, in consequence of a better photon statistics in most of their observed spectra. The unweighted mean yields $\alpha = -1.8 \pm 0.3$. A linear function fitted to all photon-indices doesn't result in an acceptable correlation, in agreement with the large variation of the data points. This is still true, if field and millisecond pulsars are fitted separately. The latter means that the data are still in agreement with having no significant aging effect in the slope of the pulsars' non-thermal X-ray spectra. This result is in agreement with the observation that, e.g., the young Crab-like pulsar B0540−69 and the seventeen million years old pulsar B0950+08 both turn out to have an observed pulse-phase averaged photon-index of $\alpha = -1.92$, even with comparable errors (cf. Table 6.6). It is therefore not justified to conclude that older pulsars in general have softer X-ray spectra.

Chandra and XMM-Newton have obtained spectral information from 78 rotation-powered pulsars. In more than fifty pulsars a power law spectral component is required in the spectral fits. Back in 1997 at the end of the ROSAT mission the number of detected pulsars was roughly only one third of that. Nevertheless, the

ROSAT data allowed for the first time to investigate the spectral emission properties of pulsars for a larger sample, covering a wide range of spin-down ages, magnetic field strengths and spin-periods. With this data Becker and Trümper [15] found the pulsars' X-ray efficiency in the 0.1–2.4 keV band to follow in good approximation the linear trend $L_x = 10^{-3}\,\dot{E}$.

Today, the sample of X-ray detected pulsars is much larger than it was in 1997, including high signal-to-noise spectra from cooling neutron stars, million years old pulsars and recycled millisecond pulsars. The question is whether a linear correlation of the X-ray luminosity as a function of the pulsars' spin-down energy is still in agreement with the new and more significant data. To test this the full sample of X-ray detected pulsars for which spectra have been measured (cf. Tables 6.8 and 6.9) was used to correlate the isotropic X-ray luminosity with the spin-down energy. No beaming correction is applied. As both, emission from heated polar caps and non-thermal emission finally appears to be powered by the rotation of the star the X-ray luminosities from both spectral components were added and correlated with $\dot{E}$. Proper motion corrected period derivatives and spin-down energies were used if available. For the 47 Tuc millisecond pulsars the period derivatives corrected for the influence of the cluster potential were used [24]. Figure 6.22 shows the data points (cf. column L_x^{BB+PL} in Tables 6.8 and 6.9 for the 0.1–2 keV band) with their error bars along with the linear correlation:

$$L_x(0.1\text{–}2\,\mathrm{keV}) = 10^{-3.24^{+0.26}_{-0.66}}\,\dot{E}^{0.997^{+0.008}_{-0.001}}\,. \tag{6.1}$$

The errors in L_x have been fully taken into account and were used to weight the data points. The 1σ-confidence region of the correlation is indicated by the gray shaded bar in Fig. 6.22. The correlation coefficient is found to be $r = 0.9$. As can be seen from the plot the $L_x - \dot{E}$ correlation is still in good agreement with $L_x = 10^{-3}\,\dot{E}$, although it becomes apparent that this relation represents more an upper bound to the X-ray efficiency than a fixed correlation. This was already suggested by Becker and Trümper [15] and is due to the fact that ROSAT by its limited sensitivity detected only the brightest pulsars. With the higher sensitivity of XMM-Newton and Chandra more faint pulsars have been detected for which, e.g., the orientation of the magnetic/rotational axes to the observers line of sight might not be optimal. As no beaming correction can be applied the X-ray efficiency of those pulsars appears to be smaller.

As far as the X-ray efficiency from the 47 Tuc millisecond pulsars are concerned it can be seen from Fig. 6.22 that the X-ray luminosity of these pulsars is well within the scatter of other data points at this spin-down energy level. Within the uncertainties of the deduced X-ray luminosities it is therefore not justified to conclude that these pulsars have an X-ray efficiency which is different from the efficiency observed for field millisecond pulsars.

The X-ray efficiency in the harder X-ray band was investigated by various authors. Seward and Wang [142] used data from the Einstein observatory and found $L_x \propto \dot{E}^{1.39}$ for the 0.2–4 keV energy range. Saito [139] investigated the X-ray efficiency in the 2–10 keV ASCA band by correlating the X-ray luminosities of

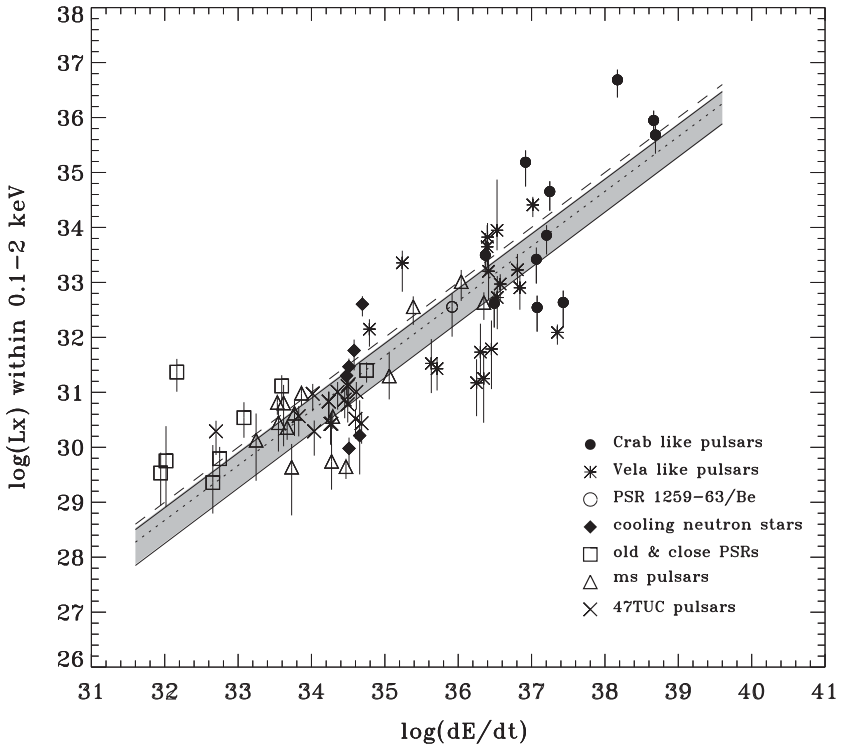

Fig. 6.22 X-ray luminosity of rotation-powered pulsars as a function of the pulsars' spin-down energy. The *dashed line* represents $L_x = 10^{-3}\,\dot{E}$. The *dotted line and gray shaded bar* represent the linear correlation $L_x(0.1\text{–}2\,\mathrm{keV}) = 10^{-3.24}\,\dot{E}^{0.997}$ and its $1-\sigma$ uncertainty range

16 pulsars. They found a relation $L_x \propto \dot{E}^{1.5}$. Possenti et al. [134] found for the 2–10 keV band a correlation $L_x \propto \dot{E}^{1.34}$, although in their work many X-ray luminosities were simply extrapolated from the ROSAT energy range by assuming that the spectrum in the hard X-ray band would be the same as in the soft band. Li et al. [98] investigated the X-ray efficiency by correlating the luminosities of a sample of 27 mostly young pulsars. They found $L_x \propto \dot{E}^{0.92}$ for the energy band 2–10 keV. Figure 6.23 shows the data points L_x^{BB+PL} from Tables 6.8 and 6.9 for the 2–10 keV band along with the fitted linear correlation:

$$L_x(2\text{–}10\,\mathrm{keV}) = 10^{-15.72^{+0.7}_{-1.7}}\,\dot{E}^{1.336^{+0.036}_{-0.014}}\,. \tag{6.2}$$

As for the soft band the errors in L_x were fully taken into account and were used to weight the data points in the linear fit. By reason of a smaller contribution from the thermal spectral components above $\sim$2 keV the scatter in the data points below $\sim 10^{35}\,\mathrm{erg\,s^{-1}}$ seems larger. The result from a linear fit, however, is found to be fully in agreement with the earlier results based on Einstein, ASCA and ROSAT data [134, 139, 142].

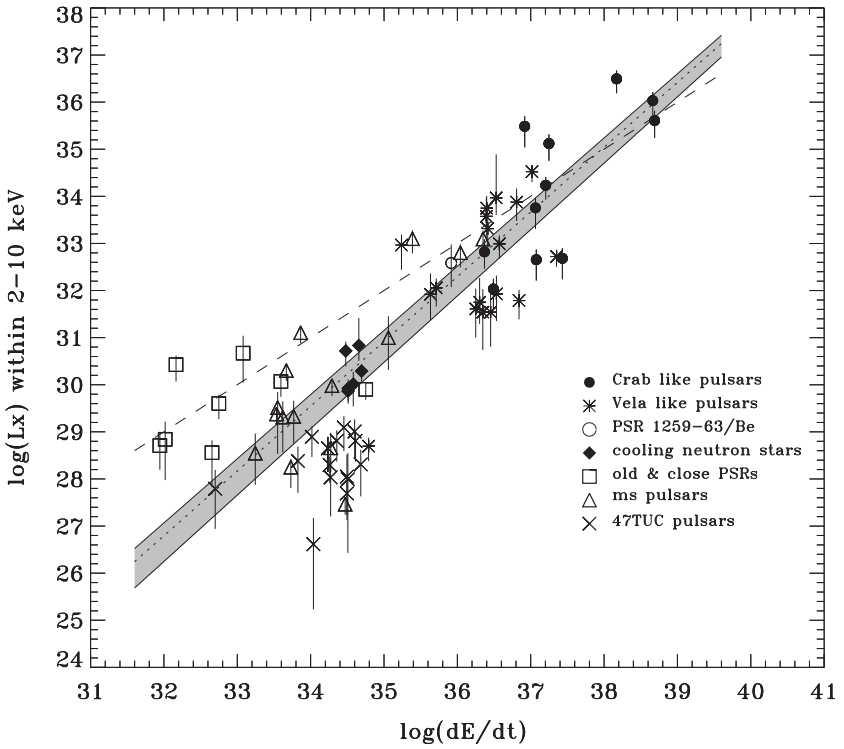

Fig. 6.23 X-ray luminosity (2–10 keV) of rotation-powered pulsars as a function of the pulsars' spin-down energy. The *dashed line* represents $L_x = 10^{-3}\,\dot{E}$. The *dotted line and gray shaded bar* represent the linear correlation $L_x(2\text{–}10\,\mathrm{keV}) = 10^{-15.72}\,\dot{E}^{1.336}$ and its $1-\sigma$ uncertainty range

Albeit the higher sensitivity of Chandra and XMM-Newton which observed the detected pulsars with much better photon statistics than possible in earlier experiments we find the X-ray efficiencies of the rotation-powered pulsars in the soft and hard X-ray bands still in agreement with the earlier measurements [15, 134, 139, 142]. However, what gets conspicuous in the larger data sample is that with an increase in sensitivity also apparently less efficient X-ray pulsars were detected, leading to a larger scatter in L_x vs. $\dot{E}$ for pulsars of the same category. The smaller efficiency, though, does not necessarily mean that the X-ray to spin-down energy conversion process in these pulsars is less efficient but that, e.g., the orientation of the magnetic/rotational axes to the observers line of sight might not be optimal. With an increasing number of detections any linear fit thus will become less correlated. Beaming factors, however, are generally unknown, so that it might be more adequate to express the empirical relation between L_x and $\dot{E}$ without loss of generality in the form:

$$L_x \lesssim 10^{-3}\,\dot{E}\,. \tag{6.3}$$

Table 6.6 Observed spectral properties of X-ray detected rotation-powered field pulsars. (See next page for the column description).

Pulsar	$N_H/10^{21}$ (cm^{-2})	Spectrum	Photon-Index	$T^{\infty}_{cool}/10^5$ (K)	R^{∞}_{cool} (km)	$T^{\infty}_{pc}/10^6$ (K)	R^{∞}_{pc} (km)	Ref.
B0531 + 21	$3.45^{+0.02}_{-0.02}$	PL	$1.63^{+0.07}_{-0.07}$	-	-	-	-	[15, 161]
B0833 − 45	0.22	BB + PL	$2.70^{+0.40}_{-0.40}$	-	-	1.49 ± 0.04	2.10 ± 0.2	[128]
J0205 + 6449	$3.40^{+0.1}_{-0.1}$	PL	$1.67^{+0.03}_{-0.03}$	-	-	-	-	[144]
J2229 + 6114	$6.30^{+1.3}_{-1.3}$	PL	$0.99^{+0.27}_{-0.27}$	-	-	-	-	[65]
J0633 + 1746	0.11	BB + BB + PL	$1.70^{+0.10}_{-0.10}$	5.00 ± 0.1	8.60 ± 1.0	1.90 ± 0.3	0.04 ± 0.01	[43]
B1951 + 32	3.00	PL	$1.74^{+0.03}_{-0.03}$	-	-	-	-	[97]
B1509 − 58	8.60	PL	$1.19^{+0.04}_{-0.04}$	-	-	-	-	[39, 41]
B1706 − 44	5.50	BB + PL	$1.49^{+0.09}_{-0.08}$	-	-	$2.01^{+0.18}_{-0.20}$	$1.81^{+0.43}_{-0.29}$	[105]
J1357 − 6429	$4.90^{+0.20}_{-0.20}$	BB + PL	$1.30^{+0.20}_{-0.20}$	-	-	1.70 ± 0.2	2.50 ± 0.5	[165]
J1930 + 1852	16.0	PL	$1.35^{+0.06}_{-0.10}$	-	-	-	-	[29]
J1617 − 5055	32.0^{+4}_{-4}	PL	$1.30^{+0.10}_{-0.20}$	-	-	-	-	[12]
B0656 + 14	$0.43^{+0.02}_{-0.02}$	BB + BB + PL	$2.10^{+0.30}_{-0.30}$	6.50 ± 0.1	$20.90^{+2.7}_{-3.8}$	1.25 ± 0.03	1.80 ± 0.15	[43]
J1747 − 2958	$27.0^{+1.0}_{-1.0}$	PL	$1.80^{+0.08}_{-0.08}$	-	-	-	-	[48]
J1124 − 5916	$3.10^{+0.40}_{-0.4}$	PL	$1.60^{+0.10}_{-0.10}$	-	-	-	-	[76]
B1046 − 58	$9.00^{4.00}_{-2.00}$	PL	$1.70^{+0.40}_{-0.20}$	-	-	-	-	[56]
J1811 − 1925	$22.2^{+5.70}_{-7.80}$	PL	$0.97^{+0.39}_{-0.32}$	-	-	-	-	[136]
J0537 − 6910	$9.50^{+0.70}_{-0.70}$	PL	$1.80^{+0.10}_{-0.10}$	-	-	-	-	[109]
B1259 − 63[a]	$2.90^{+0.20}_{-0.20}$	PL	$1.69^{+0.04}_{-0.04}$	-	-	-	-	[34]
B1823 − 13	7.00	PL	$1.98^{+0.40}_{-0.36}$	-	-	-	-	[125]
J1420 − 6048	22.0	PL	$1.60^{+0.40}_{-0.40}$	-	-	-	-	[137]
B1800 − 21	13.8	PL	$1.40^{+0.60}_{-0.60}$	-	-	-	-	[86]
J1809 − 1917	7.00	PL	$1.23^{+0.62}_{-0.62}$	-	-	-	-	[87]
B1757 − 24	35.0	PL	$1.60^{+0.60}_{-0.50}$	-	-	-	-	[91]
J1119 − 6127	$18.0^{+1.5}_{-0.6}$	BB + PL	$1.90^{+1.10}_{-0.90}$	-	-	2.46 ± 0.12	2.70 ± 0.7	[140]
B0540 − 69	4.60	PL	$1.92^{+0.11}_{-0.11}$	-	-	-	-	[84]
B1055 − 52	$0.27^{+0.02}_{-0.02}$	BB + BB + PL	$1.70^{+0.10}_{-0.10}$	7.90 ± 0.3	$12.30^{+1.3}_{-1.1}$	1.79 ± 0.06	0.46 ± 0.06	[43]
J1105 − 6107	7.00^{+2}_{-2}	PL	$1.80^{+0.40}_{-0.40}$	-	-	-	-	[60]
B1853 + 01	50.0	PL	$1.28^{+0.36}_{-0.36}$	-	-	-	-	[129]
B0355 + 54	8.80	BB + PL	$1.00^{+0.20}_{-1.00}$	-	-	$2.32^{+1.16}_{-0.81}$	$0.12^{+0.16}_{-0.07}$	[104]
J1509 − 5850	$8.0^{+2.3}_{-2.1}$	PL	$1.00^{+0.20}_{-0.30}$	-	-	-	-	[78]
J0538 + 2817	2.21	BB	-	-	-	$2.12^{+0.04}_{-0.03}$	1.68 ± 0.05	[106]
J2021 + 3651	$7.80^{+1.70}_{-1.40}$	PL	$1.70^{+0.23}_{-0.15}$	-	-	-	-	[71]
B1929 + 10	$1.60^{+0.20}_{-0.18}$	PL	$2.72^{+0.12}_{-0.09}$	-	-	-	-	[8]
B1610 − 50	20.0	PL	2.00	-	-	-	-	[132]
J1846 − 0258	39.6	PL	$1.39^{0.04}_{-0.04}$	-	-	-	-	[68]
J2043 + 2740	0.00^{+20}	PL	$3.10^{+1.10}_{-0.60}$	-	-	-	-	[10]
B1719 − 37	$2.40^{+2.4}_{-1.7}$	BB	-	-	-	$2.70^{+0.70}_{-0.58}$	$0.31^{+0.51}_{-0.16}$	[116]
B0950 + 08	$0.26^{+0.27}_{-0.24}$	PL	$1.92^{+0.14}_{-0.12}$	-	-	-	-	[10]
B2334 + 61	$2.60^{+2.6}_{-0.4}$	BB	-	-	-	1.62 ± 0.17	$1.66^{+0.45}_{-0.30}$	[105]
J0631 + 1036	$2.00^{+2.00}_{-1.00}$	PL	$2.30^{+0.38}_{-0.30}$	-	-	-	-	[150]
B0823 + 26	$0.00^{+0.88}$	PL	$2.50^{+0.90}_{-0.45}$	-	-	-	-	[10]
B1133 + 16	0.15	PL	$2.51^{+0.36}_{-0.33}$	-	-	-	-	[90]
B2224 + 65	0.90	PL	$1.58^{+0.43}_{-0.33}$	-	-	-	-	[79]
J0108 − 1431	0.073	PL	$2.20^{+0.24}_{-0.23}$	-	-	-	-	[124]
B0943 + 10	0.43	PL	$2.60^{+0.70}_{-0.50}$	-	-	-	-	[170]
B0628 − 28	$0.62^{+0.31}_{-0.18}$	PL	$2.63^{+0.23}_{-0.15}$	-	-	-	-	[9]

[a] Observed 0.5^0 past apastron

Table 6.7 Observed spectral properties of X-ray detected rotation-powered millisecond pulsars. The individual columns are as follows: (1) Pulsar name; (2) column density (if no error is listed the value was deduced from the radio dispersion measure); (3) spectral components required to fit the observed spectra, PL: power law, BB: blackbody; (4) Pulse-phase averaged photon index; (5) surface temperature; (6) projected blackbody radius of the thermal surface spectral component; (7) polar cap temperature; (8) projected blackbody radius of the thermal polar cap spectral component; (9) references. Errors represent the 1σ confidence interval. If no errors are listed the value represents a best guess.

Pulsar	$N_h/10^{21}$ (cm^{-2})	Spectrum	α	$T^{\infty}_{pc-rim}/10^6$ (K)	R^{∞}_{pc-rim} (km)	$T^{\infty}_{pc-core}/10^6$ (K)	$R^{\infty}_{pc-core}$ (km)	Ref.
J0437 − 4715	0.02	BB+BB+PL	$2.00^{+0.40}_{-0.40}$	0.52 ± 0.16	2.6 ± 0.4	1.40 ± 0.2	$0.12^{+0.04}_{-0.02}$	[14, 17, 167]
J0034 − 0534	0.43	BB	-	-	-	~ 2.20	~ 0.05	[167]
J2124 − 3358	$0.30^{+0.2}_{-0.2}$	BB+PL	$2.10^{+0.70}_{-0.70}$	-	-	1.30 ± 0.1	0.32 ± 0.04	[14, 167]
B1937 + 21	$12.7^{+4.0}_{-3.0}$	PL	$1.1^{+0.15}_{-0.2}$	-	-	-	-	
J1744 − 1134	0.2	PL	2.0	-	-	-	-	[14]
B1257 + 12	0.30	PL	$2.75^{+0.34}_{-0.36}$	-	-	-	-	[126]
B1821 − 24	$1.60^{+0.53}_{-0.61}$	PL	$1.20^{+0.11}_{-0.10}$	-	-	-	-	[11]
J1824 − 2452H	1.8	PL	2 .0	-	-	-	-	[6]
B1957 + 20	0.80	PL	$2.03^{+0.51}_{-0.36}$	-	-	-	-	[75]
J0030 + 0451	$0.125^{+0.095}_{-0.095}$	BB+PL	$3.05^{+0.30}_{-0.30}$	-	-	2.45 ± 0.19	0.075 ± 0.019	[12]
J1024 − 0719	$0.20^{+0.2}_{-0.2}$	BB	-	-	-	2.90 ± 0.3	0.03 ± 0.01	[167]
J0737 − 3039A	0.5	PL	$2.93^{+0.29}_{-0.31}$	-	-	-	-	[31, 89]
J1012 + 5307	0.07	PL	1.78 ± 0.36	-	-	-	-	[156]
J0218 + 4232	0.50	PL	1.10 ± 0.06	-	-	-	-	[157]
B1620 − 26	2.36	PL	$2.30^{+0.40}_{-0.40}$	-	-	-	-	[126]
J1740 − 5340	1.00	PL	~ 1.5	-	-	-	-	[62]
J1911 − 6000C	0.20	PL	2.5	-	-	-	-	[40, 133]
J0751 + 1807	0.40	PL	1.59 ± 0.20	-	-	-	-	[14, 156]
B1534 + 12	0.36	PL	3.17 ± 0.52	-	-	-	-	[89]
J0021 − 72F	0.13	BB	-	-	-	2.19 ± 0.09	0.22 ± 0.11	[24]
J0021 − 72E	0.13	BB	-	-	-	1.75 ± 0.09	0.28 ± 0.17	[24]
J0024 − 7204O	0.13	BB+PL	$1.33^{+0.79}_{-0.79}$	-	-	1.76 ± 0.15	0.28 ± 0.18	[24]
J0024 − 7204U	0.13	BB	-	-	-	2.76 ± 0.22	0.08 ± 0.06	[24]
J0024 − 7204T	0.13	BB	-	-	-	1.56 ± 0.16	0.19 ± 0.17	[24]
J0024 − 7204Q	0.13	BB	-	-	-	2.24 ± 0.2	0.11 ± 0.07	[24]
J0024 − 7204W	0.13	BB+PL	$1.36^{+0.24}_{-0.24}$	-	-	1.52 ± 0.28	0.29 ± 0.29	[24]
J0024 − 7204S	0.13	BB	-	-	-	2.19 ± 0.09	0.22 ± 0.11	[24]
J0024 − 7204R	0.13	BB	-	-	-	2.51 ± 0.16	0.15 ± 0.08	[24]
J0024 − 7204Y	0.13	BB	-	-	-	2.24 ± 0.18	0.11 ± 0.07	[24]
B0021 − 72N	0.13	BB	-	-	-	2.07 ± 0.18	0.13 ± 0.09	[24]
B0021 − 72M	0.13	BB	-	-	-	2.22 ± 0.18	0.11 ± 0.07	[24]
B0021 − 72L	0.13	BB	-	-	-	2.27 ± 0.10	0.20 ± 0.10	[24]
B0021 − 72J	0.13	BB+PL	$1.00^{+0.56}_{-0.56}$	-	-	1.73 ± 0.21	0.22 ± 0.17	[24]
B0021 − 72I	0.13	BB	-	-	-	2.21 ± 0.12	0.18 ± 0.10	[24]
B0021 − 72H	0.13	BB	-	-	-	1.93 ± 0.13	0.17 ± 0.11	[24]
B0021 − 72G	0.13	BB	-	-	-	2.21 ± 0.12	0.18 ± 0.10	[24]
B0021 − 72D	0.13	BB	-	-	-	2.20 ± 0.17	0.13 ± 0.06	[24]
B0021 − 72C	0.13	BB	-	-	-	2.02 ± 0.18	0.11 ± 0.08	[24]

Table 6.8 List of rotation-powered field pulsars that have been detected in the radio, optical, X- and/or γ-ray wavebands, ordered according to their spin-down flux density at Earth $\dot{E}/4\pi d^2$. The individual columns are as follows: 1. Pulsar name; 3–8. Energy ranges in which pulsed (p), unpulsed (d) radiation has been detected: R – radio, O – optical, Xs – soft X-rays ($E_\gamma \sim 1\,\mathrm{keV}$), X_h – hard X-rays ($E_\gamma \sim 10\,\mathrm{keV}$), γ_s – soft γ-rays ($E_\gamma \sim 1\,\mathrm{MeV}$) and γ_h – hard γ-rays ($E_\gamma > 100\,\mathrm{MeV}$). Possible detections are indicated by a question mark. $\dot{E}$ is the pulsar spin-down power; L_x^{PL} is the non-thermal luminosity. L_x^{BB+PL} luminosity from heated polar caps plus non-thermal contributions; $L_x^{BB+BB+PL}$ like L_x^{BB+PL} but plus a surface cooling contribution. η is the X-ray efficiency in the 0.1–2 keV and 2–10 keV bands for the PL spectral component. η^{BB+PL} is the X-ray efficiency in the 0.1–2 keV and 2–10 keV bands for the heated polar caps plus non-thermal components. Radio pulsar parameters have been taken from the ATNF catalog.

Pulsar	Comment	Detected						$\dot{E}/(4\pi d^2)$	$\log\dot{E}$	L_x^{PL}	L_x^{BB+PL}	$L_x^{BB+BB+PL}$	L_x^{PL}	$\log\tau$	P	$\dot{P}\cdot 10^{-15}$	D	$\log B_\perp$	η	η	η^{BB+PL}	Ref.
		R	O	X_s	X_h	γ_s	γ_h	erg/s/cm^2		0.1–2 keV	0.1–2 keV	0.1–2 keV	2–10 keV	yrs	s	s/s	kpc	G	0.1–2 kev	2–10 keV	0.1–2 keV	
B0531 + 21	Crab	p	p	p	p	p	p	$9.6\cdot10^{-7}$	38.66	$35.95^{+0.18}_{-0.31}$	-	-	$36.03^{+0.18}_{-0.31}$	3.09	0.03308	$4.23\cdot10^{-13}$	2.00	12.58	$1.90\cdot10^{-3}$	$2.30\cdot10^{-3}$	-	[15,161]
B0833 − 45	Vela	p	p	p	p	p	p	$9.2\cdot10^{-7}$	36.84	$32.81^{+0.25}_{-0.44}$	$32.90^{+0.23}_{-0.40}$	-	$31.79^{+0.37}_{-0.67}$	4.05	0.08932	$1.25\cdot10^{-13}$	0.25	12.53	$9.35\cdot10^{-5}$	$8.86\cdot10^{-6}$	$1.15\cdot10^{-4}$	[16,128]
J0205 + 6449[a]	3C58	p	-	p	-	-	-	$3.3\cdot10^{-8}$	37.43	$32.64^{+0.22}_{-0.45}$	-	-	$32.68^{+0.22}_{-0.45}$	3.73	0.06568	$1.94\cdot10^{-13}$	2.60	12.56	$4.73\cdot10^{-6}$	$2.54\cdot10^{-5}$	-	[144]
J2229 + 6114[a]	G106.6+2.9	p	-	p	-	-	d	$2.0\cdot10^{-8}$	37.35	$32.09^{+0.22}_{-0.45}$	-	-	$32.72^{+0.22}_{-0.45}$	4.02	0.05162	$7.83\cdot10^{-14}$	3.00	12.31	$5.45\cdot10^{-6}$	$2.34\cdot10^{-5}$	-	[65]
J0633 + 1746	Geminga	p	p	p	-	-	p	$1.0\cdot10^{-8}$	34.51	$29.90^{+0.20}_{-0.35}$	$29.92^{+0.19}_{-0.33}$	$31.41^{+0.21}_{-0.38}$	$29.98^{+0.20}_{-0.35}$	5.53	0.23709	$1.10\cdot10^{-14}$	0.16	12.21	$2.46\cdot10^{-5}$	$2.57\cdot10^{-5}$	$2.95\cdot10^{-5}$	[12,43]
B1951 + 32	CTB 80	p	-	d	-	-	p	$7.8\cdot10^{-9}$	36.57	$32.97^{+0.18}_{-0.31}$	-	-	$32.95^{+0.18}_{-0.31}$	5.03	0.03953	$5.84\cdot10^{-15}$	2.00	11.69	$2.49\cdot10^{-4}$	$2.41\cdot10^{-4}$	-	[16,97]
B1509 − 58	MSH 15-52	p	-	p	p	p	-	$5.4\cdot10^{-9}$	37.25	$34.64^{+0.19}_{-0.35}$	-	-	$35.12^{+0.20}_{-0.37}$	3.19	0.15065	$1.54\cdot10^{-12}$	5.20	13.19	$2.54\cdot10^{-3}$	$7.45\cdot10^{-3}$	-	[39,41]
B1706 − 44	G343.1-02.3	p	-	p	-	-	p	$4.5\cdot10^{-9}$	36.53	$32.20^{+0.46}_{-0.59}$	$32.72^{+0.39}_{-0.58}$	-	$31.93^{+0.30}_{-0.45}$	4.24	0.10245	$9.30\cdot10^{-14}$	2.50	12.49	$4.60\cdot10^{-5}$	$2.48\cdot10^{-5}$	-	[16,105]
J1357 − 6429		p	-	p	-	-	-	$4.1\cdot10^{-9}$	36.49	$31.66^{+0.22}_{-0.45}$	$32.62^{+0.22}_{-0.45}$	-	$32.03^{+0.22}_{-0.45}$	3.86	0.16610	$3.60\cdot10^{-13}$	2.50	12.89	$1.46\cdot10^{-5}$	$3.47\cdot10^{-5}$	$1.23\cdot10^{-4}$	[165]
J1930 + 1852[a]	G54.1+0.3	p	-	p	-	-	-	$3.8\cdot10^{-9}$	37.06	$33.42^{+0.22}_{-0.45}$	-	-	$33.75^{+0.22}_{-0.45}$	3.46	0.13685	$7.51\cdot10^{-13}$	5.00	13.01	$2.03\cdot10^{-4}$	$4.38\cdot10^{-4}$	-	[29]
J1617 − 5055	near RCW 103	p	-	p	-	-	-	$3.7\cdot10^{-9}$	37.20	$33.85^{+0.19}_{-0.35}$	-	-	$34.23^{+0.18}_{-0.31}$	3.91	0.06935	$1.35\cdot10^{-13}$	6.00	12.49	$4.49\cdot10^{-4}$	$1.07\cdot10^{-3}$	-	[12]
B0656 + 14		p	p	p	-	-	?	$3.5\cdot10^{-9}$	34.58	$30.38^{+0.35}_{-0.54}$	$31.76^{+0.20}_{-0.36}$	$32.71^{+0.22}_{-0.45}$	$30.01^{+0.26}_{-0.47}$	5.05	0.38489	$5.50\cdot10^{-14}$	0.30	12.67	$6.36\cdot10^{-5}$	$2.70\cdot10^{-5}$	$1.51\cdot10^{-3}$	[12,43]
J1747 − 2958	Mouse	p	-	d	-	-	-	$3.3\cdot10^{-9}$	36.40	$33.82^{+0.26}_{-0.23}$	-	-	$33.75^{+0.24}_{-0.23}$	4.41	0.09881	$6.14\cdot10^{-14}$	2.49	12.40	$2.66\cdot10^{-3}$	$2.23\cdot10^{-3}$	-	[48]
J1124 − 5916[a]	G292.0+1.8	p	-	p	-	-	-	$2.7\cdot10^{-9}$	37.08	$32.54^{+0.22}_{-0.45}$	-	-	$32.66^{+0.22}_{-0.45}$	3.46	0.13531	$7.47\cdot10^{-13}$	6.00	13.01	$2.94\cdot10^{-5}$	$3.80\cdot10^{-5}$	-	[76]
B1046 − 58	Vela twin	p	-	d	-	-	d	$2.3\cdot10^{-9}$	36.30	$31.73^{+0.52}_{-0.46}$	-	-	$31.75^{+0.30}_{-0.43}$	4.31	0.12367	$9.63\cdot10^{-14}$	2.70	12.54	$2.68\cdot10^{-5}$	$2.80\cdot10^{-5}$	-	[56]
J1811 − 1925	G11.2-0.3	-	-	p	p	-	-	$2.1\cdot10^{-9}$	36.81	$33.23^{+0.29}_{-0.40}$	-	-	$33.88^{+0.18}_{-0.31}$	4.37	0.06466	$4.40\cdot10^{-14}$	5.00	12.23	$2.64\cdot10^{-4}$	$1.17\cdot10^{-3}$	-	[136]
J0537 − 6910	N157B, LMC	p	-	p	-	-	-	$1.8\cdot10^{-9}$	38.69	$35.68^{+0.19}_{-0.34}$	-	-	$35.61^{+0.20}_{-0.37}$	3.69	0.01612	$5.18\cdot10^{-14}$	47.00	11.97	$9.85\cdot10^{-4}$	$8.34\cdot10^{-4}$	-	[109]
B1259 − 63[b]	Be-star bin	p	-	d	d	d	-	$1.7\cdot10^{-9}$	35.92	$32.55^{+0.25}_{-0.54}$	-	-	$32.58^{+0.39}_{-0.51}$	5.52	0.04776	$2.28\cdot10^{-15}$	2.00	11.52	$4.27\cdot10^{-4}$	$4.57\cdot10^{-4}$	-	[34]
B1823 − 13	Vela-like	p	-	d	-	-	-	$1.4\cdot10^{-9}$	36.45	$31.80^{+0.52}_{-0.73}$	-	-	$31.55^{+0.38}_{-0.62}$	4.33	0.10146	$7.51\cdot10^{-14}$	4.00	12.45	$2.16\cdot10^{-5}$	$1.22\cdot10^{-5}$	-	[125]
J1420 − 6048		p	-	p	-	-	-	$1.4\cdot10^{-9}$	37.02	$34.41^{+0.22}_{-0.45}$	-	-	$34.52^{+0.22}_{-0.45}$	4.11	0.06818	$8.32\cdot10^{-14}$	7.70	12.38	$2.48\cdot10^{-3}$	$3.20\cdot10^{-3}$	-	[137]
B1800 − 21	G8.7-0.1	p	-	d	-	-	-	$1.2\cdot10^{-9}$	36.35	$32.35^{+0.49}_{-0.80}$	-	-	$32.64^{+0.26}_{-0.53}$	4.20	0.13361	$1.34\cdot10^{-13}$	3.80	12.63	$8.01\cdot10^{-6}$	$1.56\cdot10^{-5}$	-	[86]

(Continued)

Table 6.8 (continued)

Pulsar	Comment	Detected						$\dot{E}/(4\pi d^2)$	$\log\dot{E}$	L_x^{PL}	L_x^{BB+PL}	$L_x^{BB+BB+PL}$	L_x^{PL}	$\log\tau$	P	$\dot{P}\cdot 10^{-15}$	D	$\log B_\perp$	η	η	η^{BB+PL}	Ref.
		R	O	X_s	X_h	γ_s	γ_h	erg/s/cm^2		0.1–2 keV	0.1–2 keV	0.1–2 keV	2–10 keV	yrs	s	s/s	kpc	G	0.1–2 kev	2–10 keV	0.1–2 keV	
J1809 − 1917		p	-	d	-	-	-	$1.2\cdot10^{-9}$	36.25	$31.11^{+0.43}_{-0.61}$	-	-	$31.55^{+0.75}_{-1.46}$	4.71	0.08274	$2.55\cdot10^{-14}$	3.50	12.17	$8.39\cdot10^{-6}$	$2.28\cdot10^{-5}$	-	[87]
B1757 − 24	G5.4-1.2, Duck	p	-	d	-	-	-	$8.6\cdot10^{-10}$	36.41	$33.10^{+0.54}_{-0.53}$	-	-	$33.21^{+0.26}_{-0.53}$	4.19	0.12492	$1.28\cdot10^{-13}$	5.00	12.61	$4.90\cdot10^{-4}$	$6.31\cdot10^{-4}$	-	[91]
J1119 − 6127	G292.2-0.5	p	-	p	-	-	-	$5.4\cdot10^{-10}$	36.37	$32.15^{+0.40}_{-0.42}$	$33.50^{+0.40}_{-0.38}$	-	$32.36^{+0.25}_{-0.31}$	3.21	0.40774	$4.02\cdot10^{-12}$	6.00	13.61	$6.46\cdot10^{-4}$	$2.17\cdot10^{-4}$	$1.35\cdot10^{-3}$	[57]
B0540 − 69	N158A, LMC	p	p	p	p	-	-	$5.0\cdot10^{-10}$	38.17	$36.68^{+0.19}_{-0.32}$	-	-	$36.49^{+0.21}_{-0.37}$	3.22	0.05035	$4.79\cdot10^{-13}$	49.40	12.70	$3.27\cdot10^{-2}$	$2.11\cdot10^{-2}$	-	[84]
B1055 − 52		p	d	p	-	-	p	$4.4\cdot10^{-10}$	34.48	$30.70^{+0.22}_{-0.35}$	$31.03^{+0.22}_{-0.37}$	$32.58^{+0.23}_{-0.36}$	$30.72^{+0.58}_{-0.33}$	5.73	0.19710	$5.83\cdot10^{-15}$	0.75	12.04	$1.66\cdot10^{-4}$	$1.73\cdot10^{-4}$	$3.55\cdot10^{-4}$	[12, 43]
J1105 − 6107		p	-	d	-	-	-	$4.2\cdot10^{-10}$	36.39	$33.65^{+0.39}_{-0.50}$	-	-	$33.57^{+0.18}_{-0.31}$	4.80	0.06319	$1.58\cdot10^{-14}$	7.00	12.00	$1.79\cdot10^{-3}$	$1.51\cdot10^{-3}$	-	[60]
B1853 + 01	W44	p	-	d	-	-	-	$3.9\cdot10^{-10}$	35.63	$31.53^{+0.44}_{-0.54}$	-	-	$31.92^{+0.19}_{-0.34}$	4.31	0.26744	$2.08\cdot10^{-13}$	3.00	12.88	$7.81\cdot10^{-5}$	$1.93\cdot10^{-4}$	-	[129]
B0355 + 54		p	-	d	-	-	-	$3.5\cdot10^{-10}$	34.66	$30.21^{+0.64}_{-0.71}$	$30.31^{+0.55}_{-0.63}$	-	$30.83^{+0.57}_{-0.33}$	5.75	0.15638	$4.40\cdot10^{-15}$	1.04	11.92	$3.59\cdot10^{-5}$	$1.50\cdot10^{-4}$	-	[104]
J1301 − 6305		p	-	d	-	-	-	$3.3\cdot10^{-10}$	36.23	32.30	-	-	-	4.04	0.18452	$2.67\cdot10^{-13}$	6.62	12.85	-	$1.17\cdot10^{-4}$	-	
J1509 − 5850		p	-	d	-	-	-	$2.9\cdot10^{-10}$	35.71	$31.43^{+0.20}_{-0.40}$	-	-	$31.55^{+0.35}_{-0.54}$	5.19	0.08892	$9.17\cdot10^{-15}$	3.81	11.96	$5.23\cdot10^{-5}$	$1.93\cdot10^{-4}$	-	[78]
J0538 + 2817	SNR S147	p	-	p	-	-	-	$2.8\cdot10^{-10}$	34.69	-	$32.60^{+0.22}_{-0.45}$	-	-	5.79	0.14315	$3.67\cdot10^{-15}$	1.20	11.87	-	-	$8.1\cdot10^{-3}$	[106]
J2021 + 3651		p	-	p	-	-	?	$2.8\cdot10^{-10}$	36.53	$34.13^{+0.23}_{-0.56}$	-	-	$33.97^{+0.18}_{-0.33}$	4.24	0.10372	$9.56\cdot10^{-14}$	10.00	12.50	$4.03\cdot10^{-3}$	$2.74\cdot10^{-3}$	-	[71]
B1929 + 10		p	d	p	-	-	-	$2.5\cdot10^{-10}$	33.59	$31.12^{+0.20}_{-0.33}$	-	-	$30.07^{+0.18}_{-0.33}$	6.49	0.22651	$1.16\cdot10^{-15}$	0.36	11.71	$3.32\cdot10^{-3}$	$2.97\cdot10^{-4}$	-	[8]
B1610 − 50	Kes 32	p	-	d	-	-	-	$2.4\cdot10^{-10}$	36.20	$33.25^{+0.22}_{-0.45}$	-	-	$32.98^{+0.22}_{-0.45}$	3.87	0.23169	$4.95\cdot10^{-13}$	7.30	13.03	$1.13\cdot10^{-3}$	$6.09\cdot10^{-4}$	-	[132]
J1846 − 0258[a]	Kes 75	p	-	p	d	-	-	$1.9\cdot10^{-10}$	36.92	$35.19^{+0.22}_{-0.45}$	-	-	$35.49^{+0.22}_{-0.45}$	2.86	0.32359	$7.10\cdot10^{-12}$	19.00	13.69	$1.86\cdot10^{-2}$	$3.70\cdot10^{-2}$	-	[68]
J2043 + 2740[a]		p	-	d	-	-	-	$1.4\cdot10^{-10}$	34.75	$31.40^{+0.22}_{-0.45}$	-	-	$29.90^{+0.22}_{-0.45}$	6.08	0.09613	$1.27\cdot10^{-15}$	1.80	11.55	$4.44\cdot10^{-4}$	$1.42\cdot10^{-5}$	-	[10]
B1719 − 37		p	-	d	-	-	-	$8.0\cdot10^{-11}$	34.51	-	$31.47^{+0.22}_{-0.45}$	-	-	5.54	0.23617	$1.09\cdot10^{-14}$	1.84	12.21	-	-	$9.05\cdot10^{-4}$	[116]
B0950 + 08		p	d	p	-	-	-	$6.9\cdot10^{-11}$	32.75	$29.80^{+0.22}_{-0.36}$	-	-	$29.61^{+0.19}_{-0.33}$	7.24	0.25306	$2.30\cdot10^{-16}$	0.26	11.39	$1.10\cdot10^{-3}$	$7.12\cdot10^{-4}$	-	[10]
B2334 + 61		p	-	d	-	-	-	$5.0\cdot10^{-11}$	34.79	-	$32.15^{+0.18}_{-0.32}$	-	-	4.61	0.49530	$1.92\cdot10^{-13}$	3.20	12.99	-	-	$2.28\cdot10^{-3}$	[105]
J0631 + 1036		p	-	p	-	-	-	$3.3\cdot10^{-11}$	35.24	$33.36^{+0.22}_{-0.53}$	-	-	$32.77^{+0.34}_{-0.49}$	4.64	0.28777	$1.05\cdot10^{-13}$	6.55	12.74	$1.31\cdot10^{-2}$	$3.44\cdot10^{-3}$	-	[150]
B0823 + 26		p	-	d	-	-	-	$3.2\cdot10^{-11}$	32.66	$29.36^{+0.69}_{-0.56}$	-	-	$28.56^{+0.26}_{-0.73}$	6.69	0.53066	$1.71\cdot10^{-15}$	0.34	11.98	$5.02\cdot10^{-4}$	$7.98\cdot10^{-5}$	-	[10]
B1133 + 16		p	-	d	-	-	-	$5.6\cdot10^{-12}$	31.94	$29.46^{+0.37}_{-0.60}$	-	-	$28.66^{+0.29}_{-0.51}$	6.70	1.18791	$3.73\cdot10^{-15}$	0.36	12.33	$3.86\cdot10^{-3}$	$5.80\cdot10^{-4}$	-	[90]
B2224 + 65	Guitar	p	-	d	-	-	-	$2.9\cdot10^{-12}$	33.08	$30.53^{+0.28}_{-0.37}$	-	-	$30.66^{+0.37}_{-0.62}$	6.05	0.68253	$9.66\cdot10^{-15}$	1.86	12.41	$2.88\cdot10^{-3}$	$3.89\cdot10^{-3}$	-	[79]
J0108 − 1431		p	?	d	-	-	-	$2.9\cdot10^{-12}$	30.75	$28.41^{+0.21}_{-0.21}$	-	-	$27.93^{+0.30}_{-0.30}$	8.22	0.80756	$7.70\cdot10^{-17}$	0.13	11.40	$4.57\cdot10^{-3}$	$1.49\cdot10^{-3}$	-	[124]
B0943 + 10		p	-	d	-	-	-	$2.1\cdot10^{-12}$	32.02	$29.75^{+0.63}_{-0.84}$	-	-	$28.84^{+0.38}_{-0.87}$	6.70	1.09770	$3.49\cdot10^{-15}$	0.63	12.30	$5.43\cdot10^{-3}$	$6.66\cdot10^{-4}$	-	[170]
B0628 − 28		p	-	p	-	-	-	$5.8\cdot10^{-13}$	32.16	$31.37^{+0.24}_{-0.36}$	-	-	$30.42^{+0.19}_{-0.36}$	6.44	1.24441	$7.12\cdot10^{-15}$	1.45	12.48	$1.62\cdot10^{-1}$	$1.82\cdot10^{-2}$	-	[10]

[a]No errors are specified in the literature. A 40% flux uncertainty was assumed.
[b]Pulsar observed at 0.5° apastron.

Table 6.9 List of rotation-powered millisecod pulsars that have been detected in the radio, optical, X- and/or γ-ray wavebands, ordered according to their spin-down flux density at Earth $\dot{E}/4\pi d^2$. The individual columns are as follows: 1. Pulsar name; 3–8. Energy ranges in which pulsed (p), unpulsed (d) radiation has been detected: R – radio, O – optical, Xs – soft X-rays ($E_\gamma \sim 1\,\mathrm{keV}$), X_h – hard X-rays ($E_\gamma \sim 10\,\mathrm{keV}$), γ_s – soft γ-rays ($E_\gamma \sim 1\,\mathrm{MeV}$) and γ_h – hard γ-rays ($E_\gamma > 100\,\mathrm{MeV}$). Possible detections are indicated by a question mark. $\dot{E}$ is the pulsar spin-down power; L_x^{PL} is the non-thermal luminosity. L_x^{BB+PL} luminosity from heated polar caps plus non-thermal contributions; η is the X-ray efficiency in the 0.1–2 keV and 2–10 keV bands for the PL spectral component. η^{BB+PL} is the X-ray efficiency in the 0.1–2 keV and 2–10 keV bands for the heated polar caps plus non-thermal components. Radio pulsar parameters have been taken from the ATNF catalog.

Pulsar	Comment	Detected						$\dot{E}/(4\pi d^2)$	log$\dot{E}$	L_x^{PL}	L_x^{BB+PL}	L_x^{PL}	log τ	P	$\dot{P}\cdot 10^{-15}$	D	log $B_\perp$	η	η	η^{BB+PL}	Ref.
		R	O	X_s	X_h	γ_s	γ_h	erg/s/cm^2		0.1–2 keV	0.1–2 keV	2–10 keV	yrs	s	s/s	kpc	G	0.1–2 kev	2–10 keV	0.1–2 keV	
J0437 − 4715	bin	p	d	p	-	-	-	$5.077\cdot10^{-9}$	33.62	$29.94^{+0.28}_{-0.78}$	$30.81^{+0.33}_{-0.78}$	$29.32^{+0.33}_{-0.75}$	9.20	0.00575	$2.00\cdot10^{-20}$	0.18	8.76	$2.08\cdot10^{-4}$	$6.98\cdot10^{-5}$	$1.53\cdot10^{-4}$	[14, 17, 167]
J0034 − 0534[a,b]		p	-	d	-	-	-	$8.488\cdot10^{-10}$	34.47	-	$29.65^{+0.22}_{-0.45}$	-	9.78	0.00187	$4.96\cdot10^{-21}$	0.54	7.99	-	-	$1.51\cdot10^{-5}$	[14, 167]
J2124 − 3358	sol	p	-	p	-	-	-	$7.754\cdot10^{-10}$	33.55	$29.89^{+0.39}_{-0.63}$	$30.45^{+0.31}_{-0.52}$	$29.52^{+0.33}_{-0.99}$	9.58	0.00493	$1.10\cdot10^{-20}$	0.27	8.51	$2.18\cdot10^{-4}$	$9.33\cdot10^{-5}$	$7.86\cdot10^{-4}$	[15, 82]
B1937 + 21	sol	p	-	p	-	-	-	$7.097\cdot10^{-10}$	36.04	$33.01^{+0.22}_{-0.35}$	-	$32.80^{+0.18}_{-0.31}$	8.37	0.00155	$1.05\cdot10^{-19}$	3.60	8.61	$9.37\cdot10^{-4}$	$5.78\cdot10^{-4}$	-	[115]
J1744 − 1134	sol	p	-	d	-	-	-	$6.457\cdot10^{-10}$	33.28	$29.18^{+0.22}_{-0.45}$	-	$28.91^{+0.22}_{-0.45}$	9.86	0.00407	$8.60\cdot10^{-21}$	0.26	8.29	$7.94\cdot10^{-5}$	$4.27\cdot10^{-5}$	-	[14, 15]
B1257 + 12	sol	p	-	d	-	-	-	$6.288\cdot10^{-10}$	34.27	$29.74^{+0.31}_{-0.52}$	-	$28.66^{+0.32}_{-0.52}$	8.94	0.00621	$1.14\cdot10^{-19}$	0.50	8.93	$2.94\cdot10^{-5}$	$2.43\cdot10^{-6}$	-	[126]
B1821 − 24	sol, M28	p	-	p	-	-	-	$6.192\cdot10^{-10}$	36.35	$32.63^{+0.19}_{-0.32}$	-	$33.09^{+0.18}_{-0.31}$	7.48	0.00305	$1.62\cdot10^{-18}$	5.50	9.35	$1.92\cdot10^{-4}$	$5.56\cdot10^{-4}$	-	[11]
B1957 + 20	bin	p	-	d	-	-	-	$5.946\cdot10^{-10}$	35.06	$31.30^{+0.44}_{-0.43}$	-	$31.00^{+0.46}_{-0.69}$	9.18	0.00160	$1.20\cdot10^{-20}$	1.50	8.22	$1.74\cdot10^{-4}$	$8.71\cdot10^{-5}$	-	[15, 75]
J0030 + 0451	sol	p	-	p	-	-	p	$5.421\cdot10^{-10}$	33.54	$30.71^{+0.22}_{-0.45}$	$30.81^{+0.22}_{-0.45}$	$29.34^{+0.22}_{-0.45}$	9.89	0.00486	$1.00\cdot10^{-20}$	0.23	8.35	$1.48\cdot10^{-3}$	$6.97\cdot10^{-5}$	$1.86\cdot10^{-3}$	[12]
J1024 − 0719		p	-	d	-	-	-	$2.925\cdot10^{-10}$	33.73	-	$29.64^{+0.42}_{-0.88}$	-	9.64	0.00516	$1.85\cdot10^{-20}$	0.39	8.50	-	-	$8.06\cdot10^{-5}$	[167]
J0737 − 3039A	bin	p	-	p	-	-	-	$1.963\cdot10^{-10}$	33.77	$30.62^{+0.23}_{-0.41}$	-	$29.33^{+0.34}_{-0.58}$	8.32	0.02269	$1.76\cdot10^{-18}$	0.50	9.80	$7.08\cdot10^{-4}$	$3.62\cdot10^{-5}$	-	[31, 89]
J1012 + 5307[a]	bin	p	-	d	-	-	-	$1.441\cdot10^{-10}$	33.67	$30.36^{+0.22}_{-0.45}$	-	$30.30^{+0.22}_{-0.45}$	9.69	0.00525	$1.71\cdot10^{-20}$	0.52	8.48	$4.89\cdot10^{-4}$	$4.30\cdot10^{-4}$	-	[156]
J0218 + 4232	bin	p	-	p	-	-	-	$6.279\cdot10^{-11}$	35.39	$32.56^{+0.19}_{-0.33}$	-	$33.10^{+0.18}_{-0.31}$	8.68	0.00232	$7.74\cdot10^{-20}$	5.70	8.63	$1.02\cdot10^{-4}$	$3.57\cdot10^{-4}$	-	[157]
B1620 − 26[a]	triple sys.	p	-	-	-	-	-	$5.448\cdot10^{-11}$	34.29	$30.55^{+0.22}_{-0.45}$	-	$29.97^{+0.22}_{-0.45}$	8.42	0.01107	$6.71\cdot10^{-19}$	1.73	9.44	$1.85\cdot10^{-4}$	$4.10\cdot10^{-5}$	-	[126]
J0751 + 1807[a]	bin	p	-	d	-	-	-	$1.526\cdot10^{-11}$	33.86	$30.98^{+0.22}_{-0.45}$	-	$31.10^{+0.22}_{-0.45}$	9.85	0.00347	$7.79\cdot10^{-21}$	2.00	8.22	$1.32\cdot10^{-3}$	$1.74\cdot10^{-3}$	-	[156]
B1534 + 12	NS-bin	p	-	d	-	-	-	$1.472\cdot10^{-11}$	33.25	$30.13^{+0.49}_{-0.74}$	-	$28.55^{+0.42}_{-0.67}$	8.39	0.03790	$2.42\cdot10^{-18}$	1.00	9.99	$7.61\cdot10^{-4}$	$2.00\cdot10^{-5}$	-	[89]
J1824 − 2452H	M28	P	-	d	-	-	-	$9.133\cdot10^{-12}$	34.51	$29.97^{+0.22}_{-0.45}$	-	$29.70^{+0.22}_{-0.45}$	8.95	0.00462	$2.42\cdot10^{-20}$	5.50	?	-	-	-	[6]
J1953 + 1846A	M71	p	-	d	-	-	-	-	?	$30.81^{+0.22}_{-0.45}$	-	$30.87^{+0.22}_{-0.45}$	?	0.00488	?	4.00	?	-	-	-	[46]
B0021 − 72F	47-Tuc	p	-	d	-	-	-	$1.689\cdot10^{-11}$	34.61	-	$31.15^{+0.18}_{-0.32}$	$28.81^{+0.23}_{-0.44}$	8.81	0.00262	$6.45\cdot10^{-20}$	4.5	8.62	$2.49\cdot10^{-4}$	$1.57\cdot10^{-6}$	-	[24]
B0021 − 72E	47-Tuc	p	-	d	-	-	-	$1.288\cdot10^{-11}$	34.49	-	$30.78^{+0.18}_{-0.33}$	$27.69^{+0.30}_{-0.57}$	8.75	0.00353	$9.85\cdot10^{-20}$	4.5	8.78	$1.94\cdot10^{-4}$	$1.58\cdot10^{-7}$	-	[24]
J0024 − 7204O	47-Tuc	p	-	p	-	-	-	$1.288\cdot10^{-11}$	34.49	$30.23^{+0.22}_{-0.45}$	$31.11^{+0.21}_{-0.34}$	$28.05^{+0.47}_{-0.82}$	9.14	0.00264	$3.04\cdot10^{-20}$	4.5	8.46	$4.13\cdot10^{-4}$	$3.59\cdot10^{-7}$	$4.72\cdot10^{-4}$	[24]
J0024 − 7204U	47-Tuc	p	-	d	-	-	-	$1.643\cdot10^{-11}$	34.60	-	$30.52^{+0.18}_{-0.37}$	$29.01^{+0.26}_{-0.58}$	8.86	0.00434	$9.52\cdot10^{-20}$	4.5	8.81	$8.28\cdot10^{-5}$	$2.55\cdot10^{-6}$	-	[24]
J0024 − 7204T	47-Tuc	p	-	d	-	-	-	$4.501\cdot10^{-12}$	34.04	-	$30.29^{+0.20}_{-0.44}$	$26.61^{+0.56}_{-1.39}$	8.61	0.00758	$2.94\cdot10^{-19}$	4.5	9.18	$1.79\cdot10^{-4}$	$3.78\cdot10^{-8}$	-	[24]
J0024 − 7204Q	47-Tuc	p	-	d	-	-	-	$7.515\cdot10^{-12}$	34.26	-	$30.43^{+0.18}_{-0.38}$	$28.29^{+0.18}_{-0.38}$	9.27	0.00403	$3.40\cdot10^{-20}$	4.5	8.57	$1.46\cdot10^{-4}$	$1.08\cdot10^{-6}$	-	[24]

(Continued)

Table 6.9 (continued)

Pulsar	Comment	Detected						$\dot{E}/(4\pi d^2)$	log$\dot{E}$	L_x^{PL}	L_x^{BB+PL}	L_x^{PL}	log τ	P	$\dot{P}\cdot 10^{-15}$	D	log $B_\perp$	η	η	η^{BB+PL}	Ref.
		R	O	X_s	X_h	γ_s	γ_h	erg/s/cm^2		0.1–2 keV	0.1–2 keV	2–10 keV	yrs	s	s/s	kpc	G	0.1–2 kev	2–10 keV	0.1–2 keV	
J0024 – 7204W	47-Tuc	p	-	d	-	-	-	-	?	$30.97^{+0.19}_{-0.48}$	$30.83^{+0.22}_{-0.45}$	$31.29^{+0.23}_{-0.55}$	?	0.00235	?	4.5	?	-	-	-	[24]
J0024 – 7204S	47-Tuc	p	-	d	-	-	-	$9.373\cdot 10^{-12}$	34.36	-	$31.01^{+0.18}_{-0.32}$	$28.81^{+0.23}_{-0.44}$	9.53	0.00283	$1.32\cdot 10^{-20}$	4.5	8.29	$4.49\cdot 10^{-4}$	$2.83\cdot 10^{-6}$	-	[24]
J0024 – 7204R	47-Tuc	p	-	p	-	-	-	$1.173\cdot 10^{-11}$	34.45	-	$30.87^{+0.18}_{-0.34}$	$29.09^{+0.24}_{-0.50}$	8.77	0.00348	$9.45\cdot 10^{-20}$	4.5	8.52	$2.60\cdot 10^{-4}$	$4.33\cdot 10^{-6}$	-	[24]
J0024 – 7204Y	47-Tuc	p	-	d	-	-	-	$1.990\cdot 10^{-11}$	34.68	-	$30.44^{+0.18}_{-0.37}$	$28.31^{+0.31}_{-0.68}$	?	?	?	4.5	?	$5.68\cdot 10^{-5}$	$4.22\cdot 10^{-7}$	?	[24]
B0021 – 72N	47-Tuc	p	-	d	-	-	-	$7.721\cdot 10^{-12}$	34.27	-	$30.43^{+0.19}_{-0.40}$	$28.03^{+0.36}_{-0.83}$	9.56	0.00305	$1.34\cdot 10^{-20}$	4.5	8.31	$1.44\cdot 10^{-4}$	$5.76\cdot 10^{-7}$	-	[24]
B0021 – 72M	47-Tuc	p	-	d	-	-	-	-	?	-	$30.43^{+0.86}_{-0.53}$	$28.27^{+0.86}_{-0.53}$	?	0.00367	?	4.5	?	-	-	-	[24]
B0021 – 72L	47-Tuc	p	-	d	-	-	-	$4.294\cdot 10^{-12}$	34.02	-	$30.97^{+0.18}_{-0.32}$	$28.89^{+0.22}_{-0.43}$	9.50	0.00434	$2.12\cdot 10^{-20}$	4.5	8.49	$9.03\cdot 10^{-4}$	$7.52\cdot 10^{-6}$	-	[24]
B0021 – 72J	47-Tuc	p	-	d	-	-	-	$1.329\cdot 10^{-11}$	34.51	$30.27^{+0.22}_{-0.45}$	$31.15^{+0.20}_{-0.41}$	$27.99^{+0.56}_{-1.56}$	9.64	0.00210	$7.60\cdot 10^{-21}$	4.5	8.11	$4.34\cdot 10^{-4}$	$3.05\cdot 10^{-7}$	$4.94\cdot 10^{-4}$	[24]
B0021 – 72I	47-Tuc	p	-	d	-	-	-	$7.102\cdot 10^{-12}$	34.24	-	$30.83^{+0.18}_{-0.34}$	$28.65^{+0.25}_{-0.50}$	9.47	0.00348	$1.86\cdot 10^{-20}$	4.5	8.41	$3.40\cdot 10^{-4}$	$2.59\cdot 10^{-6}$	-	[24]
B0021 – 72H	47-Tuc	p	-	d	-	-	-	-	?	-	$30.56^{+1.03}_{-0.59}$	$27.88^{+1.04}_{-0.60}$	?	0.00321	?	4.5	?	-	-	-	[24]
B0021 – 72G	47-Tuc	p	-	d	-	-	-	$7.102\cdot 10^{-12}$	34.24	-	$30.83^{+0.18}_{-0.34}$	$28.65^{+0.25}_{-0.50}$	9.34	0.00404	$2.90\cdot 10^{-20}$	4.5	8.54	$3.40\cdot 10^{-4}$	$2.59\cdot 10^{-6}$	-	[24]
B0021 – 72D	47-Tuc	p	-	p	-	-	-	$2.766\cdot 10^{-12}$	33.83	-	$30.57^{+0.18}_{-0.37}$	$28.28^{+0.31}_{-0.68}$	9.51	0.00535	$2.63\cdot 10^{-20}$	4.5	8.58	$5.49\cdot 10^{-4}$	$1.94\cdot 10^{-4}$	-	[24]
B0021 – 72C	47-Tuc	p	-	d	-	-	-	$2.065\cdot 10^{-13}$	32.70	-	$30.29^{+0.19}_{-0.43}$	$27.79^{+0.40}_{-0.85}$	9.58	0.00575	$2.43\cdot 10^{-21}$	4.5	9.20	$3.90\cdot 10^{-3}$	$1.24\cdot 10^{-5}$	-	[24]
J1740 – 5340	NGC 6397	p	-	d	-	-	-	$9.837\cdot 10^{-11}$	35.13	-	~ 30.9	-	8.54	0.00365	$1.68\cdot 10^{-19}$	3.4	8.89	$5.88\cdot 10^{-5}$	-	-	[62]
J1701 – 3006B	NGC 6266	p	-	d	-	-	-	-	?	~ 32.62	-	~ 32.35	?	0.00359	?	6.6	?	-	-	-	[36]
J1910 – 5959B	NGC 6752	p	-	d	-	-	-	-	?	~ 30.53	-	~ 29.73	?	0.00835	?	4.5	?	-	-	-	[40]
J1911 – 6000C	NGC 6752	p	-	d	-	-	-	$2.51\cdot 10^{-13}$	32.78	~ 30.84	-	~ 30.04	10.58	0.00527	$2.16\cdot 10^{-21}$	4.5	8.03	$1.15\cdot 10^{-2}$	$1.81\cdot 10^{-3}$	-	[40]
J1910 – 5959D	NGC 6752	p	-	d	-	-	-	$2.11\cdot 10^{-11}$	34.71	~ 31.06	-	~ 30.79	8.17	0.00903	$9.64\cdot 10^{-19}$	4.5	9.47	$2.24\cdot 10^{-4}$	$1.20\cdot 10^{-4}$	-	[40]

[a] No errors are specified in the literature. A 40% flux uncertainty was assumed.
[b] Photon statistics is not sufficient to distinguish between a thermal and non-thermal spectrum.

6.4.1 Concluding Remarks

The results on the X-ray emission properties of pulsars presented in this chapter and elsewhere in the book demonstrate that X-ray astronomy has made great progress in the past several years thanks to telescopes with larger effective areas and greatly improved spatial, temporal and spectral resolutions. But even in view of these great observational capabilities and the intense neutron star research made over a period of more than 40 years there are fundamental questions which still have not be answered. How are the different manifestations of neutron stars related to each other? What are the physical parameters which differentiate AXPs/SGRs/CCOs/XDINs and rotation-powered pulsars? What is the maximal upper bound for the neutron star mass and what is the range of possible neutron star radii? Is there any exotic matter in neutron stars? Do strange stars exist? And what are the physical processes responsible for the pulsars' broad band emission observed from the infrared to the gamma-ray band? These are just a few of the long standing open questions which can be addressed with the next generation of proposed instruments, eROSITA, Simbol-X and IXO are supposed to bring again a major improvement in sensitivity, making these instruments even more suitable for pulsar and neutron star astronomy.

References

1. Alpar, M.A., Cheng, A.F., Ruderman, M.A., Shaham, J., 1982, Nature, 300, 728
2. Aschenbach, B., Brinkmann, W., 1975, A&A, 41, 147
3. Aschenbach, B., 1998, Nature, 396, 141
4. Bhattacharya, D., van den Heuvel, E.P.J., 1991, Phys. Rep., 203, 1
5. Becker, W., Tennant, A., Kanbach, G., et al., 2008, in preparation, submitted to A&A
6. Becker, W., Hui, C.Y., 2007, A&A, astro-ph/07050119
7. Becker, W., Hui, C.Y., Aschenbach, B., Iyudin, A., 2007, A&A, astro-ph/0607081
8. Becker, W., Kramer, M., Jessner, A., et al., 2006, ApJ, 645, 1421
9. Becker, W., Jessner, A., Kramer, M., et al., 2005, ApJ, 633, 367
10. Becker, W., Weisskopf, M.C., Tennant, et al., 2004, ApJ, 615, 908
11. Becker, W., Swartz, D.A., Pavlov, G.G., et al., 2003, ApJ, 594, 798
12. Becker, W., Aschenbach, B., 2002, in *Neutron Stars, Pulsars and Supernova Remnants*, eds. W. Becker, H. Lesch, J. Trümper, MPE-Report 278, p. 64, (astro-ph/0208466)
13. Becker, W., Pavlov, G.G., 2001, in *The century of Space Science*, eds. J. Bleeker, J. Geiss, M. Huber, Kluwer, Dordrecht, p. 721, astro-ph/0208356
14. Becker, W., Trümper, J., 1999, A&A, 341, 803
15. Becker, W., Trümper, J., 1997, A&A, 326, 682
16. Becker, W., Truemper, J., 1996, A&AS, 120C, 69
17. Becker, W., Trümper, J., 1993, Nature, 365, 528
18. Bégin, S., 2006, Thesis, Faculty of Physics, University of British Columbia
19. Bell, J.F., Bailes, M., Manchester, R.N., Weisberg, J.M., Lyne, A.G., 1995, ApJ, 440, L81
20. Bell, J., 1977, Ann. NY Acad. Sci., 302, 685
21. Beskin, V.S., Gurevich, A.V., Istomin, Ya.N., 1993, Physics of the Pulsar Magnetosphere, Cambridge University Press, Cambridge, ISBN 0-521-41746-5
22. Bisnovatyi-Kogan, G.S., Komberg, B.V., 1974, Sov. Astron., 18, 217

23. Blaschke, D., Glendenning, N.K., Sedrakian, A., 2001, Physics of Neutron Star Interiors, Springer, Berlin, ISBN 3540423400
24. Bogdanov, S., Grindlay, J.E., Heinke, C.O., et al., 2006, ApJ, 646, 1104
25. Bowyer, C.S., Byram, E.T., Chubb, T.A., Friedman, H., 1964, Nature, 201, 1307
26. Cameron, P.B., Rutledge, R.E., Camilo, F., et al., 2007, ApJ, 660, 587
27. Camilo, F., Ransom, S.C., Halpern, J.P., et al., 2006, Nature, 442, 892
28. Camilo, F., Rasio, A.F., 2005, in *Binary Radio Pulsars*, eds. F.A. Rasio, I.H. Stairs, ASP Conf. Ser., 328, p. 147
29. Camilo, F. et al., 2002, ApJ, 574, L71
30. Cassam-Chenai, G., Decourchelle, A., Ballet, J., et al., 2004, A&A, 427, 199
31. Chatterjee, S. et al., 2007, ApJ, 670, 1301
32. Cheng, K.S., Ho, C., Ruderman, M.A., 1986, ApJ, 300, 500
33. Cheng, K.S., Ho, C. Ruderman, M.A., 1986, ApJ, 300, 522
34. Chernyakova, M., et al., 2006, Mon. Not. R. Astron. Soc., 367,1201
35. Chiu, H.Y., Salpeter, E.E., 1964, Phys. Rev. Letters, 12,413
36. Cocozza, G., Ferraro, F.R., POssenti, A., et al., 2008, ApJ 679, L105
37. Cool, A.M., Grindlay, J.E., Krockenberger, M., et al., 1993, ApJ, 410, L103
38. Cordes, J.M., Lazio, T.J.W., 2002, astro-ph/0207156
39. Cusumano, G. et al., 2001, A&A, 375, 397
40. D'Amico, N., Possenti, A., Fici, L., et al., 2002, ApJ, 570, L89
41. DeLaney, T., Gaensler, B.M., 2006, ApJ, 640, 929
42. De Luca, A., Caraveo, P.A., Mereghetti, S., et al., 2006, Science, 313, 814
43. De Luca, A., Caraveo, P.A., Mereghetti, S., et al., 2005, ApJ, 623, 1051
44. De Luca, A., Mereghetti, S., Caraveo, P.A., 2004, A&A, 418, 625
45. Dickel, J.R., Carter, L.M., 1998, MdSAI, 69, 845
46. Elsner, R.F., Heinke, C.O., Lugger, P.M., et al., 2008, submitted to ApJ (astro-ph/08072404)
47. Fesen, R.A., Pavlov, G.G., Sanwal, D., 2006, ApJ, 636, 848
48. Gaensler, B.M. et al., 2004, ApJ, 616, 383
49. Gaensler, B.M., 2004, Adv. Space Res., 33, 645
50. Gaensler, B.M., Jones, D.H., Stappers, B.W., 2002, ApJ, 580, L137
51. Giacconi, R., 1974, in *X-ray Astronomy*, eds R. Giacconi and H. Gursky, R. Reidel, Holland, ISBN 90 277 02950
52. Giacconi, R., Gursky, H., Paolini, F.R., et al., 1962, Phys. Rev. Lett., 9, 439
53. Glendenning, N.K., 2001, Compact Stars, Springer, Berlin, ISBN 0387989773
54. Gold, T., 1968, Nature, 218, 731
55. Gold, T., 1969, Nature, 221, 25
56. Gonzalez, M.E. et al., 2006, ApJ, 652, 569
57. Gonzalez, M.E. et al., 2005, ApJ, 630, 489
58. Gotthelf, E.V., Halpern, J.P., Seward, F.D., 2005, ApJ, 627, 390
59. Gotthelf, V.E., Halpern, J., 2007, ApJ, 664, L35
60. Gotthelf, E.V., Kaspi, V.M., 1998, ApJ, 497, L29
61. Green D.A., 2006, *A Catalogue of Galactic Supernova Remnants (2006 April version)*, Astrophysics Group, Cavendish Laboratory, Cambridge
62. Grindlay, J.E., Camilo, F., Heinke, C.O., et al., 2002, ApJ, 581, 470
63. Grindlay, J.E., Heinke, C.O., Edmonds, P.D., et al., 2001, ApJ, 563, 53
64. Gudmundsson, E.H., Pethick, C.J., Epstein, R.I., 1983, ApJ, 272, 286
65. Halpern, J.P. et al., 2002, *Neutron Stars in Supernova Remnants*, ASP Conference Series, Vol. 271
66. Harding, A.K., Muslimov, A.G., 2001, ApJ, 556, 1001
67. Hwang, U., Kaming, J.M., Badenes, C., et al., 2004, ApJ, 615, L117
68. Helfand, D.J., Collins, B.F., Gotthelf, E.V, 2003, ApJ, 582, 783
69. Helfand, D.J., Becker, R.H., 1984, Nature, 307, 215
70. Hertz, P., Grindlay, J.E, 1983, ApJ, 275, 105
71. Hessels, J.W.T. et al., 2004, ApJ, 612, 389
72. Hester, J.J., Mori, K., Burrows, D., et al., 2002, ApJ, 577, 49

73. Hewish, A., Bell, S.J., Pilkington, J.D.H., et al., 1968, Nature, 217, 709
74. Hoyle, R.A., Narlikar, J., Wheeler, J.A., 1964, Nature, 203, 914
75. Huang, H.H., Becker, W., 2007, A&A, 463, L5
76. Hughes, J.P. et al., 2003, ApJ, 591, L139
77. Hui, C.Y., Becker, W., 2008, A&A, 486, 485
78. Hui, C.Y., Becker, W., 2007, A&A, 470, 965
79. Hui, C.Y., Becker, W., 2007, A&A, 467, 1209
80. Hui, C.Y., Becker, W., 2006, A&A, 454, 543
81. Hui, C.Y., Becker, W., 2006, A&A, 457, L33
82. Hui, C.Y., Becker, W., 2006, A&A., 448, L13
83. Johnston, H.M., Verbunt, F., 1996, A&A, 312, 80
84. Kaaret, P. et al., 2001, ApJ, 546, 1159
85. Kargaltsev, O., Pavlov, G.G., Wong, J.A., 2008, astro-ph/08051041
86. Kargaltsev, O., Pavlov, G.G., Garmire, G.P., 2007, ApJ, 660, 1413
87. Kargaltsev, O., Pavlov, G.G., 2007, ApJ, 670, 655
88. Katsuda, S., Tsunemi, H., Mori, K., 2008, ApJ, 678, L35
89. Kargaltsev, O., Pavlov, G.G., Garmire, G.P., 2006, ApJ, 646, 1139
90. Kargaltsev, O., Pavlov, G.G., Garmire, G.P., 2006, ApJ, 636, 406
91. Kaspi, V.M. et al., 2001, ApJ, 562, L163
92. Kaspi, V.M., Crawford, F., Manchester, R.N., et al., 1998, ApJ, 503, L161
93. Kendziorra, E., Staubert, R., Pietsch, W., et al., 1977, ApJ, 217, L93
94. Kuiper, L., Hermsen, W., Verbunt, F., et al., 2002, ApJ, 577, 917
95. Large, M.I., Vaughan, A.E., Mills, B.Y., 1968, Nature, 220, 340
96. Lazendic, J.S., Slane, P.O., Gaensler, B.M., et al., 2003, ApJ, 593, L27
97. Li, X.H., Lu, F.J., Li, T.P., 2005, ApJ, 628, 931
98. Li, X.H., Lu, F.J., Li, Z., 2008, astroph/07074279
99. Lommen, A., Donovan, J., Gwinn, C., et al., 2007, ApJ, 657, 436
100. Lyne, A.G., Brinklow, A., Middleditch, J., et al., 1987, Nature, 328, 399
101. Malofeev, V.M., Malov, O.I., Teplykh, D.A., V.M., 2006, Chin. J. Astron. Astrophys., 6(2), 68
102. Manchester, R.N., Hobbs, G.B., Teoh, A., Hobbs, M., 2005, AJ, 129, 1993
103. Manzali, A., De Luca, A., Caraveo, P.A., 2007, ApJ, 669, 570
104. McGowan, K.E. et al., 2007, Astrophys. Space Sci., 308, 30
105. McGowan, K.E. et al., 2006, ApJ, 639, 377
106. McGowan, K.E. et al., 2003, ApJ, 591, 380
107. Mereghetti, S., Chiarlone, L., Israel, G.L., et al., 2002, in *Neutron Stars, Pulsars and Supernova Remnants*, eds. W. Becker, H. Lesch, J. Trümper, MPE-Report 278, p. 29, astro-ph/0205122
108. Michel, F.C., 1991, Theory of Neutron Star Magnetospheres, University of Chicago Press, Chicago, ISBN 0-226-52331-4
109. Mignani, R.P., et al., 2005, A&A, 431, 659
110. Mineo, T., Cusumano, G., Massaro, E., 2004, A&A, 423, 1045
111. Moffett, D.A., Hankins, T.H., 1996, ApJ, 468, 779
112. Morrison, P., 1958, Nuovo Cimento, 7, 858
113. Morrison, P., Olbert, S., Rossi, B., 1954, Phys. Rev., 94, 440
114. Nasuti, F.P., Mignani, R., Caraveo, P.A., Bignami, G.F., 1997, A&A, 323, 839
115. Nicastro, L., Cusumano, G., Loehmer, O., et al., 2004, A&A, 413, 1065
116. Oosterbroek, T., Kennea, J., Much, R., Cordova, F.A., 2004, Nucl. Phys. B (Proc. Suppl.), 132
117. Ostriker, J.P., Gunn, J.E., 1969, ApJ, 157, 1395
118. Ögelman, H., 2005, in *The Lives of the Neutron Stars*, eds. Alpar, Kiziloglu, van Paradijs, NATO ASI Series, Kluwer, Dordrecht, p. 101
119. Ögelman, H., Finley, J.P., Zimmerman, H.U., 1993, Nature, 361, 136
120. Pacini, F., 1967, Nature, 216, 567
121. Pacini, F., 1968, Nature, 219, 145

122. Page, D., 2007, in Lecture Notes on *Pulsars and Neutron Stars: 40 Years After the Discovery*, eds. W. Becker, Springer, Berlin
123. Page, D., Reddy, S., 2006, ARoNucPS, 56, 1, p. 327
124. Pavlov, G.G., Kargaltsev, O., Wong, J.A., et al., 2008, astro-ph/08030761
125. Pavlov, G.G., Kargaltsev, O., Brisken, W.F., 2008, ApJ, 675, 683
126. Pavlov, G.G. et al., 2007, ApJ, 664, 1072
127. Pavlov, G.G., Teter, M.A., Kargaltsev, O., et al., 2003, ApJ, 591, 1157
128. Pavlov, G.G. et al., 2001, ApJ, 552, L219
129. Petre, R., Kuntz, K.D., Shelton, R.L., 2002, ApJ, 579, 404
130. Petre, R., Canizares, C.R., Kriss, G.A., Winkler, P.F., Jr., 1982, ApJ, 258, 22
131. Pfeffermann, E., Aschenbach, B., 1996, in *Roentgenstrahlung from the Universe*, eds. H.H. Zimmermann, J. Trümper, H. Yorke, MPE Rep. 263, p. 267
132. Pivovareff, M.J., Kaspi, V.M., Gotthelf, E.V., 2000, ApJ, 528, 436
133. Pooley, D., Lewin, W.H.G., Homer, L., et al., 2002, 569, 405
134. Possenti, A. et al., 2002, A&A, 387, 993
135. Rasio, F.A., Pfahl, E.D., Rappaport, S., 2000, ApJ, 532, 47
136. Roberts, M.S.E., et al., 2003, ApJ, 588, 992
137. Roberts, M.S.E., Romani, R.W., Johnston, S., 2001, ApJ, 561, L187
138. Ruderman, M., Sutherland, P.G., 1975, ApJ, 196, 51
139. Saito, Y., 1998, PhD Thesis, University of Tokyo (S98)
140. Safi-Harb, S., Kumar, H.S., 2008, ApJ, 684, 532
141. Seward, F.D., Slane, P.O., Smith, R.K., Sun, M., 2003, ApJ, 584, 414
142. Seward, F.D., Wang Z.R., 1988, ApJ, 332, 199
143. Shibata S., Tomatsuri H., Shimanuki M., et al., 2003, MNRAS, 346, 841
144. Slane, P. et al., 2004, ApJ, 616, 403
145. Staelin, D.H., Reifenstein, III, E.C., 1968, Science, 162, 1481
146. Stappers, B.W., Gaensler, B.M., Kaspi, V.M., et al., 2003, Science, 299, 1372
147. Tananbaum, H., 1999, IAU Circ. #7246
148. Tananbaum, H., Gursky, H., Kellogg, E.M., et al., 1972, ApJ, 174, L143
149. Tennant, A.F., Becker, W., Juda, et al., 2001, ApJ, 554, L173
150. Torii, K., et al., 2001, ApJ, 551, L151
151. Torii, K., Kinugasa, K., Toneri, T., et al., 1998, ApJ, 494, L207
152. Trümper, J.E., Pietsch, W., Reppin, C., et al., 1978, ApJ, 219, L105
153. Tsuruta S., 1998, Phys. Rep., 292, 1
154. Tuohy, I.R., Garmire, G.P., 1980, ApJ, 239, L107
155. Verbunt, F. 2001, A&A, 368, 137
156. Webb, N.A. et al., 2004, A&A, 419, 269
157. Webb, N.A., Olive, J.-F., Barret, D., 2004, A&A 417, 181
158. Weber, F. 1999, Pulsars as Astrophysical Laboratories for Nuclear and Particle Physics, Institute of Physics, ISBN 0-7503-0332-8
159. Weisskopf, M.C., Hester, J.J., Tennant, A.F., et al. 2000, ApJ, 536, L81
160. Wijnand, R., 2005, in *Nova Science Publishers: Pulsars New Research*, astro-ph/0501264
161. Willingale, R., Aschenbach, B., Griffiths, R.G., et al., 2001, A&A, 365, L212
162. Woods, P.M., Thompson, C., 2006, in *Compact Stellar X-Ray Sources*, eds W. Lewin, M. van der Klis, pp. 547–586, Cambridge University Press, Cambridge, ISBN 978-0-521-82659-4, astro-ph/0406133
163. Yakovlev, D.G., Pethick, C.J., 2004, Ann. Rev. Astron. Astrophys. 42, 169
164. Yakovlev, D.G., Levenfish, K.P., Shibanov, Yu.A., 1999, Phys. Usp., 169, 825
165. Zavlin, V.E., 2007, ApJ, 665, L143
166. Zavlin, V.E., 2007, in *Astrophysics and Space Science*, eds. D. Page, R. Turolla, S. Zane, 308, 297
167. Zavlin, V.E., 2006, ApJ, 638, 951
168. Zavlin, V.E., Pavlov, G.G., 2004, ApJ, 616, 452
169. Zavlin, V.E., Pavlov, G.G., Sanwal, D., Trümper, J., ApJ, 540, L25
170. Zhang, B., Sanwal, D., Pavlov, G.G., 2005, ApJ, 624, L109

Chapter 7
Isolated Neutron Stars: The Challenge of Simplicity

Roberto Turolla

7.1 Introduction

The seven soft, thermal sources discovered by ROSAT offer an unprecedented opportunity to unveil the temperature and magnetic field surface distribution of isolated neutron stars. This makes a direct measurement of the star radius and mass within reach and will allow to place tight constraints on matter equation of state at nuclear densities. In this chapter the main observational properties of the *Magnificent Seven* are reviewed, and the current status of theoretical modeling presented. Emphasis is placed on the main challenge these objects pose to theorists, namely how can a cooling neutron star emit a nearly perfect blackbody spectrum. Open issues concern the origin of the broad absorption features (or lack thereof) detected around a few hundred electron volts, the search for new candidates and the (possible) links of the Magnificent Seven with other classes of Galactic neutron star sources, the newly discovered rotating radio transients and the magnetar candidates in particular.

First hypothesised in the 1930s, neutron stars have been for more than 40 years a theoretician's dainty, until the discovery of the first radio pulsar [27]. Since then, neutron stars have been mostly detected at radio wavelengths, and the number of known radio pulsars exceeds now 1,800.[1] This vast success contributed to spread the general belief that isolated (i.e. those not in binary systems) neutron stars are with no exception active radio pulsars. It was thanks to X-ray telescopes flown in the last 20 years that our picture of isolated neutron stars gradually started to change.

Search for the soft X-ray radiation given off by the cooling surface of aging neutron stars has been already one of the goals of the EINSTEIN mission. However, its limited spatial resolution and low-energy sensitivity made it difficult to

R. Turolla
Department of Physics, University of Padova, Italy
e-mail: turolla@pd.infn.it

[1] ATNF pulsar catalogue, http://www.atnf.csiro.au/research/pulsar/psrcat/.

W. Becker (ed.), *Neutron Stars and Pulsars,* Astrophysics and Space Science Library 357,

resolve the point-like emission of the pulsar itself from the harder component which originates in the surrounding nebula. Despite the inherent difficulties, the pulsar X-ray signature was picked up in EINSTEIN data for PSR 0656+14 [9] and in EINSTEIN/EXOSAT data for Vela (PSR 0833−45 [54]).

It was ROSAT which some years later opened a new window for the detection and the study of isolated neutron stars at X-ray energies, thanks to its vastly superior spatial resolution and unprecedented sensitivity in the 0.15–2 keV band. ROSAT observations provided a clear detection of the pulsed surface emission from Vela and PSR 0656+14, Geminga, PSR 1055−52 (the "Three Musketeers"), and gave for the first time ever a measure of the star surface temperature (see, e.g. [2, 53] and references therein). The discovery of thermal emission in pulsars has been indeed a great achievement, although in a sense an expected one. We know that pulsars *are* neutron stars, that neutron stars are born very hot, cool down and for some million years have a surface temperature of $\approx 10^6$ K (see, e.g. [57] and Page, this volume), in the right range to make them shine in X-rays, and that many pulsars are of the right age. ROSAT data gave the much needed, long-sought observational proof that this picture is correct. What came completely unexpected, and this was a genuine breakthrough of the ROSAT mission, was the discovery that there are neutron stars which emit in the X-rays but *are not* active radio (or γ-ray) pulsars. ROSAT has shown that these sources may be as numerous as radio pulsars [52, 70], although their detection in the soft X-rays is severely hindered by Galactic absorption.

Thermal emission was successfully detected in other INS sources as well, bringing the total number of known sources to 14 at the dawn of the new millennium, when XMM-Newton and Chandra took over. At present the list of isolated neutron stars with detected thermal emission totals more than 30 sources, including, besides radio pulsars, the (relatively) hot Anomalous X-ray Pulsars and Soft γ-repeaters (AXPs and SGRs; e.g. [103] for a review and Israel, this volume), the yet mysterious Central Compact Objects in Supernova remnants (CCOs in SNRs; e.g. [59]), Geminga and its twin RX J1836.2+5925 (e.g. [3,24,36]), one of the puzzling Rotating Radio Transients (RRATs; [46, 75]) and, last but not least, the seven close-by sources with purely thermal spectrum known sometimes as XDINSs (X-ray Dim Isolated Neutron Stars), or as *The Magnificent Seven*.[2] These latter are the topic of the present paper.

Before going into more details, in the following I shall briefly address some basic questions, like: What are exactly the *Magnificent Seven*? Why are they important? And what can we learn from them?

- *What are they?* The neutron star nature of these sources was already clear when the first candidate was discovered by Walter et al. [102]. The main points at the basis of such a claim are the very soft, thermal X-ray spectrum and the exceedingly large X-ray-to-optical flux ratio. Unfortunately this particular source did not appear to pulsate, so the determination of the star spin could not be used to back the neutron star hypothesis. The gap was however quickly filled when the second source followed [17] and now pulsations have been detected in six out of seven sources (see Sect. 7.2.1).

[2] © Sergei Popov.

Although little doubt is left that these are isolated neutron stars, for some time the mechanism powering their X-ray emission was under debate. Following the original suggestion by Ostriker, Rees and Silk [55], several authors predicted that the large ($\approx 10^8 - 10^9$) Galactic population of old ($\gtrsim 10^7$ yr) dead pulsars could be resurrected from the graveyard by accretion of the interstellar medium (e.g. [4, 85, 108], see also [86]). Accretion at the Bondi rate ($\dot{M} \propto n_{ISM}/v^3$, where n_{ISM} is the ISM particle density and v the star velocity) could produce a detectable X-ray flux if the star is close-by ($D \lesssim 500$ pc) and moves slowly ($v \lesssim 50$ km s^{-1}). However, when the discovery of the faint optical counterparts of some of the Seven made it possible to measure their proper motion (see Sect. 7.2.3), it become soon clear that these sources are too fast to be powered by accretion. The only hypothesis left standing is then that the Seven are just middle aged neutron stars giving off thermal radiation as they cool down. This is further supported by the quite recent determination of the spin-down age in two sources, which provided values of $\approx$1 Myr [33, 34].

- *Why are they important?* The holy grail of neutron star astrophysics is the determination of the equation of state (EOS) of matter at supra-nuclear densities. The most direct way of constraining the EOS is to measure simultaneously the neutron star mass and radius (e.g. [40, 41]). If a neutron star emits blackbody radiation from its surface of radius R at homogeneous temperature T, the received flux at distance D is just $F = \sigma T^4 (R/D)^2$. So, if distance is known and T could be determined by spectral analysis, the previous relation immediately yields the star radius. Not surprisingly reality is a trifle more complicated, as it is discussed in more detail in the next sections. Still, this oversimplified analysis catches the essence of what is needed in order to measure the neutron star radius: distance, flux and surface temperature. Observing the star thermal emission is therefore crucial. Among all thermally emitting neutrons stars the Magnificent Seven are the only ones with a purely blackbody spectrum. Their clean thermal emission, unmarred by contaminations from magnetospheric activity, a surrounding nebula or supernova remnant, makes these sources ideal targets for such a study: the Magnificent Seven are the perfect neutron stars!
- *What can we learn from them?* Measuring the star radius is per se a goal of paramount importance but it is not the only mystery that investigations of the Seven promise to unveil. In the presence of a strong magnetic field thermal conduction is highly anisotropic: heat tends to flow preferentially along the field lines. This means that the star surface temperature is not homogeneous: there will be hotter zones where the field lines are more closely packed, e.g. near the magnetic poles. If the star spins it will expose different portions of the surface to view at different phases. The shape of the lightcurve bears therefore the imprint of the surface temperature distribution. Same goes for spectra taken at different spin phases. Since temperature and magnetic field are interwoven, lightcurve analysis and phase-resolved spectroscopy give unique information on the magnetic field structure. Present results (see Sect. 7.3.1) already seem to exclude that a simple dipolar geometry can account for the observed properties of the Seven. X-ray spectroscopy, available thanks to instruments on board XMM-Newton and

Chandra, allows to search for spectral features with an unprecedented level of detail. Up to now broad absorption features have been detected in almost all XDINSs. Although their origin is not clear yet, it is almost certain that the star strong magnetic field plays a fundamental role in their formation. Absorption features may then provide a powerful diagnostics for the strength of the surface field. Once the nature of the lines has been settled and if an independent measurement of the magnetic field is available (e.g. through spin-down), a measure of the gravitational red-shift will be possible, paving the way to the simultaneous determination of both the star mass and radius.

7.2 The *Magnificent Seven* in Parade

Besides exhibiting a purely thermal spectrum with typical temperatures in the range $\sim$50–100 eV, without any evidence for the hard power-law component observed in other isolated neutron stars, the Seven share a number of common properties:

- Very low values of the column density ($N_H \sim 10^{20}\,\mathrm{cm}^{-2}$)
- No association with a supernova remnant
- No evidence for a binary companion
- Pulsation periods in a restricted range $P \sim 3$–12 s
- Very faint optical counterparts implying an exceedingly large X-ray-to-optical flux ratio ($f_X/f_{opt} > 10^4$)
- No radio emission

Until recently the list would have contained one item more:

- Steady X-ray flux

It was however found that at least one source, RX J0720.4−3125, is positively variable (see Sect. 7.2.1). Even the statement that these sources are radio-silent is to be taken with some care, since the detection of pulsed radio emission at very short wavelengths has been claimed for two XDINSs [44, 45].

The *Magnificent Seven* and their main observational properties are summarized in Table 7.1 where the last two entries give the (semi)amplitude of the X-ray lightcurve and the magnitude of the optical counterpart, when detected. For more details and further references see, e.g. [16].

7.2.1 Timing Properties

In the case of the prototype of the class and brightest object, RX J1856.5−3754, a very long (500 ks) Chandra observation was unable to detect pulsations and placed an upper limit on the pulsed fraction of $\lesssim$1% [74]. Very recently however, Tiengo and Mereghetti [84] positively identified the source period ($P = 7.055$ s), confirming the very low value of the pulsed fraction (1.5%). Apart from RX

Table 7.1 The Magnificent Seven

Source	kT eV	P s	Amplitude/2 %	Optical	Refs.
RX J1856.5−3754	60	7.06	1.5	V = 25.6	[7, 12, 101, 102]
RX J0720.4−3125[a]	85	8.39	11	B = 26.6	[17, 23, 37, 47]
RX J0806.4−4123	96	11.37	6	–	[18, 22]
RX J0420.0−5022	45	3.45	13	B = 26.6?	[18, 19]
RX J1308.6+2127 (RBS 1223)	86	10.31	18	$m_{50CCD} = 28.6$	[20, 25, 31, 79]
RX J1605.3+3249 (RBS 1556)	96	–	–	$m_{50CCD} = 26.8$	[32, 48, 93]
1RXS J214303.7+065419 (RBS 1774)	104	9.43	4	–	[104, 105]

[a]Variable source

J1605.3+3249 for which present data do not allow to reach a firm conclusion, all other sources show pulsations in their X-ray lightcurves with similar periods. The pulsed fractions are modest, but in a few cases (notably that of RX J1308.6+2127) they exceed 25%. The lightcurve shapes are quasi-sinusoidal and single-peaked. However, RX J1308.6+2127 displays a double-peaked lightcurve [20, 77], and in RX J0420.0−5022 there is some evidence for a skewness in the pulse profile, with a slower rise and faster decline [18] (see Fig. 7.1). Rather counter-intuitively, the spectrum of both RX J0720.4−3125 and RX J1308.6+2127 becomes harder at pulse minimum. A coherent timing solution has been recently obtained for RX J0720.4−3125 and RX J1308.6+2127 [33, 34]. The period derivatives are 7×10^{-14} s/s and 10^{-13} s/s, respectively. The derived dipolar field is $2–3 \times 10^{13}$ G and the spin-down ages are 2 and 1.5 Myr.

For a long time the Seven were considered to be steady sources, to the point that RX J0720.4−3125 was included among the calibration sources for the EPIC and RGS instruments on board XMM-Newton. The continuous monitoring revealed however that the source underwent conspicuous changes in the period 2001–2003 [11,96]. In particular, while the total flux stayed more or less constant, the blackbody temperature steadily increased, going from ∼86 to over 90 eV. This was accompanied by a change of the pulse profile, with an increase of the pulsed fraction. More recently this trend seems to have reversed. Starting from 2004, the temperature decreased and there are hints that the overall evolution may be cyclic, with a period of 7–8 yr [21]. The implications of this behavior for the models are discussed in Sect. 7.3.1.

7.2.2 Spectral Properties

As it has been stressed before, a key feature which discriminates the Seven from all the other isolated neutron stars detected in X-rays, is their thermal spectrum, with

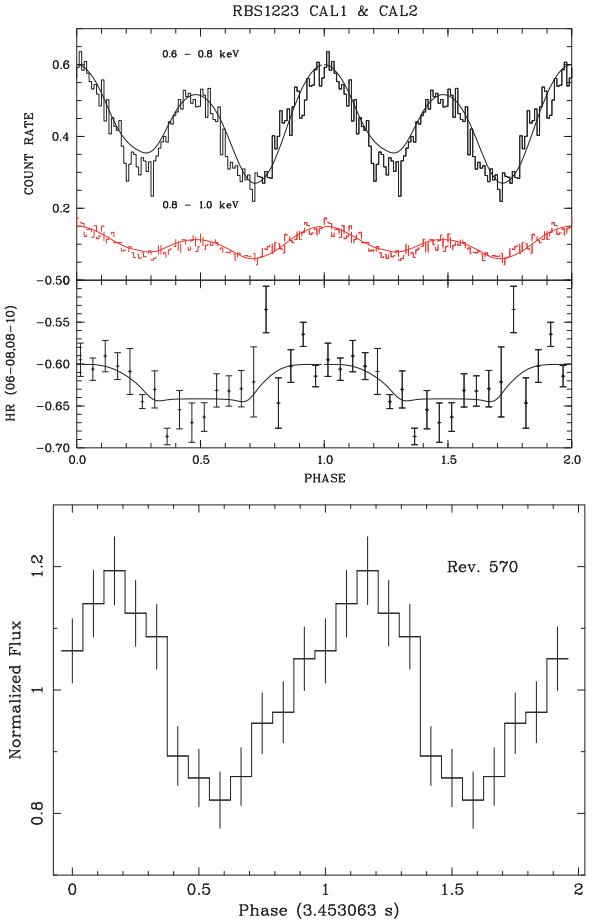

Fig. 7.1 *Left*: the pulse profile of RX J1308.6+2127 (RBS 1223) in two energy bands; the *lower panel* shows the variation of the hardness ratio with phase (from [77]). *Right*: the pulse profile of RX J0420.0−5022 (from [18])

no evidence for a power-law tail extending at higher energies. The derived temperatures span a limited range, from ∼40 to ∼100 eV (see Table 7.1). Although a blackbody provides a good description of the overall X-ray emission, XMM-Newton data revealed the presence of absorption features in XDINS spectra. First detected in RX J0720.4−3125 [20], a spectral feature was subsequently discovered in RX J1308.6+2127 RX J0806.4−4123 and RX J0420.0−5022 [18], RX J1605.3+3249 [93], and 1RXS J214303.7+065419 [105]. Very recently, Schwope et al. [78] reported the possible presence of a second, harmonically spaced feature in RX J1308.6+2127, and Haberl [16] that of up to three lines (with energy ratios 1, 1.5, 2) in RX J1605.3+3249. The properties of the features are similar in the different sources (see Table 7.2): they are centered at energies of some hundreds electron volts and are quite broad (typical equivalent width of several tens

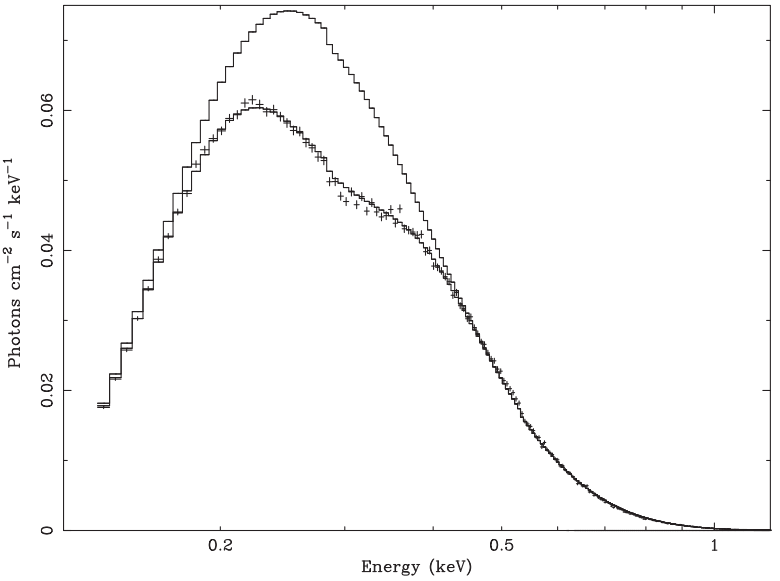

Fig. 7.2 The unfolded XMM EPIC-pn spectrum of RX J0720.4−3125 together with the best fitting model (a blackbody plus absorption line); the blackbody component is also shown for comparison (from [23])

electron volts). This is illustrated in Fig. 7.2 which shows the unfolded spectrum of RX J0720.4−3125. Absorption features appear to vary with the spin phase, as in RX J0720.4−3125 [18] and in RX J1308.6+2127 [77]. Moreover, in RX J0720.4−3125 the line EW follows the long-term ($\sim$ yrs) evolution of the source and correlates with the blackbody temperature. The prototype, and brightest source, of the class, RX J1856.5−3754, is peculiar since its spectrum convincingly appears featureless [12], although possible broadband deviations from a blackbody have been reported [7].

The nature of the absorption features is unclear as yet. At present, two main explanations for their origin have been suggested: either proton cyclotron resonances or atomic transitions in light elements. In both cases the required value of the magnetic field is quite high, $B \gtrsim 10^{13}$ G. The derived values of the magnetic field, assuming that the features are proton cyclotron resonances,

$$E_{line} = 0.63(1+z)^{-1}(B/10^{14}\ \mathrm{G}) \tag{7.1}$$

where $(1+z)^{-1} \sim 0.8$ is the gravitational redshift factor at the star surface, are listed in Table 7.2. Interestingly, for the two sources in which a spin-down measure is available, the values of B obtained from $\dot{P}$ assuming magneto-dipolar braking are in reasonable agreement with those inferred from the line energy (see Sect. 7.2.1 and Table 7.2 where the spin-down values of B are in parentheses).

Finally, it should be noted that more sophisticated and physically motivated spectral models, in particular atmospheric models, give a worst interpretation of the data with respect to a simple blackbody. Although this is the case also for some other

Table 7.2 Spectral features

Source	Energy eV	EW eV	B 10^{13} G
RX J1856.5−3754	no	no	?
RX J0720.4−3125[a]	270	40	5 (2.4)
RX J0806.4−4123	460	33	9
RX J0420.0−5022	330	43	7
RX J1308.6+2127	300	150	6 (3.4)
RX J1605.3+3249	450	36	9
1RXS J214303.7+065419	700	50	14

[a]Variable source

isolated NSs with a thermal spectral component, it is particularly puzzling for the Seven. In these sources, in fact, there is no evidence for any form of activity which could influence the emission from the star surface (e.g. particle bombardment by magnetospheric particles).

7.2.3 Optical Counterparts, Proper Motions and Distances

Under the assumption that XDINSs emit a single component, blackbody spectrum at all wavelengths, the expected luminosity in the optical band is

$$L_{opt} \approx L_X \times 10^{-5.5-\log(kT/100\,\mathrm{eV})}\,, \tag{7.2}$$

where L_X and T are the X-ray luminosity and temperature (e.g. [86]). This implies that their optical counterparts are very weak, with magnitudes $\gtrsim$25. The first XDINS identified in the optical (with HST) has been the brightest one, RX J1856.5−3754 [101]. Up to now, three further sources have been detected in the optical: RX J0720.4−3125 [37,47], RX J1308.6+2127 [31] and RX J1605.3+3249 [32]. A possible optical counterpart has been proposed also for RX J0420.0−5022 [18] but this still awaits confirmation. The magnitudes of the presently known XDINS counterparts are listed in Table 7.1.

In all cases in which multi-colour photometry is available [32,35,94], the optical data follow, more or less closely, a λ^{-4} law, as expected by a thermally emitting surface. However, the optical fluxes are a factor ∼5–10 above the extrapolation at low energies of the best-fitting X-ray blackbody, a fact commonly referred to as the *optical excess*. Strong deviations from a purely Rayleigh–Jeans behavior at optical wavelengths have been reported in RX J1605.3+3249 [50]. Whether this is due to contamination from a nearby diffuse source, or it is the signature of a non-thermal continuum, possibly extending from the hard X-rays to the optical, as in other isolated NSs (e.g. Geminga [36]), is still an open issue. Unique among the seven, RX J1856.5−3754 has a H_α nebula around it [95]. The nebula is arc-shaped and its apex is nearly aligned with the star proper motion vector.

The discovery of XDINS counterparts made it possible to measure their proper motions, and, up to now in two cases, their parallax. The proper motions of RX J1856.5−3754, RX J0720.4−3125 and RX J1605.3+3249 are in the range $\sim$100–300 mas yr^{-1} [50, 51, 99]. For two more XDINSs without a (certain) optical counterpart, RX J0806.4−4123 and RX J0420.0−5022, quite stringent upper limits on their proper motion ($\lesssim$100 mas yr^{-1}) have been derived in the X-rays, exploiting the superb spatial resolution of Chandra [49]. Back tracing the stars path along the proper motion vector reveals that the most likely birthplaces of RX J1856.5−3754, RX J0720.4−3125 and RX J1605.3+3249 are the Sco and Vela OB2 associations. These are associations rich in OB stars, part of a vast, ring-like structure (in which the Sun is embedded) known as the Gould Belt. The role of the Gould Belt as the nursery of most of the close-by isolated neutron stars has been discussed by Popov et al. [69], who have shown that the contribution of type II supernova events in the Belt is necessary to explain the bright end of the Galactic NS $\log N$–$\log S$ distribution. Parallactic distances have been obtained for RX J1856.5−3754 and RX J0720.4−3125 [31, 92, 99, 100]. Most updated figures are 161^{+18}_{-14} pc and 330^{+170}_{-80} pc, respectively. Together with the proper motion, they provide a transverse velocity of $\sim$280 and $\sim$115 km s^{-1}, much too high to make accretion from the interstellar medium efficient as the source of their X-ray luminosity.

7.3 Modeling the Surface Emission

Much as normal stars, isolated NSs are expected to be covered by an atmosphere, although the properties are quite different in the two cases. The exceedingly large surface gravity ($g \approx 10^{14}$ cm s^{-2}) makes the atmosphere very thin ($h \approx$ 1–10 cm) and this allows to treat radiative transfer in the plane-parallel approximation. However, despite the very limited distance traveled, the blackbody spectrum emitted at the base of the gaseous layer gets distorted as photons propagate towards lower optical depths. The shape of the emerging spectrum depends on several parameters: besides the star surface (or effective) temperature, chiefly the atmosphere composition (either H/He or heavy elements) and the star magnetic field (see, e.g. [109] for a review and Zavlin, this volume). The net result is that, irrespective of details, the observed spectrum is not a blackbody, although it retains a blackbody-like appearance. Usually, atmospheric models are used assuming that the star surface has a given temperature, and that **B** is fixed. For the sake of conciseness, in the following I shall refer to this approach as the "standard" model.

Direct application of the "standard" model to real sources is meaningful only if the star/atmosphere can be assumed to be homogeneous, i.e. nothing changes at different locations on the star surface. While this may be reasonable for the chemical composition, it is definitely not the case for the temperature and magnetic field. In a strongly magnetized medium photon propagation is anisotropic and occurs preferentially along the field (magnetic beaming, e.g. [59]). Even assuming a star-centred dipolar field, the simplest possible choice, both the field strength and orientation

depends on magnetic co-latitude θ. This implies that annuli at different θ do not emit the same spectrum. The structure of the internal magnetic field also deeply influences the surface temperature distribution of the cooling neutron star. Because thermal conductivity is suppressed perpendicularly to the field, heat flows from the core through the crust following the field lines. The star surface temperature depends then on the angle α between the radial and magnetic field directions (see [15, 56])

$$T_s = T_p \left(\cos^2 \alpha + \frac{K_\perp}{K_\parallel} \sin^2 \alpha \right)^{1/4} \sim T_p |\cos \alpha|^{1/2} , \tag{7.3}$$

where T_p is the temperature at the magnetic pole and the ratio of the conductivities perpendicular ($K_\perp$) and parallel ($K_\parallel$) to the field is assumed to be constant. The second (approximate) equality holds in most cases of interest (and for XDINSs in particular, see Sect. 7.2.2), since it is $K_\perp / K_\parallel \ll 1$ for $B \gg 10^{11}$ G.

A quite obvious point in favor of the fact that XDINSs do possess a non-homogeneous surface temperature distribution is the discovery of pulsations (in six out of seven cases) in their X-ray flux. The moderate pulsed fractions detected in these sources (see Sect. 7.2.1) argue against the presence of very small, hot regions (caps) and favor a picture in which the emitting area is a sizeable fraction of the star surface. This, in turn, points towards a smooth temperature distribution, like that induced by a large-scale magnetic field. Realistic modeling of NS surface emission should therefore account for temperature and magnetic field surface distributions. A particularly useful way to obtain information on XDINS temperature distribution and magnetic field is to compare the observed X-ray pulse profiles with those predicted by models, as is discussed in the next subsection.

7.3.1 Pulse Profiles

The problem of calculating the pulse profile produced by a given surface temperature map on a spinning neutron star was first tackled by Page [56] (see also [64]). In essence the approach is as follows. The magnetic field is assigned (e.g. a dipole) and the temperature distribution follows, once its value at the pole is chosen. Then, the star surface is divided into patches by means of suitable grid (the natural one being that induced by the magnetic co-latitude and azimuth). Each patch is associated with a value of T_s and $\mathbf{B}$, and the local spectrum is computed. The simplest possible choice (as in [56]) is that the spectrum is a blackbody, which amounts to neglect the effects of $\mathbf{B}$ and of the atmosphere. The next step in order to derive the spectrum observed at infinity is to collect the contributions of all the patches which are into view at a given spin phase. Since the star appears point-like, there is a single ray which leaves each patch and reaches the observer. Light propagation is affected by the strong gravitational field of the neutron star with the result that the exposed portion of the star is larger than one hemisphere because of ray-bending.

Page [56] found that, under the assumptions of local isotropic blackbody emission and a purely dipolar magnetic configuration, the lightcurves are always symmetrical and the pulsed fractions quite small, $\lesssim$10%. Gravity, making more than half the star visible at the same time, contributes to reduce the pulsed fraction. Despite they produce an increase in the pulsed fraction [61], dipole-induced temperature distributions fail to provide a satisfactory description of the observed lightcurves also in the case in which the spectrum from each surface patch is computed using a magnetized atmosphere model [106]. More complex (star-centred) magnetic field configurations, obtained including quadrupolar components, have been investigated by Page and Sarmiento [58] for local blackbody emission. Zane and Turolla [106], using an atmosphere model, have shown that the pulse profiles of the Seven can be quite accurately reproduced in this case. Although a star-centred dipole+quadrupole topology might not be entirely realistic, the results of these investigations provide quite a strong indication that the magnetic field in these sources is more complicated than a simple dipole.

The structure of the internal magnetic field of a neutron star depends much on the physical state of the star interior, a still largely debated issue. In particular, were neutrons superfluid and protons superconducting, it might be impossible for the magnetic field to penetrate the star core. If this is indeed the case, the field is confined in the crust, together with the currents. Conversely, the presence of a non-superconducting superfluid may allow the field to permeate the entire star. Although at present no definite observational evidence in favor either possibility exists, the long precession periods observed in PSR B1828−11 [80] and RX J0720.4−3125 [21] (see discussion further on) have been interpreted as a possible evidence in favor of the crustal field scenario [42, 43].

As shown by Geppert et al. [13], the thermal surface distribution induced by heat transport through the envelope in the presence of a poloidal crustal field is sensibly different from that of a core-centred dipole. In the latter case the field lines, along which heat flows, are predominantly radial while in the former they are mostly meridional. As a consequence, the crust can sustain a sizable temperature gradient, opposite to the core field case, in which it is almost exactly isothermal. The strong insulating effect of the poloidal field allows heat to flow mostly towards the polar regions, where field lines attain a more radial pattern (see Fig. 7.3). This results in less extended hot polar caps and in cooler equatorial regions with respect to the core-centred field geometry. The addition of a toroidal crustal field magnifies both effects, and can introduce a N-S asymmetry, giving rise to polar regions of different sizes [14, 66]. Such surface temperature distributions can account for the observed pulsed fractions and also explain pulse patterns more complex than a simple sinusoid, like the double peaked lightcurve of RX J1308.6+2127 in which the height of the two maxima are not equal. Actually, the two peaks appear shifted in phase not exactly by half a period, and this points towards the presence of two warm regions which are not antipodal [77]. However, because of the crustal field axial symmetry, such a configuration can not be produced by present models, which always give symmetric pulse profiles.

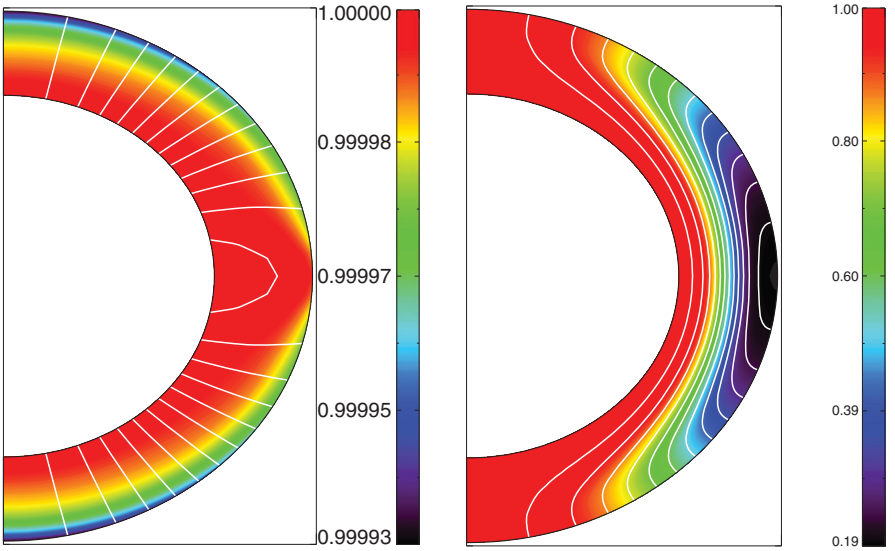

Fig. 7.3 The magnetic field lines and temperature distribution in the neutron star envelope for a core-centred dipolar (*left*) and a crustal field (*right*); the vertical bars give the temperature scale in units of the core temperature (from [13])

Further indications on the star surface temperature distribution come from the recent observations of RX J0720.4−3125. This source, unique among the Seven, exhibited a long-term variability in the blackbody temperature, radius and pulse shape while the X-ray flux stayed pretty constant [11, 96]. The suggestion that the (monotonic) trend found during 2001–2004 is associated to the change in the NS viewing angle due to free precession of the NS was already put forward in the two papers referenced above. The precession scenario is strengthened by the more recent XMM-Newton observations of 2004–2005 which revealed a trend reversal, that is to say temperature started to decrease [97]. Although a complete precession cycle has been not observed as yet (X-ray data cover about 6 yr), Haberl et al. [21] found evidence for a cyclic behaviour with a period of $\sim$7.1 yr. This is further supported by the presence of a comparable (within the errors) periodicity ($\sim$7.7 yr) obtained by fitting a sine wave to the phase residuals of the time coherent solution of Kaplan and Van Kerkwijk [33], as shown in Fig. 7.4. The latter spans a much longer period, $\sim$12 yr, and more than one oscillation is present. Haberl et al. [21] presented a simple model for the surface emission which can explain, within the precession scenario, the basic observational properties of RX J0720.4−3125. Both the blackbody temperature variations and the (anti-correlated) changes in the radiation radius are reproduced assuming that the X-rays come from two warm regions, slightly different in temperature and size, which emit a blackbody spectrum and are not antipodal. Moreover, such a configuration also accounts for the observed hardening of the spectrum near the pulse minimum and for the time evolution of the pulse profile.

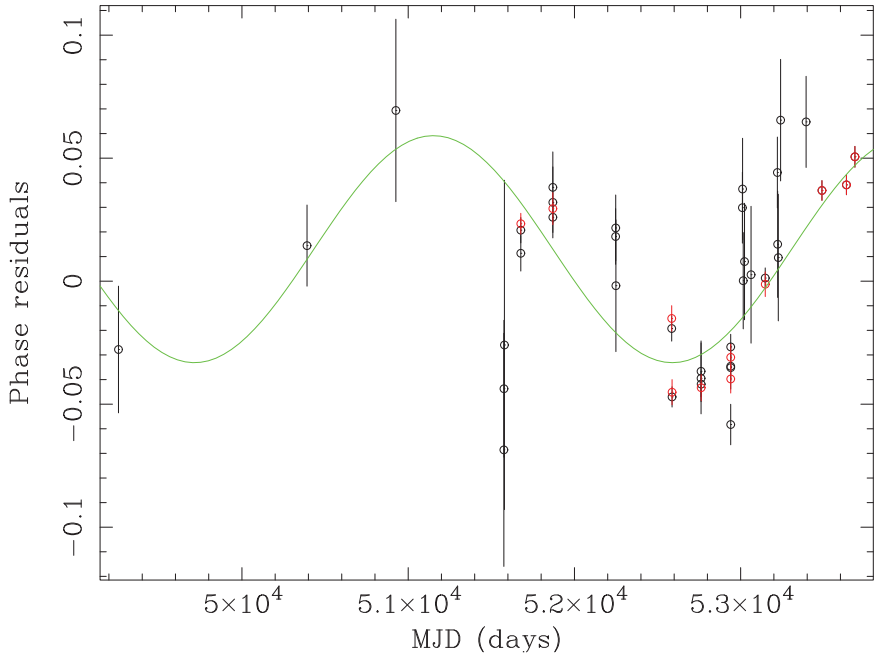

Fig. 7.4 Phase residuals for RX J0720.4−3125, together with the best fitting sine function (from [16])

Although a real fit of the lightcurves has not been presented, the pulsed fraction of RX J0720.4−3125 is correctly reproduced if the star is a nearly aligned rotator (magnetic and rotation axes are parallel) seen at an angle of $\sim 75^\circ$ (i.e. almost equator on, line-of-sight perpendicular to the rotation axis). The issues of the long-term variations of the absorption feature equivalent width, and of its changes with phase, have not have been properly addressed as yet.

The fact that the pulsed fractions of the Seven span a sizable range (from as low as 1.5% for RX J1856.5−3754 to $\sim$18% in the case of RX J1308.6+2127, see Table 7.1) may find a quite natural interpretation in terms of different viewing angles and/or different sizes of the warm, emitting regions. In this respect it is worth noticing that the source with the largest pulsed fraction, RX J1308.6+2127, is the only one with a double peaked pulse profile, an indication that this NS is probably a nearly orthogonal rotator seen at quite a large angle with respect to its rotation axis (see [77]). If the sources with lower pulsed fractions are nearly aligned rotators observed at large angles, this could explain why no radio emission has been detected from them. At large rotational periods, in fact, the radio beam narrows and it can easily miss the Earth for an unfavorable viewing geometry. The claim for a radio detection of RX J1308.6+2127 at very low frequencies (111 MHz [45]) is then particularly intriguing, and, if confirmed, will give support to this picture.

7.3.2 Spectra

The nearly perfect blackbody shape of the XDINS X-ray continuum, most notably that of RX J1856.5−3754, together with their optical excess (see Sect. 7.2.3) has been intriguing all along. The conundrum is: XDINSs are expected to be covered by an atmosphere, but spectra produced by an atmosphere are not blackbody. Burwitz et al. [7] were the first to suggest that the planckian spectrum of RX J1856.5−3754 may arise in a bare neutron star, i.e. a star *without* an atmosphere.

The possibility that the surface layers of a neutron star may be in a condensed (either solid or liquid), instead of gaseous state depends critically on the strength of the magnetic field. The properties of atoms and condensed matter are qualitatively changed by magnetic effects when $B \gg B_0 = m_e e^3 c/\hbar^3 \simeq 2.35 \times 10^9$ G. Under such conditions electrons are strongly confined in the direction perpendicular to the magnetic field and atoms attain a cylindrical shape. Moreover, it is possible for these elongated atoms to form molecular chains by covalent binding along the field direction. Interactions between the linear chains can then lead to the formation of three-dimensional condensates. As discussed in [38, 39], in the case of hydrogen the infinite linear chains (and metallic hydrogen) are certainly bound, favoring the possibility of condensation for sufficiently low temperatures and/or strong magnetic fields. For heavier elements (such as Fe), the lattice structure and the cohesive properties of the condensed state are very uncertain and are different from those of H and He. For instance, unless the field is extremely high ($B \gg 10^{14}$ G), it is likely that the linear chains are unbound for $Z \gtrsim 6$. On the other hand (see again [38]), even such a weak cohesion of the Fe condensate can give rise to a phase transition for temperatures below

$$T_{crit}^{Fe} \approx 27 B_{12}^{2/5}\,\mathrm{eV}\,. \tag{7.4}$$

Calculations for heavier elements are still quite crude and they should be regarded as being typically accurate to an order of magnitude. Also, only when the temperature drops below $\sim T_{crit}/2$ the vapor density becomes much less than the condensation density and a phase transition is unavoidable.

The critical condensation temperatures for H and Fe are plotted as a function of B in Fig. 7.5 together with the position in the B–T plane of the coolest ($T \lesssim 100$ eV), thermally emitting INSs for which an estimate of the magnetic field is available [89]. RX J1856.5−3754, for which the magnetic field in presently unknown, is represented by a horizontal line. It is apparent from Fig. 7.5 that all INSs have a temperature well in excess of the H critical temperature: if surface layers are H-dominated, the presence of a gaseous atmosphere is unavoidable. On the other hand, if INSs have not accreted much gas, one might expect to detect thermal emission directly from the iron surface layers. If this is the case, the outermost layers of RX J1856.5−3754 (depending on the magnetic field), and possibly RX J0720.4−3125 and RX J1308.6+2127, might be in form of hot condensed matter, in which case the usual radiative transfer computations do not apply.

In a neutron star with metallic (Fe) surface layers the density at zero pressure is given by [38]

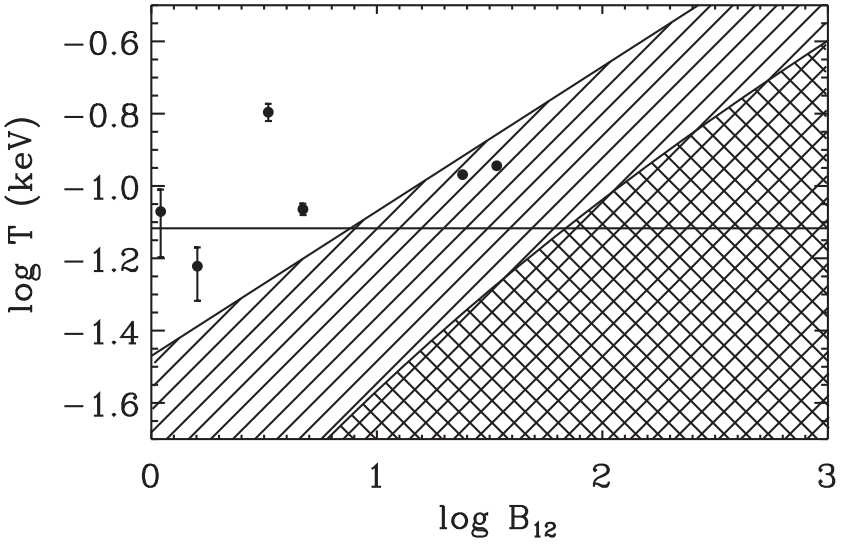

Fig. 7.5 The critical temperature for H and Fe as a function of the magnetic field. Condensation is possible in the *shaded region* for Fe and in the *cross-hatched region* for H. The *full circles* with error bars mark the position of six cool, isolated neutron stars for which a measure of the magnetic field is available (in order of increasing temperature: Geminga, PSR 1055−52, PSR 0656+14, RX J0720.4−3125, RX J1308.6+2127 and Vela). The *horizontal line* is drawn in correspondence to the blackbody temperature of RX J1856.5−3754 (adapted from [89])

$$\rho_s \approx 560 A Z^{-3/5} (B/10^{12}\,\mathrm{G})^{6/5}\,\mathrm{g\,cm^{-3}}\,, \tag{7.5}$$

where $Z = 26$ and $A = 56$. The electron plasma frequency is then

$$\hbar\omega_p \approx 0.7 Z^{1/5} \left(\frac{B}{10^{12}\,\mathrm{G}}\right)^{3/5} \left(\frac{\rho}{\rho_s}\right)^{1/2} \mathrm{keV}\,. \tag{7.6}$$

Cool NSs ($T \lesssim 100\,\mathrm{eV}$) emit most of their thermal radiation below the plasma frequency and substantial deviations from a pure blackbody spectrum are expected owing to the large absorption at $\omega \lesssim \omega_p$.

The emitted spectrum from a given star surface element can be obtained first computing the total reflectivity ρ_ω of the surface for incident unpolarized radiation. Then, since the absorption coefficient is simply $\alpha_\omega = 1 - \rho_\omega$, Kirchhoff's law yields the emissivity $j_\omega = \alpha_\omega B_\omega(T)$, where T is the temperature of the emitting element. In general, ρ_ω depends on the direction of the refracted ray, so that the monochromatic flux f_ω emitted by the surface element must be computed by integrating over all incident directions [6, 89],

$$f_\omega = \int_0^{2\pi} \int_{-\pi/2}^{\pi/2} j_\omega(i, \beta, \theta) \sin i\, di\, d\beta\,. \tag{7.7}$$

Further integration over the entire surface yields the total flux

$$F_\omega = \frac{1}{2}\int_0^\pi \sin\theta\, d\theta \int_0^{2\pi}\int_{-\pi/2}^{\pi/2} j_\omega(i,\beta,\theta)\sin i\, di\, d\beta\,. \tag{7.8}$$

Unfortunately, owing to our poor present knowledge of the physical conditions of the material inside the star, the correct form of the dielectric tensor, which is essential for the evaluation the emissivity, is still an open issue. Turolla et al. [89] considered both a cold electron plasma in which the damping of free electrons due to collisions is neglected, and the, more realistic, case where electron–ion collisions, mainly due to scattering by crystal lattice vibrations (phonons) are accounted for. No contributions from the ions were included in the dielectric tensor, which amounts to treat them as fixed particles. Examples of the spectra computed using the two different assumptions are shown in Figs. 7.6 and 7.7. In both cases the spectrum appears blackbody-like in shape but is depressed wrt the blackbody at the star temperature at low energies by $\sim$30–50%. When electron damping is included, the surface emissivity is more depressed. In this case, although deviations from a planckian distribution are modest ($\lesssim$20%) in the range of interest (0.1–1 keV), they increase at low energies and spectral features may be present.

The problem of the spectrum emitted by a bare NS was further addressed in [65, 91]. In these investigations the contribution of ions to the dielectric tensor was included. The main effect of adding free ions is to increase the emissivity at low frequencies. Resulting spectra are then closer to a (depressed) blackbody in a broader energy range and this might remove the deviations at low energies reported in [89]. While ions, even if they are confined in a lattice, may experience some motion,

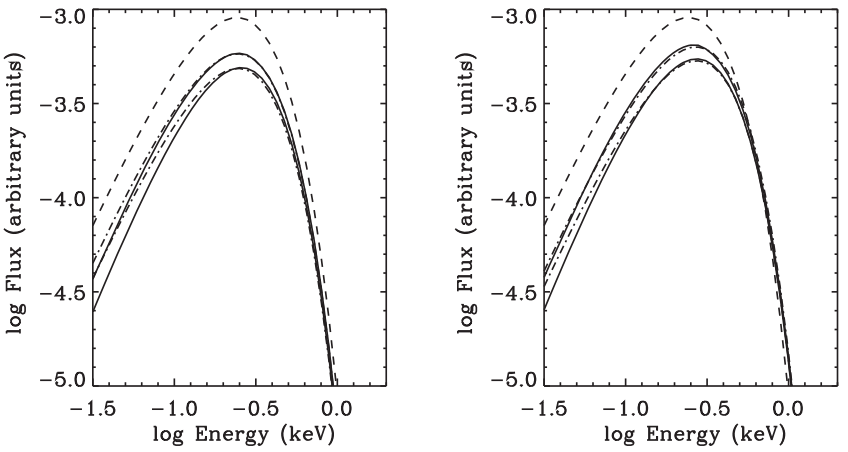

Fig. 7.6 The emitted spectrum in the cold plasma limit for $B_p = 3\times10^{13}$ G and $T_{surf} = 75$ eV. *Left panel*: uniform surface temperature; *right panel*: dipole-induced temperature map. The *dashed line* is the blackbody at T_{surf} and the *dash-dotted line* the blackbody which best fits the calculated spectrum in the 0.1–2 keV range. The two models shown in each panel are for different values of the surface density (from [89])

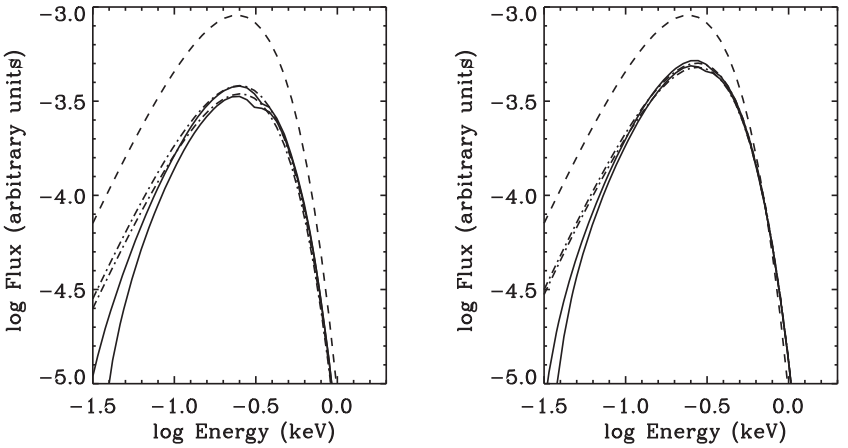

Fig. 7.7 Same as in Fig. 7.6 for the case in which electron–ion collisions are accounted for (from [89])

treating them as free gas is probably not quite realistic. Although results from these investigations substantially differ al lower energies, they all concur that departures from a planckian shape in the ∼0.1–1 keV spectrum are small and bare NS spectra can therefore provide an acceptable fit to XMM and Chandra data.

As shown in [63] soon after the identification of the optical counterpart of RX J1856.5−3754, H atmosphere models largely over predict the observed optical-to-X-ray flux ratio (∼6). According to [68], (non-magnetic) heavy element atmospheres can account for the observed multi-wavelength spectral energy distribution (SED) of RX J1856.5−3754 if a meridional temperature gradient exists on the star surface. The problem of the many features present in such spectra at X-ray energies and which are not observed, however, remains. Nevertheless, if the emitted spectrum can be assumed to be close to a blackbody, the existence of a (smaller) warm and a (larger) cool region (or of a continuous temperature distribution with the same properties) may indeed explain the observed SED [5, 87]. Although the stringent upper limit on the pulsed fraction has been used as an argument against such a picture (e.g. [12]), RX J1856.5−3754 may be an almost aligned rotator seen nearly equator on, as supported by the recent measurement of the pulse period [84]. Up to now, spectra from a condensed surface appear the best candidates in order to produce a nearly blackbody (in shape) distribution. Moreover, as discussed in Sect. 7.3.1, crustal fields and/or quadrupolar components may produce more complex surface thermal maps. A model based on these two ingredients has been recently proposed in order to explain the multi-wavelength SED (and its long term evolution in terms of precession) of RX J0720.4−3125 [67]. A satisfactory fit to the optical fluxes can be obtained, however, only assuming free ions, a still quite controversial issue (see discussion above).

An alternative possibility to reproduce the optical excess, originally suggested in [51] and further explored in [107], is that the bare NS is covered by a thin gaseous

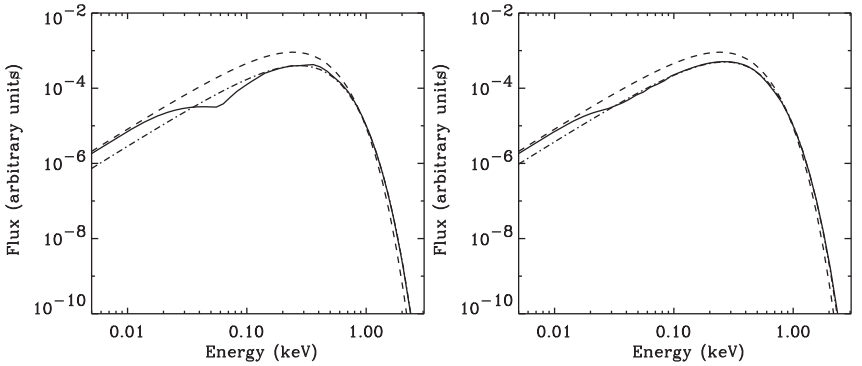

Fig. 7.8 *Solid line*: the emergent spectrum after crossing a pure H (unmagnetised) layer in the case of meridional temperature variation. The spectrum emitted by the condensed surface is that illustrated in Fig. 7.7 and the star is seen equator on. The *dashed line* is the blackbody at T_{surf} and the *dash-dotted line* is the best-fitting blackbody in the 0.1–2 keV band. *Left panel*: $B_{pole} = 2 \times 10^{13}$ G; *right panel*: $B_{pole} = 5 \times 10^{13}$ G

layer, which may have been acquired by the star accreting a small quantity of interstellar H. Since at optical wavelengths the albedo is very small, free-free absorption always dominates over scattering. The free-free absorption depth at optical/UV wavelengths ($E_{opt} \sim 10\,\mathrm{eV}$) is a factor

$$\frac{\tau_{opt}}{\tau_X} \sim \left(\frac{E_X}{E_{opt}}\right)^3 \frac{E_{opt}/kT}{1-\exp\left(-E_X/kT\right)} \approx 200 \tag{7.9}$$

larger than in the X-rays ($E_X \sim 100\,\mathrm{eV}$). Therefore, the gaseous layer is expected to be optically thin in the X-rays and thick to optical photons for a wide range of average densities. This implies that the bare surface X-ray spectrum traverses the layer with no modifications, while at optical/UV energies the spectrum is close to the Rayleigh–Jeans tail of a blackbody at the layer temperature (see Fig. 7.8). Very recently a detailed model based on such a picture has been proposed for RX J1856.5−3754 [30]. A key point in such a model is the thermal balance of the layer, which needs to be maintained at (or close to) the surface temperature against radiative losses, although heat may be efficiently transferred to the layer by thermal conduction from the solid crust.

7.4 Open Issues and Future Perspectives

The large body of observations performed in the last years both at the X-ray and optical wavelengths considerably strengthened the picture according to which the Magnificent Seven are middle-aged cooling neutron stars. The determination of the period derivative provided age estimates of $\approx 10^6$ yr and, together with the energy

of the absorption features in the X-ray spectrum, points towards magnetic fields of $\approx 10^{13} - 10^{14}$ G. Lightcurve analysis and pulsed-phase spectroscopy revealed a rather complex surface temperature distribution, almost certainly different from what is expected in the case of a core-centred dipolar field. Theoretical modeling did not lag behind. Temperature distributions induced by crustal magnetic fields and emission from a condensed surface may be the right ingredients to explain the XDINS observed SED. Despite the considerable progresses, however, many of the properties of these sources, and their relations, if any, with other classes of isolated neutron stars still await a definite explanation. In the following are some important issues that need to be addressed in the near future.

Spectral energy distribution. The nature of the broad absorption features detected in XDINS spectra, their changes with spin phase and over longer timescales, their absence in the spectrum of RX J1856.5−3754 are fundamental questions which need to be addressed by future studies. Possible explanations put forward until now for their origin, either proton cyclotron resonance or atomic transitions, require the presence of an atmosphere. Indeed, as discussed in [92], the line energies can be easily matched by invoking a H atmosphere. This, however, appears difficult to reconcile with the overall SED of XDINSs and with the nearly planckian shape of the spectrum of RX J1856.5−3754 and, to a certain extent in the XMM observation of 2000, also of RX J0720.4−3125. Moreover, if the presence of harmonically spaced lines will be confirmed, the proton cyclotron hypothesis may become untenable, since the predicted strength of higher harmonics is depressed by a factor $E_{line}/m_p c^2$, where m_p is the proton mass [62]. On the other hand, emission from a condensed surface (with the possible inclusion of a thin atmospheric layer) seems capable of reproducing the main features of the observed SED. In this case the nature of the absorption features is likely different and related to the appearance of "spectral edges" (distortions with respect to a pure blackbody shape around the maximum, see, e.g. [66, 89] and Fig. 7.7). According to [67], such a model can explain the observed evolution of the feature properties in RX J0720.4−3125.

More definite conclusions will come from a thorough investigation of the properties of magnetised atmospheres, including partial H ionization and vacuum polarisation effects, which is presently being carried out [28,29,73,90] (see also [26]). In this respect, the role played in line formation by He [60] and bound species, like the "exotic" molecular ions (e.g. [88], may prove important. At the same time, further investigations are required to assess what is the contribution of ions to the emissivity from the condensed surface. This will clarify if the optical flux of XDINSs can be produced by surface radiation alone, or the presence of a thin atmosphere is indeed required.

Search for new candidates. Even if this means giving up the nickname *the Magnificent Seven*, finding new XDINS candidates is of paramount importance. Although no positive detection has been claimed up to now, searches for new sources are in progress. The searching strategy is based on the very large X-ray-to-optical flux ratio of XDINSs ($f_X/f_{opt} \gtrsim 10^4$) and aims at identifying "blank field" sources in large scale X-ray surveys, chiefly the ROSAT All Sky Survey (RASS). These are objects without a counterpart within their X-ray error circle up to the limiting

magnitude of the optical survey which is cross-correlated with the RASS. The RASS covers about 99.7% of the sky in the 0.1–2.4 keV band up to a limiting flux of a few times $10^{-13}\,\mathrm{erg/cm^2/s}$ [98]. Rutledge et al. [76] matched the RASS Bright Source Catalogue (BSC) with the United States Naval Observatory (USNO A2.0) survey. More recently, Agüeros et al. [1] extended the analysis to the entire RASS catalogue ($\sim$124,000 sources), used in conjunction with the Sloan Digital Sky Survey (SDSS), finding about 10 blank field sources. All potential candidates have $f_X/f_{opt} \gtrsim 10$–100 which make them worth of dedicated pointings with XMM/Chandra, although present lower limits can not exclude that these are sources belonging to other classes of "exotic" X-ray emitters (e.g. type 2 quasars, extreme BL-Lac objects, X-ray binaries). A search for XDINSs in HRI observations, which cover 1.8% of the sky, produced a few more candidates [10]. Despite no large scale survey is available for Chandra and XMM-Newton, a possibility worth exploring is the search for XDINS candidates in archive observations of promising regions of the sky, like those in the direction of nearby OB associations at low interstellar absorption (see [72]).

The XDINS-RRAT connection. The recently discovered Rotating Radio Transients (RRATs [46]) exhibit many striking similarities with the Seven. In fact, the values of the rotational periods, period derivatives, estimated ages, besides the spatial distribution and the lack of persistent pulsed radio emission, are all features shared by both classes of sources. Moreover, Chandra detected a dim (thermal, $kT \sim 120\,\mathrm{eV}$) X-ray source positionally coincident with RRAT J18189−1458 [75]. On the basis of these considerations and of simple estimates on the birth rates of the different Galactic NS populations (radio pulsars, XDINSs, RRATs and SGRs/AXPs), Popov et al. [71] concluded that RRATs may well be far away XDINSs. While the faint X-ray emission from RRATs is difficult to detect since they are about a factor 10 more distant than XDINSs, bursting, RRAT-like emission from the latter could be easily observed, but it has not yet searched for.

The XDINS-magnetar connection. XDINSs are likely to be quite strongly magnetized neutron stars. If magnetic field strengths derived assuming that the absorption lines are proton cyclotron resonances will be confirmed (as for RX J0720.4−3125 and RX J1308.6+2127), some of these sources have $B \sim 10^{14}$ G, close to the magnetar range. Magnetic fields in excess of $B_{QED} \simeq 4.4 \times 10^{13}$ G have been discovered also in radio pulsars [8]. The question as to why isolated neutron stars with similar magnetic fields manifest themselves as inconspicuous, dim X-ray sources, ordinary radio pulsars or very energetic soft gamma repeaters, then naturally arises. A related issue is if, and to which extent, there is an evolutionary link between SGRs/AXPs and XDINSs. Are XDINSs "worn out magnetars", what is left after the star has dissipated much of its internal field electricity, the alleged culprit for the observed activity in SGRS and AXPs [81–83]?

Future X-ray missions are bound to shift our understanding of XDINSs into a higher gear. In particular, IXO, thanks to their large effective area and superb spectral resolution in the soft X-ray range, will probe the X-ray SED of the Seven to an unprecedented level of detail. This will allow to better characterize the spectral properties of the faintest sources, and to perform accurate phase-resolved spectroscopy in those brighter objects, like RX J1856.5−3754, with a low pulsed fraction. This

will clarify if indeed the spectrum of RX J1856.5−3754 is featureless, or if absorption features, which appear only at certain phases, are present. The X-ray polarimeter (XPOL) which is presently under consideration for the IXO mission will be, if flown, the first instrument of this kind to go into operation. X-ray polarimetry will provide a decisive diagnostics to discriminate among the different mechanisms proposed to explain the surface emission from XDINSs, and, in particular, will allow to put the condensed surface model through a direct observational test.

References

1. M.A. Agüeros, S.F. Anderson, B. Margon et al.: AJ, **131**, 1740 (2006)
2. W. Becker, J. Trümper: A&A, **326**, 682 (1997)
3. G.F. Bignami, P.A. Caraveo: ARA&A, **34**, 331 (1996)
4. O. Blaes, P. Madau: ApJ, **403**, 690 (1993)
5. T.M. Braje, R.W. Romani: ApJ, **580**, 1043 (2002)
6. W. Brinkmann: A&A, **82**, 352 (1980)
7. V. Burwitz, F. Haberl, R. Neuhäuser et al.: A&A, **399**, 1109 (2003)
8. F. Camilo, V.M. Kaspi, A.G. Lyne et al.: ApJ, **541**, 367 (2000)
9. F.A. Córdova, J. Middleditch, R.M. Hjellming et al.: ApJ, **345**, 451 (1989)
10. M. Chieregato, S. Campana, A. Treves et al.: A&A, **444**, 69 (2005)
11. C.P. de Vries, J. Vink, M. Méndez et al.: A&A, **415**, L31 (2004)
12. J.J. Drake, H.L. Marshall, S. Dreizler et al.: ApJ, **573**, 157 (2002)
13. U. Geppert, M. Küker, D. Page: A&A, **426**, 267 (2004)
14. U. Geppert, M. Küker, D. Page: A&A, **467**, 937 (2006)
15. G. Greenstein, G.J. Hartke: ApJ, **271**, 283 (1983)
16. F. Haberl: The Magnificent Seven: Magnetic fields and surface temperature distributions. In *Isolated Neutron Stars: From the Interior to the Surface*, ed. by S. Zane, R. Turolla, D. Page (Springer, Berlin Heidelberg New York, 2007, astro-ph/0609066)
17. F. Haberl, C. Motch, D.A.H. Buckley et al.: A&A, **326**, 662 (1997)
18. F. Haberl, C. Motch, V.E. Zavlin et al.: A&A, **424**, 635 (2004)
19. F. Haberl, W. Pietsch, C. Motch: A&A, **351**, L53 (1997)
20. F. Haberl, A.D. Schwope, V. Hambaryan et al.: A&A, **403**, L19 (2003)
21. F. Haberl, R. Turolla, C.P. de Vries et al.: A&A, **451**, L17 (2006)
22. F. Haberl, V. Zavlin: A&A, **391**, 571 (2002)
23. F. Haberl, V.E. Zavlin, J. Trümper et al.: A&A, **419**, 1077 (2004)
24. J.P. Halpern, E.V. Gotthelf, N. Mirabal et al.: ApJ, **537**, L41 (2002)
25. V. Hambaryan, G. Hasinger, A. Schope et al.: A&A, **381**, 98 (2002)
26. A.K. Harding, D. Lai: Rep. Prog. Phys., **69**, 2631 (2006)
27. A. Hewish, S.J. Bell, J.D. Pilkington et al.: Nature, **217**, 709 (1968)
28. W. Ho, D.Lai, A.Y. Potekhin et al.: ApJ, **599**, 1293 (2003)
29. W. Ho, D.Lai: ApJ, **607**, 420 (2004)
30. W. Ho, D.L. Kaplan, P. Chang et al.: MNRAS, **375**, 821 (2007)
31. D.L. Kaplan, S.R. Kulkarni, M.H. van Kerkwijk: ApJ, **579**, L29 (2002)
32. D.L. Kaplan, S.R. Kulkarni, M.H. van Kerkwijk: ApJ, **588**, L33 (2003)
33. D.L. Kaplan, M.H. van Kerkwijk: ApJ, **628**, L45 (2005)
34. D.L. Kaplan, M.H. van Kerkwijk: ApJ, **635**, L65 (2005)
35. D.L. Kaplan, M.H. van Kerkwijk, H.L. Marshall et al.: ApJ, **590**, 1008 (2003)
36. O.Y. Kargaltsev, G.G. Pavlov, V.E. Zavlin et al.: ApJ, **625**, 307 (2005)
37. S.R. Kulkarni, M.H. van Kerkwijk: ApJ, **507**, L49 (1998)
38. D. Lai: Rev. Mod. Phys., 73, 629 (2001)

39. D. Lai, E.E Salpeter: ApJ, **491**, 270 (1997)
40. J.M. Lattimer, M. Prakash: ApJ, **550**, 426 (2001)
41. J.M. Lattimer, M. Prakash: Science, **304**, 536 (2004)
42. B. Link: Phys. Rev. Lett., **91**, 101011 (2003)
43. B. Link: A&A, **458**, 881 (2006)
44. V.M. Malofeev, O.I. Malov, D.A. Teplykh: Radio emission from AXP and XDINS. In *Isolated Neutron Stars: From the Interior to the Surface*, ed. by S. Zane, R. Turolla, D. Page (Springer, Berlin Heidelberg New York, 2007)
45. V.M. Malofeev, O.I. Malov, D.A. Teplykh et al.: Astron. Rep., **49**, 242 (2005)
46. M.A. McLaughlin, A.G. Lyne, D.R. Lorimer et al.: Nature, **439**, 817 (2006)
47. C. Motch, F. Haberl: A&A, **333**, L59 (1998)
48. C. Motch, F. Haberl, F.-J.Zickgraf et al.: A&A, **351**, 177 (1999)
49. C. Motch, A.M. Pires, F. Haberl et al.: Measuring proper motions of isolated neutron stars with Chandra. In *Isolated Neutron Stars: From the Interior to the Surface*, ed. by S. Zane, R. Turolla, D. Page (Springer, Berlin Heidelberg New York, 2007, astro-ph/0608589)
50. C. Motch, K. Sekiguchi, F. Haberl et al.: A&A, **429**, 257 (2005)
51. C. Motch, V. Zavlin, F. Haberl: A&A, **323**, 408 (2003)
52. R. Neuhäuser, J.E. Trümper: A&A, **343**, 151 (1999)
53. H. Ögelman: X-ray observations of cooling neutron stars. In *The Lives of the Neutron Stars*, ed. by M.A. Alpar, U. Kiziloglu, J. van Paradijs (Kluwer Academic, Dordrecht, 1995), p. 101
54. H. Ögelman, H.-U. Zimmermann: A&A, **214**, 179 (1989)
55. J.P. Ostriker, M.J. Rees, J. Silk: Astrophys. Lett., **6**, 179 (1970)
56. D. Page: ApJ, **442**, 273 (1995)
57. D. Page, U. Geppert, F. Weber: Nucl. Phys. A, **777**, 497 (2006)
58. D. Page, A. Sarmiento: ApJ, **473**, 1067 (1996)
59. G.G. Pavlov, D. Sanwal, M.A. Teter: Central compact objects in supernova remnants. In: *Young Neutron Stars and Their Environments, IAU Symposium no. 218*, ed. by F. Camilo, B.M. Gaensler (Astronomical Society of the Pacific, San Francisco, 2004), p. 239
60. G.G. Pavlov, V.G. Bezchastnov: ApJ, **635**, L61 (2005)
61. G.G. Pavlov, Yu.A. Shibanov, J. Ventura et al.: A&A, **289**, 837 (1994)
62. G.G. Pavlov, Yu.A. Shibanov, D.G. Yakovlev: Ap&SS, **73**, 33 (1980)
63. G.G. Pavlov, V.E. Zavlin, J. Trümper et al.: ApJ, **472**, L33 (1996)
64. K.R. Pechenick, C. Ftaclas, J.M. Cohen: ApJ, **274**, 846 (1983)
65. J.F. Pèrez-Azorin, J.A. Miralles, J.A. Pons: A&A, **433**, 275 (2005)
66. J.F. Pèrez-Azorin, J.A. Miralles, J.A. Pons: A&A, **451**, 1009 (2006)
67. J.F. Pèrez-Azorin, J.A. Pons, J.A. Miralles et al.: A&A, **459**, 175 (2006)
68. J.A. Pons, F.M. Walter, J.M. Lattimer et al.: ApJ, **564**, 981 (2002)
69. S.B. Popov, M. Colpi, M.E. Prokhorov et al.: A&A, **406**, 111 (2003)
70. S.B. Popov, M. Colpi, A. Treves et al.: ApJ, **530**, 896 (2000)
71. S.B. Popov, R. Turolla, A. Possenti: MNRAS, **369**, L23 (2006)
72. B. Posselt, S.B. Popov, F. Haberl et al.: The Magnificent Seven in the dusty prairie – The role of interstellar absorption on the observed neutron star population. In *Isolated Neutron Stars: From the Interior to the Surface*, ed. by S. Zane, R. Turolla, D. Page (Springer, Berlin Heidelberg New York, 2007, astro-ph/0609275)
73. A.Y. Potekhin, D. Lai, G. Chabrier et al.: ApJ, **612**, 1034 (2004)
74. S.M. Ransom, B.M. Gaensler, P.O. Slane: ApJ, **570**, L75 (2002)
75. S.P. Reynolds, K.J. Borkowski, B.M. Gaensler et al.: ApJ, **639**, L71 (2006)
76. R.E. Rutledge, D.W. Fox, M. Bogosavljevic et al.: ApJ, **598**, 458 (2003)
77. A.D. Schwope, V. Hambaryan, F. Haberl et al.: A&A, **441**, 597 (2005)
78. A.D. Schwope, V. Hambaryan, F. Haberl et al.: The complex X-ray spectrum of the isolated neutron star RBS1223. In *Isolated Neutron Stars: From the Interior to the Surface*, ed. by S. Zane, R. Turolla, D. Page (Springer, Berlin Heidelberg New York, 2007, astro-ph/0609705)
79. A.D. Schwope, G. Hasinger, R. Schwarz et al.: A&A, **341**, L51 (1999)
80. I.H. Stairs, A.G. Lyne, S.L. Shemar: Nature, **406**, 484 (2000)
81. C. Thompson, A.M. Beloborodov: ApJ, **634**, 565 (2005)

82. C. Thompson, R.C. Duncan: ApJ, **561**, 980 (2001)
83. C. Thompson, M. Lyutikov, S.R. Kulkarni: ApJ, **574**, 332 (2002)
84. A. Tiengo, S. Mereghetti: ApJ, **657**, L101 (2007)
85. A. Treves, M. Colpi: A&A, **241**, 107 (1991)
86. A. Treves, R. Turolla, S. Zane et al.: PASP, **112**, 297 (2000)
87. J. Trümper, V. Burwitz, F. Haberl et al.: Nucl. Phys. B, **132**, 560 (2004)
88. A.V. Turbiner, J.C. Lopez-Vieyra: Phys. Reps., **424**, 309 (2006)
89. R. Turolla, S. Zane, J.J. Drake: ApJ, **603**, 265 (2004)
90. M. Van Adelsberg, D. Lai: MNRAS, **373**, 1495 (2006)
91. M. Van Adelsberg, D. Lai, A.Y. Potekhin et al.: ApJ, **913**, 628 (2005)
92. M.H. van Kerkwijk, D.L. Kaplan: Isolated neutron stars: Magnetic fields, distances, and spectra. In *Isolated Neutron Stars: From the Interior to the Surface*, ed. by S. Zane, R. Turolla, D. Page (Springer, Berlin Heidelberg New York, 2007, astro-ph/0607320)
93. M.H. van Kerkwijk, D.L. Kaplan, M. Durant et al.: ApJ, **608**, 432 (2004)
94. M.H. van Kerkwijk, S.R. Kulkarni: A&A, **379**, 986 (2001)
95. M.H. van Kerkwijk, S.R. Kulkarni: A&A, **380**, 221 (2001)
96. J. Vink, C.P. de Vries, M. Méndez et al.: ApJ, **609**, L75 (2004)
97. J. Vink, F. Haberl, C.P. de Vries et al.: The Astronomer's Telegram, #650 (2005)
98. W. Voges, B. Aschenbach, Th. Boller et al.: A&A, **349**, 389 (1999)
99. F.M. Walter: ApJ, **549**, 433 (2001)
100. F.M. Walter, J. Lattimer: ApJ, **576**, L145 (2002)
101. F.M. Walter, L.D. Matthews: Nature, **389**, 358 (1997)
102. F.M. Walter, S.J. Wolk, R. Neuhäuser: Nature, **379**, 233 (1996)
103. P.M. Woods, C. Thompson: Soft gamma repeaters and anomalous X-ray pulsars: magnetar candidates. In: *Compact Stellar X-ray Sources*, ed. by W. Lewin, M. van der Klis (Cambridge Astrophysics Series, No. 39, Cambridge University Press, Cambridge, 2006), pp. 547–586
104. L. Zampieri, S. Campana, R. Turolla, et al.: A&A, **378**, L5 (2001)
105. S. Zane, M. Cropper, R. Turolla et al.: ApJ, **627**, 397 (2005)
106. S. Zane, R. Turolla: MNRAS, **366**, 727 (2006)
107. S. Zane, R. Turolla, J.J Drake: Adv. Sp. Res., **33**, 531 (2004)
108. S. Zane, R. Turolla, L. Zampieri et al.: ApJ, **451**, 739 (1995)
109. V.E. Zavlin, G.G Pavlov: Modeling neutron star atmospheres. In: *Proceedings of the 270. WE-Heraeus Seminar on Neutron Stars, Pulsars, and Supernova Remnants*, ed. by W. Becker, H. Lesch, and J. Trümper (MPE Report 278, 2002), p. 263

Chapter 8
Millisecond Pulsars in Globular Clusters and the Field

Jonathan E. Grindlay and Slavko Bogdanov

8.1 Introduction

Globular clusters are preferred for the study of millisecond pulsars (MSPs), given the $\gtrsim$100 increase in their number per unit stellar mass than in the Galaxy at large. X-ray observations of globulars with imaging grazing incidence telescopes have proven to be at least as sensitive as radio telescopes for MSP detection and spectral classification, but not (yet) for period discovery due to the relatively low count rates. However, for known periods, pulse-phase spectroscopy studies are remarkably effective. We provide an initial overview of the current X-ray studies of MSPs in globular clusters as well as in the Galaxy field. Early X-ray studies of MSPs with *ROSAT*, *ASCA*, and *RXTE* are reviewed briefly and put into the context of current results. Globular clusters observed with the *Chandra* X-ray Observatory, given its exceptional angular resolution, have clarified the range of MSP types (thermal vs. non-thermal) and overall populations. Observations of several nearby field MSPs with *XMM-Newton*, with its temporal-spectral resolution, have given new measurements of the M/R (compactness) of neutron stars from precise measures of their soft X-ray pulse profiles as a function of energy. X-ray spectral-timing of MSPs can then best constrain the equation of state of neutron stars when future broadband (0.1–10 keV) X-ray telescopes with very high throughput ($\gtrsim$10$\times$ *Chandra* or *XMM-Newton*) are in operation.

Millisecond pulsars (MSPs) are remarkable objects in many respects. As the fastest spinning known astronomical objects, neutron stars with mass $\sim$1.4 $M_\odot$ and radius R $\sim$ 10 km have a surface equatorial velocity of 0.15 c for the shortest period (1.38 ms) known MSP [36]. All $\sim$200 MSPs currently known have been discovered as radio pulsars (see [40] for a review). Compared to "normal" rotation powered pulsars (defined here as those with spin periods P $\gtrsim$30 ms), MSPs have

J.E. Grindlay and S. Bogdanov
Harvard-Smithsonian Center for Astrophysics, 60 Garden St., Cambridge, MA 02138, USA
e-mail: josh@cfa.harvard.edu; sbogdano@cfa.harvard.edu

W. Becker (ed.), *Neutron Stars and Pulsars,* Astrophysics and Space Science Library 357,

exceptionally small spin-down rates, with $\dot{P} \times 10^{-15} \lesssim 10^{-19}$, and thus spin-down ages $\tau = P/2\dot{P} \gtrsim 10^{8.5}$ yrs for most MSPs. Their spin histories are essentially free of discontinuities, or glitches, making them the most stable astronomical clocks known. Although MSPs were discovered in the radio, a significant fraction ($\sim 10^{-3}$) of their spin-down luminosity and the bulk of their radiated photon luminosity is emitted in the X-ray band [9].

In this review, we summarize X-ray observations of MSPs in globular clusters and, for comparison, the field of the Galaxy. After an overview of the observations, we discuss how the most recent studies made with *Chandra* and *XMM-Newton* have revealed the X-ray emission regions for MSPs as due to three different processes: thermal emission from the heated polar caps [8, 10], already hinted at by ROSAT studies [9, 10, 54]; non-thermal emission from the pulsar magnetosphere, already evident from *RXTE* [45, 49], and non-thermal emission from the pulsar wind shock (PWS) at a binary companion star (e.g. [37]), first suggested for re-recycled MSPs in globular clusters by *Chandra* data for the MSP in the globular cluster NGC 6397 [30] and, in much more detail, for the MSP 47 Tuc-W for which the PWS is partly eclipsed by the binary companion main sequence star in the globular cluster 47 Tuc [15].

8.2 Early X-Ray Studies of MSPs

Here we summarize the early X-ray studies of MSPs, both in and out of globular clusters. The first MSP to be discovered as a field radio pulsar, PSR B1937+21 with the remarkably short period 1.6 ms [2], was only much later detected by the *ASCA* X-ray telescope [51], as discussed below. However other MSPs, closer and brighter, were detected earlier with the *ROSAT* soft X-ray telescope, and a few with the *RXTE* and *BeppoSAX* X-ray missions. These early detections enabled the first understanding of the high energy emission in these fastest-spinning neutron star systems. However, it was not until (much) larger samples of MSPs were detected in X-rays with *Chandra* and *XMM-Newton*, as summarized in several sections of this Review, that the full range of MSP emission processes were possible to disentangle.

8.2.1 ROSAT, RXTE, *and* ASCA *Observations*

Prior to the launch of *ROSAT*, nothing was known about the X-ray properties of MSPs. The first targeted X-ray observation of a MSP was that of the "black-widow" pulsar, PSR B1957+20 , in the field, and so named because the PWS of this MSP is ablating its low-mass binary companion star. A faint X-ray counterpart was detected with the *ROSAT* PSPC and HRI detectors [27, 39], but no spectral and timing analysis could be carried out. The first secure detection of X-ray pulsations from a

MSP was of the nearest known system, PSR J0437−4715, in a serendipitous 6 ks *ROSAT* all-sky survey observation in which pulsations at the 5.76 ms spin period were detected [8].

Subsequently, PSR B1821−24 in the globular cluster M28 was detected by *ROSAT* [23], *ASCA* [49], *RXTE*, and *BeppoSAX* [42]. PSR B1937+21 was detected by *ASCA* [50, 51]. The bulk of X-rays for B1821−24 and B1937+21 are emitted in two very narrow pulses, similar to the radio pulses and indicative of highly beamed, non-thermal radiation from the pulsar magnetosphere. As expected, the spectral continuum of these MSPs is well described by a power-law spectrum. These MSPs have characteristically the highest spin-down luminosities and radiated X-ray luminosities ($\gtrsim 10^{32}$ ergs s^{-1}).

Over its lifetime, *ROSAT* detected 10 MSPs in the field of the Galaxy and 1 in a globular cluster (see [10] for a summary). However, due to the intrinsic faintness of these sources, the exact nature of the X-ray emission (thermal vs. non-thermal) was uncertain for most of them. The substantial increase in sensitivity provided by the recent observations with *Chandra* and *XMM-Newton* was required for further study of these intriguing objects. In stark contrast to the most luminous MSPs detected with ROSAT, RXTE, ASCA and BeppoSAX for which non-thermal magnetospheric emission dominated, the bulk of the MSPs in globular clusters were found to be relatively low luminosity (10^{30-31} ergs s^{-1}) soft thermal sources [13, 30, 31].

8.3 *Chandra* Studies of MSPs in Globular Clusters

8.3.1 47 Tuc

The first *Chandra* observation of the globular cluster NGC 104, 47 Tucanae (hereafter 47 Tuc), was the 70-ks exposure with ACIS-I [31] (Fig. 8.1). This revealed that the dominant mode of X-ray emission from MSPs in globulars was thermal emission from their heated polar caps [30]. As summarized above, this had been recognized as a dominant emission mechanism for several nearby field MSPs [10] from *ROSAT* studies and in more detail with recent *XMM-Newton* studies. However, the first *Chandra* results showed that the *thermal emission is the dominant source for MSPs, generally*. By detecting a significant sample (12 convincingly, and 2–3 marginally) of the total (15) MSPs with then known precise positions from radio timing [26] in 47 Tuc in which there were then a total of 20 MSPs [18], and finding that all but three were soft thermal sources, this established that the early detections of luminous hard spectra MSPs (e.g. B1821−24 in M28) were the rare exception for MSPs in general. The complete analysis of the 47 Tuc MSPs is given by Bogdanov et al. [13], who used the followup deep (300 ks) observations and source catalog reported by Heinke et al. [34]. The spectral analysis revealed that the X-ray emission of the majority (16 of 19) of these MSPs was found to be well described by a thermal (blackbody or neutron star hydrogen atmosphere) spectrum

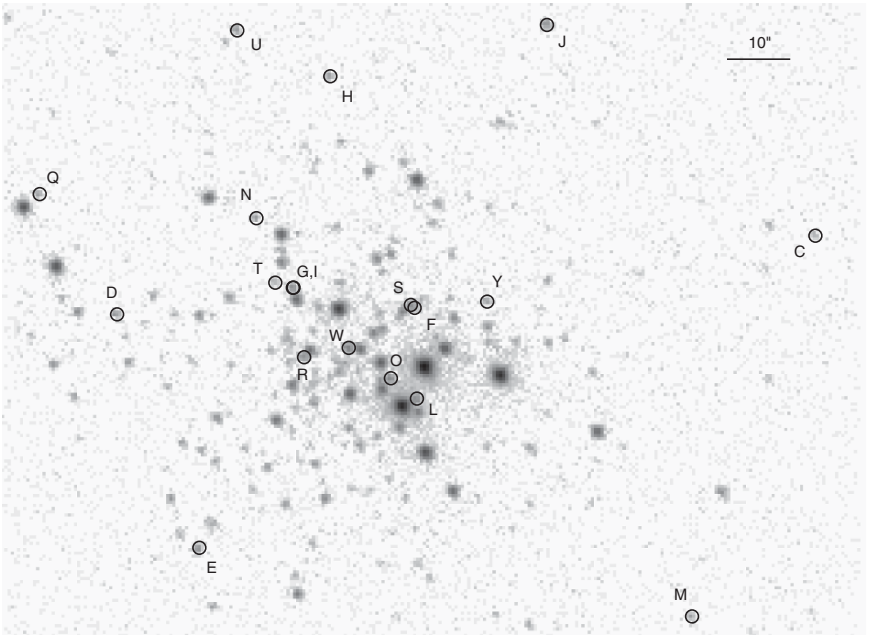

Fig. 8.1 *Chandra* ACIS-S 270-ks exposure of the core of the globular cluster 47 Tuc. An X-ray counterpart is associated with the radio positions (*circles*) of all 19 MSPs with known (from radio timing) source positions (see [13] for details of the cluster MSPs)

with a temperature $T_{\rm eff} \sim (1-3) \times 10^6$ K, emission radius $R_{\rm eff} \sim 0.1$–3 km, and luminosity $L_X \sim 10^{30-31}$ ergs s^{-1}. Note that the initial Chandra observations could not distinguish between simple blackbody vs. neutron star atmosphere (hereafter NSA) spectral models. This was to come later, with pulse phase spectroscopy (see Sect. 8.4.1, Fig. 8.4) which showed BB fits are not acceptable.

For several of the 47 Tuc MSPs, there is indication that a second thermal component is required, similar to what is seen in some nearby field MSPs. The observed radiation most likely originates from the heated magnetic polar caps of the MSPs. The small apparent scatter in L_X is consistent with thermal emission from the polar caps of a global dipole field although the small emission areas may imply either a more complex small-scale magnetic field configuration near the neutron star surface or non-uniform polar cap heating. The radio-eclipsing binary MSPs 47 Tuc J, O, and W were found to show a significant non-thermal (power-law) component, with spectral photon index $\Gamma \sim 1$–1.5, which most likely originates in an intra-binary shock formed due to interaction between the relativistic pulsar wind and matter from the stellar companion. A re-examination of the X-ray–spin-down luminosity relation ($L_X - \dot{E}$) has revealed that for the MSPs with thermal spectra $L_X \propto \dot{E}^{\beta}$, where $\beta \sim 0.2 \pm 1.1$. Due to the large uncertainties in predominantly $\dot{E}$, the result is consistent with both the linear $L_X - \dot{E}$ relation and the flatter $L_X \propto \dot{E}^{0.5}$ predicted by polar cap heating models [33]. In terms of X-ray properties, there appear to be no clear systematic differences between MSPs in 47 Tuc (the only globular cluster

with a large MSP population for which both soft thermal spectra can be measured and $\dot{E}$ values have been reported from radio timing observations) and in the field of the Galaxy. Globulars with higher collision rates (e.g. core collapse clusters, such as NGC 6397, or clusters like Terzan 5) remain to be studied in detail to ascertain if their larger-expected total numbers or re-recycled MSPs show measurable differences. Such differences could arise, for instance, due to single (or repeated) recycling episodes of cluster MSPs [20, 30]. Thus, either most MSPs in 47 Tuc have not undergone such "re-recycling" episodes or these do not alter the basic emission properties of these objects. Note that the only examples of MSPs with main-sequence or slightly evolved secondaries are found in globulars (see below) and point strongly to their original binary companions (typically a white dwarf) being re-exchanged for cluster main-sequence stars. It may be the case that the magnetic field of the original MSP has been substantially altered by the likely period of renewed accretion just after exchange encounter [30], since MSPs themselves provide evidence that spin frequency and neutron star mass (which together track total mass accretion) correlate with inferred neutron star magnetic field for the MSP [29].

47 Tuc W

The most notable MSP in 47 Tuc is the binary PSR J0024−7204W (47 Tuc W), which exhibits peculiar X-ray spectral variability. The emission consists of a dominant non-thermal component, which is eclipsed for a portion of the orbit, and a thermal component, which appears to be persistent. The non-thermal X-rays likely originate in a relativistic intra-binary shock, formed due to interaction between the relativistic particle wind from the pulsar and matter from the main-sequence companion star, while the thermal photons are from the heated magnetic polar caps of the millisecond pulsar (Fig. 8.2). At optical wavelengths, the emission exhibits large-amplitude ($\sim$0.3 mag) variations at the orbital period, which can be attributed to heating of one side of the tidally-locked secondary star by the pulsar wind. The observed X-ray and optical properties of 47 Tuc W are strikingly similar to those of the low mass X-ray binary and X-ray millisecond pulsar SAX J1808.4−3658 in quiescence [19]. This supports the conjecture that the non-thermal X-ray emission and optical modulations seen in the SAX J1808.4−3658 system in a quiescent state are due to interaction between the wind from a reactivated rotation-powered pulsar and matter from the companion star. The remarkable similarities between the two systems provide direct evidence for the long-sought connection between accretion- and rotation-powered MSPs [15].

8.3.2 NGC 6397

The sole MSP known in NGC 6397, PSR J1740−5340 [21], is bound to a peculiar $\sim 0.2 - 0.3\,M_{\odot}$ "red-straggler" companion in a 32.5-h binary orbit [25]. Optical observations of this system [48] have revealed the presence of ellipsoidal variations

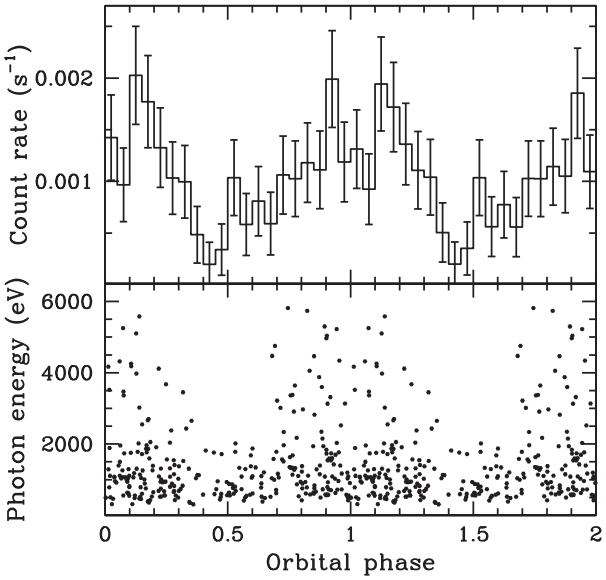

Fig. 8.2 Lightcurve of 47 Tuc W folded at its 3.2-h binary period. The X-ray flux is characterized by an asymmetric occultation of the hard X-ray flux, which can be explained by a geometric occultation of the intra-binary shock by the main-sequence secondary star [15]

as well as a stream of gas protruding from the $1.6\,R_{\odot}$ secondary star through the L1 point implying that the companion is Roche-lobe filling. However, the fact that PSR J1740−5340 (hereafter J1740) is observed as a radio pulsar implies that this gas stream never reaches the underlying NS and is instead swept back and ultimately expelled from the binary system by the relativistic particle wind from the MSP. The presence of this swept-back gas stream is evident in the very unusual HI emission line profile [48]. This unbound gas is likely the cause for the irregular eclipses observed at radio frequencies the MSPs exhibits over a wide range of orbital phases.

The J1740 system is known to be coincident with a moderately luminous X-ray source (Fig. 8.3; see also [32] and [28]). The relatively hard X-ray emission from this source is consistent with the picture of the intra-binary PWS model described above given that synchrotron emission is expected to be the primary energy loss mechanism in the shock wave resulting from the interaction between the MSP wind and the infalling gas from the secondary (see Fig. 2 in [15]). Indeed, the observed X-ray spectrum is best described by a non-thermal model with power-law photon index $\Gamma = 1.6 \pm 0.1$ and X-ray luminosity $L_X = 1.5 \times 10^{31}$ ergs s^{-1} (0.3–8.0 keV) assuming the nominal column density towards NGC 6397, $N_H = 1 \times 10^{21}$ cm^{-2} and distance $d = 2.3$ kpc. We note that the moderate spin-down luminosity of $\dot{E} \approx 3.3 \times 10^{34}$ ergs s^{-1} [4] does not favor a magnetospheric origin of the observed X-rays considering that other MSPs with comparable values of $\dot{E}$ exhibit much softer, thermal spectra. The spectrum of PSR J1740−5340 likely contains a soft thermal component (with $T_{\rm eff} \sim 10^6$ K and L_X of order a few $\times 10^{30}$ ergs s^{-1})

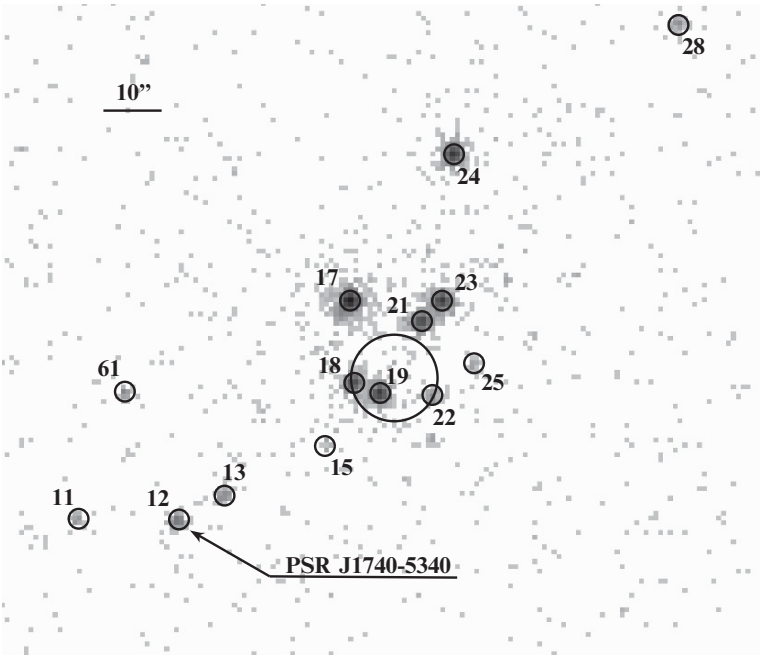

Fig. 8.3 Chandra ACIS-S image of NGC 6397 (from [28]). The X-ray source 12 was discovered by Grindlay et al. [32] to be coincident with the radio and optical position of PSR J1740−5340. Source 18 exhibits very similar X-ray and optical properties and may also be a re-exchanged MSP system [28]. The *large circle* shows the cluster core radius

originating from the hot magnetic polar caps of the MSP, as most 47 Tuc MSPs. However, the column density towards the cluster (1×10^{21} cm^{-2}) and the short exposure time of the existing observations make the detection of such a soft emission component difficult.

In the temporal domain, the X-ray flux from the shock is expected to undergo modulations at the binary period [1]. Such variability may be the result of a total or partial eclipse of the shock emission by the secondary star, depending on the binary inclination and the proximity of the shock to the companion and its thickness in the direction perpendicular to the orbital plane. Furthermore, around superior conjunction there should be enhanced emission due to Doppler boosting in the direction of the flow downstream from the shock as predicted by [1]. Unfortunately, the limited exposure time of the existing ACIS-I and ACIS-S observations coupled with the long binary period, resulting in incomplete phase coverage, does not permit a detailed investigation of the temporal behavior of the X-ray emission. This will be possible with the analysis of the recently acquired deep (250 ks) *Chandra* observation of NGC 6397.

It is interesting to note that X-ray source #18 in NGC 6397 displays remarkably similar X-ray and optical properties as PSR J1740−5340, making it a strong candidate “re-exchanged” binary MSP [28]. As this source has not been detected as

a radio pulsar it is likely that the radio pulsations are perpetually obscured by the intra- and circum-binary gas driven off the secondary star by the relativistic pulsar wind. The recent deep *Chandra* ACIS-S observation of NGC 6397, together with recent deep HST studies, will allow the properties of source #18 to be compared in detail with those of the known MSP, J1740, as well as a definitive search for still more MSP candidates in this closest core collapse globular cluster.

8.3.3 M28 and Terzan 5

The unprecedented angular resolution of *Chandra* has enabled the first measurement of the unconfused spectrum of PSR B1821−24 (M28A) (cf. [7] and Chap. 6). The phase-averaged X-ray spectrum of M28A is best described by a power-law with photon index $\Gamma \simeq 1.2$ and $L_X = 1.3 \times 10^{33}$ ergs s^{-1} (phase integrated for 0.5–8 keV), 2–3 orders of magnitude greater than most MSPs.[1] Unexpectedly, Becker et al. [7] found intriguing but marginal (at 98% confidence) evidence of a broad emission feature centered at 3.3 keV, which can be most plausibly interpreted as cyclotron emission from the magnetosphere above the pulsar's polar cap if the magnetic field strongly deviates from a centered dipole. Confirmation of this feature would provide the first direct measurement of the magnetic field of a rotation-powered pulsar (MSP or otherwise). This is of great importance given that the standard method for estimating the magnetic field of pulsars using P and $\dot{P}$ relies on assuming a radius (R_{NS}) and moment of inertia (I_{NS}) of the NS, $B_{\rm surf} \propto R_{NS}^{-3}(I_{NS}P\dot{P})^{1/2}$, as well as the exact field geometry (a centered dipole). In fact, the field strength inferred from the electron cyclotron line ($B \simeq 3\times10^{11}$ G) implies that the field is either multipolar or substantially off-center. For comparison, the conventional (centered) dipole spin-down formula gives $B_{\rm surf} \simeq 4.5 \times 10^9$ G (assuming $M_{NS} = 1.4\,{\rm M}_\odot$, $R_{NS} = 10$ km, and $I_{NS} = 10^{45}$ g cm^2), already the highest for any MSP.

For the off-center dipole case a 3×10^{11} G field can be produced if the magnetic dipole moment is shifted along the axial direction so that it is only ∼1.9 km beneath one of the polar caps. An off-centered dipole field is directly suggested from X-ray data for another MSP: J0437−4715; see below. Thus invoking this geometry for M28A now has some new support. The putative cyclotron line from M28A can be formed by an optically thin, hot corona ($kT \sim 10$ keV) above the MSP polar caps. The required particle densities needed to produce the observed line luminosity are in full agreement with those expected in the MSP magnetosphere above the polar cap (see Sect. 2.2.1 of [7] for details). Thus, the cyclotron interpretation of the line is quite plausible and its confirmation with a deeper observation would provide unique insight into the local magnetic field near the surface of a pulsar. Such an observation is approved for Chandra cycle 9 and will be reported by us elsewhere.

Rutledge et al. [47] have found that in addition to the two sharp pulses from M28A there is an unpulsed component (15% of total flux), possibly due to thermal

[1] Only two of the ∼35 other X-ray detected MSPs (B1937+21 and J0218+4232, both field MSPs) have comparable L_X of a few $\times10^{32}$ ergs s^{-1} and purely PL spectra.

polar cap emission. Further observations of B1821−24 will also permit a search for such a component in its spectrum.

In recent years, intensive radio timing search campaigns have uncovered a host of MSPs in globular clusters, including 33 in Terzan 5 [44] and 10 new MSPs in M28 [12]. Of these, two MSPs in Ter 5 (PSRs J1748−2446P and J1748−2446ad) and one in M28 (PSR J1821−24 H) appear to have main-sequence-like companions based on their binary parameters and the presence of unusual radio eclipses. At X-ray energies, these objects are found to be positionally coincident with relatively hard X-ray sources with $L_X \sim 10^{31}\,\mathrm{ergs\,s^{-1}}$ (cf. [6] and Chap. 6), very similar to 47 Tuc W and J1740. Therefore, it is likely that these systems have also formed as a result of past exchange encounters and that their winds are interacting with material from the secondary. While these may be "black widow" type systems (i.e. very compact binaries with their MSPs ablating their very low mass brown dwarf companions as in PSR B1957+20) their presence in globular clusters suggests they are longer period systems with "re-exchanged" main sequence companions. The discovery of main sequence (or slightly evolved) companions would suggest that "re-exchanged" MSP binaries are not uncommon in the dense cores of globular clusters, as originally suspected from 47 Tuc [30] data. A recently approved Cycle 9 deep ACIS-S observation, accompanied by multiband *HST* WFPC2 observations, of M28 will shed more light on the properties of PSR J1821−2452H and its peculiar companion. In the case of Terzan 5, the high absorption column density along the line of sight towards this cluster ($N_{\mathrm{H}} \sim 10^{22}\,\mathrm{cm^{-2}}$), renders most of its known 33 MSPs very difficult to detect in X-rays as the predominantly soft emission from these thermal sources is heavily absorbed. Indeed, in the existing *Chandra* ACIS-S observations of this cluster [35], X-ray counterparts are found only for the two candidate "exchanged" MSPs, PSRs J1748−2446P and J1748−2446ad, which are expected to have hard, non-thermal spectra from their intra-binary shocks.

8.3.4 Other Clusters

Observation of globular clusters with *Chandra* have identified X-ray counterparts to other MSPs, including PSR J1911−6000C in NGC 6752 [22], B1620−26 in M4 [3], and J1953+1846A in M71, a radio eclipsing binary [24]. However, due to the limited photon statistics it is difficult to determine the spectral properties of these MSPs. As more clusters are surveyed by *Chandra*, the number of X-ray detected MSPs is expected to increase, and the relative populations of possibly re-recycled MSPs can be further recognized by the partial hard X-ray eclipses that are expected over a range of binary inclinations since the intra-binary shock is close to the relatively large binary companion. Note that such systems will *not* be expected to be pulsed (except for their underlying soft, thermal component) since their dominant hard emission arises in the shock. Detection of pulsations from hard MSPs is expected only from the very most luminous (and highest $\dot{E}$ spin-down luminosities), for which the dominant emission is magnetospheric.

8.4 MSPs as Beacons for Constraining the Neutron Star Equation of State

Pavlov and Zavlin [43,54], and Bogdanov et al. [16] have developed models of thermal X-ray emission from hot polar caps on the surface of a rotating compact star with a weakly magnetized light-element atmosphere (see Fig. 8.4), applicable to MSPs. This model produces lightcurves characterized by broad modulations with relatively low pulsed fractions (<50%), consistent with the observed pulse profiles of nearby field MSPs [53] and those in 47 Tuc [17]. In addition to the obvious dependence on the viewing angle and magnetic inclination, the thermal pulse profile is very sensitive to the mass-to-radius (M/R) ratio of the NS, due to the different gravitational bending and thus temporal view of the polar cap that differing M/R values impose. Therefore, modeling the X-ray pulse profiles of MSPs may, in principle, allow strict constraints on the neutron star (NS) equation of state (EOS), provided sufficiently sensitive spectral-temporal soft X-ray observations can be made which can distinguish the correct spectral model (simple black body vs. H-atmosphere on the NS polar cap) as well as constrain the polar cap emission geometry or regions. This has only now become possible with new analysis tools and *Chandra*, and *XMM-Newton* data.

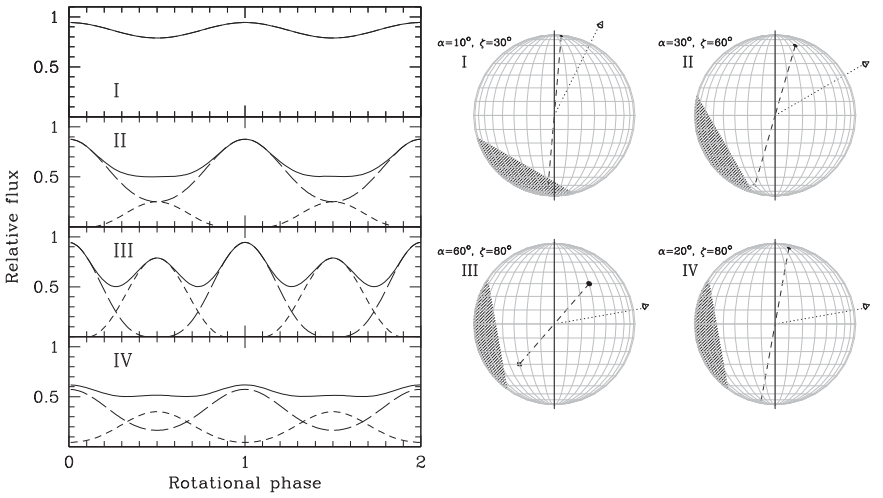

Fig. 8.4 (*Left*) Representative synthetic lightcurves for a rotating $M = 1.4\,M_{\odot}$, $R = 10\,\mathrm{km}$ NS with two antipodal hot spots for the four lightcurve classes (I–IV, *from top to bottom*, respectively), defined by Beloborodov (2002). The *dashed lines* show the individual flux contribution from the two hot spots while the *solid line* shows the total observed flux. All fluxes are normalized to the value corresponding to $\alpha = \psi = 0$. Two rotational cycles are shown for clarity. (*Right*) Orthographic map projection of the MSP surface for each of the four pulse profile classes. The *dashed line* shows the magnetic axis while the *dotted line* shows the line of sight to the observer. The hatched region corresponds to the portion of the star not visible to the observer [14]

8.4.1 PSR J0437−4715

An application to *ROSAT*, *Chandra*, and *XMM-Newton* X-ray observations of the nearest known rotation-powered millisecond pulsar (MSP) PSR J0437−4715 revealed that the thermal emission from this pulsar is fully consistent with such a model (Fig. 8.5), enabling constraints on important properties of the underlying neutron star [16]. This modeling confirmed that the observed thermal X-ray pulsations from J0437−4715 are incompatible with simple blackbody emission and require the presence of an optically thick, light element atmosphere on the neutron star surface, as suggested (but not required) by previous studies using *ROSAT* observations [43, 54]. The morphology of the X-ray pulse profile was found to be consistent with a global dipole configuration of the pulsar magnetic field but suggest an off-center magnetic axis, with a displacement of $\gtrsim$1 km from the stellar

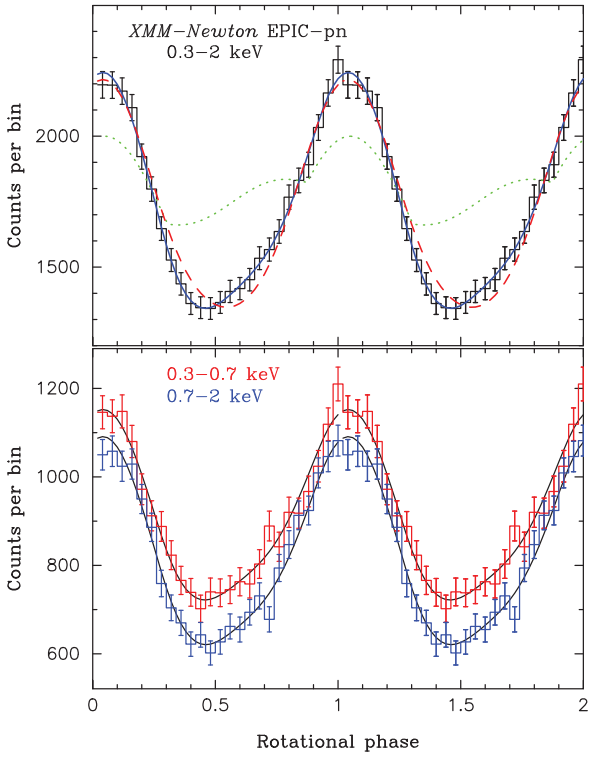

Fig. 8.5 (*Top*) *XMM-Newton* EPIC-pn pulse profiles of PSR J0437−4715 (0.3–2 keV). The *solid blue line* shows the best fit hydrogen atmosphere polar cap model for an off-center magnetic dipole field while the *dashed line* is for a best fit centered dipole. The *dotted green line* shows the blackbody polar cap model that best fits the spectrum of J0437−4715, showing that simple blackbody spectra do *not* fit MSP thermal spectra. (*Bottom*) Best fits in soft (*red*) vs. hard (*blue*) bands for an off-centered dipole. The choice of phase 0 is arbitrary [16]

center. For an assumed mass of $1.4\,M_{\odot}$, the model restricts the allowed stellar radii to $R = 6.8$–13.8 km (90% confidence) and $R > 6.7$ km (99.9% confidence), which is consistent with standard NS equations of state and rules out ultra-compact stars [41].

8.4.2 PSRs J0030+0451 and J2124−3358

Useful information regarding the basic properties of the NS can be extracted even from X-ray data with fairly limited photon statistics, such as the archival *XMM-Newton* spectroscopic and timing observations of the nearby isolated PSRs J0030+0451 [5, 11] and J2124−3358 [52] (hereafter J0030 and J2124, respectively). The X-ray emission from these pulsars is found to be consistent with the presence of a H atmosphere and a dipolar magnetic field configuration (Fig. 8.6), in agreement with previous findings for PSR J0437−4715. For both MSPs J0030 and J2124, the favorable viewing geometry allows interesting limits on the allowed

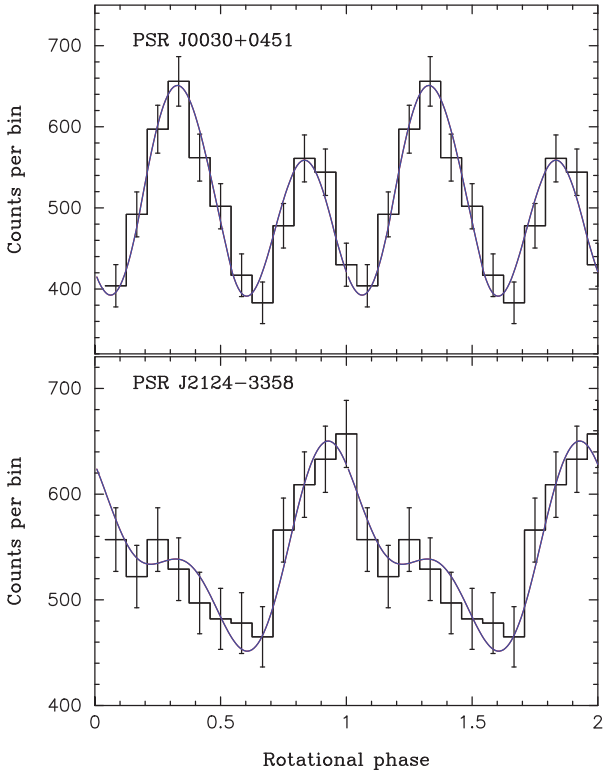

Fig. 8.6 XMM-Newton EPIC-pn pulse profiles of PSRs J0030+0451 and J2124−3358 in the 0.3–2 keV band. The *solid lines* show the best fit hydrogen atmosphere polar cap emission model [14]

mass-to-radius ratios of the NS. In particular, assuming $1.4\,M_\odot$, the radius is constrained to be $R > 9.4$ km and $R > 7.8$ km (68% confidence) for PSRs J0030+0451 and J2124−3358, respectively [14]. In addition, the available data permits strong constraints on the magnetic field evolution model proposed by [46]. In particular, the observational constraints on the pulsar obliquities imply that the magnetic field of an MSP does not have a tendency to align itself with the spin axis nor migrate towards the spin pole during the low-mass X-ray binary phase.

8.5 Future Prospects

With the currently active X-ray observatories *Chandra* and *XMM-Newton*, only a few of the nearest and brightest MSPs can be studied effectively for their detailed X-ray properties using deep exposures. Naturally, further improvement in telescope sensitivity will permit much more detailed phase-resolved spectroscopic analyses of these objects and a study of a substantially larger sample of sources. The primary motivation of these observations would be detailed modeling of the pulsed thermal radiation, which appears to be a promising means for obtaining tight constraints on M/R. We [14] have shown that future X-ray facilities such as IXO could, in principle, provide constraints on M/R to $\sim$5%. Ultimately a very high throughput and angular resolution mission such as *Gen-X* could provide constraints to $\lesssim$2%, and simultaneously for a large population of MSPs as in the core of 47 Tuc.

8.5.1 Searches for Radio-Quiet MSPs

The effect of light bending combined with the (nearly) antipodal configuration of the two MSP hot spots ensure that the thermal radiation is emitted into all 4π steradians of the sky and is thus seen by all distant observers for any combination of α and ζ. On the other hand, at radio frequencies a pulsar is not observable if $|\alpha - \zeta|$ exceeds the opening half-angle ρ of the radio emission cone. This implies that, in principle, it may be possible to detect and identify such radio quiet MSPs in X-rays using pulsation searches. With the current generation of X-ray observatories (*Chandra* and *XMM-Newton*) this endeavor is difficult due to the intrinsic faintness of MSPs (see e.g. [17]) and the low X-ray pulsed fractions of these sources ($\leq$50%). On the other hand, for IXO, the great increase in sensitivity makes such a survey of field MSPs quite feasible. In the more distant future, *Gen-X* would permit a complete census of MSPs in many globular clusters of differing dynamical state (e.g. 47 Tuc vs. the archetype core collapse cluster M15), where both high sensitivity and angular resolution significantly greater that of *Chandra* are required.

Figure 8.7 shows the X-ray pulsed fraction of a 10 km, $1.4\,M_\odot$ MSP as a function of α and ζ [14]. Also shown are lines defining the region for which a pulsar with a

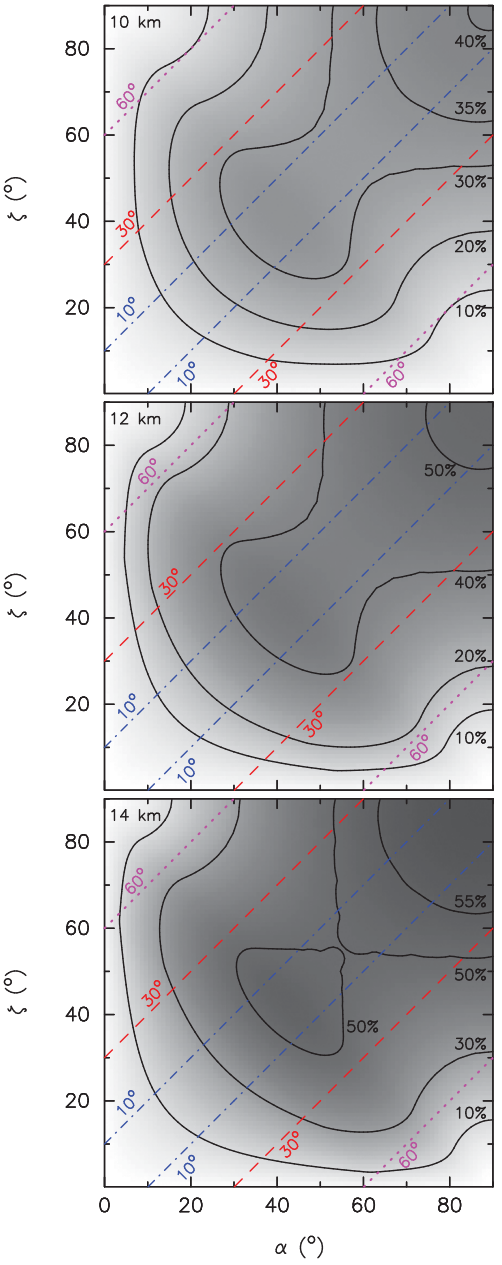

Fig. 8.7 Contours of constant pulsed fraction (*solid lines*) for thermal polar cap X-ray H atmosphere emission in the 0.3–2 keV band as a function of the pulsar obliquity (α) and viewing angle (ζ) for a 1.4 $M_\odot$ MSP with radii 10, 12, and 14 km (*from top to bottom*, respectively). The diagonal *dot-dashed*, *dashed* and *dotted lines* show 10°, 30°, and 60° radio emission cones, respectively. All MSPs found between each pair of lines are radio-loud [14]

given radio emission cone width is observable at radio frequencies. Note that the true opening angle of the radio emission cone for a given MSP is not known and difficult to measure reliably but could be as high as $\sim 60^\circ$ [38]. For a uniform distribution of pulsar obliquities (α) and viewing angles (ζ), for $\rho <\simeq 30^\circ$ a substantial portion ($\sim$45%) of the MSP population is invisible to us in the radio. On the other hand, if we consider an X-ray timing survey with a limiting pulsed fraction sensitivity of $\sim$10%, only $\sim$5–15% (depending on M/R) of the MSPs will go undetected as pulsed sources though they will still be detected as X-ray sources. The Galactic population of MSPs may in fact be preferentially clustered in a certain range of α due to the poorly understood effects of the accretion and magnetic field reduction processes during the LMXB phase on the NS. A deep X-ray timing survey of nearby ($\lesssim$1–2 kpc) MSPs may, in principle, reveal whether this is indeed the case.

References

1. Arons, J., Tavani, M., 1993, ApJ, 403, 249
2. Backer, D.C., Kulkarni, S.R., Heiles, C., et al., 1982, Nature, 300, 615B
3. Bassa, C.G., Pooley, D., Homer, L., et al., 2004, ApJ, 609, 755
4. Bassa, C.G., Stappers, B.W., 2004, A&A, 425, 1143
5. Becker, W., Achenbach, B., 2002, in Neutron Stars, Pulsars, and Supernova Remnants, Eds. W. Becker, H. Lech, J. Trümper, MPE-Report 278, p. 64
6. Becker, W., Hui, C.Y., 2007, submitted to A&A, astro-ph/07050119
7. Becker, W., Swartz, D.A., Pavlov, G.G., et al., 2003, ApJ, 594, 798
8. Becker, W., Trümper, J., 1993, Nature, 365, 528
9. Becker, W., Trümper, J., 1997, A&A, 326, 682
10. Becker, W., Trümper, J., 1999, A&A, 341, 803
11. Becker, W., Trümper, J., Lommen, A.N., et al., 2000, ApJ, 545, 1015
12. Bégin, S., Thesis submitted to the Faculty of Physics, University of British Columbia, 2006
13. Bogdanov, S., Grindlay, J.E., Heinke, C.O., et al., 2006, ApJ, 646, 1104
14. Bogdanov, S., Grindlay, J.E., Rybicki, G.B., 2008, ApJ, in press
15. Bogdanov, S., Grindlay, J.E., van den Berg, M., 2005, ApJ, 630, 1029
16. Bogdanov, S., Rybicki, G., Grindlay, J.E., 2007, ApJ, 670, 668
17. Cameron, P.B., Rutledge, R.E., Camilo, F., et al., 2007, ApJ, 660, 587
18. Camilo, F., Lorimer, D.R., Freire, P., et al., 2000, ApJ, 535, 975
19. Campana, S., D'Avanzo. P., Casares, J., et al., 2004, ApJ, 614, L49
20. Cheng, K.S., Taam, R.E., 2003, ApJ, 598, 1207
21. D'Amico, N., Lyne, A.G., Manchester, R.N., et al., 2001, ApJ, 548, L171
22. D'Amico, N., Possenti, A., Fici, L., et al., 2002, ApJ, 570, L89
23. Danner, R., Kulkarni, S.R., Thorsett, S.E., 1994, ApJ, 436, L153
24. Elsner, R.F., Heinke, C.O., Lugger, P.M., et al., 2008, in press
25. Ferraro, F.R., Sabbi, E., Gratton, R., et al., 2003, ApJ, 584, 2003
26. Freire, P.C., Camilo, F., Lorimer, D.R., et al., 2001, MNRAS, 326, 901
27. Fruchter, A.S., Bookbinder, J., Garcia, M.R., et al., 1992, Nature, 359, 303
28. Grindlay, J.E., 2006, Adv. Space Res., 38, 2923–2929
29. Grindlay, J.E., 2006, Science, 311, 1876
30. Grindlay, J.E., Camilo, F., Heinke, C.O., et al., 2002, ApJ, 581, 470
31. Grindlay, J.E., Heinke, C., Edmonds, P.D., et al., 2001, Science, 292, 2290
32. Grindlay, J.E., Heinke, C.O., Edmonds, P.D., et al., 2001, ApJ, 563, L53
33. Harding, A.K., Muslimov, A.G. 2002, ApJ, 568, 862

34. Heinke, C.O., Grindlay, J.E., Edmonds, P.D., et al., 2005, ApJ, 625, 796
35. Heinke, C.O., Wijnands, R., Cohn, H.N., et al., 2006, 651, 1098
36. Hessels, J.W.T., Ransom, S.M., Stairs, I.H., et al, 2006, Science, 311, pp. 1901
37. Huang, H.H., Becker, W., 2007, A&A, 463, 5L
38. Kramer, A., Xilouris, K.M., Lorimer, D.R., et al., 1998, ApJ, 501, 270
39. Kulkarni, S.R., Phinney, E.S., Evans, C.R., et al., 1992, Nature, 359, 300
40. Manchester, R.N., Hobbs, G.B., Teoh, A., et al., 2005, AJ, 129, 1993
41. Nemiroff, R.J., Becker, P.A., Wood, K.S., 1993, ApJ, 406, 590
42. Nicastro, L., Cusumano, G., Löhmer, O., et al., 2004, A&A, 413, 1065
43. Pavlov, G.G, Zavlin, V.E., 1997, ApJ, 490, L91
44. Ransom, S.M., Hessels, J.W.T., Stairs, I.H., et al., 2005, Science, 307, 892
45. Rots, A.H., Jahoda, K., Macomb, D.J., et al., 1998, ApJ, 501, 749
46. Ruderman, M., 1991, ApJ, 366, 261
47. Rutledge, R.E., Fox, D.W., Kulkarni, S.R., et al., 2004, ApJ, 613, 522
48. Sabbi, E., Gratton, R., Ferraro, F.R., et al., 2003, ApJ, 589, L41
49. Saito, Y., Kawai, N., Kamae, T., et al., 1997, ApJ, 477, L37
50. Takahashi, M., Shibata, S., Gunji, S., et al., 1999, Astron. Nachr., 320, 340
51. Takahashi, M., Shibata, S., Torii, K., et al., 2001, ApJ, 554, 316
52. Zavlin, V.E., 2006, ApJ, 638, 951
53. Zavlin, V.E., 2007, Ap&SS, 308, 297
54. Zavlin, V.E., Pavlov, G.G., 1998, A&A, 329, 583

Chapter 9
Theory of Radiative Transfer in Neutron Star Atmospheres and Its Applications

Vyacheslav E. Zavlin

9.1 Introduction

Before the first neutron star was discovered in 1967 as a radio pulsar[1] by Jocelyn Bell [22] it had been predicted that neutron stars can be powerful sources of thermal X-ray emission, having surface temperatures of about one million Kelvin [11, 78]. This prediction and the discovery of the first pulsar became one of many motivations for further developing X-ray astronomy at the end of the 1950s. Observational study of thermal radiation from neutron stars began in 1978 with the launch of the Einstein observatory which detected X-ray emission in the 0.2–4 keV range from a number of neutron stars and neutron star candidates. The ROSAT mission which was sensitive in the 0.1–2.4 keV range marks the beginning of the "decade of space science", which in the 1990s provided many important results on observing X-ray emission from neutron stars. By extending the energy range up to 10 keV ASCA and BeppoSAX added important information on the pulsar emission in the harder band pass whereas EUVE and HST allowed to study neutron stars in the very soft 0.07–0.2 keV and optical/UV bands. More details on results from observations of neutron stars can be found in the Chaps. 6–8. New excellent observational data on neutron stars collected with two currently operating powerful X-ray observatories, *Chandra* and *XMM*-Newton (both launched in 1999), provide a breakthrough in studying emission properties of these enigmatic objects.

V.E. Zavlin
Space Science Laboratory, NASA Marshall Space Flight Center, SD59, Huntsville, AL 35805, USA
e-mail: vyacheslav.zavlin@msfc.nasa.gov

[1] PSR B1919+21

W. Becker (ed.), *Neutron Stars and Pulsars,* Astrophysics and Space Science Library 357,

9.2 Properties of X-ray Emission from Isolated Neutron Stars

Generally, X-ray radiation from an isolated[2] neutron star can consist of two distinguished components: the non-thermal emission due to the pulsar activity and the radiation originating from the stellar surface. The non-thermal component is usually described by a power-law spectral model and attributed to radiation produced by synchrotron and/or inverse Compton processes in the pulsar magnetosphere, whereas the thermal emission can originate from either the entire surface of a cooling neutron star or small hot spots around the magnetic poles (polar caps) on the star surface, or both. The sketch shown in Fig. 9.1 represents an evolutionary picture of these two radiative components in the X-ray spectrum of neutron stars. In the majority of very young pulsars ($\tau \sim 1$ kyr) the non-thermal component dominates (see the left panel in Fig. 9.1), making it virtually impossible to accurately measure the thermal flux; only upper limits on the surface temperature $T_{\rm surf}$ could be derived, as it was done for the famous Crab pulsar [77] and PSR J0205+6449 in the SNR 3C 58 [75]. As a pulsar becomes older, its non-thermal luminosity decreases (roughly) proportional to its spin-down power $\dot{E} = 4\pi^2 I P^{-3} \dot{P}$ (I, P, and $\dot{P}$ are the neutron star moment of inertia, spin period and its derivative, respectively). The latter is thought to drop with the star age τ as $\dot{E} \sim \tau^{-m}$, where $m \simeq 2$–4 (depending on the pulsar magneto-dipole braking index). On the other hand, the thermal luminosity of an aging and cooling neutron star decreases at a lower rate than the non-thermal one does for ages $\tau \sim 10$–100 kyr, up to the end of the neutrino-cooling era ($\tau \sim 1$ Myr). Thus, the thermal radiation from the *entire* stellar surface can dominate at soft X-ray energies for middle-aged pulsars ($\tau \sim 100$ kyr) and some younger pulsars ($\tau \sim 10$ kyr). This situation is shown in the middle panel of Fig. 9.1. For neutron stars older than about 1 Myr, the surface temperature is too low, $T_{\rm surf} \lesssim 0.1$ MK, to detect the thermal radiation from the whole surface in X-rays; only magnetospheric and/or thermal radiation from hot polar caps can be detected.

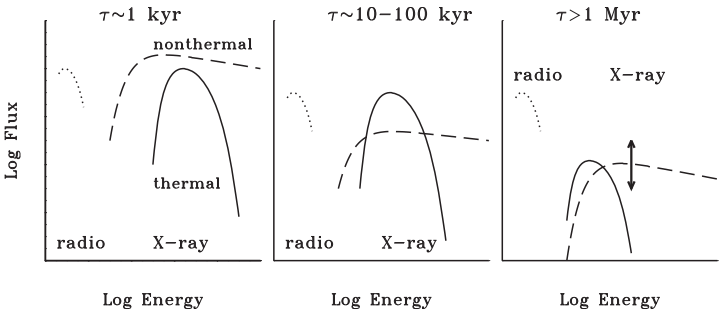

Fig. 9.1 Sketch illustrating what radiative component, non-thermal (*dashed*) or thermal (*solid curves*), is expected to dominate in the X-ray flux of neutron stars of different ages τ. The *double-ended arrow* in the *right panel* indicates two possible situations for old and millisecond pulsars

[2] The term "isolated" is omitted hereafter in the text.

As predicted by virtually all pulsar models, these polar caps can be heated up to X-ray temperatures ($\sim$1 MK) by relativistic particles generated in pulsar acceleration zones. A conventional assumption about the polar cap radius is that it is close to the radius within which open magnetic field lines originate from the pulsar surface, $R^*_{\rm pc} = [2\pi R^3/cP]^{1/2} \simeq 0.5\,[P/0.1\,{\rm s}]^{-1/2}\,{\rm km}$ (for a neutron star radius $R = 10\,{\rm km}$). As the spin-down power $\dot{E}$ is the energy source for both non-thermal and thermal polar-cap components, it is hard to predict which of them would prevail in X-ray flux of an old neutron star (as indicated in the right panel of Fig. 9.1). However, it cannot be ruled out, and is proven by observations of several millisecond pulsars, that the thermal one may be dominant. Remarkably, of about 80 neutron stars currently detected in X-rays, more than a half reveal thermal emission of different origin. To interpret these observations, one needs reliable models of neutron star thermal radiation. This paper reviews theoretical and observational aspects of studying thermal radiation from neutron stars.

9.3 Modeling Thermal Radiation from Neutron Stars

There are a few questions to be answered before immersing into details on the theory of neutron star thermal emission.

9.3.1 Why Is the Thermal Radiation Important?

The main question is why studying the thermal emission is needed and interesting. Shortly, comparing observed thermal spectrum of a neutron star with theoretical models can allow one to infer the surface effective temperature $T^\infty_{\rm eff}$ and total bolometric flux $F^\infty_{\rm bol}$. These are redshifted quantities, i.e., as measured by a distant observer, which are connected to the actual (un-redshifted) parameters, $T_{\rm eff} = g_{\rm r}^{-1} T^\infty_{\rm eff}$ and $F_{\rm bol} = g_{\rm r}^{-2} F^\infty_{\rm bol}$ ($g_{\rm r} = [1 - R_{\rm S}/R]^{1/2}$ is the gravitational redshift, $R_{\rm S} = 2GM/c^2 = 2.952[M/M_\odot]\,{\rm km}$ is the Schwarzschild radius, $M_\odot$ is the solar mass). If the distance to the neutron star, D, is known, then the measured temperature and flux yield the apparent (redshifted) radius of the star,

$$R^\infty = D\left[\frac{F^\infty_{\rm bol}}{\sigma_{\rm SB}(T^\infty_{\rm eff})^4}\right]^{1/2}, \tag{9.1}$$

where $\sigma_{\rm SB}$ is the Stefan–Boltzmann constant. This in turn links the actual neutron star radius and mass to each other via the relation $R^\infty = g_{\rm r}^{-1} R$, or

$$M = \frac{c^2 R}{2G}\left[1 - \left(\frac{R}{R^\infty}\right)^2\right]. \tag{9.2}$$

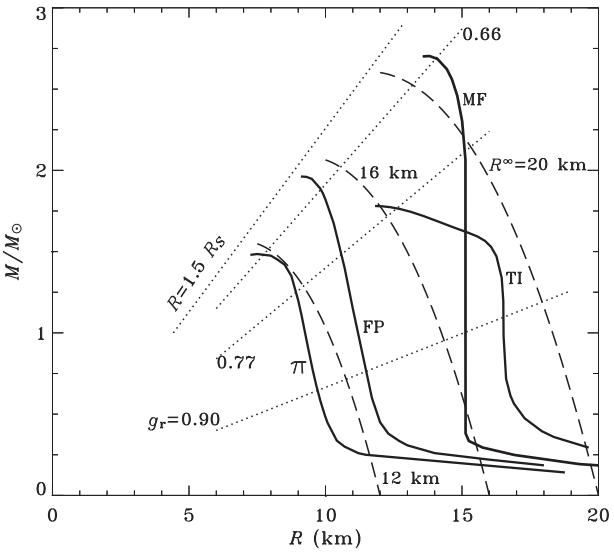

Fig. 9.2 Neutron star mass-radius diagram with lines of constant values of the gravitational parameter g_r (*dots*), redshifted radius $R^\infty = g_r^{-1}R$ (*dashes*) and four $M(R)$ relations (*solid curves*) corresponding to different equations of state of superdense matter ([72], Chap. 10). The values of M and R for realistic equations of state lie below the *straight line* $R = 1.5R_S$ (or $g_r = 1/\sqrt{3}$)

As seen in Fig. 9.2, the latter puts constraints on equation of state of the superdense neutron star matter (Chap. 10). If the gravitational redshift g_r is measured for a few neutron stars, for example, via detecting and identifying spectral features in the observed X-ray flux, then it would yield a unique solution for the equation of state of the matter in the neutron star interior.

Next, investigating thermal emission from neutron stars of different ages can trace their thermal evolution, that in turn sheds light on internal composition and nucleon superfluidity of the superdense matter ([86], Chaps. 11 and 12). In addition, inferring surface properties of a neutron star (temperature, magnetic field, chemical composition) tells about its formation and interaction with environment.

9.3.2 Properties of Neutron Star Surfaces

Like in usual stars, thermal radiation of neutron stars is formed in the superficial (surface) layers. Hence, the next question to be asked in this study is about the state of the neutron star surface. In principle, it can be in the gaseous state or in a condensed state (liquid or solid), depending on the surface temperature, magnetic field B and chemical composition. For instance, according to the estimates given in [35], hydrogen is condensed in surface layers if $T_{\rm surf} \lesssim 0.1$ MK at $B = 1 \times 10^{13}$ G and $T_{\rm surf} \lesssim 1$ MK at $B = 5 \times 10^{14}$ G. At higher temperatures and/or lower magnetic

fields, hydrogen does not condensate and forms an atmosphere. As most of known neutron stars are believed to possess surface magnetic fields of $B \lesssim 10^{12}$, they are expected to have an atmosphere. Therefore, properties of neutron star atmospheres are mainly discussed below.

The chemical composition affects not only the state of the surface, but it also determines the properties of emitted radiation. What could the composition of the stellar surface be? In case of neutron stars, one can expect that the emitting layers are comprised of just one, lightest available, chemical element because heavier elements sink into deeper layers due to the immense neutron star gravitation [1]. For instance, even a small amount of hydrogen, with a surface density of $\sim 1\,\mathrm{g\,cm^{-2}}$, is sufficient for the radiation to be indistinguishable from that emitted from a purely hydrogen atmosphere. Such an amount of hydrogen, $\sim 10^{-20} M_\odot$, can be delivered onto the neutron star surface by, e.g., a weak accretion from the interstellar medium during the neutron star life and/or fallback of a fraction of the envelope ejected during the supernova explosion. If no hydrogen is present at the surface (e.g., because of diffuse nuclear burning; [10]), a heavier chemical element is responsible for the radiative properties of the neutron star atmosphere. However, a mixture of elements can be observed in the emitting layers if a neutron star is experiencing accretion with such a rate that the accreting matter is supplied faster than the gravitational separation occurs.

What else makes neutron star atmospheres very special? It is of course the enormous gravity at the neutron star surface, with typical gravitational acceleration $g \sim 10^{14}$–$10^{15}\,\mathrm{cm\,s^{-2}}$, and very strong, even huge, surface magnetic fields. The gravity makes the atmospheres very thin, with a typical thickness $H \sim kT_{\rm surf}/[m_{\rm p} g] \sim 0.1$–$10\,\mathrm{cm}$ (k is the Boltzmann constant, $m_{\rm p}$ is the mass of a proton), and very dense, $\rho \sim 10^{-2}$–$10^{2}\,\mathrm{g\,cm^{-3}}$. Such a density causes strong non-ideality effects (pressure ionization, smoothed spectral features) which must be taken into account [53]. In addition, the strong gravitational field bends the photon trajectories near the neutron star surface [59], as illustrated in Fig. 9.3. This effect depends on the gravitational parameter $g_{\rm r}$, and it can even make the whole surface visible if the neutron star is massive enough, $1.92\,[10\,\mathrm{km}/R] < [M/M_\odot] < 2.25\,[10\,\mathrm{km}/R]$. In particular, the gravitational bending strongly affects the observed pulsations of thermal emission [101]. As shown in [8, 54, 92, 94], analyzing pulsed thermal radiation can put constraints on the mass-to-radius ratio, M/R, and the neutron star geometry (orientation of spin and magnetic axes with respect to each other and direction to a distant observer – see Fig. 9.3).

Huge magnetic fields, up to $B \sim 10^{14}$–$10^{15}\,\mathrm{G}$, expected in the surface layers of neutron stars change the properties of the atmospheric matter and the emergent radiation very drastically. Strongly magnetized atmospheres are essentially anisotropic, with radiative opacities depending on the magnetic field and the direction and polarization of radiation. Moreover, since the ratio of the cyclotron energy, $E_{\rm ce} = \hbar e B/m_{\rm e} c$, to the Coulomb energy is very large (e.g., $\beta \equiv E_{\rm ce}/[1\,\mathrm{Ry}] = 850\,[B/10^{12}\,\mathrm{G}]$ for a hydrogen atom), the structure of atoms is strongly distorted by the magnetic field. For instance, the binding (ionization) energies of atoms are increased by a factor of $\sim \ln^2 \beta$ (e.g., the ionization potential of a hydrogen atom

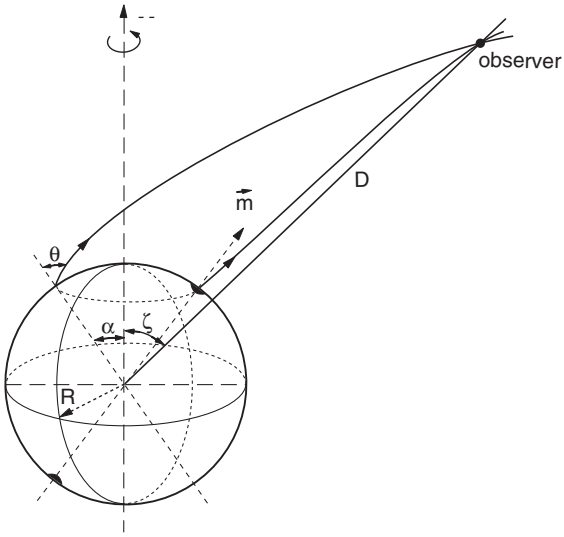

Fig. 9.3 Sketch illustrating bending of photon trajectories near the surface of a neutron star. The star's spin and magnetic (**m**) axes are indicated. *Black spots* around the magnetic poles show possible heated polar caps on the stellar surface

is about 0.3 keV at $B = 10^{13}$ G). This in turn significantly modifies ionization equilibrium of the neutron star atmospheric plasma. Another important effect is that the heat conductivity of the neutron star crust is anisotropic, being higher along the magnetic field. This results in a nonuniform surface temperature distribution [19], which can lead to pulsations of the thermal radiation due to neutron star rotation.

Depending on the magnetic field strength, models of neutron star atmospheres are differentiated in two groups, "non-magnetic" and "strongly magnetized". The non-magnetic models are constructed for $B \lesssim 10^9$ G, when the electron cyclotron energy, $E_{\rm ce} \lesssim 0.01$ keV, is lower than the binding energy of atoms and thermal energy of particles, $E \sim kT_{\rm surf}$. As a result, the effect of the magnetic field on the radiative opacities and emitted spectra is negligible at X-ray energies, $E \gtrsim 0.1$ keV. These models are constructed assuming $B = 0$ G and can be applicable to, for example, millisecond pulsars and neutron star transients in quiescence, whereas the magnetized models are intended mostly for radio pulsars with $B \sim 10^{10}$–10^{14} G. More details on the neutron star atmosphere models can be found in [93].

9.3.3 Non-Magnetic Atmosphere Models

Modeling non-magnetic neutron star atmospheres was started in the pioneering work [64]. Since then, models for various surface chemical compositions have been developed in [14, 21, 56, 60, 62, 83, 98, 99].

The general approach of the atmosphere modeling is as follows. Very small thickness of a neutron star atmosphere, $H \ll R \approx 10\,\mathrm{km}$, allows one to use the plane-parallel (one-dimensional) approximation. In addition, because of rather high densities of the surface layers, the atmospheres are expected to be in the local thermodynamic equilibrium. The atmosphere modeling involves solving three main equations. The first one is the radiative transfer equation for the specific spectral intensity I_ν (e.g., [39]):

$$\mu \frac{\mathrm{d}}{\mathrm{d}y} I_\nu = k_\nu (I_\nu - S_\nu)\,, \tag{9.3}$$

where ν is photon frequency, μ is the cosine of the angle θ between the normal to the surface and the wave-vector of outgoing radiation, y is the column density ($\mathrm{d}y = \rho\,\mathrm{d}z$, with z being the geometrical depth), $k_\nu = \alpha_\nu + \sigma_\nu$ is the total radiative opacity which includes the absorption, α_ν, and scattering, σ_ν, opacities, $S_\nu = (\sigma_\nu J_\nu + \alpha_\nu B_\nu) k_\nu^{-1}$ is the source function, $J_\nu = \frac{1}{2}\int_{-1}^{1} I_\nu \mathrm{d}\mu$ is the mean spectral intensity, and B_ν is the Planck function. The boundary condition for this equation is $I_\nu = 0$ for $\mu < 0$ at $y = 0$, assuming no incident radiation at the surface (valid at $R > 1.5R_\mathrm{S}$ – see Fig. 9.2).

The atmospheres are supposed to be in radiative and hydrostatic equilibrium. The first condition implies that the total energy flux through the atmosphere is constant, transferred solely by radiation (electron heat conduction and convection are of no importance for typical parameters of interest) and determined by the effective surface temperature T_eff,

$$\int_0^\infty \mathrm{d}\nu \int_{-1}^{1} \mu I_\nu \,\mathrm{d}\mu = \sigma_\mathrm{SB}\, T_\mathrm{eff}^4\,. \tag{9.4}$$

The second condition means that the atmospheric pressure is $p = g\,y$ (the radiative force is insignificant unless $T_\mathrm{eff} \gtrsim 10\,\mathrm{MK}$). Finally, these three equations are supplemented with the equation of state for the atmospheric plasma and equations of ionization equilibrium. The latter are needed for computing the electron number density and the fractions of ions in different stages of ionization to obtain the radiative opacity with account for free-free, bound-free and bound–bound atomic transitions.

The main results of the atmosphere modeling are the properties of the emergent radiation demonstrated in Fig. 9.4. The left panel of this figure presents the spectral fluxes of emergent radiation at a local surface point, $F_\nu = \int_0^1 \mu I_\nu \mathrm{d}\mu$ (at $y = 0$), for several effective temperatures and chemical compositions (pure hydrogen, helium, and iron), together with blackbody spectra at the same values of T_eff. The atmosphere model spectra differ substantially from the blackbody ones, particularly in high-energy Wien tails of the radiation from the light-element (hydrogen and helium) atmospheres. The reason is in the combination of two effects: rapid decrease of the light-element opacities with energy, $k_\nu \sim E^{-3}$, and temperature growth in the surface layers, $T(y)$, with depth y. Hence, the high-energy radiation is formed in deeper and hotter layers, with $T > T_\mathrm{eff}$. The spectra emitted from the heavy-element atmospheres (see also [93] for spectra of solar-mixture compositions) exhibit numerous spectral lines and photoionization edges (e.g., M, L, and K spectral complexes in the iron spectra, at about 0.1, 0.8, and 7.1 keV, respectively) produced by ions in various

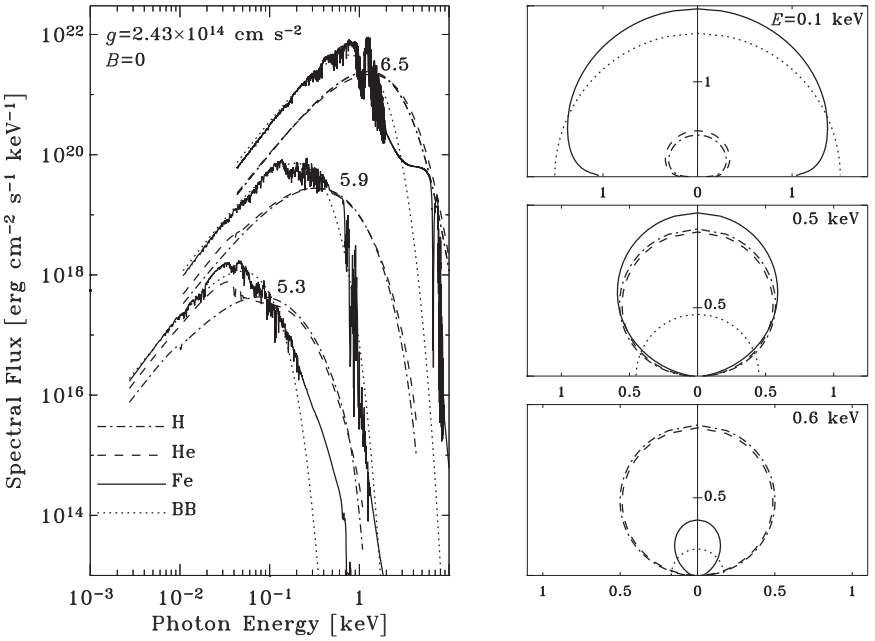

Fig. 9.4 *Left*: Spectra of emergent radiation for pure hydrogen, helium, and iron non-magnetic atmospheres with different effective temperatures (numbers near the curves label $\mathrm{Log}\,T_{\rm eff}$ [K]). "BB" stands for blackbody spectra. *Right*: Polar diagrams of normalized spectral specific intensities at different photon energies, E, and $\mathrm{Log}\,T_{\rm eff} = 5.9$, and for the same chemical compositions. The normal to the surface is directed upward

ionization stages. Generally, they are closer to the blackbody radiation because the energy dependence of the heavy-element opacities is, on average, flatter than that for the light elements.

Although the opacity of the atmospheric plasma is isotropic in the non-magnetic case, the emitted radiation shows substantial anisotropy, i.e., the specific intensity I_ν depends on the direction of emission due to the limb-darkening effect (see the right panel in Fig. 9.4): the larger angle θ (Fig. 9.3) between the normal to the surface and direction of a specific intensity is, the longer path throughout the surface layers emerging photons travel to escape. This results in a stronger absorption the of the emitted radiation. The anisotropy depends on photon energy and chemical composition of the atmosphere. This effect should be taken into account to model thermal radiation from a nonuniform neutron star surface.

The emergent radiation depends also on the surface gravity: a stronger gravitational acceleration increases the density of the atmospheric plasma, changes temperature run $T(y)$ and enhances the non-ideality effects, which results in weaker (more smoothed) spectral features. The hardness of the spectral Wien tail at higher photon energies also alters with varying surface gravity because of the changes in the atmosphere structure [21, 98]. However, these effects are rather subtle and may be important only for analyzing observational data of extremely good statistics.

9.3.4 Magnetized Atmosphere Models

First magnetized hydrogen models have been developed in [52, 53, 73, 74, 100]. These models used simplified radiative opacities of strongly magnetized, partially ionized plasma, which did not include the bound–bound transitions. However, they are considered to be reliable enough in the case of high temperatures, $T_{\rm eff} \approx 1$ MK, at typical pulsar fields, $B \sim 10^{12}$ G, when the atmospheric plasma is almost fully ionized even in the strong magnetized fields. Later on, completely ionized hydrogen models for superstrong magnetic fields, $B \sim 10^{14}$–10^{15} G, have been presented in [5, 23, 24, 47, 88] dealing mainly with the vacuum polarization effects first discussed in [49] and the proton cyclotron lines whose energies shift into the X-ray band at $B \gtrsim 2 \times 10^{13}$ G. Models for partially ionized hydrogen atmospheres with magnetic fields up to 5×10^{14} G and effective temperatures down to about 0.5 MK were presented in [25]. This work showed that the vacuum polarization affects not only the proton cyclotron line but also it suppresses spectral features caused by bound species, making them virtually unobservable in thermal spectra of strongly magnetized neutron stars. First set of magnetized atmospheres with a heavy-element composition (pure iron) was constructed in [63], with the use of a rather crude approximations for the very complicated properties of iron ions in strong magnetic fields. Recently, a next step in modeling magnetized heavy-element (carbon, oxygen, neon) atmospheres with $B = 10^{12}$–10^{13} G and $T_{\rm eff} = 1$–5 MK has been undertaken in [43]. These models imply latest developments in atomic physics and radiative opacities in strong magnetic fields [41, 42]. Like in the non-magnetic case, the magnetized heavy-element atmosphere emission shows many prominent spectral features which, if observed in real X-ray observational data, could be very useful to measure the neutron star magnetic field and mass-to-radius ratio, M/R.

All the above-mentioned works used the same approach for constructing magnetized atmosphere models, which is generally similar to the non-magnetic case. The main difference is that the atmospheric radiation is polarized, and the radiative opacities depend on the polarization and direction of radiation. The radiative transfer in a strongly magnetized plasma is described in terms of coupled equations for specific intensities of two normal modes, $I_{\nu,1}$ and $I_{\nu,2}$, with different polarizations and opacities [15]:

$$\mu \frac{\mathrm{d}}{\mathrm{d}y} I_{\nu,j}(\mathbf{n}) = k_{\nu,j}(\mathbf{n}) I_{\nu,j}(\mathbf{n}) - \left[\sum_{i=1}^{2} \oint \mathrm{d}\mathbf{n}' I_{\nu,i}(\mathbf{n}')\, \sigma_{\nu,ij}(\mathbf{n}', \mathbf{n}) + \alpha_{\nu,j}(\mathbf{n}) \frac{B_\nu}{2} \right], \tag{9.5}$$

where $\mathbf{n}$ is the (unit) wave-vector, $\alpha_{\nu,j}$ is the absorption opacity for the jth mode, $\sigma_{\nu,ij}$ is the scattering opacity from mode i to mode j, and $k_{\nu,j} = \alpha_{\nu,j} + \sum_{i=1}^{2} \oint \mathrm{d}\mathbf{n}' \sigma_{\nu,ij}(\mathbf{n}', \mathbf{n})$ is the total opacity. It should be noted that the opacity depends on the angle between the wave-vector and the magnetic field, so that I_ν depends not only on θ but also on $\Theta_{\rm B}$, the angle between the local magnetic field and the normal to the surface element. Similar to the non-magnetic case, (9.5) are

supplemented with the equations of hydrostatic and radiative equilibrium (for the latter, (9.4) applies with $I_\nu = I_{\nu,1} + I_{,2}$).

To deal with the problems caused by the sharp angular dependence of the radiative opacities [27], a two-step method for modeling of magnetic neutron star atmospheres was developed [52, 74]. At the first step, the radiative transfer is solved in the diffusion approximation for the mean intensities $J_{\nu,j} = (4\pi)^{-1} \oint I_{\nu,j}(\mathbf{n})\,\mathrm{d}\mathbf{n}$:

$$\frac{\mathrm{d}}{\mathrm{d}y} d_{\nu,j} \frac{\mathrm{d}}{\mathrm{d}y} J_{\nu,j} = \bar{\alpha}_{\nu,j} \left[J_{\nu,j} - \frac{B_\nu}{2} \right] + \bar{\sigma}_\nu \left[J_{\nu,j} - J_{\nu,3-j} \right] , \tag{9.6}$$

where $\bar{\alpha}_{\nu,j} = (4\pi)^{-1} \oint \mathrm{d}\mathbf{n}\, \alpha_{\nu,j}(\mathbf{n})$ and $\bar{\sigma}_\nu = (4\pi)^{-1} \oint\oint \mathrm{d}\mathbf{n}\,\mathrm{d}\mathbf{n}'\, \sigma_{\nu,12}(\mathbf{n},\mathbf{n}')$ are the angle-averaged absorption and scattering opacities. The diffusion coefficient is $d_{\nu,j} = d^{\mathrm{p}}_{\nu,j} \cos^2\Theta_{\mathrm{B}} + d^{\mathrm{o}}_{\nu,j} \sin^2\Theta_{\mathrm{B}}$, with $d^{\mathrm{p}}_{\nu,j} = \int_0^1 \mu^2 k^{-1}_{\nu,j}\,\mathrm{d}\mu$ and $d^{\mathrm{o}}_{\nu,j} = \int_0^1 (1-\mu^2)\, k^{-1}_{\nu,j}\,\mathrm{d}\mu$. Next, the atmospheric structure obtained at the first step is corrected using an iterative procedure applied to the exact equations of the radiative transfer. Finally, the emergent intensity (at $y = 0$) is

$$I_{\nu,j} = \mu^{-1} \int_0^\infty \left[\alpha_{\nu,j} \frac{B_\nu}{2} + \sum_{i=1}^{2} \sigma_{\nu,ij} J_{\nu,i} \right] \exp\left[-\nu^{-1} \int_0^y k_{\mu,j}\,\mathrm{d}z \right] \mathrm{d}y , \tag{9.7}$$

and the emitted spectral flux is computed as $F_\nu = \int_0^1 \mu \sum_{i=1}^2 I_{\nu,i}\,\mathrm{d}\mu$. More details on the modeling of magnetized atmospheres can be found in [53].

Figure 9.5 (left panel) shows polarization-summed spectral fluxes of the emergent radiation, F_ν, emitted by a local element of the neutron star surface, for two values of effective temperature and two magnetic field orientations, perpendicular and parallel to the surface ($\Theta_{\mathrm{B}} = 0$ and 1, respectively). The main result is that the magnetized atmosphere spectra are harder than the blackbody radiation of the same T_{eff}, although they are softer than the non-magnetic spectra. Similar to the non-magnetic case, this is explained by the temperature growth with depth and the opacity decrease at higher energies, which is more gradual ($\propto E^{-1}$ for the mode with the smaller opacity) in the magnetized plasma. At lower effective temperatures, $T_{\mathrm{eff}} \lesssim 1\,\mathrm{MK}$, the photoionization opacity (due to bound-free transitions) becomes important, that affects the shape of the emitted spectra (see the example with $\mathrm{Log}\,T_{\mathrm{eff}} = 5.8$ in Fig. 9.5). The proton cyclotron lines are seen at energies $E = 6.3\,(B/10^{12}\,\mathrm{G})\,\mathrm{eV}$. If the magnetic field is very large, $B \gtrsim 10^{14}\,\mathrm{G}$, the proton cyclotron line shifts into the X-ray band. On the other hand, if the magnetic field is not so large, $B = 10^{10}$–$10^{12}\,\mathrm{G}$, the neutron star atmosphere spectra may exhibit the electron cyclotron lines in the X-ray band, at $E_{\mathrm{ce}} = 11.6\,(B/10^{12}\,\mathrm{G})$ keV. Calculations of hydrogen atmosphere models which include bound–bound atomic transitions [25, 93] show that spectral lines, considerably broadened by the motional Stark effect [50, 51], may emerge at $T_{\mathrm{eff}} \lesssim 0.5\,\mathrm{MK}$. The strongest line corresponds to the transition between the ground state and the lowest excited state; its energy is $E \approx [75 + 0.13\ln(B/10^{13}\,\mathrm{G}) + 63(B/10^{13}\,\mathrm{G})]\,\mathrm{eV}$.

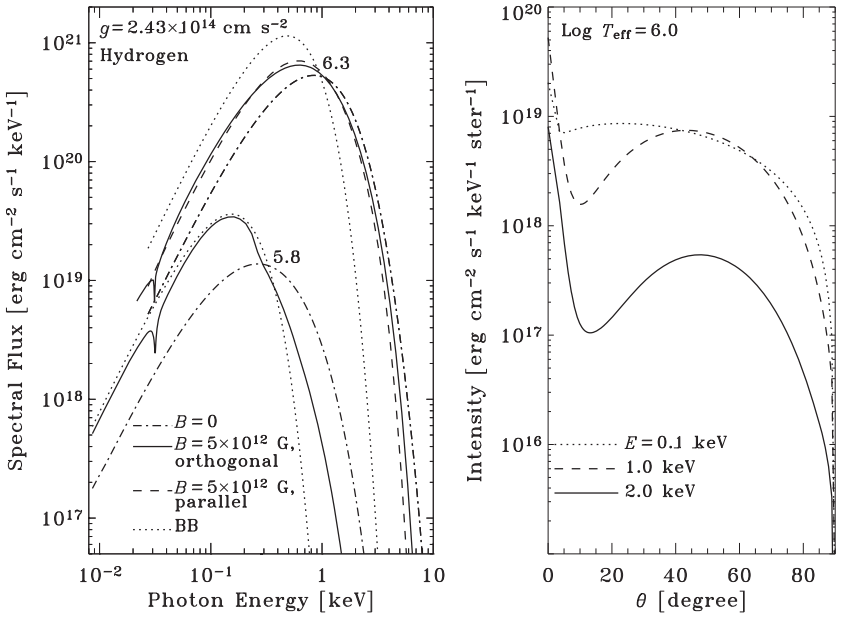

Fig. 9.5 *Left*: Spectra of radiation emergent from neutron star atmospheres for a magnetic field orthogonal and parallel to the surface with different effective temperatures (numbers near the curves label $\mathrm{Log}\,T_{\rm eff}$ [K]). "BB" stands for blackbody spectrum. *Right*: Dependences of specific intensities on the angle between the photon wave-vector and the magnetic field directed along the surface normal

Radiation emerging from a magnetized atmosphere is strongly anisotropic. Angular dependences of the local specific intensities, $I_\nu = I_{\nu,1} + I_{\nu,2}$ (9.7), show a complicated "pencil-plus-fan" structure – a narrow peak along the direction of the magnetic field (where the atmospheric plasma is most transparent for the radiation), and a broader peak at intermediate angles. The widths and strengths of the peaks depend on magnetic field and photon energy (see examples in the right panel of Fig. 9.5). Obviously, it is very important to account for this anisotropy while modeling the radiation from a neutron star with nonuniform surface magnetic field and effective temperature.

9.3.5 Thermal Radiation as Detected by a Distant Observer

Results presented in Sects. 9.3.3 and 9.3.4 describe spectral radiation emitted by a *local* element at the neutron star surface. The effective temperature and/or magnetic field distributions over the surface can be nonuniform (for example, if a neutron star has a dipole magnetic field, the effective temperature decreases from the magnetic poles to the equator). To calculate the *total* emission, one should integrate the local

intensities, computed for local temperatures and magnetic fields, over the visible part of the surface S, with account for the gravitational redshift and bending of photon trajectories:

$$F(E_{\rm obs}) = g_{\rm r}\frac{1}{D^2}\int_S \mu\, I(E_{\rm obs}/g_{\rm r})\,{\rm d}S\,, \tag{9.8}$$

where $E_{\rm obs} = g_{\rm r}E$ is the observed (redshifted) photon energy. To take into account the interstellar absorption, a factor, $\exp(-n_{\rm H}\sigma_{\rm eff}[E])$, should be added in (9.8) ($n_{\rm H}$ is absorption column density towards a specific object, $\sigma_{\rm eff}[E]$ is the absorption cross section per hydrogen atom). More details about the integration over the neutron star surface can be found in [55]. It is worthwhile to mention that if a neutron star has a nonuniform distribution of the magnetic field, the surface integration broadens the spectral features. In addition, if a neutron star is a fast rotator, one should take into account the Doppler shifts of energies of photons emitted from surface elements moving with different radial velocities. Maximum values of these velocities, $v_r = 2\pi RP^{-1}\sin\zeta$ (ζ is the inclination of the rotation axis with respect to observer's line of sight – see Fig. 9.3), can be as high as 10–15% of the speed of light for millisecond periods. For instance, a fast rotation, $P \lesssim 10\,$ms, may lead to complete smearing of weak and narrow spectral lines [93], leaving only most prominent spectral jumps around the strongest photoionization edges.

If thermal radiation originates from small polar caps on the neutron star surface, it greatly simplifies (9.8):

$$F(E_{\rm obs}) = g_{\rm r}\frac{S_{\rm a}}{D^2}I(E_{\rm obs}/g_{\rm r},\,\theta^*)\,, \tag{9.9}$$

where the apparent spot area $S_{\rm a}$ and the angle θ^* between the wave-vector of escaping radiation and the radius-vector to the hot spot are computed with account for the effect of gravitational bending. These quantities depend on the angles α (between the rotational and magnetic axes) and ζ (Fig. 9.3), and the gravitational parameter $g_{\rm r}$ [101].

The flux given by (9.7) and (9.8) varies with the period of neutron star rotation. One can obtain a large variety of pulse profiles at different assumptions on the angles α and ζ and M/R ratio. Examples of pulse profiles computed for radiation from the entire neutron star surface are shown in [93], whereas pulse profiles of thermal radiation from heated polar caps are presented in [94, 101] for magnetized atmosphere models, and in [8, 92] for non-magnetic ones.

9.3.6 Atmosphere Emission vs. Blackbody Radiation

Although the model atmosphere spectra are different from blackbody radiation, very often an observed thermal spectrum can be fitted equally well with a blackbody spectrum and a neutron star atmosphere model (see examples below), particularly

when the instrumental energy resolution is low and/or the energy band is narrow, and/or observational data are of a poor quality. However, the parameters obtained from such fits are quite different, especially when the hydrogen or helium atmospheres are used. Since the light-element atmosphere spectra are much harder than the blackbody spectra at the same effective temperatures, an atmosphere model fit results in a temperature $T_{\rm eff}$ significantly lower than the inferred blackbody temperature $T_{\rm bb}$, with a typical ratio $T_{\rm bb}/T_{\rm eff} \sim 2$–3. On the other hand, to provide the same total energy flux, the blackbody fit yields a smaller normalization factor, proportional to S/D^2 [see (9.7)], than the atmosphere model does. In other words, the light-element atmosphere fit gives a considerably larger size of the emitting region, $S_{\rm eff}/S_{\rm bb} \sim 50$–200. Note however that both neutron star atmosphere and blackbody spectral fits yield about the same values of bolometric luminosity, $L^{\infty}_{\rm bol} = g_{\rm r}^2 L_{\rm bol} = 4\pi g_{\rm r}^2 \sigma_{\rm SB} R^2 T_{\rm eff}^4$, as measured by a distant observer.

It is also worth to remember that blackbody radiation is isotropic and, hence, it results in weak pulsations of the model flux, with a typical pulsed fraction around a few percents only.

Finally, the atmosphere models discussed here, both non-magnetic and magnetized, are available for analyzing thermal X-ray emission observed from neutron stars as a part of the X-ray Spectral Fitting Package[3] (XSPEC codes "NSA" and "NSAGRAV") provided by the NASA's High Energy Astrophysics Science Archive Research Center.

9.3.7 Modeling Radiation from Condensed Neutron Star Surface

As mentioned above, if magnetic field of the neutron star surface is strong enough and the surface temperature is rather low, then the outermost surface layers could be in any state other than gaseous. For example, at $B = 10^{14}$ G and $T_{\rm surf} \lesssim 0.5$ MK and $T_{\rm surf} \lesssim 2$ MK for hydrogen and iron compositions, respectively, the surface would be in a condensed (solid) state. First models of thermal radiation emitted by a condensed surface of a neutron star were constructed in [79, 80]. These works showed that the overall spectral shape of X-ray flux emitted by the condensed surface is mostly featureless (only weak spectral features associated with ion cyclotron and electron plasma frequencies can appear in some cases) and fairly close to the blackbody spectrum of the same temperature. The main difference between these two model spectra is that, because of suppressed emissivity of the condensed surface, the surface radiation is reduced from the blackbody one by a factor of a few. Hence, applying the condensed surface models to observed thermal emission is expected to result in temperature estimates close to and flux normalizations (proportional to the factor $[R^{\infty}/D]^2$) larger by a factor of a few than those yielded by the blackbody radiation. For more details on this topic, see Chap. 7.

[3] `http://heasarc.gsfc.nasa.gov/docs/xanadu/xspec/`

9.4 Thermal Emission from Neutron Stars: Observational Results

As already mentioned in Sect. 9.2, thermal emission has been observed from a rather large number of neutron stars of various types. Most of them radio pulsars of different ages ranging from very young neutron stars to old and very old (millisecond) ones. In addition to active pulsars, a number of radio-quiet neutron stars emitting only thermal-like X-rays have been detected, with typical temperatures $\sim$0.5–5 MK. They are usually subdivided in four classes: Anomalous X-ray Pulsars (AXPs; [33]), Soft Gamma-ray Repeaters (SGRs; [32], Chap. 21), "dim" or "truly isolated" radio-quiet neutron stars (i.e., not associated with SNRs; [20, 81], Chap. 7) and compact central sources (CCOs) in SNRs (Chap. 6) which have been identified with neither active pulsars nor AXPs/SGRs. Observational manifestations (particularly, multi-wavelength spectra) of radio-quiet neutron stars are quite different from those of active pulsars, and their properties have not been investigated as extensively, but the presence of the thermal component in their radiation provides a clue to understand the nature of these objects. While a detailed review on thermal emission detected from neutron stars can be found in, e.g., [57], a few most interesting and illustrative examples are discussed below, concentrating mainly on spectral properties of detected thermal emission.

9.4.1 PSR J1119−6127

It is the youngest,[4] $\tau_c = 1.6\,\mathrm{kyr}$, and very energetic in terms of the spin-down power, $\dot{E} = 2.3 \times 10^{36}\,\mathrm{ergs\,s^{-1}}$, radio pulsar whose X-ray flux reveals a strong thermal component. The best representation of the pulsar's spectrum detected with *XMM*-Newton is a two-component, thermal plus non-thermal, model [16]. The non-thermal emission dominating at energies $E \gtrsim 2.5\,\mathrm{keV}$ is well fitted with a power-law spectrum of a photon index $\Gamma \simeq 1.5$ and X-ray luminosity $L^{\mathrm{nonth}} \simeq 0.8 \times 10^{33}\,\mathrm{ergs\,s^{-1}}$ in the 0.2–10 keV range.[5] The thermal component can be fitted with a blackbody spectrum of an apparent (redshifted) temperature $T_{\mathrm{bb}}^{\infty} \simeq 2.4\,\mathrm{MK}$ and radius $R_{\mathrm{bb}}^{\infty} \simeq 3.4\,\mathrm{km}$ (for the estimated distance[6] to the pulsar $D = 8.4\,\mathrm{kpc}$), implying the measured bolometric luminosity $L_{\mathrm{bol}}^{\infty} \simeq 2.7 \times 10^{33}\,\mathrm{ergs\,s^{-1}}$. This model fit would mean that the thermal radiation originates from a small hot area on the pulsar's surface (polar caps?), although the inferred radius of the emitting area significantly exceeds the canonical radius $R_{\mathrm{pc}}^{*} \simeq 0.2\,\mathrm{km}$ predicted by theoretical models for PSR J1119−6127 with a spin period $P = 0.41\,\mathrm{s}$ (see Sect. 9.2). Alternatively, the thermal component can be interpreted as X-ray flux of an effective (actual)

[4] The characteristic age, $\tau_c = P/(2\dot{P})$, is a standard age estimate for the vast majority of radio and X-ray pulsars. Note, however, that it may be very inaccurate.

[5] This energy range is used for all other estimates on L^{nonth} given in this work.

[6] Distances cited in Sect. 9.4 are either those estimated to SNRs which host some of discussed objects, or derived from pulsar parallaxes or dispersion measures.

temperature $T_{\rm eff} \simeq 1.6\,{\rm MK}$ (or $T^{\infty}_{\rm eff} = g_{\rm r}^{-1} T_{\rm eff} \simeq 1.2\,{\rm MK}$) emitted from the whole pulsar's surface covered with a magnetized ($B \approx 1 \times 10^{13}$ G) hydrogen atmosphere (assuming the standard neutron star mass $M = 1.4\,M_{\odot}$ and radius $R = 10\,{\rm km}$), yielding $L_{\rm bol} \simeq 4.7 \times 10^{33}\,{\rm ergs\,s^{-1}}$ ($L^{\infty}_{\rm bol} = g_{\rm r}^{2} L_{\rm bol} \simeq 2.8 \times 10^{33}\,{\rm ergs\,s^{-1}}$). In this interpretation, the parameters of the non-thermal component are virtually the same as those in the fit with the blackbody radiation. The best fit with the magnetized atmosphere model and power-law spectrum is shown in Fig. 9.6.

Very importantly, the X-ray flux of PSR J1119−6127 detected in the 0.5–2 keV range, where the thermal component dominates, is pulsed, with a very large pulsed fraction, $f_{\rm p} \approx 75\%$ [16]. It should be noted that because of the strong gravitational bending effect (Sect. 9.3.2) such pulsations can be reconciled with neither (isotropic) blackbody radiation nor atmospheric emission from an *uniform* surface. On the other hand, no pulsations have been detected at energies $E > 2\,{\rm keV}$, that is rather a surprising result as non-thermal emission is expected to be strongly pulsed, especially that emitted by young and energetic pulsars.

The example of PSR J1119−6127 is remarkable in the sense that the situation with observing thermal emission from very young and active pulsars is not in fact as "pessimistic" as it may follow from the general picture described in Sect. 9.2, and more such detections can be expected in future (see, e.g., [91] for the case of PSR J1369−6429).

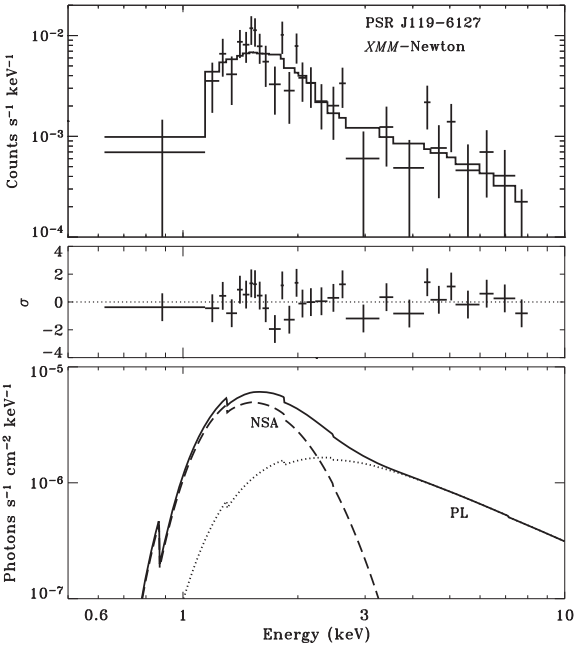

Fig. 9.6 Two-component, hydrogen magnetized atmosphere (NSA) model plus power law (PL), fit to the X-ray spectrum of PSR J1119−6127 detected with *XMM*-Newton (*upper panel*). The *middle panel* shows residuals in the fit, whereas the *lower panel* presents the contributions (attenuated by interstellar absorption) from the thermal (*dashes*) and non-thermal (*dots*) components

9.4.2 The Vela Pulsar and PSR B1706−44

The superb angular resolution of *Chandra* made it possible to separate X-ray flux of the famous Vela pulsar ($P = 0.09\,\mathrm{s}$, $\tau_c = 11\,\mathrm{kyr}$, $\dot{E} = 6.9 \times 10^{36}\,\mathrm{ergs\,s^{-1}}$) from its bright pulsar-wind nebula and study the properties of the pulsar's emission [58]. The *Chandra* observations revealed that the bulk of the X-ray flux detected from Vela is of a thermal origin, and non-thermal emission dominates only at energies $E \gtrsim 2\,\mathrm{keV}$, similar to the case of PSR J1119−6127. The thermal component can be described equally well with either a blackbody spectrum or a magnetized ($B \approx 5 \times 10^{12}\,\mathrm{G}$) hydrogen atmosphere model. However, the parameters of the thermal component are significantly different in the blackbody and atmosphere model fits: $T_{\mathrm{bb}}^{\infty} \simeq 1.6\,\mathrm{MK}$ and $R_{\mathrm{bb}}^{\infty} \simeq 2.8\,\mathrm{km}$, $T_{\mathrm{eff}} \simeq 0.9\,\mathrm{MK}$ (or $T_{\mathrm{eff}}^{\infty} \simeq 0.7\,\mathrm{MK}$) and $R \simeq 13\,\mathrm{km}$ (for the estimated distance to the pulsar $D = 300\,\mathrm{pc}$), respectively. The bolometric luminosity of the thermal emission is $L_{\mathrm{bol}} \simeq 0.8 \times 10^{33}\,\mathrm{ergs\,s^{-1}}$. Moreover, the slope of the non-thermal emission depends on the thermal model applied for interpreting the pulsar's spectrum. It has a rather large photon index $\Gamma \simeq 2.7$ if the blackbody radiation is used. The non-thermal component with this slope greatly exceeds the optical emission of the pulsar. In the analysis involving the atmosphere model the non-thermal component is much flatter, with $\Gamma \simeq 1.5$. Remarkably, the extrapolation of this power-law spectrum (with $L^{\mathrm{nonth}} \simeq 0.2 \times 10^{32}\,\mathrm{ergs\,s^{-1}}$, or about 40 times lower than L_{bol}) matches fairly well the optical and hard X-ray/soft γ-ray fluxes detected from the pulsar. This is shown in Fig. 9.7.

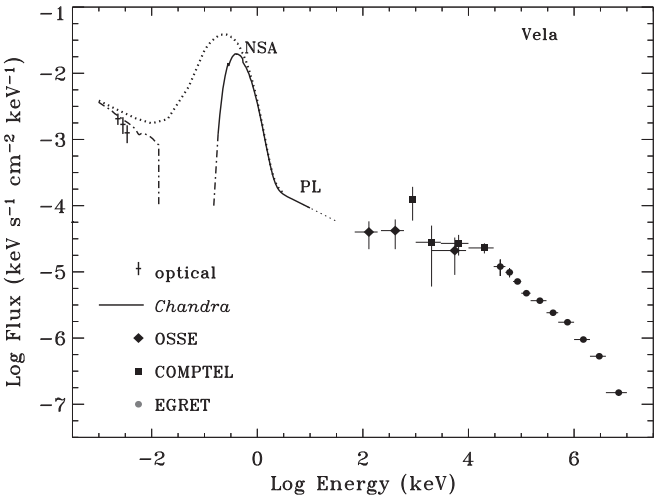

Fig. 9.7 Multiwavelength spectrum of the Vela pulsar detected with different missions. The *solid line* shows the X-ray spectrum obtained with *Chandra* and fitted with a two-component, neutron star atmosphere (NSA) and power law (PL), model. *Dots* correspond to the unabsorbed model spectrum. The *dash-dotted lines* show the extrapolated optical and EUV absorbed spectra

The X-ray pulsed profile of Vela is very unusual and complicated, with at least three peaks per rotational period and $f_p \approx 8\%$ [57]. A combined spectral and timing analysis is crucial to further elucidate mechanisms generating the X-ray emission of this pulsar.

PSR 1706−44 is one more young and energetic pulsar ($P = 0.10$ s, $\tau_c = 18$ kyr, $\dot{E} = 3.4 \times 10^{36}$ ergs s^{-1}) emitting thermal X-rays, with spectral properties very similar to those of Vela [37]. The thermal component of PSR 1706−44 detected with *XMM*-Newton can be described by a magnetized hydrogen atmosphere model with $T_{\rm eff} \simeq 1.0$ MK and $R \simeq 12$ km (for $D = 2.3$ kpc), or $L_{\rm bol} \simeq 1.0 \times 10^{33}$ ergs s^{-1}. The non-thermal emission is fitted with a power-law spectrum of $\Gamma \simeq 1.4$, but its luminosity, $L^{\rm nonth} \simeq L_{\rm bol}$, is much higher than that of Vela. The X-ray pulsed profile of PSR 1706−44 is energy-dependent and shows a broad pulse per period with $f_p \approx 10\%$ at energies $E \lesssim 1.4$ keV, where the thermal flux dominates. The *Chandra* data on this pulsar [65], which is surrounded by a PWN, agreed with the results given in [37] on the thermal component, although the *Chandra* data provided a more accurate, a factor of 3 smaller, estimate on the non-thermal flux.

9.4.3 PSRs J0538+2817 and B2334+61

These two neutron stars have similar pulsar parameters (age, spin period, spin-down power) and could be considered as "twins", or at least "coevals", if their ages were derived in the same way.

PSR J0538+2817 ($P = 0.14$ s, $\dot{E} = 4.9 \times 10^{34}$ ergs s^{-1}) represents a rare case when neutron star age is well determined. It was inferred from the pulsar's proper motion measurements [34], $\tau \simeq 30$ kyr, and is much smaller than the standard estimate $\tau_c = 618$ kyr.

No non-thermal emission was observed from PSR J0538+2817. The pulsar's spectrum detected with *XMM*-Newton [36] can be fitted with a single blackbody spectrum of $T_{\rm bb}^{\infty} \simeq 2.1$ MK and $R_{\rm bb}^{\infty} \simeq 1.7$ km ($D = 1.2$ kpc). As shown in [95], a hydrogen atmosphere model with $B = 10^{12}$ G fits the observational data even better, yielding the surface temperature $T_{\rm eff} \simeq 1.1$ MK and the star's radius $R \simeq 10.5$ km (at $M = 1.4\,M_{\odot}$), or $L_{\rm bol} \simeq 1.2 \times 10^{33}$ ergs s^{-1}. An upper limit on luminosity of a possible non-thermal component is $L^{\rm nonth} < 1.0 \times 10^{31}$ ergs s^{-1} (assuming $\Gamma = 1.5$).

The X-ray flux of PSR J0538+2817 is pulsed, with a broad, asymmetric pulse per period and pulsed fraction of $f_p \approx 25\%$. The phases of pulse maxima at energies below and above 0.8 keV differ by $\sim 75^{\circ}$ [95]. This indicates that the thermal emission is intrinsically anisotropic and the pulsar has a strong non-uniformity of the surface temperature and magnetic field.

The estimate on the age of PSR B2334+61 ($P = 0.50$ s, $\dot{E} = 6.2 \times 10^{34}$ ergs s^{-1}) is obtained in the standard way, $\tau_c = 41$ kyr. Similar to the case of PSR J0538+2817, the X-ray flux of PSR B2334+61 detected with *XMM*-Newton if of a thermal origin, and the pulsar's spectrum can be fitted with a single thermal model [38]. The blackbody fit yields $T_{\rm bb}^{\infty} \simeq 1.5$ MK and $R_{\rm bb}^{\infty} \simeq 2.8$ km ($D = 3.1$ kpc). A hydrogen

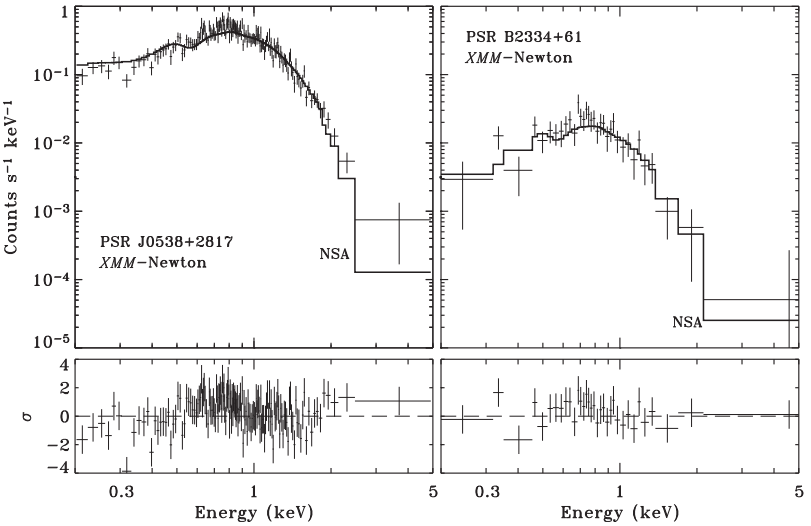

Fig. 9.8 X-ray spectra of PSRs J0538+2817 and B2334+61 detected with *XMM*-Newton (*crosses*) and fitted with magnetized neutron star atmosphere models. Residuals in the fits are shown in the *lower panels*

atmosphere model with $R = 10\,\mathrm{km}$, $M = 1.4 M_\odot$ and $B = 10^{13}\,\mathrm{G}$ fits the observational data equally well, resulting in the surface temperature $T_{\rm eff} \simeq 0.9\,\mathrm{MK}$ and $L_{\rm bol} \simeq 0.5 \times 10^{33}\,\mathrm{ergs\,s^{-1}}$. A lower limit on luminosity of a possible non-thermal component is $L^{\rm nonth} < 0.7 \times 10^{31}\,\mathrm{ergs\,s^{-1}}$ (for $\Gamma = 1.5$). Based on the results of the spectral fits, one can assume that these two pulsars are indeed "twins" and the estimate $\tau_{\rm c}$ on the age of PSR B2334+61 is close to the pulsar's true age. Figure 9.8 shows the spectra detected from PSRs J0538+2817 and B2334+61 and fitted with the best neutron star atmosphere models. The only difference in the X-ray properties of these two objects is that the emission observed from PSR B2334+61 revealed no pulsations, with a 5% upper limit on the pulsed fraction, indicating different neutron star geometries of these pulsars (e.g., PSR B2334+61 may have smaller ζ and/or α angles – see Fig. 9.3).

9.4.4 Middle-Aged Pulsars: B0656+14, B1055−52 and Geminga

As discussed in Sect. 9.2, middle-aged (a few hundred thousand years old) pulsars are believed to be best targets for observing thermal neutron star emission. The well-known three neutron stars with close pulsar parameters, PSRs B0656+14, B1055−52, and Geminga,[7] support this. Observations with ROSAT first showed that soft X-ray emission from these objects are of a thermal origin [45], and later *Chandra* and *XMM*-Newton allowed a detailed study of this radiation [12,31,57,95].

[7] Dubbed as "Three Musketeers" by [3].

PSR B0656+14 ($P = 0.39\,\mathrm{s}$, $\tau_\mathrm{c} = 111\,\mathrm{kyr}$, $\dot{E} = 3.8 \times 10^{34}\,\mathrm{ergs\,s^{-1}}$) is the brightest of these three neutron stars. Its X-ray spectrum cannot be fitted by a two-component model like those describing the spectra of PSRs J1119−6127, B1706−44 and Vela. If fitted with a blackbody radiation, the pulsar's thermal emission requires two components, a "soft" one (TS) with $T^{\infty}_{\mathrm{bb,s}} \simeq 0.8\,\mathrm{MK}$ and $R^{\infty}_{\mathrm{bb,s}} \simeq 7.5\,\mathrm{km}$, and a "hard" one (TH) with $T^{\infty}_{\mathrm{bb,s}} \simeq 1.7\,\mathrm{MK}$ and $R^{\infty}_{\mathrm{bb,s}} \simeq 0.6\,\mathrm{km}$ (for $D = 300\,\mathrm{pc}$). The TS component of the bolometric luminosity $L^{\infty}_{\mathrm{bol,s}} \simeq 1.6 \times 10^{32}\,\mathrm{ergs\,s^{-1}}$ may be regarded as emitted from the whole star's surface, whereas the TH component ($L^{\infty}_{\mathrm{bol,s}} \simeq 0.2 \times 10^{32}\,\mathrm{ergs\,s^{-1}}$) could be interpreted as radiation from heated polar caps. In addition to these two thermal components, a power-law spectrum is needed to fit the pulsar's emission detected at energies above 2 keV. With the available data, the slope of the non-thermal component is not well constrained, but one can assume that the photon index does not change from optical to X-rays, like in the Vela pulsar. Then, it results in a power-law spectrum with $\Gamma \simeq 1.5$ and $L^{\mathrm{nonth}} \simeq 0.3 \times 10^{31}\,\mathrm{ergs\,s^{-1}}$. Figure 9.9 presents the broadband emission of PSR B0656 + 14.

The X-ray spectrum of PSR B1055−52 ($P = 0.20\,\mathrm{s}$, $\tau_\mathrm{c} = 535\,\mathrm{kyr}$, $\dot{E} = 3.0 \times 10^{34}\,\mathrm{ergs\,s^{-1}}$) is very similar to that of PSR B0656+14. It can be fitted only with a three-component model, "soft" and "hard" blackbody spectra plus a power law, with the following parameters (as inferred by [57] from the combined ROSAT and *Chandra* data on the pulsar): $T^{\infty}_{\mathrm{bb,s}} \simeq 0.8\,\mathrm{MK}$ and $R^{\infty}_{\mathrm{bb,s}} \simeq 8.4\,\mathrm{km}$, $T^{\infty}_{\mathrm{bb,s}} \simeq 1.6\,\mathrm{MK}$ and $R^{\infty}_{\mathrm{bb,s}} \simeq 0.6\,\mathrm{km}$ (for $D = 700\,\mathrm{pc}$), a photon index $\Gamma \simeq 1.7$ and $L^{\mathrm{nonth}} \simeq 0.9 \times 10^{31}\,\mathrm{ergs\,s^{-1}}$.

Compared to the spectra of PSRs B0656+14 and B1055−52, the X-ray flux of the famous γ-ray and X-ray Geminga pulsar ($P = 0.24\,\mathrm{s}$, $\tau_\mathrm{c} = 342\,\mathrm{kyr}$,

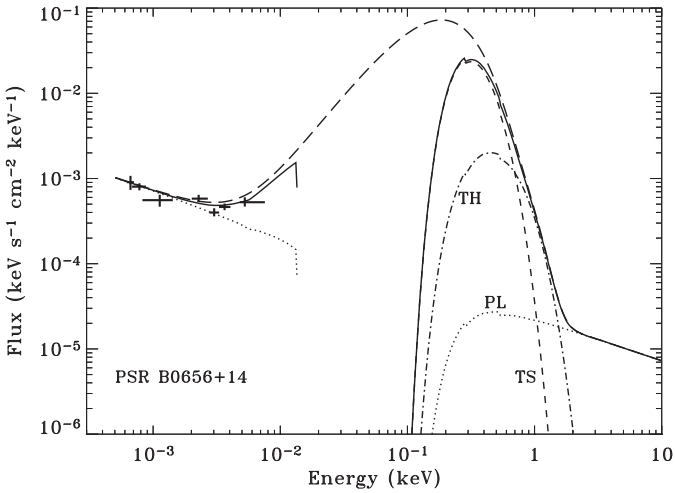

Fig. 9.9 Broadband spectrum of PSR B0656+14 for a three-component model (TS+TH+PL) extrapolated in optical. The *solid and long-dashed curves* show the absorbed and unabsorbed spectra, respectively. *Crosses* indicate the IR-optical fluxes

$\dot{E} = 3.3 \times 10^{34}$ ergs s^{-1}) alone does not require a three-component model. It can be fitted with two components, a blackbody spectrum and a power law of $\Gamma \simeq 2.0$. However, the non-thermal component extrapolated to low energies greatly exceed optical fluxes observed from the pulsar. To describe the optical/UV/FUV and X-ray data with the same model, one needs to invoke a three-component interpretation of the X-ray flux, similar to that applied for the other "Musketeers", with $T^{\infty}_{\rm bb,s} \simeq 0.5$ MK and $R^{\infty}_{\rm bb,s} \simeq 12.9$ km, $T^{\infty}_{\rm bb,s} \simeq 2.3$ MK and $R^{\infty}_{\rm bb,s} \simeq 0.05$ km (for $D = 200$ pc), and a photon index $\Gamma \simeq 1.5$ and $L^{\rm nonth} \simeq 0.2 \times 10^{31}$ ergs s^{-1} [31]. Figure 9.10 shows the multi-wavelength spectrum of Geminga based on this three-component interpretation. It is worthwhile to mention that, although this spectral model is similar to those suggested for the X-ray emission of PSRs B0656+14 and B1055−52, the $R^{\infty}_{\rm bb,h}$ radius inferred for Geminga is smaller by about a factor of 10 than the estimates obtained for the other two pulsars. Note that according to theoretical pulsar models these three objects should have about the same polar cap radii.

Applying magnetized hydrogen atmosphere models for the thermal components observed from these three pulsars yields formally acceptable fits. However, they imply very large radii for the TS component, $R \gtrsim 40$ km. Therefore, applicability of the available neutron star atmosphere models to these objects is questionable. Most likely, these pulsars are too cold to possess an atmosphere and, hence their surfaces are in a condensed state, as discussed in [31].

The pulsations of the X-ray fluxes from these pulsars shows a complex behavior, with energy-dependent variations in pulsed fraction, phase of main pulses, and pulse

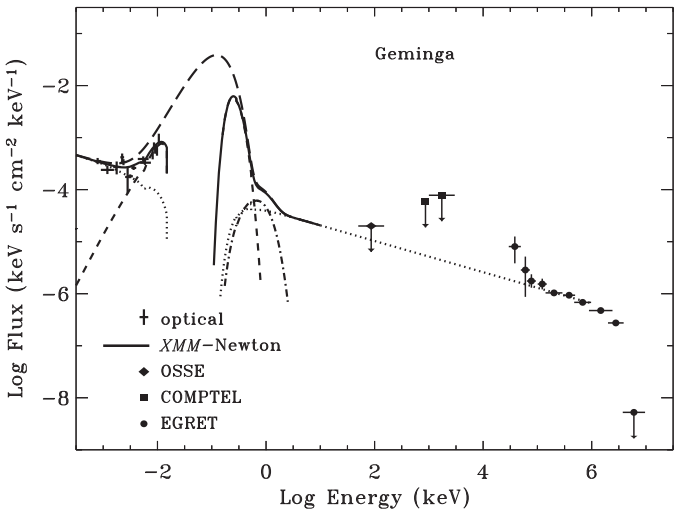

Fig. 9.10 Multiwavelength spectrum of Geminga observed with different missions. The X-ray flux is described with a three-component (TS+TH+PL) model. The *solid and long-dashed curves* are the absorbed and unabsorbed fluxes, respectively. *Short dashes, dash-dots, and dots* show the TS, TH, and PL components, respectively

shape [31, 57, 95]. This indicates that their thermal radiation is locally anisotropic, in obvious contradiction with the simplistic blackbody interpretation of the phase-integrated spectra. Moreover, the observed pulsed profiles hints that the surface distributions of temperature and magnetic field are not azimuthally symmetric, suggesting a strong multipolar component of the magnetic field or a de-centered magnetic dipole.

9.4.5 Old Radio Pulsars

Because of their age, $\tau_c > 1\,\mathrm{Myr}$, old ordinary (with spin periods $P \gtrsim 0.05\,\mathrm{s}$, i.e., not millisecond) radio pulsars are expected to be and actually are much less energetic and fainter than their younger "stellar mates". Up to now, of about 1,100 such pulsars known,[8] only seven have been firmly detected in X-rays [4,29,94]. The analysis of X-rays collected from these old neutron stars revealed very diverse properties of their emission, with possible thermal radiation detected from two objects, PSRs B0950+08 and J2043+2740 [94]. See also Chap. 6 and [4] for an alternative interpretation, involving only non-thermal emission.

PSR B0950+08

The X-ray spectrum of PSR B0950+08 ($P = 0.25\,\mathrm{s}$, $\tau_c = 17.4\,\mathrm{Myr}$, $\dot{E} = 5.6 \times 10^{32}\,\mathrm{ergs\,s^{-1}}$) detected with *XMM*-Newton can be described with a two-component model, thermal plus non-thermal. The thermal component, dominating at energies $E \lesssim 0.7\,\mathrm{keV}$, is interpreted as radiation from two heated polar caps on the star's surface covered with a magnetized ($B \simeq 3 \times 10^{11}\,\mathrm{G}$) hydrogen atmosphere. The applied model takes into account the GR effects (redshift and gravitational bending). The inferred temperature, radius, and luminosity of the polar caps are $T_{\mathrm{pc}} \simeq 1.0\,\mathrm{MK}$, $R_{\mathrm{pc}} \simeq 0.25\,\mathrm{km}$, and $L_{\mathrm{bol}}^{\mathrm{pc}} \simeq 0.3 \times 10^{30}\,\mathrm{ergs\,s^{-1}}$ (for $D = 260\,\mathrm{pc}$), respectively. Remarkably, the obtained polar cap radius is in excellent agreement with the conventional estimate $R_{\mathrm{pc}}^{*} \simeq 0.3\,\mathrm{km}$. The non-thermal emission is fitted with a power-law spectrum of a photon index $\Gamma \simeq 1.3$ and luminosity $L^{\mathrm{nonth}} \simeq 1.0 \times 10^{30}\,\mathrm{ergs\,s^{-1}}$. This power-law model also matches well optical fluxes detected from the pulsar. Figure 9.11 presents the broadband, from optical to X-rays, spectrum of PSR B0950+08. The analysis of the temporal behavior of the pulsar's X-ray flux, with energy-dependent pulse shape and pulsed fraction, also supports this two-component interpretation. The combined optical and X-ray data put the upper limit on the temperature of the bulk of the neutron star surface, $T_{\mathrm{surf}} < 0.1\,\mathrm{MK}$ (assuming the standard neutron star radius $R = 10\,\mathrm{km}$).

[8] According the pulsar catalog provided by the Australia Telescope National Facility; `http://www.atnf.csiro.au/research/pulsar`.

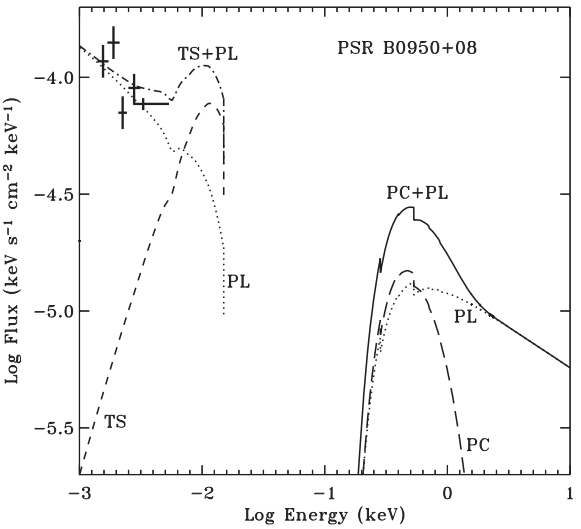

Fig. 9.11 Broadband spectrum of PSR B0950+08 for a two-component, polar caps (PC) plus power law (PL), model extrapolated in optical. *Crosses* show the optical fluxes. Radiation from the whole surface (TS) is also indicated

PSR J2043+2740

Analysis of the X-ray flux of PSR J2043+2740 ($P = 0.10\,\mathrm{s}$, $\tau_\mathrm{c} = 1.2\,\mathrm{Myr}$, $\dot{E} = 5.6 \times 10^{34}\,\mathrm{ergs\,s^{-1}}$) observed with *XMM*-Newton firmly showed, despite a low number of photons collected, that the pulsar's spectrum is very soft, with no emission detected at energies $E \gtrsim 2\,\mathrm{keV}$. A single power-law fit to these data yields a photon index $\Gamma \simeq 5$, that greatly exceeds a typical value $\Gamma = 1$–2 found in non-thermal radiation of a large sample of radio pulsars (including the examples discussed in this paper), with ages varying in a broad range, from about 1–20 Myr. This fact can be considered as an argument to disfavor a non-thermal interpretation of the pulsar's X-ray emission. Applying blackbody radiation to these X-ray data yields $T_\mathrm{bb}^\infty \simeq 0.9$ and $R_\mathrm{bb}^\infty \simeq 2.7\,\mathrm{km}$ (for $D = 1.8\,\mathrm{kpc}$), that could be suggestive that the X-ray emission originates from polar caps. However, this radius estimate is a factor of 5 larger than the theoretical prediction $R_\mathrm{pc}^* \simeq 0.5\,\mathrm{km}$. On the other hand, the fits with magnetized ($B \simeq 4 \times 10^{11}\,\mathrm{G}$) hydrogen atmosphere models gives the surface effective temperature $T_\mathrm{eff} \simeq 0.6\,\mathrm{MK}$ for the neutron star radius $R = 9\,\mathrm{km}$. The latter fit indicates that the detected X-ray emission most likely emerges from the bulk of the star's surface, with the bolometric luminosity $L_\mathrm{bol} \simeq 0.8 \times 10^{30}\,\mathrm{ergs\,s^{-1}}$. This result is rather unexpected because PSR J2043+2740 has the highest spin-down power among all known ordinary pulsars with $\tau_\mathrm{c} > 1\,\mathrm{Myr}$ and, hence, it should have been the strongest non-thermal emitter among old ordinary pulsars. A longer observation of this pulsar is required to provide more details on the properties of its thermal X-ray emission.

9.4.6 Millisecond Pulsars

Millisecond pulsars, with unique properties, represent an evolutionarily distinct group among radio pulsars. First of all, they possess very short and stable spin periods, $P \lesssim 0.05\,\mathrm{s}$ with $\dot{P} \lesssim 10^{-18}\,\mathrm{s\,s^{-1}}$, and low surface magnetic fields, $B \lesssim 10^{10}\,\mathrm{G}$. They are thought to be extremely old neutron stars ($\tau_c \sim 0.1$–$10\,\mathrm{Gyr}$) presumably spun up by angular momentum transfer in binary systems. X-ray detections have been reported for about 35 (nonaccreting) millisecond pulsars (of more than a hundred currently known). The majority of them are located in the globular cluster 47 Tuc and exhibit thermal X-rays most probably emitted from heated polar caps [7]. However, detailed spectral and timing information on X-ray emission has been obtained only for eight of the detected millisecond pulsars [90]. One half of them are non-thermally emitting pulsars. The bulk of X-rays from the other four objects originates from heated polar caps. These are PSRs J0030+0451, J2124−3358, J1024−0719 and J0437−4715, with similar characteristics of the detected X-ray flux. The latter is the nearest ($D = 140\,\mathrm{pc}$) and brightest millisecond pulsar, and its X-ray properties are discussed below.

PSR J0437−4715

Pulsed X-ray emission from this pulsar ($P = 5.8\,\mathrm{ms}$, $\tau_c = 6.5\,\mathrm{Gyr}$, $\dot{E} = 3.8 \times 10^{33}\,\mathrm{ergs\,s^{-1}}$) was discovered with ROSAT [2], and observations with *Chandra* and *XMM*-Newton have finally established its X-ray spectrum [89, 96]. The model describing the pulsar's X-ray flux consists of a thermal and no-thermal components. The thermal component is emitted from two identical polar caps covered with a (non-magnetic) hydrogen atmosphere and located at the poles of a magnetic dipole. As first proposed in [92], the polar caps of a millisecond pulsar would have a nonuniform temperature because low surface magnetic field does not prevent the energy (heat) released by relativistic particles from propagating along the surface to an area of a radius larger than the conventional estimate R^{*}_{pc}. The uniform temperature is approximated by a step-function mimicking a smaller and hotter polar cap "core" and a larger and colder "rim". The GR effects (redshift and gravitational bending) are accounted for in this interpretation. The thermal model, supplemented with a power-law component, fits well the X-ray emission detected from PSR J0437−4715 up to 10 keV and yields reasonable spectral parameters: $T^{\mathrm{core}}_{\mathrm{pc}} \simeq 1.4\,\mathrm{MK}$ and $T^{\mathrm{rim}}_{\mathrm{pc}} \simeq 0.5\,\mathrm{MK}$, $R^{\mathrm{core}}_{\mathrm{pc}} \simeq 0.4\,\mathrm{km}$ and $R^{\mathrm{rim}}_{\mathrm{pc}} \simeq 2.6\,\mathrm{km}$, with the total bolometric luminosity $L^{\mathrm{pc}}_{\mathrm{bol}} \simeq 1.8 \times 10^{30}\,\mathrm{ergs\,s^{-1}}$. The non-thermal component has a photon index $\Gamma \simeq 1.8$ and luminosity $L^{\mathrm{nonth}} \simeq 0.5 \times 10^{30}\,\mathrm{ergs\,s^{-1}}$. Figure 9.12 presents this model and the fit to the data on PSR J0437−4715 collected with *XMM*-Newton. Interestingly, PSR J0437−4715 was detected in UV/FUV with HST [30]. The shape of the inferred spectrum suggests thermal emission from the whole neutron star surface of a surprisingly high temperature of about 0.1 MK. A powerful

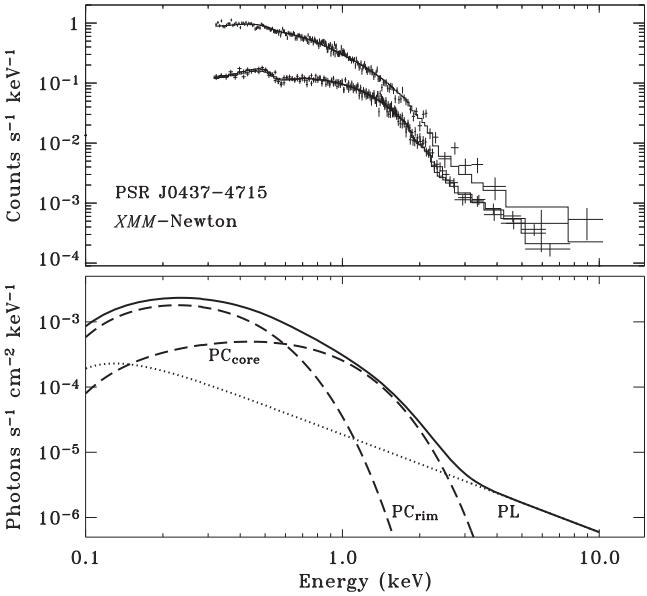

Fig. 9.12 X-ray spectrum of PSR J0437−4715 detected with different instruments onboard *XMM*-Newton (*crosses in the upper panel*) and fitted with a composite model, two-temperature ("core" and "rim") polar caps (PC) and power law (PL), shown in the lower panel

energy source (most likely, internal chemical and/or frictional heating) should be operating in a Gyr-old neutron star to keep its surface at such temperature.

X-ray emission from all four thermally emitting millisecond pulsars is pulsed, with pulsed fraction $f_{\rm p} \simeq 35$–50%. Such pulsed fraction can be produced only by intrinsically anisotropic radiation, that supports the assumption on presence of a hydrogen atmosphere on the surface of millisecond pulsars. The pulsed profiles of PSRs J0437−4715, J2124−3358, and J1024−0719 are rather similar in shape, with single broad pulses, whereas the light curve of PSR J0030+0451 exhibits two pulses per period indicating that the geometry of this pulsar (the angles ζ and α – see Fig. 9.3) is different from those of the three others. For example, in the framework of the conventional pulsar model with the magnetic dipole at the neutron star center, PSR J0030+0451 can be a nearly orthogonal rotator (i.e., $\zeta \simeq \alpha \simeq 90^\circ$) with two pulses in its light curve being due to contributions from two polar caps seen during the pulsar's rotation. For the others, the bulk of the detected X-ray flux is expected to come mostly from one polar cap. Importantly, as first demonstrated in [54, 92] on the X-ray emission of PSR J0437−4715 detected with ROSAT, analyzing pulsed emission with thermal polar cap models can put stringent constraints on the neutron star mass-to-radius ratio M/R if the star's geometry is known (e.g., from radio polarization data). This analysis was extended in [8] to model the temporal data on PSR J0437−4715 collected with *XMM*-Newton (see also Chap. 8).

9.4.7 Putative Pulsars: CXOU J061705.3+222127 (J0617) and RX J0007.0+7302 (J0007)

The compact source J0617 discovered in a short *Chandra* observation [46] is located within a bright X-ray comet-like nebula. Most likely, J0617 is a young, fast and energetic pulsar that powers this nebula. To firmly confirm this very plausible hypothesis, pulsations of emission from this object (in radio and/or X-rays) have to be detected yet. A longer *Chandra* observation of J0617 and the nebula provided more details on X-ray properties of the source and surrounding diffuse emission [13, 82]. The X-ray spectrum of J0617 reveals a thermal component which dominates at energies $E \lesssim 1.7$ keV. At higher energies, a non-thermal emission prevails. The fact that the spectrum of J0617 is very similar to those found in the young and powerful pulsars, J1119−6127, Vela, and B1706−44, strongly supports the assumption on this compact source being a neutron star and a pulsar. The detected spectrum can be equally well fitted with both blackbody plus power law and hydrogen atmosphere plus power law combinations. Applying magnetized atmosphere models interprets the thermal flux as emitted from the whole neutron surface of $T_{\rm eff} \simeq 0.8$ MK and radius $R = 10$ km (for $D = 1.5$ kpc), with $L_{\rm bol} \simeq 2.9 \times 10^{32}$ ergs s^{-1}, and yields the non-thermal spectrum of $\Gamma \simeq 1.2$ with $L^{\rm nonth} \simeq 0.2 \times 10^{32}$ ergs s^{-1}, about 15 times smaller than the thermal luminosity. The spectrum of J0617 fitted with this two-component model is presented in Fig. 9.13. It should be noted that, like in the case of Vela, using blackbody radiation instead of atmosphere models results in much steeper power-law component of $\Gamma \simeq 2.7$, that is not typical for non-thermal emission from radio pulsars. Hence, the interpretation involving the atmosphere model can be regarded as more preferable.

Another putative pulsar with a possible γ-ray counterpart and powering an X-ray nebula is the compact source J0007 at the center of the SNR CTA 1. As found in [76], its X-ray spectrum detected with *XMM*-Newton is well fitted with a magnetized hydrogen atmosphere model of the same parameters as those derived for J0617 (assuming $D = 1.4$ kpc), plus a power-law component of $\Gamma \simeq 1.6$ and $L^{\rm nonth} \simeq 0.5 \times 10^{32}$ ergs s^{-1}. Extrapolation of this power-law spectrum to high energies is consistent with the flux detected from the proposed γ-ray counterpart, strengthening the proposition that J0007 is a γ-ray emitting pulsar.

9.4.8 1E 1207.4−5209 (1E1207)

All objects presented in Sects. 9.4.1–9.4.7 are either radio pulsars or show other manifestations of the non-thermal activity. Below is briefly discussed a very interesting example of radio-quiet neutron stars emitting only thermal X-ray emission.

1E1207 belongs to the small group of currently seven CCOs known in SNRs (see Chap. 6 for a review). One of them, the CCO in the SNR RCW 103, is rather outstanding because it shows a highly variable X-ray flux and its emission is presumably powered by accretion from a companion in a close binary system with a

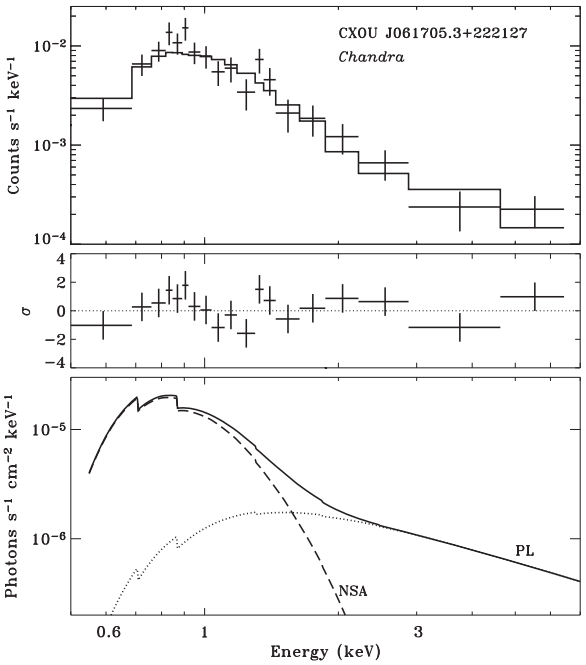

Fig. 9.13 Two-component, hydrogen magnetized atmosphere (NSA) model plus a power law (PL), fit to the X-ray spectrum of CXOU J061705.3+222127 detected with *Chandra* (*upper panel*). The *middle panel* shows residuals in the fit, whereas the *lower panel* presents the contributions (attenuated by interstellar absorption) from the thermal (*dashes*) and non-thermal (*dots*) components

$\sim$6.5-h orbital period. The other six CCOs have not shown any long-term variability of their thermal emission, characterized by blackbody temperatures $T_{\rm bb}^{\infty} \approx 2$–$5$ MK and emitting areas $R_{\rm bb}^{\infty} \approx 0.3$–$3$ km, and seem to be similar to each other. However, the spin periods of two objects, 1E1207 in the SNR PKS 1209−51/52 with $P = 0.42$ s [97] and CXOU J185238.6+004020 in the SNR Kes 79 with $P = 0.11$ s [18], make them distinct from the rest.

1E1207 is even more unique: it is the only known nonaccreting neutron star whose X-ray flux contains two firmly detected spectral features. Figure 9.14 presents the spectrum of 1E1207 with two absorption lines at about 0.7 and 1.4 keV discovered with *Chandra* [71]. Data on this CCO collected in a long *XMM*-Newton observation [6] suggested additional lines, at 2.1 and 2.8 keV, although the reality of these lines has been disputed [40]. First magnetized oxygen atmosphere models with a magnetic field $B \sim 10^{12}$ G [43] seem to be in apparent qualitative agreement with the X-ray spectrum of 1E1207. However, it has to be demonstrated yet whether these models could explain the observational data in the quantitative way. The timing analysis presented in [17] put an upper limit on the surface magnetic field, $B < 3.3 \times 10^{11}$ G, suggesting the interpretation of the spectral lines as electron cyclotron harmonics. In any case, regardless of what the true origin of these spectral lines is, they make 1E1207 one of the most important objects for astrophysics of

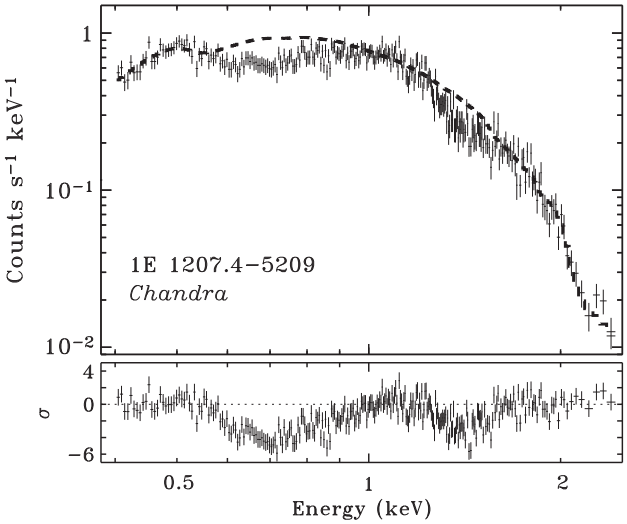

Fig. 9.14 *Upper panel*: Spectrum of 1E 1207.4−5209 detected with *Chandra* (*crosses*) vs. a featureless thermal model (*dashes*). *Lower panel*: Residuals between the observed and model spectra demonstrating the presence of the two absorption features in the X-ray emission of this object

neutron stars and physics of superdense matter because it provides an opportunity to measure the gravitational redshift at the neutron star surface and constrain the equation of state of the superdense matter in the neutron star interiors.

9.5 Concluding Remarks

This section completes the review with a brief discussion about what has been learned during the extensive studying of thermal emission from neutron stars.

Undoubtedly, a substantial progress has been made on the theoretical front. Best investigated models are non-magnetic atmospheres of various chemical compositions and magnetized fully-ionized hydrogen atmospheres. These models have been successfully applied to interpretation of thermal emission to a number of neutron stars, mainly, radio pulsars of different ages, including millisecond pulsars, and yielded reasonable neutron star parameters (surface temperatures and radii of emitting areas). In addition to the active pulsars, there is a group of neutron stars transiently accreting in X-ray binaries (e.g., Aquila X-1, KS 1731−260, Centaurus X−4, 4U 1608−522, MXB 1659−29, 4U 2129+47) whose X-ray emission in quiescence has been analyzed with use of atmosphere models [21, 44, 66, 68–70, 84, 85]. Although these objects are not isolated, their quiescent radiation is interpreted as emitted from the whole neutron star surface covered with a non-magnetic hydrogen atmosphere heated by energy released in pycnonuclear reactions of the compressed accreted material. Importantly, based on the results obtained on the

thermal emission from these objects, a new method for studying neutron stars internal structure and equation of state of the inner matter has been proposed in [87]. Also, as suggested in [67], the atmosphere models can be useful for distinguishing between transiently accreting neutron stars and black holes, in quiescence. First steps have been undertaken in modeling partially ionized atmosphere models with strong magnetic fields and different chemical compositions, as well as in modeling thermal emission from condensed neutron star surfaces, although both these types of models are still awaiting application to observational data.

Despite a lot of interesting and encouraging results obtained in modeling the thermal emission and applying these models to observational data, a number of problems remains to be solved. First of all, the approach based on two polarization modes currently used in magnetized atmosphere models is in fact inaccurate and inapplicable for a partially ionized plasma. To construct more advanced models, the problem of radiative transfer in strongly magnetized plasmas should be solved in terms of the four Stokes parameters, with use of the polarizability tensor constructed with aid of the Kramers–Kronig relations [9, 61]. Next, investigations of the structure of various atoms, molecules, and molecular chains in strong magnetic fields, as well as radiative transitions in these species [48], are necessary to construct magnetized atmosphere models of a next generation for different chemical compositions. Very interesting and important are the (virtually unknown) radiative properties of matter in superstrong magnetic fields, $B \gtrsim 10^{14}$ G, apparently found in AXPs and SGRs. More reliable models are required for radiative properties of non-ideal plasmas and condensed matter, as well as further investigations of phase transitions between different states of matter in such strong magnetic fields.

Not only the models of neutron star atmospheres and condensed surfaces require improvements. Analysis of observational data on thermal flux from neutron stars, especially temporal behavior of detected X-ray emission, shows that the idealized picture of a neutron star with a centered magnetic dipole and uniform surface temperature is oversimplification. Therefore, future computations of thermal emission from a neutron star applied to observational data should use realistic surface temperature distributions to reproduce *both spectral and temporal* properties of observed emission. In particular, the problem of temperature distribution over heated polar caps of millisecond pulsars is of a special importance because modeling pulsed thermal emission from these objects is a promising way to constrain neutron star mass-to-radius ratio. For that, more elaborated models of magnetospheric pulsed emission are required to disentangle non-thermal and thermal components.

Confronting the surface temperatures derived from observation data with theoretical models of neutron star thermal evolution [86, 91] indicates that the neutron star interiors are most probably superfluid and that these objects may have different masses (e.g., $M \simeq 1.47 M_\odot$ for Vela and Geminga, and $M \simeq 1.35 M_\odot$ for PSR B1055−52). But these results are quite uncertain because they are based on simplified spectral models and assumption that the characteristic age of a neutron star is its true age.

Next, thermal emission mechanisms operating in neutron stars are not completely understood yet, especially in colder objects. Only rather simple conclusions

could be drawn from the obtained results. It looks plausible that younger and hotter objects (this $\tau \simeq \tau_c \lesssim 50\,\mathrm{kyr}$ and $T_{\mathrm{surf}} \gtrsim 1\,\mathrm{MK}$) are indeed covered with a gaseous atmosphere, strongly ionized if comprised of hydrogen. To explain why the simple blackbody model fits well thermal radiation from colder neutron stars with strong magnetic fields, whereas atmosphere models do not provide reasonable parameters, one may suggest that cooling hydrogen-depleted neutron star envelopes undergo a phase transition, forming a condensed surface. But this assumption is challenged by very complicated temporal behavior of the thermal flux detected from many these objects – it can be hardly explained without invoking a strong anisotropy of surface radiation similar to that characteristic to the atmospheric radiation. Therefore, the parameters inferred from the blackbody spectral fits should be taken with caution. It also concerns the two-blackbody ("soft" and "hard") model suggested for the thermal phase-integrated spectra of the middle-aged pulsars. It is not clear whether the harder thermal component is real or it emerges because the simplified spectral models were used (e.g., this component is not required in the interpretation involving a power-law spectrum with a phase-dependent photon index; [26]).

There are even much more unanswered questions related to thermal radiation of neutron stars (concerning, for example, the nature of CCOs and connection between them and other types of neutron stars, the origin of spectral lines in thermal emission of a number of objects and why no features are present in spectra of other neutron stars with similar temperatures and magnetic field, etc.) To answer these questions, not only improved models are necessary but also a larger sample of neutron stars of various types observed in different energy ranges, from optical/UV to X-rays, is required. In particular, as shown in [28, 31], the UV/FUV range is very important for elucidating properties of thermal emission emerging from the whole neutron star surface. Contrary to the X-ray (Wien) part of the thermal emission whose shape is strongly affected by surface chemical composition and temperature inhomogeneities, the UV/FUV (Rayleigh–Jeans) tail, proportional to the product $[T_{\mathrm{surf}}R^2]$, can put tight constraints on the surface temperature. Hopefully, enough observational time will be allocated in future for studying these enigmatic objects, neutron stars.

References

1. C. Alcock, A.F. Illarionov, 1980, ApJ, **235**, 534
2. W. Becker, J. Trümper, 1993, Nature, **365**, 528
3. W. Becker, J. Trümper, 1997, A & A, **326**, 682
4. W. Becker, M.C. Weisskopf, A.F. Tennant, A. Jessner, J. Dyks, et al., 2004, ApJ, **615**, 908
5. V.G. Bezchastnov, G.G. Pavlov, Yu.A Shibanov, V.E. Zavlin, 1996, in *Gamma-ray Bursts*, ed. C. Kouveliotou, M. Briggs, G.J. Fishman, AIP Conf. Proc. 384, (New York: Woodbury), p. 907
6. G.F. Bignami, P.A. Caraveo, A. De Luca, S. Mereghetti, 2003, Nature, **423**, 725
7. S. Bogdanov, J.E. Grindlay, C.O. Heike, F. Camilo, P.C.C. Freire, et al., 2006, ApJ, **646**, 1104
8. S. Bogdanov, G.B. Rybicki, J.E. Grindlay, 2007, ApJ, **670**, 668
9. T. Bulik, G.G. Pavlov, 1995, ApJ, **469**, 373

10. P. Chang, L. Bildsten, 2004, ApJ, **605**
11. H.-Y. Chiu, E.E. Salpeter, 1964, Phys. Rev. Lett., **12**, 413
12. A. De Luca, P.A. Caraveo, S. Mereghetti, M. Negroni, G.F. Bignami, 2005, ApJ, **623**, 1051
13. B.M. Gaensler, S. Chatterjee, P.O. Slane, E. van Swalw, F. Camilo, et al., 2006, ApJ, **648**, 1037
14. B.T. Gänsicke, T.M. Braje, R.W. Romani, 2002, A&A, **386**, 1001
15. Yu.N. Gnedin, G.G. Pavlov, 1974, JETP, **38**, 903
16. M.E. Gonzalez, V.M. Kaspi, F. Camilo, B.M. Gaensler, M.J. Pivovaroff, 2005, ApJ, **630**, 489
17. E.V. Gotthelf, J.P. Halpern, 2007, ApJ, **664**, L35
18. E.V. Gotthelf, J.P. Halpern, F.D. Seward, 2005, ApJ, **627**, 390
19. G. Greenstein, G.J. Hartke, 1983, ApJ, **271**, 283
20. F. Haberl, 2007, Ap&SS, **308**, 181
21. C.O. Heinke, G.B. Rybicki, R. Narayan, J.E. Grindlay, 2006, ApJ, **664**, 1090
22. A. Hewish, S.J. Bell, J.D.H. Pilkington, P.F. Scott, R.A. Collins, 1968, Nature, **217**, 709
23. W.C.G. Ho, D. Lai, 2001, MNRAS, **327**, 1081
24. W.C.G. Ho, D. Lai, 2003, MNRAS, **338**, 233
25. W.C.G. Ho, D. Lai, A.Y. Potekhin, G. Chabrier, 2003, ApJ, **599**, 1293
26. M.S. Jackson, J.P. Halpern, 2006, ApJ, **633**, 1114
27. A.D. Kaminker, G.G. Pavlov, Yu.A. Shibanov, 1982, Ap&SS, **86**, 249
28. O.Y. Kargaltsev, G.G. Pavlov, 2007, Ap&SS, **308**, 287
29. O.Y. Kargaltsev, G.G. Pavlov, G.P. Garmire, 2006, ApJ, **636**, 406
30. O.Y. Kargaltsev, G.G. Pavlov, R.W. Romani, 2004, ApJ, **602**, 327
31. O.Y. Kargaltsev, G.G. Pavlov, V.E. Zavlin, R.W. Romani, 2005, ApJ, **625**, 307
32. V.M. Kaspi, 2004, in *Young Neutron Stars and Their Environments*, ed. F. Camilo, B.M. Gaensler, IAU Symp. 218 (San Francisco: ASP), p. 231
33. V.M. Kaspi, 2007, Ap&SS, **308**, 1
34. M. Kramer, A.G. Lyne, G. Hobbs, O. Löhmer, P. Carr, et al., 2003, ApJ, **593**, L31
35. D. Lai, E.E. Salpeter, 1997, ApJ, **491**, 270
36. K.E. McGowan, J.A. Kennea, S. Zane, F.A. Córdova, M. Cropper, et al., 2003, ApJ, **591**, 380
37. K.E. McGowan, S. Zane, M. Cropper, J.A. Kennea, F.A. Córdova, et al., 2004, ApJ, **600**, 343
38. K.E. McGowan, S. Zane, M. Cropper, W.T. Vestrand, C. Ho, 2006, ApJ, **639**, 377
39. D. Mihalas, 1978, *Stellar Atmospheres* (San Francisco: Freeman)
40. K. Mori, J.C. Chonko, C.J Hailey, 2005, **631**, 1082
41. K. Mori, C.J. Hailey, 2002, ApJ, **564**, 914
42. K. Mori, C.J. Hailey, 2006, ApJ, **648**, 1139
43. K. Mori, W.C.G. Ho, 2007, MNRAS, **377**, 905
44. M.A. Nowak, S. Heinz, M.C. Begelman, 2002, ApJ, **573**, 778
45. H. Ögelamn, 1995, in *The Lives of Neutron Stars*, ed. A. Alpar, U. Kilizóglu, J. van Paradijs (Dordrecht: Kluwer), p. 101
46. C.M. Olbert, C.R. Clearfield, N.E. Willams, J.W. Keohane, D.A. Frail, 2001, ApJ, **554**, L205
47. F. Özel, 2001, ApJ, **563**, 276
48. G.G. Pavlov, 1998, in *Atoms and Molucules in Strong External Fields*, ed. P. Schmelcher, W. Schweizer (New York: Plenum), p. 37
49. G.G. Pavlov, Yu.N. Gnedin, 1984, Astr. Space Phys. Rev., **3**, 197
50. G.G. Pavlov, P. Mészáros, 1993, ApJ, **416**, 752
51. G.G. Pavlov, Y.A. Potekhin, 1995, ApJ, **450**, 883
52. G.G. Pavlov, Yu.A. Shibanov, J. Ventura, V.E Zavlin, 1994, A&A, **289**, 847
53. G.G. Pavlov, Yu.A. Shibanov, V.E Zavlin, R.D. Meyer, 1995, in *The Lives of Neutron Stars*, ed. A. Alpar, U. Kilizóglu, J. van Paradijs (Dordrecht: Kluwer), p. 71
54. G.G. Pavlov, V.E Zavlin, 1997, ApJ, **490**, L91
55. G.G. Pavlov, V.E Zavlin, 2000, ApJ, **529**, 1011
56. G.G. Pavlov, V.E Zavlin, 2000, in *Highly Energetic Physical Processes and Mechanisms for Emission from Astrophysical Plasmas*, ed. P.C.H. Martens, S. Tsuruta, M.A. Weber (PASP: IAU Symp. 195), p. 103

57. G.G. Pavlov, V.E. Zavlin, D. Sanwal, 2002, in *Neutron Stars, Pulsars, and Supernova Remnants*, ed. W. Becker, H. Lesch, J. Trümper (MPE Report 278), p. 273
58. G.G. Pavlov, V.E. Zavlin, D. Sanwal, V. Burwitz, G.P. Garmire, 2001, ApJ, **552**, L129
59. K.R. Pechenick, C. Ftaclas, J.M. Cohen, 1983 ApJ, **274**, 846
60. J.A. Pons, F.M. Walter, J.M. Lattimer, M. Prakash, R. Neuhäuser, 2002, ApJ, **564**, 981
61. A.Y. Potekhin, D. Lai, G. Chabrier, W.C.G. Ho, 2004, ApJ, **612**, 1034
62. M. Rajagopal, R.W. Romani, 1996, ApJ, **461**, 327
63. M. Rajagopal, R.W. Romani, M.C. Miller, 1997, ApJ, **479**, 347
64. R.W. Romani, 1987, ApJ, **313**, 718
65. R.W. Romani, C.-Y. Ng, R. Dodson, W. Brisken, 2005, ApJ, **631**, 480
66. R.E. Rutledge, L. Bildsten, E.F. Brown, G.G. Pavlov, V.E. Zavlin, 1999, ApJ, **514**, 945
67. R.E. Rutledge, L. Bildsten, E.F. Brown, G.G. Pavlov, V.E. Zavlin, 2000, ApJ, **529**, 985 (2000)
68. R.E. Rutledge, L. Bildsten, E.F. Brown, G.G. Pavlov, V.E. Zavlin, 2001, ApJ, **551**, 921
69. R.E. Rutledge, L. Bildsten, E.F. Brown, G.G. Pavlov, V.E. Zavlin, 2001, ApJ, **559**, 1054
70. R.E. Rutledge, L. Bildsten, E.F. Brown, G.G. Pavlov, V.E. Zavlin, et al., 2002, ApJ, **580**, 413
71. D. Sanwal, G.G. Pavlov, V.E. Zavlin, M.A Teter, 2002, ApJ, **574**, L61
72. S. Shapiro, S. Teukolsky, 1983, *Black Holes, White Dwarfs, and Neutron Stars* (New York: Wiley)
73. Yu.A. Shibanov, V.E. Zavlin, G.G. Pavlov, J. Ventura, 1992, A&A, **266**, 313
74. Yu.A. Shibanov, V.E. Zavlin, 1995, Astron. Lett., **21**, 3
75. P. Slane, D.J. Helfand, E. van der Swaluw, S.S. Murray, 2004, ApJ, **616**, 403
76. P. Slane, E.R. Zimmerman, J.P. Hughes, F.D. Seward, B.M. Gaensler, et al., 2004, ApJ, **601**, 1045
77. A.F. Tennant, W. Becker, M. Juda, R.F. Elsner, J.J. Kolodziejczak, et al., 2001, ApJ, **554**, 173
78. S. Tsuruta, 1964, Ph.D. Thesis (New York: Columbia University)
79. R. Turolla, S. Zane, J.J. Drake, 2004, ApJ, **603**, 265
80. M. van Adelsberg, D. Lai, A.Y. Potekhin, P. Arras, 2005, ApJ, **628**, 902
81. M.H. van Kerkwijk, D.L. Kaplan, 2007, Ap&SS, **308**, 279
82. M.C. Weisskopf, M. Karovska, G.G. Pavlov, V.E. Zavlin, T. Clarke, 2007, Ap&SS, **308**, 151
83. K. Werner, J. Deetjen, 2000, in *Pulsar Astronomy – 2000 and Beyond*, ed. M. Kramer, N. Wex, R. Wielebinski (ASP Conf. Ser. 202), p. 623
84. R. Wijnands, G. Matteo, M. van der Klis, M. Mèndez, 2002, ApJ, **573**, L45
85. R. Wijnands, M. Nowak, J.M. Miller, J. Homan, S. Wachter, et al., 2003, ApJ, **594**, 952
86. D.G. Yakovlev, O.Y. Gnedin, M.E. Gusakov, A.D. Kaminker, K.P. Levenfish, et al., 2005, Nuc. Phys. A, **752**, 590
87. D.G. Yakovlev, K.P. Levenfish, P. Haensel, 2003, A&A, **407**, 265
88. S. Zane, R. Turolla, L. Stella, A. Treves, 2001, ApJ, **560**, 384
89. V.E. Zavlin, 2006, ApJ, **638**, 951
90. V.E. Zavlin, 2007, Ap&SS, **308**, 297
91. V.E. Zavlin, 2007, ApJ, **665**, L143
92. V.E. Zavlin, G.G. Pavlov, 1998, A&A, **329**, 583
93. V.E. Zavlin, G.G. Pavlov, 2002, in *Neutron Stars, Pulsars, and Supernova Remnants*, ed. W. Becker, H. Lesch, J. Trümper (MPE Report 278), p. 263
94. V.E. Zavlin, G.G. Pavlov, 2004, ApJ, **616**, 452
95. V.E. Zavlin, G.G. Pavlov, 2004, Mem. Soc. Astron. Ital., **75**, 458
96. V.E. Zavlin, G.G. Pavlov, D. Sanwal, R.N. Manchester, J. Trümper, et al., 2002, ApJ, **569**, 894
97. V.E. Zavlin, G.G. Pavlov, D. Sanwal, J. Trümper, 2000, ApJ, **540**, L25 (2000)
98. V.E. Zavlin, G.G. Pavlov, Yu.A. Shibanov, 1996, A&A, **315**, 141
99. V.E. Zavlin, G.G. Pavlov, Yu.A. Shibanov, F.J. Rogers, C.A. Iglesias, 1996, in *Röntgenstrahlung from the Universe*, ed. H.-U. Zimmermann, J. Trümper, H. Yorke (MPE Report 263), p. 209
100. V.E. Zavlin, G.G. Pavlov, Yu.A. Shibanov, J. Ventura, 1995, A&A, **297**, 441
101. V.E. Zavlin, Yu.A. Shibanov, G.G. Pavlov, 1995, Astron. Lett., **21**, 149

Chapter 10
Neutron Star Interiors and the Equation of State of Superdense Matter

Fridolin Weber, Rodrigo Negreiros, and Philip Rosenfield

10.1 Introduction

Neutron stars contain matter in one of the densest forms found in the Universe. This feature, together with the unprecedented progress in observational astrophysics, makes such stars superb astrophysical laboratories for a broad range of exciting physical studies. This paper gives an overview of the phases of dense matter predicted to make their appearance in the cores of neutron stars. Particular emphasis is put on the role of strangeness. Net strangeness is carried by hyperons, K-mesons, H-dibaryons, and strange quark matter, and may leave its mark in the masses, radii, moment of inertia, dragging of local inertial frames, cooling behavior, surface composition, and the spin evolution of neutron stars. These observables play a key role for the exploration of the phase diagram of dense nuclear matter at high baryon number density but low temperature, which is not accessible to relativistic heavy ion collision experiments.

Neutron stars are dense, neutron-packed remnants of stars that blew apart in supernova explosions. Many neutron stars form radio pulsars, emitting radio waves that appear from the Earth to pulse on and off like a lighthouse beacon as the star rotates at very high speeds. Neutron stars in X-ray binaries accrete material from a companion star and flare to life with a burst of X-rays. The most rapidly rotating, currently known neutron star is pulsar PSR J1748−2446ad, which rotates at a period of 1.39 ms (which corresponds to a rotational frequency of 719 Hz) [1]. It is followed by PSRs B1937+21 [2] and B1957+20 [3] whose rotational periods are 1.58 ms (633 Hz) and 1.61 ms (621 Hz), respectively. Finally, the recent discovery of X-ray burst oscillations from the neutron star X-ray transient XTE J1739−285 [4] could suggest that XTE J1739−285 contains the most rapidly rotating neutron star yet

F. Weber, R. Negreiros, and P. Rosenfield
Department of Physics, San Diego State University, 5500 Campanile Drive, San Diego, CA 92182-1233, USA
e-mail: fweber@sciences.sdsu.edu

W. Becker (ed.), *Neutron Stars and Pulsars,* Astrophysics and Space Science Library 357,

discovered. Measurements of radio pulsars and neutron stars in X-ray binaries comprise most of the neutron star observations. Improved data on isolated neutron stars (e.g., RX J1856.5-3754, PSR 0205+6449) are now becoming available, and future investigations at gravitational wave observatories focus on neutron stars as major potential sources of gravitational waves (see [5] for a recent overview). Depending on star mass and rotational frequency, the matter in the core regions of neutron stars may be compressed to densities that are up to an order of magnitude greater than the density of ordinary atomic nuclei. This extreme compression provides a high-pressure environment in which numerous subatomic particle processes are likely to compete with each other [6, 7]. The most spectacular ones stretch from the generation of hyperons and baryon resonances ($\Sigma, \Lambda, \Xi, \Delta$), to quark (u, d, s) deconfinement, to the formation of boson condensates (π^-, K^-, H-matter) [6–9, 11, 12] (see Fig. 10.1). In the framework of the strange matter hypothesis [15–17], it has also been suggested that 3-flavor strange quark matter – made of absolutely stable u, d, and s quarks – may be more stable than ordinary atomic nuclei. In the latter event, neutron stars should in fact be made of such matter rather than ordinary (confined) hadronic matter [18–20]. Another striking implication of the strange matter hypothesis is the possible existence of a new class of white-dwarfs-like strange stars (strange dwarfs) [21]. The quark matter in neutron stars, strange stars, or strange dwarfs ought to be in a color superconducting state [22–25]. This fascinating possibility has renewed tremendous interest in the physics of neutron stars and the physics

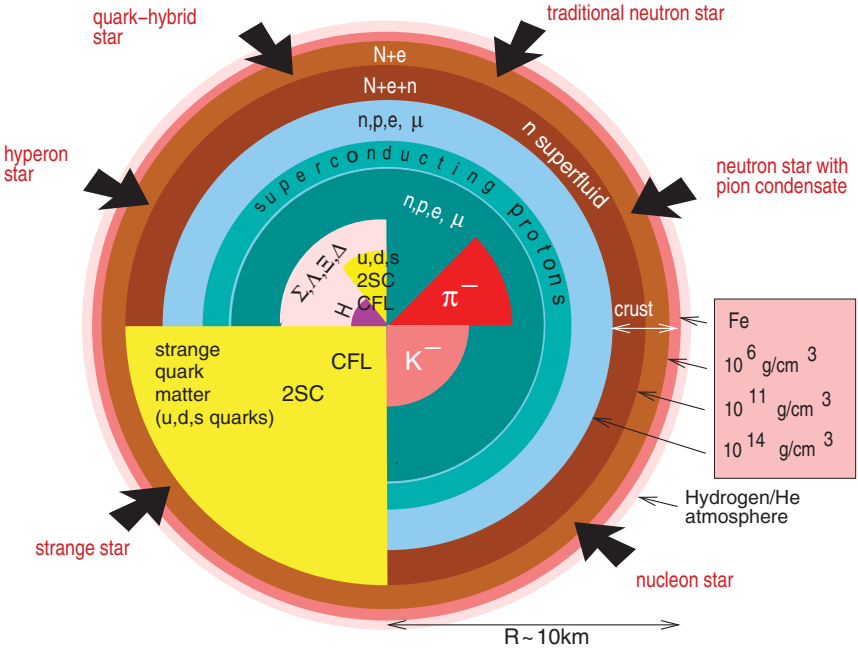

Fig. 10.1 Neutron star compositions predicted by theory

and astrophysics of (strange) quark matter [11,22,23]. This paper discusses the possible phases of ultra-dense nuclear matter expected to exist deep inside neutron stars and reviews selected models derived for the equation of state (eos) of such matter (see also [6–14]).

10.2 Neutron Star Masses

In 1939, Tolman, Oppenheimer and Volkoff performed the first neutron star calculations, assuming that such objects are entirely made of a gas of non-interacting relativistic neutrons [26, 27]. The eos of such a gas is extremely soft, i.e., very little additional pressure is gained with increasing density, as can be seen from Fig. 10.2, and predicts a maximum neutron star mass of just 0.7 $M_\odot$ (Fig. 10.3) at an unrealistically high density of 17 times the density of nuclear matter (Fig. 10.4). It is interesting to note that the inclusion of interactions among the neutrons increases the star's maximum mass from 0.7 $M_\odot$ to around 3 $M_\odot$ (Figs. 10.3 and 10.4). However, the radii of the latter are so big that mass shedding from the star's equator occurs at rotational frequencies that are considerably smaller than those observed for PSR J1748−2446ad, 716 Hz (1.39 ms) [1], or B1937+21, 630 Hz (1.58 ms) [2].

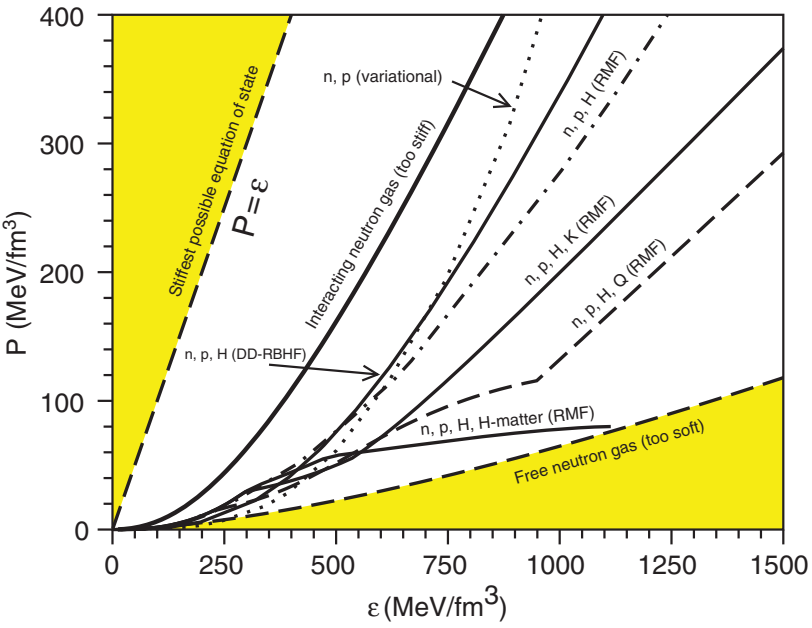

Fig. 10.2 Models for the equation of state (pressure vs. energy density) of neutron star matter [11]. The notation is as follows: RMF, relativistic mean-field model; DD-RBHF, density dependent relativistic Brueckner–Hartree–Fock model; n, neutrons; p, protons; H, hyperons, K, $K^-[u,\bar{s}]$ meson condensate; Q, u,d,s quarks; H-matter, H-dibaryon condensate

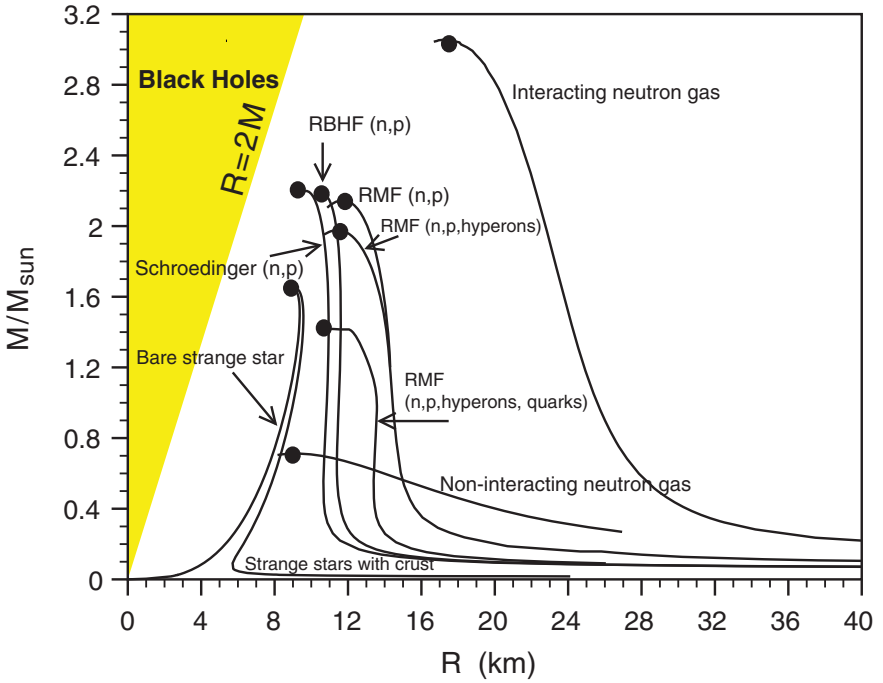

Fig. 10.3 Mass–radius relationship of neutron stars and strange stars [11]. The strange stars may be enveloped in a crust of ordinary nuclear material whose density is below neutron drip density [18, 62, 63]

An interacting neutron gas thus fails to accommodate the observed rapidly rotating neutron stars. The other extreme, a non-interacting relativistic neutron gas, fails too since it does not accommodate the Hulse–Taylor pulsar ($M = 1.44\ \mathrm{M}_\odot$) [28], and also conflicts with the average neutron star mass of $1.350 \pm 0.004\ \mathrm{M}_\odot$ derived by Thorsett and Chakrabarty [29] from observations of radio pulsar systems. More than that, recent observations indicate that neutron star masses may be as high as around $2\ \mathrm{M}_\odot$. Examples of such very heavy neutron stars are $M_{\mathrm{J0751+1807}} = 2.1 \pm 0.2\ \mathrm{M}_\odot$ [30], $M_{\mathrm{4U\,1636+536}} = 2.0 \pm 0.1\ \mathrm{M}_\odot$ [31], $M_{\mathrm{Vela\,X-1}} = 1.86 \pm 0.16\ \mathrm{M}_\odot$ [32], $M_{\mathrm{Cyg\,X-2}} = 1.78 \pm 0.23\ \mathrm{M}_\odot$ [33, 34]. Large masses have also been reported for the high-mass X-ray binary 4U 1700−37 and the compact object in the low-mass X-ray binary 2S0921−630, $M_{\mathrm{4U\,1700-37}} = 2.44 \pm 0.27\ \mathrm{M}_\odot$ [35] and $M_{\mathrm{2S0921-630}} = 2.0$–$4.3\ \mathrm{M}_\odot$ [36], respectively. The latter two objects may be either massive neutron stars or low-mass black holes with masses slightly higher than the maximum possible neutron star mass of $\sim 3\ \mathrm{M}_\odot$. This value follows from a general, theoretical estimate of the maximal possible mass of a stable neutron star as performed by Rhoades and Ruffini [37] on the basis that (1) Einstein's theory of general relativity is the correct theory of gravity, (2) the eos satisfies both the microscopic stability condition $\partial P/\partial \varepsilon \geq 0$ and the causality condition $\partial P/\partial \varepsilon \leq c^2$, and (3) that the eos below some matching density is known. From these assumptions, it follows

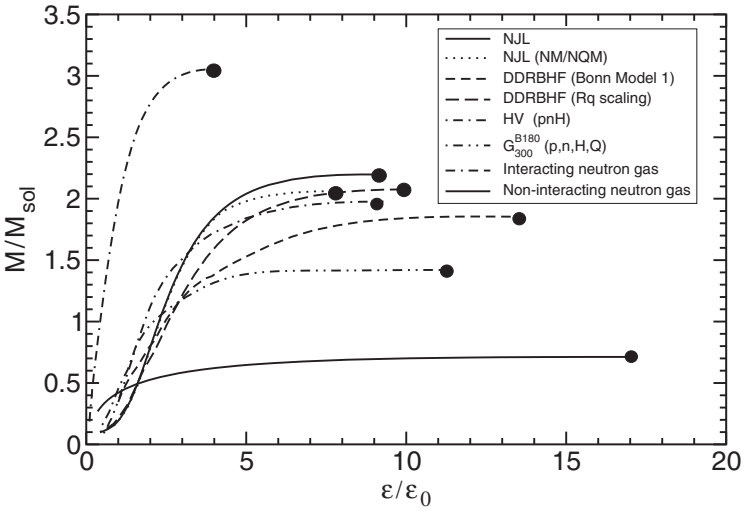

Fig. 10.4 Neutron star mass vs. central density (in units of nuclear matter density, $\varepsilon_0 = 140\,\mathrm{MeV\,fm^{-3}}$)

that the maximum mass of the equilibrium configuration of a neutron star cannot be larger than $3.2\,M_\odot$. This value increases to about $5\,M_\odot$ if one abandons the causality constraint $\partial P/\partial\varepsilon \leq c^2$ [38, 39], since it allows the eos to behave stiffer at asymptotically high nuclear densities. If either one of the two objects 4U 1700−37 or 2S0921−630 were a black hole, it would confirm the prediction of the existence of low-mass black holes [40]. Conversely, if these objects were massive neutron stars, their high masses would severely constrain the eos of dense nuclear matter.

10.3 Composition of Cold and Dense Neutron Star Matter

A vast number of models for the equation of state of neutron star matter has been derived in the literature over the years. These models can roughly be classified as follows:

- Thomas–Fermi based models [41, 42]
- Schroedinger-based models (e.g., variational approach, Monte Carlo techniques, hole line expansion (Brueckner theory), coupled cluster method, Green function method) [8, 43–48]
- Relativistic field-theoretical treatments: relativistic mean field (RMF), Hartree–Fock (RHF), standard Brueckner–Hartree–Fock (RBHF), density dependent RBHF (DD-RBHF) [49–54]
- Nambu–Jona–Lasinio (NJL) models [55–60]
- Chiral SU(3) quark mean field model [61]

A collection of equations of state computed for several of these models is shown in Fig. 10.2. Mass–radius relationships of neutron stars based on these equations of state are shown in Fig. 10.3. Any acceptable nuclear many-body calculation must correctly reproduce the bulk properties of nuclear matter at saturation density, $n_0 = 0.16\ \mathrm{fm}^{-3}$. These are the binding energy, $E/A = -16.0\,\mathrm{MeV}$, effective nucleon mass, $m_{\mathrm{N}}^{*} = 0.79\,m_{\mathrm{N}}$, incompressibility, $K \simeq 240\,\mathrm{MeV}$, and the symmetry energy, $a_{\mathrm{s}} = 32.5\,\mathrm{MeV}$.

10.3.1 Hyperons and Baryon Resonances

At the densities in the interior of neutron stars, the neutron chemical potential, μ^n, is likely to exceed the masses, modified by interactions, of Σ, Λ and possibly Ξ hyperons [64]. Hence, in addition to nucleons, neutron star matter may be expected to contain significant populations of strangeness carrying hyperons. The thresholds of the lightest baryon resonances ($\Delta^-, \Delta^0, \Delta^+, \Delta^{++}$) are not reached in relativistic mean-field (Hartree) calculations. This is different for many-body calculations performed at the relativistic Brueckner–Hartree–Fock level, where Δ's appear very abundantly [65]. In any event, pure neutron matter constitutes an excited state relative to hyperonic matter which, therefore, would quickly transform via weak reactions like

$$\mathrm{n} \rightarrow \mathrm{p} + \mathrm{e}^- + \bar{\nu}_e \tag{10.1}$$

to the lower energy state. The chemical potentials associated with reaction (10.1) in equilibrium obey the relation

$$\mu^n = \mu^p + \mu^{e^-}, \tag{10.2}$$

where $\mu^{\bar{\nu}_e} = 0$ since the mean free path of (anti) neutrinos is much smaller than the radius of neutron stars. Hence (anti) neutrinos do not accumulate inside neutron stars. This is different for hot proto-neutron stars [66]. Equation (10.2) is a special case of the general relation

$$\mu^\chi = B^\chi \mu^n - q^\chi \mu^{e^-}, \tag{10.3}$$

which holds in any system characterized by two conserved charges. These are in the case of neutron star matter electric charge, q^χ, and baryon number charge, B^χ. Application of (10.3) to the Λ hyperon ($B^\Lambda = 1$, $q^\Lambda = 0$), for instance, leads to

$$\mu^\Lambda = \mu^n. \tag{10.4}$$

Ignoring particle interactions, the chemical potential of a relativistic particle of type χ is given by

$$\mu^\chi = \omega(k_{F_\chi}) \equiv \sqrt{m_\chi^2 + k_{F_\chi}^2}\,, \tag{10.5}$$

where $\omega(k_{F_\chi})$ is the single-particle energy of the particle and k_{F_χ} its Fermi momentum. Substituting (10.5) into (10.4) leads to

$$k_{F_n} \geq \sqrt{m_\Lambda^2 - m_n^2} \simeq 3 \text{ fm}^{-1} \Rightarrow n \equiv \frac{{k_{F_n}}^3}{3\pi^2} \simeq 6n_0, \tag{10.6}$$

where $m_\Lambda = 1,116$ MeV and $m_n = 939$ MeV was used. That is, if interactions among the particles are ignored, neutrons are replaced with Λ's in neutron star matter at densities of around six times the density of nuclear matter. This value is reduced to around two times the density of nuclear matter by the inclusion of particle interactions [64]. Densities of just $\sim 2n_0$ are easily reached in the cores of neutron stars. Hence, in addition to nucleons and electrons, neutron stars may be expected to contain considerable populations of strangeness-carrying Λ hyperons, possibly accompanied by smaller populations of the charged states of the Σ and Ξ hyperons [64]. Depending on the star's mass, the total hyperon population can be very large [64], which is illustrated graphically in Figs. 10.5 and 10.6 for rotating neutron stars whose equation of state is computed in the framework of the relativistic

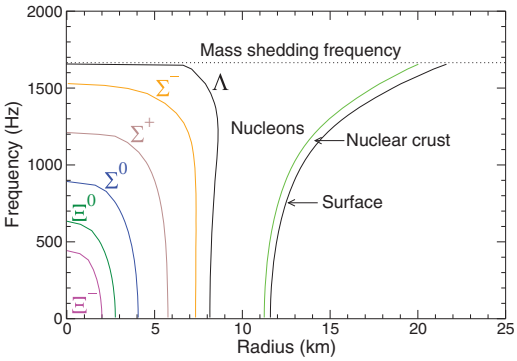

Fig. 10.5 Hyperon composition of a rotating neutron star in equatorial direction

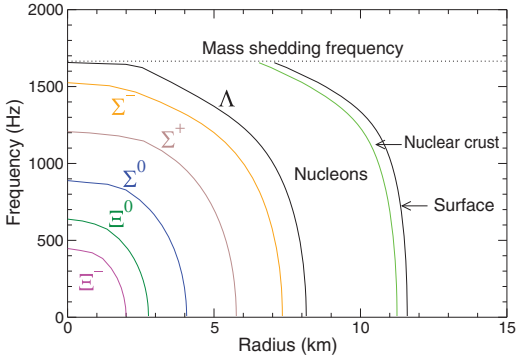

Fig. 10.6 Same as Fig. 10.5, but in polar direction

DD-RBHF formalism [52]. Aside from chemical equilibrium, the condition of electric charge neutrality of neutron star matter,

$$\sum_{\chi=p,\Sigma^{\pm},\Xi^{-},\Delta^{++},\ldots;e^{-},\mu^{-}} q^{\chi}\, k_{F_\chi}^3 \;+\; 3\pi^2 n^M\, \Theta(\mu^M - m_M) \equiv 0\,, \tag{10.7}$$

where M stands for π^- or K^- mesons, plays a key role for the particle composition of neutron star matter too. The last term in (10.7) accounts for the possible existence of either a π^- or a K^- meson condensate in neutron star matter, which will be discussed in more detail in Sect. 10.3.2. Before, however, we illustrate the importance of (10.2) and (10.7) for the proton-neutron fraction of neutron star matter. The beta decay and electron capture processes among nucleons, $\mathrm{n} \rightarrow \mathrm{p} + \mathrm{e}^- + \bar{\nu}_e$ and $\mathrm{p} + \mathrm{e}^- \rightarrow \mathrm{n} + \nu_e$ respectively, also known as nucleon direct Urca processes , are only possible in neutron star matter if the proton fraction exceeds a certain critical value [67]. Otherwise energy and momentum can not be conserved simultaneously for these reactions so that they are forbidden. For a neutron star made up of only nucleons and electrons, it is rather straightforward to show that the critical proton fraction is around 11%. This follows from $\mathbf{k}_{F_n} = \mathbf{k}_{F_p} + \mathbf{k}_{F_e}$ combined with the condition of electric charge neutrality of neutron star matter. The triangle inequality then requires for the magnitudes of the particle Fermi momenta $k_{F_n} \leq k_{F_p} + k_{F_e}$, and charge neutrality dictates that $k_{F_p} = k_{F_e}$. Substituting $k_{F_p} = k_{F_e}$ into the triangle inequality leads to $k_{F_n} \leq 2k_{F_p}$ so that for the particle number densities of neutrons and protons $n_n \leq 8n_p$. Expressed as a fraction of the system's total baryon number density, $n \equiv n_p + n_n$, one thus arrives at $n_p/n > 1/9 \simeq 0.11$, which is the figure quoted just above. Medium effects and interactions among the particles modify this value only slightly but the presence of muons raises it to about 0.15. Hyperons, which may exist in neutron star matter rather abundantly, produce neutrinos via direct Urca processes like $\Sigma^- \rightarrow \Lambda + \mathrm{e}^- + \bar{\nu}_e$ and $\Lambda + \mathrm{e}^- \rightarrow \Sigma^- + \nu_e$ [68]. The direct Urca processes are of key importance for neutron star cooling (see D. Page's contribution elsewhere in this volume). In most cases, the nucleon direct Urca process is more efficient than the ones involving hyperons [69, 70].

10.3.2 Meson Condensation

The condensation of negatively charged mesons in neutron star matter is favored because such mesons would replace electrons with very high Fermi momenta. Early estimates predicted the onset of a negatively charged pion condensate at around $2n_0$ (see, for instance, [71]). However, these estimates are very sensitive to the strength of the effective nucleon particle-hole repulsion in the isospin $T = 1$, spin $S = 1$ channel, described by the Landau Fermi-liquid parameter g', which tends to suppress the condensation mechanism. Measurements in nuclei tend to indicate that the repulsion is too strong to permit condensation in nuclear matter [72, 73]. In the mid 1980s, it was discovered that the in-medium properties of $K^-[u\bar{s}]$ mesons may be such that this meson rather than the π^- meson may condense in neutron star matter [74–76].

The condensation is initiated by the schematic reaction $e^- \rightarrow K^- + \nu_e$. If this reaction becomes possible in neutron star matter, it is energetically advantageous to replace the fermionic electrons with the bosonic K^- mesons. Whether or not this happens depends on the behavior of the K^- mass, $m^*_{K^-}$, in neutron star matter. Experiments which shed light on the properties of the K^- in nuclear matter have been performed with the Kaon Spectrometer (KaoS) and the FOPI detector at the heavy-ion synchrotron SIS at GSI [77–81]. An analysis of the early K^- kinetic energy spectra extracted from Ni+Ni collisions [77] showed that the attraction from nuclear matter would bring the K^- mass down to $m^*_{K^-} \simeq 200\,\mathrm{MeV}$ at densities $\sim 3\,n_0$. For neutron-rich matter, the relation $m^*_{K^-}/m_{K^-} \simeq 1 - 0.2n/n_0$ was established [82–84], with $m_K = 495\,\mathrm{MeV}$ the K^- vacuum mass. Values of around $m^*_{K^-} \simeq 200$ MeV may be reached by the electron chemical potential, μ^e, in neutron star matter [7, 64] so that the threshold condition for the onset of K^- condensation, $\mu^e = m^*_K$ might be fulfilled for sufficiently dense neutron stars, provided other negatively charged particles (Σ^-, Δ^-, d and s quarks) are not populated first and prevent the electron chemical potential from increasing with density.

We also note that K^- condensation allows the conversion reaction $n \rightarrow p + K^-$. By this conversion the nucleons in the cores of neutron stars can become half neutrons and half protons, which lowers the energy per baryon of the matter [85]. The relative isospin symmetric composition achieved in this way resembles the one of atomic nuclei, which are made up of roughly equal numbers of neutrons and protons. Neutron stars are therefore referred to, in this picture, as nucleon stars. The maximum mass of such stars has been calculated to be around 1.5 $M_\odot$ [86]. Consequently, the collapsing core of a supernova, e.g., 1987A, if heavier than this value, should go into a black hole rather than forming a neutron star, as pointed out by Brown et al. [40, 82, 83]. This would imply the existence of a large number of low-mass black holes in our galaxy [40]. Thielemann and Hashimoto [87] deduced from the total amount of ejected ^{56}Ni in supernova 1987A a neutron star mass range of 1.43–1.52 $M_\odot$. If the maximum neutron star mass should indeed be in this mass range ($\sim$1.5 $M_\odot$), the existence of heavy neutron stars with masses around 2 $M_\odot$ (Sect. 10.2) would be ruled out. Lastly, we mention that meson condensates lead to neutrino luminosities which are considerably enhanced over those of normal neutron star matter. This would speed up neutron star cooling considerably [70, 86].

10.3.3 H-Matter and Exotic Baryons

A novel particle that could be of relevance for the composition of neutron star matter is the H-dibaryon (H=$([ud][ds][su])$), a doubly strange six-quark composite with spin and isospin zero, and baryon number two [88]. Since its first prediction in 1977, the H-dibaryon has been the subject of many theoretical and experimental studies as a possible candidate for a strongly bound exotic state. In neutron star matter, which may contain a significant fraction of Λ hyperons, the Λ's could combine to form H-dibaryons, which could give way to the formation of H-dibaryon matter at

densities somewhere above $\sim 4\,n_0$ [89–91]. If formed in neutron stars, however, H-matter appears to unstable against compression which could trigger the conversion of neutron stars into hypothetical strange stars [90, 92, 93].

Another particle, referred to as exotic baryon, of potential relevance for neutron stars, could be the pentaquark , $\Theta^+([ud]^2\bar{s})$, with a predicted mass of 1,540 MeV. The pentaquark, which carries baryon number one, is a hypothetical subatomic particle consisting of a group of four quarks and one anti-quark (compared to three quarks in normal baryons and two in mesons), bound by the strong color-spin correlation force (attraction between quarks in the color $\bar{\mathbf{3}}_c$ channel) that drives color superconductivity [94, 95]. The pentaquark decays according to $\Theta^+(1540) \rightarrow K^+[\bar{s}u] + n[udd]$ and thus has the same quantum numbers as the K^+n. The associated reaction in chemically equilibrated matter would imply $\mu^{\Theta^+} = \mu^{K^+} + \mu^n$.

10.3.4 Quark Deconfinement

It has been suggested already many decades ago [96–103] that the nucleons may melt under the enormous pressure that exists in the cores of neutron stars, creating a new state of matter know as quark matter. From simple geometrical considerations it follows that for a characteristic nucleon radius of $r_N \sim 1$ fm, nucleons may begin to touch each other in nuclear matter at densities around $(4\pi r_N^3/3)^{-1} \simeq 0.24\ \mathrm{fm}^{-3} = 1.5\,n_0$, which is less than twice the density of nuclear matter. This figure increases to $\sim 11\,n_0$ for a nucleon radius of $r_N = 0.5$ fm. One may thus speculate that the hadrons of neutron star matter begin to dissolve at densities somewhere between around 2–10 n_0, giving way to unconfined quarks. Depending on rotational frequency and neutron star mass, densities greater than two to three times n_0 are easily reached in the cores of neutron stars so that the neutrons and protons in the cores of neutron stars may indeed be broken up into their quark constituents [6, 7, 11, 104]. More than that, since the mass of the strange quark is only $m_s \sim 150$ MeV, high-energetic up and down quarks will readily transform to strange quarks at about the same density at which up and down quark deconfinement sets in. Thus, if quark matter exists in the cores of neutron stars, it should be made of the three lightest quark flavors. A possible astrophysical signal of quark deconfinement in the cores of neutron stars was suggested in [105]. The remaining three quark flavors (charm, top, bottom) are way to massive to be created in neutron stars. For instance, the creation of charm quark requires a density greater than 10^{17} g cm^{-3}, which is around 100 times greater than the density reached in neutron stars. A stability analysis of stars with a charm quark population reveals that such objects are unstable against radial oscillations and, thus, can not exist stably in the universe [7, 11]. The same is true for ultra-compact stars with unconfined populations of top and bottom quarks, since the pulsation eigen-equations are of Sturm-Liouville type.

The phase transition from confined hadronic (H) matter to deconfined quark (Q) matter is characterized by the conservation of baryon charge and electric charge.

The Gibbs condition for phase equilibrium then is that the two associated chemical potentials, μ^n and μ^e, and the pressure in the two phases be equal [6, 104],

$$P_{\rm H}(\mu^n,\mu^e,\{\chi\},T) = P_{\rm Q}(\mu^n,\mu^e,T)\,, \tag{10.8}$$

The quantity $P_{\rm H}$ denotes the pressure of hadronic matter computed for a given hadronic Lagrangian $\mathcal{L}_{\rm M}(\{\chi\})$, where $\{\chi\}$ denotes the field variables and Fermi momenta that characterize a solution to the field equations of confined hadronic matter,

$$(i\gamma^\mu\partial_\mu - m_\chi)\psi_\chi(x) = \sum_{M=\sigma,\omega,\pi,\ldots} \Gamma_{M\chi} M(x)\,\psi_\chi(x)\,, \tag{10.9}$$

$$(\partial^\mu\partial_\mu + m_\sigma^2)\sigma(x) = \sum_{\chi=p,n,\Sigma,\ldots} \Gamma_{\sigma\chi}\,\bar\psi_\chi(x)\psi_\chi(x)\,, \tag{10.10}$$

plus additional equations for the other meson fields ($M = \omega,\pi,\rho,\ldots$). The pressure of quark matter, $P_{\rm Q}$, is obtainable from the bag model [106,107]. The quark chemical potentials $\mu^u,\ \mu^d,\ \mu^s$ are related to the baryon and charge chemical potentials as

$$\mu^u = \frac{1}{3}\,\mu^n - \frac{2}{3}\,\mu^e\,, \qquad \mu^d = \mu^s = \frac{1}{3}\,\mu^n + \frac{1}{3}\,\mu^e\,. \tag{10.11}$$

Equation (10.8) is to be supplemented with the two global relations for conservation of baryon charge and electric charge within an unknown volume V containing A baryons. The first one is given by

$$n \equiv \frac{A}{V} = (1-\eta)\,n_{\rm H}(\mu^n,\mu^e,T) + \eta\,n_{\rm Q}(\mu^n,\mu^e,T)\,, \tag{10.12}$$

where $\eta \equiv V_{\rm Q}/V$ denotes the volume proportion of quark matter, $V_{\rm Q}$, in the unknown volume V, and $n_{\rm H}$ and $n_{\rm Q}$ are the baryon number densities of hadronic matter and quark matter. Global neutrality of electric charge within the volume V can be written as

$$0 = \frac{Q}{V} = (1-\eta)\,q_{\rm H}(\mu^n,\mu^e,T) + \eta\,q_{\rm Q}(\mu^n,\mu^e,T) + q_{\rm L}\,, \tag{10.13}$$

with q_i the electric charge densities of hadrons, quarks, and leptons. For a given temperature, T, (10.8)–(10.13) serve to determine the two independent chemical potentials and the volume V for a specified volume fraction η of the quark phase in equilibrium with the hadronic phase. After completion $V_{\rm Q}$ is obtained as $V_{\rm Q} = \eta V$. Because of (10.8) through (10.13) the chemical potentials depend on the proportion η of the phases in equilibrium, and hence so also all properties that depend on them, i.e., the energy densities, baryon and charge densities of each phase, and the common pressure. For the mixed phase, the volume proportion of quark matter varies from $0 \le \eta \le 1$ and the energy density is the linear combination of the two phases [6, 104],

$$\varepsilon = (1-\eta)\,\varepsilon_{\rm H}(\mu^n,\mu^e,\{\chi\},T) + \eta\,\varepsilon_{\rm Q}(\mu^n,\mu^e,T)\,. \tag{10.14}$$

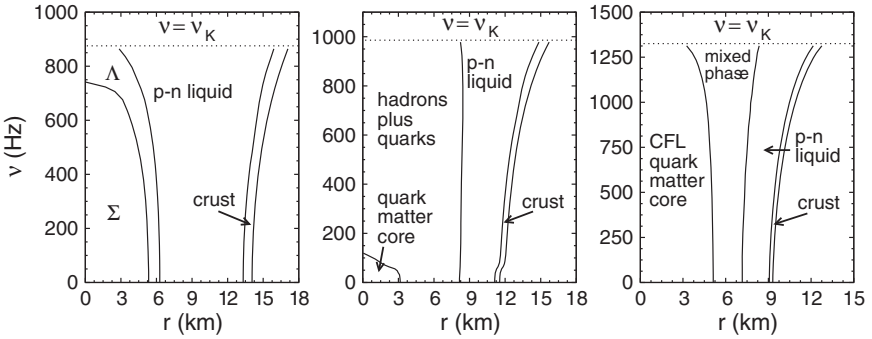

Fig. 10.7 Dependence of neutron star composition on spin frequency, ν, for three sample compositions (*left*: hyperon composition, *middle*: quark-hybrid composition, *right*: quark-hybrid composition with quark matter in the color-flavor locked (CFL) phase [108]). The non-rotating stellar mass in each case is 1.4 $M_\odot$. ν_K denotes the Kepler (mass-shedding) frequency, which sets an absolute limit on stable rotation

Hypothetical neutron star compositions computed along the lines described above are shown in Fig. 10.7. Possible astrophysical signals associated with quark deconfinement, the most striking of which being "backbending" of isolated pulsars, are discussed in [6, 7, 11, 109, 110].

10.3.5 Color-Superconductivity

There has been much recent progress in our understanding of quark matter, culminating in the discovery that if quark matter exists it ought to be in a color superconducting state [22–25]. This is made possible by the strong interaction among the quarks which is very attractive in some channels. Pairs of quarks are thus expected to form Cooper pairs very readily. Since pairs of quarks cannot be color-neutral, the resulting condensate will break the local color symmetry and form what is called a color superconductor. The phase diagram of such matter is expected to be very complex [22, 23]. The complexity is caused by the fact that quarks come in three different colors, different flavors, and different masses. Moreover, bulk matter is neutral with respect to both electric and color charge, and is in chemical equilibrium under the weak interaction processes that turn one quark flavor into another. To illustrate the condensation pattern briefly, we note the following pairing ansatz for the quark condensate [111],

$$\langle \psi^{\alpha}_{f_a} C\gamma_5 \psi^{\beta}_{f_b} \rangle \sim \Delta_1 \varepsilon^{\alpha\beta 1}\varepsilon_{f_a f_b 1} + \Delta_2 \varepsilon^{\alpha\beta 2}\varepsilon_{f_a f_b 2} + \Delta_3 \varepsilon^{\alpha\beta 3}\varepsilon_{f_a f_b 3}\,, \qquad (10.15)$$

where $\psi^{\alpha}_{f_a}$ is a quark of color $\alpha = (r, g, b)$ and flavor $f_a = (\mathrm{u,d,s})$. The condensate is a Lorentz scalar, antisymmetric in Dirac indices, antisymmetric in color, and thus antisymmetric in flavor. The gap parameters Δ_1, Δ_2 and Δ_3 describe d–s, u–s and

u–d quark Cooper pairs, respectively. The following pairing schemes have emerged. At asymptotic densities ($m_s \to 0$ or $\mu \to \infty$) the ground state of QCD with a vanishing strange quark mass is the color-flavor locked (CFL) phase (color-flavor locked quark pairing), in which all three quark flavors participate symmetrically. The gaps associated with this phase are

$$\Delta_3 \simeq \Delta_2 = \Delta_1 = \Delta\,, \tag{10.16}$$

and the quark condensates of the CFL phase are approximately of the form

$$\langle \psi^{\alpha}_{f_a} C\gamma_5 \psi^{\beta}_{f_b} \rangle \sim \Delta\, \varepsilon^{\alpha\beta X} \varepsilon_{f_a f_b X}\,, \tag{10.17}$$

with color and flavor indices all running from 1 to 3. Since $\varepsilon^{\alpha\beta X}\varepsilon_{f_a f_b X} = \delta^{\alpha}_{f_a}\delta^{\beta}_{f_b} - \delta^{\alpha}_{f_b}\delta^{\beta}_{f_a}$ one sees that the condensate (10.17) involves Kronecker delta functions that link color and flavor indices. Hence the notion color-flavor locking. The CFL phase has been shown to be electrically neutral without any need for electrons for a significant range of chemical potentials and strange quark masses [112]. If the strange quark mass is heavy enough to be ignored, then up and down quarks may pair in the two-flavor superconducting (2SC) phase. Other possible condensation patterns are CFL-K^0 [113], CFL-K^+ and CFL-$\pi^{0,-}$ [114], gCFL (gapless CFL phase) [111], 1SC (single-flavor-pairing) [111, 115, 116], CSL (color-spin locked phase) [117], and the LOFF (crystalline pairing) [118–120] phase, depending on m_s, μ, and electric charge density. Calculations performed for massless up and down quarks and a very heavy strange quark mass ($m_s \to \infty$) agree that the quarks prefer to pair in the two-flavor superconducting (2SC) phase where

$$\Delta_3 > 0\,, \quad \text{and} \quad \Delta_2 = \Delta_1 = 0\,. \tag{10.18}$$

In this case the pairing ansatz (10.15) reduces to

$$\langle \psi^{\alpha}_{f_a} C\gamma_5 \psi^{\beta}_{f_b} \rangle \propto \Delta\, \varepsilon_{ab}\varepsilon^{\alpha\beta 3}\,. \tag{10.19}$$

Here the resulting condensate picks a color direction (three or blue in the example (10.19) above), and creates a gap Δ at the Fermi surfaces of quarks with the other two out of three colors (red and green). The gapless CFL phase (gCFL) may prevail over the CFL and 2SC phases at intermediate values of m_s^2/μ with gaps given obeying the relation $\Delta_3 > \Delta_2 > \Delta_1 > 0$. For chemical potentials that are of astrophysical interest, $\mu < 1{,}000\,\text{MeV}$, the gap is between 50 and 100 MeV. The order of magnitude of this result agrees with calculations based on phenomenological effective interactions [25,121] as well as with perturbative calculations for $\mu > 10\,\text{GeV}$ [122]. We also note that superconductivity modifies the equation of state at the order of $(\Delta/\mu)^2$ [123, 124], which is even for such large gaps only a few percent of the bulk energy. Such small effects may be safely neglected in present determinations of models for the equation of state of quark-hybrid stars . There has been much recent work on how color superconductivity in neutron stars could affect their properties [22, 23, 118, 125–127]. These studies reveal that possible signatures include

the cooling by neutrino emission, the pattern of the arrival times of supernova neutrinos, the evolution of neutron star magnetic fields, rotational stellar instabilities, and glitches in rotation frequencies.

10.4 Strange Quark Matter

It is most intriguing that for strange quark matter made of more than a few hundred up, down, and strange quarks, the energy of strange quark matter may be well below the energy of nuclear matter [15–17], $E/A = 930\,\mathrm{MeV}$, which gives rise to new and novel classes of strange matter objects, ranging from strangelets at the low baryon-number end to strange stars at the high baryon number end [7, 11, 18, 20, 128]. A simple estimate indicates that for strange quark matter $E/A = 4B\pi^2/\mu^3$, so that bag constants of $B = 57\,\mathrm{MeV\,fm^{-3}}$ (i.e., $B^{1/4} = 145\,\mathrm{MeV}$) and $B = 85\,\mathrm{MeV\,fm^{-3}}$ ($B^{1/4} = 160\,\mathrm{MeV}$) would place the energy per baryon of such matter at $E/A =$ 829 MeV and 915 MeV, respectively, which correspond obviously to strange quark matter which is absolutely bound with respect to nuclear matter [20, 129].

10.4.1 Nuclear Crust on Strange Stars

Strange quark matter is expected to be a color superconductor which, at extremely high densities, should be in the CFL phase [22, 23]. This phase is rigorously electrically neutral with no electrons required [112]. For sufficiently large strange quark masses, however, the low density regime of strange quark matter is rather expected to form other condensation patterns (e.g., 2SC, CFL-K^0, CFL-K^+, CFL-$\pi^{0,-}$) in which electrons are present [22, 23]. The presence of electrons causes the formation of an electric dipole layer on the surface of strange matter, with huge electric fields on the order of $10^{19}\,\mathrm{V\,cm^{-1}}$, which enables strange quark matter stars to be enveloped in nuclear crusts made of ordinary atomic matter [18, 19, 63, 131].[1] The maximal possible density at the base of the crust (inner crust density) is determined by neutron drip, which occurs at about $4 \times 10^{11}\,\mathrm{g\,cm^{-3}}$ or somewhat below [63]. The eos of such a system is shown in Fig. 10.8. Sequences of compact strange stars with and without (bare) nuclear crusts are shown in Fig. 10.3. Since the nuclear crust is gravitationally bound to the quark matter core, the mass–radius relationship of strange stars with crusts resembles the one of neutron stars and even that of white dwarfs [21]. Bare strange stars obey $M \propto R^3$ because the mass density of quark matter is almost constant inside strange stars.

[1] Depending on the surface tension of blobs of strange matter and screening effects, a heterogeneous crust comprised of blobs of strange quark matter embedded in an uniform electron background may exist in the surface region of strange stars [132]. This heterogeneous strange star surface would have a negligible electric field which would make the existence of an ordinary nuclear crust, which requires a very strong electric field, impossible.

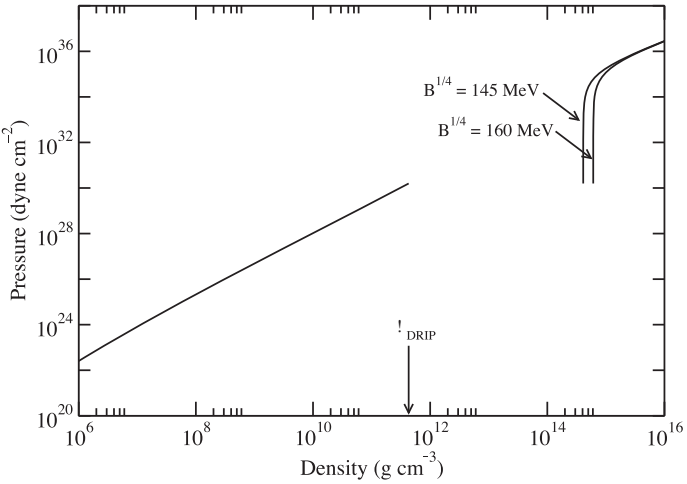

Fig. 10.8 Illustration of the eos of strange stars with nuclear crusts (from [130])

10.4.2 Strange Dwarfs

For many years only rather vague tests of the theoretical mass–radius relationship of white dwarfs were possible. Recently the quality and quantity of observational data on the mass–radius relation of white dwarfs has been reanalyzed and profoundly improved by the availability of Hipparcos parallax measurements of several white dwarfs [133]. In that work Hipparcos parallaxes were used to deduce luminosity radii for 10 white dwarfs in visual binaries of common proper-motion systems as well as 11 field white dwarfs. Complementary HST observations have been made to better determine the spectroscopy for Procyon B [134] and pulsation of G226−29 [135]. Procyon B at first appeared as a rather compact star which, however, was later confirmed to lie on the normal mass–radius relation of white dwarfs. Stars like Sirius B and 40 Erin B, fall nicely on the expected mass–radius relation too. Several other stars of this sample (e.g., GD 140, G156−64, EG 21, EG 50, G181−B5B, GD 279, WD2007−303, G238−44) however appear to be unusually compact and thus could be strange dwarf candidates [136]. The situation is graphically summarized in Fig. 10.9.

10.4.3 Surface Properties of Strange Matter

The electrons surrounding strange quark matter are held to quark matter electrostatically. Since neither component, electrons and quark matter, is held in place gravitationally, the Eddington limit to the luminosity that a static surface may emit does not apply, and thus the object may have photon luminosities much greater than $10^{38}\,\mathrm{erg\,s^{-1}}$. It was shown by Usov [137] that this value may be exceeded

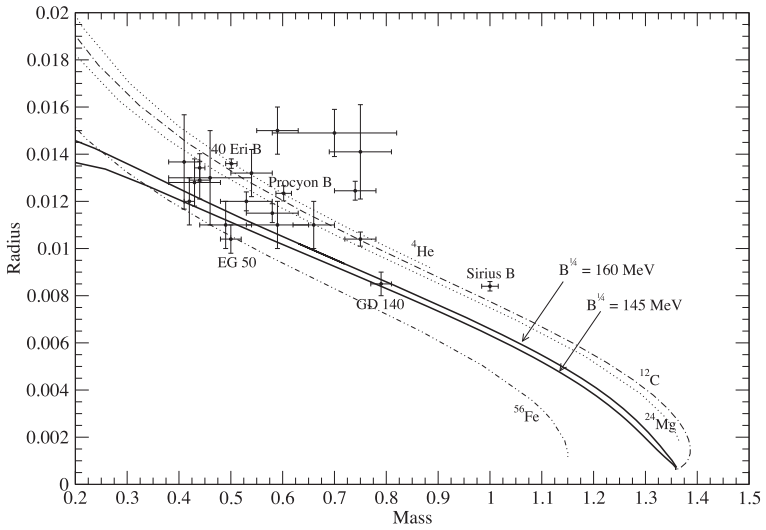

Fig. 10.9 Comparison of the theoretical mass–radius relationships of strange dwarfs (*solid curves*) and normal white dwarfs [130]. Radius and mass are in units of $R_\odot$ and $M_\odot$, respectively

by many orders of magnitude by the luminosity of e^+e^- pairs produced by the Coulomb barrier at the surface of a hot strange star. For a surface temperature of $\sim 10^{11}$ K, the luminosity in the outflowing pair plasma was calculated to be as high as $\sim 3 \times 10^{51}$ erg s^{-1}. Such an effect may be a good observational signature of bare strange stars [137–140]. If the strange star is enveloped by a nuclear crust however, which is gravitationally bound to the strange star, the surface made up of ordinary atomic matter would be subject to the Eddington limit. Hence the photon emissivity of such a strange star would be the same as for an ordinary neutron star. If quark matter at the stellar surface is in the CFL phase the process of e^+e^- pair creation at the stellar quark matter surface may be turned off, since cold CFL quark matter is electrically neutral so that no electrons are required and none are admitted inside CFL quark matter [112]. This may be different for the early stages of a hot CFL quark star [141].

10.5 Proto Neutron Star Matter

Here we take a brief look at the composition of proto neutron star matter. The composition is determined by the requirements of charge neutrality and equilibrium under the weak processes, $B_1 \rightarrow B_2 + l + \bar{\nu}_l$ and $B_2 + l \rightarrow B_1 + \nu_l$, where B_1 and B_2 are baryons, and l is a lepton, either an electron or a muon. For standard neutron star matter, where the neutrinos have left the system, these two requirements imply that $Q = \sum_i q_i n_{B_i} + \sum_{l=e,\mu} q_l n_l = 0$ (electric charge neutrality) and $\mu_{B_i} = b_i \mu_n - q_i \mu_l$ (chemical equilibrium), where $q_{i/l}$ denotes the electric charge

density of a given particle, and n_{B_i} (n_l) is the baryon (lepton) number density. The subscript i runs over all the baryons considered. The symbol μ_{B_i} refers to the chemical potential of baryon i, b_i is the particle's baryon number, and q_i is its charge. The chemical potential of the neutron is denoted by μ_n. When the neutrinos are trapped, as it is the case for proto-neutron star matter, the chemical equilibrium condition is altered to $\mu_{B_i} = b_i\mu_n - q_i(\mu_l - \mu_{\nu_l})$ and $\mu_e - \mu_{\nu_e} = \mu_\mu - \mu_{\nu_\mu}$, where μ_{ν_l} is the chemical potential of the neutrino ν_l. In proto-neutron star matter, the electron lepton number $Y_L = (n_e + n_{\nu_e})/n_B$ is initially fixed at a value of around $Y_{L_e} = Y_e + Y_{\nu_e} \simeq 0.3 - 0.4$ as suggested by gravitational collapse calculations of massive stars. Also, because no muons are present when neutrinos are trapped, the constraint $Y_{L_\mu} = Y_\mu + Y_{\nu_m u} = 0$ can be imposed. Figures 10.10 and 10.11 show sample compositions of proto-neutron star matter and standard neutron star matter (no neutrinos) computed for the relativistic mean-field approximation. The presence of the Δ particle in (proto) neutron star matter at finite temperature is striking. This particle is generally absent in cold neutron star matter treated in the relativistic mean-field approximation [6, 7, 143].

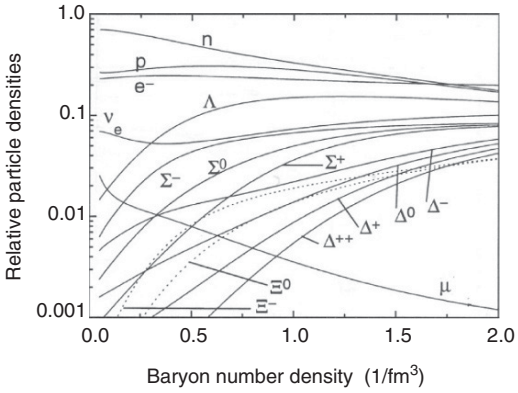

Fig. 10.10 Composition of hot ($T = 40$ MeV) proto-neutron star matter for $Y_L = 0.3$ [142]

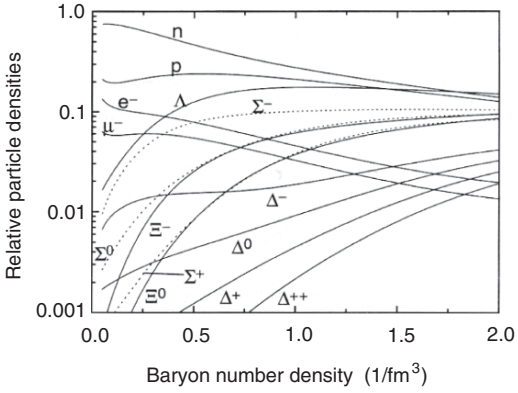

Fig. 10.11 Same as Fig. 10.10, but for standard neutron star matter [142]

10.6 Rotational Instabilities

An absolute limit on rapid rotation is set by the onset of mass shedding from the equator of a rotating star. However, rotational instabilities in rotating stars, known as gravitational radiation driven instabilities, set a more stringent limit on rapid stellar rotation than mass shedding. These instabilities originate from counter-rotating surface vibrational modes which at sufficiently high rotational star frequencies are dragged forward, as schematically illustrated in Fig. 10.12. In this case gravitational radiation, which inevitably accompanies the aspherical transport of matter, does not damp the instability modes but rather drives them. Viscosity plays the important role of damping these instabilities at a sufficiently reduced rotational frequency such that the viscous damping rate and power in gravity waves are comparable.

The most critical instability modes that are driven unstable by gravitational radiation are f-modes [7, 144] and r-modes [145, 146]. Figure 10.13 shows the stable

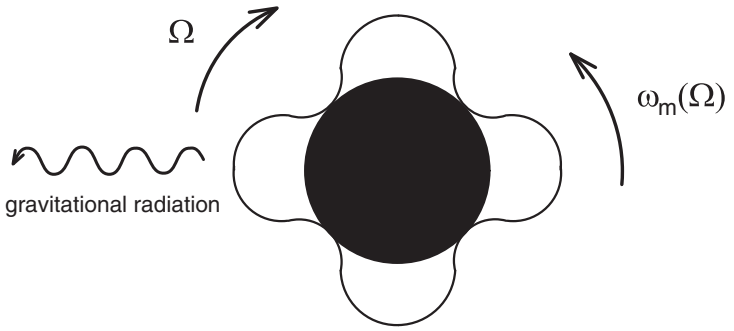

Fig. 10.12 Representation of an $m = 4$ perturbation of a rotating neutron star. Ω denotes the star's rotational frequency, ω_m is the frequency of the counter-rotating perturbation [7]

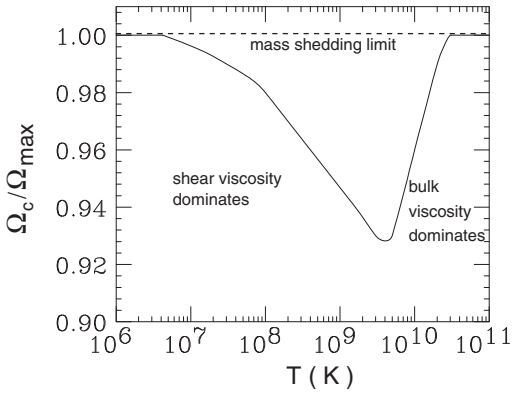

Fig. 10.13 Gravitational radiation driven f-mode instability suppressed by shear and bulk viscosity (figure from [7])

neutron star frequencies if only f-modes were operative in neutron star. One sees that hot as well as cold neutron stars can rotate at frequencies close to mass shedding, because of the large contributions of shear and bulk viscosity, respectively, for this temperature regime. The more recently discovered r-mode instability [145, 148] may change the picture completely, as can be seen from Fig. 10.14. These modes are driven unstable by gravitational radiation over a considerably wider range of angular velocities than the f-modes (cf. dashed curve labeled ($m = 2$) r-mode instability). In stars with cores cooler than $\sim 10^9$ K, on the other hand, the r-mode instability may be completely suppressed by the viscosity originating from the presence of hyperons in neutron star matter, so that stable rotation would be limited by the f-mode instability again [147].

Figures 10.15 and 10.16 are the counterparts to Figs. 10.13 and 10.14 but calculated for strange stars made of CFL and 2SC quark matter, respectively [149, 150]. The r-mode instability seems to rule out that pulsars are CFL strange stars, if the characteristic time scale for viscous damping of r-modes are exponentially increased

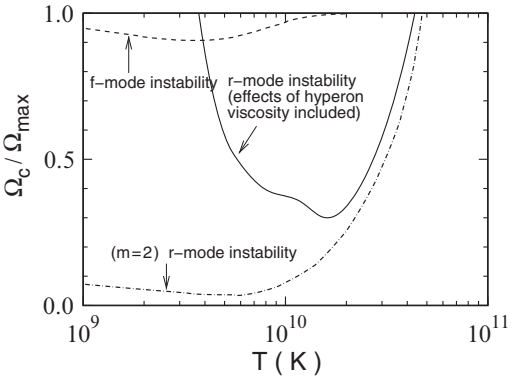

Fig. 10.14 Comparison of f-mode instability with r-mode instability (data from [144, 147])

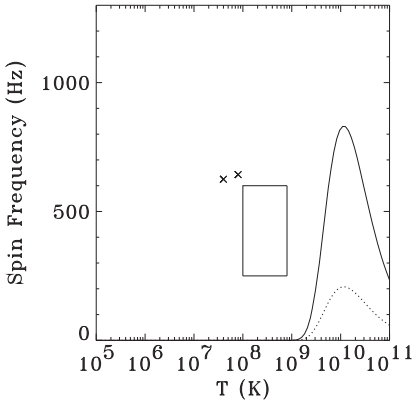

Fig. 10.15 Critical rotation frequencies vs. stellar temperature for CFL strange stars [150]

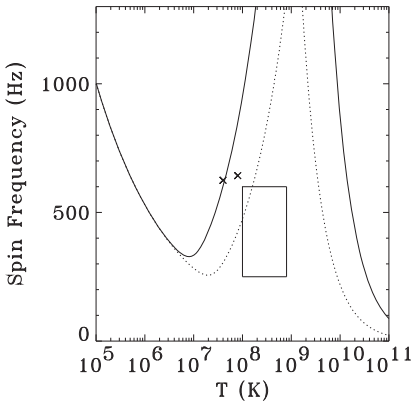

Fig. 10.16 Same as Fig. 10.15, but for 2SC quark stars [150]

by factors of $\sim\Delta/T$ as calculated in [149]. An energy gap as small as $\Delta = 1\,\mathrm{MeV}$ was assumed. For much larger gaps of $\Delta \sim 100\,\mathrm{MeV}$, as expected for color superconducting quark matter (see Sect. 10.3.5), the entire diagram would be r-mode unstable. The full curve in Fig. 10.15 is calculated for a strange quark mass of $m_s = 200\,\mathrm{MeV}$, the dotted curve for $m_s = 100\,\mathrm{MeV}$. The box marks the positions of most low mass X-ray binaries (LMXBs) [151], and the crosses denote the most rapidly rotating millisecond pulsars known. All strange stars above the curves would spin down on a time scale of hours due to the r-mode instability, in complete contradiction to the observation of millisecond pulsars and LMXBs, which would rule out CFL quark matter in strange stars (see, however, [152]). Figure 10.16 shows the critical rotation frequencies of quark stars as a function of internal stellar temperature for 2SC quark stars. For such quark stars the situation is less conclusive. Rapid spin-down, driven by the r-mode gravitational radiation instability, would happen for stars above the curves.

10.7 Net Electric Fields and Compact Star Structure

Here we consider the possibility that the electric charge density inside compact stars (neutron stars, strange stars) is not identically zero. This may be the case, for example, for compact stars accreting ionized hydrogen. Another example are strange quark stars. They could have electric charge distributions on their surfaces that generate electric fields on the order of $10^{18}\,\mathrm{V\,cm^{-1}}$ [7, 11, 18, 131] for ordinary quark matter, and $10^{19}\,\mathrm{V\,cm^{-1}}$ [153] if quark matter is a color-superconductor. Although the electric field on strange stars exists only in a very narrow region of space, it is interesting to study the effects of such ultra-high electric fields on the structure of the star.

It has already been shown that the energy densities of ultra-high electric fields can substantially alter the structure (mass–radius relationship) of compact stars [154],

depending on the strength of the electric field. In contrast to electrically uncharged stars, the energy–momentum tensor of charged stars has two key contributions, the usual matter-energy term plus the energy density term that originates from the electric field. The latter plays a dual role for compact star physics. Firstly, it acts as an additional source of gravity and, secondly, it introduces Coulomb interactions inside the star. Both features can alter the properties of compact stars significantly, as we shall demonstrate below.

We will restrict ourselves to spherically symmetric compact stars. The metric of such objects is given by

$$ds^2 = e^{\nu(r)}c^2dt^2 - e^{\lambda(r)}dr^2 - r^2(d\theta^2 + \sin^2\theta d\phi^2)\,. \tag{10.20}$$

The energy–momentum tensor consists of the usual perfect fluid term supplemented with the electromagnetic energy–momentum tensor,

$$T_\kappa{}^\mu = (p+\rho c^2)u_\kappa u^\mu + p\delta_\kappa{}^\mu + \frac{1}{4\pi}\left[F^{\mu l}F_{\kappa l} + \frac{1}{4\pi}\delta_\kappa{}^\mu F_{kl}F^{kl}\right], \tag{10.21}$$

where u^μ is the fluid's four-velocity, p and $\rho c^2 \equiv \varepsilon$ are the pressure and energy density, respectively, and $F^{\mu\kappa}$ satisfies the covariant Maxwell equation,

$$[(-g)^{1/2}F^{\kappa\mu}]_{,\mu} = 4\pi J^\kappa(-g)^{1/2}. \tag{10.22}$$

The quantity J^κ denotes the four-current which represents the electromagnetic sources in the star. For a static spherically symmetric system, the only non-zero component of the four-current is J^1, which implies that the only non-vanishing component of $F^{\kappa\mu}$ is F^{01}. We therefore obtain from (10.22)

$$F^{01}(r) = E(r) = r^{-2}e^{-(\nu+\lambda)/2}\int_0^r 4\pi j^0 e^{(\nu+\lambda)/2}dr\,, \tag{10.23}$$

which is nothing other than the electric field. This relation can be identified as the relativistic version of Gauss' law. In addition we see that the electric charge of the system is given by

$$Q(r) = \int_0^r 4\pi j^0 e^{(\nu+\lambda)/2}dr\,. \tag{10.24}$$

With the aid of (10.24) the energy–momentum tensor of the system can be written as

$$T_\kappa{}^\mu = \begin{pmatrix} -\left(\varepsilon + \frac{Q^2(r)}{8\pi r^4}\right) & 0 & 0 & 0 \\ 0 & p - \frac{Q^2(r)}{8\pi r^4} & 0 & 0 \\ 0 & 0 & p + \frac{Q^2(r)}{8\pi r^4} & 0 \\ 0 & 0 & 0 & p + \frac{Q^2(r)}{8\pi r^4} \end{pmatrix}. \tag{10.25}$$

Using the energy–momentum tensor (10.25), Einstein's field equation leads to

$$e^{-\lambda}\left(-\frac{1}{r^2}+\frac{1}{r}\frac{d\lambda}{dr}\right)+\frac{1}{r^2}=\frac{8\pi G}{c^4}\left(p-\frac{Q^2(r)}{8\pi r^4}\right), \tag{10.26}$$

$$e^{-\lambda}\left(\frac{1}{r}\frac{d\kappa}{dr}+\frac{1}{r^2}\right)-\frac{1}{r^2}=-\frac{8\pi G}{c^4}\left(\varepsilon+\frac{Q^2(r)}{8\pi r^4}\right). \tag{10.27}$$

At this point we define the radial component of the metric g^{11}, in analogy to the exterior solution of Reissner–Nordström, as [155]

$$e^{-\lambda}(r)=1-\frac{Gm(r)}{rc^2}+\frac{GQ^2(r)}{r^2c^4}. \tag{10.28}$$

From (10.26), (10.27) and (10.28), we derive an expression for $m(r)$, which is interpreted as the total mass of the star at a radial distance r. This expression reads

$$\frac{dm(r)}{dr}=\frac{4\pi r^2}{c^2}\varepsilon+\frac{Q(r)}{c^2 r}\frac{dQ(r)}{dr}, \tag{10.29}$$

which reveals that, in addition to the standard term originating from the eos of the stellar fluid, the electric field energy contributes to the star's total mass too. Next, we impose the vanishing of the divergence of the energy–momentum tensor, $T^{\mu}{}_{\kappa;\mu}=0$, which leads to the Tolman–Oppenheimer–Volkoff (TOV) equation of electrically charged stars,

$$\frac{dp}{dr}=-\frac{2G\left[m(r)+\frac{4\pi r^3}{c^2}\left(p-\frac{Q^2(r)}{4\pi r^4c^2}\right)\right]}{c^2r^2\left(1-\frac{2Gm(r)}{c^2r}+\frac{GQ^2(r)}{r^2c^4}\right)}(p+\varepsilon)+\frac{Q(r)}{4\pi r^4}\frac{dQ(r)}{dr}. \tag{10.30}$$

Summarizing the relevant stellar structure equations, we end up with the following set of equations:

$$\frac{d\lambda}{dr}=\frac{8\pi G}{c^4}\left(\varepsilon+\frac{Q^2(r)}{8\pi r^4}\right)re^{\lambda}-\left(\frac{e^{-\lambda}-1}{r}\right), \tag{10.31}$$

$$\frac{d\nu}{dr}=\frac{2G\left[m(r)+\frac{4\pi r^3}{c^2}\left(p-\frac{Q^2(r)}{4\pi r^4c^2}\right)\right]}{c^2r^2\left(1-\frac{2Gm(r)}{c^2r}+\frac{GQ^2(r)}{r^2c^4}\right)}. \tag{10.32}$$

$$\frac{dm(r)}{dr}=\frac{4\pi r^2}{c^2}\varepsilon+\frac{Q(r)}{c^2r}\frac{dQ(r)}{dr}, \tag{10.33}$$

$$\frac{dQ(r)}{dr}=4\pi r^2 j^0 e^{-(\nu+\lambda)/2}. \tag{10.34}$$

$$\frac{dp}{dr} = -\frac{2G\left[m(r) + \frac{4\pi r^3}{c^2}\left(p - \frac{Q^2(r)}{4\pi r^4 c^2}\right)\right]}{c^2 r^2\left(1 - \frac{2Gm(r)}{c^2 r} + \frac{GQ^2(r)}{r^2 c^4}\right)}(p+\varepsilon) + \frac{Q(r)}{4\pi r^4}\frac{dQ(r)}{dr}\,. \tag{10.35}$$

Equations (10.31) and (10.32) arise from Einstein's field equation, (10.33) is the mass continuity equation, (10.34) comes from the Maxwell equations, and (10.35) is the TOV equation. This system of coupled differential equations is subject to the following boundary conditions

$$p(0) = p_c\,, \qquad e^{\lambda} = 0\,, Q(0) = 0\,, \qquad m(0) = 0\,. \tag{10.36}$$

In addition to these conditions, one needs to specify the star's central density (or, equivalently, the central pressure) for a given equation of state and a given electric charge distribution. This will be discussed in more details in the next sections.

As already mentioned at the beginning of this section, strange stars may be expected to carry huge electric fields on their surfaces [7, 11, 18, 131, 153]. We want to study the effects of such fields on the overall structure of strange stars. To this aim, we model the charge distribution by superimposing two Gaussian functions. The first Gaussian is chosen to be positive, representing the accumulation of a net positive charge. The second Gaussian, slightly displaced from the first one, is chosen negative to represent the accumulation of a net negative charge. Mathematically, we thus have

$$j(r) = \frac{\sigma}{b\sqrt{\pi}}\left(e^{-\left(\frac{r-r_1}{b}\right)^2} - e^{-\left(\frac{r-r_2}{b}\right)^2}\right), \tag{10.37}$$

where σ is a constant that controls the magnitude of the Gaussians and b the widths of the Gaussians. The graphical illustration of (10.37) is shown in Fig. 10.17. To obtain a noticeable impact of the electric field on the structure of strange stars, one needs to have Gaussians with a width of at least around 0.05 km. For such

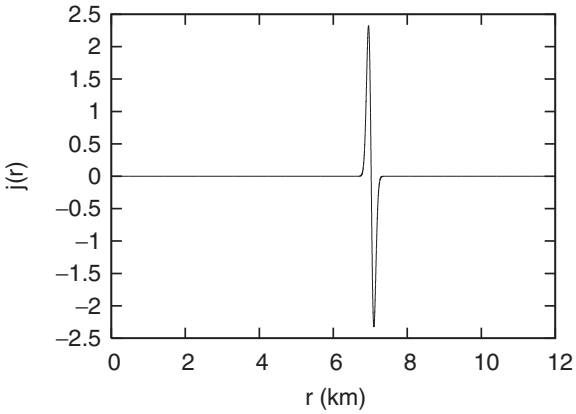

Fig. 10.17 Displacement of electric charges on the surface of a strange star. The mathematical form is obtained by superimposing two Gaussian functions

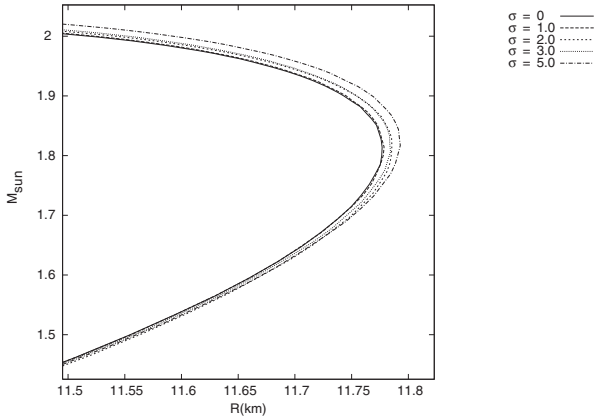

Fig. 10.18 Mass–radius relationships of electrically charged strange stars

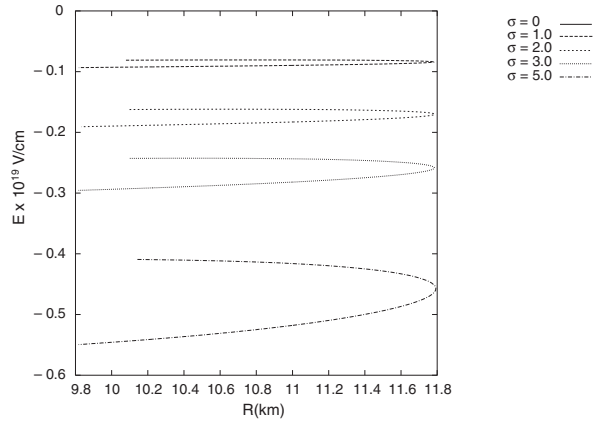

Fig. 10.19 Electric fields at the surface of strange stars

widths we find the mass–radius relationships shown in Fig. 10.18. The deviations from the mass–radius relationships of uncharged strange stars are found to increase with mass, and are largest for the maximum-mass star of each stellar sequence.

The radial distribution of the electric charge over the surface of a strange star is particularly interesting. The reason being the occurrence of the metric functions in (10.24), which defines the star's total net charge. Since the metric functions are not symmetric in the radial distance, the charge distribution is rendered asymmetric and stars that are strictly electrically charge neutral in flat space-time become electrically charged and thus possess non-zero electric fields. Figure 10.19 shows the electric field at the surface of strange stars. Figure 10.20 shows the net electric charge at the surface of strange stars. Both plots account for the general relativistic charge separation effect.

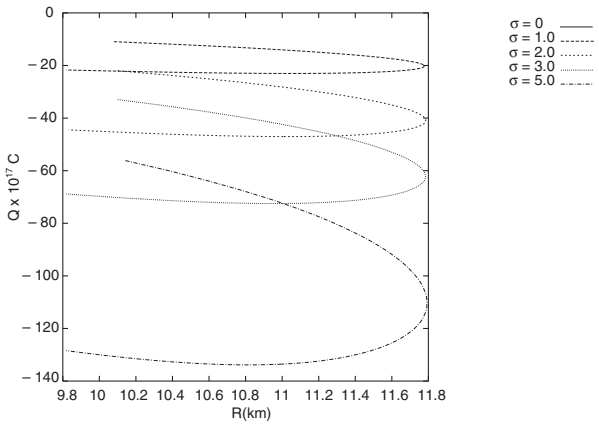

Fig. 10.20 Electric charge on strange quark stars

10.8 Conclusions and Outlook

It is often stressed that there has never been a more exciting time in the overlapping areas of nuclear physics, particle physics and relativistic astrophysics than today. This comes at a time where new orbiting observatories such as the Hubble Space Telescope (HST), Rossi X-ray Timing Explorer, Chandra X-ray satellite, and the X-ray Multi Mirror Mission (XMM Newton) have extended our vision tremendously, allowing us to observe compact star phenomena with an unprecedented clarity and angular resolution that previously were only imagined. On the Earth, radio telescopes like Arecibo, Green Bank, Parkes, VLA, and instruments using adaptive optics and other revolutionary techniques have exceeded previous expectations of what can be accomplished from the ground. Finally, the gravitational wave detectors LIGO, LISA, VIRGO, and Geo-600 are opening up a window for the detection of gravitational waves emitted from compact stellar objects such as neutron stars and black holes. This unprecedented situation is providing us with key information on neutron stars, which contain cold and ultra-dense baryonic matter permanently in their cores. As discussed in this paper, a key role in neutron star physics is played by strangeness. It alters the masses, radii, moment of inertia, frame dragging of local inertial frames, cooling behavior, and surface composition of neutron stars. Other important observables influenced by strangeness may be the spin evolution of isolated neutron stars and neutron stars in low-mass X-ray binaries. All told, these observables play a key role for the exploration of the phase diagram of dense nuclear matter at high baryon number density but low temperature [184], which is not accessible to relativistic heavy ion collision experiments.

Obviously, our understanding of neutron stars has changed dramatically since their first discovery some 40 years ago. In what follows, I briefly summarize what we have learned about the internal structure of these fascinating object since their discovery. I will address some of the most important open questions regarding the

composition of neutron star matter and its associated equation of state, and will mention new tools, telescopes, observations, and calculations that are needed to answer these questions:

- There is no clear picture yet as to what kind of matter exists in the cores of neutron stars. They may contain significant hyperon populations, boson condensates, a mixed phase of quarks and hadrons, and/or pure quark matter made of unconfined up, down, and strange quarks.
- Pure neutron matter constitutes an excited state relative to many-baryon matter and, therefore, will quickly transform via weak reactions to such matter.
- Neutron stars made up of pure, interacting neutron matter cannot rotate as rapidly as the very recently discovered pulsars PSR J1748−2446ad, which spins at 716 Hz. The equation of state of such matter, therefore, imposes an upper bound on the equation of state of neutron star matter that is tighter than the usual $P = \varepsilon$ constraint (see Fig. 10.2).
- Charm quarks do not play a role for neutron star physics, since they become populated at densities which are around 100 times greater than the densities encountered in the cores of neutron stars. While hydrostatically stable, "charm" stars are unstable against radial oscillations and, thus, cannot exist stably in the universe [131].
- Multi-quark states like the H-particle appear to make neutron stars unstable.
- Significant populations of Δ's are predicted by relativistic Brueckner–Hartree–Fock calculations, but not by standard mean-field calculations which do not account for dynamical correlations among baryons computed from the relativistic T-matrix equation.
- The finite temperatures of proto neutron stars favors the population of Δ's already at the mean-field level.
- The r-modes are of key interest for several reasons: (1) they may explain why young neutron stars spin slowly, (2) why rapidly accreting neutron stars (LMXB) spin slowly and within a narrow band, and (3) they may produce gravitational waves detectable by LIGO. Knowing the bulk viscosity originating from processes like $\mathrm{n} + \mathrm{n} \rightarrow \mathrm{p}^{+} + \Sigma^{-}$ and the superfluid critical temperature of Σ^{-}, both are poorly understood at present, will be key.
- The loss of pressure resulting from the appearance of additional hadronic degrees of freedom at high densities reduces the (maximum) mass of neutron stars. This feature may serve as a key criteria to distinguish between, and eliminate certain, classes of equations of state [6, 7, 185].
- Heavy neutron stars, with masses of around two solar masses, do not automatically rule out the presence of hyperons or quarks in the cores of neutron stars [186].
- Depending on the densities reached in the cores of neutron stars, both Schroedinger-based models as well as relativistic field-theoretical models may be applicable to neutron star studies.
- The density dependence of the coupling constants of particles in ultra-dense neutron star matter needs be taken into account in stellar structure calculations. Density dependent relativistic field theories are being developed which account for this feature.

- The models used to study the quark–hadron phase transition in the cores of neutron stars are extremely phenomenological and require considerable improvements.
- If quark matter exists in the cores of neutron stars, it will be a color superconductor whose complex condensation pattern is likely to change with density inside the star. The exploration of the numerous astrophysical facets of (color superconducting) quark matter is therefore of uppermost importance. What are the signatures of color superconducting quark matter in neutron stars? So far it has mostly been demonstrated that color superconductivity is compatible with observed neutron star properties.
- A two-step quark–hadron phase transition – (1) from nuclear matter to regular quark matter, (2) from regular quark matter to color superconducting quark matter – may explain long quiescent gamma-ray bursts due to the two phase transitions involved.
- Are there isolated pulsar that are spinning up? Such a (backbending) phenomenon could be caused by a strong first-order-like quark–hadron phase transitions in the core of a neutron star [105, 187, 188].
- Was the mass of the neutron star created in SN 1987A around 1.5 $M_{\odot}$? And did SN 1987A go into a black hole or not? If the answer to both questions were yes, a serious conflict with the observation of heavy neutron stars would arise. On the other hand, it could also indicate the existence generically different classes of "neutron" stars with very different maximum masses.
- Sources known to increase the masses of neutron stars are differential rotation, magnetic fields, and electric fields. Some of these sources are more effective (and plausible) than others though.
- Nuclear processes in non-equilibrium nuclear crusts (e.g., pycnonuclear reactions) and/or cores (heating caused by changes in the composition) of neutron stars can alter the thermal evolution of such stars significantly. We are just beginning to study these processes in greater detail.
- What is the shell structure for very neutron rich nuclei in the crusts of neutron stars?
- Do $N = 50$ and $N = 82$ remain magic numbers? Such questions will be addressed at GSI (Darmstadt) and RIKEN.
- Are there pulsars that rotate below one millisecond? Such objects may be composed of absolutely stable strange quark matter instead of purely gravitationally bound hadronic matter. Experimental physicists have searched unsuccessfully for stable or quasistable strange matter systems over the past two decades. These searches fall in three main categories: (a) searches for strange matter (strange nuggets or strangelets) in cosmic rays, (b) searches for strange matter in samples of ordinary matter, and (c) attempts to produce strange matter at accelerators. An overview of these search experiments is given in Table 10.1.
- Strange stars may be enveloped in a crust. There is a critical surface tension below which the quark star surfaces will fragment into a crystalline crust made of charged strangelets immersed in an electron gas [128, 132].

Table 10.1 Past, present, and future search experiments for strange quark matter [11]

Experiment	References
Cosmic ray searches for strange nuggets:	
AMS-02[a]	[156, 157]
CRASH[b]	[158–160]
ECCO[c]	[161]
HADRON	[162]
IMB[d]	[163]
JACEE[e]	[164, 165]
MACRO[f]	[166–169]
Search for strangelets in terrestrial matter:	[170]
Tracks in ancient mica	[171, 172]
Rutherford backscattering	[173, 174]
Search for strangelets at accelerators:	
Strangelet searches E858, E864, E878, E882-B, E896-A, E886	[175–177]
H-dibaryon search	[178, 179]
Pb+Pb collisions	[180–183]

[a]AMS: Alpha Magnetic Spectrometer (scheduled for 2005–2008)
[b]CRASH: Cosmic Ray And Strange Hadronic matter.
[c]ECCO: Extremely-heavy Cosmic-ray Composition Observer.
[d]IMB: Irvine Michigan Brookhaven proton-decay detector (1980–1991)
[e]JACEE: Japanese-American Cooperative Emulsion Chamber Experiment.
[f]MACRO: Monopole, Astrophysics and Cosmic Ray Observatory (1989–2000)

- If bare, the quark star surface will have peculiar properties which distinguishes a quark star from a neutron star [137, 138, 189, 190].
- A very high-luminosity flare took place in the Large Magellanic Cloud (LMC), some 55 kpc away, on 5 March 1979. Another giant flare was observed on 27 August 1998 from SGR 1900+14. The inferred peak luminosities for both events is $\sim 10^7$ times the Eddington limit for a solar mass object, and the rise time is very much smaller than the time needed to drop $\sim 10^{25}$ g (about 10^{-8} $M_\odot$) of normal material onto a neutron star. Alcock et al. [18] suggested a detailed model for the 5 March 1979 event burst which involves the particular properties of strange matter (see also [190, 191]). The model assumes that a lump of strange matter of $\sim 10^{-8}$ $M_\odot$ fell onto a rotating strange star. Since the lump is entirely made up of self-bound high-density matter, there would be only little tidal distortion of the lump, and so the duration of the impact can be very short, around $\sim 10^{-6}$ s, which would explain the observed rapid onset of the gamma ray flash. The light curves expected for such giant bursts [137–140] should posses characteristic features that are well within the capabilities of ESA's INTErnational Gamma-Ray Astrophysics Laboratory (INTEGRAL [192]) launched by the European Space Agency in October of 2002.

References

1. J. W. T. Hessels, S. M. Ransom, I. H. Stairs, P. C. C. Freire, V. M. Kaspi, and F. Camilo, Science **311** (2006) 1901.
2. D. C. Backer, S. R. Kulkarni, C. Heiles, M. M. Davis, and W. M. Goss, Nature **300** (1982) 615.
3. A. S. Fruchter, D. R. Stinebring, and J. H. Taylor, Nature **334** (1988) 237.
4. P. Kaaret et al., Astrophys. J. **657** (2007) L97.
5. L. Villain, EAS Publ. Ser. **21** (2006) 335.
6. N. K. Glendenning, *Compact Stars, Nuclear Physics, Particle Physics, and General Relativity*, 2nd ed. (Springer, New York, 2000).
7. F. Weber, *Pulsars as Astrophysical Laboratories for Nuclear and Particle Physics*, High Energy Physics, Cosmology and Gravitation Series (IOP, Bristol, Great Britain, 1999).
8. H. Heiselberg and V. Pandharipande, Ann. Rev. Nucl. Part. Sci. **50** (2000) 481.
9. J. M. Lattimer and M. Prakash, Astrophys. J. **550** (2001) 426.
10. D. Blaschke, N. K. Glendenning, and A. Sedrakian (ed.), *Physics of Neutron Star Interiors*, Lecture Notes in Physics **578** (Spring, Berlin, 2001).
11. F. Weber, Prog. Part. Nucl. Phys. **54** (2005) 193, (astro-ph/0407155).
12. A. Sedrakian, Prog. Part. Nucl. Phys. **58** (2007) 168.
13. D. Page and S. Reddy, Ann. Rev. Nucl. Part. Sci. **56** (2006) 327.
14. D. Blaschke and H. Grigorian, Prog. Part. Nucl. Phys., **59** (2007) 139 (arXiv:astro-ph/0612092).
15. A. R. Bodmer, Phys. Rev. D **4** (1971) 1601.
16. E. Witten, Phys. Rev. D **30** (1984) 272.
17. H. Terazawa, INS-Report-338 (INS, Univ. of Tokyo, 1979); J. Phys. Soc. Japan, **58** (1989) 3555; **58** (1989) 4388; **59** (1990) 1199.
18. C. Alcock, E. Farhi, and A. V. Olinto, Astrophys. J. **310** (1986) 261.
19. C. Alcock and A. V. Olinto, Ann. Rev. Nucl. Part. Sci. **38** (1988) 161.
20. J. Madsen, Lecture Notes in Physics **516** (1999) 162.
21. N. K. Glendenning, Ch. Kettner, and F. Weber, Phys. Rev. Lett. **74** (1995) 3519.
22. K. Rajagopal and F. Wilczek, *The Condensed Matter Physics of QCD*, At the Frontier of Particle Physics / Handbook of QCD, ed. M. Shifman, (World Scientific, Singapore) (2001).
23. M. Alford, Ann. Rev. Nucl. Part. Sci. **51** (2001) 131.
24. M. Alford, K. Rajagopal, and F. Wilczek, Phys. Lett. **422B** (1998) 247.
25. R. Rapp, T. Schäfer, E. V. Shuryak, and M. Velkovsky, Phys. Rev. Lett. **81** (1998) 53; Ann. Phys. **280** (2000) 35.
26. J. R. Oppenheimer and G. M. Volkoff, Phys. Rev. **55** (1939) 374.
27. R. C. Tolman, Phys. Rev. **55** (1939) 364.
28. J. H. Taylor and J. M. Weisberg, Astrophys. J. **345** (1989) 434.
29. S. E. Thorsett and D. Chakrabarty, Astrophys. J. **512** (1999) 288.
30. D. J. Nice, E. M. Splaver, I. H. Stairs, O. Loehmer, A. Jessner, M. Kramer, and J. M. Cordes, *A 2.1 solar mass pulsar measured by relativistic orbital decay*, (astro-ph/0508050).
31. D. Barret, J.-F. Olive, and M. C. Miller, *The coherence of kHz quasi-periodic oscillations in the X-rays from accreting neutron stars*, (astro-ph/0605486).
32. O. Barziv, L. Kaper, M. H. van Kerkwijk, J. H. Telting, and J. van Paradijs, Astron. Astrophys. **377** (2001) 925.
33. J. Casares, P. A. Charles, and E. Kuulkers, Astrophys. J. **493** (1998) L39.
34. J. A. Orosz and E. Kuulkers, Mon. Not. R. Astron. Soc. **305** (1999) 132.
35. J. S. Clark, S. P. Goodwin, P. A. Crowther, L. Kaper, M. Fairbairn, N. Langer, and C. Brocksopp, Astron. Astrophys. **392** (2002) 909.
36. T. Shahbaz, J. Casares, C. A. Watson, P. A. Charles, R. I. Hynes, S. C. Shih, and D. Steeghs, Astrophys. J. **616** (2004) L123.
37. C. E. Rhoades and R. Ruffini, Phys. Rev. Lett. **32** (1974) 324.
38. A. G. Sabbadini and J. B. Hartle, Ann. Phys. (N.Y.) **104** (1977) 95.

39. J. B. Hartle, Phys. Rep. **46** (1978) 201.
40. G. E. Brown and H. A. Bethe, Astrophys. J. **423** (1994) 659.
41. W. D. Myers and W. J. Swiatecki, Nucl. Phys. A **601** (1996) 141.
42. K. Strobel, F. Weber, M. K. Weigel, and Ch. Schaab, Int. J. Mod. Phys. E **6**, No. 4 (1997) 669.
43. V. R. Pandharipande and R. B. Wiringa, Rev. Mod. Phys. **51** (1979) 821.
44. R. B. Wiringa, V. Fiks, and A. Fabrocini, Phys. Rev. C **38** (1988) 1010.
45. A. Akmal, V. R. Pandharipande, and D. G. Ravenhall, Phys. Rev. C **58** (1998) 1804.
46. M. Baldo, G. F. Burgio, and H. J. Schulze, Phys. Rev. C **61** (2000) 055801.
47. M. Baldo and F. Burgio, Lect. Notes Phys. **578** (2001) 1.
48. G. F. Burgio, M. Baldo, H.-J. Schulze, and P. K. Sahu, Phys. Rev. C **66** (2002) 025802.
49. H. Lenske and C. Fuchs, Phys. Lett. **345B** (1995) 355.
50. C. Fuchs, H. Lenske, and H. H. Wolter, Phys. Rev. C **52** (1995) 3043.
51. S. Typel and H. H. Wolter, Nucl. Phys. A **656** (1999) 331.
52. F. Hofmann, C. M. Keil, and H. Lenske, Phys. Rev. C **64** (2001) 034314.
53. T. Nikšić, D. Vretenar, P.Finelli and P. Ring, Phys. Rev. C **66** (2002) 024306.
54. S. F. Ban, J. Li, S. Q. Zhang, H. Y. Jia, and J. P. Sang, and J. Meng, Phys. Rev. C **69** (2004) 045805.
55. M. Buballa, Phys. Rept. **407** (2005) 205.
56. D. Blaschke, S. Fredriksson, H. Grigorian, A. M. Öztas and F. Sandin, Phys. Rev. D **72** (2005) 065020.
57. S. B. Ruster, V. Werth, M. Buballa, I. A. Shovkovy, and D. H. Rischke, Phys. Rev. D **72** (2005) 034004.
58. H. Abuki and T. Kunihiro, Nucl. Phys. A **768** (2006) 118.
59. S. Lawley, W. Bentz, and A. W. Thomas, J. Phys. G: Nucl. Part. Phys. **32** (2006) 667.
60. S. Lawley, W. Bentz, and A. W. Thomas, Phys. Lett. **B632** (2006) 495.
61. P. Wang, S. Lawley, D. B. Leinweber, A. W. Thomas, and A. G. Williams, Phys. Rev. C **72** (2005) 045801.
62. N. K. Glendenning and F. Weber, Astrophys. J. **400** (1992) 647.
63. M. Stejner and J. Madsen, Phys. Rev. D **72** (2005) 123005.
64. N. K. Glendenning, Astrophys. J. **293** (1985) 470.
65. H. Huber, F. Weber, M. K. Weigel, and Ch. Schaab, Int. J. Mod. Phys. E **7**(3), (1998) 301.
66. M. Prakash, I. Bombaci, M. Prakash, P. J. Ellis, J. M. Lattimer, and R. Knorren, Phys. Rep. **280** (1997) 1.
67. J. M. Lattimer, C. J. Pethick, M. Prakash, and P. Haensel, Phys. Rev. Lett. **66** (1991) 2701.
68. M. Prakash, M. Prakash, J. M. Lattimer, and C. J. Pethick, Astrophys. J. **390** (1992) L77.
69. P. Haensel and O. Yu. Gnedin, Astron. Astrophys. **290** (1994) 458.
70. Ch. Schaab, F. Weber, M. K. Weigel, and N. K. Glendenning, Nucl. Phys. A **605** (1996) 531.
71. G. Baym, *Neutron Stars and the Physics of Matter at High Density*, in: Nuclear Physics with Heavy Ions and Mesons, Vol. 2, Les Houches, Session XXX, ed. by R. Balian, M. Rho and G. Ripka (North-Holland, Amsterdam, 1978) p. 745.
72. S. Barshay and G. E. Brown, Phys. Lett. **47B** (1973) 107.
73. G. E. Brown, K. Kubodera, D. Page, and P. Pizzochero, Phys. Rev. D **37** (1988) 2042.
74. D. B. Kaplan and A. E. Nelson, Phys. Lett. **175B** (1986) 57; Nucl. Phys. A **479** (1988) 273.
75. G. E. Brown, K. Kubodera, and M. Rho, Phys. Lett. **192B** (1987) 273.
76. C.-H. Lee and M. Rho, *Kaon condensation in dense stellar matter*, Proc. of the International Symposium on Strangness and Quark Matter, ed. by G. Vassiliadis, A. Panagiotou, B. S. Kumar, and J. Madsen (World Scientific, Singapore, 1995) p. 283.
77. R. Barth et al., Phys. Rev. Lett. **78** (1997) 4007.
78. P. Senger, Nucl. Phys. A **685** (2001) 312c.
79. C. Sturm et al., Phys. Rev. Lett. **86** (2001) 39.
80. A. Devismes, J. Phys. G: Nucl. Part. Phys. **28** (2002) 1591.
81. Ch. Fuchs, Prog. Part. Nucl. Phys. **56** (2006) 1.
82. G. Q. Li, C.-H. Lee, and G. E. Brown, Nucl. Phys. A **625** (1997) 372.
83. G. Q. Li, C.-H. Lee, and G. E. Brown, Phys. Rev. Lett. **79** (1997) 5214.

84. G. E. Brown, Phys. Bl. **53** (1997) 671.
85. G. E. Brown, *Supernova Explosions, Black Holes and Nucleon Stars*, in: Proceedings of the Nuclear Physics Conference – INPC '95, ed. by S. Zuxun and X. Jincheng (World Scientific, Singapore, 1996) p. 623.
86. V. Thorsson, M. Prakash, and J. M. Lattimer, Nucl. Phys. A **572** (1994) 693.
87. F.-K. Thielemann, M.-A. Hashimoto, and K. Nomoto, Astrophys. J. **349** (1990) 222.
88. R. L. Jaffe, Phys. Lett. **38** (1977) 195.
89. R. Tamagaki, Prog. Theor. Phys. **85** (1991) 321.
90. T. Sakai, J. Mori, A. J. Buchmann, K. Shimizu, and K. Yazaki, Nucl. Phys. A **625** (1997) 192.
91. N. K. Glendenning and J. Schaffner-Bielich, Phys. Rev. C **58** (1998) 1298.
92. A. Faessler, A. J. Buchmann, M. I. Krivoruchenko, and B. V. Martemyanov, Phys. Lett. **391B** (1997) 255.
93. A. Faessler, A. J. Buchmann, and M. I. Krivoruchenko, Phys. Rev. C **56** (1997) 1576.
94. R. Jaffe and F. Wilczek, Phys. Rev. Lett. **91** (2003) 232003.
95. R. L. Jaffe, Phys. Rep. **409** (2005) 1; Nucl. Phys. Proc. Suppl. **142** (2005) 343.
96. D. D. Ivanenko and D. F. Kurdgelaidze, Astrophys. **1** (1965) 251.
97. N. Itoh, Progr. Theor. Phys. **44** (1970) 291.
98. H. Fritzsch, M. Gell-Mann, and H. Leutwyler, Phys. Lett. **47B** (1973) 365.
99. G. Baym and S. Chin, Phys. Lett. **62B** (1976) 241.
100. B. D. Keister and L. S. Kisslinger, Phys. Lett. **64B** (1976) 117.
101. G. Chapline and M. Nauenberg, Phys. Rev. D **16** (1977) 450.
102. W. B. Fechner and P. C. Joss, Nature **274** (1978) 347.
103. G. Chapline and M. Nauenberg, Ann. New York Academy of Sci. **302** (1977) 191.
104. N. K. Glendenning, Phys. Rev. D **46** (1992) 1274.
105. N. K. Glendenning, S. Pei, and F. Weber, Phys. Rev. Lett. **79** (1997) 1603.
106. A. Chodos, R. L. Jaffe, K. Johnson, C. B. Thorne, and V. F. Weisskopf, Phys. Rev. D **9** (1974) 3471.
107. A. Chodos, R. L. Jaffe, K. Johnson, and C. B. Thorne, Phys. Rev. D **10** (1974) 2599.
108. F. Weber, A. Torres i Cuadrat, A. Ho, and P. Rosenfield, (`astro-ph/0602047`).
109. F. Weber, J. Phys. G: Nucl. Part. Phys. **25** (1999) R195.
110. N. K. Glendenning and F. Weber, *Signal of Quark Deconfinement in Millisecond Pulsars and Reconfinement in Accreting X-ray Neutron Stars*, Lecture Notes in Physics, vol. 578, (Springer, Berlin, 2001), p. 305.
111. M. Alford, C. Kouvaris, and K. Rajagopal, Phys. Rev. Lett. **92** (2004) 222001.
112. K. Rajagopal and F. Wilczek, Phys. Rev. Lett. **86** (2001) 3492.
113. P. F. Bedaque and T. Schäfer, Nucl. Phys. A **697** (2002) 802.
114. D. B. Kaplan and S. Reddy, Phys. Rev. D **65** (2002) 054042.
115. M. Buballa, J. Hosek and M. Oertel, Phys. Rev. Lett. **90** (2003) 182002.
116. A. Schmitt, *Spin-one Color Superconductivity in Cold and Dense Quark Matter*, Ph.D. thesis, `nucl-th/0405076`.
117. T. Schäfer, Phys. Rev. D **62** (2000) 094007.
118. M. Alford, J. A. Bowers, and K. Rajagopal, Phys. Rev. D **63** (2001) 074016.
119. J. A. Bowers and K. Rajagopal, Phys. Rev. D **66** (2002) 065002.
120. R. Casalbuoni and G. Nardulli, Rev. Mod. Phys. **76** (2004) 263.
121. M. Alford, K. Rajagopal, and F. Wilczek, Nucl. Phys. **B537** (1999) 443.
122. D. T. Son, Phys. Rev. D **D59** (1999) 094019.
123. M. Alford and S. Reddy, Phys. Rev. D **67** (2003) 074024.
124. M. Alford, J. Phys. G **30** (2004) S441.
125. K. Rajagopal, Acta Physica Polonica B **31** (2000) 3021.
126. M. Alford, J. A. Bowers, and K. Rajagopal, J. Phys. G **27** (2001) 541.
127. D. Blaschke, D. M. Sedrakian, and K. M. Shahabasyan, Astron. Astrophys. **350** (1999) L47.
128. M. Alford, K. Rajagopal, S. Reddy, and A. W. Steiner, Phys. Rev. D **73** (2006) 114016.
129. J. Madsen, Phys. Rev. Lett. **61** (1988) 2909.

130. G. J. Mathews, I.-S. Suh, B. O'Gorman, N. Q. Lan, W. Zech, K. Otsuki, and F. Weber, J. Phys. G: Nucl. Part. Phys. **32** (2006) 1.
131. Ch. Kettner, F. Weber, M. K. Weigel, and N. K. Glendenning, Phys. Rev. D **51** (1995) 1440.
132. P. Jaikumar, S. Reddy, A. W. Steiner, Phys. Rev. Lett. **96** (2006) 041101.
133. J. L. Provencal, H. L. Shipman, E. Hog, and P. Thejll, Astrophys. J. **494** (1998) 759.
134. J. L. Provencal, H. L. Shipman, D. Koester, F. Wesemael, and P. Bergeron, Astrophys. J. **568** (2002) 324.
135. S. O. Kepler et al., Astrophys. J. **539** (2000) 379.
136. G. J. Mathews, B. O'Gorman, K. Otsuki, I. Suh, and F. Weber, Univ. of Notre Dame preprint (2003).
137. V. V. Usov, Phys. Rev. Lett. **80** (1998) 230.
138. V. V. Usov, Astrophys. J. **550** (2001) L179.
139. V. V. Usov, Astrophys. J. **559** (2001) L137.
140. K. S. Cheng and T. Harko, Astrophys. J. **596** (2003) 451.
141. C. Vogt, R. Rapp, and R. Ouyed, Nucl. Phys. A **735** (2004) 543.
142. F. Weber, M. Meixner, R. P. Negreiros, and M. Malheiro, *Ultra-Dense Neutron Star Matter, Strange Quark Stars, and the Nuclear Equation of State*, (astro-ph/0606093).
143. N. K. Glendenning, Phys. Lett. **114B** (1982) 392; Astrophys. J. **293** (1985) 470; Z. Phys. A **326** (1987) 57; Z. Phys. A **327** (1987) 295.
144. L. Lindblom, *Neutron Star Pulsations and Instabilities*, in: Gravitational Waves: A Challenge to Theoretical Astrophysics, edited by V. Ferrari, J. C. Miller, and L. Rezzolla, ICTP Lecture Notes Series, Vol. III, (ISBN 92-95003-05-5, May 2001), (astro-ph/0101136).
145. N. Andersson, Astrophys. J. **502** (1998) 708.
146. N. Andersson and K. Kokkotas, Int. J. Mod. Phys. **D10** (2001) 381.
147. L. Lindblom and B. Owen, Phys. Rev. D **65** (2002) 063006.
148. J. L. Friedman and S. M. Morsink, Astrophys. J. **502** (1998) 714.
149. J. Madsen, Phys. Rev. Lett. **81** (1998) 3311.
150. J. Madsen, Phys. Rev. Lett. **85** (2000) 10.
151. M. van der Klis, Ann. Rev. Astron. Astrophys. **38** (2000) 717.
152. C. Manuel, A. Dobado, and F. J. Llanes-Estrada, *Shear Viscosity in a CFL Quark Star*, (hep-ph/0406058).
153. V. V. Usov, Phys. Rev. D **70** (2004) 067301.
154. S. Ray, A. L. Espíndola, M. Malheiro. J. P. S. Lemos, and V. T. Zanchin, Phys. Rev. D **68** (2003) 084004.
155. J. D. Bekenstein, Phys. Rev. D **4** (1971) 2185.
156. The AMS home page is http://ams.cern.ch.
157. J. Sandweiss, J. Phys. G: Nucl. Part. Phys. **30** (2004) S51.
158. T. Saito, Y. Hatano, Y. Fukuda, and H. Oda, Phys. Rev. Lett. **65** (1990) 2094.
159. T. Saito, *Test of the CRASH experiment counters with heavy ions*, Proc. of the International Symposium on Strangeness and Quark Matter, ed. by G. Vassiliadis, A. D. Panagiotou, B. S. Kumar, and J. Madsen (World Scientific, Singapore, 1995) p. 259.
160. M. Ichimura et al., Nuovo Cimento A **36** (1993) 843.
161. Information about ECCO can be found at http://ultraman.berkeley.edu.
162. S. B. Shaulov, APH N.S., Heavy Ion Physics **4** (1996) 403.
163. A. De Rújula, S. L. Glashow, R. R. Wilson, and G. Charpak, Phys. Rep. **99** (1983) 341.
164. O. Miyamura, Proc. of the 24th International Cosmic Ray Conference, 1 (Rome, 1995) p. 890.
165. J. J. Lord and J. Iwai, Paper 515, presented at the International Conference on High Energy Physics, Dallas (1992); H. Wilczynski et al., Proceedings of the XXIV International Cosmic Ray Conference, HE Sessions, Rome (1995), Vol. 1, p. 1.
166. MACRO Collaboration, Phys. Rev. Lett. **69** (1992) 1860.
167. M. Ambrosio et al., EPJ **C13** (2000) 453.
168. M. Ambrosio et al., for the MACRO Collaboration, *Status Report of the MACRO Experiment for the year 2001*, (hep-ex/0206027).
169. G. Giacomelli, for the MACRO Collaboration, (hep-ex/0210021).

170. Z.-T. Lu, R. J. Holt, P. Mueller, T. P. O'Connor, J. P. Schiffer, and L.-B. Wang, *Searches for Stable Strangelets in Ordinary Matter: Overview and a Recent Example*, (nucl-ex/0402015).
171. A. De Rújula and S. L. Glashow, Nature **312** (1984) 734.
172. P. B. Price, Phys. Rev. Lett. **52** (1984) 1265.
173. M. Brügger, K. Lützenkirchen, S. Polikanov, G. Herrmann, M. Overbeck, N. Trautmann, A. Breskin, R. Chechik, Z. Fraenkel, and U. Smilansky, Nature **337** (1989) 434.
174. M. C. Perillo Isaac et al., Phys. Rev. Lett. **81** (1998) 2416; *ibid.* **82** (1999) 2220 (erratum).
175. J. Thomas and P. Jacobs, *A Guide to the High Energy Heavy Ion Experiments*, UCRL-ID-119181.
176. A. Rusek et al., (E886 collaboration), Phys. Rev. C **54** (1996) R15.
177. G. Van Buren (E864 Collaboration), J. Phys. G: Nucl. Part. Phys. **25** (1999) 411.
178. J. Belz et al., (BNL E888 collaboration), Phys. Rev. D **53** (1996) R3487.
179. J. Belz et al., (BNL E888 collaboration), Phys. Rev. Lett. **76** (1996) 3277.
180. F. Dittus et al. (NA52 collaboration), *First look at NA52 data on Pb–Pb interactions at 158 A GeV/c*, International Conference on Strangeness in Hadronic Matter, ed. by J. Rafelski, AIP 340 (American Institute of Physics, New York, 1995) p. 24.
181. G. Appelquist et al., Phys. Rev. Lett. **76** (1996) 3907.
182. G. Ambrosini et al., Nucl. Phys. A **610** (1996) 306c.
183. R. Klingenberg, J. Phys. G: Nucl. Part. Phys. **25** (1999) R273.
184. T. Klahn *et al.*, Phys. Rev. C **74** (2006) 035802.
185. J. Lattimer and M. Prakash, Phys. Rev. Lett. **94** (2005) 111101.
186. M. Alford, D. Blaschke, A. Drago, T. Klahn, G. Pagliara, J. Schaffner-Bielich, Nature 445 (2007) E7, (astro-ph/0606524).
187. J. L. Zdunik, P. Haensel, E. Gourgoulhon, and M. Bejger, Astron. Astrophys. **416** (2004) 1013.
188. E. Chubarian, H. Grigorian, G. Poghosyan, and D. Blaschke, Astron. Astrophys. **357** (2000) 968.
189. D. Page and V. V. Usov, Phys. Rev. Lett. **89** (2002) 131101.
190. V. V. Usov, Phys. Rev. Lett. **87** (2001) 021101.
191. J. E. Horvath, H. Vucetich, and O. G. Benvenuto, Mon. Not. R. Astron. Soc. **262** (1993) 506.
192. See, for instance, astro-ph/0207527.

Chapter 11
Neutron Star Cooling: I

Dany Page

11.1 Introduction

This chapter presents a basic, but detailed, introduction to the physical and astrophysical issues involved in the study of the thermal evolution of isolated neutron stars. Results of numerical calculations,[1] for both minimal and enhanced cooling scenarios, are presented and compared with observational data.

The first conjectures about the possible existence of stellar neutron cores by Landau [37] and Baade and Zwicky [6] and the pioneering work of Oppenheimer and Volkoff [48] pointed to very mysterious, exotic, small and dense objects. Forty years after the actual discovery of neutron stars [28] these early thoughts have been fully confirmed: neutron stars are demonstrably very small and dense, they very probably enclose some exotic form(s) of matter, and they are still mysterious.[2]

A theorist view of the interior of a neutron star is depicted in Fig. 11.1: the central region, marked as "?", is the mysterious part and it is the main goal of the study of neutron star cooling, necessarily complemented with the study of many other facets of neutron star phenomenology, to elucidate it. However, any information about this central part which we can glean by observing the surface is conditioned by our understanding and correct modeling of the outer parts of the star. The core, where neutrons and protons form a homogeneous quantum liquid, is distinguished from the crust, where the nucleons cluster and matter is hence inhomogeneous at

D. Page
Departamento de Astrofísica Teórica, Instituto de Astronomía, Universidad Nacional Autónoma de México, México D.F 04510, México
e-mail: page@astroscu.unam.mx

[1] A 1D (i.e., assuming spherical symmetry) cooling code, `NSCool`, with which most calculations presented in this chapter were performed, is available at http://www.astroscu.unam.mx/neutrones/NS-Cooler/.

[2] The existence of pulsars with periods around 1.5 ms implies, by causality, that they have radii smaller than 75 km and, if they are bound by gravity, that their average density is, at least, of the order of 10^{14} g cm^{-3}.

W. Becker (ed.), *Neutron Stars and Pulsars,* Astrophysics and Space Science Library 357,

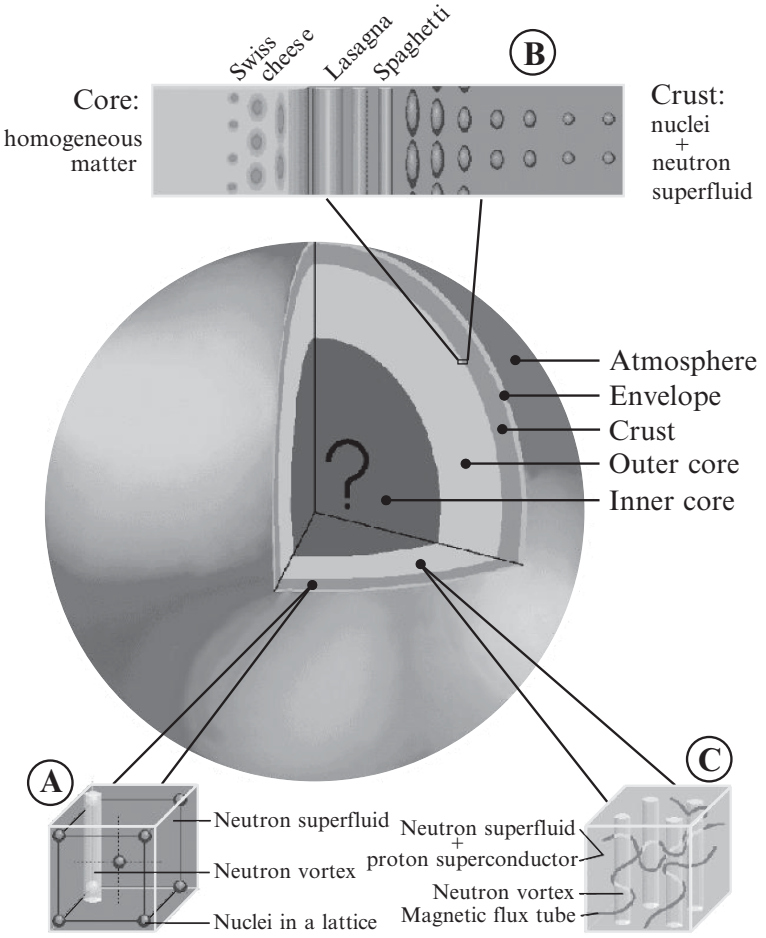

Fig. 11.1 A pictorial vision of the inside of a neutron star (drawing by the author, from [58])

the microscopic level. This crust–core separation is currently estimated [44] to be located at a density $\rho_{cc} \simeq 1.6 \times 10^{14}\,\mathrm{g\,cm^{-3}}$, i.e., about 60% of nuclear matter density, $\rho_{nuc} \simeq 2.8 \times 10^{14}\,\mathrm{g\,cm^{-3}}$. ($\rho_{nuc}$ refers to symmetric nuclear matter, i.e., made of 50% neutrons and 50% protons, at zero pressure and is deduced from the central density of heavy nuclei, while at ρ_{cc} in a neutron star, pressure is non zero and matter consists of about 95% neutrons with a small 5% proton component.)

At the surface of the star we expect a very thin atmosphere composed of hydrogen and in some cases perhaps a mix of heavy elements, or even a condensed magnetic surface [36]. This surface is of utmost observational importance because it is where the observable thermal flux $F(E)$ is emitted. An envelope exists just below the atmosphere where matter is not yet fully degenerate and, with a thickness of a few tens of meters, it acts as a thermal insulator between the hot interior and the surface. The outer 500–1,000 m of the star, its crust, contain nuclei, forming a lattice

immersed in a quantum liquid of electrons and, when density exceeds the neutron drip point at $\rho_{\rm drip} \simeq 4 - 7 \times 10^{11}\,{\rm g\,cm^{-3}}$, accompanied by free neutrons which most probably are in a superfluid state (Fig. 11.1, insert A). Owing to the rotation of the star, the neutron superfluid forms vortices, which possibly pin on the nuclei and may be responsible for the pulsar glitches. As we go deeper into the crust, when approaching nuclear density there is a first-order phase transition from the inhomogeneous regime of the crust to the homogeneous core. In this regime, termed the nuclear pasta (Fig. 11.1, insert B), as density grows, nuclei are increasingly elongated (the spaghetti phase), then form bidimensional structures (lasagnas) – with the space between them still filled by the superfluid neutrons – until the geometry inverts in the Swiss cheese phase, where bubbles of neutrons are immersed in the homogeneous neutron+proton liquid. (For a review of the physics of the neutron star crust see [61].)

In the outer core, protons very likely form a type II superconductor where the magnetic field is confined to fluxoids and neutrons possibly form a superfluid containing rotation-induced vortices as in the inner crust (Fig. 11.1, insert C). In the inner core (marked as "?" in Fig. 11.1), one may have charged meson, π^- or K^-, condensates, hyperons and/or deconfined quark matter. The transition from baryonic to quark matter also likely involves a mixed pasta phase [21]. Almost any form of dense matter beyond the simple neutron+proton liquid will allow very large neutrino emissivities and strongly affect the cooling of the star.[3] This situation is precisely one of the main motivations for the study of neutron star cooling with the hope to find candidates for "exotic" neutron stars.

The reader will find longer descriptions of the physics of neutron star structure in [88] or [58], and a very detailed and extensive presentation in the recent book of [27].

In the present chapter the physics of neutron star cooling, and results of cooling simulations, will be described in a very progressive and elementary manner. The literature in this field is so extended that I have been able to cite only key entries to it, as well as some essential works, and the reader can refer to several recent reviews [54, 58, 84, 93] for complementary presentations. In Sect. 11.2 a description of the physical ingredients needed to model the cooling of a neutron star is presented and at the end of the section the simplest model, described by (11.1), is solved analytically. The next three sections present models, and numerical results, of increasing complexity as well as comparisons with observational data. Finally, Sect. 11.6 summarizes the present state of the field and discusses prospects for the future.

11.2 The Essential Physics of Neutron Star Cooling

The study of the cooling of a neutron star can reach high levels of sophistication, several of them being presented in the next sections. However, the basic features can be easily grasped by simply considering the energy balance equation for the

[3] Notice, however, that even a simple neutron+proton liquid with a high enough proton concentration also allows intense neutrino emission by the direct Urca process.

star. In its Newtonian formulation, if $E_{\rm th}$ is the thermal energy content of the star and $C_{\rm v}$ its specific heat, this equation reads

$$\frac{dE_{\rm th}}{dt} = C_{\rm v}\frac{dT}{dt} = -L_\nu - L_\gamma + H\,. \tag{11.1}$$

This simply states that the change in $E_{\rm th}$ must be given by the sum of the energy losses due to neutrinos, L_ν, from the whole stellar interior and photons, L_γ, emitted at the stellar surface, possibly compensated by some "heating" mechanism(s), H. (These three quantities, L_ν, L_γ, and H, have dimension of luminosities, i.e., erg s^{-1}.) In this simple version, the energy balance equation assumes the stellar interior has a uniform temperature T. This latter assumption is not valid for young stars but all observed thermally emitting neutron star are old enough that the isothermal interior approximation is quite good. Modern models of neutron star cooling use a general relativistic formulation and perform heat transport in the interior:[4] the corresponding formalism is briefly described in Appendix B of [56] and the evolution of a young neutron star toward isothermality will be described in Sect. 11.4.2. Notice, however, that in case the star is permeated by a strong magnetic field, this approximation of an isothermal interior may break down, as will be discussed in Sect. 11.5.

The heating term H can include many possible dissipative processes which convert rotational, magnetic or "chemical" energy into heat. I will not consider it here and refer the reader to [54] for further discussion.

Preliminary to solving (11.1) one needs to have a star, i.e., choose an equation of state and obtain the density profile by solving the Oppenheimer–Volkoff equation of hydrostatic equilibrium. I refer the reader to [88] or [58] for this preliminary step and a presentation of the many possible choices. The following subsections present the basic ingredients entering (11.1).

11.2.1 Specific Heat

Since matter is highly degenerate in most of the interior, one can use the Fermi-liquid result by summing the contributions of each constituent species i (electrons, muons, neutrons, protons, ...)

$$c_{\rm v} = \sum_i c_{{\rm v,i}} \quad \text{with} \quad c_{{\rm v,i}} = \left(\frac{m_{\rm i}^* p_{\rm F,i}}{\pi^2\hbar^3}\right)\frac{\pi^2}{3}k_{\rm B}^2 T \tag{11.2}$$

to obtain the specific heat, per unit volume, at constant volume $c_{\rm v}$ (which, for degenerate Fermions, is equal to the one at constant pressure $c_{\rm p}$). For each particle species, its Fermi momentum $p_{\rm F}$ is related to its number density n through the same relation as in the case of an ideal Fermi gas

[4] See footnote 1.

$$n = \frac{p_{\rm F}^3}{3\pi^2\hbar^3} \,. \tag{11.3}$$

The effective mass m^* and Fermi velocity $v_{\rm F}$ are defined from the *single particle excitation energy* $\varepsilon(p)$ by the relation

$$\left.\frac{\partial\varepsilon(p)}{\partial p}\right|_{p=p_{\rm F}} \equiv \frac{p_{\rm F}}{m^*} \equiv v_{\rm F} \,. \tag{11.4}$$

For momenta close to $p_{\rm F}$ one can thus write

$$\varepsilon(p) = E_{\rm F} + v_{\rm F}\,(p - p_{\rm F}) \,, \tag{11.5}$$

where, by definition, the Fermi energy $E_{\rm F}$ is the value of $\varepsilon(p)$ at the Fermi surface. For a non relativistic free particle of mass m one has $\varepsilon(p) = mc^2 + p^2/2m$ and thus $m^* = m$. In the case of electrons and muons, electromagnetic interaction effects on $\varepsilon(p)$ are negligible once density exceeds $\sim 10^4$–$10^5\,{\rm g\,cm^{-3}}$, hence $\varepsilon(p) = (m^2c^4 + p^2c^2)^{1/2}$ and when they become highly relativistic $m^* = \varepsilon(p_{\rm F})/c^2 = E_{\rm F}/c^2$: in this case $m^* \gg m$. When interactions are important $\varepsilon(p)$ is modified and for strongly interacting particles, i.e., nucleons and hyperons, which never become highly relativistic, m^* is usually *smaller* than the free mass m.

Notice that m^* in (11.4) is defined by evaluating the derivative at the Fermi surface. Finite temperature effects can only excite particles with energies close to $E_{\rm F}$, since $k_{\rm B}T \ll E_{\rm F}$ in a highly degenerate Fermion system. Physical quantities dependent on thermal excitations will usually contain a factor $N(0)$, called the density of states at the Fermi surface, defined through

$$g\iint \frac{dp^3}{(2\pi\hbar)^3} = g\frac{4\pi p_{\rm F}^2\,dp}{(2\pi\hbar)^3} = N(0)d\varepsilon \qquad \text{or} \qquad N(0) \equiv \frac{m^* p_{\rm F}}{\pi^2\hbar^3} \tag{11.6}$$

when integrating over the surface of the Fermi sphere (and $g = 2$ for spin 1/2 Fermions). $N(0)$ naturally appears in the expression for $c_{\rm v}$ in (11.2), reflecting the fact that, when $k_{\rm B}T \ll E_{\rm F}$, only particles close to the Fermi surface can be thermally excited and store heat.

The $C_{\rm v}$ in (11.1) is simply the integral of $c_{\rm v}$ over the whole star. An example of the contributions of the various components in the core is shown in Fig. 11.2 which plots $c_{\rm v}$ per unit volume vs. volume so that the area, in the figure, of the strip corresponding to each component directly gives its contribution to $C_{\rm v}$. In the crust, electrons are also highly degenerate, except in the upper part of the envelope (see below), as are the free neutrons in the inner crust. The contribution of the crustal lattice has to be added for detailed calculations, as described, e.g., in Chap. 4 of Shapiro and Teukolsky [79].

An important point is that superfluidity and superconductivity strongly alter the value of $C_{\rm v}$ as discussed in the following subsection.

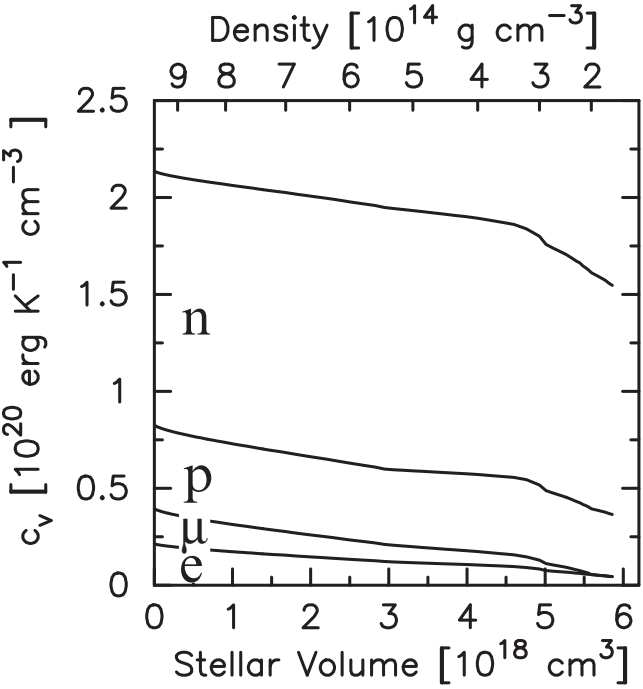

Fig. 11.2 Cumulative specific heats of e, μ, p, and n vs. stellar volume in the core of a 1.4 $M_\odot$ star built using the APR (Akmal, Pandharipande, and Ravenhall [3]) equation of state, at temperature $T = 10^9$ K. Nucleons are assumed to be unpaired. (Notice that $C_v \propto T$ in absence of pairing.) (Figure from [56])

11.2.2 Pairing: Superfluidity and Superconductivity

The presence of superfluidity and superconductivity in the neutron star interior is one of the most important features of these stars. Soon after the development of the BCS theory [9], Bohr, Mottelson, and Pines [10] argued that the same phenomenon of pairing is occurring inside nuclei and Migdal [45] moreover extended the idea to the interior of neutron stars. Formation of Cooper pairs and the resulting condensate is expected to occur, at low enough temperature, in any degenerate system of Fermions in which there is an attractive interaction between particles whose momenta lie close to the Fermi surface: this is the Cooper theorem [14]. The strength of the interaction determines the critical temperature T_c at which the pairing phase transition will occur. In laboratory superconductors one can identify a very weak residual attraction between electrons, once e–e, e–ion, and ion–ion interactions are properly modeled, which results in pairing, with small critical temperatures. In nuclei and neutron star matter, the strong interaction between neutrons, between protons, and also probably between hyperons, immediately provides attractive channels for pairing.

In a normal system the energy $\varepsilon(p)$ varies smoothly when p crosses the Fermi surface as described by (11.5) while in the presence of pairing a discontinuity develops

$$\begin{aligned} \varepsilon(p) &= E_{\rm F} - \sqrt{v_{\rm F}^2(p-p_{\rm F})^2 + \Delta^2} \quad \text{for} \quad p < p_{\rm F} \,, \\ \varepsilon(p) &= E_{\rm F} + \sqrt{v_{\rm F}^2(p-p_{\rm F})^2 + \Delta^2} \quad \text{for} \quad p > p_{\rm F} \,, \end{aligned} \tag{11.7}$$

where Δ is called the (energy) gap and can be seen as half the binding energy of a Cooper pair. Thus, states with $p \lesssim p_{\rm F}$, which in the absence of pairing have energy $\varepsilon(p) \lesssim E_{\rm F}$, see their energy being pushed down below $E_{\rm F} - \Delta$ in the presence of pairing; and vice versa for states with $p \gtrsim p_{\rm F}$. The transition from the normal state to the superfluid, or superconducting, state is a second order phase transition. The gap Δ acts as an order parameter, is temperature dependent, $\Delta = \Delta(T)$, and its value at $T = 0$ is related to the critical temperature $T_{\rm c}$ by

$$k_B T_c \approx 0.57 \Delta(0) \,. \tag{11.8}$$

For $T > T_{\rm c}$ the gap vanishes while it rapidly grows when $T < T_{\rm c}$.

Let us consider, as an example, the storage of thermal energy, i.e., the specific heat. For a normal degenerate Fermi system $c_{\rm v}$ is given by (11.2) where the presence of m^* reflects the fact that, since $\varepsilon(p)$ varies smoothly across the Fermi surface, any amount of energy, no matter how small, can be imparted to a particle. Once this systems pairs, because $\varepsilon(p)$ develops a discontinuity at $E_{\rm F}$, a thermal excitation requires an amount of energy of at least Δ and hence one can expect that $c_{\rm v}$ will be suppressed, when $k_{\rm B}T \ll \Delta$, roughly by a Boltzmann-like factor $\exp(-\Delta/k_{\rm B}T)$. However, when $T \sim T_{\rm c}$ the system copiously forms pairs and, since at these temperatures $k_{\rm B}T \gg \Delta(T)$, also easily breaks them: storing thermal energy becomes very easy and this results in a jump of $c_{\rm v}$, typical of the strong fluctuations at a second order phase transition. In numerical calculations these effects are incorporated through a control coefficient $\mathcal{R}$ so that

$$c_{\rm v} = c_{\rm v}^{\rm normal} \to c_{\rm v}^{\rm paired} = \mathcal{R}(T/T_{\rm c}) \times c_{\rm v}^{\rm normal} \,. \tag{11.9}$$

Such coefficients have been calculated in [42] for several types of pairing and two of them are illustrated in the upper panel of Fig. 11.5. Besides its effect on the specific heat, pairing has an even more dramatic effect on neutrino emission, as presented in the next subsection.

In the BCS *weak coupling approximation* the zero temperature pairing gap can be estimated as

$$\Delta(0) \sim E_{\rm F} e^{-1/N(0)V} \,, \tag{11.10}$$

where $N(0)$ is the density of states at the Fermi surface, defined in (11.6), and V the pairing potential. The exponential dependence of Δ on the pairing interaction V (and also on the details of the energy spectrum $\varepsilon(p)$ contained in $N(0)$ through its m^* dependence), illustrated in this simple formula, implies that accurate calculations are extremely difficult. For nucleons, pairing channels can be searched for

by considering the "bare" nucleon–nucleon interaction studied in low-energy laboratory experiments. It turns out that at low momentum p, which will translate into low $p_{\rm F}$ and hence low density, the dominant attraction occurs in the spin-angular momentum $^1S_0$ channel.[5] At higher momentum, and hence higher density in a neutron star, the preferred pairing channel becomes the spin triplet $^3P_2$, which is moreover coupled to $^3F_2$ by the tensor interaction, giving a $^3P_2$–$^3F_2$ pairing. Considering the *bare* interaction only gives a presumption that the corresponding coupling can induce pairing *in-medium*: response of the medium can naturally be expected to have a significant influence on the interactions. Medium polarization has been the most studied effect to date, and it can result in a reduction, because of screening, or an enhancement, because of anti-screening, of the pairing. Neutron $^1S_0$ pairing is by far the most studied case and, with time, results have converged and show that medium polarization reduces the gap by almost a factor of 3. Among the many calculations of proton $^1S_0$ gaps there is a much larger spread in predictions and medium effects have not yet been thoroughly investigated. The case of neutron $^3P_2$ gaps is even more difficult and even the *bare* interaction in this channel is not yet satisfactorily described by current theories, leading to an enormous spread in predicted values of $T_{\rm c}$ [8]. Moreover, Schwenk and Friman [75] recently showed that a strongly repulsive force in this channel develops *in-medium*, which is not present *in-vacuum*, and possibly results in a vanishingly small gap. Two good recent reviews of these issues can be found in [43] and [77], the latter also describing many other consequences of superfluidity and superconductivity in neutron star phenomenology. A range of prediction for $T_{\rm c}$'s is presented in Fig. 11.3 for neutron $^1S_0$ and $^3P_2$ pairing and in Fig. 11.4 for proton $^1S_0$ pairing.

Hyperons (see, e.g., [81] and references therein) and quarks (see, e.g., [4, 5] and references therein) are also likely to pair, if they appear in the inner core, but uncertainties about the size of the gaps are even larger than the ones for nucleons.

Things Are Likely Much More Complicated!

To make matters worse, the gap at the Fermi surface is actually a matrix in angular momentum space, $\Delta = \|\Delta_l^{j,m_j}\|$, and a function of the Fermi momentum $\mathbf{k}_{\rm F} \equiv \mathbf{p}_{\rm F}/\hbar$, i.e., it can depend on the particle momentum's orientation. It is only in the case of $^1S_0$ pairing that Δ is a scalar, since $j = l = s = 0$, and is isotropic, i.e., $\Delta = \Delta(k_{\rm F})$. However, for $^3P_2$ pairing the many components of Δ ($j = 2$ and $l = 1$) describe many different phases, and Zverev et al. [95] have shown that there are at least thirteen of them! Each phase results in a different *energy* gap deduced from the corresponding expressions of the non-vanishing components of Δ. Fortunately, in absence of external perturbations, one phase seems to be energetically preferred, corresponding to $m_j = 0$, and the angular dependence of the energy gap is $\propto 1 + 3\cos^2\theta_k$ where θ_k is the azimuthal angle of the Fermi momentum $\mathbf{k}_{\rm F}$ for an arbitrary

[5] In spectroscopic notations: this means Cooper pairs have orbital angular momentum $\mathbf{L}$ with $l = 0$ ("S"), total spin $\mathbf{S}$ with $s = 0$, i.e., spin-singlet and hence the superscript "1", and total angular momentum $\mathbf{J}$ with $j = 0$, the "0" subscript.

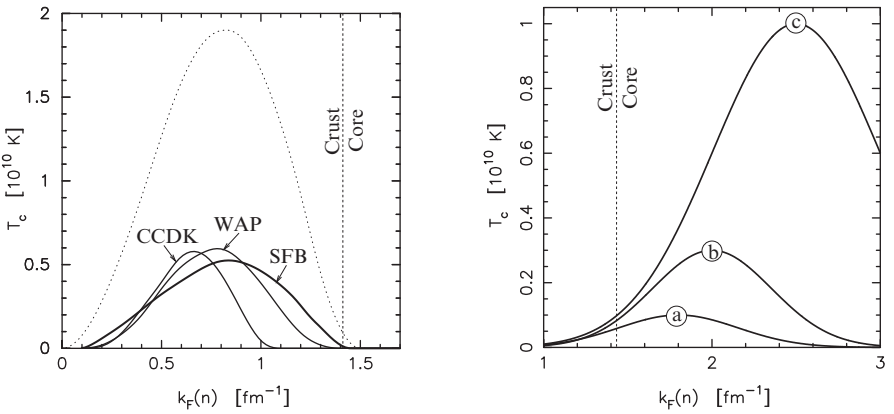

Fig. 11.3 *Left panel*: neutron $^1S_0$ pairing critical temperatures T_c from the calculations of [12] ("CCDK"), [87] ("WAP"), and [76] ("SFB"), all three including medium polarization effects using various many-body technics. The *dotted line* shows a typical result when medium polarization effects are neglected. *Right panel*: three typical neutron $^3P_2$ pairing critical temperatures curves representatives of present uncertainties (from the simple parameterization of [56]). The *vertical dashed line* shows the approximate location of the crust–core transition. The *horizontal axis* shows the Fermi momentum $k_F \equiv p_F/\hbar$. (Figures from [56])

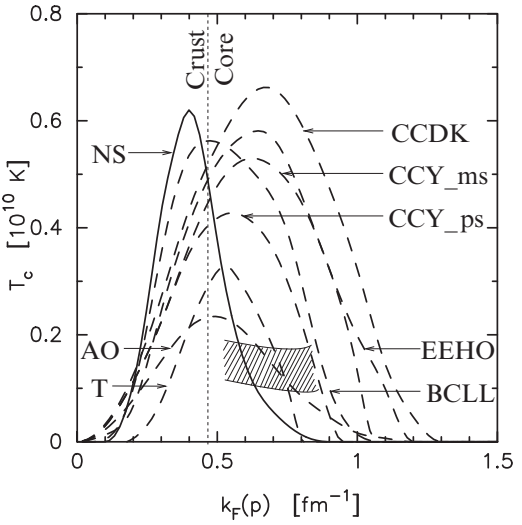

Fig. 11.4 Proton $^1S_0$ pairing critical temperatures T_c from a large set of calculations (see [56] for references). The model "NS" is the only one to have included medium polarization effects while the *shaded region* shows the estimates of [2] for the range of values in which T_c is expected to lie due to medium polarization. The *vertical dashed line* shows the approximate location of the crust–core boundary. (Figure from [56])

angular momentum quantization axis. However, another phase, corresponding to $|m_j| = 2$, has an energy gap proportional to $\sin^2\theta_k$ which hence *vanishes* on the Fermi sphere equator: such a gap with *nodes* has a much less efficient suppression effect on the specific heat, and also on neutrino emission (see next subsection). Nevertheless, for an appropriate definition of the angle-average of the energy gap its value is still related to T_c through the relation of (11.8), at least for several studied cases (see, e.g., [7]).

11.2.3 Neutrino Emission

The most efficient neutrino emission process (see Table 11.1), in the core of a neutron star, is the so-called direct Urca (or "DUrca") process

$$n \to p + e^- + \bar{\nu}_e \quad \text{and} \quad p + e^- \to n + \nu_e \,, \tag{11.11}$$

which is simply the β-decay of the neutron and its inverse reaction. Such reactions can only occur if they satisfy energy and momentum conservation. For degenerate matter, possible energies and momenta are very close, to within $\sim k_{\rm B}T$, to the particle Fermi energies and momenta. Since $E_{\rm F,i}$ is practically equal to the chemical potential $\mu_{\rm i}$, energy conservation is simply $\mu_n = \mu_p + \mu_e$ (assuming the ν's leave the star and have vanishing chemical potentials), which is just the condition for chemical equilibrium and is always satisfied. However, momentum conservation is non-trivial and the reaction (11.11) requires $p_{F,n} \le p_{F,p} + p_{F,e}$ (the triangle inequality). Considering the simplest case where the only present charged particles are p and e, charge neutrality requires $n_p = n_e$, i.e., from (11.3), $p_{F,p} = p_{F,e}$ and the triangle inequality gives $p_{F,n} \le 2p_{F,p}$. In terms of density this is $n_n \le 8n_p$ or, using the "proton fraction" $x_p \equiv n_p/n_B$, with $n_B \equiv n_n + n_p$ being the baryon density, the reaction (11.11) requires

$$x_p \ge \frac{1}{9} \simeq 11\% \,. \tag{11.12}$$

Since we are considering "neutron stars" it was assumed during many years that such a high proton fraction was unrealistic and that the DUrca process is kinematically forbidden. Hence, the modified Urca (or "MUrca") process

Table 11.1 Examples of neutrino emitting processes in neutron star cores[a]

Name	Process	Emissivity[b] (erg cm^{-3} s^{-1})	
Modified Urca (neutron branch)	$n+n \to n+p+e^- + \bar{\nu}_e$ $n+p+e^- \to n+n+\nu_e$	$\sim 2\times 10^{21}\,\mathcal{R}\,T_9^8$	Slow
Modified Urca (proton branch)	$p+n \to p+p+e^- + \bar{\nu}_e$ $p+p+e^- \to p+n+\nu_e$	$\sim 10^{21}\,\mathcal{R}\,T_9^8$	Slow
Bremsstrahlung	$n+n \to n+n+\nu\bar{\nu}$ $n+p \to n+p+\nu\bar{\nu}$ $p+p \to p+p+\nu\bar{\nu}$	$\sim 10^{19}\,\mathcal{R}\,T_9^8$	Slow
Cooper pair formations	$n+n \to [nn]+\nu\bar{\nu}$ $p+p \to [pp]+\nu\bar{\nu}$	$\sim 5\times 10^{21}\,\mathcal{R}\,T_9^7$ $\sim 5\times 10^{19}\,\mathcal{R}\,T_9^7$	
Direct Urca	$n \to p+e^- + \bar{\nu}_e$ $p+e^- \to n+\nu_e$	$\sim 10^{27}\,\mathcal{R}\,T_9^6$	Fast
π^- condensate	$n+<\pi^->\to n+e^- + \bar{\nu}_e$	$\sim 10^{26}\,\mathcal{R}\,T_9^6$	Fast
K^- condensate	$n+<K^->\to n+e^- + \bar{\nu}_e$	$\sim 10^{25}\,\mathcal{R}\,T_9^6$	Fast

[a] Table from [54].
[b] For each process the "control coefficient" $\mathcal{R} = \mathcal{R}(T/T_{\rm c})$ is introduced to take into account the extra temperature dependence due to pairing [92].

$$n + n' \to p + n' + e^- + \bar{\nu}_e \quad \text{and} \quad p + n' + e^- \to n + n' + \nu_e \tag{11.13}$$

was considered as the standard neutrino cooling agent. In the reactions (11.13) the spectator neutron n' is present to satisfy momentum conservation but makes it a process with five degenerate Fermions instead of three and introduces a suppression of the order of $(k_{\rm B}T/E_{F,n})^2$, reducing its efficiency by about six orders of magnitude when $T \sim 10^9$ K compared to the DUrca process. However, as was shown by Lattimer et al. [38], the constraint of (11.12) is not as restrictive as had been thought and practically *all* modern equations of state allow the occurrence of the DUrca process at high enough densities.

When other species of baryons are present similar DUrca and MUrca processes are possible. For example, if Λ hyperons can appear one has the DUrca process $\Lambda \to p + e^- + \bar{\nu}_e$ and its inverse, whereas in deconfined quark matter one has $d \to u + e^- + \bar{\nu}_e$ and its inverse, both subjected to the fulfillment of their respective triangle inequalities. In the presence of a charged meson condensate, such as π^- or K^-, other versions of the Urca process become possible, even if the triangle inequality is not satisfied, which are not as efficient as the pure DUrca process (11.11) but still much more efficient than the MUrca process. Notice, moreover, that it is possible that medium effects on the MUrca process, leading to the Medium Modified Urca (MMUrca) process (see, e.g., [86]), may imply a significantly higher rate than what has been used in most cooling simulations.

Besides these Urca type processes there are many other processes based on neutral current which produce $\nu_i\bar{\nu}_i$ pairs, where here ν_i can be any neutrino flavor, ν_e, ν_μ or ν_τ. For example

$$n + n \to n + n + \nu_i\bar{\nu}_i \,, \tag{11.14}$$

which is called n–n-bremsstrahlung. Almost any process known to emit a photon has an analogous one in which the photon is substituted by a $\nu\bar{\nu}$ pair (in the Standard Model: the photon is replaced by a Z^0 boson, the photon's heavy brother, which itself decays into a $\nu\bar{\nu}$ pair). Electron–electron bremsstrahlung [31] is such an example:

$$e^- + e^- \to e^- + e^- + \gamma \quad \text{becomes} \quad e^- + e^- \to e^- + e^- + \nu_i\bar{\nu}_i \,. \tag{11.15}$$

In the presence of superfluidity/superconductivity neutrino emission is strongly altered, an effect similar to what happens with the specific heat and also due to the presence of a gap Δ in the single particle excitation spectrum $\varepsilon(p)$. All processes described above involve particle excitations and if one of the participating particles has a gap Δ in its spectrum this energy cost reduces the number of such excitations and leads to a strong suppression of the process. When $T \ll T_{\rm c}$ one can expect a Boltzmann-like suppression, $\sim\exp[-\Delta(T)/k_{\rm B}T]$, and detailed calculations (see, e.g., [92]) confirm this naive expectation. In the same fashion as is done for the specific heat, (11.9), control functions are used to incorporate this effect on the emissivity $\varepsilon_{\nu X}$ of a process "X" when some of the participating particle(s) undergo(es) pairing:

$$\varepsilon_{\nu,X} = \varepsilon_{\nu,X}^{\rm normal} \to \varepsilon_{\nu,X}^{\rm paired} = \mathcal{R}_X(T/T_c) \times \varepsilon_{\nu,X}^{\rm normal} \,. \tag{11.16}$$

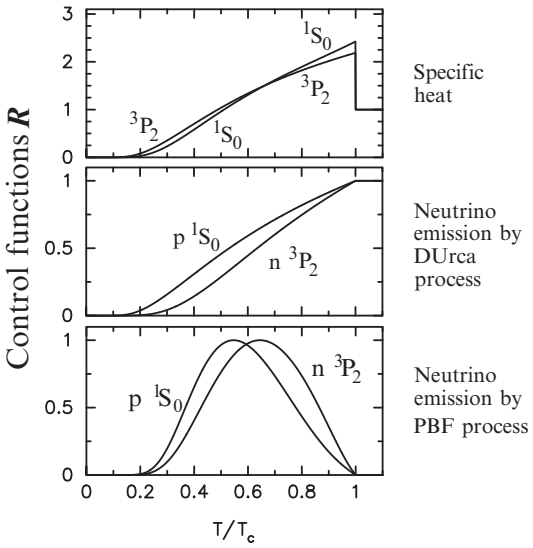

Fig. 11.5 Some examples of control functions for c_ν, (11.9) (*upper panel*), DUrca ε_ν, (11.16) (*middle panel*), and PBF ε_ν, (11.18) and (11.19) (*lower panel*). In the $^3P_2$ case the nodeless $m_j = 0$ phase is assumed. (Figure from [58])

There is a large family of such control functions [92] which not only depend on the details of each reaction but also on which participating particle(s) has a gap, and two of these are shown in the middle panel of Fig. 11.5.

An important family of neutrino emission processes appears when particles become paired [17]. The formation (and, to a lesser extent, the breaking) of a Cooper pair releases energy which can be emitted as a $\nu\bar{\nu}$ pair, as, for example, in

$$n + n \to [nn] + \nu_i \bar{\nu}_i \,, \tag{11.17}$$

which is analogous to the process (11.14) but where $[nn]$ designates a neutron Cooper pair (so this process can be viewed as a bremsstrahlung with a very strong correlation in the final state). These processes have been dubbed as "PBF" processes, for "pair breaking and formation". At temperatures slightly below the pairing critical temperature T_c single particles (i.e., "broken pairs") are abundant and in thermal equilibrium with the condensate (i.e., the paired particles) and the corresponding PBF process is a copious neutrino emitter. The PBF process (11.17) is actually more efficient than the simple bremsstrahlung (11.14) and even more efficient than the MUrca process (11.13), its emissivity being of the order of

$$\varepsilon_{\nu\, PBF\, n\, ^3P_2} \sim 5 \times 10^{21}\, T_9^7\, \mathcal{R}_{^3P_2}(T/T_c) \,. \tag{11.18}$$

Recent more detailed calculations by Leinson and Peréz [39,40], see also [78], have shown that correct introduction of charge conservation in the calculation results in a suppression of the vector part of the PBF process by several orders of magnitude. The axial part thus makes the dominant contribution, but in the case of $^1S_0$ gaps this axial part is suppressed for non relativistic particles. As a result, the PBF process probably has a negligible effect in the case of the inner crust $^1S_0$ superfluid neutrons

while for the core $^1S_0$ superconducting protons its emissivity, essentially given by the axial part, is of the order of

$$\varepsilon_{\nu\, PBF\; p\, ^1S_0} \sim 5 \times 10^{19}\, T_9^7\, \mathcal{R}_{^1S_0}(T/T_c)\,. \tag{11.19}$$

In the case of the neutron $^3P_2$ pairing, the suppression of the vector channel results only in a small reduction, $\sim$25%, of the total emissivity of (11.18). The two control functions $\mathcal{R}$, for $^1S_0$ proton and $^3P_2$ neutron pairing, are plotted in the lower panel of Fig. 11.5 and show that the process turns on when T reaches T_c, increases sharply when T decreases and then becomes exponentially suppressed at $T \ll T_c$.

Table 11.1, taken from [54], lists some of these processes with order of magnitude estimates of their emissivities. The last column indicates if the process leads to "slow" or "fast" neutrino cooling, a qualification which results from both the overall efficiency and the temperature dependence: T^6 for the fast processes and T^8 for the slow ones. The PBF processes are intermediate between slow and fast ones. It is important to notice that when muons are present each process involving an electron has a analogous one where e^- is replaced by a μ^- and when hyperons or quarks are present most processes of Table 11.1 have analogous processes where n and/or p are replaced by hyperons or quarks. Including all direct and modified Urca, bremsstrahlung, and PBF processes with all possibly present particles one obtains more than a hundred possible neutrino emission mechanisms! This presentation of neutrino processes is very sketchy and the reader is referred to [54, 58] for longer presentations and to the review of [92] where a detailed presentation of many processes may be found.

Neutrino Processes in the Crust

In most cases the neutrino cooling is driven by core emission, exceptions being models in which baryon in the whole core are paired with high T_c's. However, at early times when the star's age is smaller than the thermal diffusion time, the crust and core cooling are almost independent and crust neutrino emission controls the cooling of the crust (this will be described in detail at the end of Sect. 11.4). The two dominant processes in the crust are the plasmon (Γ) decay

$$\Gamma \to \nu\overline{\nu} \tag{11.20}$$

and the electron–ion bremsstrahlung[6]

$$e^- + \text{Nucleus} \to e^- + \text{Nucleus} + \nu\overline{\nu}. \tag{11.21}$$

In vacuum the photon decay, $\gamma \to \nu\overline{\nu}$, is forbidden by energy-momentum conservation but in a dense medium the plasmon dispersion relation renders the decay of a Γ possible. The bremsstrahlung process (11.21) is another example where a classical process emitting a γ has an analogous one emitting a $\nu\overline{\nu}$ pair. At very high temperatures when positrons are present one also has the pair annihilation

[6] When ions form a crystal one should rather call this process electron–phonon bremsstrahlung.

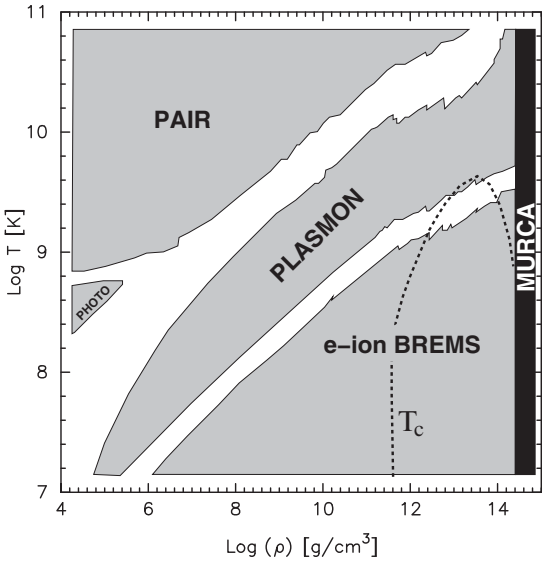

Fig. 11.6 Dominant neutrino emission processes in the crust. *Each shaded region* shows the regime in which a given process contributes more than 90% of the neutrino energy losses. An example of neutron $^1S_0$ superfluidity T_c curve is also plotted, below which the PBF process starts to act with an emissivity similar to the one of the e–ion bremsstrahlung. (Figure produced using the calculations of [30])

process, $e^- + e^+ \to \nu\overline{\nu}$. These processes have complicated T and ρ dependences, but Fig. 11.6 illustrates the regimes in which each makes the dominant contribution. (The photo-neutrino process, $\gamma + e^- \to e^- + \nu\overline{\nu}$, is not relevant for our purposes.) Once neutrons become superfluid in the inner crust, the corresponding PBF process was thought to dominate over e–ion bremsstrahlung by several orders of magnitude, but the recent results of [39, 40, 78] show that it is actually of the same order of magnitude as the e–ion bremsstrahlung. The free neutrons in the inner crust also emit neutrinos through the bremsstrahlung process of (11.14), but this emission is suppressed by the neutron superfluidity which makes it only a minor process.

11.2.4 Photon Emission and the Envelope

The photon luminosity L_γ is traditionally expressed as

$$L_\gamma = 4\pi R^2 \cdot \sigma_{\rm SB} T_{\rm e}^4 , \tag{11.22}$$

which *defines* the effective temperature $T_{\rm e}$ ($\sigma_{\rm SB}$ being the Stefan–Boltzmann constant and R the stellar radius). The quantities L, R, and $T_{\rm e}$ are local quantities as measured by an observer at the stellar surface. An external observer "at infinity" will measure these quantities red-shifted, i.e., $L_\infty = e^{2\phi} L_\gamma$, $T_\infty = e^{\phi} T_{\rm e}$, and $R_\infty = e^{-\phi} R$, where $e^{2\phi} \equiv g_{00}$ is the time component of the metric and is related to the red-shift z by $e^{-\phi} = 1 + z$, so that

$$L_\infty = 4\pi R_\infty^2 \cdot \sigma_{\rm SB} T_\infty^4 . \tag{11.23}$$

The radius at infinity, R_∞, and temperature at infinity, T_∞, are quantities which are, in principle, directly observable and whose values are often quoted by observers.[7]

Non-Magnetized Envelopes

The temperature T_e, or T_∞, is of course different from the interior temperature T which appears in (11.1): even under the assumption of a uniform interior temperature T one cannot avoid having strong temperature gradients in the upper layers of the star. In the deep interior heat transport is usually dominated by the electrons which are highly degenerate and have a very high thermal conductivity. As a result, within a few years after the star's birth its interior temperature will become uniform, as will be described in Sect. 11.4.2, a situation commonly referred to as "isothermality". In the atmosphere, in case the surface is not in a condensed state, and in the lowest density layers beneath it, photons dominate the heat transport but there is an intermediate layer where photon transport is inefficient because of the higher density and where electrons are not yet highly degenerate. Dubbed the "sensitivity strip", this layer acts as a heat throttle and controls the heat flow toward the surface. As is traditional in stellar structure modeling, one usually separates out the outer part of the star where strong temperature gradients are always present and treat it as the outer boundary condition in cooling calculations. This outer zone is termed the *envelope* and, with a typical cut density $\rho_b = 10^{10}\,\mathrm{g\,cm^{-3}}$, it has a thickness of the order of 100 m. Gudmundsson et al. [24] presented a detailed study of neutron star envelopes and summarized their results by a simple "T_b–T_e relationship"

$$T_e \simeq 0.87 \times 10^6\, g_{s\,14}^{1/4} \left(\frac{T_b}{10^8\ \mathrm{K}} \right)^{0.55} , \tag{11.24}$$

where T_b is the temperature at the bottom of the envelope, at density $\rho_b = 10^{10}\,\mathrm{g\,cm^{-3}}$, and equal to the interior temperature T in the uniform temperature approximation, and $g_{s\,14}$ is the surface gravity acceleration in units of $10^{14}\,\mathrm{cm\,s^{-2}}$. (As rule of thumb: $T_e \sim T_b^{1/2}$ and $T_e \sim 10^6$ K $\leftrightarrow T_b \sim 10^8$ K.)

The results of (11.24) had been obtained assuming that matter in the envelope is made of ^{56}Fe and iron-like nuclei, i.e., so-called "catalyzed matter". However, this is the textbook chemical composition of neutron star upper layers and real stars may be more dirty: depending on the early history of the star, during or just after the supernova explosion, lighter elements may have been deposited at the surface. They can significantly alter the heat transport since the electron thermal conductivity in the liquid layers of the sensitivity strip is approximately proportional to Z^{-1}, Z being the charge number of the nuclei. Light elements, as, e.g., H, He, C, or O, hence result in a more efficient heat transport and may induce a higher surface temperature T_e for a given T_b if they are present deep enough to reach the sensitivity strip [11]. Since the temperature gradient in the envelope is essentially limited to the region where

[7] Notice that R_∞ has the interpretation of being the radius an observer would measure were she/he able to resolve the angular size of the star, considering the effect of gravitational light bending [49].

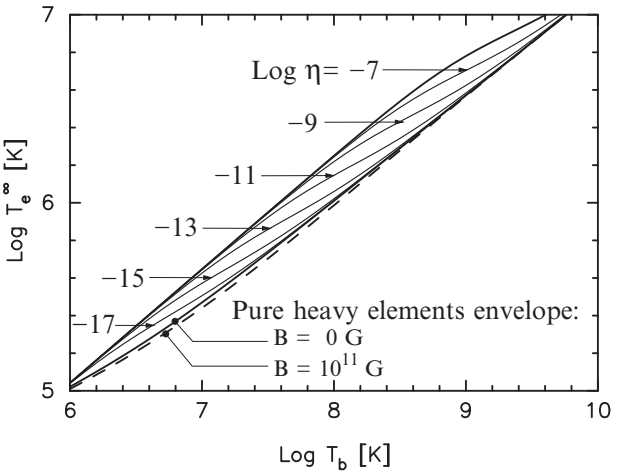

Fig. 11.7 T_b–T_e^∞ relationships for various amounts of light elements, parameterized by $\eta \equiv g_{s14}^2 \Delta M_\mathrm{L}/M$ (ΔM_L is the mass in light elements in the envelope, g_{s14} the surface gravity in units of $10^{14}\,\mathrm{cm\,s^{-1}}$, and M is the star's mass), in the absence of a magnetic field [67]. Also shown are the relationships for an envelope of heavy elements with and without the presence of a dipolar field of strength of 10^{11} G, following [68]. (Figure from [56])

electrons are non degenerate it reaches larger densities at high T_e than at low T_e. As a result, a thicker layer of light elements is necessary to affect the outcoming heat flux in a hot star than in a cold one. The resulting T_b–T_e relationships are exhibited in Fig. 11.7 which shows that such a small amount of light elements as $10^{-7} M_\odot$ is enough to significantly increase T_e and, since $L_\gamma \propto T_\mathrm{e}^4$, result in photon luminosities almost one order of magnitude higher than in cases where only iron-like elements are present.

It is important to emphasize that the chemical composition of the uppermost layers, the atmosphere, has no effect on the outcoming integrated flux F, since it is determined by the underlying sensitivity strip and the temperature profile in the atmosphere will simply adjust to let this flux go through it, possibly becoming convective (see, e.g., [11]). However, the atmosphere is of upmost observational importance since it is where the spectral distribution $F(E)$ is determined.

Heat Transport in the Presence of a Strong Magnetic Field

In the absence of magnetic field the thermal conductivity κ, which relates the heat flux $\mathbf{F}$ to the temperature gradient ∇T through $\mathbf{F} = -\kappa \cdot \nabla T$, is conveniently written as

$$\kappa_0 = \frac{1}{3} c_\mathrm{v}^\mathrm{hc} \bar{\mathrm{v}}^2 \tau = \frac{\pi^2 k_\mathrm{B}^2 T n_e}{3 m_e^*} \tau \,, \tag{11.25}$$

where c_v^hc is the specific heat of the heat carriers, $\bar{\mathrm{v}}$ their mean velocity, and τ their collisional time; the second expression is particularized to relativistic electrons [94].

In the presence of a magnetic field, due to the classical Larmor rotation of electrons, heat flow may be anisotropic and κ becomes a tensor

$$\kappa = \begin{pmatrix} \kappa_\perp & \kappa_\wedge & 0 \\ -\kappa_\wedge & \kappa_\perp & 0 \\ 0 & 0 & \kappa_\parallel \end{pmatrix} \tag{11.26}$$

(assuming the field **B** oriented along the z-axis) whose components have the form

$$\begin{aligned} \kappa_\parallel &= \kappa_0 \,, \\ \kappa_\perp &= \frac{\kappa_0}{1+(\omega_B\tau)^2} \,, \\ \kappa_\wedge &= \frac{\kappa_0\,\omega_B\tau}{1+(\omega_B\tau)^2} \,, \end{aligned} \tag{11.27}$$

where $\omega_B = eB/m_e^* c$ is the electron gyrofrequency. The condition $\omega_B\tau \gg 1$, or $\omega_B \gg \nu$ where $\nu = 1/\tau$ is the collisional frequency, which implies strong anisotropy, is easily understood: electrons will undergo many Larmor revolutions between collisions and their motion is essentially controlled by the magnetic field. They can then easily move along the magnetic field, and hence $\kappa_\parallel = \kappa_0$, but cannot move perpendicularly to it, and hence $\kappa_\perp \ll \kappa_0$. In the opposite case, $\omega_B \ll \nu$, electrons only complete a very small part of a revolution between collisions and thus behave almost as if there were no magnetic field. Values of the magnetization parameter $\omega_B\tau$ are plotted in Fig. 11.8 and show that the condition $\omega_B\tau \gg 1$ may be realized in the whole crust [19].

In case the field is strong enough to be quantizing, the expressions (11.27) have to be modified (in particular τ also becomes anisotropic) but the essential result that $\kappa_\perp \ll \kappa_\parallel$, when $\omega_B\tau \gg 1$, remains valid [66].

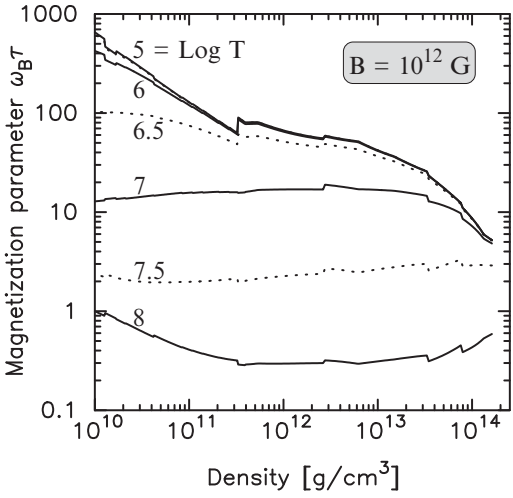

Fig. 11.8 Magnetization parameter $\omega_B\tau$ vs. density at six different temperatures (as labeled on the curves) assuming a uniform magnetic field of strength $B = 10^{12}$ G. Its value for different field strengths scales linearly in B. (Figure from [19])

Magnetized Envelopes

The presence of a magnetic field stronger than 10^{10} G is already sufficient to alter heat transport in the envelope. The magnetic field is of course not uniform over the stellar surface but if we assume that it does not vary much on a length scale of a few hundred meters we can isolate a small patch at the surface and consider **B** to be uniform within it and, given its thinness, also within the underlying envelope. We will see that the surface temperature $T_{\rm s}(\theta,\phi)$ can vary by a factor of a few over the stellar surface while T varies by a much larger factor (one to two orders of magnitude) in the radial direction through the envelope: it is a good approximation to assume that the heat flux **F** and the temperature gradient ∇T are essentially radial. If Θ_B is the angle between **B** and the radial direction, see Fig. 11.9, then the thermal conductivity in the direction of the radially pointing **F**, from the tensor of (11.26), is given by

$$\kappa(\Theta_B) = \cos^2\Theta_B \times \kappa_{\parallel} + \sin^2\Theta_B \times \kappa_{\perp} \ . \tag{11.28}$$

With this form of $\kappa(\Theta_B)$ and radial **F** and ∇T, heat transport in the envelope at this surface patch is a one-dimensional problem, similar to the case of a non-magnetized envelope but with a different thermal conductivity, and also a modified equation of state [91]. The solution is a "local $T_{\rm b} - T_{\rm e}$ relationship", valid only at the small patch of the surface under study, which depends on B and Θ_B: the obtained effective temperature $T_{\rm e}$ is a local one which we will rather write as $T_{\rm s}(\theta,\phi)$ in the sense that the flux emerging from this patch is $\sigma_{\rm B} T_{\rm s}(\theta,\phi)^4$. Given the form of $\kappa(\Theta_B)$, (11.28), Greenstein and Hartke [23] proposed the simple interpolation formula

$$\begin{aligned} T_{\rm s}(\theta,\phi)^4 &\equiv T_{\rm s}(T_{\rm b};B,\Theta_B)^4 \\ &\approx \cos^2(\Theta_B) \times T_{\rm s}(T_{\rm b};B,\Theta_B=0)^4 \\ &\quad + \sin^2(\Theta_B) \times T_{\rm s}(T_{\rm b};B,\Theta_B=90^\circ)^4 \end{aligned} \tag{11.29}$$

for arbitrary angle Θ_B in terms of the two cases of radial ($\Theta_B = 0^\circ$) and tangential ($\Theta_B = 90^\circ$) field. This formula is useful in the sense that only the two cases $\Theta_B = 0^\circ$ and $\Theta_B = 90^\circ$ have to be calculated. Schaaf [74] had performed, with many

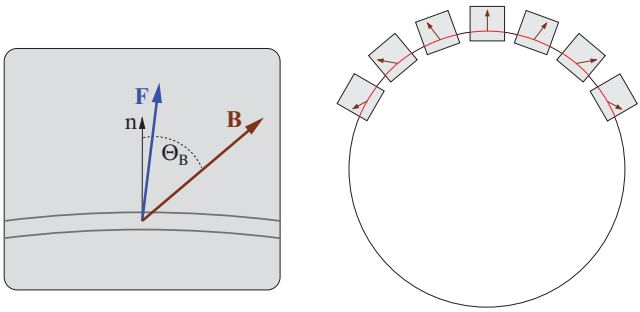

Fig. 11.9 *Left*: a small patch of the neutron star surface-envelope. *Right*: piecing together of such patches, (11.29), for a given field geometry

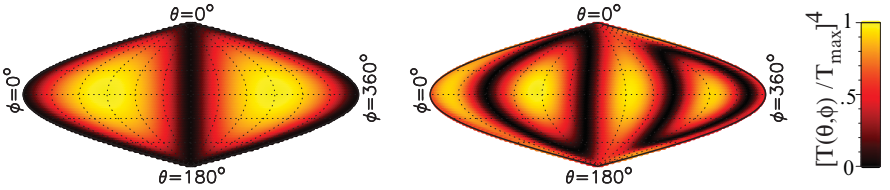

Fig. 11.10 Two examples of surface temperature distribution obtained from (11.29). The maps cover the whole neutron star surface in an area preserving projection. The *left panel* has a dipolar field only while the *right panel* also contains a quadrupolar field superposed to the same dipole. The color coding represents the intensity of emitted flux, i.e., T^4, as indicated on the right scale. For better viewing the dipole magnetic field axis is located in the equatorial plane, oriented from $\phi = 90^\circ$ to $\phi = 270^\circ$. (Figure drawn form the results of [59])

approximations, 2D transport calculations and his results are very well fitted by the simple relation (11.29). Recently, Potekhin et al. [68, 69] have presented detailed calculation and fitted their results by an expression similar to (11.29).

Considering now any surface magnetic field geometry, not necessarily dipolar, one can use a relation of the type of (11.29) to calculate the whole surface temperature distribution [49, 59], under the assumption that, given the high thermal conductivity of the interior, the bottom temperature T_b is uniform. Two examples of such temperature distributions are illustrated in Fig. 11.10. Having the temperature distribution $T_\mathrm{s}(\theta,\phi)$ determined by this method one naturally defines the star's effective temperature , see (11.22), through

$$T_\mathrm{e}^4 \equiv \int\!\!\int \frac{\sin\theta\, d\theta d\phi}{4\pi}\, T_\mathrm{s}(\theta,\phi)^4 \tag{11.30}$$

and, by varying T_b, obtains the resulting T_b–T_e relationship. However, the effect of the magnetic field in the envelope on the T_b–T_e relationship turns out to be relatively small: the blanketing effect in regions where $\Theta_B \sim 90^\circ$ reduces the luminosity but at high enough fields the enhancement of $\kappa_\parallel$ by quantum effects increases T_s in regions where $\Theta_B \sim 0^\circ$ and compensates the previous reduction.

Finally, one has to mention that the assumption of a uniform T_b is questionable: the high thermal conductivity in the interior is largely due to the long collisional time τ and, with strong magnetic fields, this implies that the magnetization parameter $\omega_B\tau$ is very large and may result in a strongly non-uniform crustal temperature. This issue will be discussed in Sect. 11.5.

11.2.5 Some Simple Analytical Solutions

Based on the previous description of physical processes involved in the cooling of a neutron star we can obtain several simple and illustrative analytical results. In line with (11.2) and the neutrino emissivities of Table 11.1 we can write

Table 11.2 Typical numerical coefficients for simplified power-law cooling models

	C erg K^{-2}	$N^{\rm s}$ erg s^{-1} K^{-8}	$N^{\rm f}$ erg s^{-1} K^{-6}	S erg s^{-1} K$^{-2-4\alpha}$	α
high	10^{30}	10^{-32}	10^{-9}	4×10^{14}	0.1
low	10^{29}	10^{-34}	0	2×10^{15}	0.05

Comments:
Values "low" for C and the two $N^{\rm s}$ and $N^{\rm f}$ correspond to a maximum pairing suppression, with a minimum for C due to leptons which never pair and for $N^{\rm s}$ due to neutrino emission from the crust, while for $N^{\rm f}$ it corresponds to absence of fast neutrino emission. For S and α: "high" corresponds to an envelope with a maximum amount of light elements while "low" corresponds to an envelope made of heavy elements, in both cases with a stellar radius $R\sim12\,$km

$$C_{\rm v}=C\cdot T\,,\qquad L_\nu^{\rm slow}=N^{\rm s}\cdot T^8\,,\qquad L_\nu^{\rm fast}=N^{\rm f}\cdot T^6\,, \tag{11.31}$$

explicitly separating fast and slow neutrino processes. For the photon surface emission we can write

$$L_\gamma\equiv4\pi R^2\sigma_{\rm SB}T_{\rm e}^4=ST^{2+4\alpha}\qquad\text{using}\qquad T_{\rm e}\propto T^{0.5+\alpha}\quad(\alpha\ll1)\,, \tag{11.32}$$

where $T_{\rm e}$ has been converted into the internal temperature T through an envelope model with a power-law dependence. In Table 11.2, taken from [54], typical values of the parameters of (11.31) and (11.32) are listed.

Due to the much stronger T-dependence of L_ν compared to L_γ, at early times ν emission drives the cooling, this is the *neutrino cooling era* , and when T has sufficiently decreased photons will take over, the *photon cooling era* . The temperature $T_{\rm shift}$ at which photon cooling takes over can easily be estimated by equating L_ν to L_γ. For slow ν emission one obtains

$$T_{\rm shift}^{\rm s}\simeq\left(\frac{S}{N^{\rm s}}\right)^{1/6}\sim10^8\ {\rm K}\quad\text{and}\quad T_e\sim10^6\ {\rm K}\,, \tag{11.33}$$

whereas for fast ν cooling

$$T_{\rm shift}^{\rm f}\simeq\left(\frac{S}{N^{\rm f}}\right)^{1/4}\sim10^6\ {\rm K}\quad\text{and}\quad T_e\sim10^5\ {\rm K}\,. \tag{11.34}$$

Analytical solutions to (11.1) are easy to obtain:

(1) During the *neutrino cooling era* we can neglect L_γ and find

$$\text{Slow }\nu\text{ cooling}:\quad t=\frac{C}{6N^{\rm s}}\left(\frac{1}{T^6}-\frac{1}{T_0^6}\right), \tag{11.35}$$

$$\text{Fast }\nu\text{ cooling}:\quad t=\frac{C}{4N^{\rm f}}\left(\frac{1}{T^4}-\frac{1}{T_0^4}\right), \tag{11.36}$$

where T_0 is the initial temperature at time $t_0 \equiv 0$. For $T \ll T_0$, this gives

$$\text{Slow } \nu \text{ cooling}: \quad T = \left(\frac{C}{6N^{\rm s}}\right)^{\frac{1}{6}} t^{-\frac{1}{6}} \quad \text{and} \quad T_{\rm e} \mathrel{\widetilde{\propto}} t^{-\frac{1}{12}}\,, \tag{11.37}$$

$$\text{Fast } \nu \text{ cooling}: \quad T = \left(\frac{C}{4N^{\rm f}}\right)^{\frac{1}{4}} t^{-\frac{1}{4}} \quad \text{and} \quad T_{\rm e} \mathrel{\widetilde{\propto}} t^{-\frac{1}{8}} \tag{11.38}$$

(we have used that $\alpha \sim 0$ in the conversion from T to $T_{\rm e}$). The very small exponent of t in the $T_{\rm e}$ evolution during neutrino cooling is a direct consequence of the strong temperature dependence of L_ν. The neutrino cooling time scales are also very suggestive:

$$\text{Slow } \nu \text{ cooling}: \quad \tau_\nu^{\rm slow} = \frac{C}{6N^{\rm s}T^6} \simeq 6 \text{ months} \cdot \left[\frac{C_{30}}{6N^{\rm s}_{-32}T_9^6}\right], \tag{11.39}$$

$$\text{Fast } \nu \text{ cooling}: \quad \tau_\nu^{\rm fast} = \frac{C}{4N^{\rm f}T^4} \simeq 4 \text{ minutes} \cdot \left[\frac{C_{30}}{4N^{\rm f}_{-9}T_9^4}\right], \tag{11.40}$$

and justify the names of "slow" and "fast" neutrino cooling! Notice that 10^9 K is a typical value for the baryon pairing $T_{\rm c}$, and hence, in case of fast neutrino cooling, one can expect that a few minutes after the star is born its core may become superfluid/superconducting, and the neutrino emission very strongly suppressed.

(2) During the *photon cooling era* ($L_\gamma \gg L_\nu$) one similarly obtains

$$t = t_1 + \frac{C}{4\alpha S}\left(\frac{1}{T^{4\alpha}} - \frac{1}{T_1^{4\alpha}}\right), \tag{11.41}$$

where T_1 is the temperature at time t_1. When $t \gg t_1$ and $T \ll T_1$, we have

$$T = \left(\frac{C}{4\alpha S}\right)^{\frac{1}{4\alpha}} t^{-\frac{1}{4\alpha}} \quad \text{and} \quad T_{\rm e} \mathrel{\widetilde{\propto}} t^{-\frac{1}{8\alpha}}\,. \tag{11.42}$$

Since $\alpha \ll 1$, we see that, during the photon cooling era, the evolution is very sensitive to the nature of the envelope, i.e., α and S, and to changes in the specific heat, as induced by pairing.

After this description of the essential physical ingredients needed to model neutron star cooling and the insight gained by these simple analytical models we are ready to embark into descriptions of more sophisticated numerical models in the next sections.

11.3 Minimal Cooling of Neutron Stars

Before presenting fast cooling scenarios in the next section, we will first consider models within the *minimal cooling paradigm* [56], i.e., the modern version of the previous "standard" cooling scenario (see, e.g., Nomoto and Tsuruta [46,47]). Minimal cooling means restricting ourselves to scenarios where fast neutrino emission is not occurring: no charged meson condensate, π^- or K^-, no hyperons, no deconfined quark matter is allowed to be present (i.e., no inner core as "?" in Fig. 11.1 is allowed to exist) and, moreover, the proton fraction must be low enough for the nucleon DUrca process to be kinematically forbidden. However, minimal cooling is not naive cooling: it must take into account all other possible factors affecting the star's thermal evolution. Of particular importance is the occurrence of pairing, for neutrons and/or protons, with the resulting strong alterations of the specific heat and neutrino emission, including the one from the formation, and breaking, of Cooper pairs (the PBF process). A second important ingredient is the chemical composition of the envelope which can significantly alter the photon emission as described in Sect. 11.2.4 and also, but to a much smaller extent, the structure of the magnetic field in the envelope. A third major effect may come from the structure of the magnetic field in the deeper layers of the crust: this was not considered in the original version [56] of the minimal cooling and will be discussed in Sect. 11.5.

The minimal cooling paradigm imposes tight constraints on the equation of state and among the many proposed models of supra-nuclear matter only a handful of them do not allow fast neutrino emission. Very soft equations of state are usually obtained when charged meson condensates and/or hyperons are present while stiff ones commonly pertain to relativistic models which also result in large proton fractions, but both of these families of models are excluded from the minimal cooling paradigm. Figure 11.11 shows the mass-radius relationship for four allowed equations of state: radii at the "canonical" mass of $1.4\,M_\odot$ are between 11 and 12 km and radii at the maximum mass are between 9 and 10 km. The maximum mass, however, shows a broader range, 1.7–$2.2\,M_\odot$.

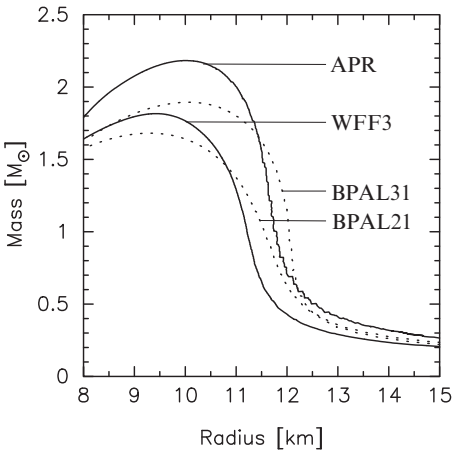

Fig. 11.11 Mass–radius curves for four equations of state satisfying the requirements of the minimal cooling paradigm: "APR" from Akmal et al. [3], "WFF3" from Wiringa et al. [90], "BPAL21" and "BPAL31" from Prakash et al. [71]. (Figure from [56])

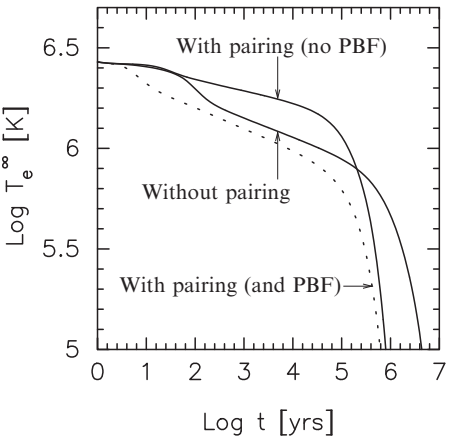

Fig. 11.12 Comparison of the cooling of a $1.4\,M_\odot$ star, built using the equation of state of APR [3], without and with nucleon pairing. Neutron $^1S_0$ pairing is from WAP, $^3P_2$ pairing from case "c" and p $^1S_0$ pairing from AO, as labeled in Figs. 11.3 and 11.4. A heavy elements envelope has been assumed. (Figure from [56])

Let us consider, as a first step, the effect of neutron/proton pairing as illustrated in Fig. 11.12. The two continuous lines correspond to the old "standard" cooling scenario: core neutrino emission is provided by the MUrca process family, either freely acting in the "without pairing" case or suppressed in the "with pairing" case (where neutrino emission by the PBF process is not taken into account). During the neutrino cooling era both C_v and L_ν are suppressed in the "with pairing" case, but L_ν more strongly than C_v and hence this model cools more slowly than the "without pairing" model. During the photon cooling era L_γ is unaffected by pairing and the model "with pairing" cools faster because of the reduction of C_v. However, when the neutrino emission from the PBF process is taken into account, the previous trend reverses during the neutrino cooling era: the model "with pairing" cools faster than the model "without pairing" because of the high L_ν^PBF. During the photon cooling era the two models with pairing, with and without the PBF process, converge since they have the same C_v and the previous neutrino cooling history is progressively forgotten.

The previous examples of Fig. 11.12 illustrated the importance of the PBF process. However, this process is very strongly temperature dependent: it has an overall T^7 dependence and is, moreover, turned on by pairing, when $T = T_\mathrm{c}$, and then almost completely suppressed once $T \lesssim 0.2\,T_\mathrm{c}$ (see its control function $\mathcal{R}$ in Fig. 11.5). The result is a strong neutrino emission within a small range of temperatures, between T_c down to about $0.2\,T_\mathrm{c}$, and, since T_c is density dependent, this emission occurs at different time in different layers of the star. Considering the enormous uncertainty on the values of T_c in the core, for both neutrons and protons, it becomes mandatory to examine many cooling models, scanning the whole range of possible pairing gaps. Figure 11.13 compares cooling histories when the neutron $^3P_2$ gap is assumed to correspond to the three very different cases shown in the right panel of Fig. 11.3 and the case where it is vanishingly small. From the discussion in the previous paragraph one can easily understand the thermal evolutions during the photon cooling

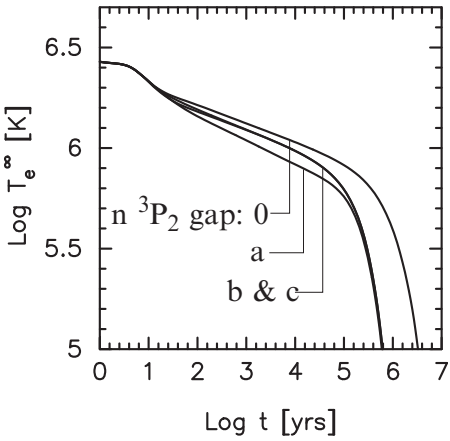

Fig. 11.13 Comparison of the cooling of the same star as in Fig. 11.12 but considering the four cases of neutron $^3P_2$ gaps of Fig. 11.3. (Figure from [56])

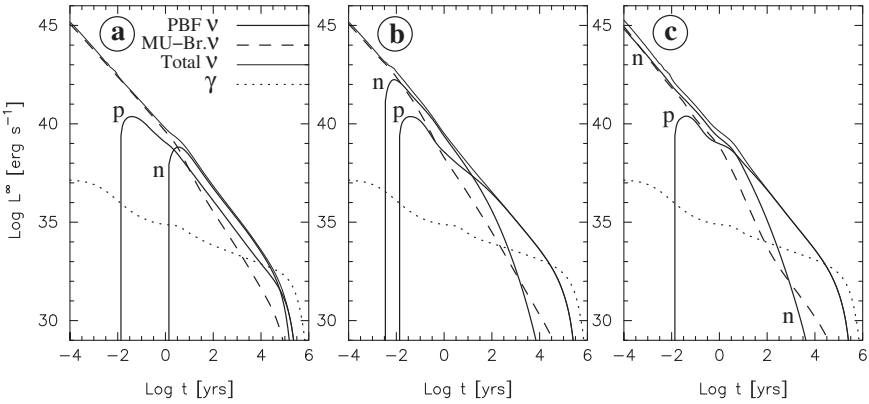

Fig. 11.14 Comparison of luminosities from various processes during three realistic cooling histories: photon ("γ"), all ν-processes ("Total ν"), modified Urca and nucleon bremsstrahlung ("MU-Br. ν"), and PBF ("PBF ν") from n $^3P_2$ and p $^1S_0$ pairing marked by "n" and "p", respectively. PBF neutrinos from the n $^1S_0$ gap are not shown explicitly, since their contribution is always dominated by other processes, but they are included in the total ν luminosity. In all three cases, the p $^1S_0$ gap is from AO, the n $^1S_0$ gap from WAP, whereas the n $^3P_2$ gap is from model "a" (*left panel*), "b" (*central panel*) and "c" (*right panel*) of Fig. 11.3. Notice the crossing of the "γ" and "Total ν" curves, at ages $\sim 10^5$ yrs, which marks the transition from the neutrino to the photon cooling era, and the resulting change in the slope of the photon luminosity curve, in agreement with (11.37) and (11.42). (Figure from [56])

era: the three models with non-vanishing neutron $^3P_2$ gaps are very similar simply because at this phase $T \ll T_c$ in the whole core and the neutron contribution to C_ν has practically vanished resulting in models with the same C_ν, and the same L_γ since they also have the same type of envelope, and hence the same evolution. During the earlier neutrino cooling era differences appear and the dominant neutrino luminosities, as well as the photon one, are plotted in Fig. 11.14. Neutron $^3P_2$ gaps "b" and

"c" give indistinguishable results in Fig. 11.13: such high values of T_c result in efficient neutrino emission from the neutron $^3P_2$ PBF process at early times, but this process is later strongly suppressed, once $T \ll T_c$, and the neutrino luminosity is then dominated by the proton $^1S_0$ PBF process. The model with the neutron $^3P_2$ gap "a" gives the lowest effective temperatures during the neutrino cooling era because this gap has T_c's which maximize neutrino emission from the PBF process at the right time, i.e., at ages between 10 and 10^5 yrs. Thus, the four cooling curves of Fig. 11.13 show us the range of uncertainty inherent to the minimal cooling because of present uncertainty on the size of the neutron $^3P_2$ gap. This range becomes even broader once the uncertainty on the proton $^1S_0$ gap is taken into account: all models of Fig. 11.13 used the same proton $^1S_0$ gap and the effect of varying this gap will be considered in the final results presented below.

All minimal cooling calculations shown here were performed before it was realized that the $^1S_0$ neutron PBF process is strongly suppressed. However, the neutron $^1S_0$ gap is restricted to the star's crust and the neutrino emission from the corresponding PBF process has very little effect on the long term cooling of the star: these calculations will be up-dated soon [57].

A large uncertainty is also introduced due to the unknown chemical composition of the envelope. As described in Sect. 11.2.4, the presence of light elements in the upper layers increases their thermal conductivity, compared to heavy iron-like elements, resulting in a larger T_e for a given interior temperature. The effect is significant and acts in opposite directions during the neutrino cooling era and the photon cooling era. During the neutrino cooling era the star's evolution is driven by L_ν, modulo C_v, which determines the time evolution of the interior temperature T while T_e simply follows this evolution: L_γ is irrelevant for the star's evolution and different envelopes structures will simply result in a different T_e evolution for the same T evolution. This is clearly visible in Fig. 11.15 where panel B shows that T^∞_{center} is the same for both envelope models when $L_\nu > L_\gamma$ (shown in panel C), while T^∞_e is higher in case of a light element envelope than in the iron-like element one (panel A). Later on, during the photon cooling era, the evolution of the interior temperature T is driven by L_γ, modulo C_v, and a higher T_e, for a given T, results in a higher L_γ and faster cooling: a model with a light element envelope cools faster than the analogous model with an iron-like envelope.

Other ingredients, within the minimal cooling paradigm, have much less impact on the results. All equations of state compatible with the assumption of minimal cooling are very similar and lead to very similar evolutions, keeping other ingredients, as pairing and the envelope, unchanged. In a similar way the mass of the star has little impact: there is, by assumption, no critical density above which matter's structure dramatically changes and hence no critical stellar mass above which some new mechanism begins to act.

Having considered in some detail the various processes at work in the cooling of a minimal neutron star we can compare the prediction of this paradigm with observational data, as presented in Fig. 11.16. The two grey bands correspond to models using either a heavy element envelope or an envelope with a maximum amount of light elements, the lighter grey intermediate area showing the location of cooling

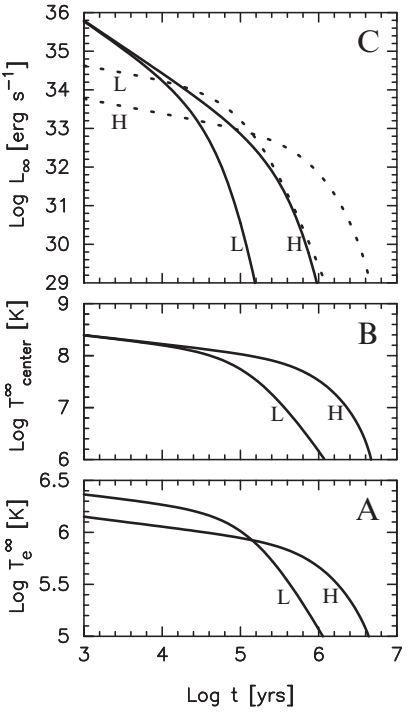

Fig. 11.15 Neutrino and photon cooling eras for two models of non magnetized envelopes formed by heavy iron-like elements (labeled "H") and a maximum amount of light elements (labeled "L"). The effective temperature (*panel A*), the central temperature (*panel B*) and neutrino (*continuous lines*) and photon (*dotted lines*) luminosities (*panel C*), all redshifted to infinity, are shown as a function of time. No pairing effects are included in these calculations. (Figure from [56])

trajectories with an intermediate amount of light elements in the envelope. For both extreme types of envelope the thickness of the band comes from considering various assumptions about proton $^1S_0$ and neutron $^3P_2$ pairing, i.e., cooling models were calculated for all combinations of gaps shown in Figs. 11.3 and 11.4 (for displays of all these trajectories the reader is referred to Figs. 28 and 29 in [56]). Considering the stars with the best data, displayed as boxes, the agreement between theory and observation is quite good, given uncertainties in both the theoretical predictions and the estimates of luminosities and ages. The Vela pulsar (6) (and possibly PSR 1706−44: 5) nevertheless appears suspicious, as only extreme values of L_∞ and t are compatible with the coldest minimal cooling trajectories. On the other side, PSR 1055−52 (7) and RX J0720.4−3125 (11) may be too hot unless their ages fall in the lower part of the estimated range. These two stars may be good candidates for the occurrence of significant heating, the term "H" of (11.1) which has been neglected in all models presented in this chapter. However, in the cases of the objects PSR J0205+6449 (B) in SNR 3C58 and RX J0007.0+7302 (D) in SNR CTA 1, the discrepancy is significant.

There are other objects, and candidates, for comparison with cooling models. Kaplan et al. [34, 35] have searched for a compact object in several supernova remnants in which there is, to date, no evidence for the presence of such object. They obtained upper limits on the thermal luminosity of the presumptively existing neutron star which in most cases are well below the cooling curves exhibited in

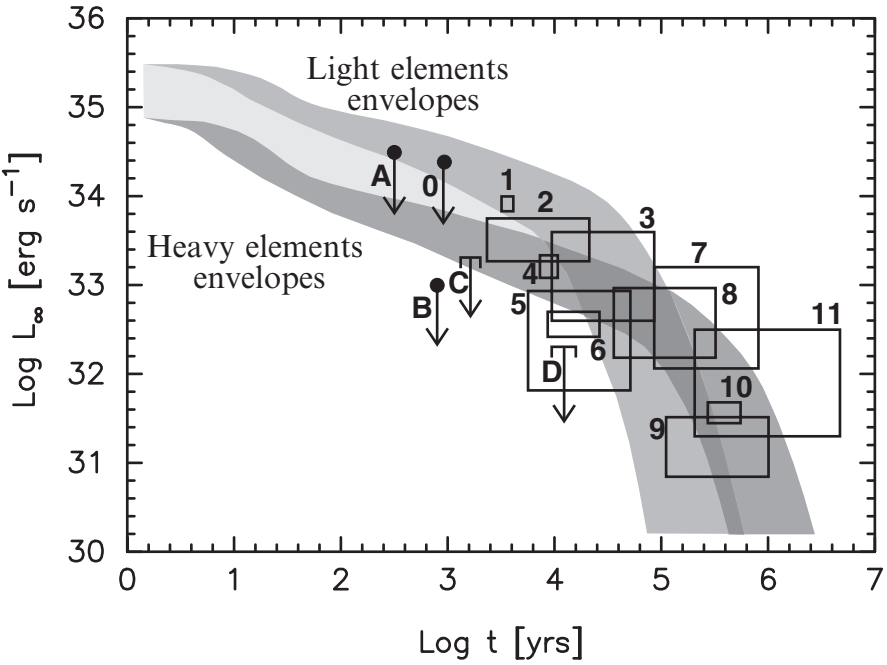

Fig. 11.16 Comparison of the predictions of the Minimal Model of neutron star cooling with the best presently available data. *Boxes* correspond to neutron stars where surface thermal emission is clearly detected and which have been studied in detail: 1–6 are obtained from spectral fits with magnetized hydrogen atmospheres while 7–11 are from blackbody fits, this choice being based on which type of spectra resulted in an observed radius $R_{\rm Obs}$ the closest to 10–15 km. These stars are: 1, RX J0822−4247 (in SNR Puppis A); 2, 1E 1207.4−5209 (in SNR PKS 1209−52); 3, PSR 0538+2817; 4, RX J0002+6246 (in SNR CTB 1); 5, PSR 1706−44; 6, PSR 0833−45 (in SNR "Vela"); 7, PSR 1055−52; 8, PSR 0656+14; 9, PSR 0633+1748 ("Geminga"); 10, RX J1856.5−3754; and 11, RX J0720.4−3125. The next four stars, labeled as A, B, C, and D, are barely detected and in case C there is no evidence for thermal emission: A, CXO J232327.8+584842 (in SNR Cas A); B, PSR J0205+6449 (in SNR 3C58); C, PSR J1124−5916 (in SNR G292.0+1.8); and D, RX J0007.0+7302 (in SNR CTA 1). The last point: 0, PSR 0531+21; is the Crab pulsar, for which there is to date no detection of a surface thermal component and only an upper limit on $L_{\rm Obs}$ is possible. Discussion of each data point and references can be found in [56], except for the upper limit on the Crab pulsar, taken from [89]. (Figure adapted from [56])

Fig. 11.16. However, the supernovas could have been of type Ia, in which case no compact remnant was formed, or may have produced black holes. In case a neutron star were detected in one of these remnants, it would probably be our best candidate for the occurrence of fast neutrino emission. Finally, magnetars also exhibit surface thermal emission with high luminosities, above $10^{35}\,{\rm erg\,s^{-1}}$, which is powered by magnetic field decay and they are, hence, not appropriate for comparison with the passive cooling models discussed in this chapter.

In their variant of minimal cooling, Gusakov et al. and Kaminker et al. [25, 26, 32] have reached similar conclusions, but with different assumptions about nucleon pairing.

Some Comments on the Data

Figure 11.16 plots the red-shifted photon luminosity L_∞ vs. time: this is *theoretically* equivalent to a plot of the red-shifted effective temperature T_∞, through (11.23) and considering that R_∞ is well defined for any given theoretical cooling model. However when plotting data, the observed luminosity and temperature, $L_{\rm Obs}$ and $T_{\rm Obs}$ resp., are not equivalent:

1. $T_{\rm Obs}$ is obtained from a spectral fit and the result depends on which kind of theoretical spectra are used in the fit. For example, fits with magnetized hydrogen atmosphere model spectra give $T_{\rm Obs}$ a factor 2–3 lower than when blackbodies are used. Moreover, even in cases where the theoretical spectra are accurate there is no a priori guarantee that the deduced $T_{\rm Obs}$ is an effective temperature: the non-uniform surface temperature distribution makes that the spectral fit, in the X-ray band, will be biased toward measuring the temperature of the warmest part of the stellar surface (while the spectrum in the optical region may come from the coldest part of the star).
2. $L_{\rm Obs}$ could be obtained from the flux F through $L_{\rm Obs} \equiv 4\pi D^2 F$, once a star's distance D is assumed. However, the flux F is not directly observed: part of it falls outside the detector's energy range and a part, often very large, of it is absorbed by the interstellar medium. The contribution of a hard tail, either due to polar cap thermal emission or some magnetospheric processes, and possible contamination from a surrounding pulsar wind nebula also have to be taken into account to extract the surface thermal emission. As a consequence, reconstructing F from an observed $F_{\rm Obs}$ requires a spectral model, i.e., for thermal spectra, is based on $T_{\rm Obs}$ (and deducing an $L_{\rm Obs}$ from F moreover involves an assumption about the R/D ratio).

A consistency check can be performed imitating (11.23) to write $L_{\rm Obs} = 4\pi R_{\rm Obs}\,\sigma_{\rm SB} T_{\rm Obs}^4$ and thus obtain $R_{\rm Obs}$: the "measured" star's radius $R_{\rm Obs}$ should be around 10–20 km, the expected range of R_∞ from theoretical models. Obviously the deduced $R_{\rm Obs}$ is proportional to the assumed D. In the case of the Vela pulsar, this consistency check can be meaningfully performed, since D is accurately known, and gives $R_{\rm Obs} \sim 13 - 15$ km when magnetized hydrogen atmosphere spectra are used, while blackbodies give $R_{\rm Obs} \sim 3{-}5$ km. Thus in this case, spectral fits with magnetized hydrogen atmosphere spectra satisfactorily fulfill the consistency check and comparing theory with the observed L or T is equivalent. Unfortunately, for most other candidates the consistency check does not give such good results and the best which can be done is to use spectral fits which give $R_{\rm Obs}$ the closest to the expected value of 10–20 km. This approach was used in [56] for the objects labeled "1" to "11" in Fig. 11.16. However, for the other objects, labeled "A" to "D" the

data are not good enough to perform the check and, hence, a L vs. t plot is much more adequate than a T vs. t plot.

Next to the luminosity/temperature measurements come the age "measurements". It is only for the Cab pulsar that we have a definite age from its association with the historical supernova of 1054 A.D., while 3C58 is likely associated with the supernova of 1181 A.D., and an association of Cas A with a late seventeenth century supernova is possible. When the neutron star is associated with a supernova remnant, one can obtain an age estimate, the "kinematic age" $t_{\rm kin}$, either from the study of the kinematics of the remnant expansion and/or from the observed proper motion of the pulsar and its offset from the remnant expansion center. For RX J1856.5−3754, the age is estimated from the observed proper motion and its backward extrapolation which points toward a cluster of massive OB stars where the neutron star was probably born. In the other cases, we are left with a rough estimate of the star's age from the observed pulsar spin-down using the so-called "spin-down age" $t_{\rm sd} = P/2\dot{P}$. For objects where $t_{\rm sd}$ is the only available information about the age, an uncertainty of a factor 3 in both directions was assigned in [56]. This factor of three is representative of typical discrepancies between $t_{\rm sd}$ and $t_{\rm kin}$ for young objects when both age estimates are available, but larger, and smaller, discrepancies are not uncommon (see Tables 1, 2 and 3 in [56]). However, $t_{\rm sd}$ is certainly affected by glitches in young objects and may possibly be more reliable in older stars which do not present glitches, but for these older stars there is, to date, no other observed properties against which one could test the reliability of $t_{\rm sd}$.

For more details on these issues I refer the reader to the Chaps. 6 & 9 in this book.

11.4 Fast Cooling of Neutron Stars

We will now consider the cooling of neutron stars in which some part of the inner core, the "pit", is emitting neutrinos through one of the many possible fast processes. As was shown in (11.39) and (11.40), fast neutrino emission means that matter can cool down to 10^9 K in a few minutes, compared to a year under slow neutrino emission. This is further illustrated in Fig. 11.17 which shows the resulting effective temperature for a series of stars with increasing masses. The early plateau, at $\mathrm{Log}\, T_{\rm e} \sim 6.4$, which we had already identified in minimal cooling models, is also present here since it is due to the cooling of the crust and will be discussed in details at the end of this section: its duration depends on the thickness of the crust and models of increasing mass, having a thinner crust, leave the plateau earlier. Once the star has relaxed to isothermality the difference between slow and fast neutrino cooling is spectacular. Notice that the 1.4 $M_\odot$ model has an inner "pit" of only 0.038 $M_\odot$ which, given the emissivity of the DUrca process, is enough to result in very low temperatures.

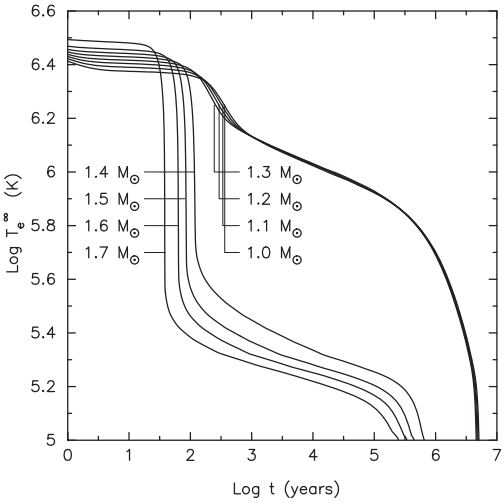

Fig. 11.17 Cooling of neutron stars of increasing masses for an equation of state model, from [70], which allows the DUrca process at densities above $1.25 \times 10^{15}\,\mathrm{g\,cm^{-3}}$, i.e., above a critical neutron star mass of $1.35\,M_\odot$. Notice that the equation of state used is a parametric one and parameters were *specifically adjusted* to obtain a critical mass of $1.35\,M_\odot$ which falls within the expected range of isolated neutron star masses; other equations of state can result in very different critical masses. (Figure from [52])

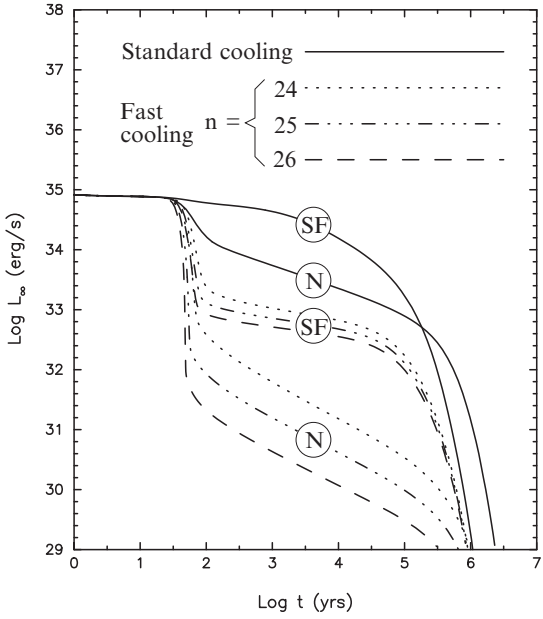

Fig. 11.18 Comparison of "standard" cooling vs. three scenarios with fast cooling without (labeled as "N" for "Normal") and with (labeled as "SF" for "SuperFluid") pairing suppression. Notice that in these models, from [51], neutrino emission from the PBF processes had not been included

Once pairing is taken into account the situation may change dramatically (the models of Fig. 11.17 do not take into account pairing), as shown in Fig. 11.18. The fast neutrino emissivity in these models is set as $\varepsilon_\nu^{\mathrm{fast}} = 10^n\, T_9^6\,\mathrm{erg\,cm^{-3}\,s^{-1}}$ with $n = 24$, 25, and 26, and they are also compared to the "standard" cooling. The T^6 dependence is typical of all fast cooling processes and the three values of n correspond, very roughly, to kaon and pion condensates and to DUrca processes, resp. (see Table 11.1). The superfluid models in this figure assume a neutron $^3P_2$ gap

intermediate between the models "a" and "b" of Fig. 11.3, i.e., a T_c of the order of 2×10^9 K down to the center of the star: as a result, neutrino emission is strongly suppressed when $T < 10^9$ K and the surface temperature of the three models with fast neutrino cooling remain almost constant at ages between 10^2 and 10^5 yrs. The "standard" cooling models show the same behavior as was displayed in Fig. 11.12, but for the fast cooling models the effect of superfluidity is much more dramatic: the inner fast cooling "pit" will see its temperature drop very fast till it reaches T_c and then $\varepsilon_\nu^{\rm fast}$ becomes suppressed. Actually, T_c is reached within less than a minute for $n = 26$ and in less than an hour for $n = 24$! Once $T \ll T_c$ fast neutrino emission has practically disappeared and this is why the three models, despite different $\varepsilon_\nu^{\rm fast}$, have very similar temperatures: they have the same superfluid gaps and having reached T_c in seconds or minutes after their birth does not make much of a difference when one looks at the star thousands of years later.

An example of comparison of a fast neutrino emission scenario with data is presented in Fig. 11.19. The equation of state used is the same as in Fig. 11.17 but a set of neutron and proton pairing gaps is assumed and their effects wholly taken into account. The same data as in Fig. 11.16 are also plotted: the full set of observed stars can be interpreted in this scenario by allowing them to have different masses and different envelope chemical composition. Most stars should undergo slow neutrino cooling, but the young ones with low luminosities should have higher masses with fast neutrino cooling controlled by pairing.

11.4.1 A Warning About Fast Neutrino Cooling Scenarios

Figure 11.17 clearly showed what "fast" neutrino cooling means and Fig. 11.18 illustrated the possibly dramatic effect of the pairing suppression of ε_ν. However, this latter figure also shows that different neutrino emission mechanisms can lead to very similar cooling trajectories (see the "SF" fast cooling curves). As an example, [56] presented cooling models with equations of state which contained nucleons only, and also including hyperons and/or quarks (a "maximal" cooling scenario!) and showed that, given uncertainties on the possible pairing gaps of all these components, essentially indistinguishable cooling trajectories could be obtained. The scenarios presented here are based on pairing control of the fast neutrino emission and this control must occur at high densities where pairing gaps are essentially unknown. Presence of a π^--condensate is likely to favor large gaps and may be a good candidate (see [85], and references therein). Quarks are expected to develop very large gaps [4, 5] making deconfined quark matter another good candidate (see, e.g., [65], and references therein). However, K^--condensate with sufficient heating can also be made compatible with observational data *without* invoking pairing suppression of its not so fast neutrino emission [50], as well as scenarios using the MMUrca process [73].

Obviously more information than just the thermal evolution is required in order to attempt to draw any conclusion about the state of matter in the inner core of

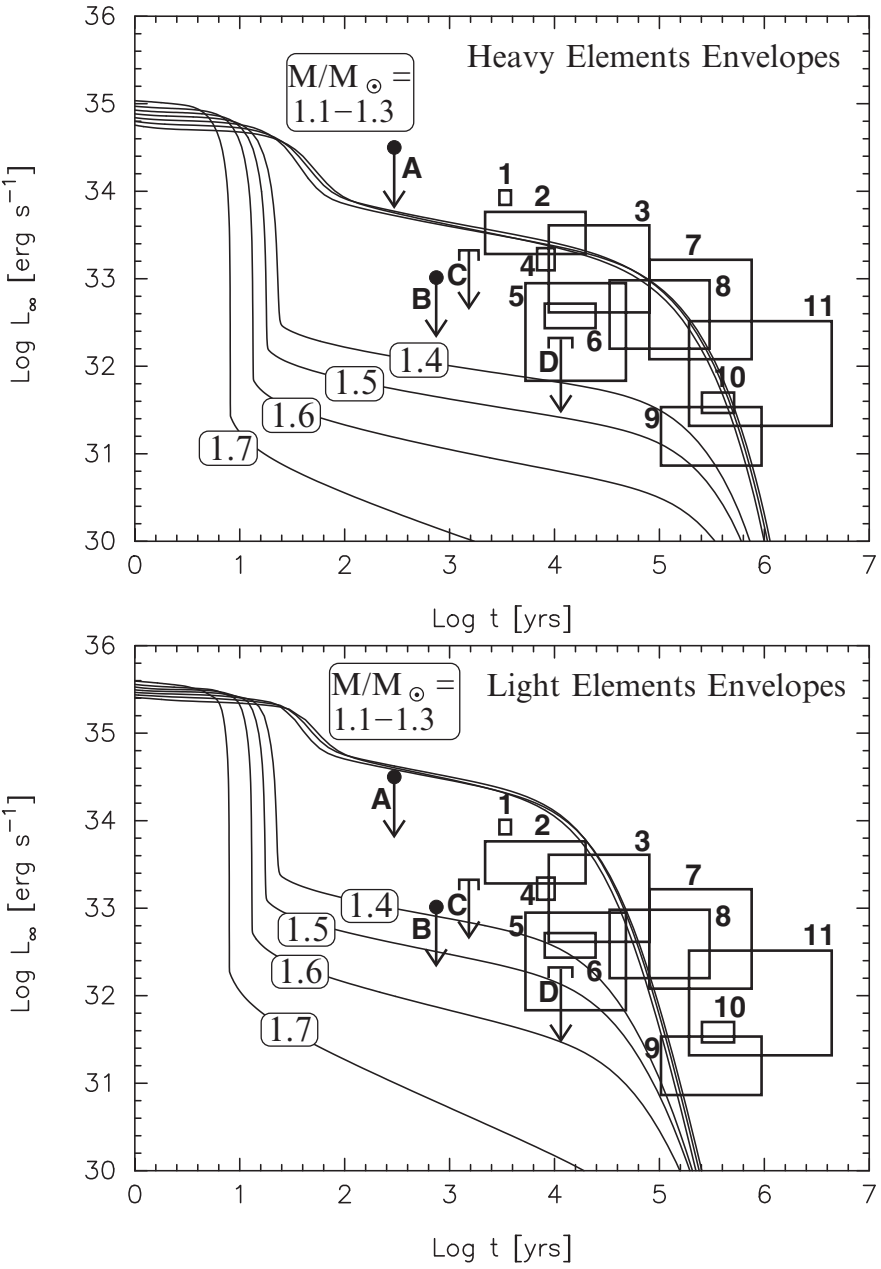

Fig. 11.19 Cooling of the same stars as in Fig. 11.17, with masses from 1.1 up to 1.7 $M_\odot$ as labeled on the curves, with a heavy element (*upper panel*) or light element (*lower panel*) envelope. Neutrons are paired with a $^1S_0$ gap from model "SFB" and a $^3P_2$ gap from model "b" of Fig. 11.3 and protons with a $^1S_0$ gap from model "T" of Fig. 11.3. Plotted data are the same as in Fig. 11.16

the heavier neutrons stars. In particular, the critical mass at which some fast neutrino emission mechanism becomes allowed is very model dependent, and drawing conclusions about the masses of cooling isolated neutron stars by comparing their thermal luminosity with some fast cooling model is dangerous since very different scenarios, and EOSs, can lead to very similar results.

11.4.2 A Look at the Evolution of Temperature Profiles

It is most instructive to look in detail at the evolution of the temperature profile inside the star during its cooling. Two examples, for fast and slow neutrino cooling, are shown in Fig. 11.20 (see also the longer description in [22] where the same equation of state as the present one is used. These authors, however, had not considered

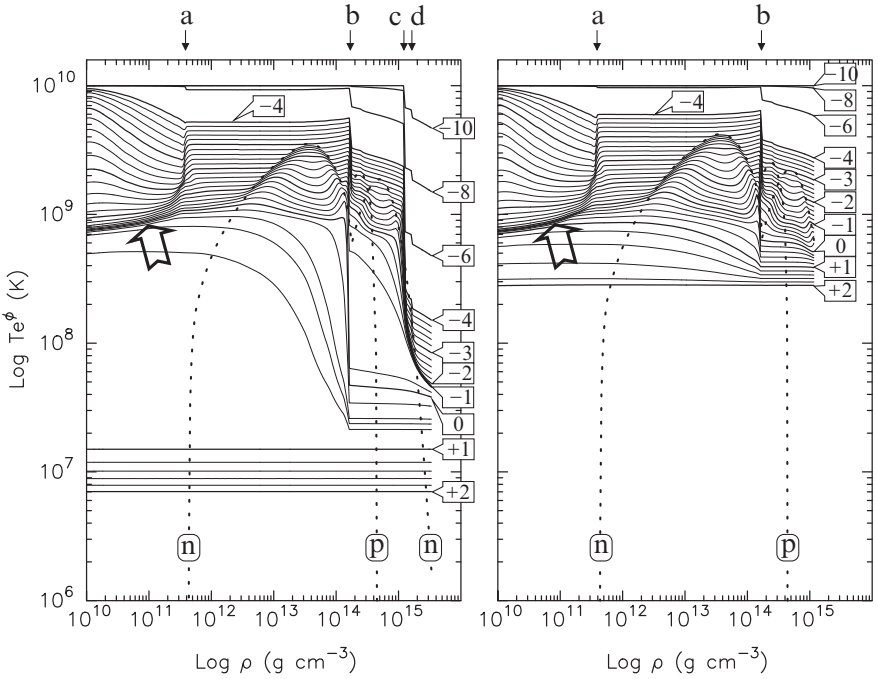

Fig. 11.20 Temperature profiles for the $1.7\,M_{\odot}$ (*left panel*) and $1.3\,M_{\odot}$ (*right panel*) models of the upper panel, i.e., with heavy element envelopes, of Fig. 11.19. The vertical scale plots the red-shifted temperature $T\,\mathrm{e}^{\phi}$ (since isothermality is given by $T(r)\,\mathrm{e}^{\phi(r)} = \text{constant}$). T profiles are shown for ages (in years) with $\mathrm{Log}\,t = -10$, up to $+2$ (*thick lines*, with $\mathrm{Log}\,t$ labeled next to the curves), and from -2 to $+2$ profiles in steps of 0.2 are also shown (*thin lines*). Also shown are the T_{c} profiles for neutrons (labeled "n") $^1S_0$ and $^3P_2$ and proton (labeled "p") $^1S_0$ pairing. The two densities marked "a" and "b" are the neutron drip point and the crust–core boundary. The two densities marked as "c" and "d" for the $1.7\,M_{\odot}$ models are the critical densities above which the two DUrca processes, $n \to p + e + \overline{\nu}_e$ and $n \to p + \mu + \overline{\nu}_{\mu}$, resp., become kinematically allowed

the suppression of the neutron $^1S_0$ Cooper pair process described in [39, 40]). The initial temperature was (arbitrarily) set at $T(r)\,e^{\phi(r)} = 10^{10}$ K in the whole star for both cases: the earliest T-profiles should not be taken too seriously (and, moreover, neutrino trapping is not considered in these cooling calculations).

Considering first the *early cooling of the crust*, it is initially driven by neutrino emission from plasmon decay (see Fig. 11.6), and the temperature in the outer crust (below point marked as "a" in Fig. 11.20) relaxes in about 1 year to some almost universal profile, indicated by the inclined bold arrows in both panels of the figure, which correspond to the temperature where the plasmon process becomes exponentially suppressed and neutrino emission is provided by the inefficient e–ion bremsstrahlung process (compare with Fig. 11.6). This is the origin of the early flat plateau, lasting a few years and visible in all cooling curves shown in previous figures. The much slower cooling of the inner crust, i.e., between the point "a" and "b" in both panels of Fig. 11.20, is due to much larger specific heat of this region because of the abundant free neutrons. Notice that once T reaches T_c the cooling of the layer slows down because of the sudden increase of the neutron c_v just below T_c while when $T \ll T_c$ the cooling accelerates because of the exponential suppression of c_v.

When looking at the *early cooling of the core*, one can see that the evolution of the 1.3 $M_\odot$ model's core is identical to the evolution of the outer core, i.e., the region between points "b" and "c", of the 1.7 $M_\odot$ model. However the inner core of the 1.7 $M_\odot$ model cools much faster due to the DUrca process. Notice the even faster cooling above point "d" where the second DUrca process with muons is also allowed.

In the early phases, when the neutrino cooling time scale is much shorter than the heat transport time scale, different layers cool independently of the evolution of their neighbors, which is apparent as sharp temperature variation at points "a", "b", "c", and "d". The heat diffusion time scale $\tau_l^{\rm Heat}$ over a distance l is roughly given as $\tau_l^{\rm Heat} \sim l^2\kappa/c_v$ and takes very different values at different regions and different ages during the cooling. As time runs, the effect of heat diffusion is easily seen in Fig. 11.20 as a progressive smoothing of the T profiles. Most spectacular is the emptying of the crustal heat into the core in the 1.7 $M_\odot$ model at ages between $\mathrm{Log}\, t = 0$ and 1, which results in the fast drop of surface temperature seen in Figs. 11.17, 11.18, and 11.19. After this phase the star has reached isothermality and its evolution is much simpler, allowing some analytical solutions as described in Sect. 11.2.5.

11.5 More than Only Dense Matter: Magnetic Fields

The final result of the early evolution described in Sect. 11.4.2 is a neutron star with an isothermal interior, a strong temperature gradient only surviving in the upper layers in the envelope. These results were obtained with a cooling code which assumes spherical symmetry and thus explicitly excludes any anisotropy effect in the internal heat transport due to the presence of a strong magnetic field, possible magnetic

effects being only included in the envelope through the outer boundary condition (see Sect. 11.2.4). However, anisotropy is expected to be present much deeper than just the envelope, in the case of a strong enough magnetic field or low enough temperatures, as can be seen from the large values of the magnetization parameter displayed in Fig. 11.8. This effect which, we will see below, potentially alters the cooling of the star and may result in surface temperature distributions drastically different from the ones presented in Fig. 11.10, implies that *the geometry of the magnetic field in the stellar interior may have observable consequences*. In order to study this problem we thus have to model the structure of the field in the stellar interior. This approach actually only depends on the structure of the field within the crust: in the core, at least in the outer part of it, protons are expected to form a type II superconductor with the result that the magnetic flux is confined into fluxoids which occupy only a very small part of the material's volume and, hence, thermal conductivity is not expected to be so strongly anisotropic than in the crust. In this case, an isothermal core, which forms within a few years after the neutron star birth, is a reasonably good approximation.

At present time, studies have been performed with 2D heat transport codes, i.e., axisymmetric configurations. If we consider only dipolar field structures, it is convenient to decompose the magnetic field $\mathbf{B}$ in two components

$$\mathbf{B} = \mathbf{B}^{\rm pol} + \mathbf{B}^{\rm tor} \,, \tag{11.43}$$

where, working in spherical coordinates with the $\theta = 0$ axis along the field's symmetry axis, the poloidal part $\mathbf{B}^{\rm pol}$ only has r and θ components while the toroidal one $\mathbf{B}^{\rm tor}$ only has a ϕ component. The field lines of $\mathbf{B}^{\rm tor}$ are then simply circles centered on the symmetry axis. Outside the star $\mathbf{B}^{\rm tor}$ vanishes while $\mathbf{B}^{\rm pol}$ turns into a simple vacuum dipolar field. Our concern is the structure of $\mathbf{B}$ *inside* the star, and defining it is equivalent to choosing the location of the electric currents $\mathbf{j}$, since $\nabla \wedge \mathbf{B} = \frac{4\pi}{c}\mathbf{j}$. The next natural step is to separate currents flowing in the core, which are proton supercurrents located around each magnetic field fluxoid tube, from the ones located in the crust which are due to electrons. For $\mathbf{B}^{\rm tor}$ we only need the crustal part, since by axisymmetry the core part is totally confined to the core, but for $\mathbf{B}^{\rm pol}$ we can write

$$\mathbf{B}^{\rm pol} = \mathbf{B}^{\rm core} + \mathbf{B}^{\rm crust} \,. \tag{11.44}$$

This, oversimplified, internal magnetic field structure is illustrated in Fig. 11.21.

With these definitions we are ready to study the effects of a strong internal magnetic field on the thermal structure of a neutron star [19, 20, 60]. The left panel of Fig. 11.22 depicts the crustal temperature distribution in the case $\mathbf{B}$ is reduced to a $\mathbf{B}^{\rm crust}$ component: electrical currents are only present in the crust and generate a purely poloidal dipolar magnetic field (a probably unrealistic, but illustrative, configuration). What have to be noted are, first, the magnetic field lines which, being confined to the crust, are predominantly meridional becoming radial only close to the surface and near the symmetry axis, and, second, since $\kappa_\perp \ll \kappa_\parallel$, that the magnetic field lines are practically isothermal lines. In the central panel of Fig. 11.22 the three components of $\mathbf{B}$ are present. The pictured field lines are the ones of $\mathbf{B}^{\rm pol}$

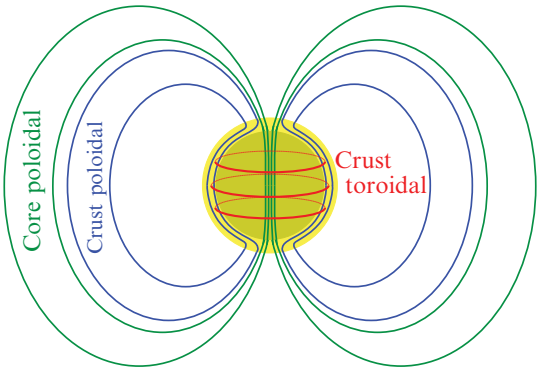

Fig. 11.21 The three components of the magnetic field

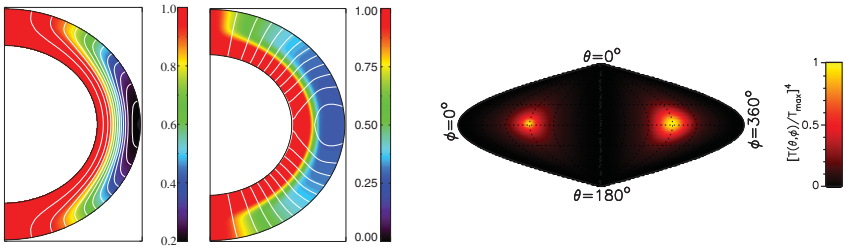

Fig. 11.22 *Left and central panels* show the temperature distribution in a magnetized neutron star crust with a poloidal dipolar field confined to the crust, $\mathbf{B}^{\rm crust}$ (*left*), and a more general configuration including a toroidal component, $\mathbf{B}^{\rm core}+\mathbf{B}^{\rm crust}+\mathbf{B}^{\rm tor}$ (*center*), with $\mathbf{B}^{\rm tor}$ concentrated in the middle of the crust. Field lines of $\mathbf{B}^{\rm pol}$ are shown as *white lines* and the color coding maps $T(r,\theta)/T_{\rm core}$. The thickness of the crust has been increased for better viewing. The *right panel* shows the surface temperature resulting from the crustal temperature of the *central panel* using the same projection as in Fig. 11.10. (Figures from [19, 20])

only and, due to the presence of a very strong $\mathbf{B}^{\rm tor}$, the field lines of the total $\mathbf{B}$ are strongly wrapped around the symmetry axis: the thermal barrier due to $\mathbf{B}^{\rm tor}$ is clearly seen and results in heat flowing toward the surface mostly along the symmetry axis where $\mathbf{B}^{\rm tor}$ vanishes. The right panel of Fig. 11.22 shows the resulting surface temperature distribution which should be compared to the ones shown in Fig. 11.10.

These results open up the possibility of detecting the presence of a strong toroidal field confined to the stellar interior. Good candidates for this purpose are the "Magnificent Seven" (see Chap. 7). These are nearby, isolated, cooling neutron stars which share several properties, one of them being that the size of the thermally emitting region, obtained from blackbody fits of the X-ray band thermal spectrum, is much smaller than the total area of a neutron star. Moreover, several of them have been detected in the optical band where they are brighter than the Raleigh–Jeans tail of the blackbody X-ray spectrum. A proposed interpretation of this optical excess, inspired by the small X-ray thermally emitting region, is that a large part

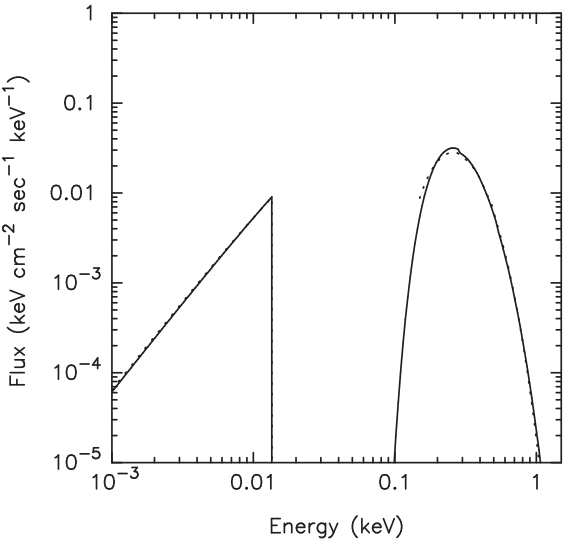

Fig. 11.23 Fit of the X-ray and optical spectrum of the isolated neutron star RX J1856.5−3754: the *continuous line* shows the composite spectrum originating from the surface temperature distribution of the *right panel* Fig. 11.22, assuming blackbody emission from each surface element at the local $T_s(\theta,\phi)$, while the *dotted lines* show the double blackbody fit to the data from [83]. (Figure from [20])

of the stellar surface is cold and detectable in the optical while not being seen in the X-ray band [62, 83]. A surface temperature distribution as the one shown in the right panel of Fig. 11.22 could provide support for such an interpretation, as illustrated in Fig. 11.23. Notice, however, that the model of Fig. 11.23 assumes isotropic blackbody emission from the surface, which is certainly not realistic, and the good fit to the data cannot be considered yet as more than a hint about the presence of a toroidal field. Moreover, other explanations of the mismatch of the optical spectrum with the extrapolation of the X-ray spectrum may be possible, as, e.g., a peculiar surface structure with a condensed matter surface made of iron and covered by a thin hydrogen atmosphere [29].

The presence of an extended cold region at the surface, because of the existence of a strong toroidal field, also has the immediate consequence that the photon thermal luminosity is lower than the one of a star with a purely poloidal magnetic field. In other words, a toroidal component can significantly alter the T_b–T_e relationship as is shown in the left panel of Fig. 11.24. Notice however that in these results T_b now refers to the interior temperature at a density $\rho_b = 10^{14}\,\mathrm{g\,cm^{-3}}$, instead of $10^{10}\,\mathrm{g\,cm^{-3}}$ as was the case in envelope models discussed in Sect. 11.2, so that the whole effect of the magnetic field in the crust is taken into account in the outer boundary condition. From the description of minimal cooling in Sect. 11.3 the effect of such modified T_b–T_e relationships is easily foreseen, and confirmed by the cooling models presented in the right panel of Fig. 11.24: during the neutrino cooling era models with strong toroidal fields have lower luminosities than a model without

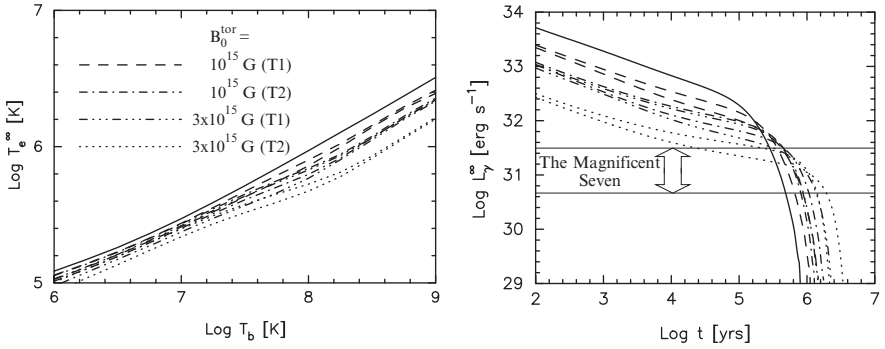

Fig. 11.24 *Left panel*: T_b–T_e relationships corresponding to four different toroidal field structure. In models "T2" $\mathbf{B}^{tor}$ is concentrated in the middle of the crust while in "T1" it is close to the crust–core boundary and, for each case, two different maximum toroidal field strength are considered. In all cases $\mathbf{B}^{pol}$ has a strength of 10^{13} G at the magnetic pole but two different distributions of the electrical currents in the stellar interior are considered. The continuous curve shows the T_b–T_e relationship corresponding to an isothermal crust. *Right Panel*: cooling of neutron stars with the magnetic field structures of the *left panel*. The observed range of luminosities of the "Magnificent Seven" is indicated. (Figure from [53])

toroidal field, although the core temperatures of all of them are practically identical, while during the photon cooling era the situation is inverted and models with lower T_e, and hence a lower L_γ, for a given T_b cool more slowly. The significance of these results resides in this last effect, i.e., neutron stars with strong toroidal magnetic fields can live longer as detectable thermally emitting X-ray sources [53, 55]. A more detailed study of cooling neutron stars with a strong toroidal field as been recently presented by Aguilera et al. [1].

11.6 Conclusions and Future Prospects

The detailed study of the minimal cooling of neutron stars, presented in Sect. 11.3, has allowed us to reach the conclusion that most observed thermally emitting isolated neutron stars are compatible with the predictions of this scenario. We could nevertheless identify several good candidates for non-minimal neutron stars. Considering the expected mass range of isolated neutron stars, shown in Fig. 11.25, we can conclude that:

- This strongly indicates that the critical mass for the appearance of a new state of matter in neutron stars is close to the upper edge of this mass range, i.e., around $\mathbf{1.5 \pm 0.1\, M_\odot}$.

Identification of this new state of matter will, however, require complementary studies, particularly of the many other facets of neutron star phenomenology. One must

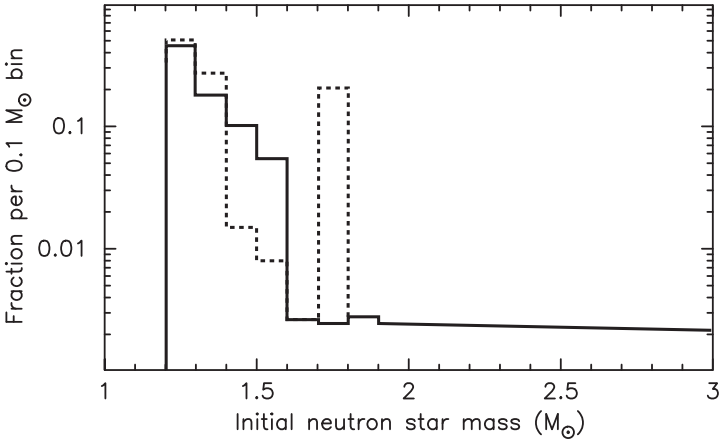

Fig. 11.25 The initial mass function of neutron stars as predicted by stellar evolution theory. The *continuous line* shows results from Fryer and Kalogera [18] and the *dotted line* is adapted from Timmes et al. [82]. The difference between these two predictions is that the former authors included fall-back after the supernova explosion. (Figure from [58])

also keep in mind that "new state of matter" may simply be nucleon matter with a proton fraction above the DUrca threshold, or the existence of the MMUrca process.

The "Magnificent Seven" have proven to be a gold mine for neutron star studies and are still far from being understood. It was shown in Sect. 11.5 that they may be examples of neutron stars with strong toroidal fields, and their strong magnetic fields make them a population intermediate between run of the mill pulsars and magnetars. Many of the observed nearby cooling neutron stars come from the Gould belt [64], making the Solar neighborhood a favorable region in the Galaxy for neutron star studies: population synthesis studies [63] with cooling models [65] and future increase of the sample will be a valuable and complementary tool to the traditional approach presented in this chapter.

Magnetars, either SGRs or AXPs, are also laboratories which, in spite of the complications brought in by their huge magnetic fields, may provide insight on the neutron star interior. Theoretical modeling of their thermal behavior is still in its infancy but the possibility that their large "persistent" thermal X-ray emission is due to the long term cooling of the inner crust heated by a giant burst [16] opens a new window in the study of neutron star thermal behavior. Many aspects of the problem remain to be explored (see, e.g., [33]), including the effects of the magnetic field introduced in Sect. 11.5 where only the first steps have been performed to date [1].

Very promising for complementary studies are compact stars in accreting binary systems, particularly those undergoing transient accretion. When accretion stops we are most certainly directly seeing the surface of the heated compact star and the evolution of these stars parallels that of isolated ones (see, e.g., the recent work of Levenfish and Haensel [41] and references therein). In several cases, the compact star appears to be very cold and these provide serious candidates for fast neutrino

cooling [13]. When an accretion period has lasted several years, the crust has been driven out of thermal equilibrium with the core and the relaxation of the star can be directly observed after accretion stopped, i.e., an evolution similar to the one described in Sect. 11.4.2 can be directly observed [72, 80]. Moreover, the internal thermal state of an accreting compact star has a direct impact on the properties of long type I X-ray bursts (see, e.g., [15]). Since in these low-mass X-ray binaries (LMXBs) accretion can last 10^8–10^9 years one expects some of them to contain more massive compact stars than the ones present in the isolated neutron star sample. Future observations, and theoretical studies, of LMXBs will certainly be a major tool to unravel several of the neutron star mysteries.

References

1. Aguilera, D. N., Pons, J. A., & Miralles, J. A. 2007, e-print: arXiv:0710.0854 [astro-ph]
2. Ainsworth, T. L., Wambach, J., & Pines, D. 1991, in *Neutron Stars: Theory and Observation*, ed. by J. Ventura, & D. Pines (Dordrecht: Kluwer) 37
3. Akmal, A., Pandharipande, V. R., & Ravenhall, D. G. 1998, Phys. Rev., C58, 1804
4. Alford, M. G. 2001, Annu. Rev. Nucl. Part. Sci., 51, 131
5. Alford, M. G., Rajagopal, K., Schaefer, T., et al. 2007, submitted to Rev. of Mod. Phys., e-print: arXiv:0709.4635 [hep-ph]
6. Baade, W., & Zwicky, F. 1934, Proc. Natl. Acad. Sci., 20, 259
7. Baldo, M., Cugnon, J., Lejeune, A., et al. 1992, Nucl. Phys., A536, 349
8. Baldo, M., Elgaroy, O., Engvik, L., et al. 1998, Phys. Rev., C58, 1921
9. Bardeen, J., Cooper, L. N., & Schrieffer, J. R. 1957, Phys. Rev., 108, 1175
10. Bohr, A., Mottelson, B. R., & Pines, D. 1958, Phys. Rev., 110, 936
11. Chabrier, G., Potekhin, A. Y., & Yakovlev, D. G. 1997, ApJ, 477, L99
12. Chen, J. M. C., Clark, J. W., Davé, R. D., et al. 1993, Nucl. Phys., A555, 59
13. Colpi, M., Geppert, U., Page, D., & Possenti, A. 2001, ApJ, 548, L175
14. Cooper, L. N. 1956, Phys. Rev., 104, 1189
15. Cumming, A., Macbeth, J., in't Zand, J. M. M., et al. 2006, ApJ, 646, 429
16. Eichler, D., Lyubarsky, Y., Kouveliotou, C., et al. 2007, e-print: arXiv:astro-ph/0611747
17. Flowers, E., Ruderman, M., & Sutherland, P. 1976, ApJ, 205, 541
18. Fryer, C. L., & Kalogera, V. 2001, ApJ, 554, 548
19. Geppert, U., Küker, M., & Page, D. 2004, A&A, 426, 267
20. Geppert, U., Küker, M., & Page, D. 2006, A&A, 457, 937
21. Glendenning, N. K. 1992, Phys. Rev., D46, 1274
22. Gnedin, O. Y., Yakovlev, D. G., & Potekhin, A. Y. 2001, MNRAS, 324, 725
23. Greenstein, G., & Hartke, G. J. 1983, ApJ, 271, 283
24. Gudmundsson, E. H., Pethick, C. J., & Epstein, R. I. 1982, ApJ, 259, L19
25. Gusakov, M. E., Kaminker, A. D., Yakovlev, D. G., et al. 2004, A&A, 423, 1063
26. Gusakov, M. E., Kaminker, A. D., Yakovlev, D. G., et al. 2004, Astron. Lett., 30, 759
27. Haensel, P., Potekhin, A. Y., & Yakovlev, D.G. 2007, *Neutron Stars 1: Equation of State and Structure* (New York: Springer)
28. Hewish, A., Bell, S. J., et al. 1968, Nature, 217, 709
29. Ho, W. C. G., Kaplan, D. L., Chang, P., et al. 2007, MNRAS, 375, 821
30. Itoh, N., Hayashi, H., Nishikawa, A., et al. 1996, ApJS, 102, 411
31. Jaikumar, P., Gale, C., & Page, D. 2005, Phys. Rev. D, 72, 123004
32. Kaminker, A. D., Gusakov, M. E., Yakovlev, D. G., et al. 2006, MNRAS, 365, 1300

33. Kaminker, A. D., Yakovlev, D. G., Potekhin, A. Y., et al. 2006, MNRAS, 371, 477
34. Kaplan, D. L., Frail, D. A., Gaensler, B. M., et al. 2004, ApJS, 153, 269
35. Kaplan, D. L., Gaensler, B. M., Kulkarni, S. R., et al. 2006, ApJS, 163, 344
36. Lai D. 2001, Rev. Mod. Phys., 73, 629
37. Landau, L. D. 1932, Phys. Z. Sowjetunion, 1, 285
38. Lattimer, J. M., Pethick, C. J., Prakash, M., et al. 1991, Phys. Rev. Lett., 66, 2701
39. Leinson, L. B., & Pérez, A. 2006, Phys. Lett., B648, 114
40. Leinson, L. B., & Perez, A. 2006, e-print: arXiv:astro-ph/0606653
41. Levenfish, K. P., & Haensel, P. 2007, Ap&SS, 308, 457
42. Levenfish, K. P., & Yakovlev, D. G. 1994, Astron. Rep., 38, 247
43. Lombardo, U., & Schulze, H.-J. 2001, in *Physics of Neutron Star Interiors*, ed. by D. Blaschke, N. K. Glendenning, & A. Sedrakian, Lect. Notes in Phys., 578 (Berlin: Springer), 30, e-print: arXiv:astro-ph/0012209
44. Lorentz, C. P., Ravenhall, D. G., & Pethick, C. J. 1993, Phys. Rev. Lett., 70, 379
45. Migdal, A. B. 1959, Zh. Eksp. Teor. Fiz., 37, 249 [1960, Sov. Phys. JETP, 10, 176]
46. Nomoto, K., & Tsuruta S. 1986, ApJ, 305, L19
47. Nomoto, K., & Tsuruta S. 1987, ApJ, 312, 711
48. Oppenheimer, J. R., & Volkoff, G. M. 1939, Phys. Rev., 55, 374
49. Page, D. 1995, ApJ, 442, 273
50. Page, D. 1997, ApJ, 479, L43
51. Page, D. 1998, in *The Many Faces of Neutron Stars*, ed. by A. Alpar, R. Buccheri, & J. van Paradijs (Dordrecht: Kluwer), p. 539, e-print: arXiv:astro-ph/9706259
52. Page, D., & Applegate, J. H. 1992, ApJ, 394, L17
53. Page, D., Geppert, U., & Küker, M. 2007, Ap&SS, 308, 403
54. Page, D., Geppert, U., & Weber, F. 2006, Nucl. Phys. A, 777, 497
55. Page, D., Henderson, J. A., & Geppert, U. 2008, in preparation
56. Page, D., Lattimer, J. M., Prakash, M., et al. 2004, ApJS, 155, 623
57. Page, D., Lattimer, J. M., Prakash, M., & Steiner, A. W. 2008, in preparation
58. Page, D., & Reddy, S. 2006, Annu. Rev. Nucl. Part. Sci., 56, 327
59. Page, D., & Sarmiento, A. 1996, ApJ, 473, 1067
60. Pérez-Azorín, J.F., Miralles, J.A., & Pons, J.A. 2006, A&A, 452, 1009
61. Pethick, C. J., & Ravenhall, D. G. 1995, Annu. Rev. Nucl. Part. Sci., 45, 429
62. Pons, J.A., Walter, F.M., Lattimer, J.M., et al. 2002, ApJ, 564, 981
63. Popov, S. B., Colpi, M., Prokhorov, M. E., et al. 2000, ApJ, 544, L53
64. Popov, S. B., Colpi, M., Prokhorov, M. E., et al. 2003, A&A, 406, 111
65. Popov, S. B., Grigorian, H., & Blaschke, D. 2006, Phys. Rev., C74, 025803
66. Potekhin, A.Y. 1999, A&A, 351, 797
67. Potekhin, A. Y., Chabrier, G., & Yakovlev, D. G. 1997, A&A, 323, 415
68. Potekhin, A. Y., & Yakovlev, D. G. 2001, A&A, 374, 213
69. Potekhin, A. Y., Yakovlev, D. G., Charbier, G., et al. 2003, ApJ, 594, 404
70. Prakash, M., Ainsworth, T. L., & Lattimer, J. M. 1988, Phys. Rev. Lett., 61, 2518
71. Prakash, M., Bombaci, I, Prakash, M., et al. 1997, Phys. Rep., 280, 1
72. Rutledge, R. E., Bildsten, L., Brown, E. F., et al. 2002, ApJ, 580, 413
73. Schaab, C., Voskresensky, D., Sedrakian, A. D., et al. 1997, A&A, 321, 591
74. Schaaf, M. E. 1990, A&A, 235, 499
75. Schwenk, A., & Friman, B. 2004, Phys. Rev. Lett., 92, 082501
76. Schwenk, A., Friman, B., & Brown, G. E. 2003, Nucl. Phys., A713, 191
77. Sedrakian, A., & Clark, J. W. 2006, in *Pairing in Fermionic Systems: Basic Concepts and Modern Applications* (World Scientific: Singapore), in press. e-print: arXiv:nucl-th/0607028
78. Sedrakian, A., Müther, H., & Schuck, P. 2007, e-print: arXiv:astro-ph/0611676
79. Shapiro S. L., Teukolsky S. A. 1984, *Black Holes, White Dwarfs, and Neutron Stars: the Physics of Compact Objects* (New York: Wiley)
80. Shternin, P. S., Yakovlev, D. G., Haensel, P., & Potekhin, A. Y. 2007, e-print: arXiv:0708.0086 [astro-ph]

81. Takatsuka, T., Nishizaki, S., Yamamoto, Y., Tamagaki, R. 2006, Prog. Th. Phys., 115, 355
82. Timmes, F. X., Woosley, S. E., & Weaver, T. A. 1996, ApJ, 457, 834
83. Trümper, J., Burwitz, V., Haberl, F., et al. 2004, Nucl. Phys. B, Proc. Supp., 132, 560
84. Tsuruta, S. 1998, Phys. Rep., 292, 1
85. Tsuruta, S., Teter, M. A., Takatsuka, T., et al. 2002, ApJ, 571, L143
86. Voskresensky, D. N. 2001, Lect. Notes Phys. 578, 467, e-print: arXiv: astro-ph/0101514
87. Wambach, J., Ainsworth, T. L., & Pines, D. 1993, Nucl. Phys., A555, 128
88. Weber, F., Negreiros, R., & Rosenfield, P. 2008, this volume.
89. Weisskopf, M. C., O'Dell, S. L., Paerels, F., et al. 2004, ApJ, 601, 1050
90. Wiringa, R. B., Fiks, V., & Fabrocini, A. 1988, Phys. Rev., C38, 1010
91. Yakovlev, D. & Kaminker, A. 1994, in *The Equation of State in Astrophysics*, ed. by G. Chabrier, & E. Schatzman (Cambridge: Cambridge University Press), 214
92. Yakovlev, D. G., Kaminker, A. D., Gnedin, O. Y., et al. 2001, Phys. Rep., 354, 1
93. Yakovlev, D. G., & Pethick, C. J. 2004, Annu. Rev. Astron. Astrophys., 42, 169
94. Yakovlev, D.G., & Urpin, V.A. 1980, Sov. Astron., 24, 303
95. Zverev, M. V., Clark, J. W., & Khodel, V. A. 2003, Nucl. Phys., A720, 20

Chapter 12
Neutron Star Cooling: II

Sachiko Tsuruta

12.1 Introduction

12.1.1 Historical Background

It was more than 70 years ago when Baade and Zwicky [3] speculated that an "exotic" star consisting mostly of neutrons, now known as a neutron star, may be formed when a normal star collapses through a supernova explosion. During the subsequent years in the 1930s several theorists, including Oppenheimer and Volkoff [35], discussed the properties of neutron stars. However, it was not until the late 1950s to the early 1960s, when curiosity on such a hypothetical object revived [11,73]. As far as I am aware Cameron [11] is the first author who discussed thermodynamic problems of neutron stars. This article's author chose to explore this problem as one of the projects on neutron stars as her PhD thesis [59]. The research started as a purely theoretical endeavor, but before the calculations were completed we learned of the discovery of the first Galactic X-ray source Sco X−1, which was soon followed by the second such Galactic X-ray source detection, this time in the Crab supernova remnant [15]. It was immediately suggested by several theorists [19, 59, 66] that these strong X-ray sources might be neutron stars, because if these X-rays are blackbody radiation as expected, the radius of the emitting region has to be as small as $\sim$10 km (because the temperature is so high), just the correct size predicted for a neutron star.[1]

The first series of our detailed cooling calculations [59, 66] indeed showed that these stars can be hot enough to emit X-rays for approximately a million years

S. Tsuruta
Department of Physics, Montana State University, Bozeman, MT 59717, USA
e-mail: uphst@gemini.msu.montana.edu

[1] For blackbody radiation the photon luminosity $L_\gamma \propto R^2 T_s^4$ (R is the stellar radius, and T_s is the surface temperature), and to emit X-rays T_s must be $\sim 10^6$ K or so [19, 59]. Then, for L_γ to be observable, e.g., solar luminosity, the radius must be about 10 km.

W. Becker (ed.), *Neutron Stars and Pulsars,* Astrophysics and Space Science Library 357,

after a supernova explosion. However, subsequent observations indicated that the Crab X-ray source is "extended", and the spectrum of Sco X−1 radiation is not blackbody [9]. At about the same time Bahcall and Wolf (1965) [4] suggested that if pions are present in a neutron star, the star will cool too fast to be observable. The unexpected discovery of a neutron star, however, was soon reported in 1968, in the form of a radio pulsar [20]. With the subsequent discovery of many more radio pulsars [57], as well as X-ray pulsars by *UHURU* and other X-ray satellite missions [24], a neutron star is now an established, no longer "exotic" member of the celestial family. On the other hand, the prospect of directly "seeing" a neutron star, in the sense of detecting the radiation directly from the stellar surface, as in the case for ordinary stars, has turned out to be elusive. This is because the circumstellar plasmas, in accretion disks and/or the stellar magnetosphere, can emit X-rays, too, often stronger than the stellar surface radiation, and it was beyond the capability of the earlier pioneering detectors to separate one from the other.

The first imaging X-ray telescope on board the *Einstein* Observatory launched in 1978 [16], however, offered the first opportunity for detecting radiation directly from the surface of neutron stars (see, e.g., [33]). Prompted by this new challenge the subsequent years have seen revival of neutron star thermal evolution studies [34,44,61]. In the earlier years neutron star cooling calculations were carried out by adopting a simple isothermal approximation.[2] In the subsequent years during the 1980s more detailed neutron star cooling calculations were carried out [34,44], by adopting fully general relativistic stellar structure evolution equations (see Sect. 12.2.1) and up-to-date microphysics, and by utilizing the "exact evolutionary method" without making an isothermal approximation (see footnote 2). The results of these calculations were then carefully compared with the data from the *Einstein* observations [33,61]. The conclusion is that the upper limits to the temperatures of some neutron stars are consistent with the "standard" neutron star cooling scenario, but the Vela pulsar temperature upper limit is too low for the standard cooling scenario. However, the Vela data is consistent with a fast "nonstandard" cooling scenario.[3] The earlier developments as outlined above have been reviewed by two major articles by Tsuruta [60,61].

Although the launch of the *Einstein* Observatory gave the first hope for detecting thermal radiation directly from the surface of cooling neutron stars, the data from the *Einstein* were only temperature upper limits [33,34]. However, the *ROSAT* X-ray satellite mission, launched in 1990, offered the first turning point. Due to its

[2] When the integration of basic stellar structure evolution equations is carried out simultaneously without making an isothermal approximation, we refer to that method, for convenience, as the "exact evolutionary method". However, the interior of a neutron star becomes essentially isothermal after several hundred to a few thousand years of thermal evolution, and then the structure equations and the thermodynamic equations can be decoupled. When these two sets of equations are solved separately, the method is generally referred to, as the "isothermal method". See Sect. 12.2.1 for the details.

[3] In the "standard" cooling scenario a star cools through the conventional neutrino processes, such as the modified Urca process. On the other hand, the accelerated cooling, such as pion cooling, is often referred to, as "nonstandard" cooling. In this article, for convenience, we will adopt this terminology. See Sect. 12.2.2 for the details.

favorable soft response it offered for the first time confirmed detections of the stellar surface thermal radiation from at least three cooling neutron stars, PSR 0656+14, PSR 0630+18 (Geminga) and PSR 1055−52, and possibly from PSR 0833−45 (Vela pulsar) also [6]. Consequently, the 1990s saw renewed activities in the studies of thermal radiation from neutron stars. These activities were reviewed, e.g., by Tsuruta in 1998, hereafter T98 [62].

12.1.2 Recent Developments

Recently, the prospect for measuring the surface temperature of isolated neutron stars, as well as obtaining better upper limits, has increased tremendously, thanks to the superior X-ray data from *Chandra* and *XMM-Newton* X-ray satellite missions launched in 1999 (see, e.g., [8] for the review). Consequently, the number of confirmed surface temperature detections has increased to at least eleven, and the upper limits to the temperatures were obtained for all pulsars from the *ROSAT* All Sky Survey [8]. New X-ray spectral data from these satellite missions enabled us to estimate the surface composition (see, e.g., [39]). The distance and the age of the stars have been among the most uncertain parameters, which have made it difficult to discriminate among different competing theoretical models. Most recently, however, we have gained hope for some improvements, e.g., by the direct distance measurement by very long baseline interferometry (VLBI) observations, e.g., for Vela pulsar [12].

On the theoretical side, in recent years important progress has been underway in the area of nuclear and particle physics which are essential for testing neutron star (NS) cooling theories, such as the equation of state (EOS) and the influence of superfluid neutrons and protons in the inner neutron star crust (see [32, 51–56], and references therein). These developments have started to give us better hope for differentiating between various competing neutron star cooling models.

In this paper we will consider isolated "ordinary" NSs which are suitable for testing cooling theories with observation – "ordinary" in the sense that surface magnetic fields do not exceed $\sim 10^{13}$ G. Therefore, magnetars, accreting NSs in binaries and millisecond pulsars are not included. Quark stars are not covered due to lack of detailed theories necessary for testing NS cooling models, to the extent that is currently already available for other types of NSs covered in this review.

After an introduction in this section, Sect. 12.2 describes basic equations, methods of calculations and input microphysics. Section 12.3.1 summarizes cooling models obtained by these equations before the *Chandra* and *XMM-Newton* X-ray missions offered more detailed cooling data. Section 12.3.2 will introduce currently up-dated observational data, and in Sect. 12.3.3 the latest theoretical thermal evolution models are presented and compared with these new observational data. Future prospects are discussed in Sect. 12.4, and concluding remarks are given in Sect. 12.5.

12.2 Basic Equations and Input Physics

12.2.1 Basic Equations and Methods of Solution

The general relativistic equations for solving the structure and evolution of neutron stars (NSs hereafter) are given as [58, 61]:

Hydrostatic Equilibrium:

$$dP/dr = \frac{-G(m+4\pi r^3 P/c^2)(P/c^2+\rho)}{r^2(1-2Gm/rc^2)}, \tag{12.1}$$

$$dm/dr = 4\pi r^2 \rho, \tag{12.2}$$

$$d\phi/dr = \frac{-dP/dr}{(\rho c^2+P)}, \tag{12.3}$$

Energy Balance:

$$d(Le^{2\phi})/dr = \frac{-4\pi r^2 n e^{\phi} C_v dT/dt}{(1-2Gm/rc^2)^{1/2}}. \tag{12.4}$$

Radiative Energy Transport:

$$d(Te^{\phi})/dr = \frac{-3\kappa\rho L_\gamma e^{\phi}}{16\sigma T^3 4\pi r^2 (1-2Gm/rc^2)^{1/2}}, \tag{12.5}$$

where P, ρ, m, T, L, L_γ, κ, C_v, n, r, and t are pressure, total mass density, mass, temperature, total luminosity, photon luminosity, total opacity, total specific heat, total number density, radial distance from the center of the star, and time, respectively, measured locally. G, σ, and c are Gravitational constant, Stefan–Boltzmann constant, and speed of light, respectively. ϕ is the gravitational potential and e^{ϕ} is the general relativistic correction factor. In the non-relativistic limit e^{ϕ} reduces to 1, $m \gg 4\pi r^3 P/c^2, P \gg \rho c^2$, and $1 \gg 2Gm/rc^2$, and these equations reduce to the familiar Newtonian stellar structure evolution equations found in any standard astrophysics textbooks.

The first equation (12.1) tells just the mechanical balance, i.e., that at each point in a star the gravity must be supported by the internal pressure and the second equation (12.2) is just the relation between mass and density. The third equation defines the gravitational potential due to general relativity which becomes negligible in the Newtonian limit, and hence this equation does not appear in the Newtonian version of these basic equations. The first three equations determine the structure and mechanical properties of the star such as the relations between mass, radius and central density, while the last two equations determine the thermodynamic properties of the star, such as specific heat, luminosity and internal and surface temperatures.

In order to solve these equations, we require additional supplementary equations:
Equation of State (EOS):

$$P = P(X, \rho, T), \tag{12.6}$$

Opacity Equation:

$$1/\kappa = 1/\kappa_R + 1/\kappa_C, \tag{12.7}$$

Luminosity Equations:

$$d(L_\nu e^{2\phi})/dr = \frac{4\pi r^2 n e^{\phi} q_\nu}{(1 - 2Gm/rc^2)^{1/2}}, \tag{12.8}$$

$$L_\gamma = 4\pi\sigma R^2 T_s^4, \tag{12.9}$$

$$L = L_\nu + L_\gamma, \tag{12.10}$$

where κ_R and κ_C are the radiative and conductive opacity, L_ν and q_ν are total neutrino luminosity and total neutrino emissivity (= luminosity per volume), respectively, X refers to the composition, R is stellar radius, and T_s is stellar surface temperature, respectively.

Note that in the above equations the total mass density, total number density, total opacity and total specific heat are the values obtained by adding the respective components contributed by all constituent particles.

Solving (12.1)–(12.10) simultaneously, we obtain the mechanical structure such as stellar mass M, radius R and central density ρ^c, and thermodynamic properties such as temperature T, total internal energy E, specific heat C_v, as well as the radial distribution of these parameters across the stellar interior. In this article, for convenience, this method without making any approximations will be called the "exact evolutionary method". On the other hand, the stellar interior is essentially isothermal, and any temperature decrease from the interior to the surface takes place within very skinny layers near the surface. Therefore, except during the earlier stages before the thermal equilibrium is reached (about 100–10,000 years after a supernova explosion), the first three mechanical equations (12.1)–(12.3) and the last two thermodynamic equations (12.4) and (12.5) can be decoupled. Then we first integrate (12.1)–(12.3) to obtain mechanical properties such as M, R and ρ^c. Using these quantities thus obtained as the input, we solve the last two equations (12.4) and (12.5), to obtain thermodynamic properties such as T vs. t relations (cooling curves) and the relation between the internal core temperature T_c and surface temperature T_s.[4] This method, of decoupling the mechanical and thermodynamic parts, is generally called the "isothermal method".[5] In this article, all cooling/heating curves shown were obtained by adopting the exact evolutionary method without making an isothermal approximation.

Typical results for the mechanical properties are presented in Fig. 12.1, where the central density vs. stellar mass relation is shown, for the density regime from

[4] This T_c vs. T_s relation is necessary because neutrino luminosity depends on T_c (since neutrinos escape from the stellar interior directly), while photon luminosity depends on T_s.

[5] It many be emphasized that although various physical properties can be explored qualitatively by using the isothermal method, in order to obtain detailed cooling curves which are to be compared with the improved observational data, it is desirable that we adopt the exact evolutionary method.

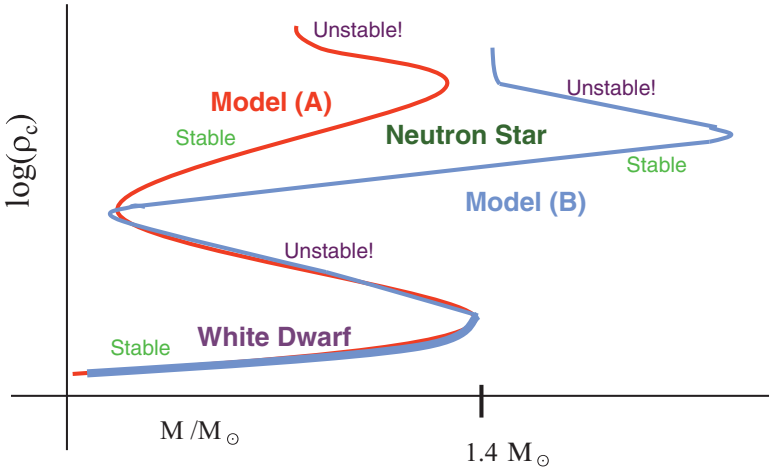

Fig. 12.1 Mass–central density relation of dense stars. In the lower stable region stable white dwarfs lie, while in the upper two stable regions two stable NS models (A) and (B) are located. The compactness (M/R) depends on the nuclear force

the white dwarf region (lower stable region) to the NS region (upper two stable regions which represent two different NS models (A) and (B)). Model(A) represents a denser and more compact star, while Model (B) refers to a more extended and less dense star. See Sect. 12.2.2 for further details of the models.

The quantities such as T, L, R, etc., which appear in the above equations refer to the local values at the star. However, since an NS is very dense, gravitational effects can not be neglected. Consequently, the values at infinity (the observed values) are gravitationally redshifted. The observed surface temperature and photon luminosity are, accordingly, expressed as

$$T_s^{\infty} = T_s e^{\phi_s}, \tag{12.11}$$

$$L_{\gamma}^{\infty} = L_{\gamma} e^{2\phi_s}. \tag{12.12}$$

Combining these equations, the observed photon luminosity and surface temperature are related as

$$L_{\gamma}^{\infty} = 4\pi\sigma R_e^2 (T_s^{\infty})^4, \tag{12.13}$$

where R_e is the effective (observed) radius

$$R_e = e^{-\phi_s} R. \tag{12.14}$$

In these equations ϕ_s is the gravitational potential at the stellar surface, and

$$e^{\phi_s} = (1 - 2GM/Rc^2)^{1/2}. \tag{12.15}$$

It may be noted that (12.4) is especially important for NS cooling theories because it essentially determines cooling. That can be seen more easily if we look at this equation in the Newtonian limit, which reduces to

$$dE/dt = C_v dT/dt = -L_\gamma - L_\nu + H, \tag{12.16}$$

where E is the total internal energy, L_γ and L_ν are photon luminosity and neutrino luminosity , respectively, and C_v is the total specific heat. Sometimes heating becomes important, and hence the heating term H is added in this equation. This equation represents the rate of decrease of temperature with time dT/dt. It determines cooling/heating, i.e., the T vs. t relation, which can be obtained by integrating $(-L_\gamma - L_\nu + H)/C_v$ over time.

Typical standard cooling curves are shown in Fig. 12.2. Total photon luminosity L_γ^∞ (to be observed at infinity) is plotted against stellar age t (taken from T98 [62]).[6] These cooling curves were obtained by the exact evolutionary method. The different curves refer to the different NS models BPS, PS and FP. The BPS model represents a dense, more compact star with the EOS constructed by Baym, Pethick and Sutherland [5], the PS model a less dense, very extended star with the EOS constructed by Pandharipande, Pines and Smith [37], and the FP model with the EOS constructed by Friedman and Pandharipande [14] which represents a model which is medium in its compactness (see Sect. 12.2.2). The data points indicated by the name of each pulsar were up-dated as of 1995. Bars and downward arrows represent detections and upper limits, respectively. Until the age of about 10^{5-6} years neutrino luminosity L_ν dominates photon luminosity L_γ [in (12.10)], and hence the star cools by neutrinos escaping from the interior. This period is called *neutrino cooling era*. After about that age, however, photon luminosity overtakes neutrino luminosity, and the star cools predominantly by photons escaping from the stellar

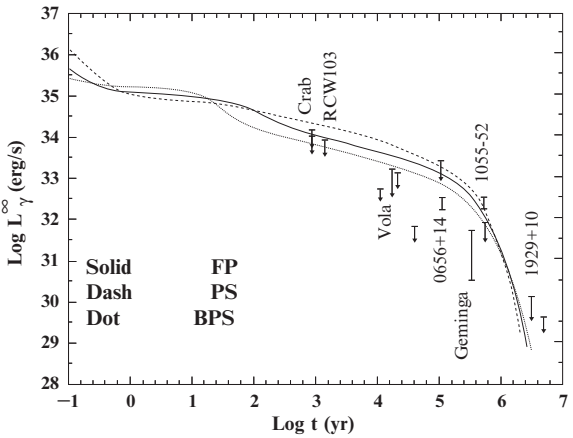

Fig. 12.2 Typical standard cooling curves for different NS models BPS (*dotted curve*), PS (*dashed*), and FP (*solid*), taken from [62]

[6] Note that since surface photon luminosity is directly related to surface temperature through the blackbody radiation equation (12.13), cooling curves are often shown as photon luminosity vs. age relations. See Sect. 12.3.2 for the reason.

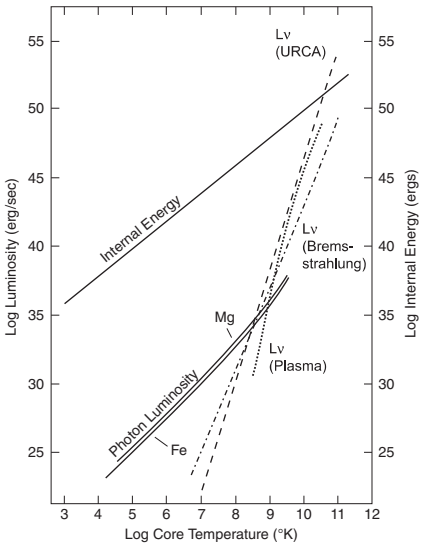

Fig. 12.3 Various components of neutrino luminosity, photon luminosity and internal energy as a function of internal core temperature, taken from [66]

surface. This latter period is called *photon cooling era* . We see that the effect of EOS is relatively small, but more extended stars cool somewhat more slowly during the neutrino cooling era between $\sim$100 and 10^6 years.

This behavior takes place because neutrino luminosity far exceeds at high temperatures during the earlier stages but it has a sharp decrease with temperature, as $\propto T_c^{6-8}$, and hence it decreases quickly as the star cools, while photon luminosity depends on temperature more moderately as $\propto T_s^4$. The situation is illustrated in Fig. 12.3, where various components of luminosity and internal energy are shown as a function of internal temperature. In this figure three curves with steeper slopes marked (URCA), (Plasma) and (Bremsstrahlung) are modified Uruca, plasmon and crust bremsstrahlung neutrino luminosity, respectively, while two other lines with much milder slope marked (Photon Luminosity) refer to photon luminosity, with two surface composition Mg and Fe (as marked). See Sect. 12.2.2 for the details.

12.2.2 Major Input Parameters and Their Effects

Among the important factors which potentially can affect the nature of NS cooling seriously are: EOS, composition, neutrino emission processes, superfluidity of constituent particles, heating, and stellar mass. In the following we shall consider these factors.[7]

[7] The effect of magnetic fields on cooling itself is not important for isolated neutron stars and ordinary pulsars with magnetic fields less than about 10^{13} G. Other related properties affected by magnetic fields are discussed in Page's contribution to this volume, and also in [62].

Equation of State (EOS)

An equation of state (EOS) for neutron matter in the stellar core depends strongly on the nuclear force among nucleons. (Similarly, an EOS for exotic particles such as hyperons depends on the strong force.) The behavior of nuclear force is illustrated in Fig. 12.4, where nuclear interaction potential V is plotted against separation distance between two nucleons. As shown in Fig. 12.4 the interaction force generally becomes negative and hence attractive first as the inter-particle distance decreases, but eventually it turns positive and hence repulsive at short distances. How deep the attractive force is and when the repulsive effect overtakes determine the nature of an EOS of the central core. EOS with stronger attractive forces (e.g., Model (A) in Fig. 12.4) produces a denser, more compact and smaller star, while an EOS with stronger repulsive forces (e.g., Model (B) in Fig. 12.4) will result in a less dense, more extended and larger star. The maximum mass of the former (e.g., Model (A)), accordingly, is less than that of the latter (e.g., (B)). That is clearly seen in Fig. 12.1 in Sect. 12.2.1. See also the table accompanying Fig. 12.4. For convenience, in this paper we follow the terminology generally used: the former EOS (e.g., Model (A)) is called "soft", while the latter EOS (e.g., (B)) "stiff". See, e.g., [62, 66] for further details.

Note that BPS, PS and FP Models, the EOS models introduced in Fig. 12.2 in Sect. 12.2.1 and adopted in some subsequent figures shown in this article, represent typical soft, stiff, and medium EOS.

Composition and Structure

The composition of different parts of an NS is shown in Fig. 12.5, where a cross section of the interior of an NS is given.

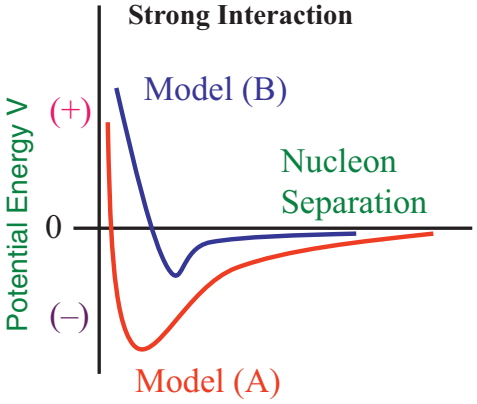

Model	(A)	(B)
ρ^c (gm/cm^3) /10^{14}	3 ~ 70	3 ~ 10
Mass/$M_\odot$	0.1~1.5	0.1 ~ 2
Radius (km)	20 ~ 8	20 ~15

Properties of NS - Model dependent!

Fig. 12.4 Nuclear force: Simplified representation of the nuclear potential shown as a function of the separation between two nucleons (neutrons and/or protons)

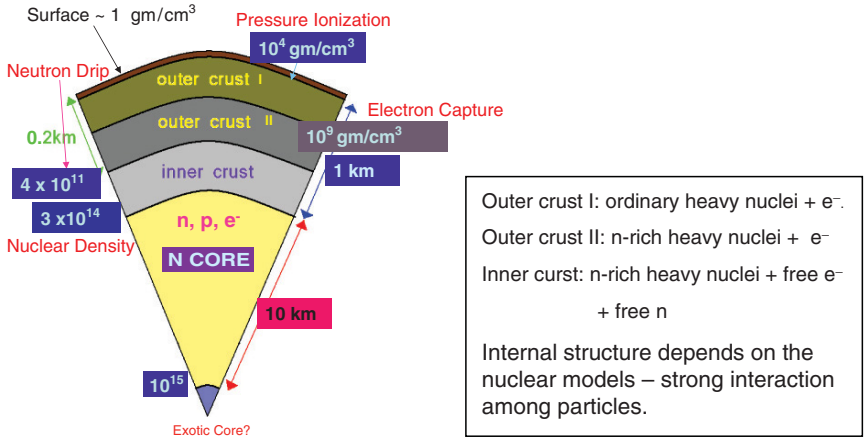

Fig. 12.5 A cross section of an NS showing the structure and composition of different parts of the star. Note that neutrons and protons may be in a superfluid state

The composition of different parts of an NS is theoretically predicted from properties of dense matter where a zero-temperature approximation is valid: that is, Fermi energy E_F of constituent particles, which depends on density, exceeds thermal energy kT [59]. With densities from terrestrial values up to $\rho_p \sim 10^4\,\mathrm{gm\,cm^{-3}}$ ordinary terrestrial matter exists. Calculations show that the equilibrium composition peaks at iron [59]. Therefore, in this range the most abundant element is predicted to be ordinary $^{56}\mathrm{Fe}_{26}$ atoms, and hence we expect the atmosphere and the outermost layers just beneath the surface consist of ordinary heavy atoms peaking at $^{56}\mathrm{Fe}_{26}$. At ρ_p, the density is so large that the pressure ionization, where atoms are ionized by pressure due to high density (rather than temperature), takes place. This is where the outer crust I (see Fig. 12.5), consisting of ordinary heavy ions and free electrons, starts. With further increase of density another critical point is reached where free electrons become so abundant that they are captured by nuclei. It takes place at density $\rho_e \sim 10^9\,\mathrm{gm\,cm^{-3}}$. A captured electron combines with a proton and becomes a neutron within a nucleus. In this way neutron-rich nuclei are formed. This is where the outer crust II (Fig. 12.5) starts. Here the mater consists of neutron-rich heavy nuclei and free electrons. With further increase of density, another critical point is reached when there are so many neutrons in a nucleus that some neutrons drip out of the nucleus. This point is called the "neutron-drip" point, with the critical density $\rho_n \sim 4 \times 10^{11}\,\mathrm{gm\,cm^{-3}}$. At this density the inner crust starts which consists of free neutrons, electrons and neutron-rich heavy nuclei. Finally when density approaches the nuclear density, $\rho_N = 2.8 \times 10^{14}\,\mathrm{gm\,cm^{-3}}$, there are so many neutrons within nuclei that heavy ion nuclei disintegrate into free neutrons, protons and electrons (called "photo disintegration"). By this time there are so many neutrons that about 95% of particles are neutrons, with a small amount of protons and electrons. This is where a predominantly neutron core starts. (Muons

also appear at somewhat higher densities.) With still further increase of density it becomes energetically more economical if some nucleons transform to "exotic" particles such as hyperons, pions, etc.

Consequently, when the density is not high the composition of the central core of NSs is predominantly neutrons (n) with only a small fraction of protons (p) and electrons (e^-). That occurs for density ranges from about ρ_N to ρ^{tr}, the transition density to the "exotic" particles, such as hyperons and pion and kaon condensates, which is $\sim(0.6\text{–}2) \times 10^{15}\,\mathrm{gm\,cm^{-3}}$. For higher densities these "exotic" particles will appear. Therefore, when a star is less massive and hence less dense, we have an ordinary NS with the core consisting predominantly of neutrons. On the other hand, the interior of a heavier, denser star (exceeding this transition density) consists of the inner core mixed with exotic particles and the outer core with the ordinary neutron matter. The thin stellar envelopes outside the core consist of the inner crust with neutron-rich heavy nuclei, free neutrons and electrons, and the outer crust with heavy nuclei and electrons. The stellar surface is covered with very thin atmospheres [62].

Neutrino Emissivity

Neutrino emissivity, q_ν, appearing in (12.8) which calculates neutrino luminosity, can be divided into two parts: emissivity for slower, more conventional "standard" processes $q_\nu(st)$ and emissivity for fast "nonstandard" processes $q_\nu(nonst)$:

$$q_\nu = q_\nu(st) + q_\nu(nonst), \tag{12.17}$$

$q_\nu(st)$ can be expresses as

$$q_\nu(st) = q_\nu^{MU} + q_\nu^{NN} + q_\nu^{pl} + q_\nu^{B}(C) + (others), \tag{12.18}$$

where $q_\nu^{MU}, q_\nu^{NN}, q_\nu^{pl}$, and $q_\nu^{B}(C)$ are modified Urca, nucleon bremsstrahlung (involving both neutrons and protons), plasmon, and crust bremsstrahlung neutrino emissivity, respectively. Urca process is essentially beta decays and their inverse reactions. However, since nucleons and electrons in a NS core are highly degenerate, the Pauli Exclusion Principle prohibits direct beta processes and the modification is needed, which causes the process to become slower than the direct processes [29]. Modified Urca and plasmon neutrino processes take place both in the core (involving nucleons) and in the inner crust (involving heavy ions). Nucleon neutrino bremsstrahlung takes place in the core, while crust neutrino bremsstrahlung takes place in the inner crust. (Others) represent other minor processes such as pair neutrino, photo-neutrino processes, etc. These processes are called "standard" because the mechanisms are relatively straightforwardly predicted, and they have hence been adopted since the early days in the 1960s (see [59, 62, 66] for further details).[8]

[8] Also see Page's contribution to this volume.

It was Bahcall and Wolf (1965) [4] who first showed that a NS can cool very fast if pions are present in the interior. Since then it was shown that these pions are in the form of condensates (see, e.g., [48]). It has been shown that the presence of not only pion condensates, but also other "exotic" particles, such as hyperons, quarks and kaon condensates, also causes fast cooling (see, e.g., [62]). Furthermore, it has been pointed out that if the proton fraction in neutron matter is relatively high (e.g., $\gtrsim$11%) a fast direct Urca process involving nucleons alone (with no "exotic" particles) also can take place in the neutron-dominated core (with no exotic particles) [28]. For convenience, we refer to all these fast processes as "nonstandard" cooling.

Figure 12.6 shows standard and nonstandard cooling curves for a $1.4\,M_{\odot}$ star, taken from T98 [62]. The upper solid curve marked "stan" refers to standard cooling [where all processes in (12.18) are included]. Various lower curves represent nonstandard curves, where "kaon", "qu(KS)", "qu(IWA)", "pi06", "pi+ka", and "direct" refer to fast direct Urca cooling with kaons, quarks (constructed by Kiguchi/Sato), quarks (constructed by Iwamoto), pions, pions and kaons, and nucleons only, respectively. The medium EOS Model UU constructed by Umeda, Tsuruta and Nomoto (1995) [70] was adopted. Other notations are the same as in Fig. 12.2. It is obvious that all nonstandard cooling scenarios are too fast to be consistent with the detection data.

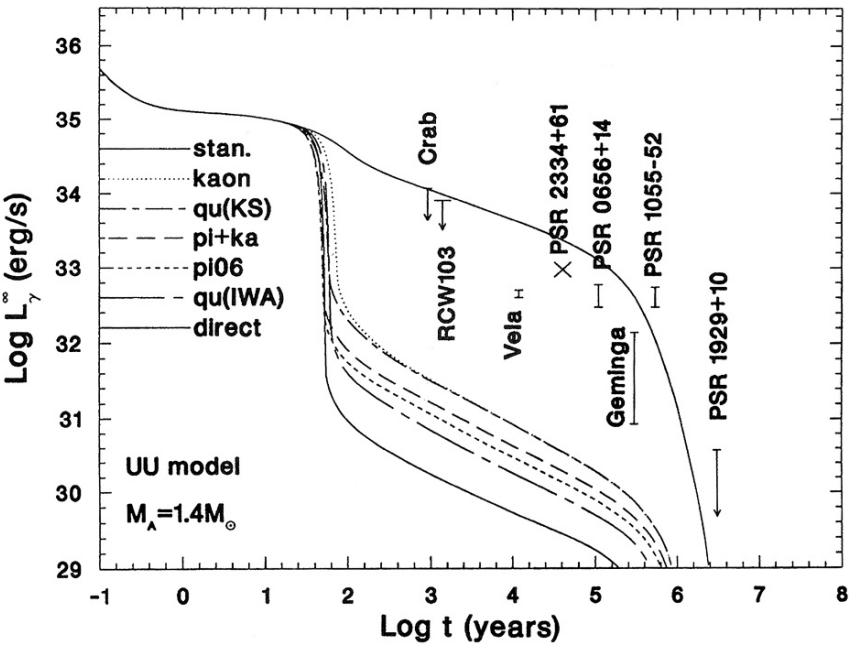

Fig. 12.6 Standard and non-standard cooling curves (from [62]). The sharp luminosity drop at ~100 yrs is because of a temperature inversion. In the accelerated cooling models the inner neutron star regions cool more efficient by neutrino cooling than the outer parts do. This causes the heat to flow from the outer regions to the inner parts of the star and thus causes a fast decrease of the surface temperature

Superfluidity of Constituent Particles

As the central collapsed star cools after a supernova explosion and the interior temperature falls below the superfluid critical temperature T_{cr}, the constituent particles in question (nucleons, hyperons, pion condensates, etc., though not electrons and muons) become superfluid. Superfluid neutrons in the inner crust and in the core are expected to be in the $^1S_0$ and $^3P_2$ state, respectively, while protons in the core are in the $^1S_0$ state. Hereafter, for convenience, we shall refer to neutron superfluid in the $^1S_0$ state in the crust as "neutron S", and neutron superfluid in the $^3P_2$ state in the core as "neutron P" superfluid.

The superfluid critical temperature T_{cr} is related to the superfluid energy gap Δ according to

$$kT_{cr} \sim 0.57\Delta, \tag{12.19}$$

where k is Boltzmann constant. Δ represents a measure of strength of superfluidity. The stronger the attractive nuclear force, the larger is the energy gap. It depends on density. Typical examples of density dependence of T_{cr} for various core neutron P superfluid models are shown in Fig. 12.7 (taken from T98 [62]). T_{cr} is plotted against ρ_m, matter density. Various superfluid models are: T72 constructed by Takatsuka (1972) [47], AO constructed by Amundsen and Ostgarrd (1985) [2], and HGRR constructed by Hoffberg et al. (1970) [21], respectively. The other models, NPC, ETA, E1 and E2 were constructed by Takatsuka and Tmagaki (1980, 1982) [48].

The major effect of superfluidity on cooling is that when the interior temperature T becomes below T_{cr}, all neutrino processes involving the superfluid particles decrease roughly as

$$L_\nu(super) = L_\nu(normal)R(T/T_{cr}), \tag{12.20}$$

where $L_\nu(super)$ and $L_\nu(normal)$ are neutrino luminosity with and without superfluid particles, respectively, and $R(T/T_{cr})$ is the reduction factor, i.e., the luminosity

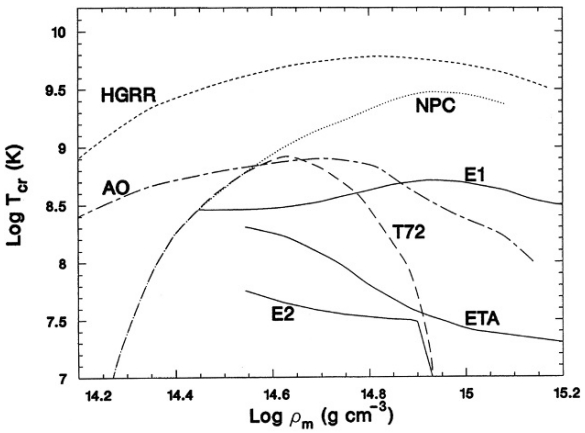

Fig. 12.7 Density dependence of T_{cr} for various core neutron P superfluid models, taken from [62]

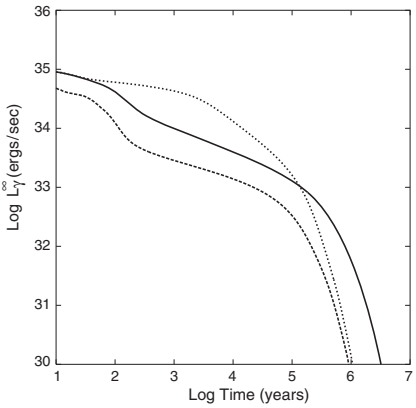

Fig. 12.8 The effects of core neutron superfluidity and the Cooper pairing neutrino processes on standard cooling

is suppressed by this factor in the presence of superfluidity. Roughly it reduces as $\exp(-a_c T_{cr}/T)$ (for $T \ll T_{cr}$, where a_c is a constant), although the precise dependence is somewhat more complicated.[9] The net effect is that in the presence of superfluidity a star cools more slowly due to suppression of neutrino cooling, which raises surface temperature during the neutrino cooling era. The suppression is larger for stronger superfluidity, meaning a larger energy gap and hence higher T_{cr}. This effect on cooling is small for crust neutrons, but it can be significant for core particles, especially neutrons [62].

A typical example of the effects of core neutron P superfluidity on standard cooling is shown in Fig. 12.8, which shows cooling of $1.3\,M_\odot$ stars with an EOS of medium stiffness. The solid curve is for a star with no superfluid P neutrons, while the thin dotted curve (upper curve) shows the effect of superfluid P neutrons. Other notations are the same as in Fig. 12.2. We see that the effect of superfluid core neutrons is to raise the surface temperature during the neutrino cooling era. Proton superfluidity also gives similar effects.

Another important factor is that superfluidity causes additional neutrino processes, hereafter referred to as the "Cooper pairing neutrino processes". They were originally suggested by Flowers, Ruderman and Sutherland (1976) [13], and recently "rediscovered". These processes have proven to be very important under certain circumstances (see, e.g., [76]). The net effect is to enhance, in complicated ways, the neutrino emission involving the superfluid particles right after the superfluidity sets in [13, 76]. The effect is especially important when core neutrons are in a superfluid state (see footnote 8, and also [36]). In Fig. 12.8 the effect of Cooper pairing neutrino processes is displayed by the thick dashed curve (lower curve). It is clear that this effect is to accelerate cooling significantly and hence the star cools faster.

We have noted that suppression of standard cooling by superfluid nucleons raises the cooling curve during the neutrino cooling era (see Fig. 12.8). This effect can be drastic for nonstandard cooling. The situation is illustrated in Fig. 12.9, where

[9] Specific heat C_v also decreases similarly with superfluidity.

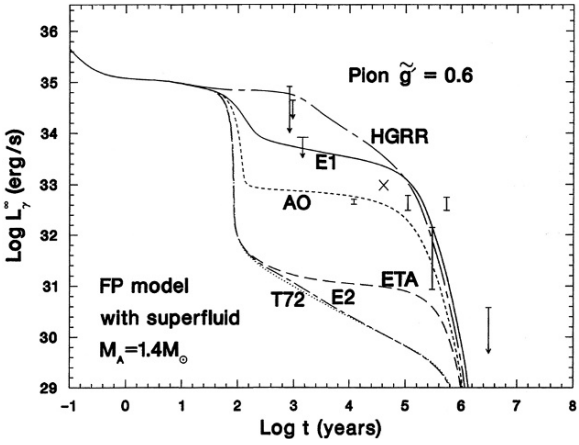

Fig. 12.9 The effect of superfluidity on non-standard cooling

cooling curves for 1.4 $M_\odot$ stars with FP EOS (introduced in Sect. 12.2.1) are shown. Neutron P superfluid models of various strengths (i.e., varying T_{cr}) are applied to a nonstandard pion cooling scenario. Different models HGRR, E1, AO, etc., refer to the superfluid models introduced in Fig. 12.7. We see that for a weak superfluid model such as Model E2 (small T_{cr}) suppression is essentially negligible, while for a strong model such as HGRR the suppression is so complete that the cooling is essentially the same as standard cooling. Other intermediate models such as AO and E1 models lie between these two extremes.

The Effect of Heating

For ordinary isolated neutron stars and pulsars where surface magnetic fields do not exceed $\sim 10^{13}$ G, the only heating mechanism which can seriously affect cooling is the frictional heating which takes place in the inner crust. Neutrons there are expected to be in a superfluid state. Then, as the star is spinning down, while the rigid crustal heavy ions spin down with the star superfluid neutrons will not. Therefore, there arise frictions between the heavy ion crustal material and superfluid neutrons which cause heating. The efficiency of this frictional heating depends on how strongly the superfluid vortex is pinned to the crust, and hence the strength of this pinning determines heating [1, 62, 69–71].

Typical examples are shown in Fig. 12.10, where the surface temperature (to be observed at infinity) vs. age relation is given, for PS Model introduced in Sect. 12.2.1, taken from T98 [62]. The solid curve represents cooling without heating. The upper three curves refer to models with frictional heating included, with varied degrees of heating. The uppermost curve (long dashed) refers to the maximum heating expected from the frictional heating theory. The bars and downward arrows refer to the data for detections and upper limits, respectively, which were available in 1993. We note that heating is significant for this stiff PS Model. We find that heating is less significant for models with softer EOSs [62].

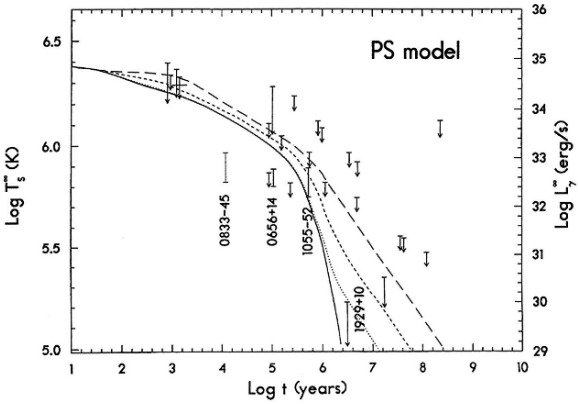

Fig. 12.10 The effects of frictional heating on neutron star cooling

Effect of Stellar Mass

For standard cooling of NSs without superfluid particles the effect of mass is relatively small (see, e.g., [62, 66]).[10]

The situation changes dramatically when nonstandard cooling is included, in the following way. Less massive, and hence less dense stars whose central density ρ^c is less than the transition density to an exotic process ρ^{tr}, are ordinary neutron stars, and hence they will cool with a slower, standard scenario. On the other hand, in more massive, denser stars where ρ^c exceeds ρ^{tr}, nonstandard fast cooling takes over, and the effect of mass becomes very important (see, e.g., [62]). When density dependence of superfluid suppression is taken into account nonstandard curves generally go down smoothly with increasing stellar mass (see, e.g., Figs. 12.11–12.13 in Sect. 12.3.3).

12.3 Neutron Star Thermal Evolution Models

12.3.1 Earlier Work

In the pioneering work on NS cooling by Tsuruta and Cameron (1966), hereafter TC66 [66] various standard neutrino emissivities, such as modified Urca, neutrino bremsstrahlung and plasmon neutrino processes involving nucleons in the core and heavy ions in the crust (see Fig. 12.3), as well as more minor processes, are included. To solve the basic structure evolution equations the isothermal method was used. General relativity was included in the Oppenheimer–Volkoff equations

[10] However, the situation can be more complicated in the presence of superfluidity due to the sensitive dependence of superfluid energy gaps on density.

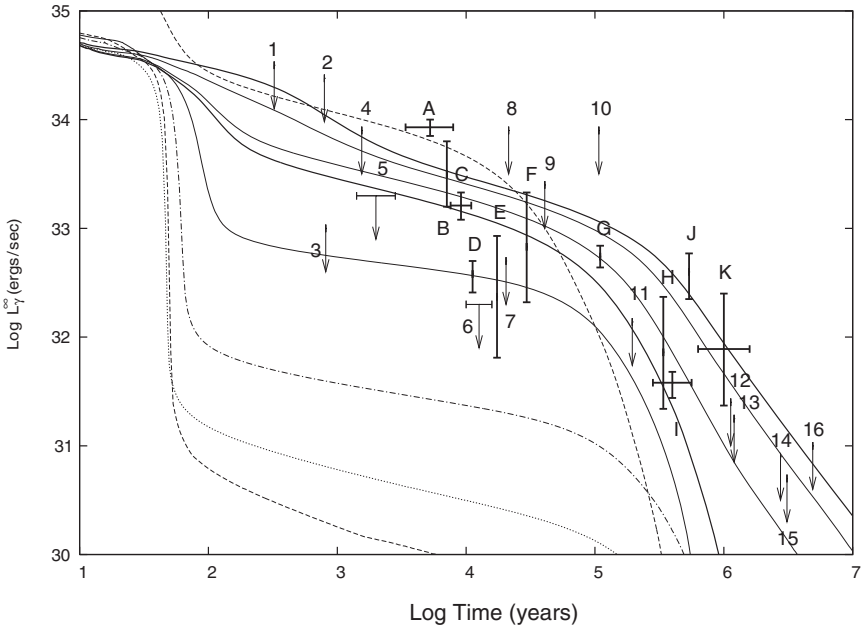

Fig. 12.11 Thermal evolution of hyperon-mixed stars with various mass and the EOS TNI6u of medium stiffness

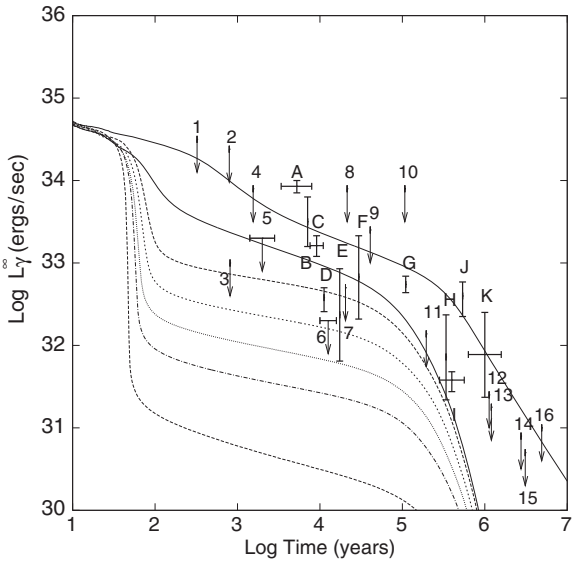

Fig. 12.12 Thermal evolution of hyperon-mixed stars with various mass and with the soft EOS TNI2u/TNI2. Notations are the same as in Fig. 12.11

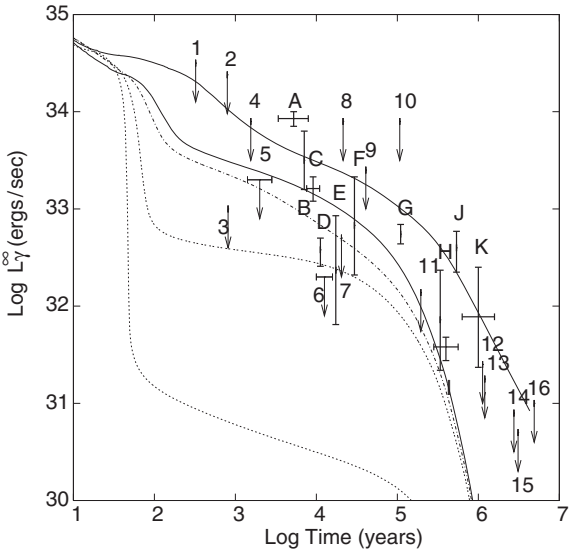

Fig. 12.13 Thermal evolution of pion-mixed stars with various mass and with the stiff EOS TNI3p/TNI3. Notations are the same as in Fig. 12.11

for hydrostatic equilibrium [(12.1)–(12.3) in Sect. 12.2.1], but not in the last two thermodynamic equations (12.4) and (12.5). The results showed that NSs should be hot enough to be observable for about a million years. Since then, more isothermal cooling calculations have been carried out for NSs, including nonstandard pion cooling and cooling of magnetic and superfluid NSs, etc. These studies in the pioneering days are reviewed by Tsuruta (1979) [60].

The first major improvement on NS cooling models was applied by Nomoto and Tsuruta (1987) [34] when the *Einstein* X-ray observatory launched in 1979 offered the first upper limits to NS surface temperatures. In their calculations, for the first time the exact evolutionary code was constructed and adopted. Also, the general relativistic version was used not only for hydrostatic, but also for thermodynamic equations. Otherwise, the input microphysics was an improved version of TC66 [66]. The results were compared with temperature upper limits from *Einstein*, by Nomoto and Tsuruta (1981, 1986) [33].

A breakthrough in the NS cooling-related area came in the 1990s when *ROSAT* reported, for the first time, the detection of NS surface temperatures (see, e.g., [6]), not just the upper limits, for at least three pulsars, PSR 0656+14, PSR 1055−52, and PSR 0633+1748 (Geminga), and possibly PSR 0833−45 (Vela pulsar) also. Therefore, more thorough investigations of cooling and related problems were carried out. For instance, Umeda et al. (1993, 1994) [69,71] included, for the first time, the effect of the frictional heating. Umeda et al. (1994) [69] and Umeda, Tsuruta and Nomoto (1995), hereafter UTN95 [70] investigated the effects of superfluidity, stellar mass, EOS, heating, and different versions of nonstandard direct Urca cooling, with nucleons, pion, kaon, and kaon + pion condensates, and quarks, in more thorough ways,

adopting fully general relativistic exact evolutionary code. Newer EOS, PS, FP and BPS, which were introduced in Sect. 12.2.1 were used. In these calculations the most up-dated input microphysics which were available at the time, the improved version of the earlier microphysical input in Nomoto and Tsuruta (1987) [34] were adopted. In order to compare different nonstandard models, a simple assumption was adopted that the transition to all of these different "exotic" nonstandard processes takes place at the same density $\rho^{tr} = 4\rho_N$, (where $\rho_N = 2.8 \times 10^{14}\,\mathrm{gm\,cm^{-3}}$ is the nuclear density). The major results were:

- The effect of stellar mass is relatively small for standard cooling (although note footnote 10 for the complications which can be caused by superfluidity of particles). However, the effect of mass is very important when nonstandard cooling is introduced, in the sense that larger mass stars with the central density exceeding the transition density to the exotic fast cooling processes, cool very fast due to enhanced direct Urca processes (see Sect. 12.2.2).
- If the transition density is the same, various nonstandard cooling scenarios behave similarly, although nucleon direct Urca is the fastest (see Fig. 12.6 and Sect. 12.2.2).
- All nonstandard cooling mechanisms are too fast for the Vela data. Significant superfluid suppression of nonstandard cooling is needed for Vela pulsar detection data. See Figs. 12.6 and 12.9 in Sect. 12.2.2.
- For standard cooling the net effect of superfluidity is to raise the temperature somewhat during the neutrino cooling era, due to superfluid suppression of leading neutrino emission mechanisms such as modified Urca and nucleon neutrino bremsstrahlung (see Fig. 12.8 in Sect. 12.2.2).
- The superfluid suppression effect can be more drastic for nonstandard cooling when the superfluid energy gap is substantial. See Fig. 12.9 in Sect. 12.2.2.
- Depending on the size of a superfluid energy gap (hence T_{cr}) consistent with the existing superfluid models, all observed data are consistent with NS thermal evolution theories, within the limit of uncertainty in both theory and observation, if the superfluid suppression is moderately effective for nonstandard cooling. See Figs. 12.9 and 12.10 in Sect. 12.2.2.
- The frictional heating can be significant, especially for a stiff EOS model. See, e.g., Fig. 12.10 in Sect. 12.2.2.

Further details are found in a review article by T98 [62]. In this review, some other related problems such as the effects of magnetic fields, axion cooling, are also reported.

In the late 1990s some others also investigated NS cooling. These studies are reviewed, e.g., by Yakovlev and Pethick (2004) [77]. Their findings and conclusions are generally in line with those reported in T98 [62] and just summarized in this section above. Some additional major findings are (1) when the stellar envelope is contaminated by light elements the net effect on cooling is to raise surface temperatures during the earlier neutrino cooling era while the trend is reversed during the later photon cooling era [43], and (2) the Cooper pairing neutrino processes can be very important for a certain combinations of proton S and neutron P superfluidity [76].

In the following, after presenting the currently up-dated observational data, we report on the latest work on thermal evolution (cooling/heating) models, which are compared with observation.

12.3.2 Currently Up-Dated Observational Data

We introduce the NS cooling data up-dated as of December 2007, which are adopted in our latest studies to be introduced in Sect. 12.3.3.[11] There are at least eleven isolated NSs with confirmed detection. These are: (A) RX J0822−4247 (in Puppis A), (B) 1E 1207.4−5209, (C) RX J0002+6246, (D) PSR 0833−45 (Vela pulsar), (E) PSR 1706−44, (F) PSR 0538+2817, (G) PSR 0656+14, (H) PSR 0630+1748 (Geminga), (I) RX J1856.5−3754, (J) PSR 1055−52, and (K)RX J0720.4−3125. Their data and references are listed in Table 12.1, and they are shown in Figs. 12.11 through 12.13. Here t is the age and L_γ^∞ is the total surface photon luminosity to be observed at infinity.

In our figures we do not adopt rectangular shapes for data uncertainties (cf. Page, this volume) for clarity. Furthermore, an age uncertainty factor of 3 (as assumed by Page, cf. this volume) is arbitrary and not constrained by observations.

There are already about two dozen upper limits given [8]. However, some are not interesting, in the sense that they are too high above the cooling curves to constrain theories and/or too old when our purpose is to test NS cooling theories. Also including some of them will only unnecessarily overcrowd the figures to be presented. Therefore they are not included. We choose sixteen which are either better known sources (e.g., pulsars in Crab and Cas A) or more interesting for our purpose of constraining theories. These, together with the references, are listed in Table 12.2 and shown in subsequent figures. The notations used are the same as in Table 12.1.

Table 12.1 NS luminosity detections

	Source	$\log_{10} t$ (age)	$\log_{10} L_\gamma^\infty$ (erg s^{-1})	Reference
A	RX J0822−4300 (Puppis A)	3.53–3.90	33.85–34.00	[23]
B	1E 1207.4−5209	3.85	33.20–33.80	[74]
C	RX J0002+6246	3.88–4.04	33.08–33.33	[36]
D	PSR 0833−45 (Vela)	4.04	32.41–32.70	[40]
E	PSR 1706−44	4.24	31.81–32.93	[30]
F	PSR 0538+2817	4.47	32.32–33.33	[78]
G	PSR 0656+14	5.04	32.64–32.84	[79]
H	PSR 0633+1748 (Geminga)	5.53	31.34–32.37	[27]
I	RX J1856.5−3754	5.45–5.75	31.44–31.68	[41]
J	PSR 1055−52	5.75	32.35–32.77	[7]
K	RX J0720.4−3125	5.8–6.2	31.37–32.40	[31]

[11] More thorough investigation of the data is currently underway [7].

Table 12.2 NS luminosity upper limits

	Source	$\log_{10} t$ (age)	$\log_{10} L_\gamma^\infty$ (erg s^{-1})	Reference
1	CXO J232327.8+584842 (Cas-A)	2.51	34.5	[38]
2	PSR B0531+21 (Crab)	2.9	34.45	[72]
3	J0205+6449 (3C 58)	2.95	33.0	[46]
4	PSR B1509−58 (MSH−15−52)	3.19	33.9	[8]
5	PSR J1124−5916 (G292.0+1.8)	3.15–3.45	33.3	[22]
6	RX J0007+7302 (CTA 1)	4–4.2	32.3	[18]
7	PSR B1046−58 (Vela Twin)	4.31	32.7	[8]
8	PSR B1823−13 (Vela-like)	4.33	33.9	[8]
9	PSR B2334+61	4.61	33.4	[8]
10	PSR B1951+32 (CTB 80)	5.03	33.9	[8]
11	PSR J0154+61	5.29	32.14	[17]
12	PSR B2224+65	6.053	31.4	[7]
13	PSR J2043+2740	6.08	31.25	[7]
14	PSR B0628−28	6.44	30.9	[7]
15	PSR B1929+10	6.49	30.7	[7]
16	PSR B0823+26	6.69	31.0	[8]

Among these, especially interesting sources are (1) CXO J232327.8 (Cas A), (2) PSR 0531+21 (Crab pulsar), (3) PSR J0205+6449 (in 3C 58), (4) PSR 1124−5916 (in G292.0+1.8), (5) PSR 1509−58 (in MSH−15−52), (6) RX J0007.0+7302 (in CTA 1), (7) PSR 1046−58 (Vela twin), (8) PSR 1823−13 (Vela-like), (12) PSR 2224+61, (13) PSR 2043+2740, (14) PSR 0628−28, (15) PSR 1929+10, and (16) PSR B0823+26.

PSR J0205+6449 in 3C 58 and RX J0007.0+7302 in CTA 1 [marked (3) and (6) in figures] are especially important because they are relatively cold and they probably will require nonstandard cooling (see figures in Sect. 12.3.3). The pulsars marked (12) through (15), the newest data from XMM/Newton, are also interesting because they may constrain heating (cf. Sect. 12.3.3).

Among these NSs the precise age is known only for the Crab, as its historical age. Other ages have to be estimated, e.g., from the pulsar spin-down age or the age of the hosting SNR. We choose the age of their supernova remnants (SNRs) for (3) J0205+6449 (3C 58), and (D) PSR 0833−45 (Vela pulsar), because that is more accurate and reliable than both kinetic age and spin-down age. When horizontal error bars are given for pulsars in our subsequent figures, they refer to the pulsar spin-down age (minimum) and kinetic age (maximum) when both are known. The age we adopt for pulsars whose kinetic age and SNR age both are not known is their spin-down age, but their error bars are not given because any reliable error bars for pulsar spin-down age itself do not exist.

Recently, a possibility for very cold NSs in at least four SNRs (G084.2−0.8, G093.3−6.9, G127.1+0.5, and G315.4−2.3) was reported by [26]. We do not show these sources in our subsequent figures, because the X-ray luminosity is less than the total bolometric luminosity with which theoretical cooling curves should be

compared.[12] It further is not clear whether the supernova remnants indeed are from a type II core collapse event which has produced a compact remnant. The upper limits by [26] are for this reason not relevant to constrain neutron star cooling models.

It may be noted that when we present our cooling results, we mostly chose the surface photon luminosity (to be observed at infinity) L_γ^∞ vs. age t relation, not the temperature vs. age. The major reason is:

- Theoretical cooling curves are obtained by calculating the rate of change of the internal temperature as a function of luminosity (of both neutrinos and photons), not directly as a function of temperature. When we convert the surface photon luminosity thus obtained to the surface temperature T_s vs. age t relation, we have to use the blackbody relation which involves radius R. Both EOS and mass depend on R. That means that the theoretical cooling curves with different mass values and/or EOS plotted on the same graph belong to different R if surface temperature vs. age relation is adopted. On the other hand, if luminosity is used the theoretical cooling curves will be independent of radius. Therefore, when we present different theoretical curves with different mass and EOS in the same graph together, luminosity is more preferable.

Luminosities from observations depend on distance, but if the distance is well known, choosing the luminosity instead of temperature for cooling curves will be generally more accurate when theory is to be compared with observation.

12.3.3 Recent and Current Thermal Evolution Models

Tsuruta et al. (2002) [67] included the Cooper pairing neutrino emissivity in the standard cooling calculations and chose the direct Urca cooling involving pion condensates as a nonstandard scenario. Otherwise the method and microphysical input are similar to T98 [62] introduced in Sect. 12.3.1. The conclusion is that both standard and nonstandard cooling are required, and for nonstandard cooling superfluid suppression is needed to be consistent with observation. These authors conclude that among nonstandard cooling scenarios direct Urca involving pion condensates is valid, while direct Urca involving both nucleons and kaon condensates are not valid because in both cases the stars would cool too fast due to the lack of superfluid suppression (see also [49, 50]).

Page et al. [36] also calculated NS cooling models utilizing an exact evolutionary method. Standard cooling including the Cooper pairing neutrino processes, which these authors called "minimal cooling" was investigated. When the similar input physics is adopted, their cooling models qualitatively agree with our results for standard cooling as reported in this article. The effects of magnetic fields on related problems, such as the anisotropic nature of surface radiation under strong magnetic fields, are also discussed. The details are presented in Page's contribution to this

[12] For instance, $L_{bol} \sim 80\, L_x(0.5\text{–}10\,\text{keV})$ for PSR 0656+14 (the former, $\sim 8 \times 10^{32}$ erg s^{-1}, vs. the latter, $\sim 10^{31}$ erg s^{-1}).

volume. Page's work on nonstandard cooling in this volume and elsewhere, however, is qualitative in nature. For instance, he uses simple parameterized equations for neutrino emissivity. Therefore, it is not suitable to be compared quantitatively, with the results reported below which we obtained with more quantitative calculations based on the outcome of detailed new nuclear theory investigations. Heating is also omitted in Page et al. [36].

In recent years Yakovlev et al. [75] and Kaminker et al. [25] also calculated NS cooling models – some "minimal cooling" but some also including direct Urca cooling of nucleon matter. Both nonstandard cooling with "exotic" particles (e.g., pions, hyperons) and heating were not included. When the same input is used, their results qualitatively agree with our results reported in this article. However, we find that the core neutron P superfluid models adopted by these authors, which seriously affect our interpretations of the models and observational data, are unrealistic. These models do not agree with nuclear theories, in the sense that they are outside the limits of theoretical uncertainties [68].

More recently, Kyoto/Iwate theorists have been investigating thoroughly the basic nuclear and particle physics involving neutron matter, hyperon-mixed matter, and matter mixed with pion condensates – especially their EOS and superfluid properties (see, e.g., [32, 51–56], and reference therein). We have been taking advantage of these new developments on the theoretical side, by carrying out thermal evolution calculations (both cooling and heating) utilizing the more reliable results (than earlier ones) from these new theoretical investigations. The work is still in progress, but here we introduce our current findings – to be reported more in detail in [68] (hereafter T07a) and [68] (hereafter T07b). Hopefully our results will offer, not just "possible models", but "most-likely" models. The preliminary reports on these studies have been given in [63–65].

(1) Thermal Evolution of Hyperon-Mixed Neutron Stars

T07a [68] calculated NS cooling/heating by adopting the results of most recent EOS and superfluid studies for neutron and hyperon matter by NYT02, TT01, TT04, and Ta06 [32, 52–54]. The calculations were carried out with most up-to-date microphysical input and by adopting a fully general relativistic, "exact evolutionary code" which was originally constructed by Nomoto and Tsuruta [34] but which has been continuously up-dated. The input neutrino emissivity consists of all possible standard mechanisms (see T98 [62] and Sect. 12.2.2 of this paper) including the Cooper pairing neutrino emission. As a nonstandard scenario direct Urca for hyperon-mixed matter (hereafter referred to as "hyperon cooling") is chosen. Some of the results are summarized in Figs. 12.11 and 12.12.

In these figures (Figs. 12.11 and 12.12) the EOS adopted are as follows. The most recent studies of nuclear theories predict that the critical transition density from neutron to hyperon-mixed matter, ρ_{tr}^{Y}, is $4\rho_N$ [54], and this is the value we choose for ρ_{tr}^{Y}. (Here $\rho_N = 2.8 \times 10^{14}$ gm cm^{-3} is the nuclear density.) For $\rho < \rho_{tr}^{Y}$ we adopt TNI6 EOS for neutron matter and for $\rho > \rho_{tr}^{Y}$ TNI6u EOS for hyperon-mixed matter,

both constructed by Ta06 [54]. (The EOS TNI6u becomes TNI6 below the transition density.) The EOS generally softens for hyperon matter. However, recently it was shown [32, 54] that many-body effects will reduce the softening effect sufficiently so that TNI6u (for hyperon-mixed matter) is only slightly softer than the neutron counterpart TNI6. As a hyperon superfluid model we adopt the Soft-D Model (see [54]) and as the neutron superfluid model the OPEG-B Model [53], both among the realistic models recently constructed. The Cooper pairing neutrino emissivity of [76] is adopted for both neutrons and protons. For our heating calculations we adopt the frictional heating model introduced in [70] (see also [62]). Other input microphysics is similar to T98.

In Fig. 12.11 the upper three thick solid curves refer to $1.3\,M_\odot$ stars with the frictional heating of various degrees, with the highest curve referring to the maximum heating estimated from theories. The lowest thick solid curve refers to no heating for the same model. The hottest thick dashed curve shows a model which is the same as the lowest thick solid curve ($1.3\,M_\odot$ star with no heating) but with the envelope contaminated by light elements (with maximum light element mass fraction) [42]. The bars refer to detections while downward arrows are upper limits. See Tables 12.1 and 12.2 and Sect. 12.3.2 for the explanation of the data points. We note that the hottest dashed curve is higher than the lowest thick solid curve (without the contaminated envelope) during the neutrino cooling era.[13] Since for all these stars the central density $\rho^c < \rho_{tr}^Y$, they are neutron stars undergoing standard cooling.

The rest of the curves (the lower four curves) represent nonstandard cooling for $1.5\,M_\odot$, $1.6\,M_\odot$, $1.7\,M_\odot$ and $1.8\,M_\odot$ hyperon-mixed stars, respectively, all without heating, in the order of decreasing luminosity. For the TNI6u EOS adopted, we find that $\rho^c = \rho_{tr}^Y$ for a $1.4\,M_\odot$ star. Therefore, our stars with mass larger than $\sim 1.4\,M_\odot$ contain a hyperon-mixed core and hence the predominant cooling mechanism is the nonstandard hyperon direct Urca process. Note that T_{cr} first increases, reaches a peak and then decrease to zero as density increases – see, e.g., Fig. 12.7. The heavy $1.8\,M_\odot$ star cools very fast because the internal density is so high that the superfluidity disappears. For the intermediate mass stars with $1.5\,M_\odot$, $1.6\,M_\odot$ and $1.7\,M_\odot$, on the other hand, superfluid suppression is still effective, and therefore their cooling curves lie between the standard curve and the nonstandard curve without suppression.

To show the effects of EOS and stellar mass further, Fig. 12.12 shows thermal evolution of various mass stars for another EOS, TNI2u, as an example of soft EOS constructed by NYT02 [32] for densities $\rho > \rho_{tr}^Y$. This EOS for hyperon-mixed matter reduces to the same EOS for neutron matter, TNI2 [32], at densities lower than the transition density. The hottest two solid curves refer to $1.2\,M_\odot$ stars with and without maximum heating for the higher and lower curves, respectively. The rest (the cooler five curves) are for hyperon-mixed stars with $1.28\,M_\odot$, $1.3\,M_\odot$, $1.32\,M_\odot$, $1.35\,M_\odot$ and $1.4\,M_\odot$, respectively, in the order of decreasing luminosity. For the

[13] This is because conductivity decreases with atomic number Z, and hence contamination of the envelope layers by lighter elements means higher conductivity, causing less temperature difference between the interior and surface temperatures. Neutrino emissivity depends on the interior temperature, and hence we have higher surface temperatures during the neutrino cooling era.

most massive star with $1.4\,M_\odot$, the internal density is so high that the superfluid gap disappears and hence it cools without superfluid suppression, while superfluid suppression is not negligible for the other intermediate mass stars. The results are:

- As expected, all stars with the same mass are hotter with heating than without heating. The trend is especially significant for the maximum heating.
- The effect of stellar mass in the case of hyperon cooling is that by increasing stellar mass, cooling curves change smoothly from close to the standard down to the nonstandard scenario without superfluid suppression, due to the density dependence of superfluid energy gaps.
- As to the effect of EOS, we note that the overall qualitative behavior is similar, but the transition from neutron to hyperon-mixed stars takes place for lower mass stars for soft EOS. For instance, it takes place for $1.4\,M_\odot$ and $1.25\,M_\odot$ stars, respectively, for medium TNI6u and soft TNI2u EOS, respectively.

(2) Thermal Evolution of Pion-Mixed Neutron Stars

Recently we re-investigated thermal evolution of NSs with an inner core including pion condensates, which we will refer to, from here on, as "pion-mixed neutron stars" for convenience. The method of calculations, microphysical input, etc., are very similar to those presented in the previous subsection, (1), except that the direct Urca cooling involving pion condensates is chosen as the nonstandard scenario.

To begin with, we first adopted the earlier superfluid models for charged pion condensates constructed by Takatsuka and Tamagaki (1980, 1982) [48] and adopted by Umeda et al. (1994) [69] and UTN95 [70] (also see [62].) However, we created a new EOS, TNI3p, which is a modified version of TNI3 constructed by NYT02 [32], which represents a stiff model. It was modified to include pion condensates for densities exceeding ρ_{tr}^{π}, the critical density for transition to pion condensates [67]. We chose a stiff EOS because in this model charged pion condensates appear at a lower density than hyperons do. The results are shown in Fig. 12.13. Two upper solid curves are for $1.3\,M_\odot$ stars with and without maximum heating for the higher and lower curves, respectively. The rest (the cooler three curves) are for pion-mixed NSs with $1.5\,M_\odot$, $1.7\,M_\odot$ and $1.9\,M_\odot$, respectively, in the order of decreasing luminosity. For the stiff EOS and the pion superfluid model adopted, we see that superfluid suppression is still effective for a $1.7\,M_\odot$ star although it becomes negligible for a $1.9\,M_\odot$ star. Otherwise, the trend is very similar to the hyperon case. Further details are found in [63–65].

Most recently, TT06a,b [55] and TT07 [56] re-investigated basic physics of pion condensates for charged pions, neutral pions and the mixture of the two. The new finding is that the mixed phase of charged and neutral pions should appear at densities lower than anticipated earlier, at as low as $\sim 2\rho_N$. It is significantly lower than that for hyperons. Then, lower mass stars with lower densities will already be pion-mixed stars. However, these authors also re-investigated the properties of superfluidity of mixed phase pion condensates, and find that the superfluid energy gaps (and hence superfluid critical temperatures) are considerably large – in fact, sufficiently

large so that for pion stars superfluid suppression is sufficient to bring the temperatures to the level of standard cooling. In view of these new findings, T07b [68] are currently carrying out cooling and heating of pion-mixed stars in this new mixed phase. Except that this new mixed-phase pion model is adopted, the methods, other microphysical input, etc., are very similar to [63–65, 68].[14] Preliminary results indicate that due to sufficient superfluid suppression of pion cooling at lower densities we obtain cooling behavior qualitatively similar to the earlier pion-mixed star models (as shown in Fig. 12.13), although the microphysics behind is different. Further details will be reported in T07b [68].

(3) Comparison with Observation

The observational data are inhomogeneous, suggesting NSs with a variety of cooling rates, from the hottest (e.g., (A) RX J0822−4300, (J) PSR 1055−52), to the intermediate (e.g., (G) PSR 0656+14)), to the cooler (e.g., (D) Vela pulsar, (3) PSR J0205+6449 in 3C 58, (6) RX J70007+7303 in CTA 1). In Figs. 12.11 through 12.13 theoretical thermal evolution models are compared with the latest observational data introduced in Sect. 12.3.2.

Note that when all possible theoretical models are included, possible cooling curves generally occupy regions with wide stripes (often marked as shaded) in cooling figures – see, e.g., Fig. 11.16 of Page's contribution to this volume. However, many of the curves within such stripes are mutually exclusive. For instance, suppose we choose the cooling curve closest to PSR 1055−52 (e.g., no neutron P superfluid model) which does not require heating. Then, to be consistent, we must choose the corresponding curve (i.e., the same no neutron P superfluid model) for Vela pulsar also (although the envelope composition can be different). Then, clearly we see already that the Vela pulsar data will require nonstandard cooling. In other words, it can not be that the currently existing data require both "no heating" and "no nonstandard cooling" at the same time. This kind of self-consistency tests can help us narrow down acceptable models when we carefully compare theoretical models with observed data.

By applying such self-consistency tests to our results, we are led to the following interpretation: (1) The warmer sources are consistent with standard thermal evolution of less massive stars. (2) For PSR 1055−52 (marked (J) in figures) both age and luminosity uncertainty can be relatively large, but still it will probably require at least moderate heating. (3) Vela pulsar (marked (D) in figures) is most likely a massive star undergoing nonstandard cooling, but then significant superfluid suppression is required. (4) Nonstandard cooling of massive stars is required also for the cooler sources such as PSR J0205+6449 in 3C 58 and RX J70007+7303 in CTA 1 [marked (3) and (6) in figures]. (5) Among nonstandard cooling scenarios, both hyperon and pion cooling scenarios are consistent with observation, while nucleon and kaon direct Urca cooling scenarios are not [49, 50]. The details are found in [68] and [68].

[14] We assume that the gaps decrease at higher densities as in the hyperon case.

12.4 Future Prospects

Some of the results presented may be currently still inconclusive due to various uncertainties, both in theory and observation. However, this situation will change if we succeed in achieving some improvements, which appear to be within our reach in the foreseeable future. For instance:

On the observational side:

- Next generation X-ray space missions, such as NEXT and IXO, will offer more detections with smaller error bars and more and better upper limits. The detections and upper limits to be obtained by these missions will be important especially for the fainter sources currently out of our reach.
- Better measurement of distance can decrease luminosity and age uncertainties. We have already noted that using surface photon luminosity for cooling curves is more accurate than using temperatures when testing cooling/heating theories with observation if distance is accurately known (see Sect. 12.3.2). In fact, luminosity error bars for some pulsars, e.g., PSR 0656+14, were reduced significantly already due to recent success of direct radio parallax measurements of the distance by VLBI (Very Long Baseline Interferometry) [10]. Larger radio array systems planed for the future, e.g., SKA (Square Kilometer Arrays), will increase the prospect of such direct distance measurements for more objects.
- For instance, the luminosity error bar for PSR 1055−52 in Table 12.1 in Sect. 12.3.2 (and figures in Sect. 12.3.3) is estimated by assuming 20% uncertainty to the currently best available distance of 710 pc [7]. However, the method adopted, the dispersion measure, is not as accurate as direct radio measurements. More direct distance measurement is highly desirable for this pulsar, for that will enable us to make more conclusive interpretation of this pulsar.
- Currently we simply do not know the error bars to be placed on pulsar's spin-down ages. If sufficient number of pulsars with both spin-down age and kinetic and/or SNR age are in our data base, some statistical approach may become possible to better estimate the error bars for spin-down ages. That should help us the interpretation of sources such as PSR 1055−52 – for instance, whether heating is required.

On the theoretical side:

- Among all existing theoretical models some are more realistic while some are definitely less realistic. Separating these two may eliminate some of these models, or at least help us distinguish the more likely options from the less likely.
- In this connection, we may emphasize the importance of the kind of careful investigations most recently carried out by the Kyoto/Iwate group (see Sect. 12.3.3), although admittedly the task was extremely tedious.
- Continuation of such new theoretical studies of nuclear and elementary particle physics will help us distinguish between different models. That will also open opportunities for more realistic studies of quark cooling than currently available.

- Currently we do not know whether the SNRs G084.2−0.8, G093.3−6.9, G127.1+0.5, and G315.4−2.3 in [26] contain NSs or not. By studying the property and nature of these SNRs (especially the progenitor mass) we may be able to estimate the presence or absence of NSs in these SNRs.
- One puzzling issue is that for older pulsars Fe lines are expected in their spectra, and yet their observed spectra are smooth blackbody-like continuum with no signs of lines. This could be caused by, e.g., the effects of magnetic fields, but studies of magnetic atmospheres are still in pioneering stages. This is another area which can be explored in future studies.

12.5 Concluding Remarks

Some of the works reported in this paper, for instance, cooling/heating of stars involving pion condensates (Sect. 12.3.3) are still in progress. In this sense this paper is meant as a progress report. However, hopefully some of the current situations involving cooling NS problems are clarified, and we can already differentiate the "best-buy" models from those "less likely". In this connection we may emphasize that current nuclear theories do soundly predict the natural transition from neutron matter to matter mixed with hyperons or pion condensates within the density regime of observable NSs.

Due to theoretical uncertainties, some authors treat various important parameters, such as superfluidity, as free parameters, and then fix these parameters to agree with observational data. However, we find that some of these "free parameters" are, under close examinations, in fact *not free*. These parameters still must be constrained by acceptable theoretical limits. Theoretical models which violate these limits should not be acceptable even if they can explain observational data.

References

1. M.A. Alpar, K.S. Cheng, D. Pines, et al.: ApJ **346**, 823 (1989)
2. L. Amundsen, E. Ostgarrd: Nucl. Phys. A **442**, 163 (1985)
3. W. Baade, F. Zwicky: Phys. Rev. **46**, 76 (1934)
4. J.N. Bahcall, R.A. Wolf: Phys. Rev. B **140**, 1452 (1965)
5. G. Baym, C. Pethick, P. Sutherland: ApJ **170**, 299 (1971)
6. W. Becker: PhD Thesis, University of Munich, Munich (1995)
7. W. Becker: X-Ray emissions from pulsars and neutron stars. In: *Neutron Stars and Pulsars*, ed. by W. Becker (Springer, Heidelberg, 2008)
8. W. Becker, G. Pavlov: Pulsars and isolated neutron stars. In: *The Century of Space Science*, ed. by J. Breeker et al. (Kluwer, Dordrecht, 2002) (Astro-ph/0208356) (BP02)
9. S. Bowyer, E.T. Byram, T.A. Chubb, et al.: Science **146**, 912 (1964); R. Giacconi, H. Gursky, J. Waters: Nature **207**, 572 (1965); G. Clark: Phys. Rev. Lett. **14**, 91 (1965)
10. W.F. Brisken, S.E. Thorsett, A. Golden, W.M. Goss: ApJ **593**, L89 (2003)
11. A.G.W. Cameron: ApJ **130**, 884 (1959)
12. R. Dodson, D. Legge, J.A. Reynolds, et al.: ApJ **596**, 1137 (2003)

13. E.G. Flowers, M. Ruderman, P.G. Sutherland: ApJ **205**, 541 (1976)
14. B. Friedman, V.R. Pandharipande: Nucl. Phy. A **361**, 502 (1981)
15. R. Giacconi, H. Gursky, F.R. Paolini, et al.: Phys. Rev. Lett. **9**, 439 (1962); H. Gursky, R. Giacconi, F.R. Paolini, et al.: Phys. Rev. Lett. **11**, 530 (1963); S. Bowyer, E.T. Byram, T.A. Chubb, et al.: Nature **201**, 1307 (1964)
16. R. Giacconi, E.J. Schreier, F.D. Seward, CFA/HEA preprint 78–214
17. M.E. Gonzalez, V.M. Kaspi, A.G. Lyne, M.J. Pivovaroff: ApJ **610**, L37 (2004) (Gon04)
18. J.P. Halpern, E.V. Gotthelf, F. Camilo, et al.: ApJ **612**, 398 (2004) (H04)
19. S. Hayakawa: Prog. Theor. Phys. (1964); H.Y. Chiu, E.E. Salpeter: Phys. Rev. Lett. **12**, 412 (1964)
20. A. Hewish, S.J. Bell, J.D.H. Pikington, et al.: Nature **217**, 709 (1968)
21. M. Hoffberg, A.E. Glassgold, R.W. Richardson, et al.: Phys. Rev. Lett. **24**, 775 (1970)
22. J.P. Hughes, P.O. Slane, S. Park, et al.: ApJ **591**, L139 (2003) (H03)
23. C.Y. Hui, W. Becker: A&A **454**, 543(2006)
24. P.C. Joss, S. Rappaport: Nature **264**, 219 (1976); W. Lewin, P. Joss: In: *X-ray binaries*, ed by W.H.G. Lewin, et al. (Cambridge University Press, Cambridge 1995), and references therein
25. A.D. Kaminker, M.E. Gusakov, D.G. Yakovlev, et al.: MNRAS **365**, 1300 (2006), Astro-ph/0511179, and references therein
26. D.L. Kaplan, S.R. Kulkarni, D.A. Frail, B.M. Gaensler, P.O. Slane, E.V. Gotthelf: In: *Young neutron stars and their environments*, ed by F. Camilo et al. (ASP, San Francisco, 2004) pp. 123–126 (Ka04)
27. O.Y. Kargaltsev, G.G. Pavlov, V.E. Zavlin, et al.: ApJ **625**, 307 (2005) (Astro-ph/0502076) (Ka05)
28. J.M. Lattimer, C.J. Pethick, M. Prakash, et al.: Phys. Rev. Lett. **66**, 2701 (1991)
29. O.V. Maxwell: ApJ **231**, 201 (1979)
30. K.E. McGowan, S. Zane, M. Cropper, et al.: ApJ **600**, 343 (2004) (M04)
31. C. Motch, V.E. Zavlin, F. Haberl: A&A **408**, 323 (2003) (MZH03)
32. S. Nishizaki, Y. Yamamoto, T. Takatsuka: Prog. Theor. Phys. **108**, 703 (2002) (NYT02)
33. K. Nomoto, S. Tsuruta: ApJ **250**, L19 (1981); K. Nomoto, S. Tsuruta: ApJ **305**, L19 (1986)
34. K. Nomoto, S. Tsuruta: ApJ **312**, 711 (1987)
35. J.R. Oppenheimer, G.M. Volkoff: Phys. Rev. **55**, 374 (1939)
36. D. Page, J.M. Lattimer, M. Prakash, A.W. Steiner: ApJ Suppl. Series **155**, 623 (2004) (PLPS04)
37. V.R. Pandharipande, D. Pines, R.A. Smith: ApJ **208**, 550 (1976)
38. G.G. Pavlov, V.E. Zavlin, B. Aschenbach, et al.: ApJ **531**, L53 (2000) (P00)
39. G.G. Pavlov, V.E. Zavlin, D. Sanwal: In: *Proc. 270th WE-Heraeus Seminar on Neutron Stars, Pulsars and Supernova Remnants, MPE Rep. 278*, ed by W. Becker, H. Lesch, J. Trümper (Garching: MPE 2002) p. 273 (2002)(P02)
40. G.G. Pavlov, V.E. Zavlin, D. Sanwal, et al.: ApJ **552**, L129 (2001) (P01)
41. J.A. Pons, F.M. Walter, J.M. Lattimer, et al.: ApJ **564**, 981 (2002) (Pon02)
42. A.Y. Potekhin, G. Chabrier, D.G.Yakovlev: A&A **323**, 415 (1997) (PCY97)
43. A.Y. Potekhin, D.G. Yakovlev, G. Chabrier, et al.: ApJ **594**, 404 (2003), and reference therein
44. M.B. Richardson, H.M. Van Horn, K.F. Ratcliff, et al.: ApJ **255**, 624 (1982), and references therein
45. D. Sanwal, M.A. Teter, V.E. Zavlin, et al.: ApJ, in preparation (2007) (S07)
46. P. Slane: In: *Young neutron stars and their environments*, ed by F. Camilo et al. (ASP, San Francisco, 2004), pp. 185–188, and reference therein (S04)
47. T. Takatsuka: Prog. Theor. Phys. **48**, 1517 (1972)
48. T. Takatsuka, R. Tamagaki: Prog. Theor. Phys. **64**, 2270 (1980); T. Takatsuka, R. Tamagaki: Prog. Theor. Phys. **67**, 1649 (1982)
49. T. Takatsuka, R. Tamagaki: Prog. Theor. Phys. **94**, 457 (1995) (TT95)
50. T. Takatsuka, R. Tamagaki: Prog. Theor. Phys. **97**, 345 (1997) (TT97)
51. T. Takatsuka, R. Tamagaki: Prog. Theor. Phys. **102**, 1043 (1999)
52. T. Takatsuka, R. Tamagaki: Prog. Theor. Phys. **105**, 179 (2001) (TT01)
53. T. Takatsuka, R. Tamagaki: Prog. Theor. Phys. **112**, 37 (2004) (TT04)

54. T. Takatsuka, S. Nishizaki, Y. Yamamoto, et al.: Prog. Theor. Phys. **115**, 355 (2006), and references therein (Ta06)
55. R. Tamagaki, T. Takatsuka: Prog. Theor. Phys. **115**, 245 (2006a) (TT06a); R. Tamagaki, T. Takatsuka: Prog. Theor. Phys. **116**, 573 (2006b) (TT06b)
56. R. Tamagaki, T. Takatsuka: Prog. Theor. Phys. **117**, No. 5 (2007) (TT07)
57. J.H. Tayler, R.N. Manchester, A.G. Lyne: ApJ (Suppl.) **88**, 529 (1993); T. Gold: Nature **218**, 731 (1968); F. Pacini: Nature **219**, 145 (1968)
58. K.S. Thorne: ApJ **212**, 825 (1977)
59. S. Tsuruta: Neutron star models. PhD Thesis, Columbia University, New York (1964)
60. S. Tsuruta: Phys. Rep. **56**, 237 (1979)
61. S. Tsuruta: Comm. Astrophys. **11**, 151 (1986)
62. S. Tsuruta: Phys. Rep. **292**, 1–130 (1998) (T98)
63. S. Tsuruta: In: *Young neutron stars and their environments*, ed by F. Camilo et al (ASP, San Francisco, 2004) pp. 21–28
64. S. Tsuruta: In: *Origin of matter and evolution of galaxies*, ed by Kubono et al (AIP 2006) pp. 163–170 (Astro-ph/0602138)
65. S. Tsuruta: In: *Stellar astrophysics*, ed by Y.W. Wang et al., ASP, 362, 111 (ASP, 2007)
66. S. Tsuruta, A.G.W. Cameron: Canad. J. Phys. **44**, 1863 (1966) (TC66)
67. S. Tsuruta, M. A. Teter, T. Takatsuka, T. Tatsumi, R. Tamagaki: ApJ **571**, L143 (2002)
68. S. Tsuruta, et al., in preparation (2008)
69. H. Umeda, K. Nomoto, S. Tsuruta, et al.: ApJ **431**, 309 (1994)
70. H. Umeda, S. Tsuruta, K. Nomoto: ApJ **433**, 256 (1995) (UTN95)
71. H. Umeda, N. Shibazaki, K. Nomoto, et al.: ApJ **408**, 186 (1993)
72. M.C. Weisskopf, S.L. O'Dell, F. Paerels, et al.: ApJ **601**, 1050 (2004) (W04)
73. J.A. Wheeler, B.K. Harrison, M. Wakano: In: *La Structure et l'evolution de l'univers*, ed by T. Stoops (Brussels, 1958); E.E. Salpeter: ApJ. **134**, 669 (1961)
74. P.M. Woods, V.E. Zavlin, G.G. Pavlov: Appl. Space Sci., 308, 239 (2007) (WZP06)
75. D.G. Yakovlev, O.Y. Gnedin, A.D. Kaminker, et al.: Adv. Space Res. **33**, 523 (2004), and references therein
76. D.G. Yakovlev, K.P. Levenfish, Yu.A. Shibanov: Phys. Usp. **42**, 737 (1999) (YLS99)
77. D.G. Yakovlev, C.J. Pethick: Ann. Rev. Astron. Astrophys. **42**, 169 (2004)
78. V.E. Zavlin, G.G. Pavlov: In: *Proc. XMM-Newton EPIC Consotium Memorie della Societa' Astronomica Italiana*, **75**, 458 (2004) (ZP04)
79. V.E. Zavlin, G.G. Pavlov, D. Sanwal: ApJ **606**, 444 (2004)

Chapter 13
Turning Points in the Evolution of Isolated Neutron Stars' Magnetic Fields

Ulrich Geppert

13.1 Introduction

During the life of isolated neutron stars (NSs) their magnetic field passes through a variety of evolutionary phases. Depending on its strength and structure and on the physical state of the NS (e.g., cooling, rotation), the field looks qualitatively and quantitatively different after each of these phases. Three of them, the phase of MHD instabilities immediately after NS's birth, the phase of fallback which may take place hours to months after NS's birth, and the phase when strong temperature gradients may drive thermoelectric instabilities, are concentrated in a period lasting from the end of the proto-NS phase until 100, perhaps 1,000 years, when the NS has become almost isothermal. The further evolution of the magnetic field proceeds in general inconspicuous since the star is in isolation. However, as soon as the product of Larmor frequency and electron relaxation time, the so-called magnetization parameter ($\omega_B \tau$), locally and/or temporally considerably exceeds unity, phases, also unstable ones, of dramatic changes of the field structure and magnitude can appear.

The energy of the magnetic fields of neutron stars is even for magnetar field strengths ($\sim 10^{15}$ G) negligible in comparison with the gravitational energy of even the least massive NSs. Except for the magnetars, this is true also when comparing with the rotational and thermal energy of the majority of NSs which appear as radio pulsars. Nevertheless, the magnetic field plays a decisive rôle for practically all observable quantities. Together with a sufficiently rapid rotation it allows them to detected as pulsars. For magnetars it is believed that their thermal radiation and burst activities are powered dominantly by their ultrastrong magnetic field (for a review see [42]). In standard NSs, possessing surface fields in the range of $10^{11.5...13.5}$ G, observations as, e.g., thermal radiation (see reviews of D. Page and R. Turolla in this volume), drifting subpulses [32], glitches [76], cyclotron lines in X-ray spectra,

U. Geppert
German Aerospace Center, Institute of Space Systems, System Conditioning, Rutherfordstr. 9, 12489 Berlin, Germany
e-mail: ulrich.geppert@dlr.de

W. Becker (ed.), *Neutron Stars and Pulsars,* Astrophysics and Space Science Library 357,

or the variety of magnetospheric emissions [4, 100] are significantly affected by the magnetic field and consequences of its evolution. On the other hand, the cooling process affects the field evolution (see [96] for a core field; [59] for a crustal field), and the braking of the NS's rotation, almost completely determined by the dipolar magnetic field, may have a backreaction onto the field decay by affecting the flux expulsion from the superfluid core [3, 16, 48]. The magnetic field evolution in millisecond pulsars will not be discussed here, since their progenitors went most likely through a phase of spin-up by accreting matter from a low mass companion star in a binary system [6, 65, 86], thereby manifolding the factors which influence the field evolution.

At first glance an isolated NS seems to be a sphere where its inborn magnetic field evolves only slowly because the electric conductivity is enormous and external influences don't affect it. However, there are periods during which the field evolution proceeds comparatively fast, sometimes even dramatic, and the field arrives repeatedly at a crossroad. There, depending on the physical state of the NS and on the strength and structure of the magnetic field itself, the field can evolve in two qualitatively different ways. Which of them is taken will have of course consequences for the further evolution of the whole NS. This is a natural implication of the tight connection between the magnetic and the thermal and rotational evolution.

Three of these phases appear quite early in a NS's life. The first turning point occurs immediately after a NS's birth. Here, the birth moment is understood to be that moment, when the proto-NS phase has been completed: the isolated NS has almost reached its final mass–radius relation and density profile, convective motions have ceased and the matter is uniformly rotating, and in a liquid and normal (i.e., non-superfluid) state. At this stage the field, whatever structure and strength it has acquired after collapse and proto-NS stage, must possibly go through magnetohydrodynamic (MHD) instabilities and may suffer from the most dramatic changes conceivable for any magnetic field evolution: during the first $\lesssim 10$ s of its life MHD instabilities may reduce an initially perhaps $\sim 10^{15}$ G dipolar field down to standard pulsar field strengths of $\sim 10^{12}$ G, depending on the rotation period and the inclination angle between magnetic and rotation axis [28].

The second point comes when after the supernova explosion the hypercritical fallback accretion, produced by a reversed shock, reaches the NS surface. In the case of SN 1987 A this happened about 2 h after bounce [17]. However, depending on the detailed properties of each particular supernova this moment will vary [18]. In some cases and influenced by many factors depending on the medium surrounding the NS, its kick and rotation velocities, and on its magnetic field strength just after the mentioned MHD instabilities, this fallback can be significantly reduced or will not take place at all. When it, however, proceeds similar as estimated for SN 1987 A, it will submerge a pre-existing magnetic field in the crust, perhaps down to the crust–core interface. The strength of the fallback accretion and the conductive properties of the crust decide whether the NS appears as a radio pulsar already at its birth or, in case of weak fallback and shallow submergence, after say some 100 years [55]. For heavier fallback and deeper submergence the rediffusion of the field to the surface takes millions or hundreds of millions of years and the NS is either radio quiet or its

active age (given by the rotational period and its time derivative, P and $\dot{P}$), is much larger than its real age, making relatively young NSs to old looking ones [26].

The third turning point happens when the conditions are such that a thermoelectric instability may efficiently convert thermal into magnetic energy (see [30, 87] and references therein). The preferred region where that instability takes place is the low density liquid shell ($\rho \leq 10^{10}\,\mathrm{g\,cm^{-3}}$) where a sufficiently strong temperature gradient prevails. The thermoelectric instability in that layer will act as long as $T_{s6}^4/g_{s14} > 100$, where T_{s6} is the surface temperature in 10^6 K and g_{s14} is the gravitational acceleration at the NS's surface in $10^{14}\,\mathrm{cm\,s^{-2}}$ [93]. For a typical NS with $g_{s14} \approx 1$ this means that the surface temperature should exceed 3×10^6 K, which, depending on the cooling scenario is likely only for the first 100 years, in case of the slowest cooling perhaps 1,000 years of NS's life. During the initial, linear stage of the thermoelectric instability only small scale ($\sim$100 m) toroidal field components are exponentially growing on a timescale of 50...100 days. After about 10 years nonlinear interactions raise to large scale toroidal components. However, the studies stopped at that point and all attempts failed up to now to create the observable poloidal large scale fields of $10^{12...13}$ G at the surface of the star by that instability.

There are however very promising regions in young NSs, where the thermoelectric instability may act even more efficiently than in the outer liquid crust. As shown by Gnedin et al. [33] there exist extremely strong temperature gradients deep in the crust during first year of the early thermal relaxation phase. A strong magnetic field created in those layers by the thermoelectric instability during the first hours of the NS's life could alter the magneto-thermal evolution qualitatively.

The fourth "turning point" of the magnetic field evolution in an isolated NS can not be dedicated to a certain phase of its life but appears always if the magnetization parameter $\omega_B\tau$ significantly exceeds unity, either temporally or spatially. Here, $\omega_B = eB/(m_e^* c)$ is the Larmor frequency, where B is the strength of the magnetic field, e the elementary charge, c the velocity of light and m_e^* the effective electron mass which depends on density and chemical composition. The relaxation time τ, that is the period between collisions of the electrons with the relevant impact partners as, e.g., ions, phonons or impurities in the crust or protons and neutrons in the core, is a complicated function of the density, temperature, chemical composition, impurity concentration, the occurrence of superfluidity, and perhaps other factors and increases usually significantly when the NS cools down. The magnetization parameter may therefore exceed unity in different phases of a NS's life and perhaps only locally in certain regions of the NS: when either the magnetic field strength or the relaxation time increases beyond a certain threshold. Thereby, the strength of one quantity may overcompensate the smallness of the other. In crusts of magnetars, e.g., the relaxation time is relatively short because of the high temperatures, but the extremely strong magnetic field ensures that $\omega_B\tau \gg 1$ there.

Two consequences of situations with $\omega_B\tau \gg 1$ will be discussed in this review. Firstly, the situation will be considered when a large magnetization parameter causes a domination of the magnetic field evolution by the Hall-drift. Although the Hall-e.m.f. is conservative, it redistributes magnetic energy from large scales into smaller ones which eventually decay much faster ohmically than pure dipole fields

would do. Goldreich and Reisenegger [34] studied this process in detail, coining for the continuous transfer of magnetic energy towards smaller scaled field modes the term "Hall-cascade".

Alternatively to or simultaneously with the Hall-cascade, a non-local unstable energy transfer may proceed from a relatively large scaled background field into smaller scaled perturbations, if the second derivative of the background field with respect to at least one spatial variable is non-zero, i.e., if this field is sufficiently curved [71]. This instability is driven by the shear in the electron velocity of the current maintaining the background field (see [19, 72] and references therein). The large braking indices observed in some middle aged pulsars could be explained very well by an energy drain out of the dipolar field, which determines the braking, into smaller scaled perturbations just on the time scale of the Hall instability [27]. In all, both the Hall-cascade and the Hall-instability will play a role for the transient acceleration of the magnetic field decay as well as for the generation of strong small scale field structures at the surface, necessary for the pulsar mechanism to work. Their relative importance, however, has not yet been clarified.

Secondly, the situation will be considered when a large magnetization parameter causes significant deviations from the isotropic transport through the NS's crust, leading to comparatively small hot spots around the magnetic poles, leaving the largest part of the surface so cool that it can not contribute substantially to the observed X-ray flux of thermally emitting isolated NSs. Meanwhile a large number of X-ray and combined X-ray and optical observations (revealing in some cases a significant larger optical flux than to be expected by the continuation of the blackbody spectrum from the X-ray energies, called "optical excess") of these NSs (called "The Magnificent Seven") are available and both spectral and lightcurve analyses justify quite well the conclusion, that the surface temperatures are indeed highly anisotropic (see, e.g., [5, 15, 37, 39, 67, 85]). It is known already since Greenstein and Hartke [35] that a dipolar magnetic field which penetrates the envelope (upper crustal region where $\rho < 10^{10}\,\mathrm{g\,cm^{-3}}$) being stronger than, say, 10^{11} G causes a surface temperature gradient from the pole to the equator. The observed surface temperature profiles, however, can not be explained by assuming anisotropy of the heat transfer in the envelope only, but considering the whole crust from the crust–core interface up to the bottom of the envelope as isothermal. A satisfactory agreement with the observational facts can be reached, when the anisotropy of the heat transport in the whole crust is taken into account [24, 25, 60, 61, 98, 99]. The strong crustal field enforces heat transport prevailingly parallel to the field lines, while the heat flux perpendicular to them is strongly suppressed. In contrast, a star centered core field causes only very little anisotropy of the heat flux through the crust. Only a crustal field consisting of sufficiently strong poloidal and toroidal components may create such a temperature distribution at the bottom of the envelope that the further heat transfer through it creates the observed large surface temperature gradients in meridional direction. Although due to the variety of possible emission processes at the NS surface, being either an atmosphere, a liquid or a solid, having an unknown chemical composition, etc., other reasons for the observed temperature profiles and the "optical excess" are conceivable [91], the good agreement of the observations

with the model calculations of the anisotropic heat transfer is a quite reliable hint for the existence of strong crustal field configurations.

As can be seen already from the references, the instabilities immediately after NS's birth and the effect of a large magnetization parameter on field evolution and heat transport currently gain intensive attention, while the consideration of the consequences of the supernova fallback as well as the study of thermoelectric instabilities in NSs is recently not in the very focus of the community. I believe, however, that all these five possible "turning moments" of the field evolution deserve further research activities and I will now try to describe the corresponding physics and the results available up to now in some detail. The article presupposes some basic background knowledge of plasma physical processes under astrophysical conditions. An introduction to that topic can be found in [50].

13.2 MHD Instabilities Immediately After Birth: Magnetar or Radio Pulsar?

When the proto-NS phase is completed a (quasi-)isolated NS is born. Unfortunately, no newborn NS is observable. The nearly simultaneously formed supernova remnant obscures the star for hundreds of years almost completely. Therefore, theoretical models have to promote the understanding of the physical conditions at a NS's birth.

During the pre-supernova phase of the massive progenitor star, during its core's collapse and during the proto-NS stage, which lasts about 30 s, any pre-existing magnetic field can be amplified tremendously.

In the pre-supernova phase the so-called "Spruit dynamo" [80, 81] is probably a powerful amplification mechanism. It transfers the energy of differential rotation into magnetic energy. A poloidal seed field will be wound up by differential rotation, thereby creating a toroidal field component. This component undergoes a MHD instability [82], thereby forming poloidal components which can tap the energy of differential rotation again, closing in that way the dynamo cycle. Estimates show, that the toroidal component of the generated field may reach up to 5×10^9 G for a $15 M_\odot$ star while its poloidal component will be considerably weaker [43].

In the core collapse another enhancement of the magnetic field strength proceeds, at least simply by flux conservation in the highly conductive matter. Depending on the mass of the progenitor, the amplification factor can be as large as $10^4 \ldots 10^5$.

The proto-NS phase is characterized by vigorous convective motions which are driven by the usual Ledoux instability and/or by doubly diffusive instabilities [14, 47, 52–54, 66]. Thompson and Duncan [83] argue that under the conditions prevalent in the proto-NS these rapid convective motion may generate fields as strong as 10^{16} G by dynamo action. However, the situation in the proto-NS is characterized by extremely large magnetic Reynolds numbers $R_m \sim 10^{19}$ which are by about 16 orders of magnitude over critical with respect to the onset of the dynamo. Since the proto-NS convection is anyway a transient phenomenon, lasting at most $\sim$20 s, there exist various scenarios of magnetic field amplification [73], including

that the dynamo acts only at the end of the convective stage, when the convective velocity decreases. Then, $R_m \lesssim 1{,}000$ and the backreaction of the growing field can no longer efficiently counteract the dynamo process.

Since the fluid in the proto-NS is – at least during its early stage – for sure in turbulent motion and differentially rotating, the description of the magnetic field evolution by mean field models, i.e., by α- and/or Ω-dynamos, is suggestive (see [8] and references therein). However, the mean-field coefficients of these models are derived in second order correlation approximation (SOCA). The SOCA results (in the high-conductivity limit) have been justified so far for a Strouhal number $St = \tau V/l \ll 1$ and are perhaps still useful as "order of magnitude estimates" if $St \sim 1$ (see in [49] (3.12) and (4.10), [63]). In the proto-NS, however, the minimum of both the overturn time and the characteristic life time of velocity pattern $\tau \gtrsim 10\,\mathrm{ms}$, the convective velocity $V \sim 10^8 \ldots 10^9\,\mathrm{cm\,s^{-1}}$ and the typical scale of the convective eddies $l \lesssim 10^5\,\mathrm{cm}$; therefore $St \gtrsim 10$, making the results obtained by Bonanno et al. [8] questionable. Another field amplifying instability, the magneto-rotational instability (MRI), acts very efficiently during the first $\lesssim 1\,\mathrm{s}$ after bounce. The MRI is supposed to be able to tap the energy of differential rotation for the generation of fields exceeding even $10^{16}\,\mathrm{G}$ [1, 84].

Therefore, though a satisfactory understanding of the field amplification processes during pre-NS-stages is still not well-elaborated, there are good reasons to assume that at the beginning of its life the NS is endowed with an ultrastrong magnetic field, perhaps in excess of $10^{15}\,\mathrm{G}$.

At the same time, the NS is likely in a state of very rapid ($P < 60\,\mathrm{ms}$) but rigid rotation. Ott et al. [57] argue that NSs reach at the end of the proto-NS phase the state of rigid rotation. The growth of the magnetic field in that phase is initially at least partly powered by the differential rotation. However, the growing magnetic field causes via the MRI a turbulent viscosity, much larger than the molecular one, which enables a rapid angular momentum redistribution. Therefore, at least at the end of the proto-NS phase, when convection ceased and the field is as strong as $\sim 10^{15}\,\mathrm{G}$, the state of uniform rotation will be reached, which is the lowest-energy state of a rotating body for a given angular momentum.

Another statement about the newborn NS can be made with great certainty: since the temperature at birth exceeds $10^{10}\,\mathrm{K}$, the complete NS is liquid, the crystallization of the crust has not yet been started and the core matter has not yet performed the transition into the superfluid state.

It is observationally evident that a NS which starts its life with a magnetic field exceeding $10^{15}\,\mathrm{G}$ will evolve in a completely different manner than another which starts with a typical radio pulsar field of $10^{11\ldots13}\,\mathrm{G}$ or, practically non-magnetized, as a millisecond pulsar with $\sim 10^8\,\mathrm{G}$. Therefore, the knowledge about the initial magnetic field strength and structure is basic for the understanding of the further evolution of NSs. More precisely, the question arises whether the inborn field can reach in a relatively short time – until the onset of crystallization and superfluidity – a stable equilibrium configuration. This is the old question for stable magnetostatic equilibria in a conducting sphere.

Prendergast [69] already discussed that the coexistence of a poloidal and toroidal magnetic field can enable an equilibrium configuration within an infinitely conducting sphere. It was Wright [95], who postulated the stability of a magnetic field configuration the poloidal and toroidal constituents of which are of comparable strength. Tayler [82], Markey and Tayler [51], Wright [95], and Pitts and Tayler [64] performed a series of analytical stability analyses of magnetic field configurations in stars. The outcome of these analyses is that a purely toroidal axisymmetric field without rotation in a stratified medium is always unstable with respect to large scale perturbations. The growth rate of this instability is on the order of the Alfvèn frequency $\Omega_A = v_A/r$, where $v_A = B/\sqrt{4\pi\rho}$, B the magnetic field strength, ρ the density, and r the radial coordinate. This "Tayler-instability" acts locally in meridional (r, θ) planes but globally in the azimuthal (φ) direction.

Markey and Tayler [51] and Wright [95] performed similar adiabatic stability analyses for axisymmetric poloidal fields and concluded its general instability if at least some of its field lines are closed within the star. The instability generates small scale, rapidly decaying field structures on the same time scale as for a toroidal field. They discuss the possibility that sufficiently rapid rotation and/or the simultaneous existence of equipollent toroidal and poloidal components may stabilize the axisymmetric background fields. Pitts and Tayler [64] performed an analytical stability analysis of a very special combination of toroidal and poloidal fields also with respect to rotation and to the magnetic inclination angle α. They found a tendency of rotation to counteract the instability but concluded that "rotation is unlikely to lead to a complete stability of general magnetic field configurations".

In 2005 the interest in the stability of magnetostatic equilibria in stars became revitalized in a series of papers by Braithwaite, Spruit and Nordlund [9, 11–13]. The latter authors studied the stability of magnetic fields in the radiative interiors of non-rotating Ap stars and found that any random field is generally unstable but evolves in a stably stratified star towards a "twisted torus" configuration with approximately equipollent toroidal and poloidal components. Braithwaite and Spruit [13] considered the stability of MHD configurations in magnetars. They found that, quite similar to the Ap stars, stable magnetic fields exist when being concentrated to a relatively small region around the center of the star and after having evolved into the poloidal–toroidal twisted torus shape.

While [10] showed that sufficiently fast rotation may stabilize purely toroidal field configurations, until now the effect of rotation on the stability of purely poloidal field configurations has not been considered in general. When NSs have inborn magnetic fields of order 10^{15} G, than the corresponding Alfvèn crossing time $\tau_A = r/v_A$ is very short; for $r = R = 10^6$ cm and $\rho = 2 \times 10^{14}\,\mathrm{g\,cm^{-3}} \approx 50$ ms. The rotation period at the NS's birth however, is supposed to be even smaller, at least in some cases, theoretically it can be as small as $\sim$0.8 ms (for a $1.4 M_\odot, R = 10^6$ cm NS, Villain et al. 2004 [92]). Therefore, rotation in new-born NSs and its effect on any inborn magnetic field can for sure not be neglected. Since the dipolar magnetic field determines both observability and rotational evolution, Geppert and Rheinhardt [28] studied the consequences of rotation for the stability of such fields in detail.

Besides the above mentioned assumptions, that the whole star is liquid and in a normal state (for at least the first few 100 s), that it rotates rigidly, and that it has an inborn field of order 10^{15} G, they assumed incompressibility, constant density, maintenance of the spherical shape of the star, and uniform rotation. The assumption of incompressibility can be quite well justified a posteriori by comparing the maximum fluid velocities with the sound velocity. The deviations from a spherical shape can be neglected as long as both the magnetic and kinetic energies inherent in the conducting sphere are small in comparison with its gravitational binding energy. However, the assumption of constant density for a NS is of course a questionable one, the more since a stable stratification exerts a stabilizing effect on to the field. Although a certain amount of compressibility gives rise to other (e.g., Parker) instabilities, and although the bulk of the induced flow is in the core where the density gradient is by far not as large as in the crustal region, further calculations have to relax that premise.

The preceding considerations result in the following ruling equations for magnetic field B and velocity u and corresponding boundary conditions written in dimensionless form:

$$\begin{aligned} \frac{\partial B}{\partial t} &= \Delta B + \mathrm{curl}(u \times B) && \text{for} \quad r \le 1\,, \\ \mathrm{curl}\, B &= 0 && \text{for} \quad r > 1\,, \\ \mathrm{div}\, B &= 0 && \forall r\,, \\ [B] &= 0 && \text{for} \quad r = 1\,, \end{aligned} \tag{13.1}$$

$$\left.\begin{aligned} \frac{\partial u}{\partial t} = \; & -\nabla(p - \frac{1}{2}\Omega^2 r^2 \sin^2\vartheta + \Phi) \\ & -(u\nabla)u + Pm\,\Delta u \\ & -2\Omega e_z \times u + \mathrm{curl}\, B \times B \\ \mathrm{div}\, u = \; & 0 \end{aligned}\right\} \quad \text{for} \quad r \le 1\,, \tag{13.2}$$

$$\left.\begin{aligned} u_r &= 0 \\ (\hat{D}(u)\cdot e_r)_{\vartheta,\varphi} &= 0 \end{aligned}\right\} \quad \text{for} \quad r = 1\,. \tag{13.3}$$

Here, length is normalized on the NS radius R, time on the magnetic diffusion time $\tau_{\mathrm{Ohm}} = R^2/\eta$, where $\eta = c^2/4\pi\sigma$ is the magnetic diffusivity and σ the electric conductivity. [.] denotes the jump of a quantity across a surface. The magnetic field is measured in units of $(4\pi\rho)^{1/2}\eta/R$, the velocity in units of η/R, the pressure p in units of $\rho\eta^2/R^2$, and the gravitational potential Φ in units of η^2/R^2. $\hat{D}(u)$ denotes the deformation tensor. (r, ϑ, φ) are spherical co-ordinates, the polar axis ($\vartheta = 0$, $\uparrow\uparrow e_z$) of which coincides with the axis of rotation.

Equations (13.1) and (13.2) contain two parameters which together with the initial field strength B_0 (for a fixed initial field geometry) define the problem completely: the magnetic Prandtl number Pm and the normalized rotation rate Ω.

Pm, is the ratio of kinematic viscosity, ν, and magnetic diffusivity, η, and is chosen to be 0.1, 1, and 10, resp., what is partly dictated by numerical restrictions, but on the other hand represents a subset of the NS-relevant range determined by the prevailing densities ($\rho = (1\ldots2.8)\times10^{14}\,\mathrm{g\,cm^{-3}}$) and temperatures ($\sim10^{11\ldots9}$ K). These values result in $Pm = 0.1\ldots6\times10^{8}$ [21, 97] reflecting mainly the strong temperature dependence of $Pm \propto T^{-4}$.

The two remaining parameters are best expressed as ratios of characteristic times: $\Omega = 2\pi/P$ by $q_P = P/\tau_{\mathrm{A},0}$, and P the rotation period of the NS, where $\tau_{\mathrm{A},0} = R/v_{\mathrm{A},0}$ is the Alfvèn crossing time related to the initial field, and the initial field amplitude B_0 by $q_{B_0} = \tau_{\mathrm{A},0}/\min\{\tau^{B}_{\mathrm{decay}}, \tau^{u}_{\mathrm{decay}}\}$,. Note, that the "decay times" of the magnetic and velocity fields, $\tau^{B}_{\mathrm{decay}}$, $\tau^{u}_{\mathrm{decay}}$, are different from the often used magnetic and viscous "diffusion times", $\tau_{\mathrm{Ohm}} = R^2/\eta$, $\tau_{\mathrm{visc}} = R^2/\nu$, by factors $1/\pi^2$ and 0.06676, respectively.

For q_{B_0} values $\sim10^{-2}$ are assumed, which are of course by far too large for highly magnetized young NSs where this ratio can go down to 10^{-16} for a surface magnetic field of 10^{15} G. However, as long as the growth/decay times of the examined perturbations are on the order of at most a few Alfvèn times, dissipation of the background state does not affect their linear stage (quasi-stationary approximation). The artificially enhanced dissipation is a concession to numerical feasibility only, in order to avoid excessive requirements for spatial resolution (see [12], where q_{B_0} was chosen to be 0.1). Hence, the use of the results from the nonlinear stage has to be considered with caution when the elapsed time since birth exceeds about $100\tau_{\mathrm{A},0}$. However, the non-linear treatment returns at least reliable saturation values.

For the models presented here the following parameters were chosen:

$$R = 10^{6}\mathrm{cm}, \qquad \rho = 2\times10^{14}\mathrm{g\,cm^{-3}}, \qquad \tilde{B}(t=0) = 10^{15}\mathrm{G}, \tag{13.4}$$

where $\tilde{B}$ is the de-normalized r.m.s. value. Therefore, $\tau_{\mathrm{A},0} = 0.05$ s. With rotation periods chosen between 0.6 ms and 0.6 s, where the former value is somewhat below the generally accepted minimum for new-born NSs, but the latter is in that respect not very likely, these model parameters result in $q_P = 0.012\ldots12$. As a reference and for comparison with known results for non-rotating stars $q_P = \infty$ is considered, too.

Two qualitatively different initial field configurations are considered. Each of these consists of an axisymmetric dipolar background field, the stability of which is examined, and imprinted magnetic perturbations. The fluid is assumed to be at rest initially, and the initial magnetic inclination α is defined by the dipole axis. The two background fields are shown in Fig. 13.1 for $\alpha = 0$. The energy of the perturbations is set to 0.1% of the magnetic background energy, and their geometry ensures that the initial state has no preferred equatorial symmetry.

The uniform background field configuration, a more academic example, consisting of a field uniform throughout the sphere, but being a dipolar vacuum field outside:

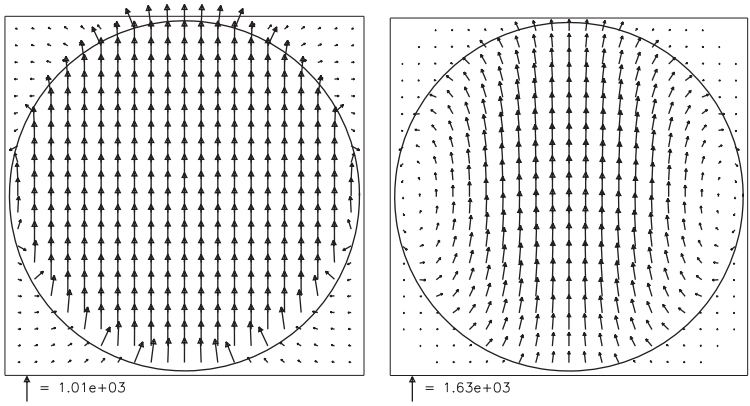

Fig. 13.1 *Left panel*: internal uniform field according to (13.5) in a meridional plane. The *arrow* indicated below marks a magnetic field of 10^{15} G. *Right panel*: dipolar magnetostatic equilibrium field according to (13.6). The *arrow* indicated below marks a magnetic field of 1.63×10^{15} G

$$\begin{aligned} B = &\quad B_0 e_z && \text{for } r \le 1, \\ B = &-B_0 \operatorname{curl} r \times \nabla \left(\frac{\cos\vartheta}{2r^2} \right) && \text{for } r > 1, \\ [B_r] = &\ 0 && \text{for } r = 1. \end{aligned} \tag{13.5}$$

Here, B_0 denotes the polar surface field strength. Of course, the continuity of the normal component of B has to be required, but the tangential components remain discontinuous and give rise to surface currents. This model field was chosen, because it was the one considerations on magnetic stability in NSs were first exemplified on by Flowers and Ruderman [23] and because [13] report on its instability in the non-rotating case.

A more realistic initial configuration consists of the poloidal magnetostatic equilibrium field the angular dependence of which is the same as for a dipolar field [74, 75]:

$$\begin{aligned} B = &\quad B_0 \ \operatorname{curl} r \times \nabla \left(\frac{1}{4}(3r^3 - 5r)\cos\vartheta \right) && \text{for } r \le 1, \\ B = &-B_0 \ \operatorname{curl} r \times \nabla \left(\frac{\cos\vartheta}{2r^2} \right) && \text{for } r > 1, \\ [B] = &\ 0 && \text{for } r = 1. \end{aligned} \tag{13.6}$$

As the Lorentz force of this field is a pure gradient it can, in the constant-density case, be balanced by the quantity $-\nabla\left(p - (\Omega^2 r^2 \sin^2\vartheta)/2 + \Phi\right)$ (see (13.2)). If stable, this state could be a final equilibrium to which an arbitrary initial configuration relaxes during the fluid stage of a newly born NS. As known from analytical studies [51], however, any purely poloidal field is in the absence of rotation surely unstable, hence the evolution of the field (13.6) under the influence of rotation is a crucial question.

Because the star is modeled as a spherical body and incompressibility is assumed, the problem is especially suited to be tackled by a spectral method. The one used here employs an expansion of B and u into their modes of free decay.

The numerical solution of (13.1), (13.2) returns qualitatively very different results for the magnetic field evolution in dependence on the rotational period and the inclination angle α. If the rotation is fast enough and/or the inclination angle sufficiently small, the background field is stable and reaches quite fast a stable equilibrium configuration. If, in contrast, rotation is too slow and/or α too large, the background field becomes unstable and looses almost all of its initial energy by transferring it to small scale modes of the velocity and the magnetic field, for which dissipation acts efficiently. For the parameter range considered up to now, the transition from stabilization to unstable behaviour happens at a rotational period $P \gtrsim 6$ ms and $\alpha \approx 45°$. To illustrate it, in Table 13.1 the results for a model with $Pm = 1$ and the two different initial background field configurations are presented.

Note, that for the model parameters (13.4) $q_P = 0.12$ corresponds to $P = 6$ ms. Most informative about the effect of rotation and inclination is the third row, where the final magnetic energies after equal evolution times is related to the final energy of the purely ohmic case $E_{\rm mag}^{\rm Ohm}$, i.e., when no coupling to the fluid flow is allowed. It is clearly seen that with increasing rotational velocity, an increasingly smaller part of the magnetic energy is dissipated and/or transferred into kinetic energy (fourth row). That an increasing α exacerbates the stabilization of the background field is also shown by the fact, that for $\alpha = 90°$ an extremely fast rotation with $P = 0.6$ ms would be necessary to stabilize the dipolar magnetostatic equilibrium field. It is informative to consider in comparison the evolution of the initial uniform background field (left panel of Fig. 13.1). The general tendencies are the same as for the dipolar equilibrium field. Again, the significant influence of α on the stability is proven.

Table 13.1 Left part: results for the dipolar magnetostatic equilibrium model. All quantities are taken after a period of $\tau_{\rm decay}^{B}$. Subscripts "kin" and "mag" refer to velocity and magnetic-field related quantities, respectively. The calculations for the non-rotating NS, $q_P = \infty$, were performed only for $\alpha = 0$ because in this case the choice of the axis is of course arbitrary. Right part: the corresponding results for the internal uniform field model

$\alpha\,(°)$	q_P	$E_{\rm mag}/E_{\rm mag}^{\rm Ohm}$	$E_{\rm kin}/E_{\rm mag}$	$\alpha\,(°)$	q_P	$E_{\rm mag}/E_{\rm mag}^{\rm Ohm}$	$E_{\rm kin}/E_{\rm mag}$
0	∞	0.0002	4.67	0	∞	0.00009	147.6
	12.	0.0004	6.6		12.	0.001	2.92
	1.2	0.0076	0.0007		1.2	0.083	0.0034
	0.12	0.98	0.00003		0.12	1.02	0.00002
45	1.2	0.075	0.001	45	0.12	0.56	0.00006
	0.12	0.824	0.00005		0.012	1.006	0.0023
90	12.	0.0033	0.64	90			
	1.2	0.043	0.003				
	0.12	0.14	0.00014		0.12	0.193	0.0005
	0.012	0.98	0.0013		0.012	0.976	0.0013

It is interesting to see how an unstable background field configuration evolves through the instability. In Fig. 13.2 a snapshoot of both the velocity and magnetic field evolution is shown at $10\tau_A = 0.5$ s for a newborn NS rotating initially with $P = 60$ ms (second line in Table 13.1).

A comparison of both the final spectra and field geometries of the initially quite different background field configurations shown in Fig. 13.1 for $P = 6$ ms and $\alpha = 0^\circ$ (fourth lines in Table 13.1 gives strong evidence for a tendency to approach the same state for $t \to \infty$; see Fig. 13.3). Not only the difference in the initial geometry (cf. Fig. 13.1), but also the difference in the initial energies is obviously equalized after having gone through the nonlinear stage. The relative r.m.s. value of the difference of both fields is only 1.6%. The same coincidence is found for $\alpha = 45^\circ, 90^\circ$, $q_P = 0.012$.

The temporal evolution of the magnetic and kinetic energies for both the stabilized and the destabilized background field configurations are shown in Figs. 13.4 and 13.5: A comparison of Fig. 13.4 with Fig. 13.5 shows that while for sufficiently

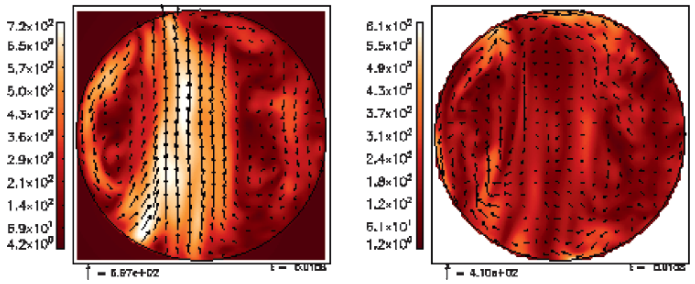

Fig. 13.2 Field geometries of magnetic field (*left*) and flow (*right*) around the end of the dramatic field reduction phase (see *upper panels* of Fig. 13.5 at $t \approx 0.01$) in a meridional plane for the dipolar equilibrium model with q_P=12, $Pm = 1$, $\alpha = 0$. *Arrows* indicate vector components parallel to the paper plane. Their maxima are 6.93×10^{14} G and 8.3×10^6 cm s^{-1}, respectively. Colors encode the field moduli: the brightest tone corresponds to 7.2×10^{14} G and 1.2×10^7 cm s^{-1}, respectively

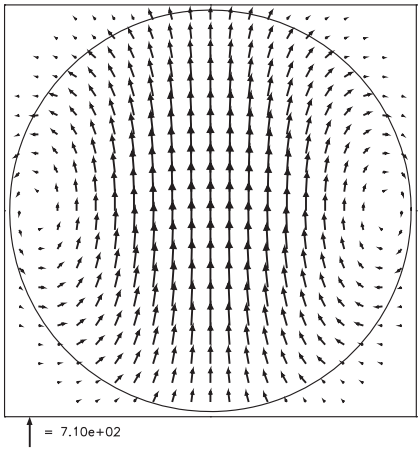

Fig. 13.3 Final field geometry for the internal uniform field model in a meridional plane (the field is almost exactly axisymmetric) for $\alpha = 0$, $q_P = 0.12$, $Pm = 1$. With the denormalization based on (13.4) the maximum field strength is $\approx 7.1 \times 10^{14}$ G

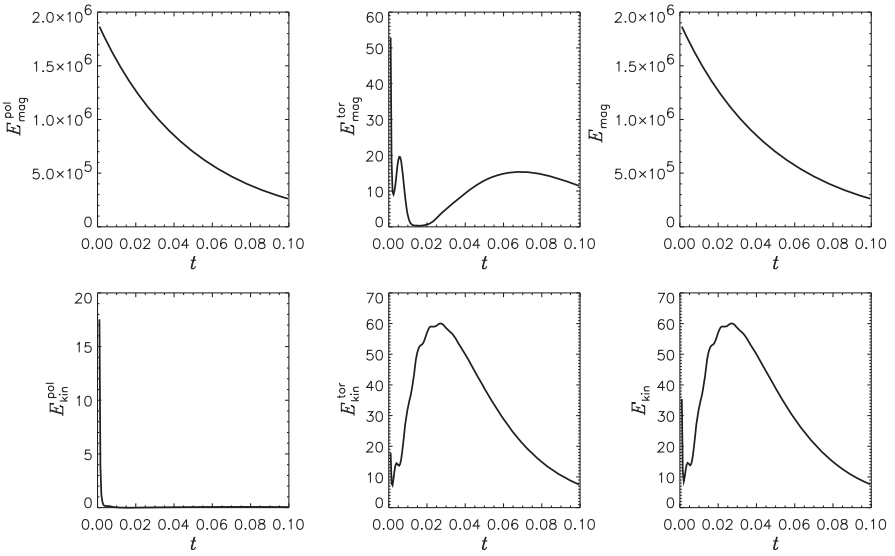

Fig. 13.4 Temporal evolution of the disturbed dipolar magnetostatic equilibrium for q_P=0.12, $Pm = 1$, $\alpha = 0$ (a stable case). Time is in units of $\tau_{\rm Ohm}$, energy in units of $\rho\eta^2/R^2$. Subscripts "kin" and "mag" refer to velocity and magnetic-field related quantities, respectively. The magnetic and kinetic energies, $E_{\rm mag}$ and $E_{\rm kin}$, are each further subdivided in their poloidal and toroidal parts

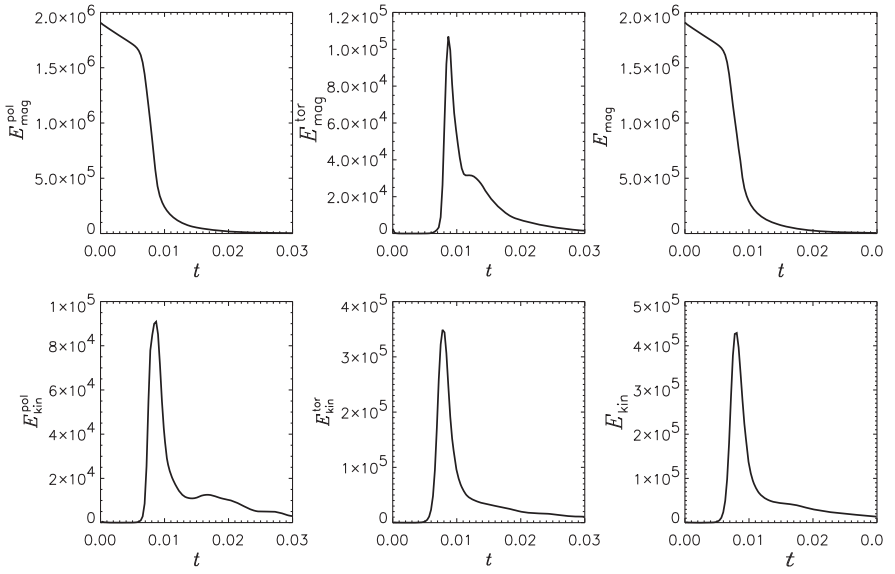

Fig. 13.5 Temporal evolution of the disturbed dipolar magnetostatic equilibrium. $q_P = 12$, $Pm = 1$, $\alpha = 0$ (an unstable case). For further explanations see Fig. 13.4. Note, that using the parameters (13.4) $t = 0.01$ corresponds to 0.5 s!

fast rotation the magnetic energy is decreased to 15% of its initial value (which corresponds to a decrease of the field strength from 1.71×10^{15} G to 7.1×10^{14} G) in the unstable , slower rotating NS, 99.99% of the magnetic energy has been redistributed into kinetic one and is finally dissipated into heat, so that the remaining NS magnetic field has a strength of 1.71×10^{13} G, typical for the majority of young radio pulsars.

Concluding, the effect of the MHD instability occurring immediately after the birth of NSs with ultra-strong dipolar fields is that:

1. Those whose rotation period is less than $\sim$6 ms and whose magnetic inclination angle α is smaller than $\sim 45^\circ$ will retain their extremely large surface field strength and appear, after a rapid spin down, as magnetars.
2. Those which rotate less rapidly, say with $P \gtrsim 6$ ms and/or for which is $\alpha \gtrsim 45^\circ$ will lose almost all of their inborn magnetic energy and appear as radio pulsars.

It turns out that rotation is likely to be the only stabilizing agent which allows of the existence of magnetars whereas the stable configurations found by [13] are less suited to support such strong surface fields; due to their concentration to the very inner core region it demands too large field strengths for typical magnetar surface fields. Thus, the much smaller number of observed magnetars in comparison with that of all the other observed realizations of NSs may be a consequence of the fact that only a small fraction of all new-born NSs are rotating as fast as or faster than $P \sim 6$ ms.

13.3 Fallback Accretion, Submergence and Rediffusion: Pulsar or Radio Quiet Neutron Star?

Whether and if so how much fallback accretion can change the magnetic field evolution qualitatively depends on two questions:

- Can the fallback matter reach the NS surface at all, i.e., is the dynamical pressure of the matter flow stronger than the pressure of NS's magnetic field which exists after the first $\sim$10 s of NS's life (see Sect. 13.2), and is the rotation sufficiently fast that the rotating dipole acts like a propeller?
- If the fallback matter reaches the surface, how deep can the magnetic field be submerged and how fast can it rediffuse to the surface up to its strength before the hypercritical accretion started?

For other factors which may either reduce the rate of fallback accretion or prevent it at all (decay of ^{56}Ni and ^{56}Co, rapid rotation, kick velocity) see [26]. A rough estimate with respect to the first question is whether the Alfvèn radius, determined by the equilibrium of the pressure of the dipolar field and the ram pressure of the gravitationally captured fallback matter, is larger or smaller than the NS radius R.

$$R_A = \left(\frac{R^6 B^2}{4\dot{M}\sqrt{GM}} \right)^{2/7} \approx 1.3 \times 10^5 \left(\frac{B_{12}^2}{\dot{M}_{350}} \right)^{2/7} \text{ cm}, \tag{13.7}$$

where $B_{12} = B/10^{12}\,\mathrm{G}$ and $\dot{M}_{350} = \dot{M}/350 M_\odot \mathrm{yr}^{-1}$. The accretion rate of $350 M_\odot \mathrm{yr}^{-1}$ was estimated for the initial accretion on to the NS in SN 1987A [17]; the factor in (13.7) is given for a NS with $M = 1.4 M_\odot$ and $R = 10^6$ cm. Clearly, the majority of NSs, having after the period of MHD instabilities "only" surface field strength in of order 10^{12} G, will suffer from fallback if the accretion rate is as huge as in case of SN 1987A. If, however, the field strength after that periods is $\gtrsim 3 \times 10^{13}$ G and the fallback accretion rate is only one tenth as strong as in the case of SN 1987A, the Alfvèn radius $R_A \approx 1.75 \times 10^6$ cm, just the radius of a NS with quite stiff equation of state (EoS). In that case the submergence of the field can be attenuated drastically. Even for fallback as heavy as in case of SN 1987A, a magnetar field ($\gtrsim 10^{15}$ G) ensures $R_A \approx 6.9 \times 10^6$ cm, a precondition for preventing fallback accretion.

Another condition to impede fallback concerns sufficient fast rotation. The rotation period which separates the propeller from the accretor regime is given by the so-called equilibrium period P_{eq} [2]. Thus, the NS is in the propeller regime and can eject the inflowing fallback as long as

$$\left(\frac{2\pi}{P}\right)^2 R_A^3 > GM \approx 1.9 \times 10^{25}\ \mathrm{cm^3 s^{-2}}\,, \tag{13.8}$$

i.e., for the magnetic field of standard pulsars $\sim 10^{12}$ G, even a rotation as fast as $P = 10$ ms can not prevent accretion if it starts as heavy as in case of SN 1987 A (see (13.7)). The same rotation combined with magnetar field strength, however, would drive the propeller mechanism. This mechanism prevents heavy accretion, but has an enormously efficient braking effect (see, e.g., [86]. Since on the other hand the fallback accretion rate drops rapidly with time (in case of SN 1987A after the onset of accretion $\dot{M} \propto t^{-3/2}$ during the Bondi-accretion regime, after the transition to the dust-like regime $\dot{M} \propto t^{-5/3}$) it is possible that a magnetar field together with an rapid initial rotation may prevent the fallback accretion. For the majority of newborn NSs it is quite likely, that fallback accretion will appear, albeit not as heavy and field submerging as in case of SN 1987A. The onset of the powerful propeller regime which prevents the submergence of the magnetar field but spins the NS rapidly down might be one reason, why those NSs having magnetar field strength, the anomalous X-ray pulsar (AXPs) and the soft gamma repeaters (SGRs), are relatively young ($\sim 10^4$ yrs) and rotate so slow ($5 < P < 12$ s).

The question how deep the field can be submerged during fallback accretion and how fast it can rediffuse towards the surface has been addressed, e.g., by [20,26,55].

The magnetic field present at the surface of the NS when accretion stops will be the field which was present in the accreted matter and compressed. Following the standard hypothesis that the pulsar magnetic field is a fossil of the progenitor's core field, the accreted matter, being material of the progenitor's core too, could bring in a field comparable to the field already present in the NS, i.e., the NS may be born with a strong surface field.

However, the hypothesis that the fall-back matter brings in a well-ordered large scale field is questionable since there is still the possibility that this accreting matter has suffered a turbulent episode during which the plasma behaved as a diamagnet

[90] and its field could have been severely reduced, which would mean that the final surface field of the NS would also be weak. In contrast, within the proto-NS dynamo scenario for the origin of NS magnetic fields [83] the core of the progenitor is only required to have a small field which will act as a seed for the dynamo action. In this case the field present at the NS surface after accretion will be small. The strength of the surface magnetic field of a new-born NS which has undergone hypercritical accretion may thus be very different if its magnetic field is fossil or of proto-NS dynamo origin. Hence, the assumption that the accreting matter is only weakly, magnetized, is natural within the proto-NS dynamo scenario and may also be compatible with the fossil field hypothesis.

How deep the field will be submerged depends on the details of the supernova explosion as well as on the magnetic field strength and on the rotation rate of the NS when the fallback hits the surface. The submergence process in a NS whose field is that of "standard" pulsars and for the fallback parameters of SN 1987A (for details see [26] is shown in Fig. 13.6.

When the accretion has ceased, the field starts re-diffusion back toward the surface. This problem has been considered by [55] in the case of very shallow

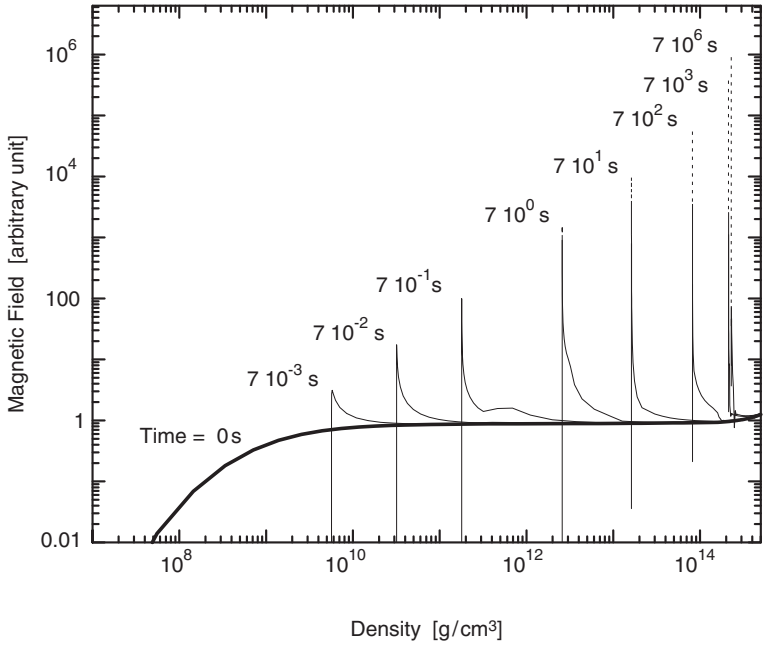

Fig. 13.6 Distribution of the angle averaged magnetic field strength in the NS as a function of time for the fallback rate estimated for SN1987A. Initial time corresponds to the beginning of the accretion phase. In less than 2 h the initial field is submerged down to the crust–core interface. Notice that the maximum value attained by the field depends on its initial value at low density since the low density region is the most strongly compressed. The calculation assumes ideal MHD, but these zones of highly compressed field have very small length scale and thus a very small ohmic diffusion time: these fields, shown as *dashed lines*, will eventually washed out by diffusion when time becomes comparable to the ohmic diffusion time

submergence, i.e., the total amount of accreted matter $M_{\rm acc} \sim 10^{-5} M_\odot$. They showed that after a few hundred years the surface field strength becomes comparable to the interior one, resulting in a delayed switch-on of the pulsar. For a typical type II SN [17] estimated that the accreted mass should be at least 100 times smaller than in SN 1987A, i.e., less than $10^{-3} M_\odot$.

The rediffusion process in isolated NSs is solely determined by the conductive properties of the crustal matter. This, in turn, depends on the cooling scenario and on the impurity content Q of the crust. The rediffusion processes shown in Fig. 13.7

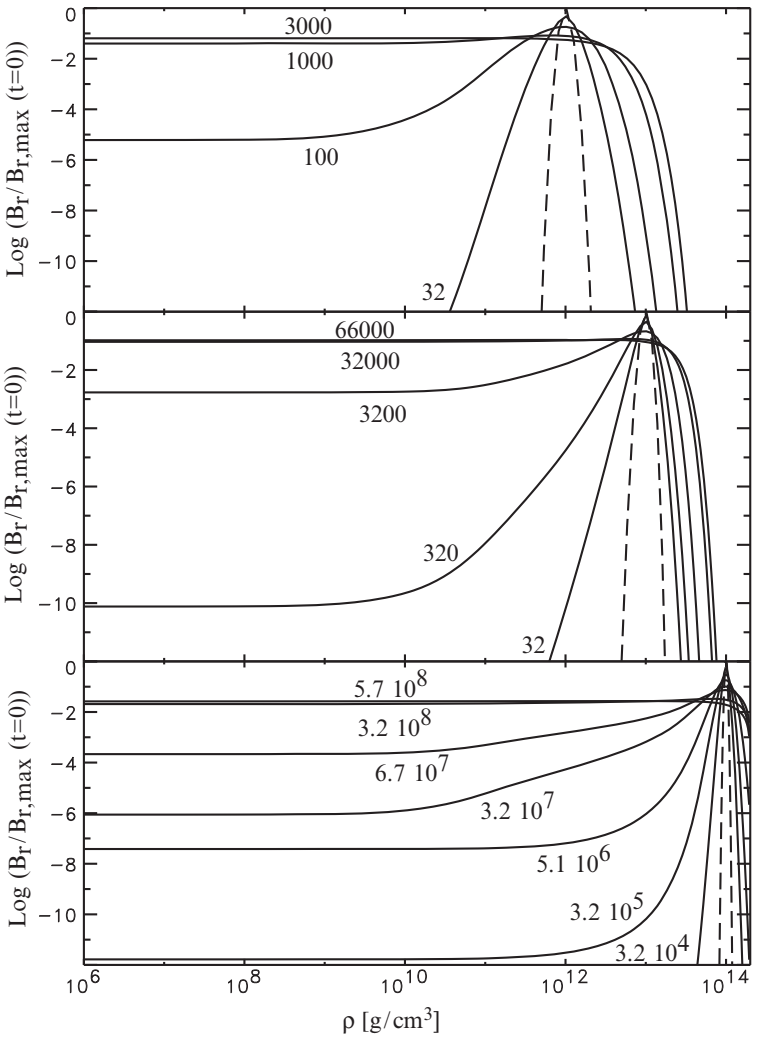

Fig. 13.7 Rediffusion of the interior magnetic field after the hypercritical accretion phase for three different submergence depths. Only the radial component is plotted. The assumed initial field location is shown by *dashed lines*. The ages of the star are indicated on the lines

are based on the standard (slow) cooling scenario [58] and an impurity content of $Q = 0.01$. The latter is controversially discussed, see Jones [46] who argues in favor of a much larger Q which would accelerate the rediffusion. The final depths into which the field has been submerged after accretion of a certain amount of fallback matter (see Fig. 2 in [26] correspond roughly to a rediffusion time of about 10^3 (3×10^4) yrs for $M_{\rm acc} \sim 10^{-4}$ $(\sim 10^{-3})\, M_\odot$, while for $M_{\rm acc} \sim 10^{-2} M_\odot$ rediffusion takes more than 10^8 yrs. Moreover, in the case of $M_{\rm acc} \sim 10^{-1} M_\odot$ the rediffusion time will exceed the Hubble time and, as far as SN1987A is concerned, it is likely that a pulsar will never be seen in it.

This re-magnetization scenario relies upon the assumption that the accreted matter is weakly magnetized, either because the progenitor's core had a very weak magnetic field or because the explosion and/or accretion process demagnetized it.

There remains also the possibility that immediately after the fallback a mechanism generates a strong field in the very surface layers based on a thermoelectric instability (Sect. 13.4) driven by the strong temperature gradient in the outer crust. Even stronger temperature gradients may appear transiently during the thermal relaxation of the young NS in deeper crustal layers [33], which would be preferred locations for the transfer of thermal in to magnetic energy. In that case, the pulsar in the remnant of SN 1987A could be switched on relatively soon.

13.4 Thermoelectric Instabilities: Strong Fields Despite Deep Submergence?

Wherever in nature large temperature gradients are maintained in a medium of sufficiently high conductivity, a suitably structured arbitrarily weak magnetic seed field can be amplified by an instability which is based on two thermomagnetic effects, the thermo-Hall effect, by which the magnetic field affects the heat flux (see Sect. 13.5.2) and the thermoelectric effect, by which a temperature gradient creates an e.m.f. (battery effect). This instability is, e.g., used to confine plasmas in thermonuclear reactor devices [94].

The existence of huge temperature gradients is one of the many superlatives which are assigned to NSs. For the first time Dolginov and Urpin [22] studied the possibility of an thermomagnetic instability in the cores of white dwarfs. Soon it became clear that in the envelopes of NSs much larger temperature gradients are prevalent [36] which, together with the high electric conductivity may guarantee that the field generation overwhelms the ohmic diffusion. Blandford et al. [7] considered thermoelectric field amplification in the solid crust which should via Lorentz forces drive a dynamo process in the liquid layer above the solid. Urpin et al. [87] showed that the thermomagnetic instability may act efficiently in the liquid layer only and that a sufficiently fast rotation is necessary to keep the instability alive. The latter condition is fulfilled by the vast majority of young NSs.

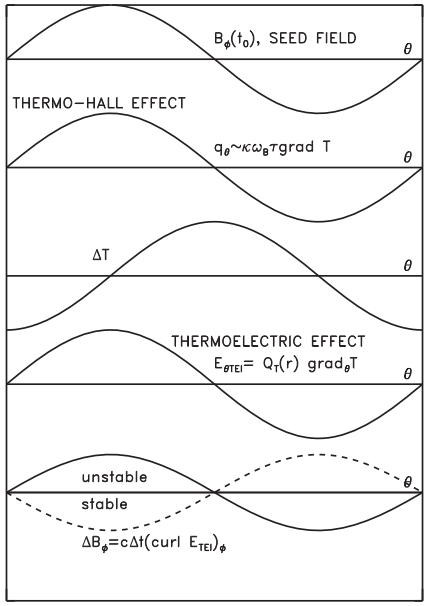

Fig. 13.8 Schematic presentation of the thermoelectric instability caused by the interaction of an toroidal (in axial symmetry purely azimuthal (φ)) magnetic field with the radial temperature gradient. The magnetic field B_φ and ΔB_φ, temperature T and ΔT, the related heat flux q_Θ, and the thermoelectric field $E_{\Theta\,\mathrm{TEI}}$ vary along the meridional (Θ) direction (according Fig. 1 in [87]). During the linear stage of the instability only toroidal seed fields can be amplified

The basic scenario is sketched in Fig. 13.8 and can be described as follows: A pre-existing small scaled toroidal (in axisymmetry: azimuthal) component of the NS magnetic field in the liquid creates via the thermo-Hall effect by means of the strong radial temperature gradient thermal flux variations in meridional direction having approximately the same scale length as the seed field. This meridional heat flux causes temperature variations and the thermoelectric effect generates by them an additional electric field also pointing in meridional direction. Due to the non-uniformity of the liquid layer in radial direction that electric field has a curl component in azimuthal direction which, under suitable conditions, may amplify the seed field.

The set of equations which govern the thermoelectric instability is

$$\begin{aligned} \frac{\partial B}{\partial t} &= -\,\mathrm{curl}\Big(\frac{c^2}{4\pi\sigma}\,\mathrm{curl}\,B\Big) + c\ \mathrm{grad}\,Q_T \times \mathrm{grad}\,T + \mathrm{curl}\left[(v_j + v_{TD}) \times B\right]\ , \\ 0 &= \mathrm{div}\left[(\kappa_{\mathrm{ei}} + \kappa_{\mathrm{rad}})\,\mathrm{grad}\,T + \kappa_{\mathrm{ei}}\omega_B\tau(b \times \mathrm{grad}\,T)\right]\ . \end{aligned} \tag{13.9}$$

The first term in the induction equation describes the ohmic diffusion of the field, the second term is the battery term. Its strength is determined by the temperature gradient and the gradient of the thermopower Q_T. This kinetic coefficient quantifies the efficiency of the thermoelectric (Seebeck) effect and is the ratio of the electric voltage gained by the temperature gradient (see, e.g., [101]). Because all transport coefficients are in good approximation dependent on the radial coordinate only as long as $\omega_B\tau < 1$, the battery term can amplify a seed field only if the temperature gradient has, besides its strong radial component, a meridional one too. The third

term resembles the usual advection term. Here, however, the velocity is not the hydrodynamical motion, perhaps affected by the Lorentz force. Since the instability starts with weak seed fields, the coupling to the hydrodynamics is neglected. This assumption becomes wrong only if the field strength exceeds $\sim 10^{12}$ G. Instead, the velocity consists here of the thermal drift v_{TD} which describes the drift of the magnetic field in the liquid caused by the temperature gradient and is a consequence of the thermoelectric effect. The electron mobility ($v_j \propto \mathrm{curl}\, B$) is responsible for the Hall-drift; it makes the induction equation nonlinear in B while the thermal drift together with the battery effect as well as the thermo-Hall effect couples the field evolution to the thermal one.

The thermal conductivities $\kappa_{\rm ei}$ and $\kappa_{\rm rad}$ correspond to the heat transport due to electron–ion collisions and to radiation, respectively, where the latter dominates with decreasing density in the liquid layer. For the field strength expected to appear at this stage of field evolution the radiative conductivity will not be affected by the field. It can only influence the electron–ion collisions which, together with the magnetization parameter and the temperature gradient determine the relative importance of the thermo-Hall effect, coupling the heat flux to the field (b is the unit vector of B). For details of the derivation of (13.9) see [30].

Note, if there is initially a purely radial temperature gradient, initially only the toroidal component of the seed field can be amplified. Any amplification of the poloidal field component, which forms the dipole field outside the NS, is only possible via nonlinear interactions of the poloidal and toroidal field components and each of them with the temperature variations.

In a series of studies Geppert and Wiebicke (see [93] and references therein) tried to follow the evolution from a weak toroidal seed field to a poloidal field of observed pulsar strength, but they failed. They could show the scheme of thermoelectric field generation in the surface layers of young NSs which is characterized by a rapid growth of small scale toroidal field components in less than 10 yrs saturating at field strengths $\sim 10^{13}$ G, provided the surface temperature is $\gtrsim 3 \times 10^6$ K. Below that surface temperature the temperature gradient in the liquid crust becomes too flat and ohmic decay and/or the Hall drift will dominate the field evolution. During the exponential growth of the small-scale toroidal field modes nonlinear (quadratic) interactions drive an (twice as) fast growth of large scale (say quadrupolar) toroidal fields which reach in about $100 \ldots 1{,}000$ yrs field strength of $10^{11 \ldots 12}$ G (see Fig. 13.9). While after about 10 years the exponential growth of the small-scale modes saturate, the large-scale modes are still growing. However, the growth of the large-scale toroidal modes after saturation of the small-scale modes as shown in Fig. 13.9 is questionable. There are two reasons why the modeling of their growth and that of the poloidal field component, fed by the rapidly growing small-scale toroidal components, did not return correct results. Firstly, the decoupling of the field from the hydrodynamic motions is not justified when the field attains strengths $\gtrsim 10^{12}$ G. Then, Lorentz forces may drive matter circulations which can act dynamo-like and amplify the poloidal component of the seed field, too. Secondly, it is well

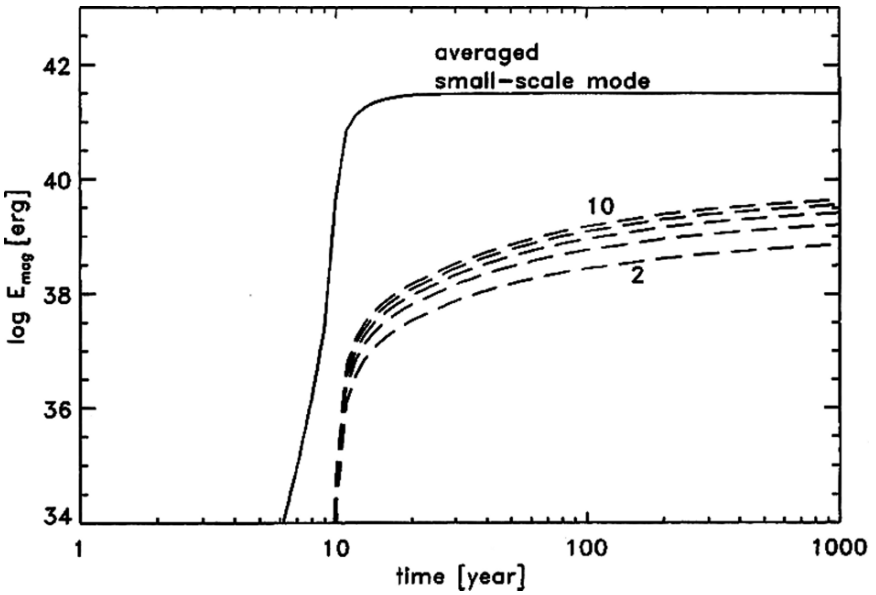

Fig. 13.9 Magnetic energy content of the toroidal field modes as function of time. The result has been obtained for a NS model with $T_s = 5 \times 10^6$ K by a nonlinear calculation which couples the five largest scale modes (*dashed lines*, even multipolarities n = 2,4,6,8,10) to each other and the small scale "locomotives" The energy content of the large scale modes remains two orders of magnitude smaller than that of the "collective" fastest growing small scale mode. For details see [31]

possible that the Hall-instability sets in as discussed in Sect. 13.5.1. An indication of this scenario is that as soon as the toroidal field component exceeded $\approx 10^{12}$ G, the Hall-drift caused a rapid growth of smaller scaled components and the code crashed.

Although the complete thermoelectric field generation process in the crust is by far not yet understood and both the adding of the equations of hydrodynamics and the numerical handling of the Hall instability are quite challenging complex problems, I would like to mention a place and a situation in the NS, where the thermoelectric instability may act even more efficiently than in the outer liquid layer of the crust.

Gnedin et al. [33] studied the thermal relaxation in young NSs which proceeds when during the first 100 yrs the core and the outer crust of the NS cools by neutrino emission faster than the bulk of the crust in the range $5 \times 10^{11} < \rho < 2 \times 10^{14}$ g cm^{-3} for a standard (slow) cooling scenario. This causes naturally two temperature gradients just around these limiting densities (see Fig. 13.10). The temperature gradient, e.g., at the crust–core boundary is of order 2.5×10^6 K cm^{-1}, i.e., about 50...100 times stronger than in the outer liquid layer discussed above. Since the growth time scales are proportional to the square of the inverse of the temperature gradient [22] and the growth time in the outer crust is for surface temperatures $T_s \gtrsim 3 \times 10^6$ K of order 50...100 days, one can expect that, for the instability acting just above

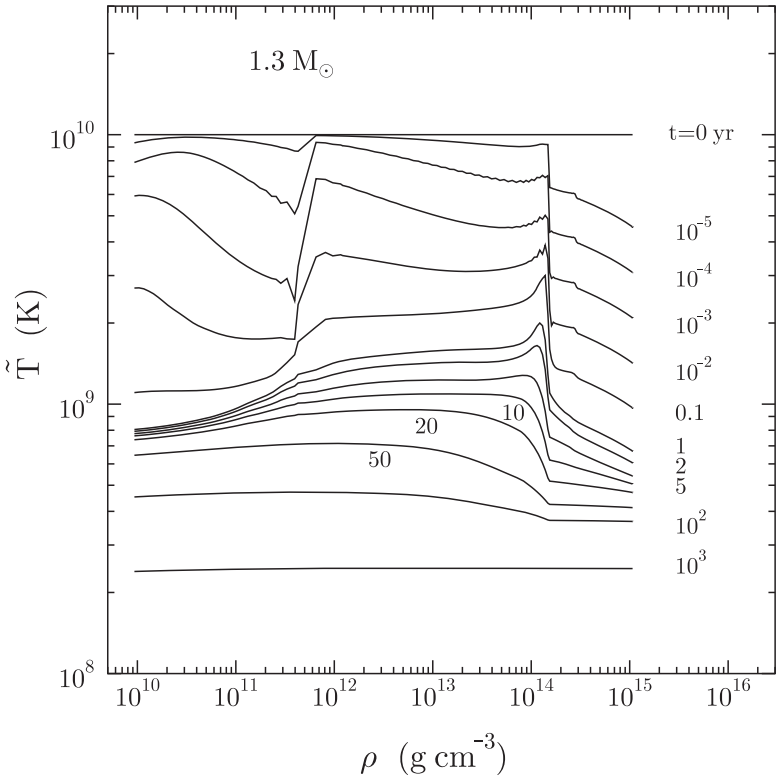

Fig. 13.10 Temperature profile in a $1.3\,M_\odot$ NS without superfluidity effects as shown by [33] depending on the age which is indicated by the numbers next to the curves

the core, the growth time is $\sim$500…2,000 s only. Depending on the cooling, which determines the onset of crystallization, there could be conditions realized, under which a large magnetic field is very fast generated. Another support for the instability is the much larger electric conductivity in comparison with that appearing in the outer crust. Additionally the inverse direction of the temperature gradient may help, which tends to drive the field in regions with even larger conductivity. Perhaps, the rapidly growing magnetic field in the inner crust will prevent the liquid matter for a while from crystallization. Moreover, strong toroidal fields present in the vicinity of the crust–core boundary are necessary to explain the existence of small hot polar regions as discussed in Sect. 13.5.2. I believe it worthwhile to consider the possibility, that very early on, just after the MHD instabilities in the newborn NS ceased, deep in the star, strong fields may be created by use of extreme temperature gradients. It seems, however, that for this purpose the hydrodynamics has to be coupled to (13.9).

13.5 Large Magnetization Parameters: Hall-Drift Induced Instabilities and Strongly Anisotropic Surface Temperatures?

As already mentioned in Sect. 13.1, a magnetization parameter $\omega_B\tau$ exceeding unity will change the magnetic field evolution and cooling history, causing various, possibly observable consequences. The reason is that both the electric and the heat conductivity are in the presence of a magnetic field no longer only *scalar* functions of density, temperature, chemical composition and other quantities, but become *tensors*. Tensorial transport coefficients can only be used to describe correctly the magnetic field effects on electric and heat fluxes in the crystallized crust. There, the ions are fixed to the crystal lattice sites and the electrons are the only moving particles. The more general case, when both the electrons and ions (protons) can move with respect to each other and to the neutral background of neutrons has been studied in detail by Goldreich and Reisenegger [34] and Reisenegger et al. [70]. Such a situation is materialized in the NS core, where, besides the Hall-drift, the ambipolar diffusion plays an important role for the magnetic field evolution. As an immediate consequence of $\omega_B\tau$ being larger than unity, the induction equation becomes predominantly nonlinear and the heat transport will tend to proceed parallel to the magnetic field. While the nonlinear induction equation comprises the multifaceted effects of the Hall drift, a significant deviation from isotropic heat transfer through the crust affects the surface temperature distribution of thermally emitting isolated NSs.

13.5.1 Hall-Drift in the Crust

In a NS's crust, where the positively charged ions are fixed to their lattice sites and no significant "flux" of the crustal matter is possible, the Hall drift is the only (nonlinear) modification of the usual Ohmic decay, expressed by the term $\propto \omega_B\tau$ in (13.10):

$$\dot{B} = -c\ \mathrm{curl}\left[\frac{c}{4\pi\sigma}\left(\mathrm{curl}B + \omega_B\tau(\mathrm{curl}B \times b)\right)\right]. \tag{13.10}$$

Many authors discussed the consequences of the Hall drift in isolated NSs, see, e.g., [19,34,41,44,56,79,88,89] and references therein. They discussed the redistribution of magnetic energy from an initially large-scaled (e.g., dipolar) field into small-scale components due to the nonlinear Hall term. Though the Hall drift itself is a non-dissipative process, the tendency to redistribute the magnetic energy into small scales may accelerate the field decay considerably.

Vaĭnshteĭn et al. [89] found that the Hall drift creates current sheets in configurations where a large density gradient exists. These current sheets can be sites for rapid ohmic dissipation of magnetic energy. Since crusts of NSs have a very large density gradient ($\sim 10^{14}\,\mathrm{g\,cm^{-3}}/10^5\,\mathrm{cm}$) [89] concluded that in current sheets created by a

crustal magnetic field this could decay an timescales of $3{,}000 \ldots 30$ years, depending on the location of the current sheets within the crust.

When starting with a large scale magnetic field the *Hall cascade* derived by [34] will generate small scale field components down to a scale length l_{crit}, where the ohmic dissipation begins to dominate the Hall drift. This cascade, however, can be accompanied or superimposed by a non-local (in the spectral space) magnetic energy transfer from a slowly, (ohmically) decaying, larger scale background field into smaller scale components. This *Hall instability* may have observable consequences [27, 71]. Moreover, the Hall instability and/or cascade are well conceivable processes which produce the strong surface field components of smaller scale ($l \sim R/10$), necessary for the pulsar mechanism to work [29].

The occurrence of the Hall instability is based on certain properties of the electric currents maintaining the background field: the motion of the electrons which create the currents must show a sufficiently strong shear [19, 72]. A linear stability analysis performed in a plan-parallel slab assuming for simplicity constancy for the transport coefficients reveals the mechanism of the instability.

With $B = B_0 + \delta b$, where B_0 denotes the background field (chosen such, that its Lorentz force is a gradient) and δb a small perturbation, the linearized dimensionless induction equation

$$\dot{\delta b} = \Delta\, \delta b - \mathrm{curl}(\,\mathrm{curl}\, B_0 \times \delta b \,+ \mathrm{curl}\, \delta b \times B_0), \;\; \mathrm{div}\, \delta b = 0 \qquad (13.11)$$

describes the behaviour of the perturbations of the reference state (for details see [71]). Along with the term $\mathrm{curl}\, \delta b \times B_0$ which is energy-conserving like the original Hall term $\mathrm{curl}\, B \times B$ here a second Hall term $\mathrm{curl}\, B_0 \times \delta b$ occurs which may well deliver or consume energy (to/from δb!) since in general the integral $\int_V (\mathrm{curl}\, B_0 \times \delta b) \cdot \mathrm{curl}\, \delta b\, dV$ will not vanish. This reflects the fact that (13.11) describes the behavior of only a part of the total magnetic field. Actually, perturbations may grow only on expense of the energy stored in the background field.

Performing a standard stability analysis, the perturbations $\delta b \propto \exp pt$ are found to have for a certain range of background field strengths positive growth rates p which correspond to characteristic growth times of $10^3 \ldots 10^5$ years; has the background field magnetar strength the growth time reduces to $\sim$10 yrs. Note, that from (13.11) the critical scale length below which ohmic dissipation dominates the Hall drift is $l_{crit} \leq L/(\omega_B \tau)$ (L being the scale length of the background field); at the same l_{crit} the Hall cascade ceases.

This rapid transfer of magnetic energy may cause observable consequences. The drain of energy from the large scale background field, which determines the rotational evolution by magneto-dipole radiation and stellar wind, weakens – at least episodically – the ability of that large scale field to spin down the NS. This should be reflected observationally by braking indices $n = 2 - P\ddot{P}/\dot{P}^2$ exceeding markedly the value $n = 3$ for a constant dipole. Such values have been found for a number of radio pulsars as old as $10^5 \ldots 10^6$ years [45]. Geppert and Rheinhardt [27] have shown that the Hall instability may reduce the dipolar field with a rate of $\sim 10^8\,\mathrm{G\,yr^{-1}}$, in coincidence with some of the observations.

Another consequence of the Hall cascade and/or instability is the generation of small scale field structures close to the NS surface, which automatically cause small scale Lorentz forces and Joule heating sources. A typical structure which may arise due to the Hall instability is shown in Fig. 13.11. It is obtained by solving the Hall induction equation at a certain moment of the NS's cooling, reasonably assuming that for NSs older than 10^5 yrs its cooling time scale is larger than the growth time of the Hall instability in case of $B_0 \gtrsim 10^{13}$ G. Moreover, in calculating that structure a realistic crustal density profiles has been applied. Thus, in comparison with (13.11), the Hall induction equation is no longer dimensionless and has an additional term. For a background field of 3×10^{13} G the maximum growth time of the perturbations is on the order of 3×10^3 years; it scales inversely with the background field strength. The generated small scale poloidal field structures have just length scales as required by the Ruderman and Sutherland pulsar model to drive the pulsar's radio emission [77]. Since the currents which maintain these small scale fields are circulating in relatively low density crustal layers, they decay on a timescale of $\sim 10^6$ years after the Hall instability lost its power because the energy loss of the background field became so large that it is no longer unstable.

It is conceivable that these consequences of the Hall-instability in case of magnetar background field strengths ($\geq 10^{15}$ G) are responsible both for the bursts observed in the SGRs and the thermal emission of SGRs and AXPs.

13.5.2 Temperature Distribution in the Magnetized Crust

In the crust of NSs electrons are the by far dominating carriers of the heat flow. By collisions with impurities and phonons in the crystallized crust and with ions in its liquid layer they transfer the heat following the temperature gradient from the core through the crust and its envelope towards the surface where it is finally irradiated. In case of weak magnetization, the heat will be transferred almost isotropically and a uniform surface temperature T_s would be seen by an observer.

Observations of many isolated NSs, however, indicate with great significance that the surface temperature T_s is not uniform but has (in some cases even large) meridional gradients. For slowly rotating, radio quiet, isolated NSs as the "Magnificent Seven" the magnetic field can be the source of a significant deviation from an isotropic surface temperature distribution. Outstanding common features as seen for the "Magnificent Seven" are the apparent smallness of their radii derived from X-ray spectra, the slow rotation, and the existence of a remarkable optical excess (see, e.g., [39, 61]).

The motion of the electrons is free parallel to the field lines but impeded by Larmor rotation perpendicular to them, the tensor component of the heat conductivity perpendicular to the field lines is strongly suppressed by the square of the magnetization parameter. Therefore, it is suggesting to consider the magnetic field to be the primary source for the observed anisotropies.

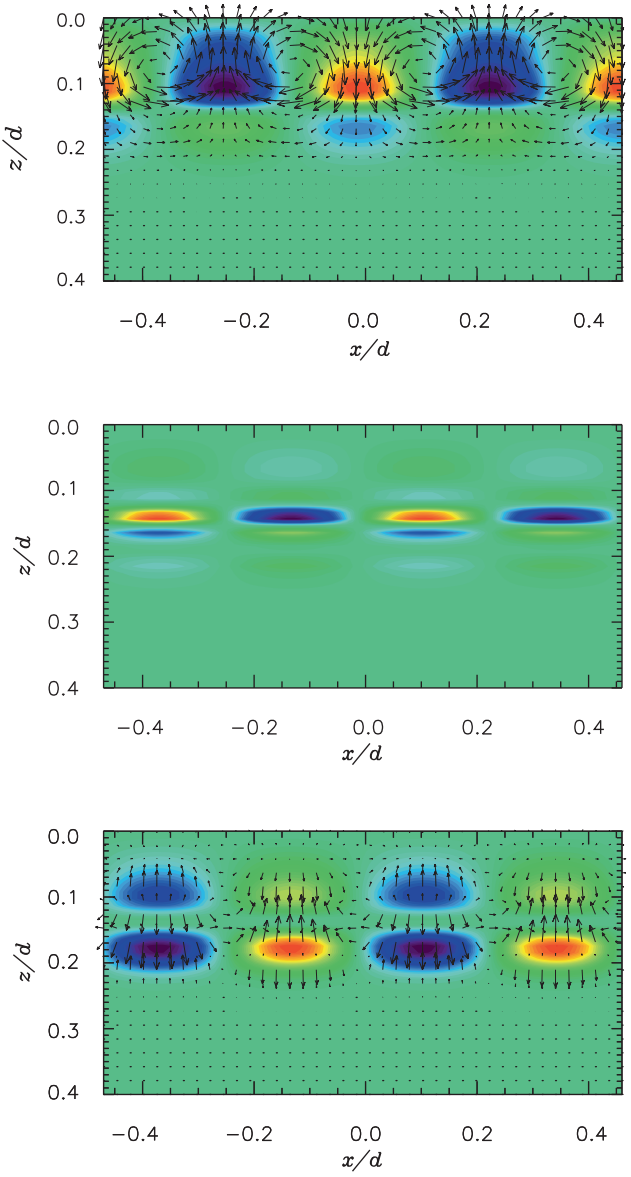

Fig. 13.11 Consequences of the Hall drift. *Upper panel*: typical structure of the small scale field generated on a growth time of 3×10^3 years by the Hall instability from a large scale toroidal crustal field of 3×10^{13} G. The thickness of the crust is $d \approx 3,800$ m. Thus, the typical meridional and azimuthal scale of the perturbations is about 1 km. The field is concentrated in a depth of about 400 m below the NS surface $z = 0$. Colour encoding corresponds to the azimuthal field component (for details see [74]). *Middle panel*: Perturbation of the Joule heat sources density $\propto 2\,\mathrm{curl}\,B_0 \times \mathrm{curl}\,\delta b$ in arbitrary units corresponding to the perturbation field shown in the upper panel. Positive (*Green to red*), negative (*green to blue*) deviations from the background heat sources. *Lower panel*: Lorentz force density perturbations $\propto \mathrm{curl}\,B_0 \times \delta b + \mathrm{curl}\,\delta b \times B_0$ corresponding to the perturbation field shown in the *upper panel*. The *arrows* denote radial and meridional force components, colour encoded is the azimuthal force component

The thermal evolution of the crust is determined by the energy balance equation which has, in axial symmetry and with general relativistic effects included, the following form:

$$\frac{e^{-\Lambda}}{r^2}\frac{\partial}{\partial r}(r^2\, F_r\, e^{2\Phi}) + \frac{e^{2\Phi}}{r\,\sin\theta}\frac{\partial}{\partial\theta}(\sin\theta F_\theta) = \left(e^{\Phi}C_\nu\frac{dT}{dt} + e^{2\Phi}Q_\nu\right), \quad (13.12)$$

where T is the local temperature, $e^{\Phi(r)}, e^{\Lambda(r)}$ are the redshift and length correction factors, F_r and F_θ are the local radial and meridional components of the heat flux and r and θ the local coordinates. Q_ν and C_ν are the neutrino emissivity and specific heat, respectively, per unit volume. Studying stationary configurations and neglecting neutrino energy losses, the right-hand side of (13.12) can be set to zero, and it results in

$$\frac{1}{x^2}\frac{\partial}{\partial\tilde{x}}(x^2\,\tilde{F}_r) + \frac{1}{x\,\sin\theta}\frac{\partial}{\partial\theta}(\sin\theta\tilde{F}_\theta) = 0\,, \quad (13.13)$$

where $x = r/R$, $\partial/\partial\tilde{x} \equiv e^{-\Lambda}\partial/\partial x$ and $\tilde{F}_{r,\theta} \equiv e^{2\Phi}F_{r,\theta}/R$. While in the envelope, the outer shell with densities $\rho \leq 10^{10}\,\mathrm{g\,cm^{-3}}$, the magnetic field has both classical and quantum effects on the electron motion, in the crustal regions below the envelope, the quantized motion of electrons transverse to the magnetic field lines doesn't play any rôle for the magnetic modification of the heat transport and the field acts dominantly via the classical Larmor rotation of the electrons. The components of the heat conductivity tensor $\hat{\kappa}$ and that of the temperature gradient determine the heat flux vector

$$\begin{aligned} e^{\Phi}F &= -\hat{\kappa}\cdot\nabla(e^{\Phi}T) \\ &= -\frac{\kappa_0}{1+(\omega_B\tau)^2} \\ &\quad\times\left[\nabla(e^{\Phi}T) + (\omega_B\tau)^2\, b\,(\nabla(e^{\Phi}T)\cdot b) + \omega_B\tau\, b\times\nabla(e^{\Phi}T)\right]. \end{aligned} \quad (13.14)$$

For a prescribed magnetic field structure, which determines the components of the heat conductivity tensor, (13.13) is solved with the heat flux components given by (13.14) until a stationary solution is found. The temperature at the crust–core interface is taken fixed. For the outer boundary condition the analytical expression derived by [68] is applied. It comprises the relation between the temperatures the bottom and the surface of the envelope, taking into account all the complex physics of the heat flux through the strongly magnetized envelope.

The essence of the effect of a strong magnetic field is that the heat flux F is forced to be almost aligned with the local field B when $(\omega_B\tau)^2 \gg 1$ since then the component of the thermal conductivity tensor $\hat{\kappa}$ parallel to B is $\kappa_\parallel = \kappa_0$ while the components in the perpendicular directions are $\kappa_\perp = \kappa_0/(1+(\omega_B\tau)^2) \ll \kappa_\parallel$.

For a magnetic field configuration consisting of axially symmetric toroidal and poloidal constituents, the azimuthal component of the heat flux F_φ is independent of φ but certainly *not* equal to zero, in spite of having $\partial T/\partial\varphi \equiv 0$. Since for strong fields heat essentially flows along the field lines, when B^{tor} is dominant, F_φ will

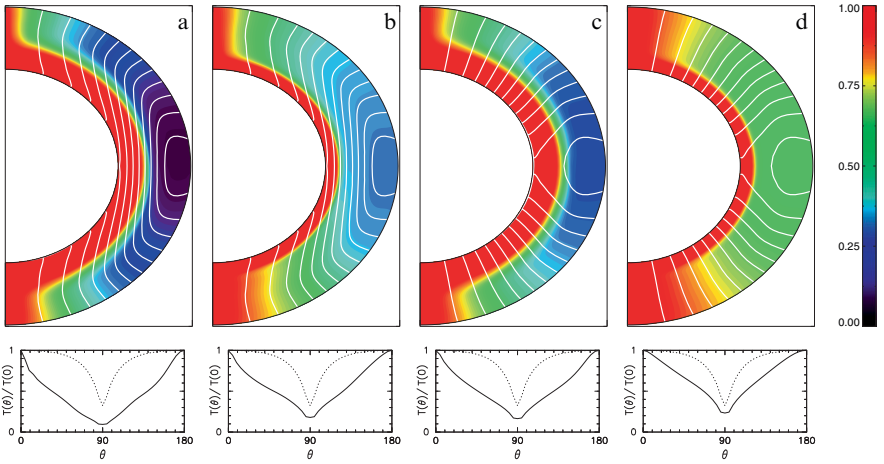

Fig. 13.12 Thermal structure of the NS crust between the crust–core interface and the bottom of the envelope at $\rho = 10^{10}\,\mathrm{g\,cm^{-3}}$. The radial scale of the crust is stretched by a factor of 5 for clarity. The magnetic field includes the three constituents B^{crust}, B^{core} and B_0^{tor}. In *panels a and b* the crustal poloidal field dominates the core field ($B_0^{\mathrm{crust}} = 7.5 \times 10^{12}$ G, $B_0^{\mathrm{core}} = 2.5 \times 10^{12}$ G) while in *panels c and d* the core field is dominant ($B_0^{\mathrm{crust}} = 2.5 \times 10^{12}$ G, $B_0^{\mathrm{core}} = 7.5 \times 10^{12}$ G. In *all panels* $B_0^{\mathrm{tor}} = 3 \times 10^{15}$ G. Here, the index "0" denotes the polar surface (for the crustal and core poloidal field) and the maximum (for the crustal toroidal field) values. In the *lower panels* the *full lines* show the resulting surface temperature profiles $T_{\mathrm{s}}(\theta)$ and the *dotted lines* illustrate the same profile when an isothermal crust is assumed, i.e., if the magnetic field would influence the heat transfer in the envelope only

also be much larger than F_θ and F_r and produce a winding of the heat flow around the symmetry axis: F follows the shortest possible paths with the highest possible conductivity and this winding effectively acts as a heat blanket.

Typical crustal temperature distributions with the corresponding surface temperature profiles are shown in Fig. 13.12. A noticeable general feature is the asymmetry between the two magnetic hemispheres, resulting from the asymmetry of the total field B, since the dipolar poloidal crustal and star centered field constituents, B^{crust} and B^{core}, are anti-symmetric with respect to the equatorial plane, while the crustal toroidal field, B^{tor}, (as chosen here) is symmetric. In cases where the poloidal component is almost comparable to the toroidal one, the asymmetry is barely detectable but in all other cases it is clearly visible. The star centered core field, which superimposes the poloidal and toroidal crustal fields causes practically no deviations from isothermality of the crust for densities $\rho > 10^{10}\,\mathrm{g\,cm^{-3}}$. In the envelope, however, that core field produces a meridional temperature gradient as shown by [35], recently refined by [68]. If sufficiently strong, it may counteract the effects of the crustal field and tries to establish a temperature distribution closer to crustal isothermality. For a detailed discussion see [25].

The very distinct surface temperature distributions resulting from significantly non-isothermal crusts have several immediate observational consequences. In presence of a strong toroidal field in the crust, the channeling of heat toward the

polar regions results in the appearance of two hot spots of very reduced size in comparison with the hot polar regions which would appear in case of an almost isothermal crust, having the magnetic field effects caused by a star centered field only. Figure 13.13 shows five examples of surface temperature distributions and the

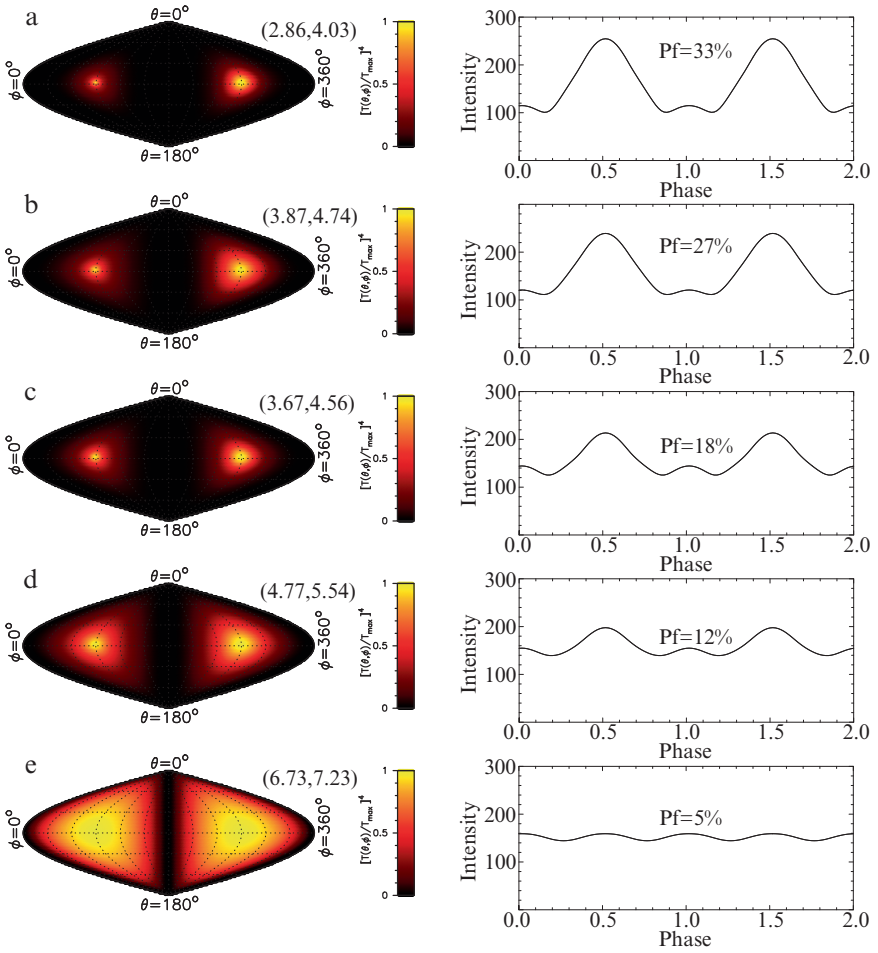

Fig. 13.13 Surface temperature distributions (*left panels*) in an area preserving-representation with a color scale following the emitted flux ($\propto T^4$). *Panels a–d* use the internal field structures of the corresponding panels in Fig. 13.12 while *panel e* assumes an isothermal crust. In contrast to Fig. 13.12 the dipolar symmetry axis is in all cases oriented in the equatorial plane defined with respect to the rotation axis $\theta = 0, \pi$. The *right panels* show the resulting pulse profiles (in arbitrary units) which an observer, also located in the equatorial plane, would detect. In all cases the core temperature is the same but the star's distance has been adjusted to give the same average flux (see Fig. 13.14). Number pairs within parentheses give ($T_{\rm ave}$, $T_{\rm eff}$) with $T_{\rm ave}$ the optical flux and $T_{\rm eff}$ for the X-ray flux (see [25]), resp., in units of 10^5 K. All five models have almost the same maximum surface temperature $T_{\rm max} \simeq 8.45 \times 10^5$ K but different minimal temperatures

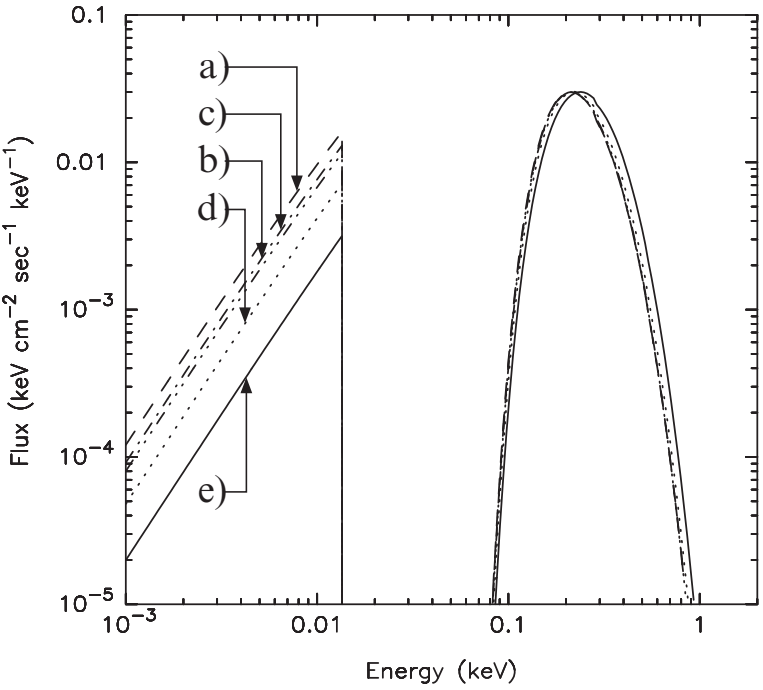

Fig. 13.14 Observable spectra for the five surface temperature distributions and pulse profiles, "a" to "e", shown in Fig. 13.13. The stars, with radius $R = 11.4$ km (radius seen at infinity $R_\infty = 14.28$ km) and $M = 1.4\,M_\odot$, are assumed to be at distances of 100, 142, 131, 202, and 220 pc, resp., to produce almost identical observable spectra in the X-ray band (column density $N_{\rm H} = 1 \times 10^{20}$ cm^{-2} for interstellar absorption) but resulting in significantly different fluxes in the optical range

resulting observable pulse profiles of the X-ray light curve. Naturally, models with the smallest hot spots result in the highest pulsed fractions, P_f, with values above 30%, in contrast to the case of an almost isothermal crust which results in $P_f \sim 5\%$. The composite blackbody spectra resulting from the same five cases of Fig. 13.13 are shown in Fig. 13.14. The distances to the model stars have been adjusted to give the same maximum flux in the X-ray band, and thus very similar X-ray spectra. Given this adjustment the differences between the relative areas of the hot and cold regions in the various cases result in differences in the predicted optical fluxes. Comparison of the surface temperature plots (left panels of Fig. 13.13) with the relative optical fluxes shows a direct correlation between the relative size of the cold region with the optical flux. Obviously, the presence of two small warm regions separated by an extended cold belt has two immediate observational consequences. The first one is that the observable pulsed fraction in the X-ray band can be very large, above 30% assuming isotropic blackbody emission. As the second one, the emission of the cold region contributes little to the X-ray flux but dominates the detectable flux in the optical range, appearing as an "optical excess". These successes in explaining

the observations are strong indicators, that the heat transfer through the strongly magnetized crust of isolated NSs is indeed responsible for the small hot spots.

However, the above discussed dipolar axisymmetric field configurations produce symmetric, but not sinusoidal, light-curves. For RBS 1223 and RX J0720.4−3125 the light-curves are clearly not symmetric. This could be interpreted by assuming that the hot spots are not in antipodal position but have a meridional distance of $\approx 160^\circ$ [38, 40, 78]. The non-uniqueness of the light curve interpretation allows also an axisymmetric arrangement of hot regions. A superposition of dipolar and quadrupolar magnetic field constituents could as well be able to produce precise fits of the observed pulse profiles of the "Magnificent Seven" [99].

Indeed, very recently [62] have shown that a crustal field configuration consisting of dipolar and quadrupolar parts in both the toroidal and the poloidal constituents produces a warm equatorial belt in addition to the polar hot spots. The corresponding surface temperature distribution explains convincingly well all observational evidences seen for RX J0720.4−3125, a prominent member of the "Magnificent Seven", namely the X-ray spectrum, the "optical excess", the pulsed fraction, the spectral feature around 0.3 keV, and the light curves including their strong anti-correlation of the hardness ratio with the pulse profiles in both the hard and the soft band. It is compelling that these model calculations rely on an axisymmetric field configuration instead of a non-axisymmetric one which could also explain the light curve by the non-alignment of the northern and southern hot spot. The latter model, however, implies a complicated structure of the currents which maintain the non-axisymmetric field. Since it is hard to believe that such a field can be stable over a long period, the model of [62] is perhaps likely to be realized in isolated NSs.

13.6 Concluding Remarks

The magnetic field of NSs is a complex entity, maintained by currents which circulate both in the core and in the crust. While the former support essentially the large scale, long living ($\gtrsim 10^8$ yrs) dipolar field which is responsible for the rotational evolution, the latter have a considerably shorter decay time ($\sim 10^{6\ldots7}$ yrs) and cause the anisotropic heat transport through the crust, its cracking, and the Joule heating. The crustal field may consist of a toroidal and poloidal part. The large scale modes of the latter join at the surface the star centered core field. For the typical pulsar lifetime the core and crust field "collaborate" to establish the conditions for radio emission. Thus, a strong sub-surface toroidal field could provide via Hall-drift induced processes the small scaled field structures necessary to produce sufficient electron positron pairs in the polar gap. Sometimes it is argued by means of population synthesis results that the NS magnetic field decays – if at all – on timescales which exceed the typical pulsar lifetime ($\sim 10^7$ yrs) considerably. The population syntheses, however, reflect almost only the effect of the core field on the rotational evolution, which is affected by the poloidal part of the crust field only during its shorter lifetime.

At the discussed turning points the NS's magnetic field will evolve into qualitatively different ways. Should the inborn field be stabilized against MHD instabilities, the NS has a perspective as magnetar, otherwise it becomes a "standard" radio pulsar. Depending on the power of fallback accretion and on the electric conductivity of the crust, the NS will appear as a radio pulsar soon after its creation in a supernova or will evolve with a weak surface field which has minor braking effects on the rotation. If temperature gradients in the crust are strong enough and maintained for a sufficient long period, a magnetic field may be rapidly generated and the NS becomes a pulsar in spite of heavy fallback accretion. Exceeds the magnetization parameter significantly unity locally and/or temporally both the magnetic and thermal evolution will proceed differently from that of a weakly magnetized NS. This may have observational consequences both for the rotational and cooling history.

Although the basic ideas of the physical processes discussed above are known, there is still a lot of work necessary to understand them in more detail. This concerns both the properties of NS matter (e.g., its conductivity) and the processes around the NS's birth (initial α, P, and field configuration) as well as the nonlinear and non-axial symmetric processes of field evolution. Since the NS's life is so intimately connected with the magnetic field, any better insight into its evolution will return a better understanding of the physics of the most fascinating stellar objects in the universe.

References

1. S. Akiyama, C. Wheeler, D. Meier, & I. Lichtenstadt: ApJ **584**, 954 (2003)
2. A. Alpar: ApJ **554**, 1245 (2001)
3. A. Alpar, S. Langer, & J. Sauls: ApJ **282**, 533 (1984)
4. W. Becker & B. Aschenbach: Proceedings of the 270. WE-Heraeus Seminar on Neutron Stars, Pulsars, and Supernova Remnants. MPE Report 278. Edited by W. Becker, H. Lesch, and J. Trümper. Garching bei München: Max-Plank-Institut für extraterrestrische Physik, 2002, p. 64
5. W. Becker & J. Trümper: A&A **326**, 682 (1997)
6. D. Bhattacharya & E. van den Heuvel: Phys Rep **203**, 1 (1991)
7. R. Blandford, J. Applegate, & L. Hernquist: MNRAS **204**, 1025 (1983)
8. A. Bonanno, V. Urpin, & G. Belvedere: A&A **451**, 1049 (2006)
9. J. Braithwaite: ArXiv:astro-ph/0512182
10. J. Braithwaite: A&A **453**, 87 (2006)
11. J. Braithwaite & A. Nordlund: A&A **450**, 1077 (2006)
12. J. Braithwaite & H. Spruit: Nature **431**, 819 (2004)
13. J. Braithwaite & H. Spruit: A&A **450**, 1097 (2006)
14. S. Bruenn, E. Raley, & A. Mezzacappa: arXiv:astro-ph/0404099 (2004)
15. V. Burwitz, F. Haberl, F. Neuhäuser, P. Predehl, J. Trümper, & V. Zavlin: A&A **399**, 1109
16. H. Chau, K. Cheng, & K. Ding: ApJ **399**, 213 (1992)
17. R. Chevalier: ApJ **346**, 847 **345**, 847 (1989)
18. M. Colpi, S. Shapiro, & I. Wassermann: ApJ **470**, 1075 (1996)
19. A. Cumming, P. Arras, & E. Zweibel: ApJ **609**, 999 (2004)
20. A. Cumming, E. Zweibel, & L. Bildsten: ApJ **557**, 958 (2001)
21. C. Cutler & L. Lindblom: ApJ **314**, 234 (1987)
22. A. Dolginov & V. Urpin: Ap&SS **69**, 259 (1980)

23. E. Flowers & M. Ruderman: ApJ **215**, 302 (1977)
24. U. Geppert, M. Küker, & D. Page: A&A **426**, 267 (2004)
25. U. Geppert, M. Küker, & D. Page: A&A **457**, 937 (2006)
26. U. Geppert, D. Page, & T. Zannias: A&A **345**, 847 (1999)
27. U. Geppert & M. Rheinhardt: A&A **392**,1015 (2002)
28. U. Geppert & M. Rheinhardt: A&A **456**, 639 (2006)
29. U. Geppert, M. Rheinhardt, & J. Gil: A&A **412L**, 33 (2003)
30. U. Geppert & H.-J. Wiebicke: A&AS **87**, 217 (1991)
31. U. Geppert & H.-J. Wiebicke: A&A **300**, 429 (1995)
32. J. Gil, G. Melikidze & U. Geppert: A&A **407**, 315 (2003)
33. O. Gnedin, D. Yakovlev, & A. Potekhin: MNRAS **324**, 725 (2001)
34. P. Goldreich & A. Reisenegger: ApJ **395**, 250 (1992)
35. G. Greenstein & G. Hartke: ApJ **271**, 283 (1983)
36. E. Gudmundsson, C. Pethick, & R. Epstein: ApJ **272**, 286 (1983)
37. F. Haberl: AdSpR **33**, 638 (2004)
38. F. Haberl: MPE Report **288**, 29; arXiv:astro-ph/0510480 (2005)
39. F. Haberl: Ap&SS **308**, 181 (2007)
40. F. Haberl, R. Turolla, C. de Vries et al., A&A **451**, L17 (2006)
41. P. Haensel, V. Urpin, & D. Yakovlev: A&A **229**, 133 (1990)
42. A. Harding & D. Lai: arXiv:astro-ph/0606674 (2006)
43. A. Heger, S. Woosley, & H. Spruit: ApJ **626**, 350 (2005)
44. R. Hollerbach & Rüdiger: MNRAS **347**, 1273 (2004)
45. S. Johnston & D. Galloway: MNRAS **306**, l50
46. P. Jones: PhRvL **93**, 221101 (2004)
47. W. Keil, H.-T. Janka, & E. Müller: ApJ **473**, L111 (1996)
48. D. Konenkov & U. Geppert: MNRAS **360**, 1052, (2000)
49. F. Krause & K.-H. Rädler: Mean-Field Magnetohydrodynamics and Dynamo Theory. Akademie/Pergamon, Berlin/Oxford (1980) 271 pages
50. R. Kulsrud: Plasma Physics for Astrophysics. Princeton University Press, Princeton (2007)
51. P. Markey & R. Tayler: MNRAS **163**, 77, (1973)
52. J. Miralles, J. Pons, & V. Urpin: ApJ **543**, 1001 (2000)
53. J. Miralles, J. Pons, & V. Urpin: ApJ **574**, 356 (2002)
54. J. Miralles, J. Pons, & V. Urpin: ApJ **420**, 245 (2004)
55. A. Muslimov & D. Page: ApJ **440**, L77 (1995)
56. T. Naito & Y. Kojima: MNRAS **266**, 597 (1994)
57. C. Ott, A. Burrows, T. Thompson, E. Livne, & R. Walder: ApJS **164**, 1300 (2006)
58. D. Page, U. Geppert & F. Weber: Nucl. Phys. A **777**, 497, (2006)
59. D. Page, U. Geppert & T. Zannias: A&A **360**, 1052 (2000)
60. J. Pérez-Azorín, J. Miralles, & J. Pons: A&A **433**, 1009 (2006)
61. J. Pérez-Azorín, J. Miralles, & J. Pons: A&A **451**, 275 (2005)
62. J. Pérez-Azorín, J. Pons, J . Miralles, & G. Miniutti: astro-ph/0603752 (2006)
63. K. Petrovay & J. Zsago: MNRAS **296**, 245 (1998)
64. E. Pitts & R. Tayler: MNRAS **216**, 139 (1985)
65. P. Podsiadlowski, S. Rappaport, & E. Pfahl: ApJ **565**, 1107 (2002)
66. J. Pons, S. Reddy, M. Prakash, J. Lattimer, & J. Miralles: ApJ **513**, 780 (1999)
67. J. Pons, F. Walter, J. Lattimer, M. Prakash, R. Neuhäuser, & P. An: ApJ **564**, 981 (2002)
68. A. Potekhin & D. Yakovlev; A&A **374**, 213 (2001)
69. K. Prendergast: ApJ **123**, 498 (1956)
70. A. Reisenegger, J. Prieto, R. Benguria, D. Lai, & P. Araya: in, Magnetic Fields in the Universe: From Laboratory and Stars to Primordial Structures. AIP Conf. Proc., 784, 263 (2005)
71. M. Rheinhardt & U. Geppert: PhRvL **88**, 101103 (2002)
72. M. Rheinhardt & U. Geppert: PhRvE **71**, 038301 (2005)
73. M. Rheinhardt & U. Geppert: A&A **435**, 201 (2005)
74. M. Rheinhardt, D. Konenkov, & U. Geppert: A&A **420**, 631 (2004)
75. P. Roberts: Astron. Nachr. **302**, 65 (1981)

76. M. Ruderman: arXiv: astro-ph/0510623 (2005)
77. M. Ruderman & P. Sutherland: ApJ **196**, 51 (1975)
78. A. Schwope, V. Hambaryan, F. Haberl,& C. Motch: A&A **441**, 597 (2005)
79. D. Shalybkov & V. Urpin: A&A **321**, 685 (1997)
80. H. Spruit: A&A **349**, 397 (1999)
81. H. Spruit: A&A **381**, 397 (2002)
82. R. Tayler: MNRAS **161**, 365 (1973)
83. C. Thompson & R. Duncan: ApJ **408**, 194 (1993)
84. T. Thompson, E. Quataert, & A. Burrows: ApJ **620**, 861 (2005)
85. J. Trümper, V. Burwitz, F. Haberl,& V. Zavlin: NuPhS **132**, 560 (2004)
86. V. Urpin, U. Geppert, & D. Konenkov: MNRAS **295**, 907 (1998)
87. V. Urpin, S. Levshakov, & D. Yakovlev: MNRAS **219**, 703 (1986)
88. V. Urpin & D. Shalybkov: A&A **294**, 117 (1995)
89. S. Vaĭnshteĭn, S. Chitre, & A. Olinto: PhRvE **61**, 4422 (2000)
90. S. Vaĭnshteĭn & Y. Zel'dovich: Sov. Phys. Usp. **15**, 159 (1972)
91. M. van Adelsberg, D. Lai, A. Potekhin, & P. Arras: ApJ **628**, 902 (2005)
92. L. Villain, J. Pons, P. Cerdá-Durán, & E. Gourgoulhon: A&A **418**, 283 (2004)
93. H.-J. Wiebicke & U. Geppert: A&A **309**, 203 (1996)
94. F. Winterberg: Phys. Lett. A **336**, 188 (2005)
95. G. Wrihgt: MNRAS **162**, 339 (1973)
96. D. Yakovlev, A. Kaminker, O. Gnedin, & P. Haensel: Phys. Rep. **354**, 1 (2001)
97. D. Yakovlev, D. Shalybkov: Ap&SS **176**, 191 (1991)
98. S. Zane & R. Turolla: AdSpR **35**, 1162 (2005)
99. S. Zane & R. Turolla: MNRAS **366**, 727 (2006)
100. V. Zavlin & G. Pavlov: MmSAI **75**, 458 (2004)
101. J. Ziman: Principles of the Theory of Solids. Cambridge University Press, Cambridge (1972)

Chapter 14
Pulsar Spin, Magnetic Fields, and Glitches

Malvin Ruderman

14.1 Introduction

As the number of nucleons in stable atomic nuclei increases, their neutron to proton ratios grow larger. So does the fraction of each atom's electrons which is contained within its nuclear volume. If an atomic weight (A) were to exceed 10^4 that atom would resemble a canonical neutron star: a huge nucleus consisting mainly of neutrons, several percent protons, and an electron cloud almost entirely contained within the nucleus. In the commonly observed nuclei this limit cannot be reached because nucleon-nucleon attractive forces can no longer prevent nuclear fission from Coulomb repulsion when A exceeds 300. However, if A were to reach 10^{55}, gravitational attraction would become sufficiently strong to hold the star together and we can have a stable conventional neutron star. In it, the dominant neutron sea is a quantum fluid with properties very similar to those of very low temperature superfluid Helium. The much less abundant protons form a superconductor whose properties closely resemble those of a BCS (Bardeen, Cooper, Schrieffer) electron superconductor. Both of these quantum fluids are well understood and their expected properties confirmed in laboratory experiments. Most astrophysically relevant features do not depend on the fermion masses or fluid densities and lead to the model presented below for various phenomena in the development of a canonical neutron star.

In a cooled core below the relatively thin crust of a spinning neutron star (NS) superconducting protons (SC-p)coexist with much more abundant superfluid neutrons (SF-n) to form a giant atomic nucleus which contains within it a neutralizing sea of degenerate ultra-relativistic electrons. Superfluid neutrons in a star with a spin-period $P(sec)$ rotate by forming a nearly uniform array of co-rotating quantized

M. Ruderman
Department of Physics and Columbia Astrophysics Laboratory, Columbia University, New York, NY, USA
e-mail: mar@phys.columbia.edu

W. Becker (ed.), *Neutron Stars and Pulsars,* Astrophysics and Space Science Library 357,

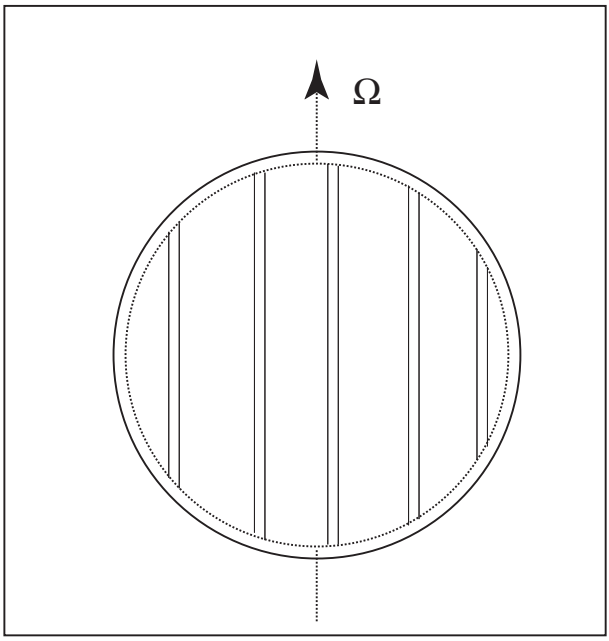

Fig. 14.1 Five of the $\sim 3 \times 10^{16}/P\,(\mathrm{sec})$ SF-n vortex lines in the superfluid core of a cooled neutron star

vortex lines parallel to the star's spin axis. This array has a number of vortices per unit area density $n_v \sim 10^4\ P^{-1}\ \mathrm{cm}^{-2}$ (cf. Fig. 14.1).

The array must contract (expand) when the NS spins up (down). Vortices at distance $r_\perp$ from the spin-axis generally move away from the NS spin-axis with a velocity $r_\perp(\dot{P}/2P)$ until $r_\perp$ reaches the core's neutron superfluid radius,only slightly less than the stellar radius(R). A stellar magnetic field passing below the stellar crust (the outer km. of the R = 10 km. NS) must, in order to penetrate through the core's superconducting protons, become a very dense array of quantized flux-tubes (area density $n_\phi \sim 5 \times 10^{18}\ \mathrm{B}_{12}\ \mathrm{cm}^{-2}$ with B the local average magnetic field). Each tube carries a flux of $2 \times 10^{-7}\ \mathrm{G\,cm}^2$ and a magnetic field $B_c \sim 10^{15}\ \mathrm{G}$.[1] There is negligible interaction between flux tubes as long as $B \ll B_c$. The initial magnetic field within the core of a newly born hot neutron star is expected to have both toroidal and very non-uniform poloidal components. The web of flux-tubes formed after cooling to the transition to superconductivity is then much more complicated and irregular than the neutron vortex-array. It also is of the order of 10^{14} times more dense (cf. Fig. 14.2).

[1] This assumes Type II proton-superconductivity in the NS core below the crust, the common result of many calculations. If it were Type I, with many thin regions with $B >$ several B_c, and $B \sim 0$ in between [17], the impact on surface B of changing NS spin proposed below would not change significantly. If, however, the locally averaged B inside the NS core exceeds a critical field somewhat greater than B_c, the core's protons would not become superconducting. This may well be the case for some (or all) "magnetars".

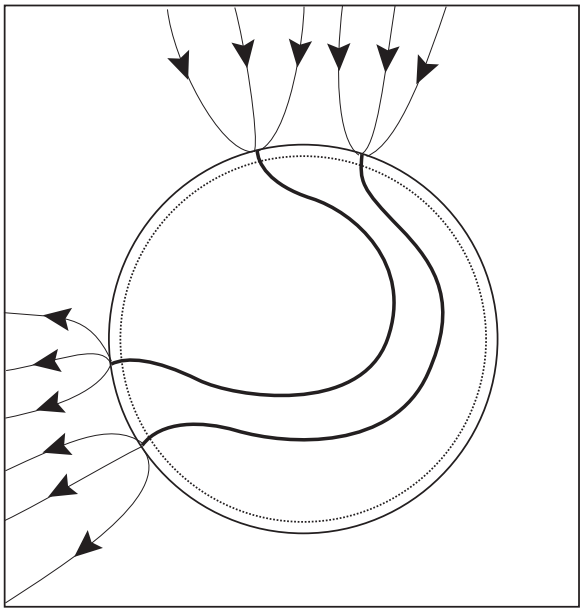

Fig. 14.2 Two of the $6 \times 10^{31} B_{12}$ magnetic flux-tubes in the superconducting core of a NS. Each flux-tube has a flux of 2×10^{-7} G cm^2 (the same as that of a laboratory BCS electron superconductor) and a magnetic field $B_c \sim 10^{15}$ G

Because of the velocity dependence of the short range nuclear force between neutrons and protons, there is a strong interaction between the neutron-superfluid's vortex-lines and the proton-superconductor's flux-tubes if they come closer to each other than about 10^{-11} cm. Consequently, when $\dot{P} \neq 0$, flux-tubes will be pushed (or pulled) by the moving neutron vortices [9, 12, 16, 24, 27, 30, 31, 34], (cf. also Fig. 14.3). A realistic flux-tube array will be forced to move along with a changing SF-n vortex array which threads it as long as the force at a vortex-line flux-tube junction does not grow so large that vortex-lines cut through flux-tubes. In spinning-down pulsars cold enough to have SF-n cores ($T_{core} \lesssim 3 \times 10^8$ K) outward moving n-vortex velocities are generally less than a cm/day (about the vortex array's expansion speed in the Crab pulsar's core). During NS spin-up to millisecond pulsars the inward moving n-vortex velocities are usually <cm/century. The drag on flux-tubes caused by such slow movement is too small to cause cut-through of flux-tubes by moving n-vortices. Jones [14] has recently found that electron scattering on flux-tubes allows easier passage of flux-tubes through the SF-n than had been estimated. In addition, an expected motion-induced flux-tube bunching instability could more easily allow co-motion of flux-tubes with the local electron plus SC-p fluid in which they are embedded [25]. If not for the anchoring of flux-tubes at the base of the metallic crust (idealized in Fig. 14.4a) flux-tubes positions at the core–crust interface could closely follow changes in the core's SF-n vortex array. (Large forces resulting in considerable cut-through may also come from stretching toroidal bundles of flux

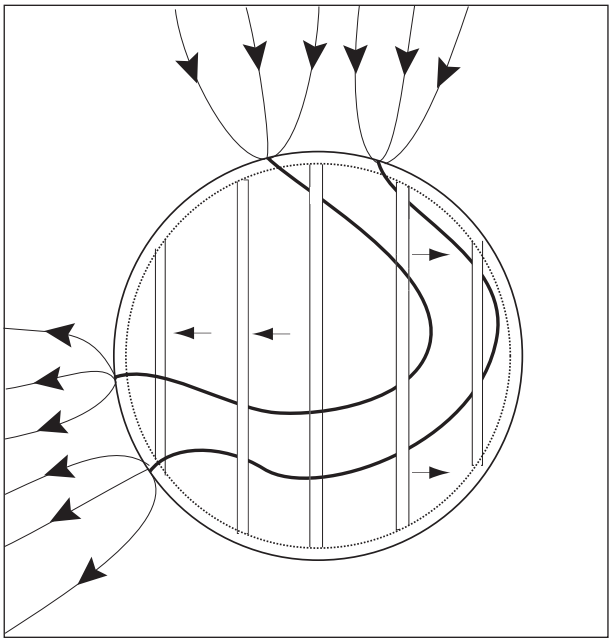

Fig. 14.3 Interacting flux-tubes and vortex-lines during initial spin-down

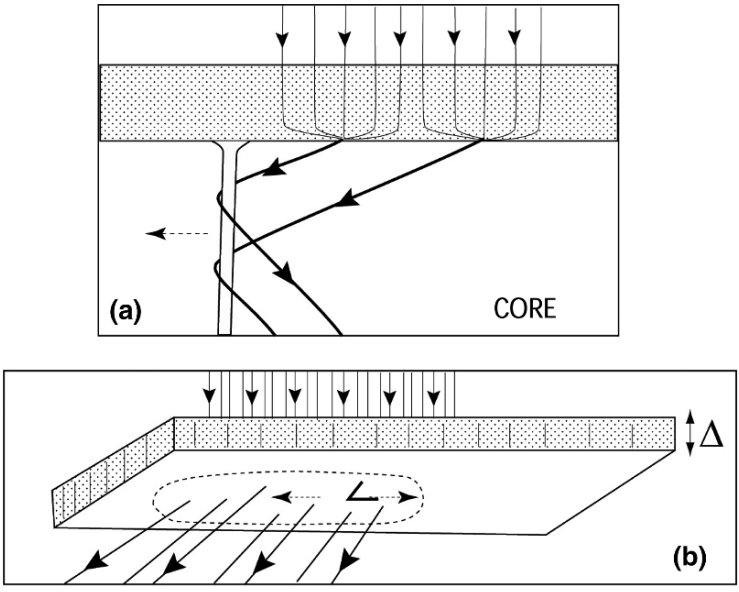

Fig. 14.4 **a** A moving quantized vortex-line in a NS core's superfluid neutrons puling a pair of the core's proton superfluid quantized flux-tubes anchored in the star's solid, conducting crust (*shown dotted*). **b** The scale L of (14.1) for shearing stress on the crust from flux-tube pull

tubes by an expanding n-vortex array. Further study is needed of the evolution of this component and its consequences.

The magnetic field at the crust-surface should always be almost equal to the average field from the flux-tubes at the core–crust interface below it on time-scales exceeding the "impurity"-dominated ohmic (Eddy) diffusion time through the crust, estimated to be several million years. On much shorter time-scales the crust acts like a thin, incompressible, solid, shearable, breakable(?), perfect conductor. Because of crustal stratification and the huge gravitational field it yields mainly to huge tangential shear-stresses (from $BB_c/8\pi \sim 3 \times 10^{17} B_{12}$ tons cm^{-2}) larger than its yield strength. This happens on scales L (>crust thickness Δ; Fig. 14.4b) such that the total shearing force on a large crustal area can no longer be balanced by the restraining stress from the rest of the star on that area's perimeter. The crust yield strength is exceeded when a shear stress of

$$\frac{BB_c}{8\pi} L^2 \gtrsim (\sigma\, \theta_m \Delta) L \ , \tag{14.1}$$

or

$$L \gtrsim \frac{10^6 \mathrm{cm}}{B_{12}} \sim \frac{R}{B_{12}} \tag{14.2}$$

for typical estimates of crust shear modulus $\sigma \sim 10^{30}$ dyne cm^{-2}, $B_c \sim 10^{15}$ G, crust-thickness $\Delta \sim 10^5$ cm, and maximum sustainable strain $\theta_m \sim 3 \times 10^{-4}$, is reached. This forms the basis for a very simple model for describing predicted changes in pulsar magnetic fields during NS spin-up or spin-down which agrees well with different families of pulsar observations. On small scales (<L) the magnetic field through the crust of a NS can be frozen locally in the crust it penetrates for the first several 10^6 years after the crust solidifies (several hours after the formation of the NS). It changes during this long epoch only when huge $BB_c/8\pi$ shearing stresses overstrain the crust on large scales (>L), inducing "platelets" (usually with different B) to interchange positions by slow "plastic flow" or more sudden discontinuous crust-breaking. After the formation of SF-n vortex arrays ($t \gtrsim 10^3$ yrs) large scale magnetic fields and dipole moments follow underlying core n-vortex movement but local polar cap fields in small areas (a typical polar cap radius $\sim 10^4$ cm) do not change substantially because of such movement. However, after several 10^6 years both surface dipole moments and surface polar cap field strengths follow closely the movement of SF-n vortices near the surface of a NS's core SC-p.

There are some quantitative uncertainties in the predictions from this model of the response of NS surface field to NS spin-down (cf. Sect. 14.2). These relate mainly to the structure and magnitude of toroidal components of the core's magnetic field and to how a NS crust responds to very strong stresses (slow plastic "creep" vs. sudden cracking). Neither is important during NS spin-up slow enough for crust conductivity to be negligible so the description of Sect. 14.3 should then be quite robust.

14.2 Magnetic Field Changes in Spinning Down Neutron Stars

Effects from the coupling between a spin-down expansion of a NS's SF-n vortex-array and its SC-p flux-tubes should appear in several observable phases after a neutron star spin-period P_o is reached, i.e., after $\sim 10^3$ yrs when the NS has cooled down enough so that the vortex-line and the flux-tube array have both formed.

The distance from the spin-axis of SF-n vortex lines ($r_\perp$) increases with decreasing NS spin rate (Ω) to conserve $\Omega r_\perp^2$, the number of vortices in each expanding vortex-lattice area. This has the following consequences:

(a) When $P > P_o$, $\mu_\perp$, the component of the NS-core's magnetic dipole moment perpendicular to NS spin, initially grows as $P^{1/2}$ for any configuration of surface B (cf. Fig. 14.5):

$$\frac{\mu_\perp(P)}{\mu_\perp(P_o)} \sim \left(\frac{P}{P_o}\right)^{1/2} . \tag{14.3}$$

(b) When $P \sim$ several P_o, a good fraction of a NS's core flux-tubes will have been pushed outwards from the spin-axis into the equatorial region ($r_\perp \sim R$). These vortices cannot, of course, continue to move outward (Fig. 14.5) so that (14.3) no longer holds. Rather, the mixture of expanding and crust-constrained flux-tubes gives

$$\frac{\mu_\perp(P)}{\mu_\perp(P_o)} \sim \left(\frac{P}{P_o}\right)^{\hat{n}} \quad (0 < \hat{n} < 1/2) \tag{14.4}$$

with the exact value of $\hat{n}$ dependent on details of the core's B-field configuration.

(c) The crust can delay, but not indefinitely prevent, expulsion of this magnetic field from the NS. When $P \sim$ several P_o, intertwined vortices plus flux which have been pushed into the core–crust interface will stress the crust enough to exceed its shear-strength (Sect. 14.5. and Figs. 14.5 and 14.6). Then crust movements begin that can lead to B-field reconnections. Flux that is threaded by SF-n vortex

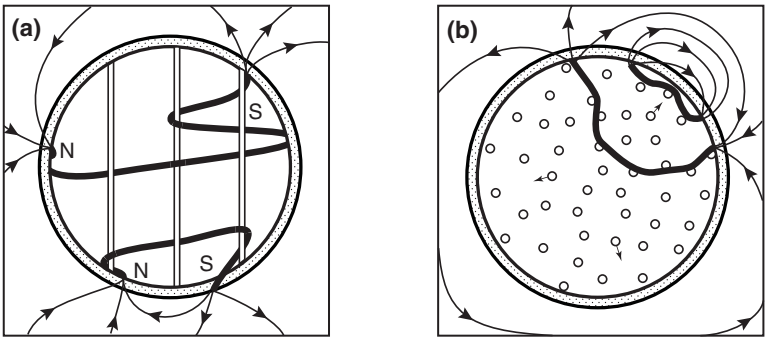

Fig. 14.5 Two flux-tubes whose North and South magnetic poles moved away from a NS's spin-axis during spin-down: **a** side view with one of the North poles moved to its maximum $r_\perp \sim R$; **b** top view of the core's equatorial plane with one of the flux tubes being pushed out of the NS core

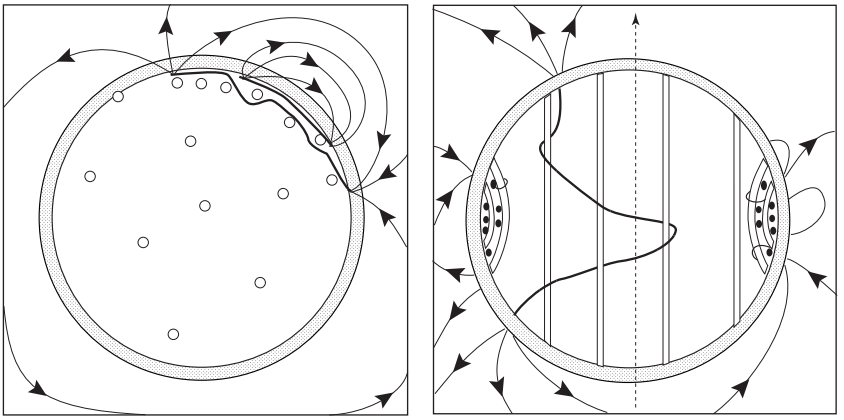

Fig. 14.6 *Left*: The configuration (top view) of Fig. 14.5b after further spin-down. Flux-tubes are piling up in an equatorial annulus at the core–crust interface. The blocked flux-tubes, in turn, block short segments of vortex lines which forced them into this annulus. *Right*: A side view of the representation shown in the *left figure* with the addition of a flux-tube, which the expanding vortex-array has not yet forced out to a radius $\sim R$

lines that have not yet reached $r_\perp \sim R$, and thus have not yet disappeared are then -the remaining source for the NS's dipole moment. The sum of all this remaining flux is proportional to the total number of remaining vortex-lines ($\propto \Omega$). Then, (14.4) holds with $\hat{n} = -1$.

(d) When the average B remaining in the core drops below about 10^{12} G, shear-stress on the crust from it would no longer be expected to be capable of exceeding the crust's yield-strength. The NS's surface B may then lag that at the base of its crust by the crust's ohmic (Eddy current) dissipation time (perhaps of order, but not greater than, 10^7 years).

14.3 Magnetic Dipole Field Changes in Spinning Up NSs

NS spin-up, when sustained long enough so that one of the above criteria for limiting shear-stress from crust-anchored magnetic flux before cut-through is met, leads to a "squeezing" of surface B toward the NS spin-axis. After a large decrease in spin-period from an initial P_o to $P \ll P_o$ all flux would enter and leave the core's surface from a small area within a radius $R(P/P_o)^{1/2}$ of the NS's spin-axis. This surface B-field change is represented in Fig. 14.7 for the special case when the magnetic flux which exits the NS surface from its upper (lower) spin-hemisphere returns to the stellar surface in its lower (upper) one. Potentially observable features of such a "spin-squeezed" surface B configuration include the following:

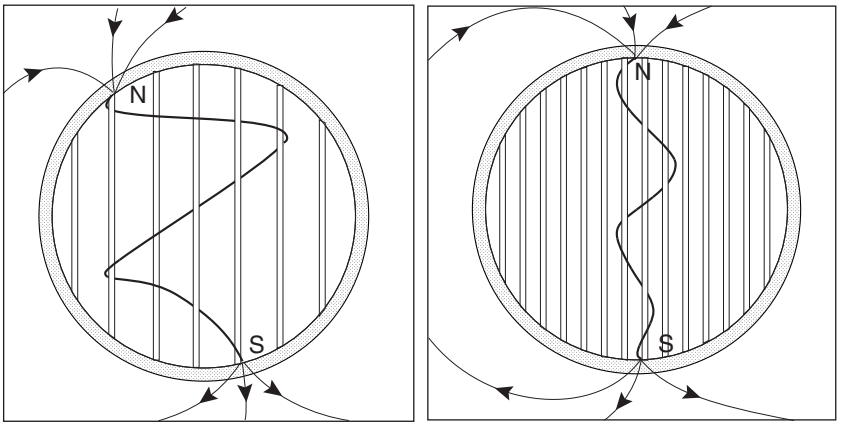

Fig. 14.7 *Left*: A single flux-tube (one of 10^{31}) and some of the NS's arrayed vortices (7 of 10^{17}) with surface poles in opposite spin-hemispheres. *Right*: The flux-tube and vortex array after a large stellar spin-up

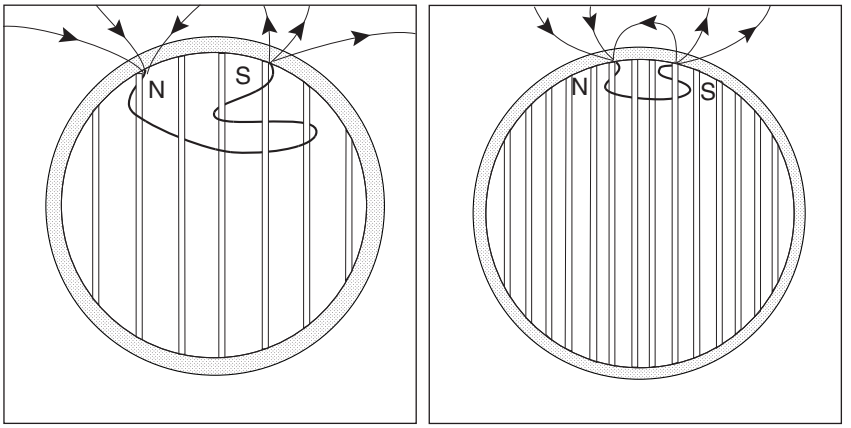

Fig. 14.8 *Left*: A single flux-tube, part of a sunspot-like B-field geometry in which flux from a spin-hemisphere of the surface returns to the surface in that same hemisphere. *Right*: Flux-tube and vortex array after a large stellar spin-up

(a) The dipole moment becomes nearly aligned along the NS spin-axis.
(b) The canonical polar cap radius at the stellar surface, $r_p \equiv R(\Omega R/c)^{1/2}$, shrinks to $r'_p \equiv \Delta(\Omega R/c)^{1/2}$. The B-field just above the polar cap has almost no curvature.
Evolutionary squeezing of a pre-spin-up surface B with a sunspot-like configuration (i.e., flux returning to the NS surface in the same hemisphere as that from which it left) is represented in Fig. 14.8. In this case, potentially observable features after $P \ll P_o$ include:
(c) A pulsar dipole moment oriented nearly orthogonal to the NS spin-axis

(d) Positioned at the crust–core interface with
(e) A magnitude μ greatly reduced from its pre-spin-up size

A more general (probably more realistic) pre-spin-up configuration has flux emitted from one spin-hemisphere returning to the stellar surface in both, as shown in Fig. 14.9. Spin-up squeezing then typically gives the surface field configuration in Fig. 14.10, a spin-squeezed, nearly orthogonal dipole on the NS spin-axis with properties (c), (d), and (e), together with an aligned dipole on the spin-axis whose external field is well-represented by North and South poles at a distance of 2R apart.

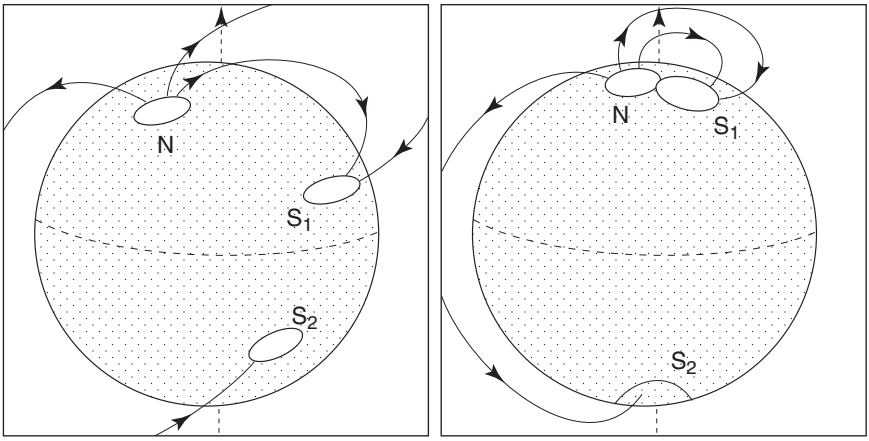

Fig. 14.9 *Left*: A surface field which has magnetic flux tubes of both Figs. 14.7 and 14.8 configurations. *Right*: The same field configuration after a large stellar spin-up

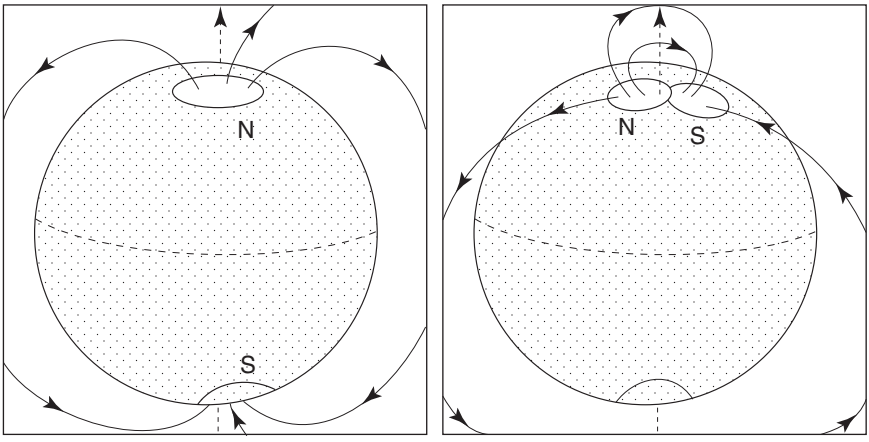

Fig. 14.10 *Left*: The field from Fig. 14.9 after very large further spin-up. The new N is reduced by S_1 from its initial value. *Right*: The field from Fig. 14.9 after large spin-up when S_2 can be neglected. Only a squeezed orthogonal dipole, greatly reduced in magnitude by the spin-up, is left

14.4 Comparisons of Pulsar Dipole Field Observations with Model Expectations

Figure 14.11 shows inferred magnetic dipole field strength at the neutron star surface as a function of P for about 1,500 radio pulsars from measured P and $\dot{P}$, used with $I\dot{\Omega} = -\mu^2\Omega^3 c^{-3}; B = \mu\ R^{-3}$ and NS moment of inertia $I = 10^{45}$ g cm^2. Segments of B(P) based upon the model of Sects. 14.2 and 14.3 are shown for a typical pulsar by solid lines. The dashed line is the steady state "spin-up line" which relates the dipole moment of a spun-up neutron star (B) to its spin period (P) when the spin-up has been accomplished by expected accretion from a surrounding accretion disk:

1. Point A is a (B, P) where, typically, flux-tubes and vortex lines begin coexistence.
2. $(A \rightarrow C)$ is the expanding array prediction of Sect. 14.2b: $B \propto P^{\hat{n}}$ with the model prediction $0 < \hat{n} < 0.5$. The index $\hat{n}$ is known only in the several cases where $\ddot{P}$ is also measured: $\hat{n}$ = + 0.3, 0.1, 0.6, 0.1, 0.05 [5, 15, 19, 40]. The compatibility of $\hat{n}$ = 0.6 for Vela with the model is considered in [27]. (The canonical "braking index" $n = 3 - 2\hat{n}$, where $\dot{\Omega} \propto \Omega^n$).

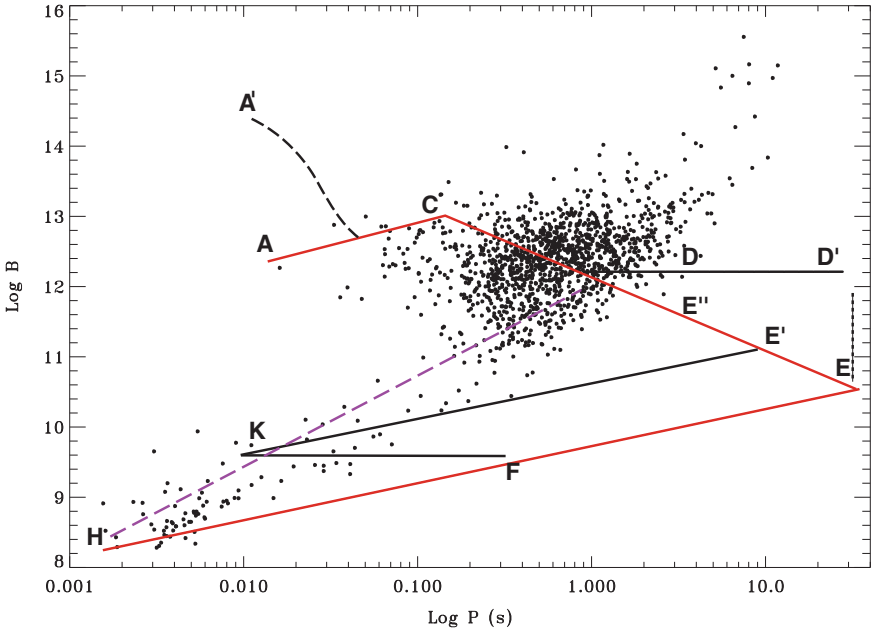

Fig. 14.11 Dipole-B observed on pulsar surfaces (inferred from measured P and $\dot{P}$) as a function of pulsar period. The *solid line segments* are the evolutionary segments for B of Sect. 14.4, based upon the model of Sects. 14.2 and 14.3. The *dashed diagonal* is the steady state "spin-up line" from an accretion disk fed at 0.1 the Eddington limit. The horizontal $(D \rightarrow D')$ is B at a NS crust surface above core surface $(D \rightarrow E)$ when not enough time has passed ($\lesssim 10^6$ yrs.) for crustal dissipation to result in B about the same at both surfaces. The E″–E′ segment would be typical for an isolated NS after 10^{10} yrs

3. $(C \rightarrow D)$ describes the core flux-expulsion and reconnection segment. The model predicts $< \hat{n} >= -1$ for $\hat{n}$ averaged over the $(C \rightarrow D)$ history of any one pulsar. Reliable $\ddot{P}$ are not generally measurable in this (B,P) region. However comparison of presently observed $P/2\dot{P}$ with actual pulsar ages inferred from observed pulsar velocities and probable distance traveled since birth [8], gives $< \hat{n} >= -0.8 \pm 0.4$, not inconsistent with the model prediction $\hat{n} = -1$.
4. $(D \rightarrow E)$ is the core-surface/crust-base B evolution after about $\sim 10^{10}$ yrs. The horizontal $(D \rightarrow D')$ is the NS crust's surface field, remaining near 10^{12} G for $\sim 10^7$ yrs. as discussed in Sect. 14.2d. This segment should be characteristic of typical X-ray pulsars NSs in binaries spun up or down by active companions through a wide range of P (e.g., Hercules X$-$1 with $P \sim 1$ s to Vela X$-$1 with $P \sim 10^3$ s) until crustal Eddy current decay allows a $(D' \rightarrow E)$ decay from some D' region. A small minority of NSs, after (D $\rightarrow$ E$''$ $\rightarrow$ E$'$) segments, will be resurrected as pulsars after accretion from a previously passive nearby companion which now overflows its Roche lobe (LMXBs). These NSs have entered into the spin-up phase of Sect. 14.3 until they reach a steady state on the canonical "spin-up line" represented by the dashed diagonal of Fig. 14.11 (for $\dot{M} = 10^{-1}\dot{M}_{Eddington}$).
5. $(E \rightarrow F \rightarrow H)$ is the spin-up segment when the NS surface B has the sunspot geometry which allows spin-up to minimal P before spin-up equilibrium is reached. Observations of maximally spun-up millisecond pulsars (MSPs) support the Sect. 14.3 model for such MSP formation. Figure 14.12 show Sect. 14.3d's high fraction of MSPs with two subpulses about 180° apart, characteristic of orthogonal rotators [2,6,8,13,26]. For additional support from radio pulse polarization and its frequency dependence in such subpulses see [6].
6. (E $\rightarrow$ F $\rightarrow$ K) is the track of total dipole B predicted after large spin-up from (E) with Fig. 14.9 geometry to (F) with Fig. 14.10 geometry. Further spin-up diminishes only the orthogonal component of μ until an almost aligned rotator results when (K) is reached. X-ray emission from the almost aligned MSP PSR J0437$-$4715 ($P = 6$ ms) (cf. Fig. 14.12) supports the predicted tiny polar cap area about $(\Delta/R)^2 \sim 10^{-2}$ that from a central dipole moment configuration for the same P (see [2,6,26] and (14.5) below).

Expected consequences for pulsar dipole-B changing according to the model described in Sects. 14.2–14.3 are supported by many kinds of observations. However, for almost all there are usually other and more popular explanations (e.g., B getting from (D) to (H) because of burial of B by accreted matter from a companion (cf. [4,38,40]).

14.5 Polar Cap Areas

A NS's polar cap area (A_{pc}) depends upon the ratio of its dipole field B_d to its polar cap field (B_{pc}). Conservation of magnetic flux within the "open" field line bundle between the NS's polar cap and its "light cylinder" at $r_\perp = c/\Omega$ gives

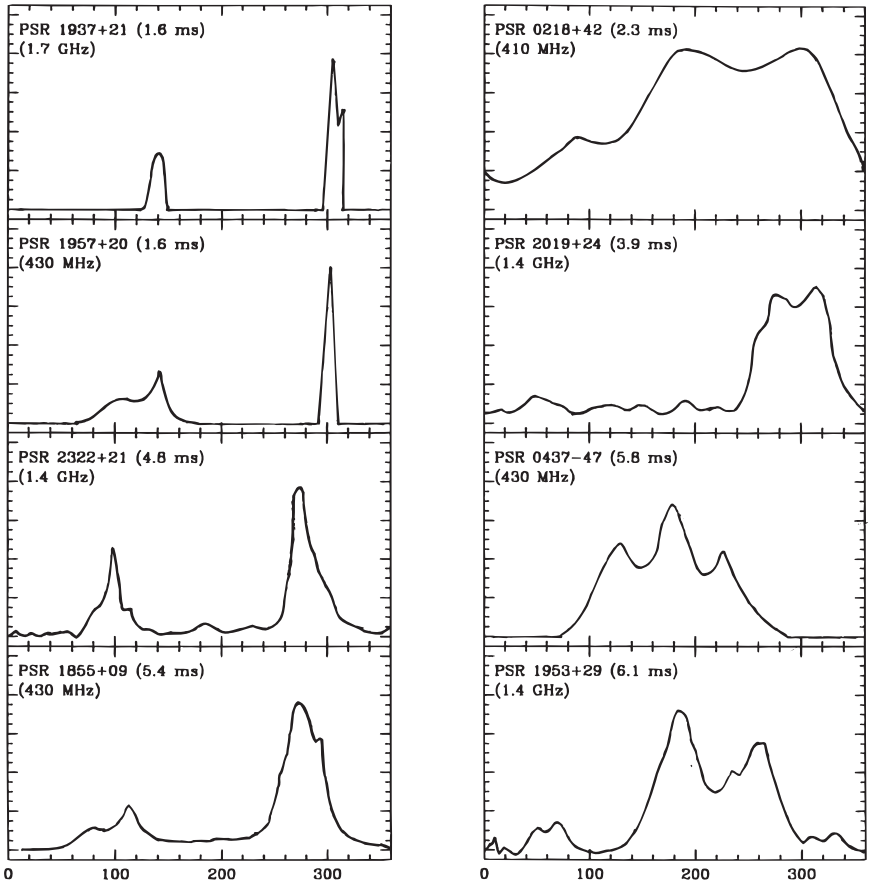

Fig. 14.12 Radio pulse profiles of eight of the fastest 11 disk population millisecond pulsars in 1997 [7]. Among non-MSPs about one pulsar in 10^2 has two substantial subpulses (amplitudes within an order of magnitude of each other) near half a period apart

$$A_{pc} \sim \frac{\Omega R^3}{c} \frac{B_d}{B_{pc}} \,. \tag{14.5}$$

Since B_{pc} is expected to be approximately constant for the first few $\times 10^6$ yrs after crust formation $A_{pc} \propto B_d/P$ in that interval. It is not clear, however, what the appropriate initial value of B_{pc} is. In many cases it may well be very much larger than B_d after 10^3 yrs when the controlling $SF-n$ vortex arrays form and the model considered above could be expected to become applicable (cf. Sect. 14.5).

Very slow ($t \gg 10^6$ yrs) spin-up of a NS to a millisecond pulsar squeezes all the core's flux-tubes, together with the NS polar caps, toward the spin axis. A_{pc} then decreases because $B_d \propto \Omega^{-\frac{1}{2}}$ on E $\rightarrow$ F $\rightarrow$ H in Fig. 14.11 and $B_{pc} \propto \Omega$. Spin-up

from a spin-period $\sim$10 s to near the minimum $P \sim 10^{-3}$ s on the "spin-up" line for near maximum NS spin-up by a companion-fed accretion disk gives a polar cap radius at the core–crust intercase which is $\ll$ the crust thickness Δ. For an aligned spun-up MSP the polar cap area at the crust surface becomes

$$A_{pc} \sim \pi \frac{\Omega R}{c} (R\Delta)^2 \sim 10^{-2}\ \mathrm{km}^2, \tag{14.6}$$

about two orders of magnitude less than the conventionally assumed polar cap area $\pi\Omega R^3/c \sim 1$ km^2 when $P \sim$ several ms. Such very small A_{pc} are consistent with those reported by [42] for the almost aligned rotator PSR J0437−4715, and two orthogonal rotators, J0030 and J2124. There are, however, still considerable uncertainties in inferring observed A_{pc} from X-ray observations. For an orthogonal dipole on the spin-axis at the crust core interface the surface polar cap area is much larger than the A_{pc} of (14.6). However, MSPs are identified by observations of their radio emission beams, a nearly aligned one from PSR J0437−4715, and an expected gravitationally elongated (in latitude) fan beam from a rotating orthogonal dipole. An aligned MSP is, therefore, usually observed from a direction nearly normal to its polar cap. The observing angle would generally be much closer to tangential in the orthogonal case. Then the polar cap area inferred from its thermal X-ray emission would be near that of (14.6) for PSR J0437−4715, but a smaller projection of a larger A_{pc} for an orthogonal rotator whose dipole is on the spin-axis very near the stellar surface. Despite this ambiguity, support for a predicted very large reduction in observed polar cap areas for strongly spun-up MSPs seems quite strong.

14.6 Pulsar Spin-Period Glitches from Spin-Induced *B*-Field Changes

Moving core flux-tubes continually build up shearing stress in the conducting crust which anchors *B*-field that traverses it. If this stress grows to exceed the crust's yield strength, subsequent relaxation may, at least partly, be through relatively sudden crustal readjustments ("crust-breaking"). Such events would cause very small spin-up jumps in spinning-down NSs (spin -period "glitches"). The Sects. 14.2–14.3 model for the evolution of a core's flux-tube array suggests glitch details in pulsars similar to those of the two observed glitch families: Crab-like glitches and the very much larger giant Vela-like ones of Fig. 14.13.

14.6.1 Crab-Like Glitches

In both the $(A \rightarrow C)$ and $(C \rightarrow D)$ segments of Fig. 14.11, an expanding quasi-uniform vortex-array carries a flux-tube array outward with it. Where growing

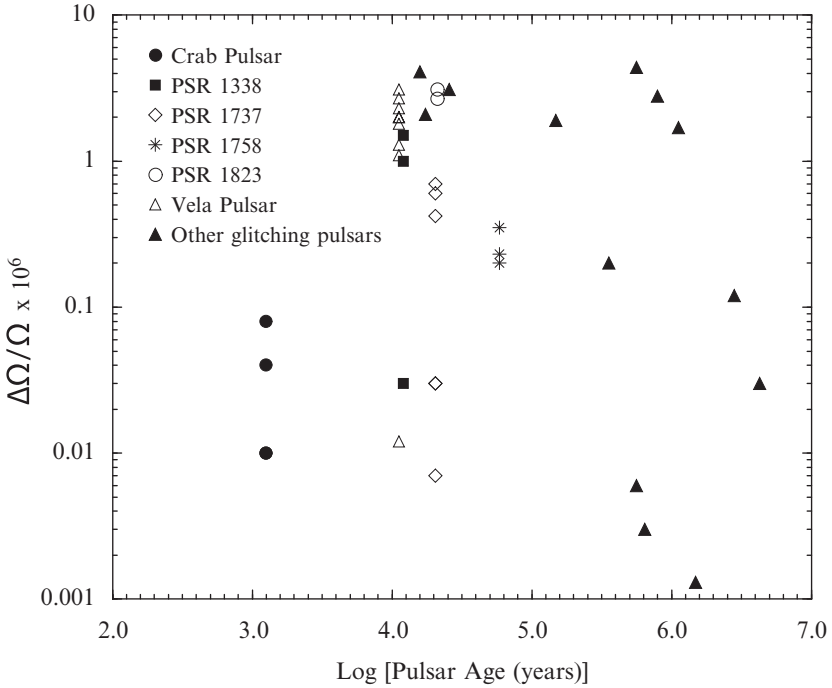

Fig. 14.13 Observed jumps ("glitches") in pulsar spin-rates ($\Delta\Omega/\Omega$) of pulsars with various spin-down ages. The vela-like pulsars have $\Delta\Omega/\Omega \sim (1-10)\times 10^{-6}$. The Crab-like ones have $(\Delta\Omega/\Omega) \sim (0.01-0.1)\times 10^{-6}$ [21,41]

flux-tube-induced stress on the crust is partly relaxed by "sudden" outward crust movements (of magnitude s) where the stress is strongest (with density preserving back-flow elsewhere in the stratified crust) the following consequences are expected:

1. A "sudden" permanent increase in $\mu_\perp$, spin-down torque, and $\dot{\Omega}$ with $\frac{\Delta\dot{\Omega}}{\dot{\Omega}} \sim$ typical tangential crust fractional displacement $s/R \sim \Delta\theta$ (strain relaxation) $\lesssim \theta_{max} \sim 10^{-3}$. A permanent glitch-associated fractional jump in NS spin-down rate of this sign and magnitude ($\sim 3\times 10^{-4}$) is indeed observed in the larger Crab glitches (cf. Fig. 14.14 and [11, 18, 20, 39]).
2. A "sudden" reduction in shear stress on the crust by the flux-tubes attached to it from below. This is matched by an equivalent reduction in pull-back on the core's expanding vortex array by the core's crust anchored flux-tube array attached to it. The n-vortices therefore "suddenly" move out to a new equilibrium position where the Magnus force on them is reduced by just this amount. The high density SF-n sea therefore spins down a bit. All the (less dense) charged components of the NS (crust, core-p and-e) together with the flux-attached n-vortex-array spin-up much more. (The total angular momentum of the NS does not change significantly in the brief time for development of the glitch.) A new equilibrium is established in which the charged components (all that can be observed, of

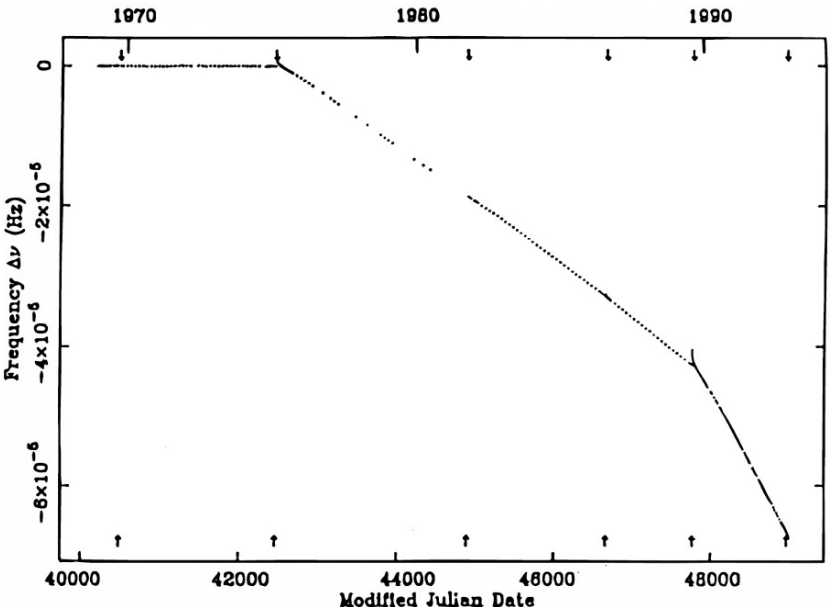

Fig. 14.14 The difference between Crab pulsar spin-frequencies observed over a 23-yr interval and those predicted from extrapolation from measurement of P, $\dot{P}$, and $\ddot{P}$ at the beginning of that interval. These "sudden" permanent fractional jumps in spin-down rate ($\Delta\dot{\Omega}/\dot{\Omega} \sim +5 \times 10^{-4}$) occur at glitches ($\Delta\dot{\Omega}/\dot{\Omega} \sim 10^{-8}$–$10^{-7}$) but are 10^4 times greater in magnitude [11, 39]

course, is P of the crust's surface) have been spun up. For Crab B and P, estimated $\Delta\Omega/\Omega \sim 10^{-4}(\Delta\dot{\Omega}/\dot{\Omega})$ [26, 32, 33] are consistent with both the Crab glitches of Fig. 14.13 and also with much smaller Crab glitches not shown there [39]).

14.6.2 Giant Vela-Like Glitches

Those glitches differ from that of Crab-like pulsars in several ways:

1. $\left(\frac{\Delta\Omega}{\Omega}\right)_V \sim 10^2 \times \left(\frac{\Delta\Omega}{\Omega}\right)_C$.
2. Vela-like glitches develop their $\Delta\Omega$ in less than 10^2 s; the $\Delta\Omega$ of a Vela-like glitch is already decreasing in magnitude when first resolved, while Crab-like glitches are still rising toward their full $\Delta\Omega$ for almost 10^5 s [22, 23].
3. Vela-like glitches are observed in pulsars (mainly, but not always) in Fig. 14.11 along ($C \rightarrow D$) while C-glitches are observed all along ($A \rightarrow C \rightarrow D$).
4. The Crab-like glitch proportionality between $\Delta\dot{\Omega}/\dot{\Omega}$ and $\Delta\Omega/\Omega$ would greatly overestimate $\Delta\dot{\Omega}/\dot{\Omega}$ after Vela-like glitches.

The existence of a second glitch family, with Vela-like properties, is expected from a second effect of vortex-driven flux-tube movement in a spinning down NS

core. If there were no very dense, comoving, flux-tube environment around them, outward moving core-vortices could smoothly shorten and then disappear as they reached the core's surface at its spin-equator. (We ignore crustal SF-n here.) However, the high conductivity of the crust at its base resists entry of the flux-tubes which the vortices bring with them to the crust's base. This causes a pile-up of pushed flux-tubes into a small equatorial annulus which delays the final vortex-line disappearance. The vortex movement in which they vanish occurs either in vortex-line flux-tube cut-through events, or perhaps in a sudden breaking of the crust which has been over stressed by the increasing shear-stress on it from the growing annulus. Giant Vela-like glitches have been proposed as such events [25, 26] allowing a "sudden" reduction of part of this otherwise growing annulus of excess angular momentum and also some of the magnetic flux trapped within it. These would not begin until enough vortex-lines, initially distributed almost uniformly throughout the core, have piled up in the annulus for the flux-tubes they bring with them to supply the needed shear stress. Estimates of Vela-like glitch magnitudes $\Delta\dot{\Omega}/\dot{\Omega}$ are less reliable than those for Crab-like glitches. A very rough one, based upon plausible guesses and an assumed strain relaxation about the same as those in the larger Crab-like glitches, suggest that Vela-like glitch repetition rates and magnitudes are similar to observed ones.

14.7 Open Questions and Summary

Several areas stand out as needing much more study:

1. The origin of a NS's magnetic field – Speculations include (a) conservation during a NS's violent birth of flux already inside its ancestor. NS fluxes are comparable to those in magnetic White Dwarfs, and the toroidal field within the sun; (b) short-lived post-partum dynamos [35]; (c) field amplification in asymmetric supernova explosions; (d) toroidal field breakout after wind-up from different rotation imparted at birth [29]; (e) thermoelectric generation [**?**, 3, 36, 37]; and (f) exterior field reduction from burial by fall-back of some of the initially exploded matter.
2. Prehistory – The proposed spin-down biography of a NS surface B presented in Sect. 14.2 began at A (or perhaps A') in Fig. 14.11 when that typical NS is expected to be about 10^3 yrs old. Before that its crust had solidified (age $\sim$ a minute), its core protons had become superconducting (age $\sim$ 1 yr?), and core neutrons became superfluid (age $\sim 10^3$ yrs?). If so, there would be a nearly 10^3-year interval between formation of the NS core's magnetic flux-tube array and control of that array's movement by a SF-n vortex array. During that interval an early magneto-hydrodynamic equilibrium involving poloidal and toroidal fields, and some crustal shear stress could be upset. Dramatically altered B-field stresses after flux-tube formation could induce movements in the overstrained crust which cause B_d to change [25, 26]. Recent reconsideration of drag on moving flux-tubes [14] suggests the core flux-tube adjustment might take $\sim 10^3$ yrs. For many

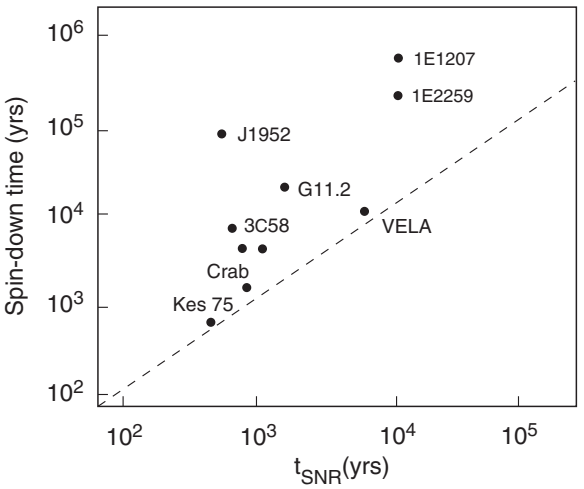

Fig. 14.15 Observed spin-down times for pulsars ($P/2\dot{P}$) vs. the time since birth of these same pulsars as inferred by the ages of the supernova remnants in which they are still embedded (t_{SNR})

NSs, depending on details of their initial B structure, dipole moments could then become much smaller in that 10^3-yr epoch. Large post-partum B_d values and such subsequent drops in their sizes have been estimated and proposed [25, 26] as the reason some young pulsars have present spin-down ages $(P/2\dot{P})$ 10^2 times greater than their true ages (Fig. 14.15).

If present $P < 10^{-1}$s it may not be implausible that such pulsars simply were born with a spin-period near that observed now. In others (e.g., 1E 1207 with $P \sim 0.4$ s) the case for an earlier epoch with very much larger B_d may be more attractive. It has been suggested by [10] and others that this might have been caused by burial of surface field by slow fall-back.

A second consequence of a very early, large reduction in B_d of some NSs would be a comparable reduction in their A_{pc} to far below the canonical $\pi\Omega R^3/c$ (cf. (14.5)). The A_{pc} of Sect. 14.5 would then be small because presently observed pulsars "remember" their early very large B_{pc} but not the B_d they then had. Subsequent changes in B_d and (14.1) and (14.2) would need reconsideration.

An early epoch between the formation of SC-p flux-tubes and SF-n vortices arrays is rich in possibilities and needs further exploration.

3. Precession – Large, long lasting and long period (∼yr) free precession of a NS appears to be incompatible with simple, canonical neutron star models [17, 32, 33]. This is especially the case for the model considered above in which the NS core's SF-n vortex lines are "tied" to the NS crust by magnetic flux which interacts strongly with both. However, there are a substantial number of observations of significant long period (∼year) oscillations around expected pulse arrival times [22] which have been interpreted as evidence for large amplitude free precession of NSs. How to modify the canonical model of a spinning-down (-up)

NS to allow such sustained free precession and also preserve the consequences described above for magnetic fields and glitches seems a severe and crucial problem [1, 17]. (One proposed resolution [28] is that the observations attributed to free precession of the NS are from slow oscillations in emission beam direction and spin-down torque coming from a very slow "drifting" (precession) only of the current-pattern above a polar cap accelerator.) Until it is satisfactorily resolved other model predictions will remain somewhat suspect.

Summary

In the core of a canonical spinning magnetized neutron star a nearly uniform superfluid neutron vortex-array interacts strongly with a twisted array of magnetic flux-tubes threading the core's superconducting protons. One consequence is that changes in NS-spin alter both arrays and also the magnetic field distribution on the surface of the surrounding crust. Among predicted consequences for very young spinning-down NSs are "spin-down indices" increasing from 2 to 3, and a family of (Crab-like) spin-period "glitches" with permanent fractional jumps in spin-down torque 10^5 times greater than those in NS-spin. For older NSs, average spin-down indices increase to around 5, and an additional (Vela-like) family of giant glitches develops. NS spin-up to millisecond pulsars results in a high abundance of orthogonal and aligned rotators, and anomalously small polar cap areas. Observations do not conflict with these expectations. An epoch of NS magnetic field evolution between the onset of proton superconductivity ($\sim$yr) and neutron superfluidity ($\sim 10^3$ yrs) may be important for large surface magnetic field changes and needs further study. Observations generally interpreted as compelling evidence for NS precession may need reconsideration.

References

1. Alpar, A., 2005, In: Proc. of the Electromagnetic Spectrum of Neutron Stars, Baykal et al. (ed)
2. Becker, W. & Aschenbach, B., 2002, MPE Rpt. 278, astro-ph/0208466
3. Blandford, R.D., Applegate, J.H. & Hernquist, L., 1983, MNRAS, 204, 1025
4. Burderi, L. & D'Amico, N., 1997, ApJ, 490, 343
5. Camilo, F., Kaspi, V.M., Lyne, A.G., Manchester, R.N., Bell, J.F., D'AMico, N., McKay, N.P.F., & Crawford, F., 2000, ApJ, 541, 367
6. Chen, K. & Ruderman, M., 1993, ApJ, 408, 179
7. Chen, K., Ruderman, M., Znu, T., 1998, ApJ, 493, 397
8. Cordes, J. & Chernoff, D., 1998, ApJ, 505, 315
9. Ding, K., Cheng, K.S., & Chau, H., 1993, ApJ, 408, 167
10. Geppert, U., Page, D., & Zannias, T., 1999, A&A, 345, 847
11. Gullahorn, G., Isaacman, R., Rankin, J. & Payne, R., 1997, AJ, 81, 309
12. Jahan-Miri, M., 2000, ApJ, 532, 514
13. Jayawardhana, R. & Grindlay, J., 1995, J. Astron. Soc. Pac. Conf. Ser., 105, 231
14. Jones, P., 2006, MNRAS, 365, 339
15. Kaspi, V., Manchester, R., Siegman, B., Johnston, S. & Lyne, A., 1994, ApJ, 422, 544, L177

16. Konenkov, D. & Geppert, U., 2001, MNRAS, 325, 426
17. Link, B., 2003, Phys. Rev. Lett., 91, 101101
18. Lyne, A., Graham-Smith, F. & Pritchard, R., 1992, Nature, 359, 706
19. Lyne, A., Pritchard, R., & Graham-Smith, F., 1998, MNRAS, 233, 267
20. Lyne, A., Pritchard, R., Graham-Smith, F., & Camilo, F., 1996, Nature, 381, 497
21. Lyne, A., Pritchard, R., & Shemar, S., 1995, J. Astrophys. Astron., 16, 179
22. Lyne, A., Shemar, S., & Graham-Smith, F., 2000, MNRAS, 315, 534
23. McCulloch, P., Hamilton, P., McConnel, D., & King, E., 1990, Nature, 346, 822
24. Ruderman, M., 1991, ApJ, 366, 261 and ApJ, 382, 576
25. Ruderman, M., 2004, in *From X-Ray Binaries to Gamma-Ray Bursts*, E. van den Heuvel, L. Kapper, E. Rol, & R. Wijers (ed), ASP Conf. Series 308, 251
26. Ruderman, M., 2004, in *X-ray and γ-ray Astrophysics of galactic Sources*, Proc. 4th Agile Science Workshop, 2003, M. Tavani, A. Pellizoni, & S. Varcellone (ed), IASF
27. Ruderman, M., 2005, The Electromagnetic Spectrum of Neutron Star, A. Baykal et al. (eds), (Berlin: Springer), 47–61
28. Ruderman, M. & Gil, J., 2006, A&A, 460, 31
29. Ruderman, M., Tao, L. & Kluzniak, W., 2000, ApJ, 542, 243
30. Ruderman, M., Zhu, T. & Chen, K., 1998, ApJ, 492, 267 and 493, 397
31. Sauls, J., 1989, Timing Neutron Stars, H. Ögelman & E. van den Heuval (eds.), (Dordrecht: Kluwer)
32. Sedrakian, A., Wasserman, I., & Cordes, J.M., 1999, ApJ, 524, 341
33. Shaham, J., 1977, ApJ, 214, 251
34. Srinivasan, G., Bhattacharya, D., Muslimov, A., & Tsygan, A., 1990, Curr. Sci., 59, 31
35. Thompson, R. & Duncan, R., 1996, ApJ, 473, 322
36. Urpin, V., Geppert, U. & Konenkov, D., 1997, MNRAS, 295, 907
37. Urpin, V., Levshakov, S., & Iakovlev, D., 1986, MNRAS, 219, 703
38. van den Heuvel, E. & Bitzaraki, O., 1995, A&A, 297L, 41V
39. Wong, J., Backer, D. & Lyne, A., 2001, ApJ, 548, 447
40. Zhang, C., Kojima, Y., 2006, MNRAS, 366, 137
41. Zhang, W., Marshall, F., Gotthelf, E., Middleditch, J. & Wang, Q., 2001, ApJ, 544, L177
42. Zavlin, V., 2006, ApJ, 638, 951

Chapter 15
Pulsar Emission: Where to Go

Jonathan Arons

15.1 Introduction

Pulsars are the quintessential dogs that don't bark in the night – their observed loss of rotational energy mostly disappears into the surrounding world while leaving few traces of that energy loss in observable photon emission. They are the prime example of compact objects which clearly lose their energy through a large scale Poynting flux.

In this chapter I survey recent successes in the application of relativistic MHD and force-free electrodynamics to the modeling of the pulsars' rotational energy loss mechanism as well as to the structure and emission characteristics of Pulsar Wind Nebulae. I suggest that unsteady reconnection in the current sheet separating the closed from the open zones of the magnetosphere is responsible for the torque fluctuations observed in some pulsars, as well as for departures of the braking index from the canonical value of 3. I also discuss the theory of high energy pulsed emission from these neutron stars, emphasizing the significance of the boundary layer between the closed and open zones as the active site in the outer magnetosphere. I elaborate on the conflict between the models currently in use to interpret the gamma-ray and X-ray pulses from these systems with the electric current flows found in the spin down models. Because the polar cap "gap" is *the* essential component in the supply of plasma to pulsar magnetospheres and to pulsar wind nebulae, I emphasize the importance of high sensitivity gamma-ray observations of pulsars with core components of radio emission and high magnetospheric voltage, since observations of these stars will look directly into the polar plasma production region and will probe the basic plasma parameters of these systems. I also discuss the current state

J. Arons
Departments of Astronomy and of Physics, and Theoretical Astrophysics Center,
University of California, Berkeley
and
Kavli Institute of Particle Astrophysics and Cosmology, Stanford University
e-mail: arons@astro.berkeley.edu

W. Becker (ed.), *Neutron Stars and Pulsars,* Astrophysics and Space Science Library 357,

of understanding and problems in the shock conversion of flow energy into the spectra of the synchrotron emitting particles in the Nebulae, emphasizing the possible role of heavy ions in these processes. I comment on the prospects for future developments and improvements in all these areas.

This chapter is entitled "Pulsar Emission: Where to Go" in the theory of pulsar radio and high energy emission. "Where to Go" on these topics depends greatly on where one thinks the energy and the particles are. Therefore, I mostly discuss here questions of dynamics, and return to the emission physics through the lens of the successes and problems of dynamical models of rotation powered pulsars' magnetospheres. Also, I emphasize results and problems common to all pulsars. I will give an impressionistic rather than a comprehensive review, more in the spirit of setting goals as I see them rather than providing a scholarly survey.[1] I have focused on issues that can be addressed by timing and by high energy photon observations.

15.2 Pulsar Electrodynamics: Follow the Energy

Astrophysical understanding comes from using observation and theory to find and follow the flow of energy, mass and momentum in the macroscopic systems of interest. For pulsars, this has been a challenge. They are quintessential "dogs that don't bark in the night", with only a small fraction of the energy they broadcast into the Universe appearing in directly observable forms. The interpretation of the regular pulse periods from sources distant enough to require stellar and sub-stellar luminosity in the radio (and in the infrared, optical, X-ray and gamma-ray) discovered by the radio astronomers led immediately to the understanding that the observed periods are the consequence of rotation of massive stellar flywheels (neutron stars). The steady lengthening of the pulse period, shown in Fig. 15.1, led immediately to a permanently successful model of that spin-down, the electromagnetic torques exerted if the stars are sufficiently well magnetized.

One can readily estimate the magnitude of such torques from the observation that rotation of a stellar magnetic field B induces a poloidal electric field of magnitude $E \sim (\Omega r/c)B_p$, with $\Omega = 2\pi/P$ and B_p the poloidal magnetic field – from the point of view of the torque, that field is well approximated by a dipole with dipole moment $\mu = R_*^3 B_p$. The winding up of the magnetic field as the conducting star rotates requires the existence of a toroidal magnetic field of magnitude $B_\phi \sim (\Omega r/c)B_p$. This E field corresponds to energy loss in a Poynting flux $cE \times B/4\pi$. If the electromagnetic energy density exceeds all the material energy densities, one obtains the total energy loss $\dot{E}_R$ and therefore the torque $\dot{J} = \dot{E}_R/\Omega$ by summing the Poynting flux over a sphere of radius R_A, expected to be comparable to the light cylinder

[1] Much of what I have to say derives from collaborations, most recently with Elena Amato, Phil Chang, Niccolo Bucciantini, Eliot Quataert, Todd Thompson and especially Anatoly Spitkovsky; in earlier years, with Ted Scharleman, Bill Fawley, Colin Norman, David Alsop, Don Backer, Brian Gaensler, Yves Gallant, Vicky Kaspi, Bruce Langdon, Claire Max and Marco Tavani. However, I am solely responsible for the views expressed in the subsequent pages.

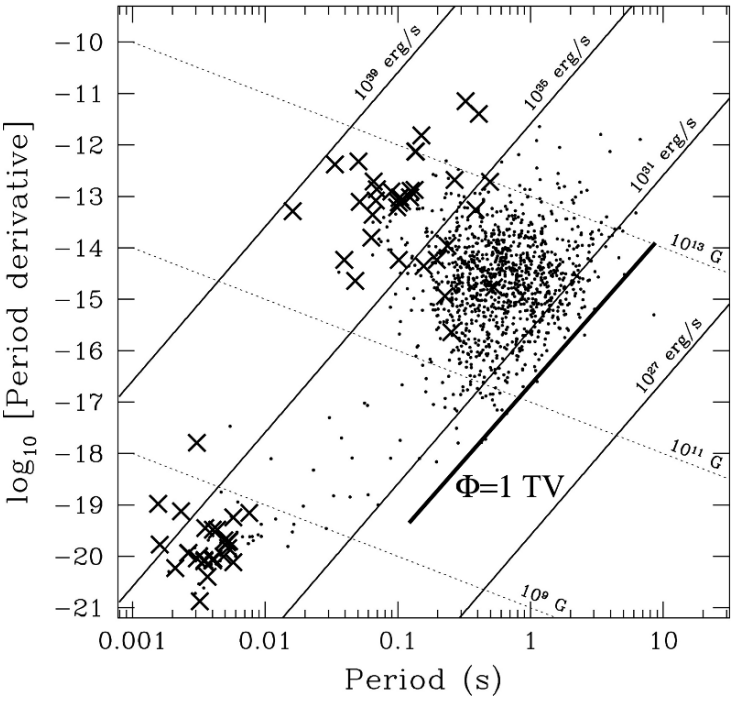

Fig. 15.1 Observed RPP periods and period derivatives, from [75]. "X" marks a pulsar with $P, \dot{P}$ measured from X-rays as well as radio observations. The line $\Phi = 10^{12}\,\mathrm{V} = 1\,\mathrm{TV}$ is the locus in the $P\dot{P}$ diagram where the rotation induced voltage drops to $10^{12}\,\mathrm{V}$, clearly marking a boundary beyond which pulsar emission is unlikely

distance $R_L = c/\Omega$, where the electromagnetic inertia $B^2/4\pi c^2$ causes the poloidal field to depart from the imposed stellar (dipole) field by an amount on the order of B_p itself. Then R_A is the smallest radius where B_ϕ becomes comparable to B_p, and $B_p \approx \mu/R_A^3$. Therefore

$$\dot{E}_R \sim 4\pi R_A^2 c \frac{E(R_A)B_\phi(R_A)}{4\pi} \approx \left(\frac{\Omega^4\mu^2}{c^3}\right)\left(\frac{R_L}{R_A}\right)^2. \tag{15.1}$$

For radio emitting Rotation Powered Pulsars (RPPs), stars are known with $\dot{E}_R = I\Omega\dot{\Omega}$ from as small as $10^{30}\,\mathrm{erg\,s^{-1}}$ to as large as $10^{39}\,\mathrm{erg\,s^{-1}}$ – I is the stellar moment of inertia, $I \approx 10^{45}$ cgs for currently acceptable equations of state for neutron stars.

Modeling of RPPs has one great advantage over modeling of other compact objects – observations of P, $\dot{P}$ determine the energy supply, to within the uncertainties in the moment of inertia. In contrast, modeling of accreting black holes always suffers from major uncertainty as to whether the systems are, or are not, accreting at a well determined rate, e.g., the Eddington limit. This fact runs through much

of what I discuss below – with the total energy budget known, the effort turns to aspects of the machine's physics at a level of sophistication not sustainable in many other aspects of compact object physics.

15.2.1 Force-Free Model: Heuristics

Expression (15.1) makes no reference at all to charged particles, and indeed the first theories of RPP spin-down (some invented before RPPs were discovered) invoked the electrodynamics of a vacuum rotator as an explanation of the observed $\dot{P}$ [45, 111, 112]. Except for geometric factors, vacuum theories yield expression (15.1), but with the special addition that as the angle $i \equiv \angle(\mu, \Omega)$ becomes small, so does the torque, in proportion to $\sin^2 i$. Application of this model to the spin-down data for normal RPPs yields dipole moments on the order of 10^{30} cgs, corresponding to surface dipole fields $B_* \equiv \mu R_*^3 \sim 10^{12}$ G for "normal" neutron stars.[2]

Vacuum models have large electric fields parallel to the magnetic field at the stellar surface, a fact which led Deutsch (in the context of the oblique rotator $i \neq 0$) to suggest that a vacuum rotator has to form a charged magnetosphere, as charged particles move from the surface to short out $\boldsymbol{E} \cdot \boldsymbol{B}$. Simultaneously with the appearance of the vacuum torque models after RPP discovery, [55] independently made the same observation in the context of the aligned rotator. They went further to suggest that a charge separated outflow forms, creating a conduction current $\boldsymbol{J} = \eta_R \boldsymbol{v}$, where η_R is the charge density required to force $E_{\|} = \boldsymbol{E} \cdot \boldsymbol{B}/B$ to zero, $\eta_R = -\Omega \cdot B/2\pi c +$ relativistic corrections. They also introduced the idea that the magnetosphere is "force-free", that is, the electromagnetic energy density is so large that all inertial, pressure and dissipative forces can be neglected, a concept consistent with the fact that RPPs are non-barking dogs – the large energy loss manifested in spin-down does not appear in any radiative emission associated with the magnetosphere (here defined as the region interior to R_A, probably $\approx R_L$.) Conceived of as a system which is strictly steady in the co-rotating frame – after all, pulsars form superb clocks, therefore the rotating lighthouse picture should apply, which it does, at least to averages of many pulses – the flow of the charges decompose into any velocity parallel to $\boldsymbol{B}$ plus rotation $\Omega \times \boldsymbol{r}$. The same charge density and velocity decomposition apply to the magnetohydrodynamic (MHD) model introduced by [100] in the same year, with the difference that the MHD model assumes a density large compared to η_R/q. Charge separated/MHD outflow and magnetospheric dynamics occurs for densities equal to or less than/greater than

[2] "Normal" means neutron stars discovered via their "normal" radio emission, an obvious selection effect. More recent discoveries, of millisecond radio pulsars and of X-ray selected objects, have revealed neutron stars with magnetic moments from $\sim 10^{33}$ cgs down to "zero" in the X-ray burst sources, which effectively means $\mu < 10^{26}$ cgs [75]. In particular, X-ray cyclotron lines confirm the existence of 10^{12} G surface fields.

$$\frac{|\eta_R|}{e} \approx \frac{\mu}{R_L^4 e}\left(\frac{R_L}{R_A}\right)^3 \frac{B}{B(R_A)}$$
$$\approx 6\times 10^3 \frac{\mu_{30}}{P_{100}^4}\left(\frac{R_L}{R_A}\right)^3\left[\left(\frac{R_A}{r}\right)^3+\left(\frac{R_A}{r}\right)^2\right]\ \mathrm{cm}^{-3}, \qquad (15.2)$$

if the particles have Larmor radii small compared to r. Here $P_{100} = P/100\,\mathrm{ms}$ and $\mu_{30} = \mu/10^{30}$ cgs. Interpreted as a particle outflow, this density corresponds to a particle loss rate

$$\dot{N}_R = 4\pi R_A^2 c\frac{|\eta_R(R_L)|}{e} = \frac{I_R}{e} = \frac{c\Phi}{e} = 2.7\times 10^{32}\frac{\mu_{30}}{P_{100}^2}\ \mathrm{s}^{-1}. \qquad (15.3)$$

The poloidal electric current I_R is the current expected such that the induced magnetic field becomes comparable to the dipole field at the light cylinder. In Goldreich and Julian's charge separated picture of the aligned rotator, the charges in I_R, composed of the charges in the fully charge separated plasma flowing parallel to the poloidal magnetic field, provides the support for B_ϕ and the Poynting flux. $\Phi = \sqrt{\dot{E}_R/c} = 1.3\times 10^{15}\mu_{30}/P_{100}^2$ V is the magnetospheric electric potential.

Observations of the synchrotron emission from young pulsar wind nebulae (PWNe) (e.g., [48, 51, 77, 122]) reveal particle injection rates $\dot{N}$ (in the form of electrons and – probably – positrons) corresponding to densities in a wind outflow $n = \dot{N}/4\pi r^2 c$ (at distances *much* larger than R_L) a factor of 10^3 and more larger than the density of the charge separated flow predicted by the charge separated wind idea. Thus the nebular observations suggest MHD models with a quasi-neutral plasma (which can only be electron–positron pairs, see Sect. 15.3), appear to be a good starting place for understanding these systems.

15.2.2 Force-Free Model: Results

Thus the simplest idea is that a dense plasma exists everywhere in the magnetosphere and beyond, with the plasma energy density much lower than $B^2/8\pi$ – for the young, high voltage pulsars, plasmas with energy density remotely comparable to that of the EM fields and still under the rotational control of the stars would lead to pulsed photon emission orders of magnitude greater than what is observed. The force free idea was elegantly formulated in the early 1970s in the "pulsar equation" for the aligned rotator [101, 128], a variation of the Grad-Shafronov equation familiar from the theory of magnetic confinement [15]:

$$\left(1-\frac{\varpi^2}{R_L^2}\right)\left(\frac{\partial^2\psi}{\partial\varpi^2}+\frac{\partial^2\psi}{\partial z^2}\right)-\left(1+\frac{\varpi^2}{R_L^2}\right)\frac{1}{\varpi}\frac{\partial\psi}{\partial\varpi}+I(\psi)\frac{\partial I}{\partial\psi}=0. \qquad (15.4)$$

Here ψ is the magnetic flux, with the poloidal magnetic field related to ψ by $B_p = -\varpi^{-1}\hat{\phi}\times\nabla\psi$, ϖ is the cylindrical distance from the rotation (z) axis, while

the toroidal magnetic field is $B_\phi = I(\psi)/\varpi$, with I the current enclosed within a circle around the z axis of radius ϖ. These fields are supported by charge and current densities all derivable from ψ, once a solution of (15.4) is determined. The electromagnetic structure of this non-pulsing model was (and is) thought to capture the essence of what is needed to make a full, oblique rotator model. The model says nothing about particle energetics – thus it, and its oblique rotator descendants, provides a geometric platform and an accounting of the dominant electromagnetic energy flow tapped by the subdominant dynamical processes that lead to the observable emissions. In particular, it does provide a basic model for the invisible processes that lead to pulsar spin-down.

Solution of (15.4) in the simplest relevant case (a star centered dipole with rotation axis parallel to the magnetic moment) has taken a remarkably long time. Solutions appeared immediately for a) a strictly co-rotating magnetosphere $I(\psi) = 0$, which is not relevant since it does not spin down (this dog really doesn't bark!) and implies particle motions faster than the speed of light at $\varpi > R_L$ and b) a star centered monopole, with an elegant result obtained by [102] whose most important element is the poloidal current function

$$I(\psi) = c\Phi \frac{\psi}{\psi_0}\left(\frac{2\psi_0 - \psi}{\psi_0}\right), \tag{15.5}$$

where $\psi_0 \approx \pi\varpi_{cap}^2(2\mu/R_*^3) \approx (\mu/R_L)(R_L/R_Y)$ is the open magnetic flux in one hemisphere of the monopole – R_Y is the equatorial radius of the Y point in the magnetic field which marks the largest extent of the closed magnetic field lines in the rotational equator, $\varpi_{cap} \approx (R_*/R_Y)^{1/2}$ is the cylindrical radius of the magnetic polar cap, and $\psi_0 = R_Y\Phi = \mu/R_Y$. Finding these solutions required inspired guessing of $I(\psi)$. In the years between 1973 and 1999, many attempts were made to solve (15.4) by guessing various forms for $I(\psi)$ and applying ever more clever analytic techniques to this fundamentally non-linear model. None yielded anything credible – see [98] for a summary of much of this work.

The situation changed when [35] took seriously the nonlinear eigenvalue and eigenfunction character of (15.4) and its associated boundary and regularity conditions and successfully applied an iterative numerical technique to find B and $I(\psi)$ to produce a result with $E \cdot B = 0$ and $E^2 - B^2 < 0$ everywhere – the latter condition is required if the model is to be taken seriously as a representation of a physical magnetosphere, since the $E \times B$ velocity must be sub-luminal, for a physical model.[3] This solution, in which the last closed field line is assumed to have equatorial radius equal to R_L, has been reproduced with increasing numerical accuracy by [57,94,132,138]. It exhibits a number of long expected features [104]. In particular, the last closed field line has a Y-type neutral point on the equator, with return current flowing (mostly) in an unresolved current sheet along the boundary of the closed zone, then extending as an equatorial current sheet to radii $\varpi > R_Y$. Figure 15.2, taken

[3] $E^2 - B^2 > 0$ is possible, in principle. However, in the absence of losses particles then accelerate to energy $\sim q\Phi$ in distances not greater than R_L. In the younger pulsars, the acceleration becomes radiation reaction limited, implying radiation emission from RPPs far in excess of what is observed.

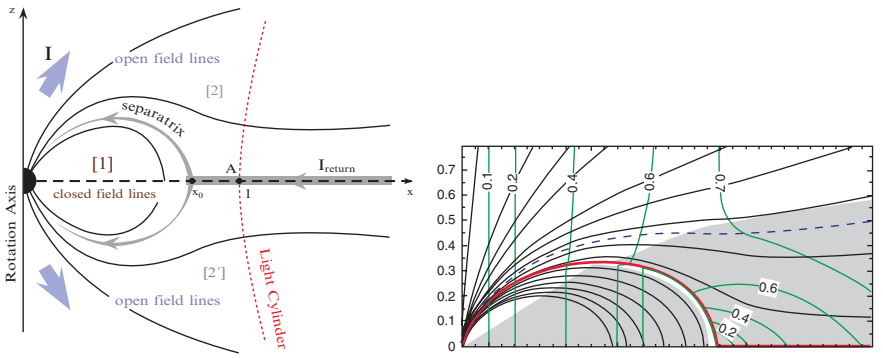

Fig. 15.2 *Left*: Cartoon of the aligned rotator's magnetosphere, showing the primary polar current and the return current flowing along the separatrix at the equatorial current sheet. The anti-aligned case, with μ anti-parallel to Ω is shown. The aligned case has the same topology, with the sign of the current flows reversed. *Right*: Field lines (magnetic flux surfaces) of the aligned rotator solution, for the case $R_Y = 0.992 R_L$

from [138], shows the poloidal magnetic geometry of the aligned rotator. The solution illustrated has $\psi_0 = 1.23\mu/R_L$, in the case $R_Y/R_L = 0.992$, in excellent agreement with [57] and with [35], who assumed $R_Y = R_L$ exactly. All authors agree on the spin-down energy losses of the aligned rotator, $\dot{E}_R = k\Omega^4\mu^2/c^3$, $k = 1 \pm 0.1$.

As predicted by [103], the asymptotic structure ($r = \sqrt{\varpi^2 + z^2} \gg R_L$) approaches that of the (split) monopole, as appears most clearly in McKinney's and Timokhin's results. Thus the poloidal current flow is almost that of the monopole, a point discussed further below. Also, as shown by [56], [34] and [138], the steady state force free magnetosphere has a whole range of possible solutions, parameterized by $R_Y/R_L \leq 1$.

By solving the time dependent force free equations, [132] showed that the force-free magnetosphere evolves with $R_Y \rightarrow R_L$, starting from a static vacuum magnetic dipole on a star instantaneously set into rotation with angular velocity Ω; at $t = 0$, the electric field on the stellar surface was set equal to $-(\Omega \times r) \times B$. The rate of approach of R_Y to R_L depends on the artificial resistivity used to control singular behavior at current sheets. Komissarov [81] and Bucciantini et al. [29] found similar results using a relativistic MHD model (i.e., inertial forces included). Spitkovsky's method allowed the current sheet to have an arbitrary shape. Thus, he also succeeded in finding the force free solution for arbitrary i; the resulting 3D model of the magnetic field appears in Fig. 15.3. Within the assumption of a magnetosphere everywhere filled with plasma of density sufficient to short out parallel electric fields (and no physics that might support such electric fields in a plasma of density greater than $|\eta_R|/e$), a full solution for the electromagnetic structure of the RPP's magnetosphere (both aligned and oblique rotators) is now available, after 38 years of discussion. Spitkovsky's result,

$$\dot{E}_R = k\frac{\mu^2\Omega^4}{c^3}(1 + \sin^2 i),\ k = 1 \pm 0.1, \tag{15.6}$$

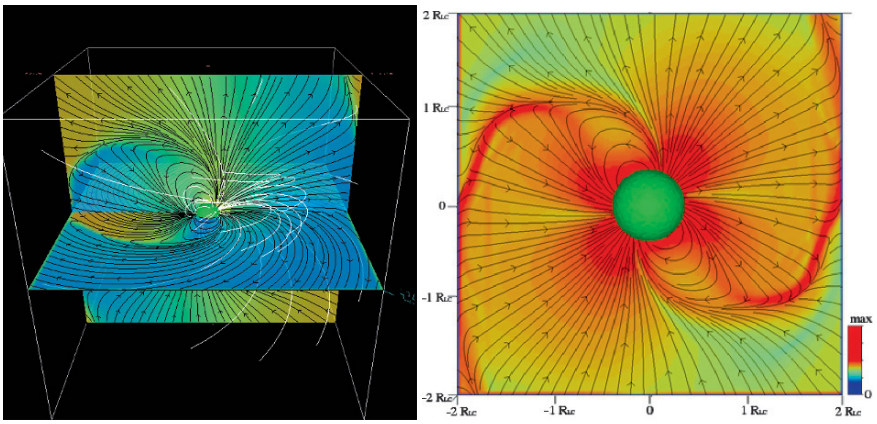

Fig. 15.3 *Left*: A snapshot of a force free simulation of a RPPs magnetosphere, for $r < 2R_L$ (from [132]). *Right*: Total current $(c/4\pi)\nabla \times B$, the sum of conduction and displacement currents

contains all the aligned rotator studies as a special case. As is clear from Fig. 15.3, the magnetic topology of the oblique rotator (closed field lines terminating at a Y line, current sheet extending from the Y line separating regions of oppositely directed field in the wind) is a rotationally distorted version of the simpler aligned rotator geometry.

15.2.3 Beyond the Force-Free Model: Plasma Sighs and Whispers

Until recently, the magnetosphere was assumed to have $R_Y = R_L$, an assumption consistent with the observation that radio emission from low altitude appears to occupy a polar flux tube which, if modeled as being in a static vacuum dipole's geometry, is bounded by a closed zone which appears to extend to the light cylinder [84, 120], i.e., have a polar cap opening angle $\theta_c = (R_*/R_Y)^{1/2}$ with $R_Y = R_L$; of course, the observations and the simplified model do not come close to *proving* that $R_Y = R_L$, or even that static dipole model for the B field is accurate all the way to $r = R_Y$. But if $R_Y/R_L \leq 1$ is some constant, then since R_L increases as the pulsar spins down, there must be net conversion of open field lines to closed field lines (transfer of open magnetic flux to closed flux) on the spin-down time scale. This topological change requires reconnection and a violation of ideal MHD, at least in local regions – the likely culprit is the Y-line and the current sheet, as has been observed by [34, 36]. Having made this observation, [34] suggests that for pulsars near the death line in Fig. 15.1, reconnection proceeds sporadically – the magnetosphere "coughs" – because of failure in the supply of plasma from the polar cap accelerator and pair creation region – see Sect. 15.3. He applies this idea to a scenario for the major outburst observed in the magnetar SGR1806−20 on December 27, 2004 [72, 117].

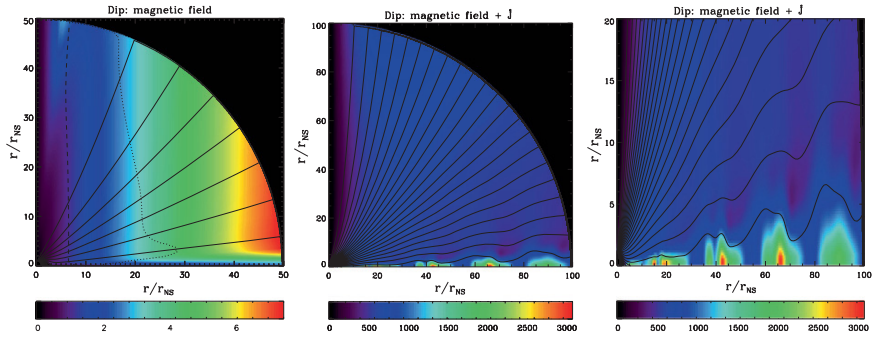

Fig. 15.4 *Left*: Magnetic structure of a relativistic magnetosphere with mass outflow, in a case when the magnetic pressure at the light cylinder exceeds the relativistic plasma inertia by a factor approaching 20, a record high for MHD calculations. The *contours* represent poloidal magnetic field lines, while *colors* represent the ratio B_ϕ/B_r. Reconnection have been artificially suppressed. *Middle*: Snapshot of the magnetic structure when the reconnection components of the electric field are not suppressed. Reconnection occurs because of numerical resistivity introduced by the finite difference scheme. Plasmoids emerge along the equatorial current sheet, grow and flow out at the local Alfvén speed ($\sim c$). *Right*: Blow up of the plasmoid structure

In fact reconnection is likely have an unsteady, "bursty" character for all pulsars[4] – the magnetosphere should be noisy at some level all the time. Figure 15.4 shows a snapshot of the magnetosphere of a rotating neutron star with large plasma supply, taken from [29]. This relativistic MHD (not force-free) model was designed to represent the wind from a young, rapidly rotating magnetar, with the wind driven by the enormous thermal pressure at the neutron star's surface. The wind, formed by plasma flowing out on open field lines, converges on the equatorial current sheet. That convergence causes driven reconnection, operating in a bursting mode – the sheet forms "plasmoids", islands of reconnected poloidal field with closed, O-point magnetic topology[5] which flow away at the local Alfvén speed, $\sim c$. Numerical resistivity in the code provided the dissipation required to allow the transformations of field topology shown – the GEM study of non-relativistic reconnection [21] demonstrated that any non-ideal effect allows rapid driven reconnection with inflow velocity into the separatrix (the current sheet separating the closed field from the open field regions in Figs. 15.2 and 15.3) being $(0.1\text{–}0.2)v_A$, outside the restrictive bounds of incompressible MHD with uniform resistivity. Note that the reconnection sporadically transforms the Y-line into a X-line, with the current sheet then containing a series of *dynamical* X-lines, all leaving the star – [89] objection to the formation of a *stationary* X-line (the field lines inside the separatrix on the open side of the X-line are not anchored to the magnetosphere) is answered simply by the fact that the plasmoids indeed are not anchored to the magnetosphere and fly

[4] Reconnection measured in the laboratory and in space plasmas, and observed in solar plasmas, does occur with bursty, often explosive, behavior.

[5] In these axisymmetric models, the islands are magnetic torii.

away, but constantly reform. The Poynting flux was found to be time dependent, fluctuating around the mean by ∼30%.

The Bucciantini et al. model was not designed specifically for classical RPPs, or for magnetars in their currently observed state – future work on reconnection in configurations with electron–positron plasma, where the Hall effect, so important in the nonrelativistic studies, is absent (and is replaced either by pressure anisotropy as the facilitator of rapid reconnection, as pointed out by [19], or by particle inertia), in a state suggested by the models of plasma supply in RPPs' magnetospheres, are required to quantify this "noisy magnetosphere" picture. In particular, extending such modeling to the full 3D rotator in strongly magnetized MHD has not yet been done. Also, *it remains to be demonstrated that noise in the current sheet at and beyond R_Y communicates back to the inner magnetosphere and the star*, through (kinetic) Alfvén waves traveling back along field lines at and near the separatrix (see Sect. 15.3).

But if this picture does apply to RPPs, it has a number of consequences for observables and outstanding questions, some of which I touch on further in Sect. 15.3. From the point of view of the basic energetics embodied in spin-down, the fluctuating Poynting flux may imply a fluctuating torque. Noise in pulsar spin-down has been known since the early days – it limits the ability to time pulsars coherently. If the magnetic field interior to but near R_Y fluctuates by tens of per cent on time scales comparable to the rotation period, and these fluctuations represent variations in the poloidal current that communicates stress to the star, then the torque is noisy with magnitude the same as is inferred from representing the observed random walks in the rotation frequency [37, 38, 59] as being the consequence of white noise in the electromagnetic torque [6] – reconnection may provide the mechanism for magnetospheric instability and torque fluctuations that was not specified in this early attempt at scenario building).

Magnetospheric noise opens the possibility that R_Y/R_L evolves. One can readily show [29] that the braking index, defined as $n = \bar{\Omega}\ddot{\bar{\Omega}}/\dot{\bar{\Omega}}^2$ (with averages indicating the usual average over subpulses taken in measuring pulsars' periods, here taken to be the same as an average over plasmoid emission and torque fluctuations), in a magnetosphere with evolving R_Y/R_L but fixed μ and i, is

$$n = \frac{\bar{\Omega}\ddot{\bar{\Omega}}}{\dot{\bar{\Omega}}^2} = 3 + 2\frac{\partial \ln\left(1+\frac{R_Y}{R_L}\right)}{\partial \ln \bar{\Omega}}. \tag{15.7}$$

Braking indices less than 3 ([88] and references therein) thus may indicate a progressive lag of the closed zone's expansion, measured by the radius of the Y line, behind the expansion of the light cylinder as a pulsar spins down.

This is hardly the only thinkable explanation of $n < 3$. Magnetic moment evolution has long been advocated as the origin of small braking indices, going back to the crustal field growth model of [23] – which doesn't actually work in those authors' formulation, the threshold for growth set by crustal resistivity is too high – to Ruderman's model for growth of $\mu_\perp = \mu \sin i \propto \sqrt{P}$ due to interaction of interior magnetic

flux tubes with the quantized vorticity of the superfluid interior (e.g., Ruderman, this book). When combined with expression (15.6), this model yields

$$n = \frac{3 + 4\frac{\Omega_0}{\Omega}\tan^2 i_0}{1 + 2\frac{\Omega_0}{\Omega}\tan^2 i_0}\,, \tag{15.8}$$

where Ω_0, i_0 are the angular velocity and obliquity at the time when the arrays of quantized magnetic flux tubes and vortex tubes have both formed, thought to be perhaps 10^3 years after the neutron star's birth. This model can produce any braking index between 2 and 3.

Fluctuations and oscillations in the co-rotating frame of the currents at the light cylinder also offer a possible explanation for the long known fact that pulsars are *flickering* lighthouses. The well-known pulse stability that allows exquisitely precise timing applies to average pulses, formed by summing hundreds to thousands of individual pulses. However, individual pulses arrive with at varying times within the pulse window, usually at random in those pulsars with "core" emission characteristics, and either at random or with an organized drift of the arrival times through the pulse window, in stars with "conal" emission characteristics (see [119] for pulsar beam classification). Figure 15.5 shows an example of pulse to pulse variability. Typically one or at most two pulse components are within the pulse window at any one time, suggesting the individual pulse variability time is on the order of the rotation period. That time scale is consonant with the Alfvén wave transit time from the low altitude emission region to the radius of the Y-line, where current fluctuations are formed, a coincidence suggesting the subpulse variability (both random and drifting) is a consequence of current variations created by activity in the outer magnetosphere [6]. In this picture, drifting and chaotic subpulses are both the consequence of the same dissipative dynamics of the currents coupling the magnetosphere to the wind, with drifting subpulses reflecting limit cycle behavior of magnetospheric reconnection while chaotic subpulses represent a more random, bursty behavior of the field lines topological changes. Objects such as PSR B0943+10, in which transitions from organized drifting to chaotic single pulse behavior and back are observed [121], are particularly telling laboratories for investigation of the connection between current flow and pulsar emission, and thus offer insight into magnetospheric dynamics.

15.2.4 Electrospheres?

There is, however, a ghost hiding inside the force-free/MHD magnetospheric machine. These theories assume that a plasma dense enough to enforce $E_\parallel = 0$ is present everywhere in the magnetosphere, an assumption which relies upon the pair creation physics summarized in Sect. 15.3. Pair creation assumes relativistic beams contribute a substantial fraction – possibly all – of the electric currents embodied in the force-free and MHD models, since only these beams can (plausibly) emit the gamma-rays that convert to $e^{\pm}$. One can think of pair creation as an instability of the

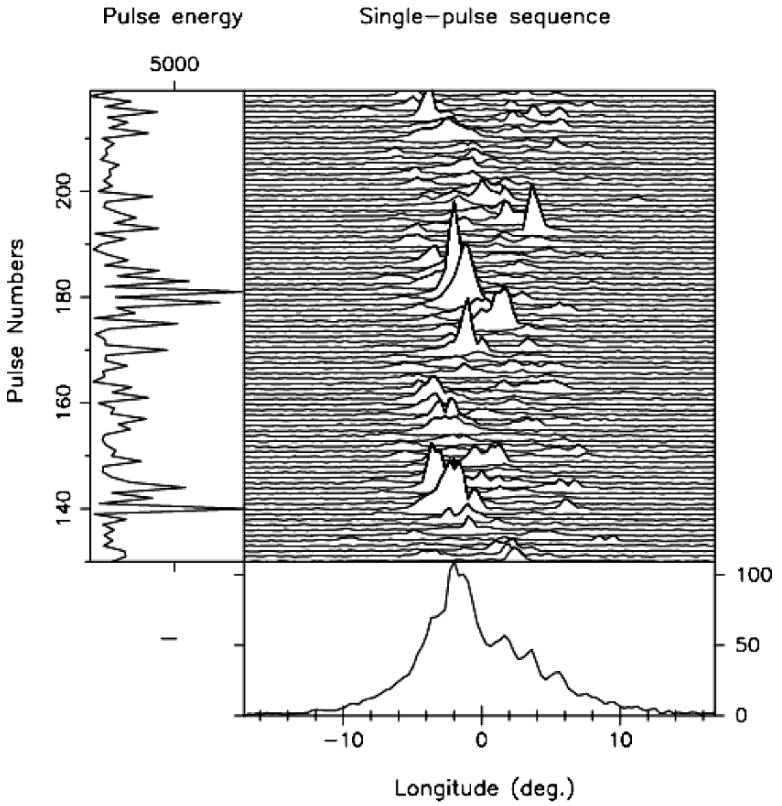

Fig. 15.5 A series of individual pulses from PSR B0943+10 (*center*). The average pulse is shown in the *bottom panel*, as a function of pulse number and longitude, with 360° or longitude corresponding to one rotation of the star. This star shows organized drifting of the pulses through the pulse window. From [44]

current flow originally hypothesized in the fully charge separated scenario of [55]. But, as was recognized not long after the charge separated outflow scenario was suggested, the charge separated wind model must fail, so long as charged particle flow across field lines is forbidden – many field lines of a dipole (not a monopole) must pass through a surface where $\Omega \cdot B = 0$. The charge (and plasma) density of the charge separated medium on the exterior (larger) radius side of this "null surface" has sign opposite to that of the plasma that can be supplied from the stellar surface by particle motion parallel to B. The plasma in this exterior region has no source, if the only allowable charged particle motions are sliding along the magnetic field plus bulk flow $E \times B$ drift [67,68]. Thus, one expects such a magnetosphere to open large gaps, and probably have no charged particle wind – certainly no wind with particle flux greatly in excess of $\dot{N}_R = c\Phi/e$.

Such "electrospheres" [85] do *not* appear to be unstable to pair creation [114], thus do not collapse to the plasma filled state hypothesized in the force free models,

by pair creation alone. However, they are unstable to cross field transport even without pair creation. A large gap separates the equatorial regions of the electrosphere from the stellar surface, leading to differential rotation of the equatorial plasma. This differential rotation is subject to the diocotron instability – a variation of a Kelvin–Helmholtz instability [115, 134]. Simulations [113, 116, 134] suggest the resulting time dependent (in the co-rotating frame) $E \times B$ drifts create cross-field "diffusion" which may relax the charge separated magnetosphere to something approximating the state envisaged by Goldreich and Julian. Expansion of the equatorial plasma is illustrated in Fig. 15.6.

Bottoms-up models based on these results have not been investigated. The fact that young pulsars supply their nebulae with particle fluxes greatly in excess of $\dot{N}_R$

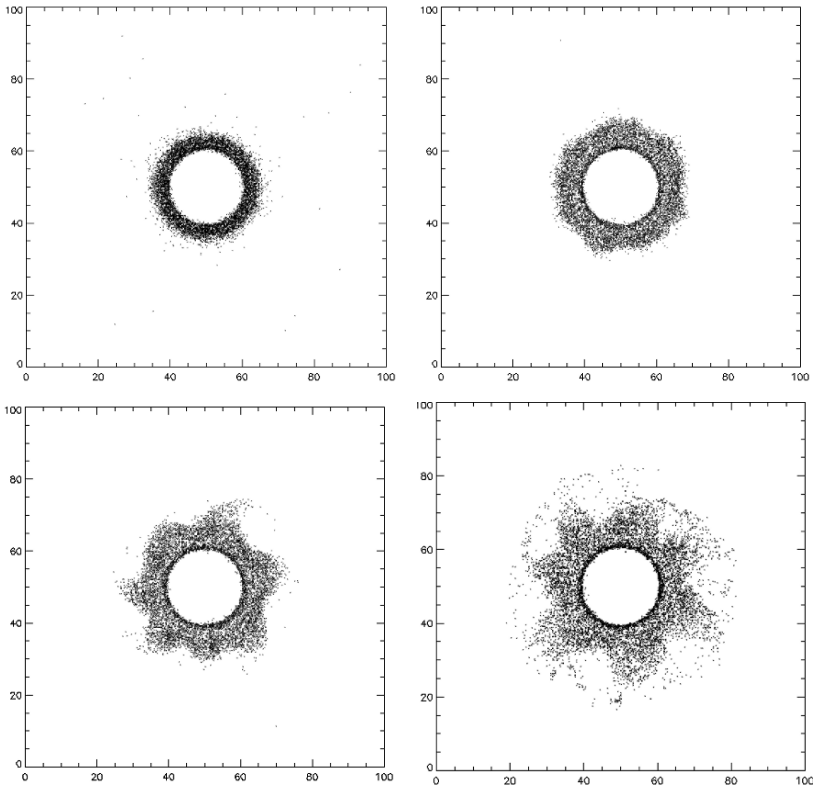

Fig. 15.6 Spreading of the equatorial charged disk in the electrosphere of an aligned rotator under the influence of the diocotron instability, from a PIC simulation of the flow, from [134]. The figure shows a series of snapshots of the disk's density in the rotational equator of the neutron star, which fills the central circle – the spatial scale is in units of computational cells, with 10 cells equaling one neutron star radius. The time sequence goes *from left to right*, with the lower row following the upper row. The simulation begins with the small disk of the equilibrium electrosphere. At later times the disk spreads and develops non-axisymmetric rolls and fingers, characteristic of Kelvin–Helmholtz instabilities, to which diocotron instability is closely related

lends support to the perhaps more practical view that the filled magnetosphere model has consequences in reasonable accord with observations of high energy pulsed emission and of pulsar wind nebulae, thus deserves the main focus of scientific attention. Such models may have charge separated current flows possibly unstable to pair creation.

The force free solutions and their possible extensions have a number of implications for emission models, and for the pair creation models that underlie the emission physics.

15.2.5 Magnetic Geometry of Radiating Layers

The oblique rotator solution determines a polar cap/polar flux tube size and shape. These are non-circular, and have centroid displaced from the magnetic axis (Spitkovsky, personal communication). Such changes in magnetic geometry from the conventional assumptions need to be folded into radio beaming and polarization, and polar cap X-ray emission models, which often invoke *ad hoc* changes in polar cap size and shape, perhaps created by surface anomalies in the surface magnetic field (e.g., [97]), in order to explain departures from the simplest, static dipole geometry. The need for such extra parameters in the models needs to be evaluated in the context of realistic magnetic geometry of the rotating dipole.

The surface of last closed field lines (the separatrix) and of the return current flowing along that separatrix has been determined within the force-free approximation. Particle acceleration in gaps (regions of low density where a parallel electric field $E_\parallel = E \cdot B/B$ forms because of charge starvation below the Goldreich–Julian density) on the open field lines close to this surface has been advanced as the origin of the pulsed gamma-rays observed from a small number of pulsars ([66, 108] and references therein) by the EGRET experiment [139] and by other high energy detectors, with a substantial increase in the population observed expected with the launch of the GLAST telescope [96].

These models use magnetic geometry borrowed from the vacuum oblique rotator, with plausible but ad hoc prescriptions for the shape of the separatrix and for the choice of field lines assumed to participate in the gap. Strictly steady flow (and therefore electrostatic accelerating electric fields in variety of free parameters (especially the thickness of the assumed accelerating layer) allows fits of the resulting radiation spectra and pulse profiles to observations with greater or lesser success. Since such geometric constructions are sensitive to the exact form of the geometry such model construction would be a step toward probing the basic structure of the magnetosphere, a task made possible since all the phenomenological gap models contain parallel voltage drops $\Delta\Phi_\parallel = \int E_\parallel ds$ small compared to Φ, therefore allowing the force-free theory to be a good zeroth order platform for parallel accelerator and radiation model construction.

15.2.6 Current Flow Profile and Gap Electrodynamics

The force free electrodynamic solutions also exhibit an important result which affects *all* the gap models constructed for the last 30 years, starting with the vacuum surface and outer gaps of [32, 126] and their many successors, as well as the space charge limited flow beam models, both with and without slot gaps, of [5,8,12] and the many successors of this modeling idea.

All these schemes embody the idea that $E_\parallel$ appears as a result of the magnetosphere's attempt to restore charge neutrality in the co-rotating frame by accelerating non-neutral beams of particles with density comparable to the Goldreich–Julian density η_R/q, with that adjustment to perfect charge neutrality in the co-rotating frame being incomplete – an $E_\parallel$ due to charge starvation. In such configurations, the field aligned current $J_\parallel = J \cdot B/B$ adjusts to a value controlled by the local electrostatics of the hypothesized region of charge starvation, not to a value determined by the energetically dominant magnetospheric dynamics.

For currents emerging from the star's atmosphere, the accelerating $E_\parallel$ appears from the gravitational depletion of density below the Goldreich–Julian value, due to the low temperature and low radiation pressure which prevents the filling of the magnetosphere and formation of a wind with a charge neutral plasma pushed up by pressure and centrifugal forces from the stellar surface. The current supplies the charge needed to support a polarization electric field which (almost) cancels the vacuum field. The residual ("starvation") electric field still supports enough of a voltage drop to allow the accelerated particles to emit gamma-rays that can convert to electrons and positrons. The resulting gap structure, elaborated assuming strictly steady flow in the co-rotating frame, thus enforces a current density almost uniform with distance from the magnetic axis, with value close to the canonical value $c\eta_R$. Since this current fills (almost) the whole polar cap, the total current from a polar cap is $I \approx c\eta_R \pi r_{cap}^2 \approx c(\Omega B_{cap} \cos i/2\pi c)\pi R_*^3/R_Y = c\Phi$, which suggested that such a gap *might* be an element of the magnetospheric circuit, although with the peculiar property that the charge density (and therefore the current density) is an eigenfunction of the local electrostatics. The return current is not included in these local acceleration models, being explicitly or implicitly assigned to the current sheet.

Such local determination of $J_\parallel$ is not what one expects on energetic grounds, since the current density reflects the induced magnetic field, through which all the spin-down energy loss flows. That energy flow is much larger than the energy flowing through the proposed electrostatic accelerator, which is thought of as a small perturbation of the force-free structure. In the absence of further information from full magnetospheric solutions, or specific features coming from phenomenological models of radio or high frequency pulse observations which characterize the current flow in more detail, the hope expressed by the approximate correspondence between the total gap current and the current of the magnetospheric circuit has stood unchallenged.[6]

[6] That one might be able to use observations to probe the current flow structure has been an almost untouched subject. One of the few counterexamples was provided by [63], who pointed out that

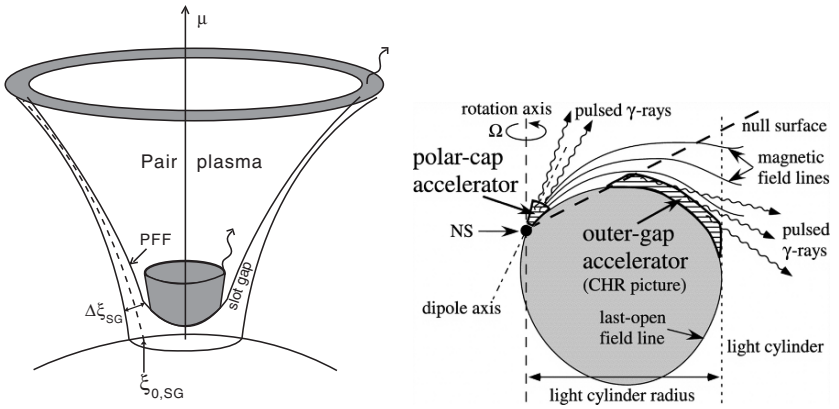

Fig. 15.7 Location of proposed charge starvation gaps in the magnetosphere, employed in models for pulsed high energy emission. *Left*: slot gap model of [8, 12, 107, 108]; figure from [107]. *Right*: classical outer gap geometry of [32, 33, 123, 125]; figure from [66]

For outer gaps, whose morphology appears in Fig. 15.7, the current density is also established by the effect of pair plasma shorting out the starvation $E_{\parallel}$, since within the gap counter streaming electron and positron beams coexist, with acceleration ceasing at the end points where the pair density rises to be approximately equal to the Goldreich–Julian density – or not at all, along field lines closest to the (assumed) conducting boundary formed by the last closed field line, where pair creation is weak, for reasons traceable to the assumed geometry. Figure 15.8 shows the place outer gaps might have in a hypothetical picture of the global circuit. The starvation electric field can be sustained only if the $e^{\pm}$ beams have density not exceeding $c\eta_R/e$, therefore the current density necessarily approximates the Goldreich–Julian current *density*. Since the gap must be thin in the poloidal direction across B (otherwise the photon emission from the gap would not make a narrow pulse, the express purpose for which the gap model was designed), the total gap current has to be small compared to the magnetospheric current – outer gaps cannot close the whole magnetospheric circuit, if they are to have any pretensions as a successful model for pulsed gamma-rays. Their biggest success, which they share with the slot gap model, is the assignment of the radiating geometry for gamma-ray pulsars to a thin sheet which closely follows the last closed flux surface of the oblique rotator.

Outer gaps, as regions of field aligned acceleration relying upon starvation electric fields, can occur only on field lines not supplied with a dense plasma either from the polar caps, as comes from the polar and slot gap space charge limited acceleration region, or from the recirculation of polar outflow by reconnection flows in the vicinity of the Y-line. Also, the outer gap, if it exists, sends almost all of its pair plasma back to the stellar surface, rather than supplying the wind [66]. Thus the outer gap has a hard time being a major supplier of the known large ($\dot{N}_{\pm} \gg \dot{N}_R$)

thin return current layers might create observable signatures in the radio polarization data. Their predicted signature of the return current layer may have been seen in PSR J1022+1001 [118].

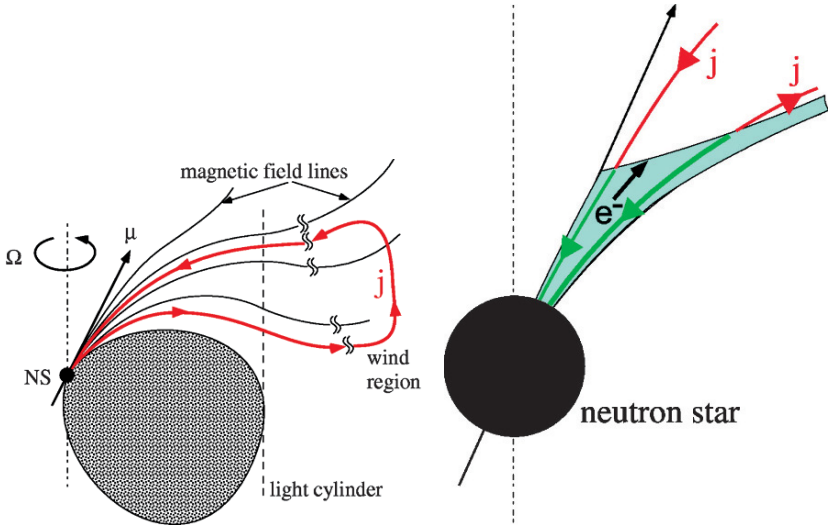

Fig. 15.8 Current flow patterns hypothesized for modern outer gap models [66], which include possible outward ion flow on field lines near the separatrix (in $i < 90^\circ$ geometry). *Left*: global pattern assuming a closed circuit, with currents closing in the wind. *Right*: hypothetical current flow from the star through the null surface. No attempt is made to account for the return current in the current sheet in these models, nor has there been any correspondence made between these hypothetical current flows and the currents in the force free solutions

particle fluxes known to be injected into the young Pulsar Wind Nebulae, as discussed further in Sect. 15.3. Outer gaps also run the risk of supplying too much energy in precipitating particles to the stellar surface, thus powering too much thermal emission. Outer gap modelers have mostly swept these issues under the rug.

15.2.7 Gap Subversion: Non-Uniform Current Profiles

All gap models (vacuum polar cap gaps, space charge limited flow polar cap and slot gaps, outer gaps) function as suppliers of plasma which come as close as possible to restoring the charge density to the Goldreich–Julian density η_R. They rely on starvation electric fields, since the gaps' charge densities fall below η_R (by a little or a lot, depending on the model). Since the voltage drops developed in the gaps are highly relativistic, such plasma takes the form of relativistic particle beams, with the resulting current density parallel to B being $J_\parallel = c\eta_R(1-h)$, where $h \ll 1$ for polar cap and slot gaps (the stellar surface supplies a beam of charge density almost equal to η_R, thus trapped particle back-flow formed at the PFF is small), while in traditional outer gaps, $h \approx -1$, (the pair formation front at each end has to trap plasma with the full Goldreich–Julian density, forming two counter streaming beams of approximately equal density). This current is almost constant, as a

function of distance across the magnetic flux surfaces (formally, $J_\parallel(\psi) \approx$ constant). All the models assume strictly steady current and plasma flow in the co-rotating frame (electrostatic approximation), even though the models' authors frequently indulge in discussion of time dependence that they think should be part of their proposals. Steady current flow *has* been found in evolutionary force-free and relativistic MHD models [81, 132] – these show no signs of variability in the co-rotating frame (they also cannot capture reconnection physics, which requires probably requires higher resolution simulations than have been employed so far, and probably also requires incorporating more physical models of dissipation and inertia). But, even though global and local theories both have stationary lighthouse behavior built in, the consequences of gap electrostatics for the current flow distribution are entirely *inconsistent* with the results of force free modeling, because of a serious mismatch between the current profiles found in the gap and in the global models.

Figure 15.9 shows the poloidal current density, as a function of magnetic flux, exhibiting the fact that a fraction ($\sim$20%) of the return current flows on open field lines just within the boundary of the closed zone if $R_Y = R_L$; the rest of the return current lies within the unresolved current sheet separating the closed from the open field lines. Thus, as far as current flow is concerned, 30 years of research on the force free rotator can be summarized by saying that to within 20% accuracy, the current flow distribution of the force free dipole is that of the monopole, whose total current appears in (15.5) – as far as the open field lines are concerned, the dipolar magnetosphere is the monopole mapped onto a polar cap, in each hemisphere. The current density as a function of distance from the magnetic axis then is (ignoring the small piece of the return current required on open field lines)

$$J_\parallel = \frac{dI}{d\psi} = j_{GJ}\left(1 - \frac{\psi}{\psi_{cap}}\right) = j_{GJ}\left(1 - \frac{\varpi_*^2}{\varpi_{pc}^2}\right), \tag{15.9}$$

where $j_{GJ} = c\eta_R(\varpi_* = 0) = \Omega B_{cap}\cos i/2\pi$ and ϖ_* is the cylindrical distance of a field line's footpoint from the dipole axis. If the polar current is a charge separated, steadily[7] flowing beam extracted from the star's atmosphere by $E_\parallel$ with charge density $\eta = J_\parallel/c\beta$, with $\beta \approx 1$ except in a thin region at the surface of thickness 10 or so times the atmospheric scale height, then the difference of this beam charge density from the Goldreich–Julian density is of order η_R itself over most of the polar flux tube:

$$\frac{J_\parallel}{c} - \eta_R = \frac{j_{GJ}}{c}\left(1 - \frac{\psi}{\psi_{cap}}\right) - \frac{j_{GJ}}{c} = +\frac{|j_{GJ}|}{c}\frac{\varpi^2}{\varpi_{cap}^2} \to \frac{|j_{GJ}|}{c}, \varpi \to \varpi_{cap}. \tag{15.10}$$

Expression (15.10) means that the parallel electric field is not almost shorted out by the space charge density of the particle beam from the surface, thus returning the space charge limited flow to an environment with an electric field akin to what was envisaged for vacuum gaps (if the plasma forming the return current on the polar flux tube's boundary behaves as a perfect conductor, as has been assumed in all

[7] Steady on times long compared to the polar cap transit timescale $\varpi_{cap}/c \sim 10\,\mu$s.

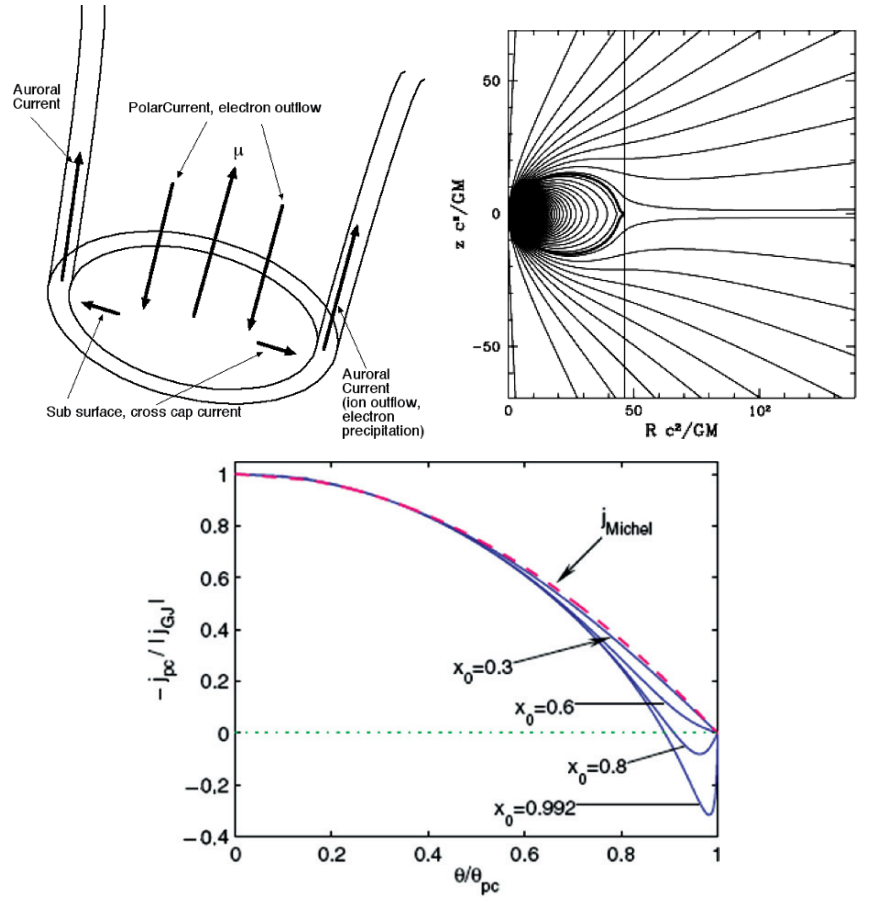

Fig. 15.9 Polar current flow patterns hypothesized and found from force free models. *Top Left*: Polar current flow with all return current in the current sheet, and illustrating balancing the charge loss with an ion current extracted from the surface, in response to electrons and plasma precipitating from the Y-line [6,7]. *Top Right*: Magnetic field lines of the aligned rotator when $R_Y/R_L = 1.0$, from [94], showing the asymptotically monopolar character of the poloidal field structure. *Bottom*: Current flow in a force free solution of the aligned rotator, for various values of $x_0 = R_Y/R_L$ [138]. θ is the magnetic colatitude of a field line's footpoint, and θ_{pc} is the magnetic colatitude of the polar cap's edge, defined as the intersection of the separatrix between closed and open field lines with the stellar surface

models to date), but now with the requirement (since the stars have dense, thermal X-ray emitting atmospheres) that $E_{\|}(r = R_*) = 0$.

The resulting huge acceleration inevitably leads to massive pair creation, in the manner of the [136] picture of a high energy beam coexisting with massive pair creation and acceleration with almost all of Φ being dropped by the electric field within a height about equal to the polar cap width. Such a situation has both interesting possibilities and large problems, both theoretical and observational.

Pairs forming in an approximately vacuum electric field will short out $E_\parallel$ at a height such that the voltage drop $\Delta\Phi_\parallel$ is sufficient to allow the accelerating particles of the beam from the surface to emit magnetically convertible gamma-rays. Typically, $\Delta\Phi_\parallel \sim 10^{12}\ \mathrm{V} \ll \Phi$. Because the difference charge density (15.10) is a large fraction of $-\eta_R$ over most of the open flux tube, the pairs have to supply most of the charge density needed to shut down $E_\parallel$ at the pair formation front (PFF). Because the pair formation front is now formed at lower altitude than is the case in space charge limited flow models with the current density determined by the local electrostatics, pair cascades may be better able to supply the total plasma flux inferred from pulsar wind nebulae, as discussed in Sect. 15.3. However, the pairs generally are born with energies small compared to $e\Delta\Phi$. Therefore, particles with charges having the same sign as the particles of the beam extracted from the stellar atmosphere are added to the outbound beam, while particles with the opposite sign of charge are trapped electrically and go backwards – backflow from the PFF enhances the current. If the potential is monotonic, the particle backflow collides with the stellar surface with number flux $\approx (c|\eta_R|/e)(\varpi/\varpi_{cap})^3$ and energy/particle $\sim e\Delta\Phi$. The particles in the backflow lose their energy after penetrating several hundred gm/cm^2 into the crust, heating the atmosphere from below. Then each pole would have thermal X-ray emission with luminosity/pole $L_{X\,pole} \approx 0.5\dot{E}_R(\Delta\Phi_\parallel/\Phi)$. With $\Delta\Phi_\parallel \sim 10^{12}$ V (the voltage defining the theoretical death line in Fig. 15.1), these heated polar caps would emit substantially more thermal X-rays than are observed in many RPPs. Similar backflow in "spark" models runs into the same difficulty.

The traditional space charge limited polar caps, in which the current carrying beam extracted already has density close to $|\eta_R|/e$, greatly reduce this emission – in modern models, in which dragging of inertial frames controls the difference between the beam's density and $|\eta_R/e|$, the reduction is by a factor $\sim 0.4GM/R_*c^2 \approx 0.06$. This reduction is enough to give polar cap X-ray emission either in accord with observations of some pulsars, or small enough to be hidden by magnetospheric nonthermal emission. But the price paid is an electric current (formed by response to backflow from the PFF as well as by emission from the atmosphere) over the whole polar cap (stationary or non-stationary) which is large compared to (15.9) except near the magnetic axis. Furthermore, just as in the early spark gap models of [126], the difference charge density in (15.10) implies a nonzero $E_\parallel$ incident on the star's surface – really, the top layers of the atmosphere required to explain polar cap thermal emission in many pulsars.

A number of ideas have been advanced to resolve this conundrum:

- The PFF has a different structure than has been found in studies starting with [12] all the way through recent work on the full slot gap [107, 108]. If somehow electrons could be made to precipitate from pair plasma above the PFF and enter the current flow region, the current would be reduced [138]. However, this is quite hard to achieve, the electric field below the PFF acts to expel such particles -they could not enter unless they already had energy $\sim e\Delta\Phi_\parallel$. For curvature gamma-ray emission generated pair cascades, the pairs are born with energies far below $e\Delta\Phi_\parallel$, which make formation of a PFF that reduces $J_\parallel$ impossible.

- The PFF and the acceleration region below it is fully time dependent, with the current flickering on the polar cap transit time $\sim \varpi_{cap}/c \sim 10\,\mu$s, in the manner of the [136] and [126] diode instability and spark scenarios, respectively. Given stars with atmospheres which make charges freely available to the magnetospheres above, the most significant gap question is, how does the star adjust to provide the magnetospherically required current density, while at the same time adjusting the charge density to reduce $E_\parallel$ below its vacuum value in a manner that does not do violence to thermal X-ray emission (for example).
- All the models of relativistic field aligned acceleration considered to date have assumed unidirectional flow, or at most counter streaming beams with no trapped particles in the acceleration zone – that is, monotonic accelerating potentials and electric fields. The possible presence of trapped particles, implicit in the non-monotonic, non-relativistic acceleration model of a singly charged fluid of [99], can break the straight jacket of current being proportional to charge density, even if the plasma is completely non-neutral. Furthermore, the outer magnetosphere can modify the local polar cap (and outer gap, if it exists) electric field through return current control of the currents and charge densities in the polar flux tube boundary layer separating the open from the closed field lines, which opens the possibility of relaxing the assumption of perfect conductivity on the boundaries of the acceleration region used in all models to date. All models to date have assumed the open field lines are bounded by a surface whose behavior mimics a perfect conductor, which makes a very specific statement about the surface charge density along the separatrix. As with the total current and current density, there is no reason for the surface charge to adopt this locally determined value – it depends not only on the charges contained within the open flux tube, but also on the dynamics controlling the formation of the return current, both at the stellar surface and at the magnetospheric Y line. I discuss these speculative points further below.

The magnetosphere is a high inductance system – the magnetic fields induced by particle and displacement current flow can change on times no shorter than the Alfvén transit time between surface and Y line and back, $T_A \approx 2R_Y/v_A \approx (2/\Omega)(R_Y/R_L)$, very much greater than the polar cap transit time, or the plasma period based on the Goldreich–Julian density $\omega_{pGJ} = \sqrt{4\pi e^2|\eta_R|/m_\pm e} = \sqrt{2\Omega\Omega_{c\pm}} = \Omega\sqrt{2\Omega_{c\pm}/\Omega} \gg \Omega$ [here $\Omega_{c\pm} = eB/m_\pm c$ is the nonrelativistic cyclotron frequency $\sim 10^{19}(B/10^{12}\mathrm{G})\ \mathrm{s}^{-1}$ of an electron or positron]. Thus one possibility is that the atmosphere supplies the current demanded through pair creation discharges, which launch charge bunches accompanied by pulses of much denser pair plasma, a popular idea frequently mentioned in the cartoon approximation but rarely studied.

Homogeneous and spatially 1D models of time dependent pair creation have been studied by [2, 46, 87] – the first considers only time dependent oscillations in a uniform medium (a "0D" model), the second, using a 1D Particle-in-Cell method, considers the propagating transitions between vacuum $E_\parallel$ and an $E_\parallel \approx 0$ region created by a burst of pair creation (motivated by the [126] spark scenario), while the third considers nonlinear uniform oscillations similar to those studied by [2] and also spatially inhomogeneous nonlinear limit cycle oscillations. Levinson et al. [87]

incorporated the existence of the magnetospheric current as a fixed constant in the model, as is appropriate since the oscillations occur on the time scale ω_{pGJ}^{-1}, much shorter than all possible time scales of magnetospheric variability. They point to the interesting possibility that the charge and current oscillations might become chaotic, a topic of substantial interest to possible radio emission mechanisms, but present no specific calculations that exhibit such behavior.

None of these explicitly time dependent models showed approach to the steady flow in the co-rotating frame assumed at the start in the models of [12] and [108], in which the current density is fixed by the local electrostatics. Significantly, none of these local, 0D or 1D time dependent models included the effects of pair outflow from the system, nor included the Poynting fluxes (in effect, the collective radiation losses) from the regions of pair oscillation. Considered as an instability, the oscillations studied are probably sensitive to the loss of plasma and Poynting flux from the system, since the pair creation (in 1D) has the character of a spatial amplifier. Thus the question of whether pair oscillations approach a steady state with the local value of the magnetospheric current density emerging as a steady flow or as an average over the oscillations remains open, requiring calculations which are able to give a more complete account of the coupling to the stellar surface and the losses from the region of oscillatory dynamics. Giving an account of the effects of plasma flow onto the star and the consequent heating and X-ray emission is of substantial importance, since the Levinson et al. model suggests a local current density $c\eta_R$ accelerated through $\sim 10^{13}$ V colliding with the surface, which leads to observable thermal X-ray emission which may, or may not, be in excess of what is observed from many stars.

On the opposite side, [8] and [106] point to how their steady flow, spatially inhomogeneous models ("gap-PFF") might become unstable, due to inhomogeneity of the pair creation, in older stars where the pair creation gain lengths are large. Such instability would be of the spatial, traveling wave amplifier variety, a possibility also of interest to the outer gap models, whose local time dependence has also begun to be studied. Hsu et al. [71] have opened the first door to time dependent (in the co-rotating frame) outer gap models, showing that their models, which do incorporate particle outflow from the accelerator region – mostly toward the star – converge to a steady state flow. Strictly speaking, however, these models are inconsistent, allowing for full time dependence of the current and plasma densities but treating the electric field as electrostatic, which is quantitatively incorrect in a relativistic, multidimensional (2D, in their model) system. The approach to a steady state is attributed to the screening of $E_\parallel$ if too many pairs materialize, while underscreening results in an increase of $E_\parallel$. This mechanism is the same as underlies the nonlinear limit cycle oscillations appearing in the polar cap pair oscillation model of Levinson et al.. Thus the approach to a steady state in the time dependent outer gap model more likely owes its origin to the spatial loss of plasma from the acceleration region, an effect broadly akin to transit time damping of electromagnetic oscillations in a plasma.

Given the large, almost vacuum conditions above much of the polar cap implied by (15.10), coupling to the stellar atmosphere almost certainly requires consideration of trapped particles' contribution to the charge density, in either steady flow or time dependent current flow conditions.

A full theoretical resolution of pair creation driven oscillations in *any* "gap" geometry awaits more definitive study, along with any sort of serious attempt to relate such oscillations to observable phenomena – current and torque fluctuations, radio microstructure, variability in thermal X-rays created by surface bombardment, etc. All such modeling needs to be set into the context of the global force-free models – so long as the potential drop in a local accelerator $\Delta\Phi_{\parallel}$ is small compared to the magnetospheric potential Φ, field aligned accelerators of any sort (employing starvation $E_{\parallel}$ in all the schemes available in the literature) appear as small departures from force-free conditions, allowing the use of force-free models as the basic zeroth order description of the current flow and magnetic geometry.

15.2.8 Gamma Ray Tests of Existing Gap Models

The modern force-free magnetosphere models open the possibility of using the upcoming gamma ray observatory GLAST [30, 54] to test and improve our understanding of pulsars' magnetospheres, along the lines suggested above or in other directions. Gamma rays afford the possibility of probing the magnetosphere using well understood radiation processes, leaving the modeling and the synergy between models and observations living in the domain of the geometry and the acceleration physics – "gapology", in the existing theoretical frameworks. In particular, the advent of the force free-models should allow the outer gap and slot gap modelers to significantly reduce the geometric uncertainties in their constructions of the beaming profiles and energy dependent light curves, thus allowing much more stringent empirical tests of the hypothesized geometric scenarios – if the necessary extensions of the models to 3D, and perhaps to time dependence, are incorporated. Even more important, the improved sensitivity of GLAST over past gamma-ray telescopes will allow, for the first time, a direct test of whether polar caps and polar cap pair creation occur in a significant population of pulsars. Given that no proposed outer gap (or slot gap, for that matter) model makes a significant contribution to pair creation and gamma-ray emission for periods much in excess of $\sim$200 ms ($\Phi < 10^{15}$ V), the much heralded association of pair creation with pulsar photon emission and, more significantly, with relativistic wind formation must come from activity in the polar cap region just above the surface. Indirect evidence for such pair creation comes from the simple $\Phi = 10^{12}$ V radio pulsar death line shown in Fig. 15.1, which corresponds roughly to where polar cap/slot gap acceleration models predict pair creation to cease [12, 126, 136]. Previous gamma-ray telescopes lacked the sensitivity to probe the predicted gamma-ray emission, which, in the models, is absorbed at energies above 1 GeV (in simple, star centered static dipole geometry) through gamma-ray conversion to $e^{\pm}$ pairs.

Figure 15.10, taken from [62], gives a simple version of this opportunity, in good accord with more recent evaluations of pulsar gamma-ray emission from the inner magnetosphere. Testing the existing polar gap acceleration and gamma-ray emission models, or better, improved models that take proper account of the magnetospheric

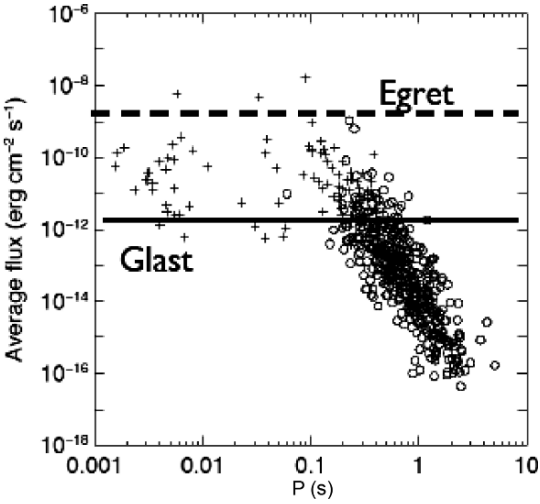

Fig. 15.10 Sensitivity of the EGRET and GLAST telescopes to low altitude (below and just above the PFF) gamma-ray emission at energies $\varepsilon > 100\,\mathrm{MeV}$, in a simple dipole model for the low altitude geometry (which affects the magnetic curvature and therefore the maximum photon energy that can escape) and unidirectional space charge limited flow *with current density* $J_{\parallel} \simeq c\eta_R$, not the force-free current given (approximately) by (15.9). The different symbols refer to the different major contributors to gamma-ray emission and absorption – see [62] for the details

current system, can be done best by studying pulsars that show *core* component radio emission, since one looks down the "barrel of the gun" into the low altitude magnetic field, where the core emission arises (see [84] for the evidence that the core emission arises from a few kilometers above the surface in a substantially dipolar B field).

I can safely predict that GLAST observations of pulsars deeper in the P–$\dot{P}$ plane than could be detected by previous gamma-ray telescopes, which should begin to become available in 2008–09, will stimulate a small host of improved gap models which take advantage of the geometric and current flow constraints coming from the force-free models. They might stimulate investigations into origins of $E_{\parallel}$ based on physics differing from the starvation models that have been explored for the last 30 years – for example, invoking the $E_{\parallel}$ accompanying the kinetic Alfvén waves that couple the outer magnetosphere to the star, a conceivable acceleration mechanism that might augment or even replace outer gap and slot gap accelerators, especially if plasma precipitating from reconnection flows at the Y-line floods the regions envisaged for these gaps and poison their starvation electric fields.

To amplify this issue, which is a prospect for future research, consider the hypothetical global reconnection flow illustrated in Fig. 15.11, shown here for an aligned rotator but just as applicable to the Y-line of the oblique rotator illustrated in Fig. 15.3.

As appears in the [29] model, pairs supplied from the polar gap supplying the wind should allow reconnection of the current sheet to occur all the time. It has not yet been shown that the reconnection propagates back into the magnetosphere in the manner envisaged in Fig. 15.11. In the somewhat analogous problem of reconnection at the Y line in the rapidly rotating Jovian magnetosphere, [140] showed, using a PIC simulation of the electron–ion plasma at the Y-line, that reconnection

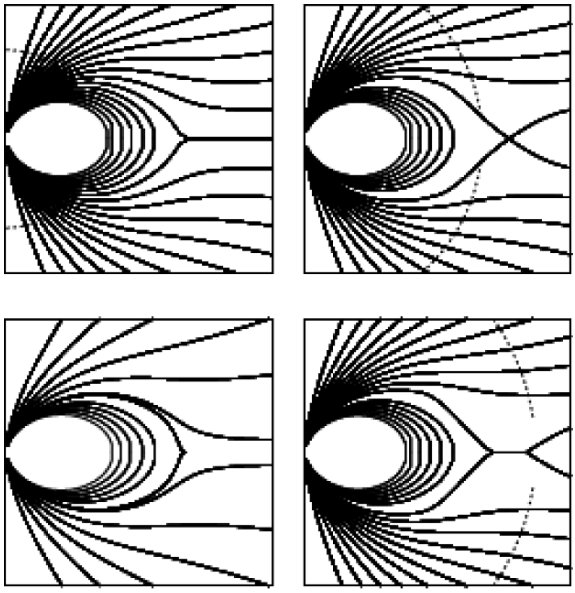

Fig. 15.11 A cartoon of a pulsar magnetosphere undergoing sporadic reconnection, (from [34])

qualitatively akin to that illustrated in Fig. 15.4 occurs, with finite but not large reaction along the separatrix interior to the sporadically forming X-line. That back reaction includes generating precipitating $J_{\|}$ *and* plasma with density well in excess $|J_{\|}|/ec$ on and around the separatrix. The field aligned currents are part of the kinetic Alfvén waves that couple the time variable

Y-line to the inner magnetosphere and the star, thus generating a time variable torque. The space charge in these boundary layer flows can alter, in a major way, the electric field within the polar cap accelerator (as well as poison both outer and slot gaps), while the parallel electric fields in the kinetic Alfvén waves offer a new mechanism for field aligned acceleration in the boundary layer geometry already known, from the outer and slot gap models, to be extremely useful in understanding gamma-ray pulsars' beaming morphology. If these waves have a chaotic time series, the chaos in the resulting polar $J_{\|}$ offers a good candidate for understanding the random arrival times of radio subpulses within a pulse window; if the reconnection induced waves have a limit cycle time series, the phenomenon of subpulse drifting can be reproduced, assuming the radio emission intensity and beaming is a direct product of the field aligned current density. The electric fields in these Alfvén waves have a central role in the formation and extraction of the return current required to maintain the average charge balance of the star. Finally, the shear between the plasma flow in the polar flux tube and the neighboring boundary layer offers a promising candidate for the collective radiation mechanism in "conal" radio emission.

An important constraint which must be met by any model of outer magnetospheric variability is that magnetic fluctuations must not broaden the beaming of photons emitted with momenta parallel to the instantaneous magnetic field beyond the characteristic pulse widths observed in the gamma-ray and associated optical and

X-ray emission (and radio emission, in the Crab), thought to come from $r > 0.5R_L$ [123] – although this number, derived from a geometry based on a vacuum dipole with a phenomenological prescription for the location of the last closed field lines, will change when the magnetic field of the oblique force free rotator is put to use as the geometric platform for the beaming. If reconnection (or any other mechanism) causes the magnetic field at the light cylinder to fluctuate by an amount δB at $r \sim R_L$, then the Alfvén waves traveling along the boundary layer have, from conservation of energy flux, amplitude $\delta B = B(R_L)(\delta B/B)_{r=R_L}(r/R_L)^{3/2}$ – for convenience, I have here assumed $R_Y = R_L$. These are shear waves, with $\delta B \perp B$, thus causing the local magnetic direction to vary about the mean by an angle $\delta\theta \approx \delta B/B$. The observed sharpness of the gamma-ray pulsars' light curves then suggests $\delta\theta < 0.2(B/\delta B)^{2/3}_{r=R_L}$, while order of magnitude application of this idea to the observed torque fluctuations in the Crab pulsar and others suggests $(B/\delta B)_{r=R_L} < 2$ [6]. The correspondence of the limits on the emitting radius from geometric fluctuation pulse broadening, from measurements of the torques and from modeling the beaming geometry provides an example of how gamma-ray observations of pulse profiles and radio observations of torque variability over a substantial range of the P–$\dot{P}$ diagram can be used to seriously constrain both the electrodynamics and acceleration physics of these magnetospheres.

I have left out all discussion of the hoary problem of pulsar radio emission and transfer – that would require an additional paper – other than the few comments above concerning radiation beaming and single pulse fluctuations, which appear to me to provide probes into the magnetospheric dynamics. In connection with the dynamical importance of the boundary layer between closed and open field lines – the location of the return current – it is perhaps worth emphasizing that this region is likely to be the dynamical realization of the site of "conal" emission, with velocity shear between the boundary layer plasma and the plasma filling the open flux tube (and that filling the closed zone) as a prime candidate for the free energy driving the collective radio emission process(es).

Perhaps a few bold souls will explore these issues more quantitatively *before* the GLAST observations become available, thus offering up their predictions to the sharp knives of experimental tests. There is an urgent need for *physical* models of the boundary layer between the open and closed regions, either with or without gaps, which account for the coupling with the stellar surface as well as the transition from the magnetosphere to the wind. This is a collection of non-trivial problems – predictions of future progress are uncertain.

15.3 Follow the Mass

While there has been lots of attention to pair creation and particle acceleration *within* pulsars' magnetospheres from the community interested in observing and modeling these stars' lightcurves and SEDs, the most obvious evidence for particle acceleration and pair creation comes from observations and models of Pulsar Wind Nebulae

(PWNe). These have recently been well reviewed from the observational standpoint by [130] and [49]. The young PWNe and their pulsars – those still not crushed by the reverse shock – provide calorimetric information on both the energy and mass loss budgets of the underlying pulsars. Indeed, since the earliest days, the energy budget has been used to constrain the moment of inertia of the neutron stars, thus the equation of state of nuclear matter. The mass loss budget provides a powerful constraint on all models of plasma behavior within the magnetosphere, whether designed to explain specific observations or constructed to investigate basic theoretical issues.

15.3.1 Observations and Consequences

There has been major observational progress on these systems, coming most of all from high resolution optical and X-ray imaging, as shown in Fig. 15.12, and from related studies of temporal variability.

Observations and models of the PWNe tell us about the particle loss rates $\dot{N}_{\pm}$, $\dot{N}_{beam}$ from the neutron stars. In the case of the Crab, with its strong magnetic field and rapid synchrotron cooling of the particles radiating photons at energies above infrared frequencies, the now well resolved optical, X-ray and the unresolved gamma-ray sources require a particle input of around $10^{38.5}\ \mathrm{s}^{-1}$, about 10^4 times the basic electric current flow $c\Phi/e \sim 10^{34.5}\ \mathrm{s}^{-1}$ for this pulsar (e.g., [135]). Similar conclusions have been reached for other PWNe as has been done, for example, in G320 around PSR B1509−58 [41, 48], even though in this case the radiative losses are not as rapid and therefore inferring $\dot{N}$ is not as straightforward. See [40] for pair injection rate inferences for several other pulsars/PWNe. These inferred rates come from examining the brightness of the X-ray and (when they can be seen)

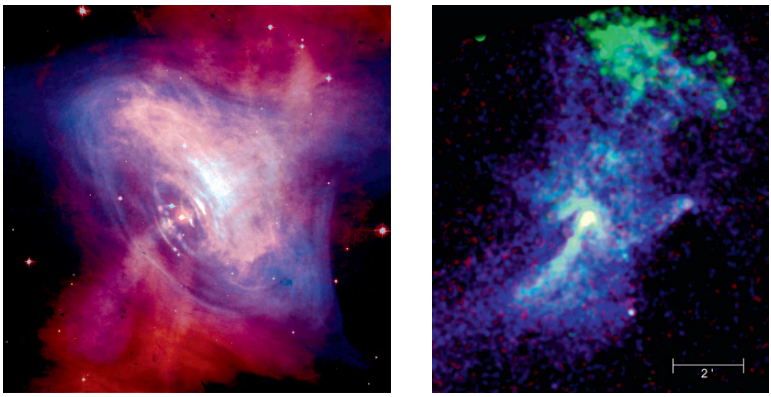

Fig. 15.12 *Left*: composite of Hubble Space Telescope and Chandra images of the inner $1'$ of the Crab Nebula, showing the torus–plume structure around (torus) and along (plumes) the pulsar's rotation axis. *Right*: Chandra image of the supernova remnant MSH 15−52 (G320.4+1.2), showing its torus–plume structure

optical nebulae, augmented by hard X-ray and gamma-ray (GeV to TeV) observations of the young nebulae, when the hard photon telescopes can detect anything – for a recent summary of the rapidly developing TeV observations of TeV PWNe, see [50] and [47]. The TeV observations are sensitive to particles of energy comparable to those that give rise to synchrotron X-ray emission. 10 MeV to 10 GeV observations constrain the highest energy particles, which produce synchrotron X- and γ-ray emission. A survey of PWN emission in this energy range awaits GLAST.

While the pair production rates found from polar cap models based on starvation electric fields do seem adequate for the understanding of the high energy photon emission in PWNe ([65] – these results remain the only attempt to survey pair creation across all observed P–$\dot{P}$), other models have been developed specifically for the purpose of explaining gamma-ray pulsar SEDs and light curves), there are substantial indications that something of qualitative significance is missing. It has long been known (e.g., [129]) that the total radiating particle content of the Crab Nebula (mostly in the form of radio emitting electrons or pairs, which lose energy only because of adiabatic expansion) requires an injection rate averaged over the 1,000-year history of the system on the order of 10^{40}–$10^{41}\ \mathrm{s}^{-1}$ electrons plus positrons, in order to understand the total radio emission from the Nebula. Recently [40] has revisited this same question in the light of the TeV observations of VelaX, G320 and the newly discovered nebula of PSR B1823−13, again finding pair injection rates greatly in excess of the rates found for particle *outflows* from either polar cap/slot gap or outer gap models[8] constructed using starvation electric fields shorted out by the pair creation.[9] Only the early polar cap model by [137], in which the effect of pairs' ability to limit the voltage drop was completely neglected, comes even close to yielding the observed time average injection rates. Since incorporating the pairs' polarizability destroys Tademaru's model, his empirical success has been ignored.

The starvation electric field models also have difficulty in coming up with enough pair plasma to meet the desires of most (not all) models of radio emission over the whole $P\dot{P}$ diagram. The results of [64] appearing in Fig. 15.13 show clearly that for lower voltages ($\Phi < 10^{13.5}$ V), where most pulsars lie, the pair multiplicities drop well below unity, far below the level assumed in almost all models of the radio emission, and also required in models of propagation effects that have had some success in the interpretation of radio polarization and beaming structure (e.g., [14, 95]), or indeed needed to explain the death line in Fig. 15.1.

It is possible that offset of the dipole from the stellar center (cf. Ruderman, this book), a central aspect of the model for magnetic field evolution, might substantially enhance a polar cap's pair yield, while still remaining consistent with the apparently dipolar morphology of the low altitude magnetic field. If the axis of the offset dipole is tipped with respect to a radius vector, gravitational bending of the gamma-rays'

[8] However, his conclusion requires extrapolation of the particle spectra inferred from the TeV emission to radio emitting energies, a big jump.

[9] Some outer gap models applied to the Crab pulsar do find total particle production rates in the range 10^{39}–$10^{40}\ \mathrm{s}^{-1}$, but these refer to particles flowing in toward the star, where they collide with and are absorbed by the surface and (over)heat it. See [66] for the most recent version of this kind of model.

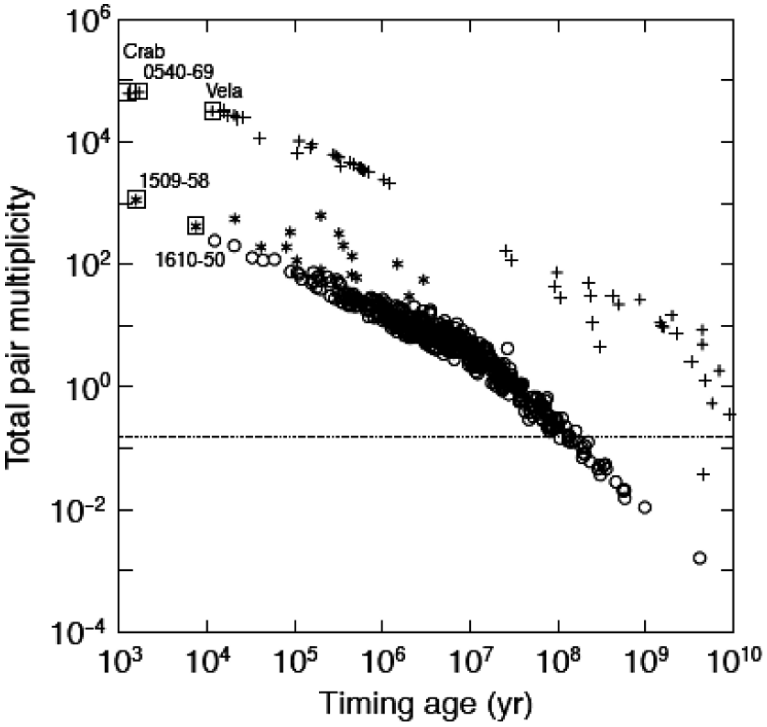

Fig. 15.13 Multiplicities (number of pairs per particle in the Goldreich–Julian density) across the $P\dot{P}$ diagram, from [64]. Harding et al. [58] report similar results, using a more elaborate analysis. Both used similar versions of space charge limited beam acceleration in the polar cap region, and both included the contribution of synchrotron cascades to the total multiplicity. *Crosses* refer to objects where curvature emission provides the gamma-rays that convert to pairs, *circles* to objects where non-resonant inverse Compton up-scatter of thermal X-rays (both from the polar cap heated by backflow bombardment and from the whole surface of he cooling neutron star) provides the gamma-rays, while asterisks show the more strongly magnetized stars where the cyclotron resonance in the scattering cross section makes a significant contribution to the gamma-ray production rate. All these calculations used a star centered dipole for the magnetic geometry, and can be substantially affected by surface magnetic anomalies, e.g., offsets of the dipole center from the stellar center, as in [10], or higher order multipoles, as in [97]. The modern force-free model of the oblique rotator [132] offers the possibility of investigating the pair multiplicity within a self-consistent geometric setting, either with the traditional starvation electric fields or with improvements that take into account the full magnetospheric current system and charge densities, as outlined in Sect. 15.2.7

orbits leads to much larger one photon pair creation opacity in the magnetic field than is the case for the star centered dipole [10]. That opacity increase allows the more numerous low energy curvature gamma-rays to contribute to pair creation, thus enhancing the particle flux. This effect certainly does have a favorable impact on reconciling theoretical with observational death lines; whether it seriously enhances the pair yield in pulsars feeding plasma into young PWNe, which are far from death valley, remains an unexplored topic.

The fact that pulsars (at least the young ones) must supply a plasma with particle outflow rate well above the Goldreich–Julian rate $c\Phi/e$ is undeniable, based on the behavior of the PWNe – undeniable progress. The problems described here are quantitative, perhaps to be resolved by possible larger pair output if the polar flow is time dependent ("flicker" flow), possibly to be resolved in a steady flow model if the charge density in the return current alters and increases the local electric field, perhaps by other effects not yet investigated. These possibilities have potential connections to time variability in the radio emission. Flickering of the polar current and pair creation might be connected to the radio microstructure (e.g., [18, 73, 126]); modification of the electric field by boundary layer space charge controlled by outer magnetospheric unsteady reconnection (see above) may be connected to subpulse variability. Improved sensitivity in infrared and shorter wavelength detection techniques that would allow probing for variability (in the co-rotating frame) of the higher frequency emission would be invaluable. Progress in this area in the next few years is to be expected.

15.3.2 Pulsar Wind Nebula Models

MHD Nebular Models

Modeling the PWNe themselves has advanced greatly in the last decade. Driven by the wealth of spatially and temporally resolved X-ray observations [130] of the "torus-jet" structures shown in Fig. 15.12 in the Crab and PSR B1509 nebulae and now known to be present in an increasing number of PWNe [110, 124], modeling and simulation have advanced from the elementary "spherical cow" models of [122] and [77] to two dimensional, axisymmetric time dependent relativistic MHD simulations of the flow structure [25, 42, 83].

These simulations exploit the suggestions of [26] and [90], that energy injected into these nebulae follows the $\cos^2\lambda$ profile (λ = latitude with respect to a star's rotational equator) of the toroidal field energy density exhibited by the split monopole and oblique split monopole [24] models of the Poynting fluxes from the neutron star. They suggested that the consequence of such anisotropic energy injection into the surrounding nebulae would be greatly enhanced emission in a belt around the rotational equator – the "torus" appearing in the X-ray and optical imagery. In addition, [90] suggested the outflow from the torus, since it is injected into the non-relativistically expanding cavity formed by the supernova, would be deflected into a subsonic backflow at higher latitudes, where magnetic hoop stress could act to focus plasma into a magnetically compressed, outflowing, subsonic *plume* along the pulsar's rotation axis, thus creating the appearance of a jet.

The simulations amply confirm the implications of the initial toy models, with flow velocities in the equator and the plume ($v \sim 0.5c$) comparable to those inferred from motions of features in the published time series of motions in the central regions of the Crab Nebula [60]. Snapshots taken from that time series are shown in Fig. 15.15.

The σ Problem

The MHD models do well at reproducing the torus–plume structure, as is shown in Fig. 15.14, *if* the wind upstream from the termination shock is weakly magnetized – the average of $\sigma = B^2/4\pi\rho\gamma c^2$ over the equatorial shock must be $\sim$0.02 in order to generate the good looking simulated image, a value $\sim 4\times$ larger than what had been previously inferred from the 1D time stationary models of [77]. But this value is still far below what the asymptotic σ expected in ideal MHD outflow *of an unconfined wind*, exhibited in (15.11),[10] and the asymptotic Lorentz factor and four velocity (in units of c) are

$$\sigma_\infty \approx \sigma_0^{2/3}, \qquad u_\infty \approx \sigma_0^{1/3} \tag{15.11}$$

$$\sigma_0 \equiv \frac{\Omega^2 \Psi_B^2}{\dot{M} c^3 \gamma_0} = \frac{e\Phi}{2 m_{eff} c^2 \gamma_0}, \qquad m_{eff} = m_{ion} + 2m_\pm \kappa_\pm \, . \tag{15.12}$$

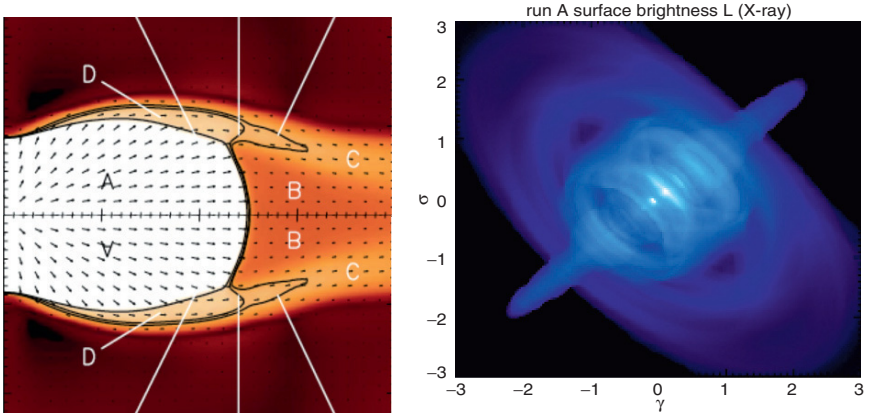

Fig. 15.14 *Left*: Outflow structure in MHD models with energy injection concentrated in the equator. A: Upstream relativistic wind. B: Subsonic equatorial outflow, downstream of the equatorial termination shock. C: Fast downstream outflow emerging from the higher latitude oblique shock. D: Supersonic flow just downstream of the high latitude oblique shock. The backflow that focuses downstream plasma onto the axis is not shown. From [42]. *Right*: Synthetic torus–plume image, from [43]

[10] Relativistic MHD jets accelerating within confining boundaries – "walls" – may have quite different behavior, as has been most recently exhibited by [82]. Here, the effect of a confining boundary, perhaps representing confining pressure in an outflow from a disk, forces poloidal field lines and stream lines to depart from monopolar form, which allows magnetic hoop stress to confine and accelerate a polar flow. For a wind emerging from a star, essentially a point source, there is no analog of confining walls to break the balance between magnetic hoop stress and electric repulsion that lies behind the slow acceleration.

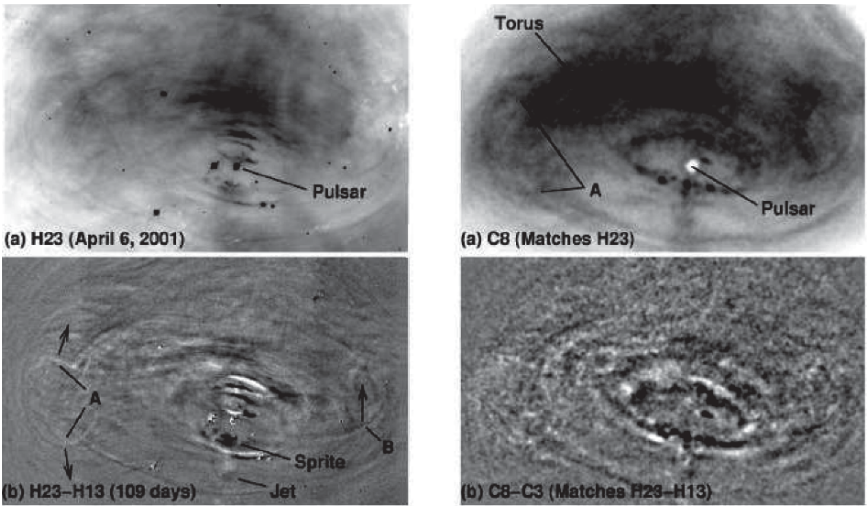

Fig. 15.15 The torus and plume in the center of the Crab Nebula, as seen by HST and Chandra in 2001, from [60]. *Left column*: HST; *right column*: Chandra. *Upper row*: total structure, showing the knotty inner ring in the Chandra image morphologically identified with the wind's termination shock in the rotational equator. The *elliptical shape* reflects the 60° angle between the equatorial plane (which contains the torus) and the plane of the sky. *Lower row*: large scale structure subtracted by differencing between a pair of early and later images in the series, producing a snapshot of the moving wisps emerging from the Chandra ring and expanding at speed $\sim 0.5c$

Here $\Psi_B = \mu/R_L = R_L\Phi$, $\kappa_\pm$ the pair multiplicity and γ_0 the bulk four velocity of the plasma emerging from the plasma source (pair creation at the polar cap, since outer gaps – if they exist as particle production zones – send most of their plasma back toward the neutron star), itself an unknown function of magnetic latitude (possibly lower in the equator than at the poles, since pair creation should be weaker near the magnetospheric boundary layer). For the Crab pulsar, pair creation theory suggests the multiplicity of the plasma feeding the nebular optical and X-ray source is $\kappa_{\pm OX} \sim 10^{4.5}$, based on spectral imaging modeling [43], a value consistent with starvation gap modeling of the polar cap [65], who also find $\gamma_0 \sim 100$ for this star. If this piece of the mass loss budget corresponds to the total mass loss, $\sigma_0 \sim 1 \times 10^4$ and $u_\infty = 22 \approx \gamma_\infty$.

If one includes the whole mass flow, $\dot{N}_\pm \sim 10^{40.5}\,\mathrm{s}^{-1}$ [40], which includes the particles required to feed the Nebular radio emission, then $\kappa_\pm \sim 10^6$ and σ_0 is $\sim 10^{4.6}/\gamma_0$ – since the origin of the large mass flux is unknown, γ_0 is also unknown, although surely it is smaller than the value ~ 100 found in existing gap models – then $u_\infty = 16(10/\gamma_0)^{1/3}$.

The ideal MHD values of σ_∞ and γ_∞ are for a wind with monopolar poloidal field and flow geometry at large r. Theory and simulation to date all support the poloidal field of the wind being monopolar well outside the light cylinder – see, for example, [29], whose high σ simulation of outflow from the aligned rotator extended to $r \approx 900R_L$, well outside the fast magneto-sonic surface, with the field becoming closely

monopolar with no polar focusing or hoop stress apparent. Then the asymptotic magnetization σ_∞ and 4-velocity $c\gamma_\infty$ (outside the current sheet, which is infinitely thin in ideal MHD) are predicted to be as in (15.11).

The MHD models do answer the oft repeated question of just what is going on at higher latitudes – if the torus structure is the manifestation of the shock termination of the wind, why don't we see evidence for the shock at high latitude (e.g., [22])? The MHD model asserts that the polar regions at distances we can resolve are occupied by the backflow that forms the plume. The shock shown in Fig. 15.14 curves down toward the star, reaching into radii too small to observationally resolve on the polar axis. Furthermore, the shock is quite oblique at higher latitude, which weakens the efficacy of shock acceleration. The MHD model and the curvature of the shock relies on the total energy flux being proportional to $\cos^2\lambda$. In the Crab, the higher latitude parts of the curved shock do manifest themselves as the bright knots, which appear in projection as if they are right next to the pulsar [83]. Thus, qualitatively and semi-quantitatively, a satisfactory picture of PWNe plasma flow on nebular scales has appeared.

Ideal MHD models may also do well at reproducing the wisp structures shown in Fig. 15.15, which are of interest for the diagnosis of the relativistic shock wave terminating the outflow. These are now known to be structures (probably waves, [127]) appearing to be emitted from the Chandra ring with a periodicity $\sim$6 months, traveling out with a speed $\sim 0.5c$, possibly with some deceleration with increasing radius [105]. The wisps occur on scales too small to be resolved by the published MHD simulations of the whole nebular flow. Of the various suggestions made over the years to interpret the wisps, the most promising MHD model for these is that they are due to MHD Kelvin–Helmholtz instabilities occurring at the boundary between a fast equatorial and a slower high latitude flow [17]. The global flow models have such a shear layer, as flow emerging from the equatorial shock in the nebular cavity returns at higher latitudes toward the axis. Bucciantini and Del Zanna [28] used high resolution MHD simulations of a shear layer in a box, repeated with periodic boundary conditions, to draw the conclusion that this hypothesis is quantitatively inadequate to reproduce the observed variability. However, recent (summer of 2007) high resolution MHD simulations of the whole nebular flow by Bucciantini and by Komissarov, both still in progress, suggest that either Kelvin–Helmholtz instability or, perhaps more likely, secondary instability of the vortices formed in the shear layer near the base of the plume, do show many features similar to the observed moving wisp structures.

If these models do exhibit as much ability to reproduce the observations as has been found in the preliminary work, the multi-dimensional MHD model of PWN structure will have accumulated three major successes: a model for thermal filament formation, through Rayleigh–Taylor instability of the boundary between the non-thermal bubble, as first pointed out by [61] and developed extensively by [27]; mildly relativistic plume (a.k.a. jet) formation, as first suggested by [90] and modeled numerically by [25, 42, 83]; and now the wisp variability near the termination shock. Such models probably will turn out to be successful in interpreting the more slowly expanding outer structures of the torus – the current round of high resolution

simulations will soon show whether or not these features of the nebular "weather" can be captured numerically.

The MHD dynamics does have strong sensitivity to σ_{wind} at the termination shock. The models are insensitive to the wind's 4-velocity (Lorentz factor) just upstream of the termination shock, and are insensitive to the composition, other than that the particles must have small Larmor radii and that they be efficient radiators. The last requirement leaves electron–positron plasma as the only option, in the young systems with bright PWNe – the particle injection rates greatly exceed the Goldreich–Julian value.

15.3.3 Beyond MHD

Striped Winds

However, the equator where the equatorial shock forms is a current sheet, a region notorious for breakdown of ideal MHD. Such breakdown has been assumed in the MHD models, which achieve their successful fits of nebular appearance to observation only when there is a finite region around the equator where the magnetic field at the shock is small compared to what one would expect in the ideal MHD flow with an infinitely thin, flat current sheet. Coroniti [39] suggested the apparent low value of σ in the equator – inferred to be $\sim$0.005 in the 1D, spherically symmetric [77] model – is due to annihilation of the equatorial magnetic field in the current sheet. Close to the star but outside the light cylinder the magnetic field takes the form of the striped magnetic structure, with oppositely directed fields from the opposite poles of the dipole wound into a frozen in wave, shown in Fig. 15.16. Coroniti's idea was that some form of current sheet dissipation causes the magnetic energy to annihilate in the inner wind, causing conversion of magnetic energy to flow energy, and reducing the structure to something approximating that of an aligned rotator's outflow with a magnetic field in the asymptotic wind $R_L \ll r \ll R_{shock}$ (= $10^9\, R_L$ in the case of the Crab) much weaker than that what one expects from ideal MHD transport of the light cylinder field inferred from the star's spin-down. The resulting (dissipative) MHD model has an equatorial current sheet built in, since the $\lambda > 0$ hemisphere has a toroidal magnetic field wound in the opposite direction to that found for $\lambda < 0$. Figure 15.17 shows a cartoon of the resulting magnetic "sandwich" wind at large radius, along with magnetic field strength as a function of λ considered in the MHD models of the nebulae beyond the shock.

One almost model independent constraint on this idea is that an acceptable theory of stripe dissipation in the wind zone necessarily leads to the wind's four velocity in the dissipation region being small compared to the value $\Gamma_{wind} \sim 10^{6.5}$ inferred from 1D dynamical models of the nebular high energy photon spectra [77]. The reason is simple.

The magnetic field in the stripes, which have proper wavelength $\lambda' = \Gamma_{wind} R_L$, need proper dissipation time $T'_d > \lambda'/c = \Gamma_{wind} R_L/c$, since the current sheets can't

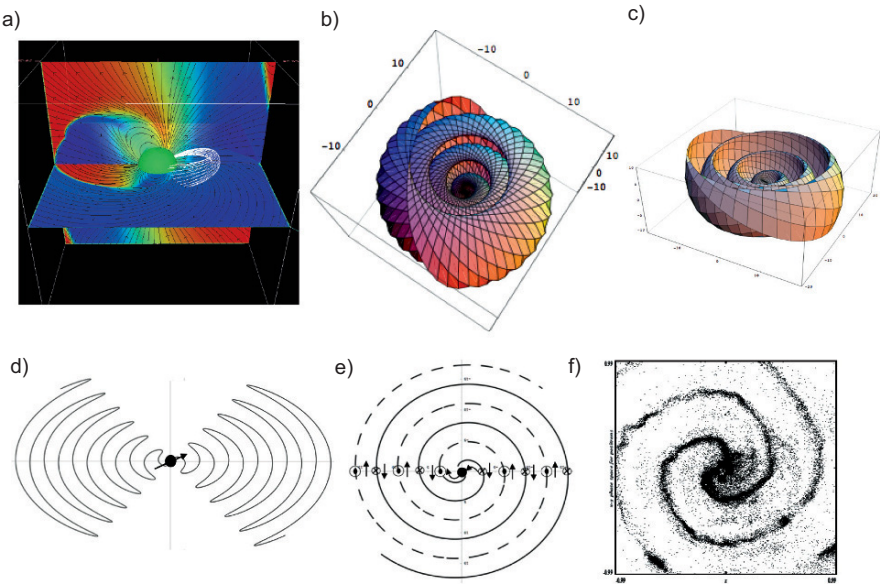

Fig. 15.16 Magnetic geometry of the inner regions of a striped wind emerging from an oblique rotator with a large obliquity i. **a** Magnetic structure of the force free rotator for $i = 60°$, from [132]. **b** One of the two interleaved current sheets for the 60° rotator, derived from Bogovalov's oblique split monopole model [24]. **c** The same as **b** but for $i = 9°$, shown for clarity. **d** and **e** Meridional and equatorial cross sections of the striped wind current sheet, for the 60° rotator. **f** A snapshot of a 2D PIC simulation of the equatorial stripes, by [131]

expand any faster than the speed of light; alternatively, in a reconnection model, the magnetic field flows into the sheets, to disappear in expanding islands of hot plasma around O-lines, with velocity $\varepsilon_R v_A \approx \varepsilon_R c$ [92], with ε_R expected[11] to be on the order of 0.1–0.2. In the pulsar's center of mass frame, the dissipation time then has the lower limit $T_d > \Gamma_{wind}^2 R_L/c$; in a reconnection model, $T_d \approx \Gamma_{wind}^2 R_L/\varepsilon_R c$. A successful model for the apparent low value of σ at the termination shock in the Crab Nebula, where the equatorial shock occurs at $R_{shock} \approx 10^9 R_L$, requires that the dissipation go to completion in a region where $\Gamma_{wind} < 10^{4.5}$; using the reconnection model reduces this upper limit to $\Gamma_{wind} < 10^4$. In MSH15−52, where $R_{shock} \sim 0.4 - 0.5$ pc and $R_L = 7825$ km, $\Gamma_w < 10^{4.7}$ is a firm upper limit; in a reconnection model, $\Gamma_{wind} < 10^{4.2}$.

It is interesting to note that the full average particle loss rate $\dot{N}_\pm \sim 10^{40}$–10^{41} s^{-1} inferred for the Crab Nebula requires, from energy conservation, that the asymptotic value of the wind 4 velocity is $\Gamma_{wind\infty} \leq \dot{E}/\dot{N}_\pm m_\pm c^2 = 10^{4.3}/\dot{N}_{40.5}$ in this system, much less than inferred in 1D models that neglect the plasma required for the radio emission such as that of [77] – the upper limit is achieved if the plasma is cold

[11] An expectation based on kinetic simulations and experiments on non-relativistic reconnection, as in [21]; relativistic reconnection in a pair plasma, the case relevant here, has just started to receive attention [19].

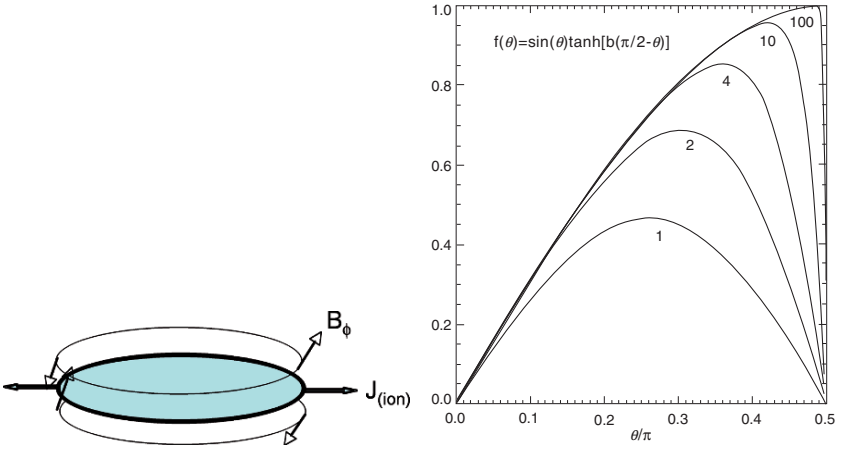

Fig. 15.17 *Left*: Magnetic sandwich geometry of the equatorially concentrated outflow, with radial electric current flowing in a extremely weakly magnetized midplane between oppositely directed toroidal magnetic field at higher latitudes. *Right*: Typical magnetic profiles as a function of latitude, from [42]

by the time it reaches the termination shock. The acceleration from the inner wind, launched by the pulsar's magnetic spring to $\Gamma_w = u_\infty$ given in (15.11), occurs if the current sheets dissipate and the wind heats, accelerating from the resulting internal pressure gradient. This is a relatively slow process [93], reaching completion before a fluid element collides with the termination shock in the Crab Nebula only if $\Gamma_w < 10^{4.8}$, $\dot{N} > 10^{40}\,\mathrm{s}^{-1}$. This requires maximal dissipation of the current sheets – in a sheet broadening model, as originally proposed by [39], the sheets must expand at a substantial fraction of the speed of light in the proper frame of the flow. Recently [11] showed that the interaction of the relativistic currents in neighboring sheets drives a Weibel-like instability in each sheet, with a resulting anomalous resistivity that supports such maximal dissipation in the inner wind of the Crab pulsar, $r < 10^6 R_L$, a conclusion consistent with the maximal dissipation rate model of [80]. However, it is safe to say that the transition of the wind from high to low σ and from low to high four velocity remains not fully understood, and not well constrained by direct observation of the winds.

For a long time, winds have been modeled as having an asymptotic flow velocity $\Gamma_{w\infty} \sim 10^6$, with various arguments being used, ranging from radiation modeling of the post-shock flow to the dynamics of high energy particles injected by the wind at the shock, with Larmor radii comparable to the termination shock's radius, invoked as a dynamical model for the variable wisp dynamics near the shock. Such particles, if they exist, have 4 velocities much larger than the maximum flow 4-velocity of the wind inferred from energy conservation. They might occur due to acceleration in the current sheet (perhaps due to relativistic runaway, in a current sheet with anomalous resistivity), thus are confined to the equatorial sector.

Some of the dissipated energy might reappear as an unpulsed photon source superposed (because of relativistic beaming) on the pulsar. The Crab pulsar exhibits linearly polarized (33%), unpulsed optical emission, with intensity $\sim$1.25% of the main pulse peak intensity with a fixed polarization position angle [74], polarization properties consistent with emission from the toroidal field in the wind zone [13]. If it proves possible to interpret such unpulsed flux as radiation from the wind, one might obtain significant observational constraints on this difficult problem.

Wisps as Ion Cyclotron / Magnetosonic Waves

A non-MHD hypothesis based on kinetic structure in the current sheets' plasma (a "beyond MHD" model) does as well as MHD schemes at reproducing the observed variability near the wind termination shock. Gallant and Arons [51] proposed this current contains a high energy ion beam, accompanied by a flux of $e^{\pm}$ pairs, with ion energy/particle approaching the total magnetospheric potential energy, and that this ion current carries a large fraction of the spin-down energy, while still being a minority population by number density.

It is important to note that as far as the dynamics is concerned, high energy ions in the equatorial return current, expected to emerge from an "acute" pulsar – $\angle(\Omega,\mu) < \pi/2$ – can be replaced by high energy electrons, expected to form the return current in an "obtuse" pulsar, $\angle(\Omega,\mu) > \pi/2$. In both cases, the required acceleration to energy/particle comparable to $e\Phi$ must occur in the wind, perhaps as particle runaways in the current sheet's resistive electric field [11]. In the electron case, radiation reaction can limit the energy/particle that can be achieved, which makes the acute pulsar model slightly preferable, and for the rest of this discussion I confine discussion to the ion beam case.

Since such ions have Larmor radii comparable to the radius, the compressions induced in the pair plasma at the ion stream's turning points can appear as surface brightening spaced with separation comparable to the spacing of the wisps. Spitkovsky and Arons [135] implemented this idea in a time dependent simulation, showing that in a 1D model in a toroidal magnetic field winding in one direction in the equatorial flow (i.e., ignoring the reversal of the field direction in latitude), the ions' deflection into circular motion in the abruptly increased magnetic field at the equatorial shock in the pairs is ion cyclotron unstable, with gyro-phase bunching forming a compressional limit cycle which launches finite amplitude magnetosonic waves in the pairs. This launching occurs approximately once per ion Larmor period, which is about six months for the parameters determined by comparing the model to the images. These waves travel out at speeds $\approx$ (0.3–0.5)c, with the precise velocity value depending on the degree of isotropization of the pairs.

The resulting synthesized surface brightness map looks more than a little like the observed waves emitted from the inner X-ray ring in the Crab Nebula, as shown in Fig. 15.18. The observed wave emission period [105], announced at a conference *after* the model was developed and published, is in good accord with the model's predictions. Application of the model to PSR B1509/G320 suggests that "wisp"

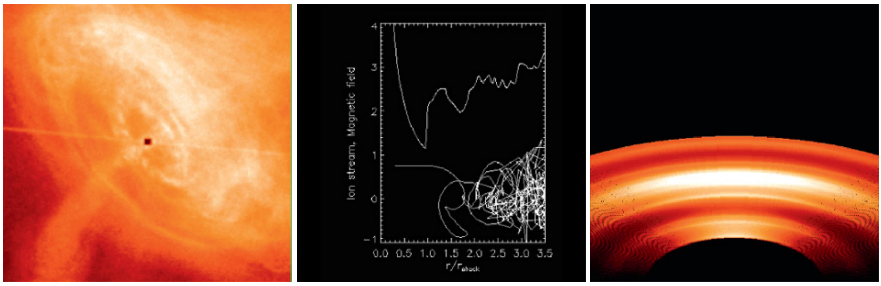

Fig. 15.18 Ion cyclotron instability model of pulsar wind termination shock variability. *Left*: Chandra snapshot of the X-ray ring and torus in the Crab Nebula. The ring is the location of the magnetosonic shock wave in the pairs, whose thickness is unresolved. *Center*: Snapshot of a 1D hybrid (PIC ions, MHD pairs) simulation of the equatorial ion outflow as it encounters the enhanced magnetic field in the pairs. The *upper half* shows the magnetic field with the ion induced compressions.The *lower half* shows the ion phase space ($p_r/\gamma_{upstream}m_{ion}c$ vs. r/R_{shock}, p_r = radial momentum of an ion), with the gyro-phase bunch formed as the ions encounter enhanced B and acquire a reduced Larmor radius. The rotating, reforming bunch (a limit cycle) emits a train of compressional magnetosonic waves that propagate to larger radius. *Right*: Snapshot of the synthetic surface brightness map, assuming the pairs emit synchrotron radiation in the compressed magnetic field with no non-thermal acceleration included (from [135])

variability on a time scale of years should be found. There is weak, but not very convincing, evidence for such variability in the partial torus near this pulsar [41].

By far the most attractive theoretical feature of the model when it is fit to the HST and Chandra movies – fit by eye, there is little use in more elaborate fitting procedures, given the 1D model's departures from the observationally obvious requirement of at least 2D – is the inference that the ion flux required to produce the observed surface brightness enhancements is $\dot{N}_{ion} \approx c\Phi/e$, the equatorial return current of the force free rotator, in the case of the Crab pulsar. Of course, since the magnetic field has largely dissipated in the wind, the pairs accompanying the ions must largely neutralize the electric current in the ions, but the result is an indication that back at the magnetosphere and the stellar surface, some piece of non-force-free electrodynamics does work to extract this ion flux so as to maintain the star's charge balance. In turn, that suggests $i < 90°$, although i certainly should be a large fraction of $\pi/2$. Another feature of the model is that the fact that the ions in the wind are inferred to have Larmor radii comparable to the wind's termination radius R_s – this yields ion energy/particle $E_{ion} = e\Phi(m_p/m_{eff,eq})$, and $\gamma_{ion} \approx 10^{6.5}$ with the pair multiplicity evaluated *in the equator*, a value close to the MHD wind 4-velocity inferred by [77].

The model *assumes* the underlying acceleration from the neutron star is like MHD even in the current sheet, with all the particles – ions and pairs – traveling with a single (fluid) 4-velocity until a fluid element encounters the shock, even though the flow in question is in the current sheet, where different plasma components may have different velocities. Thus Spitkovsky and Arons' inference that $\Gamma_{wind} \approx 10^{6.5}$ is based on the *assumption* that the ions, which carry the electric return current in this model, have the same 4-velocity as the underlying and surrounding MHD wind.

The upper limit $\Gamma_{wind} < 10^4$ clearly is inconsistent with a single fluid velocity for ions and pairs. The 1D model averages over the whole equatorial sector that feels the equatorial belt shock, shown in Fig. 15.14, thus mixes the ion flux with the whole flux of pairs feeding the torus, $\sim 10^{38.5}$ pairs/s for the optical, X- and γ-ray emission from the Crab. It yields an average value of σ within a factor of 3 of the average value of σ inferred from the MHD nebular models. However, the assumption $\Gamma_{wind} = \gamma_{ion}$ clearly violates the upper limit on Γ_{wind}, a limit which comes from assuming the whole flux of pairs feeds the equatorial torus,[12] an assumption supported by the approximate correspondence of the radio wisps [20] with the optical features.

The sandwich magnetic field model, a fundamentally 2D construct, suggests substantial alterations of the [135] scheme. The magnetic field inside the current sheet is weak compared to that in the MHD flow outside the sheet. That weakened B alters the character of the ion orbits from simple magnetic reflections to partial deflections from radial flow, thus altering the momentum transfer to the pairs and therefore the compressions. If most of the ions flow in an essentially unmagnetized region, γ_{ion} is no longer coupled by the magnetic field to the flow 4-velocity of the pairs, thus allowing $\gamma_{ion} \gg \Gamma_{wind}$ [11].

Taking such improvements of the model into account is needed before one can realistically assess the model's consequences for observations, including possible hadronic TeV gamma ray and neutrino emission from the nebulae, a definite prediction of the model at some flux level. At this writing, models of the TeV SED based on the 1D dynamical model [4, 16] show that the hadronic gamma-rays at $\varepsilon < 20$ TeV are masked by inverse Compton emission; recent HESS observations of the Crab [1] suggest that an interesting constraint on ions in the outflow may be attainable. Recently [69] suggested that the TeV emission observed from the Vela-X PWN might be due to hadronic emission from the p–p interaction. Simple evolutionary models (Bucciantini and Arons, in preparation) suggest that such an interpretation is supported by the ion current sandwich model, when proper account is taken of the expansion and compression history of this older (age $\sim 10^{4.3}$ years) PWN.

Whatever the ultimate fate of models of this sort, they suggest the usefulness of stepping beyond MHD (which does not by itself constrain the wind velocity or density) in modeling the observations with the goal of extracting the plasma content and constraining just what does come out of pulsars, and other compact objects. See Chap. 16 for a parallel review of this subject.

Shock Acceleration

Starting with the seminal work of [122], the conversion of flow energy to the nonthermal particles emitting nebular synchrotron and inverse Compton radiation has

[12] Arons [9] suggested the large flux of radio emitting particles might be in higher latitude flow, a possibility I now disfavor, both because continuity of the Crab Nebula's spectral energy distribution militates against the accident that would be required, if the particle spectra were formed from such different flow components, and because the modern MHD models have no such distinction between low and high latitude particle fluxes.

been attributed to some form of "shock acceleration". Most commonly, Diffusive Fermi Acceleration (DFA) has been invoked, even though in relativistic shocks it faces a number of substantial difficulties, especially when the magnetic field is transverse to the flow. Mechanisms have not been apparent to supply the very large amplitude turbulence required [109], which must extend to large distances ($\sim R_{shock}$) both up and downstream of the shock so as to have a large "optical depth" for scattering of the largest Larmor radius particles both up- and down-stream. The spectrum of test particles accelerated depends sensitively upon the isotropy (or lack thereof) of the scattering process. However, in the case of isotropic scattering in the fluid frame, the test particle spectra are encouraging – Monte Carlo [79] and analytic [78] calculations with assumed scattering rules and infinite optical depth for particle scattering up and downstream yield an accelerated particle spectrum in the downstream medium $N(E) \propto E^{-20/9}$, which is almost exactly that inferred by modeling the synchrotron emission in a 1D post-shock flow in the Crab Nebula [77] – this simplified flow model should be a not unreasonable approximation to flow right outside the equatorial belt shock shown in Fig. 15.14. The efficiency depends entirely on what is assumed for the particle injection rate into the process, and the acceleration rate depends entirely on the assumed turbulence amplitude that goes into the scattering law adopted.

Hoshino et al. [70] suggested an alternate process, especially well tuned to the mixture of heavy ions and pairs injected in the equator with the magnetic field transverse to the flow.[13] Using 1D PIC simulations, they, and, more recently, [3] with higher mass ratio and resolution, showed that high harmonics of the ion cyclotron waves generated by the ions as they pass through the shock in the pairs can be resonantly absorbed by the positrons *and* electrons, which are non-thermally heated, yielding power law downstream distributions with a spectral slope that depends on the ratio of the upstream ion energy density to that of the pairs. The non-thermal part of the $e^{\pm}$ spectra shown in Fig. 15.19 extends from the pairs' flow energy/particle all the way up to the ions flow energy/particle.

If all the species have the same upstream flow velocity, the resulting spectra nicely span the range required for optical, X-ray and γ-ray emission from the Crab [70], and for X-ray and γ-ray emission from G320 [48]. As demonstrated by [3], however, when applied to the 1D model of [51] of the Crab Pulsar wind's termination shock, this mechanism has trouble providing an accelerated spectrum of pairs in accord with the observation. The ion flux by number is fixed at Goldreich–Julian value (it can hardly be anything else). If $\gamma_{ion} = \Gamma_{wind}$, the upstream energy density ratio $(U_{\pm}/U_{ion})_1 = (2n_{\pm}\Gamma_{wind}m_{\pm}/\gamma_{ion}n_{ion}m_i) \sim 10^3$ leads to the pairs' particle energy distribution hardly differing from a relativistic Maxwellian, the downstream distribution for a relativistic transverse shock in a pure pair plasma [**?**,52,86], not at all in accord with the observations.

[13] As in the high energy beam, cyclotron instability interpretation of the wisps, an electron current accelerated in the equatorial current sheet of an "obtuse" pulsar can replace the ion beam accelerated in the current sheet of an "acute" pulsar without altering the conclusions – at equal relativistic energy/particle, the only difference is the sense of gyration with respect to the unknown vector direction of the magnetic field.

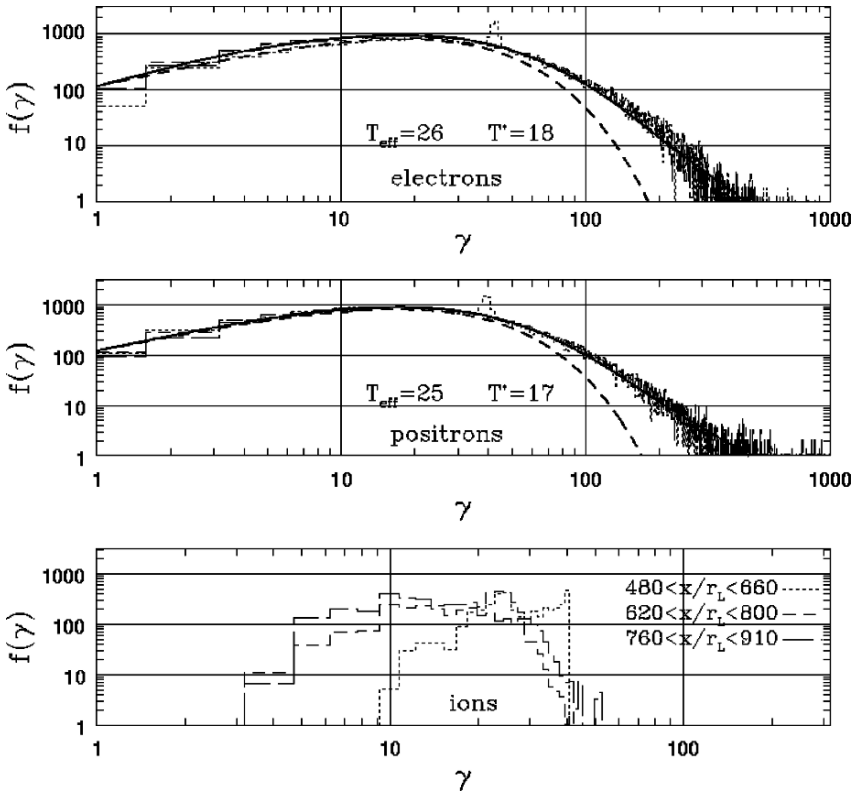

Fig. 15.19 Downstream particle spectra of a PIC simulation of a shock with upstream magnetic field transverse to the flow in an electron–positron–proton plasma with mass ratio $m_p/m_\pm = 100$ and upstream flow Lorentz factor of all species $\gamma_1 = 40$. The upstream Lorentz factor sets the scale; the results are otherwise independent of the specific value of γ_1, so long as it is larger than 2 or 3. $f(\gamma)$ are the distribution functions, with $\int f(\gamma)\gamma d\gamma =$ species density. The ratio of the proton number density to the number density of electrons plus positrons was 1/19, therefore the energy density in upstream protons was 2.1 times the energy density in pairs. The *dashed curves* in the panels showing the electron and positron spectra are the best fit Maxwellians, while the temperatures stated in the figure (which are in units of mc^2) rows are inferred from fitting a Maxwellian with a power law tail to the numerical data. The slope of the power supra-thermal component is $\alpha = 3.2$, corresponding to an energy space spectrum $dN/d\gamma \propto \gamma^{-(\alpha-1)} \propto \gamma^{-2.2}$, quite close to what is required in modeling the optical and X-ray synchrotron emission from the Crab Nebula and other young pulsar wind nebulae. The power law spectral index is a strong function of the upstream energy density ratio, thus making the downstream nonthermality of the pairs a strong function of the upstream composition. For the details, including the power law spectra index as a function of density ratio, see [3]

If acceleration occurs near the sandwich midplane, the obstacles to acceleration by either mechanism may be reduced. The cyclotron mechanism benefits from $\gamma_{ion} \gg \Gamma_{wind}$. With pair multiplicity $\kappa_\pm = 2n_\pm/n_{GJ} > 10^6$ (required to supply the radio emission of the Crab Nebula) and therefore $\Gamma_w \leq 10^4$ (since most of the energy

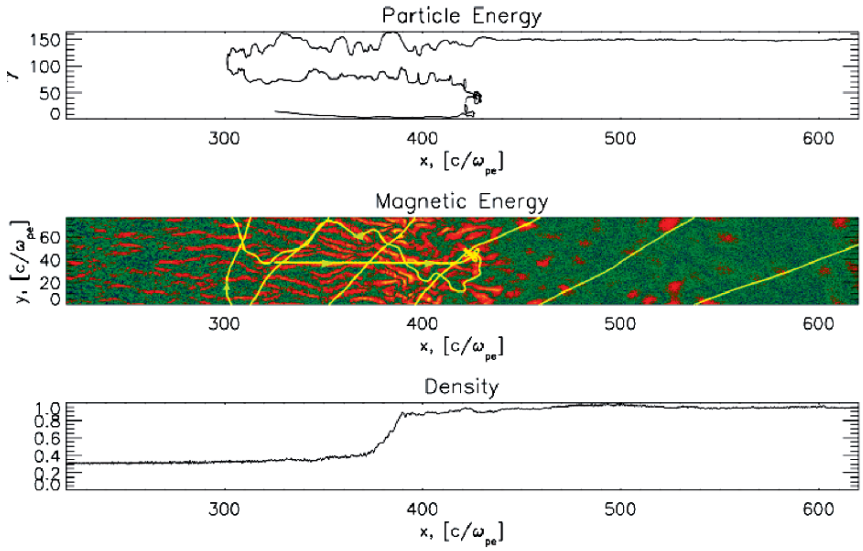

Fig. 15.20 Shock structure and test particle gaining energy at the shock front, from a PIC simulation of an unmagnetized $e^{\pm}$ shock by [133]. Lengths are measured in units of the upstream skin depth. *Bottom panel*: Density as a function of position, exhibiting the factor of 3 jump (properties of this shock in a 2D plasma are measured in the downstream frame). *Middle panel*: $(B^2)^{1/4}$, showing the upstream magnetic filaments characteristic of the Weibel instability in the linear regime, the scrambled magnetic structures formed when the currents reach the Alfvén critical current, magnetic trapping disrupts the flow and the shock transition forms [76]. Note the transition of the magnetic structure to spatially intermittent (widely separated) islands in the downstream. The orbit of a test particle is superimposed. Because of the finite thickness of the strongly turbulent scattering layer, particles escape downstream after a finite number of scatterings. The sideways dimension is periodic, thus a particle leaving the box at the top reappears at the lower bottom. *Top panel*: Energy of the test particle, which started with the upstream flow energy ($\gamma = 15$) and increased its energy by a factor of 10 before escaping

flux is carried by the pairs) while $\gamma_{ion} \sim 10^{6.5}$, now $(U_{\pm}/U_{ion})_1 \sim 3$, which leads to a downstream particle spectrum possibly as flat as the $E^{-1.5}$ radio emitting particles. DFA might benefit from a weaker transverse magnetic field – for $\sigma_{local} < 10^{-3}$ within the current sheet, magnetized shocks in pair plasmas become indistinguishable from shocks formed in a flow with no magnetic field at all [?]. Figure 15.20 shows a snapshot of a 2D PIC simulation of a shock in a $B = 0$, $e^{\pm}$ plasma, exhibiting a test particle gaining energy as it scatters in the magnetic turbulence in and behind the shock front, which forms due to the Weibel instability driven by the upstream flow penetrating into the heated downstream medium.

The downstream pair spectra found in this simulation are shown in Fig. 15.21, which exhibit the formation of a supra-thermal particle spectrum through scattering in the turbulence in and near the shock front. To go to energies much higher requires turbulence that persists to much greater depths in the downstream than are studied in the simulations, with amplitudes that do not decay. Phase mixing between particles and fields may cause the decay of the downstream magnetic fields [31], in

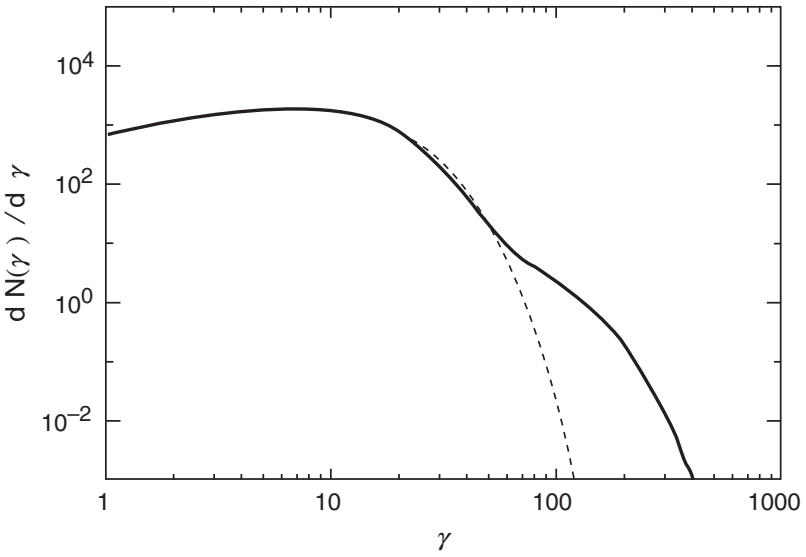

Fig. 15.21 Downstream particle distribution function in the large PIC simulation of a pair shock with no systematic magnetic field in the upstream medium used to create Fig. 15.20. The *lowest dashed* is a Maxwellian distribution fit. The *solid curve* is the actual particle distribution. Clearly, scattering in and around the shock front produces supra-thermal particles (in this example, these are 5% by number and 20% by energy)

completely unmagnetized shocks. Nevertheless, these results, which show how non-thermal particles can be created out of the thermal pool in a very weakly magnetized shock (upstream $\sigma < 10^{-3}$, as might be characteristic of the central regions of the equatorial current sheet), there to act as seeds for DFA. Identifying the necessary scattering turbulence remains a challenge.

These speculative possibilities suggest a solution to the vexing question of how the peculiar spectrum of particles injected into the Crab Nebula and other PWNe might be formed. These systems all have very flat power law distributions of particles $N(E) \propto E^{-p}$, $1 \leq p \leq 1.5$ giving rise to their radio synchrotron emission, while the inferred injection spectra of particles required for the harder photon emissions (optical when seen, X-ray) have much steeper spectra, $p = 2.2$–2.4. The continuity observed between the radio and the harder photon spectra suggests the shock injects a broken power law spectrum. Cyclotron resonant acceleration, driven by an ion flow in the current sheet with $\gamma_{ion} \gg \Gamma_w$, might be responsible for the very flat spectrum of radio and infrared emitting electrons, whose upper cutoff is determined by energy conservation to be not large compared to Γ_{wind}. DFA might be responsible for continued acceleration to optical, X-ray and gamma-ray synchrotron emitting energies. This combination was first suggested by [53]. In their formulation, in which $\gamma_{ion} = \Gamma_{wind}$, the ions had negligible energy density compared to the much denser pairs and therefore could not act as the desired accelerator, while in the version suggested here, the ions having a 4 velocity much larger than that of the pairs allows

them to act as an effective agent in creating the non-thermal radio emitting particles. A quantitative expression of these thoughts is under investigation.

The scheme outlined above assumes the stripes in the wind do in fact disappear well upstream of the shock, as is suggested by the rapid dissipation results of [11]. Lyubarsky [91], starting from the slow stripe dissipation model of [93], showed, using 1D and 2.5D kinetic simulations in $e^{\pm}$ plasma, that the striped field can annihilate in a broad "shock" region with strong plasma heating – thus, the effect is as if σ was low in the upstream medium, even when it was not in fact small. He also presented evidence that reconnection at individual sheets might create a flat particle distribution $N \propto E^{-1.1}$ which might be of use in understanding the radio emission from PWNe. However, a full 3D treatment is needed in order to properly evaluate the non-thermal particle acceleration, since the periodicity of the simulation in the electric field direction can lead to artificial results for particle acceleration.

A clear theoretical picture has yet to emerge, never mind models with readily checkable observational predictions. And all of these models and the observations underlying them tell us that a fully quantitative account of the pair plasma supply is still lacking. There will be progress on the theoretical front in the next few years. The much anticipated launch of GLAST may add a new observational handle on these problems, since the highest energy radiating particles have rapid radiation losses, therefore leading to interesting time series in the gamma-ray emission as the particles simultaneously accelerate and radiate in the time variable termination shock region.

15.4 Conclusion: Pulsar Problems and Prospects

Pulsar physics has made substantial progress in the last decade. The emergence of the MHD model of relativistic plasma flow in Pulsar Wind Nebulae has given a plausible account of the plume–torus (a.k.a. jet-torus) structures observed in these systems, thus reconciling the external response of the surrounding world to the well known difficulties in forming a jet in the relativistic winds themselves. These models also explain the lack of shock excitation of the nebulae at high latitude as a result of the shock's lack of spherical symmetry, itself a consequence of the anisotropy of the energy outflow found in the energy flux emerging from the magnetosphere.

Application of force-free electrodynamics and relativistic MHD to the winds emerging from magnetospheres with dipole magnetic fields has led to the first theory of the oblique rotator's energy loss that incorporates qualitative changes from the vacuum theory imposed by electric current flow, leading to the delightfully simple formula for the spin-down energy loss given in expression (15.6). For the model of the magnetosphere, the most important result is that the polar electric current distribution is close to that of the monopolar magnetosphere, reflecting the asymptotically monopolar poloidal magnetic field beyond the light cylinder.

The role of reconnection in the transfer of open to closed magnetic flux (and back again, since this is an unsteady process) has begun to be assessed, and is full

of promise as a path to a physical theory of the boundary layer between the closed and open magnetosphere, where existing gamma-ray observations and gap models suggest the most prominent photon emissions from pulsars occur. Prominent issues waiting assessment include reconciling the creation of pairs with the monopolar current distribution in expression (15.9) and Fig. 15.9, with various solutions being on the table, awaiting surgery – these range from rapid local current fluctuations (averaging to the force-free current) to manipulation of the polar cap electrostatics by return currents on the open flux tube boundaries. These models all have consequences for long standing issues such as the origin of torque fluctuations, radio subpulse phase randomness and drifting, possibly for the origin of the departures of the braking index from its canonical value of 3, and for the origin of the large particle fluxes inferred from nebular radio emission. The modeling will be observationally illuminated by the results of the upcoming GLAST gamma-ray mission. If high sensitivity X-ray astronomy has a future, observations with the ability to inspect variability in the X-rays, both non-thermal and thermal from polar caps heated by magnetospheric currents would be invaluable.

The longstanding problem of the origin of the weak magnetic fields inferred downstream of pulsar winds' termination shocks in the young nebulae is still an outstanding question, with dissipation of the magnetic stripes in the wind being the prime suspect. Whether this occurs in the wind far upstream form the shock, or in the shock itself, is an open question under active investigation.

Finally, the basic physics of relativistic shock waves is receiving significant attention, which opens the prospect of having a testable theory of the conversion of flow energy to non-thermal particle spectra in these relativistic systems within the next few years. Significant issues that will receive attention include the mixture (if any) of Diffusive Fermi Acceleration and other shock related processes, the possible role of protons and other heavy ions as well as pairs in the acceleration physics (and testing for these ions' presence through VHE gamma-ray and neutrino observations), and an understanding of how the nebular radio emitting electrons can be accelerated by the curved termination shock. – Exciting times lie ahead!

References

1. Aharonian, F., Akhperjanian, A.G., Bazer-Bachi, A.R., et al., 2006, A&A, 457, 899
2. Al'ber, Y.I., Krotova, Z.N., and Eidman, V.Y. 1975, Astrophys., 11, 189
3. Amato, E., and Arons, J., 2006, ApJ, 653, 325
4. Amato, E., Guetta, D., and Nlasi, P., 2003, A&A, 402, 827
5. Arons, J., 1981, ApJ, 248, 1099
6. Arons, J., 1981, in *Proc. IAU Symp. No. 95 'Pulsars'*, W. Sieber and R. Wielebinski, eds. (Dordrecht: Reidel), 69
7. Arons, J., 1983, in *Positron–Electron Pairs in Astrophysics* (New York: AIP), 163
8. Arons, J., 1983, ApJ, 266, 215
9. Arons, J., 1998, Mem. Soc. Ast. It., 69, 989 (astro-ph/9809392)
10. Arons, J., 1998, in *Neutron Stars and Pulsars: Thirty Years after the Discovery*, N. Shibazaki et al., eds. (Tokyo: Universal Academy Press), 339, (astro-ph/9802198)

11. Arons, J., 2008, submitted to ApJ. A summary can be found in Arons, J. 2008, in *40 Years of Pulsars: Millisecond Pulsars, Magnetars and More*, C.G. Bassa, Z. Wang, A. Cumming and V.M. Kaspi, eds., AIP Conference Proceedings vol. 983 (Melville, NY: AIP), 200–206 (astro-ph/0710.5261)
12. Arons, J., and Scharleman, E.T., 1979, ApJ, 231,854
13. Barnard, J.J., 1986, ApJ, 303, 280
14. Barnard, J.J., and Arons, J., 1986, ApJ, 302, 138
15. Bateman, G., 1978, *MHD Instabilities* (Cambridge: MIT Press), 66–69
16. Bednarek, W., and Bartosik, M., 2003, A&A, 405, 689
17. Begelman, M., 1999, ApJ, 512,755
18. Benford, G., 1977, MNRAS, 179, 311
19. Bessho, N., and Bhattacharjee, A., 2005, Phys. Rev. Lett., 95, 245001
20. Bietenholz, M., Hester, J.J., Frail, D.A., and Bartel, N., 2004, ApJ, 615, 794
21. Birn, J., Drake, J.F., Shay, M.A., et al., 2001, JGR, 106, 3715
22. Blandford, R., 2002, in *Lighthouses of the Universe*, M. Gilfanov, R. Sumyaev and E. Churazov, eds. (New York: Springer), 381 (astro-ph/0202265)
23. Blandford, R., Applegate, J., and Hernquist, L., 1982, MNRAS, 204, 1025
24. Bogovalov, S.V., 1999, A&A, 349, 1017
25. Bogovalov, S.V., Chechetkin, V.M., Koldoba, A.V., and Ustyugova, G.V., 2005, MNRAS, 358, 705
26. Bogovalov, S.V., and Khangoulian, D.V., 1999, MNRAS, 336, L53
27. Bucciantini, N., Amato, E., Bandiera, R., Blondin, J.M., and Del Zanna, L., 2004, A&A, 423, 253
28. Bucciantini, N., and Del Zanna, L., 2006, A&A, 454, 393
29. Bucciantini, N., Thompson, T., Arons, J., et al., 2006, MNRAS, 368, 1717
30. Carson, J., 2006, astro-ph/0610960
31. Chang, P., Spitkovsky, A., and Arons, J., 2008, ApJ, 674, 378
32. Cheng, K.S., Ho, C., and Ruderman, M., 1986, ApJ, 300, 500 and 522
33. Chiang, J., and Romani, R., 1994, ApJ, 46, 754
34. Contopoulos, I., 2005, A&A, 442, 579
35. Contopulos, I., Kazanas, D., and Fendt, C., 1999, ApJ, 511, 351
36. Contopoulos, I., and Spitkovsky, A., 2006, ApJ, 643, 1139
37. Cordes, J., 1980, ApJ, 239, 640
38. Cordes, J., and Helfand, D.J., 1980, ApJ 239, 640
39. Coroniti, F., 1990, ApJ, 349, 538
40. de Jager, O., 2007, ApJ, 658, 1177
41. DeLaney, T., Gaensler, B., Arons, J., and Pivovaroff, M., 2006, ApJ, 640, 929
42. Del Zanna, L., Amato, E., and Bucciantini, N., 2004, A&A, 421, 397
43. Del Zanna, L., Volpi, D. Amato, E., and Bucciantini, N., 2006, A&A, 453, 621
44. Deshpande, A., and Rankin, J., 1999, ApJ, 524, 1008
45. Deutsch, A., 1955, Ann. d'Ap., 18, 1
46. Fawley, W.M., 1978, PhD Dissertation, UC Berkeley (Ann Arbor: http://wwwlib.umi.com/dissertations/)
47. Funk, S., 2007, astro-ph/070147
48. Gaensler, B., Arons, J., Kaspi, V., et al., 2002, ApJ, 569, 878
49. Gaensler, B., and Slane, P., 2006, Ann. Rev. Astro. Astrophys., 44, 17
50. Gallant, Y.A., 2007, Ap & SS, 309, 197
51. Gallant, Y.A., and Arons, J., 1994, ApJ, 435, 230
52. Gallant, Y.A., Hoshino, M., Langdon, A.B., Arons, J., and Max, C.E., 1992, ApJ, 391, 73
53. Gallant, Y.A., van der Swaluw, E., Kirk, J.G., and Achterberg, A., 2002, in *Neutron Stars in Supernova Remnants*, P.O. SLane and B.M. Gaensler, eds. (San Francisco: ASP Conference Series Vol. 271), 99
54. Gehrels, N., and Michelson, P., 1999, Astroparticle Phys., 11, 277
55. Goldreich, P., and Julian, W.H., 1969, ApJ, 157, 869
56. Goodwin, S.P., Mestel, J., Mestel, L., and Wright, G., 2004, MNRAS, 349, 213

57. Gruzinov, A., 2005, Phys. Rev. Lett., 94, 021101
58. Harding, A.K., Muslimov, A.G., and Zhang, B., 2002, ApJ, 576, 366
59. Helfand, D.J., et al., 1980, ApJ, 237, 206
60. Hester, J.J., Mori, K., Burrows, D., et al., 2002, ApJ, 577, L49
61. Hester, J.J., Stone, J.M., Scowen, P.A., et al., 1996, ApJ, 456, 225
62. Hibschman, J.A., 2002, ApJ, 565, 1183
63. Hibschman, J.A., and Arons, J., 2001, ApJ, 546, 382
64. Hibschman, J.A., and Arons, J., 2001, ApJ, 546, 624
65. Hibschman, J.A., and Arons, J., 2001, ApJ, 560, 871
66. Hirotani, K., 2006, ApJ, 652, 1475
67. Holloway, N., 1973, Nat. Phys. Sci., 246, 6
68. Holloway, N., 1975, MNRAS, 171, 619
69. Horns, D., Aharonian, F., Santangelo, A., et al., 2006, A&A, 451, L54
70. Hoshino, M., Arons, J., Gallant, Y.A., and Langdon, A.B., 1992, ApJ, 390, 454
71. Hsu, P.-C., Hirotani, K., and Chang, H.K., 2006, in *Proc. 363rd W.E. Heraeus Seminar "Neutron Stars and Pulsars"*, W. Becker and H.H. Huang, eds. (Munich: MPE Report No. 291), 141 (astro-ph/0612677)
72. Hurley, K., et al., 2005, Nature, 434, 1098
73. Jessner, A., Slowikowska, A., Klein, B., et al., 2005, Adv. Space Res., 35, 1166
74. Kanbach, G., Slowikowska, A., Kellner, S., and Stenle, H., 2005, in *Astrophysical Sources of High Energy Particles and Radiation* (New York: AIP Conference Proceedings), 306
75. Kaspi, V., Roberts, M., and Harding, A., 2006, in *Compact Stellar X-ray Sources*, W. Lewin and M. van der Klis, eds. (Cambridge: Cambridge University Press), 279–339 (astro-ph/0402136)
76. Kato, T.N., 2005, Phys. Plasmas, 12, 080705 (astro-ph/0501110)
77. Kennel, C.F., and Coroniti, F.V., 1984, ApJ, 283, 694; 283, 710
78. Keshet, U., and Waxman, E., 2005, Phys. Rev. Lett., 94, 111102
79. Kirk, J.G., Guthmann, A.W., Gallant, Y.A., and Achteberg, A., 2000, ApJ, 542, 235
80. Kirk, J.G., and Skjæraasen, O., 2003, ApJ, 591, 366
81. Komissarov, S., 2006, MNRAS, 367, 19
82. Komissarov, S., Barkov, M., Vlahakis, N., and Konigl, A., 2007, MNRAS, 380, 51
83. Komissarov, S., and Lyubarsky, Y., 2003, MNRAS, 344, L93; 2004, MNRAS, 349, 779
84. Kramer, M., Xilouris, K.M., Lorimer, D., et al., 1998, ApJ, 501, 270
85. Krause-Polstorff, J., and Michel, F.C., 1985, MNRAS, 213, 43
86. Langdon, A.B., Arons, J., and Max, C.E., 1988, Phys. Rev. Lett., 61, 779
87. Levinson, A., Melrose, D., Judge, A., and Luo, Q., 2005, ApJ, 631, 456
88. Livingstone, M., et al., 2005, ApJ, 619, 1046
89. Lyubarsky, Y., 1990, Pis'ma Astron. Zh., 16, 34 (Sov. Astron. Lett., 16, 16)
90. Lyubarsky, Y., 2002, MNRAS, 329, L34
91. Lyubarsky, Y., 2003, MNRAS, 345, 153; 2005, Adv. Space Res., 35, 1112
92. Lyubarsky, Y., 2005, MNRAS, 358, 113
93. Lyubarsky, Y., and Kirk, J., 2001, ApJ, 547, 437
94. McKinney, J.C., 2006, MNRAS, 368, L30
95. McKinnon, M.M., 1997, ApJ, 475, 763
96. McLaughlin, M., and Cordes, J., 2000, ApJ, 538, 818
97. Melikidze, G.I., Gil, J., and Szary, A., 2006, in *Proceedings of the 363rd WE-Heraeus Seminar on: Neutron Stars and Pulsars*, W. Becker, H.H. Huang, eds., MPE Report 291, 157 (astro-ph/0612683)
98. Mestel, L., 1999, *Stellar Magnetism* (Oxford: Clarendon)
99. Mestel, L., Robertson, J., Wang, Y.M., and Westfold, K., 1985, MNRAS, 217, 443
100. Michel, F.C., 1969, ApJ, 158, 727
101. Michel, F.C., 1973, ApJ, 180, 207
102. Michel, F.C., 1973, ApJ, 180, L133
103. Michel, F.C., 1974, ApJ, 187, 585
104. Michel, F.C., 1975, Apj, 197, 193

105. Mori, K., et al., 2006, in *36th COSPAR Assembly* (Beijing), http://www.cosis.net/abstracts/COSPAR2006/02615/COSPAR2006-A-02615.pdf, and personal communication
106. Muslimov, A., and Harding, A., 2003, ApJ, 485, 735
107. Muslimov, A., and Harding, A., 2003, ApJ, 588, 430
108. Muslimov, A., and Harding, A., 2004, ApJ, 606, 1143
109. Niemic, J., and Ostrowski, M., 2006, ApJ, 641, 984
110. Ng, C.-Y., and Romani, R., 2004, 601, 479
111. Ostriker, J., and Gunn, J., 1969, ApJ, 157, 139
112. Pacini, F., 1967, Nature, 434, 1107
113. Petri, J., 2007, A&A, 464, 135 (astro-ph/0611936)
114. Petri, J., Heyvaerts, J., and Bonnazola, S., 2002, A&A, 384, 414
115. Petri, J., Heyvaerts, J., and Bonnazola, S., 2002, A&A, 387, 520
116. Petri, J., Heyvaerts, J., and Bonnazola, S., 2003, A&A, 411, 203
117. Palmer, D.M., et al., 2005, Nature, 434, 1107
118. Ramachandran, R., and Kramer, M., 2003, A&A, 407, 1085
119. Rankin, J., 1983, ApJ, 274, 333
120. Rankin, J., 1990, ApJ, 352, 247
121. Rankin, J., and Suleymanova, S.A., 2006, A&A, 453, 679
122. Rees, M.J., and Gunn, J.E., 1974, MNRAS, 167, 1
123. Romani, R., 1996, ApJ, 470, 469
124. Romani, R., Ng, C.-Y., Dodson, R., and Brisken, W., 2005, ApJ, 631, 480
125. Romani, R., and Yadigoroglu, I.A., 1995, ApJ, 438, 314
126. Ruderman M., and Sutherland, P., 1975, ApJ, 196, 51
127. Scargle, J., 1969, ApJ, 156, 401
128. Scharlemann, E.T., and Wagoner, R.V., 1973, ApJ, 182, 951
129. Shklovsky, I.S., 1968, *Supernovae* (New York: Wiley)
130. Slane, P., 2005, Adv. Space Res., 35, 1092
131. Spitkovsky, A., 2002, PhD dissertation, UC Berkeley
132. Spitkovsky, A., 2006, ApJ., 648, L51
133. Spitkovsky, A., 2008, ApJ, 673L, 39
134. Spitkovsky, A., and Arons, J. 2002, in *Neutron Stars and Supernova Remnants*, P.O. Slane and B.M. Gaensler, eds. (San Francisco: Astronomical Society of the Pacific), 81 (astro-ph/0201360)
135. Spitkovsky, A., and Arons, J., 2004, ApJ, 603, 669
136. Sturrock, P.A., 1971, ApJ, 164, 529
137. Tademaru, E., 1973, ApJ, 183, 625
138. Timokhin, A., 2006, MNRAS, 368, 1055
139. Thompson, D., 2000, Adv. Sp. Res., 25, 659
140. Yin, L., Coroniti, F.V., Pritchett, P.L., et al., 2000, JGR, 25, 345

Chapter 16
The Theory of Pulsar Winds and Nebulae

John G. Kirk, Yuri Lyubarsky, and Jérôme Pétri

16.1 Introduction

The theory of pulsar winds and the nebulae they energize is currently celebrating its golden jubilee. Ten years before the discovery of pulsars it was already apparent that the magnetic field and relativistic particles that produce the radiation of the Crab Nebula must have their origin in a central stellar object [104]. Today, about 50 similarly powered objects are known, and some of them, like the Crab, are detected and even resolved at all accessible photon frequencies, from the radio to TeV gamma-rays. The rotation of the central neutron star [98] is now universally accepted as the energy source fuelling these objects, but the details of the coupling mechanism are still unclear. In this article we review current theoretical ideas on this subject and their relationship to observations. We concentrate on the magnetohydrodynamic description of the relativistic outflow driven by the pulsar and on the bubble it inflates in the surrounding medium.

The discussion is organised as follows: in Sect. 16.2 we consider the region between the surface of the neutron star and the *light cylinder* a surface of cylindrical radius $r_{\rm L} = cP/(2\pi)$, where P is the pulsar period. The speed of an object that co-rotates with the star becomes luminal on this surface, and the wavelength of the radiation that would be emitted by the pulsar in vacuum is $2\pi r_{\rm L}$. In the terminology of radiating systems, the region within the light cylinder is, therefore, the "near zone", where the fields can be approximated as being in rigid co-rotation. Conventionally, this region is called the pulsar *magnetosphere*. It is thought to be the site of copious pair creation, and, in most theories, is the region in which the pulsed radiation itself is emitted.

J.G. Kirk and J. Pétri
Max-Planck-Institut für Kernphysik, Postfach 10 39 80, 69029 Heidelberg, Germany
e-mail: John.Kirk@mpi-hd.mpg.de, Jerome.Petri@mpi-hd.mpg.de

Y. Lyubarsky
Department of Physics, Ben Gurion University, P.O. Box 653, Beer-Sheva 84105, Israel
e-mail: lyub@bgu.ac.il

W. Becker (ed.), *Neutron Stars and Pulsars,* Astrophysics and Space Science Library 357,

Electric and magnetic fields dominate the dynamics in the near zone inside the light cylinder. However, this is also true in at least part of the "far zone", that lies well outside the light cylinder – a region that is not conventionally thought of as the pulsar magnetosphere. Here, we follow conventional terminology, and call this the *wind zone*;[1] it extends up to the *termination shock*, where the ordered, relativistic flow of particles and fields is randomised. Electromagnetic fields dominate the inner part of the wind zone, where the plasma flows subsonically with respect to the fast magnetosonic mode. As we describe in Sect. 16.3, force-free solutions to the aligned rotator problem show that the plasma accelerates up to the critical point where its velocity equals the fast magnetosonic speed, and, presumably, passes through it into a supersonic domain. In this part of the flow, the dynamics is strongly influenced by the particles, although most of the energy flux continues to be carried by the fields. The oblique rotator is a more suitable model for a pulsar, and the key difference it introduces in the wind zone is wave-like structure on the very small length scale $r_{\rm L}$. We discuss the structure of such a *striped wind* in Sect. 16.4, and consider the possibility that dissipative processes play a role in converting Poynting flux into kinetic energy. In both the sub and supersonic parts, the pulsar wind is highly relativistic. If it radiates at all, its emission is beamed predominantly in the radial direction. This simple kinematic effect has an important influence on the radiative signature of this region, as we discuss in Sect. 16.5.

Observationally, the termination shock can be identified as the outer boundary of an underluminous region that lies at the centre of the diffuse synchrotron emission of the nebula. The nebula itself, therefore, lies between the termination shock and an outer boundary, where the relativistic particles produced by the pulsar impinge on either the debris of its natal supernova explosion, or on the interstellar medium. These particles are most plausibly accelerated at the termination shock, and we consider the acceleration processes operating here in Sect. 16.6. Finally, in Sect. 16.7, we discuss models of the nebula and its emission.

16.2 The Magnetosphere

An enormous electric field is induced by the rotation of a magnetised neutron star. This field tears particles from the stellar surface and accelerates them up to high energies. As a result, these "primary" particles initiate an electron–positron cascade, which, according to conventional wisdom, populates the entire magnetosphere with plasma. In the aligned case, solutions have been found for the region well within the light cylinder in which this plasma is confined to domes above the poles and a differentially rotating equatorial disk [77, 101]. If, on the other hand, the magnetosphere is filled with plasma, the strength of the magnetic field is sufficient to ensure that the

[1] Note that we designate the entire far zone outside the light cylinder as the *pulsar wind*, although this term is really only appropriate for the supersonic part of the flow.

plasma co-rotates [56, 100]. At some point near the light cylinder, co-rotation must cease, and the particles escape, carrying away magnetic flux and energy in the form of an ultra-relativistic, magnetised wind.

If one traces the escaping ("open") magnetic field lines back to the stellar surface, they define areas which, in a dipole geometry, lie close to the magnetic axis and are called "polar caps". To maintain a steady state, plasma must be continuously generated on the open field lines in these polar regions. It then streams along them with relativistic velocity and eventually escapes through the light cylinder. It is usually assumed that the mechanism responsible for creating the pulsed radiation is somehow associated with the materialisation of these plasma streams, which presumably takes place at either an "inner gap" or "outer gap", [55]. However, this is not necessarily true (see Sect. 16.5), and, at least for the optical pulses, there are indications that the site of pulse production could lie outside the light cylinder [46, 73, 102].

The rate at which pairs escape is conveniently measured in terms of the the pair multiplicity, κ, which is the number of pairs produced by a single primary particle that emerges from one of the polar caps. The primary beam consists of particles of a single charge, and its density is expected to be close to the Goldreich–Julian density, defined as that required to screen the induced electric field, namely

$$n_{\rm GJ} \equiv |(\Omega \cdot \mathbf{B})/(2\pi ec)| \ , \tag{16.1}$$

where Ω is the angular velocity of the star and $\mathbf{B}$ the magnetic field [42, 61, 94]. In an aligned dipole geometry, the foot-points of those field lines that cross the light cylinder lie within polar caps of (cylindrical) radius $r_{\rm pc} \approx \sqrt{R_*^3/r_{\rm L}}$, where R_* is the stellar radius, and this is a reasonable approximation also in the oblique case [46]. Assuming the pairs stream away from the polar cap at relativistic speed, the total number ejected per unit time may therefore be estimated as

$$\begin{aligned} \dot{N} &= \kappa \frac{\Omega^2 B_* R_*^3}{ec} \\ &= 2.7 \times 10^{30} \kappa \left(\frac{B_*}{10^{12}\,{\rm G}} \right) \left(\frac{P}{1\,{\rm s}} \right)^{-2} {\rm s}^{-1} \ , \end{aligned} \tag{16.2}$$

where $\mathbf{B}_*$ is the magnetic field at the polar cap.

The actual value of the multiplicity, κ, is rather uncertain. Theoretical models [59, 60], give values of κ ranging from a few to thousands, but some observations suggest that the real value might be substantially higher (see Sect. 16.7 and [25, 51]). If $\Omega \cdot \mathbf{B}_* < 0$, the primary particles are positively charged ions. Because these particles do not breed in cascades, they make up a fraction of at most $1/\kappa$ by number of the wind particles. Nevertheless, if κ is indeed as low as predicted theoretically, the energy flux carried by ions could be as large as that carried by pairs.

16.3 The Wind of an Aligned Rotator

Pairs are produced with an energy that ranges from dozens to hundreds of MeV, and the total energy density of the produced plasma remains small compared to the magnetic energy density. Nevertheless, the presence of the plasma is crucially important, because the electromagnetic structure in the far zone is strongly influenced by the currents it carries. The overall structure may be pictured by taking into account that the magnetic field is frozen into the plasma. As the plasma cannot rotate with superluminal velocity, the magnetic field lines beyond the light cylinder are wrapped backwards with respect to the rotation of the neutron star. As a result of this, even an axisymmetric rotator loses energy by driving a plasma wind, provided its inner zone is filled with plasma. In contrast, an aligned magnetic dipole rotating in vacuum does not lose energy.

In the case of an aligned rotator (with parallel magnetic dipole and rotation axes), the entire system is axisymmetric. Essentially, the rotational energy of the neutron star is spent in the generation of azimuthal magnetic field in the wind. This can be seen by noting that the electric field ($\mathbf{E}'$) in the proper frame of the flow vanishes because the plasma conductivity is infinite, which implies

$$\mathbf{E} + (1/c)\mathbf{v} \times \mathbf{B} = 0. \tag{16.3}$$

In a radial, relativistic wind, the poloidal component of $\mathbf{B}$ is also radial, so that the magnitude of the electric field is close to that of the azimuthal magnetic field, which then determines the radial component of the Poynting flux: $P_R \approx cB_\varphi^2$.

In a steady, axisymmetric solution, the displacement current vanishes, and the azimuthal magnetic field is generated by poloidal currents that flow either into or out of the polar caps of the star, depending on the sign of $\Omega \cdot \mathbf{B}_*$. The circuit is closed in a current carrying surface – a "current sheet". Well outside the light cylinder, this sheet lies in the equatorial plane and separates the field lines that originate from the two magnetic poles. Inside the light cylinder, the current flows in the surface that encloses the volume containing closed field lines.

At the light cylinder, the azimuthal and poloidal fields are comparable. In the wind zone, conservation of magnetic flux in a diverging flow implies that the poloidal field decreases faster than the azimuthal field, which is proportional to $1/r$, where r is the cylindrical radius. Thus, the field in the far zone of the wind may be considered as purely azimuthal; even though each magnetic field line is a spiral anchored on the surface of the star, the spiral becomes so tightly wound in the far zone that it can be approximated locally as separate coaxial magnetic loops moving together with the flow.

The relative strength of magnetic field and particles is an important characteristic of the wind. This is best defined, in an ideal MHD description, as the ratio in the proper frame (where $\mathbf{E}' = 0$) of the magnetic to particle enthalpy densities:

$$\sigma \equiv \frac{B'^2}{4\pi w c^2}\,, \tag{16.4}$$

where w is the proper enthalpy density of the plasma and $\mathbf{B}'$ is the magnetic field in the proper frame. If, as we assume, the plasma is cold, the enthalpy density is simply the rest mass energy density: $w = m_e c^2 n/\Gamma$, where n is the number density in the lab. frame, (in which the centre of mass of the neutron star is at rest) and Γ is the Lorentz factor of the wind in this frame. Then, since the velocity of the wind is perpendicular to $\mathbf{B}' = \mathbf{B}/\Gamma$, σ equals the ratio of the energy carried by Poynting flux to that carried by particles:

$$\sigma = B^2/4\pi m_e c^2 n\Gamma \,. \tag{16.5}$$

According to all available models of the multiplicity, $\sigma \gg 1$ close to the light cylinder, so that the wind is Poynting dominated at that point. This means that the fast magnetosonic speed $v_{\rm fms}$ is very close to c:

$$\begin{aligned} v_{\rm fms} &= \frac{cB'}{\sqrt{4\pi w + B'^2}} \\ &\approx \sqrt{\frac{\sigma}{1+\sigma}} \end{aligned} \tag{16.6}$$

[70] and the corresponding Lorentz factor is $\Gamma_{\rm fms} = \sqrt{\sigma}$. In the cold wind, σ is related to Γ via (16.5), so that the fast magnetosonic point is located at the point where

$$\Gamma = \Gamma_{\rm fms} = \left(\frac{B^2}{4\pi m_e c^2 n}\right)^{1/3} , \tag{16.7}$$

$$\equiv \mu_{\rm M}^{1/3} , \tag{16.8}$$

where $\mu_{\rm M}$ is the magnetisation parameter introduced by [90]. The propagation of the fast magnetosonic wave is a result of the interplay between magnetic tension and plasma inertia. If, as seems likely, the flow emerges through the light cylinder subsonically, i.e., with $\Gamma \ll \sqrt{\sigma}$, the dynamics simplify significantly, because the inertia terms in the equation of motion are unimportant. Since gravity and gas pressure are also unimportant in the pulsar case, this "force-free"approximation implies that the Lorentz force is exactly cancelled by the electric force:

$$\rho_e \mathbf{E} + (1/c)\mathbf{j} \times \mathbf{B} = 0 \,. \tag{16.9}$$

The description of the dynamics is complete when this equation is complemented by Maxwell's equations, connecting the charge and current densities ρ_e and $\mathbf{j}$ with the fields $\mathbf{E}$ and $\mathbf{B}$, and by the ideal MHD condition (16.3).

The force-free MHD equations for the pulsar magnetosphere are strongly nonlinear and must, in general, be solved numerically [40, 54, 74, 88, 112]. In particular, the oblique rotator, being a three-dimensional problem, has only recently been treated [110]. Nevertheless, an exact axisymmetric solution describing a magnetosphere of a rotating star, namely that of the split monopole, has been known for many

years [92]. In this solution, magnetic field lines extend from the origin to infinity in the upper hemisphere and converge from infinity to the origin in the lower hemisphere. The hemispheres are separated by an equatorial current sheet. The magnetic surfaces have the form of coaxial cones whose vertices lie at the origin. Plasma flows radially from the origin to infinity. Of course, the flow lines in a realistic (dipole) magnetosphere cannot be radial everywhere; there should be a zone of closed field lines inside the light cylinder. However, [64] and [93] showed that, independently of the field structure near the origin, the flow lines beyond the light cylinder become asymptotically radial in the force-free approximation, just as in the split monopole solution. This is in contrast with the situation in axisymmetric nonrelativistic MHD winds where hoop stresses collimate the flow along the rotation axis. The reason is that in the relativistic case, the electric force compensates these stresses almost exactly.

In axisymmetric MHD, the flow lines lie in magnetic surfaces and the electric field is perpendicular to these surfaces, which are, therefore, equipotentials. The force-free condition (16.9) implies that the currents also flow along the magnetic surfaces. Taking this into account, one can find the asymptotic behaviour of the basic quantities in the radial wind:

$$\begin{aligned} B_\varphi &\propto r_\mathrm{L}/R\,, & E &\propto r_\mathrm{L}/R\,, \\ B_R &\propto r_\mathrm{L}^2/R^2\,, & n &\propto r_\mathrm{L}^2/R^2\,, \end{aligned} \tag{16.10}$$

where R is the radius in spherical polar coordinates. It follows from the higher order terms in the asymptotic solutions presented by [64] and [93] that the difference between E and B decreases with radius and the flow velocity approaches closer and closer to c, i.e., it accelerates. Buckley [37] showed that, in the force-free approximation, the Lorentz factor of the flow grows linearly with the radius [39]. Eventually, the Lorentz factor becomes comparable to that of the fast magnetosonic mode $\Gamma_\mathrm{fms} = \sqrt{\sigma}$. The plasma inertia becomes important at this point, and the force-free approximation breaks down.

If the pulsar wind is launched with $\sigma_0 \gg 1$ and $\Gamma_0 \ll \sqrt{\sigma_0}$, it is initially subsonic, the force-free approximation holds, and the flow accelerates. As Γ increases, σ decreases, since, in a radial flow with purely toroidal field, B^2/n remains constant and $\sigma \propto \Gamma^{-1}$ according to (16.5). At the fast magnetosonic point, $\sigma = (\sigma_0\Gamma_0)^{2/3} \gg 1$, and the flow is still Poynting dominated. This is in contrast with the nonrelativistic situation, where $v_\mathrm{fms} = B/\sqrt{4\pi\rho}$ so that the energy flux carried by particles equals the Poynting flux at the fast magnetosonic point. The reason is that in the relativistic case, the electric and magnetic forces almost compensate each other, allowing inertial effects to come into play at an early stage.

Beyond the fast magnetosonic point the full relativistic MHD equations must be solved. However, the flow remains nearly radial even there [22, 26, 38, 82, 113], because the additional inertial forces tend to resist collimation. Thus, if the flow is radial in the force-free region, it remains radial further out. In fact, the flow is practically ballistic, i.e., the plasma moves radially with negligible acceleration, so that Γ and, hence, σ remain constant. Thus, within the scope of ideal MHD, the

wind can be accelerated to at most Lorentz factors of a few times $\Gamma_{\rm fms}$, at which point σ is still large. Beyond this point, electromagnetic energy is not transferred to the plasma[2].

16.4 The Striped Wind

In the real world, pulsar winds are neither axisymmetric nor steady. In fact, the defining characteristic of a pulsar is that it is an oblique rotator, in the sense that its magnetic and rotation axes are not parallel. The time-varying electromagnetic fields excited by such an oblique rotator propagate outwards in the form of electromagnetic waves. The wavelength of these oscillations is at most $2\pi r_{\rm L}$. In the far zone, this is much smaller than the radius. For this reason, dissipative processes, which operate only on short length scales, are likely to be much more important in the wind of an oblique rotator than in a steady, axisymmetric wind. Therefore, the dissipation or damping of these waves could be an important mechanism of energy transformation in a pulsar wind.

A rarefied magnetised plasma supports a variety of electromagnetic waves. However, it seems reasonable to simplify the problem by assuming that only MHD waves (i.e., those satisfying the ideal MHD condition (16.3)) survive in the far zone. The reason is that, according to the conventional picture, the plasma density at the base of the pulsar wind (at $r \sim r_{\rm L}$) is sufficiently large that low-frequency electromagnetic waves are heavily damped [10, 89]. In this case, it is once again useful to think of magnetic field lines as frozen into the plasma flow. In the equatorial belt, the magnetic field at a fixed radius alternates in direction at the frequency of rotation, being connected to a different magnetic pole every half-period. Michel [91] pointed out that the flow in this zone should evolve into regions of cold, magnetically dominated plasma separated by very narrow, hot current sheets. Such a structure can be thought of as containing four tangential discontinuities per wavelength, each of which separates field lines from one magnetic pole from the thin, bounding layer of hot plasma which constitutes the current sheet. The corresponding structure in hydrodynamics is called an entropy wave. It is simply a stationary pattern of spatially varying temperature and density that is in pressure equilibrium in a motionless plasma.

[2] This does not mean that σ remains large in *any* Poynting-dominated flow. The relativistic MHD equations do not forbid acceleration of the flow and conversion of Poynting flux into kinetic energy. There exist many solutions that demonstrate explicitly the reduction of Poynting flux to the equipartition level or even below [23, 80, 118]. However this can happen only if the flow lines are not radial. In the above-mentioned solutions, this is achieved by a special choice of the poloidal flux distribution such that the total poloidal flux is infinite and the magnetic surfaces do not converge to origin. (Note that although the poloidal field is small beyond the light cylinder, the stress of this field may be not negligible in some cases because the hoop stress is nearly compensated by the electric force.) Whereas it is quite plausible that such solutions could be matched to boundary conditions above a disk, it is difficult to imagine that they could be made compatible with a star (effectively a point source) threaded by a finite magnetic flux. For this reason, we do not discuss them further here.

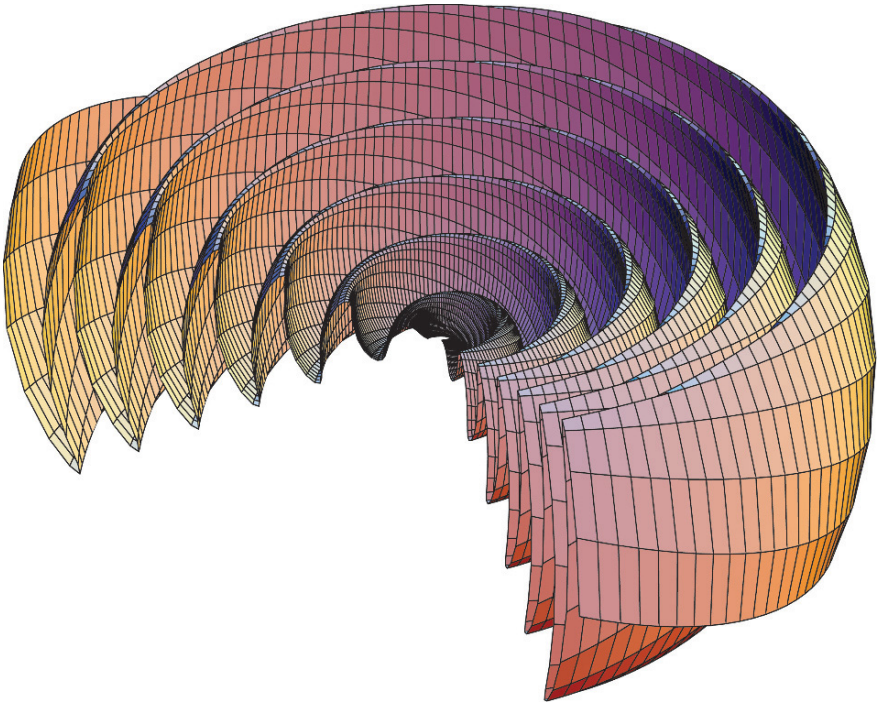

Fig. 16.1 The *striped wind* [41, 91]. A snapshot is shown of the surface that is traced out by the inclined magnetic equator when it rotates and is carried outwards by a radially propagating wind of constant velocity. This surface corresponds precisely to the current sheet in the oblique split-monopole solution [27]

The global picture of the resulting flow is shown in Fig. 16.1. As in the aligned rotator, the current sheet is a single surface that separates magnetic field lines that are attached to opposite magnetic hemispheres on the stellar surface. However, in the oblique case a pattern similar to that observed in the solar wind emerges: the sheet develops corrugations, whose amplitude increases linearly with distance from the star, as the radial wind draws out the flux lines. The current sheet now cuts the equatorial plane along twin spirals, that separate stripes of magnetic field of opposite polarity – hence the name *striped wind*. In the far zone, the distance between successive corrugations is small compared to the radius of curvature of their surfaces, and the spiral in the equatorial plane becomes tightly wound. Within a belt around the equator, whose thickness depends on the angle between the magnetic and rotation axes (see below), the flow locally resembles a sequence of concentric, spherical current sheets.

This picture can be made more precise by noting that, in an ideal MHD solution, the polarity of the field between two magnetic surfaces can be reversed without affecting the structure of the solution, provided a current sheet is inserted on the bounding surfaces. Bogovalov [27] applied this argument to the split monopole solution by anchoring the inner edge of the current sheet to the obliquely rotating

magnetic equator on the stellar surface. This effectively transforms the aligned split-monopole solution into one for an obliquely rotating split monopole. The resulting picture coincides precisely with that illustrated in Fig. 16.1. Recently, numerical solutions of the force-free equations have been found that have a similar appearance [110], although the dimensions of the calculational box extend as yet to only a few $\times\, r_{\rm L}$.

At high latitudes, the magnetic field does not change sign, and there are no current sheets embedded in the flow. Here, the magnetic oscillations can propagate as fast magnetosonic waves; the generation of such waves by the rotating, slightly nonaxisymmetric magnetosphere was considered by [28]. They could decay by nonlinear steepening leading to the formation of multiple shocks [85]. But this could release only a fraction of the Poynting flux into the plasma, since, at these latitudes, most of it is carried by the mean magnetic field.

The X-ray image of the inner Crab Nebula clearly suggests that most of the energy is transported in the equatorial belt of the pulsar wind [9, 32, 119]. The split monopole solution indeed has a pronounced maximum of the Poynting flux at the equator: $\mathrm{d}L/\mathrm{d}\Omega \propto \sin^2\theta$, where $\mathrm{d}L/\mathrm{d}\Omega$ is the luminosity per solid angle interval and θ is the colatitude [92]. In an equatorial belt, $\pi/2-\zeta<\theta<\pi/2+\zeta$, where ζ is the angle between the magnetic and rotation axes, the energy is carried predominantly by alternating fields (the mean field of oblique rotator vanishes in the equatorial plane). This means that most of the energy is transported in the form of a striped wind; therefore the fate of the striped wind is of special importance.

In an ideal MHD picture, the entropy wave that makes up the striped wind propagates without damping, and the dynamics is the same as in the case of the aligned rotator: in the supersonic region, the flow is essentially ballistic and propagates radially at constant speed. However, as noticed by [114], this cannot continue to arbitrarily large radius. The reason is that the amplitude of the magnetic oscillations, which is proportional to the current flowing in the sheets, decays only as $1/R$, whereas the number of particles contained by the sheet decays as $1/R^2$. At some radius, therefore, there cease to be enough particles to carry the required current.

This problem can be avoided, or at least postponed, if the current sheet is able to "recruit" additional charge carriers from the surrounding, magnetised plasma. However, such a process corresponds to the annihilation of the magnetic flux that originally threaded the newly recruited charge carriers. It hinges on the existence of an entropy creating dissipation mechanism, and the rate at which it can proceed depends on the details of the microphysics of this mechanism.

A convenient analytical approach to this problem is to employ the small wavelength approximation. This was first done by [41]. He adopted an implicit model of the dissipation by assuming that it proceeded just fast enough to maintain the minimum required number of charge carriers. An equivalent formulation of this assumption is the requirement that the thickness of the current sheet should be equal to the gyro-radius of the sheet particles. The full set of relativistic MHD equations, complemented by this assumption about dissipation in the sheet, was solved by [83] in the small wavelength approximation. They found that dissipation causes the supersonic flow to accelerate, thus effectively converting Poynting flux

into kinetic energy. Unfortunately, an inescapable side effect of this acceleration is the relativistic dilation of the dissipation time scale. Taking account of this, one finds that the Lorentz factor of the flow grows only slowly, according to $\Gamma \propto R^{1/2}$. Applying these results to the Crab Nebula, [83] concluded that this kind of dissipation could not convert a significant fraction of the wind luminosity into kinetic energy before the flow encountered the termination shock.

The implicit assumption about the dissipation rate in this calculation is clearly both fundamental and arbitrary. In an attempt to improve this situation, [72] compared the effects of three different prescriptions for the dissipation rate. As well as the minimum rate used by [41] and [83], they found solutions corresponding to dissipation on the timescale of the growth of the relativistic tearing mode, and to dissipation at the maximum plausible rate, governed by the transit time of sound waves across the sheet. Applying these to the Crab Nebula, they concluded that conversion of the Poynting flux to kinetic energy was indeed possible in the most favourable case, but only if the outflow carried substantially more pairs than predicted by the cascade models of [59, 60].

Although the short-wavelength approximation enables one to find analytical solutions and sketch out possible scenarios for the solution of the σ problem, it does not necessarily follow that these scenarios are realised in any given pulsar. It could be, for example, that dissipation becomes important even before the wind is accelerated to supersonic speed. The deposition of a substantial amount of energy into heat in the wind zone is likely to result in an observable signature, as discussed in Sect. 16.5. Finally, if the analytical solutions indeed describe the wind accurately, it could be that relatively little Poynting flux is converted into kinetic energy before the termination shock is reached. The observed morphology of the Crab Nebula could, nevertheless, be recovered if the conversion were to take place instead in the termination shock itself [86]. According to the results of one-dimensional particle-in-cell simulations [81, 103], this appears plausible, and may open up a way to understand the particle acceleration process operating at this shock front (see Sect. 16.6).

16.5 Observability of the Wind

16.5.1 Point-Like Appearance

Whereas the termination shock and nebula are visible in the X-ray [119] and optical [57, 58] images of the Crab Nebula, the wind zone they enclose appears to be dark, as was noticed in early optical images [108]. The standard explanation of this phenomenon is that the MHD wind is expected to be cold. In the comoving frame, a volume element in a ballistic wind would expand by a factor of 10^{18} between the light cylinder and the termination shock of the Crab, so that any random motion should quickly disappear. Cold, ordered motion of a highly conducting plasma, does not, however, produce synchrotron radiation. According to the ideal MHD condition, (16.3), the acceleration of each particle vanishes, so that all trajectories are

rectilinear. I.e., in the comoving frame, all particles are stationary. The emissivity for bremsstrahlung and for other "thermal" processes also vanishes in this case. The only possibility of producing radiation in this case is by coupling the bulk motion to the photon field. Inverse Compton scattering of photons of the cosmic microwave background or other target fields could do this, but would give rise to gamma-rays rather than X-rays or optical photons (see Sect. 16.5.2). Unfortunately, the resolution of current gamma-ray detectors does not enable such photons to be distinguished from the nebular emission.

However, even if the plasma somehow remains hot, perhaps because of internal dissipation, the emission should be strongly beamed into a cone of (half)-opening angle $1/\Gamma$ in the radial direction. One might naively expect that the image of the wind on the sky should not exceed an angular size of $1/\Gamma$. In fact, the maximum possible size of the image is much smaller, and depends on the radial dependence of the emissivity, as well as on the radial dependence of Γ. To see this, consider a simple model in which the emissivity of the wind is such that emission from all radii R is visible, provided that the radius vector $\mathbf{R}$ makes an angle of less than $1/\Gamma(R)$ with the line of sight, and provided that $R < R_{\rm T}$, where $R_{\rm T}$ is the radius of the termination shock, here assumed, for simplicity, to be spherical in shape.

The solutions found in the short-wavelength approximation (Sect. 16.4) suggest the Lorentz factor can be parameterised as

$$\Gamma(R) = \Gamma_{\rm T} \left(\frac{R}{R_{\rm T}} \right)^q , \tag{16.11}$$

where $\Gamma_{\rm T}$ is the Lorentz factor at the termination shock and q (≥ 0) describes the radial acceleration. Making the reasonable assumption that the distance D to the pulsar is large, specifically, $D \gg \Gamma_{\rm T} R_{\rm T}$, it follows that radiation is emitted in the direction of the observer provided $\sin\theta \leq 1/\Gamma(R)$, and $R \leq R_{\rm T}$. This defines a surface that limits the visible part of the wind to

$$R \leq R_{\rm T} {\rm Min} \left[1, 1/\left(\Gamma_{\rm T} \sin\theta\right)^{1/q} \right] . \tag{16.12}$$

On the plane of the sky, this surface appears to have an angular diameter $\alpha = \alpha_{\rm T} R \sin\theta / R_{\rm T}$ where $\alpha_{\rm T}$ is the angular diameter of the termination shock. Hence, the diameter of the visible part of the wind is

$$\alpha \leq \frac{\alpha_{\rm T}}{\Gamma_{\rm T}} {\rm Min} \left[\Gamma_{\rm T} \sin\theta, \left(\Gamma_{\rm T} \sin\theta\right)^{1-1/q} \right] . \tag{16.13}$$

For $q < 1$, such as is found for all the dissipation models tested by [72], the maximum angular diameter of the wind emission is reached at the termination shock:

$$\alpha_{\rm max} = \frac{\alpha_{\rm T}}{\Gamma_{\rm T}} , \tag{16.14}$$

whereas, for more rapidly accelerating flows ($q > 1$), the maximum diameter is determined at the launching point.

Optical observations reveal a point-like source, of angular size less than 0.1 arcsec at the position of the pulsar, whereas the termination shock has an angular diameter of approximately 12 arcsec. If there is substantial dissipation within the wind, then these observations establish a minimum Lorentz factor that is required in order that the wind should still appear point-like. For $q < 1$, this is simply

$$\begin{aligned} \Gamma_{\rm T} &> \frac{\alpha_{\rm T}}{\alpha_{\rm max}} \\ &\gtrsim 100\,. \end{aligned} \tag{16.15}$$

This is a modest requirement when compared to most estimates, which lie in the range from $\Gamma \sim 10^5$ to 10^6. In the case of more rapid acceleration $q > 1$, the constraint is even less stringent. For a launching point R_0 it reads $\Gamma \gtrsim 24 R_0/R_{\rm T} \ll 100$. Thus, one concludes that the appearance of the optical and X-ray nebula, with its central point-like source and dark region within the termination shock, does not rule out the possibility that a substantial fraction of the pulsar luminosity is dissipated and radiated away in the wind zone, provided only that the flow speed remains high. This same argument applies also to those parts of the nebula that remain in relativistic, approximately radial motion. Such regions are indeed found in two-dimensional MHD models (see Sect. 16.7) and are expected to produce almost point-like images close to the pulsar.

16.5.2 Inverse Compton Scattering

As mentioned above, the wind, though cold, could in principle be detected through the emission produced by inverse Compton (IC) scattering of an external, soft photon field [15, 29]. There are several possible external origins of the target photon population: the cosmic microwave background radiation, the synchrotron radiation of the nebula (dominant for the Crab from radio wavelengths to X-rays), the thermal far-infrared radiation (probably associated with dust), from the surroundings of the nebula [12] and, in the case of a pulsar in a binary system, photons from the companion star [14]. For a wind of constant Lorentz factor, the emission is very strongly peaked in frequency space. Even for an accelerating wind, an almost monochromatic line should appear in the gamma-ray range. The integrated (over frequency) luminosity of the scattered photons is well below the sensitivity of current gamma-ray telescopes – only if the peculiarities of the predicted spectral distribution could be exploited might it be possible to extract a signal.

Another possibility is an internal source of target photons, i.e., photons from the pulsar itself. These photons suffer the obvious disadvantage that they propagate radially outwards together with the wind. Scattering events are, therefore, likely to be almost forward in direction, which implies relatively small energy gain. However, if, by some mechanism, the wind becomes kinetic energy dominated quite close to the light cylinder, the angular momentum it must carry ensures that its velocity vec-

tor makes a substantial angle with the radius vector. Photons from the stellar surface could then be significantly boosted in energy. Bogovalov and Aharonian [29] investigated this possibility for the Crab, taking into account as target photons not only the thermal X-rays from the surface of this young pulsar, but also the non-thermal, pulsed emission (assuming it too comes from close to the stellar surface). Because the predicted high-energy flux depends sensitively on the location of the transition from a magnetically to a kinetically dominated wind, the observed gamma-ray flux (which probably originates from the nebula) puts a lower limit on this conversion radius $R_{\rm w}$. Assuming thermal X-rays as targets, they found $R_{\rm w} \geq 5\, r_{\rm L}$ whereas including also the pulsed component tightens this limit to $R_{\rm w} \geq 30\, r_{\rm L}$. Unfortunately, however, the constraint is not only quite weak in the sense that it does not extend far into the wind zone, but it is also sensitive to the angular dependence of the pulsar wind: if the conversion from Poynting flux to kinetic energy affects only the striped wind in the equatorial belt, the gamma-rays would be visible only to observers located in this belt, thus invalidating the constraint.

On the other hand, a lower limit on the Lorentz factor of wind follows from the fact that induced Compton scattering by the electrons in the wind does not appear to influence the radio pulses significantly. Wilson and Rees [120] investigated this effect in detail and estimated that, for the Crab pulsar wind, $\Gamma > 10^4$ at a radius of roughly $100\, r_{\rm L}$.

16.5.3 Pulses from the Wind

In the striped wind scenario, dissipation of magnetic energy occurs primarily in the current sheets. If this gives rise to a significant synchrotron emissivity, the resulting radiation will, as discussed above, appear to be point-like. Furthermore, provided that $R/r_{\rm L} \lesssim \Gamma^2$, where R is the radius of the radiation source, it will be pulsed at the neutron star rotation period. This was noticed quite early in the development of pulsar theory [7, 91] and has been revived recently [73]. Thus, the striped wind is a possible site of production of the incoherent, high energy (optical to gamma-ray) non-thermal radiation observed from numerous pulsars. A priori, there is no compelling reason to favour this site over the inner or outer gaps in the magnetosphere. However, in contrast to these theories, the wind model has the advantage that an analytical description of the magnetic field structure is available. This removes from its predictions much of the arbitrariness present in those of the magnetospheric models.

Both the point-like appearance and the pulsations of the radiation from the wind are a consequence of relativistic beaming. Assume for simplicity that the striped wind consists of thin, concentric, spherical, radiating shells. In the equatorial plane, successive shells, n and $n+1$, are separated by half a wavelength of the stripes, $\Delta l = \pi\, r_{\rm L}$, (see Fig. 16.2). Furthermore, assume that these shells radiate only after they cross a spherical surface of radius R_0. The maximum time delay between the

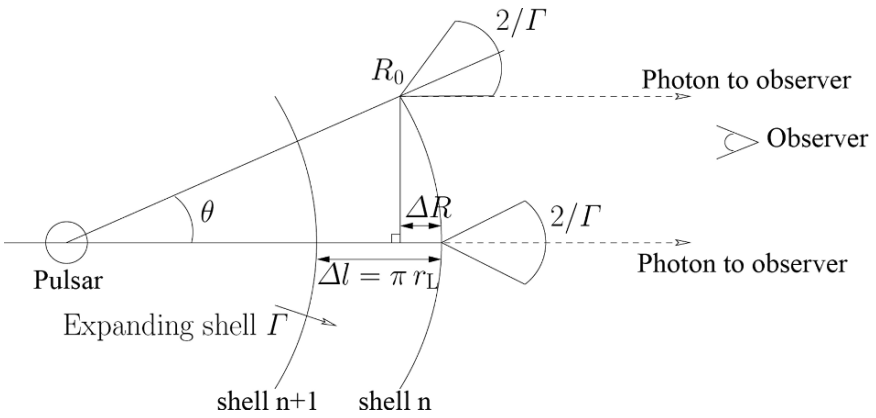

Fig. 16.2 Spherically symmetric shells expanding with relativistic Lorentz factor Γ and emitting within a cone of opening angle $2/\Gamma$ when crossing the surface R_0

arrival times at a distant observer of photons emitted on shell n is $\Delta t = \Delta R/c = (1-\cos\theta)R_0/c$. For relativistic flows, $\theta \approx 1/\Gamma \ll 1$. Therefore,

$$\Delta t \approx \frac{R_0}{2\Gamma^2 c}\,. \tag{16.16}$$

In order to observe pulses, this time delay should be less than the time delay between emission of two consecutive shells, n and $n+1$, crossing R_0, given by $\Delta T = \Delta l/c = \pi r_{\rm L}/c$. As a consequence, pulses are observed if

$$R_0 \lesssim 2\pi\Gamma^2 r_{\rm L} \tag{16.17}$$

(cf. (47) and [7]). Using the oblique split monopole solutions, [73] computed the pulse profiles expected from the striped wind. In general, two pulses per period are predicted, as observed in all gamma-ray pulsars. The spacing of these pulses is uniquely determined by the angles between the rotation axis and the magnetic axis (α) and the rotation axis and the line of sight (ζ). In the case of the Crab, the pulses are spaced by 0.4 of a period, consistent with $\alpha = 60^\circ$ and $\zeta = 60^\circ$, as independently suggested by the morphology of the X-ray torus [96]. The width of the main pulse and interpulse observed in the Crab is much larger than would be expected of a thin current sheet in a wind of Lorentz factor of 10^5 or more. Furthermore, there is a significant unpulsed component of emission. These properties suggest that at least some of the radiating electrons diffuse out of the sheet.

As well as pulse profiles, the polarisation of the optical pulses from the Crab pulsar has motivated detailed comparative studies of the emission predicted by different magnetospheric models [46, 66]. The analogous computations for the wind model have been performed by [102]. Extending the oblique, split-monopole solutions, these authors model the radial dependence of a current sheet of finite thickness, including an electron density that peaks in the centre of the sheet, and falls to a

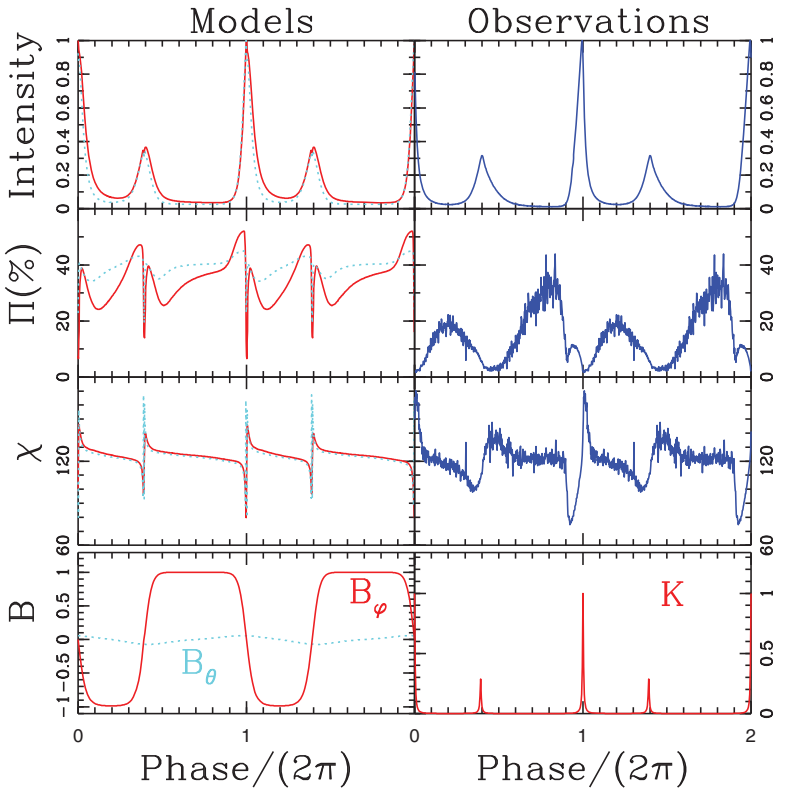

Fig. 16.3 Light curve of intensity, degree of polarisation and position angle of the pulsed synchrotron emission obtained for the striped wind model and measurements of these quantities for the Crab pulsar. Models with Lorentz factor $\Gamma = 20$ (*solid red*) and 50 (*dotted cyan*) are shown. The *bottom panels* show the dependence on phase of the assumed magnetic field components B_θ and B_φ and the particle density K in the comoving frame (figure from [102])

small, but finite value in between them, such that overall pressure balance is maintained with the varying magnetic field. An arbitrary, but small, poloidal component of the magnetic field is also added, in order to prevent the magnetic field vanishing on the neutral surface.

These extensions result in the radial dependences of magnetic field components and electron density plotted in the lower two panels of Fig. 16.3. The thickness and relative number of electrons in each sheet is chosen to fit the observed pulse profiles, shown in the top two panels (model on the left, observations [65] on the right). The B_θ component is chosen to fit the sweep of the linear polarisation as it enters and leaves the pulse and interpulse (see the angle of polarisation χ in Fig. 16.3). The fact that B_θ oscillates with the same period as B_φ implies that the pulsar wind itself has a small degree of circular polarisation, whose sense is determined by the sense of rotation of the neutron star, and is, therefore, the same in both the pulse and interpulse.

The detailed fits to all three observed components (intensity, degree of polarisation Π and angle of polarisation χ) are quite good. On the other hand, as in the magnetospheric models, a degree of arbitrariness has been introduced in order to achieve this. However, one important prediction of the wind model is independent of these uncertainties. The direction on the sky of the polarisation vector associated with the d.c. component of emission between the pulses should be determined by B_φ alone, i.e., it should lie along the projection onto the sky of the rotation axis of the neutron star. This prediction is testable, because the morphology of the X-ray image of the nebula enables a symmetry axis to be identified [96]. In Fig. 16.3 this measurement was used to orient the model predictions of the angle χ. Thus, the agreement of the predicted off-pulse values of χ with the measured off-pulse polarisation direction is a strong argument in support of the wind model.

16.6 The Termination Shock

Pulsar wind nebulae (PWNe) are observed from the radio to TeV gamma-rays [48]. The spatially integrated spectrum contains information on the distribution in energy of the radiating particles that are presumably injected at the termination shock. The best observed example, the Crab Nebula, is shown in Fig. 16.4. Most of the radiation (from the radio up to 100 MeV) is synchrotron emission, and only the peak

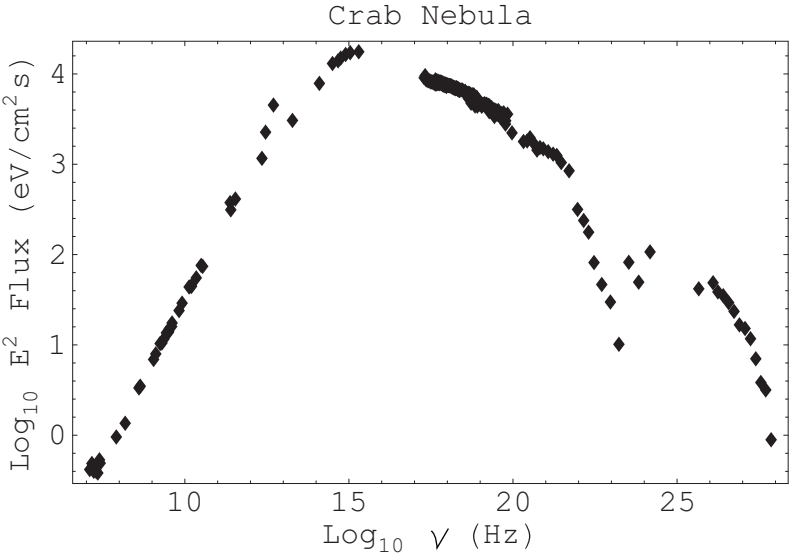

Fig. 16.4 The integrated spectrum of the Crab Nebula. Radio data are taken from [13], infrared from [53], optical from [117], and X-ray through gamma-ray data (EGRET, COMPTEL and BeppoSAX) from [78]. The TeV data points ($>10^{25}$ Hz) are from H.E.S.S. observations [3]

in the very-high energy gamma-ray band is attributed to the inverse Compton scattering of synchrotron photons on high-energy electrons. The synchrotron part may be described as power laws with spectral breaks around 10^{13}, 10^{15} Hz and 100 keV. This extremely broad frequency range implies that the spectrum of relativistic electrons and positrons in the nebula extends from $\lesssim$100 MeV to $\sim$1 PeV. The energy density (and pressure) of this relativistic plasma is dominated by leptons with an energy of around 100 GeV.

The spectra of other PWNe are generally similar to that of the Crab. In the radio band, they are hard: $\mathcal{F}_\nu \propto \nu^{-\alpha}$, with α between 0 and 0.3. At high frequencies the spectrum softens, and in the X-ray band $\alpha > 1$.

Kennel and Coroniti [68] postulated that the wind from the Crab pulsar has a Lorentz factor $\Gamma_\mathrm{T} \approx 3 \times 10^6$ at the termination shock, where a power-law particle spectrum is created at energies exceeding $E \sim m_\mathrm{e}c^2\Gamma_\mathrm{T} \sim 1$ TeV. These electrons and positrons emit from the UV to the gamma-ray bands. Optically emitting electrons appear in the nebula as a result of the synchrotron cooling of the TeV electrons. The formation of the power-law spectrum at $E > m_\mathrm{e}c^2\Gamma_\mathrm{T}$ was considered by [63] and [4]. They suggested that the pulsar wind is loaded by ions. Ion cyclotron waves are then collectively emitted at the shock front, and positrons and electrons are accelerated by resonant absorption of these waves. Their simulations of a relativistic shock in an electron–positron–ion plasma show that a power-law spectrum of positrons and electrons is formed. This model not only accounts for the optical to X-ray spectrum of the Crab but offers an explanation of the variable synchrotron emission of the wisps observed in the vicinity of the termination shock [57, 108]. Gallant and Arons [49] and Spitkovsky and Arons [111] argue that the wisps arise in regions where reflection of the ions in the self-consistent magnetic field causes compressions of the electron–positron plasma and, thus, enhanced emission. The characteristic variability time-scale of the wisps (a few months) is determined in this model by the Larmor period of ions with Lorentz factors of a few$\times 10^6$.

The main problem with this model is that it does not account for the radio to IR emission of the nebula, which is generated by electrons and positrons with energies between 100 MeV and 100 GeV. The large number of these electrons and positrons requires a pair injection rate of $\dot{N} = 10^{40}$ to $10^{41}\,\mathrm{s}^{-1}$ [105], implying $\kappa \sim 10^6$ (see 16.2). The spin-down power of the pulsar L_sd, when divided by this pair output, yields a Lorenz-factor of the wind $\Gamma_\mathrm{T} = 6 \times 10^4 (10^{40}/\dot{N})$, incompatible with the value of a few$\times 10^6$ required by the ion model. Kennel and Coroniti, [68] and [11] avoided this problem by assuming that the low energy electrons were injected at a very early stage of the history of the nebula. The synchrotron lifetime of the radio emitting electrons is significantly longer than the age of the nebula, so that one cannot exclude *a priori* that the overall spectrum depends on history of the nebula. Nevertheless, a convincing explanation of this rather convenient event in the past is lacking. Another possibility, proposed by [8], is that the radio and X-ray emitting particles are injected by different sectors of the termination shock, X-ray particles being accelerated in the equatorial belt and the radio ones in the polar region. However, the apparent continuity of the overall spectrum of the nebula from the radio to the gamma-ray band favours for a single population of emitting electrons. Moreover,

recent observations of the wisps in the radio band [24, 25] suggest that the radio emitting electrons are currently accelerated in the same region as those responsible for the optical to X-ray emission.

The spectral slope of the Crab is $\alpha = 0.3$ in the radio band [13] and $\alpha = 0.72$ in the optical [117], which is compatible with the assumption that the break at about 10^{13} Hz is due to the synchrotron burn-off effect in a magnetic field of 300 μG, which is close to the equipartition value [87]. The implied energy spectrum of the injected electrons and positrons has the form $N(E) \propto E^{-1.6}$. This view is supported by [50,51] who found that the infra-red spectral index in the central parts of the Crab is close to that in the radio, and gradually steepens as one moves outwards. The high frequency break lies in the ultra-violet band at about a few $\times 10^{15}$ Hz, which implies that at $E > E_{\rm br} \sim 1$ TeV the injection spectrum becomes steeper[3]; the spectral slope in the X-ray band, $\alpha = 1.1$, corresponds, when the synchrotron burn-off effect is taken into account, to an injection spectrum of $N(E) \propto E^{-2.2}$ at $E > E_{\rm br}$, so that the injection spectrum is a broken power-law. Taking into account that no sign of a low frequency cut-off is observed in the Crab spectrum down to about 30 MHz (at lower frequencies the spectrum is dominated by the pulsar), one concludes that the injection spectrum of electrons and positrons extends down to $E_{\rm min} \leq 100$ MeV.

Such an injection spectrum implies a rather unusual acceleration process. The energy density of the injected plasma, $\int E N(E) {\rm d}E$, is dominated by particles with $E \sim E_{\rm br}$ whereas most of the particles find themselves at $E \sim E_{\rm min} \ll E_{\rm br}$ so that the acceleration process should somehow transfer most of the total energy of the system to a handful of particles leaving for the majority only a small fraction of the energy. This is not what one would normally expect from a shock-associated acceleration process, where the particle flow is randomised at the shock and only a fraction of the upstream kinetic energy is converted into the energy of a few accelerated particles. In this case, the temperature T downstream roughly corresponds to the upstream particle kinetic energy and the high-energy tail of accelerated particles merges, at its low energy end, with the quasi-thermal distribution at $E \sim$ few $\times k_{\rm B}T$. For the Crab, this means that the Lorentz factor of the wind at the termination shock, $\Gamma_{\rm T}$, should not exceed a few hundred in order to deliver the majority of the electrons and positrons into the downstream region with $E_{\rm min} \sim 100$ MeV. On the other hand, the particle energy spectrum implies that the energy per electron in the system is much larger, about 10 GeV, so there would appear to exist an energy reservoir in the flow that eventually dissipates in a small fraction of the particles.

Gallant et al. [52], modifying the original idea of [63], suggested that the wind is loaded by so many ions that their kinetic energy dominates the wind energy flux. At the shock front, the pairs are thermalized with $k_{\rm B}T \sim m_{\rm e}c^2\Gamma_{\rm T} \leq 100$ MeV whereas the ions collectively emit about one half of their energy as cyclotron waves. The radio emitting electrons and positrons are accelerated by these waves according to the mechanism by [63] and [4]. The problem with this theory, is that the

[3] Del Zanna et al. [44] argue that the UV break is due to the synchrotron cooling, which assumes that the magnetic field in the nebula remains a few times less than the equipartition level. In this case, the 10^{13} Hz break should be attributed to the break in the injection spectrum so that $E_{\rm br} \sim 100$ GeV.

required injection rate of ions, $\sim L_{\rm sd}/(m_{\rm p}c^2\Gamma_{\rm T}) \sim 10^{39}\,{\rm s}^{-1}$, vastly exceeds the fiducial Goldreich–Julian elementary charge loss rate, $\dot{N}_{\rm GJ} \sim 10^{34}\,{\rm s}^{-1}$, obtained by substituting $\kappa = 1$ into (16.2). It is difficult to imagine how the electric field at the surface of the star could extract ions with a density orders of magnitude higher than that required to screen out this same field. On the other hand, one cannot exclude by observation that pulsars emit the required number of ions. Their presence in the plasma injected into the nebula could, in principle, be revealed by observations of ultra high energy gamma-rays and/or neutrinos [5, 16, 17]; the data currently available on the Crab Nebula are, however, compatible with the assumption that all the observed emission is generated by electrons and positrons and no relativistic ions are present [3]. However, it has recently been proposed that the high energy emission of the PWN Vela X can be understood if a significant fraction of the pulsar spin-down power is carried by relativistic nuclei [62].

Another possible energy reservoir for particle acceleration is present if most of the pulsar spin-down energy is still stored in the striped magnetic field when the flow enters the termination shock [86,103]. As discussed in Sect. 16.4, this would be expected if the microphysics of the dissipation process proceeds relatively slowly. The flow then accelerates only slowly, and the Lorentz factor at the termination shock is compatible with a low $E_{\rm min}$ in the energy distribution of the accelerated particles. When the flow enters the shock, the alternating magnetic fields annihilate transferring the energy to the particles and one can speculate that the radio-to-optical emission of PWNe is generated by electrons and positrons accelerated in the course of reconnection of the alternating magnetic field at the pulsar wind termination shock. One-dimensional PIC simulations indeed show that the alternating fields easily annihilate at the shock [81, 103], but do not show evidence of a non-thermal distribution. This may be attributed to a highly idealised one-dimensional field structure in the simulations. In the real case, reconnection is expected to occur at X-points, and particles gain energy according to how close they approach such a point. Higher dimensional studies of the reconnection process in a relativistic electron–positron plasma without a striped field [79,107,121–123] demonstrate efficient acceleration of non-thermal particles. However, even though the obtained spectra can be roughly described by a power-law with an exponential cutoff, there is as yet no evidence of a hard power-law spectrum over the wide energy range observed in PWNe.

The formation of the high-energy tail in the spectrum at $E > E_{\rm br}$, on the other hand, can be attributed to the first-order Fermi acceleration mechanism. In the absence of strong cross-field diffusion, this mechanism does not operate at a perpendicular shock (where the magnetic field is perpendicular to the shock normal), because particles are prevented from diffusing back upstream by the fact that their guiding centres must follow the field lines, which run parallel to the shock front. Because the perpendicular field component is compressed in the proper frame by a large factor, relativistic shocks almost always fall into this category [20]. However, in reality, some degree of cross field transport must occur, and the question of whether or not the first-order mechanism operates at a relativistic shock hinges on the relative magnitudes of the ordered magnetic field and the stochastic component

that produces the cross-field transport. Simulations of acceleration in prescribed stochastic fields indeed show that acceleration is less effective for stronger ordered fields [97], and corroborating evidence is beginning to accumulate from 3D, relativistic, particle-in-cell simulations [109]. On the other hand, in the pulsar case, annihilation of the ordered magnetic field in the wind (or in the shock) may leave a highly turbulent, small-scale magnetic field, whose chaotic component significantly exceeds the regular field [106]. Particle scattering off these strong inhomogeneities may then allow the first-order Fermi mechanism to operate. It is interesting that the first-order Fermi mechanism operating at an ultra-relativistic shock yields, in the case of isotropic diffusion of the accelerated particles, an energy distribution $E^{-2.2}$ [1, 18, 71] – exactly the value required to explain the X-ray spectrum of the Crab.

16.7 The Nebula

The physical conditions in pulsar winds, though difficult to determine directly, can be inferred from the observed properties of PWNe, which are simply the bubbles inflated by the wind in the surrounding medium. It is the wind plasma that fills the nebula and produces the observed non-thermal electromagnetic emission. The typical size of the PWN is a few parsecs. Specifically, the Crab Nebula is an ellipsoid of projected dimension $2\,\mathrm{pc} \times 3\,\mathrm{pc}$.

The nebula is confined by its nonrelativistic surroundings, and the termination shock of the pulsar wind is located at a radius defined by the condition that the confining pressure balances the momentum flux of the wind. In the case of the Crab Nebula, the shock radius was estimated by [105] to be 0.1 pc, in excellent agreement with the radius of the apparent central hole in the nebula brightness distribution [108]. At the shock front, the wind energy is released into the relativistic particles responsible for the observed radiation. Rapidly moving wisps and variable knots were found in this region [57, 58, 108], confirming it as the site of energy injection into the nebula.

Early spherically symmetrical MHD models of the Crab Nebula [47, 67, 68, 105] seem to describe its main properties perfectly well. The observed brightness and the spectral index distributions are generally consistent with the assumption that the relativistic particles are injected by the pulsar in the centre of the nebula and then expend their energy on synchrotron emission and $p\mathrm{d}V$ work [6, 68]. The size of the nebula decreases with observed frequency because the higher the energy of a particle, the faster it loses energy by synchrotron emission. The synchrotron life-time of the radio emitting electrons is larger than the age of the nebula. Therefore, they fill the whole nebula. The life-time of the optically emitting electrons is comparable or somewhat shorter than the age of the nebula and, therefore, the optical image is smaller than the radio one. The X-ray emitting electrons lose their energy in only a few years. Therefore, X-rays are emitted only close to the pulsar. This makes the X-rays an exceptional tool for the study of the interaction of the pulsar wind with

the nebula. Whereas the radio and optical images are dominated by the outer parts of the nebula and distorted by interaction with the surroundings, the X-rays trace the freshly injected plasma and reveal the physical processes in the very heart of the nebula.

The basic conclusion of these early models was that the pulsar wind must be particle dominated. The magnetic field in the lab. frame increases by a factor of roughly three across a relativistic shock front. In the subsonic postshock flow, the plasma density remains approximately constant, so that conservation of the magnetic flux within a radially expanding magnetic loop implies linear growth of the field strength with radius. In order for the magnetic pressure at the outer boundary of the nebula not to exceed the plasma pressure, the magnetisation of the wind just upstream of the termination shock should be at most $\sigma \sim 3 \times 10^{-3}$ [47, 67]. Such a low value of σ is puzzling, because the pulsar wind is launched as a Poynting dominated flow with $\sigma \gg 1$, and, as discussed in Sects. 16.3 and 16.4, it is not easy to invent a realistic mechanism to reduce σ to the required level.

On the other hand, σ cannot be significantly lower than the above value, because magnetic stresses play an important role in shaping the nebula: the observed elongation is convincingly explained as the result of pinching by an azimuthal magnetic field [21, 115]. The discovery of the jet-torus structure confirmed that the nebula is elongated along the pulsar spin axis so that the magnetic field in the nebula should indeed be wrapped around the major axis of the ellipsoid.

The jet-torus structure was revealed already in earlier X-ray observations [9, 32, 58] and was clearly resolved by Chandra [57, 95, 119]. Similar structures have been found in other PWNe (for a review see [48], suggesting that this is a generic phenomenon. The inner boundary of the X-ray torus of the Crab coincides with the position of the standing shock predicted by early spherically symmetric models, but the morphology of the inner nebula forces one to abandon the assumption of spherical symmetry. The observed structure suggests that the pulsar wind itself is highly anisotropic, with most of the energy being transported in the equatorial belt. Encouragingly, simple (split-monopole) models of the pulsar wind indeed have the property that the energy flux reaches a maximum at the equator (see Sect. 16.4). However, the origin of the polar jet is not so evident.

The jet in the Crab Nebula, as well as the jets in other PWNe, appears to originate from the pulsar and propagate along the rotation axis. This seems to indicate that they are a part of the pulsar wind, possibly collimated by magnetic hoop stresses. However, as discussed in Sect. 16.3, this mechanism does not work in ultra-relativistic flows. Moreover, such a jet would presumably be ultra-relativistic, whereas the observed jets certainly are not, as follows both from direct measurements of the proper motion in the jets of the Crab and Vela [57, 99], and from the fact that both the jet and counter-jet are visible. Lyubarsky [84] pointed out that magnetic collimation, though ineffective in the pulsar wind, could be responsible for the formation of the jets *beyond* the termination shock. In the equatorial belt, which carries most of the energy, annihilation of the striped field (see Sect. 16.4) ensures that the residual magnetic field is low and does not affect the dynamics of the post-shock plasma. However, the magnetisation of the high latitude flow remains significant.

This naturally results in the separation of the post-shock flow into an equatorial disk and a magnetically collimated polar outflow. In this model, the observed jet arises as a result of the axial compression of the shocked plasma.

In the split monopole model of the pulsar wind, the angular distribution of the total energy flux $f_{\rm tot}$ can be written as

$$f_{\rm tot} = \frac{f_0}{R^2}(\sin^2\theta + 1/\sigma_0) \tag{16.18}$$

[27,92], where R and θ are the usual spherical coordinates, f_0 and $\sigma_0 \gg 1$ constants. The first term in parentheses represents the Poynting flux, whereas the second one accounts for the small initial contribution of particles. As discussed above, a significant part of the Poynting flux is transferred by variable fields, and can be converted into plasma energy relatively easily. But the total energy per particle is conserved along the streamlines and, as they are radial, the angular distribution (16.18) remains unchanged. Lyubarsky [84] showed that in such a strongly anisotropic wind, the termination shock is highly aspherical, forming a cusp on the axis of the flow. Therefore, the jet could appear to originate from the pulsar simply because the termination shock lies much closer to the pulsar in the polar regions than in the equatorial belt. By neglecting magnetic stresses in the vicinity of the shock, [31] independently found that the subsonic region lies much closer to the pulsar in the polar region than in the equatorial plane. However, the formation of a jet on the axis depends on the additional effect of magnetic collimation [69].

To test this qualitative picture [75,76] performed axisymmetric relativistic MHD simulations of a flow produced by an anisotropic pulsar wind within a slowly expanding cavity of cold heavy gas. They adopted (16.18) for the angular distribution of the total energy in the wind and assumed that all waves decayed either in the wind or at the termination shock so that the postshock flow is completely determined by the total energy flux, $f_{\rm tot}$ and the mean field, B, in the wind. As the postshock MHD parameters are independent of where exactly the waves decay, one can assume for simplicity that all the wave energy has already been converted into the flow kinetic energy on entering the shock, $\rho\Gamma v = f_{\rm tot} - cB^2/4\pi$. For an ultra-relativistic flow, $\Gamma \gg 1$, the post-shock plasma is relativistically hot and the dynamics of the downstream flow depends only on the total energy flux and magnetisation, i.e., it does not depend on ρ and Γ separately, but only on their product. Therefore, the flow is determined by the two functions, $f_{\rm tot}(\theta)$ and $B(\theta)$.

The distribution of the mean field in the pulsar wind is not known but certainly goes to zero on the equator of a flow driven by an obliquely rotating, centred dipole. Moreover the mean field vanishes on the axis of the flow, because an unphysical singular current would otherwise be required. Taking into account that the field is frozen into a radial flow and, therefore, the radial dependence is given by (16.10), [75,76] chose a simple model for the mean field:

$$B = \sqrt{\frac{4\pi f_0}{c}}\,\frac{\xi}{R}\,\sin\theta\left(1 - \frac{2\theta}{\pi}\right), \tag{16.19}$$

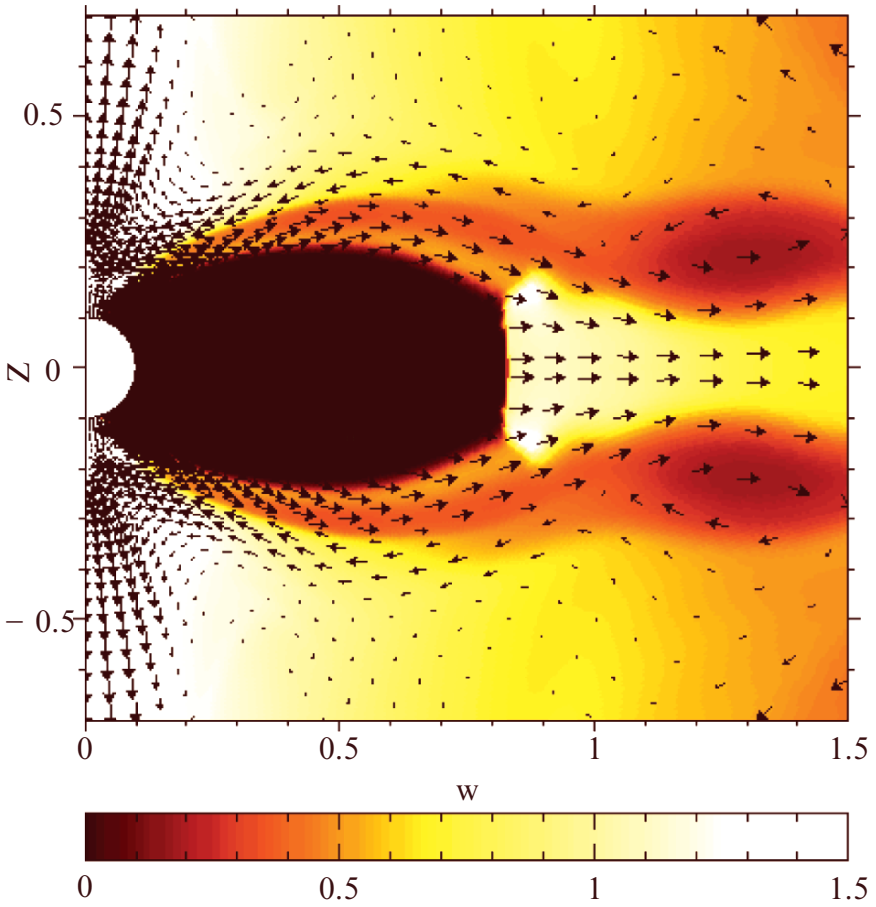

Fig. 16.5 The flow around the termination shock [75]. The flow velocity is shown by *arrows*, the plasma energy density by *colour*

where the free parameter $\xi \leq 1$ controls the magnetisation of the wind. The ratio of the energy transported by the mean electromagnetic field to the energy transported by the particles is $\sigma = 0.1\xi^2$.

The results of these simulations are shown in Fig. 16.5. The termination shock is highly aspherical being significantly closer to the pulsar in the polar zone than in the equatorial plane. Most of the downstream flow is initially confined to the equatorial plane. The magnetic hoop stresses stop the outflow in the surface layers of this equatorial disk and redirect it into magnetically confined polar jets, which, therefore, are formed outside of the termination shock. Velocities both in the disk and in the jet were found to be about $0.5c$, close to those inferred from observation [45,57,99].

Images of the nebula in synchrotron emission were also simulated, taking into account the relativistic beaming effect and particle energy losses (Fig. 16.6). These

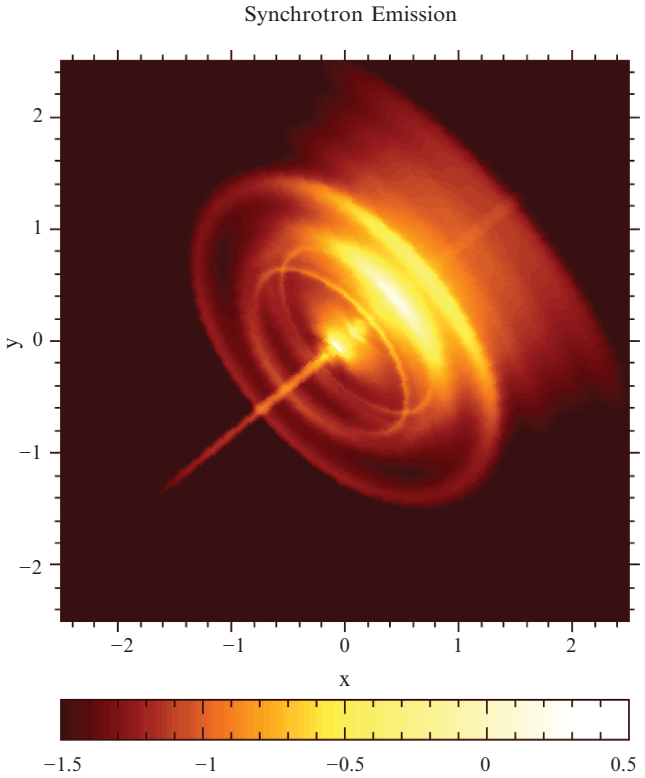

Fig. 16.6 The simulated image of the synchrotron emission of the Crab Nebula [75]

images resemble those of the Crab and other PWNe obtained by Chandra. They exhibit both a system of rings, giving the impression of an equatorial disk-like or even toroidal structure, and well-collimated polar jets, which give the illusion of originating directly from the pulsar.

The simulated images also reveal a bright central source. At high latitudes, plasma enters the shock highly obliquely, and, therefore, the post-shock velocity remains high, $\sim 0.9c$ and is not deflected far from its upstream radial direction. As discussed in Sect. 16.5.1, this results in an almost point-like feature close to the pulsar. However, it is not connected with emission from the Crab pulsar itself, but may be identified with the bright knot discovered by [58] and located 0.65 arcsec to the southeast.

[43] investigated the sensitivity of the morphology of the nebula to the angular dependence of the wind magnetisation. They simulated the evolution of the pulsar wind nebula within the expanding supernova ejecta adopting (16.18) for the total energy flux, but parameterising the angular dependence of the mean magnetic field as $B \propto \sin\theta \tanh[b(\pi/2-\theta)]$ (cf. (16.19)). The effect on the flow of the width of the low magnetisation region in the equatorial belt (associated with the striped wind)

was investigated by varying b. They found that collimation occurs at any b but that the overall picture of the flow changes completely if there is no belt of low magnetisation, i.e., when $b \to \infty$.

In this case, the magnetic hoop stresses in the equatorial plane completely suppress the radial flow after a few termination shock radii, diverting the plasma towards the axis. A part of the flow then enters a polar outflow whereas another part is directed towards the pulsar forming a large-scale vortex. The polar outflow is quite wide (the radius is comparable with the equatorial radius of the termination shock) and is formed rather far from the pulsar. The outflow starts at a distance larger than the equatorial radius of the termination shock, whereas, below the base of the outflow, the plasma moves towards the pulsar. A wide outflow starting far from the pulsar was also found by [30] who simulated the nebula formed by a pulsar wind with $B \propto \sin\theta$. This picture does not match the observed structure of the nebula, where the jet is very narrow and appears to start close to the pulsar.

The clearly observed polar-equator dichotomy arises only if the magnetisation is low in the equatorial belt of the pulsar wind; according to [43], $b = 10$ is enough. Only in this case is the equatorial outflow not significantly affected by the magnetic stresses, and is able to extend deep into the nebula, whilst the high latitude wind is collimated into a narrow polar jet. In this sense, the jet-torus structure provides evidence in favour of magnetic dissipation in the striped wind. One can speculate that the smaller the angle between the magnetic and rotation axes of the pulsar, the narrower the striped zone and, therefore, the larger is the fraction of the flow that is collimated into a polar jet.

The MHD model thus captures many properties of the Crab Nebula quite well and, in spite of some quantitative differences with the observational data, is probably basically correct. By incorporating more physics into the model, one can hope to achieve even better agreement with the observations and infer the parameters of the pulsar wind in different systems. Thus, [36] computed polarisation maps of the nebula, and [44] investigated the effects of synchrotron cooling on the images and spectral properties of PWNe. Bucciantini and Del Zanna [35] addressed the development of the Kelvin-Helmholtz instability in the disk outflow and the resulting small-scale modulation of the synchrotron radiation. Global variations of the flow are also clearly visible in simulations; [30] has reported quasiperiodic oscillations on timescales from years to dozens of years, but the origin of these variations is still unclear.

The interaction of a PWN with the surrounding gas is another phenomenon that can be studied using relativistic MHD simulations, and the results are a valuable tool in the interpretation of the wide variety shown by X-ray images. Thus, the evolution of the nebula within the expanding supernova ejecta, including interaction with the reverse shock, was simulated by [116] in a spherically symmetric model, and [33] studied the Rayleigh-Taylor instability at the interface between an expanding PWN and its surrounding supernova remnant. Bucciantini et al. [34] presented axisymmetric simulations of pulsar wind bow-shock nebulae arising around pulsars, that have already emerged from the progenitor supernova remnant.

These detailed results are strongly dependent on the angular structure of the pulsar wind. Recent progress in simulating the obliquely rotating dipole magnetosphere and wind [110], suggests that a more realistic model of the angular dependence of the pulsar wind might soon be available to replace parameterisations such as (16.18) and (16.19). Then one might even hope to constrain the angle between the rotation and magnetic axes of the pulsar from the observed structure of the inner nebula.

All PWNe models discussed so far are either spherically or axially symmetric. However, in MHD flows with non-negligible magnetic stresses, 3D effects could come into play because the underlying symmetric configurations could be unstable. Inadequacy of the axisymmetric picture may be suggested by the fact that all models of the Crab Nebula require a very low overall magnetisation $\sigma \approx 0.01$ – if the magnetisation were larger the nebula would be distorted by the pinch effect beyond observational limits. However, the ideas on magnetic dissipation discussed in Sect. 16.4 are capable of removing only the oscillating part of the magnetic field in the equatorial belt. This apparent problem can be alleviated if, as suggested by [19], the kink instability destroys the concentric field structure in the nebula. In the axisymmetric case, magnetic loops in the expanding flow are forced to expand and perform work against the magnetic tension. The kink instability allows the loops to come apart and one can expect that in 3D, the hoop stress would be less effective than suggested by axisymmetric simulations. These stresses cannot disappear altogether, because they are responsible for driving the kink instability itself. Nevertheless, this effect could have important implications for the inferred magnetisation of the pulsar wind.

16.8 Summary

The suggestions of [104] that the relativistic particles and magnetic fields in PWNe originate in a central stellar object, as well as that of [98] that the ultimate energy source lies in the rotational energy of the neutron star, have both stood the test of time and the scrutiny of increasingly high resolution observations at all accessible wavelengths. We also now know that the pulsar wind has differing equatorial and polar components, as suggested by [9]. The Crab Nebula, in particular, can be quite well described by an axisymmetric, relativistic MHD model. This establishes without much doubt that the energy is injected into the nebula at the wind termination shock, with most of it being concentrated into an equatorial belt in a particle dominated form, and that the jets consist of shocked plasma collimated by azimuthal fields, rather than a polar wind.

Consensus is more difficult to achieve in the case of the wind. That it is highly relativistic on entering the termination shock, with bulk Lorentz factor $\Gamma_{\rm T} > 100$, seems secure. This lower limit, which applies only if the flow remains magnetically dominated up to the shock front, is still controversial; other models generally place $\Gamma_{\rm T}$ between 10^4 and 10^6. That the equatorial flow is born as a "striped wind" [41,91] seems likely. That it is almost perfectly radial and accelerates at least to the fast magnetosonic point is also not controversial.

Perhaps the most puzzling open question is the matter content of the wind. Detailed models of pair creation in the magnetosphere produce far too few leptons to explain all of the nebular emission. The ion content is also puzzling: observations of the wisps or, alternatively, of the integrated spectrum, could be nicely explained if ions contributed to the energy flux, but they are even harder to extract from the pulsar.

The much discussed σ-problem also remains an open question, especially for the Crab Nebula. Although two solutions work for the equatorial part of the wind (dissipation of the stripes either in the wind or at the termination shock), neither of these works in the polar wind region. The only possibilities here seem to be either that the equatorial belt is initially very broad (i.e., a highly oblique rotator) or that kink instabilities in the outer nebula ultimately release the magnetic tension.

The particles responsible for the non-thermal emission are almost certainly accelerated at the termination shock front. However, which mechanisms are responsible is controversial. It seems that at least two different ones must be operating, one at low energies, (100 MeV to 1 TeV) which may be either resonant absorption of coherently emitted ion cyclotron waves, or the annihilation of magnetic flux in the shock front, and one at high energy ($>$1 TeV) which is most likely the first order Fermi mechanism. However, none of these mechanisms can be regarded as fully worked out from a theoretical point of view.

Progress, as always, will flow from more and improved observations. For the nebula, X-ray and optical images continue to be of crucial importance, and maps in the TeV band are just starting to appear [2]. For the wind, the observational signatures will be point-like, and might be pulsed. High time-resolution optical polarimetry of pulsar emission will have important input on the question of the location of the pulse-forming region. Finally, the large number of new gamma-ray pulsars that will be discovered by GLAST is also highly likely to lead to the extinction of some theories of high energy pulsed emission, as well as providing much more accurate spectra for comparison with models of PWNe.

References

1. Achterberg, A., Gallant, Y. A., Kirk, J. G., & Guthmann, A. W., 2001, MNRAS, 328, 393
2. Aharonian, F., Akhperjanian, A. G., Aye, K.-M., et al., 2005, A&A, 435, L17
3. Aharonian, F., Akhperjanian, A. G., Bazer-Bachi, A. R., et al., 2006, A&A, 457, 899
4. Amato, E. & Arons, J. 2006, ApJ, 653, 325
5. Amato, E., Guetta, D., & Blasi, P. 2003, A&A, 402, 827
6. Amato, E., Salvati, M., Bandiera, R., Pacini, F., & Woltjer, L., 2000, A&A, 359, 1107
7. Arons, J., 1979, Space Sci Rev, 24, 437
8. Arons, J., 1998, Mem Soc Astron Ital, 69, 989
9. Aschenbach, B. & Brinkmann, W., 1975, A&A, 41, 147
10. Asseo, E., Kennel, C. F., & Pellat, R., 1978, A&A, 65, 401
11. Atoyan, A. M., 1999, A&A, 346, L49
12. Atoyan, A. M. & Aharonian, F. A., 1996, MNRAS, 278, 525
13. Baars, J. W. M., Genzel, R., Pauliny-Toth, I. I. K., & Witzel, A., 1977, A&A, 61, 99
14. Ball, L. & Dodd, J., 2001, Publ Astron Soc Aust, 18, 98

15. Ball, L. & Kirk, J. G., 2000, Astroparticle Phys, 12, 335
16. Bednarek, W., 2003, A&A, 407, 1
17. Bednarek, W. & Bartosik, M., 2003, A&A, 405, 689
18. Bednarz, J. & Ostrowski, M., 1998, Phys Rev Lett, 80, 3911
19. Begelman, M. C., 1998, ApJ, 493, 291
20. Begelman, M. C. & Kirk, J. G., 1990, ApJ, 353, 66
21. Begelman, M. C. & Li, Z.-Y., 1992, ApJ, 397, 187
22. Beskin, V. S., Kuznetsova, I. V., & Rafikov, R. R., 1998, MNRAS, 299, 341
23. Beskin, V. S. & Nokhrina, E. E., 2006, MNRAS, 367, 375
24. Bietenholz, M. F., Frail, D. A., & Hester, J. J., 2001, ApJ, 560, 254
25. Bietenholz, M. F., Hester, J. J., Frail, D. A., & Bartel, N., 2004, ApJ, 615, 794
26. Bogovalov, S. & Tsinganos, K., 1999, MNRAS, 305, 211
27. Bogovalov, S. V., 1999, A&A, 349, 1017
28. Bogovalov, S. V., 2001, A&A, 367, 159
29. Bogovalov, S. V. & Aharonian, F. A., 2000, MNRAS, 313, 504
30. Bogovalov, S. V., Chechetkin, V. M., Koldoba, A. V., & Ustyugova, G. V., 2005, MNRAS, 358, 705
31. Bogovalov, S. V. & Khangoulian, D. V., 2002, MNRAS, 336, L53
32. Brinkmann, W., Aschenbach, B., & Langmeier, A., 1985, Nature, 313, 662
33. Bucciantini, N., Amato, E., Bandiera, R., Blondin, J. M., & Del Zanna, L., 2004, A&A, 423, 253
34. Bucciantini, N., Amato, E., & Del Zanna, L., 2005, A&A, 434, 189
35. Bucciantini, N. & Del Zanna, L., 2006, A&A, 454, 393
36. Bucciantini, N., del Zanna, L., Amato, E., & Volpi, D., 2005, A&A, 443, 519
37. Buckley, R., 1977, MNRAS, 180, 125
38. Chiueh, T., Li, Z.-Y., & Begelman, M. C., 1998, ApJ, 505, 835
39. Contopoulos, I. & Kazanas, D., 2002, ApJ, 566, 336
40. Contopoulos, I., Kazanas, D., & Fendt, C., 1999, ApJ, 511, 351
41. Coroniti, F. V., 1990, ApJ, 349, 538
42. Davis, L., 1947, Phys Rev, 72, 632
43. Del Zanna, L., Amato, E., & Bucciantini, N., 2004, A&A, 421, 1063
44. Del Zanna, L., Volpi, D., Amato, E., & Bucciantini, N., 2006, A&A, 453, 621
45. DeLaney, T., Gaensler, B. M., Arons, J., & Pivovaroff, M. J., 2006, ApJ, 640, 929
46. Dyks, J., Harding, A. K., & Rudak, B., 2004, ApJ, 606, 1125
47. Emmering, R. T. & Chevalier, R. A., 1987, ApJ, 321, 334
48. Gaensler, B. M. & Slane, P. O., 2006, Ann. Rev. Astron. Astrophys., 44, 17
49. Gallant, Y. A. & Arons, J., 1994, ApJ, 435, 230
50. Gallant, Y. A. & Tuffs, R. J. 2000, in *ASP Conf. Ser., 202: IAU Colloq. 177: Pulsar Astronomy – 2000 and Beyond*, ed. M. Kramer, N. Wex, & R. Wielebinski, 503
51. Gallant, Y. A. & Tufs, R. J., 2002, in *ASP Conf. Ser. 271: Neutron Stars in Supernova Remnants*, ed. P. O. Slane & B. M. Gaensler, 161
52. Gallant, Y. A., van der Swaluw, E., Kirk, J. G., & Achterberg, A., 2002, in *ASP Conf. Ser. 271: Neutron Stars in Supernova Remnants*, 99–104
53. Green, D. A., Tuffs, R. J., & Popescu, C. C., 2004, MNRAS, 355, 1315
54. Gruzinov, A., 2005, Phys Rev Lett, 94, 021101
55. Harding, A. K., 2005, in *AIP Conf. Proc. 801: Astrophysical Sources of High Energy Particles and Radiation*, ed. T. Bulik, B. Rudak, & G. Madejski, 241–252
56. Harding, A. K. & Lai, D., 2006, Rep Prog Phys, 69, 2631
57. Hester, J. J., Mori, K., Burrows, D., et al., 2002, ApJ, 577, L49
58. Hester, J. J., Scowen, P. A., Sankrit, R., et al., 1995, ApJ, 448, 240
59. Hibschman, J. A. & Arons, J., 2001, ApJ, 554, 624
60. Hibschman, J. A. & Arons, J., 2001, ApJ, 560, 871
61. Hones, Jr., E. W. & Bergeson, J. E., 1965, JGR, 70, 4951
62. Horns, D., Aharonian, F., Santangelo, A., Hoffmann, A. I. D., & Masterson, C., 2006, A&A, 451, L51

63. Hoshino, M., Arons, J., Gallant, Y. A., & Langdon, A. B., 1992, ApJ, 390, 454
64. Ingraham, R. L. 1973, ApJ, 186, 625
65. Kanbach, G., Kellner, S., Schrey, F. Z., et al., 2003, in *Instrument Design and Performance for Optical/Infrared Ground-based Telescopes*. Edited by Iye, Masanori; Moorwood, Alan F. M., Proceedings of the SPIE, Volume 4841, pp. 82–93 (2003)
66. Kaspi, V. M., Roberts, M. S. E., & Harding, A. K., 2004, ArXiv Astrophysics e-prints
67. Kennel, C. F. & Coroniti, F. V., 1984, ApJ, 283, 694
68. Kennel, C. F. & Coroniti, F. V., 1984, ApJ, 283, 710
69. Khangoulian, D. V. & Bogovalov, S. V., 2003, Astron Lett, 29, 495
70. Kirk, J. G. & Duffy, P., 1999, J Phys G Nucl Phys, 25, 163
71. Kirk, J. G., Guthmann, A. W., Gallant, Y. A., & Achterberg, A., 2000, ApJ, 542, 235
72. Kirk, J. G. & Skjæraasen, O., 2003, ApJ, 591, 366
73. Kirk, J. G., Skjæraasen, O., & Gallant, Y. A., 2002, A&A, 388, L29
74. Komissarov, S. S., 2006, MNRAS, 367, 19
75. Komissarov, S. S. & Lyubarsky, Y. E., 2003, MNRAS, 344, L93
76. Komissarov, S. S. & Lyubarsky, Y. E., 2004, MNRAS, 349, 779
77. Krause-Polstorff, J. & Michel, F. C., 1985, A&A, 144, 72
78. Kuiper, L., Hermsen, W., Cusumano, G., et al., 2001, A&A, 378, 918
79. Larrabee, D. A., Lovelace, R. V. E., & Romanova, M. M., 2003, ApJ, 586, 72
80. Li, Z.-Y., Chiueh, T., & Begelman, M. C., 1992, ApJ, 394, 459
81. Lyubarsky, Y., 2005, Adv Space Res, 35, 1112
82. Lyubarsky, Y. & Eichler, D., 2001, ApJ, 562, 494
83. Lyubarsky, Y. & Kirk, J. G., 2001, ApJ, 547, 437
84. Lyubarsky, Y. E., 2002, MNRAS, 329, L34
85. Lyubarsky, Y. E., 2003, MNRAS, 339, 765
86. Lyubarsky, Y. E., 2003, MNRAS, 345, 153
87. Marsden, P. L., Gillett, F. C., Jennings, R. E., et al., 1984, ApJ, 278, L29
88. McKinney, J. C., 2006, MNRAS, 368, L30
89. Melatos, A. & Melrose, D. B., 1996, MNRAS, 279, 1168
90. Michel, F. C., 1969, ApJ, 158, 727
91. Michel, F. C., 1971, Comments Astrophys Space Phys, 3, 80
92. Michel, F. C., 1973, ApJ, 180, L133+
93. Michel, F. C., 1974, ApJ, 187, 585
94. Michel, F. C., 1991, *Theory of neutron star magnetospheres* (Chicago, IL, University of Chicago Press, 1991, 533 p.)
95. Mori, K., Burrows, D. N., Hester, J. J., et al., 2004, ApJ, 609, 186
96. Ng, C.-Y. & Romani, R. W., 2004, ApJ, 601, 479
97. Ostrowski, M. & Bednarz, J., 2002, A&A, 394, 1141
98. Pacini, F., 1967, Nature, 216, 567
99. Pavlov, G. G., Teter, M. A., Kargaltsev, O., & Sanwal, D., 2003, ApJ, 591, 1157
100. Pétri, J., 2006, in *Stellar Fluid Dynamics and Numerical Simulations: From the Sun to Neutron Stars*. Edited by M. Rieutord and B. Dubrulle, 355–382
101. Pétri, J., Heyvaerts, J., & Bonazzola, S., 2002, A&A, 384, 414
102. Pétri, J. & Kirk, J. G., 2005, ApJ, 627, L37
103. Pétri, J. & Lyubarsky, Y., 2007, A&A 473, 683
104. Piddington, J. H., 1957, Aust J Phys, 10, 530
105. Rees, M. J. & Gunn, J. E., 1974, MNRAS, 167, 1
106. Reville, B., Kirk, J. G., & Duffy, P., 2006, Plasma Phys Controlled Fusion, 48, 1741
107. Romanova, M. M. & Lovelace, R. V. E., 1992, A&A, 262, 26
108. Scargle, J. D., 1969, ApJ, 156, 401
109. Spitkovsky, A., 2005, in *AIP Conf. Proc. 801: Astrophysical Sources of High Energy Particles and Radiation*, ed. T. Bulik, B. Rudak, & G. Madejski, 345–350
110. Spitkovsky, A., 2006, ApJ, 648, L51
111. Spitkovsky, A. & Arons, J., 2004, ApJ, 603, 669
112. Timokhin, A. N., 2006, MNRAS, 368, 1055

113. Tomimatsu, A., 1994, Publ. Astron. Soc. Japan, 46, 123
114. Usov, V. V., 1975, Astrophys. Space Sci., 32, 375
115. van der Swaluw, E., 2003, A&A, 404, 939
116. van der Swaluw, E., Achterberg, A., Gallant, Y. A., & Tóth, G., 2001, A&A, 380, 309
117. Veron-Cetty, M. P. & Woltjer, L., 1993, A&A, 270, 370
118. Vlahakis, N., 2004, ApJ, 600, 324
119. Weisskopf, M. C., Hester, J. J., Tennant, A. F., et al., 2000, ApJ, 536, L81
120. Wilson, D. B. & Rees, M. J., 1978, MNRAS, 185, 297
121. Zenitani, S. & Hoshino, M., 2001, ApJ, 562, L63
122. Zenitani, S. & Hoshino, M., 2005, ApJ, 618, L111
123. Zenitani, S. & Hoshino, M., 2005, Phys Rev Lett, 95, 095001

Chapter 17
Implications of HESS Observations of Pulsar Wind Nebulae

Ocker C. de Jager and Arache Djannati-Ataï

17.1 Introduction

Even before the discovery of pulsars, pulsar wind nebulae (PWN) like the Crab Nebula were identified as belonging to a class of cosmic radio sources with relativistic electrons moving in magnetized plasmas to give the continuum radiation as observed. Visionaries like [36] already predicted that we should be able to measure the magnetic field strength in PWN using the combination of synchrotron and inverse Compton (IC) radiation. Following this, [43] were the first to provide us with a sophisticated one dimensional (1D) magneto hydrodynamical models (MHD) model of the Crab Nebula, which predicted a magnetic field strength distribution, consistent with broadband multi-wavelength (radio through very high energy gamma-ray) constraints [12, 25, 39].

The discovery of the Crab pulsar in 1968 confirmed suspicions that a rapidly spinning neutron star should provide the energy input into the Crab Nebula, but soon questions concerning the spin-down of pulsars in relation to the evolution of the nebulae arose. Whereas a few Crab-like remnants were discovered, Vela X, assumed to be associated with the 11,000 year old Vela pulsar, raised the question about the evolution of PWN as described by [63]. More serious evolutionary studies of PWN in supernova remnants (SNR) were launched by [56] and [55], but the offset of Vela X relative to the Vela pulsar raised the question if Vela X is indeed associated with the Vela pulsar. We also focus on Vela X in this discussion for the very specific reason that it serves as a prototype of evolved PWN. A wealth of new information on Vela X and similar evolved PWN became recently available as discussed in this review paper.

O.C. de Jager
Unit for Space Physics, North-West University, Potchefstroom 2520, South Africa
e-mail: fskocdj@puk.ac.za

A. Djannati-Ataï
CNRS, Universite Paris 7, Denis Diderot, 75005 Paris, France

W. Becker (ed.), *Neutron Stars and Pulsars,* Astrophysics and Space Science Library 357,

An excellent review of the structure and evolution of PWN from a radio and X-ray perspective was recently given by [33], whereas investigations on the population of galactic very high energy (VHE) HESS sources considered to be associated with PWN were given by [45] and [34].

17.2 The Evolving Definition of Pulsar Wind Nebulae

The term "pulsar wind nebulae" (PWN), or "plerions" (derived from Ancient Greek *pleres*) – a term coined by [62], is described by the following:

- Filled center or blob-like form
- A flat radio spectrum where the radio energy flux depends on frequency ν as $F_\nu \propto \nu^\alpha$, with $\alpha \sim 0$ to -0.3
- A well-organised internal magnetic field with high integrated linear polarisation at high radio frequencies

The origins of the last property will be revisited in Sect. 17.6.

The main body of information on PWN came mainly from radio and X-ray observations, whereas interstellar absorption makes it difficult to detect most of these diffuse sources in optical as well. The study of PWN was therefore confined to a study of the synchrotron component only, which depends on the nebular field strength. This, and the fact that only radio and X-ray observations (representing widely divergent particle populations) have been used in theoretical studies, must have restricted progress in the understanding of PWN evolution and the conversion of spin-down power into energetic particles in such nebulae.

With the growth of X-ray Astronomy, aided by sensitive instruments like Chandra and XMM-Newton, the definition of PWN has been broadened. We may add the following three important aspects:

- A torus and jet near the pulsar, with the direction of the jet reflecting the direction of the pulsar spin axis and the torus showing an underluminous region inside a characteristic scale radius $R_s \sim 10^{17}$cm to $\sim 10^{18}$cm, believed to be the pulsar wind shock radius (see [51] for parameter fits to such torii).
- Evidence for re-acceleration of particles somewhere between the pulsar light cylinder and R_s, leading to a hard X-ray spectrum with a photon index $\sim$1.5 to $\sim$2 near R_s (a review thereof will be given Sect. 17.3).
- Evidence for synchrotron cooling (spectral steepening) at $R > R_s$, with the size of the PWN decreasing towards increasing energies, as seen from the Crab and several other PWN. The photon indices of the cooled spectra range between 2.0 and 2.5 (see also Sect. 17.3).

The drawback of having only radio and X-ray synchrotron information on PWN was realised by [26,28,30], who were probably the first to predict that PWN evolved beyond the Crab phase (i.e., those would have field strengths smaller than the Crab)

would accumulate sufficient amounts of relic electrons so that the inverse Compton (IC) scattering of these PWN electrons on the CMBR and possibly far infrared photons from galactic dust would be detectable by space and ground-based γ-ray telescopes. Furthermore, current generation ground based γ-ray telescopes have an angular resolution of a few arcminutes [40], so that the ratio $\theta_{\rm PWN}/\theta_\gamma$ of the PWN angular radius $\theta_{\rm PWN}$ relative to the telescope angular resolution θ_γ increases to values greater than unity as the pulsar/PWN evolves beyond the Crab phase. They effectively become resolved, which allows us to measure spatially resolved spectra to the resolution of the VHE γ-ray telescopes. These complementary γ-ray observations then allow us to probe the electron spectra in the sources, as well as the associated magnetic field distribution, provided that comparable electron energies contribute to the observed (spatially resolved) synchrotron and IC spectra.

The HESS telescope has the advantage of a large field-of-view, few arcminute angular resolution and good sensitivity against background rejection to probe extended sources [40] which allowed this telescope to see for the first time a population of evolved (resolved) VHE γ-ray emitting PWN [3, 7]. Such detections imply one or more of the following properties (see also [29]):

- The overall (total) wind magnetization parameter of the PWN $\sigma_{\rm tot}$ may be much less than unity (i.e., a particle dominated wind as discussed by [18], whereas [26] considered evolved PWN in equipartition. If the PWN is well below equipartition ($\sigma_{\rm tot} \ll 1$), synchrotron losses on the VHE emitting particles will be relatively small, leading to an intrinsically bright VHE source.
- Rapid expansion of the PWN during its early phases of high power input from the pulsar (such as G0.9+0.1 and the PWN of PSR B1509−58 [18]) results in a relatively low field strength in the PWN and hence the survival of the majority of VHE emitting electrons since early epochs. If the progenitor was part of an OB association, the combined stellar wind would blow a cavity so that the PWN expands nearly uninhibited for tens of kyr. The magnetic field strength in such an expanded PWN can in principle drop below a few micro-gauss, so that synchrotron losses become less important relative to IC, ending up in a "dark VHE source", since we can no longer rely on synchrotron emission to provide a multi-wavelength counterpart. One such possibility is HESS J1303−631 which may be associated with Cen OB as reported by [4].
- The ideal condition (which includes the first two conditions) is to have the radiation lifetime $\tau(E_\gamma)$ of VHE radiating particles comparable to, or longer than, the age T of the system, and therefore surviving even the earlier epochs when the field was stronger, so that the total amount of energy in electrons in the PWN is a significant fraction of the maximal rotational kinetic energy of the neutron star $I\dot{\Omega}_0^2/2$ at birth. Only adiabatic losses are then the main source of losses. In this case we do not expect to see an energy dependence of the PWN size with changing γ-ray energy – a well known phenomenon for PWN where the lifetime of particles exceeds the age of the system. The predicted VHE γ-ray flux will then depend on the birth period of the pulsar.

The discovery of VHE γ-rays from HESS J1825−137 [5] and Vela X [6], both offset from their pulsars, confirm predictions of [14, 32, 60] that anisotropic reverse shocks can offset PWN from their original positions. We will discuss this further in this review paper. This conclusion led [29] to propose that a systematic investigation of middle-aged pulsars at the edges of resolved center-filled VHE γ-ray sources, combined with follow-up radio and X-ray imaging information, should result in the identification of a new class of PWN, with Ground-Based Gamma-Ray Astronomy taking the lead in this new direction. GLAST operations at its highest energies (where the angular resolution is best) is also expected to make a contribution to this field. In fact, with GLAST we expect to see a population of electrons with ages even longer than those seen by HESS.

Lemiére et al. [46] were the first to search for molecular clouds (based on CO and HI data) associated with such HESS sources, and in the case of HESS J1825−137, they found a cloud at the same kinematic distance to its associated pulsar PSR B1823−13. This cloud also has the correct orientation relative to the pulsar and γ-ray center of gravity to explain the observed offset in terms of an early reverse shock from the cloud location. A more detailed study on this topic was performed in the thesis of Lemiére [45] whose study have revealed this new class of offset, filled center VHE PWN.

17.3 Energy Scales and Lifetimes of X-Ray Synchrotron and VHE IC Emitting Electrons

The IC scattering of VHE electrons on the 2.7 K CMBR radiation is relatively efficient, since most scattering relevant to the observed VHE γ-ray range is in the Thomson limit. Far infrared photons from galactic dust at an average temperature of 25 K tend to preselect lower energy electrons where the Thomson limit still applies, whereas the cross-section for IC scattering decreases towards higher energies in the Klein–Nishina limit. The net effect is a steepening in the observed spectrum if far IR photons due to dust grains dominate, whereas the spectral index for IC in the Thomson limit is the same as that for synchrotron radiation by the same spectrum of electrons in a magnetic field. The reader is referred to the treatment by [15] on these topics.

In the prediction of a population of VHE γ-ray emitting PWN due to CMBR and far IR photons from dust, [26] remarked that the effect of dust would become more dominant towards the galactic center region. The most interesting application of this is the convincing prediction that a significant fraction of the galactic center HESS source (HESS J1745−290) at the location of Sgr A* is due to a pulsar wind nebula: The relativistic electrons of this PWN suffers severe energy losses as a result of inverse Compton scattering on the dense IR radiation field [41].

In the scaling equations below we will focus on the contribution from the CMBR alone, but refer the reader to [22, 26] for first order analytical Klein–Nishina corrections when including the dust component (also based on [15].

The required electron energy in a transverse magnetic field of strength $B = 10^{-5}B_{-5}$ G, to radiate synchrotron photons of mean energy $E_{\rm keV}$ (in units of keV) is given by

$$E_e = (70\ {\rm TeV})B_{-5}^{-1/2}E_{keV}^{1/2}. \tag{17.1}$$

Similarly, the mean electron energy required to inverse Compton scatter the CMBR seed photons to energies $E_{\rm TeV}$ (in units of TeV) is typically lower at

$$E_e = (18\ {\rm TeV})E_{\rm TeV}^{1/2}. \tag{17.2}$$

The mean synchrotron photon energy (in units of keV) can be written in terms of the mean IC photon energy (following scattering on the CMBR) E_{TeV} (in units of TeV)

$$E_{\rm keV} = 0.06B_{-5}E_{\rm TeV}. \tag{17.3}$$

If we define the synchrotron lifetime ($\tau = E/\dot{E}$) of a VHE electron in a field of strength $B = 10^{-5}B_{-5}$ G, scattering cosmic microwave background (CMBR) photons to energies $E_\gamma = 10^{12}E_{\rm TeV}$ eV (in the Thomson limit) can be shown to be

$$\tau(E_\gamma) \sim (4.8\ {\rm kyr})B_{-5}^{-2}E_{\rm TeV}^{-1/2}. \tag{17.4}$$

Note that the constant above depends on the assumed pitch angle of the electron relative to the magnetic field direction. Other constants will also be obtained if we define the final electron energy to be an arbitrary fraction of the initial energy. Assuming (17.4), the corresponding lifetime of keV emitting electrons would be shorter

$$\tau(E_{\rm X}) = (1.2\ {\rm kyr})B_{-5}^{-3/2}E_{\rm keV}^{-1/2}, \tag{17.5}$$

where $E_{\rm keV}$ is again the synchrotron photon energy in units of kiloelectronvolt. In very extended nebular MHD flows it is possible to get field strengths below the typical 3 μG ISM value, in which case we should include inverse Compton energy losses on the 2.7 K CMBR. Following [8] we also include a Klein–Nishina suppression factor (relative to the Thomson limit) of 2/3 for the HESS range to give a lifetime for TeV emitting electrons of

$$\tau(E_\gamma) \sim \frac{(100\,{\rm kyr})}{[1+0.144(B_{\mu\rm G})^2]E_{\rm TeV}^{1/2}}\ , \tag{17.6}$$

where $B_{\mu\rm G}$ is now the field strength in unit of micro-gauss. This hints at a terminating VHE lifetime of 100 kyr. Note however that the X-ray synchrotron surface brightness in such extended low-field environments may be well below detectable levels, in which case a PWN will only be visible in the γ-ray domain (via the IC process), whereas no radio, optical and/or X-ray (synchrotron) plerionic counterpart

is found. Furthermore, the parent neutron star's thermal and/or non-thermal X-ray component(s) may also no longer be visible, since the lifetime of VHE emitting electrons may even exceed the neutron star's cooling and non-thermal radiating timescales!

Such γ-ray detections are expected to contribute to the growing population of Unidentified Gamma-Ray Sources or Dark Accelerators/Sources, but given our growing knowledge through experimentation and theory, we should eventually be able to lift these PWN to the status of "gamma-ray pulsar wind nebulae without multi-wavelength counterpart".

17.4 Particle Acceleration at PWN Shocks

Although electrons and positrons from magnetospheric electromagnetic cascades escape with relatively low energy from the pulsar light cylinder, where the ratio σ_L of electromagnetic energy density to particle energy density must be much larger than unity ($\sigma_L \sim 10^4$ for the Crab pulsar [21] this σ parameter must reduce drastically beyond the light cylinder for two reasons: (1) Wilson and Rees [64] have shown that the Crab pulsar's radio pulses would have been smeared unless the Lorentz factor of the $e^{\pm}$ wind exceeds 10^4; (2) Observations at the pulsar wind shock indicate that this ratio must have reduced to $\sigma \sim 3 \times 10^{-3}$ for the Crab [17,43], but in the range 0.01–0.1 for the Vela PWN shock [17,57]. The reader is referred to [11] for a review of this particle energization process.

The first observational evidence of a pulsar wind nebular shock was seen in the Crab Nebula, where the observation of the underluminous region within $\sim$10 arcsec from the pulsar made it natural for [53] to associate the pulsar wind shock ($R_s \sim$ 0.1 pc) with the boundary of this region.

Even though energy is converted from fields to the bulk of the particle population between R_L and R_s, we require an additional mechanism to accelerate electrons and positrons to ultra-relativistic energies with an electron spectral index of $\sim$2 (see Sect. 17.4 for observational evidence). Recently [10] have shown that the fractional energy content in the accelerated $e^- - e^+$ component increases with increasing energy content in upstream (unshocked) ultra relativistic ions. These authors also found that the ratio of accelerated e^+ to e^- components become significantly more than unity as the upstream wind energy flux becomes ion dominated. The reader is also referred to [10] for a review of the literature on ion mediated lepton acceleration in pulsar wind shocks.

Another fundamental question regarding pulsar wind nebulae is the maximum energy to which $e^- - e^+$ can be accelerated at a pulsar wind shock to produce the observed high energy synchrotron and inverse Compton radiation downstream of the shock? We will attempt to answer this question without restricting ourselves to the microphysics of the acceleration process.

This limit for low field strength pulsar wind shocks was first discussed by [38] who considered the gyro-radius limit and by [27] for synchrotron limited acceleration as discussed below.

17.4.1 The Synchrotron Limit

For any ion gyro resonant (as discussed before) or Fermi I type acceleration process in a relativistic pulsar wind shock, electrons and/or positrons can be accelerated at a rate as fast as the gyro-period, as reviewed by [27]. The latter authors then balanced this rate with synchrotron losses for relatively strong fields to derive a maximum characteristic (cutoff) synchrotron energy (in the lab frame) of

$$E_\gamma(\max) = \left(\frac{3}{4\pi}\right)^2 \left(\frac{hc}{r_0}\right) = (25\,\mathrm{MeV}) \tag{17.7}$$

for electrons/positrons in such relativistic shocks. This limit reproduces the observed characteristic synchrotron cutoff energy of $\sim$25 MeV for the Crab Nebula as seen by COMPTEL and EGRET [27]. The corresponding 90% confidence interval for this cutoff is 15–70 MeV.

We note that [1] approached this problem from a totally different perspective by calculating the electron cycle times upstream and downstream of a relativistic shock. They finally arrived at exactly the same expression (17.7), or (A2) of [27] within a factor of 2π. Aharonian [2] also extended this limit to account for synchrotron limited acceleration of protons and electrons by considering an acceleration timescale given by a scale factor η times the gyro-radius relative to c, so that (A2) of [27] is retrieved if we set $\eta = 2\pi$ (gyro-period timescale). His maximum for electrons is then

$$E_\gamma(\max) = (160\,\mathrm{MeV})\eta^{-1} \tag{17.8}$$

similar to [1]. EGRET observations of the Crab Nebula are however consistent with (17.7), or, $\eta \sim 2\pi$ [27].

17.4.2 The Gyro-Radius Limit

For lower field strengths (i.e., PWN evolved beyond the Crab-like phase), where synchrotron losses no longer constrain the maximum electron energy, we generalise the gyro-radius limit of [38], which states that the highest energy particles must still be contained in the shock at R_s while participating in the acceleration process. In other words, the gyro-radius of particles with energy $E_{\max}$ should be significantly smaller than R_s, or,

$$r_L = \frac{E_{\max}}{eB_s} = \varepsilon R_s < R_s, \tag{17.9}$$

where $\varepsilon < 1$ is the required fractional size of R_s for containment during any Fermi or gyro resonant type of acceleration to provide the bright synchrotron radiation downstream of the pulsar wind shock. This result does not depend explicitly on the acceleration timescale, but relatively fast acceleration (relative to escape and radiation losses) will result in maximal values of $\varepsilon < 1$, until containment becomes a problem.

We can again generalise this expression by adding the charge number Z (= 1 for electrons and positrons) for the possible acceleration of ions to give

$$E_{\max} = Ze\varepsilon B_s R_s. \tag{17.10}$$

Equation (17.10) converges to (52) of [1] if we set the abovementioned containment factor $\varepsilon = (\ell_c/3r_L)^{1/2} < 1$, where ℓ_c is the coherence length of the field, if the latter is assumed to be randomly oriented. We, however, do not specify the exact physics of acceleration so that ε is kept as a free parameter, which is constrained to be less than unity from a general containment principle.

We apply this constraint to PWN by using the [43] formalism to write the post-shocked field strength in terms of the pulsar spin-down power and parameters related to the pulsar wind shock to give

$$B_s = \kappa \left[\frac{\sigma \dot{E}}{(1+\sigma)c}\right]^{\frac{1}{2}} \frac{1}{R_s}, \tag{17.11}$$

with σ the wind magnetization parameter ($\sigma \equiv$ electromagnetic energy density to particle energy density at R_s) and $\dot{E}$ the spin-down power of the pulsar. The magnetic compression ratio $1 < \kappa < 3$ [43] depends on the strength of this relativistic shock (and hence σ). For strong shocks ($\sigma \ll 1$) we have $\kappa \sim 3$, whereas $\kappa \sim 1$ for weaker Vela-like shocks [43], where $\sigma \sim 0.01$ to 0.1 [17, 57].

The expression for the maximum particle energy for remnants with field strengths weaker than the Crab (i.e., where radiation losses do not limit the energy) can now be written in terms of σ and $\dot{E}$, without having to know where the shock is located (since R_s cancels)

$$E_{\max} = \varepsilon \kappa e \left(\frac{\sigma}{1+\sigma}\frac{\dot{E}}{c}\right)^{1/2} = (110\,\mathrm{TeV})\kappa \left(\frac{\varepsilon}{0.2}\right)\left(\frac{\sigma}{0.1}\dot{E}_{36}\right)^{1/2}, \tag{17.12}$$

where the spin-down power has been rescaled in terms of a typical Vela-like value of $\dot{E} = 10^{36}\dot{E}_{36}$ erg s^{-1} and a Vela-like $\sigma \sim 0.1$. However, according to [38] the maximum energy is equal to the polar cap potential, in which case the term $\varepsilon\kappa\sigma/(1+\sigma)$ should drop away (i.e., no field compression and magnetisation). In this case the maximum energy for a Vela-like pulsar would be ∼350 TeV if $\varepsilon = 0.2$.

The discussion of this maximum is very relevant from an observational viewpoint, since the highest photon energy at any location in the PWN will always be bounded by such a quantity, which should evolve with time as a result of pulsar spin-down.

17.4.3 PSR B1929+10: A Challenge for Particle Acceleration in PWN Shocks

The aforementioned maximum electron energy imposes an important boundary condition when modeling the extended X-ray and γ-ray emission from PWN, since this maximum will suffer synchrotron and adiabatic losses during electron transport to the outer edge of the PWN. While this long-term transport process is taking place, the spin-down power will also be decreasing with time, resulting in a decrease of $E_{\max}$ at R_s for freshly injected electrons (making compact nebular X-rays) as well. For the sake of simplicity we will assume that the maximum electron energy is set by the pulsar polar cap potential [38].

The detection of an X-ray synchrotron trail from PSR B1929+10 by [13,61] from X-ray observations should challenge the maximum electron energy set by (17.12), since the spin-down power $\dot{E} = 3.9 \times 10^{33}\,\mathrm{erg\,s^{-1}}$ is low compared to even Vela-like pulsars. Becker et al. [13] considered the case where the time $t = R_t/V_p$ (with R_t the length of the trail seen in X-rays and V_p the pulsar proper motion velocity) is equal to the synchrotron lifetime τ_s, which can be several thousand years for a trail field strength $B < 10\,\mu\mathrm{G}$. Even if we assume that the electrons never lost any energy along their transport from R_s to the present weak-field trail location, we find from (17.12) that the maximum electron energy is given by

$$E_{\max}(\mathrm{B1929}) \sim (20\,\mathrm{TeV})\left(\frac{\varepsilon}{0.2}\right), \tag{17.13}$$

whereas the corresponding characteristic synchrotron energy in a nebular magnetic field, normalised to a strength of $B_{-5} = B/10\,\mu\mathrm{G}$, would be given by

$$h\nu_{\max}(1929) < (300\,\mathrm{eV})B_{-5}\left(\frac{\varepsilon}{0.2}\right)^2. \tag{17.14}$$

This limit is clearly in the soft X-ray band, falling short to explain synchrotron emission up to 10 keV as observed.

If the pulsar has spun down significantly during a time t into the past, then we are looking at relic electrons in the trail, but accelerated at the pulsar wind shock when the age of the pulsar was equal to $T - t$, where T is the current true age. Assuming a pulsar braking index of $n = 3$, the retarded spin-down power would then be

$$\dot{E} = \frac{\dot{E}_0}{(1 + (T-t)/\tau_0)^2}, \tag{17.15}$$

where $\dot{E}_0$ is the spin-down power at birth and $\tau_0 = P_0/2\dot{P}_0$ the characteristic age at birth when the initial spin period was P_0 and period derivative $\dot{P}_0$. For those not familiar with the concept of a retarded spin-down power: The author borrowed this concept from electrodynamics where the term retarded potential is used to describe

radiating systems, where the changing vector potential seen by the observer is the result of particle movement some time in the past. Also, for those not familiar with the concept of a braking index: The spin-down power of a pulsar can be written as a function of the rotational frequency Ω as $-\dot{E} = K\Omega^{n+1}$, where K depends on several neutron star properties and n the braking index. For magnetic dipole radiation and energy losses via particle outflow through the pulsar polar cap as in the well-known Goldreich–Julian model, $n = 3$. However, even this retarded spin-down may not solve the problem of PSR B1929+10 since the age $T = 3 \times 10^6$ years (i.e., already too large), so that quantity $(T - t)/T \sim 1$ does not give us any advantage.

We can therefore only speculate about possible explanations for the existence of X-ray synchrotron photons from the trail of PSR B1929+10: One possibility is re-acceleration due to adiabatic compression in the bow shock. A detailed discussion of this is however beyond the scope of this general review paper, except to mention that more X-ray observations, as well as future ground based VHE γ-ray observations are important to characterise this important laboratory for particle acceleration. Whereas X-rays measure the convolution of the electrons with the field strength in the trail, the VHE γ-rays would directly probe the particle population via the IC scattering of this relic component on the CMBR and known far infrared photons from galactic dust grains.

17.5 The Energy Dependent Cooling Radius of a PWN

In Fig. 17.1 we summarise the observed spectral steepening with radius $r > R_s$, where $R_s = d\theta_s$ is the pulsar wind shock radius, d is the distance between earth and the pulsar, and θ_s is the angular distance between the pulsar and its wind shock as seen on the sky: If Γ_s is the photon spectral index (as seen in X-rays) at the pulsar wind shock, a steepening $\Gamma_x > \Gamma_s$ corresponding to $r > R_s$ is observed as a result of radiative losses. This effect is mostly seen in the X-ray (synchrotron) domain, but may be less so in the VHE (IC) domain where lower energy electrons (producing the VHE γ-rays) suffer less radiative losses compared to the synchrotron emitting electrons.

Theoretically we would expect a convergent value of $\Gamma_X = \Gamma_s + 0.5$ as a result of radiative (mostly synchrotron) cooling, since the energy loss rate scales as electron energy squared. It is clear that the points all lie either on this (solid) line in Fig. 17.1, or above it. The reason for the latter is because the spectral cutoff associated with the highest energy electrons at the observed angular radius θ_X may only contribute to energy bins below the upper spectral edge used in the analysis, in which case the spectral index Γ_X may asymptotically diverge to relatively large numbers near $\theta_X = r/d$. However, even this information is useful in sophisticated models where the maximum electron energy in the PWN shock serves as one of the inputs. This can help us to constrain the maximum electron energy at θ_s in time dependent models which takes the full evolution into account.

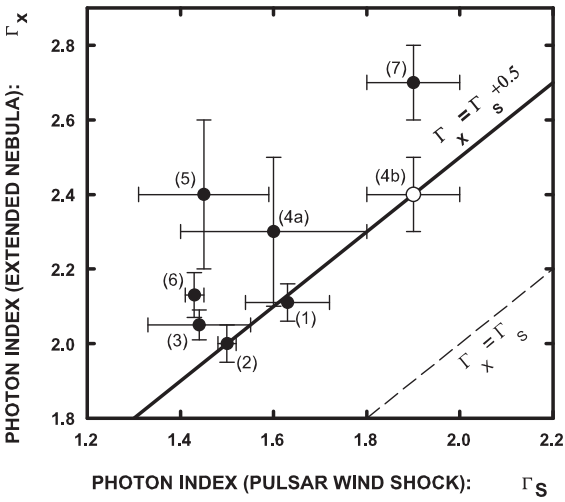

Fig. 17.1 Plot of the X-ray spectral index Γ_X around ∼1 keV at the maximal observable radius (or "extended nebula") vs. the spectral index Γ_s for the same energy range near the pulsar wind shock. The *dashed line* indicates $\Gamma_X = \Gamma_s$ whereas the *solid line* represents the line $\Gamma_X = \Gamma_s + 0.5$ expected for $dE/dt \propto -E^2$ (e.g., synchrotron) cooling if we assume that the maximum observable photon energy is still above the upper spectral edge of the observations in the extended nebula (typically >10 keV). References: (1) Crab [35], (2) Vela [47,48], (3) PSR B1509−58 [31], (4a) G18.0−0.9 [32], (4b) HESS J1825−137 [8], (5) G0.9+0.1 [52], (6) G21.5−0.9 [49], and (7) 3C58 [16,58]

Any PWN has a terminating radius $\theta_{\rm PWN}$, which pushes against the SNR ejecta, swept-up gas or ISM. This edge is usually seen in radio (if the PWN is also detectable in radio), because the lifetime of radio synchrotron emitting electrons is longest and they survive in the oldest expanding volume at the radial distance $\theta_{\rm PWN}$. Suppose we define the angular radius $\theta_{1/2}$, with $\theta_s < \theta_{1/2} \leq \theta_{\rm PWN}$, as that radius where $\Gamma_X = \Gamma_s + 0.5$ is reached. We then define the energy dependent scaled cooling radius as

$$\xi_{1/2} \equiv \frac{\theta_{1/2}}{\theta_{\rm PWN}}, \qquad \text{where} \qquad \frac{d\xi_{1/2}}{dE_e} < 0. \tag{17.16}$$

The scaled radius $\xi_{1/2}$ should thus decrease towards increasing electron energies E_e. Although this is well-known, there is little experimental data to support this: Detectors with good angular resolution to resolve PWN also have limited bandwidth (typical 0.5–10 keV), but if the statistics are good enough, observers should consider splitting the data into two energy bands of equal statistics to identify a possible shift in $\xi_{1/2}$ between the two energy bands.

In the Sect. 17.7 we will review the HESS detection of the PWN G18.0−0.7 = HESS J1825−137 associated with the Vela-like pulsar PSR B1823−13, which clearly shows a similar steepening of the photon index with radius.

17.6 Pleres Pera or "Filled Bags"

The most fundamental principle in PWN flows is that the pulsar wind slows down from relativistic to relatively low expansion velocities as a result of the confining pressure. This slow down typically occurs after the pulsar wind has been shocked at some distance R_s from the pulsar (see e.g., [43]). The decelerating post shock ($r > R_s$) pulsar wind flow velocity $\mathbf{V}$ would typically be radial, i.e., $\mathbf{V} \sim V_r \mathbf{e_r}$. Furthermore, the associated magnetic field at $r > R_s$ would be described by the equation (see, e.g., [43])

$$\nabla \times (\mathbf{V} \times \mathbf{B}) \sim 0, \tag{17.17}$$

in which case $\mathbf{B} \sim B\mathbf{e}_\perp$: The field direction would also be approximately perpendicular relative to the radial flow direction. The reader is probably familiar with the Chandra image of the Crab Nebula and other X-ray plerions, showing exactly the toroidal (azimuthal) structures implied by this vector equation.

Given this introduction, we now raise two questions: (1) Is it possible for a high energy particle to overtake this convective flow as a result of diffusion? (2) Under which conditions would it be possible for such a particle to escape through the boundary of a PWN? We will therefore compare radial diffusion vs. radial convective flow, where the diffusion is *perpendicular* to the (e.g., toroidal) magnetic field line.

The most general form of the perpendicular diffusion coefficient is given by

$$\kappa_\perp = \frac{1}{3}\lambda_\perp c\,, \tag{17.18}$$

where $\lambda_\perp$ is the mean free path for scattering in a direction which is perpendicular to the field line direction (i.e., cross field diffusion). The case we consider here therefore corresponds to diffusion in the radial direction relative to the pulsar. We parameterize this quantity further by writing it as a factor f times the particle gyro-radius ρ_L, so that

$$\lambda_\perp = f(\Omega\tau)\rho_L\,, \tag{17.19}$$

where Ω is the particle gyrofrequency and τ is the mean time between scatterings. The Bohm limit corresponds to $\Omega\tau \sim 1$ and $f(\Omega\tau) = 1$. Assuming hard sphere scattering, it can be easily shown for both weak scattering ($\Omega\tau \ll 1$) and strong scattering ($\Omega\tau \gg 1$) that $f(\Omega\tau) \ll 1$ [59]. Thus, under the assumption of hard sphere scattering, the mean free path against diffusion perpendicular to a field line is always less or equal to the particle gyro-radius. This is intuitively expected: It is difficult for charged particles to cross field lines - a principle we have learned from undergraduate days!

Scaling a PWN to a distance of $d = 1 d_{\rm kpc}$ kpc with an age of $\tau = 20$ kyr and an associated field strength of $B = 3\,\mu$G, we arrive at an angular spread due to diffusion of VHE electrons scattering CMBR photons in the Thomson limit to VHE γ-rays of energy $E_{\rm TeV}$ (from 17.2)

$$\theta_{\rm diff}(e^{\pm}) = 0.07^{\circ} d_{\rm kpc}^{-1} \left[\left(\frac{f(\Omega\tau)}{0.1}\right)\left(\frac{3\,\mu{\rm G}}{B}\right)\left(\frac{\tau}{10\,{\rm kyr}}\right)\right]^{1/2} E_{\rm TeV}^{1/4}. \tag{17.20}$$

Thus, the toroidal field line structures in PWN tend to contain relativistic particles much better than would have been the case if the field line structures had radial components, in which case the parallel diffusion coefficient is relatively large ($\lambda_{||} \gg \rho_L$). In the latter case much larger cosmic ray type diffusion coefficients would have been appropriate as employed by [9] for PSR B1706−44, so that relic charged particles accumulated over the source lifetime would have escaped much more easily from the convective plasma, with the latter reflected by the radio morphology.

We therefore conclude that PWN act as well-contained "filled bags" (or pleres pera in Ancient Greek) with high integrity against diffusion losses over Vela-like lifetimes. Such sources will expand convectively until the PWN pressure becomes small enough so that particles start to leak into the interstellar medium. The same principle is also expected to hold for ultra-relativistic ions injected into the PWN over the lifetime of the PWN: If E_i is the total energy per ultra relativistic ion with charge X, the spatial ion spread due to diffusion alone is then

$$\theta_{\rm diff}({\rm ion}) = 0.05^{\circ} d_{\rm kpc}^{-1} \left[\left(\frac{1}{Z}\right)\left(\frac{f(\Omega\tau)}{0.1}\right)\left(\frac{3\,\mu{\rm G}}{B}\right)\left(\frac{\tau}{10\,{\rm kyr}}\right)\left(\frac{E_i}{10\,{\rm TeV}}\right)\right]^{1/2}. \tag{17.21}$$

If we claim that several of the unidentified filled-center HESS sources near Vela-like pulsars in the galactic plane are PWN, diffusion would spread them by undetectable amounts (given the HESS angular resolution of $\sim 0.07^{\circ}$) relative to convective sizes $\theta_{\rm PWN}$. For example, scaling the $\sim 2^{\circ}$ convective size of the Vela X PWN to a distance of 1 kpc gives $\theta_{\rm PWN} = 0.3^{\circ} d_{\rm kpc}^{-1}$, which is large compared to the diffusive size.

17.7 HESS J1825−137 and the "Three Princes of Serendip"

The serendipitous discovery of the source HESS J1825−137 as part of the Galactic plane HESS survey [3] serves as a good example of the correct use of the word serendipity as coined by Horace Walpole in the eighteenth century, based on the old Persian tale of the "Three of Princes of Serendip". In this story the rewards did not come at the time of discovery, but only later. We will also identify three main discoveries following the collection of sufficient statistics on this source.

The first HESS observations of this region occurred as part of a systematic survey of the inner Galaxy from May to July 2004 (with 4.2 h of exposure within 2° of HESS J1825−137). Evidence for a VHE γ-ray signal in these data triggered re-observations from August to September 2004 (5.1 h), resulting in a significance of 13σ. This led to the announcement by the HESS Collaboration [5] of a possible association of this source with the Vela-like pulsar PSR B1823−13 and its associated PWN G18.0−0.7 as identified in X-rays by [32].

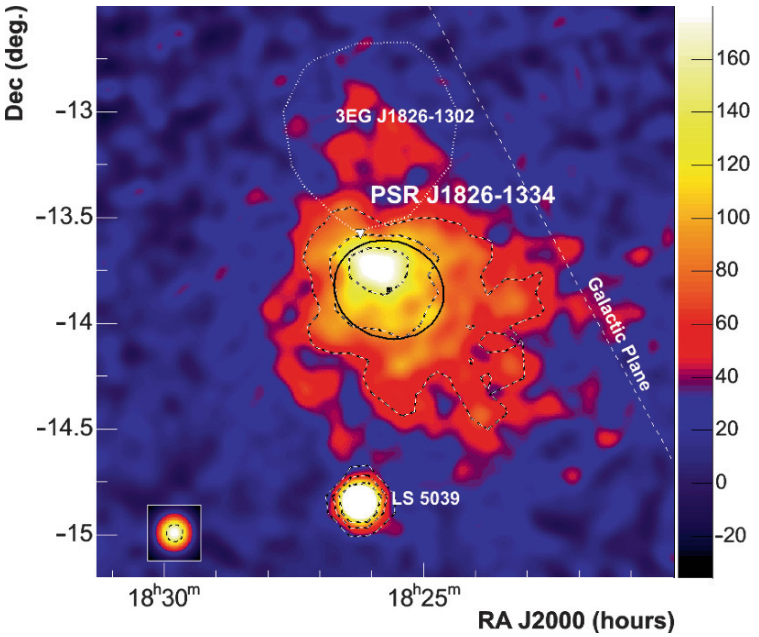

Fig. 17.2 Acceptance-corrected smoothed map of HESS J1825−137 [8] showing the extended emission relative to PSR B1823−13 = PSR J1826−1334. The *dotted line* indicates the 95% confidence contour of the unidentified EGRET source 3EG J1826−1302. The point source at the bottom corresponds to the microquasar LS 5039. (Figure from [8])

Further observations during 2005 resulted in improved statistics to study the energy dependent morphology [8]. One of the main reasons for this was to get full orbital coverage on the source LS 5039 as seen in Fig. 17.2. The total lifetime then increased to 52.1 h with a significance of 34σ.

The three main discoveries with respect to HESS J1825−137 are the following:

17.7.1 The Anomalously Large Size of HESS J1825−137 and Its Implied SNR Shell

Since the X-rays already show the effect of full cooling from a photon index of $\sim$1.6 to $\sim$2.3 (Fig. 17.1) within a distance of $\sim$5 arcmin from the pulsar [32], we would expect that the X-ray PWN G18.0−0.7 already reached it terminal size. If this is not the terminal size, further cooling well beyond 5 arcmin should then result in $\Gamma_X \gg 2.3$ as discussed in Sect. 17.3 accompanied by the loss of X-ray statistics.

The VHE γ-ray size is however $\sim 1^\circ$ as seen from Fig. 17.1, which is much larger than G18.0−0.7 and the anomalously large size of the pulsar wind nebula can be explained if the pulsar PSR B1823−13 was born with a relatively large initial

spin-down power and braking index $n \sim 2$, provided that the SNR expanded into the hot ISM with relatively low density ($\sim 0.003\,\mathrm{cm}^{-3}$). This pulsar is a 101 ms evolved pulsar with a spin-down age of $T = 2.1 \times 10^4$ years for an assumed braking index of $n = 3$ [19] and in these properties very similar to the Vela pulsar. It is located at a distance of $d = 3.9 \pm 0.4$ kpc [20].

The average VHE γ-ray radius of the PWN of $\sim 0.5^\circ$ corresponds to $R_\gamma = 35 d_4$ pc for a distance of $d = 4 d_4$ kpc. Since the observed ratio of SNR forward shock radii to PWN radii are all a factor 4 or larger [60], the expected SNR forward shock radius $R_{\mathrm{SNR}} > 140 d_4$ pc, making this one of the largest expected SNR in our galaxy. De Jager et al. [24] derived a constraint on this forward shock radius, which can be stretched to a value of

$$R_{SNR} = (120\,\mathrm{pc}) \left(\frac{E_{SN}}{3 \times 10^{51}\mathrm{erg}} \frac{0.001\,\mathrm{cm}^{-3}}{N} \right)^{0.2} \left(\frac{1}{n-1} \right)^{0.4}. \tag{17.22}$$

Finally, returning to the question about the apparent discrepancy between the VHE and X-ray sizes: We can achieve the observed ratio of 1° (VHE) relative to 5 arcmin (X-rays) easily in a low-B environment (with $E_{\mathrm{TeV}} \sim 0.3$ and $E_{\mathrm{keV}} = 1$) if we adopt the equation for conservation of magnetic flux in spherical coordinates (assuming the steady state solution, giving $RVB = \mathrm{const}$), and that the radius R is equal to the expansion velocity V times radiation lifetime. This would give a field strength in the outer VHE nebula, which is about three times smaller than the field strength in the smaller X-ray nebula. In fact, we do need a small field strength in the outer nebula to allow VHE emitting electrons to survive while producing a VHE spectral break as observed. The latter will also be covered in this review.

17.7.2 The Offset PWN in X-Rays and VHE γ-Rays

At the time of the X-ray discovery of G18.0−0.7, it was found that whereas the uncooled X-ray compact nebula is symmetric around the pulsar, the extended cooled nebula is offset to the south. To explain this offset, [32] introduced the reverse shock explanation of [14] for Vela X, where hydrodynamical simulations have shown that SNR expansion into an inhomogeneous medium would result in a reverse shock returning first from the region of higher density. After crushing the PWN, the latter is offset from its original position, resulting in a new center of gravity. We also observe that the entire VHE image is shifted relative to the pulsar (Fig. 17.2) and the same explanation for HESS J1825−137 was also offered by us in [5].

By extending a line from this shifted VHE center of gravity through the pulsar, [45] discovered a molecular cloud in CO at a distance from earth, which is consistent with the dispersion based distance to the pulsar. This means that the SNR forward shock most likely struck this cloud, resulting in a reverse shock returning first to the expanding PWN of PSR B1823−13, which then resulted in a predictable offset direction for the VHE center of gravity.

Since this process takes of the order of 3–10 kyr to offset a PWN, we can expect several Vela-like PWN (with ages older than 10 kyr) to be offset in VHE γ-rays, since SNR expansion is always expected to take place in an inhomogeneous medium (i.e., the ISM is rarely expected to be homogeneous).

17.7.3 Energy Dependent Morphology and the Cooling Break

(a) Spectral Steepening away from the Pulsar

The most astonishing discovery of this source (given the extended statistics) was the discovery of a steepening spectrum as a function of increasing distance from the pulsar as described in [8] as shown on the left side of Fig. 17.3, where we see the photon index in intervals of 0.1° (along the sector of brightest emission) increasing from 1.9 ± 0.1 to 2.4 ± 0.1 at the outer part. The corresponding surface brightness for the same slice/sector is shown in the right-hand panel of Fig. 17.3 and note the peak at a distance of 0.15° from the pulsar. We will revisit this feature below.

We can clearly see the energy dependence of the surface brightness with radius if we take the power law fits corresponding to each radial interval (from [8]) and calculate the relative surface brightness for energies chosen within the energy limits of the power law fits. The results are shown in Fig. 17.4. Note that these relative surface brightness plots therefore represent smoothed averages over energy, whereas the radial scale remains uncorrelated.

In this plot we can see that the size of the source shrinks with increasing energy and that the peak surface brightness (corresponding to the shifted PWN due to the effect of the reverse shock) in Fig. 17.3 is located at a radius of $\theta_{\rm peak} \sim 0.2^\circ$ from the

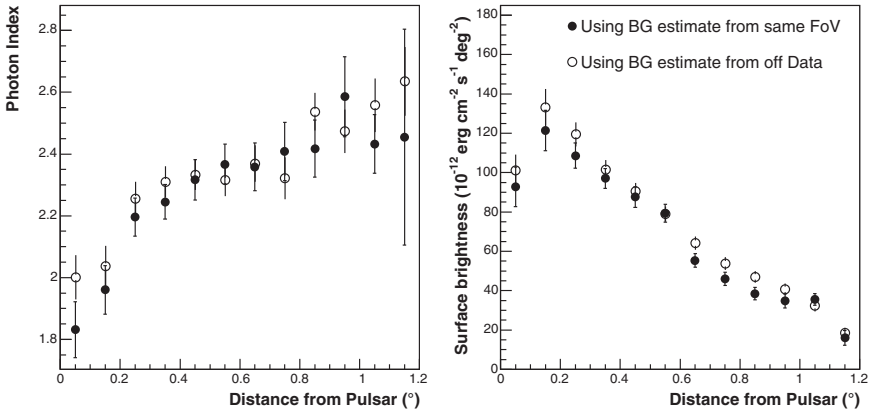

Fig. 17.3 *Left*: Photon index vs. radius along the sector of brightest emission from the pulsar as defined by [8]. *Right*: Relative surface brightness (all energies) corresponding to the *left panel*

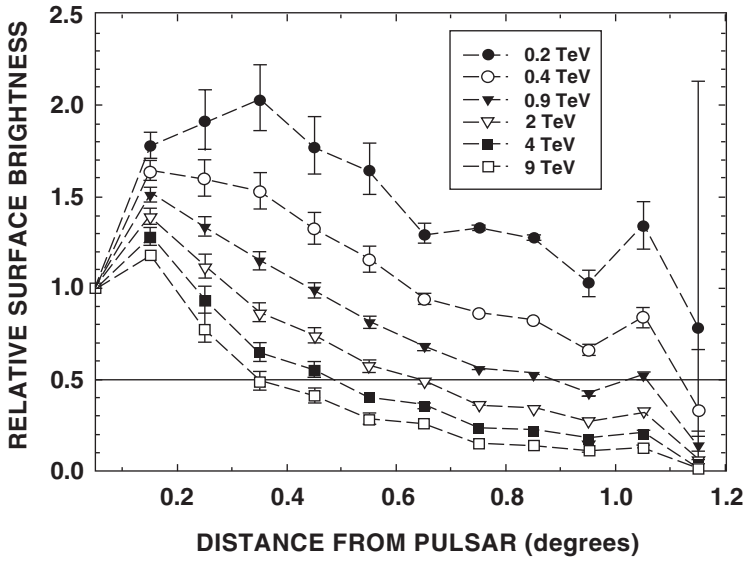

Fig. 17.4 Relative surface brightness vs. distance from the pulsar for energies between 0.2 and 9 TeV as indicated in the legend. The relative brightness along the energy scale is correlated (because these points and their errors were derived from power law fits to individual radial slices), whereas it is uncorrelated along the radial scale

pulsar for $E_\gamma \sim 0.2$ TeV in Fig. 17.4. This peak however shifts towards the pulsar for increasing energies (i.e., $\theta_{\rm peak} \leq 0.1^\circ$ for $E_\gamma > 0.9$ TeV). Also, the relative surface brightness drops below the 50% level only for $E > 0.9$ TeV.

With this clear evidence of an energy-dependent morphology we also show the first color image in the history of Gamma-Ray Astronomy (Fig. 17.5): Defining the three basic colors RGB as $\mathrm{R} \equiv [E_\gamma < 0.8\,\mathrm{TeV}]$, $\mathrm{G} \equiv [0.8\,\mathrm{TeV} < E_\gamma < 2.5\,\mathrm{TeV}$ and $\mathrm{B} \equiv [E_\gamma > 2.5\,\mathrm{TeV}]$, we could combine these colors in a single colour image showing the extended red image, which shrinks with increasing energy towards the blue nebula above 2.5 TeV close to the pulsar. Note that the point source LS 5039 shows up as a white image because of its broad band nature and the fact that it is a point source.

We are now also in a position to compare the scaled cooling radii $\xi_{1/2}$ (17.16) between X-rays and VHE γ-rays: For X-rays $\xi_{1/2} \sim 5'/1^\circ \sim 0.1$, whereas $\xi_{1/2} \sim 1$ as measured by HESS Thus, clearly $d\xi_{1/2}/dE_e < 0$ as required by (17.16), where E_e is the electron energy, which is higher for X-rays than for VHE γ-rays, as required by (17.2) and (17.1) for a relatively low magnetic field strength as motivated above. Furthermore, since $\xi_{1/2}$ is already close to unity for the VHE (IC) domain, we expect that $\xi_{1/2}$ should become undefined for the GLAST (IC) domain since the electron lifetime will become longer than the age of the system for all positions in the PWN – similar to the radio emission in the Crab Nebula below the spectral break of 10^{13} Hz, which does not show any cooling effects anymore.

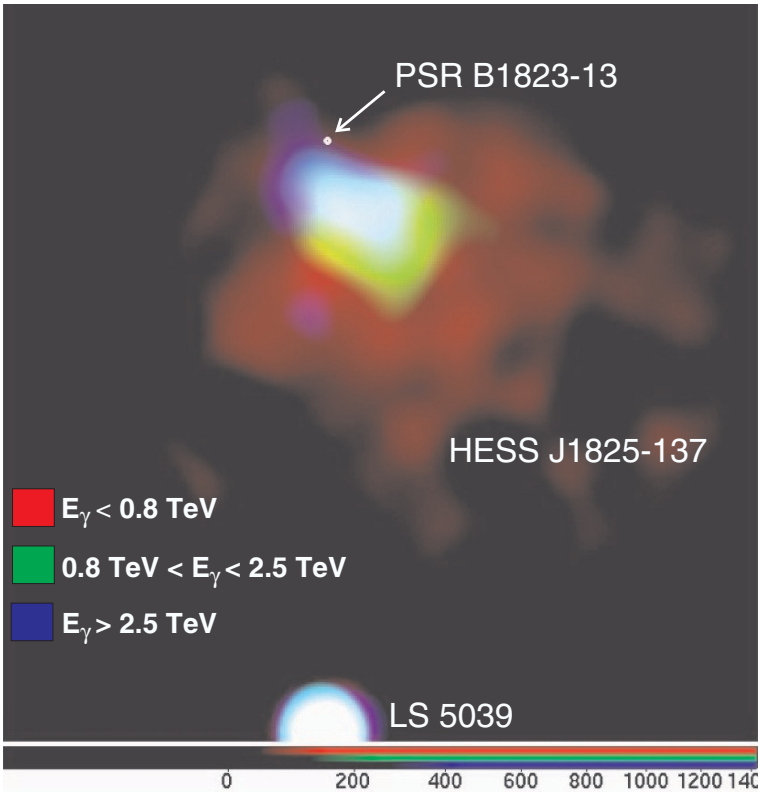

Fig. 17.5 First color image in the history of Gamma-Ray Astronomy showing the energy dependent morphology resolved in the three basic colors as indicated in the legend. The white point source at the bottom is the μ-quasar LS 5039. Produced by S. Funk and O.C. de Jager for the HESS Collaboration

(b) The Cooling Break in the Total Spectrum

The above mentioned behaviour is also summarised when we plot the total spectrum of HESS J1825−137 as shown in Fig. 17.6, where we see that this photon spectral index steepens from ∼1.9 to ∼2.6 as expected for a cooling break. It is important to measure this cooling break, since we can then determine the average nebular field strength of the PWN, independently from a comparison of synchrotron and IC brightnesses, for which we do not have comparative data corresponding to the same electron energies. There are two problems if we attempt to "read" this break energy E_b from the energy spectrum as shown in Fig. 17.6: (a) We do not know what the convergent (uncooled) photon spectral index below the HESS range is, although this should be reflected by the synchrotron photon index (∼1.6) of the uncooled electrons near the PWN shock. Therefore, most likely the electron spectral index for this domain is around 2.2. (b) Klein–Nishina effects due to dust IR photons tend to steepen spectra with increasing photon energy as described by [26] for such PWN.

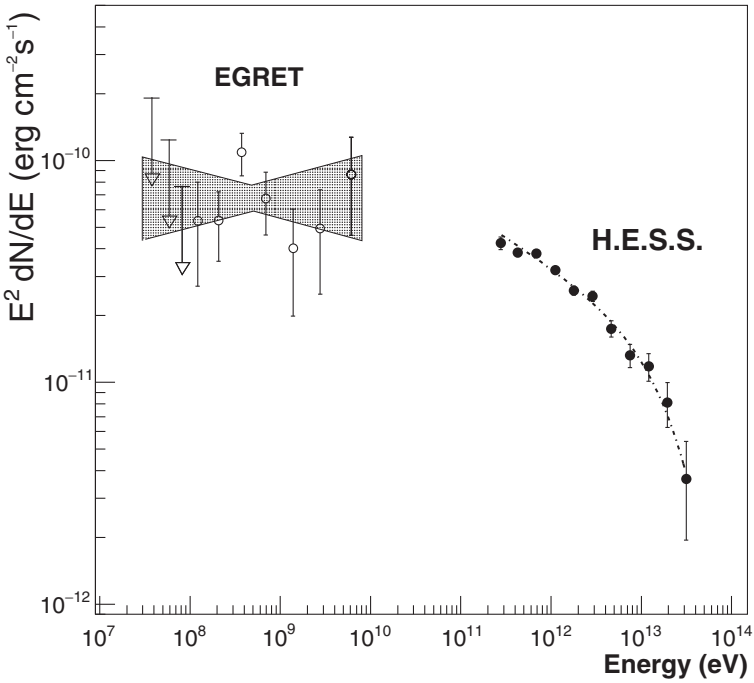

Fig. 17.6 The photon spectra of HESS J1825−137 and the nearby source 3EG J1826−1302 (multiplied by E^2) showing the curvature in the spectrum of HESS J1825−137 [8]

A more accurate procedure would then be either through direct modeling as done by [45] for HESS J1825−137, or, simply through fitting a two component electron spectrum scattering the CMBR and dust IR photons and rewriting the expressions for the cooling break directly in terms of the electron spectral break energy. Fortunately the estimate for the nebular field strength depends weakly on E_b as discussed below:

The anomalously large size of the unseen SNR forward shock radius is best met if the pulsar braking index n is closer to 2 than 3, giving a pulsar spin-down age

$$T_p = (40\,\mathrm{kyr})\left(\frac{1}{n-1}\right), \tag{17.23}$$

which is closer to 40 kyr, rather than the canonical 20 kyr. It is possible to probe the field strength in most of the PWN volume by solving the expression

$$-\int_{E(\max)}^{E} \frac{dE_e}{(dE_e/dt)_s + (dE_e/dt)_{\mathrm{IC}}} = T_p \tag{17.24}$$

for the electron energy E_e, where we include both synchrotron and inverse Compton losses [15]. In this case electrons injected with the maximum energy $E_e(\max)$ at the

PWN shock during the earliest epochs (when the spin-down power was a maximum, see Sect. 17.3), move with the outer edge of the PWN. While losing most energy in the PWN, they must still be able to radiate VHE photons with energy at least $\sim$4 TeV to account for the highest energy spectral point at a distance of $\sim 1^\circ$ from the pulsar as shown in Fig. 4 of [8].

For inverse Compton energy losses on the 2.7 K CMBR we include a Klein–Nishina suppression factor (relative to the Thomson limit) of $2/3$ in the HESS range [8]. By setting the spin-down age equal to the total radiation lifetime of VHE γ-ray emitting electrons, we can write the electron energy in terms of the VHE γ-ray energy (17.2) to give the observed spectral break energy of $E_b \sim 2.5$ TeV [45], which is observed as a steepening in Fig. 17.6:

$$E_b = \frac{(6.2\,\mathrm{TeV})(n-1)^2}{[1+0.144(B_{\mu\mathrm{G}})^2]^2}\,. \tag{17.25}$$

Thus, for $n = 2$ ($T = 40$ kyr age) and a $B \sim 2\,\mu$G field, the VHE γ-ray break would be around 2.5 TeV, whereas for $n = 3$ (i.e., a $T = 20$ kyr age), the required field strength would be 3.9 μG. Whereas [45] found the abovementioned break energy from broad band modeling of HESS J1825$-$137, GLAST should be able to measure the uncooled spectral index at γ-ray energies $E_\gamma \ll E_b$, which will allow us to constrain E_b more accurately in future.

17.7.4 Conclusion: A Particle Dominated Wind in HESS J1825−137

With both the spectral break around a TeV and the survival of $\sim$5 TeV emitting electrons to the edge of the PWN, it is clear that we require a magnetic field strength $B < 3\,\mu$G in the extended nebula. Such a low field strength also supports the relatively low observed X-ray to VHE γ-ray luminosity. A detailed treatment of this is however beyond the scope of this paper.

A concern which may be raised from a lay perspective: We know that the field strength in the ISM is about 3 μG or more, then why do we get an apparent field strength below this value?

The total pressure in the PWN is the sum of the magnetic pressure plus particle pressure, and we can already derive the total particle pressure from the electron spectrum responsible for the HESS signal: de Jager [23] derived the pulsar pair production multiplicities from the HESS data alone, as well as an upper limit by extrapolating the HESS spectrum along the harder uncooled pre-break $e^+ - e^-$ spectrum with an index of $\sim$2 down to $E_0 \sim 1$ GeV [23]. The total energy in electrons in the HESS range is $\sim 10^{48}$ erg, but if we take the total energy down to E_0 also into account, the total energy would be $E_\pm \sim 8 \times 10^{48}$ erg. This would have required a pulsar birth period $2\pi/\Omega_0 = P_0 < 50$ ms to give a total rotational kinetic energy of $0.5 I \Omega_0^2 > E_\pm$.

The total energy density in leptons is then $U_e \sim (1\,\mathrm{eV\,cm^{-3}})d_4^{-3}$ for a PWN radius of 0.5°. The accuracy of this number is expected to improve when GLAST observations are added, which should measure the spectral hardening well below the break with better accuracy. The energy density in a $B = 2\,\mu\mathrm{G}$ PWN field is $U_B = (0.1\,\mathrm{eV\,cm^{-3}})(B/2\,\mu\mathrm{G})^2$. Thus, to a first order we find that $U_e \sim 10U_B$, so that:

- The PWN of HESS J1825−137 is particle dominated with lepton energy density about 10 times the field energy density, thus adding this PWN to the [18] list of particle dominated winds.
- The pressure U_e still appears to be significant to press against the ISM medium, which resulted in the anomalously large PWN as observed today.

17.8 Vela X: The Prototype for Evolutionary Studies

Vela X, the bright flat spectrum radio component of the Vela SNR served as the prototype PWN for evolutionary studies [63]. The offset of the radio nebula to the south of the pulsar had Astronomers doubting if this association is real, until ROSAT discovered a cocoon of X-ray emission, also extending south of the pulsar, and aligned with a bright radio filament in Vela X [50]. The length of both features to the south is ∼45′. More revealing was that even though this is one of the brightest polarised radio filaments, the degree of polarisation is low (∼15–20%). The reason for this is the presence of thermal material mixed into the plasma of highly relativistic particles [50]. A natural explanation for this two-fluid mixing and offset to the south was offered by [14] for Vela X: The reverse shock returning from a denser ISM offsets the PWN to the south while forcing this two-fluid mixing. Further evidence for this mixing came from the combined ASCA/ROSAT analysis of the bright cocoon (radio filament) region by [48] which shows evidence of mixing of a non-thermal component with photon index of ∼2 with a thermal component. Analyses by [42] with new ASCA results, as well as *XMM-Newton* observations of the cocoon of Vela X also confirmed this two-component spectrum [44].

17.8.1 HESS Detection of the Vela X "Cocoon": Radio and X-Ray Correlation

The High Energy Stereoscopic System of telescopes observed the Vela region and discovered a structure resembling the Vela X cocoon in X-rays [6] as shown in Fig. 17.7. The relative sizes however differ significantly: Whereas the size of the X-ray cocoon is $45 \times 12\,\mathrm{arcmin^2}$, the corresponding VHE cocoon size is $58 \times 43\,\mathrm{arcmin^2}$.

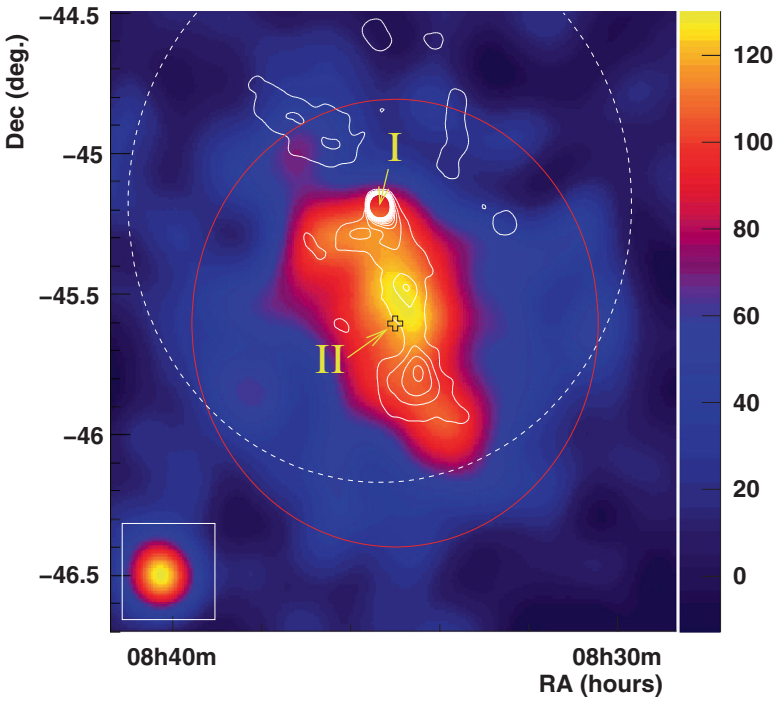

Fig. 17.7 Gaussian smoothed sky map of region surrounding Vela pulsar, showing significant emission to the south of the pulsar position, coincident with an X-ray feature seen by ROSAT PSPC (*white contours*). The *solid circle* represents the HESS integration region for the spectral measurement, while the *dashed circle* represents the field of view for the ROSAT observations. (From [6]; see also this paper for more details)

To complete the multi-wavelength comparison, we also compare the VHE detection with the radio map: Fig. 17.8 shows an overlay of the HESS γ-ray contours on the 8.4 GHz radio map of Vela X [37, 50], showing that the γ-ray map does overlap with the bright radio filament, which in turn overlaps with the X-ray cocoon as remarked by [50]. The latter author made the following observation based on the [54] model: The radio filaments are the result of Rayleigh Taylor instabilities in the SNR expansion. We conclude further that these filaments were also offset to the south of the pulsar by the early reverse shock. If the γ-ray signal is then due to hadronic interactions with this thermal gas, we would also expect to see a correlation between the γ-ray and filamentary structures.

The approximate full size of the Vela X PWN is $\sim 3^\circ$ in RA and $\sim 2^\circ$ in DEC as seen from a $8^\circ \times 8^\circ$ HartRAO radio map of the Vela region at 2.3 GHz by Jonas (2006, personal communication). Note that the status of VHE γ-radiation from Vela X as a whole was not discussed by [6], although this total flux cannot be much larger than that from the VHE cocoon itself. We can then summarize the morphological multi-wavelength properties of the cocoon detection as follows:

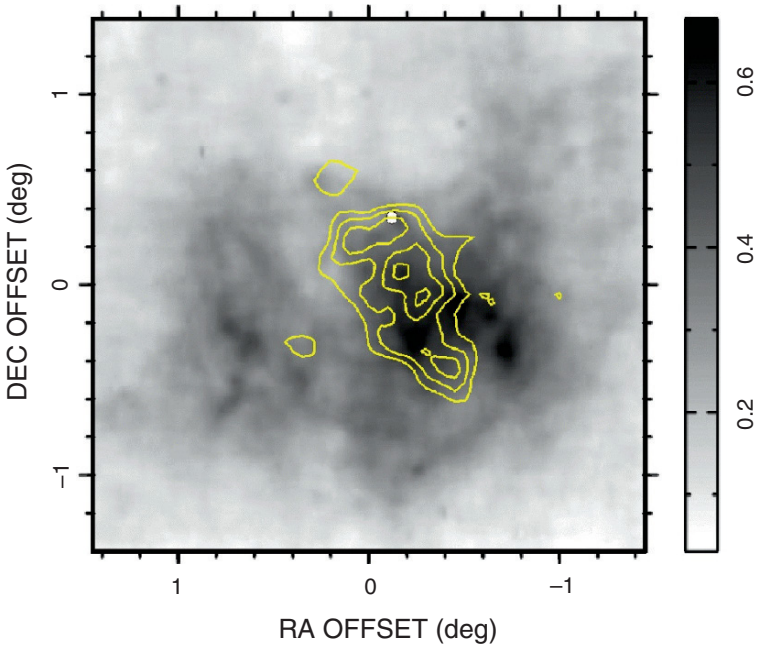

Fig. 17.8 Destriped radio image of Vela X at 8.4 GHz in grey-scale [37] with the HESS map in Fig. 17.7 converted to contours, overlayed in *yellow*. The pulsar position is marked by a *white circle*. The origin (zero point) of this image is (RA,DEC) = (129.02°,−45.54°) (J2000), which is different from the origin defined by [37]

- The volume of the VHE γ-ray cocoon is $\sim$5% relative to the total volume of Vela X.
- The cocoon contains both a non-thermal and thermal component, which is indicative of a reverse shock mixing gases of adiabatic indices $\gamma = 4/3$ and 5/3 during the crushing phase.
- The offset of the cocoon to the south of the pulsar is explained by the reverse shock crushing the PWN to the south (see next section).
- The position angle (P.A.) of the VHE γ-ray cocoon (41 ± 7 degrees, measured from north through east) is similar to that of the X-ray cocoon orientation (see next section).
- The X-ray cocoon overlaps in position with a bright radio filament, although there are other similarly bright radio filaments further to the west without any X-ray or VHE γ-ray counterparts.
- Deeper, but wide FoV VHE observations of the entire Vela X structure shown in Fig. 17.8 should indicate if there are γ-rays with lower surface brightness compared to the bright cocoon region.

17.8.2 Constraints on the Cocoon Field Strength from the Upper Synchrotron Cutoff Energy

Since the cocoon has been shifted to the SW of the pulsar by the reverse shock, the highest energy electrons mixed in the thermal gas in the cocoon provide a powerful diagnostic of the age since shift and associated field strength. Markwardt and Ögelman [48] measured a power law component up to at least 7 keV from the cocoon area. Horns et al. [42] and LaMassa et al. [44] also confirmed this two-component composition with ASCA and XMM-Newton observations respectively.

This means that ultra-relativistic electrons and thermal gas were mixed during the reverse shock crushing phase and with the offset PWN, the relativistic component is removed from its pulsar source, so that the upper spectral cutoff energy moves down in energy with time, without any source of replenishment. From Fig. 3 of [42], it is clear that this cutoff is currently $\sim$10 keV. The electrons radiating at this cutoff are not replenished by the Vela pulsar, since they have already been removed from the pulsar over a time interval $T - T_c$, which represents the time between the southward shift of the PWN from the pulsar (at time T_c) and the present time T. These 10 keV emitting electrons were also the highest energy electrons accelerated by the PWN shock at the epoch T_c when the reverse shock started to crush the PWN. For such high energy electrons, IC scattering would be in the extreme Klein–Nishina limit, so that we only consider synchrotron losses, giving the time interval between the time of crushing and the present time of

$$T - T_c = (2.3\,\mathrm{kyr}) \left(\frac{3\,\mu\mathrm{G}}{B} \right)^{3/2} \left(\frac{10\,\mathrm{keV}}{E_X(\mathrm{max})} \right)^{1/2} . \tag{17.26}$$

For Vela X [14] calculated $T_c \sim 3$ kyr, whereas 2-D time dependent MHD simulations for the Vela SNR shows that the reverse shock was expected to reach the pulsar position around 5 kyr after the birth of the pulsar. Thus, a field strength around 3 μG (or smaller) in the cocoon of Vela X is required to allow 10 keV synchrotron emitting electrons to survive between the time of crossing of the reverse shock and the present epoch. If the field strength was 10 μG or larger (as required by [42]) these electrons had to be shifted within 400 yr, which is unlikely to be achieved given any realistic reverse shock parameters.

17.8.3 Diffusion of VHE Particles from the Cocoon

Horns et al. [42] considered the problem of diffusion of X-ray synchrotron emitting electrons away from the X-ray cocoon, stating that a high field strength is required to contain the ultra-relativistic electrons in the 45×12 arcmin^2 cocoon. Assuming that the cocoon is still expanding under its own pressure, a perpendicular field component is expected to be maintained by virtue of (17.17), so that (17.19) with $f \ll 1$ for $\Omega\tau \ll 1$ or $\Omega\tau \gg 1$ is expected to hold, which protects the integrity of this PWN

against diffusive escape. Replacing the time $T - T_c$ with (17.26) in the diffusion equation, the electron energy cancels, so that the angular spread due to diffusion at a distance of $d = 0.3\,\mathrm{kpc}$ can be written as

$$\theta_{\mathrm{diff}} = 0.5^\circ \left(\frac{f}{0.1}\right)^{1/2} \left(\frac{3\,\mu\mathrm{G}}{B}\right)^{3/2} . \tag{17.27}$$

With a minimum X-ray cocoon dimension of 0.2°, it is clear that we have to set $f < 0.02$ for $B = 3.3\,\mu\mathrm{G}$, which places a restriction on the scattering parameter $\Omega\tau$ based on hard-sphere scattering [59].

17.8.4 No "Missing" Leptonic Component in Vela X

Horns et al. [42] suggested that there is a missing leptonic component in Vela X. Whereas this is true for the cocoon, the actual volume of the Vela PWN (called "Vela X") is about 20 times larger than the size of the cocoon as seen in VHE and to get the total energy in leptons, we have to take the bolometric spectrum from the total Vela X, which is one of the brightest radio nebulae in the sky. Using the radio spectrum of Vela X, [23] found that the total lepton energy in the radio nebula is $W_e = 6.2 \times 10^{47}\,\mathrm{erg}$ (for $B = 10\,\mu\mathrm{G}$) or $3.8 \times 10^{48}\,\mathrm{erg}$ ($B = 3\,\mu\mathrm{G}$), giving respective conversion efficiencies of $W_e/(0.5I\Omega_0^2) = 5\%$ and 30% for a birth period of 40 ms [60]. Thus, there does not appear to be a "missing" leptonic component and it is clear is that most lepton energy has been processed in the low energy leptonic domain. However, there are also observational lower limits to the Vela X averaged field strength: Using EGRET upper limits, [28] have shown that we can already constrain the volume averaged field strength to $<B>> (4\,\mu\mathrm{G})(\nu_b/10^{11}\,\mathrm{Hz})^{0.4}$ where ν_b is the unknown radio spectral break frequency. GLAST/LAT observations should either detect this radio counterpart of Vela X, or, provide more stringent lower limits on $<B>$. This also calls for a separate study on variations in B: How does B in the cocoon differ relative to $<B>$, given the presence of filaments in the PWN as well as the filling factor question?

17.8.5 The HESS Signal: Hadrons or Leptons?

In the previous two sections we have shown the field strength in the cocoon must be relatively low for X-ray emitting electrons to survive at the southern tip of the cocoon, which would argue for an IC origin. This also implies a limit on the scattering parameter $\Omega\tau$ for containment against diffusion through a weak perpendicular field. We have no theory to predict this number, but future research on turbulence theory may be able to make some predictions.

Another potential problem with a hadronic interpretation is the following: With the high required ion energy budget of 10^{48} erg (iron) to 10^{49} erg (protons) in the VHE cocoon, [42] invoked the early epoch of pulsar output to account for the observed γ-ray flux via hadronic interactions. However, protons ejected during such early epochs (and convected by the pulsar wind) should fill the total (old) radio emitting Vela X PWN and not just the smaller (and younger) cocoon. Thus, the total energy budget in Vela X implied by the HESS detection will then be (to a first order) 20 times larger than calculated for the cocoon: $\sim 2 \times 10^{49}$ erg (for iron) to 2×10^{50} erg (for protons). Furthermore, [60] estimated a birth period of $P_0 \sim 40$ ms for the Vela pulsar to account for the observed classical ratio of PWN radius to SNR radius of 0.25. The total integrated kinetic energy provided by the pulsar since birth is then $0.5 I \Omega_0^2 = 1.2 \times 10^{49}$ erg, which means that we may have a conversion efficiency of $>100\%$ of spin-down power to ions in Vela X. Thus, the VHE signal is more likely to be of leptonic than hadronic origin.

17.8.6 The VHE γ-Ray Spectral Break in the Vela X Cocoon

If we assume that the HESS signal is due to IC scattering on the CMBR in a relatively weak field of $B \sim 3\,\mu$G, then we should be able to predict the cooling break as that energy where radiation losses become comparable to the age of the PWN/SNR. This may then explain the spectral break in Fig. 17.9: In this case (17.25) would predict a VHE γ-ray spectral break energy of $E_b \sim 12$ TeV for such a field strength,

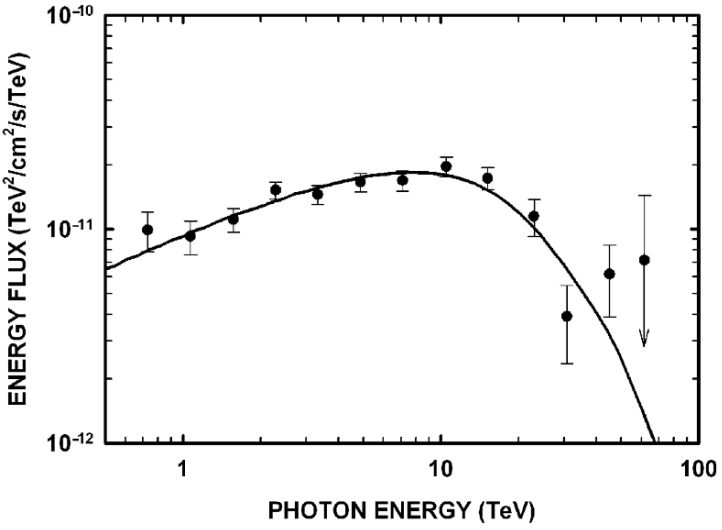

Fig. 17.9 Energy spectrum of the Vela X cocoon as measured by HESS [6], with integration area shown in Fig. 17.7. The *solid line* represents a fit assuming an inverse Compton origin as specified in the text

given a total age of 11 kyr. Note that this break energy E_b evolves downward in energy with time, and if we assume that the cocoon field strength did not change significantly over the past few thousand years, the break energy is predicted to be

$$E_b = \frac{(15\,\mathrm{TeV})}{[1+0.144(B/3\,\mu\mathrm{G})^2]^2}\left(\frac{11\,\mathrm{kyr}}{T}\right)^2. \tag{17.28}$$

Note also that Fig. 17.9 represents *the first detection of a spectral maximum in VHE γ-ray Astronomy*, which allows this clear measurement of a spectral break energy.

17.9 Summary

In this review paper of pulsar wind nebulae (as seen by HESS), we attempted to interpret the observed properties within a unified framework: We first reviewed the known properties of PWN as derived over many years from radio, IR, optical and X-ray observations. We then introduced new properties which are expected to make PWN bright high-energy to VHE γ-ray sources: For example, if the energy density in the soft radiation field (acting as target for IC scattering) dominates the energy density of the magnetic field, electron energy losses would be dictated by the IC rather than the synchrotron process. This principle is demonstrated when we compare the general properties of HESS PWN with the Crab Nebula: The Crab Nebula is an efficient synchrotron radiator but inefficient γ-ray emitter (i.e., a high ratio of optical/X-ray energy flux to VHE γ-ray flux) as a result of the relatively large magnetic field energy density, but for most other HESS PWN, the ratio of synchrotron to IC energy fluxes are comparable to, or even less than unity. This then hints at a relatively small magnetic energy density. Furthermore, in such cases we may also find that the energy density in relativistic electrons dominates the magnetic energy density, leading to the description of "particle dominated winds", as opposed to the Crab Nebula which is known to be in equipartition.

We then reviewed the γ-ray lifetimes of PWN by considering electrons losing energy due to both synchrotron and inverse Compton radiation in the expanding post-shocked flow. As the PWN expands well beyond its X-ray phase (this X-ray phase terminates when the overall field strength becomes too small as a result of expansion), IC losses on the CMBR is then expected to dominate, in which case the terminating lifetime would converge to a value of 100 kyr. Thus, if we observe a PWN at an energy near 1 TeV, the lifetime of the PWN is expected to be $\leq$100 kyr. This discussion naturally led to the concept of particle spectral steepening as a function of increasing radius, but only as long as either synchrotron or IC radiation dominates the electron energy loss process.

The concept of dispersion in a PWN was also discussed: Is the observed size of a PWN mostly due to post-shocked convective (pulsar wind) flow, or, would diffusion dominate the process? At first glance (from this review paper) it seems as

if the ordered magnetic field in a PWN would inhibit dispersion due to diffusion. The result of this is that the expanding PWN "bubble" contains its radiating charged particles, but only as long as the magnetic field direction maintains its perpendicular direction relative to the radial direction. This question is relevant if we want to calculate the luminosity of a PWN as a function of time.

This review paper then concluded with a discussion of two important HESS sources, where aspects such as (1) size, (2) spectral energy distribution (SED) maximum, (3) the offset of the center of gravity (of the VHE emission) relative to the pulsar position as a result of SNR expansion into an inhomogeneous interstellar medium, (4) energy dependent morphology (i.e., the effect of spectral steepening in the radial direction) and (5) the observed VHE spectral break were discussed (if interpreted as the SED maximum). For both these sources it appears as if IC losses dominate over synchrotron losses, which has the advantage that the age of the PWN can be relatively accurately determined from the observed VHE spectral break: Assuming this, we showed that we indeed get consistent ages for both HESS sources.

References

1. Achterberg, A., Gallant, Y.A., Kirk, J.G., et al., 2001, MNRAS, 328, 393
2. Aharonian, F.A., 2000, New Astron, 5, 377
3. Aharonian, F.A., et al. (H.E.S.S. Collaboration), 2005, Science, 307, 1938
4. Aharonian, F.A., et al. (H.E.S.S. Collaboration), 2005, A&A, 439, 1013
5. Aharonian, F.A., et al. (H.E.S.S. Collaboration), 2005, A&A, 442, L25
6. Aharonian, F.A., et al. (H.E.S.S. Collaboration), 2006, A&A, 448, L43
7. Aharonian, F.A., et al. (H.E.S.S. Collaboration), 2006, ApJ, 636, 777
8. Aharonian, F.A., et al. (H.E.S.S. Collaboration), 2006, A&A, 460, 365
9. Aharonian, F.A., Atoyan, A.M. & Kifune, T., 1997, MNRAS, 291, 162
10. Amato, A. & Arons, J., 2006, ApJ, 653, 325
11. Arons, J., 2004, Acceleration and dissipation in relativistic winds, In *Young Neutron Stars and Their Environments*, IAU Symposium no. 218, Sydney, Australia, ed. by Fernando Camilo and Bryan M. Gaensler. San Francisco, CA: Astronomical Society of the Pacific, p. 163
12. Atoyan, A.M. & Aharonian, F.A., 1996, MNRAS, 278, 525
13. Becker, W.E., Kramer, M., Jessner, A., et al., 2006, ApJ, 645, 1421
14. Blondin, J.M., Chevalier, R.A., & Frierson D.M., 2001, ApJ, 563, 806
15. Blumenthal, G.R. & Gould, R.J., 1970, Rev. Mod. Phys., 42, 237
16. Bocchino, F., Warwick, R.S., Marty, P., et al., 2001, A&A, 369, 1078
17. Bogovalov, S.V., Chechetkin, V.M., Koldoba, A.V., et al., 2005, MNRAS, 358, 705
18. Chevalier, R.A., 2004, Adv Space Res, 33, 456
19. Clifton, T.R., Lyne, A.G., Jones, A.W., et al., 1992, MNRAS, 254, 177
20. Cordes, J.M. & Lazio, T.J.W., 2002, unpublished (Astro-ph/0207156)
21. Coroniti, F.V., 1990, ApJ, 349, 538
22. de Jager, O.C., 2005, H.E.S.S. Observations of Pulsar Wind Nebulae, in *Astrophysical Sources of High Energy Particles and Radiation*, ed. by B. Rudak, (AIP Conf. Proc. 2005), 801, 298
23. de Jager, O.C., 2007, ApJ, 658, 1177
24. de Jager, O.C., Funk, S., & Hinton, J.A., 2005, in *Proc. of the 29th International Cosmic Ray Conference*, 4, 239
25. de Jager, O.C. & Harding, A.K., 1992, ApJ, 396, 161

26. de Jager, O.C., Harding, A.K., Baring, M., et al., 1995, Gamma-Ray Plerions, in *Proc. of the 24th Int. Cosmic Ray Conf.*, OG 2, 528
27. de Jager, O.C., Harding, A.K., Michelson, P.F., et al., 1996, ApJ, 457, 253
28. de Jager, O.C., Harding, A.K., Sreekumar, P., et al., 1996, A&AS, 120, 441
29. de Jager, O.C. & Venter, C., 2005, in *Towards a Network of Atmospheric Cherenkov Detectors VII, Cherenkov 2005 Proceedings*, ed. by B. Degrange, G. Fontaine. (astro-ph/0511098)
30. du Plessis, I., de Jager, O.C. & Buchner, S., et al., 1995, ApJ, 453, 746
31. Gaensler, B.M., Arons, J., & Kaspi, V.M., et al., 2002, ApJ, 569, 878
32. Gaensler, B.M., Schulz, N.S., & Kaspi, V.M., et al., 2003, ApJ, 588, 441
33. Gaensler, B.M. & Slane, P.O., 2006, Ann. Rev. A&A, 44, 17
34. Gallant, Y.A. (for the H.E.S.S. Collaboration), 2007, Ap&SS, 309, 197
35. Gotthelf, E.V. & Olbert, C.M. in *Proc. of the 270 WE-Heraeus Seminar on Neutron Stars, Pulsars, and Supernova Remnants*, MPE Report 278, ed. by W. Becker, H. Lesch, & J. Trümper (Garching bei München: Max-Plank-Institut für Extraterrestrische Physik, 2002), 159
36. Gould, R.J., 1965, Phys Rev Lett, 15, 577
37. Hales, A.S., Casassus, S., Alvarez, H., et al., 2004, ApJ, 613, 977
38. Harding, A.K. & Gaisser, T.K., 1990, ApJ, 358, 561
39. Hillas, A.M., et al. (Whipple Collaboration) 1998, ApJ, 503, 744
40. Hinton, J.A., et al. (the H.E.S.S. Collaboration) 2004, New Astron Rev, 48, 331
41. Hinton, J.A & Aharonian, F.A., 2007, A&A., 657, 302
42. Horns, D., Aharonian, F.A., Santangelo, A., et al., 2006, A&A, 451, L51
43. Kennel, C.F. & Coroniti, F.V., 1984, ApJ, 283, 710
44. LaMassa, A., Slane, P.O. & de Jager, O.C. 2006, American Astronomical Society Meeting 208, No. 3.03
45. Lemiére, A., 2006, Ph.D. thesis, Univ. of Paris 7 and College de France, Paris
46. Lemiére, A., Terrier, R., & Djannati-Ataï, A., 2005, in *Proc. of the 29th International Cosmic Ray Conference*, 4, 105
47. Mangano, V., Massaro, E., Bocchino, F, et al., 2005, A&A, 436, 917
48. Markwardt, C.B. & Ögelman, H., 1997, ApJ, 480, L13
49. Matheson, H. & Safi-Harb, S., 2005, Adv Space Res, 35, 1099
50. Milne, D.K., 1995, MNRAS, 277, 1435
51. Ng, C.-Y. & Romani, R.W., 2004, ApJ, 601, 479
52. Porquet, D., Decourchelle, A., & Warwick, R.S., 2003, A&A, 401, 197
53. Rees, M.J. & Gunn, J.E., 1974, MNRAS, 167, 1
54. Reynolds, S.P., 1988, ApJ, 327, 853
55. Reynolds, S.P. & Chanan, G.A., 1984, ApJ, 281, 673
56. Reynolds, S.P. & Chevalier, R.A., 1984, ApJ, 278, 630
57. Sefako, R.R. & de Jager, O.C. 2003, ApJ, 593, 1013
58. Slane, P.O., Helfand, D., van der Swaluw, E., et al., 2004, ApJ, 616, 403
59. Steenberg, C.D. 1988, Ph.D. thesis, North-West University, Potchefstroom Campus
60. van der Swaluw, E. & Wu, Y. 2001, ApJ, 555, L49
61. Wang, Q.D., Li, Z.Y. & Begelman, M.C. 1993, Nature, 364, 127
62. Weiler, K.W. & Panagia, N. 1978, A&A, 70, 419
63. Weiler, K.W. & Panagia, N. 1980, A&A, 90, 269
64. Wilson, D.B. & Rees, M.J. 1978, MNRAS, 185, 297

Chapter 18
High Energy Emission from Pulsars and Pulsar Wind Nebulae

Kwong Sang Cheng

18.1 Introduction

Pulsars are accidentally discovered by the Cambridge scientists [48]. Shortly thereafter, Gold [39] and Pacini [72] proposed that pulsars are rotating neutron stars with surface magnetic fields of around 10^{12} G. Gold [39] pointed out that such objects could account for many of the observed features of pulsars, such as the remarkable stability of the pulsar period, and predicted a small increase in the period as the pulsar slowly lost rotational energy. With the discovery of the Vela pulsar with a period of 88 ms [65], the identification of the Crab pulsar with a period of 33 ms [86] and the discovery of slowdown of Crab pulsar [77], it was essentially confirmed that pulsars are rapidly rotating neutron stars. So far, over 1,500 radio pulsars have been found (see the most updated list of pulsars in www.atnf.csiro.au/research/pulsar/). The radio luminosities of these pulsars are small compared with the energy loss rate due to the pulsar spin down ($\sim 10^{-6}$–10^{-5}). Strong high-frequency radiation in the X-ray band has been observed from about two dozens pulsars (for recent review cf. [6, 7]), but only eight pulsars have been confirmed to emit high energy γ-rays (cf. [94] for a recent review). The observed radiated power for the γ-ray pulsars is concentrated mainly in the γ-ray range and the γ-ray luminosities are a substantial fraction (10^{-3}–10^{-1}) of the spin-down power. This makes studies of high energy radiation from a pulsar a promising way to better understand the physical processes which result in their non-thermal radiation.

Theoretically, a common idea is that emissions ranging from radio to γ-rays are produced in different regions of the pulsar magnetosphere. To an excellent approximation, the pulsar may be considered as a non-aligned rotating magnet with a very strong surface magnetic field. Just outside the surface of the neutron star, the Lorentz force on a charged particle is very strong and far exceeds the force of gravitational

K.S. Cheng
Department of Physics, University of Hong Kong
e-mail: hrspksc@hkucc.hku.hk

W. Becker (ed.), *Neutron Stars and Pulsars,* Astrophysics and Space Science Library 357,

attraction, i.e., $e((\mathbf{v}/c)\times\mathbf{B})/(GMm/r^2)\gg 1$. As a result, the structure of the magnetosphere of the neutron star is completely dominated by electromagnetic forces. Because the induced electric fields at the surface of a neutron star are so strong that the force on the charged particle in the surface exceeds the work function of the surface material, there must be a plasma surrounding the neutron star. In this way, there is a fully conducting plasma surrounding the neutron star, and electric currents can flow in the magnetosphere (e.g., [69]). If the component of the electric field $E_\parallel = \mathbf{E}\cdot\mathbf{B}/B$ along the magnetic field direction ($\mathbf{B}$) is non-zero in the pulsar magnetosphere, and this component of the electric field can accelerate particles to ultra-relativistic energies. The accelerated particles emit γ-rays due to curvature emission and other processes, e.g., inverse Compton scattering. Some of these γ-rays are absorbed giving rise to secondary electron-positron pairs. The created electron-positron pairs screen the electric field $E_\parallel$ in the pulsar magnetosphere everywhere except for certain compact regions. The regions where $E_\parallel$ is not screened are called accelerators or gaps. These gaps serve as an engine which is responsible for the pulsar non thermal radiation. There are two kinds of magnetosphere gaps: polar gaps and outer gaps , their location and potential drop being determined by the dipolar magnetic field, the rotation speed Ω and the angle between them called the inclination angle (α). The polar gaps place the source of the emission immediately above a magnetic pole. The evidence for the polar gaps came from radio observations of beam width and polarization. The outer gap place the source of emission far out in the magnetosphere, close to the velocity of light cylinder. The evidence for the origin of the outer gaps came from the high energy radiation observed from young pulsars such as the Crab, Vela and Geminga. It has been proved that all radiation from young pulsars cannot come from a single location.

We will organize this review paper as follows. In Sect. 18.2, we introduce the standard pulsar magnetosphere. In Sect. 18.3, we summarize some interesting observed X-ray and gamma-ray data. Some of these data look contradictory to each other. In Sect. 18.4, we review the high energy radiation produced by polar gaps and slot gaps. In Sect. 18.5, we introduce various outer magnetospheric gap models. In Sect. 18.6, we apply the three-dimensional outer gap to explain the observed phase-resolved spectrum and the polarization properties of the Crab pulsar. In Sect. 18.7, we introduce a simple pulsar wind nebula model, which can be used to explain high energy emission from region beyond the light cylinder. In Sect. 18.8, we use the simple pulsar wind model to explain the relation between the X-ray luminosity and the spin-down power. We also explain why millisecond pulsars in globular cluster behave so much different from those millisecond pulsars in the field. Finally we present a brief discussion in Sect. 18.9.

18.2 Standard Pulsar Magnetospheric Models

The standard emission theory for pulsars is based on the concept that pulsars are rapidly rotating, strongly magnetized, neutron stars. Detailed discussions of the structure of pulsar magnetospheres can be found, for example, in [69] and [9].

Here, we introduce some basic features of the magnetosphere of an aligned pulsar. It should be pointed out that these features do not differ drastically from those given by the more sophisticated treatments of oblique, self-consistent charged magnetospheres.

In an aligned pulsar, its magnetic dipole moment μ is aligned with its rotation axis Ω. The magnetic field far from the surface of the star is dominated by the dipole contribution of the star's intrinsic magnetic field. If the neutron star can provide the necessary negative charges (electrons) and positive charges (ions and/or positrons), and the currents in the magnetosphere are negligible, the electric field in steady state in the corotation frame, $\mathbf{E}' = 0$, which implies

$$\mathbf{E} + \frac{\mathbf{1}}{\mathbf{c}}(\Omega \times \mathbf{r}) \times \mathbf{B} = 0. \tag{18.1}$$

where $\mathbf{E}$ and $\mathbf{B}$ are the electric and magnetic fields measured in a non-rotating frame, and $\Omega \times \mathbf{r}$ is the co-rotating velocity. Equation (18.1) implies a local charge density

$$\rho_c = -\frac{\Omega \cdot \mathbf{B}}{2\pi c} \frac{1}{1 - |\Omega \times \mathbf{r}/c|^2}, \tag{18.2}$$

which is co-rotating with the local magnetic field. Such a charge density is a called corotation charge density, or Goldreich–Julian charge density [40]. There are surfaces defined by $\Omega \cdot \mathbf{B} = 0$ on which this charge density is zero, called null charge surfaces. The charge density on both sides of the null charge surface are of different sign. This property plays an essential role in the formation of acceleration regions in the vicinity of null surfaces [15, 57]. Equation (18.2) corresponds to a charge number density $n_c = 7 \times 10^{-2} B_z P^{-1} (q/e)^{-1}$ cm^{-3}, where B_z is z-component of the magnetic field in gauss, P is the pulsar period in seconds and q/e is the charge of the particle in the charge unit of proton. The corotation region of the magnetosphere is limited to within a surface on which the magnetic field lines will be swept along at the speed of light. This cylindrical surface is called the light cylinder; it has a radius given by

$$R_L = c/\Omega \approx 5 \times 10^9 P \text{ cm}. \tag{18.3}$$

Field lines which cross the light cylinder do not return to the surface of the neutron star, and are referred to as open field lines. Otherwise, they are referred as closed field lines. The edge of the polar cap is defined by the locus of the last closed magnetic field lines (i.e., the field lines which just touch the light cylinder). In spherical polar coordinates, the radius of the polar cap region which contains the open field lines is given by $r_{pc} = R \sin\theta_{pc}$, where θ_{pc} is the angular radius of the polar cap. For an aligned pulsar with radius R (i.e., one with its rotation axis parallel to its magnetic axis), one can get

$$\sin\theta_{pc} = \left(\frac{R}{R_L}\right)^{1/2}, \tag{18.4}$$

since for dipole field lines $\sin^2\theta/r$ =constant and the last closed field lines will touch the light cylinder at 90°. The polar cap radius is then given by

$$r_{pc} = R\theta_{pc} \approx 1.4 \times 10^4 R_6 P^{-1/2} \text{ cm}, \tag{18.5}$$

where R_6 is the stellar radius in units of 10^6cm. Charged particles streaming out of the polar caps, which can escape to infinity along the open field lines, generate a toroidal magnetic field component. This toroidal component is largest near the critical field lines that separate the open from the closed regions. Because the potential at the base of the open field lines near the axis is negative with respect to the exterior, negative charges stream out. But, overall, a net charge cannot flow out from the star, so the potential of the magnetic field lines near the edge of the polar cap must be positive with respect to the exterior, and positive charges stream out from the star along these lines which form an annulus on the outer part of the polar cap. There is an intermediate set of critical field lines separating the regions of negative and positive outflow, and there the potential on the surface of the star equals the potential of the exterior interstellar medium. The magnetosphere of an aligned pulsar is shown in Fig. 18.1.

If, in addition, a strong potential is available to accelerate charge away from the stellar surface, a current of primary particles flows out from a single polar cap which is approximately given by

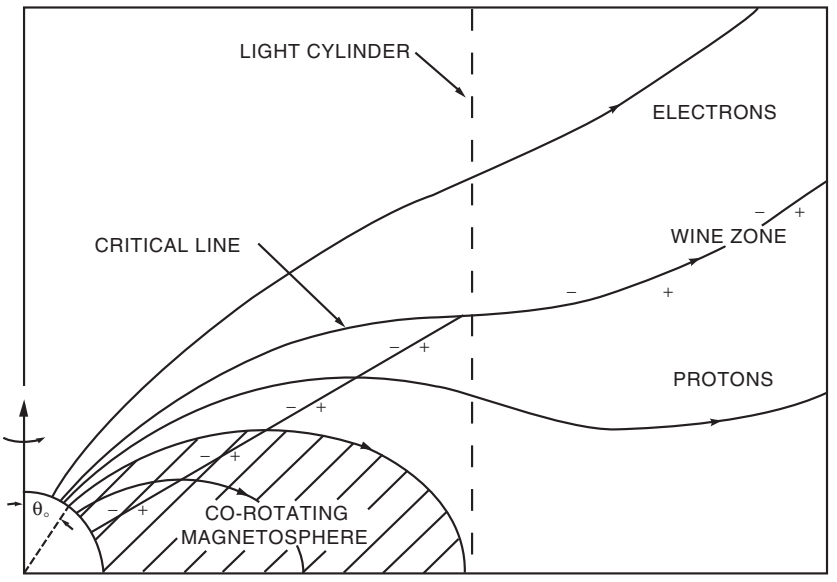

Fig. 18.1 Magnetosphere of an aligned pulsar. The *open-field lines* are swept back to form a toroidal component after crossing the light cylinder. The *closed-field lines* encompass the co-rotating portion of the magnetosphere. The *critical field line* divides regions of positive and negative current flow, while the *diagonal dashed line* gives the locus of $B_z = 0$ where the sign of the Goldreich–Julian space charge changes [40]

$$\dot{N}_{GJ} \approx \pi r_{pc}^2 \left(\frac{\rho_c}{e}\right) c \approx \frac{\Omega^2 R^3 B_s}{2ec} = 2.7 \times 10^{30} B_{12} P^{-2} R_6^3 \ \mathrm{s}^{-1}, \tag{18.6}$$

where B_s is the surface magnetic field. From (18.1) and (18.4), the potential difference between the center and the edge of the polar cap is

$$\Delta\Phi = \int \mathbf{E} \cdot d\mathbf{s} \approx \frac{\Omega^2 R^3 B_s}{2c^2} = 6.6 \times 10^{12} B_{12} P^{-2} R_6^3 \ \mathrm{V}. \tag{18.7}$$

The quantities given by (18.4), (18.6) and (18.7) define the characteristic polar cap values for the standard pulsar model.

Theoretically, it is suggested that high energy γ-rays from a pulsar are produced by the radiation of charged particles that are accelerated in the pulsar magnetosphere. Nowadays, two general types of γ-ray pulsar models are popular in the literature: polar cap models and outer gap models. Both models predict that electrons and positrons are accelerated in a charge depletion region, called a gap, by an electric field along the magnetic field lines and assume that charged particles loose their energies via some radiation mechanisms (say curvature radiation) in both polar and outer gaps. We introduce these models briefly in Sects. 18.4 and 18.5 respectively.

18.3 Summary of Some Interesting Observed Results in X-Rays and Gamma-Rays

In past two decades, there are tremendous progresses of X-ray and gamma-ray observations to rotation-power pulsars by ROSAT, ASCA, RXTE, BeppoSAX, CGRO, Chandra, XMM-Newton, INTEGRAL, etc. These satellites provide very important information for us to understand the properties of their emission regions including local energy distribution of charged particles, local electric field and magnetic field, geometry, etc. The observed information also constrains for theoretical models.

There are eight pulsars have been detected in gamma-ray energy range (cf. [94] for a recent review) with period ranging from 0.033 to 0.237 s and age younger than million years old. Most of these gamma-ray pulsars also emit X-rays (e.g., [6, 7]). However, there are over 50 pulsars detected with X-ray emission but most of them are old pulsars including more than 30 millisecond pulsars, which have age older than billion years.

Theoretically, it is suggested that high-energy photons are produced by the radiation of charged particles that are accelerated in the pulsar magnetosphere. There are two kinds of theoretical models: one is the polar gap model (e.g., [32, 43], for more detail review of polar cap model cf. [44]), and another is the outer gap model (e.g., [18, 19, 29, 33]). Both models predict that electrons and positrons are accelerated in a charge depletion region called a gap by the electric field along the magnetic field lines and assume that charged particles lose their energies via curvature

radiation in both polar and outer gaps. The key differences are: polar gaps are located near stellar surface and the outer gaps are located near the null charge surface, where are at least several tens stellar radii away the star.

The study of the emission characteristics from rotation powered pulsars has been a subject of long standing interest. Our knowledge of the fundamental properties (e.g., mass, spin, and magnetic field) of the underlying neutron star stems from detailed spectral and timing investigations. To facilitate an understanding of the mechanism by which the loss of rotational energy is converted into high energy radiation, many observational and theoretical studies have sought to determine the relationship between the X-ray luminosity, L_x, and the rate of rotational energy loss or spin down power, L_{sd}. Indeed, a correlation of the form $L_x \propto L_{sd}^{1.39}$ was found in Einstein data by [85]. Subsequent, [7,8] used 27 rotation powered pulsars including 9 millisecond pulsars in the field and led to a relation of the form, $L_x \propto L_{sd}$ based on ROSAT data. However [84] used 16 rotation-power pulsars observed by ASCA and obtained a different relation, $L_x \propto L_{sd}^{1.5}$. Recently, a reanalysis of 39 pulsars based on data obtained from several X-ray satellites by [74] led to an intermediate relation $L_x \propto L_{sd}^{1.34}$, similar to that of [85]. However, the situation became more complicated when [42] reported that the MSPs in 47 Tuc obeyed a much shallower relation $L_x \propto L_{sd}^{0.5}$.

Qualitatively we believe that although the deduced existence of a correlation between L_x and L_{sd} suggests that the observed X-rays are produced by a process which taps the rotational energy of the neutron star, a detailed description of the mechanism remains elusive. This is, in part, a result of the fact that the data from different satellites are obtained in different energy ranges. The results can be affected, for example, by interstellar absorption especially for those pulsars studied in the soft X-ray regime of ROSAT (0.1–2.4 keV). In addition, the total X-ray luminosity is composed of contributions from both the pulsed and non pulsed components, and these components are likely to reflect physical conditions in diverse spatial environments. In general the pulsed thermal emission likely originates in regions within the light cylinder, where the magnetic field is so strong that radiation emission must be beamed. For examples, the pulsed non-thermal emission may be produced in the vicinity of the polar cap as a result of inverse Compton scattering of higher order generation pairs of particles on soft photons emitted by the neutron star [103] or in the outer magnetosphere as a result of synchrotron radiation of downward cascades from the outer gap electron/positron particles [26]. On the other hand, the non-thermal non pulsed X-ray radiation likely is produced in the surrounding wind nebula [27]. Since the pulsed and non pulsed emission have different origins, the relationship between the total X-ray luminosity and spin down power is not expected, in general, to be represented by a single power law. In fact, the non-thermal pulsed and non pulsed emission components are distinguished by different spectral signatures and conversion efficiencies.

The continuous observations of powerful young pulsars, including the Crab, the Vela and the Geminga, have collected large number of high energy photons, which allow us to carry out much more detailed analysis. Fierro et al. [36] divided the whole phase into eight phase intervals, i.e., leading wing, peak 1, trailing 1, bridge,

leading wing 2, peak 2, trailing 2 and off-pulse. They showed that the data in each of these phases can be roughly fitted with a simple power law. However, the photon indices of these phases are very different, they range from 1.6 to 2.6. Massaro et al. [68] have shown that X-ray pulse profile is energy dependent and the X-ray spectral index also depends on the phase of the rotation.

Recently [64] have combined the X-ray and gamma-ray data of the Crab pulsar, they showed that the phase-dependent spectra exhibit a double-peak structure, i.e., one very broad peak in soft gamma-rays and another broad peak in higher energy gamma-rays. The position of these peaks depend on the phase. Although the double-peak structure is a signature of synchrotron self-Compton mechanism, it is impossible to fit the phase dependent spectrum by a simple particle energy spectrum.

Actually it is not surprised that the spectrum is phase dependent because photons are emitted from different regions of the magnetosphere. The local properties, e.g., electric field, magnetic field, particles density and energy distribution are very much different for different regions. Therefore these phase dependent data provide very important information for emission region.

18.4 Polar Cap and Slot Gap Models

Sturrock [89] first proposed the polar cap model, and later many authors (e.g., [2, 4, 31, 43, 83]) developed it. Sturrock [89] studied the consequences of the particle outflow from the star along the open field lines. Assuming that the electric field is primarily radial for heights $h < r_{pc}$ and transverse at heights $h > r_{pc}$, primary charged particles (e.g., $e^{\pm}$ pairs) are accelerated in a small zone with typical height h above the polar cap surface, and the primary emission region is confined to the dipole open field lines. Using the approximation $\rho_c = (1/4\pi)\nabla^2\Phi \sim (1/4\pi)\Phi/h^2$ and (18.2), the accelerating potential responsible for the charged particle flow given by (18.6) is $\Phi \sim (2\Omega B_s/c)h^2$. The potential difference between the center and the edge of the polar cap is

$$\Delta\Phi \sim (\Omega B_s/2c)h^2. \tag{18.8}$$

Sturrock assumed that $h \sim r_{pc}$, so $\Delta\Phi \sim (\Omega^2 R^3 B_s/2c^2)$, which is essentially equivalent to (18.7), and amounts to a potential drop of $\Delta V \sim 6\times10^{12}B_{12}P^{-2}R_6^3$ V. Sturrock further assumed that this potential would be sufficient to rip charged particles (say electrons) from the stellar surface and accelerate them up to relativistic velocities along the strong magnetic field lines. The perpendicular energies of the accelerated electrons would be rapidly radiated away through synchrotron radiation, but their longitudinal energies would be radiated away in form of high energy γ-rays due to curvature radiation mechanism, which is the dominant energy lost process for charged particles moving with relativistic velocity along the curved magnetic field lines. The typical curvature photon energy is

$$E_\gamma \approx (3/2)\hbar\gamma_e^3/s \sim 10^9\gamma_7^3 s_8^{-1}\ \text{eV}\,, \tag{18.9}$$

where γ_7 is the electron Lorentz factor in units of 10^7, and $s_8 \sim (rR_L)^{1/2}/10^8$ is the typical curvature radius in units of 10^8 cm. When these extremely energetic photons move transverse to the strong magnetic field, they will produce $e^{\pm}$ pairs via $\gamma + B \longrightarrow e^+e^-$. Sturrock therefore envisaged that, for a sufficiently strong electric field, these secondary pairs would also be accelerated and create γ-rays leading to further pairs, resulting in a pair cascade. This cascade produces the coherent low frequency emission necessary to explain the brightness temperature implied from radio observations. From (18.7), as the pulsar slows down, the potential drop will decrease, and would eventually reach the critical value below which pair production will not be possible and pulsed emission will cease. However, (18.8) means that the acceleration of charged particles is caused by the full vacuum potential across the polar cap, which is now recognized to be incorrect. In fact, the charged particles will only be accelerated in the vacuum gap where $\mathbf{E}\cdot\mathbf{B} \neq \mathbf{0}$ (see below).

Ruderman and Sutherland [83] carried out a major development of this model, and addressed some of the concerns associated with the standard pulsar model, such as trying to maintain a force-free $\mathbf{E}\cdot\mathbf{B} = \mathbf{0}$ condition while the charge density moves everywhere at the speed of light along divergent field lines. In their model $\Omega\cdot\mathbf{B} < 0$, therefore the polar cap electric field can only pull out ions. Since electrons will not be stripped from the stellar surface while the ions will be retained due to their higher surface binding energy, the stellar surface does not supply the positive charges to replace the positive charges in the magnetosphere which are accelerated outward, as a result a vacuum gap will form above the polar cap. This gap will continue to expand at a speed $\sim c$ until it reaches a maximum height h, which corresponds to a gap potential large enough to ignite an $e^{\pm}$ cascade. In the vacuum gap, $\mathbf{E}\cdot\mathbf{B} \neq \mathbf{0}$, it means that the magnetic field lines in this region are not forced to co-rotate. Above the vacuum gap, the magnetosphere co-rotates with the pulsar. The gap potential and h can be determined by the condition of pair production which is

$$\frac{E_\gamma}{2m_ec^2}\frac{Bh/s}{B_q} \geq \frac{1}{15} \tag{18.10}$$

[35, 83]. Since the electrons/positrons are accelerated in the gap, $\gamma_e = e\Delta\Phi/m_ec^2$. Combining (18.8)–(18.10), we obtain

$$h_{RS} = 5\times 10^3\, s_6^{2/7} P^{3/7} B_{12}^{-4/7}\ \text{cm} \tag{18.11}$$

and

$$\Delta\Phi \equiv \Delta V_{RS} = 1.6\times 10^{12} s_6^{4/7} P^{-1/7} B_{12}^{-1/7}\ \text{V}\,. \tag{18.12}$$

Here s_6 is the radius of curvature in units of 10^6 cm instead of 10^8 cm, it is because non-dipolar field with a characteristic curvature radius $\sim 10^6$ cm is assumed to exist on the neutron star surface. Ruderman and Sutherland suggested that, when the gap potential drop reaches ΔV_{RS}, a spark discharge occurs inside the gap, triggering an avalanche of $e^{\pm}$ pairs, which in turn will result in the pair production cascade envisaged by Sturrock. The difference from Sturrock's model is that here the acceleration occurs only in the vacuum gap ($\mathbf{E}\cdot\mathbf{B} \neq 0$) with height $h = h_{RS} < r_{pc}$. Outside the gap

($\mathbf{E}\cdot\mathbf{B}=0$), the pairs are no longer accelerated and stream outward with a Lorentz factor ∼3. Ruderman and Sutherland showed that the density of the streaming pairs is much higher than the Goldreich–Julian density, so the plasma will be essentially charge neutral. Furthermore, they suggested that radio emission occurs above the spark regions in the filled, streaming region where bunching by plasma instabilities would lead to coherent radio emission.

When $\Omega\cdot\mu>0$, the polar cap charge density is negative. Electrons with much weaker binding energy can be pulled out from the stellar surface and form a steady outflow current. Because of the finite inertia of the electron, the potential of the polar gap cannot be zero. Arons and Scharlemann [4] presented solutions for steady, space charge limited flow (which is shorted out by pair creation) of an electron beam above the polar cap of a pulsar in this case. Because of curvature of the magnetic field, the space charge limited particle beam from the stellar surface is accelerated to an energy high enough to emit curvature γ-rays. The particles accelerate along the magnetic field through a potential drop [4]

$$\Delta V_s \approx \frac{\Omega^2\mu}{c^2}\frac{R}{s} \sim 10^{11}\mu_{30}P^{-5/2}\ \mathrm{V}\,, \tag{18.13}$$

which is called the space-charge-limited potential (also see [3] for a review). However, [71] have shown that the actual potential drop for the space-charge-limited flow is much larger than that in (18.13) if the inertial frame dragging effect is included. The corrected space-charge-limited potential should be

$$\Delta V_s \approx \frac{10R}{s}\frac{\Omega^2\mu}{c^2}[1-(R/r)^3] \sim 10^{14}\mu_{30}P^{-5/2}[1-(R/r)^3]\ \mathrm{V}\,, \tag{18.14}$$

which is even larger than ΔV_{RS}, where μ_{30} is the pulsar's magnetic moment in units of 10^{30} cgs and s is the radius of curvature of the magnetic field lines. It is further suggested that a large potential drop may explain γ-ray emission from young pulsars (e.g., [70]). However, (18.14) has ignored the pair production inside the gap which is possible if the surface magnetic field is pure dipolar, otherwise the pair cascade should restrict the potential of the cap as shown in (18.12). Harding and Muslimov [45] have investigated a self-consistent particle acceleration mechanism by the electrostatic field due to the effect of inertial dragging near the polar cap. They computed the potential self-consistently, including pair formation in the polar gap.

In explaining the high energy emission from pulsars, [32] have used the traditional polar cap model to calculate the light curve and gamma-ray spectrum. They provided a very successful model fitting for the observed phase average spectrum of the Vela pulsar. However, they have to artificially put the acceleration region at three stellar radii and assume the polar cap rim enhancement. The viewing angle is assumed to be 10°. All these assumptions are not easy to be justified.

In order to seeking the possibility of a wide hollow cone emission due to flaring B-field lines, [2] first examined a gap formation in higher altitudes along the last open field line. This type of accelerator is called slot gap. The more recent review of slot gap can be found in [44]. Based on the slot gap properties, some light curve and

polarization properties of the Crab pulsar can be explained very well (cf. [33, 34]). Another successful application of slot gap is in millisecond pulsars, [46] have used the slot gap geometry and assumed that secondary particles can maintain their pitch angles due to the interaction with the radio. The model predictions can explain the observed high energy radiation spectrum of the millisecond pulsar PSR J0218+4232 very successfully.

18.5 Outer Gap Models

18.5.1 CHR Model

Cheng et al. [18, 19], (hereafter CHRI and CHR II) constructed a semi-analytical outer-magnetospheric gap model of rapidly spinning neutron stars. They assumed that a global current flow pattern through the magnetosphere of a rapidly spinning magnetized neutron star results in large regions of magnetospheric charge depletion (gaps). This would result in a large electric field along the magnetic field lines ($\mathbf{E}\cdot\mathbf{B}\neq\mathbf{0}$) in those regions, which, through various mechanisms, including inverse Compton scattering and photon-photon pair production, could sustain enough $e^{\pm}$ pair production to:

1. Short out $\mathbf{E}\cdot\hat{B}$ except in an almost slab like volume (the "outer gap")
2. Maintain the huge magnetospheric current flow

According to this model, there are two kinds of pulsars: Crab-type and Vela-type pulsars. For the Crab-type pulsars, a Crab-type gap produces GeV photons via curvature radiation and subsequently produce $e^{\pm}$ which radiate synchrotron radiation and inverse Compton-scattered photons (CHRII; [24, 56]). The detailed pair production and radiation mechanisms of the Vela-type outer gap (for the conditions in pulsars with a Vela-type outer gap refer to CHRII; [16]) are the following. The members of paired $e^{\pm}$ are created within the gap (primary pairs) and accelerated in opposite direction to extreme relativistic energies. These primary $e^{\pm}$ produce γ-rays (primary) through inverse Compton scattering on *IR* photons. Here primary γ-ray are sufficiently energetic to produce $e^{\pm}$ pairs (secondary) in collision with the same *IR* photon flux; synchrotron radiation of these secondary pairs gives crossed fan beams of secondary γ-rays and weaker ones of X-rays. Collisions of the secondary γ-rays and X-rays produce a large flux of lower energy $e^{\pm}$ pairs (tertiary), much further from the outer gap, which fill much of the outer-magnetosphere. It is the (tertiary) *IR* synchrotron radiation from tertiary pairs through the outer gap which causes the initial primary inverse Compton scattering in the gap and converts the scattered γ-rays, thus initiating the entire series of pair production processes. It should be noted that in Vela-like pulsars the CHR model use the infrared photons to extract energy from the outer gap via Inverse Compton Scattering with the primary particles which predicts a large observed TeV flux, which has not yet been observed

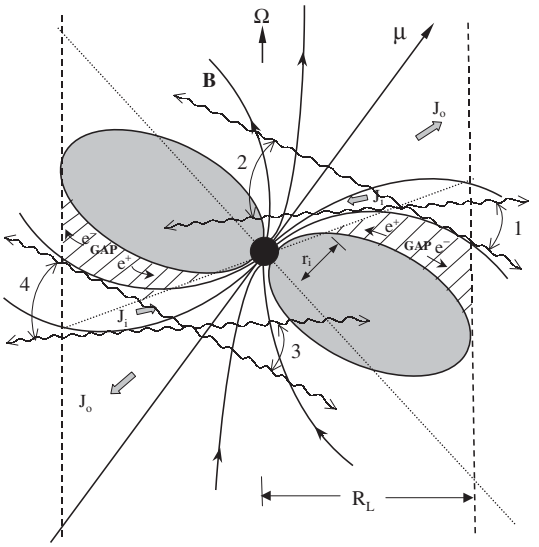

Fig. 18.2 Schematic illustration of the location and geometry of the outer gaps, the current flow pattern in the magnetosphere and the radiation beaming of secondary radiation from four emission regions. The outer gaps, where $\mathbf{E}\cdot\hat{B}\neq 0$, starts at r_i where the null surface intersect the last closed field lines and extends to R_L

(e.g., [96]). Figure 18.2 schematically shows the location of the outer gap and the radiation beaming of secondary radiation from the two emission regions.

The pair production and radiation mechanisms of the Vela-type outer gap and the Crab-type outer gap are quite different. The primary $e^{\pm}$ of the Crab pulsar lose most of their energies via curvature radiation instead of synchrotron radiation as in the case of the Vela pulsar. As a result, the power of the Crab-type and Vela-type pulsars have different parametric dependence on P and B_s. The radiation power loss of the Crab-type pulsars is given by

$$L_\gamma \simeq 1.5\times 10^{37} P \text{ erg s}^{-1}. \tag{18.15}$$

On the other hand the radiation power loss of the Vela-type is very sensitive to the spin period P as well as the dipole magnetic field strength B and it is given by $L_\gamma \propto P^{-4}B_s^2$.

In calculating the γ-ray spectrum of the Vela pulsar, Cheng Ho and Ruderman (CHRI, II) made some simplifying assumptions. They argue that the secondary e^-/e^+ production distribution in the Vela-type outer gap would scale like γ^{-1}, where γ is the e^-/e^+ Lorentz factor and most of the secondary $e^{\pm}$ have similar pitch angles, θ, with respect to the local magnetic field, B. Then the steady state distribution is roughly given by [12],

$$N_e(\gamma) \sim \gamma^{-2} \ln\left(\frac{\gamma_{max}}{\gamma}\right), \tag{18.16}$$

where γ_{max} is the maximum energy of the primary e^-/e^+ which is determined by the fact that the energy of the primary photons must be just enough to make pairs on collision with the *IR* photons with a typical energy, E_{IR}, therefore, $\gamma_{max} \sim mc^2/E_{IR}$. The typical energy of the *IR* photons is estimated to be (CHRII)

$$E_{IR} \sim \frac{\hbar}{\omega_B^3}\left(\frac{mc^3\Omega}{e^2}\right)^2 , \tag{18.17}$$

where $\omega_B = \frac{eB}{mc}, B(r) = B_s R^3/r^3$ for a dipole field, $r \equiv \eta R_L$ is the observed emission distance to the outer gap and R is the stellar radius. Because the maximum energy of secondary $e^\pm$ is $\gamma_{max} mc^2$, the typical energy of the synchrotron photons from the secondary $e^\pm$ is [16]

$$E_{max} = 9 \times 10^5 \eta^{-21} P_{-1}^{17} B_{12}^7 \sin\theta \text{ eV}, \tag{18.18}$$

where θ is the mean pitch angle of the secondary pairs with respect to the local magnetic field and αR_L is the mean distance to the outer gap. If the primary photons are emitted tangential to the local field then $\sin\theta \approx (\frac{1}{\gamma_{max}} + \frac{\lambda}{S}) \sim \lambda/S$ where λ is the mean free path of the primary photons and S is the radius of curvature of the local magnetic field lines. In general, $\sin\theta$ should vary from pulsar to pulsar. For $E_\gamma > E_{max}$, the photon flux will drop exponentially, so this energy is regarded as an upper spectral cut-off. Because of the weakness of the magnetic field in the outer magnetosphere of Vela-type pulsars, a relativistic e^-/e^+ does not radiate away all of its energy through synchrotron loss before it leaves the light cylinder. Thus, the distribution of secondary pairs given by (18.16) is valid only for $\gamma > \gamma_{min}$ where γ_{min} is roughly given by

$$\gamma_{min} \sim \frac{\Omega mc^3}{e^2\omega_B^2 \sin^2\theta} . \tag{18.19}$$

Such a γ_{min} corresponds to a lower energy spectral break in the photon spectrum at an energy given by

$$E_{min} = 11\alpha^9 P_{-1}^7 B_{12}^{-3} \sin^{-3}\theta \text{ eV}. \tag{18.20}$$

Therefore, the distribution of the secondary pairs can be approximated by

$$N_e(\gamma) \sim \begin{cases} \gamma^{-2}\ln(\gamma_{max}/\gamma), & \gamma_{min} \le \gamma \le \gamma_{max} , \\ 0, & \gamma < \gamma_{min} . \end{cases} \tag{18.21}$$

Here, we have assumed that no e^-/e^+ is created below γ_{min}.

The pulsed radiation spectrum from a Vela-type outer gap is calculated by using the $e^\pm$ pair distribution of (18.21) with the single particle synchrotron radiation spectrum,

$$\frac{d^2N_\gamma}{dE_\gamma dt} \propto \frac{1}{E_\gamma}\int_{\gamma_{min}}^{\gamma_{max}} d\gamma N_e(\gamma) F(x) , \tag{18.22}$$

where $F(x) = x\int_x^\infty K_{5/3}(y)dy$ with $K_{5/3}$ the modified Bessel function, whose values and asymptotic form are given by [38], and $x = E_\gamma/E_{syn}$ with $E_{syn} = 3\gamma^2 \sin\theta\hbar\omega_B/2$.

18.5.2 A Self-Consistent Outer Gap Model

Pulsars are rapidly rotating, strongly magnetized, neutron stars surrounded by co-rotating plasma up to the light cylinder (R_L, where the co-rotating speed is c). Detailed discussions of the structure of pulsar magnetospheres can be found, for example, in [69] and [9]. It is generally believed that pulsed gamma-rays are emitted within the light cylinder. There are two popular classes of charged accelerator models, i.e., polar cap models (e.g., [32, 47]) and outer gap models. Here we will focus on the outer gap models.

Cheng et al. [18] proposed a two-dimensional outer gap model to explain the observed data of the Crab and Vela pulsars. Their model assumed that the radiation regions are thin in the longitudinal direction. Their double peak γ-ray structure was from two topologically disconnected outer gaps, each of which is associated with different magnetic poles. However, Romani and co-workers [29, 79] have shown that only one outer gap with only outgoing current can already produce a broad, irregularly-shaped emission beam of which is particularly dense near the edge, so that two γ-ray peaks would be observed when the line of sight from the Earth crosses these enhanced γ-ray beam regions; the inner region of the beam provided a significant amount of emission between the peaks. Cheng et al. [20], (hereafter CRZ) have re-considered the three-dimensional magnetospheric gap model by introducing various physical processes (including pair production which depends sensitively on the local electric field and the local radius of curvature, surface field structure, reflection of $e^{\pm}$ pairs because of mirroring and resonant scattering) to determine the three-dimensional geometry of the outer gap. They have shown that two outer gaps and both outgoing and incoming currents are in principle allowed, but it turns out that outgoing currents dominate the emitted radiation intensities. According to CRZ, the azimuthal extension of the outer gap ($\Delta\Phi \sim 160^\circ$ for the Crab pulsar) is finite and is determined by the local pair production condition. According to [104], the size of the outer gap (f_0) is limited by the pair production between the soft thermal X-rays from the stellar surface and the curvature photons with energy $E_\gamma(f_0)$ emitted by the primary electrons/positrons accelerated in the outer gap. Furthermore, the energy of the soft X-ray photons is determined by the back-flow of the primary electrons/positrons, therefore the soft X-ray energy $E_X(f_0)$ is also a function of the gap size. Using $E_X(f_0)E_\gamma(f_0) \sim (mc^2)^2$, the size of the outer gap can be expressed as

$$f_0 = 5.5P^{26/21}B_{12}^{-4/7}\,, \tag{18.23}$$

where, $f_0 \leq 1$ is the ratio between the outer gap volume $\sim R_L^3$, $R_L = cP/2\pi$ is the light cylinder radius, P is pulsar period in seconds and B_{12} is the surface magnetic field in units of 10^{12} G. It should be emphasized that $f_0 \leq 1$ otherwise the outer gap does not exist. Zhang et al. [105] have considered how the inclination angle (α) can affect the outer gap size. They find that the size of outer gap will increase for larger inclination angle. The maximum change can be near 75%.

Furthermore, the return particles emit curvature photons with typical energy $E_\gamma = (3/2)(c/s)\hbar\gamma(x)^3$, where $x = s/R_L$, s is the local radius of curvature and

$\gamma(x) \approx 2\times10^7 f_s^{1/2} B_{12}^{1/4} P^{-1/4} x^{-3/4}$ [26]. These photons will be converted into the secondary pairs by the neutron star magnetic field if the pair production condition in strong magnetic field is satisfied. From this condition and assuming the local field is dipole field, then the distance to the star of the first generation of $e^{\pm}$ pairs can be given by [17] $r_s/R = (15E_\gamma B_s/(2mc^2 B_g))^{1/3}$, where B_s is the surface magnetic field and $B_g = m_e^2 c^3/e\hbar = 4.4\times10^{13}$ G. These secondary pairs will lose their energy via synchrotron radiation with the following typical energy $E_{syn} = E_\gamma/20$. Since these synchrotron photons are emitted toward the star, they will encounter stronger magnetic field and convert into $e^{\pm}$ pairs which again radiate their energy via synchrotron radiation. We can easily show that each new generation of $e^{\pm}$ pairs will reduce their energy by a factor of $\sim$0.05 and comes closer to the star by a factor of $\sim$0.37 [17]. The synchrotron spectral index starts with -1.5 and evolves to become -1.9. We argue that an electromagnetic cascade will take place until the energy of synchrotron photons is $\sim$1 MeV and the spectral index ~-2. Therefore, the expected X-ray spectrum for $E_X <$ MeV, which consists of soft thermal X-rays and hard non-thermal X-rays, is given by

$$\frac{d\dot{N}_X}{dE_X} = F_{bb}(T_s, E_X) + AE_X^{-2}\,, \tag{18.24}$$

where F_{bb} is the blackbody spectrum with a characteristic temperature $kT_s = E_X^s$, which satisfies $\int F_{bb}E_X dE_X = L_X^{soft}$ and $A \approx 1.7\times10^{35}\ f^{1/2}P^{-65/12}\ B_{12}^{29/12}\ \tan^4\alpha/\ln(\mathrm{MeV}/\hbar eB(r_s)/mc)$, where r_s is the distance to the star at which the magnetic field becomes strong enough to convert the curvature photons into pairs. We can see that the X-rays consist of two components. Therefore when we fit a finite energy range in X-rays by a simple power law, the photon index could vary for different energy range. Cheng and Zhang [26] have found that the model predicted photon index in the energy range from 100 eV to 2.4 keV is $\sim$1 whereas the photon index in the energy range from 2–10 keV is $\sim$1.15, which is only slight steeper than the softer energy band. In fact, they argue that X-ray emission from rotation-powered pulsars in general consist of one non-thermal component, two hard thermal components, and one soft thermal component. The non-thermal X-rays come from synchrotron radiation of $e^{\pm}$ pairs created in the strong magnetic field near the neutron star surface by curvature photons emitted by charged particles on their way from the outer gap to the neutron star surface. The first hard thermal X-ray component results from polar-cap heating by the return current in polar gap. The second hard thermal X-ray component results from polar-cap heating by the return particles from the outer gap. Because of cyclotron resonance scattering, most of the hard thermal X-rays will be effectively reflected back to the stellar surface and eventually re-emitted as soft thermal X-rays. However, some of the hard thermal X-rays can still escape along the open magnetic field lines, where the $e^{\pm}$ pair density is low. Furthermore, the characteristic blackbody temperatures of the two hard X-ray components emitted from the polar-cap area inside the polar gap and the polar cap area defined by the footprints of the outer-gap magnetic field lines are strongly affected by the surface magnetic field, which can be much larger than the dipolar field. In fact, the strong

surface magnetic field can explain why the effective blackbody radiation area is nearly two orders of magnitude larger than that deduced from the dipolar field for young pulsars (two orders of magnitude less for old pulsars). However, how many components can be observed depend on the magnetic inclination angle and viewing angle. Their model can explain the observed X-ray spectra from Geminga, PSR B1055−52, PSR B0656+14, and PSR B1929+10 very well. Unlike those two hard thermal X-ray components, which can only be observed in a small solid angle, the non-thermal component and the soft thermal component can cover a much larger solid angle and they are also the strongest components. Therefore (18.24) should be the most likely observed X-ray spectrum.

18.5.3 Single Gap Models

After studying the γ-ray production and light curves for various magnetosphere geometries based on the CHR model, [28] assumed that gap-type regions could be supported along all field lines which define the boundary between the closed region and open field line region rather than just on the bundle of field lines lying in the plane containing the rotation and magnetic dipole axes. In this case, photons are generated which travel tangential to the local magnetic field lines, and there are beams in both the outward (away from the neutron star) and inward directions, because the accelerating gaps are populated by pair production. They considered the pulse profile of radiation produced in the outer gap and showed that a single pole will produce a broad, irregularly-shaped, emission which is particularly dense near the edge. As a result, double γ-ray pulses will be observed when the line of sight from the Earth crosses these enhanced regions of the γ-ray beam, while the inner region of the beam provides a significant amount of emission between the pulses. With a proper choice of the observer viewing angle, a wide range of peak phase separations can be accommodated. Furthermore, [29] refined the calculation of high energy emission from the rotation-powered pulsars based on the CHR model. Their major refinements include (1) the approximate location of the emission at each point in phase along a given line of sight was inferred by using a pulse phase map, and (2) because the spectral emissivities at different emission points will differ, so the outer gap is divided into small sub-zones in the plane containing the rotation and dipole axes. The photon densities and beaming directions for different zone are also different, in which case the particle transport needs to be considered. Under their refinements, they found that the spectral variation of the γ-radiation over the pulsar period is the result of the different emission processes which play a role throughout the outer magnetosphere, however, they were not able to obtain a self-consistent spectrum which resembled the observed high energy spectra, and they attributed this shortcoming to the inability to model appropriately the extremely complex emission processes and their interactions.

Romani and Yadigaroglu [79] modeled the emission geometry and calculated the pulse profile from the single pole outer gap, including the full effects of aberration,

retarded potential and time-of-flight across the magnetosphere. In their model, the radio to γ-ray pulse offset of the known pulsars, and the shapes of the high energy pulse profiles, were determined by using the knowledge of inclination angle α and viewing angle ζ. They gave a range of α and ζ for γ-rays from a pulsar which can be detected at the Earth, and showed that the values of α and ζ for the known γ-ray pulsars can be chosen within observational constraints which not only fall within the parameter space required for γ-ray observability but can explain the measured phase profile offsets and phase separations. Their results indicate that the phase offset is inversely related to the phase separation, and that γ-ray emission can only be observed from pulsars for which the viewing angle is large ($\zeta \geq 45^\circ$), while nearly aligned pulsars ($\alpha \leq 35^\circ$) with their radio emission pointed toward the Earth will have their γ-ray emission beamed away from the Earth (for example PSR B0656+14). Based on this model, Yadigaroglu and Romani [101] calculated the variation of the beaming fraction as a function of the efficiency of high energy γ-ray production. They argued that as the pulsar slows down, the gap should widen and the distance between the last closed field lines and the radiating surface should increases, so more of the open field lines occupy the gap, which implies that older pulsars have larger gaps and will be more efficient at producing $\sim$GeV γ-rays. Moreover, high energy photons from the outer gaps are primarily radiated along the upper surface of the vacuum gap [29], so a broader outer gap will produce emission closer to the dipole axis. Therefore, the γ-ray beaming solid angle is smaller for an old pulsar. Yadigaroglu and Romani [101] used the fact that the efficiency should increase with age and the observed values of PSR B1706$-$44 and PSR B1055$-$52 to derive a phenomenological scaling law for all high energy pulsed emission

$$\eta_\gamma = 3.2 \times 10^{-5} \tau^{0.76}, \tag{18.25}$$

with the characteristic age τ in years. The cut-off to this evolution occurs as the beaming factor drops to zero at $\sim 10^6$ yr.

Romani [78] described a revised picture of gap closure and an emission model for γ-ray pulsars based on curvature radiation reaction-limited charges in the outer magnetosphere. In this model, the following assumptions are made: (1) there is a gap which start near the intersection of the null charge surface and the surface of last closed field lines for which particles can rotate with the star, where the acceleration electric field $E_\parallel \sim r^{-1}$; (2) charges are created in this gap and a modest fraction of the local corotation charge density $n_{GJ} = 7 \times 10^8 B_z(r)/P\,\mathrm{cm}^{-3}$ experiences this acceleration field, these charges are limited by curvature radiation to $\gamma_{lim} = (eE_\parallel/5.6 \times 10^{-3} mc)^{1/4}/s^{1/2}$ and emit curvature photons with a typical energy $E_c \propto \gamma^3/s$, which comprise the main observed EGRET spectrum of the γ-ray pulsars; (3) the gap is maintained by photon-photon pair production, in which soft photons come from the thermal surface emission of the neutron star, with an evolutionary temperature $T(t) = 10^6 (t/10^5)^{-0.05} \exp(-t/10^6)$ K, where time t is in units of years. Because the primaries each radiate $n_\gamma \approx eE_\parallel R_L/2E_c$ photons in transversing the outer gap and the optical depth for primary photons traveling through the magnetosphere is small ($\leq 10^{-3}$ to 10^{-2}), the bulk of the primary flux escapes to

produce the observed beams, but a small fraction of the n_γ primary photons produced by each primary charge produces pairs in the gap, and (4) the electron energy spectrum in the gap is $dN_e/dE_e \propto E_e^{-p}$ with $p = 4$, which causes a curvature spectrum with a spectral index ~ -1.7 extending from $E_c \sim 3$ GeV down to $\sim$20 MeV for parameters similar to Vela's. Moreover, since photons are aberrated across field lines, pairs are initially produced with a significant pitch angle $\sim$0.1 radian and the pairs near the null charge line will emit synchrotron radiation with a typical energy $E_{syn} \sim$2 MeV for Vela parameters. Obviously, one of the key quantities in this model is the fractional width of the gap, Romani estimated it by calculating the pair multiplication $n_{mul} = n_\gamma n_2 \sigma_{\gamma\gamma} r_i$, where, n_2 is the soft photon density above threshold and r_i is the radius of the gap closure point. He also estimated the efficiency for GeV photon production and the γ-ray beaming fraction, which are functions of the fractional width of the gap. This model produces phase-resolved GeV spectra for Vela-like parameters which are consistent with those observed by EGRET.

18.5.4 CRZ Model

Cheng et al. [20], (hereafter CRZ) re-consider the three-dimensional magnetospheric outer gap model, following the important ground-breaking work of Romani and co-workers. But instead of assuming a *single* outer gap with *only* an outgoing current, and no restriction on azimuthal directions, they use various physical processes (including pair production which depends sensitively on the local electric field and the local radius of curvature, surface field structure, reflection of $e^{\pm}$ pairs because of mirroring and resonant scattering) to determine the three-dimensional geometry of the outer gap. In their model, two outer gaps and both outgoing and incoming currents are in principle allowed, but it turns out that outgoing currents dominate the emitted radiation intensities. Furthermore, the three-dimensional structure of outer gaps is completely determined by pair production conditions. Since the potential drop of the gap is

$$\Delta V \approx 6.6 \times 10^{12} f_0^2 B_{12} P^{-2} \text{ V} , \tag{18.26}$$

where $f_0 = h(<r>)/R_L$, $h(<r>)$ is the average width of the gap boundaries in the (Ω, μ) plane and $R_L = c/\Omega$ is the light cylinder radius, and $<r>$ is the average distance to the gap; its value depends on magnetic inclination angle α ($<r> \sim R_L/2$). The particle current passing through the gap is

$$\dot{N}_{gap} = 3 \times 10^{30} f_0 \xi B_{12} P^{-2} \text{ s}^{-1} , \tag{18.27}$$

where $\xi = \Delta\phi/2\pi$; $\Delta\phi$ is the transverse extension of the gap. Each of the charged particles inside the gap will radiate high-energy curvature photons with a characteristic energy

$$E_\gamma(f_0) = 2 \times 10^8 f_0^{3/2} B_{12}^{3/4} P^{-7/4} \text{ eV} . \tag{18.28}$$

About half of $\dot{N}_{gap}$ will move toward the star. Although they continue to radiate their energies on the way to the star, they still carry $10.5P^{1/3}$ erg of energy on to the stellar surface. The energy will be radiated back out in hard X-rays. However, resonant scattering with pairs near the star may reflect hard X-rays back to the stellar surface [17,98], to be re-emitted as soft X-rays with a temperature

$$T_s \approx 3.8 \times 10^6 f_0^{1/4} \xi^{1/4} B_{12}^{1/2} P^{-5/12} \text{ K} . \tag{18.29}$$

The X-ray photon density is very low but each pair produced by an X-ray-curvature photon collisions in the outer gap will emit almost 10^5 curvature γ-rays for further pair creation in that gap. Once the pair production threshold condition $kT_sE_\gamma \geq (m_ec^2)^2$ is satisfied, the gap is unlikely to grow much larger. This pair production condition gives

$$f_0 = 5.5P^{26/21} B_{12}^{-4/7} \xi^{1/7} . \tag{18.30}$$

Here, ξ is still an unknown quantity. However, f_0 is weakly dependent on ξ which is likely of order of unity. In first approximation, they assume $f_0 = 5.5P^{26/21}B_{12}^{-4/7}$ [104]. To determine ξ, they consider local pair production processes. The pair production per unit length inside the gap is a decreasing function of r. According to [18], $E_{||} \propto r^{-1/2}$ for the thin outer gap (e.g., the Crab pulsar), which gives $E_\gamma(r) \propto r^{-1/8}$ after using the large r limit $s(r) = (rR_L)^{1/2}$. Since E_γ is only weakly dependent on r, they assume $\sigma_{\gamma\gamma} \approx const$.

The local pair production per unit length is

$$N_{e^\pm}(r) = (1 - e^{-\tau_{\gamma\gamma}}) N_\gamma(r) \approx \tau_{\gamma\gamma} N_\gamma(r) , \tag{18.31}$$

where $\tau_{\gamma\gamma} = n_X(r)\sigma_{\gamma\gamma} l(r)$ is the local optical depth, $n_X = R^2 T_s^4 \sigma / r^2 kT_s c$ is the X-ray number density at r, $l(r) \approx (2s(r)f(r)R_L)^{1/2}$ is the local optical path, $f(r) = h(r)/R_L$ is the local vertical extension of the gap (since $B(r)h^2(r)$ is a constant, which gives $f(r) \propto r^{3/2}$ and $f_0 \sim f(R_L/2)$), and $N_\gamma = eE_{||}(r)/E_\gamma(r)$ is the number of curvature photons emitted at r per e^+/e^- per unit length. Then

$$N_{e^\pm}(r) \propto r^{-11/8} . \tag{18.32}$$

Since most pairs are produced near the null surface where $r = r_{in}$, so the pair production take place mainly in the range $r_{in} \leq r \leq r_{lim}$ where r_{lim} is estimated as $r_{lim}N_{e^\pm}(r_{lim})/r_{in}N_{e^\pm}(r_{in}) \sim (r_{lim}/r_{in})^{-3/8} \sim 1/2$, which gives $r_{lim} \sim 6r_{in}$. This limits pair production both along the field lines and in transverse directions, and gives

$$\Delta\Phi \sim 160^\circ . \tag{18.33}$$

Within the pair production regions, outgoing and incoming directions for particle flows are allowed. For $r > r_{lim}$ only outgoing current is possible.

The total gamma-ray luminosity is given by $L_\gamma = f_0^3 \dot{E}$, where $\dot{E}$ is the spin-down power of pulsar or it can be expressed as

$$L_\gamma \approx 3.6 \times 10^{31} f^3 B_{12}^2 P^{-4} \text{ erg s}^{-1}. \quad (18.34)$$

The radiation spectrum produced by the primary particles with power-law distribution through synchro-curvature radiation [25] in the outer gap has been obtained by [104]. Therefore, the differential flux at the earth is given by

$$F(E_\gamma) = \frac{1}{\Delta\Omega d^2} \frac{d^2 N_\gamma}{dE_\gamma dt}, \quad (18.35)$$

where $\Delta\Omega$ is the solid angle of γ-ray beaming and d is the distance to the pulsar.

Inside the light cylinder, high energy photons will be emitted nearly tangent to the magnetic field lines in the co-rotating frame because of the relativistic $1/\gamma$ beaming inherent in high energy processes unless $|\mathbf{E} \times \mathbf{B}| \sim \mathbf{B^2}$. Then the propagation direction of each emitted photons by relativistic charged particles can be expressed as (ζ,Φ), where ζ is the polar angle from the rotation axis and Φ is the phase of rotation of the star. Effects of the time of flight and aberration are taken into account. A photon with velocity $\mathbf{u} = (u_x, u_y, u_z)$ along a magnetic field line with a relativistic addition of velocity along the azimuthal angle gives an aberrated emission direction $\mathbf{u}' = (u'_x, u'_y, u'_z)$. The time of flight gives a change of the phase of the rotation of the star. Combining these two effects, and choosing $\Phi = 0$ for radiation in the (x,z) plane from the center of the star, ζ and Φ are given by $\cos\zeta = u'_z$ and $\Phi = -\phi_{u'} - \mathbf{r} \cdot \hat{u'}$, where $\phi_{u'}$ is the azimuthal angle of $\hat{u'}$ and $\mathbf{r}$ is the emitting location in units of R_L. In numerical calculation we assume that the radiation comes a layer of magnetic field lines, which can be identified from their footprints on the polar cap surface. First we determine the coordinate values (x_0, y_0, z_0) of the last closed field lines at the stellar surface, where should be the lower boundary of the outer gap. Then the coordinate values (x'_0, y'_0, z'_0) for the actual emission region can be determined by using $x'_0 = a_1 x_0$, $y'_0 = a_1 y_0$ and $z'_0 = (1 - (x'^2_0 + y'^2_0))^{1/2}$ for given value of a_1.

In panel A of Fig. 18.3, the emission morphology in the (ζ, Φ) plane is shown. For a given observer with a fixed viewing angle ζ, a double-pulsed structure is observed because photons are clustered near two edges of the emission pattern due to the relativistic effects (cf. panel B of Fig. 18.3).

In Fig. 18.3, we can see that this model can only produce radiation between two peaks. However, the observed data of the Crab, Vela and Geminga indicate that the leading wing 1 and the trailing wing 2 are quite strong, and even the intensity in off-pulse cannot be ignored. Hirotani and his co-workers [51, 55] have pointed out that the large current in the outer gap can change the boundary of the outer gap. They solve the set of Maxwell and Boltzmann equations in pulsar magnetospheres and demonstrate the existence of outer-gap accelerators, whose inner boundary position depends the detail of the current flow and it is not necessarily located at the null charge surface. For the gap current lower than 25% of the Goldreich–Julian current, the inner boundary of the outer gap is very close to the null surface [49]. On the other hand if the current is close to the Goldreich–Julian current, the inner boundary can be as close as 10 stellar radii (cf. Fig. 18.4).

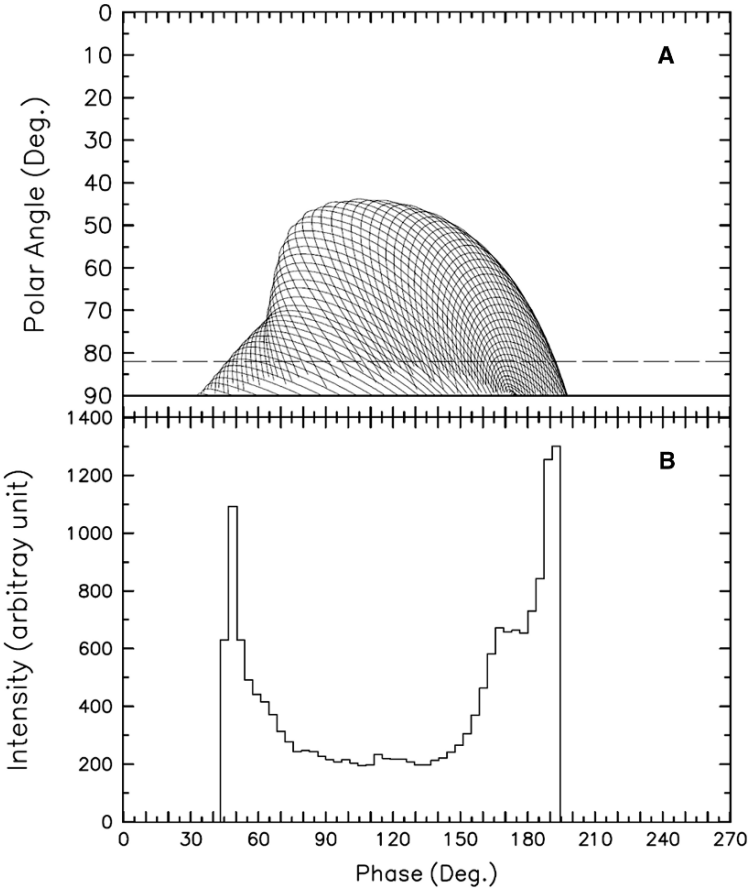

Fig. 18.3 **A** Emission projection onto the (ζ,Φ) plane and **B** pulse profile for the single pole outer gap [20]. The photons are emitted outwards from the outer gap. The choice of parameters are $a1 = 0.9$, $\alpha = 65^\circ$ and $\zeta = 82^\circ$

In Fig. 18.5, we show the light curve by assuming the inner boundary is extended inward from the null charge surface to 10 stellar radii (cf. panel A of Fig. 18.5). In panel B of Fig. 18.5, the solid line represents emission trajectory of outgoing radiation of gap 1 from the null surface to the light cylinder with $\alpha = 50^\circ$ and $\zeta = 75^\circ$ and the dashed line represents the outgoing radiation from the gap 2 from the inner boundary to the null surface. In the presence of the extended emission region from the near the stellar surface to the null charge surface, leading wing 1, trailing wing 2 and the off-pulse components can be produced. Recently, Takata et al. [91] have also shown that the extension of the outer gap plays a crucial role in explaining the polarization data of the Crab pulsar.

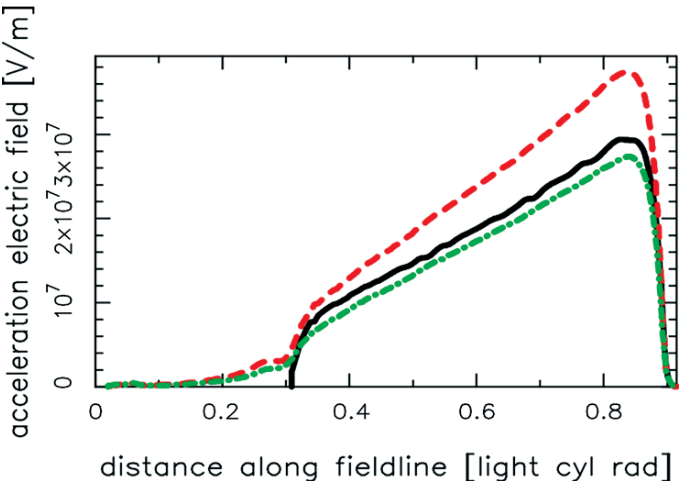

Fig. 18.4 The gap electric field for various intensities of gap current [49]. The *solid line, the dashed line and the dot-dashed line* are 25%, 50% and 75% of Goldreich–Julian current. The null charge surface is located at $\sim 0.3 r_L$

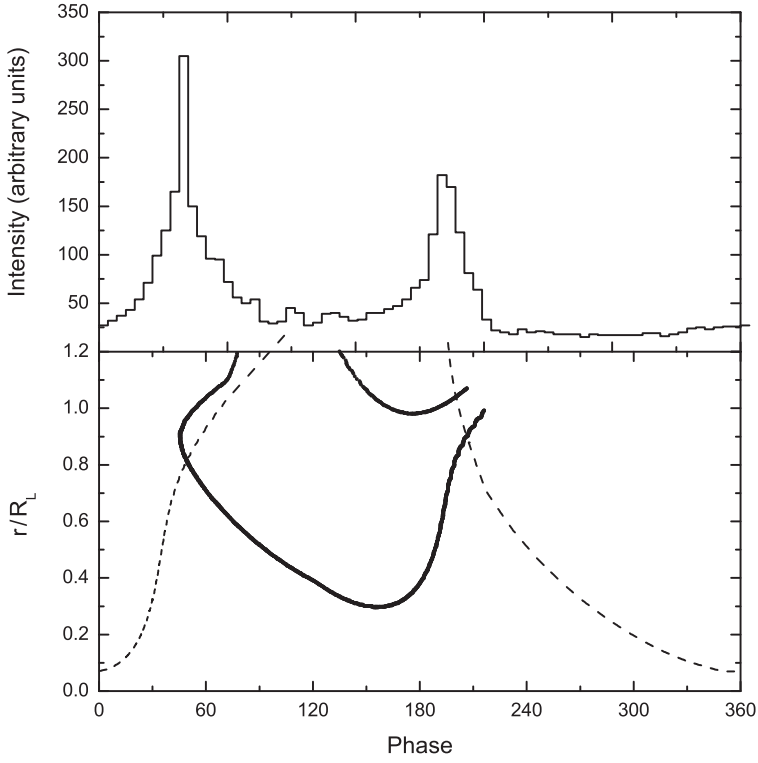

Fig. 18.5 *Upper panel*: the simulated pulse profile of the Crab pulsar; *lower panel*: variation of radial distance with pulse phase for the Crab pulsar in units of R_L, where the *bold line* represents those in the outer magnetosphere, and the *dashed line* represents those in the inner magnetosphere. The inclination angle is 50° and the viewing angle is 75° [60]

18.6 Model Fitting of the Radiation from the Crab Pulsar

In this section, we intend to use the three-dimensional outer gap models introduced in last section to explain the phase-resolved spectrum and the polarization properties of the Crab pulsar.

18.6.1 Phase-Resolved Spectrum of the Crab Pulsar

The Crab pulsar has been studied from the radio to the extremely high energy ranges, and the phase of the double-pulse with separation of 144° is found to be consistent over all wavelengths. Recent observations from COMPTEL and EGRET [64, 95] made it possible to study the phase-resolved properties of the Crab pulsar in γ-ray energies, which indicated that the radiations are from different regions inside the pulsar magnetosphere and phase-resolved spectra are locally dependent. Fierro et al. [36] divided the whole phase into eight intervals, i.e., two peaks, two leading and trailing wings, the bridge between the peaks, and the off-pulse, and we will follow this definition in this paper.

The phase-resolved properties provide more clues and constraints for the theoretical models. So far, the three-dimensional outer gap model seems the most successful model in explaining both the double-peak pulse profile and the phase-resolved spectra of the Crab pulsar (CRZ). However, the leading-edge and trailing-edge of the light curve cannot be given out, since the inner boundary of the outer gap is located at the null charge surface in this model. Recently, the electro-dynamics of the pulsar magnetosphere has been studied carefully by solving the Poisson equation for electrostatic potential and the Boltzmann equations for electrons/positrons [49, 52–54], and the inner boundary of the gap is shown to be located at several stellar radii from the star.

Here, we use the synchrotron self-Compton mechanism (e.g., [24]) to describe the high energy emission from the Crab pulsar.

The electric field of a thin outer gap (CHR) is

$$E_{\parallel}(r) = \frac{\Omega B(r) h^2(r)}{cs(r)} = \frac{\Omega B(r) f^2(r) R_L^2}{cs(r)} \,, \tag{18.36}$$

where $h(r)$ is the width of the outer gap at position r, and $f(r) = h(r)/R_L$ is the local fractional size of the outer gap. Assuming that the magnetic flux subtended in the outer gap is constant in the steady state, we get the local size factor

$$f(r) \sim f(R_L)(\frac{r}{R_L})^{3/2}, \tag{18.37}$$

where $f(R_L)$ is estimated by the pair production condition discussed in the last chapter. As the equilibrium between the energy loss in radiation and gain from

accelerating electric field, the local Lorentz factor of the electrons/positrons in the outer gap is

$$\gamma_e(r) = (\frac{3}{2}\frac{s^2}{e^2 c} eE_{\parallel}(r)c)^{1/4}. \tag{18.38}$$

For a volume element ΔV in the outer gap, the number of primary charged particles can be roughly written as

$$dN = n_{\rm GJ}\Delta A \Delta l, \tag{18.39}$$

where $n_{\rm GJ} = \frac{\Omega\cdot\mathbf{B}}{2\pi ec}$ is the local Goldreich–Julian number density, $B\Delta A$ is the magnetic flux through the accelerator and Δl is the path length along its magnetic field lines. Thus, the total number of the charged particles in the outer gap is

$$N \sim \frac{\Omega\Phi}{4\pi ce} R_L\,, \tag{18.40}$$

where $\Phi \sim f(R_L)B(R_L)R_L^2\Delta\phi$ is the angular range of the outer gap extending along the azimuthal direction. The primary $e^{\pm}$ pairs radiate curvature photons with a characteristic energy

$$E_{cur}(r) = \frac{3}{2}\hbar\gamma_e^3(r)\frac{c}{s(r)}\,, \tag{18.41}$$

and the power into curvature radiation for dN $e^{\pm}$ pairs in a unit volume is

$$\frac{dL_{cur}}{dV} \approx l_{cur} n_{\rm GJ}(r), \tag{18.42}$$

where $l_{cur} = eE_{\parallel}c$ is the local power into the curvature radiation from a single electron/positron. The spectrum of primary photons from a unit volume is

$$\frac{d^2\dot{N}}{dV dE_\gamma} \approx \frac{l_{cur} n_{\rm GJ}}{E_{cur}}\frac{1}{E_\gamma}, \qquad E_\gamma \le E_{cur}\,. \tag{18.43}$$

These primary curvature photons collide with the soft photons produced by synchrotron radiation of the secondary $e^{\pm}$ pairs, and produce the secondary $e^{\pm}$ pairs by photon-photon production. In a steady state, the distribution of secondary electrons/positrons in a unit volume is

$$\frac{d^2N}{dV dE_e} \approx \frac{1}{\dot{E}_e}\int \frac{d^2\dot{N}(E'_\gamma = 2E'_e)}{dV dE_\gamma} dE'_e \approx \frac{1}{\dot{E}_e}\frac{l_{cur} n_{\rm GJ}}{E_{cur}} \ln(\frac{E_{cur}}{E_e})\,, \tag{18.44}$$

with $\dot{E}_e$ the electron energy loss into synchrotron radiation, which is

$$\dot{E}_e = -\frac{2}{3}\frac{e^4 B^2(r)\sin^2\beta(r)}{m_e^2 c^3}(\frac{E_e}{m_e c^2})^2\,, \tag{18.45}$$

where $B(r)$ is the local magnetic field and $\beta(r)$ the local pitch angle,

$$\sin\beta(r) \sim \sin\beta(R_L)(\frac{r}{R_L})^{1/2}\,, \tag{18.46}$$

$\sin\beta(R_L)$ is the pitch angle at the light cylinder. Therefore, the energy distribution of the secondary electrons/positrons in volume $\Delta V(r)$ can be written as

$$\frac{dN(r)}{dE_e} \approx \frac{d^2N}{dVdE_e}\Delta V(r) \sim \frac{1}{\dot{E}_e}\frac{l_{cur}n_{\rm GJ}\Delta V(r)}{E_{cur}}\ln(\frac{E_{cur}}{E_e})\,. \tag{18.47}$$

The corresponding photon spectrum of the synchrotron radiation is

$$F_{syn}(E_\gamma, r) = \frac{\sqrt{3}e^3B(r)\sin\beta}{m_ec^2h}\frac{1}{E_\gamma}\int_{E_{min}}^{E_{max}}\frac{dN(r)}{dE_e}F(x)dE_e, \tag{18.48}$$

where $x = E_\gamma/E_{syn}$, and

$$E_{syn}(r) = \frac{3}{2}(\frac{E_e}{m_ec^2})^2\frac{heB(r)\sin\beta(r)}{m_ec} \tag{18.49}$$

is the typical photon energy, and $F(x) = x\int_x^\infty K_{5/3}(y)dy$, where $K_{5/3}(y)$ is the modified Bessel function of order 5/3. Also, the spectrum of the inverse Compton scattered photons in the volume $\Delta V(r)$ is

$$F_{ICS}(E_\gamma, r) = \int_{E_{min}}^{E_{max}}\frac{dN(r)}{dE_e}\frac{d^2N_{ICS}(r)}{dE_\gamma dt}dE_e, \tag{18.50}$$

where

$$\frac{d^2N_{ICS}(r)}{dE_\gamma dt} = \int_{\varepsilon_1}^{\varepsilon_2} n_{syn}(\varepsilon, r)F(\varepsilon, E_\gamma, E_e)d\varepsilon, \tag{18.51}$$

and

$$F(\varepsilon, E_\gamma, E_e) = \frac{3\sigma_Tc}{4(E_e/mc^2)^2}\times\frac{1}{\varepsilon}[2q\ln q + (1+2q)(1-q) + \frac{(\Gamma q)^2(1-q)}{2(1+\Gamma q)}], \tag{18.52}$$

where $\Gamma = 4\varepsilon(E_e/m_ec^2)/m_ec^2$, $q = E_1/\Gamma(1-E_1)$ with $E_1 = E_\gamma/E_e$ and $1/4(E_e/m_ec^2) < q < 1$. The number density of the synchrotron photons with energy ε is

$$n_{syn}(\varepsilon, r) = \frac{F_{syn}(\varepsilon)}{cr^2\Delta\Omega}, \tag{18.53}$$

where F_{syn} is the calculated synchrotron radiation flux, and $\Delta\Omega$ is the usual beam solid angle.

Figure 18.6 shows the observed data of the phase-resolved spectra from 100 eV to 100 GeV of the Crab pulsar, and the theoretical fitting results calculated by using the synchrotron self-Compton mechanism. The phase intervals are defined by division given by [36], and the amplitude of the spectrum in each phase interval is proportional to the number of photons counted in it. In this fitting, both magnetic poles contribute to the high energy radiation. We allow the properties of the north pole and south pole can be slightly different. The detailed description of fitting procedure is described in [92]. The fitting parameters are given in the figure caption. It is interesting to notice that in TW1, Bridge and LW2 there is a strong component appearing at above GeV. In P2 such component also exists but its intensity is relatively weaker. In fact this component is the survived primary photons emitted from the gap. In order to escape from the pair creation, the primary photons must be produced in regions near the light cylinder and also the local soft photon density is low. Figure 18.5 shows the emission regions of each phase. We can see that TW1, Bridge and LW2 have a relative weak synchrotron component in X-rays (cf. Fig. 18.6) and they also have regions close to light cylinder (cf. Fig. 18.5). Therefore they have a

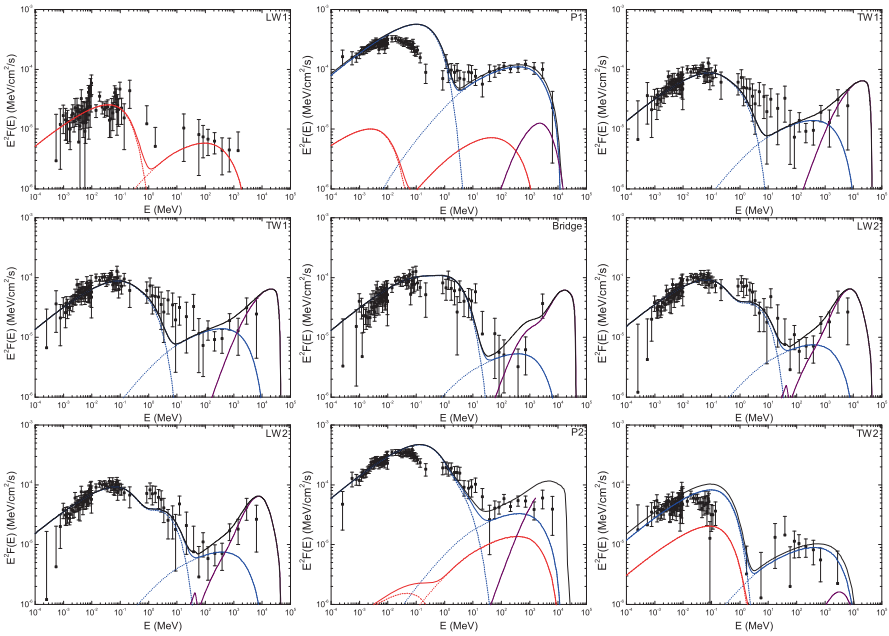

Fig. 18.6 The best model fitting of the phase resolved spectra of the Crab pulsar from 100 eV to 3 GeV in the seven narrow pulse-phase intervals (cf. [92]). Two spectra (for the TW1 and LW2) are displayed twice. The Phase-resolved spectra of the Crab pulsar fitting with $f(R_L) = 0.2$ and 0.3 for the north and the south pole, respectively. $\sin(R_L)$ varies from 0.014 to 0.065. The *red and blue colour lines* represent the contribution from north and south pole respectively. The *black lines* in P1, P2 and TW2 are the sum of the contributions from both poles. The fitting curves are compared to the observed data obtained from [64]. The *curved line* is calculated by the theoretical model, and the observed data are taken from [64]

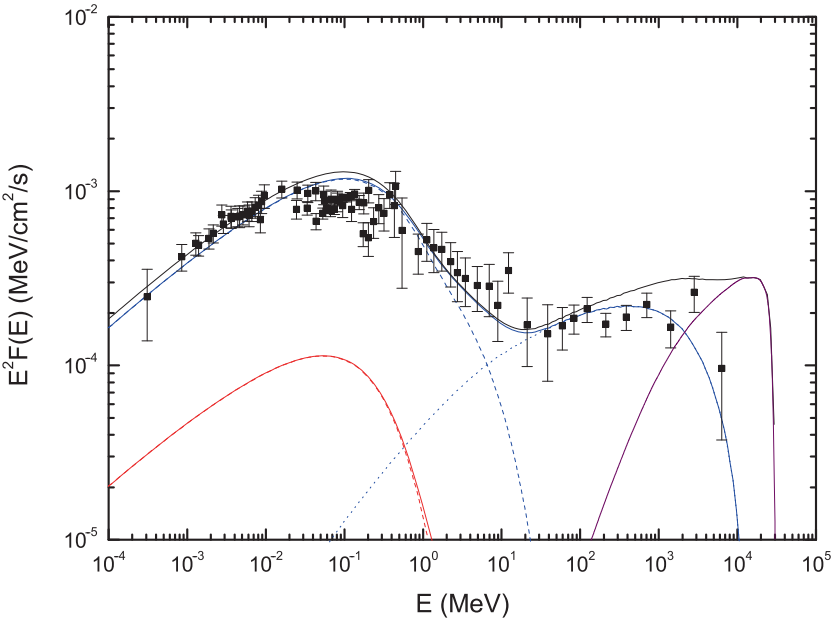

Fig. 18.7 Phase-averaged spectrum of the Crab pulsar. The *dashed line* is the synchrotron radiation and the dotted line is the inverse Compton scattering. The observed data are taken from [64]

relatively high survived primary photon component. On the other hand, the emission regions of LW1 and TW2 are always close to star, they do not have much survived primary photons. Both P1 and P2 have very intense X-rays but P2 has part of emission regions very near the light cylinder (cf. Fig. 18.5). The phase-averaged spectrum of the total pulse of the Crab pulsar is shown in Fig. 18.7. In this figure, we can see that the model has over produced the photons around 10 GeV, which seems some improvement is necessary. However, it is important to note that some curvature photons must survive in TW1, Bridge and LW2, which should be robust results.

18.6.2 Polarization of the Crab Pulsar

Takata et al. [91] investigate the polarization of the high-energy emission from the Crab pulsar based on the framework of the three-dimensional outer gap model proposed by [20], they are able to simultaneously reproduce the light curve, the spectrum, and the polarization characteristics by taking into account the gyration of the particles. In order to explain the polarization degree and angle, they conclude that the inner boundary of the outer gap cannot be located at the null charge surface. Instead the inner boundary should be located about 10 stellar radii away from the

neutron star, which is consistent with the previous studies (e.g., [50, 90]). The main reason is that when the pair creation occurs inside the outer gap, the electric field on the null surface can no longer be zero. A new inner boundary can be re-established in a region near the neutron star. The exact location of the inner boundary depends on the exact current flow in the outer gap. Takata et al. [91] has approximated the electric field inside the region from the null surface to the inner boundary by a quadratical form,

$$E_{\parallel} = E_n \frac{(r/r_i)^2 - 1}{(r_n/r_i)^2 - 1} \,, \tag{18.54}$$

where E_n is the electric field strength at the null charge surface, and r_n and r_i are the radial distances to the null charge surface and the inner boundary respectively.

Then the charged particles are accelerated inside the outer gap and they lose their energy to curvature radiation. However, the curvature photons cannot escape from the light cylinder and they will be converted into secondary electron and positrons. Synchrotron radiation of the secondary pairs produce the optical to soft gamma-rays. Some of gamma-rays will be further converted into tertiary pairs, which are important to contribute the net polarization between two peaks. They calculate the Stokes parameters to obtain the polarization position angle curve and the degree of polarization, which are compared with the Crab optical data (cf. Fig. 18.8). They

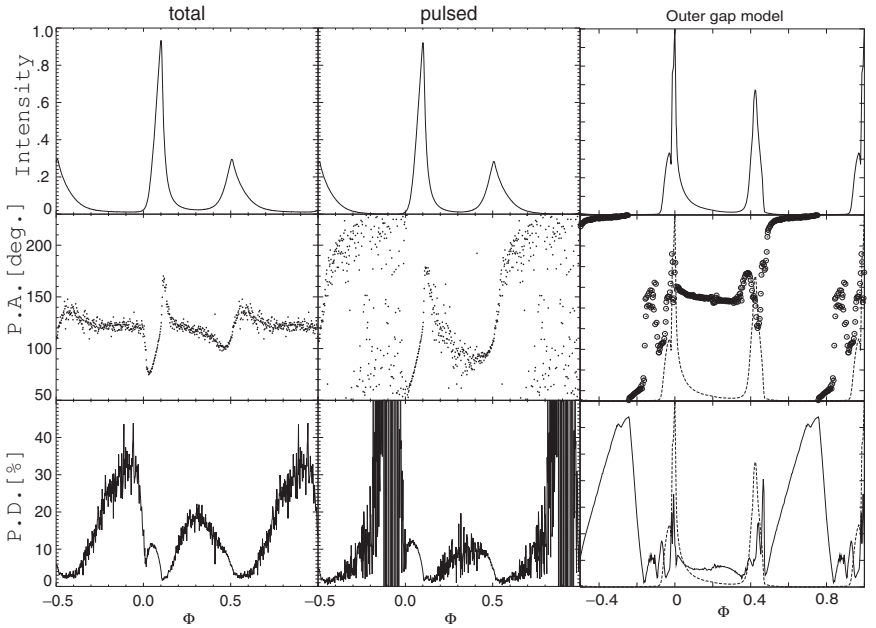

Fig. 18.8 Optical polarization for the Crab pulsar. *Left*, polarization characteristics for the total emission from the pulsar; *middle*, polarization characteristics of the emission after subtraction of the DC level [62]; *right*, predicted polarization characteristics at 1 eV for $\alpha = 50°$, $\zeta = 100°$, and $r_i = 0.67 r_n$

demonstrate that the radiation from inside the null charge surface produces the outer wing and off-pulse portions of the light curve and that the tertiary pairs contribute to the bridge emission. The emission from the secondary pairs explains the main features of the observed light curve and spectrum. On the other hand, the emissions both from inside the null charge surface and from the tertiary pairs are required in order to explain the optical polarization behavior of the Crab pulsar. The energy dependence of the polarization features is predicted by the model. From the polarization position angle curve indicates that our viewing angle as measured from the pulsar's rotational axis is greater than 90°.

18.7 A Simple Pulsar Wind Model

The non-thermal radiation can be contributed by the shock wave produced between the pulsar wind and the outflow matter of the companion star (e.g., [88, 93]) or the surrounding nebula (e.g., [27]). In pulsar binaries, the nebula non-thermal emission may be released from the shock front between the pulsar wind and the stellar wind of the companion and interstellar medium (ISM). In this section we introduce simple models to calculate the high energy spectral properties produced from pulsar wind.

Within the theoretical framework, the energy of the electrons is converted to X-ray radiation solely at the shock termination radius. For pulsar motion which is subsonic, the determination of this radius is obtained via the balance between the wind ram pressure and total magnetic and particle pressure within the nebula [76]. In this case, the wind bubble will be nearly centered about the position of the pulsar. Rees and Gunn [76] estimated $R_s \sim 3 \times 10^{17}$ cm, which is consistent with the size of the inner X-ray ring of the Crab nebula ($\sim$0.1 pc, see [63, 99]). The termination shock picture is not necessarily restricted to slowly moving pulsars since even for pulsars moving at several hundred kilometers per second the motion can be subsonic in, for example, regions where the gas has been heated to temperatures of $\sim 10^8$ K by a supernova shock. The radius of the termination shock can be estimated as

$$R_s \simeq \left(\frac{L_{\rm sd}}{B^2 c}\right)^{1/2} \sim 6 \times 10^{14} L_{\rm sd,34}^{1/2} B_{mG}^{-1} \,{\rm cm}\,, \tag{18.55}$$

where $L_{\rm sd,34}$ is the pulsar spin-down power in units of $10^{34}\,{\rm erg\,s^{-1}}$ and $B_{\rm mG}$ is the magnetic field strength in the nebula in milli-gauss. With the observed values of the Crab pulsar and its nebula ($L_{\rm sd,34} = 5 \times 10^4$ and $B_{\rm mG} = 0.5$), consistency of the shock radius is easily achieved.

For supersonic motion, the nebula will form a bow shock morphology. In this case, the termination shock radius is given by the balance of the ram pressure between the wind particles and the medium at the head of the bow shock:

$$\frac{L_{\rm sd}}{4\pi c R_s^2} = \frac{1}{2}\rho_{\rm ISM} v_p^2\,, \tag{18.56}$$

where $\rho_{\rm ISM}$ is the density of the interstellar medium and v_p is the pulsar's proper motion velocity. The termination shock radius is given as

$$R_s \simeq (\frac{L_{\rm sd}}{2\pi\rho_{\rm ISM}v_p^2 c})^{1/2} \sim 3\times10^{16}L_{\rm sd,34}^{1/2}n_1^{-1/2}v_{\rm p,100}^{-1}\,{\rm cm}\,, \tag{18.57}$$

where n_1, and $v_{\rm p,100}$ are the number density in the interstellar medium in units of 1 particle cm^{-3} and the pulsar space velocity in units of 100 km s^{-1}. For example, [14] recently discovered a bow shock structure coincident with the Geminga pulsar based on observations obtained with *XMM-Newton*. An estimate of the termination radius for Geminga follows from its spin down power, $L_{\rm sd} \simeq 3.2\times10^{34}$ erg s^{-1}, distance of $\sim$160 pc, and proper motion velocity of $v_p \sim 120$ km s^{-1} [11], leading to a radius of 4×10^{16} cm which is consistent with the observational constraint on Geminga's compact X-ray nebula.

Generally, assuming the equipartition between the electron energy and magnetic field, i.e., $\varepsilon_e \sim \varepsilon_B \sim 0.5$, the magnetic field in the emitting region of the shock can be estimated as $B = (6\varepsilon_B\dot{E}/R_s^2c)^{1/2}$. For the strong relativistic shock, the postshock electron energy distribution is $N(\gamma) \propto \gamma^{-p}$ for $\gamma_m < \gamma < \gamma_{\rm max}$, where $\gamma_m = \frac{p-2}{p-1}\varepsilon_e\gamma_w$, γ_w is the Lorentz factor of the relativistic pulsar wind. $\gamma_{\rm max}$ can be estimated by the equivalence between the electron acceleration time-scale and the synchrotron cooling time-scale. The electron synchrotron cooling time is $t_{\rm syn} = 6\pi m_e c/\sigma_T\gamma B^2$, the acceleration time is given by $t_{\rm acc} = \gamma m_e c/eB$, then $\gamma_{\rm max} = (6\pi e/\sigma_T B)^{1/2}$, where σ_T is the Thompson cross section. So the maximum photon energy emitted by the relativistic electrons is about $E_{\rm max} \sim \frac{3\hbar eB}{2m_e c}\gamma_{\rm max}^2 \sim 250$ MeV.

The number of radiating particles at γ, $N(\gamma)$, is determined by a balance between the rate at which particles are injected at the shock front $\dot{N}(\gamma)$ and synchrotron losses. The synchrotron power of an electron with γ is $P(\gamma) = \frac{4}{3}\sigma_T c\gamma^2\frac{B^2}{8\pi}$ and $\dot{N}(\gamma) = (p-1)\gamma_m^{p-1}(\gamma_w m_e c^2)^{-1}\dot{E}_{sd}\gamma^{-p}$. The balance between injection and synchrotron losses can be expressed as $\frac{1}{m_e c^2}\frac{\partial N(\gamma)P(\gamma)}{\partial\gamma} = \dot{N}(\gamma)$. The solution is $N(\gamma) = \gamma_m^{p-1}(\gamma_w P(\gamma))^{-1}\dot{E}\gamma^{-(p-1)}$. The luminosity of radiating particle in the range from γ to $\gamma+d\gamma$ is $P(\gamma)N(\gamma)$, leading to the luminosity per unit frequency

$$L_\nu = k(p)\gamma_w^{p-2}R_s^{-(p-2)/2}\dot{E}^{(p+2)/4}\nu^{-p/2}\,, \tag{18.58}$$

when $\nu_X > \nu_c$ is called the fast cooling regime. Here $k(p) = \frac{1}{2}(\frac{p-2}{p-1})^{p-1}(\frac{6e^2}{4\pi^2 m_e c^3})^{(p-2)/4}\varepsilon_e^{p-1}\varepsilon_B^{(p-2)/4}$, ν_X is the observed X-ray frequency and ν_c is called the cooling frequency. The determination of the cooling frequency is given as $\nu_c = \frac{e}{2\pi m_e c B^3}(\frac{6\pi m_e c}{\sigma_T t})^2$, where t is a characteristic timescale of the nebula estimated as the flow timescale in a characteristic radiation region, i.e., $t \sim R_s/v_p$. For the slow cooling case $\nu_X < \nu_c$, $L_\nu \sim \nu^{-(p-1)/2}$. The luminosity at a particular frequency ν can be estimated as νL_ν. Since $p = 2 \sim 3$, we expect that the photon spectral index of high energy spectrum produced by pulsar wind should be $1.5 \sim 2.5$.

Non-thermal radiation can also arise from a shock wave resulting from the interaction between the pulsar wind and the outflowing matter from the companion

star [5, 88, 93]. In this context, the neutron star is at a distance, D, from the surface of its binary companion given by $D = R + R_s$, where R_s is the shock wave termination radius as measured from the neutron star surface and R is the distance of the shock from the surface of the companion star. For millisecond pulsars in binary systems with low mass companions, we adopt an orbital separation $\sim 2 \times 10^{11}$ cm. If we assume that mass is lost isotropically from the companion star, the loss rate is given as $\dot{M} = 4\pi\rho(R_* + R)^2 v_w$, where v_w is its outflow velocity, ρ is the density at distance R from the stellar surface and R_* is the radius of the companion. The dynamic outflow pressure given by $P_w(R) = \rho(R) v_w(R)^2$ can be expressed as

$$P_w(R) = \frac{\dot{M} v_w}{4\pi(R_* + R)^2}. \tag{18.59}$$

The termination radius of the pulsar wind is given by the pressure balance between the pulsar and companion outflow and can be expressed as

$$\left(\frac{R_s}{R_* + R}\right)^2 = \frac{\dot{E}}{\dot{M} v_w c}. \tag{18.60}$$

In order to estimate the shock radius, $\dot{M}$ and v_w must be determined. Unlike the case of the progenitor of millisecond pulsars, i.e., the low mass X-ray binaries, where $\dot{M}$ can be estimated from the X-ray accretion luminosity, the mass loss rate from the neutron star companion likely results from the evaporation by a pulsar wind [82]. If the stellar wind is a consequence of evaporation by the pulsar wind, the balance between the stellar wind pressure and the pulsar wind pressure lies near the position of the companion, implying $R_s \sim D$. In taking PSR B1957+20 as an example, we find that $R_s > 0.6(R_* + D)$ under the assumption that the wind velocity is comparable to the escape speed from the companion and the mass loss rate is $< 10^{17}\,\mathrm{g\,s^{-1}}$ (see [87]).

The cooling frequency ν_c is given as $\nu_c = \frac{e}{2\pi m_e c B^3}(\frac{6\pi m_e c}{\sigma_T t_f})^2$, where $t_f \sim \sqrt{3} R_s/c$ is the dynamical flow time and the magnetic field strength at the termination radius is estimated by $B = (6\varepsilon_B \dot{E}/R_s^2 c)^{1/2}$. Taking $\dot{E} \sim 10^{35}$, $\varepsilon_B \sim 0.003$, and $R_s \sim 10^{11}$cm, we obtain $\nu_c \sim 3 \times 10^{21}$Hz. Since the cooling frequency is much larger than the frequency $\nu_x \sim 10^{18}$ Hz, the observed luminosity per frequency $L_\nu \propto \nu^{-(p-1)/2}$. Based on the work by [27], the total X-ray luminosity radiated in the intra-binary shock wave for a solid angle of Ω toward the pulsar is estimated as

$$\begin{aligned} \nu L_\nu = {} & \frac{\Omega}{4\pi} \frac{\sigma_T 6^{(p-3)/4}(p-2)^{p-1}}{2\pi m_e c^{(p+5)/4}(p-1)^{p-2}} (\frac{e}{2\pi m_e c})^{(p-3)/2} \varepsilon_e^{p-1} \varepsilon_B^{(p+1)/4} \\ & \times R_s^{-(p+1)/2} \gamma_w^{p-2} t_f \dot{E}^{(p+5)/4} \nu^{-(p-3)/2}\,, \end{aligned} \tag{18.61}$$

in the X-ray energy band (2–10 keV). It is interesting to note that if we approximate $t_f \sim \sqrt{3} R_s/c$ and $R_s = D$, the above equation can be rewritten as

$$\nu L_\nu = 5 \times 10^{30} \alpha(p) f_{0.1} D_{11}^{-(p-1)/2} \dot{E}_{35}^{(p+5)/4}\,\mathrm{erg\,s^{-1}}\,, \tag{18.62}$$

for $\nu = 10^{18}$ Hz, $\gamma_w = 10^6$, $\varepsilon_e = 0.5$, $\varepsilon_B = 0.003$ and $\alpha(p)$ is a function of p, which only varies from 1 to 2.6 as p increases from 2.2 to 2.6. For simplicity, we may assume it is a constant of order of unity. Here, $f = \Omega/4\pi$, $D_{11} = D/10^{11}$ cm and $\dot{E}_{35} = \dot{E}/10^{35}$ erg s^{-1}. We note that [93] have estimated that $\varepsilon_B \sim 0.02$ in the intra-binary shock region in order to explain the X-ray emission from PSR 1259−63. For this value, the coefficient in equation (12) will change to 3×10^{31}.

18.8 Applications to X-Ray Emission

18.8.1 L_x–L_{sd} Relations from ASCA Data

Over 50 rotation powered pulsars have been detected in the X-ray band [6], but only a fraction of them have been resolved with pulsed non-thermal components. Here, we have selected 23 X-ray pulsars with both pulsed and non pulsed emission measurements obtained from the ASCA mission (listed in Table 18.1). Our pulsar sample includes 19 normal pulsars and 4 millisecond Pulsars (cf. [22] for the description of data selection). Since the ASCA satellite does not have high spatial resolution,

Table 18.1 Characteristics of spin powered pulsars and their X-ray luminosities observed by ASCA [22]

PSR	P (s)	$\dot{P}$ (s s^{-1})	d	$L_{\rm sd}$	$L_{\rm X,tot}$	$L_{\rm X,pul}$	$L_{\rm X,npul}$
J0631+1036	0.288	1.0×10^{-13}	1.0	5.4×10^{34}	4.2×10^{31}	2.0×10^{31}	2.2×10^{31}
J1811−1926	0.065	4.4×10^{-14}	5.0	7.0×10^{36}	1.6×10^{34}	1.9×10^{33}	1.4×10^{34}
B0531+21	0.033	4.2×10^{-13}	2.0	4.5×10^{38}	1.1×10^{37}	6.8×10^{35}	1.0×10^{37}
B0833−45	0.089	1.25×10^{-13}	0.3	6.9×10^{36}	1.9×10^{33}	1.5×10^{32}	1.8×10^{33}
B0633+17	0.237	1.1×10^{-14}	0.16	3.2×10^{34}	8.2×10^{29}	4.6×10^{29}	3.6×10^{29}
B1706−44	0.1025	9.3×10^{-14}	1.82	3.4×10^{36}	6.8×10^{32}	4.1×10^{32}	2.7×10^{32}
B1509−58	0.150	1.54×10^{-12}	4.3	1.8×10^{37}	4.0×10^{34}	1.3×10^{34}	2.7×10^{34}
B1951+32	0.0395	5.8×10^{-15}	2.5	3.7×10^{36}	6.2×10^{33}	6.2×10^{32}	5.6×10^{33}
B1046−58	0.124	9.6×10^{-14}	2.98	2.0×10^{36}	9.5×10^{32}	5.5×10^{32}	4.5×10^{32}
B1929+10	0.227	1.16×10^{-15}	0.17	3.9×10^{33}	1.54×10^{30}	5.6×10^{29}	9.8×10^{29}
B0656+14	0.385	5.5×10^{-14}	0.76	3.8×10^{34}	1.7×10^{31}	1.0×10^{31}	7.0×10^{30}
B0540−69	0.05	4.8×10^{-13}	49.4	1.5×10^{38}	8.3×10^{36}	1.3×10^{36}	7.0×10^{36}
B0950+08	0.253	2.3×10^{-16}	0.12	5.6×10^{32}	4.6×10^{29}	1.6×10^{29}	3.0×10^{29}
B1610−50	0.232	4.93×10^{-13}	7.26	1.6×10^{36}	9.6×10^{33}	3.0×10^{33}	6.6×10^{33}
B1055−52	0.197	5.83×10^{-15}	1.53	3.0×10^{34}	2.7×10^{30}	2.0×10^{30}	7.0×10^{29}
B1853+01	0.267	5.4×10^{-13}	2.02	8.0×10^{35}	1.4×10^{33}	1.4×10^{32}	1.3×10^{33}
J2229+6114	0.0516	7.8×10^{-14}	3.0	2.2×10^{37}	1.7×10^{33}	4.0×10^{32}	1.3×10^{33}
B0537−69	0.016	5.13×10^{-14}	47	4.8×10^{38}	2×10^{36}	1.7×10^{35}	1.8×10^{36}
J1846−0258	0.32	7.1×10^{-12}	19	1×10^{37}	1×10^{36}	4×10^{34}	1×10^{36}
B1937+21	0.00156	1.05×10^{-20}	3.6	1.1×10^{36}	5.7×10^{32}	2.5×10^{32}	3.2×10^{32}
J2124−3358	0.005	1.08×10^{-20}	0.25	3.5×10^{33}	4.8×10^{29}	1.6×10^{29}	3.2×10^{29}
B1821−24	0.003	1.6×10^{-18}	5.1	2.2×10^{36}	6.5×10^{33}	9.4×10^{32}	5.5×10^{33}
J0437−47	0.0058	2.0×10^{-20}	0.18	4.2×10^{33}	1.3×10^{30}	4.0×10^{29}	9.0×10^{29}

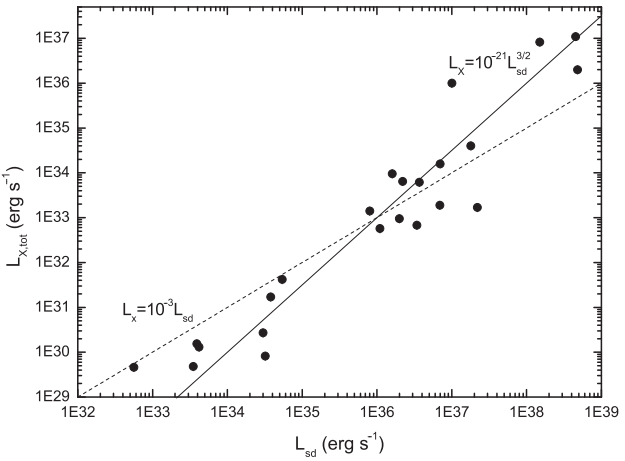

Fig. 18.9 The total X-ray luminosity (2–10 keV) from ASCA observations vs. spin-down power of 23 X-ray pulsars. The *solid line* is $L_{\rm X} = 10^{-21} L_{\rm sd}^{3/2}$ [84], and the *dashed line* represents $L_{\rm X} = 10^{-3} L_{\rm sd}$ [7]. The best fitting function is $L_{\rm X} \propto L_{\rm sd}^{1.35}$

the X-ray luminosity of the pulsars in the ASCA field is composed of emission from the pulsar's magnetosphere and compact pulsar wind nebula. For reference, the total pulsed plus non pulsed X-ray luminosity in the ASCA energy range (2–10 keV) is plotted vs. spin down power in Fig. 18.9. A correlation is found which is consistent with the form $L_x \propto L_{\rm sd}^{1.5}$ found by [84], but the best fit form of this correlation is found to be $L_x \propto L_{\rm sd}^{1.35\pm0.2}$. Here, the error in the power law exponent represents $\pm 1\sigma$ corresponding to the scatter in the observed data points, which may reflect variations in ε_e, ε_B, γ_w, and uncertainties in distance from pulsar to pulsar. Our best fit power law relation is consistent with the conclusion of [74], who used a sample of 39 pulsars observed mainly by ROSAT and data from ASCA, RXTE, BeppoSAX, Chandra and XMM-Newton. Although [74] considered their result ($L_x \propto L_{\rm sd}^{1.34}$) statistically unacceptable, our result is not subject to the uncertainties associated with the normalization of different satellite data to obtain the X-ray luminosity between 2 and 10 keV (cf. Table 18.1 of [74]), for which the extrapolation relied on the uncertain photon index in the ROSAT energy band.

The X-ray luminosity associated with the pulsed emission component is illustrated vs. spin down power in Fig. 18.10. A correlation separate from the total luminosity is found which is inconsistent with either the form $L_{\rm x} \propto L_{\rm sd}$ or $L_x \propto L_{\rm sd}^{3/2}$. The best fitting function to the data is found to be $L_{\rm X,pul} \simeq (1.0 \pm 0.6) \times 10^{-11} L_{\rm sd}^{1.2\pm0.08}$, which significantly deviates from the $3/2$ power law relation proposed by [84]. Such a relation is consistent with the relation $L_x \propto L_{\rm sd}^{1.15}$ derived from the theoretical X-ray magnetospheric emission model. However, this latter result is not without uncertainties since the inclination angle of the magnetic field with respect to the rotation axis and the viewing angle is not well determined. The observed conversion efficiencies are found to range from $\sim 10^{-5}$ to 9×10^{-3}, which is not in conflict with model predictions [17, 26].

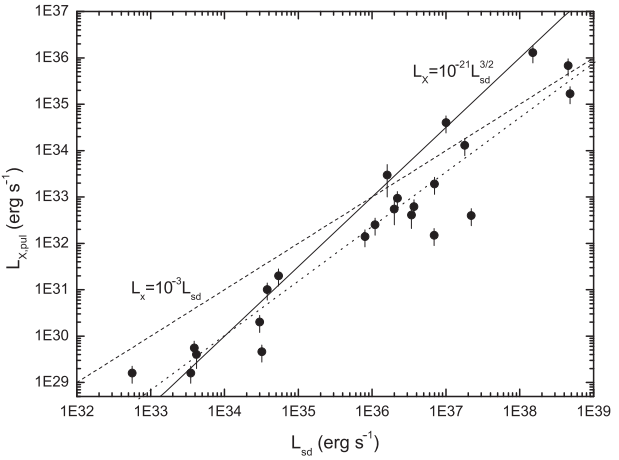

Fig. 18.10 The pulsed X-ray luminosity (2–10 keV) from ASCA observations vs. spin-down power of 23 X-ray pulsars. The *solid line* is $L_{\rm X} = 10^{-21} L_{\rm sd}^{3/2}$, and the *dashed line* represents $L_{\rm X} = 10^{-3} L_{\rm sd}$. The relation between the pulsed component and spin-down power cannot be described by both the two formulae. The best fitting function is shown as the *dotted line*, $L_{\rm X,pul} = 10^{-11} L_{\rm sd}^{1.2}$

A correlation is also found to exist between the non pulsed X-ray luminosity and the spin down power as shown in Fig. 18.3 of [22]. The data points are consistent with the previous ASCA relation of the type $L_{\rm x} \propto L_{\rm sd}^{3/2}$, but the correlation is also consistent with $L_{\rm x,npul} \propto L_{\rm sd}^{1.4\pm0.1}$. Upon comparison to the results from Fig. 18.9, this power law relation is a consequence of the fact that the pulsar emission in the ASCA sample is dominated by the non pulsed radiation component. The conversion efficiency for the non pulsed component overlaps with that for the pulsed component, but extends to efficiencies as high as 0.1.

Generally, the X-ray luminosity of pulsar wind nebulae [27] is a nonlinear function of the spin down power. As can be seen in last section, the nebula's X-ray luminosity follows from

$$L_x \propto \varepsilon_e^{p-1} \varepsilon_B^{(p-2)/4} \gamma_w^{p-2} R_s^{-(p-2)/2} L_{\rm sd}^{(p+2)/4}. \tag{18.63}$$

Here, ε_e and ε_B are assumed to be constant, but $R_s \propto L_{\rm sd}^{1/2}$ from (55) and (57). Although the above equation corresponds to the fast cooling regime, the dependence of L_X on L_{sd} for the slow cooling regime is unchanged because the ratio of the X-ray luminosities in these two regimes depends only on the cooling frequency ν_c, which is independent of L_{sd}. We note that γ_w also depends on the spin down power so the explicit dependence of L_x on L_{sd} remains to be theoretically determined. To estimate this dependence we make use of the results of [80] and [2], who argued that large fluxes of protons (ions) could also be extracted from the neutron star and accelerated in the parallel electric field in the magnetosphere. The initial Poynting flux can be converted into particle thermal and kinetic energy well within the termination radius. Since both electrons and protons are basically accelerated

by the low frequency electromagnetic wave generated by the pulsar, they will be accelerated to the same relativistic speed as they are bound by the strong electrostatic force. Hence, the Lorentz factor of the electrons and protons are the same, leading to the result that the protons may have carried away most of the spin down power [30]. Thus, we can obtain a form for the spin down power from

$$L_{\rm sd} \sim \dot{N}\gamma_w m_p c^2, \tag{18.64}$$

where $\dot{N}$ is the outflow current from the surface. This current should be of the order of the Goldreich–Julian current [40] given as $\dot{N} \simeq 1.35 \times 10^{30} B_{12} P^{-2} {\rm s}^{-1}$. Since $L_{\rm sd} \simeq 10^{31} B_{12}^2 P^{-4}\,{\rm erg\,s}^{-1}$, we find $\dot{N} \propto L_{\rm sd}^{1/2}$, leading to $\gamma_w \propto L_{\rm sd}^{1/2}$. Therefore, we obtain the relation $L_x \propto L_{\rm sd}^{p/2}$, where p generally varies between 2 and 3. The relation deduced from the non pulsed X-ray luminosity and spin down power of observed pulsars may result from a relatively high electron energy index in the nebula.

18.8.2 Why Do MSPs in the Field and Those in 47 Tuc Obey Different L_x–L_{sd} Relation?

The discovery of millisecond pulsars (MSPs) as a class of rapidly rotating ($P < 10$ ms), weakly magnetized ($B \lesssim 10^{10}$ G) neutron stars has stimulated considerable interest in the fundamental properties of these objects. The detailed observational study of these sources over periods of time have provided insights into their origin and evolution in close binary systems (see for example, [73]). The hypothesis that MSPs are neutron stars recycled in a spin up phase during which angular momentum and mass are accreted from a companion star [1, 75] has been dramatically confirmed with the observational detection of the four millisecond accreting X-ray pulsars J1808.4−3658 [100], J1751−305 [67], J0929−314 [37], and J1807−294 [66]. Their combination of short spin period and low dipole magnetic field strengths have, furthermore, provided important clues on the temporal evolution of magnetic fields in neutron stars in low mass X-ray binary systems ([97]; see also [10] for a recent review).

Insights into the nature of the emission mechanisms have been facilitated by observational investigations over broad spectral regions. As an example, the early X-ray studies of MSPs using the ROSAT satellite revealed that the MSPs in the Galactic field appear to have a non thermal character (see [7, 8]) with a power law photon index ranging from ~ -2 to -2.4. On the other hand, the recent X-ray studies with the Chandra satellite by [42] indicate that the MSPs in 47 Tuc appear to be consistent with a thermal blackbody spectrum characterized by a temperature corresponding to an energy of 0.2–0.3 keV.

Additional evidence supporting the apparent difference between the MSPs in the Galactic field and in 47 Tuc and, hence difference in their fundamental properties, can be gleaned from the relation between the X-ray luminosity, L_x, and the spin down power, L_{sd}, expressed in the form $L_x \propto L_{sd}^{\beta}$. Using ROSAT data [7,8] found that

$\beta \sim 1$ for MSPs in the Galactic field, whereas there are hints that the dependence is shallower ($\beta \sim 0.5$) for the MSPs in 47 Tuc (see [42]). An existence of a correlation between these two quantities provides strong evidence for relating the energy source of the X-ray emission to the rotational energy of the underlying neutron star. We shall, for convenience, group the MSPs with properties similar to the Galactic field as Type I and those similar to the MSPs in 47 Tuc as Type II, even though the nearest MSP J0437−4715 has an X-ray spectrum consisting of two thermal components and one non thermal component [102].

Despite the fact that these two types of MSPs have similar values in rotation period, orbital period and dipole magnetic field. They have the following differences. X-rays from MSPs in the field is dominated by the non-thermal whereas X-rays from MSPs in 47 Tuc is dominated by thermal component (cf. [41]). Furthermore, there are observation evidence that MSPs in the field with parameters similar to the Crab and the Vela could be gamma-ray sources (cf. [21]). On the other hand, the entire 47 Tuc may contains over hundreds of MSPs but it is not a EGRET source, which implies MSPs in the globular cluster are poor gamma-ray emitters even they have similar parameters as those in the field, why? Form the evolution point of view, even both types of MSPs may be recycle pulsars. Whereas the stellar density in 47 Tuc is much higher. Consequently MSPs in the globular cluster may change their companions a few time during their life time. If accretion can affect the surface magnetic field structure, which is likely the case, MSPs in the globular cluster may have much more complicated field morphology than those in the field. Finally although the spin-down age for both type of MSPs is similar, the true age of MSPs in globular cluster is most likely older than those in the field.

Cheng and Taam [21] have argued that the observed spectra and X-ray luminosities of millisecond pulsars in 47 Tuc can be interpreted in the context of theoretical models based on strong, small scale multipole fields on the neutron star surface. For multipole fields that are relatively strong as compared to the large scale dipole field, the emitted X-rays are thermal and likely result from polar cap heating associated with the return current from the polar gap. On the other hand, for weak multipole fields, the emission is non-thermal and results from synchrotron radiation of $e^{\pm}$ pairs created by curvature radiation as described by [104]. The X-ray luminosity, L_x, is related to the spin down power, L_{sd}, expressed in the form $L_x \propto L_{sd}^{\beta}$ with $\beta \sim 0.5$ and $\sim$1 for strong and weak multipole fields respectively. If the polar cap size is of the order of the length scale of the multipole field, s, the polar cap temperature is given by

$$T_s \sim 3 \times 10^6 K \left(\frac{L_{sd}}{10^{34} ergs^{-1}} \right)^{1/8} \left(\frac{s}{3 \times 10^4 cm} \right)^{-1/2}. \tag{18.65}$$

The main reason why such relation occurs is as follow. The polar cap potential with strong multipole is likely insensitive to pulsar parameters (e.g., [26, 61, 83]). The current flow in the polar cap is limited by the Goldreich and Julian current [40], which is proportional to $L_{sd}^{1/2}$. Therefore the thermal X-ray luminosity L_x resulting from the polar cap heating is simple proportional to $L_{sd}^{1/2}$. The existence of multipole also explains why MSPs in 47 Tuc are poor gamma-ray emitters. According to [81],

Table 18.2 Three types of millisecond pulsars and their X-ray properties

	D (kpc)	n (cm^{-3})	B G	v_p ($\mathrm{km\,s}^{-1}$)	$\delta\theta$	$R_{\rm obs}$ (cm)	R_s (cm)	Spectrum
GC[a]	8.5	10^2	10^{-4}	100	$1''$	6×10^{16}	3×10^{15}	Non-thermal
1957+20	1.5	1	10^{-5}	220	$5''$	6×10^{16}	4×10^{16}	Non-thermal
47 Tuc	5	0.1	10^{-5}–10^{-6}	60	$1''$	3.5×10^{16}	2×10^{17}	Thermal

[a]Millisecond pulsars in the Galactic Center and PSR B1957+20. D is the distance, n is the number density in the medium surrounding the pulsar, B is the magnetic field in the interstellar medium, v_p is the pulsar proper motion velocity, $\delta\theta$ is the detection angular limit in the different observations, $R_{\rm obs}\sim D\delta\theta/2$ is the radius of the aperture, and R_s is the predicted shock radius. For the Galactic center, we take a spin down power of $2\times10^{34}\,\mathrm{erg\,s}^{-1}$ and an average velocity of pulsars of $130\,\mathrm{km\,s}^{-1}$, which is lower than the escape speed from this region

they argue that complicated surface magnetic field can emit high curvature photons, which subsequently become pairs in those field leading to outer gap. These pairs can quench the outer gap, therefore non-thermal emission originated from this accelerator is missing. But PWNe should contribute to the non-thermal emission. However, in Table 18.2 we show that the typical shock radius in 47 Tuc is smaller than the observed radius by Chandra in order to identify each MSP in 47 Tuc. Therefore the observation will exclude the non-thermal emission from PWNe [23]. We conclude that the X-ray emission from most MSPs in 47 Tuc can described by thermal X-ray emission with temperature given by above estimation and their $\beta\sim0.5$.

However, there are some exceptions. For examples the more recent work by [13] on the spectral and long-timescale variability analyses of *Chandra* observations of 18 millisecond pulsars in 47 Tuc has led to the discovery that the three sources, 47 Tuc J, O and W, exhibit a significant non-thermal component. The photon index of these three sources are in the range 1 ± 0.56, 1.33 ± 0.79, and 1.36 ± 0.24 respectively. Of these, only 47 W exhibits dramatic X-ray variability as a function of orbital phase. We note that since 47 Tuc O lies near the center of the cluster where the number density of X-ray sources is large its non-thermal spectrum may be contaminated by background sources in the field. Of the remaining two millisecond pulsars, it is possible that the non-thermal spectral components are produced in an intra-binary shock formed by the interaction between the relativistic wind and matter from the stellar companion [13]. Thus, these observations do not suggest a magnetospheric origin for the non thermal emission at such levels. The much higher non-thermal X-ray luminosity from W ($\sim2.7\times10^{31}\,\mathrm{erg\,s}^{-1}$), in comparison to J ($\sim9.3\times10^{30}\,\mathrm{erg\,s}^{-1}$), may reflect the differing nature of the companion star. A main sequence companion star nearly filling its Roche lobe and of mass $>0.13\,\mathrm{M}_\odot$ is associated with W whereas a brown dwarf under-filling its Roche lobe and of mass $<0.03\,\mathrm{M}_\odot$ is associated with J. The X-ray luminosity of the non-thermal components from these MSPs can be estimated following the discussion given in §3.3. Taking an average spin-down power of the millisecond pulsars in 47 Tuc, $\dot{E}\sim2\times10^{34}\mathrm{erg\,s}^{-1}$, $p=2.3,\varepsilon_B\sim0.003,\varepsilon_e\sim0.5,\gamma_w\sim10^6$, and $\Omega=1$, we find an non-thermal X-ray luminosity in the band 0.1–10 keV of $4\times10^{29}\,\mathrm{erg\,s}^{-1}$ for an assumed $R_s\sim10^{11}$cm. If we choose $\varepsilon_B\sim0.1,\gamma_w\sim2\times10^5$, a larger X-ray

luminosity $\sim 4 \times 10^{30}\,\mathrm{erg\,s^{-1}}$ results, which is closer to the observed values. This may suggest that ε_B in PWN of MSPs is indeed larger. The remaining deviation by a factor of 3 may suggest an underestimate of the spin down power of these millisecond pulsars by a factor of ~ 2.

18.8.3 X-Ray Tails Associated with Pulsars

The X-ray emitting region with a characteristic frequency ($\nu_X = \frac{3\gamma^2 eB}{2m_e c}$) may exhibit a tail-like spatial structure provided that the pulsar velocity exceeds that of the termination shock front and the nebula magnetic field is sufficiently low. In this case, the distance traversed by the pulsar within the synchrotron cooling timescale can be taken as a lower limit of the elongation length. Specifically, the synchrotron cooling time in the X-ray band is $\tau_c = 6\pi m_e c/\gamma\sigma_T B^2 \sim 10^8 B_{mG}^{-3/2}(h\nu_X/\mathrm{keV})^{-1/2}\,\mathrm{s}$ where B_{mG} is the magnetic field in the emission region in milli-gauss. Thus, the typical cooling time is $\sim 10^{11}$ s for $B_{mG} = 0.01$, and the length of the X-ray elongated feature is about $l \sim v_p \tau_c \sim 10^{18}\,\mathrm{cm}$ for a pulsar moving at a velocity of $100\,\mathrm{km\,s^{-1}}$ with respect to the interstellar medium.

The X-ray images of some pulsar wind nebulae, indeed, reveal extensive X-ray tails. Seven cases are thought to be the consequence of a bow shock formed by the high velocity pulsar (e.g., Geminga, PSR B1823−13, B1757−24, B1957−20, J1747−2958, J1124−5916 and B1853+01). The two pulsars J1930+1852 and B0453−685 exhibit elongated structures and may also be bow shock structures. On the other hand, the Crab and Vela nebulae exhibit an outflow structure (X-ray jet). For more detail discussion of X-ray tails of pulsars (cf. [22, 23]).

18.9 Conclusion

In general, high energy radiations from pulsars can come from either polar gaps or outer gaps. However, from the light curve, optical emission and the energy dependent spectra of the Crab pulsar it is quite clear that they are emitted from the outer-magetopsheric regions rather than from regions near the surface. Slot gaps, which can extend to high altitudes, can also be possible alternative accelerators. However, the potential drop of the slot gap (e.g., [2]) is limited because it is connected at the polar cap. Therefore it is geometrically thin and the emission cone is quite small. It is not clear if such thin gap can provide enough power to explain the observed data in the Crab pulsar.

In order to explain the light curves and the phase-resolved spectrum of pulsars correctly, it is inevitably that three-dimensional models must be used. We have given a detailed model fitting for the phase-resolved data of the Crab pulsar. The general features of the data can be produced by the simple outer gap model. In particular, the detail optical polarization properties can be explained and the spectral break in

ultra-violet can also be obtained in the model (cf. [91]). The model also predicts that the polarization angle swing can only obtain if the viewing angle is larger than 90°. In model fitting it is important to note that the inner boundary of the outer gap cannot begin at the null charge surface otherwise the leading wing, trail wing and the off pulse can not be obtained.

We have suggested that the non-thermal non pulsed X-rays from the direction of pulsars may come from the pulsar wind nebulae. We estimate that the X-ray spin-down power and the non-thermal non pulsed X-ray luminosity should be related as $L_x \propto L^{p/2}sd$, where p is the index of the electron distribution and it is between 2 and 3 [22]. The pulsed non-thermal component of X-rays should follow $L_x \propto L^{1.15}sd$ [26]. Despite the orbital period, dipole magnetic field, rotation period and companion star for millisecond pulsars in the field and millisecond pulsar in the globular clusters are so similar, the structure of their surface may be very much different. Consequently most millisecond pulsars in globular cluster, e.g., 47 Tuc, are poor gamma-ray emitters and their X-rays are dominated by thermal X-rays [21, 81]. Since the shock radii of the pulsar wind nebulae for millisecond pulsars in the globular clusters are so large than the non-thermal emission from the nebulae will be excluded from observations. On the other hand it is interested in checking how much non-thermal X-rays from the pulsar wind nebulae of millisecond pulsars can contribute to the non-thermal X-ray emission from the entire cluster. Taking the characteristic conversion efficiency $\eta \sim 1\%(0.1\%)L_{sd}$ for the fast(slow) cooling process, the X-ray luminosity from the entire cluster contributed by the millisecond pulsars could be $10^{34}(\eta/10^{-2})(N/100)\,\mathrm{erg\,s^{-1}}$, where N is the number of millisecond in the globular cluster. It is interesting to notice that the tail length of the pulsar wind nebulae can be a nice data to estimate the local magnetic field [58, 59].

Although the general features of the Crab data can be produced by the simple outer gap model. However, a lot of fine details in data are still unable to be explained. Obviously, the detail electrodynamic structure of the accelerator in the outer magnetosphere must be studied more carefully. The successful missions of Chandra and XMM-Newton have already imposed great challenge for the existing theoretical models. After the launch of GLAST, we anticipate more challenging data will be observed. New theoretical models are anticipated to be produced to confront with all these new challenges.

References

1. M.A. Alpar, A.F. Cheng, M.A. Ruderman et al.: Nature **300**, 728 (1982)
2. J. Arons: Electron positron pairs in radio pulsars. In: *Positron-electron pairs in astrophysics; Proceedings of the Workshop, Greenbelt, MD, January 6–8, 1983*, ed by M.L. Burns, A.K. Harding, and R. Ramaty (New York: AIP 1983) pp. 163
3. J. Arons: In: *Neutron Stars and Pulsars*, eds. S. Shibata and M. Sato (Universal Academy Press, Tokyo, 1997)
4. J. Arons, E.T. Scharlemann: ApJ **231**, 854 (1979)
5. J. Arons, M. Tavani: ApJ **403**, 249 (1993)

6. W. Becker, B. Aschenbach: X-ray Observations of Neutron Stars and Pulsars: First Results from XMM-Newton. In: *Proceedings of the 270. WE-Heraeus Seminar on Neutron Stars, Pulsars, and Supernova Remnants. MPE Report 278*, ed by W. Becker, H. Lesch, and J. Trümper (Garching bei München: Max-Plank-Institut für extraterrestrische Physik 2002) pp. 64
7. W. Becker, J. Trümper: A&A **326**, 682 (1997)
8. W. Becker, J. Trümper: A&A **341**, 803 (1999)
9. V.S. Beskin, A.S. Gurevich, Ya.N. Istomin: *Physics of the Pulsar*, (Cambridge University Press, Cambridge 1992)
10. D. Bhattacharya: JAA **22**, 67 (2002)
11. G.F. Bignami, P.A. Caraveo: Nature **361**, 704 (1993)
12. G.R. Blumenthal, R.J. Gould: Rev. Mod. Phys. **42**, 237 (1970)
13. S. Bogdanov, J.E. Grindlay, M. van den Berg: ApJ **630**, 1029 (2005)
14. P.A. Caraveo, G.F. Bignami, A. de Luca et al.: Science **301**, 1345 (2003)
15. A. Cheng, M.A. Ruderman, P.G. Sutherland: ApJ **203**, 209 (1976)
16. K.S. Cheng, K.Y. Ding: ApJ **431**, 724 (1994)
17. K.S. Cheng, J. Gil, L. Zhang: ApJ **493**, L35 (1998)
18. K.S. Cheng, C. Ho, M.A. Ruderman: ApJ **300**, 500 (1986a)(CHRI)
19. K.S. Cheng, C. Ho, M.A. Ruderman: ApJ **300**, 522 (1986b)(CHRII)
20. K.S. Cheng, M. Ruderman, L. Zhang: ApJ **537**, 964 (2000)(CRZ)
21. K.S. Cheng, R.E. Taam: ApJ **598**, 1207 (2003)
22. K.S. Cheng, R.E. Taam, W. Wang: ApJ **617**, 480 (2004)
23. K.S. Cheng, R.E. Taam, W. Wang: ApJ **641**, 427 (2006)
24. K.S. Cheng, D.M. Wei: ApJ **448**, 281 (1995)
25. K.S. Cheng, J.L. Zhang: ApJ **463**, 271 (1996)
26. K.S. Cheng, L. Zhang: ApJ **515**, 337 (1999)
27. R.A. Chevalier: ApJ **539**, L45 (2000)
28. J. Chiang, R.W. Romani: ApJ **400**, 629 (1992)
29. J. Chiang, R.W. Romani: ApJ **436**, 754 (1994)
30. F.V. Coroniti: ApJ **349**, 538 (1990)
31. J.K. Daugherty, A.K. Harding: ApJ **252**, 337 (1982)
32. J.K. Daugherty, A.K. Harding: ApJ **458**, 278 (1996)
33. J. Dyks, B. Rudak: ApJ **598**, 1201 (2003)
34. J. Dyks, B. Rudak, A.K. Harding: ApJ **607**, 939 (2004)
35. T. Erber: Rev. Mod. Phys. **38**, 626 (1966)
36. J.M. Fierro, P.F. Michelson, P.L. Nolan et al.: ApJ **494**, 734 (1998)
37. D.K. Galloway, D. Chakrabarty, E.H. Morgan et al.: ApJ **576**, L137 (2002)
38. V.L. Ginzburg, S.I. Syrovatskii: Ann. Rev. Astron. Astrophy. **3**, 297 (1965)
39. T. Gold: Nature **218**, 731 (1968)
40. P. Goldreich, W.H. Julian: ApJ **157**, 869 (1969)
41. J.E. Grindlay: In: *363rd Heraeus Seminar: Neutron Stars and Pulsars Bad Honnef 14–19 May 2006* (2006)
42. J.E. Grindlay, F. Camilo, C.O. Heinke et al.: ApJ **581**, 470 (2002)
43. A.K. Harding: ApJ **245**, 267 (1981)
44. A.K. Harding: In: *363rd Heraeus Seminar: Neutron Stars and Pulsars Bad Honnef 14–19 May 2006* (2006)
45. A.K. Harding, A.G. Muslimov: ApJ **508**, 328 (1998)
46. A.K. Harding, V.V. Usov, A.G. Muslimov: ApJ **622**, 531 (2005)
47. A.K. Harding, B. Zhang: ApJ **548**, L37 (2001)
48. A. Hewish, S.J. Bell, J.D.H. Pilkington, P.F. Scott, R.A. Collins: Nature **217**, 709 (1968)
49. K. Hirotani: Ap&SS **297**, 81 (2005)
50. K. Hirotani: ApJ **652**, 1475 (2006)
51. K. Hirotani, A.K. Harding, S. Shibata: ApJ **591**, 334 (2003)
52. K. Hirotani, S. Shibata: MNRAS **308**, 54 (1999a)
53. K. Hirotani, S. Shibata: MNRAS **308**, 67 (1999b)
54. K. Hirotani, S. Shibata: PASJ **51**, 683 (1999c)

55. K. Hirotani, S. Shibata: MNRAS **325**, 1228 (2001)
56. C. Ho: ApJ **342**, 396 (1989)
57. N.J. Holloway: Nature Physical Science **246**, 6 (1973)
58. C. Y. Hui, W. Becker : A&A, 2006a, 448, 13
59. C. Y. Hui, W. Becker : A&A, 2006b, 457, 33
60. J.J. Jia, A.P.S. Tang, J. Takata, H.K. Chang, K.S. Cheng: 2007, AdSpR, 40, 1425
61. P.B. Jones: MNRAS **192**, 847 (1980)
62. G. Kanbach, A. Slowikowska, S. Kellner, H. Steinle: New optical polarization measurements of the Crab pulsar. In: *Astrophysical Sources of High Energy Particles and Radiation. AIP Conference Proceedings*, vol. 801, pp. 306 (2005)
63. C.F. Kennel, F.V. Coroniti: ApJ **283**, 710 (1984)
64. L. Kuiper, W. Hermsen, G. Cusumano et al.: A&A **378**, 918 (2001)
65. M.I. Large, A.F. Vaughan, B.Y. Mills: Nature **220**, 340 (1968)
66. C.B. Markwardt, E. Smith, J.H. Swank: IAU Circ. No. 8080 (2003)
67. C. Markwardt, J.H. Swank, T.E. Strohmayer et al.: ApJ **575**, L21 (2002)
68. E. Massaro, G. Cusumano, M. Litterio et al.: A&A **361**, 695 (2000)
69. F.C. Michel: *Theory of Neutron Star Magnetospheres*, (University of Chicago Press, Chicago, 1991)
70. A.G. Muslimov, A.K. Harding: ApJ **485**, 735 (1997)
71. A.G.Muslimov, A.I. Tsygan: MNRAS **255**, 61 (1992)
72. F. Pacini: Nature **219**, 145 (1968)
73. E.S. Phinney, S.R. Kulkarni: ARA&A **32**, 591 (1994)
74. A. Possenti, R. Cerutti, M. Colpi et al.: ApJ **387**, 993 (2002)
75. V. Radhakrishnan, F. Srinivasan: Current Science **51**, 1096 (1982)
76. M.J. Rees, J.E. Gunn: MNRAS **167**, 1 (1974)
77. D.W. Richards, J.M. Comella: Nature **222**, 551 (1969)
78. R.W. Romani: ApJ **470**, 469 (1996)
79. R.W. Romani, I.A. Yadigaroglu: ApJ **438**, 314 (1995)
80. M. Ruderman: Evolution and radiation in pulsar polar CAP models. In: *Pulsars: 13 years of research on neutron stars; Proceedings of the IAU Sym. 95, Bonn, West Germany, August 26–29, 1980*, ed by W. Sieber, R. Wielebinski (Dordrecht: Reidel, 1981) pp. 87
81. M. Ruderman, K.S. Cheng: ApJ **335**, 306 (1988)
82. M. Ruderman, J. Shaham, M. Tavani: ApJ **336**, 507 (1989)
83. M. Ruderman, P.G. Sutherland: ApJ **196**, 51 (1975)
84. Y. Saito: Title. PhD Thesis, Univ. Tokyo (1998)
85. F.D. Seward, Z.R. Wang: ApJ **332**, 199 (1988)
86. D.H. Staelin, E.C. Reifenstein: Science **162**, 1481 (1968)
87. B.W. Stappers, B.M. Gaensler, V.M. Kaspi et al.: Science **299**, 1372 (2003)
88. L. Stella, S. Campana, M. Colpi et al.: ApJ **423**, L47 (1994)
89. P.A. Sturrock: ApJ **164**, 529 (1971)
90. J. Takata, S. Shibata, K. Hirotani: MNRAS **354**, 1120 (2004)
91. J. Takata, H.K.Chang, K.S. Cheng: ApJ **656**, 1044 (2007)
92. A.P.S. Tang: The Physics of Neutron Stars. PhD Thesis, Univ. Hong Kong (2007)
93. M. Tavani, J. Arons: ApJ **477**, 439 (1997)
94. D.J. Thompson: In: *363rd Heraeus Seminar: Neutron Stars and Pulsars Bad Honnef 14–19 May 2006* (2006)
95. D.J. Thompson , M. Bailes, D.L. Bertsch et al.: ApJ **465**, 385 (1996)
96. V.V. Usov: ApJ **427**, 394 (1994)
97. E.P. van den Heuvel, J.A. van Paradijs, R.E. Taam: Nature **322**, 153 (1986)
98. F.Y.-H. Wang, M. Ruderman, J.P. Halpern, T. Zhu: ApJ **498**, 373 (1998)
99. M.C. Weisskopf, J.J. Hester, A.F. Tennant et al.: ApJ **536**, L81 (2000)
100. R. Wijnands, M. van der Klis: Nature **394**, 344 (1998)
101. I.-A. Yadigaroglu, R.W. Romani: ApJ **449**, 211 (1995)
102. V.E. Zavlin, G.G. Pavlov, D. Sanwal et al.: ApJ **569**, 894 (2002)
103. B. Zhang, A.K. Harding: ApJ **532**, 1150 (2000)
104. L. Zhang, K.S. Cheng: ApJ **487**, 370 (1997)
105. L. Zhang, K.S. Cheng, Z.J. Jiang, P. Leung: ApJ **604**, 317 (2004)

Chapter 19
High-energy Emission from the Polar Cap and Slot Gap

Alice K. Harding

19.1 Introduction

Forty years after the discovery of rotation-powered pulsars, we still do not understand many aspects of their pulsed emission. In the last few years there have been some fundamental developments in acceleration and emission models. In this Chapter I will review both the basic physics of the models as well as the latest developments in understanding the high-energy emission of rotation-powered pulsars, with particular emphasis on the polar-cap and slot-gap models. Special and general relativistic effects play important roles in pulsar emission, from inertial frame-dragging near the stellar surface to aberration, time-of-flight and retardation of the magnetic field near the light cylinder. Understanding how these effects determine what we observe at different wavelengths is critical to unraveling the emission physics.

Rotation-powered pulsars are fascinating astrophysical sources and excellent laboratories for study of fundamental physics of strong gravity, strong magnetic fields, high densities and relativity. The major advantage we have in studying pulsars is that we know they are rotating neutron stars and that they derive their power from rotational energy loss. The challenge is then to understand how they convert this source of power into the visible radiation. It is generally agreed that this occurs through acceleration of charged particles to extremely relativistic energies, using the rotating magnetic field as a unipolar inductor to create very high electric potentials. Beyond this fundamental, there is a large divergence of thought on what comes next: whether the acceleration occurs in the strong field near the neutron star surface or in the outer magnetosphere near the speed of light cylinder, or even beyond the light cylinder in the wind zone. The particle acceleration may well be occurring in all of these regions, either in the same pulsar or in pulsars of different ages.

A.K. Harding
Astrophysics Science Division, NASA Goddard Space Flight Center
e-mail: harding@twinkie.gsfc.nasa.gov

W. Becker (ed.), *Neutron Stars and Pulsars,* Astrophysics and Space Science Library 357,

In recent years, there has been much activity both in new detections and in theoretical study of rotation-powered pulsars. Multibeam radio surveys at the Parkes Telescope [23, 50] have increased the population of known radio pulsars to more than 1,700. In addition, extended radio observations of supernova remnants and unidentified γ-ray sources have discovered a number of young pulsars that are too radio-faint to be detected by surveys [12]. Although pulsed emission at other wavelengths has been detected from only a small fraction of these, this number is growing as well. At the present time, there are seven pulsars with high-confidence detection of γ-ray pulsations (cf. Chap. 23), about 30 having X-ray pulsations [42] and 10 with optical pulsations [52].

This Chapter will review both the fundamental physics and latest theoretical developments of acceleration and radiation in polar cap models. The complementary Chap. 18 reviews acceleration and radiation in the outer gap model.

19.2 Acceleration Near the Polar Cap and Beyond

A magnetic dipole rotating in vacuum will induce an electric field both along and across the magnetic field lines [18]. In the case of a pulsar, with high angular velocity Ω and surface dipole fields $B_0 \sim 10^{12}$ G, the electric force parallel to the magnetic field just above the neutron star surface exceeds the gravitational force by many orders of magnitude. Vacuum conditions therefore cannot exist outside a pulsar, since charges can be pulled from the stellar surface [24]. If the charge density reaches the Goldreich-Julian value,

$$\rho_{GJ} = \frac{\nabla \cdot \mathbf{E}}{4\pi} \approx -\frac{\Omega \cdot \mathbf{B}}{2\pi c}, \tag{19.1}$$

derived from the condition

$$\mathbf{E} = -\frac{(\Omega \times r) \times \mathrm{B}}{c}, \tag{19.2}$$

then the electric field parallel to the magnetic field vanishes. This is the force-free solution where charges and magnetic field co-rotate with the star. Corotation must break down near the light cylinder, $R_L = \Omega/c$, due to particle inertia. But if vacuum cannot surround a pulsar, neither can a completely force-free magnetosphere, since in that case no acceleration of charge, currents or radiation would exist. A real pulsar must operate somewhere between the two extremes of the vacuum and the force-free states, but a self-consistent, global solution has not yet been found. Global magnetospheric simulations study how a rotating neutron star magnetosphere fills with charge from the vacuum state. The resulting domes and torii of charge that build up near the pole and equator [44, 60] seem to be unstable [67], but the particle-in-cell codes cannot run long enough to reach a stable magnetospheric configuration. However, it seems that a near force-free magnetosphere [68] cannot result only from charges flowing out of the stellar surface, but requires some extra source of charge created in the magnetosphere above the surface. This extra source of charge

is thought to be production of electron-positron pairs by the photons radiated by accelerating particles. The pulsar magnetosphere must somehow be made up of self-consistent force-free and non-force-free regions in balance with each other. One way to determine the structure of these regions is to study the microphysics of the electrodynamics and charge flow at different sites where acceleration may occur. One of these sites, the polar cap accelerator, is near the neutron star surface on the open field lines that cross the light cylinder.

19.2.1 Polar Cap Accelerators

The two main types of polar cap accelerator are vacuum gaps [64, 72] and space-charge limited flow (SCLF) gaps [6, 33]. There are binding (or cohesive) forces on charged particles in the neutron star surface due to the lattice structure in a strong magnetic field, such that particles are free only if the surface layers are above the thermionic emission temperature. For electrons, this temperature is [72]

$$T_e \cong 3.6 \times 10^5 K \left(\frac{Z}{26}\right)^{0.8} \left(\frac{B_0}{10^{12} G}\right)^{0.4} \tag{19.3}$$

and for ions it is

$$T_i \cong 3.5 \times 10^5 K \left(\frac{B_0}{10^{12} G}\right)^{0.73} \tag{19.4}$$

where B_0 is the surface magnetic field strength and Z is the atomic number of matter in the surface layer. If the surface temperature, $T_s < T_{i,e}$, then charges are trapped in the surface and the full vacuum electric field, $E_\parallel = \Omega B_0 R$, where R is the neutron star radius, exists above the surface. If $T_s > T_{i,e}$, then charges are "boiled off" the surface layers and can flow along the open field lines in SCLF. Measured surface temperatures of pulsars are typically $T_s > 0.5 - 3.0 \times 10^6$ K, above T_e and T_i for the normal range $B_0 \lesssim 10^{13}$ of surface fields. However, a few high-field pulsars or magnetars may have $T_s < T_{i,e}$ and vacuum gaps [72, 76]. If $T_s > T_{i,e}$ and the full Goldreich-Julian charge can be supplied right about the surface, the true charge density along each field line will drop faster, $\rho \propto r^{-3}$, than ρ_{GJ} as the dipole field lines flare. A SCLF electric field, $\nabla \cdot E_\parallel = (\rho - \rho_{GJ})/\varepsilon_0$ grows with altitude. The two types of accelerator thus differ by the surface boundary condition: where $\rho(R) = 0$, $E_\parallel(R) \neq 0$ for vacuum gaps and $\rho(R) = \rho_{GJ}$, $E_\parallel(R) = 0$ for SCLF accelerators. The form of $E_\parallel$ in SCLF accelerators is thus sensitive to the detailed distribution of the charge density, which depends both on the open field line geometry as well as the compactness of the neutron star. At altitudes $\{z \ll \theta_{PC}, z \gg \theta_{PC}\}$, with $z \equiv (r/R - 1)$ being the height above the surface,

$$E_\parallel \simeq B_0 \theta_{PC}^2 \left[\{z, \theta_{PC}^2 \left(\tfrac{r}{R}\right)^{-4}\} \kappa \cos\alpha + \{z, \theta_{PC}^2 \left(\tfrac{r}{R}\right)^{-1/2}\} \tfrac{\theta_{PC}}{2} \sin\alpha \cos\varphi\right] \times [1 - \left(\tfrac{\theta}{\theta_{PC}}\right)^2] \tag{19.5}$$

[33, 59], where θ and φ are the magnetic polar and azimuth angles, α is the magnetic inclination angle to the rotation axis, $\kappa = 2GI/(c^2R^3)$ is the stellar compactness parameter, $\theta_{PC} \simeq (\Omega R/c)^{1/2}$ is the polar cap half-angle and I the neutron star moment of inertia. The first term in (19.5) is due to inertial frame dragging near the neutron star surface, and dominates for small r and low inclination, while the second term is due to the flaring of the field lines.

Both accelerators will be self-limited by the development of pair cascades, at altitudes where the particles reach high enough Lorentz factors to radiate γ-ray photons. The dominant process in most pulsars is one-photon pair production, which can occur only in very strong magnetic (or electric) fields. In this process, the magnetic field absorbs the extra momentum of a photon having the energy required to create a pair, so that the threshold condition on the photon energy is $\varepsilon_\gamma = 2mc^2/\sin\theta_{\gamma B}$, where $\theta_{\gamma B}$ is the angle between the photon propagation direction and the local magnetic field. The accelerated particles moving along magnetic field lines with high Lorentz factors radiate γ-ray photons at very small angles to the field ($\theta_0 \sim 1/\gamma$), so the one-photon pair production rate for these photons is initially zero. However, as they propagate through the curved dipole field, their angle increases until the threshold condition and the attenuation coefficient becomes large. The voltage across a vacuum gap breaks down when a stray γ-ray crosses the magnetic field within the gap and creates a pair. The electron accelerates upward/downward for $\Omega \cdot B(>,<)0$ over the polar cap, and the positron accelerates in the opposite direction as shown in Fig. 19.1. Both particles produce more pairs when their radiated photons reach the pair threshold, causing a pair avalanche and sudden discharge of the vacuum.

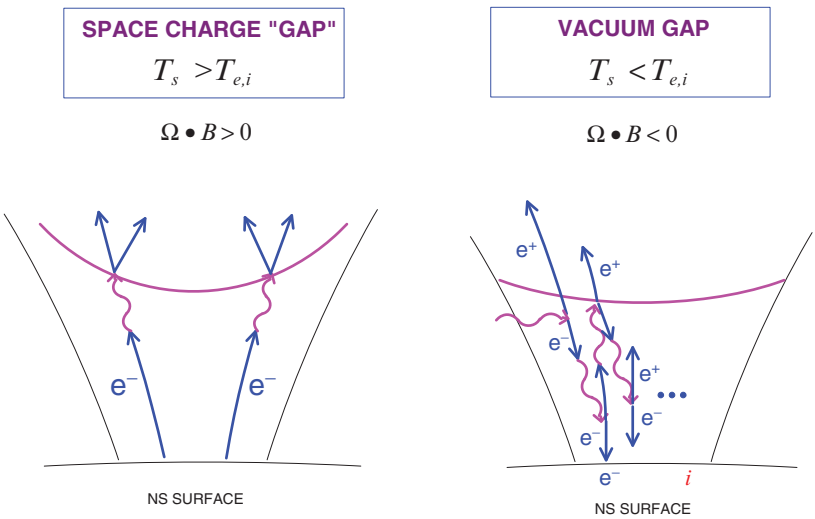

Fig. 19.1 Illustration of space-charge limited flow and vacuum gap accelerators above a pulsar polar cap. T_s is the neutron star surface temperature and $T_{i,e}$ are the ion or electron thermionic temperatures

The potential drop in the gap thus oscillates between $V_{vg} \sim \Omega B_0 (R\theta_{PC})^2/2$ and 0. In SCLF for $\Omega \cdot B(>,<)0$, an electron/positron accelerates upward from the surface until the radiated photons reach pair threshold, at which point the positrons/electrons from the pair decelerate, turn around, and accelerate downward toward the neutron star surface. The polarization of pairs above the pair formation front (PFF), discussed in more detail in Sect. 19.3, may short out the $E_\parallel$, halting any further acceleration at higher altitude. These accelerators can thus maintain a steady current of upwardly accelerating electrons, at $j_\parallel^- \simeq c\rho_{GJ}$, and a downward current of positrons, at $j_\parallel^+ \ll c\rho_{GJ}$, which heat the polar cap. The accelerator voltage is determined by the height of the PFF, which is again roughly comparable to the pair creation mean-free path. However, the stability of SCLF accelerators has not yet been verified through time-dependent models, and some simplified studies [46] have in fact shown that some oscillations in the pair creation rate could exist. This is certainly an issue that needs further investigation. Stability of vacuum gaps has also been studied by Gil et al. [25].

19.2.2 Death Lines

The pair cascades can be initiated either by curvature radiation (CR) [14] or by resonant or non-resonant inverse-Compton scattering (ICS) of stellar thermal X-rays by primary electrons [69]. Since for a given Lorentz factor the peak CR photon energy, $\varepsilon_\gamma = 3\lambda_C \gamma^3/2\rho_c$, where $\lambda_C \equiv h/mc$ is the electron Compton wavelength and ρ_c is the magnetic field radius of curvature, is much lower than the ICS peak energy, $\varepsilon_\gamma \sim \gamma$ in the extreme Klein-Nishina limit, pair production of CR photons requires a much higher particle Lorentz factor. The PFF for ICS therefore occurs at a lower altitude than the PFF for CR [33]. The PFF altitude is the sum of the acceleration length $\propto 1/E_\parallel$ and the pair attenuation length, which are both inverse functions of the magnetic field, and effectively of the pulsar age. If the PFF is larger than a stellar radius, then the magnetic field becomes too weak for pair creation to occur and a PFF does not exist. For SCLF accelerators, CR photons can produce pairs only in the case of young pulsars ($\tau \lesssim 10^7$ yr) and a few millisecond pulsars [34, 38]. One can define a 'death line' in $\dot{P} - P$ space, where $\dot{P}$ is the period derivative, shown in Fig. 19.2 below which pulsars cannot produce pairs from CR photons. Below the CR pair death line, pulsars can produce pairs only from ICS photons [35]. Below a lower, ICS pair death line, pulsars cannot produce any pairs and are expected to be radio quiet. In fact the predicted ICS death line falls close to the edge of the known radio pulsar population, as shown in Fig. 19.2 [36]. The few millisecond pulsars that lie below the ICS pair death line may be able to produce pairs through interaction of ICS photons with thermal X-ray photons from a hot polar cap [78].

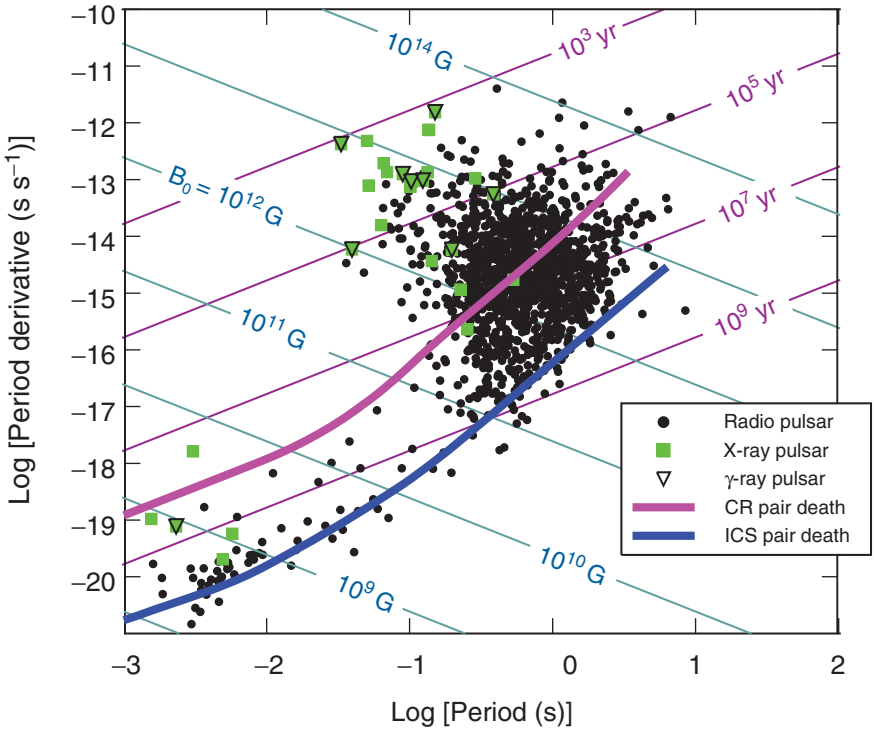

Fig. 19.2 Period derivative vs. period for radio and high-energy pulsars from the ATNF catalog, showing death lines [35] for production of electron-positron pairs through curvature radiation (CR) and inverse Compton scattering (ICS). The ICS pair death line was determined for a neutron star surface temperature of 10^6 K and a standard equation of state [8]

19.3 Electric Field Screening and Polar Cap Heating

In SCLF accelerators, the polarization of charge above the PFF acts both to screen the $E_\parallel$ and to produce heating of the polar cap by the downward flowing particles [4]. Figure 19.3 illustrates the dynamics of electric field screening. Primary electrons (e_p^-) accelerate upward from the stellar surface and produce pairs at different altitudes above the PFF. The positrons decelerate and turn around in a distance short compared to the PFF altitude and each reversing positron creates a small excess of negative charge. As more positrons are produced and decelerated, the space charge becomes more negative until the entire charge deficit $\delta\rho = (\rho - \rho_{GJ})$ that produced the $E_\parallel$ is accounted for. Since the charge deficit is small compared to the primary charge ($\delta\rho \ll \rho_{GJ}$), the screening length scale is a very small fraction of the PFF altitude. The flux of returning positrons, as a fraction of the primary flux, is approximately

$$f_+ \approx \frac{\rho_+}{\rho_{GJ}} = \frac{\rho_{GJ} - \rho}{2\rho_{GJ}}\bigg|_{z_0} \approx \frac{3}{2}\frac{\kappa}{(1-\kappa)} z_0 \tag{19.6}$$

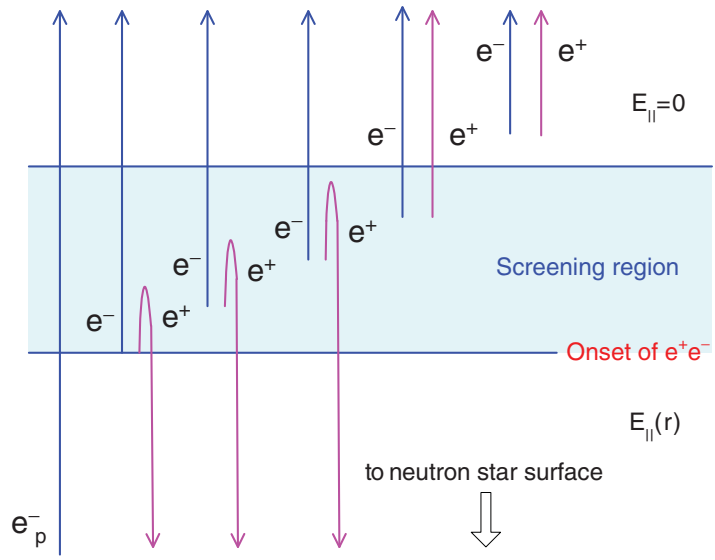

Fig. 19.3 Illustration of electric field screening in SCLF models. e_p^- represents the primary electron flux accelerating upward from the neutron star surface. e^+ and e^- represent electron-positron pairs created by the primary electron above the pair formation front

where z_0 is the PFF height above the stellar surface and κ is the general relativistic factor appearing in the SCLF electric field ((19.5)). The corresponding polar cap heating luminosity is

$$L_+^{\max} \approx f_+ \Phi(z_0)\, \dot{n}_{\rm prim} \tag{19.7}$$

where $\dot{n}_{\rm prim}$ is the primary particle flux and $\Phi(z_0)$ is the potential drop at z_0. The growth in the charge density above the CR PFF is very rapid since the CR peak energy $\varepsilon \propto \gamma^3$ increases rapidly with increasing electron Lorentz factor, γ. The CR initiated cascades have very high multiplicities and the screening of $E_\parallel$ takes place in a relatively short distance above the PFF [34]. The ICS initiated cascades on the other hand have much lower multiplicities since the ICS photon production rate decreases with increasing γ, as $\sim 1/\gamma$, for non-resonant scattering and first increases sharply, then decreases as $\sim 1/\gamma^2$ for resonant scattering. The screening above ICS PFFs takes place over a larger scale length, depending on the polar cap temperature and for a number of pulsars well below the CR pair death line, there is no screening [35]. Even when ICS screening is locally complete, an unscreened charge deficit can develop at higher altitudes since the charge density deficit $\delta\rho$ grows faster than the increase in pair density. In that case, an $E_\parallel$ reappears and acceleration continues. If a CR PFF forms at higher altitude, then screening occurs, otherwise unscreened acceleration continues to high altitude [56].

The CR pair heating luminosity is much higher than the ICS heating luminosity because the CR PFF occurs at higher altitude and a larger flux of positrons returns

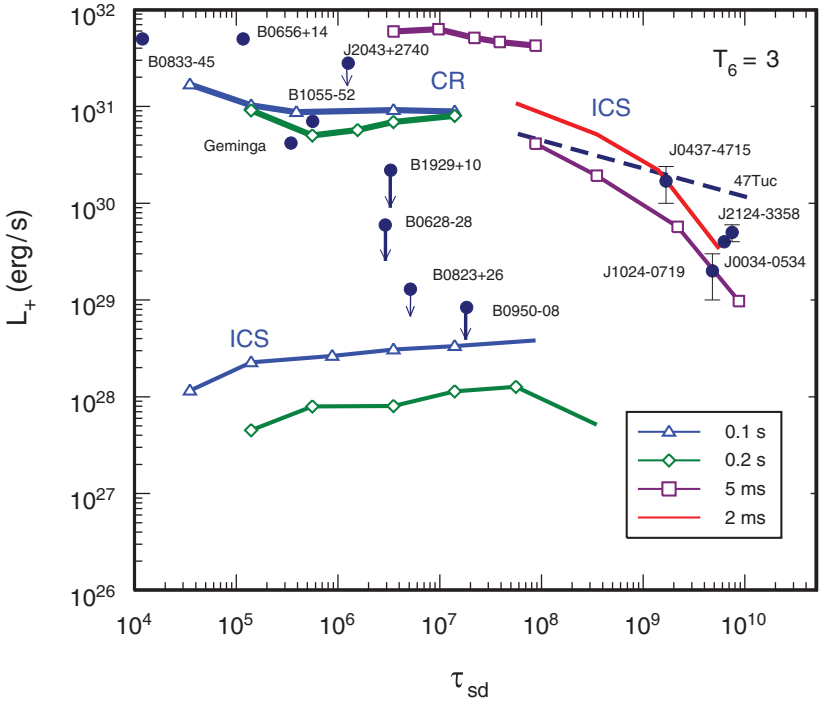

Fig. 19.4 Predicted polar cap heating luminosity, L_+, for SCLF model vs. spin down age [35], τ_{sd}, for different pulsar periods and an assumed polar cap surface temperature of 3×10^6 K. Thick curves are luminosities from curvature radiation (CR) pair heating and thin lines are luminosities from inverse Compton (ICS) pair heating. The solid circles show measured pulsar luminosities and upper limits of hot thermal components (see [42]). The dashed line is the fit of measured luminosity vs. age for the millisecond pulsars in the globular cluster 47 Tuc [10, 27]

through a higher voltage, bombarding the polar cap with higher energy. Figure 19.4 shows calculated heating luminosities from CR and ICS positrons as a function of pulsar characteristic age, $\tau_{\rm sd} = P/2\dot{P}$, for several different periods and a PC surface temperature of $T = 3 \times 10^6$ K. The CR heating lines terminate on the high $\tau_{\rm sd}$ side at the age corresponding to the CR pair death line, which is around $\tau_{sd} \sim 10^7$ yr for periods $P = 0.1, 0.2$ s and around $\tau_{sd} \sim 10^8$ yr for periods $P = 5$ ms. The CR heating luminosities are several orders of magnitude higher than the ICS heating luminosities, for normal pulsars. All the L_+ are higher for millisecond periods, because the PFFs occur at higher altitude and the gap voltage is larger. A sudden drop in L_+ is therefore predicted at the CR death line. Pulsed X-ray emission has now been detected from many middle-aged and older pulsars (cf. Chap. 6). Several thermal components are often seen, one having lower T and larger area, which may be full surface cooling, and another having a higher T and smaller area, which could be due to polar cap heating. The luminosity of the hot thermal components, which are shown in Fig. 19.4, may indicate that the heating luminosity drops suddenly around

$\tau_{sd} \sim 10^7$ yr or somewhat sooner. To within an order of magnitude, the observed luminosities of the hot thermal components agree with the predicted L_+, for both normal and millisecond pulsars.

Although the L_+ plotted in Fig. 19.4 were computed numerically, analytic expressions for L_+ provide a good estimate in the case of complete screening and upper limits in the case of incomplete screening. The heating from CR pair fronts predicts a surface X-ray luminosity of approximately [34]

$$L_+^{(CR)} \simeq 10^{31}\ \mathrm{erg\,s^{-1}} \begin{cases} 0.4\, P^{-6/7} \tau_6^{-1/7} & \text{if } P \lesssim 0.1\, B_{0,12}^{4/9}, \\ 1.0\, P^{-1/2} & \text{if } P \gtrsim 0.1\, B_{0,12}^{4/9}, \end{cases} \tag{19.8}$$

where $B_{0,12} = B_0/10^{12}$ G. The heating from ICS pair fronts predicts a surface X-ray luminosity of approximately [35]

$$L_+^{(IC)} \simeq 2.5 \times 10^{27}\ \mathrm{erg\,s^{-1}}\ P^{-3/2}. \tag{19.9}$$

Since nearly all millisecond pulsars produce only ICS pairs with incomplete screening, the above expression overestimates the predicted L_+ in these sources.

19.4 Slot Gap Accelerator

Due to the geometry of the field lines and the assumed boundary conditions of the accelerator, the altitude of the PFF varies with magnetic colatitude across the polar cap [5,33]. On field lines well inside the polar cap rim, $E_\parallel$ is relatively strong and the PFF is very near the neutron star surface. But at the polar cap rim, which is assumed to be a perfectly conducting boundary, $E_\parallel$ vanishes. Near this boundary, the electric field is decreasing and a larger distance is required for the electrons to accelerate to the Lorentz factor needed to radiate photons energetic enough to produce pairs. The PFF thus curves upward as the boundary is approached, forming a narrow slot gap (see Fig. 19.6) near the last open field line [5]. Since $E_\parallel$ is unscreened in the slot gap, particles continue to accelerate and radiate to high altitude along the last open field lines. The width of the slot gap is a function $\Lambda \equiv P B_{0,12}^{-4/7}$ of pulsar period and surface magnetic field [54], and can be expressed in magnetic colatitude as a fraction of the polar cap half-angle $\Delta\xi_{\mathrm{SG}}$, where $\xi \equiv \theta/\theta_{\mathrm{PC}}$

$$\Delta\xi_{\mathrm{SG}} \simeq \begin{cases} 4\Lambda, & \Lambda < 0.075 \\ 0.3, & \Lambda > 0.075 \end{cases} \tag{19.10}$$

The particles can achieve very high Lorentz factors which at altitudes of several stellar radii are limited by curvature radiation losses, to $\gamma_{SG} \simeq 3 - 4 \times 10^7$ [55]. Since the slot gap is very narrow for young pulsars having short periods and high fields, the corresponding solid angle of the gap emission $\Omega_{SG} \propto \theta_{PC}^2 r \Delta\xi_{SG}$ is quite small. So even though only a small fraction of the polar cap flux is accelerated in the slot

gap, the radiated flux $\Phi_{\rm SG} = L_{SG}/\Omega_{SG}\, d^2$ can be substantial. The total luminosity divided by solid angle from each pole is (from [54])

$$\frac{L_{SG}}{\Omega_{SG}} = \varepsilon_\gamma \left[0.123\cos^2\alpha + 0.51\,\theta_{PC}^2 \sin^2\alpha\right] {\rm erg\,s^{-1}\,sr^{-1}} \times \begin{cases} 9\times 10^{34}\, L_{sd,35}^{3/7} P_{0.1}^{5/7}, & B < 0.1\, B_{\rm cr} \\ 2\times 10^{34}\, L_{sd,35}^{4/7} P_{0.1}^{9/7}, & B > 0.1\, B_{\rm cr} \end{cases} \tag{19.11}$$

where $P_{0.1} \equiv P/0.1$ s, $L_{sd,35} \equiv L_{sd}/10^{35}\,{\rm erg\,s^{-1}}$ is the spin down luminosity, $B_{\rm cr} \equiv 4.4\times 10^{13}$ G is the critical magnetic field strength and ε_γ is the efficiency of conversion of primary particle energy to high-energy emission.

For $\Lambda \gg 0.075$, which corresponds to pulsars below the CR pair death line (see Fig. 19.2), the slot gap disappears since the screening of $E_\parallel$ is no longer effective. These "pair-starved" pulsars may have local screening of $E_\parallel$ near the ICS PFF, but $E_\parallel \neq 0$ at higher altitude so that acceleration can occur over nearly all of the open field volume [56]. The particle Lorentz factors, as in the slot gap, will be limited by curvature-radiation reaction to $\gamma \sim 10^7$.

19.5 High-energy Radiation

19.5.1 Polar Cap and Slot Gap Cascades

As discussed in Sect. 19.2.2, pair cascades above the polar cap may be initiated by either ICS or CR. In the strong magnetic fields near the neutron star, the Compton scattering cross section has a resonance at the cyclotron energy, $\varepsilon_B \sim 12 B_{12}$ keV, where its value is several orders of magnitude higher than the Thompson cross section. The thermal X-rays from the neutron star surface will be blue-shifted into the resonance in the rest frame of the accelerating primary electrons when $kT\gamma(1-\beta\cos\theta) \simeq \varepsilon_B$, where θ is the angle between the photon propagation and the electron velocity (i.e. the magnetic field direction). Since the enhancement of the cross section at the resonance is so large, resonance scattering will dominate if the resonance condition is met [16, 74]. For typical pulsar fields and surface temperatures, electrons with $\gamma \sim 10^2 - 10^6$ will resonant scatter surface thermal X-rays [33, 79] to energies $\varepsilon \simeq \gamma B' mc^2$, where $B' \equiv B/B_{\rm cr}$ is the magnetic field strength in units of the critical field strength, $B_{\rm cr} = 4.4\times 10^{13}$ G. X rays scattered by electrons with $\gamma \sim 10^5 - 10^6$ will produce pairs to form a PFF. Resonant scattering is the dominant mode of ICS pair production for pulsars having the highest fields [38], whereas pulsars with lower fields, that include the millisecond pulsars, produce ICS pairs through non-resonant scattering. For $\gamma \gtrsim 10^5$, the electrons will scatter non-resonantly in the Klein-Nishina limit, to energies $\varepsilon \simeq \gamma$. The ICS pair cascade multiplicities are $M_+^{ICS} \simeq N_+/N_p \sim 10^{-3} - 10$ (pairs per primary electron) [38], which is too low and produced at too low an altitude to completely shut off the acceleration.

When the primary electrons reach $\gamma \gtrsim (0.5-1)\times 10^7$, they produce CR photons that can produce pairs to form a PFF at height $0.02-0.1$ stellar radii. The CR pair cascade multiplicities reach as high as $M_+^{CR} \simeq 10^3 - 10^4$ [3, 38].

The pairs are produced in Landau states whose maximum principal quantum number is $n_{\max} = 2\varepsilon'(\varepsilon'-2)/B'$ [15], where $\varepsilon' = \varepsilon \sin\theta$ is the photon energy in the frame in which it propagates perpendicular to the local magnetic field. When the local field $B \lesssim 0.1 B_{\rm cr}$, pairs will be created above threshold in highly excited Landau states and the excitation level is quite sensitive to field strength, $n_{\max} \propto 1/B'^3$. The pairs will decay through emission of synchrotron/cyclotron photons, many of which will produce more pairs in excited states. A pair cascade can be sustained in such a way through several generations. The pairs can also produce ICS photons, through scattering surface thermal X-rays, which may produce pairs [77]. In high-field pulsars, where $B \gtrsim 0.1 B_{\rm cr}$ near the neutron star surface, the pair creation attenuation coefficient is high enough for pair creation near threshold, so pairs are produced in very low Landau states. In this case, cascade pair multiplicities are lower since the number of cyclotron photons drop significantly [7]. Bound pair production [65] also becomes important for $B \gtrsim 0.1 B_{\rm cr}$, which will further lower the pair multiplicity. When $B \gtrsim B_{\rm cr}$, photon splitting dominates over pair production [31]. The screening of the electric field is also delayed by splitting and creation of bound pairs, effectively increasing the accelerating potential. The effect of bound pair creation on polar cap acceleration has been studied by Usov & Melrose [73].

Radiated spectra from CR-initiated [14] and ICS-initiated [69] cascades are very hard (roughly power laws with indices 1.5–2.0) [30] with sharp cutoffs due to magnetic pair production at energy [28, 31]

$$E_c \sim 2\ {\rm GeV}\, P^{1/2} \left(\frac{r}{R}\right)^{1/2} \max\left\{0.1, B_{0,12}^{-1}\left(\frac{r}{R}\right)^3\right\} \tag{19.12}$$

where r is the emission radius and R is the neutron star radius. An approximate form for the polar cap pair cascade spectrum is given by

$$f(\varepsilon) = A\varepsilon^{-a} \exp\left[-C_{1\gamma}\exp\left(-\varepsilon_{\rm esc}^{1\gamma}/\varepsilon\right)\right] \tag{19.13}$$

where a is the power-law index, $C_{1\gamma} = 0.2(\alpha/\lambda\!\!\!^{-})(B'R^2/\rho)$ and $\lambda\!\!\!^{-} = \lambda_C/2\pi$ is the electron Compton wavelength. The polar cap cascade radiation produces a hollow cone of emission around the magnetic pole, with opening angle, $\theta_\gamma \simeq (3/2)(\Omega r/c)^{1/2}$, determined by the polar cap half-angle at the radius of emission r. The characteristics of emission from this type of polar cap model [17] has been successful in reproducing many features of γ-ray pulsars, including the wide double-peaked pulses observed from γ-ray pulsars like the Crab, Vela and Geminga, and the phase-revolved spectra. However, the polar cap opening angle is very small (a few degrees) unless the emission occurs more than a few stellar radii above the surface [19]. Since the pair cascades over most of the polar cap occur within several stellar radii of the stellar surface, the broad profiles which require beam opening angles of the order of the magnetic inclination angle α, cannot be produced unless the pulsar

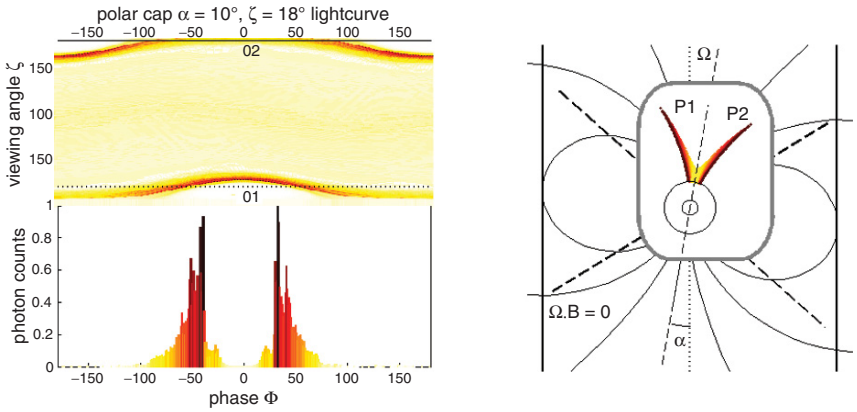

Fig. 19.5 Phase plot, sample lightcurve, and a sketch of the accelerator location for the polar cap model, for a typical inclination angle $\alpha = 10°$. The central zoom gives the gap extent relative to the star size. The dashed lines outline the null surface. The shading in the lightcurve and gap sketch is the same. The phase plot illustrates the change in lightcurve as seen by different observers and the aperture of the pulsed beams (from [26])

is nearly aligned. Daugherty & Harding [17] had to assume extended acceleration to 3 stellar radii and an artificial enhancement of primary particle flux near the polar cap rim in order to reproduce the Vela pulsar spectrum and pulse profile.

Muslimov & Harding [54] found that pair cascades on the inner edge of the slot gap occur at altitudes of 3–4 stellar radii and have higher multiplicities, $M_+ \sim 10^4 - 10^5$, than the polar cap cascades. These are the characteristics required by [17] to model γ-ray pulsars, so a combination of polar cap cascades near the stellar surface and slot gap cascades near the polar cap rim at higher altitude may be successful in explaining non-thermal radiation from some fraction of sources having small magnetic inclination α and viewing angles ζ. Figure 19.5 shows a plot of the total sky emission, phase Φ vs. viewing angle ζ relative to the rotation axis, for a slot gap cascade at inclination angle $\alpha = 10°$. In this model, the magnetic pole is at phase 0°, midway between the two peaks in the profile, which would be the predicted phase peak of polar cap thermal emission.

19.5.2 Radiation from the High-altitude Slot Gap

The electrons that accelerate in the slot gap and generate pair cascades at low altitude continue to accelerate. They will radiate curvature, inverse Compton and synchrotron radiation at high altitudes. Initially, their Lorentz factors will be limited by curvature-radiation reaction, to

$$\gamma_{CRR} = \left(\frac{3}{2}\frac{E_{||}\rho_c^2}{e}\right)^{1/4} \sim 3 \times 10^7 \tag{19.14}$$

and the peak energy of their CR spectrum will be $\varepsilon_{peak}^{CR} = 2\lambda_C \gamma_{CRR}^3 / \rho_c \approx 30\text{GeV}$. As the electrons reach higher altitude, where the local magnetic field has dropped to $B \sim 10^6 - 10^8$ G, they may be able to resonantly absorb radio photons of energy $\varepsilon_{0,GHz}$ that are at the cyclotron resonance in their rest frame. The condition for resonant absorption is

$$\gamma_R = 3 \times 10^5 \frac{B_8}{\varepsilon_{0,GHz}(1 - \beta\mu_0)} \tag{19.15}$$

where $B_8 \equiv B/10^8$ G and μ_0 is the cosine of the angle between the radio photon and the electron momentum. The electrons are then excited to higher Landau states and radiate synchrotron emission. Blandford & Scharlemann [9] investigated this process for pulsars, concluding that it was not an important source of radiation. However, they assumed that the electrons would be excited to only low Landau states and based their estimate on the cyclotron emission rate. Decades later, Lyubarsky & Petrova [48] re-examined resonant cyclotron absorption of radio emission in pulsar magnetospheres and discovered that the rate of absorption is much higher than the rate of re-emission in low-lying Landau states, so the electrons will continue to be excited to high Landau states, and their pitch angles will increase until their momentum perpendicular to the magnetic field is relativistic. The emission is then synchrotron, not cyclotron, which proceeds at a much higher rate. Petrova [61] concluded that this process could be a significant source of radiation for young pulsars. It could also be significant for millisecond pulsars with high radio luminosities like PSR J0218+4232 ([37] and Sect. 19.5.4).

In the slot gap or along open field lines of pair-starved pulsars, electrons can experience both continuous acceleration and resonant cyclotron absorption. A steady-state may be reached between synchrotron radiation (SR) losses and absorption, with perpendicular momentum

$$\frac{p_\perp^{SRR}}{mc} \simeq 302 B_8^{-1} E_{\parallel,5}^{1/2} \tag{19.16}$$

which can indeed be relativistic. In this state, the Lorentz factor can remain locked at $\gamma_R \ll \gamma_{CRR}$ to the cyclotron resonance as the electron moves along the field with the field decreasing [37]. The synchrotron peak frequency decreases with increasing altitude, spreading the emission over a range of energies up to $\sim$100 MeV, and the curvature radiation rate drops dramatically.

Non-resonant inverse Compton scattering of the radio emission by relativistic electrons in the slot gap is also possible. The scattering would be completely in the Thompson regime, and the spectrum would extend to a maximum energy of $\varepsilon_{\max} \sim \gamma_{CRR}^2 \varepsilon_{0,GHz} \sim$ a few GeV. This process might make a significant contribution to the total spectrum of the slot gap if the radio emission region is located at relatively high altitude (see Sect. 19.6.1).

19.5.3 Relativity, Geometry and Caustics

The geometry of emission at high altitude is strongly influenced by special relativistic effects of aberration, time-of-flight and retardation of the magnetic field. Aberration and time-of-flight produce phase shifts of comparable magnitudes $\Delta\Phi \sim -r/R_{LC}$ in radiation emitted at different altitudes r relative to the light cylinder radius R_{LC}. Morini [53] first noted that the combined phase shifts from aberration and time-of-flight, of photons radiated tangent to a magnetic dipole field from the polar cap to the light cylinder, nearly cancel those due to field line curvature on the trailing edge of the open-field region. Radiation along such trailing field lines bunches in phase, forming a sharp emission peak or caustic in the phase plot or profile (Fig. 19.6). On the leading side, these phase shifts add up to spread photons emitted at various altitudes over a large range of phases. The effect is most pronounced for large α and emission between altitudes $r_{\rm em} \sim 0.2 - 0.8 R_{LC}$. Sweepback of the magnetic dipole field due to retardation [18,75] affects photon emission directions near the light cylinder, and also distorts the polar cap and open field volume [2,20], even at the stellar surface. Most observer angles sweep across caustics from both magnetic poles, resulting in a double peaked pulse profile where the peaks generally have phase separation less than 180° [22]. Furthermore, emission occurs at all phases in the profile. Such profiles are very similar to those of the bright γ-ray pulsars, Crab and Vela. The predicted polarization characteristics of such a "two-pole caustic" model can also explain the observed optical polarization of the Crab pulsar [21].

Radiation from the slot gap has a geometry very similar to that of the "two-pole caustic" model and thus displays caustics in the intensity phase plots as well as Crab-like pulse profiles [55]. The high-altitude slot gap thus may be a viable model for high-energy emission from young pulsars. However particle acceleration in the slot

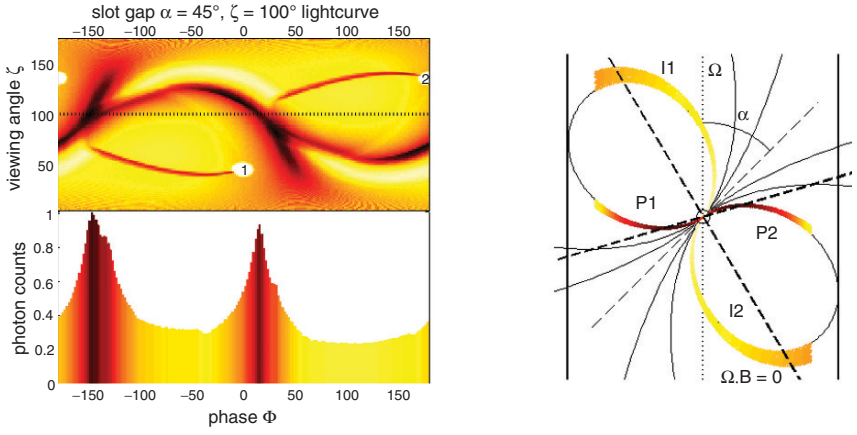

Fig. 19.6 Same as Fig. 19.5 for the slot gap model, for a typical inclination angle $\alpha = 45°$ (from [26])

gap may not operate at all inclination angles. The low altitude $E_{\parallel}$, shown in (19.5), is a function of both α and ϕ. For large α and $\cos\phi < 1$ (field lines curving away from the rotation axis), the second term in (19.5) can become large and negative at large r, causing the $E_{\parallel}$ to reverse sign. This would cause a buildup of charge at that location, and would clearly be an unstable situation. The charge flow along those field lines might then be either time-dependent or non-existent. The solution for $E_{\parallel}$ at high-altitude in the slot gap [55] may moderate this effect somewhat, but for fast rotators and $\alpha \gtrsim 70^{\circ}$ the $E_{\parallel}$ reverses sign at low altitude. The resolution to this problem is still forthcoming, but it is possible that steady current flow in the slot gap does not occur for all geometries.

19.5.4 Radiation from Millisecond Pulsars

There are more than 200 radio pulsars now known with periods between 1 and 30 ms. Many (around 30) have been detected as X-ray point sources, and seven of these have X-ray pulsations. Only the few millisecond pulsars (MSPs) that lie above or near the CR pair death line are expected to have slot gaps. These include B1821-24, B1957+20 and B1937+21, whose pulse profiles interestingly show caustic-like narrow, sharp peaks. The rest that lie below the CR death line are pair-starved and their SCLF $E_{\parallel}$ is unscreened. Particles on all open field lines will therefore accelerate to high-altitude with Lorentz factors limited by CR losses, as in the slot gap (19.14). The peak energy of the CR spectrum for MSPs is similarly high, $\varepsilon_{peak}^{CR} \approx 10\mathrm{GeV} B_8^{3/4} P_{ms}^{-5/4} \kappa_{0.15}^{3/4}$, where $P_{ms} = P/1ms$ and $B_8 = B/10^8$ G. But the very low magnetic fields of MSPs do not absorb the high energy part of the spectrum, so these sources may be visible up to energies of 50 GeV [11, 36, 49]. The CR will dominate for viewing angles near the magnetic poles because the emission comes primarily from low altitude, since the particle Lorentz factors decrease with increasing altitude. Additionally, as discussed in Sect. 19.5.2, synchrotron radiation from resonant absorption of radio emission may be important for MSPs having high radio luminosities. The synchrotron component will appear in the X-ray to γ-ray ($\lesssim$100 MeV) region of the spectrum [37], and will be visible at a larger range of observer angles since the emission comes from high altitudes. Figure 19.7 shows a model spectrum for the millisecond pulsar PSR J0218+4232 based on a (1D) cyclotron resonant absorption model described above (see 19.5.2).

19.6 Pulsar Emission at Multi-wavelengths

Since rotation-powered pulsars shine over a broad spectrum from radio to high-energy γ-ray wavelengths, the multi-wavelength spectra and profiles can give important clues to the acceleration and emission geometry. Although there are some clear patterns of spectral behavior with pulsar age (cf. Chap. 6), the observed

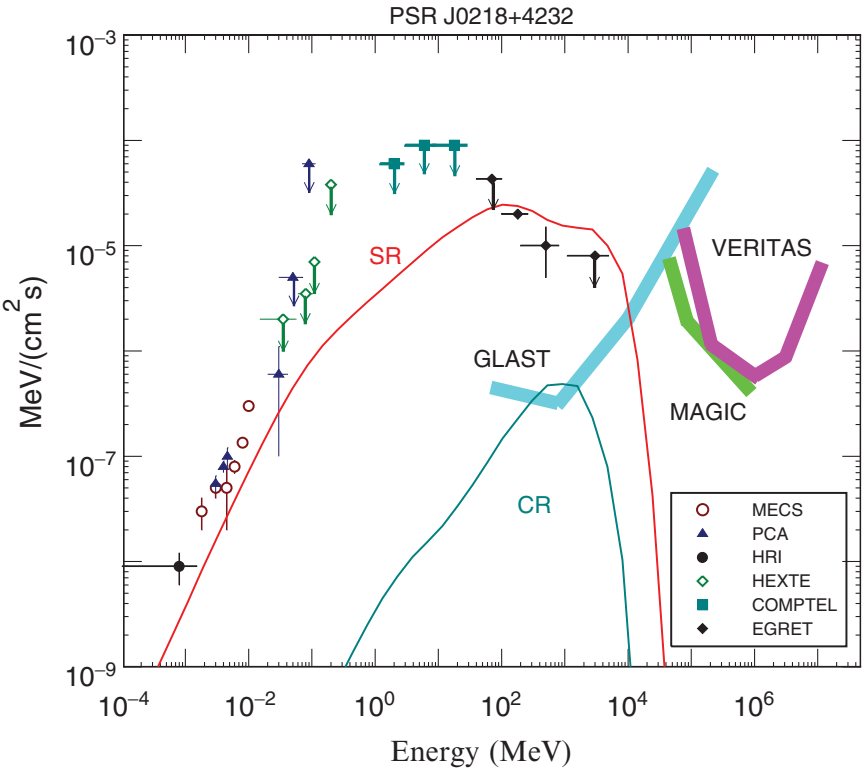

Fig. 19.7 Model spectrum for 2.3 ms PSR J0218+4232 (from [37]) showing components from synchrotron radiation (SR) and curvature radiation (CR) from unscreened acceleration of a single primary electron, from the NS surface to the light cylinder, along a field line defined by magnetic colatitude $\xi = 0.9$ in units of PC half angle, at inclination $\alpha = 50°$. Data points are from [45]

multi-wavelength lightcurves show a wide variety of characteristics that present many puzzles. As shown in Fig. 19.8, the lightcurves for the known γ-ray pulsars do not as a rule exhibit much phase correspondence between radio, X-ray and γ-ray peaks. The sole example is the Crab pulsar, where two peaks separated by $\sim$140° are in phase from radio to γ-ray energy. For the other pulsars, the radio peak usually leads the one or two γ peaks in phase and the soft X-ray peaks are broader and overlap the γ-ray peaks. Comparing X-ray and radio profiles of known rotation-powered X-ray pulsars, one sees that there is more multi-wavelength phase coherence for shorter periods ($P \lesssim 50$ ms), such as for PSR B0540-69 (50 ms), PSR J1617-5055 (69 ms) and the millisecond pulsars, PSR B1821-24, PSR B1937+21 and PSR J0218+4232. Such short-period and younger pulsars also tend to have pure power law X-ray spectra with no thermal components (cf. Chap. 6), indicating that their X-ray emission is primarily non-thermal radiation from accelerated particles. One possible picture is that pulsars with shorter periods accelerate particles mostly in the outer magnetosphere, in slot gaps or outer gaps. The high-energy

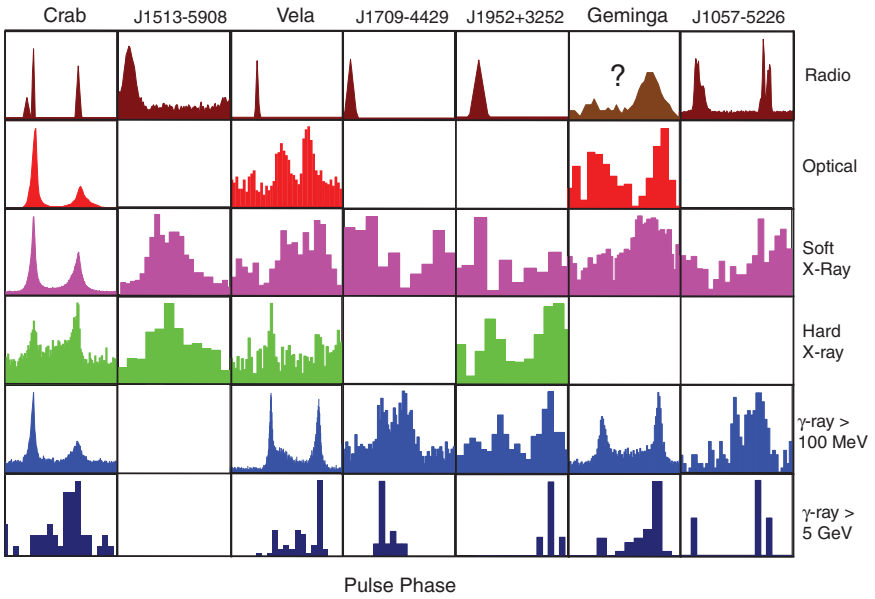

Fig. 19.8 Profiles of seven γ-ray pulsars in six energy bands, as in [70]

emission occurs at high altitudes that are large fractions of their light cylinder radii, $R_{LC} = 5 \times 10^9 P^{-1}$ cm, which are also smaller. Their emission geometry is therefore expected to be different from that of longer period pulsars, whose high-energy emission occurs closer to the neutron star surface and at altitudes that are very small fractions of R_{LC}.

19.6.1 Radio Emission Geometry

Because the mechanism responsible for the radio beams is not understood, and more importantly because the radiation is coherent, it has not been possible to describe this emission using a physical model. The emission has therefore been described using empirical models, developed over the years through detailed study of pulse morphology and polarization characteristics. The emission is also highly polarized, and displays changes in polarization position angle across the profile that often matches the swing expected for a sweep across the open field lines near the magnetic poles in the Rotating Vector Model [62]. Empirical models (e.g. [63]) characterize pulsar radio emission as having a core beam centered on the magnetic axis and one or more hollow cone beams outside of the core. The average-pulse profile widths and component separations are measured to be decreasing functions of radio frequency [66]. This is consistent with a hollow cone beam centered on the magnetic pole, emitted at an altitude that decreases with increasing frequency

(radius-to-frequency mapping). From such profile width measurements, and assuming that the edges of the pulse are near the last open field line, Kijak & Gil [43] find an emission radius of

$$r_{\rm radio} \approx .01\, R_{LC} \left(\frac{\dot{P}}{10^{-15}{\rm s\,s^{-1}}} \right)^{0.07} P^{-0.7} \nu_{GHz}^{-0.26} \tag{19.17}$$

where $\dot{P}$ is the period derivative. This result predicts that for pulsars with $P \lesssim 0.1$ s the emission radius $r_{\rm radio} \gtrsim 0.05 - 0.1\, R_{LC}$. Such a picture is independently supported by polarization studies [40] of pulsars younger than 75 kyr. They concluded that the emission of these pulsars was from a single wide cone beam, that core emission was weak or absent, and that the height of the cone emission is between 1% and 10% of the light cylinder radius.

19.6.2 The Global Picture

As discussed in Sect. 19.5.3, emission along the last open field lines at altitudes $r_{\rm em} \sim 0.2 - 0.8\, R_{LC}$ will form caustics, producing sharp peaks in the pulse profiles. According to (19.17), the radio cone emission altitude for pulsars with periods $P \lesssim 30 - 50$ ms, depending on their $\dot{P}$, will fall in the range of caustic formation. If the radio conal emission is radiated over an extended range of altitude (i.e. a few tenths of R_{LC}) then radio caustic peaks would appear in phase with high-energy caustic peaks. Such a model would explain the multi-wavelength phase coherence of the profiles of fast pulsars like the Crab and millisecond pulsars, PSR B1821-24 and PSR B1937+21. The conal emission of slower pulsars would fall below the altitude range of caustic formation and the radio conal peak(s) or core emission would lead the high-energy caustic peaks, as seen in most of the multi-wavelength profiles of Fig. 19.8. In these cases, a single radio peak leading double γ-ray peaks is most likely to be the edge of a cone beam, since it is unlikely that a viewing angle crosses the narrow core beam as well as both caustics. For example, the observer viewing angle illustrated in Fig. 19.6 would cross the outer edge of pole 2 at a phase of 180°. Due to the radius-to-frequency mapping of the cone emission, this picture would predict that the measured width of the radio beam would be smaller at higher frequency since the emission is originating at lower altitude, whereas the core emission width would not be expected to vary with frequency.

Aside from the geometry of the emission at different wavelengths, that is directly relevant to observational characteristics of pulsars, there is the more fundamental question of how the microphysics of acceleration and pair cascades fit into the studies of the pulsar magnetosphere. The magnetosphere models [13, 68] make the assumption of ideal MHD (no parallel electric fields) in order to derive the global structure of the magnetic field and currents that are solutions to the so-called pulsar equation [51] that describes a spinning neutron star with a dipole field. A notable feature of these models is the formation of a neutral sheet in the equatorial plane of the spin axis which may provide a source of the return current that flows back

to the neutron star along the last open field line. The derived currents in such models do not match the currents that have been assumed in either polar cap or outer gap accelerator models. Yet the microphysical acceleration models are needed to describe the physics of the pair creation and to check the consistency of the assumption of ideal MHD conditions over most of the magnetosphere. At present, it is not clear whether the global models can be adjusted to match the boundary conditions of the acceleration models [71] or the whether the acceleration models can produce the required cascade multiplicity with compatible boundary conditions. In the end, self-consistency between global models and acceleration models may require time-dependence or spatial-dependence of the current flow.

19.7 Open Questions

Although much of the theoretical picture presented in this article depends on a set of undisputed fundamentals, such as, that rotation-powered pulsars are neutron stars with large-scale dipole magnetic fields that are directly measurable from their period derivatives, to within uncertainties in the equation of state. But the picture also involves a number of underlying assumptions that are less well confirmed or agreed upon. The most important of these for particle acceleration are the boundary conditions on the charge flow. Both polar cap and outer gap acceleration models assume that the boundary between the open and closed field line region is a perfect conductor. This implicitly assumes that there is some microphysical screening at this boundary by charges in the closed-field region, although this process has not been modeled or simulated. The boundary condition on the electric field and potential at the neutron star depends on the binding energy of charge in the surface layers. Calculations of the cohesive force for a solid lattice in magnetic fields up to about 10^{13} G indicate that charges will not be bound in the surface at temperatures above $\sim$0.5 MK, so that most pulsars have surfaces hot enough to allow SCLF accelerators to operate. However, a number of pulsars have magnetic fields above 10^{13} G, where surface conditions have not been adequately explored. It is possible that the neutron star surface may be in a liquid rather than solid state in very high magnetic fields [32, 41] or that charges may be bound by much stronger forces. In this case, high-field pulsars could have vacuum instead of SCLF accelerators.

Models often also assume that the neutron star is a dipole field in calculating the accelerating electric potential and field. This assumption could be faulty at low altitude if there exist higher multipole fields near the neutron star surface, and is certainly invalid at very high altitude where there are distortions of the field due to retardation [20] and current flow [57]. The $E_{\parallel}$ in the high altitude slot gap [55] is only approximate and needs to be calculated using field line distortions. It is possible that the distorted field lines, having less curvature than a dipole, will have the effect of removing the sign reversals present in the approximate solutions. There are also expected to be cross field particle motions at high altitude that will modify solutions of the electric field.

The possible connection of pair cascades to radio emission morphology is an intriguing question that needs further investigation. For example, are the pairs from the near-surface polar cap and high-altitude slot gap cascades responsible for the core and cone beams? Do pairs produced in the outer gaps produce any radio emission? Whether polar caps and slot gaps can exist on the same field lines or in the same pulsar magnetosphere is also not known.

Although some of these questions require more theoretical work, it is hoped that many answers will come from observations with future detectors. The Large Area Telescope (LAT) on the Gamma-ray Large Area Space Telescope (GLAST), due to launch in 2008, will have unprecedented sensitivity and energy resolution for gamma-rays in the range of 30 MeV to 300 GeV. GLAST is therefore expected to provide major advances in the understanding of high-energy emission from rotation-powered pulsars (cf. Chap. 23 and [29]), including an increase in the number of detected radio-loud and radio-quiet gamma-ray pulsars, and millisecond pulsars, giving much better statistics for elucidating population characteristics, measurement of the high-energy spectrum and the shape of spectral cutoffs and determining pulse profiles for a variety of pulsars of different ages. Further, measurement of phase-resolved spectra and energy dependent pulse profiles of the brighter pulsars should allow detailed tests of magnetospheric particle acceleration and radiation mechanisms. Third-generation ground-based Air Cherenkov detectors, such as H.E.S.S. [58] in Namibia, MAGIC [47] in the Canary Islands and VERITAS [39] in the US, have begun operation. They are sensitive to γ-rays in the range 50 GeV to 50 TeV and are putting important constraints on pulsar spectra and emission mechanisms [1]. Further into the future are planned X-ray telescopes, such as IXO, and X-ray polarimeters, such as AXP, POGO and ACT. Polarimeters in particular will be extremely important in verifying model predictions for different pulsar emission geometries through phase-resolved measurements of position angle and polarization percent (cf. Chap. 22 by Weisskopf et al.).

References

1. Aharonian, F. et al. A & A, 466, 543 (2007)
2. Arendt, P. N. & Eilek, J. A. (astro-ph/98011257) (1998)
3. Arendt, P. N. & Eilek, J. A. ApJ, 581, 451 (2002)
4. Arons, J. ApJ, 248, 1099 (1981)
5. Arons, J. ApJ, 266, 215 (1983)
6. Arons, J. & Scharlemann, E. T. ApJ, 231, 854 (1979)
7. Baring, M. G. & Harding, A. K. ApJ, 547, 929 (2001)
8. Baym, G., Pethick, C. & Sutherland, P. ApJ, 170, 299 (1971)
9. Blandford, R. D. & Scharlemann, E. T. MNRAS, 174, 59 (1976)
10. Bogdanov, S. et al. ApJ, 646, 1104 (2006)
11. Bulik, T., Rudak, B. & Dyks, J. MNRAS, 317, 97 (2000)
12. Camilo, F. Young Neutron Stars and Their Environments, IAU Symposium 218, Ed. F. Camilo and B. M. Gaensler. San Francisco, CA: Astronomical Society of the Pacific, p. 97 (2004)
13. Contopoulos, I., Kazanas, D. & Fendt, C. ApJ, 511, 351 (1999)
14. Daugherty, J. K. & Harding, A. K. ApJ, 252, 337 (1982)

15. Daugherty, J. K. & Harding, A. K. ApJ, 273, 761 (1983)
16. Daugherty, J. K. & Harding, A. K. ApJ, 336, 861 (1989)
17. Daugherty, J. K. & Harding, A. K. ApJ, 458, 278 (1996)
18. Deutsch, A. Annales d'Astrophysique, 18, 1 (1955)
19. Dyks, J. & Rudak, B. A & A, 393, 511 (2002)
20. Dyks, J. & Harding, A. K. ApJ, 614, 869 (2004)
21. Dyks, J., Harding, A. K. & B. Rudak, ApJ, 606, 1125 (2004)
22. Dyks, J. & B. Rudak, ApJ, 598, 1201 (2003)
23. Edwards, R.T., Bailes, M., van Straten, W. & Britton, M.C. MNRAS, 326, 358 (2001)
24. Goldreich, P. & Julian, W. H. ApJ, 157, 869 (1969)
25. Gil, J., Melikidze, G. & Zhang, B. A & A, 457, 5 (2006)
26. Grenier, I. A. & Harding, A. K. In Proceedings of Einstein Centenary Conference, Paris 2005, AIP Conference Proceedings, 861, 630–637 (2006)
27. Grindlay et al. ApJ, 581, 470 (2002)
28. Harding, A. K. In High Energy Gamma-Ray Astromony, Ed. F. A. Aharonian & H. J. Volk, AIP Conference Series Vol. 558 (AIP: New York), 115 (2001)
29. Harding, A. K. In proceedings of First GLAST Symposium, ed. S. Ritz, P.F. Michelson & C. Meegan (AIP), in press (2007)
30. Harding, A. K. & Daugherty, J. K. Adv. Space Res., 21, 251 (1998)
31. Harding, A. K., Baring, M. G. & Gonthier, P. L. ApJ, 476, 246 (1997)
32. Harding, A. K. & Lai, D. Rep. Prog. Phys., 69, 2631 (2006)
33. Harding, A. K. & Muslimov, A. G. ApJ, 508, 328 (1998)
34. Harding, A. K. & Muslimov, A. G. ApJ, 556, 987 (2001)
35. Harding, A. K. & Muslimov, A. G. ApJ, 568, 862 (2002)
36. Harding, A. K., Muslimov, A. & Zhang, B. ApJ, 576, 366 (2002)
37. Harding, A. K., Usov, V. V. & Muslimov, A. G. ApJ, 622, 531 (2005)
38. Hibschman, J. A. & Arons, J. ApJ 554, 624 (2001)
39. Holder, J. In Proceedings of Science with the New Generation of High Energy Gamma-Ray Experiments. The Variable Gamma-Ray Sources: Their Identifications and Counterparts. Eds. M. M. Massai, N. Omodei, G. Spandre. ISBN-13 978-981-270-964-6. World d Scientific Publishing, p. 69 (2007)
40. Johnston, S. & Weisberg, J. M. MNRAS, 368, 1856 (2006)
41. Jones, M. D. & Ceperley, D. M. PhRvL, 76, 4572 (1996)
42. Kaspi, V. M., Roberts, M. S. E. & Harding, A. K. In Compact Stellar X-ray Sources, Ed. W.H.G. Lewin & M. van der Klis. Cambridge: Cambridge University Press, pp. 279–339 (2006)
43. Kijak, J. & Gil, J. A & A 397, 969 (2003)
44. Krause-Polstorff, J. & Michel, F. C. MNRAS, 213, 43P (1985)
45. Kuiper, L., Hermsen, W. & Stappers, B. 2003, Pulsars, AXPs and SGRs observed with BeppoSAX and Other Observatories, Proceedings of the International Workshop held in Marsala, Edited by G. Cusumano, E. Massaro, T. Mineo. Roma, Italy: Aracne Editrice, July 2003, ISBN 88-7999-514-6, pp. 31–36, astro-ph/0306622.
46. Levinson, A., Melrose, D., Judge A. & Luo Q. ApJ, 631, 456 (2005)
47. Lorenz, E. High Energy Gamma-Ray Astronomy: 2nd International Symposium, Eds. F. A. Aharonian, H. J. Vlk, and D. Horns. AIP Conference Proceedings, Volume 745. New York: American Institute of Physics, pp. 622–627 (2005)
48. Lyubarskii, Y. E. & Petrova, S. A. A&A, 337, 433 (1998)
49. Luo, Q., Shibata, S. & Melrose, D. B. MNRAS, 318, 943 (2000)
50. Manchester, R. N. et al. MNRAS, 328, 17 (2001)
51. Michel, F. C. ApJ, 180, 207 (1973)
52. Mignani, R. P., DeLuca, A. & Caraveo, P. A. In "Young Neutron Stars and Their Environments" (IAU Symposium 218, ASP Conference Proceedings), Ed. F. Camilo and B. M. Gaensler. San Francisco: ASP, p. 39 (2004)
53. Morini, M. MNRAS, 303, 495 (1983)
54. Muslimov, A. G. & Harding, A. K. ApJ, 588, 430 (2003)

55. Muslimov, A. G. & Harding, A. K. ApJ, 606, 1143 (2004a)
56. Muslimov, A. G. & Harding, A. K. ApJ, 617, 471 (2004b)
57. Muslimov, A. G. & Harding, A. K. ApJ, 630, 454 (2005)
58. Hinton, J. A. et al. New Astron. Rev., 48, 331 (2004)
59. Muslimov, A. G. & Tsygan, A. I. MNRAS, 255, 61 (1992)
60. Petri, J., Heyvaerts, J. & Bonazzola, S. A & A, 384, 414 (2002)
61. Petrova, S. A. A&A, 408, 1057 (2003)
62. Radhakrishnan, V. & Cooke, D. J. ApL, 3, 225 (1969)
63. Rankin, J. M. ApJ, 405, 285 (1993)
64. Ruderman, M. A. & Sutherland, P. G. ApJ, 196, 51 (1975)
65. Shabad, A. E. & Usov, V. V. Nature, 295, 215 (1982)
66. Sieber, W., Reinecke, R. & Wielebinski, R. Astron. Astrophys., 38, 169 (1975)
67. Spitkovsky, A. Young Neutron Stars and Their Environments, IAU Symposium 218, Ed. F. Camilo and B. M. Gaensler. San Francisco, CA: Astronomical Society of the Pacific, p. 357 (2004)
68. Spitkovsky, A. ApJ, 648, L51 (2006)
69. Sturner, S. J., Dermer, C. D. & Michel, F. C. ApJ, 445, 736 (1995)
70. Thompson D. J. In Cosmic Gamma-Ray Sources, Ed. K. S. Cheng & G. E. Romero. New York: Kluwer, ApSS, 304, 149 (2004)
71. Timokhin, A. MNRAS, 36, 1055 (2006)
72. Usov, V. V. & Melrose, D. B. Aust. J. Phys., 48, 571 (1995)
73. Usov, V. V. & Melrose, D. B. ApJ, 464, 306 (1996)
74. Xia, X. Y., Qiao, G. J., Wu, X. J. & Hou, Y. Q. Astr. Ap., 152, 93 (1985)
75. Yadigaroglu, I. A., Ph.D. Thesis, Stanford University (1997)
76. Zhang, B. & Harding, A. K. ApJ, 535, L51 (2000)
77. Zhang, B. & Harding, A. K. ApJ, 532, 1150 (2000)
78. Zhang, B. & Qiao, G. J. A & A, 338, 62 (1998)
79. Zhang, B. & Qiao, G. J. A & A, 310, 135 (1996)

Chapter 20
Physics of Drifting Sub-pulses in Radio Pulsars

Jan M.E. Kuijpers

20.1 Introduction

Sophisticated analysis of single pulses from radio pulsars with the most sensitive radio telescopes available have taught us that most pulsars exhibit the phenomenon of drifting sub-pulses [43], see Figs. 20.1 and 20.2. Already as early as 1970 [41], it has been proposed that these 'marching' sub-pulses circulate around the pulsar magnetic axis, and are caused by short-period waves which form part of a long-period wave which circulates about the star at the same angular velocity. Let P_1 be the rotation period of the pulsar, P_2 the period between sub-pulses within the primary-pulse envelope, P_3 the time interval between drifting bands of sub-pulses, and P_4 the circulation period around the magnetic axis, all expressed in units of time, then [41], see Fig. 20.2,

$$P_4 \approx \frac{P_1 P_3}{P_2(1+NP_3/P_1)} = \frac{P_1 P_3}{P_2} \tag{20.1}$$

if, in the last equality, the integer N is put to zero. After all these years, in a few cases, such a *carousel* of emission columns drifting around the magnetic axis has been constructed from the observations [4, 11, 12], see Fig. 20.7. Understanding the phenomenon of drifting sub-pulses may, therefore, well be crucial to our understanding of radio pulsar electrodynamics which despite the largely classical nature of the relevant physics is still shrouded in mysteries, to date 40 years after the discovery of pulsars.

In this Chapter I will show how drifting sub-pulses allow us to get a grip on the detailed geometry of the electric circuit and the sources of radio emission on the open field lines in the light of a number of proposed interpretations of drifting sub-pulses. In Sect. 20.2, we summarize the common characteristics of radio

J.M.E. Kuijpers
Department of Astrophysics, IMAPP, Radboud University Nijmegen, The Netherlands
e-mail: kuijpers@astro.ru.nl

W. Becker (ed.), *Neutron Stars and Pulsars,* Astrophysics and Space Science Library 357,

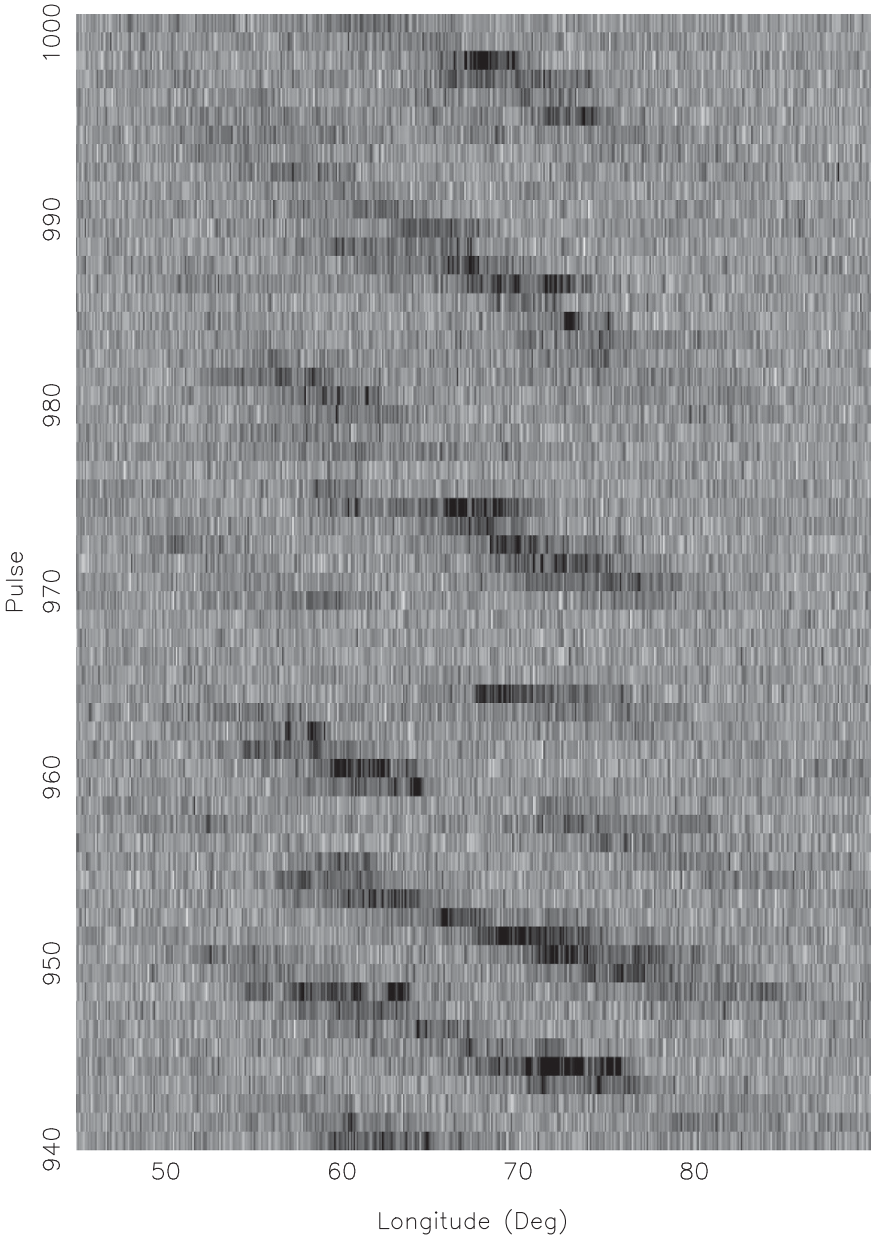

Fig. 20.1 Sequences of drifting sub-pulses are clearly visible at 328 MHz in stacked pulse observations of PSR B0031-07 (pulse period 0.943 s) taken with the Westerbork Synthesis Radio Telescope and the PuMa backend (courtesy of Dr. Roy Smits). The horizontal axis runs from 60 to 120° in 'longitude'

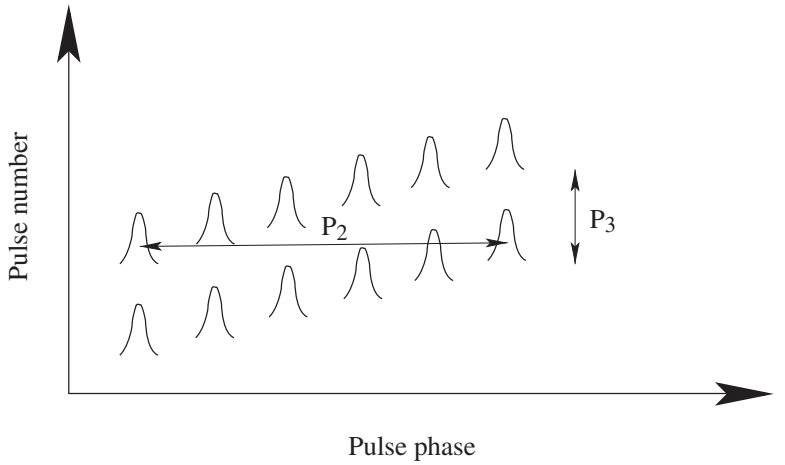

Fig. 20.2 Schematic picture of drifting sub-pulses in a stacked pulse diagram. P_2 and P_3 are measured in seconds and the pulse phase or conventional 'longitude' Φ corresponds to time according to the formula $\Phi = 360^\circ t/P_1$

pulsar models to date, and the open questions, and sketch the basic properties which any steady circuit in the magnetosphere must have. Confrontation with individual models of drifting sub-pulses will then allow us to draw conclusions regarding the details of the electric circuit, and answer some of the open questions. This is done in Sect. 20.3 where we review the existing interpretations [8, 19, 22, 26, 39, 42, 44] as far as they shed light on the physics in the pulsar magnetosphere. In Sect. 20.4 we discuss a recent interpretation in terms of a diocotron instability, on which we have worked ourselves [18], in more detail. Finally, in Sect. 20.5 we discuss directions for future progress.

20.2 Basic Pulsar Electrodynamics

The precise electrodynamics of a rotating neutron star magnetosphere is poorly known, and indeed this is what we would hope to unravel from statistical studies of pulsar radio emission and from case studies of individual radio pulsars. In particular, the geometry and temporal behavior of particle extraction from the star, particle acceleration, pair creation, emission at radio (and other) wavelengths, current closure, and transition of the wind from a Poynting flux to a kinetic energy flux dominated one are badly known. To extract such information from the observations requires a conceptual frame of reference which, on one hand, is based on general laws of physics, and on the other hand general enough so as not to exclude the actual pulsar. Figure 20.3 summarizes the main existing models for radio pulsars which are characterized by electron/positron pair creation. It compares three different models

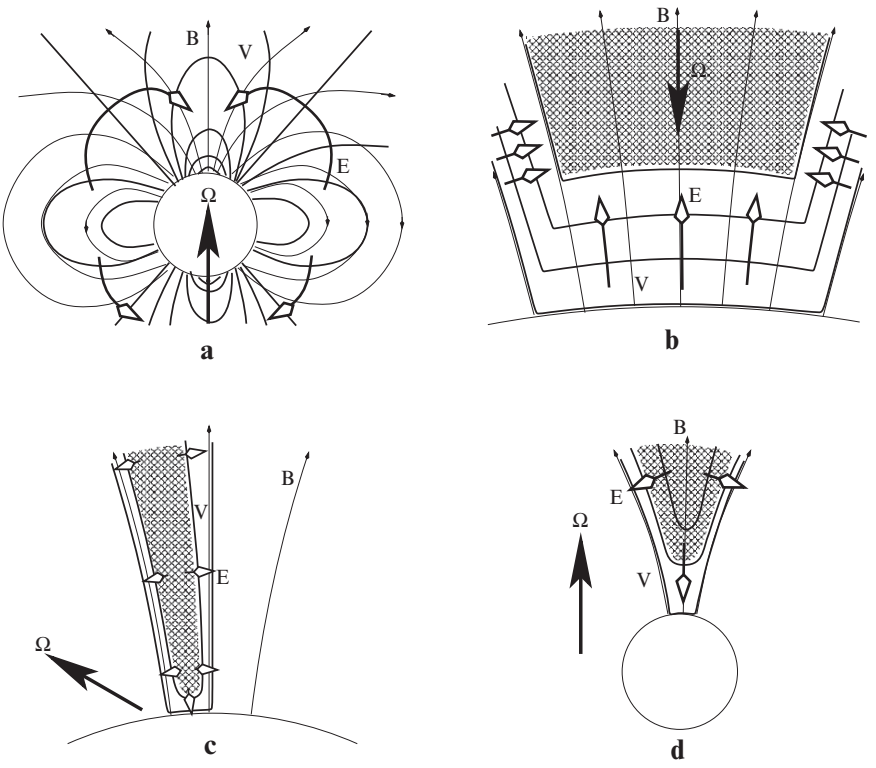

Fig. 20.3 Sketch of various models for pair creation (hatched) on the open field lines **B** in the pulsar magnetosphere with level curves of electrostatic potential **V** and corresponding electric field **E**: (**a**) axially symmetric vacuum model à la Deutsch [13]; (**b**) Ruderman and Sutherland's anti-aligned pulsar with infinite ion binding energy [39]; (**c**) Aron's model [2]; (**d**) Muslimov and Tsygan's general relativistic model [32]. The magnetic moment **m** is oriented along the vertical direction, and the rotation vector is Ω

(b, c, d) to the original Deutsch model of a rotating star in vacuo (a). Pair creation is shown hatched, and the main difference between models is in the location of the pair formation 'front' which is governed by physical and boundary conditions such as global conservation of energy and angular momentum, the requirement of a vanishing electric field component along the magnetic field in large portions of the pair wind, the binding energy of ions to the star, the initial velocity of the extracted particles, the obliquity of the rotation axis with respect to the (dipolar) magnetic field, the consideration of general relativistic effects (frame dragging), and the consideration of magnetic multi-poles. An important quantity which is useful to compare various models is the value of the electric field component along the background magnetic field at a reference altitude in the magnetosphere above the magnetic poles, for which we take an altitude of one polar cap radius $r_{pc} \equiv r_*(\Omega_* r_*/c)^{0.5}$, where r_* denotes the radius of the star and Ω_* its angular rotational frequency. The electric field at this altitude can be conveniently written as

$$E_{\parallel}(r_* + r_{pc}) \approx -pcB_* \left(\frac{\Omega_* r_*}{c} \right)^q , \tag{20.2}$$

where B_* is the surface magnetic field strength at the magnetic pole, and the parameters $\{p, q\}$ are respectively $\{1,1\}$ for the aligned vacuum model [13], $\{-2,1.5\}$ for the model by [39] which is derived for an anti-aligned rotator upon the assumption of infinite binding energy for the ions, $\{0.5,2.5\}$ for the model by [2] which has freely streaming electrons from the stellar surface, and $\{1,2\}$ for the general relativistic model of [32]. The model of [31] differs from that of [2] in the initial speed of the out-flowing primary electrons from the stellar surface which is now non-relativistic, and as a result the sets of open field lines with pair creation differ between both models. What all models have in common is that a domain exists on the open field lines which has a dense pair plasma wind (a high multiplicity of secondaries as compared to the primary particles) and a vanishing longitudinal electric field component, and which is bounded from below by a domain adjacent to the stellar surface where the electric field component along the magnetic field does not vanish and accelerates (primary) particles into the magnetosphere. In the model by [32] and the later models by Harding the pair front extends from an altitude of about one stellar radius above the stellar surface while in most other models it is located at the small altitude of about one polar cap radius. All models have in common that the primary beam is extremely relativistic with Lorentz factors $\gamma \sim 10^6 - 10^7$ while the relativistic pair wind has Lorentz factors of ten to a few hundred. The confinement of the electric potential drop along the magnetic field lines at the basis of a dense stellar pair wind with a vanishing parallel electric field component – at least over distances within the light cylinder radius $r_{lc} \equiv c/\Omega_*$ – implies a charge density in the wind given by

$$n(\mathbf{r}) \equiv -\frac{2\varepsilon_0}{e} \frac{\Omega_w \cdot \mathbf{B}_0(\mathbf{r})}{1 - \frac{|\Omega_w \times \mathbf{r}|^2}{c^2}} \approx -2\varepsilon_0 \Omega_w \cdot \mathbf{B}_0(\mathbf{r})/e. \tag{20.3}$$

where $e > 0$ is the absolute value of the electron charge, $\Omega_\mathbf{w}$ is the wind angular velocity vector, $\mathbf{B}_0(\mathbf{r})$ is the background magnetic field at position $\mathbf{r}$ and c is the speed of light. When the wind co-rotates with the star $\Omega_w = \Omega_*$ the charge density is called the Goldreich–Julian density $n(\mathbf{r}) = \mathbf{n}_{\rm GJ}(\mathbf{r})$, but in general these rotation speeds are not equal to each other, and the slippage between star and wind is determined by the magnitude of the potential drop in between.

20.2.1 Electric Circuit

The Aligned Rotator

Common belief is that the rotating magnetized star acts as a *voltage source* which – for radio pulsars – is so strong that it creates its own external *wiring* by pair formation. Along this *electric circuit* it then drives an electric current which transports

angular momentum from the star to the wind and so allows to brake the stellar rotation. We will use the simplified picture for the electric current as proposed by [23]. In a steady state the voltage generator draws a current from the star. For an aligned rotator, the current comes in through a cylinder around the magnetic axis, is then diverted through the star across the polar cap – where it brakes the stellar rotation by the Lorentz torque –, then goes outward in a cylindrical sheath, and finally closes far away from the star by crossing the magnetic field lines – where it accelerates the stellar wind and deposits stellar angular momentum. One of the unknown problems of the radio pulsar is the altitude and precise nature of current closure in the wind. For the interpretation of the drifting sub-pulses however, which are emitted well within the light cylinder, this presents no problem. Note that the incoming current consists of an *outgoing* electron/positron plasma. It is important to realize that in such a dense pair plasma – in contrast to a charge-separated flow – the current is not directly coupled to the charge density since not only convection of net charge but also relative drift between electrons and positrons creates electric current. Similarly, the outgoing current again consists of *outgoing* plasma, either in the form of positive ions from the star and/or an electron/positron plasma (Fig. 20.4). The field lines on the magnetic flux surface separating the incoming from the outgoing current are called the *critical* field lines in [23]. The critical field lines are at the same electric potential as the interstellar medium. A simple estimate of their position on the polar cap can be obtained if one assumes that everywhere on the polar cap the current density is just the Goldreich–Julian density at the stellar surface multiplied with $-$ or $+$ the speed of light depending on whether the current comes in or goes out. The foot-points of the critical field lines are therefore approximately positioned at an angle θ_c as seen from the stellar center given by $\theta_c = \theta_{pc}/\sqrt{2} = (\Omega_* r_*/2c)^{0.5}$ which differs only by a factor 0.96 from the foot-points of the field lines which pass through the cross-section of the light cylinder with the null lines – where $\Omega \cdot \mathbf{B}$ and the GJ density vanish. The foot-points of the latter are located at an angle $\theta_n = \theta_{pc}(2/3)^{1.5}$ on the stellar surface.

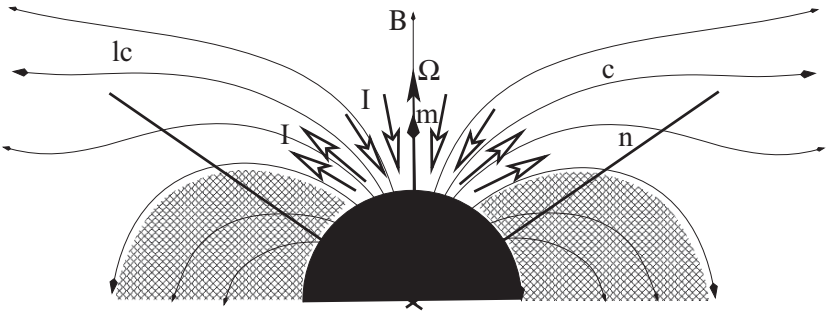

Fig. 20.4 Sketch of the current system *I* in the axially symmetric case (magnetic field **B**, magnetic moment **m**, rotation vector Ω, null line *n*, light cylinder *lc*, critical field line *c* separating incoming from outgoing current)

The Oblique Rotator

In the oblique case, the geometry lacks symmetry but still the basic elements of the electric circuit are the same. What is not always sufficiently appreciated is that the conductive properties of the star (and of the external wirings) are completely irrelevant to the existence of the external circuit (although of course it changes the value of the current somewhat). Here, we differ in opinion from other authors (e.g. [6,28]).

As we see it, the result in [6] that the current system in a perpendicular rotator leads to negligible braking of the stellar rotation is based on their assumption that the current is completely determined by the conductive properties of the stellar mantle. The authors thereby overlook the fact that even in ideal MHD (vanishing resistance) an external current circuit will be set up by an isolated rotating and magnetized star placed in and magnetically connected to an infinitely extended conductive medium. The reason is that the propagation speed of magnetic perturbations in the surrounding plasma is limited to the speed of light (it is a combination of the relativistic Alfvén and fast magneto-acoustic speeds). As a result the magnetic field lines at the stellar surface have a kink and carry a corresponding current which exerts a Lorentz torque – very much like in the front of a torsional Alfvén pulse.

In our opinion, a similar flaw underlies the objections by [28] to the existence of an external circuit.

His objections are again based on the stellar conductivity but now on the opposite inference that the large electrical conductivity of the star leads to an absurdly large electrical current. Indeed, in the extreme case of infinite conductivity of ideal MHD, it is well known that currents remain finite, and that the potential drop of the voltage source in a steady circuit is taken up, not by resistive, i.e. IR, effects but by inertial, i.e. $\int (\mathbf{v} \times \mathbf{B}) \cdot \mathbf{dl}$, effects.

Conductivity Is of Secondary Importance to Circuit Current

Let us illustrate our point of view by an example from the exhaustive literature on MHD of the solar corona and stellar flares [27]. The situation of the rotating magnetized neutron star shows much resemblance to a coronal flux tube which is differentially rotated at one of its foot-points. The foot-point motion creates a voltage source which acts as a *motor*: an Alfvénic front propagates outward and puts more and more plasma into co-rotation with the motion at the footprint. The electric current crosses the field lines at the footpoints – where the corresponding Lorentz force brakes the rotation – and goes out/comes in along the (now twisted) field lines in a nearly force-free manner (i.e. without potential drops), and closes again (but now in the reverse direction) at the outward propagating Alfvénic front where the coronal plasma is put into motion, and the angular momentum taken from the plasma at the foot-points is deposited. Of course, in the pulsar case, the situation is much more complicated, e.g. by the additional occurrence of parallel voltage drops in some regions, but the similarity with ideal MHD remains. Below, we will consider the simplified steady-state case which forms the theater where the drifting sub-pulse phenomenon is staged.

20.2.2 Rotational Drift of Wind in Oblique Pulsar

To obtain a clear picture of the *'rotational' drift* of plasma on the open field lines of an – in general oblique – magnetic rotator, it is convenient to split the electric field in the lab frame into two parts: a part which would lead to co-rotation of an otherwise static, quasi-neutral plasma, and a remaining part, which in view of the assumed steady rotation can be written in terms of an electrostatic potential Ψ:

$$\mathbf{E} = -(\Omega_* \times \mathbf{r}) \times \mathbf{B} - \nabla\Psi. \tag{20.4}$$

Note that such a decomposition can always be made, whether the pulsar is aligned or oblique. Since we assume that both the star and the closed part of the magnetosphere are in solid body rotation at the rate Ω_* by implication both the boundary of the open field bundle and the polar cap surface are at a constant potential Ψ. As a result, electric fields deriving from otherwise arbitrary Ψ distributions make the plasma circulate on nested surfaces *inside* the open bundle (see Fig. 20.5). As long as we stay well inside the light-cylinder we can approximate the open flux bundle as a cylinder which is invariant in the vertical direction which we call **s**. Each charged particle of kind α follows an equilibrium orbit which – neglecting centrifugal forces – is approximately given by $\mathbf{E} + \mathbf{v}_\alpha \times \mathbf{B} = 0$. Then, upon substitution of **E**

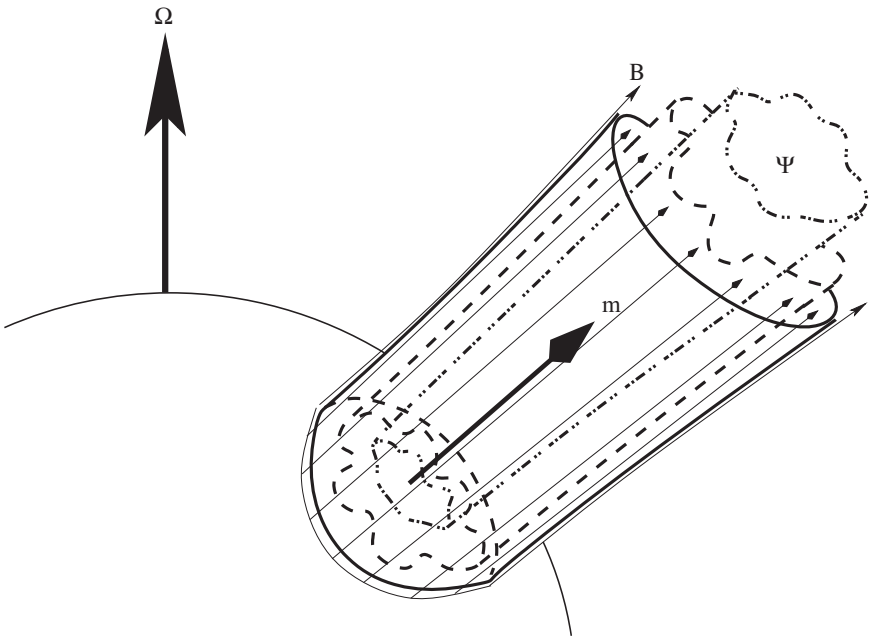

Fig. 20.5 Sketch of level curves of the electrostatic potential Ψ on the open field lines in the oblique case (magnetic field **B**, magnetic moment **m**, rotation vector Ω). The plasma circulates on surfaces of constant Ψ

from (20.4), it follows that the particle motion is described – independent of species α – by

$$\mathbf{v} = \Omega_* \times \mathbf{r} + \mathbf{u}, \tag{20.5}$$

$$\mathbf{u} = -\frac{\Psi \times \mathbf{B}}{B^2}. \tag{20.6}$$

Because of the assumption of invariance in the **s**-direction there is no electric field along the vertical, and it follows that **u** is everywhere tangent to the local magnetic flux surface which moreover coincides with a surface of constant electrostatic potential Ψ!

20.2.3 Rotational Drift of Wind in Aligned Pulsar

Longitudinal Electric Fields, Slippage and Magnetic Reconnection

We adopt cylindrical coordinates $\{R, \phi, z\}$. Faraday's law in a steady state implies that the electric field in the lab frame can be entirely written in terms of an electrostatic potential V as is true as well in the co-rotating frame in terms of the electrostatic potential Ψ. As a prelude to the exact derivation in the next section, it is instructive to discuss some general properties of the potential V. The situation in the lab frame is as is shown in Fig. 20.6 on the right. Obviously, an electric potential difference across the magnetic field is always associated with a voltage difference along field lines at the foot-points ('Kirchhoff'). A simple relation exists between the perpendicular field higher up and parallel electric fields below. Let us define a potential difference $\mathcal{V}_{ji}$ between points i and j by $\mathcal{V}_{ji} = \int_i^j \mathbf{E} \cdot \mathbf{d}\ell$ then it

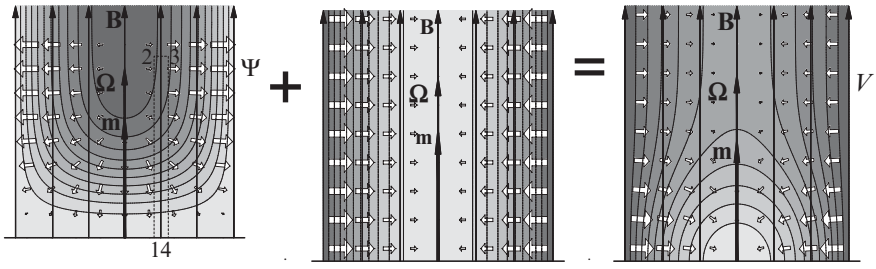

Fig. 20.6 Axially symmetric case: Both in the co-rotating frame and in the lab frame the electric fields derive from an *electrostatic* potential. Sketch of the level curves of the electrostatic potential Ψ in the frame co-rotating with the star on the left, and of the potential V in the lab frame on the right. In the middle are depicted the level curves due to pure co-rotation with the star. Darker levels of grey correspond to higher potentials. Hollow arrows mark the corresponding electric field **E**, the arrow size being proportional to the field strength. The sum of the potentials on the left equals the potential on the right. The magnetic field **B** is indicated by thin arrows, **m** is the magnetic moment and Ω the rotation vector

is immediately obvious from the loop $1,2,3,4,1$ in Fig. 20.6 on the left that the perpendicular electric field high up is given by

$$E_\perp(R) = -\frac{\partial}{\partial R}\mathcal{V}_\parallel(R) \tag{20.7}$$

Note that this relation applies both to $\mathcal{V} = \Psi$ in the co-rotating frame as well as to $\mathcal{V} = V$.

where $\mathcal{V}_\parallel(R) = \int_1^2 Edl$ is the integrated electric field along a magnetic field line from the stellar surface to point 2. In regions of pair creation and higher up, we will assume that the plasma is ideal so that the magnetic field can be considered to be 'frozen-in' into the plasma. In this domain, the electric field has no component along the magnetic field, and the situation is as sketched in Fig. 20.6. The $\mathbf{E}\times\mathbf{B}$ motion of plasma across the magnetic field at large altitudes is now matched by *slippage* of the upper part of the flux tube over the lower part which is frozen-in and co-rotates with the star at the foot-points. The continuous *rupture* of field lines is made possible by parallel electric fields. This continuous reconnection of field lines is called *generalized magnetic reconnection* as it is always associated with dissipation of magnetic – i.e. electric circuit – energy.

Absence of Co-rotation of a Charge-separated Relativistic Beam

The field in the rupture zone near the foot-points is of course not frozen into the plasma. Far above the acceleration region, the situation becomes practically independent of altitude and the electric field is entirely due to space charges inside the beam and not to any surface-charges as is the case near the stellar surface. In the [39] model, the rupture zone is located close (heights of a few polar cap radii) to the stellar surface while in the general relativistic model of [32] it extends over a few stellar radii. Since we are interested in the drift motion of a relativistic plasma beam – which creates its own transverse magnetic field $B_\phi^{\rm S}$ – the drift motion of the plasma as obtained from the approximate force equilibrium condition $\mathbf{E}+\mathbf{v}\times\mathbf{B}=0$ is given by:

$$v_{\alpha\phi}^0 = -\frac{E_R^0}{B_0} + v_{\alpha z}^0\frac{B_\phi^{\rm S}}{B_0}, \tag{20.8}$$

and is independent of species α for the same outflow velocity. Here the drift is with respect to the lab frame and positive drift is in the sense of stellar rotation. For an aligned rotator, $E_R < 0$ and $B_\phi^{\rm S} < 0$, so that the first term on the r.h.s. is positive while the second is negative. It follows that the same perpendicular electric field induces a smaller rotational drift in a charged and out-flowing beam than in a static plasma. We stress that the rotational drift we are talking about is with respect to the lab frame, that is absence of drift means complete lack of co-rotation. For a pulsar observer who translates these results into the comoving star frame this would mean counter rotation at the stellar rotation rate. In particular, for a relativistic beam of Lorentz factor γ consisting of one kind of particles only (a 'charge-separated beam'), the repulsive Coulomb electric self-field is largely – with a factor γ^{-2} – reduced

by the pinching magnetic self-field, a result well known from laboratory plasma physics. However, this fact appears to have received little attention in the literature although it has been mentioned in passing by [17]. This is a very important result in the context of pulsar physics since it implies that a charge-separated, extremely relativistic, primary beam ejected from the polar caps – which by 'construction' has at most a GJ-density – is not co-rotating with the star and, drifting with respect to the star at a negative rate comparable to the stellar rotation frequency!

Note, however, that in a relativistic beam consisting of both positive and negative charges, charge density and current density do not any more directly depend on each other because of the additional freedom of velocities of the two species. Below we will see that this is important for radio pulsars since it implies that the relativistic *pair* plasma would have no difficulty in obtaining a rotation speed not too different from that of the star.

As to the question, is the magnetic field strong enough to enforce co-rotation of any plasma with the stellar rotation, the answer depends on the global distribution of electric fields. If there be no potential drop between stellar surface and relativistic plasma beam higher up then of course in a Poynting-flux dominated situation as is the case for the pulsar, the beam would co-rotate with the star. The required relatively strong electric field would simply be given by a strong super Goldreich–Julian density. But in a realistic pulsar, the relativistic nature itself of the beam is caused by a parallel voltage drop which allows for rupture of the magnetic field lines below the beam and may cause a strong sub-rotation of the beam with respect to the stellar rotation.

20.3 Models of Drifting Sub-pulses

The existing models can be arranged into two classes: one class of models proposes to explain emission structures circulating around the stellar magnetic axis, and is characterized by the rotating carousel model in Fig. 20.7; the other class attempts to explain the drifting sub-pulses by standing waves which are oscillating in time only (period P_{time}) but which are not propagating in space. The 'archetype' of this class is given in Fig. 20.10. In the carousel models, the drifting sub-pulses arise in the radio emission as the line of sight intersects different parts of pulses and/or different pulses during each consecutive crossing of the carousel (see Fig. 20.7). The circulation time can only be derived unambiguously from the observations when a long periodicity P_4 shows up in the observations which is then interpreted as a recurring azimuthal asymmetry in the carousel (see (20.1)). In the standing wave models, the recurring bands of sub-pulses arise because P_3 is a beat between the rotation period P_1 and the wave period P_{time} so that sub-pulses follow the relationship

$$\frac{1}{P_3} = \frac{1}{P_{time}} - \frac{N}{P_1}, \tag{20.9}$$

where $NP_{time} \approx P_1$. We will first summarize a number of models of the carousel class [19, 39, 44] and then of the standing wave class [8, 22, 26].

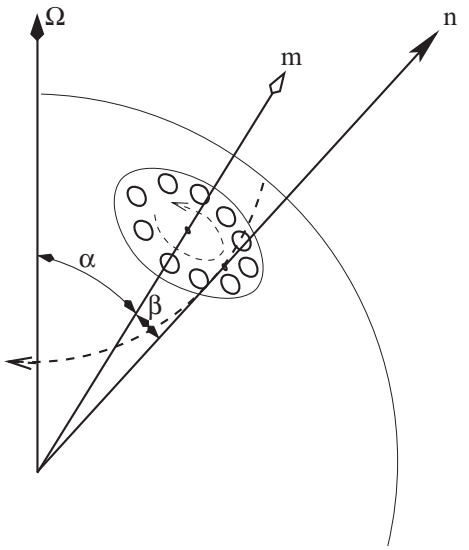

Fig. 20.7 The carousel of emission columns co-rotates as a whole with the pulsar but drifts around the magnetic axis, here with 'opposite' rotational drift. The line of sight **n** crosses the carousel as indicated with the arrow back to front. α is the angle between magnetic and rotation axis, and β is the minimal (or impact) angle of the line of sight with respect to the magnetic axis

20.3.1 Ruderman and Sutherland Models

In the model by [39, hereafter RS75], drifting sub-pulses are interpreted in terms of spark-associated plasma columns rotating around the magnetic axis due to the $\mathbf{E} \times \mathbf{B}$-drift, where $\mathbf{B}$ is the background magnetic field and $\mathbf{E}$ is the electric field in the frame co-rotating with the star (see Fig. 20.8). To the observer, the movement appears as a drift of sub-pulses in the form of sub-rotation. The assumption of the infinitely large binding energy of ions in the stellar surface, crucial for the original RS75 spark model, is probably invalid [1, 33, 34]. Also, there is a strong disagreement between the observed drift speed and the much faster one predicted by the spark model as shown by [36] in the case of PSR B0809+74. Gil et al. [19] propose a version of the spark model with a partially screened vacuum gap due to thermionic emission of ions/electrons, and are able to obtain smaller drift rates. The drift rate they predict is highly sensitive to the difference between actual polar cap temperature and the so-called critical ion temperature for free ion outflow at the GJ rate. It should also be mentioned that the model by RS75, both in its original version and in the modification by [19], requires small curvature radii of the magnetic field in the polar gap region for the pair production. Of course, although only the dipolar magnetic field strength is inferred from (indirect radio) observations at large altitudes, there is no theoretical obstacle for the assumption that strong local or multipolar

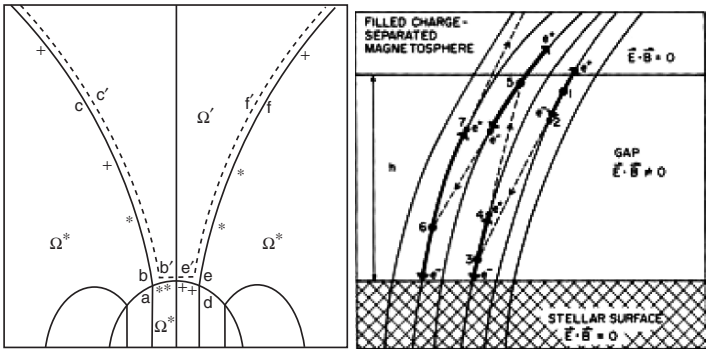

Fig. 20.8 *Left*: Magnetosphere of an anti-aligned magnetized rotating neutron star. A vacuum gap exists between the solid and dashed lines in the magnetosphere. Electric fields parallel to the magnetic field appear in the polar gap $ab'e'd$ as a result of which the wind sub-rotates at a speed $\Omega' < \Omega^*$. *Right*: Breakdown of the polar gap due to pair production from curvature radiation of accelerated electrons and positrons, and formation of a spark (from [39])

magnetic fields prevail at the neutron star surface [20, 21]. However, the implied high degree of regularity of the multipoles does present a problem [5].

20.3.2 The Phenomenological Wright-model

Recently, an empirical model has been constructed by [44] which attributes formation of a drifting regular pattern of emission nodes to constructive interaction between electron and positron beams traveling, respectively, up and down in the magnetosphere, between inner and outer acceleration gaps. The model is based on the following hypotheses: (1) radio emission comes from 'nodes' above the polar caps which lie either on the last open field lines or on field lines which pass through the cross-section of the null-surface and the light cylinder (see Fig. 20.9, left); (2) radio emission is produced only on a field line of the class defined above if the cross-section between the corresponding null line and, respectively, the closed field line or the light cylinder has an altitude within a specific range, of approximately 20,000 and 70,000 from the stellar center, and (3) the nodes are arranged in a regular pattern on two approximate circles above the foot-points of the field lines and the regularity originates from constructive interaction between repeated drifts of outgoing electrons and in-going positrons, traveling in the magnetosphere between inner and outer acceleration gaps (see Fig. 20.9, right). The model, though, does not elaborate on the detailed electrodynamics, and can be considered only as a first phenomenological step towards a physical model. The important point made in the

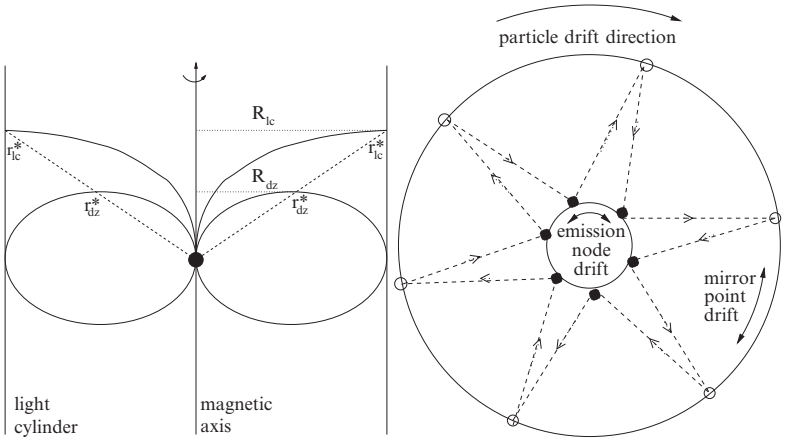

Fig. 20.9 *Left*: The geometry of the pair of magnetic surfaces – in this cross-section represented by two field lines – on which the emission nodes are supposed to be located (from [44]). *Right*: Top view of the particle drift in the co-rotating frame (from [44]). The emission nodes above the polar cap may be stationary, or drift in either direction

proposal is that drifting sub-pulses and their structure can perhaps only be understood within the context of the global magnetosphere rather than just as a local emission effect.

20.3.3 The Clemens and Rosen Model

The model by [8] is of the standing wave class, and ascribes the drifting sub-pulses to non-radial pulsations of the neutron star (Fig. 20.10). The relation (20.9) resembles the original relation proposed for drifting sub-pulses as a pulsational phenomenon (see [41]) but now P_2 is replaced by the wave period P_{time} as the two do not necessarily coincide ([8]). P_3 is now simply the beat period between P_1 and P_{time} and $NP_{time} \approx P_1$. At first sight, a difficulty with this model is the exclusive selection of one particular high-order spherical eigenmode (with a spherical harmonic number in between $l \approx 500 - 700$ and $m = 0$) at the stellar surface. It is probably true that the coupling of the magnetosphere to such stellar oscillations is so strong by the frozen-in nature of the magnetic field in the star that the generation of radio emission higher above the stellar surface would be modulated at he same rate. However, although the authors discuss the possible excitation of stellar oscillations – and in particular of ocean g-modes at some length they point out that their main point is that a *global* oscillation phenomenon may explain the drifting sub-pulses, and that another possibility for the excitation of oscillations at the locations of radio emission may be magnetic field oscillations by perturbations of the magnetosphere. Certainly, the agreement of the simulated and observed patterns of drifting sub-pulses (see Fig. 20.11) is impressive.

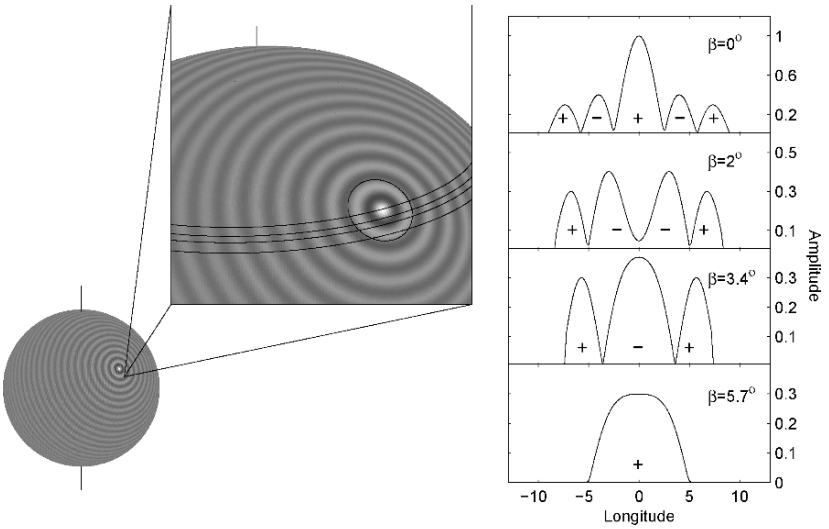

Fig. 20.10 From [8]. *Left*: Shown is an $l = 70, m = 0$ spherical harmonic aligned with the magnetic axis of the star at the altitude of radio emission, together with the boundary of the emission region (*the small black circle*), and four sight lines with different impact parameters β. *Right*: The graphs show the corresponding rectified slices of the spherical harmonic and would represent the average beam profiles. The alternating plus and minus signs denote 180° phase jumps of the sub-pulses

20.3.4 Drift Wave Models

Kazbegi et al. [26] propose to explain the sub-pulse drift in terms of modulation of the emission region by large-scale 'drift waves' on the open bundle of magnetic field lines. In a revised version of this model by [22] the drift waves are generated by oppositely directed curvature drifts of beam electrons and positrons, and form an azimuthal pattern which can be described by an azimuthal modulation $exp(im\phi)$ at mode number m. The electric field component of the drift wave which is largely along the ambient magnetic field direction is then assumed to modulate the emission process. An important point as stressed by the authors is that on a sphere, any perturbation can locally be decomposed into spherical harmonic eigenmodes (as also [8] do) but that a high mode number cannot be used as argument against such a model since what is important physically is not the ratio of wavelength to stellar radius but the wavelength as compared to the cross-section of the open flux bundle [22]. The stability of a distinct drift pattern is argued to be achieved by the non-linear accumulation of the drift modes in a specific azimuthal eigenmode. A weakness of the model seems to be the growth rate of the drift instability which typically has $\Gamma/\Omega_* < 0.01$ whereas the observed fast recovery of drifting sub-pulses after nulling would be indicative of growth rates of tens of percents.

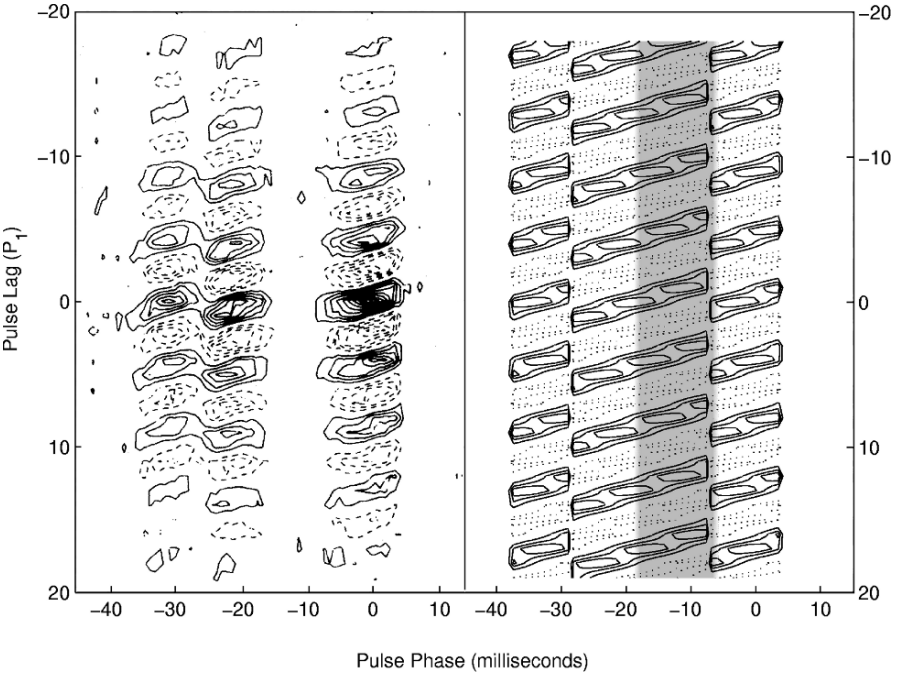

Fig. 20.11 Comparison of longitude-resolved cross-correlation maps for PSR 1919+21 (from [8]). *Left*: Cross-correlation of 1,420 MHz time series data from each longitude with that of a reference longitude. *Right*: Cross-correlation map of simulated data using an oblique pulsar model with $l = 100, \alpha - = 45^\circ, \beta = -2^\circ.35, P_1 = 1.337$ s, and $P_{time} = 32.01$ ms. Solid contours correspond to positive correlations. Note the phase reversals in the observations at approximately -30 and -8 ms which correspond to the locations of nodal lines in the model

20.3.5 Intermediate Conclusion and Forward Look

What seems to be lacking in the proposed models for drifting sub-pulses which have been presented so far is a measure of robustness which makes the outcome not too dependent on precise input of detailed physics, and moreover a precise predictive power. In the latter respect, the most promising frames of thinking are provided by the work of [8] and [44]. Perhaps, in the model of [8] one should not think of stellar pulsations as the underlying cause but directly of global magnetospheric oscillations, and then not so much of cavity modes as in [42] or of plasma frequency vibrations as in [40] but of really large-scale breathing and torsional modes of the entire magnetosphere inside the light cylinder. After all, the magnetosphere of a magnetized obliquely rotating neutron star is during every rotation period strongly perturbed on the scale of the light cylinder by the Poynting flux of the open polar field lines since the Alfvén travel timethrough he light cylinder is (by construction) of the same order as the rotation period (compare the 'ringing bell' of the Earth's

magnetosphere). Clearly, a more detailed follow-up of [8] and [44] is needed in which the described mathematical structures are provided with physics.

In the rest of the paper we will describe a model which tries to incorporate the basic electrodynamic properties of the open flux bundle, in particular the electric current and the dense relativistic pair plasma wind, as the drivers of sub-pulses.

20.4 Diocotron Instability Model

Recently, we have proposed a model for the drifting sub-pulses based on the occurrence of a diocotron instability in the pair plasma on the open field lines [18]. Since the mechanism involves a large number of properties of the polar cap wind we summarize its main characteristics and predictions in some detail here, pointing out which results are robust and which are the result of the mathematical simplifications made in the treatment of the instability. The diocotron instability (also known as 'rotational shear' or 'slipping stream' instability) is an instability of a sheared flow, much like the familiar Kelvin–Helmholtz instability in a quasi-neutral plasma, now, however, in a non-neutral plasma. This is the reason why it is sometimes also called the 'electrostatic' Kelvin–Helmholtz instability [25]. In particular, the diocotron instability occurs in a charged plasma beam propagating along a uniform background magnetic field and a vanishing background electric field component parallel to the background magnetic field, e.g. Sect. 2.10 in [9]. The electric self-field of the charged beam would lead to the familiar $\mathbf{E} \times \mathbf{B}$ drift around the cylinder axis which is now, however, as we have seen above, modified by the effect of the magnetic self-field from the beam which, in general, carries an electric current as well as a charge. When the resulting differential rotation of the beam around the cylinder axis satisfies a certain condition, a non-axially symmetric perturbation in density, velocity and electric potential can grow over the shear layer. To linear order, the unstable surface modes are characterized by a radial eigenfunction, an azimuthal mode number l, an axial wave-number $k_{\|}$, and an angular frequency ω, whose imaginary part gives the growth rate $\mathrm{Im}\,\omega = \Gamma$ and whose real part is related to the angular pattern speed through $\omega_{\mathrm{pat}} = \mathrm{Re}\,\omega/l$. In the non-linear stage, the surface waves interact with each other through the perturbed potential, which results in stable vortices [10, 14, 38]. So, the diocotron instability modulates and fragments a charged cylindrical beam in the azimuthal direction as a result of initial shear of the plasma angular velocity around the axis. Whether the instability occurs and what its characteristics (mode number, growth rate) are is completely determined by the detailed spatial distribution of the charge and current density of the relativistic pulsar wind. Therefore, if the diocotron instability be relevant at all to the sub-pulses this model provides a distinct advantage as compared to the other models in that it builds on the essential ingredient of any viable radio pulsar model, the existence of a charged and current carrying dense pair wind.

We have modeled the plasma outflow above the pair-creation front as an infinitely long, non-neutral annular beam composed of electrons and positrons propagating with relativistic speeds along the pulsar's infinite magnetic field. Stability analysis for realistic parameter values under pulsar conditions reveals a large domain of instability, where the – linear stage of the – diocotron instability indeed occurs in the form of surface waves. The link between mode number l and pattern frequency $\omega_{\rm pat}$ of the unstable mode to the observed number of sub-beams and pattern circulation time is given by

$$\tau_{\rm circ} = \Omega_*/(\Omega_* - \omega_{\rm pat}), \tag{20.10}$$

where $\Omega_* = 2\pi/P_1$ is the pulsar rotation frequency and $\tau_{\rm circ}$ is measured in units of pulsar periods P_1. In passing, we note that, in reality, the drifting sub-pulses should correspond with the vortices from the non-linear phase of the diocotron instability instead of the linear structures discussed here.

20.4.1 Equilibrium

To study the diocotron instability, the relativistic macroscopic fluid description is used. Each species α is described by the coupled fluid-Maxwell's equations. Finite temperature effects are not taken into account. The stability of equilibria are investigated under electrostatic perturbations (superscripts "0" and "1" refer to the equilibrium and perturbed quanties respectively).

Beam Models: Hollow, Beam + Core, and Beam + Return Current

In order to find suitable realistic equilibria we assume that the outgoing plasma above the pair-creation zone can be modeled as an axially symmetric cylindrical structure of out-flowing electrons and positrons (denoted with "–" and "+" respectively) in a uniform background magnetic field, $\mathbf{B}_0(\mathbf{r}) = B_0\hat{z}$. The differential rotation in the beam will then be determined by the specific equilibrium beam properties (the equilibrium radial density distribution $n^0_\pm(R)$, and the equilibrium velocity components $v^0_{\pm z}(R), v^0_{\pm\phi}(R)$). The plasma is assumed to be cold, and its quantities independent of the z-coordinate. Finally, we assume that electric fields are perpendicular to the magnetic field.

We consider three possible geometries: (1) a hollow beam; (2) a hollow beam with a core component, and (3) two hollow beams with opposite currents. We assume that the beams consist of electrons and positrons with nearly equal axial velocities (Fig. 20.12). The densities of electrons and positrons are assumed to depend only on R. Since the electric field is completely determined by the density difference $\Delta n(R) = n_+(R) - n_-(R)$ this quantity determines the equilibrium. We normalize $\Delta\tilde{n} = \Delta n/n_{\rm GJ}$ where $n_{\rm GJ} \equiv -2\varepsilon_0\Omega_* B_0/e$ is *not* the GJ-density (20.3)

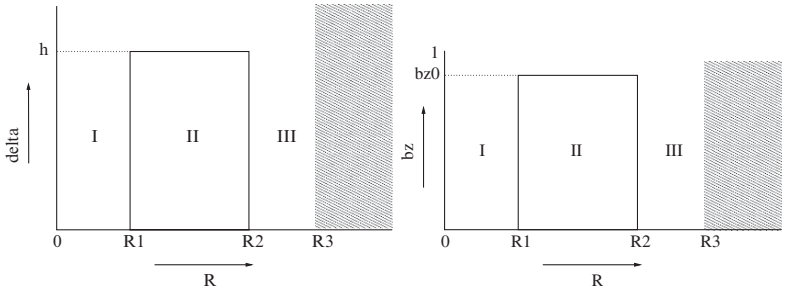

Fig. 20.12 *Left*: Model for the hollow beam. The density difference between positrons and electrons is delta$\equiv \Delta n = n_+ - n_- = h n_{\rm GJ}$ in region II, and zero in regions I and III. At $R > R_3$, the plasma is assumed to be in solid-body rotation with the star. *Right*: The axial velocity of the beam particles across the beam is taken to be constant (bz $\equiv \beta_z$ and bz0 $\equiv \beta_z^0$)

but an abbreviation involving the absolute value of the *local* magnetic field strength B_0. The closed magnetosphere occupies the region $R \geq R_3$, has a static plasma with a Goldreich–Julian density everywhere, and co-rotates with the star.

For the hollow beam $\Delta\tilde{n}(R) = h$ in region II ($R_1 < R < R_2$) and zero elsewhere. For the motion of the two species, we take $v_{+z} \approx v_{-z} = \beta_z^0 c$ independent of R. Additionally, particles are assumed to be relativistic only in the axial direction, so that $\gamma \approx (1-\beta_z^{02})^{-1/2}$. We express the axial current density of the beam formally as

$$J_z(R) = f(R)\beta_z^0(R)\, e\, n_{\rm GJ}\, c. \tag{20.11}$$

At the polar cap, the density at which the particles stream out is approximately $n_{\rm GJ}$, therefore, we expect $0 \leq f(R) \leq h$ if the current occupies the entire open flux tube, but of course $f(R)$ can be much larger if the current is confined to a thin hollow cylinder.

In Fig. 20.13 two additional configurations are depicted: a non-zero core and when part of the beam moves in the opposite direction (return current). The charge density difference in region I is $h_{\rm I}$. We expect that in this region no pair creation occurs because of the large radius of curvature of the magnetic field, and, therefore, that the beam is charge-separated. The axial velocity remains unchanged, i.e. both in region I and in region II approximately the same axial velocity applies to all particles.

As for the return current, the axial velocity of the hollow beam changes sign at the radial location

$$R_p = R_1 + p\,(R_1 - R_2) \tag{20.12}$$

which separates region IIa from IIb (see Fig. 20.13). Note that when the net ring current is zero, we have

$$R_p^2 = (R_2^2 + R_1^2)/2 \tag{20.13}$$

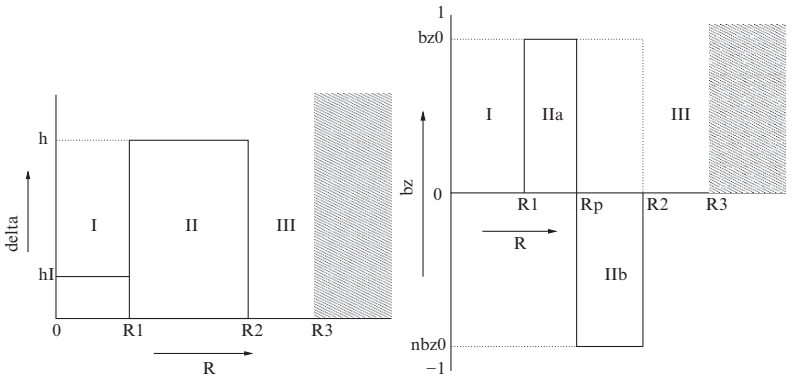

Fig. 20.13 *Left*: Similar to Fig. 20.12; now, a core component is included. The dimensionless charge difference in Region I is $h_{\rm I}$. *Right*: Similar to Fig. 20.12, but now, part of the beam moves in the opposite direction (R_p is defined by (20.12))

Differential Rotation

By the assumptions of z-invariance and axial symmetry, the equilibrium electric field as determined from Poisson's equation is given by

$$E_r^0(R) = \frac{1}{\varepsilon_0 R}\sum_\alpha e_\alpha \int_0^R \mathrm{d}R'\, R' n_\alpha^0(R') = \frac{e n_{\rm GJ}}{\varepsilon_0 R}\int_0^R \mathrm{d}R'\, \Delta\tilde{n}(R')$$

and we have used the definition of $\Delta\tilde{n}$ to obtain the latter equality. The equilibrium magnetic field is given by, $\mathbf{B}^0 = B_0\hat{z} + B_\phi^{\rm S}(R)\hat{\phi} + B_z^{\rm S}(R)\hat{z}$, where B_0 is the constant background magnetic field and $\mathbf{B}^{\rm S}$ is the field generated by the equilibrium axial and azimuthal currents J_z^0, J_ϕ^0. Since the background magnetic field is extremely large, we neglect the field $B_z^{\rm S}$ which is generated by J_ϕ^0. Furthermore, we use (20.11) for the equilibrium axial current density, so that:

$$B_\phi^{\rm S}(R) = \frac{1}{\varepsilon_0 c R}\int_0^R \mathrm{d}R'\, R' J_z(R')/c \tag{20.14}$$

Using the assumptions listed before, the zeroth order of both the continuity equation and Maxwell's equations are satisfied, while the azimuthal and axial component of the momentum equation are trivial. Thus, we are left with the radial component of the momentum equation, which relates the density distribution $n_\alpha^0(R)$, the axial velocity β_z^0, the axial current (in terms of $en_{\rm GJ}c$) $f(R)$ and the angular speed $\omega_\alpha(R) = v_{\alpha\phi}^0(R)/R$ of species α to each other:

$$\omega_\alpha^2(R) + \varepsilon_\alpha \omega_\alpha(R)\Omega_{B\alpha} + \frac{\varepsilon_\alpha e}{\gamma_\alpha(R) m_\alpha R}\left[E_R^0 - v_{\alpha z}^0(R) B_\phi^S\right] = 0 \tag{20.15}$$

where $\Omega_{B\alpha} \equiv eB_0/\gamma m_\alpha$ is the – absolute value of – the relativistic cyclotron frequency, and $\varepsilon_\alpha \equiv \mathrm{sgn}\, e_\alpha$.

If one neglects the first term in (20.15) one immediately derives the earlier result $\mathbf{E} \times \mathbf{B}$ (cf. (20.8)). Obviously, the first term represents the inertial acceleration which can be neglected even for large Lorentz factors because of the strength of the background magnetic field. Defining

$$Q \equiv \beta_z^{02} f/h, \tag{20.16}$$

$$Q_{\mathrm{I}} \equiv \beta_z^{02} f_{\mathrm{I}}/h_{\mathrm{I}}, \tag{20.17}$$

and

$$\tilde{h}_{\mathrm{I}} = h_{\mathrm{I}}/h, \tag{20.18}$$

the angular rotational velocity

$$\tilde{\omega}_\alpha(R) \equiv \omega_\alpha(R)/\Omega_* \tag{20.19}$$

for the various beams are given in Fig. 20.14.

Exact co-rotation only occurs when the beam is solid *and* $h(1-Q) \to 1$ (where h and Q are now the solid beam parameters). This can be seen both in the hollow beam

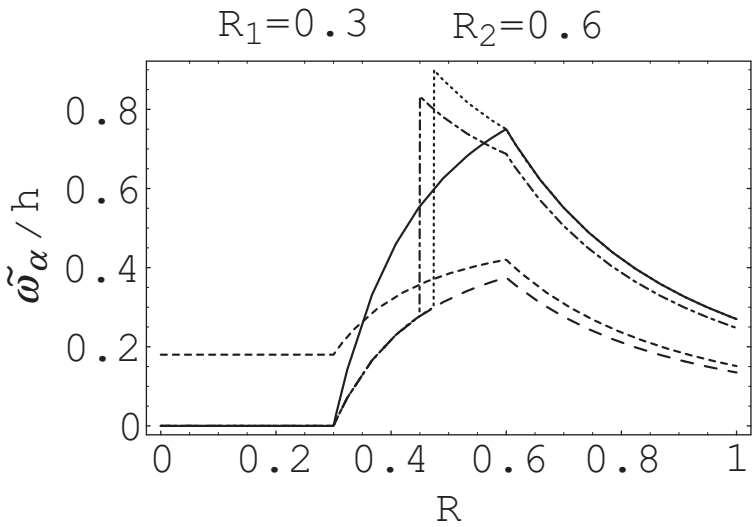

Fig. 20.14 Examples of equilibrium rotational velocity distributions across the beam. R_1, R_2 are the inner and outer boundary of the beam, and have values $R_1 = 0.3$, $R_2 = 0.6$ and $R_3 = 1$. Drawn are the equilibrium solutions for: hollow beam with $Q = 0$ (*solid*), hollow beam with $Q = 0.5$ (*long dash*), beam with core ($h_{\mathrm{I}} = 0.2, Q_{\mathrm{I}} = 0.1$) and $Q = 0.5$ (*short dash*) and beam including return current with $Q = 0.5$ where R_p is determined by a net zero current ((20.13), *dotted*) and another where $p = 0.5$ (*dash-dotted*)

case when we take $R_1 = 0$ and $\beta_z^{02} f$ close to zero for a beam with $h = 1$, and in the second case where we included a core component and co-rotation appears is only in Region I. Also, a relativistically out-flowing plasma beam with a Goldreich–Julian current density does not co-rotate at all with the star unless the charge density is of order γ^2 times the Goldreich–Julian charge density (e.g. $h = \tilde{h}_{\rm I} = 1$ in Region I. Put differently, rotational speeds exceeding the stellar rotation ('super-rotation') are possible if the charge difference density exceeds the Goldreich–Julian density sufficiently. In general, it is clear from (20.15) that a realistic pulsar outflow has a sheared rotational velocity distribution across the beam.

For illustrative purposes, a number of equilibrium rotational velocity distributions are given in Fig. 20.14. Note that the presence of a return current in a relativistic beam has the effect of pushing up the rotational velocity toward co-rotation (compare dotted and long-dashed solutions).

20.4.2 Instability

Linearizing the fluid-Maxwell's equations is done by assuming that the perturbations are electrostatic, i.e. $|\mathbf{B}^1|$ is small compared to $|\mathbf{E}^1|$ in the momentum equation and Faraday's law. With this, the perturbed electric field can be described as the gradient of a scalar potential:

$$\mathbf{E}^1 = -\nabla V^1 \tag{20.20}$$

Furthermore, each perturbed quantity is expressed as:

$$\psi^1(t,R,\phi,z) = \sum_{l=-\infty}^{\infty} \sum_{k_z=-\infty}^{\infty} \tilde{\psi}(R) \exp[-i(\omega t - l\phi - k_z z)] \tag{20.21}$$

In this way, the set of equations with five variables can be rewritten into one perturbed Poisson's equation with $\tilde{V}$ as the only variable (see Appendix in [18]). Because we are considering beams whose motion is only relativistic in the *axial* direction, terms of order $\beta_{\alpha\phi}^{02}$ and higher are neglected. Also, we assume that the beam density is low and the background magnetic field strength is large, so that $\omega_{p\alpha}^2 \ll \Omega_{B\alpha}^2$. As for the perturbations, we are interested in waves with $k_z = 0$ and $|\omega - l\omega_\alpha(R)|^2 \ll \Omega_{B\alpha}^2$ (both ω and ω_α are of the order of Ω_*). With these assumptions the perturbed Poisson equation becomes:

$$\frac{1}{R}\frac{\partial}{\partial R}\left[R\frac{\partial \tilde{V}}{\partial R}\right] - \frac{l^2}{R^2}\tilde{V} = \tilde{V}\frac{l}{R}\frac{2}{\tilde{\omega} - l\tilde{\omega}_\alpha(R)}\frac{\partial}{\partial R}\Delta\tilde{n}(R) \tag{20.22}$$

where $\tilde{\omega} = \omega/\Omega_*$.

Now, since we are using step-functions for Δn, (20.22) can be solved analytically. This applies even in the case of a 'return current', because in the derivation of (20.22) we have neglected the contributions of k_z and $\beta_{\alpha\phi}^2$.

Eigenvalue Equation

The general solution of (20.22) results in an eigenvalue equation for the perturbation $\tilde{\omega}$ which in our simple case is quadratic only. Solutions for $\tilde{\omega} = \mathrm{Re}\,\tilde{\omega} + i\,\mathrm{Im}\,\tilde{\omega}$ with positive imaginary part correspond to growing perturbations. Instability is completely determined by just two values: $\tilde{\omega}_\alpha(R_1)/h$ and $\tilde{\omega}_\alpha(R_2)/h$. For example, (see also Fig. 20.14) the same (in)stability occurs for a non-relativistic hollow beam and a non-relativistic return current. For unstable solutions, we normalize the growth rate $\tilde{\Gamma}$ to Ω_* and the rotational speed of the perturbation (or pattern speed) to $\tilde{\omega}_{\mathrm{pat}}$ to Ω_*. The pattern speed is found to have a remarkably simple expression:

$$\tilde{\omega}_{\mathrm{pat}} = \frac{\mathrm{Re}\tilde{\omega}}{l} = \frac{1}{2}\Big[\tilde{\omega}_\alpha(R_1) + \tilde{\omega}_\alpha(R_2)\Big] + \frac{h}{2l}\Big[\big\{(R_2/R_3)^{2l} - (R_1/R_3)^{2l}\big\} - \tilde{h}_{\mathrm{I}}\big\{1 - (R_1/R_3)^{2l}\big\}\Big]. \quad (20.23)$$

The pattern speed derived turns out to be approximately halfway between $\tilde{\omega}_\alpha(R_1)$ and $\tilde{\omega}_\alpha(R_2)$, just like for the Kelvin-Helmholtz instability in a quasi-neutral plasma. Physical beams are constrained by: $0 \le R_1 < R_2 \le R_3$, and for $h_{\mathrm{I}} = 0$, $Q = 1$, one obtains $\omega_\alpha(R_1) = 0$ and $\omega_\alpha(R_2) = 0$ and the solutions are always stable. Also, for $h_{\mathrm{I}} = 0$, the fundamental mode $l = 1$ is always stable.

Surface Waves

For our simple beam distributions the diocotron instability gives rise to surface waves. This is illustrated in Fig. 20.15 where the equipotential curves are drawn for $Q = 0$, $R_1 = 0.5$, $R_2 = 0.6$, $R_3 = 1$ and $l = 5$ at $t = 0$.

Obviously, extremes are formed at the two surfaces with five azimuthal nodes. Moreover, the surface waves are shifted in phase with respect to each other. The phase shift is determined by the geometry. It is this system which probably will evolve into a non-linear stage where particles get trapped and vortices form.

20.4.3 Numerical Results

We have searched the domains of instability for $l_{\max}$: the azimuthal mode number l with the largest growth rate as a function of $(R_1/R_3, R_2/R_3)$ for various beams. As an example we show the results for a hollow beam including a return current are displayed in grey-scale in Figs. 20.16–20.17. In the contour graphs, darker areas represent larger $l_{\max}$: for $l_{\max} \in [2, 10]$ we use different level of grey-scale for *each* integer $l_{\max}$ (some of which are depicted in the graphs), whereas for the ranges: [11,20], [21, 30] and [31,40], *one* grey-scale is used for each range; black represents $l_{\max} > 40$, and such values are apparent in the graphs for $Q \ge 0.6$. Complementary to the contour graphs we present the maximum of growth rates $\tilde{\Gamma}/h$ and pattern velocity $\tilde{\omega}_{\mathrm{pat}}/h$ ((20.23)) found in each $l_{\max}$-region.

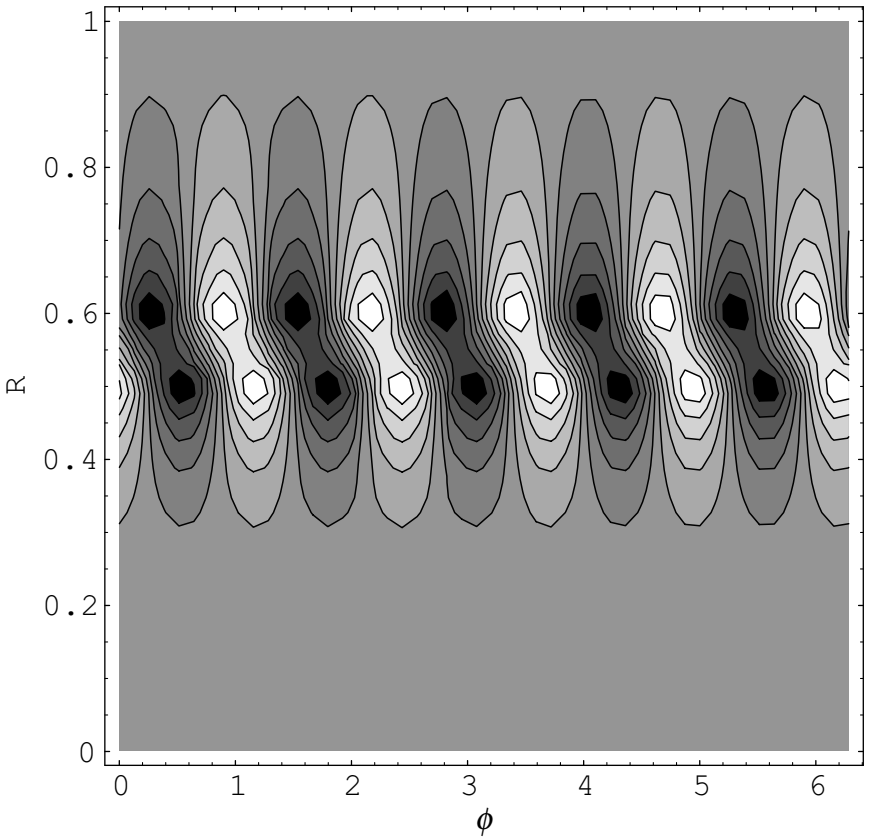

Fig. 20.15 Equipotential for annular beam with $Q = 0$, $R_1 = 0.5$, $R_2 = 0.6$ and $l = 5$ at $t = 0$

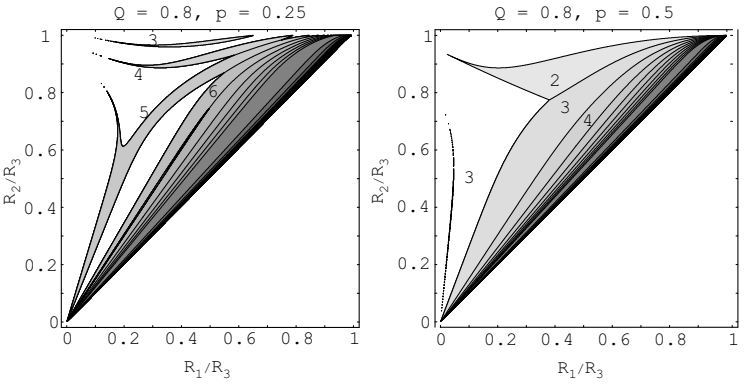

Fig. 20.16 Unstable diocotron modes in the parameter space of R_1/R_3 (along the horizontal axis) and R_2/R_3 (along the vertical axis). for examples including a return current. In levels of grey is plotted $l_{\max}$, which is the azimuthal wave number l for which the combination of R_1/R_3 and R_2/R_3 results in the largest growth rate. The parameter $Q = \beta_z^{02} f/h$ is found above each graph as well as p which defines R_p, i.e. the radius where the axial velocity of the beam particles changes sign (see (20.12))

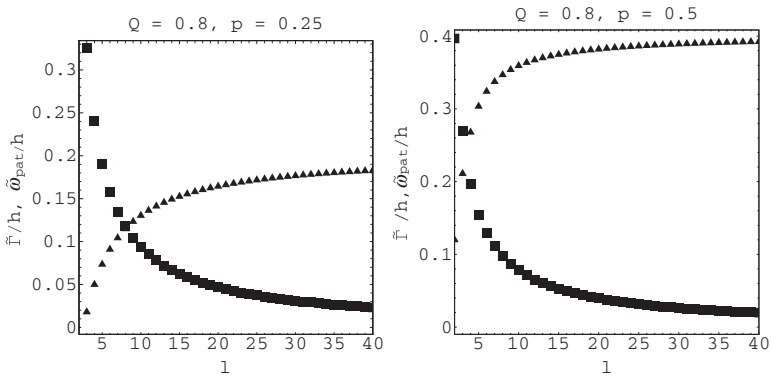

Fig. 20.17 Maximum growth rate (*triangles*) and pattern velocities (*squares*) corresponding to the case in Fig. 20.16

In the case of $Q = 0$ (i.e. either the beam is non-relativistic or the beam carries no current), the beam displays instability for all modes. The general trend for all Q's is that thinner beams, i.e. $R_1 \simeq R_2$, are unstable for higher l.

An increase in Q leads to a shift of the $l_{\max}$ regions in parameter space and a decrease in their area, until, for small $l_{\max}$, instability eventually vanishes. In the case of $Q = 0.9$, almost *any* hollow beam is stable. This is in agreement with the results of [3] for a charge-separated, relativistic, particle beam. In that case: f equals h, and solutions for $\tilde{\omega}$ are very stable unless $l \gg \gamma^2$.

20.4.4 Applications

One of the results that we obtain is that the diocotron instability can operate in a relativistic beam under typical pulsar conditions where the density distribution is not charge-separated but instead is formed by a pair plasma. In a charge-separated flow, however, the instability only occurs at extremely large azimuthal wave numbers, $l > 10^7$, which of course does not lead to observable consequences.

To demonstrate the applicability of the diocotron instability to radio pulsars, we use the hollow beam model as a simple example. To be able and apply the above investigated cases of the diocotron instability we made the following assumptions: the rotation axis is aligned with the magnetic axis, the magnetic field is uniform in the axial direction, $k_{\|} = 0$, and a core component is absent (or at least there is no *spacing* between the beam components). Since our model is valid for aligned pulsars, we have chosen two pulsars which show drifting sub-pulses and are nearly aligned: PSR B0943+10 and PSR B0826–34. To apply our results, we need to extract the following information from the observations: the azimuthal mode number l, the pattern frequency ω_{pat} in the laboratory frame, and the inner and outer radius of the subpulse, R_1, R_2, relative to the cone radius R_3 (which we assume to

Table 20.1 Observationally inferred pulsar data. Note that in [16] no value for β is quoted for B0826-34. We infer P_3 from their values of P_2 using the relation for the drift rate $D(^\circ/P_1) = P_2(^\circ)/P_3(P_1)$, which is a good approximation for this system as it is nearly aligned. Positive and negative values occur due to the definition of the drift rate

PSR	$\alpha(^\circ)$	$\beta(^\circ)$	P_1(s)	$P_3(P_1)$	l	$\tau_{\rm circ}(P_1)$	$\tilde{\omega}_{\rm circ}$
B0943+10 [12]	11.58	–4.29	1.09	1.87	20	37	0.973
B0826–34 [24]	$1-2$	1	1.848	0.50	15	7.5	0.833
B0826–34 [16]	0.5	–	1.848	$\{+6,-7\}$	13	$+78,-91$	$\{0.99,1.01\}$

correspond to the last open field line). R_1 and R_2 are retrieved from the observations of the specific pulsar. The best estimate for R_3 (at the height of emission) is obtained by using the width of the average profile together with α and β of that pulsar (see, e.g. (2) in [35]). The data available from the literature are shown in Table 20.1.

PSR B0943+10

Drifting sub-pulses have been studied extensively for this pulsar by [11, 12]. They argue that the alias problem is solved and found 20 sub-beams which sub-rotate with respect to the pulsar, and complete one circulation in 37 pulsar periods. This corresponds to an angular frequency in the laboratory frame of $\omega_{\rm pat} = 0.973\,\Omega_*$. From the average pulse profile (Fig. 1 in [12]) we obtain for the full pulse width $W = 34^\circ$. Together with $\alpha = 11^\circ.58$ and $\beta = -4^\circ.29$, we obtain for the cone radius $\rho = 5.^\circ08$. To apply our model of a hollow beam, we estimate $R_2/R_3 \sim 0.86-0.93$ (Fig. 10 in [12]). If we assume the sub-pulse shape to be circular, we get $R_1/R_3 \approx 0.65$.

For $R_1/R_3 = 0.65$ and $R_2/R_3 = 0.92$, we calculate $\tilde{\Gamma}/h$ in the parameter-space (l,Q) (see Fig. 20.18). Apparently, growth rate is not optimal for $l = 20$. Since we do not have more information on Q, we conclude that for $l = 20$ to develop, we need $Q \approx 0.8$. By combining this with measured $\tilde{\omega}_{\rm pat} = 0.973$, we find from (20.23) that $h = \Delta n/n_{\rm GJ} \approx 20$.

Since the values for R_1/R_3 and R_2/R_3 are just estimates, it is important to see what the influence is if we change the beam configuration. The results are shown in Figs. 20.18. The values of the Q-parameter, providing instability for $l = 20$, are listed in Table 20.2. If we apply the measured pattern velocity $\tilde{\omega}_{\rm pat} = 0.973$ to all five cases shown in Table 20.2 and plug the corresponding values into (20.23), we find that for the instability to develop, the charge density difference should be $\Delta n \approx 19.5\,n_{\rm GJ}$.

PSR B0826−34

This pulsar was observed by [7, 15, 30, 37] at different frequencies. Already in the first observations it was noticed that the radiation spans the full 360°. The average pulse profile is divided into four regions, labeled I–IV. At low frequencies, e.g. 408 MHz, the main pulse (III) dominates over a weak interpulse (I) in the average

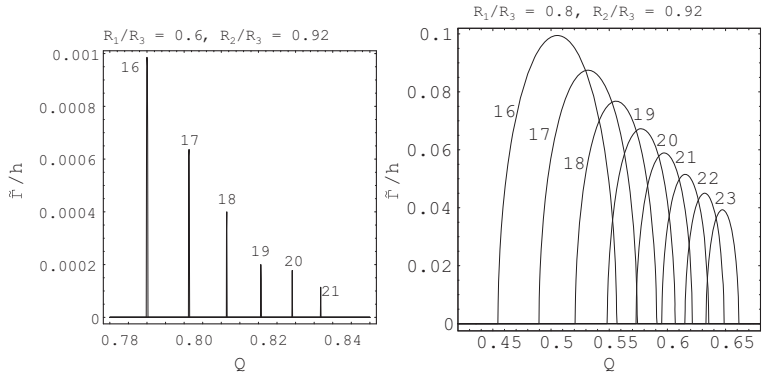

Fig. 20.18 Growth rates as functions of Q, for different values of azimuthal mode number l (indicated in the plot), for a hollow beam with $R_2/R_3 = 0.92$ and $R_1/R_3 = 0.6$ (*left*) and $R_1/R_3 = 0.8$ (*right*)

Table 20.2 The results of Q and $\tilde{\Gamma}$ for possible beam configurations of PSR 0943+10 assuming $l = 20$ and $\tilde{\omega}_{\rm pat} = 0.973$. The charge density difference is found to be $h \approx 19.5$. Initial guesses for R_1/R_3 and R_2/R_3 are taken from Fig. 10 in [12]

R_1/R_3	R_2/R_3	Q	$\tilde{\Gamma}$
0.65	0.92	0.80	1.8×10^{-2}
0.60	0.92	0.83	3.6×10^{-3}
0.80	0.92	0.60	1.14
0.65	0.86	0.77	7.2×10^{-2}
0.65	0.93	0.81	1.4×10^{-2}

pulse profile, whereas at higher frequencies, e.g. 1,374 MHz, the relative intensities switch, and the intensity in I is much higher than in III. This is seen in average pulse profiles at different frequencies, e.g. in Fig. 1 in [16]. Also, this pulsar is remarkable due to its long nulls, e.g. 70% of the time at 409 MHz [15]. Already in the early observations of PSR B0826–34, the drifting sub-pulses were observed with an unusual apparent drift pattern, namely a sign reversal of the drift rate [7].

Recently, two detailed observational studies have been made of this pulsar. Gupta et al. [24] studied the main pulse (III) with the GMRT at 318 MHz. They claim that the apparent sign reversal is merely an effect of the geometry and aliasing. Our line-of-sight is very near the magnetic axis $\beta = 1^\circ$, and this axis in turn is close to the rotation axis, $\alpha \leq 5^\circ$ (probably $\approx 1^\circ - 2^\circ$). In this way, the observations are still compatible with a Ruderman and Sutherland model. They concluded that the carousel has about 15 sparks (at 318 MHz), rotating at an angular frequency of $\tilde{\omega}_{\rm pat} = 0.867$. Another observation was made with Parkes at 1.374 GHz by [16]. They studied the whole pulse profile and used a method called 'phase tracking' where (as the name suggests) the phase of the pulse is tracked, throughout the whole profile which resulted in 13 sub-beams. At this frequency, the inter-pulse is much stronger than the main pulse, and they came to the conclusion that we observe two

nested cones, (see Fig. 10 in their paper, note that *both* cones have 13 sub-beams). They argue that the drift reversal cannot be accounted for in terms of geometry and aliasing (which would be too much of a coincidence), but that it is a *true* reversal, implying that the beams are rotating 3.6° and 3.2° per rotation period in either direction, corresponding to pattern velocities of $\tilde{\omega}_{\rm pat} = 1.01$ and 0.99, respectively. Contrary to a Ruderman and Sutherland model, the diocotron instability can account for a reverse drift as we will show.

We assume that the two observed sub-beam rings are formed by an instability of two nested hollow beams. The treatment of the inner hollow beam is unaffected by the outer beam, since the electric field causing the drift is only determined by the enclosed charge. The outer beam, on the other hand, cannot be described correctly within the context of our model without further assumptions since two different hollow beams would lead to an eigenvalue equation for $\tilde{\omega}$ of 4-th degree instead of the quadratic equation. For simplicity, we therefore assume that the outer beam can be treated independently. Although [16] suggested a polar cap geometry, R_1/R_3 and R_2/R_3 are not well enough determined. So, unlike in PSR 0943+10, we cannot first constrain Q by fixing the hollow beam geometry. Instead, we allow different Q's and plot the instability region for $l = 13$ and $Q = 0 - 0.7$ (Fig. 20.19; white regions are stable). Inside the domain we separate the regions by using grey-scales for different 'angular' velocities $\tilde{\omega}_{\rm pat}/h$ (black represents $\tilde{\omega}_{\rm pat}/h > 0.08$, and the other two have: $0 < \tilde{\omega}_{\rm pat} \leq 0.04$, $0.04 < \tilde{\omega}_{\rm pat} \leq 0.08$). Note that instead of $(R_2/R_3, R_1/R_3)$, we now use the center of the beam, $R_b = (1/2)(R_1 + R_2)$ and the beam half-width, $\Delta R = (1/2)(R_2 - R_1)$.

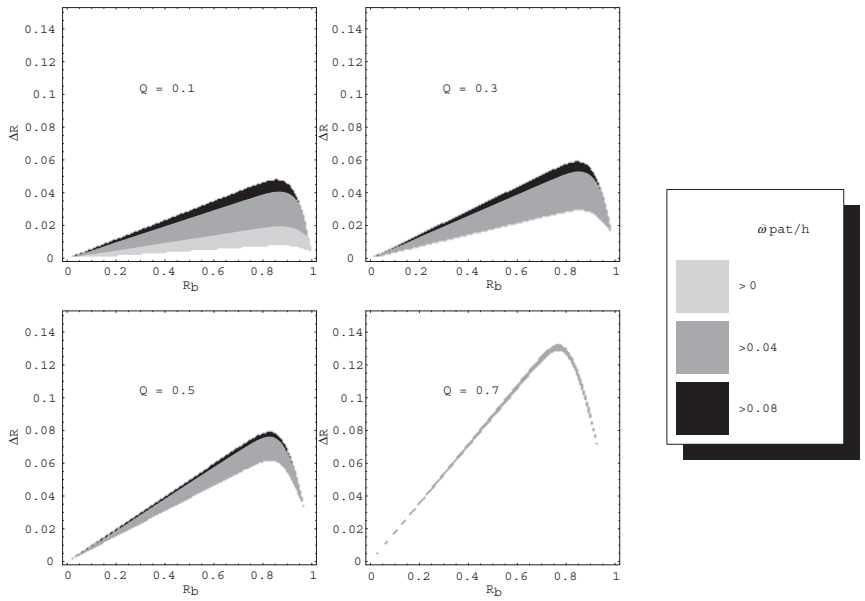

Fig. 20.19 Domain of instability for $l = 13$ as applied to PSR 0826–10. The three regions denote different intervals of $\tilde{\omega}_{\rm pat}/h$ (see legend)

To have a reverse drift, our model implies that the charge density differences are changing around a critical value. For instance, if we take $Q = 0.7$, and for the beam radius of the inner cone $R_b = 0.56$ (a rough estimate from Fig. 10 in [16]), then for $l = 13$, the maximum of $\tilde{\Gamma}/h$ occurs at $\Delta R = 0.0995$, which gives us $\tilde{\omega}_{pat}/h = 0.077$. For exact rotation with the star, we need $h = 1/0.077 \approx 13$ (which corresponds to $\tilde{\Gamma} \approx 0.12$). Thus, for slightly larger or smaller Δn, the pattern speed will be either sub- or super-rotational as compared to the stellar rotation. Also, note that the beam thickness ΔR increases with the beam radius R_b for the same (l,ω_{pat}), just like [16] suggested for the two rings on the basis of their observations (see their Fig. 10). If we choose, e.g. $R_b = 0.77$ for the outer cone, then, for this beam to be unstable for $l = 13$ *and* to have the same pattern velocity as the inner beam, we find a maximum of $\tilde{\Gamma}/h$, now corresponding to $\Delta R = 0.13$, which is indeed slightly larger than the beam thickness of the inner cone.

20.5 Future Prospects

What Have We Learned?

- The phenomenon of drifting sub-pulses is common to the majority of radio pulsars. This result has come about from a careful study of high-quality data taken with the PuMa backend of the Westerbork Synthesis Radio Telescope.
- Drifting sub-pulses can – in principle – be understood both in a rotating carousel model, and in an oscillating magnetosphere model. The precise physics leading to such an effect have, however, still to be filled in.

We have described in some detail the diocotron instability (alternatively also called a 'slipping stream' or an 'electrostatic Kelvin–Helmholtz' instability) in the context of drifting sub-pulses. We modeled the out-flowing relativistic pair plasma as a non-neutral, differentially rotating, infinitely long and azimuthally symmetric cylindrical annular beam, propagating along the pulsar's strong magnetic field. In the limit of long axial wavelengths ($k_{\|} = 0$), we find that the instability occurs for a broad range of beam geometrical parameters. We find that for charge separated flow, only the modes with very high azimuthal harmonic number, $l \geq \gamma^2$, are unstable. However, when the flow consists of both positrons and electrons, the charge density and the current density become largely independent of each other, and the beam becomes unstable in the relativistic case already for moderate azimuthal numbers, $l \leq 40$.

We have applied this model to two pulsars with sufficiently detailed carousel observations, namely PSRs B0943+10 and B0826−34, identifying the azimuthal number l of the unstable surface modes with the number of sub-beams in a particular pulsar profile. In both cases we have demonstrated that the hollow beam model can account for the observed sub-pulse drift. It is important to notice that since the drift direction is determined by the non-dimensional charge density h (i.e. relative excess of the charge of one sign over another), together with the normalized charge of one sign over another), together with the normalized current density Q, direction reversal

of the drift *is* possible within our model. The latter phenomenon is observed in PSR B0826−34. Such an application opens up the possibility to determine details of the polar cap plasma, such as charge and current densities of the particles, within the frame of the diocotron instability model.

In both applications we find that strong super GJ charge density difference is needed for the relativistic beam to nearly co-rotate with the star. It should be noticed that there are no principal difficulties for the net charge of a pair plasma beam to achieve such densities. Whether a relativistic beam has a large or small density just depends on the parallel voltage drop deep below the resonance region, close to the stellar surface. If there is no voltage drop, there is no slippage of the magnetospheric field with respect to the star, and the magnetic field is strong enough to enforce co-rotation. Moreover, we stress that a relativistic beam of electrons and positrons with a charge density difference equal to just the GJ-density does not co-rotate with the star at all, unless $1-\beta_z^{02} f$ is small, because the repelling electric radial force is largely balanced by the pinching force of the self-magnetic field. At the same time, in the pulsar application, the relativistic beam should be in a near co-rotation with the star, which implies that the charge density difference in the beam should largely exceed the GJ-value. As far as we know, this point has never been emphasized in the context of relativistic particle beams streaming away from pulsar polar caps, although the fact of strong sub-rotation of the charge-separated beam with the star was noticed long ago by [17].

What New Studies Are Needed?

In general the following points deserve attention:

- The existence of carousels has still to be confirmed or refuted for a substantial number of pulsars;
- An investigation on the excitation of global magnetospheric oscillations for an oblique, magnetized rotating neutron star;
- The relation between nulling and drifting sub-pulses is still unclear. Progress can be expected from high-sensitivity single pulse observations;
- The cause for mode-switching remains unclear. Both theoretical ideas and further detailed observations are needed.

In the context of the diocotron instability, the following studies are needed:

- For more than one cone, the number of discontinuities to match becomes more than two. This results in a higher-order polynomial equation, instead of the quadratic equation, which is not accessible to analytical treatment but rather requires involvement of numerical methods.
- In the above analysis we have simplified the problem by assuming that the pulsar is aligned, $\boldsymbol{\Omega}||\mathbf{m}$. Since it now appears that the majority of pulsars does exhibit the drifting sub-pulse phenomenon, the diocotron instability should be examined in oblique rotators, where the equilibria become time-dependent. Clearly, future theoretical work is needed to extend the treatment of the instability to such cases.

- Also, the linear stage should be followed into the non-linear regime, including the formation of vortices.
- The radio emission from pulsars presents more puzzles than the drifting sub-pulse phenomenon, the major one being the mechanism of radio emission itself. Mahajan et al. [29] have suggested that the diocotron instability can couple non-escaping longitudinal Langmuir waves to escaping electromagnetic waves. The precise influence of the diocotron instability on radio emission has not been investigated and is of course an important point for future work.

References

1. A.M. Abrahams, S.L. Shapiro: ApJ, **374**, 652 (1991).
2. J. Arons: ApJ, **266**, 215 (1983).
3. J. Arons, D.F. Smith: ApJ, **229**, 728 (1979).
4. A. Asgekar, A. Deshpande: MNRAS, **326**, 1249 (2001).
5. E. Asteo, D. Khechinashvili: MNRAS, **334**, 743 (2002).
6. V.S. Beskin, E.E. Nokhrina: Astron. Lett., **30**, 685 (2004)
7. J.D. Biggs, P.M. McCulloch, P.A. Hamilton, R.N. Manchester, A.G. Lyne: MNRAS, **215**, 281 (1985).
8. J.C. Clemens, R. Rosen: ApJ, **609**, 340 (2004).
9. R.C. Davidson: *Theory of Nonneutral Plasmas*, W.A. Benjamin, Reading, MA (1974).
10. R.C. Davidson, H. Chan, C. Chen, S. Lund: Rev. Mod. Phys., **63**, 341 (1991).
11. A.A. Deshpande, J.M. Rankin: ApJ, **524**, 1008 (1999).
12. A.A. Deshpande, J.M. Rankin: MNRAS, **322**, 438 (2001).
13. A.J. Deutsch: Annales d'Astrophysique, **18**, 1 (1955).
14. C.F. Driscoll, K.S. Fine: Phys. Fluids B, **2**, 1359 (1990).
15. J.M. Durdin, M.I. Large, A.G. Little, et al.: MNRAS, **186**, 39P (1979).
16. A. Esamdin, A.G. Lyne, F. Graham-Smith, et al.: MNRAS, **356**, 59 (2005).
17. W.M. Fawley, J. Arons, E.T. Scharlemann: ApJ, **217**, 227 (1977).
18. P. K. Fung, D. Khechinashvili, J. Kuijpers: A&A, **445**, 779 (2006).
19. J.A. Gil, G.I. Melikidze, U. Geppert: A&A, **407**, 315 (2003).
20. J.A. Gil, G.I. Melikidze, D. Mitra: A&A, **388**, 235 (2002).
21. J.A. Gil, G.I. Melikidze, D. Mitra: A&A, **388**, 246 (2002).
22. G. Gogoberidze, G.Z. Machabeli, D. Melrose, Q. Luo: MNRAS, **360**, 669 (2005).
23. P. Goldreich, W.H. Julian: ApJ, **157**, 869 (1969).
24. Y. Gupta, J. Gil, J. Kijak, M. Sendyk: A&A, **426**, 229 (2004).
25. A. Hasegawa: *Plasma instabilities and nonlinear effects, Physics and Chemistry in Space*, Springer, Berlin (1975).
26. A.Z. Kazbegi, G.Z. Machabeli, G.I. Melikidze: Aust. J. Phys., **44**, 573 (1991).
27. J. Kuijpers: Physics of Flares in Stars and Accretion Disks, in *T*he Sun: A Laboratory for Astrophysics, eds. J.T. Schmelz & J.C. Brown, NATO ASI Series C, vol. 373, p. 535 (Reidel: Dordrecht, 1992).
28. W. Kundt, Pulsar Astronomy - 2000 and Beyond, ASP Conference Series, **202**, 597 (2000)
29. S.M. Mahajan, G.Z. Machabeli, A.D. Rogava: ApJ, **479**, L129 (1997).
30. R.N. Manchester, A.G. Lyne, J.H. Taylor, et al.: MNRAS, **185**, 409 (1978).
31. L. Mestel, J.A. Robertson, Y.-M. Wang, K.C. Westfold: MNRAS, **217**, 443 (1985).
32. A.G. Muslimov, A.I. Tsygan: MNRAS, **255**, 61 (1992).
33. D. Neuhauser, S.E. Koonin, K. Langanke: Phys. Rev. A., **36**, 4163 (1987).
34. D. Neuhauser, K. Langanke, S.E. Koonin: Phys. Rev. A., **33**, 2084 (1986).

35. J.M. Rankin: ApJ, **405**, 285 (1993).
36. A.G.J. van Leeuwen, B.W. Stappers, R. Ramachandran, J.M. Rankin: A&A, **399**, 223.
37. F. Reyes, J. Aparici, F. Olmos: A&A, **301**, 182 (1995).
38. G. Rosenthal, G. Dimonte, A.Y. Wong: Phys. Fluids, **30**, 3257 (1987).
39. M.A. Ruderman, P.G. Sutherland: ApJ, **196**, 51 (1975).
40. Yu. A. Rylov: A&SS, **53**, 377 (1978).
41. D.H. Staelin, M.S. Ewing, R.M. Price, J.M. Sutton: ApJ, **160**, L7 (1970).
42. M.D.T. Young: A resonant-mode model for pulsar emission. In *Young Neutron Stars and Their Environments,* IAU Symp., Vol. 218, ed. by F. Camilo & B.M. Gaensler (2004).
43. P. Weltevrede, R. Edwards, B.W. Stappers: A&A, **445**, 243 (2006).
44. G.A. Wright: MNRAS, **344**, 1041 (2003).

Chapter 21
Soft Gamma-Ray Repeaters and Magnetars

Kevin Hurley

21.1 Introduction

The history and observational properties of the soft gamma repeaters are reviewed in this Chapter. Over the past decades, we have gone from viewing these objects as a special class of cosmic gamma-ray burst, to seeing them as one manifestation of magnetars. There is now a solid body of multiwavelength observations, as well as some more controversial properties. There are still a number of fundamental unanswered questions, which will require better theory, more sensitive observations, and many years to answer. The story of the soft gamma repeaters (SGRs) begins in 1979. On January 7th, a short duration, soft spectrum burst was observed from the direction of the Galactic center [28]. At that time, relatively little was known about cosmic gamma-ray bursts (GRBs), but their energy spectra, as observed up to that point, were clearly "hard," containing photons up to hundreds of keV and beyond. On the other hand, it was clear that the spectrum of the January 7 event was much softer than that of a GRB, i.e., with little emission beyond 100 keV. The event was called "a gamma-ray burst without the gamma-rays." Several months later, the most intense gamma-ray transient which had been observed up to that time, the March 5, 1979 burst, was detected. This event had a hard spectrum and a long duration, with a pulsating tail, and it was localized to the N49 supernova remnant in the Large Magellanic Cloud [3,7]. At the distance of the LMC, the intensity of this burst was $>10^3$ times the Eddington luminosity. And in the days that followed, smaller bursts were detected from the source [31]. Many theories were proposed to explain this event, which was generally thought to be an unusual GRB. Several weeks later, another repeating source was discovered when it emitted three short duration, soft spectrum bursts in 3 days [32]. Finally, between July and December 1987, yet another repeater was discovered [2]. This object turned out to be the same as the one which

K. Hurley
U.C. Berkeley Space Sciences Laboratory, 7 Gauss Way, Berkeley, CA 94720-7450, USA
e-mail: khurley@ssl.berkeley.edu

W. Becker (ed.), *Neutron Stars and Pulsars,* Astrophysics and Space Science Library 357,

had been detected on January 7, 1979. The source was named SGR1806-20, with SGR standing both for the constellation (Sagittarius) and for Soft Gamma Repeater, to distinguish it from the GRBs.

On the theoretical side, two papers appeared independently in 1992 which considered the role of strong magnetic fields in explaining GRBs in general, and the March 5, 1979 event in particular [5, 39]. These papers lay the groundwork for the 1995 paper which explained the SGRs as strongly magnetized neutron stars [43]. The word "magnetar" was used in it to describe these neutron stars for the first time. In these papers, one can find many roles that the magnetic field plays in explaining the SGR phenomenon, but two important ones are the following:

- It provides a robust magnetosphere that confines the hot $e^- e^+$ pair plasma required to produce the intense peak of the March 5, 1979 burst
- It suppresses the Compton scattering of outgoing radiation from the neutron star so that it can greatly exceed the Eddington limit, without invoking beaming

The definition of a magnetar is a neutron star in which the magnetic field, rather than rotation, provides the main source of free energy; the decaying field powers the electromagnetic radiation [5, 43, 44]. Note that the definition does not specify any particular field strength, but rather, is based on an energy balance argument. Today we know of several possible manifestations of magnetars, and soft gamma repeaters are one. With magnetic field strengths $B \sim 10^{15}$ Gauss, magnetars indeed have the strongest cosmic magnetic fields that we know of in the Universe. But we also know of neutron stars with strong magnetic fields that are rotation-powered, and clearly do not fit the magnetar description (e.g. [34]).

21.2 The Basic Facts

Although there are still many things that are not well understood about magnetars, there are a few basic, observational facts that are not controversial, and require little or no interpretation.

- The SGRs are sources of short ($\sim$100 ms), repeating bursts of soft γ-radiation ($<$100 keV) (Figs. 21.1 and 21.2). Figure 21.1 shows a series of bursts from SGR1900+14. When an SGR is active, it can go through periods where hundreds of bursts are emitted in a period of minutes. Active periods occur at apparently random intervals; outside of these periods, it is common for SGRs to emit no detectable bursts at all for years.
- Four SGRs are known. Three are in our galaxy (SGR1806-20, 1900+14, 1627-41), and one is in the direction of the Large Magellanic Cloud (SGR0525-66, the source of the March 5, 1979 burst). Their general locations are shown in Fig. 21.3. The fact that three are in the Galactic plane, while one is in a young SNR, indicates that all the SGRs are probably young objects (perhaps $<$10,000 years old).

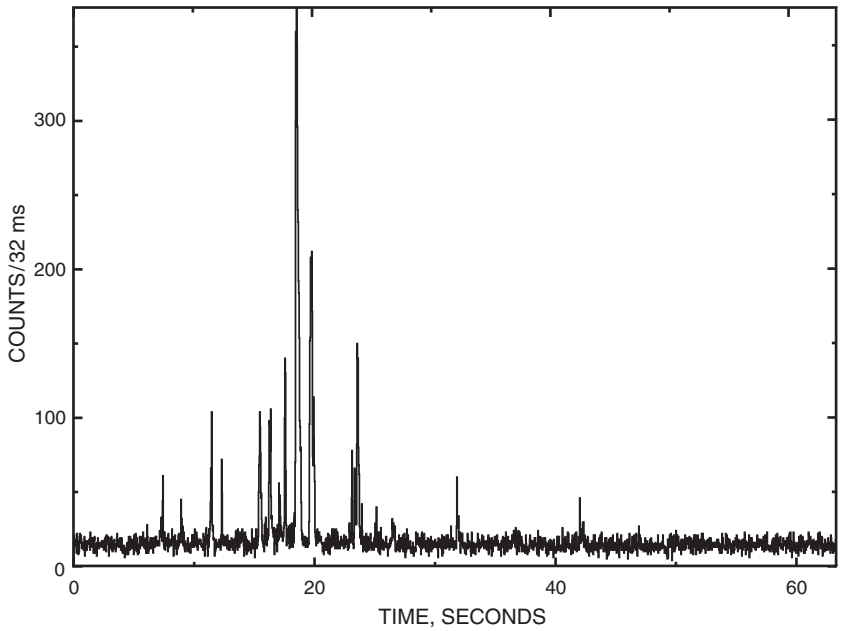

Fig. 21.1 Bursts from SGR1900+14 during a particularly active phase. The data are from the Ulysses GRB experiment, for May 30, 1998, in the 25–150 keV energy range. Active phases occur apparently at random, and no bursts are observed during quiescent phases, which can last for years

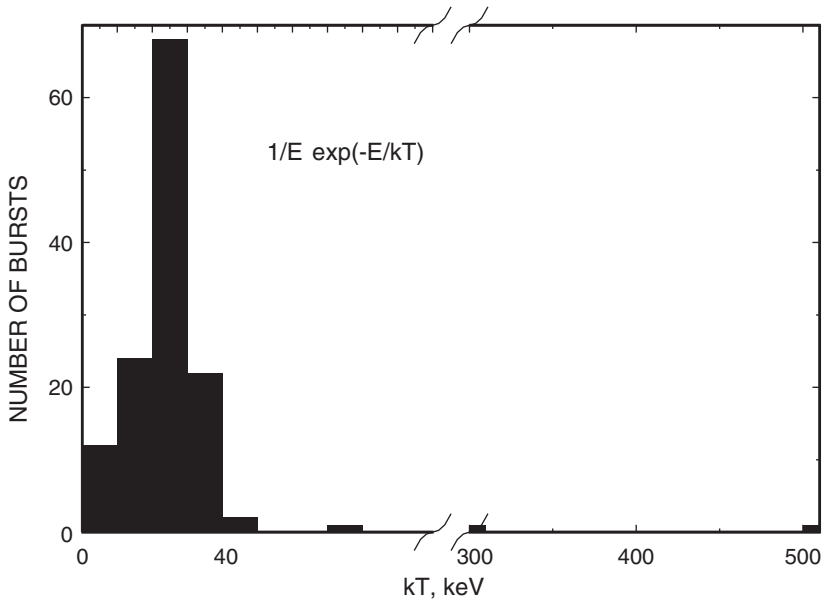

Fig. 21.2 Distribution of kT values for the energy spectra of the short bursts. The burst spectra have been fitted with a simple functional form, $E^{-1}\exp -E/kT$ (this is not to be interpreted as implying any particular emission mechanism – it is simply a convenient fitting function). The data were taken from [1]

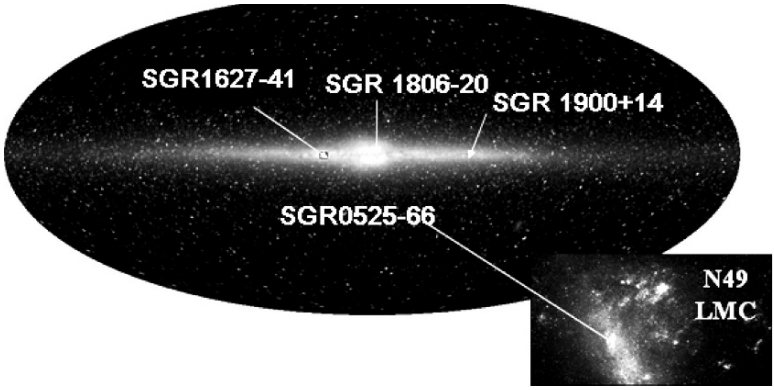

Fig. 21.3 The general locations of the four known soft gamma repeaters

- The SGRs are quiescent X-ray sources and have been imaged by most X-ray spacecraft since ROSAT. Although their luminosities are somewhat variable, they are generally strong sources ($\sim 10^{-11}\,\mathrm{erg\,cm^{-2}\,s^{-1}}$) which can easily be detected in soft X-rays, and in two cases, to energies up to 100 keV and above [14, 15]. While there is a connection between the X-ray luminosity and bursting activity, the quiescent X-ray emission is always present, even when there are no bursts.
- The SGRs have rotation periods in the 5–8 s range, which are increasing monotonically, although sometimes irregularly, with time, at rates $\sim 10^{-10}\mathrm{s\,s^{-1}}$. Figure 21.4 shows the X-ray pulse shape of SGR 1806-20. The X-ray luminosity ($\sim 2 \times 10^{35}\,\mathrm{erg\,s^{-1}}$) is much greater than the spin-down energy ($\sim 10^{33}\,\mathrm{erg\,s^{-1}}$), which leads to an estimate of the magnetic field if dipole radiation is assumed to be the cause of the spin-down, and the particle wind is negligible [26]. Also, under these conditions, the spin-down age $\mathrm{P}/2\dot{\mathrm{P}} \sim 1,500$ year, which is consistent with the idea that SGRs are young objects. SGR1627-41 may be an exception. Its periodicity is either undetectable, or its amplitude is time-variable [18, 45].
- The SGRs occasionally emit long duration, hard spectrum *giant-flares* , which produce the most intense cosmic gamma-ray fluxes ever measured at Earth. Three have been observed so far. The first was the March 5, 1979 event from SGR0525-66 [3, 7, 31]. The second was the August 27, 1998 event from SGR1900+14 [8, 17, 33]. The third was the December 27, 2004 burst from SGR1806-20, the most intense of the three [18, 35, 41]. Giant flares occur perhaps every 30 years on a given SGR (no SGR has yet been observed to emit two giant flares, so this number is based on the number of known SGRs, the number of years of more or less complete observations, and the three observed giant flares). These bursts are intense (up to $\sim 3 \times 10^{46}$ erg at the source, or $1\,\mathrm{erg\,cm^{-2}}$ at Earth), last $\sim$5 min, and have very hard energy spectra extending to MeV energies, at least. Their time histories are modulated with the neutron star periodicity. SGRs are not quiescent radio emitters [29], but giant flares create transient radio nebulae [9, 11], and even produce dramatic ionospheric disturbances [23]. Figure 21.5 shows two examples, and Fig. 21.6 compares the spectrum of a giant flare with that of a short burst.

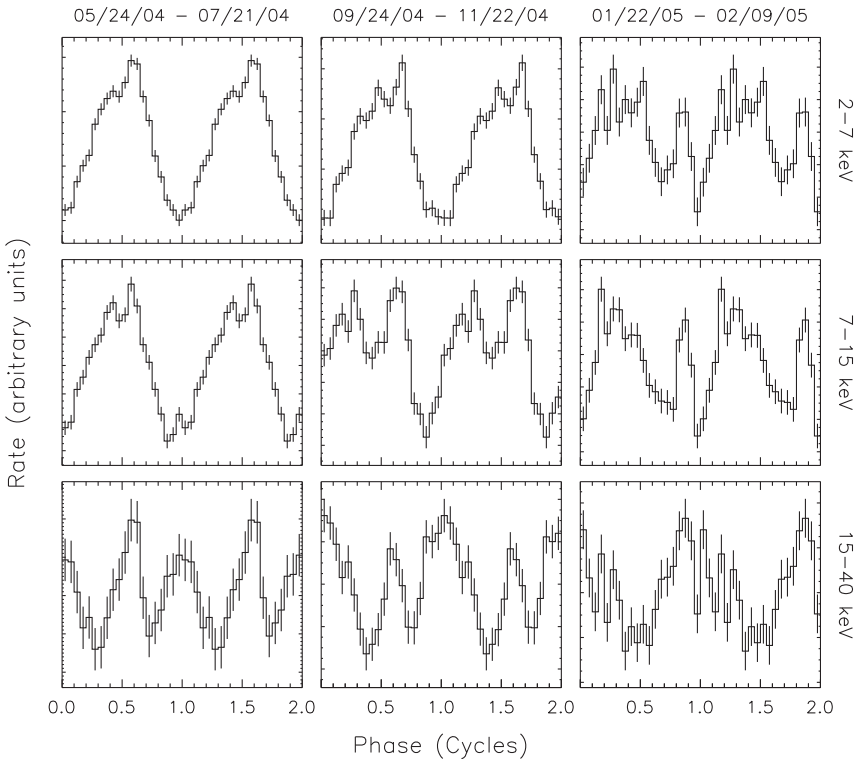

Fig. 21.4 X-ray pulse profiles of SGR 1806-20 as a function of energy, and of time before and after the giant flare of December 27, 2004, from [47]. Reproduced by permission of the AAS

21.3 The Less Certain Facts

There are a number of SGR properties whose interpretation is more complex, or less certain. The first involves burst statistics. The distributions of the short burst durations (Fig. 21.7) and the waiting time between two successive bursts have been studied by [12], who have shown that both are lognormal. (A variable x has a lognormal distribution if $\log_e(x)$ follows a Gaussian distribution). A cumulative number-intensity distribution (that is, the number of bursts N with a fluence greater than F, where F is in erg cm^{-2}) has been compiled recently using INTEGRAL–IBIS observations by [15], who has found that it follows a power law, $N \propto F^{-\alpha}$, where α is the power law index (cf. Fig. 21.8).

[12] have shown that lognormal duration and waiting time distributions, and the power law number-intensity distribution, are consistent with a system in a state of self-organized criticality. Very briefly, this is a system which evolves to a critical state due to some driving force. In this state, a slight perturbation can cause a chain reaction of almost any size. Here, the system is the neutron star crust, and it evolves to a critical state due to the force exerted by magnetic stress. The chain reaction is

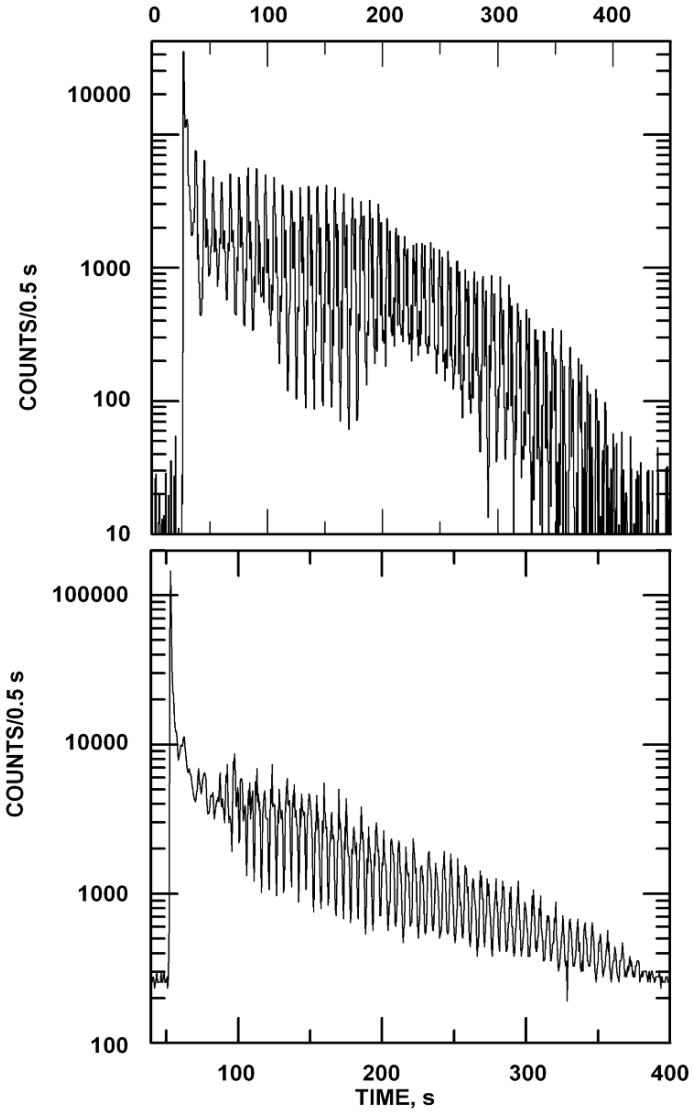

Fig. 21.5 Time histories of the giant flares from SGR1900+14 (bottom, Ulysses data) and SGR1806-20 (top, RHESSI data). The common features of giant flare time histories are (1) a fast rise ($<$1 ms) to maximum, (2) a $\sim$200 ms long intense peak, and (3) a several hundred second long tail which is modulated by the neutron star rotation period

a crust quake, and it leads to a short burst of arbitrary size (but not a giant flare). Palmer [40] has shown that this behavior is also consistent with a set of independent relaxation systems. In this picture, multiple, independent sites on the neutron star surface accumulate energy, and that energy is suddenly released seismically, producing short bursts.

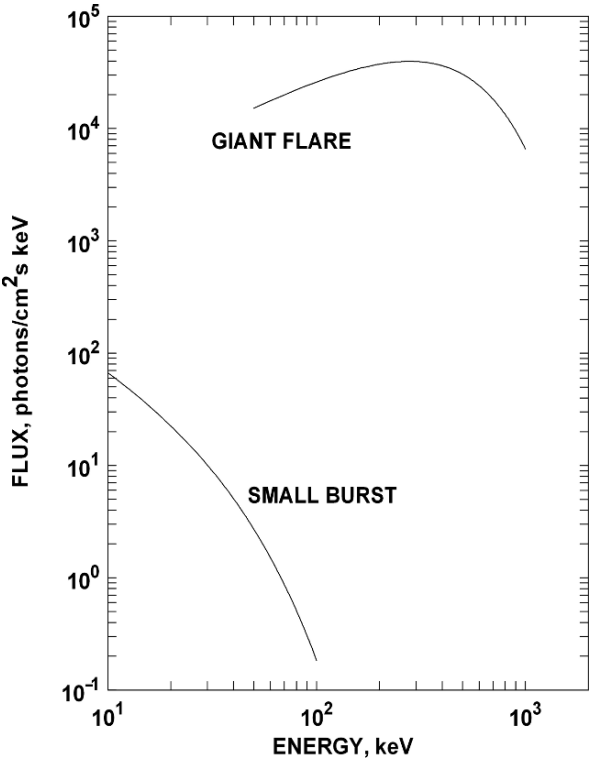

Fig. 21.6 Comparison of the typical energy spectra of a short SGR burst and a giant flare. The giant flare is not only more intense, but has a considerably harder energy spectrum during the intense peak. Emission up to ∼17 MeV has been observed

The second involves line features. The RXTE PCA spectra of ∼6 bursts from SGR1806-20 show evidence for one or more lines (at ∼5, 11, and 17 keV), which can be interpreted as cyclotron features [21, 22]. If these are assumed to be electron cyclotron features, a field strength $B \sim 6 \times 10^{11}$ G is inferred, but much greater line widths are expected due to thermal broadening. If proton cyclotron features are assumed instead, $B \sim 8 \times 10^{14}$ G is obtained, which is consistent with magnetar-strength fields. A 6.4 keV emission line has been observed in the spectrum of a burst from SGR1900+14, with a possible weaker line at 13 keV. The interpretation could be Fe fluorescence from material ablated from the neutron star surface, or again, cyclotron features [42]. Lines in the spectra of transient events, such as SGR bursts, are difficult to verify, so the interpretation of these observations remains open. Line features have not been detected in the quiescent X-ray spectra of SGRs [36].

The third is the relation between bursting and other activity. Woods et al. [46, 47] have shown that the spin-down, while monotonic, is variable, and that the variability is not related to bursting activity (cf. Fig. 21.9); for SGR1806-20 this includes both the short duration events and the giant flare. This is an argument against accretion

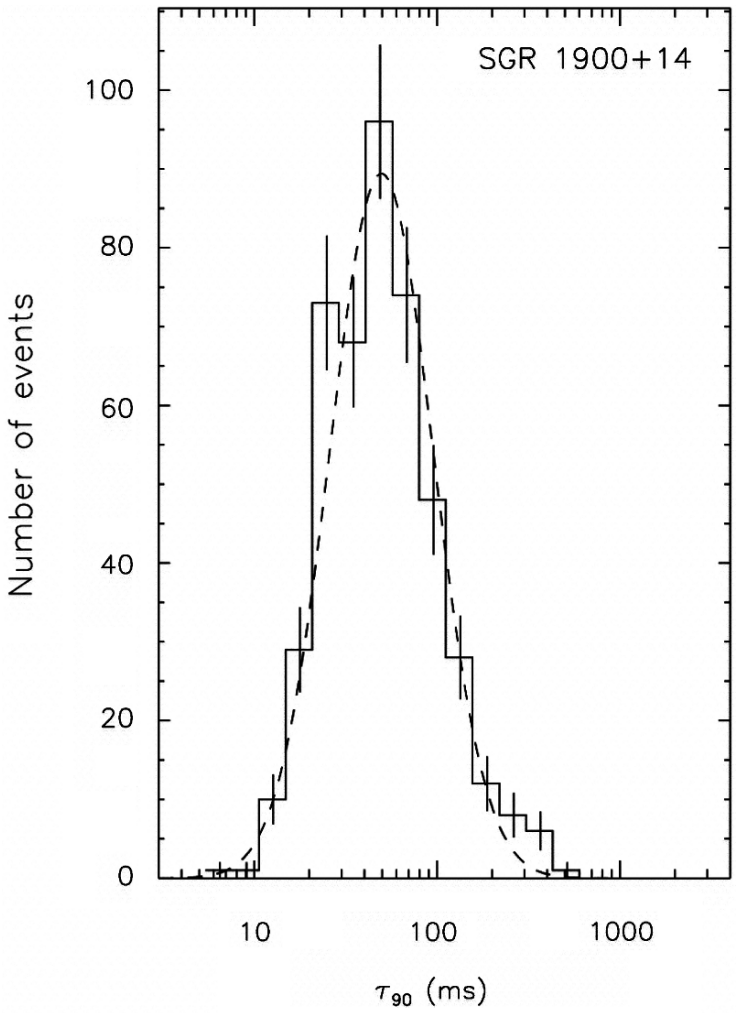

Fig. 21.7 Distribution of the durations of the short bursts from SGR1806-20 (solid line), and a log-normal fit (dashed line, from [12]. The bursts were observed by BATSE. Reproduced by permission of the AAS

as the cause of the bursts. On the other hand, bursting activity and the intensity of the quiescent emission are related (cf. Fig. 21.10). The relation between the two is probably a complex one, but a simple explanation is that both are related to magnetic stressing of the neutron star surface.

The fourth is the interpretation of the IR flux from SGR1806-20. In 2005, two groups succeeded in detecting the faint IR counterpart to this SGR in a very crowded field [24, 25]. The identification was based in large part on the IR variability, which was roughly correlated in time with the bursting activity and the quiescent flux

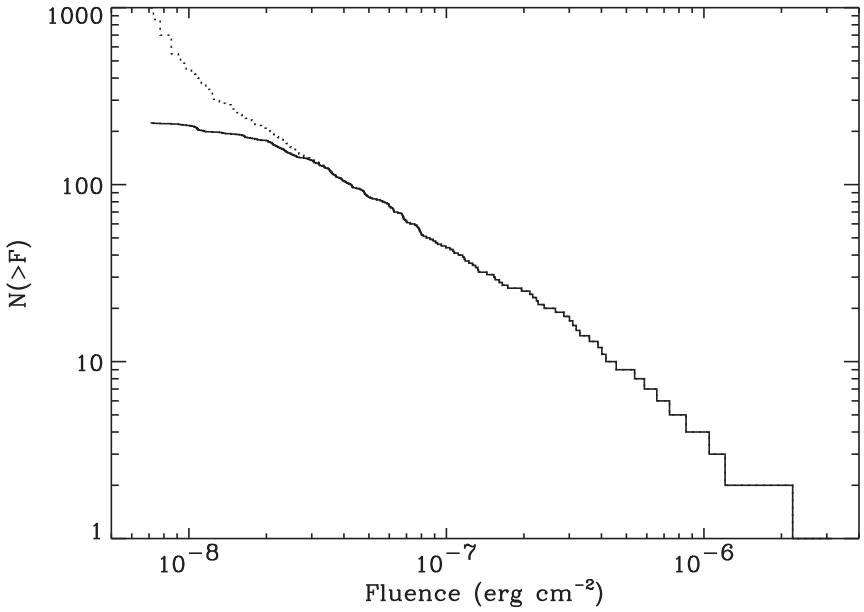

Fig. 21.8 The number-intensity relation for short duration bursts from SGR1806-20, from [14]. The bursts were observed by INTEGRAL–IBIS. The solid line represents the raw data; the dashed line is the result after correcting for efficiency

increase in 2004. However, [24] have pointed out that the IR flux is many orders of magnitude above the extrapolation of the X-ray spectrum. Thus the two probably have different origins, even though they vary in concert.

The fifth is the nature of three mystery objects, which may or may not be SGRs. SGR1801-23 was discovered by the interplanetary network when it emitted two short duration, soft spectrum bursts [4]. SGR1808-20 was discovered by the HETE spacecraft when it emitted one short duration, soft spectrum event [27]. GRB050925 was discovered by Swift; it too, has emitted just one short, soft event [16, 30]. (One should recall that SGR1806-20 was discovered when it emitted a single burst on January 7, 1979, so the lack of observed repetition to date for two of these objects is not a strong argument against an SGR origin.) All these objects lie in the Galactic plane, which is another argument in favor of an SGR interpretation. However, no quiescent X-ray source has been found for any of them, which would be unusual for an SGR.

The sixth is the relation of SGRs to supernova remnants (SNRs) and massive star clusters. While some SGRs appear to lie in or near SNRs, it can be argued that this is not unlikely based on chance superpositions [10]. Other SGRs appear to lie in massive star clusters [6], although the probability of chance alignments is harder to judge. In any case, the distances to the Galactic SGRs are generally uncertain by a factor of at least two.

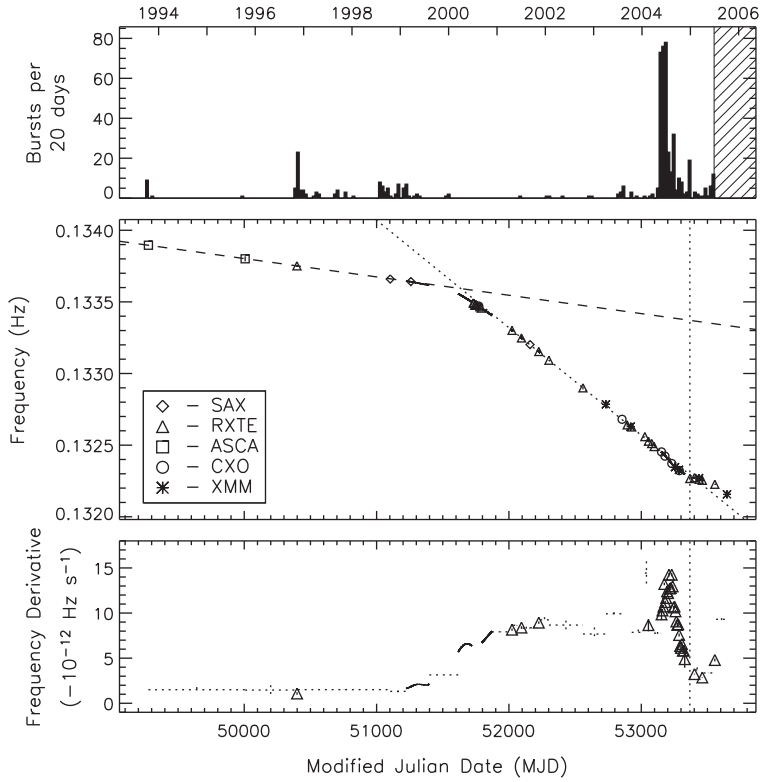

Fig. 21.9 Top panel: bursting activity of SGR1806-20 in 2004 and 2005 (from [47]). Middle panel: spin frequency as a function of time over the same period. The giant flare occurred at the end of 2004. Bottom panel: frequency derivative. Reproduced by permission of the AAS

21.4 Interpretation

Several interpretations of SGR phenomenology have been proposed. Here the magnetar model will be outlined, as it has been elaborated by [43, 44] and reviewed by [48].

In some rare supernova explosions, a neutron star is born with a fast rotation period ($\sim$ ms) and a dynamo is established which creates or amplifies a strong magnetic field. Differential rotation and magnetic braking quickly slow the period down to the observed 5–10 s range. Magnetic diffusion and dissipation heat the neutron star surface, which radiates X-rays. This X-radiation is always present, regardless of the bursting activity, so magnetars are quiescent X-ray sources. In addition, increased dissipation at the poles creates hot spots on the surface, and a periodic component whose amplitude is $\sim$10% of the total is superimposed. Thus magnetars are quiescent, periodic X-ray sources. The strong magnetic field ($\sim 10^{15}$G) stresses the iron surface of the neutron star, to which it is anchored. The surface, a crustal

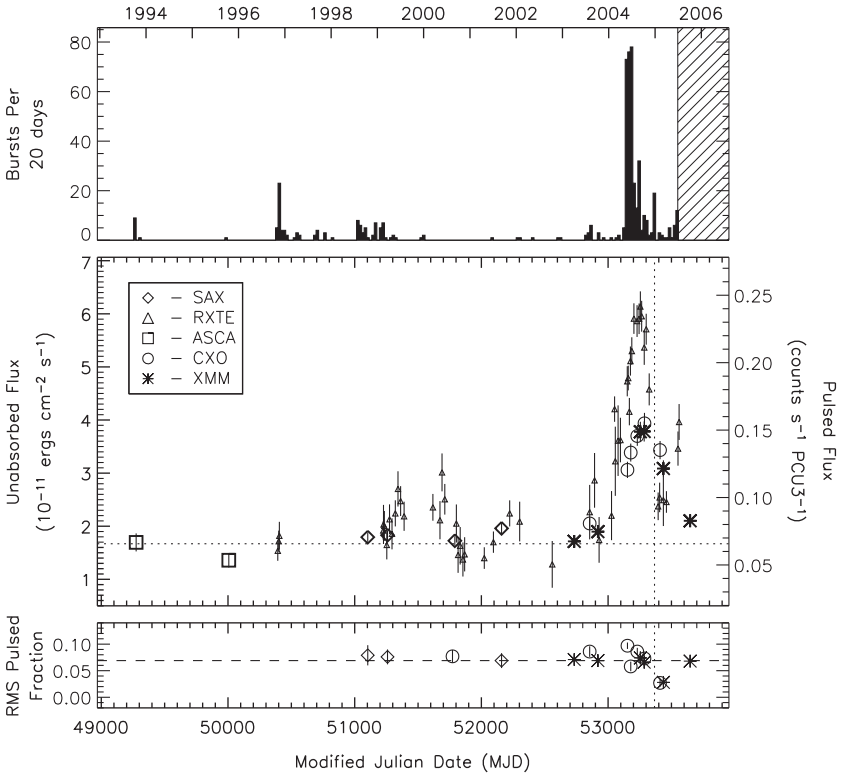

Fig. 21.10 Top panel: bursting activity of SGR1806-20 between 1993 and 2005 (from [47]). Middle panel: low energy X-ray flux, as measured by various spacecraft. The quiescent flux increases at the same time as the bursting activity in 2004. Bottom panel: pulsed fraction. Reproduced by permission of the AAS

lattice with a finite shear modulus, undergoes localized cracking, shaking the field lines and injecting energy into the magnetosphere. The resulting field line oscillations (Alfvèn waves) accelerate electrons to $\sim$100 keV; they radiate their energy in short bursts with energies around $10^{40}-10^{41}$ erg (in earthquake terms, this can be thought of as a magnitude 19.5 crust quake). These are the most common SGR bursts.

Localized cracking cannot relieve all the stress which the magnetic field exerts on the surface, and it continues to build for decades. The built-up stress eventually ruptures the surface of the star profoundly (a magnitude 23.2 star-quake), resulting in a giant flare. Magnetic field lines annihilate, accelerating electrons and positrons, and filling the magnetosphere with a hot pair plasma. The initial spike in the giant flare is radiation from the entire magnetosphere ($B > 10^{14}$ G is required to contain the pair plasma). The 5 min long, periodic component of the flare comes from hot spots on the surface of the neutron star.

Table 21.1 AXPs and SGRs compared

	SGRs	AXPs
Short duration bursts	Frequent	Rare, weaker
Giant flares	Yes	None observed
Quiescent X-ray emission	Yes	Yes
Periods	5.2–8 s	5.5–11.8 s
Spin-down	$6.1 - 20 \times 10^{-11}$ s s^{-1}	$0.05 - 10 \times 10^{-11}$ s s^{-1}
Hosts	Massive star clusters, SNRs?	SNRs?

21.5 Magnetar Manifestations

To date, we know of four definite SGRs, and three possible ones. The anomalous X-ray pulsars (AXPs, the subject of another paper in this volume) are also interpreted as magnetars, and seven of them have been identified, all in the Galaxy. Table 21.1 compares some of the essential properties of SGRs and AXPs. (For a recent review of SGR and AXP properties see [48]).

A third manifestations of SGRs might be some short duration cosmic gamma-ray bursts "in disguise" (that is, events which have been incorrectly classified as gamma-ray bursts). If an SGR giant flare were observed from a great distance, only the short duration, hard spectrum initial spike would be detectable. It would resemble a short duration GRB, and, based on the energetics of the giant flares observed so far, such a burst could be detected to a distance of perhaps 100 Mpc [19]. Evidence for an SGR origin would be a bright galaxy in the error box. Two such events have possibly been observed. The error box of GRB051103 includes part of M81 [13], and the error box of GRB070102 includes part of M31 [20]. Both cases are plausible, but not proven beyond a doubt. Thus, although it seems virtually certain that extragalactic SGRs must exist, none has been detected with certainty (apart from SGR0525-66 in the LMC). The percentage of short duration events which might be extragalactic giant magnetar flares is therefore uncertain, but estimates vary between 1 and 15% [37, 38].

21.6 Open Questions

Some of the outstanding questions about SGRs are the following:

- What are the distances of the Galactic magnetars? If this were known, the energetics of the bursts could be determined, and this would clarify the relation between giant flares and short GRBs.
- What is the number-intensity relation for giant magnetar flares? The answer to this question would also clarify the relation between giant flares and short GRBs.
- What is the SGR birth rate? If this were known, we would be able to better constrain the total number of SGRs in our galaxy, and their lifetimes.

- What kind of supernova produces an SGR? This may not matter much for understanding SGR activity, because it is probably independent of how the magnetar formed. But it is an essential open question in magnetar theory.
- What is the relation between SGRs and AXPs? Does one evolve into the other, or are they separate manifestations of magnetars? A related question is what the relation is between magnetars and the high magnetic field pulsars.
- How many other manifestations of magnetars are there waiting to be discovered?

The answers to these questions will come from three efforts. The first is more detailed theoretical modeling of magnetar formation and activity. The second is more sensitive detectors. Today the interplanetary network surveys the entire sky for magnetars, with a duty cycle close to 100%, but it only detects the more intense bursts. Swift and INTEGRAL–IBIS are extremely sensitive SGR detectors, but they view only a small fraction of the sky. Sensitivity should not be achieved by sacrificing field of view, because the entire sky needs to be surveyed for magnetar activity with greater sensitivity on a continuous basis. With these two elements in hand, one more thing will be required: about 30 years of data. This estimate comes from two facts. The first is that we have now been studying magnetars for about 30 years to arrive at our current state of knowledge. There are not many of them, and they are not active all the time. They yield their secrets very slowly. The second is that this is our best estimate of the time between giant bursts on a single SGR.

Anyone interested in getting started in this field should view these as a homework assignment, due when we meet to celebrate the 70th birthday of neutron stars in 2036.

21.7 Acknowledgments

This research has made use of data obtained from the High Energy Astrophysics Science Archive Research Center (HEASARC), provided by NASA's Goddard Space Flight Center.

References

1. Aptekar, R., Frederiks, D., Golenetskii, S., et al., ApJ (Suppl Ser), **137**, 227, 2001
2. Atteia, J.-L., Boer, M., Hurley, K., et al., ApJ, **320**, L105, 1987
3. Cline, T., Desai, U., Pizzichini, G., et al., ApJ, **237**, L1, 1980
4. Cline, T., Frederiks, D., Golenetskii, S., et al., ApJ, **531**, 407, 2000
5. Duncan, R., and Thompson, C., ApJ, **392**, L9, 1992
6. Eikenberry, S., Matthews, K., La Vine, et al., ApJ, **616**, 506, 2004
7. Evans, W.D., Klebesadel, R.W., Laros, J.G., et al., ApJ, **237**, L7, 1980
8. Feroci, M., Frontera, F., Costa, E., et al., ApJ, **515**, L9, 1999
9. Frail, D., Kulkarni, S., and Bloom, J., Nature, **398**, 127, 1999
10. Gaensler, B., Slane, P., Gotthelf, E., et al., ApJ, **559**, 963, 2001

11. Gaensler, B., Kouveliotou, C., Gelfand, et al., Nature, **434**, 1104, 2005
12. Göğüş, E., Kouveliotou, C., Woods, et al., ApJ, **558**, 228, 2001
13. Golenetskii, S. et al., GCN Circ, 4197, 2005
14. Götz, D., Mereghetti, S., Molkov, S., et al., A&A, **445**, 313, 2006
15. Götz, D., Mereghetti, S., Tiengo, A., et al., A&A, **449**, L31, 2006
16. Holland, S. et al., GCN Circ, 4034, 2005
17. Hurley, K., Cline, T., Mazets, et al., Nature, **397**, 41, 1999
18. Hurley, K., Strohmayer, T., Li, P., et al., ApJ, **528**, L21, 2000
19. Hurley, K., Boggs, S., Smith, D., et al., Nature, **434**, 1098, 2005
20. Hurley, K. et al., GCN Circ, 6103, 2007
21. Ibrahim, A., Safi-Harb, S., Swank, J., et al., ApJ, **574**, L51, 2002
22. Ibrahim, A., Swank, J., and Parke, W., ApJ, **584**, L17, 2003
23. Inan, U., Lehtinen, N., Lev-Tov, S., et al., G R L, **26(22)**, 3357, 1999
24. Israel, G., Covino, S., Mignani, R., et al., A&A, **438**, L1, 2005
25. Kosugi, G., Ogasawara, R., and Terada, H., ApJ, **623**, L125, 2005
26. Kouveliotou, C., Dieters, S., Strohmayer, T., et al., Nature, **393**, 235, 1998
27. Lamb, D. et al., GCN Circ, 2351, 2003
28. Laros, J., Fenimore, E., Fikani, M., et al., Nature, **322**, 152, 1986
29. Lorimer, D., and Xilouris, K., ApJ, **545**, 385, 2000
30. Markwardt, C. et al., GCN Circ, 4037, 2005
31. Mazets, E., Golenetskii, S., and Il Inskii, V., Nature, **282**, 587, 1979
32. Mazets, E., Golenetskii, S., and Guryan, Yu., Sov Astron Lett, **5(6)**, 343, 1979
33. Mazets, E., Cline, T., and Aptekar, R., Astron Lett, **25(10)**, 635, 1999
34. McLaughlin, M., Stairs, I., and Kaspi, V., ApJ, **591**, L135, 2003
35. Mereghetti, S., Götz, D., von Kienlin, A., et al., ApJ, **624**, L105, 2005
36. Molkov, S., Hurley, K., Sunyaev, R., et al., A&A, **433**, L13, 2005
37. Nakar, E., Gal-Yam, A., Piran, T., et al., ApJ, **640**, 849, 2006
38. Ofek, E., ApJ, **659**, 339, 2007
39. Paczyński, B., Acta Astron, **42**, 145, 1992
40. Palmer, D., ApJ, **512**, L113, 1999
41. Palmer, D., Barthelmy, S., Gehrels, N., et al., Nature **434**, 1107, 2005
42. Strohmayer, T., and Ibrahim, A., ApJ, **537**, L111, 2000
43. Thompson, C., and Duncan, R., MNRAS, **275**, 255, 1995
44. Thompson, C., and Duncan, R., ApJ, **473**, 322, 1996
45. Woods, P., Kouveliotou, C., and van Paradijs, J., ApJ, **519**, L139, 1999
46. Woods, P., Kouveliotou, C., and Göğüş, E., ApJ, **576**, 381, 2002
47. Woods, P., Kouveliotou, and C., Finger, M., ApJ, **654**, 470, 2007
48. Woods, P., and Thompson, C., in: *Compact Stellar X-Ray Sources*, ed by W. Lewin and M. van der Klis (Cambridge University Press, Cambridge, 2006), pp. 547

Chapter 22
X-Ray Polarimetry and Its Potential Use for Understanding Neutron Stars

Martin C. Weisskopf, Ronald F. Elsner, Victoria M. Kaspi, Stephen L. O'Dell, George, G. Pavlov, and Brain D. Ramsey

22.1 Introduction

In this Chapter we discuss the history and the potential scientific impact of X-ray polarimetry for the study of neutron stars. Despite major progress in X-ray imaging, spectroscopy, and timing, there have been only modest attempts at X-ray polarimetry. Indeed, the last such dedicated experiment, conducted by one of us over three decades ago, had such limited observing time and sensitivity that even $\sim 10\%^{\circ}$ of polarization would not have been detected from some of the brightest X-ray sources in the sky, and statistically significant X-ray polarization was detected in only one of the brightest celestial X-ray sources, the Crab Nebula. Radio and optical astronomers use polarimetry extensively to probe the radiation physics and the geometry of sources. Sensitive X-ray polarimetry promises to reveal unique and crucial information about physical processes and structure of neutron stars (and indeed all classes of X-ray sources). X-ray polarimetry remains the last undeveloped tool for the X-ray study of astronomical objects and needs to be properly exploited.

M.C. Weisskopf, R.F. Elsner, S.L. O'Dell, and B.D. Ramsey
NASA Marshall Space Flight Center, VP62, Huntsville, AL 35812, USA
e-mail: martin@smoker.msfc.nasa.gov

D. Hanna and V.M. Kaspi
McGill University Physics Department, Rutherford Physics Building, 3600 University St., Montreal, QC, Canada, H3A 2T8

G.G. Pavlov
Penn State University, Department of Astronomy and Astrophysics, 525 Davey Laboratory, University Park, PA 16802, USA

W. Becker (ed.), *Neutron Stars and Pulsars,* Astrophysics and Space Science Library 357,

22.2 Background

Only a few experiments have conducted successful X-ray polarimetric observations of cosmic sources. In rocket observations (Fig. 22.1), the X-ray polarization from the Crab Nebula was measured [55]. Using the X-ray polarimeter on the Orbiting Solar Observatory (OSO)-8, Weisskopf et al. [87] confirmed this result with a 19-σ

Fig. 22.1 1971 Photograph of the NASA Aerobee-350 sounding rocket No. 1709 that first detected polarization from the Crab Nebula. Left to right are R. Novick, G. Epstein, M.C. Weisskopf, R. Wolff, and R. Linke

detection ($P = 19.2\% \pm 1.0\%$), thus conclusively proving the synchrotron origin of the X-ray emission from this plerionic supernova remnant. Unfortunately, because of low sensitivity of those experiments, only upper limits were found for polarization from other X-ray sources (e.g., 13.5% and 60% for accreting X-ray pulsars Cen X-3 and Her X-1, respectively [74]). Since that time, although there have been several missions that have included X-ray polarimeters such as the original *Einstein* Observatory, and Spectrum-X, no X-ray polarimeter has actually managed to be launched. The *Einstein* mission was descoped and the polarimeter removed, and the Spectrum-X was cancelled. We discuss this point in more detail in Sect. 22.5.

22.3 Scientific Basis for Neutron Star X-Ray Polarimetry

22.3.1 Radio Pulsars

Radio pulsars are isolated, rotation-powered, neutron stars converting rotational energy to the energy of ultra-relativistic particles and radiation through electromagnetic coupling. Strong electric fields and pair production in the very strong (up to a few $\times 10^{13}$ G) magnetic field result in beamed outflow of relativistic particles and radiation and consequent "search-light" (sweeping beam) pulses. Theoretical models predict strong linear polarization varying with pulse phase due to the rotation of the neutron star. However, details of the emission, as discussed, e.g., in numerous papers presented in this Seminar, and even its location ("polar cap" versus "outer gap") remain unclear. X-ray polarimetry could provide decisive information to test detailed models, to determine the emission site, and quite possibly to verify, observationally, the phenomenon of vacuum birefringence as predicted by quantum electrodynamics (QED).

The origin of the high-energy non-thermal pulsar radiation is still a matter of debate. Controversy remains over the site of this emission: directly above the polar cap, where the coherent radio pulses originate [20, 32], or in the outer magnetosphere [13, 14, 65]. Polarization measurements would discriminate among beaming geometries (e.g., "polar-cap" vs. "outer-gap" models).

The requirements on X-ray polarimetry may be estimated by examining the optical polarimetry of the Crab pulsar [66, 76], which shows (Fig. 22.2) high linear polarization, varying rapidly through each pulse component. Because the field line projection determines the polarization position angle, we expect a close, but not necessarily identical, correspondence between the optical and X-ray sweep of the position angle. Previous X-ray polarimetry of the Crab, limited to a single energy (2.6 keV) could place only upper limits of 20–30% on the pulsar's polarization in wide phase bins [73]. What is needed are much more sensitive measurements capable of providing, at a minimum, data over a large number of pulse phase bins that are small enough to resolve different features of the pulse profile.

The pulsar's X-ray emission is almost certainly synchrotron radiation. If, however, as has been proposed [77], the optical emission were curvature radiation, the

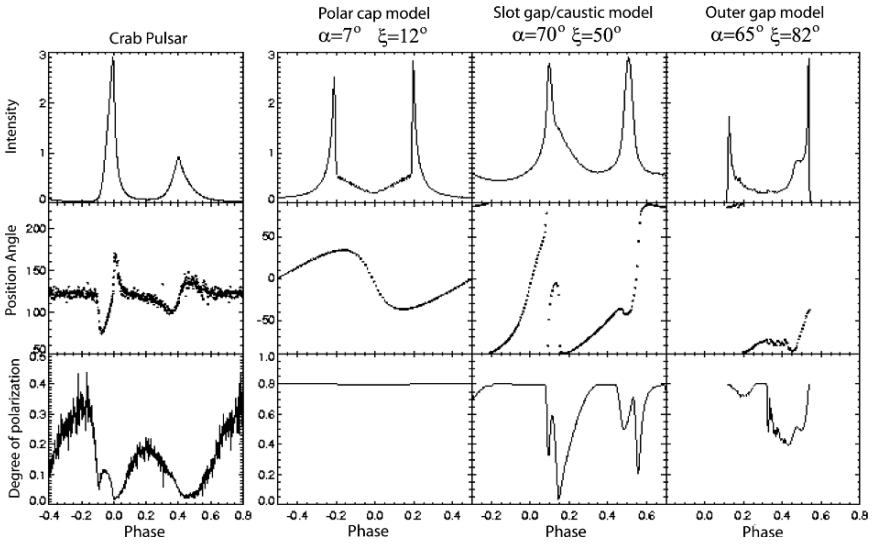

Fig. 22.2 Crab pulsar optical light curve, position angle, and degree of polarization as a function of pulse phase (from [40]). Data are compared to three different predictions of theoretical models (Courtesy A. Harding)

X-ray polarization would be orthogonal to the optical polarization (Fig. 22.2). If, instead, the remarkably flat optical spectrum were a low-pitch-angle extension of the X-ray synchrotron population [19], the larger X-ray pitch angle would smooth the position-angle sweep (the variation of the position-angle as a function of pulse phase). Thus, the X-ray-polarization profile (polarization amplitude and position angle as a function of pulse phase) would be a sensitive probe of the magnetospheric particle distribution over pitch-angles.

Polarimetry also offers an interesting opportunity to observe an exotic QED effect – vacuum birefringence – induced by a strong magnetic field. Predicted nearly 70 years ago [23, 33, 85], the effect is yet to be verified observationally. The effect follows from the result [80] that the indices of refraction for radiation polarized parallel ($n_\parallel$) and perpendicular ($n_\perp$) to the plane formed by the direction of propagation and the magnetic field are different and depend on the field strength:

$$n_\parallel \approx 1 + \frac{\alpha}{4\pi}\sin^2\theta\left[\frac{14}{45}\left(\frac{B}{B_{\rm cr}}\right)^2 - \frac{13}{315}\left(\frac{B}{B_{\rm cr}}\right)^4\right] \tag{22.1}$$

$$n_\perp \approx 1 + \frac{\alpha}{4\pi}\sin^2\theta\left[\frac{8}{45}\left(\frac{B}{B_{\rm cr}}\right)^2 - \frac{379}{5040}\left(\frac{B}{B_{\rm cr}}\right)^4\right] \tag{22.2}$$

for photon energies below the one-photon pair production threshold and magnetic fields much lower than $B_{\rm cr} = m^2c^3/e\hbar \approx 4.4\times10^{13}$ G (here α is the fine structure constant and θ is the angle between the direction of propagation of the photons and

the magnetic field). Thus, for a field of 3×10^{12} G, we have $n_{\|} - n_{\perp} \sim 4 \times 10^{-7}$ for propagation transverse to the field lines. At 1 keV, the path length for one wave retardation is only a few mm.

Pavlov, Mészáros, and co-workers investigated the influence of vacuum birefringence on X radiation from neutron stars (see [47, 58] for reviews). To accurately locate the X-ray-emitting site and infer its properties, vacuum birefringence effects on radiation propagating in a nonuniform magnetic field must be taken into account. For instance, if the emission site is near the neutron-star surface (as in polar-cap models), the vacuum birefringence leads to an energy dependence of the polarization direction at a particular rotation phase [35]. This results in a $\sim 10^{\circ}$ phase shift between the optical and X-ray polarization swings, with the X-ray sweep leading. The measurement of such a phase shift would not only locate the emission site, but it would also represent a direct observational manifestation of vacuum birefringence.

22.3.2 Magnetars

Soft Gamma-ray Repeaters (SGRs) and Anomalous X-ray Pulsars (AXPs) are presumably isolated, magnetic-powered neutron stars, converting magnetic energy ultimately into high-energy radiation. SGRs and AXPs are likely to be magnetars, i.e., neutron stars with extremely strong (10^{14-15} G) magnetic fields. Magnetically coupled seismic activity possibly results in high-energy radiation and plasma outflows, occasionally in extremely luminous (up to 10^{47} erg s^{-1}) giant flares of SGRs. Radiation emitted in such superstrong magnetic fields is inevitably highly polarized (e.g., [54] and references therein). X-ray polarimetry can provide important data for understanding the nature of magnetars and for studying physical processes in extreme magnetic fields.

In the widely accepted magnetar model [22], the neutron star's strong magnetic field powers persistent emission through low-level seismic activity and heating of the stellar interior; it powers the burst emission through large-scale crust fracture [81, 82]. However, there is no generally accepted detailed model for the SGR emission, particularly in the active (burst) phase ([45], and references therein), with peak soft-X-ray luminosities between 10^{38} and 10^{44} erg s^{-1} [36]. Sources such as SGR 1806–20 may have even brighter soft components during giant flares. The persistent radiation of magnetars is relatively faint in soft X-rays ($L_x \sim 10^{34-35}$ erg s^{-1} in the *Chandra-XMM-Newton* band). However, recent observations with *INTEGRAL* and *RXTE* have revealed hard-X-ray tails in the magnetar spectra [30, 43], with 20–100 keV luminosities up to $\sim 10^{36}$ erg s^{-1}, which makes this range promising for polarization observations. If an SGR becomes active, the polarization will be amenable to measurement. Giant flares are too rare and brief to easily observe and might saturate many instruments. Still one can expect to observe an SGR during an active period when it produces numerous short (1-s) bursts with a flux-dependent event frequency – $dN/dS \propto S^{-5/3}$ [28]. For activity such as SGR 1900+14 exhibited in 1998 August or in 2001 April, there would be about 30 short bursts, with

burst fluence 10^{-7}–10^{-5} erg cm^{-2} (25–100 keV band) in a time interval of 100 ks. It is not inconceivable to be able to detect polarization from the total fluence under these conditions.

22.3.3 XDINSs and CCOs

X-ray "dim" (although they are anything but dim in the soft X-ray range but are dim radio and optical sources) isolated neutron stars (XDINSs) are radio-quiet and non-accreting, exhibiting predominately thermal emission ($kT \approx 50$–100 eV) from the neutron-star surface. Periods in the range of 3–12 s have been measured for six of the seven currently known XDINSs (see Chap. 6 and [79]), and for two of them period derivatives have been also measured, which allows one to estimate the dipole components of magnetic field, $B = 2.4$ and 3.4×10^{13} G [41, 42], which are almost as strong as the magnetic fields of magnetars. Although the spectrum of the brightest XDINS, RX J1856.4−3754 (which also shows exceptionally weak pulsations, with a pulsed fraction of only 1.2%) is close to a perfect blackbody, most of these objects show puzzling absorption lines in their spectra, whose origin has not yet been understood (see Chap. 7 and [84]). Most likely, these lines are formed in Hydrogen or Helium atmospheres of the neutron stars, but the actual atomic transitions involved, and even the chemical composition of the atmospheres, remain to be understood. Since transitions between different types of atomic states (so-called tightly bound and hydrogen-like states) are sensitive to different (mutually orthogonal) polarizations, polarization measurements would be very helpful in understanding the type of the transitions involved, which, in turn, would establish the chemical composition and the strength and geometry of the magnetic field [57]. Moreover, even the continuum spectrum of neutron stars should be strongly polarized (typically, a few $\times 10\%$) because the atmospheric opacities are very different in different polarizations [61], and polarization degree and position angle show strong variations with pulsar rotation phase, depending on the geometry and strength of the magnetic field [60]. Therefore, using a soft-X-ray polarimeter, one has another tool to resolve the puzzle of XDINSs – the analysis of their polarization variations could establish the strength and geometry of their magnetic fields, help identify their spectral lines, and possibly explain the lack of spectral features in sources like RX J1856.4−3754. Finally, since the spectra and light curves of polarization of thermal radiation of neutron stars bear unique signatures of the vacuum polarization in a strong magnetic field ([83] and references therein), polarization observations of XDINSs could not only detect this effect but also use it for investigations of surface layers of neutron stars.

We also note that the same arguments are applicable to another class of radio-quiet neutron stars – the central compact objects (CCOs) in supernova remnants (see Chap. 6 and Pavlov et al. [63, 64] for a review). These objects also show thermal spectra, with temperatures in the range of 100–500 eV (hotter than XDINSs but somewhat colder than magnetars), and they show neither pulsar activity associated

with ultra-relativistic particles (e.g., pulsar-wind nebulae or γ-ray emission) nor magnetar behavior (e.g., bursts). Their nature is even less understood than that of magnetars and XDINSs. For instance, the CCO in the Cas A SNR, discovered in the first-light *Chandra* observations [78], shows a thermal-like spectrum emitted from a small fraction of the neutron star surface, similar to magnetars [62], but no pulsations [12]. A particularly interesting member of this class is 1E 1207.4−5209 in the PKS 1209−51/52 SNR, one of only two confirmed pulsators among the CCOs[1] [90], and the only CCO whose spectrum shows at least two absorption lines, at 0.7 and 1.4 keV [69]. The origin of the lines remains unknown. Sanwal et al. [69] have concluded that these lines cannot be associated with transitions in Hydrogen atoms at any value of the magnetic field and suggested that they could be due to absorption by once-ionized Helium in a magnetic field $B \sim 2 \times 10^{14}$ G. On the other hand, Bignami et al. [8] interpret the lines as electron cyclotron features in a magnetic field field of $\sim 10^{11}$ G, while Mori & Hailey [50] argue that the lines could be formed in an Oxygen atmosphere with $B \sim 10^{11-12}$ G. Whatever is the origin of the lines and the small, hot emitting areas in CCOs, only high magnetic fields could explain their properties because no isolated lines with such energies can be formed in the absence of a strong magnetic field [26]. This means that the CCO's radiation is inevitably strongly polarized, and, similar to XDINSs, polarization observations would be extremely useful for solving the puzzles of these unusual neutron stars.

22.3.4 Pulsating X-Ray Binaries

Pulsating X-ray binaries are accretion-fed neutron stars, converting kinetic energy of particle infall into X-ray emission at the stellar surface as the particles collide with the neutron star surface and heat it to X-ray temperatures. Rotation and accretion-flow anisotropy, induced by very strong magnetic fields (10^{12} to 10^{13} G), modulate the X rays. Most theoretical models (e.g., [47], and references therein) predict that the linear polarization of this X radiation is high and varies with pulse phase (due to rotation of the star) and also varies with energy (due to energy-dependent opacity, cyclotron resonance, and vacuum birefringence). X-ray polarimetry would provide crucial information to test detailed models, to infer parameters and geometries, and to verify vacuum birefringence observationally.

More than 50 binary X-ray sources in our Galaxy and the Magellanic Clouds exhibit pulses with periods from 69 ms to 23 min [9,51]. In about a dozen of pulsating binaries, absorption features between 10 and 100 keV have been observed ([16] and references therein). Interpreting these features as cyclotron absorption lines [27] implies very strong magnetic fields, $\sim 10^{12-13}$ G, strengths that we commonly associate with these objects. Under such conditions, X-ray emission, absorption, and scattering depend strongly on energy, direction, and polarization.

[1] The other one is CXOU J185238.6+004020 in the Kes 79 SNR [29, 71].

Detailed theoretical studies ([47, 49], and references therein) show that the linear polarization depends strongly upon the geometry of the emission region (accretion column), varies with energy and pulse phase, and reaches values as high as 60–70% for favorable orientations. Calculating the X-ray spectrum, pulse profile, and polarization from a high-temperature, strongly magnetized, rotating neutron star is complex. Further, the results depend strongly upon the assumed distribution of magnetic field, temperature, and density in the accretion column ([3, 48] and references therein). Nevertheless, theoretical modeling has now progressed to the point that X-ray polarization measurements can test models and infer parameters of the accreting matter and of the neutron star.

For example, phase-resolved polarimetry can distinguish between pencil and fan radiation patterns, corresponding to different emission-region geometries. Because the degree of linear polarization is maximum for emission perpendicular to the magnetic field, the flux and degree of polarization are in-phase for fan beams, but out-of-phase for pencil beams. Particularly interesting are those cases (e.g., Her X-1, GX1+4, and 4U1626−67) when pulse profiles change dramatically with energy, including pulse-maxima reversals between 1 and 20 keV [88]. Several authors [52, 53, 88] believe that such behavior requires both fan and pencil beam components, with each component dominating at different energies. Hence, polarimetry can differentiate among the semi-empirical models [11, 21, 37, 48] that qualitatively reproduce the pulse profiles but predict quite different phase dependences for the linear polarization.

Because the linear-polarization direction lies either parallel or perpendicular to the magnetic field (depending upon photon energy and absorption depth), the sweep of the polarization position angle with pulse phase specifies the magnetic-field geometry. For instance, abrupt position-angle changes would indicate a non-dipolar field [24]. If observed, these position-angle changes would support other evidence for such fields in some accreting pulsars [11], due perhaps to thermo-magnetic effects [10] or crustal breaking and migration of field-carrying platelets [67]. Such measurements require a polarimeter sensitive in the energy bands near the electron-cyclotron energy $E_{ec} = (11.6\,\mathrm{keV})(B/10^{12}\,\mathrm{G})$. Because the polarization dependence on energy is strongest near E_{ec}, one could establish which model is most reliable and obtain magnetic-field measurements for sources in which the cyclotron line is yet undetected.

As with radio pulsars (Sect. 22.3.1), X-ray polarimetry of pulsating X-ray binaries may detect effects of vacuum birefringence. Recent studies of neutron-star atmospheres [44] and magnetospheres [35] treat this phenomenon. The most vivid polarization signature is a 90° position-angle jump at an energy-dependent phase, occurring where normal-mode propagation through the so-called "vacuum resonance" [59] changes from adiabatic to non-adiabatic ([44, 58]). Detection of such a jump would provide a direct observation of this QED effect. Moreover, the jump's phase at a given energy depends on accretion-column inclination and density scale length in the radiating region, affording estimates of these quantities.

In the only X-ray polarimetry on pulsating X-ray binaries to date, Silver et al. [74] found 99%-confidence upper limits of 13.5% polarization for Cen X-3 and 60%

polarization for Her X-1, at 2.6 keV. In order to make significant progress one needs dramatic improvements in sensitivity whereby the polarization may be studied both as a function of energy and as a function of pulse phase.

22.3.5 Other Applications

We have concentrated on the role that X-ray polarization measurements can play in understanding the X-ray emission from neutron stars. It is worth emphasizing that X-ray polarimetry has far broader applications and would allow one to explore such systems as Galactic accretion-disks, Galactic superluminal sources, active galactic nuclei, etc.

Galactic accretion-disk systems involve accretion-powered neutron stars or black holes, converting kinetic energy into X-ray emission in the hot inner regions of the disk. While the X-ray polarization of radio pulsars, magnetars, and pulsating X-ray binaries is due to strong neutron-star magnetic fields, the polarization of accreting binaries with a low-field-neutron-star or black-hole primary will likely be dominated by scattering. Due to their complexity, accretion-disk systems as a group exhibit rich diversity: magnetodisks, winds, quasi-periodic oscillations, millisecond pulsations in spun-up pulsars, bursting, etc. X-ray polarimetry can probe the properties of the complex structure of accretion-disk systems, and explore the space-time structure close to a black hole. This latter is an especially interesting application of X-ray polarimetry.

Galactic superluminal sources (micro-quasars) and extragalactic sources such as AGNs (quasars, blazars, Seyfert galaxies, etc) are all disk-jet sources, converting kinetic energy of accreted material into X radiation and directed beams of relativistic plasma. Such sources are comprised of an interacting binary containing a black hole, stellar-mass size in the case of micro-quasars and supermassive for the others. X-ray polarimetry can provide important information on the X-ray emission mechanism and the site (disk, corona, or jet) of its origin.

22.4 Instrumental Approaches

There are a limited number of ways to measure linear polarization in the range 0.1–50 keV, sufficiently sensitive for astronomical sources. Before reviewing some of these, we emphasize that *meaningful X-ray polarimetry of such sources is difficult*:

1. In general, we do *not* expect sources to be strongly ($\gg$10%) polarized. For example, the maximum polarization from scattering in an optically thin, geometrically thin, accretion disc is only about 10% at the most favorable (edge-on) viewing angle. Hence, most of the X rays from such a source carry no polarization information and thus merely increase the background (noise) in the polarization measurement.

2. With one notable exception – namely, the Bragg-crystal polarimeter (Sect. 22.4.3) – the variation of the polarization signal, which is the signature of polarization in the detector, is much less than 100% (typically, 20–40%) even for completely polarized source. In the following we shall often refer to the variation or more precisely the modulation of the detector signal that depends on the polarization of the incident X-ray. For example, in a Bragg Crystal polarimeter, the intensity of the Bragg-reflected X-rays depends on the relative orientation of the axis normal to the crystal and the polarization vector. The reflected intensity varies (is modulated) as the crystal-detector system is rotated around the line of sight. Unfortunately, a Bragg-crystal polarimeter has a narrow spectral response, thus limiting the number of photons detected and providing little information on the spectral dependence of the polarization.
3. The degree of linear polarization is always greater than or equal to zero, so that any polarimeter will always measure (not necessarily statistically significantly) a polarization signal, even from an unpolarized source. Consequently, the statistical analysis (cf. Sect. 22.4.2) becomes somewhat complicated.

It is partly for these reasons that X-ray polarimetry has not progressed as rapidly as X-ray imaging, timing, and spectroscopy, since the pioneering experiments performed in the early 1970s. There are also sociological and psychological reasons, especially those involving the competition for observing time and the projected rate of return for instruments at the focus of telescope facilities (see also Sect. 22.5) which have played a role in stifling the development of X-ray polarimetry.

Two different types of X-ray polarimeters have flown to date – Bragg-crystal polarimeters (Sect. 22.4.3) and scattering polarimeters (Sect. 22.4.4). Note that we here differentiate between instruments that have been expressly designed and constructed to measure polarization and those that possess a degree of sensitivity to polarization, but were not designed for this purpose. We shall comment on these latter in Sect. 22.5. In this paper, we also discuss (Sect. 22.4.5) the advantages and disadvantages of a more "modern" approach to studying X-ray polarization, which uses the polarization dependence of K-shell photo-electron emission.

We emphasize the importance of the comparison we make here, as there appears to be some confusion concerning the relative merits of the different approaches. The recent literature has asserted such statements as "conventional polarimeters based on Bragg diffraction or Thompson scattering methods are characterized by a poor sensitivity..." [7]. Such broad statements are misleading, if not incorrect, in that they ignore the various contexts in which an X-ray polarimeter might fly, as well as issues of proven performance, cost, and simplicity.

22.4.1 Polarimeter Basics

All the polarimeters we discuss here have the following characteristic in common. The detected polarization signal behaves as

$$S = \bar{S}[1 + a_0 \cos(2\psi + \phi_0)], \tag{22.3}$$

where ψ is an angle with respect to the instrument's axis, in the plane transverse to the incident photon's direction. Here a_0 and ϕ_0 are related to the degree of linear polarization and its position angle, respectively.

22.4.2 Statistics

We assume that the detected signal is drawn from a broad-band noise source characterized by a mean $\bar{S}$ and variance σ^2. Then the probability of measuring a particular amplitude of modulation a and phase ϕ is given by

$$P(a,\phi) = \frac{N\bar{S}^2 a}{4\pi\sigma^2} \exp\left[-\frac{N\bar{S}^2}{4\sigma^2}(a^2 + a_0^2 - 2aa_0\cos(\Delta\phi)\right], \tag{22.4}$$

where $\Delta\phi \equiv \phi - \phi_0$ and N is the number of different values of ψ for which measurements were made – that is, the number of data points.

It follows that the probability of measuring a particular amplitude a independent of ϕ is

$$P(a) = \frac{N\bar{S}^2 a}{2\sigma^2} \exp\left[-\frac{N\bar{S}^2}{4\sigma^2}(a^2 + a_0^2)\right] I_0\left(\frac{N\bar{S}^2 a a_0}{2\sigma^2}\right), \tag{22.5}$$

where I_0 is the modified Bessel function of order zero.

The probability of measuring a particular angle ϕ independent of the amplitude a is:

$$\begin{aligned} P(\phi) = {} & \frac{1}{2\pi}\exp\left(-\frac{N\bar{S}^2 a_0^2}{4\sigma^2}\right) + \left(\frac{N}{2}\right)^{1/2} \frac{a_0\bar{S}\cos(\Delta\phi)}{2\pi\sigma} \\ & \times \exp\left[-\frac{N^2\bar{S}^2\sin^2\Delta\phi}{4\sigma^2}\right] \int_{-\infty}^{(N/2)^{1/2}\frac{a_0\bar{S}\cos\Delta\phi}{\sigma}} \exp\left(-\frac{u^2}{2}\right) du. \end{aligned} \tag{22.6}$$

In the following we assume Poisson distributed data and set $\sigma^2 = \bar{S}$. There are two interesting limiting cases which can be calculated analytically. In the first we consider large arguments of the Bessel function in (22.5) and for a close to a_0; P(a) then becomes a normal distribution with $\sigma_a = (2/N)^{1/2}$. Similarly, when the upper limit of the integral in (22.6) gets very large compared to 1 and for ϕ close to ϕ_0, P(ϕ) becomes a normal distribution with $\sigma_\phi = \sigma_a/a_0$.

To establish an instrument's sensitivity to polarized flux, the most relevant statistical question is, if the data are unmodulated (no real measure of polarization: $a_0 = 0$), what is the probability of measuring, by chance, an amplitude of modulation that is greater than or equal to the measured value? The amplitude of modulation is, after all, never negative and a value will be measured. In this case, (22.4) may be integrated analytically and, if the data are Poisson distributed, one finds

$$P(a' \geq a) = \int_a^{\inf} P(a')\, da' = \exp\left(-\frac{N\bar{S}a^2}{4}\right). \tag{22.7}$$

Note that $N\bar{S}$ is simply the total number of counts. It has become customary to single out the amplitude that has only a 1% probability of chance occurrence. Solving (22.7), this amplitude ($a_{1\%}$) is

$$a_{1\%} = \frac{4.29}{(N\bar{S})^{1/2}}. \tag{22.8}$$

The total number of counts, $\bar{S}$, is simply related to the source (R_S) and background (R_B) counting rates and the total observing time (T) through $N\bar{S} = (R_S + R_B)T$. Furthermore, we are interested in the modulation expressed as a fraction of the mean *source* counts, not the mean total counts, i.e., $a_S = a_{1\%}/\bar{S}$ so that

$$a_S = \frac{4.29}{R_S}\left[\frac{R_S + R_B}{T}\right]^{1/2}. \tag{22.9}$$

Finally, one needs to account for the possibility that the polarimeter does not fully respond to 100%-polarized radiation. It is convenient to introduce the "modulation factor", M, which is the degree of modulation expected in the absence of background and for a 100%-polarized beam. Thus, independent of the position angle, the minimal detectable polarization at the 99% confidence level, MDP_{99}, is

$$\mathrm{MDP}_{99} = \frac{a_S}{M} = \frac{4.29}{MR_S}\left[\frac{R_S + R_B}{T}\right]^{1/2}. \tag{22.10}$$

It is sometimes mistakenly assumed that (22.10) for the minimal detectable polarization describes the uncertainty of a measurement of the polarization: *That is not the case.* Equation 22.10 indicates when one may be confident that the signature of polarization has been detected – that is, that the source is *not unpolarized* – but not the uncertainty of its value (22.4). We emphasize this point because the minimal detectable polarization (MDP) often serves as *the* figure-of-merit for polarimetry. While it is *a* figure-of-merit that is useful and meaningful, a polarimeter useful for attacking astrophysical problems must have an MDP significantly smaller than the degree of polarization to be measured.

22.4.3 Crystal Polarimeters

The first successful X-ray polarimeter for astronomical application utilized the polarization dependence of Bragg reflection. Weisskopf et al. [86] describe the first sounding-rocket experiment (Fig. 22.1) using crystal polarimeters, which Schnopper & Kalata [70] had first suggested for an astronomical application.

To understand the operating principle of such devices, consider a single flat crystal. The number of reflected X-rays (N) during an observation of length T, given incident radiation with a spectral distribution I(E) (keV keV $\mathrm{cm}^{-2}\,\mathrm{s}^{-1}$), is

$$\frac{N}{T} = \int_0^\infty \frac{I(E')}{E'} R(E', \theta) A(\theta) dE', \tag{22.11}$$

where $A(\theta)$ is the projected area of the crystal in the direction of the incident flux and $R(E,\theta)$ is the probability that a photon of energy E incident on the crystal at angle θ will be reflected. For a continuum it can be shown (see, e.g., [2]) that this expression reduces to

$$\frac{N}{T} = I(E)A(\theta_B) \triangle \theta(E) cot(\theta_B), \tag{22.12}$$

where E is related to θ_B through the Bragg condition:

$$E = \frac{nhc}{2d\sin(\theta_B)}. \tag{22.13}$$

Here d is the interplanar spacing of the crystal lattice, n is the order of the reflection, and $\triangle\theta(E)$ is the integrated reflectivity at incident energy E

$$\triangle\theta(E) = \int R(E,\theta) d\theta. \tag{22.14}$$

For partially polarized radiation ($P \leq 1.0$)

$$\triangle\theta(E) = \frac{N_s^2 F^2 r_0^2}{2\mu(E)} (\frac{hc}{En})^3 \times (\frac{1}{\sin 2\theta_B} - \frac{\sin 2\theta_B}{2}(1 + P\cos 2\phi)), \tag{22.15}$$

where ϕ is the angle between the electric vector and the plane of reflection, and N_s is the number of scattering cells per unit volume, F is the crystal structure factor, r_0 is the classical electron radius, and μ is the absorption coefficient. The variation of the counting rate as a function of ϕ is maximal for θ_B at 45° and the azimuthal variation goes as $\cos 2\phi$.

The integrated reflectivity is not the same for all crystals, even of a given material, but depends on the relative orientation of the crystal domains. These latter may be viewed as small "crystalets". The integrated reflectivity is highest in the case of the "ideally imperfect" or "mosaic" crystal where perfect alignment of the the crystal planes is maintained only over microscopic domains in three dimensions. If these domains are much less than an absorption length in depth along the direction of the incident photon, then an X-ray entering the crystal may encounter many such domains, each at a slightly different Bragg angle, enhancing the probability of a Bragg reflection taking place before the photon might be absorbed. One can contrast this behavior with that which takes place in a perfect crystal where there is (essentially) only one very large domain with a single orientation; only X-rays with a very narrow bandwidth ($\ll$1 eV) can satisfy the Bragg condition, and all other X-rays are absorbed (or continue to pass through the crystal). As a consequence, perfect crystals have very low integrated reflectivity, which makes them poor candidates for polarization analyzers of the continuum fluxes prevalent from astrophysical sources. An ideally imperfect crystal can have an integrated reflectivity 10–100 times greater than that of an ideally perfect crystal of the same material. Angel & Weisskopf [2] performed a theoretical study of the integrated reflectivity of a number of naturally occurring crystals and discussed their potential

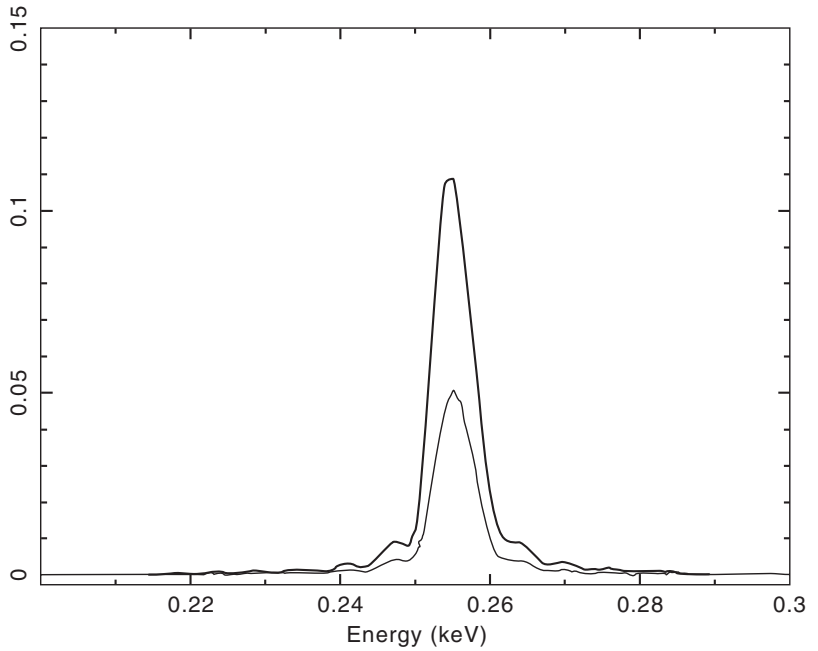

Fig. 22.3 Theoretical reflectivity vs. energy for a 40 bilayer, Ni/C synthetic multilayer, each layer being 34 RA thick. Fractional thickness Ni (0.4) and C (0.6). For 0 RA (*upper*) and 5 RA (*lower*) interlayer roughness

for X-ray astronomy applications. The highest integrated reflectivity they found was for graphite ($\triangle\theta(E) = 1.5 \times 10^{-3}$). Actual realizations using pyrolytic graphite have achieved values closer to 1×10^{-3}. Synthetic multilayer crystals, wherein alternating layers of high-Z, low-Z materials (e.g., Ni/C) are constructed, may achieve comparable and even larger integrated reflectivities at low energies. The performance of these crystals depends critically on the inter-layer surface roughness which is not easy to control. Figure 22.3, e.g., illustrates such effects. Multilayer crystals operating at low energies are especially attractive for observing effects from the XDINSs.

Only three crystal polarimeters have ever been constructed for extra-solar X-ray applications and only two – both using graphite crystals without X-ray telescopes – were ever flown (sounding rocket, [86]; OSO-8 satellite, [87]; Spectrum-X (not flown), [39] and numerous references therein.)

One of the strongest virtues of the crystal polarimeter is, for Bragg angles near 45°, that the modulation of the reflected flux approaches 100%. One can see from (22.10) that this is very powerful *all other things being equal*. Thus a factor of two increase in the modulation factor improves the minimum detectable polarization (MDP) by a factor of 2. To achieve the same improvement in sensitivity by other means would require either an increase in effective area or observing time by a factor of 4.

The most severe disadvantage of the crystal polarimeter is the narrow bandwith of the response – about 23 eV for graphite with a mosaic spread (rocking curve width) of 0.5°. The integrated reflectivity from the second order Bragg reflection is smaller than that from the first order and, of course, the typical flux from astronomical sources are usually comparatively weaker so that the overall loss in sensitivity renders the second (and higher) order(s) of marginal utility. Filling in gaps in energy coverage therefore requires using different crystals, which, in general, implies a very poor "filling factor". Here the filling factor refers to one's ability to make use of the real estate in a satellite payload that lies perpendicular to the incident flux. Unless stacked (and, because of photoelectric absorption, stacking cannot be extended arbitrarily) two crystal polarimeters, which effectively cover two energies, divide the available area in half, three – one-third, etc. This may be contrasted to the scattering and electron tracking polarimeters discussed below which cover a much larger bandwidth with a filling factor of unity, typically, however, at the price of a smaller modulation factor.

22.4.4 Scattering Polarimeters

There are two scattering processes from bound electrons that must be considered: coherent and incoherent scattering. A comprehensive discussion of both of these processes may be found in many atomic physics textbooks (see, e.g., [38]). Coherent scattering dominates at small scattering angles. In the limit of zero scattering angle, the X-ray behaves as if it were scattered from a charge Ze, where e is the charge of an electron. Coherent scattering, therefore, leads to an enhancement of forward scattering over pure Thomson scattering from free electrons. In the non-relativistic limit, the cross-section for coherent scattering for X-rays traveling along the z-axis and polarized along the y-axis is

$$\frac{d\sigma_{coh}}{d\omega} = r_0^2[\cos^2\theta\cos^2\phi + \sin^2\phi]|F|^2. \tag{22.16}$$

Here r_0 is the classical electron radius, θ is the polar scattering angle, and ϕ is the azimuthal angle measured from the x-axis. Tables of the form factor F may be found in the literature [31].

Incoherent scattering dominates at larger scattering angles and approaches the Thomson limit at sufficiently large angles. In the non-relativistic limit, the cross-section for incoherent scattering of X-rays polarized along the x-axis is:

$$\frac{d\sigma_{incoh}}{d\omega} = r_0^2[\cos^2\theta\cos^2\phi + \sin^2\phi]I. \tag{22.17}$$

Tables for the incoherent scattering function, I, are also available in the literature [17].

Various factors dominate the consideration of the design of a scattering polarimeter. The most important of these are: (1) to scatter as large a fraction of the incident

flux as possible while avoiding multiple scatterings (which clearly blurs the polarization dependence); (2) to achieve as large a modulation factor as possible; (3) to collect as many of the scattered X-rays as possible; and (4) to minimize the detector background. The scattering competes with photoelectric absorption in the material, both on the way in and, of course, on the way out. The collection efficiency competes with the desire to minimize the background. Most practical designs have the detector integrating the two scattering angles over some range which impacts the variation of flux as a function of azimuthal angle which is the variation (modulation) that is measured and is proportional to the degree of polarization.

Only two polarimeters of this type have ever been constructed for extra-solar X-ray applications and only one - utilizing blocks of lithium with proportional counters covering the four sides of the blocks orthogonal to the incident flux - was ever flown (rockets - three times: in 1968, see [1]; in 1969 see [89], and in 1971 see, e.g., [55]; satellite - Spectrum-X (never flown) see [39] and references therein.)

The virtue of the scattering polarimeter is that it has reasonable relative efficiency over a moderately large energy bandwidth, typically several keV in width. The bandwidth is large compared to the energy resolution of potential detectors, e.g., proportional counters, CCDs, etc., so that polarization measurements as a function of energy are feasible. The principal disadvantage is a modulation factor less than 100%, since only for scattering into 90° will the modulation approach unity in the absence of background and for a 100%-polarized incident beam. In order to obtain any reasonable efficiency requires integrating over a range of scattering angles and realistic modulation factors are under 50%, unless the device is placed at the focus of a telescope (the modulation factor for the scattering polarimeter on Spectrum-X reached $\sim$75%) where it is feasible to make the scattering volume small which then limits the range of possible scattering angles.

The two most popular materials that have been considered for scattering polarimeters are lithium and beryllium. The lower the Z, the lower the peak response energy, and, for cosmic X-ray sources, the higher the sensitivity. The K-absorption edges for these two materials are at 0.0554 keV (Li) and 0.188 keV (Be). The peak energy response of typical practical designs are typically $\simeq$7 keV (Li) and $\simeq$15 keV (Be) but it should be noted that the exact peak energies are somewhat design/detector-dependent.

22.4.5 Photo-Electron Tracking Polarimeters

The angular distribution (see, e.g., [34]) of the K-shell photo-electron emitted as a result of the photoelectric absorption process depends on the polarization of the incident photon. In the non-relativistic limit

$$\frac{d\sigma}{d\Omega} = f(\zeta) r_0^2 Z^5 \alpha_0^4 \left(\frac{1}{\beta}\right)^{7/2} 4\sqrt{2} \sin^2\theta \cos^2\phi . \tag{22.18}$$

Here α_0 is the fine structure constant, r_0 is the classical electron radius, Z is the charge of the nucleus of the absorbing material, and $\beta = v/c$. The variable $\zeta = \frac{Ze^2}{\hbar v}$ and $f(\zeta)$ is unity away from the absorption edge.

The considerations for the design of a polarimeter that exploits this effect are analogous to those for the scattering polarimeter. In this case the competing effects are the desire for a high efficiency for converting the incident X-ray flux into photo-electrons and the desire for those photo-electrons to travel large distances before interacting with elements of the absorbing material.

Here we will concentrate on polarimeters that use gas mixtures to convert the incident X-rays to photo-electrons. We do this for the following reasons: (1) there are two promising approaches to electron tracking polarimetry that use this approach and we are quite familiar with both of them; and (2), especially at the X-ray energies of interest here (and where the X-ray fluxes are the greatest), the range of the primary photo-electrons in solids are very tiny (e.g., $\simeq$1.5μm in silicon at 10 keV). Tracking such events in solids then requires pixels much smaller than the current state of the art, making this type of polarimetry essentially impossible at the energies of interest.

To our knowledge, the first electron tracking polarimeter specifically designed to address polarization measurements for X-ray astronomy and using a gas as the photo-electron-emitting material was that designed by Austin & Ramsey [4] (see also [5, 6]). These scientists used the light emitted by the electron avalanches which takes place after the release of the initial photo-electron in a parallel plate proportional counter. The light was focused and detected by a CCD camera. A schematic diagram of the experimental setup is shown in Fig. 22.4. The use of two multiplication stages (i.e., two parallel-plate proportional chambers) permits triggering of the camera and allows for efficient light yields. Of course the detection scheme produces a two dimensional projection of the photo-electron's track and this reduces the modulation factor.

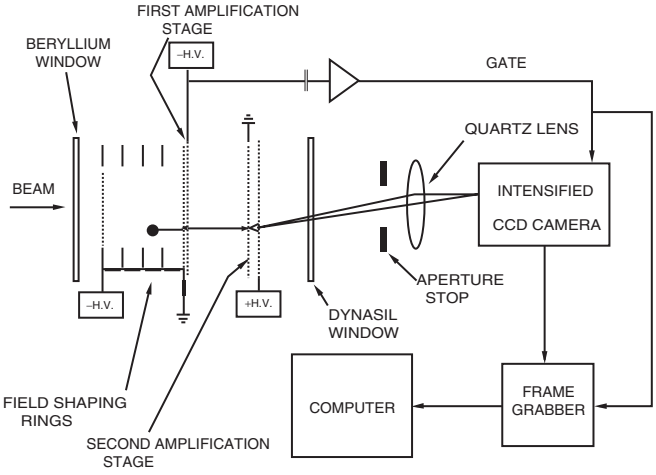

Fig. 22.4 Experimental setup for the optical imaging chamber

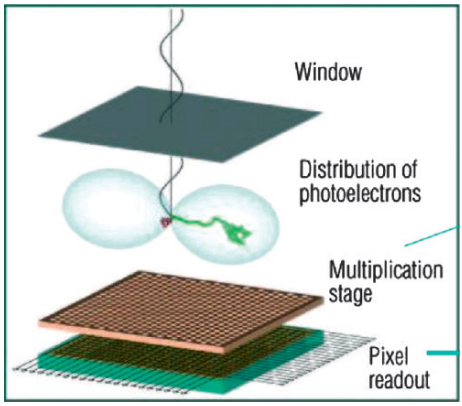

Fig. 22.5 Cartoon showing the principle of the gas-multiplication electron-tracking polarimeter. Courtesy J. Swank

Another gas-detector approach, first discussed by Costa et al. [18], uses "pixilated" proportional counters to record the avalanche of secondary electrons that result from gas-multiplication in a high field after the primary photo-electron track (and that of the original Auger electrons) drift into a region where this multiplication may take place. The concept is shown in Fig. 22.5. The resulting charge may then be read out by finely pixellated collection of electrodes. The degree of polarization is related to the variation of the flux around the position determined by where the primary interaction takes place.

Detecting the direction of the emitted photo-electron (relative to the direction of the incident flux) is itself not simple. The reason for this is that electrons, when they interact with matter, give up most of their energy at the *end* of their track, not the beginning. Of course, in the process of giving up its energy to the local medium in which the initial photo-ionization took place, the electron changes its trajectory, thus losing the information as to the initial polarization. Therefore, devices that wish to exploit the polarization dependence of the photoelectric effect have the additional challenge that they must track the ejected photo-electron's path, and the most important element of that path is the direction to the first interaction which gives up the least amount of energy.

It is instructive to examine the image of a track and we show one obtained under relatively favorable conditions with an optical imaging chamber in Fig. 22.6. The initial photoionization has taken place at the small concentration of light to the north (top) of the figure. The bright spot to the north indicates the short track of an Auger electron. As the photo-electron travels through the gas mixture it either changes direction through elastic scattering and/or both changes direction and loses energy through ionization. As these take place, the path strays from the direction determined by the incident photon's polarization. Of course, the ionization process is energy dependent and most of the electron's energy is lost at the end, not the beginning, of its track. It should be clear from this picture that, even under favorable conditions – by which we mean those where the range of the photo-electron is quite large compared to its interaction length – the ability to determine a precise angular distribution depends on the capability and sophistication of the track-recognition

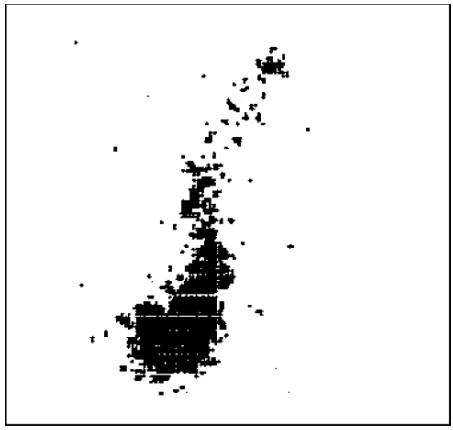

Fig. 22.6 The two-dimensional projection of a track produced when a 54 keV X-ray was absorbed in 2 atm of a mixture of argon (90%) The particular track is ≃14 mm in length

software, not only on the spatial resolution of the detection system. The burden falls even more heavily on the software at lower energies where the photo-electron track becomes very short and diffusion in the drifting photo-electron cloud conspires to mask the necessary track information.

Although polarimeters exploiting this effect have been discussed in the literature, *no device of this type has ever been flown and those built have undergone limited testing in the laboratory*. The claims for the potential performance of these devices at the energies of peak performance depend on Monte-Carlo simulations to extend experimental results. Experimental verification of performance exists at 5.4 and 6.4 keV [7]. We eagerly await experimental verification of performance at lower energies, around 3 keV, where peak performance is claimed.

Both approaches for imaging the projection of the electron track are quite interesting, especially for use at the focus of an X-ray telescope (Sect. 22.4.6). Electron tracking polarimeters must also deal with an energy dependent modulation factor. This is completely in contrast to the crystal polarimeter, and is more severe than for a typical scattering polarimeter. This energy dependence will not only complicate the calibration of such an instrument, but also the data analysis. To our knowledge, no published reports of the projected sensitivity of such devices have ever considered the impact of the finite energy resolution and the energy-dependent modulation on the data analysis. To do so here is beyond the scope of this paper, but we note that the impact of this complication on the sensitivity should not be ignored.

The considerations for the choice of the detector gases are somewhat different for the two approaches to electron tracking discussed here - high light yield versus reasonable electron amplification – but both must trade a high absorption efficiency for a long electron track in order to work efficiently as a polarimeter.

There are pros and cons in each approach. The optical imaging chamber has the advantage of flexibility in its readout scale, which can be configured by the appropriate choice of optics so that its detection pixel is small compared to the electron track length, especially at the low-energy end of the polarimeter response. In contrast, the fixed size of the pixels (≃50–100-μm) themselves determine the low-energy

response when gas-multiplication detection is used. This is probably more of a limitation than might appear at first sight since the arrangement of detection cells is, in and of itself, asymmetric in position angle, with a built in response at 2ϕ, the signature of polarization. This built-in asymmetry not only impacts the modulation factor (it vanishes if the length of the track is smaller than the size of a cell), but also introduces spurious polarization signatures when the track length is comparable to, or even somewhat larger than the characteristic size of a detection cell. We feel that it is naive to believe that such effects can be accurately accounted for by means of Monte-Carlo simulations alone.

The optical imaging chamber, however, is more limited in its selection of fill-gas mixtures in that they must produce large amounts of light via the addition of photosensitive vapors without any competing (non-light-producing) collisions with other additives. This potentially limits control over diffusion which in turn may limit the lowest-energy response of such a device. More detailed study is required to explore the fill-gas parameter space.

We encourage all experimenters working with gas-multiplication detectors for use as X-ray polarimeters to publish a calibration using polarized and, equally important, unpolarized sources in the regime for which the range of the photoelectron begins to get even close to the size of the detector pixels or to the diffusion scale so that one may understand the true response.

22.4.6 X-Ray Polarimeters at the Focus of a Telescope

We first look at polarimeters at the focus of a telescope, which as we will see, provide the highest sensitivity. We shall then turn to polarimeters without telescopes and show that, while producing lower sensitivities, these may still offer the best overall approach for a low-cost pathfinder mission.

There can be no question that for optimizing signal-to-noise, one should place the X-ray polarimeter at the focus of an X-ray telescope. Further, the electron tracking devices, if shown to work as advertised, are probably the instrument of choice. (We hedge only in that it is unclear that these devices can efficiently work at arbitrary energies, and thus may not be suitable to the study of very soft X-ray sources.) This stems from the fact that these devices will provide the broadest bandwidth together with a very low background, determined only by the size of the initial ionization convolved with the telescope's angular resolution. In contrast, the background for the scattering polarimeter is determined by the area of the surrounding detectors, which, perforce, is much larger than for detectors at the focus of a telescope. The background for the crystal polarimeter near the focus of a telescope is also very small as it is determined by the resolution of the X-ray telescope. However, the bandwidth is tiny, unless multiple crystals are utilized. A multiple-crystal design is complex, and beyond the scope of this discussion. (Possible a hybrid with thin crystals operating in series with an electron-tracking device might be interesting.)

In order to perform a comparison with the same telescope for all three types of instruments, and to make use of existing software, we consider a graphite-crystal polarimeter, a lithium-scattering polarimeter, and a photo-electron tracking polarimeter, each at the focus of the SODART telescope. This was a 60-cm-diameter, 8-m-focal-length, foil telescope of $\simeq$1,000 cm^2 at 3 keV built for the (original) Spectrum-X mission.

The configurations we consider are as follows: a graphite-crystal polarimeter followed by a lithium-scattering block surrounded by a four-proportional-counter array, as were employed for the Stellar X-Ray Polarimeter (SXRP - see Fig. 22.7 and also [39] and references therein) built for the (original) Spectrum-X mission, and an electron tracking polarimeter filled with a mixture of 80% Ne, 20% dimethylamine at 1 atm, with a 100-μm-pitch (spacing) readout, as simulated by Pacciani et al. [56].

Figures 22.8 and 22.9 compare the times to reach 3% MDP (at the 99%-confidence level) for the graphite-crystal, lithium-scattering block, and the electron-tracking polarimeter, in various energy bands for two different incident energy spectra. Figure 22.10 shows the sensitivity of each instrument as a function of energy for an observation of Her X-1. The calculations for the Spectrum-X polarimeters are based on Monte-Carlo simulations fully verified by calibration measurements at

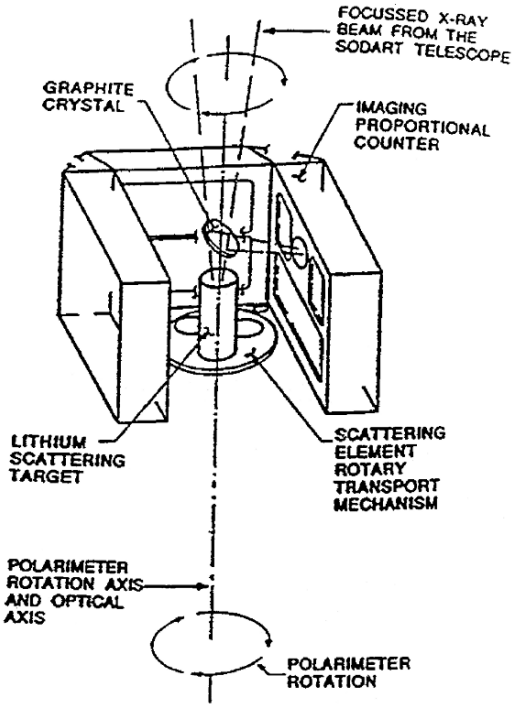

Fig. 22.7 Cartoon showing the Stellar X-ray polarimeter built for Spectrum-X

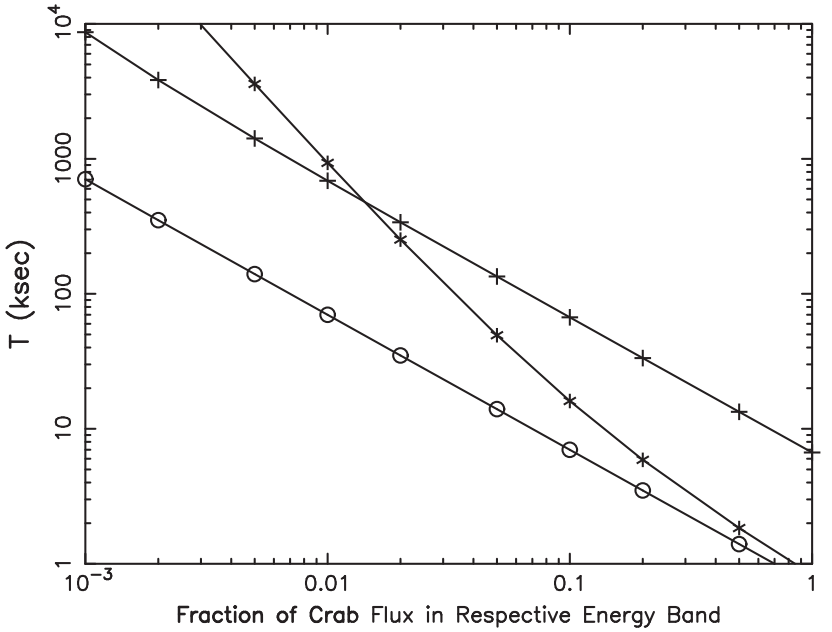

Fig. 22.8 Times to reach a MDP of 3% vs. source strength for the Crab Nebula spectrum. The numbers result from integrating over useful energy response of each instrument, The blue line (*circles*) is for an electron tracking polarimeter, the green (*crosses*) is for a lithium scattering polarimeter, and the red (*plus sign*) for a graphite crystal polarimeter. Note that the latter two operate simultaneously. All are placed at the focus of the SODART telescope

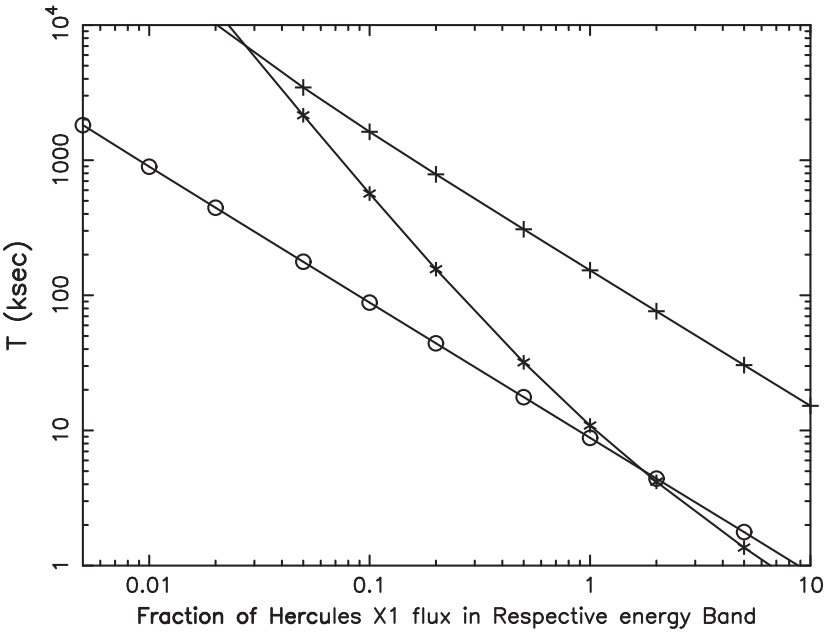

Fig. 22.9 Same as for Fig. 22.8 but for the Her X-1 spectrum

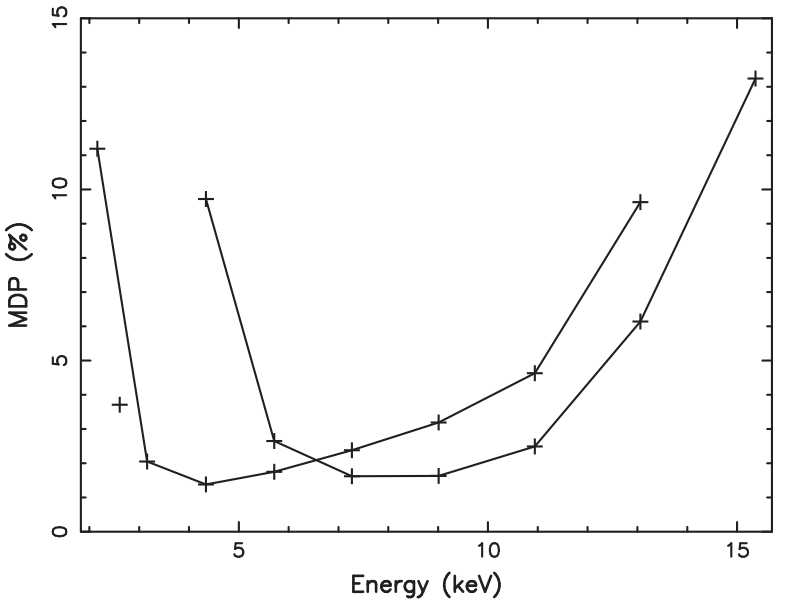

Fig. 22.10 The minimal detectable polarization for a 10^5 s integration vs. energy for the three polarimeters with a telescope (Fig. 22.8). The single point at 2.6 keV is for the graphite crystal. The continuous line extending to well below 5 keV is for the electron-tracking polarimeter. The other continuous line is for the lithium-scattering polarimeter

Lawrence Livemore National Laboratory [75], while those for the electron-tracking polarimeter are based on data taken from published simulations [56]. The graphite-crystal and electron-tracking polarimeters are not background limited, at least down to source strengths corresponding to a milli-Crab, while the lithium-scattering block polarimeter is background limited over the entire range of source strengths shown. (The flux measure is related to that of the famous Crab Nebula and its pulsar.) Since the electron-tracking polarimeter is more sensitive to fainter sources, it seems clear that *all things being equal* one would choose to place the electron-tracking polarimeter at the focus of an X-ray telescope especially if one had to choose single device.

In performing these calculations and the comparisons, we have ignored systematic effects that might lead to false signatures of polarization, and hence reduced sensitivity. Accounting for such effects is of great importance, especially at low levels of polarization which are exacerbated by below-unity modulation factors. *With all deference to high-fidelity Monte-Carlo simulations, careful ground-based calibrations over the entire operating range of a polarimeter, performed with both polarized and unpolarized beams are essential for establishing performance.* The more complex the polarimeter, the more important such calibrations become. Frankly, the literature has several examples of highly exciting new approaches to polarimetry, which, on deeper experimental examination have turned out to be incorrect and dominated by systematic effects (see, e.g., [72]).

The systematic effects may not be limited to the polarimeter itself. Items that also need to be considered are, e.g., the coupling of the telescope to the instrument – especially if the telescope is not round; off-axis effects (see [25] for one of these effects for scattering polarimeters); and solar X-rays that have become polarized through scattering through the appropriate angles from the atmosphere.

22.4.7 X-Ray Polarimeters without a Telescope

The comparison amongst the three approaches to X-ray polarimetry we are considering here is quite different if we examine polarimeters without telescopes. Now the devices that track the photo-electron, so useful at the focus of the telescope, are no longer really practical because of the large detector area and small pixel size (to establish the photo-electron track) that are both required. Thus, we examine the question how best to fill a modest aperture with a polarimeter that does not involve an X-ray telescope and in this context compare large-area scattering and crystal polarimeters.

For the purpose of this comparison we consider a beryllium scattering polarimeter (XPE) which is a realization of a design we first introduced in cartoon form in Mészáros et al. [49]. The design is illustrated in Fig. 22.11 and consists of a 0.6-m-diameter beryllium scattering cone surrounded by an annular proportional counter to record the angle and energy of scattered photons. A simple collimator limits the field of view to a few degrees. Note that the diameter of the opening is identical to that of the SODART telescope we used with the polarimeters in Sect. 22.4.6, thus the filling-factors are identical.

For a typical large-area crystal polarimeter we consider an array of multilayer-coated reflectors tuned for high throughput at large graze angles (25–40°) at

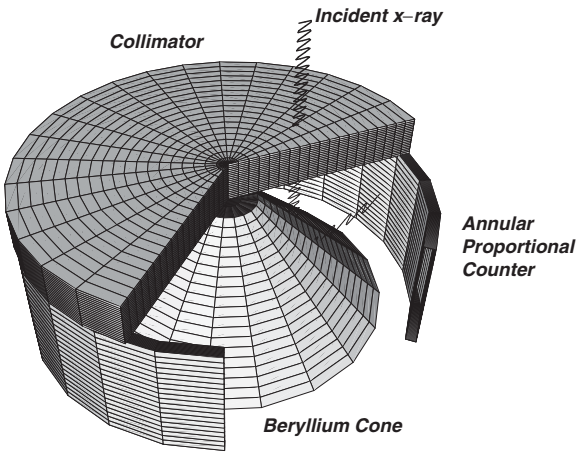

Fig. 22.11 Conceptual design for a beryllium-scattering polarimeter

0.25 keV. This is the PLEXAS design of Marshall et al. [46]. The reflectors are arrayed in three sectors, each sector reflecting onto a different detector. The concept is illustrated in Fig. 22.12. The footprint of both polarimeters is also similar.

Figure 22.13 shows polarization sensitivity for Her X-1 as a function of energy for the two polarimeters which may be compared to Fig. 22.10. The scattering

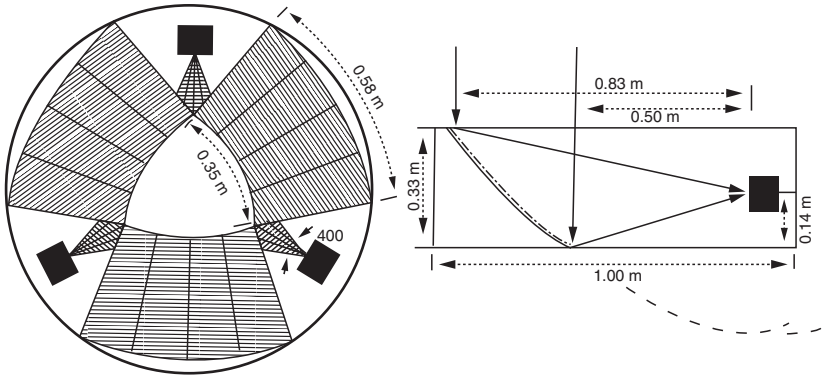

Fig. 22.12 Conceptual design for a crystal polarimeter (PLEXAS)

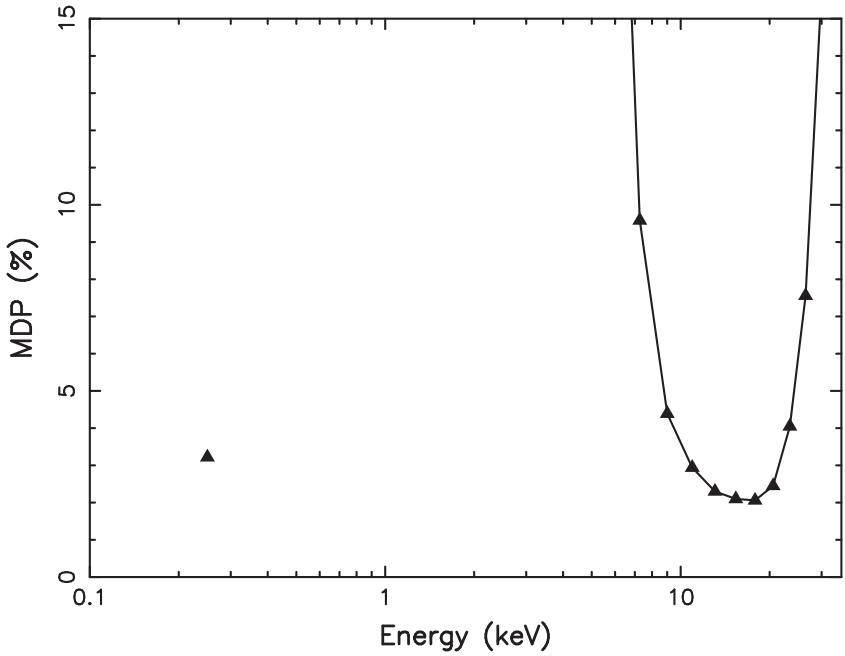

Fig. 22.13 The minimal detectable polarization for a 10^5 s integration vs. energy for the two polarimeters without a telescope. The single point at 0.25 keV is for the synthetic multilayer (PLEXAS) design. The continuous line is for the beryllium-scattering polarimeter

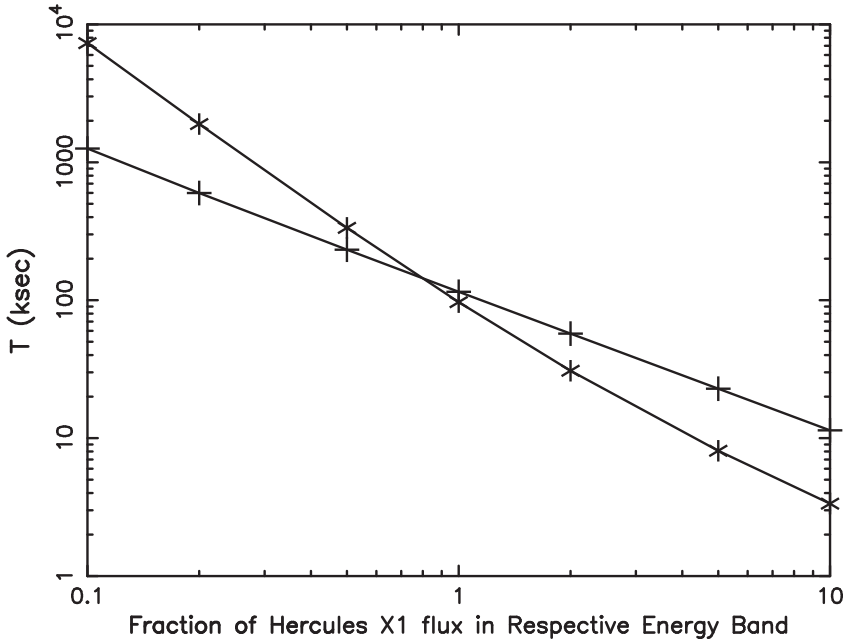

Fig. 22.14 The integration time T to reach a MDP of 3% (at 99%-confidence) vs. source strength for the Her X-1 spectrum integrated over the full energy response of each of the polarimeters (Fig. 22.13). Note that the bandwidths are quite different. The line with the star symbols is for the collimated beryllium-scattering polarimeter. The line with the plus symbols is for the synthetic multilayer operating nominally at 0.25 keV

polarimeter achieves peak performance at higher energies than the polarimeters at the focus of the long-focal-length X-ray telescope. Figure 22.14 shows the time to reach 3% MDP at 99%-confidence with such polarimeters versus source strength for the Her X-1 spectrum. Now, in contrast to Fig. 22.13, we integrate over the full bandwidth.

Although, by virtue of its concentrating reflectors, the integrated performance of the synthetic crystal polarimeter is superior for faint sources, it lacks broad band response, and one needs to answer the question as to whether or not the measurement of polarization at a single energy is capable of providing useful additional constraints of our understanding of astrophysical systems. We strongly believe that the answer to this question is no – that even a detection at a single energy is not terribly useful. In such cases we feel that the clever theorist will soon provide a myriad of ex-post-facto models to explain any unexpected result, and the ability to distinguish between models will be missing.

It should be clear then that without a telescope, a scattering polarimeter is the instrument of choice as it provides useful sensitivity over a wide energy band, especially when compared to the use of a single crystal material or an ungraded multilayer reflector.

22.5 Discussion and Conclusions

There are no free rides in X-ray polarimetry: An instrument with some polarization sensitivity, but designed primarily for other purposes, is not an adequate substitute for one optimized for polarimetry. For example, attempts to measure the polarization of GRB 021206 using the Reuven Ramaty High-Energy Solar Spectroscopic Imager (RHESSI) led to results that are controversial at best [15, 68]. In this case, the low priority for possible polarization measurements practically precluded the complete calibration needed to characterize an instrument's polarimetric sensitivity and to understand systematic effects that might produce a spurious polarization signal. For instruments operating at high energies, such a calibration could require exposing the entire spacecraft to an X-ray beam and would thus be difficult. While Monte-Carlo simulations play an important role in assessing an instrument's capabilities for polarimetry, verifying the quantitative predictions of such simulations still requires careful comparison with calibration or other experimental data.

It is reasonable to ask, "Why has there been no X-ray polarimetry of cosmic sources since the early experiments in the 1970s?" Understandably, the development of X-ray astronomy has focused on X-ray optics for imaging and spectrometric imaging, leading to facility-class missions serving a broad astronomical community. Focused imaging greatly increases the signal-to-noise ratio and mitigates source confusion, dramatically improving sensitivity and thus enabling meaningful observations of a large number of sources, their spectra, and (for resolved sources) their spatial structure. The *Einstein* Observatory evolved into the first of the facility-class X-ray missions and (unfortunately) became a paradigm for polarimetry in such missions: The original design for the *Einstein* Observatory (nee HEAO-B) included a polarimeter; however, program restructuring and descoping deleted the instrument. Although the *Chandra* call for instruments did not preclude a polarimeter, imaging and spectroscopic instruments prevailed – in large part, because many more targets are accessible to such observations than to polarimetry. In the exceptional case of Spectrum-X, which included a polarimeter insertable into the focal position, competition with the other insertable focal-plane instruments resulted in an observing plan that would have limited polarimetry to only 11 days per year! Even worse, that observatory never flew!

The absence of any X-ray polarimetric observations since the original experiments has itself impaired the development of X-ray polarimetry. Without experimental results or even the prospect thereof, progress in the theoretical framework that such experiments both require and inspire has – with notable exceptions (Sect. 22.3) – been slow. We hasten to add that this does not mean an absence of theoretical interest. Indeed, the 2004 conference on X-ray polarimetry at SLAC[2] attracted over 100 scientists, the majority of whom are theorists.

Such considerations have convinced us that a small, dedicated mission affords the best opportunity for advancing X-ray polarimetry. This permits formulation of an observing program suited to the capability of the polarimeter and avoids the

[2] http://www-conf.slac.stanford.edu/xray_polar/talks.html

limitations that a shared (e.g., facility-class) mission imposes on the least sensitive instrument aboard. Even so, it is extremely difficult – once again for many of the reasons discussed above – for a polarimetry mission to compete with other missions (most outside X-ray astronomy) seeking similar resources (e.g., in the NASA's Small Explorer Program).

Consequently, we believe that an X-ray-polarimetry pathfinder needs to be an inexpensive, simple instrument, with minimal technical requirements upon the spacecraft – for example, pointing accuracy and stability [25] – and upon the launcher. Regrettably, such budgetary constraints probably preclude use of a focusing X-ray telescope on the pathfinder. Suitable X-ray optics are costly to design and fabricate, align and assemble, integrate, and test and calibrate. Further, even

Table 22.1 Sample Polarimetry survey

Name	Type	Time (d)	MDP (%)[a]
Crab pulsar	Radio pulsar	29.6	3.0
Crab nebula	SNR		0.1
SGR 1900+14	SGR: in active state	1	3.0
4U1636-53	burster	9	3.0
GS1826-238	Clocked burster[b]	4.3	3.0
J1808.4-3658	MSP	9.1	3.0
J1751-305	MSP	10.3	3.0
Her X-1	Accreting pulsar	0.5	1.9
Cen X-3	Accreting pulsar	0.5	1.4
4U0900-40	Accreting pulsar	0.5	2.4
GX 1+4	Accreting pulsar	0.5	2.1
SMC X-1	Accreting pulsar	3.2	3.0
4U1538-58	Accreting pulsar	10.4	3.0
4U0115+63	Accreting pulsar[c]	0.5	2.4
OAO1657-41	Accreting pulsar	4	3.0
4U1626-67	Accreting pulsar	1.3	3.0
Cyg X-3	Binary	1.0	3.0
4U1822-37	Accretion-disk corona	8.3	3.0
Sco X-1	QPO	0.5	0.6
Cyg X-2	QPO	0.5	2.8
GX 5-1	QPO	0.5	2.0
Cir X-1	QPO	0.5	2.0
Cyg X-1	Black-hole binary	0.5	0.9
J1744-28	Bursting pulsar	0.5	0.6
GRS 1915+105	Microquasar[d]	0.5	0.4
J1655-40	Microquasar[c]	0.5	1.8
TBD	Weak transient	10.7	3.0
Cen A	AGN	16.2	3.0
NGC 4151	AGN	24.8	3.0

[a]99% confidence
[b]Persistent flux
[c]High state
[d]Active state

lightweight optics would burden the weight budget for a small spacecraft, especially for a telescope optimized for the higher X-ray energies at which the scientifically more interesting polarization effects (Sect. 22.3) are likely to occur.

In view of these constraints, we propose that the community consider an initial exploratory polarimetry mission, to survey bright X-ray sources, using a large-area scattering polarimeter, possibly supplemented with crystals. This type of instrument is simple (no deployables or other moving parts), low-cost, and proven. We estimate that the instrument costs would be around 5 M$ and that the total mission cost would be about 30 M$. This is roughly a quarter of the cost of the typical NASA Small Explorer program, where fixed prices for complex three-axis-stabilized catalog satellites, large launch costs, etc. mask the true cost of a simple mission.

Such a pathfinder could survey a wide range of objects at sufficient sensitivity to detect expected levels of polarization. To illustrate this, Table 22.1 lists a sample survey program, with the integration time and MDP for the XPE polarimeter (Sect. 22.4.7). Each integration time is that necessary to yield 3% MDP (integrated over energy and phase, if pulsating) or 0.5 days, whichever is longer. After the 6 months needed to complete the survey (including time for slewing and target acquisition), the remainder of the mission would conduct follow-on measurements of many of the sources exhibiting a polarization signature. In addition to performing the first X-ray-polarimetry survey, the low-cost pathfinder would serve as the foundation for a larger, more-complex mission that could include large-area focusing optics with fully developed and calibrated electron-tracking polarimeters at their foci, such as those being considered for IXO.

References

1. Angel, J.R.P., Novick, R., van den Bout, et al., 1969, Phys. Rev. Lett., 22, 861
2. Angel, J.R.P., Weisskopf, M.C., 1970, AJ, 75, 231
3. Araya-Góches, R.A., Harding, A.K., 2000, ApJ, 544, 1067
4. Austin, R.A., Ramsey, B.D.A., 1992, Proc SPIE, 1743, 252
5. Austin, R.A., Ramsey, B.D.A., 1993, Opt. Eng., 32, 1900
6. Austin, R.A., Minamitani, T., Ramsey, B.D., 1993, Proc. SPIE, 2010, 118
7. Bellazzini, R., Angelini, F., Baldini, L., et al., 2006, in *Nuclear Instruments and Methods in Physics Research Section A*, 560, 425
8. Bignami, G.F., Caraveo, P.A., de Luca, A., et al., 2003, Nature, 423, 725
9. Bildsten, L., et al., 1997, ApJS, 113, 367
10. Blandford, R., Applegate, J., Hernquist, T., 1983, MNRAS, 204, 1025
11. Bulik, T., Meszaros, P., Woo, J.W., et al., 1992, ApJ, 395, 564
12. Chakrabarty, D., Pivovaroff, M.J., Hernquist, L.E., et al., 2001, ApJ, 548, 800
13. Cheng, K.S., Ho, C., Ruderman, M.A., 1986, ApJ, 300, 500
14. Cheng, K.S., Ho, C., Ruderman, M.A, 1986, ApJ, 300, 522
15. Coburn, W., Boggs, S.E., 2003, Nature, 423, 415
16. Coburn, W., et al., 2002, ApJ, 580, 394
17. Cromer, D.T., Mann, J.B., 1967, J. Chem. Phys., 47, 1892
18. Costa, E., Soffitta, P., Bellazzini, R., et al., 2001, Nature, 411, 662
19. Crusius-Wtzel, A.R., Kunzl, T., Lesch, H., 2001, ApJ, 546, 401
20. Daugherty, J.K., Harding, A.K., 1982, ApJ, 252, 337

21. Dermer, C., Sturner, S., 1991, ApJ, 382, L23
22. Duncan, R., Thompson, C., 1992, ApJ, 392, L9
23. Euler, H., Kockel, B., 1935, Naturwiss., 23, 246
24. Elsner, R.F., Lamb, F.K., 1976, Nature, 262, 356
25. Elsner, R.F., Weisskopf, M.C., Kaaret, P., et al., 1990, Opt. Eng., 29, 767
26. Gänsicke, B.T., Braje, T.M., Romani, R.W., 2002, A&A, 386, 1001
27. Gnedin, Yu.N., Sunyaev, R.A., 1974, A&A, 36, 379
28. Göğüş, E., Kouveliotou, C., Woods, et al., 2001, ApJ, 558, 228
29. Gotthelf, E.V., Halpern, J.P., Seward, F.D., 2005, ApJ, 627, 390
30. Götz, D., Mereghetti, S., Tiengo, A., et al., 2006, A&A, 449, L31
31. Hansen H.P., Herman, F., Lea, J.D., et al., 1964, Acta Cryst., 17, 1040
32. Harding, A.K., Muslimov, G.A., 1998, ApJ, 508, 328
33. Heisenberg, W., Euler, H., 1936, Z. Phys., 38, 714
34. Heitler, W., 1954 *The Quantum Theory of Radiation*, 3rd Edition, Dover, New York
35. Heyl, J.S, Shaviv, N.J., 2000, MNRAS, 311, 555
36. Hurley, K., 2000, in *AIP Conf. Proc. 526, Gamma-ray Bursts, 5th Huntsville Sym.*, ed. R.M. Knippen, R.S. Malozzi, G.J. Fishman, AIP, New York, 763
37. Isenberg, M., Lamb, D.Q., Wang, J.C.L., 1998, ApJ, 505, 688
38. James, R.W., 1965, *The Optical Principals of the Diffraction of X-Rays*, Cornell University Press, Ithaca, NY
39. Kaaret, P.E., Schwartz, J., Soffitta, P., et al., 1994, Proc. SPIE, 2010, 22
40. Kanbach, G., Sowikowska, A., Kellner, S., et al., 2005, in *Astrophysical Sources of High Energy Particles and Radiation*, AIP Conference Proceedings, 801, 306
41. Kaplan, D., van Kerkwijk, M., 2005, ApJ, 628, L45
42. Kaplan, D., van Kerkwijk, M., 2005, ApJ, 635, L65
43. Kuiper, L., Hermsen, W., Mendez, M., 2004, ApJ, 613, 1173
44. Lai, D., Ho, W.C.G., 2003, ApJ, 588, 962
45. Lenters, G.T., Woods, P.M., Goupell, J.E., et al., 2003, ApJ, 587, 761
46. Marshall, H.L., Murray, S.S., Chappell, J.H., et al., 2003, SPIE Proc., 4843, 360
47. Mészáros, P., 1992, *High-Energy Radiation from Magnetized Neutron Stars*, University Chicago Press
48. Mészáros, P., Nagel, W., 1985, ApJ, 298, 147
49. Mészáros, P., Novick, R., Chanan, G.A., et al., 1988, ApJ, 324, 1056
50. Mori, K., Hailey, C., 2006, ApJ, 648, 1139
51. Nagase, F., 1989, Pub. Astron. Soc. Japan, 41, 1
52. Nagel, W. 1981, ApJ, 251, 278
53. Nagel, W. 1981, ApJ, 251, 288
54. Niemiec, J., Bulik, T., 2006, ApJ, 637, 436
55. Novick, R., Weisskopf, M.C., Berthelsdorf, R., et al., 1972, ApJ, 174, L1
56. Pacciani, L., Costa, E., DiPersio, G., et al., 2003, Proc SPIE, 4843, 394
57. Pavlov, G.G., Bezchastnov, V.G., 2005, ApJ, 635, L61
58. Pavlov, G.G., Gnedin, Yu. N., 1984, Ap. Space Phys. Rev. [Sov. Sci. Rev. E] 3, 187
59. Pavlov, G.G., Shibanov, Yu.A., 1979, ZhETF (Sov. Phys. JETP), 76, 1457
60. Pavlov, G.G., Zavlin, V.E., 2000, ApJ, 529, 1011
61. Pavlov, G.G., Shibanov, Yu.A., Zavlin, V.E., Meyer, R.D. 1995, in *The Lives of the Neutron Stars*, eds. A.Alpar, Ü. Kiziloglu, J. van Paradijs, Kluwer, Dordrecht, 71
62. Pavlov, G.G., Zavlin, V.E., Aschenbach, B., et al., 2000, ApJ, 531, L53
63. Pavlov, G.G., Sanwal, D., Garmire, G.P. Zavlin, V.E., 2002, in *Neutron Stars in Supernova Remnants*, eds. P.O. Slane, B.M. Gaensler, ASP Conf. Ser., v.271, ASP, San Francisco, 271
64. Pavlov, G.G., Sanwal, D., Teter, M.A., 2004, in *Young Neutron Stars and Their Environments*, eds. F. Camilo, B.M. Gaensler, ASP, San Francisco, 239
65. Romani, R.W., 1996, ApJ, 470, 469
66. Romani, R.W., Miller, A.J., Cabrera, B., et al., 2001, ApJ, 563, 221
67. Ruderman, M., 1991, ApJ, 366, 261
68. Rutledge, R.E., Fox, D.B., 2004, MNRAS, 350, 1288

69. Sanwal, D., Pavlov, G.G., Zavlin, V.E., et al., 2002, ApJ, 574, L61
70. Schnopper, H.W., Kalata, K., 1969, AJ, 854
71. Seward, F.D., Slane, P.O., Smith, R.K., et al., 2003, ApJ, 584, 414
72. Shaw, P.S., Hanany, S., Liu, Y., et al., 1991, Proc. SPIE, 1548, 118
73. Silver, E.H., Weisskopf, M.C., Kestenbaum, H.L., et al., 1978, ApJ, 221, 99
74. Silver, E.H., Weisskopf, M.C., Kestenbaum, H.L., et al., 1979, ApJ, 232, 248
75. Silver, E.H., Ziock, K.P., Dwyer, J., et al., 1994, Proc. SPIE, 2283, 60
76. Smith, F.G., Jones, D.H.P., Dick, J.S.B., et al., 1988, MNRAS, 233, 305
77. Sturrock, P.A., Petrosian, V., Turk, J.S., 1975, ApJ, 196, 73
78. Tananbaum, H., IAU Circ. 7246
79. Tiengo, A., Mereghetti, S., 2007, ApJ, 657, L101
80. Tsai, W., Erber, T., 1975, Phys. Rev. D, 12, 1132
81. Thompson, C., Duncan, R., 1995, MNRAS, 275, 255
82. Thompson, C., Duncan, R., 1996, ApJ, 473, 322
83. van Adelsberg, M., Lai, D., 2006, MNRAS, 373, 1495
84. van Kerkwijk, M., Kaplan, D., 2007, Astrophys. Space Sci., Online First
85. Weisskopf, V.F., 1936, Kgl Dansk. Vid. Selsk., 14, 1
86. Weisskopf, M.C., Berthelsdorf, R., Epstein, G., et al., 1972, Rev. Sci. Instr., 43, 967
87. Weisskopf, M.C., Cohen, C.G., Kestenbaum, et al., 1976, ApJ, 208, L125
88. White, N.E., Swank, J.H., Holt, S.S., 1983, ApJ, 270, 711
89. Wolff, R.S., Angel, J.R.P., Novick, R. et al., 1970, ApJ, 160, L21
90. Zavlin V.E., Pavlov G.G., Sanwal D., et al., 2000, ApJ, 540, L25

Chapter 23
GeV Gamma-Ray Pulsar Detection

David A. Smith and David J. Thompson

23.1 Introduction

Pulsar observations at high energies, i.e., beyond radio frequencies, shed a different light on the mechanisms at work near rotating neutron stars. This article assumes that the reader is already convinced that substantially increasing the known sample of gamma ray pulsars beyond the $\sim$8 seen with the instruments on the Compton Gamma Ray Observatory (CGRO) is a worthy goal [36, 63], to focus on *how* this goal is being pursued.

"Detection" comes in degrees. Simply counting the number of gamma ray excesses positionally coincident with known neutron stars is useful for population studies, even if source confusion will compromise some associations. Pulsed detection removes identification ambiguities while bringing precious information about beam geometry via light curve shapes: the EGRET pulsars mainly have two peaks, with the leading peak slightly offset compared to the single radio peak, and we would like to know how general this rule is [64]. Accurate determination of the cut-off energy, and, hopefully, the shape of the cut-off, is the next step. And finally, with enough photon statistics the spectral shape can be broken down by phase-interval. Having these observables on a large sample of pulsars should allow major steps forward in describing where and how high energy particles are accelerated.

Figure 23.1 illustrates the potential gain from increased detector sensitivity. The figure-of-merit $\sqrt{\dot{E}}/d^2$ assumes that the efficiency for gamma ray production decreases with the square root of the spin-down energy, $\dot{E}$ and that the observed

D.A. Smith
Centre d'études nucléaires de Bordeaux Gradignan – CENBG UMR 5797, CNRS/IN2P3 – Université Bordeaux 1, Chemin du Solarium – BP120 33175, Gradignan Cedex, France
e-mail: smith@cenbg.in2p3.fr

D.J. Thompson
Astrophysics Science Division, NASA Goddard Space Flight Center, Greenbelt, MD 20721, USA
e-mail: David.J.Thompson@nasa.gov

W. Becker (ed.), *Neutron Stars and Pulsars,* Astrophysics and Space Science Library 357,

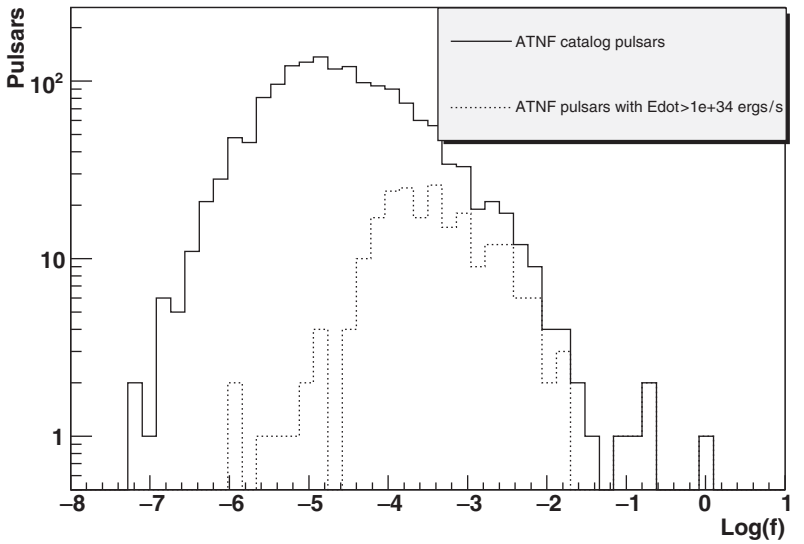

Fig. 23.1 Illustration of how increased detector sensitivity can increase the number of detectable pulsars: "f" is $\sqrt{\dot{E}}/d^2$, normalized to the value for Vela, a figure-of-merit for possible gamma ray intensity (see text). Shown are all pulsars in the ATNF database (solid histogram), and those with $\dot{E} > 1 \times 10^{34}\,\mathrm{erg\,s^{-1}}$ (*dotted histogram*). The EGRET pulsars have $f > 0.02$. Improved detector sensitivity will give access to the body of the population

flux depends on the distance d of the pulsar. If true, then EGRET saw the tip of an iceberg, and improved sensitivity will lead to a disproportionately large number of detectable objects.

Astrophysical gamma ray spectra are typically power laws, but intrinsic to pulsar dynamos is a maximum accelerating voltage. This, combined with gamma self-absorption mechanisms, leads to sharp cut-offs in the power laws. The cut-off energy E_o as well as the shape of the spectral rollover depend on the region around the neutron star where the gammas are generated, and the details of the accelerator. For a spectral shape

$$\frac{d\phi}{dE} \propto E_\gamma^{-a} e^{(-E_\gamma/E_o)^b} \tag{23.1}$$

models predict values of b from 1 ("exponential cut-off") to 2 ("super-exponential"). The 1–30 GeV energy range is particularly important. For the Cherenkov telescopes these are the lowest energies, while for the satellite detectors it is the mid- to high-end.

Unsurprisingly, these few lines imply that the instrument parameters to optimize are the same as for any telescope:

- Good sensitivity, for high photon statistics, even on weaker sources. This translates to a large detection surface and good background rejection.
- The energy resolution and scale need to be well understood.

Fig. 23.2 The four telescopes of the VERITAS Cherenkov imager array in January 2007 (Image courtesy of VERITAS Collaboration)

- Angular resolution is triply important: It helps by (1) reducing the isotropic backgrounds, thus enhancing sensitivity, (2) improving source localization to improve identification, and (3) distinguishing between the pulsar and its nebula, if there is one.

This article begins with a reminder of the basics of GeV to TeV gamma ray detection, in two domains, mainly, Atmospheric Cherenkov Telescopes ("ACT," see Figs. 23.2 and 23.6) useful for energies $E_\gamma > \mathcal{O}(100\,\mathrm{GeV})$, and orbital telescopes, useful in the GeV energy range (Figs. 23.3 and 23.12). The intent is to help the reader understand the key design trade-offs. The choices, and the results and/or prospects of the three Cherenkov telescopes most pertinent for pulsars are summarized, with a glimpse at the next generation now on the drawing boards. Further, AGILE was launched 23 May 2007, and two other satellites are also waiting. Of these, the Gamma-ray Large Area Space Telescope ("GLAST") has the best short term pulsar prospects, and receives more attention than the others.

23.2 GeV–TeV Gamma Ray Detection

Gamma ray telescopes have to overcome the background from high energy cosmic rays (ions and electrons), a background for which, e.g., radio and optical telescopes have no analogy. There is also a background of gamma rays not coming from the source under study, for example diffuse gammas from the Milky Way, or albedo gamma rays produced by cosmic rays in the atmosphere.

High energy photons and ions interact with matter in (superficially) similar ways.[1] To understand what drives instrument design and limits telescope performance, both interactions need to be considered. The Particle Physics Booklet [71] details the following considerations nicely.

[1] "High energy" in this article means the range encompassing $10^{23}\,\mathrm{Hz} = 0.42\,\mathrm{GeV}$ to $1\,\mathrm{TeV} = 1.6\,\mathrm{erg}$.

Fig. 23.3 The Large Area Telescope mounted on the (then incomplete) GLAST satellite, December 2006 (Image courtesy of NASA/General Dynamics)

The sensitive area of gamma ray telescopes derives from the longitudinal development of the electromagnetic cascade initiated by the primary photon. For an air Cherenkov telescope, this is because the area illuminated on the ground depends on the altitude at which the cascade radiates the Cherenkov light. Satellites are limited by size and especially weight. Weight scales as surface times thickness, and thickness by the targeted energy resolution via the longitudinal shower containment. The natural thickness scale is called the *radiation length*, X_0. It scales roughly as A/Z^2 of a material, where A and Z are the atomic mass and number, respectively. (And hence, even more roughly, as $1/A$.) For N_0 incident gamma rays, after penetrating a depth X there will be

$$N = N_0 e^{-X/X_0} \tag{23.2}$$

remaining. For air, tungsten, and cesium iodide (CsI), the values of X_0 are 36.66, 6.76, and 8.39 g cm^{-2}, respectively. [One atmosphere is thus (1,013 g cm^{-2}/ 36.66 g cm^{-2}) = 27.6 radiation lengths, while the GLAST LAT is a little under $10X_0$.] On average, a gamma will produce an electron–positron pair after traversing one radiation length of matter, $\gamma X \rightarrow e^+e^-$, where the X represents momentum exchange with an atom. Similarly, the distance scale over which the $e^{\pm}$ will radiate a new gamma is also X_0 ("bremsstrahlung"). Hence, after $n = X/X_0$ lengths, the number of $e^{\pm}$'s is 2^n. This increase continues until the average electron energy $E_\gamma/2^n$ becomes comparable to the pair-production threshold energy $2m_ec^2$ or, more precisely, to the somewhat lower "critical energy" E_c (where ionization and bremsstrahlung energy losses match). E_c scales inversely as Z and ranges from 10 MeV in tungsten, to 30 MeV in silicon (thus defining the minimum energy for AGILE and GLAST), to 80 MeV in air.

Angular resolution is dominated by the multiple Coulomb scattering of the $e^{\pm}$ pair(s). In simplified form, it is described by the parameter

$$\theta_{ms} \simeq \frac{13.6Z}{pc}\sqrt{X/X_0}, \tag{23.3}$$

where the charged particle momentum pc is expressed in MeV. θ is the angle between the initial charged particle direction and its direction after a thickness X, θ is distributed as a Gaussian of width θ_{ms}, with non-Gaussian tails arising from occasional hard scatters with nuclei.

Cosmic rays (protons and other nuclei) will traverse longer distances before starting a particle shower, the exponential scale length here being the *nuclear interaction length*, λ_I. For air, tungsten, and CsI, the values of λ_I are 90, 185, and 167 g cm^{-2}, respectively. The atmosphere is $>11\lambda_I$ thick – no cosmic rays get through – while the GLAST LAT lets 60% get through with only ionization signals.

The number of gamma rays recorded after time T is

$$N_\gamma = T\int_{E_0}^{\infty}\frac{d\phi}{dE}A(E)dE \tag{23.4}$$

for a differential flux at the source $\frac{d\phi}{dE}$ and an effective, energy-dependent area $A(E)$, to be discussed below. A similar rule holds for the background N_{bgd}, that is, the sum of Milky Way gammas, electrons, and cosmic ions feinting gamma rays and passing all selection cuts. The minimum flux sensitivity is for $\sigma = N_\gamma/\sqrt{N_{bgd}}$ greater than some minimum, typically 5. Detector and trigger design, and data analysis, aim to maximize the ratio $Q = \varepsilon_\gamma/\sqrt{\varepsilon_{bgd}}$, via a high efficiency for gamma rays, ε_γ, and a low efficiency for background, ε_{bgd}. Angular resolution helps.

The minimum and maximum gamma ray energies exploitable by a given instrument depend on various things. The maximum comes mainly from requiring $N_\gamma > 5$ for T as large as reasonable (months to years for a satellite, and hours to days for a Cherenkov telescope). Typically, $\frac{d\phi}{dE} \propto E^{-2}$, hence, a tenfold increase in energy means a tenfold decrease in counting rate. Other factors, e.g., backsplash for EGRET or shower truncation for a high-altitude Cherenkov telescope, will be discussed

below. The minimum energy comes essentially from the minimum signal strength: a satellite built thick enough to contain high energy showers will perform poorly near E_c, whereas Cherenkov telescopes run into the fluctuations of the night sky light, as will be discussed in the context of (23.5).

23.3 Atmospheric Cherenkov Detectors

For years, the hopes for Cherenkov telescopes were at odds with the few detections and limited science actually achieved. The seminal early review of the atmospheric Cherenkov technique is [68]. More recent reviews are [30, 46], and a pre-HESS snapshot of the state of the field is [57]. Large Cherenkov imager arrays have now crossed the barrier of 10 mCrab sensitivity, and, at least for nonpulsed sources, the results are (finally!) impressive.[2]

Can ground-based gamma-ray telescopes also contribute to pulsar science? We will now focus on how to attain sensitivity at the low end of the Cherenkov energy range adequate to study pulsars.

The electrons in the cascade are ultra-relativistic ($v \simeq c$) and above the threshold for Cherenkov radiation, that is, $v > c/n$ where c is the speed of light and n is the index of refraction at visible (blue) wavelengths. Cherenkov light is emitted above and below shower maximum, which occurs $\sim$6 radiation lengths into the atmosphere for $E_\gamma = 30$ GeV. The depth of penetration increases logarithmically with the energy, as illustrated in Fig. 27.18 of [71]. The scale height of the atmosphere is about 7 km, so the maximum development is near $h_{max} = 7 \ln(27.6/6) \simeq 11$ km above sea level, assuming normal incidence on the atmosphere (i.e., the source near zenith above the telescope). The typical luminous width of about 20 m is determined by the Moliere radius of the cascade.

The Cherenkov light is emitted at an angle $\breve{\theta} = \arccos(c/nv) \simeq 0.6^\circ$, or 10 mrad ($\delta \equiv n - 1 = 2.73 \times 10^{-4}$ for air at sea level, decreasing with the same 7 km exponential law as above). Multiple scattering is of the same order, so that the Cherenkov light is radiated into a cone of half-angle $\simeq$20 mrad. Cherenkov telescopes are generally located at sites 2–3 km above sea level, hence the radius of the light pool illuminated by the cascade is 0.02×9 km $\simeq 180$ m, for an area of $\pi \times 180^2 \simeq 10^5$ m^2. Figures 23.4 and 23.10 confirm this order-of-magnitude. The *effective* area is somewhat less, being the geometrical area multiplied by the trigger and analysis efficiencies, which depend on the distance of the Cherenkov telescope from the center of the Cherenkov light pool. (Stated backwards: the farther the extrapolated impact point of the primary gamma ray is from the telescope, the lower the detection efficiency). These simple considerations are the primary design drivers.

[2] The Crab nebula flux is used as a reference. In a νF_ν representation, near 100 GeV the spectrum is flat, at $\sim 0.8 \times 10^{-10}$ erg cm^{-2} s^{-1}. EGRET measured an integral photon flux above 100 MeV of 226×10^{-8} cm^{-2} s^{-1}, with a differential spectral index of 2.2, from both the nebula and the pulsar.

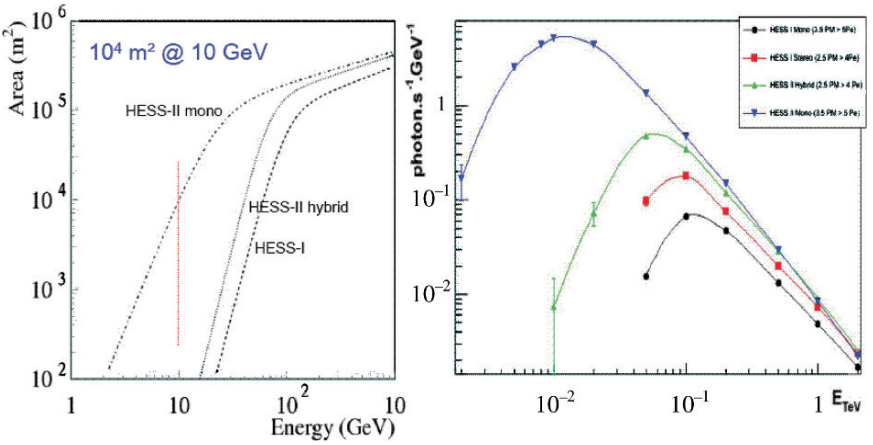

Fig. 23.4 *Left*: HESS effective areas. The left-most curve is for the HESS-II 27 m mirror running alone. The right-most curve is for the HESS-I four-telescope array. The middle curve is for the five telescopes running together. *Right*: Counting rates obtained by convoluting the effective area with the spectrum of a hypothetical source passing near zenith and having a Crab-like spectrum [31]

At 50 GeV there is roughly one Cherenkov photon per square meter, in the wavelength range of typical photocathodes. The particles and the light travel downward at nearly the same speed, with the consequence that the Cherenkov photons reach the ground within the same few nanoseconds regardless of the altitude of emission. The speed of the blue flash allows fast electronics to reject night sky background light.

The name *imager* arises because the hundred to thousand pixel camera in the mirror focal plane records the image of the shower compacted by perspective into a more or less long cigar shape (depending on the distance of the gamma's impact point from the telescope). We now know that imaging is much better than other Cherenkov detector designs [58]. Further, stereo imagers might succeed in taking their high gamma efficiency and cosmic ray rejection below 50 GeV, that is, to the pulsar regime. The detection surface is *huge*, even compared to radio telescopes, compensating for the low duty cycle (10%) imposed by the need for clear, moonless nights, and the small field of view of a few degrees, compared to satellites (>2 sr).

How to Lower the Cherenkov Energy Threshold

Don't confuse *mirror* area A_M with the *detection* area, $A(E)$. The former determines the minimum gamma ray energy, and the latter, the flux sensitivity.

The number of Cherenkov photons reaching the ground is a nearly linear function of the primary gamma ray energy, E_γ. The density (number per square meter) depends on the size of the light pool which, we have seen, depends on the observatory altitude. Multiplying by A_M gives the number of Cherenkov photons received.

Mirror reflectivities are high (>90%) but photomultiplier cathode efficiencies are low (<30%), so that the number of photoelectrons is a factor of $\mathcal{O}(10)$ smaller than the Cherenkov yield.[3]

The minimum energy is then determined by the threshold setting, in photoelectrons, of the electronic discriminators downstream of the PMTs. If set too low, the trigger rate will be saturated by fluctuations in the night sky background light, ϕ. A typical value integrated over the PMT sensitivity range is $\phi = (1.8 \pm 0.3) \times 10^{12}$ photons m^{-2} sr^{-1} s^{-1} [23]. It is the *fluctuations* in this rate that determine the minimum threshold setting. The classic formula is [58, 68]

$$E_{th} \propto \sqrt{\frac{\Omega \phi \tau}{A_M \varepsilon}}. \tag{23.5}$$

Here, Ω is the solid angle of the field-of-view of the individual PMTs. The apparent size of the air shower, (the Moliere radius of 20 m seen from 10 km gives 2 mrad), imposes a minimum value of Ω. For modern imagers, typical pixel diameters are 2 mrad, hence $\Omega \simeq \pi 0.001^2 = 3 \times 10^{-4}$ sr.

For nonzero zenith angles, shower maximum occurs a bit higher and much farther away. The illuminated ground area is broader when hit obliquely, making a lower density of Cherenkov photons and, consequently, a higher energy threshold. One gains a larger gamma ray collection area, useful for high energy studies but pulsars pretty much need to pass high above a Cherenkov telescope for any hope of detection.

In (23.5), the "easiest" variable to work with to decrease E_{th} seems to be A_M. Solar power plants built after the 1973 oil crisis have A_Ms in the tens of thousands of square meters. The review [58] summarizes their conversion into gamma ray telescopes. Indeed, the lowest energy search for a pulsed Crab signal to date comes from the experiment that used the largest mirror area, CELESTE, with $A_M = 2{,}800\,\mathrm{m}^2$ [44]. The upper limit on the Crab pulsar was expressed as an exponential cutoff $e^{-E\gamma/E_0}$ to the power law measured by EGRET, with $E_0 = 26$ GeV.

The definition of the "energy threshold" E_{th} used in the Cherenkov domain bears mention. The heroic era of the field was marked by systematic uncertainties that were large, changing, and poorly quantified. To avoid overly optimistic claims regarding the energy scale, the energy threshold was defined as the energy of the maximum counting rate. Figure 23.4 illustrates this: $A(E)$ (left panel) multiplied by a spectrum gives the differential counting rate (right panel). For modern Cherenkov instruments, this definition is somewhat unfortunate – half of the detected gamma rays are below the "threshold." For gamma-ray pulsars, likely to have a sharp spectral cut-off in the low end of the energy range, a more useful figure-of-merit is the energy for which $A(E)$ has some small but useful value, e.g., 100 m^2.

[3] Yes, photodetectors with higher quantum efficiencies ε exist. But to date none has the nanosecond speed, τ, combined with the single photon resolution of photomultiplier tubes (PMTs), available in a thousand thumbnail-sized channels. Furthermore, Cherenkov light peaks in the blue whereas the background increases towards the red, where typical CCD efficiencies peak. A factor of 2 in photoelectrons and of $\sqrt{2}$ in minimum energy threshold due to improved photodetectors may come someday.

Cherenkov Imagers

The Cherenkov imager breakthrough exemplified by HESS [3] builds on three elements: large mirrors (pioneered by the 10 m Whipple telescope [69]); fast, small-pixeled cameras (pioneered by CAT [50]); and stereo (pioneered by HEGRA [2]). The first two are driving E_{th} down to the pulsar range via (23.5), but all three contribute to the performance revolution, which comes mainly from background rejection (the Q-factor mentioned above).

Cosmic rejection exploits the differences between the generally smooth, reproducible electromagnetic cascades and the more chaotic, variable hadron-induced particle showers. Some background cannot be identified, e.g., when much of the initial energy goes to a pion, followed by $\pi^o \rightarrow \gamma\gamma$ or $\pi^{\pm} \rightarrow e\nu$ mimicking a cosmic gamma. In these cases, as for cosmic electrons, the only salvation is angular resolution. The energy spectrum of electrons is steeper than that of ions, making the electron background proportionally larger at lower energies.

Arrays of imagers help doubly. Single atmospheric muons landing a few mirror diameters from the telescope give images resembling low energy gammas in some cases, but visible in only one telescope [66], and thus easily rejected in multiple mirror arrays [29]. More importantly, the multiple images of a given shower seen from different perspectives permit tight constraints of the impact point, the primary energy, and the initial direction. The single gamma ray reconstruction has reached the point that HESS is now an *imager* in the classic sense of the term – the image of the gamma ray emitters in the field of view is sharp enough to allow detailed comparison with X-ray and radio images, that has allowed, for example, the HESS results on Vela [4].

23.3.1 VERITAS

The four-telescopes shown in Fig. 23.2 belong to VERITAS (Very Energetic Radiation Imaging Telescope Array System), and are located near the base of Mt. Hopkins, home of the Fred Whipple telescope. The facility was originally planned with seven telescopes [70], and would have had the largest effective area of any Cherenkov telescope, giving particularly good sensitivity at the highest energies. Funding and siting issues have so far limited them to four, the first of which was commissioned in February 2005 [33].

"Optimal" layout of an imager array depends on the array's goals, and the VERITAS collaboration has been a leader for blazar studies, where the high-energy end of the spectrum is of particular interest, and the sources are point-like. These favor a large inter-telescope spacing, and the traditional $\sim$2–3 km observatory altitudes (e.g., not higher). Figure 23.5 shows VERITAS' expected sensitivity [33, 35]. The "Crab-like source" refers to the nebula, not the pulsar, but the Crab pulsar and nebula fluxes match somewhere in the range between 10 and 40 GeV. VERITAS may, over time, accumulate a pulsed signal on the Crab.

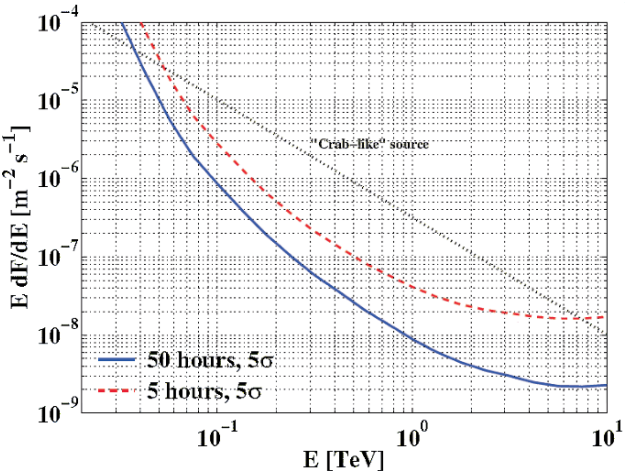

Fig. 23.5 Expected sensitivity for the VERITAS four-telescope array located at the Mt. Hopkins basecamp, i.e., lower altitude and a smaller inter-telescope distance than will be had on Kitt Peak (S. Fegan, ICRC Tsukuba)

23.3.2 MAGIC

La Palma in the Canary Islands was the site of path-breaking cosmic ray and gamma ray detectors such as AIROBICC and HEGRA. The former was an all-sky Cherenkov detector that was the first to exclude bright multi-TeV gamma ray sources over the whole sky. The latter was the first stereo Cherenkov imager array, although with relatively small mirrors (and so an energy threshold beyond the range of interest for pulsars), and achieved several interesting results. Continuing at the same site is MAGIC (Major Atmospheric Gamma-Ray Imaging Cherenkov, Fig. 23.6), a single 17 m Air Cherenkov telescope [21].

They recently published a compelling 2.9σ pulsed excess from the Crab [7]. They do not claim a detection – the standard in the field is 5σ – but unpublished results from CELESTE look quite similar [18], and the Crab pulsar likely has an exponential cut-off ($b = 1$ in (23.1)) with $E_o \simeq 25$ GeV. MAGIC points out that a super-exponential ($b = 2$) with $E_o \simeq 60$ GeV would be compatible with their data. The lowest energy point obtained for the Crab nebula with MAGIC is 60 GeV, like CELESTE's [44].

Figure 23.7 forecasts that MAGIC should access the EGRET gamma-ray pulsar PSR B1951+32 [5], and indeed their recent limits, combined with the large uncertainty on EGRET's last spectral point, make it apparent that the exponential cut-off lies in the range $10 < E_o < 30$ GeV [8]. MAGIC also obtained upper limits on the millisecond pulsars PSR B1957+20 and PSR J0218+4232 [45, 47]. About their detection of LSI +61 303 [6]: microquasars might not be as far removed from pulsars as you might think [19]!

Fig. 23.6 The second MAGIC telescope, still under construction at La Palma, with completion expected in 2007 (Figure courtesy of M. Rissi)

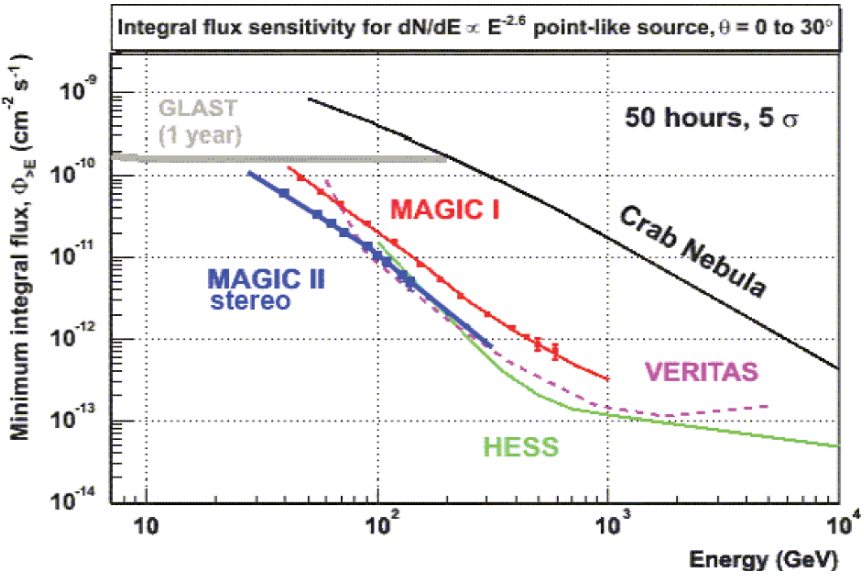

Fig. 23.7 Predicted sensitivity of the MAGIC single and double telescopes, compared to other instruments [62]

When the second telescope turns on, 85 m from the first, MAGIC 2 should have the sensitivity predicted in Fig. 23.7. They aim to halve their threshold and double their sensitivity [62]. The MAGIC collaboration has pushed towards lower energies, with the largest A_M and the most aggressive program for, e.g., improved

photocathode quantum efficiencies. The spread in predicted sensitivities between VERITAS (Fig. 23.5) and MAGIC (Fig. 23.7) cannot be easily understood in the context of (23.5). E_{th} should scale with the mirror diameter, in which case the 17 m mirror only "buys" a 30% improvement over the 12 m mirrors used by VERITAS and HESS. Furthermore, one would expect better sensitivity from the four-telescope array than from the twin telescopes.

23.3.3 H.E.S.S

Figure 23.8 shows HESS's sensitivity (High Energy Stereoscopic System, in Namibia), extending down to 100 GeV for the four 12-m telescope array. HESS and VERITAS resemble each other and the same general remarks about pulsar prospects apply. This said, the HESS design favors galactic targets (the wider camera field-of-view and a slightly smaller telescope spacing are better for extended sources) as does its southern site. An example of HESS performance for pulsars is shown in Fig. 23.9, the (best-looking) extract from a search for pulsations from the 5.8 ms pulsar PSR J0437-4715. One of the closest known pulsars (160 pc), with a robust $\dot{E}$, it has the fourth largest known $\sqrt{\dot{E}}/d^2$ (14% of Vela's) which, a criterion for selecting gamma-ray pulsar candidates (Fig. 23.1). HESS claims no detection,

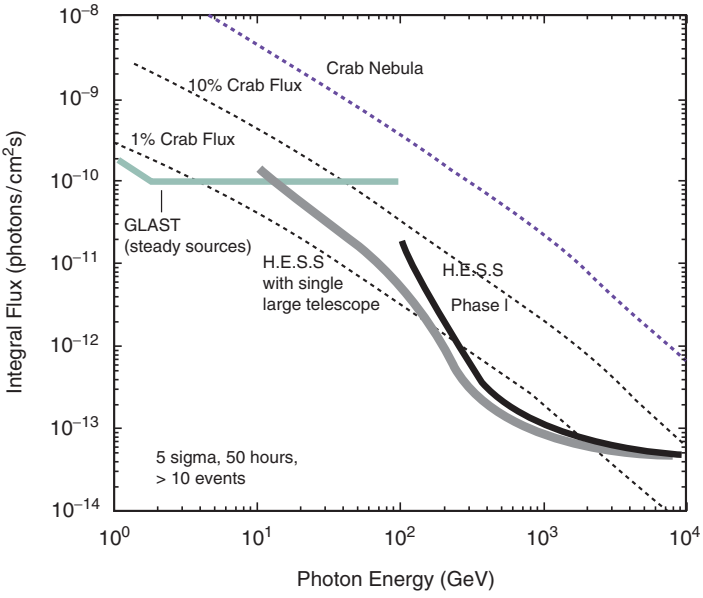

Fig. 23.8 HESS-I (four 12-m telescopes) and HESS-II (an additional 27-m unit) sensitivities [51]. The big new telescope running alone will have a lower threshold, but not the full background rejection of the array at the lowest energies. GLAST sensitivity becomes flat above a few GeV if one requires a minimum number of counts to claim a detection (here, 10 gamma rays)

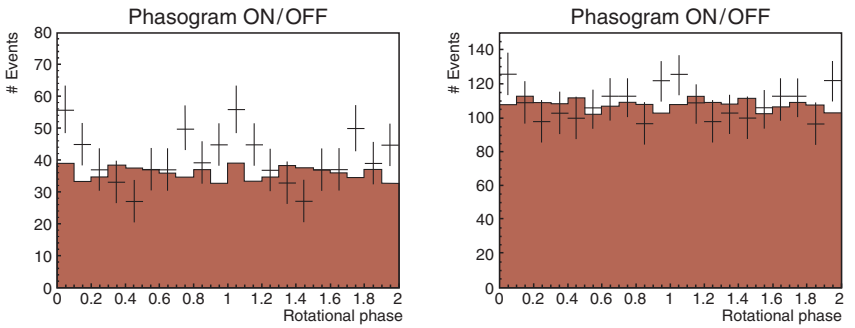

Fig. 23.9 H.E.S.S. search for pulsations from PSR J0437-4715 [20] for standard cuts (*left*) and cuts favoring lower energies (*right*). The crosses are for 8.2 h of ON-source data, and the solid histogram is from OFF-source data. The $\sim 3\sigma$ deviation from a flat light-curve shown here is diminished by several trials involved in finding the optimal gamma-ray selection cuts

nor is there a nearby EGRET source. The HESS upper limit was obtained above 100 GeV [20], less than 50 GeV beyond the cut-off predicted in [28]. HESS has also searched for pulsations from Crab, Vela, and '1706-44 [55, 56].

Construction is currently under way for a major addition to HESS. The HESS Phase II array will add a single 27 m telescope to the middle of the present array [51, 67]. The projected effective area and counting rate is shown in Fig. 23.4, and the sensitivity in Fig. 23.8. The new telescope is expected to be complete in 2008, with science in 2009.

With regards to pulsar searches, one big telescope may give them access to some first ground-based detections. The trigger rate from muons is huge, best reduced via a coincidence with another telescope. The initial HESS II design was to have *two* 30 m telescopes The energy threshold E_{th} of the existing telescopes is limited by (23.5). Hence, the potential decrease in E_{th} a pulsar afficionado might have hoped for with the new 27 m telescope will not be obtained, at least in the short term.

The Japanese-lead CANGAROO imager array located in Australia has also contributed several important results to TeV gamma ray astronomy. The instrument is not optimized for the low energies necessary for pulsar searches.

23.3.4 The Farther Future: 5@5, CTA, and LTT

Naturally, the Cherenkov community is preparing the next order-of-magnitude increase in size and performance. Part of the community is motivated to pursue spectra to the highest energies, to study blazars and the origins of UHE cosmic rays. Fluxes are low, so they want many telescopes with large separations. Cherenkov intensities are high, so the mirrors need not be huge. But the cameras need to have large fields of view, i.e., many channels of electronics, to contain large showers landing far from the mirrors. Current observatory altitudes are fine.

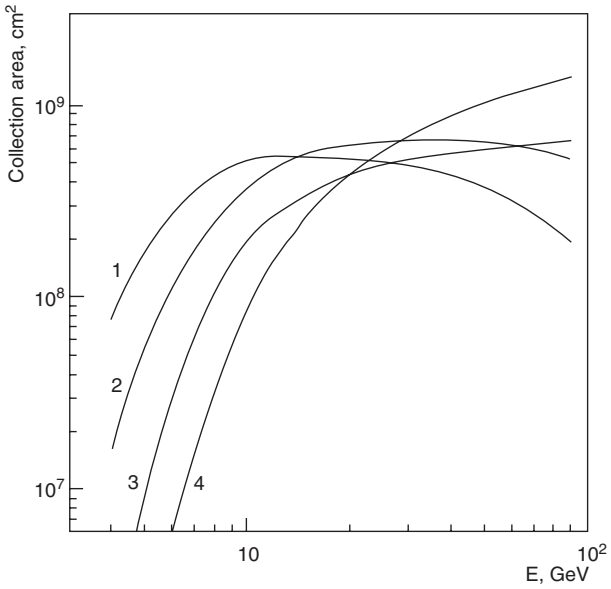

Fig. 23.10 Predicted gamma ray collection areas for a system of five 30-m Cherenkov imagers at altitude 1,800 m, requiring that a shower be seen by 2, 3, 4, and 5 telescopes (curves 1, 2, 3, and 4, respectively) [37]

Pulsar physicists favor high sensitivity and accurate spectroscopy in the $\mathcal{O}(10)$ GeV range. They push for bigger mirrors at higher altitude but would compromise on total area. Optimal cost/benefit is perceived differently by the two communities.

The first thorough study of the problem was called "5@5" [1], meaning a 5 GeV threshold with an array of 20 m mirrors 5 km above sea level. Building on the experience acquired with HESS, [37] refines these ideas, with 30 m dishes at 1,800 m. Figure 23.10 shows that twofold telescope coincidences are fully efficient at 10 GeV, meaning that systematic uncertainties in flux determinations should be small enough to allow accurate determination of the high-energy tail of pulsar spectra, with good overlap with satellite measurements.

A "Cherenkov Telescope Array" (CTA) collaboration is currently taking form, with the aim to start construction in early 2010 and do science in 2013 [32]. Further discussion of how a " Low Threshold Telescope" (LTT) would be a useful complement to space-based instruments is in [5].

Optical Pulsar Detections, and Other Fast Optical Transients

The new HESS-II mirror will be ten times larger than those of 8 m class optical telescopes. Could such a huge light bucket be put to some other use? Stellar photometry and optical Crab pulsar measurements are already routinely performed to

calibrate various aspects of the instruments. In particular, the central pixel of an ACT "sees" the point in the sky under study but is otherwise mostly useless for Cherenkov needs. The CAT imager placed a CCD there to track fiducial stars for alignment [11]. It was argued that microsecond atmospheric phenomena, or optical pulsar substructures, could be studied if the Cherenkov telescopes were designed to accommodate "guest" instruments, and these ideas have been formally discussed by the different collaborations.

23.4 Space-Based Observatories

Figure 23.10 illustrates that below a few to several GeV, Cherenkov telescopes are not viable. That's fine, because at those energies useful counting rates can be obtained for large numbers of sources using detection areas smaller than a square meter.

Figure 23.11 sketches the principle of a pair-conversion telescope. After traversing a depth X (23.2), on average a gamma ray converts to an electron–positron pair which leaves an ionization signal in a tracker. The angular resolution is enhanced if the tracks are long, i.e., enough initial radiation lengths to provoke an early conversion. But multiple scattering degrades the resolution if there is *too* much material (23.3). Interactions before the calorimeter, or secondary particles leaking out the back of the calorimeter, will degrade energy resolution. Furthermore, the rate of particle cascades (pions, kaons, protons, neutrons...) due to nuclear interactions can

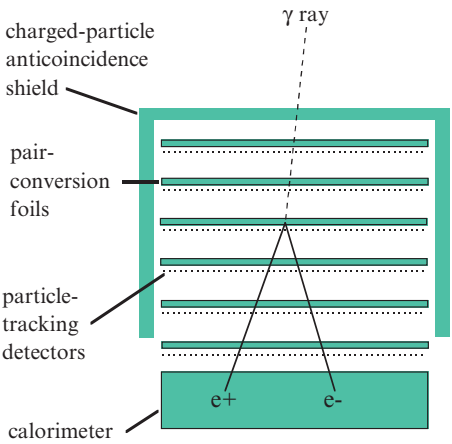

Fig. 23.11 Principle of a space-based gamma ray telescope. The primary photon converts to an electron–positron pair in the tracker. The charged particle tracks provide an estimation of the primary energy, via the opening angle and the amount of multiple scattering. More accurate energy determination comes from the energy deposited in the calorimeter. A charged-particle detector surrounding the tracker and calorimeter provides cosmic ray rejection (Figure courtesy of NASA/Sonoma State University/Aurore Simonnet)

be reduced through clever choice of materials and layout. Optimal gamma-ray telescope design requires several interlaced compromises.

EGRET is the norm, to be matched or surpassed. The main improvements stem from the invention of silicon trackers, whose high granularity allows fine pattern recognition. EGRET's sensitivity at high energies was decreased by *backsplash-induced self-veto*, that is, X-rays radiated in the cascades would leak into the scintillator detector intended to reject charged cosmic rays. The detailed information from a silicon tracker can tag these events. The cosmic ray veto scintillators have also been designed to minimize backsplash issues, with the outermost silicon layers providing further charged particle rejection. Silicon trackers are compact and allow a broader field-of-view for a given weight. They use no consumables that could limit mission duration. EGRET had significant advantages nevertheless. The conversion plates were thinner and there were twice as many tracker layers, with wider spacing, yielding more measurements per track, with less multiple scattering. Rigorous hand scans of nearly all events led to a background rejection, especially at lower energy, that the silicon detectors have yet to demonstrate.

23.4.1 AGILE

The Italian satellite AGILE (Astro-rivelatore Gamma a Immagini LEggero) was successfully launched from Madras on 23 April 2007 (Fig. 23.12) [61]. AGILE has a silicon tracker affording a large effective area compared to the instrument's overall size, over a broad range of angles: at 300 MeV, EGRET had 1,500 cm^2 on-axis, but only 50 cm^2 40° off-axis, whereas AGILE has 500 cm^2 on-axis decreasing only to 350 cm^2 50° off-axis. The cesium iodide (CsI) mini-calorimeter measures energies from 30 MeV to 50 GeV but is thin, being made of only two layers of crystals ($1.5X_0$). Energy resolution at high energies is thus degraded ($\sim$70% at 100 MeV). AGILE also has a thin, lightweight coded mask X-ray imager (called super-AGILE, "super" meaning "above" in Italian in this case), and a plastic scintillator anti-coincidence detector. AGILE should fly for two years.

AGILE pulsar prospects are excellent. The EGRET detections, as well as the hints of signals, should be confirmed, and at least a few new pulsars should come out. They rank 35 radio pulsars as gamma candidates, in order of $\dot{E}^a/d^2$, with $a = 0.5$ and 1 [49]. AGILE aims for absolute timing precision ($\sim$1 μs) significantly better than EGRET's, and could obtain effective resolution of order 50 μs with a good signal-to-noise ratio to search for pulse microstructure on bright pulsars such as Vela.

23.4.2 AMS

AMS (Alpha Magnetic Spectrometer) is designed to search for anti-matter in the cosmic radiation. The instrument weighs 7 tons, more than GLAST (4.46 tons) but

Fig. 23.12 The AGILE satellite integrated on the fourth stage of the PSLV rocket (15 April 2007). Launch on 23 April was successful, and an image of the Vela pulsar was made public on 29 May (Image courtesy of ASI)

less than CGRO (17 tons, the largest scientific payloads ever when launched in 1991). AMS is currently scheduled to be installed on the International Space Station (ISS) in mid-2009.

A Transition Radiation Detector (TRD) and other material in front of a silicon tracker amounts to $0.25X_0$ (see (23.2)). The silicon tracker sits inside a 1 T superconducting magnet, allowing momentum measurements. The silicon tracker has no tungsten to induce $\gamma \rightarrow e^+e^-$ conversions: 80% of the gammas reach the $16X_0$ thick calorimeter without interacting, but can nevertheless still be identified as gamma rays. The minimum particle detection energy is 1 GeV.

AMS' gamma ray capability is developed in the thesis at [25] (in French). At 1 GeV the sensitive area is $100\,\mathrm{cm}^2$, using only the tracker. By 10 GeV the area reaches its plateau of $400\,\mathrm{cm}^2$, and the calorimeter comes into play ($2{,}000\,\mathrm{cm}^2$). The instrument cannot be pointed, and two pieces of the sky about 30° in diameter are never seen, centered at $(l, b) = (120, 30)$ and $(320, -30)$ degrees. Simulated

response to one year on the Vela pulsar, including the exposure time for the ISS orbit and the AMS orientation, shows that cut-offs at 5 and 20 GeV would be easily distinguished. The model discrimination that could be obtained in principle with the excellent energy resolution of the calorimeter ($10\%/\sqrt{E}$, for E in GeV) may be limited by low counting statistics at high energy.

23.5 GLAST: The Gamma-Ray Large Area Space Telescope

The Large Area Telescope (LAT) on the GLAST satellite (Gamma-ray Large Area Space Telescope) will have sensitivity >30x better than EGRET's, even more above 10 GeV. Launch is foreseen for May 2008, followed by a 60-day checkout period, and then a 1-year all-sky survey. Figure 23.3 shows the LAT integrated with the satellite. Whereas the EGRET spark chamber eventually ran out of gas, GLAST could in principle run for many years beyond the five initially planned. The second instrument is the GLAST Burst Monitor, or GBM. Only the LAT is relevant for pulsars, and will be the focus of the rest of this article.

23.5.1 LAT: The Large Area Telescope

The basic elements of the LAT are very similar to those of AGILE, the fundamental difference being that the LAT is *bigger*. The instrument is described in [38, 42]. It is built as a 4-by-4 array of modules, each module having a tracker on top of a calorimeter.

The trackers have 18 silicon layers, measuring track position in both transverse directions [12, 13]. Tungsten at each layer promotes gamma conversion, with extra thickness at the first layers, for a total of $1.5X_0$. The result is a Point Spread Function (PSF) for gamma rays more than three times better than EGRET above 1 GeV. The hodoscopic CsI calorimeters are eight layers thick ($8.5X_0$) [59], allowing good resolution up to 300 GeV. The LAT's sensitivity begins at 30 MeV where the energy measurement is performed by the tracker as much as by the calorimeter. The plastic scintillators (ACD, for Anti-Coincidence Detector) used to reject charged cosmic rays are highly segmented, so that backsplash-induced X-rays radiated transverse to the gamma direction won't decrease the overall gamma efficiency.

Silicon trackers allow a low aspect ratio, giving the LAT both a large field-of-view (>2 sr, or ∼20% of the sky) *and* an effective area over four times bigger than EGRET's. Consequently, GLAST will generally scan the sky, rather than point. Scanning works as follows: on a given 95 min orbit, the LAT will point 35° below the orbital plane. When the satellite reaches the SAA (South Atlantic Anomaly) the ACD high voltages are turned down, data acquisition is suspended for a few minutes, and during this time the LAT rocks to point 35° above the orbital plane. On each orbit, 75% of the sky is covered. Thus, the whole sky is covered every 3 h.

Exposure to the different parts of the sky will be highly uniform, allowing statistical completeness unprecedented at high energy, a significant advantage for population studies. Discovery potential will be high. During the first year on-orbit, LAT will point at targets only exceptionally – standard operating procedure will be the scanning survey mode.

Absolute Timing

A GPS system on the spacecraft provides the UTC time and a Pulse Per Second (PPS) synchronization signal to the LAT and to the GBM. The LAT electronics include 20 MHz scalers. The values latched by the PPS are stored, as are the readings latched by event triggers, thus providing the elapsed time since the previous PPS. The mission requirement is to obtain 10 μs precision on the absolute time, with a goal to achieve 2 μs.

Achieving accurate absolute times in space is notoriously difficult: examples of missions that encountered difficulties are CGRO, USA, Chandra [43], and XMM [34]. As an example, the *i*th date would be assigned to the $(i+1)$th event, in software in one case and in hardware in another. For the latter, not all events were sent to the ground, so that correcting the error in analysis was effectively impossible.

Fortunately, the nature of a high energy gamma detector makes an end-to-end test relatively simple to perform on the ground. Figure 23.13 illustrates the concept. Atmospheric muons are easily detected in the LAT at a rate of ∼480 Hz. The muons are essentially unaffected by their passage through the LAT, and also traverse a suitably placed muon telescope, as in the figure. The muon telescope triggers the readout of a GPS clock in a standalone acquisition system, to be compared offline with the LAT time. Proof-of-principle measurements, made before LAT integration with the spacecraft, were successful in that they revealed some inconsequential timing artifacts of the LAT testbench at the ± 1.3 μs level [60]. By late winter the spacecraft GPS system will be complete and the true test will be performed, allowing months to diagnose and correct problems should any be observed. As a further crosscheck, we have compared GBM and LAT times for muons passing through both the silicon tracker and the BGO detector.

The spacecraft will be receiving its GPS signals through the on-board antennas for the test. Hence, the only aspect that won't have been tested on the ground is that of the GPS system itself when in orbit. This caused problems for, e.g., the USA X-ray telescope a decade ago, but modern systems are more robust. There is thus good reason to believe that LAT event timing will meet the mission requirements.

23.5.2 Detailing the Instrument Response

The LAT response to a particle depends on its energy and species, its angle relative to the detector axis, and its impact point relative to the gaps between the 16 modules.

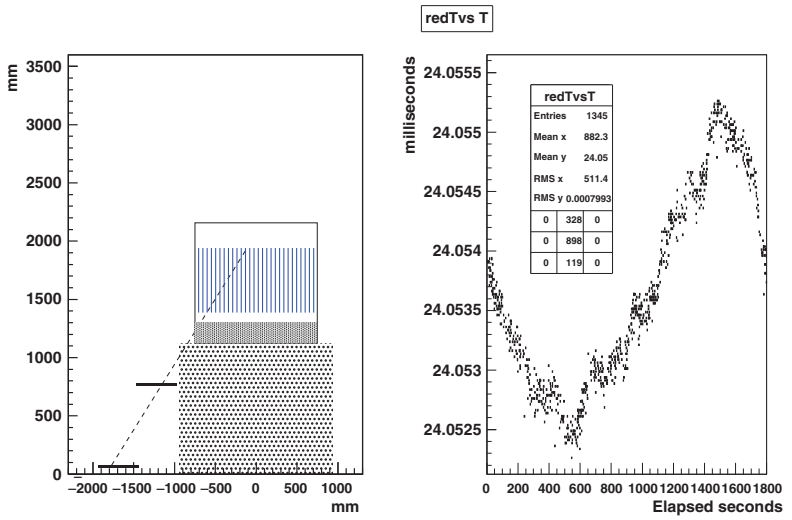

Fig. 23.13 *Left*: Ground tests of the GLAST absolute timestamps use cosmic ray muons (illustrated by the *diagonal dashed line*) traversing both the LAT (drawn perched on a support stand) and a "telescope" of two scintillators with photomultipliers. The muon telescope triggers a GPS in a standalone acquisition system. The vertical-hatched region represents the silicon tracker volume while the grey rectangle below it corresponds to the calorimeter. *Right*: The dates from the LAT and the muon telescope are compared offline. The time differences, in milliseconds, over a half-hour run are shown. The 24 ms offset is an artifact of nonflight equipment. The piecewise linear structure shows the GPS clock correcting its oscillator drift as the GPS satellite positions change. The method provides resolution at the sub-microsecond level. Tests will be performed after integration of the flight electronics, beginning in February 2007

Elaborate Monte Carlo simulations are the primary tool to master this broad phase space. They include detailed detector composition and layout, and accurate models of particle interactions. The output files have the same format as for real data, so the same analysis software is used for real and Monte Carlo data. The gamma reconstruction and background rejection algorithms can thus be refined before launch. For a choice of algorithm and event selection, the detector efficiency, Point Spread Function (PSF), and energy resolution are determined. These are collectively called the IRFs ("Instrument Response Functions"). A likelihood tool uses them to translate a gamma ray count rate into a differential flux measurement.

In this section I outline the efforts to assure the reliability of the Monte Carlo, with a view to minimizing and quantifying the systematic uncertainties that GLAST measurements will have.

The Energy Scale, and Particle Accelerator Studies

Energy determination comes primarily from the calorimeter. (The tracker also provides information: the opening angle between the e^+ and e^- tracks when both are identified, as well as the magnitude of the multiple scattering (23.3) obtained from

the track residuals both constrain the energy. Inversely, the calorimeter provides direction information). Calibrating the entire LAT, over four decades in energy, over the angles and positions mentioned above, is neither practical nor necessary. Instead, the Monte Carlo is the primary tool, used to extend a few key measurements to the entire phase space.

The pulse height observed in a single CsI crystal traversed by a minimum ionizing particle is the basic building block. The ionization energy loss for a particle of charge ze in a thickness x of material with atomic number Z and mass A is $\frac{dE}{dx}_{min} \propto z^2 \frac{Z}{A}$ ((27.1) in [71]), neglecting the energy dependence for clarity. For $z = 1$, that is, muons on the ground or protons on orbit, this gives roughly 12 MeV per crystal. For iron nuclei, the signal is $26^2 = 676$ times larger (8 GeV).

The *exact* response depends on details such as the scintillation light yield as a function of the ionization density ("quenching," [39]). A given energy deposit translates to an well-defined ionization, but the distribution of the ions in the scintillator is quite different for a cascade of electrons induced by a gamma ray and for the heavy ions used as calibrators. Detailed Monte Carlo simulation is delicate. Thus, CsI calorimeters for GLAST were exposed to accelerator beams at CERN in 2002, 2003, and 2006 (electrons, gammas, protons, and pions from a few GeV to a few hundred GeV); GANIL in 2003 (heavy ions at 73 MeV per nucleon); and GSI in 2003 and 2006 (heavy ions at a couple of GeV per nucleon).

For gamma-induced cascades in the calorimeter, the pulseheight in the crystals of each of the eight layers follows the longitudinal shower development described in [71], distorted by gaps and fluctuations. A substantial campaign of measurements at CERN in 2006 with flight-like modules provided detailed comparisons of the true response to Monte Carlo predictions [15]. Some refinements to the Monte Carlo are being made. The CERN campaign also exercised the detector configuration, acquisition, and reconstruction software chains in realistic conditions, allowing weak links to be identified and strengthened.

The energy range of atmospheric Cherenkov telescopes overlaps that of space-based detectors. The overlap range is particularly interesting (e.g., pulsar spectra cut-off) but also subject to the highest uncertainties, due to low statistics in space, and large systematics on the ground. Matching spectra for bright sources will enhance confidence in new, critical measurements. A source with a spectral feature (such as a peak in νF_ν) in the overlap range would be especially useful. HESS [24] and MAGIC [14] have begun studies to implement this idea with GLAST.

IRF Checks Using Vela, the Crab, and Geminga

As stated, the IRFs are calculated using Monte Carlo simulations, then used by the likelihood tool to convert count rates into spectra. They are available at the LAT Web page and reproduced in various places, like [14]. Demonstrating that on-orbit data behave like simulated data will bolster confidence in the accuracy of the fluxes obtained. Bright gamma ray pulsars provide a useful test case, as illustrated in Fig. 23.14. On-peak data for Vela (and Crab and Geminga) provide a gamma ray

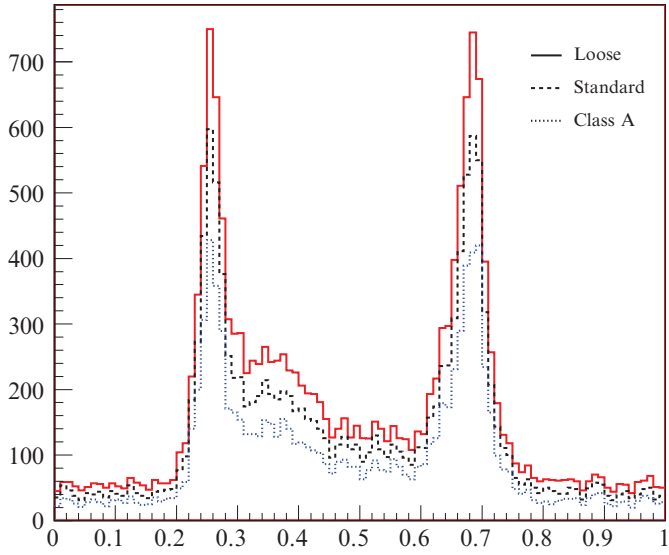

Fig. 23.14 Using bright gamma ray pulsars to validate the GLAST LAT Instrument Response Functions ("IRFs"). Here, 34.7 days of simulated Vela data in survey mode. The dotted (*blue*) histogram is for events passing selection cuts intended to maximize the gamma to cosmic ray ratio ("Class A"). The dashed (*black*) histogram is for less restrictive gamma ray selection cuts, but still more suited to high galactic latitudes. The solid (*red*) histogram loosens those cuts further, recognizing that cosmic ray backgrounds are negligible compared to diffuse gamma backgrounds from the Milky Way, allowing stronger pulsar signals. The cut efficiencies for gamma rays will be compared with real data to reduce systematic uncertainties on flux determinations [54]

sample with a high signal-to-noise ratio. We will run real and simulated data through the reconstruction software, apply the various selection cuts, and compare the real rates at each step with the predicted rates. This should allow us to identify then correct and/or quantify any systematic biases. The point-spread and energy resolution functions will also be checked against real data.

The first 60 days after launch will be used for instrument checkout and calibration ("L&EO," for Launch & Early Operations). The last two weeks of L&EO are likely to be used to adjust thresholds (i.e., data rates) for scan mode, in preparation for the 1-year all-sky survey. Under discussion is to use the two preceding weeks for *pointed* observations. Figure 23.15 shows a possible pointing direction, centered half-way between Crab and Vela. The round symbols are 45° away from the pointing direction, where LAT performance is still high. Note that Vela, Crab, and Geminga are visible. This would also be very useful to test the instrument on-orbit absolute timestamps.

We simulated a two week pointing centered midway between Crab and Vela. Figure 23.15 shows a 45° radius around the point. Using the EGRET flux for Vela [22] yields a prediction of over 10,000 photons. If we assume that the gamma ray flux scales as $\sqrt{\dot{E}}/d^2$, we find that 5(16) other pulsars in the same field of view will yield at least 100(10) gamma rays, respectively [54].

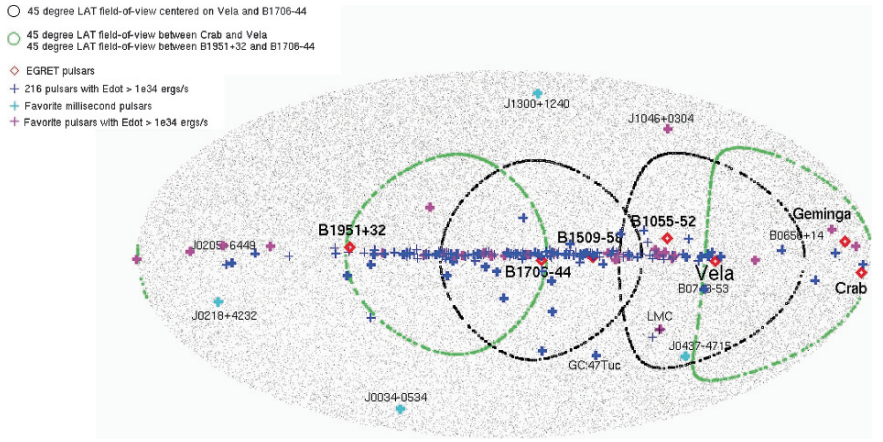

Fig. 23.15 Map in galactic coordinates of the gamma-ray pulsar candidates, i.e., the 215 pulsars from the ATNF database having $\dot{E} > 10^{34}\,\mathrm{erg\,s^{-1}}$. Cross thickness is roughly proportional to $\log(\dot{E}/d^2)^{1/2}$. Four regions of radius 45° are shown: one centered on Vela, another on a point half-way between Vela and the Crab, another centered on PSR B1706-44, and another half-way between '1706 and PSR B1951+32 (Credit: D. Parent)

Pulsar Search Sensitivities

To first order, detecting pulsed gamma radiation is limited by photon statistics (although pulse shape, diffuse gamma-ray backgrounds, spectral shape, and proximity of strong sources affect the ultimate performance). In two years with its scanning mode, LAT will detect about 30 times as many photons for most pulsars as EGRET did in its lifetime. This improvement results in detections intrinsically 25 times fainter or 5 times farther away. Some of the known gamma-ray pulsars are at distances of 2 kpc; therefore LAT will be able to detect some pulsars at the distance of the Galactic Center (7.74 ± 0.42 kpc) or farther.

Detailed simulations are yielding improved sensitivity forecasts [53], while allowing the team to develop the analysis methods to reveal pulsed sources in the LAT data. In particular, the GLAST "Data Challenge 2" was held in the spring of 2006. A very detailed gamma ray sky was modeled, including diffuse gamma and cosmic ray backgrounds. Fifty-five days of on-orbit data were simulated by a small team and then presented to the collaboration, along with the Science Tools software ensemble. Among the thousands of gamma-ray sources (dominated by blazars) there were 413 simulated pulsars, 98 having timing ephemerides provided to the users. The physics ideas used to model the pulsar population are very similar to those described in [26].

Figure 23.16 illustrates the results obtained by one of the three groups that conducted searches for pulsars with known ephemerides [16]. Over 40 of the 98 were easily detected. Other groups obtained similar results. In the figure, some undetected pulsars are brighter than ones easily seen, due to the four effects listed at the beginning of this section. Table 23.1 summarizes the sensitivities obtained from Data Challenge 2.

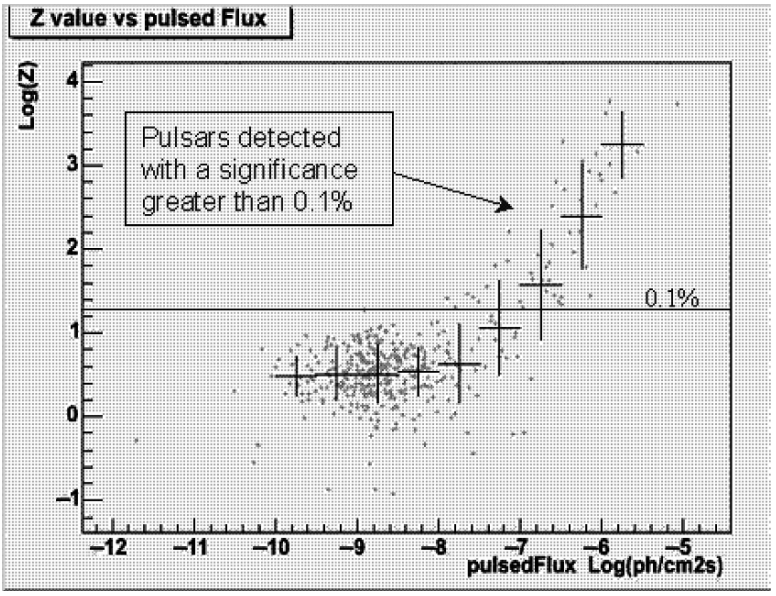

Fig. 23.16 Pulsar detection probability using the Z-test vs. simulated flux, for a population of simulated pulsars distributed over the sky, with known ephemerides but without timing noise [16]

Table 23.1 Pulsar search sensitivities, in $\mathrm{cm}^{-2}\,\mathrm{s}^{-1}$, for the GLAST LAT obtained for the 55 days of Data Challenge 2, and also extrapolated to the first year on orbit

Exposure time	With ephemerides	Blind search
Data challenge 2 (55 days)	6×10^{-8}	3×10^{-7}
1 year sky survey	2×10^{-9}	1×10^{-7}

A significant feature of the pulsar studies with LAT will be the ability to find pulsed emission without pre-knowledge of a pulsar period from radio or X-ray detections. Only the three or four gamma-brightest EGRET pulsars could have been found in a blind search (e.g., [17, 28]). The higher sensitivity of the LAT will allow searches for pulsations in most of the bright unidentified EGRET sources [52]. Geminga is unlikely to be the only radio-quiet gamma-ray pulsar.

One group applied a new time-differencing search technique blind search method [9]. The idea is that instead of a Fourier transform of the gamma ray arrival times, on studies instead the elapsed time between two consecutive events. Timing noise was not included in the simulations, but the method is expected to be less sensitive to the effects of glitches, etc, than methods based on arrival times. The group found 15 pulsars, 3 of which were not among the 98 with available ephemerides. The sensitivities obtained are in Table 23.1.

Source localization (essentially $\mathrm{PSF}/\sqrt{N_\gamma}$) is another strong point for GLAST. The angular distance between the Data Challenge 2 allocated pulsar positions and those obtained from analysis gave mis-position values of order 0.014°. Two

examples illustrate the usefulness: First, EGRET detected PSR B1951+32 only as a pulsed source, but not as a steady source in the 3EG catalog, due mainly to the high gamma background in the Cygnus region. For LAT, this pulsar should appear as a steady source within 3 days. Second, EGRET confused PSR J0218+4232 with the blazar 3C66A one degree away [36]. For LAT, both are detected at the five sigma level in a couple of days of survey mode, their localization in 10 days being of order 0.015° [27].

GLAST data become public after the first year, and the analysis software will also be made available. Information is available at the Science Support Center (GSSC), *http://glast.gsfc.nasa.gov/ssc/* .

23.5.3 Radio Timing of Gamma-Ray Pulsar Candidates

All-sky scanning mode does *not* mean that gamma ray candidates don't need to be prepared for ahead of time. Good candidates are those with the largest spin-down energies, $\dot{E}$ (Fig. 23.1). These happen to also be the pulsars with the most timing noise and glitches [10]. The LAT's performance is high relative to other orbital telescopes, but the absolute counting rates remain low: the Crab pulsar sends a >100 MeV gamma through the LAT volume for every $\sim$600 rotations of the neutron star, less often when accounting for detector efficiency or scanning mode. For PSR B1951+32 cited above, there were 300 photons with $E_\gamma > 0.1$ GeV after standard analysis cuts for the 55 days of Data Challenge 2, that is, a photon every 5 h [48]. For pulsars significantly weaker than the eight seen with CGRO, modest photon statistics will be accumulated over *years*. To have any hope to phase align them, the GLAST LAT requires good radio (or, in some cases, X-ray) timing parameters covering the mission duration.

Therefore, as was done for CGRO [10], a substantial radio timing program is being put in place. That the LAT's sensitivity is larger and that more radio pulsars are known means that the program need be even more ambitious.

The LAT pulsar sample is simply defined: all 215 pulsars (at this time) with $\dot{E} > 10^{34}\,\mathrm{erg\,cm^{-2}\,s^{-1}}$ listed in the ATNF database [40]. This covers essentially all of the pulsars described in the literature as "gamma ray interesting," and overlaps well with criteria based on, e.g., $\sqrt{\dot{E}}/d^2$ (as in [49]). The list is posted at *https://confluence.slac.stanford.edu/display/GLAMCOG/Pulsar+Timing*. Figure 23.15 shows these 215 gamma candidates distributed over the sky.

Three major radio telescopes will do the bulk of the observations, at least for the early part of the mission: these are Parkes for the southern sky, and Jodrell and Nançay for the North. Stable, radio loud pulsars can be observed briefly, as rarely as twice per year. Other pulsars need to be re-timed several times per year, and/or for longer observation times. The total telescope time required amounts to hundreds of hours.

Some particularly interesting pulsars (e.g., PSR J0205+6449 in 3C58) are both very noisy and radio faint (40 μJy at 1,400 MHz) requiring substantial time with the

most sensitive instruments. The LAT collaborators hope to reserve precious time on Arecibo and the Green Bank telescope for, e.g., deep searches of new gamma ray sources likely to be undiscovered radio pulsars.

Therefore, the LAT collaboration wants to enlist the support of other radio telescopes, to cover the long duration of the mission for small sets of pulsars ill-suited for routine automated monitoring by the three "primary" 70-m class antennas, or to simply reduce the workload of the three.

The timing solutions provided by the radio telescopes will be added to a FITS file that will be made public on the GLAST Science Support Center (GSSC) data servers, to be read by the Science Tools as part of the standard data analysis procedures.

Gamma ray analysis of faint objects with the LAT will benefit from LAT expertise even if the analysis code is public. Radio astronomers providing timing solutions will sign those LAT scientific papers which use their ephemerides. The authors believe that it is in the interest of science, and of the radio astronomers themselves, to provide timing information for gamma ray pulsars.

As a final note, let's return to two statements made above: "LAT scans most of the time" and "photons come few and far between" which leads naturally to a discussion of "to point, or not to point." Some authors predict that GLAST could discover scores to hundreds of radio-quiet gamma ray pulsars, like Geminga (for example, [26, 41]). Serendipitous discovery by LAT will require successful blind searches of data sets covering months to years. Reducing the duration over which a gamma ray sample is accumulated will improve search sensitivity. Pointing the LAT increases exposure by a factor of 3–4 for a given object, depending on its location in the sky, prompting some authors to argue in favor of pointed LAT observations, for example, 2-week observations along the plane Milky Way in the second year [52].

23.5.4 Pulsar Science with the GLAST LAT

The capabilities of the LAT will enable a wide range of high-energy pulsar studies, all aimed at greater understanding of the extreme conditions around these neutron stars. Detailed light curves, phase-resolved energy spectra over a broad energy range, and population studies of both radio-loud and radio-quiet pulsars will provide robust tests of pulsar models. Some of the specific scientific goals are described in [65].

23.6 Concluding Remarks

New gamma ray instruments are likely to provide the first GeV pulsar observations since the CGRO mission ended in the year 2000. Barring disasters, the first results should come from AGILE, and shortly after by GLAST, both in space, hopefully

before 2008. On the ground, and at higher energy, the Cherenkov imager arrays HESS and MAGIC have presented upper limits suggesting that the discovery of pulsed emission at several tens of GeV may be just around the corner. The commissioning of the VERITAS array in 2007, and the upgraded detectors HESS-II and MAGIC-2 within 2 or 3 years will drive the field forward.

A real breakthrough in the field would be i) *many* more gamma ray pulsars, and/or ii) detailed measurements of their high-energy cut-offs. GLAST will see scores to hundreds of new pulsars, with multi-GeV sensitivity adequate for cut-off determination on several of them.

This review focused on the basic design considerations limiting Cherenkov and satellite detectors, in the aim of providing the reader with insight into the relative advantages of the various approaches. Energy cut-offs, so critical to discern just where around the neutron star the particles are accelerated to such high energies, and the gammas are radiated, occur in the range where satellite statistics are low but Cherenkov systematic uncertainties are high. This is an excellent example of the complementarity of the two domains.

The next generation of Cherenkov telescopes is on the drawing boards. The trade-off between optimization for galactic vs. extragalactic studies was described, although in all cases gamma ray pulsar studies will make another significant step forward, towards the year 2015.

References

1. F. Aharonian, A.K. Konopelko, H.J. Völk and H. Quintana, Astropart. Phys., **15**, 335–356 (2001)
2. F. Aharonian et al., A & A, **370**, 112 (2001)
3. F. Aharonian et al., Science, **309**, 746 (2005)
4. F. Aharonian et al., A & A, **448**, L43 (2006)
5. J. Albert et al., Astropart. Phys., **23**, 493 (2005)
6. J. Albert et al., Science, **312**, 1771 (2006)
7. J. Albert et al., ApJ, submitted, astro-ph/0702.077
8. J. Albert et al., ApJ, submitted, astro-ph/0705.3244
9. W.B. Atwood, M. Ziegler, et al., ApJ Lett., **652**, 49 (2006)
10. Z. Arzoumanian et al., ApJ, **422**, 671–680 (1994)
11. A. Barrau et al., Nucl. Instrum. Meth., **A416**, 278–292 (1998)
12. R. Bellazzini et al., Nucl. Instrum. Meth., **A523**, 136 (2003)
13. F. Belli et al., Nucl. Instrum. Meth., **A570**, 276 (2007)
14. D. Bastieri et al., Astropart. Phys., **23**, 572–576 (2005)
15. M. Brigida, First Results from GLAST-LAT Beam Test at CERN-PS and SPS, In: *10th Topical Seminar on Innovative Particle and Radiation Detectors (IPRD06)*, October 2006, Siena, Italy, to appear in Nucl. Phys. B (Proc. Suppl.)
16. A. Caliandro, Doctoral thesis, University of Bari (2006)
17. A.M. Chandler et al., ApJ, **556**, 59 (2001)
18. E. Durand, Doctoral thesis (2003), *http://doc.in2p3.fr/themis/CELESTE/PUB/Durand_These.ps.gz*
19. G. Dubus, A & A, **456**, 801 (2006)
20. T. Eifert, Diploma thesis, *http://www-hess.physik.hu-berlin.de/theses.html*
21. D. Ferenc, NIM A, **553**, 274 (2005)

22. J.M. Fierro et al., ApJ, **494**, 734–746 (1998)
23. B. Giebels, Nucl. Instrum. Meth., **412A**, 329–341 (1998)
24. B. Giebels, GLAST and Very High Energy Astrophysics, In: *Towards a Network of Atmospheric Cherenkov Detectors VII – Palaiseau*, ed. by B. Degrange, G. Fontaine, pp 401–414 (2005)
25. L. Girard, Doctoral thesis (2004), *http://tel.archives-ouvertes.fr/tel-00008770*
26. P. Gonthier, R. Van Guilder and A. Harding, ApJ, **604**, 775–790 (2004)
27. L. Guillemot, V. Lonjou et al., Poster at the 1st GLAST Symposium
28. A.K. Harding, V.V. Usov, A.G. Muslimov, ApJ, **622**, 531 (2005)
29. J. Hinton, The Status of H.E.S.S., In: *2nd VERITAS Symposium on the Astrophysics of Extragalactic Sources*, New Astronomy Reviews, **48**, pp 331–337 (2004)
30. C.M. Hoffman, C. Sinnis, M. Punch and P. Fleury, Rev. Mod. Phys., **71**, 897 (1999)
31. W. Hofmann, Proc. ICRC, 2785 (2005)
32. W. Hofmann and M. Punch, HESS-II Technical Review, September 2006.
33. J. Holder et al., Astropart. Phys., **25**, 391–401 (2006)
34. M.G.F. Kirsch et al., Proc. SPIE, **5165**, 85–95 (2004)
35. H. Krawcyzinski et al., Astropart. Phys., **25**, 380–390 (2006)
36. L. Kuiper et al., A & A, **359**, 615 (2000)
37. A.K. Konopelko, Astropart. Phys., **24**, 191–207 (2005)
38. L. Latronico, Nucl. Instrum. Meth., **A511**, 68 (2003)
39. B. Lott, F. Piron et al., Nucl. Instrum. Meth., **560**, 395–404 (2006)
40. R.N. Manchester, G.B. Hobbs, A. Teoh and M. Hobbs, AJ, **29**, 1993–2006 (2005), see *http://www.atnf.csiro.au/research/pulsar*
41. M.A. McLaughlin, J.M. Cordes, ApJ, **538**, 818 (2000)
42. P. Michelson, In: *X-Ray and Gamma-Ray Telescopes and Instruments for Astronomy*, ed. by Trümper & Tananbaum, SPIE, vol 4851, 2003, pp 1144–1150
43. S. Murray et al., ApJ, **568**, 226–231 (2002)
44. M. de Naurois et al., ApJ, **556**, 343 (2002)
45. E. Ona-Wilhelmi et al., Proc. ICRC Pune, India, **4**, 247 (2005)
46. R.A. Ong, Phys. Rep., **305**, 93 (1998)
47. E. Ona-Wilhelmi, Doctoral thesis, Optimization of MAGIC for Pulsars (O.C. DeJager and M.V. Fonseca, advisors), *http://www.gae.ucm.es/∼emma/tesis*
48. D. Parent, M. Lemoine-Goumard et al., Poster at the 1st GLAST Symposium
49. A. Pellizoni et al., Adv. Sp. Res., **33**, 625–629 (2004)
50. F. Piron et al., A & A, **374**, 895–906 (2001)
51. M. Punch, In: *Towards a Network of Atmospheric Cherenkov Detectors VII – Palaiseau*, ed. by B. Degrange, G. Fontaine, pp 379–392 (2005)
52. P. Ray and M. Pohl, GLAST User's Committee meeting, December 2001
53. M. Razzano and A. Harding, Pulsar Sensitivity Studies of the GLAST Large Area Telescope *and* M. Razzano, Pulsar Simulation Tools for GLAST, In: *The Multi-Messenger Approach to High Energy Gamma-ray Sources, July 2006 - Barcelona*, to appear in Astrophysics and Space Science (Springer-Verlag)
54. T. Reposeur and D. Dumora et al., Poster at the 1st GLAST Symposium
55. F. Schmidt, Diploma thesis, *http://www-hess.physik.hu-berlin.de/theses.html*
56. F. Schmidt, Workshop on Pulsars, Pulsar-Wind Nebulae, and Supernova Remnants, Berlin, April 7–8 (2005)
57. D.A. Smith, Working from the Ground Up – Ground-based Gamma Ray Observations In: *The Gamma-ray Universe, XXXVIIth Rencontres de Moriond*, ed. by A. Goldwurm, D.N. Neumann, J. Trân Thanh Vân, pp 477–484 (2002)
58. D.A. Smith, Review of the Solar Array Telescopes. In: *Towards a Network of Atmospheric Cherenkov Detectors VII – Palaiseau*, ed. by B. Degrange, G. Fontaine, pp 67–79 (2005)
59. M. Strickman et al., Production, Calibration, and Environmental Testing of GLAST LAT CsI calorimeter Flight Modules In: *AAS 207th Meeting*, January 2006, Washington D.C.
60. D.A. Smith, J.E. Grove and D. Dumora, document LAT-TD-08777-03 (2006)

61. M. Tavani et al., In: *Space Telescopes and Instrumentation II: Ultraviolet to Gamma Ray.*, ed. by M.J.L. Turner, G. Hasinger, SPIE, vol 6266, 626603 (2006)
62. M. Teshima et al., Proc. ICRC Pune, India, **5**, 227 (2005)
63. D.J. Thompson et al., ApJ **516**, 297 (1999)
64. D.J. Thompson., Gamma Ray Pulsars. In: *Cosmic Gamma-Ray Sources*, ed. by K.S.Cheng, G.E. Romero (Kluwer, Dordrecht, 2004) pp 149–168
65. D.J. Thompson, In: *40 Years of Pulsars: Millisecond Pulsars, Magnetars, and More*, ed. by C. Bassa, Z. Wang, A. Cumming, V. Kaspi, AIP, in press (2008)
66. G. Vacanti et al., Astropart. Phys., **2**, 1 (1994)
67. P. Vincent, Proc. ICRC, **5**, 163 (2005)
68. T.C. Weekes., Phys. Reports, **160**, (1988)
69. T.C. Weekes et al., ApJ, **342**, 379 (1989)
70. T.C. Weekes, Astropart. Phys., **17**, 221 (2002)
71. The Particle Data Book at *http://pdg.lbl.gov/2006/*, with contents *reviews/contents_sports.html#expmethetc*. See "Passage of Particles Through Matter" (*reviews/passagerpp.pdf*) and the numerical values at (*reviews/atomicrpp.pdf*).

Chapter 24
Gravitational Waves from Spinning Neutron Stars

Reinhard Prix (for the LIGO Scientific Collaboration)

24.1 Introduction

Gravitational waves (GWs), i.e. small deformations of spacetime traveling at the speed of light, are a fundamental consequence of Einstein's general theory of relativity. There has been no direct observation of GWs so far, although first indirect evidence was found in the observed inspiral of the binary pulsar PSR 1913+16, which agreed to within 1% with the predictions of general relativity [75, 88]. Similar measurements on the recently discovered "double pulsar" system have allowed to improve these experimental tests of General Relativity to the level of 0.05%. GWs are purely transverse waves, characterized by two polarization states (denoted as '$+$' and '$\times$', respectively). These two polarization bases differ by a rotation of 45° around the propagation axis, corresponding to the quadrupolar (spin-2) nature of the gravitational field. In contrast, the two polarization bases of electromagnetic waves differ by a rotation of 90°, reflecting the dipolar (spin-1) nature of the electromagnetic field.

Any likely sources of detectable GWs will be at astrophysical distances, thus the signals reaching Earth have very small amplitudes and are nearly plane waves. A linearized version of general relativity (e.g., see [57]) can therefore be used to describe GWs in terms of a small metric perturbation $h_{\mu\nu}$, i.e. one can write the metric as $g_{\mu\nu} = \eta_{\mu\nu} + h_{\mu\nu}$, where $|h_{\mu\nu}| \ll 1$ is the gravitational wave and $\eta_{\mu\nu}$ is the Minkowski metric of the unperturbed flat spacetime. One can then show that the Einstein field equations in vacuum reduce to the familiar wave-equation for a perturbation $h_{\mu\nu}$ propagating (at the speed of light) through flat spacetime $\eta_{\mu\nu}$, i.e.

$$\Box h^{\mathrm{TT}}_{\mu\nu} = \eta^{\sigma\rho}\partial_\sigma\partial_\rho h^{\mathrm{TT}}_{\mu\nu} = 0\,, \tag{24.1}$$

R. Prix
Max-Planck-Institut für Gravitationsphysik, Albert-Einstein-Institut, Am Mühlenberg 1, 14476 Golm, Germany
e-mail: Reinhard.Prix@aei.mpg.de

W. Becker (ed.), *Neutron Stars and Pulsars,* Astrophysics and Space Science Library 357,

where $h^{\mathrm{TT}}_{\mu\nu}$ is the tensor $h_{\mu\nu}$ expressed in the transverse–traceless (TT) gauge. This is a choice of coordinates, $\{t,x,y,z\}$ say, corresponding to an inertial (Lorentz) frame in the unperturbed flat background, which makes explicit that the perturbation is *transverse*, i.e. orthogonal to the direction of propagation, and *trace-less*, namely the perturbation does not 'compress' or 'expand' elements of spacetime, but induces a (volume-preserving) 'strain' only. In this gauge a plane gravitational wave propagating along the z-axis can be written as

$$h^{\mathrm{TT}}_{\mu\nu}(t,z) = h^{\mathrm{TT}}_{\mu\nu}(t-z/c) = \begin{pmatrix} 0 & 0 & 0 & 0 \\ 0 & h_+ & h_\times & 0 \\ 0 & h_\times & -h_+ & 0 \\ 0 & 0 & 0 & 0 \end{pmatrix}, \tag{24.2}$$

where c is the speed of light and $h_{+,\times}(t-z/c)$ are the two polarizations of the wave. The effect of such a GW on two freely falling test-masses is a time-dependent change δl in their spatial distance l, which can be monitored using laser interferometry. This is the principle behind interferometric GW detectors such as the currently operating LIGO-I, GEO600, Virgo and TAMA300 (see Sect. 24.3), or future detectors such as Advanced LIGO or the space-based LISA. The measured strain $h(t)$ of such a detector is defined as the relative length-change between the two interferometer arms l_1 and l_2 (usually at right angles to each other), namely $h(t) \equiv \delta l_1/l_1 - \delta l_2/l_2$. In the long-wavelength approximation, where the reduced wavelength of the GW is assumed to be much longer than the arm length of the detector, i.e. $\lambda/2\pi \gg l_{1,2}$, it can be shown [47, 69, 77] that the measured scalar strain $h(t)$ due to the effect of a GW $h^{\mathrm{TT}}_{\mu\nu}$ is given by

$$\begin{aligned} h(t) &= \frac{1}{2}\left(e_1^i e_1^j - e_2^i e_2^j\right) h^{\mathrm{TT}}_{ij} \\ &= F_+(t)\, h_+(t) + F_\times(t)\, h_\times(t)\,, \end{aligned} \tag{24.3}$$

where e_1^i and e_2^i are spatial unit-vectors along the first and the second interferometer arm, respectively. Note that the long-wavelength approximation is generally sufficient for ground-based detectors with typical arm-lengths of $L \lesssim 4$ km and GW frequencies of up to $\lesssim$ kHz. However, in the case of the space-based LISA detector, with armlengths $\sim 5\times 10^6$ km and GW frequencies of order $\sim 10^{-2}$ Hz, the phase of the GW changes substantially during the light-travel time of photons between the space-craft. Therefore LISA requires a more detailed modeling of its response to a passing GW instead of the simple response tensor (24.3), which is achieved by "time-delay interferometry" or TDI (e.g., see [78]).

The antenna-pattern (or beam-pattern) functions $F_{+,\times}(t;\psi,\boldsymbol{n}) \in [-1,1]$ describe the sensitivity of the detector to the '+' and '×' polarization, respectively, which depend on the direction $\boldsymbol{n}$ to the source (where $\boldsymbol{n}^2 = 1$), the polarization angle ψ of the wave, and the orientation of the detector. For ground-based detectors, $F_{+,\times}$ are periodic functions over one sidereal day, due to the rotation of the Earth (while for LISA the period would be 1 year). Explicit expressions for the antenna-pattern functions can be found in [23] and [49]. GW detectors are fundamentally different from

'telescopes' for electromagnetic radiation: they are practically omni-directional due to the wide quadrupolar antenna-pattern (24.3), and they measure a single scalar function of time, $h(t)$. In this sense they are more closely analogous to acoustic microphones rather than telescopes.

The emission of GWs is generally well-described by the quadrupole formula, namely

$$h_{jk}^{\mathrm{TT}}(t) = \frac{2G}{c^4}\frac{1}{r}\left[\ddot{\mathcal{J}}_{jk}(t - r/c)\right]^{\mathrm{TT}}, \tag{24.4}$$

where G is Newton's gravitational constant, c is the speed of light, and r is the distance to the source and r/c accounts for the time delay. Dots denote time derivatives and $\mathcal{J}_{jk}$ is the mass-quadrupole moment of the source. The transverse–traceless operator 'TT' indicates the projection orthogonal to the direction of propagation and the removal of the trace. This expression was first derived by Einstein in 1916, using the assumption of weak internal gravity of the source, but it was later shown to be valid even if one only requires that the source is small compared to the reduced wavelength $\lambda/2\pi$ of the emitted waves [76, 77]. The mass-quadrupole moment $\mathcal{J}_{jk}$ of the source is defined as the coefficient of the $1/r^3$ term in an expansion in powers of $1/r$ of the Newtonian gravitational potential (far from the source). For sources with weak internal gravity, this can be directly expressed as

$$\mathcal{J}_{jk} = \int \rho(\boldsymbol{x})\left[x_j x_k - \frac{1}{3}r^2\,\delta_{jk}\right] d^3x, \tag{24.5}$$

where $\rho(\boldsymbol{x})$ is the mass density. This is simply the Newtonian moment of inertia with the trace removed. The energy emission rate L_{GW} in GWs can be expressed in the quadrupole formalism as

$$L_{\mathrm{GW}} = \frac{1}{5}\frac{G}{c^5}\left\langle \dddot{\mathcal{J}}_{jk}\,\dddot{\mathcal{J}}^{jk}\right\rangle, \tag{24.6}$$

where $\langle\ldots\rangle$ denotes the time average over several periods. The quadrupole formalism shows that time-varying mass-distributions generally emit GWs. Let us now specialize to the case of a star with mass M and radius R, rotating at a frequency ν. We see from (24.4) that a perfectly axisymmetric star rotating around its symmetry axis will *not* emit GWs, as its quadrupole moment (24.5) is constant in time. Let us characterize the deviation from axisymmetry by a dimensionless number ε, i.e. let εI be the non-axisymmetric part of the moment of inertia I. Then the order of magnitude of the GW luminosity (24.6) can be estimated as

$$L_{\mathrm{GW}} \sim \frac{G}{c^5}\,\varepsilon^2 I_{zz}^2\,\nu^6, \tag{24.7}$$

where $I_{zz} \sim MR^2$ is the moment of inertia along the rotation axis. Numerically $G/c^5 \sim 3\times 10^{-53}$ s/J, which shows that terrestrial experiments could realistically only produce infinitesimal amounts of GW radiation: if we constructed a 'dumbbell' of two masses of a few tons separated by a few meters, i.e. an $\varepsilon \sim \mathcal{O}(1)$

and a moment of inertia $I_{zz} \sim 10^5 \mathrm{kg\,m^2}$, and if we let it spin or vibrate at rates $\nu \sim 10^3$ Hz, it would still radiate only about $L_{\mathrm{GW}} \sim 10^{-25}$ W in gravitational waves. On the other hand, if we rewrite this expression in terms of the Schwarzschild radius $R_s = 2GM/c^2$ and the rotation velocity $V = 2\pi R\nu$ at the surface of the star [24], we find

$$L_{\mathrm{GW}} \sim \frac{c^5}{G}\varepsilon^2 \left(\frac{R_s}{R}\right)^2 \left(\frac{V}{c}\right)^6 . \tag{24.8}$$

This shows that *compact objects* (i.e. $R_s \sim R$) in rapid rotation (i.e. $V \sim c$), such as spinning neutron stars, can emit enormous GW luminosities even for small ε, as $c^5/G \sim 10^{52}$ W. However, spacetime is a very 'stiff' medium, i.e. large amounts of energy are carried by GWs of small amplitude. This can be seen from a similar estimate of the corresponding strain amplitude (24.4), namely

$$h \sim 10^2 \frac{G}{c^4}\frac{\varepsilon I_{zz}\nu^2}{d} \sim 3\times 10^{-25} \left(\frac{\varepsilon}{10^{-6}}\right)\left(\frac{I_{zz}}{10^{38}\,\mathrm{kg\,m^2}}\right)\left(\frac{\nu}{100\,\mathrm{Hz}}\right)^2 \left(\frac{100\,\mathrm{pc}}{d}\right), \tag{24.9}$$

where the fiducial values correspond to a neutron star with typical moment of inertia, a relatively strong deviation from axisymmetry (cf. next section), at a distance of the order of the closest known neutron star, and spinning in the millisecond regime. Even in this very optimistic case, the amplitude is about two orders of magnitude below the noise level (referring to 1 s of data) of LIGO-I, which is currently the most sensitive detector and will be discussed in more detail in Sect. 24.3. The data-analysis challenge in the search for continuous GWs from neutron stars therefore consists of finding extremely weak, nearly periodic signals buried deep in the noise of GW detectors.

24.2 Continuous Gravitational Waves from Neutron Stars

In this section we give a brief overview of the current theoretical understanding of various physical mechanisms that could operate in neutron stars to produce interesting levels of GW emission (see also [61] for a recent review). As the signal-strength is generally expected to be very weak (see previous section), long integration times of the order of $T \gtrsim$ several days to years will be required in order for the signal to be detectable in the noise (see Sect. 24.3).

Here we focus on the class of *continuous GWs*, which are long-lasting, quasi-monochromatic GWs with slowly varying intrinsic frequency. The difficulties and analysis methods for these signals differ in many respects from other types of GW signals, such as bursts (e.g., from supernovae), 'chirping' signals from the binary coalescence of compact objects, and the fossil stochastic background of GWs from the big bang. Note that neutron stars might also be interesting sources of burst-like GW emission [33], e.g., from oscillations excited by a glitch which would be damped very quickly. Another candidate for such burst-like neutron star oscillations could be crustal torsional modes, which have recently been suggested [87] as a

possible explanation for the high frequency oscillations observed in giant flares from Soft Gamma Repeaters. Although such GW 'asteroseismology' could potentially be extremely valuable for neutron-star astrophysics (e.g., see [13]), a discussion of this type of sources is not within the scope of the present paper, as the corresponding detection problem is rather different in nature from the continuous-wave type of sources considered here.

24.2.1 Emission Mechanisms for Continuous Gravitational Waves

There are three types of mechanisms usually considered for the emission of continuous GWs from spinning neutron stars in the frequency band of current ground-based detectors (i.e. $\sim$20 Hz $-$ 2kHz): (1) non-axisymmetric distortions of the neutron star, (2) unstable oscillation modes in the fluid part of the star (e.g., r-modes), and (3) free precession.

Non-Axisymmetric Distortions

Non-axisymmetric distortions, or 'mountains' on the neutron star, cannot persist in perfect fluid stars, but in realistic neutron stars such deformations can be supported either by elastic stresses in the crust or by magnetic fields. The deformation is often expressed in terms of the *equatorial* ellipticity:

$$\varepsilon \equiv \frac{I_{\mathrm{xx}} - I_{\mathrm{yy}}}{I_{\mathrm{zz}}}, \tag{24.10}$$

where I_{jj} are the three principal moments of inertia. This ellipticity is not to be confused with the centrifugal bulge, which is axisymmetric and therefore does not radiate GWs (see Sect. 24.1). A spinning non-axisymmetric neutron star at distance d, rotating with frequency ν around the I_{zz} axis emits monochromatic GWs at a frequency $f = 2\nu$ of amplitude

$$h_0 = \frac{16\pi^2 G}{c^4}\frac{I_{\mathrm{zz}}\nu^2}{d}\varepsilon\,, \tag{24.11}$$

e.g., see [49], and (24.9). The definition of the strain-amplitude h_0 refers to a GW from an optimally oriented source with respect to the detector, as will become clearer in Sect. 24.4.1.

Unfortunately, both the maximum possible as well as the most likely values for the non-axisymmetric deformation ε of neutron stars are highly uncertain. Various estimates of the maximum ellipticity ε sustainable by neutron stars have been given in the literature: the maximal deformation supported by the rigidity of the crust has been estimated [81] as

$$\varepsilon_{\mathrm{max}} \approx 5 \times 10^{-7} \left(\frac{\sigma}{10^{-2}}\right), \tag{24.12}$$

where σ is the breaking strain of the solid crust. The numerical coefficient in this equation is small mainly because the shear modulus of the inner crust is small compared to the pressure. The fiducial breaking strain of 10^{-2} in (24.12) corresponds approximately to the best terrestrial alloys. However, σ could be as high as 10^{-1} for a perfect crystal with no defects [51], or several orders of magnitude smaller for an amorphous solid or a crystal with many defects. Some exotic alternatives to standard neutron star models contain solid cores, which could support considerably larger ellipticities. The most speculative models for solid strange-quark stars can reach ellipticities of up to $\varepsilon_{\max} \approx 4 \times 10^{-4}\,(\sigma/10^{-2})$, mostly due to their higher shear modulus [60].

In addition to the problem of the maximum ellipticity that can be supported, the more relevant question is what actual deformations are likely to exist in real neutron stars. There are several mechanisms by which the spin-down of a neutron star could cause stresses in the crust to build up to the point of breaking (see [28, 66, 67]), usually considered in the context of glitch models. It is unclear, however, how long it would take to return to a smooth axisymmetric mass-distribution after such a crust quake, which could possibly leave long-lived distortions of the crust.

Another possibility are accreting neutron stars in binary systems, which have a natural way of reaching and maintaining large crust deformations: the accretion flow, guided by the neutron star's magnetic field, naturally produces 'hot spots' on the surface, which can lead to 'hills' in hotter areas, and the ellipticity might thereby build up to the maximum value [22]. The accreted material could also be held up in mountains by the magnetic field itself: the accreted matter has a very high electric conductivity, thus crosses field lines relatively slowly and could pile up in mountains larger than those supportable by elasticity alone [56, 64]. Depending on the field configuration, accretion rate, and temperature, the ellipticity from this mechanism could be up to a few times 10^{-6} even for ordinary neutron stars (cf. [61] for further discussion).

Furthermore, strong internal magnetic fields could directly produce non-axisymmetric deformations of neutron stars due to magnetic tension. A strong dipolar field that is not aligned with the rotation axis could lead to deformations of up to $\varepsilon \lesssim 10^{-6}$ in the case of type-I superconducting cores [23]. These non-aligned deformations would generally result in GW emission at *both* the first and the second harmonic of the rotation rate, i.e. $f = \nu$ and $f = 2\nu$, similar to free precession. Another possibility, suggested by [35], is that the differential rotation present after the birth of a neutron star could 'wind up' large toroidal magnetic fields. Dissipation then tends to drive the symmetry axis of a toroidal field toward the star's equator, resulting in ellipticities of the order $\varepsilon \sim 10^{-6}$ for toroidal magnetic fields of about $B_t \sim 10^{15}$ G.

Non-Axisymmetric Instabilities

At birth or during phases of accretion, rapidly rotating neutron stars can be subject to various non-axisymmetric instabilities, which would lead to GW emission

(see [12, 73] for recent reviews). If a new-born neutron star has a sufficiently high rotation rate, i.e. if the ratio $T/|W|$ of the rotational kinetic energy T to the gravitational binding energy W exceeds a critical value (typically $T/|W| \gtrsim 0.24$), it will be subject to a dynamical instability driven by hydrodynamics and gravity. Differential rotation might substantially lower this critical value to $T/|W| \gtrsim 0.14$ [29]. Through the $l = 2$ mode, this bar-mode instability will deform the star into a bar shape, which would be a strong emitter of GWs, but likely to be very short-lived (on the order of a few rotations [20]). At lower rotation rates, the star can become unstable to *secular* non-axisymmetric instabilities, driven either by gravitational radiation or viscosity (e.g., [68, 70]). It is not clear, however, how effective and long-lived any of these mechanisms would be in producing detectable GWs.

Gravitational radiation generally drives a non-axisymmetric oscillation unstable if the mode is counter-rotating with respect to the rotating frame of the star, but co-rotating with the star in the frame of a distant inertial observer. This happens when the counter-rotation rate of the mode is lower than the rotation rate of the star, so the mode gets 'dragged along' by the star. This secular instability is known as the Chandrasekhar–Friedman–Schutz (CFS) instability [31, 44]. For oscillation modes such as the fundamental mode (f-mode) and pressure-modes (p-modes), this instability would only set in at very high rotation rates close to the breakup-limit. Therefore the most promising candidate for observable GW emission from the CFS instability might be the family of r-modes, which are toroidal fluid oscillations where the Coriolis force of the rotating star is the dominant restoring mechanism (see [80] for an overview of stellar oscillations). Contrary to the polar f- and p-modes, these oscillations are generically unstable to the CFS instability at any finite rotation rate [11, 43].

Under astrophysically realistic conditions, however, their effective instability depends on a number of highly uncertain damping mechanisms and timescales (see [73] for a review). The r-mode instability has been proposed as a source of GWs (with frequency $f = 4\nu/3$) from newborn neutron stars [62] and from rapidly accreting neutron stars [15, 22]. However, the CFS instability of the r-modes in newborn neutron stars might not be a good candidate for detection because the emission will most likely be weak and would last only for a few months after the birth of the neutron stars in a supernova . Accreting neutron stars or quark stars could be a better prospect for detection [16, 85] because the emission may last several thousands of years [12, 14].

Free Precession

The third major type of emission mechanisms for continuous GWs from spinning neutron stars is free precession, i.e. the 'wobble' of a neutron star with a misaligned rotation axis with respect to its symmetry axis (defining the wobble angle θ_{w}). A large-angle wobble would typically (see [50, 82, 90]) produce GWs of amplitude

$$h_0 \sim 10^{-27} \left(\frac{\theta_{\mathrm{w}}}{0.1\,\mathrm{rad}}\right) \left(\frac{1\,\mathrm{kpc}}{d}\right) \left(\frac{\nu}{500\,\mathrm{Hz}}\right)^2 . \tag{24.13}$$

Generally, free precession results in emission at (approximately) the rotation rate ν and twice the rotation rate, i.e. $f = \nu + \nu_{\mathrm{prec}}$ (where ν_{prec} is the precession frequency) and $f = 2\nu$. Free precession may be much longer lived ($\sim 10^5$ years) than previously thought [36], but the amplitude is still quite small, which might make this mechanism relevant only for second-generation interferometers such as Advanced LIGO.

24.2.2 Loudest Expected Signal from Unknown Isolated Neutron Stars

Current models of stellar evolution suggest that our Galaxy contains $\sim 10^9$ neutron stars, while about 10^5 are expected to be active pulsars. Up to now only $\sim$1,700 pulsars have been observed (see [54]); there are numerous reasons for this, including selection effects and because many produce only faint emission. Although there is great uncertainty in the physics of the GW emission mechanisms and the strength of individual sources, one can argue for a statistical upper limit on the expected strongest GW signals from the galactic population of neutron stars. The argument is almost independent of individual source physics and goes back to Blandford. An updated version is given in [6], here we only summarize the main points and the result. One can make the (optimistic) assumption that there exists a class of neutron stars that are born rapidly rotating, and spinning down due to GWs. Assuming they are distributed uniformly throughout the galactic disc, and have a constant birthrate, one can convert these assumptions into a distribution of neutron stars with respect to GW strain and frequency. Using this, one can show that there would be a 50% chance that the strongest signal within the LIGO band ($\sim 50\,\mathrm{Hz} - 2\,\mathrm{kHz}$) has an amplitude of at least

$$h_0 \sim 4 \times 10^{-24}\,. \tag{24.14}$$

Obviously this is a purely statistical argument, and it is possible that the closest strong emitter is either far closer or further away than the typical distance expected from a random distribution of supernovae. Note also that this is an 'upper limit' only in the sense that the assumptions that went into it are optimistic, and one would generally expect a lower amplitude if some of them were not true.

24.2.3 The Spin-Down Limit for Known Pulsars

The statistical argument of the previous section applies to a population of unknown neutron stars in the galaxy. A much more robust upper limit on h_0 can be derived for known pulsars with measured frequency ν, spin-down $\dot{\nu}$ and distance d. For simplicity, let us consider the case of spinning neutron stars with a non-axisymmetric deformation ε, emitting GWs at frequency $f = 2\nu$. In this case the GW luminosity (24.6) can be written explicitly as

$$L_{\rm GW} = \frac{1}{10}\frac{G}{c^5}(\pi\nu)^6 I_{zz}^2 \varepsilon^2 . \tag{24.15}$$

If we assume that the GW emission is powered *only* by the rotational energy $E_{\rm rot} = 2\pi^2\nu^2 I_{zz}$ of the spinning neutron star, then we have the inequality

$$L_{\rm GW} \leq -\dot{E}_{\rm rot} = -2\pi^2\left(2I_{zz}\,\nu\dot{\nu} + \nu^2\dot{I}_{zz}\right) . \tag{24.16}$$

For constant moment of inertial, $\dot{I}_{zz} = 0$, this yields an upper limit on the quadrupolar deformation $\varepsilon \leq \varepsilon_{\rm sd}$, namely

$$\varepsilon_{\rm sd} = \sqrt{\frac{5c^5}{2(4\pi)^4 G I_{zz}}\frac{|\dot{\nu}|}{\nu^5}} . \tag{24.17}$$

Substituting this into (24.11), we obtain the following upper limit on the GW amplitude

$$h_0 \leq h_{\rm sd} = \frac{1}{d}\sqrt{\frac{5GI_{zz}}{2c^3}\frac{|\dot{\nu}|}{\nu}} . \tag{24.18}$$

24.2.4 Maximum Expected Signal from Accreting Neutron Stars

The statistical upper limit (24.14) on h_0 is not applicable to accreting neutron stars, since energy conservation plays a crucial role in the argument. However, if accretion replenishes the star's angular momentum, a different argument can be made, independent of the details of the emission mechanism. In this case $h_0^{\rm max}$ is set by the X-ray luminosity of the brightest X-ray source. The basic idea is that if the angular momentum lost in GWs is replenished by accretion, then the strongest GW emitters are those accreting at the highest rate, such as low-mass X-ray binaries (LMXBs). The accreted gas hitting the surface of the neutron star is heated to $\sim 10^8$ K and emits X-rays. As noted several times [22, 63, 84], if one assumes the spin-down torque from GW emission to be in equilibrium with the accretion torque, then h_0 is directly related to the observed X-ray flux $F_{\rm x}$, namely

$$h_0 \approx 5\times 10^{-27}\left(\frac{300\,{\rm Hz}}{\nu}\right)^{1/2}\left(\frac{F_{\rm x}}{10^{-8}\,{\rm erg\,cm^{-2}\,s^{-1}}}\right)^{1/2} . \tag{24.19}$$

It is interesting to note that this expression does not explicitly depend on the distance d of the system, which is implicitly contained in the observed X-ray flux $F_{\rm x}$ on Earth (both the GW and X-ray flux decrease with $1/d^2$). This theoretical argument is supported by the observation that the frequencies of most LMXBs seem to cluster in a fairly narrow range of $270\,{\rm Hz} \lesssim \nu \lesssim 620\,{\rm Hz}$ [30]. Since most neutron stars will have accreted enough matter to spin them up to near their theoretical maximum spin frequencies, estimated at $\nu_{\rm max} \sim 1{,}400\,{\rm Hz}$ (e.g., see [34]), the observed spin distribution is hard to explain without a competing mechanism to counter the

spin-up. Since the GW torque scales as $\propto \nu^5$, gravitational radiation seems like a natural explanation for the rather narrow clustering of observed frequencies. If this argument holds, then the accreting neutron star brightest in X-rays (namely Sco X-1) should also be the strongest source of GWs. Using the known X-ray flux of Sco X-1, its expected GW emission under these assumptions would have an amplitude of

$$h_0 \approx 3 \times 10^{-26} \left(\frac{540\,\mathrm{Hz}}{f} \right)^{1/2} . \tag{24.20}$$

The frequency f is unfortunately not well constrained from observations, but is generally assumed to be of the order of several hundred Hertz. This signal could in principle be detectable by second-generation interferometers such as Advanced LIGO (cf. Fig. 24.4).

24.3 Detectors of Gravitational Waves

Starting from the pioneering efforts of Joseph Weber in the early 1960s, the first GW detectors were based on the principle of monitoring the oscillations of massive resonant metal bars, the bar detectors. A GW at or near the resonance frequency of the bar would excite this oscillation mode. These designs have been successively improved over time, and today there are still a number of bar detectors operating, including ALLEGRO in Louisiana, EXPLORER at CERN and NAUTILUS in Rome. During the past decade, however, several scientific collaborations have constructed large-scale interferometric GW detectors. These include the Laser Interferometer Gravitational Wave Observatory (LIGO), consisting of three interferometers, built by a Caltech–MIT collaboration [9]; the GEO 600 detector built by a British–German collaboration [89]; the Virgo detector built by an Italian–French collaboration [27]; and the Japanese TAMA 300 detector in Tokyo [79]. In all of these detectors, the relative displacement of suspended test masses is sensed interferometrically, as illustrated schematically in Fig. 24.1. The interferometer is tuned in such a way that ideally no light would arrive at the photodetector in the absence of a GW. Therefore most of the light will be reflected back to the laser, where it is returned to the interferometer using a power recycling mirror. This increases the power of the light in the interferometer arms, which reduces 'shot noise', i.e. the statistical fluctuations of the laser light due to the quantum nature of photons.

In addition to shot noise, which is the dominant noise contribution at high frequencies, the strain measurement is affected by a large variety of noise sources. At low frequencies the dominant contributions are seismic noise and gravity-gradient noise. See [1, 77] for more detailed discussions about the functioning of GW detectors and the problems related to minimizing noise contributions affecting the strain measurements.

In the following we will focus mainly on the detectors run within the LIGO Scientific Collaboration (LSC), namely LIGO and GEO 600. The GEO 600 detector

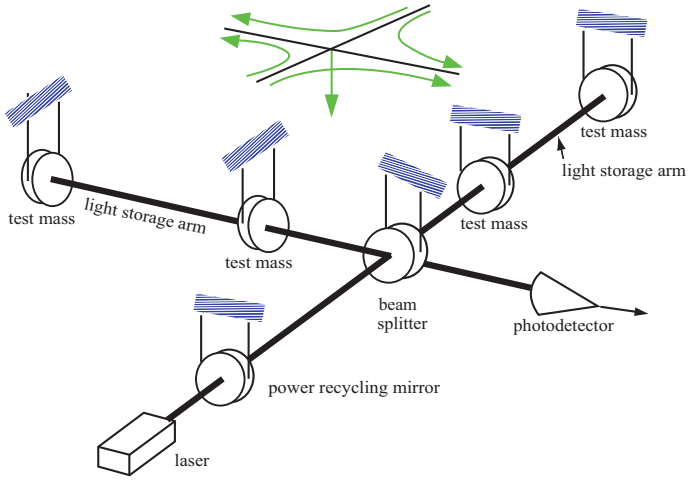

Fig. 24.1 Schematic layout of an interferometric gravitational-wave detector such as LIGO, with power recycling and Fabry–Perot arms. The quadrupolar strain deformation-field above the detector indicates an incident GW $h_{\mu\nu}^{\mathrm{TT}}$ of optimal orientation (from [1])

(G1) comprises a 4-beam Michelson delay line system of arm length 600 m. LIGO consists of three power-recycled Michelson interferometers with resonant Fabry–Perot cavity arms, installed at two sites: the Livingston site (Louisiana) contains one interferometer of 4 km arm length (referred to as L1), while the Hanford site (in Washington state) houses two interferometers, one of 4 km and one of 2 km arm length (called H1 and H2, respectively). In all four instruments (H1, H2, L1, G1), the beam splitters, recycling mirrors and test masses are hung as pendulums from multilayer seismic isolation filters to isolate them from local forces (see Fig. 24.1). The masses and beam paths are housed in high vacuum enclosures to avoid optical scintillation and acoustic interference.

24.3.1 LIGO/GEO600 Sensitivities and Scientific Runs

LIGO and GEO600 have so far completed five science-mode data-taking runs (denoted S1–S5), see Table 24.1. The ‘duty cycle’ in Table 24.1 denotes the fraction of the run time where the detector was ‘in lock’ and was taking science data. Due to seismic noise, equipment failures and alignment drifts, the duty cycle is generally less than 100%. Livingston (L1) had particularly low duty-cycles during S1 to S3 due to low-frequency noise caused by logging activity in a nearby forest. This problem has been largely overcome by installing an improved (active) seismic isolation before the start of S4, which resulted in dramatic improvements in the L1 duty cycle, as seen in Table 24.1. GEO600 has had the best duty cycles, but also lower sensitivity than LIGO, see Fig. 24.2.

Table 24.1 Summary of LIGO/GEO600 scientific runs (status in April, 2008)

Run	Start–End	Best sensitivity $\sqrt{S_n}\,(\mathrm{Hz}^{-1/2})$	Duty cycles [%] H1	L1	H2	G1
S1	Aug 23–Sept 9, 2002	2×10^{-21}	57.6	41.7	73.1	98.5
S2	Feb 14–Apr 14, 2003	2×10^{-22}	73.5	36.9	57.8	–
S3	Oct 31, 2003–Jan 9, 2004	5×10^{-23}	69.3	21.8	63.4	96.9[a]
S4	Feb 22–Mar 23, 2005	4×10^{-23}	80.5	74.5	81.4	96.6
S5	Nov 4, 2005–Oct 1, 2007	2×10^{-23}	71.0	59.1[b]	78.2	80.4

[a]Partial participation: Nov 5, 2003 – Nov 12, 2003 and Dec 30, 2003 – Jan 13, 2004
[b]Started Nov 14, 2005

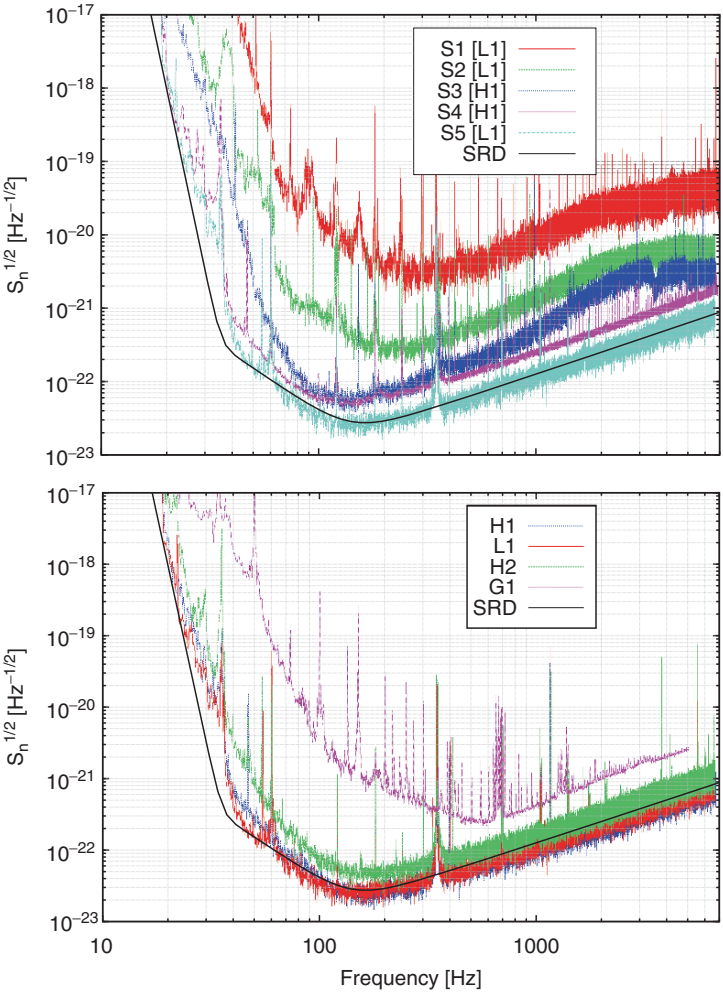

Fig. 24.2 *Top:* Successive best LIGO sensitivities achieved over the science runs S1–S5. *Bottom:* LIGO and GEO600 sensitivities during early S5 (June 2006)

As seen in this figure, the LIGO detectors have reached their design sensitivity (except at low frequencies $\lesssim 50\,\mathrm{Hz}$) during the S5 run, which took 1 year of coincident data (the run lasted for about 2 years). After S5, LIGO-I will undergo some enhancements (known as 'Enhanced LIGO') that will improve sensitivity by up to a factor of two, and will be used for another long science run (S6). After S6, work will start on the next-generation Advanced LIGO detector, which will be installed on the same sites as LIGO-I, and which is planned to start taking data within a decade.

24.4 Data Analysis of Continuous Gravitational Waves

As discussed in Sects. 24.1 and 24.2, continuous GWs reaching Earth are expected to be exceedingly weak, even compared to the sensitivities of the current generation of detectors. In order to be able to dig such signals out of the noise, one typically has to integrate for several days up to months by matching the data with a target signal ('template') of given parameters. This is the basic concept of *matched filtering*, which is the optimal method in a statistical sense (made more precise later). See also [48] for a recent review of the detection problem of continuous GWs.

As noted earlier, GW detectors are practically omni-directional. Due to the long integration time, however, it turns out that continuous GWs are in fact extremely well-localized, not only in frequency but also in sky-position. A mismatch in frequency between the true signal and a template results in a phase mismatch that is growing with observation time, and thereby rapidly degrading the output of the (mis-)matched filter. Similarly, the Doppler effect from the daily rotation and orbital motion of the Earth modulates signals in a way that depends sensitively on the direction from which they are coming. The templates therefore need to be sky-position specific, and the required precision increases with observation time.

In the case of *wide-parameter searches* for unknown sources, this makes it very expensive in terms of computing cost to increase the observation time, as it requires a much finer search in the parameter space of possible signals. There is also a purely statistical effect limiting the sensitivity of such searches: the more trials (i.e. targeting of different points in parameter space) one performs, the more 'false alarm' candidates are expected to cross a given detection threshold due to noise fluctuations alone. Therefore, a higher detection threshold is required, which reduces the sensitivity.

On the other hand, fully *targeted searches* for GW sources with known parameters (such as pulsars with known sky-position and frequency evolution) are not affected by these difficulties and can attain the best possible sensitivity by coherently integrating over all the available data.

24.4.1 The General Form of the Signal

A general, elliptically polarized GW can be written in the reference frame of the source as

$$h_+(\tau) = A_+ \cos\Phi(\tau)\,, \quad h_\times(\tau) = A_\times \sin\Phi(\tau)\,, \tag{24.21}$$

where $h_{+,\times}$ are the two polarization states of $h^{\mathrm{TT}}_{\mu\nu}$ given in (24.2), using coordinates aligned with the principal polarization axes of the coherent GW. Assuming a quasi-monochromatic signal with slowly-varying intrinsic frequency $f(\tau)$, the signal phase $\Phi(\tau)$ can be Taylor-expanded as

$$\Phi(\tau) = \phi_0 + \phi(\tau)\,, \quad \phi(\tau) = 2\pi \sum_{k=0}^{s} \frac{f^{(k)}(\tau_{\mathrm{ref}})}{(k+1)!}\,\Delta\tau^{k+1}\,, \tag{24.22}$$

where $\Delta\tau \equiv \tau - \tau_{\mathrm{ref}}$, and τ_{ref} is the reference time at which the initial phase ϕ_0 and the $s+1$ spin parameters $f^{(k)} \equiv d^k f(\tau)/d\tau^k$ are defined.

Let $\boldsymbol{n} = (\cos\delta\cos\alpha, \cos\delta\sin\alpha, \sin\delta)$ be the unit vector pointing to the source, expressed in equatorial coordinates using the standard celestial angles α (right ascension) and δ (declination). The wave-frame is then completely determined by $\boldsymbol{n}$ and the 'polarization angle' ψ, which describes the orientation of the polarization axes with respect to the equatorial-coordinate system. Following the conventions of [23], ψ can be defined as the angle between the direction $\boldsymbol{n}\times\boldsymbol{Z}$ and the $\boldsymbol{x}$-axis of the TT wave-frame (corresponding to the '+' polarization), where $\boldsymbol{Z} = (0,0,1)$ is the unit-vector pointing to the celestial north pole. As discussed in [49], the dependency of the antenna-pattern functions $F_{+,\times}$ on the wave-frame orientation $\{\boldsymbol{n},\psi\}$ can be separated as

$$\begin{aligned} F_+(t;\boldsymbol{n},\psi) &= a(t;\boldsymbol{n})\cos 2\psi + b(t;\boldsymbol{n})\sin 2\psi\,,\\ F_\times(t;\boldsymbol{n},\psi) &= b(t;\boldsymbol{n})\cos 2\psi - a(t;\boldsymbol{n})\sin 2\psi\,, \end{aligned} \tag{24.23}$$

where the expressions for the (detector-dependent) functions $a(t;\boldsymbol{n})$, $b(t;\boldsymbol{n})$ are given in (12,13) of [49].

In the detector frame the signal amplitude is modulated by the rotating antenna pattern $F_{+,\times}(t)$, as seen in (24.3). More importantly, the signal is also Doppler-modulated by the relative motion of the detector with respect to the source. This can be expressed as a relation between the detector arrival time t of a wave-front that left the source at time $\tau(t)$. Let us consider the most general case of a neutron star in a binary system with orbital parameters $\mathbf{b}$ (including orbital period, projected semi-major axis, ellipticity etc) at a sky-position $\boldsymbol{n}$. The timing relation $\tau(t)$ can then be written as

$$\tau(t;\boldsymbol{n},\mathbf{b}) = t + \frac{r(t)\cdot\boldsymbol{n}}{c} - \frac{d}{c} + \Delta_{\mathrm{bin}}(t;\mathbf{b})\,, \tag{24.24}$$

where $r(t)$ is the vector from the solar-system barycenter (SSB) to the detector location, and $r\cdot\boldsymbol{n}/c$ term is known as the Roemer-delay. For simplicity we have neglected relativistic corrections in the SSB such as the Shapiro and Einstein delays,

see [75] for details. $\Delta_{\rm bin}(t;\mathbf{b})$ is the time delay between the neutron star and its binary-system barycenter (BSB), and d is the distance between the BSB and the SSB, which for simplicity is assumed constant and can therefore be neglected. For isolated neutron stars we would obviously have $\Delta_{\rm bin} = 0$. Inserting the timing relation (24.24) into the phase (24.22) in the source frame, we see that the phase evolution $\phi(t)$ in the detector frame has the general form

$$\phi(t;\boldsymbol{\lambda}) = \phi\left(\tau(t;\boldsymbol{\lambda})\right), \quad \text{where} \quad \boldsymbol{\lambda} \equiv \{f^{(k)}, \boldsymbol{n}, \mathbf{b}\}, \tag{24.25}$$

which defines the set of *Doppler parameters* $\boldsymbol{\lambda}$. Putting all the pieces together, we can express the strain (24.3) in the detector as

$$h(t;\mathcal{A},\boldsymbol{\lambda}) = F_+(t;\boldsymbol{n},\psi)A_+\cos\left[\phi_0+\phi(t;\boldsymbol{\lambda})\right] + F_\times(t;\boldsymbol{n},\psi)A_\times\sin\left[\phi_0+\phi(t;\boldsymbol{\lambda})\right], \tag{24.26}$$

where we defined the four *amplitude parameters* $\mathcal{A} \equiv \{A_+, A_\times, \psi, \phi_0\}$. Using the form (24.23) of the antenna-pattern functions $F_{+,\times}$, it is now easy to see that the dependencies on the amplitude and Doppler parameters can be explicitly separated, namely

$$h(t;\mathcal{A},\boldsymbol{\lambda}) = \sum_{\mu=1}^{4} \mathcal{A}^\mu\, h_\mu(t;\boldsymbol{\lambda}), \tag{24.27}$$

in terms of four basis waveforms

$$\begin{aligned} h_1(t;\boldsymbol{\lambda}) &= a(t;\boldsymbol{n})\cos\phi(t;\boldsymbol{\lambda}), & h_2(t;\boldsymbol{\lambda}) &= b(t;\boldsymbol{n})\cos\phi(t;\boldsymbol{\lambda}), \\ h_3(t;\boldsymbol{\lambda}) &= a(t;\boldsymbol{n})\sin\phi(t;\boldsymbol{\lambda}), & h_4(t;\boldsymbol{\lambda}) &= b(t;\boldsymbol{n})\sin\phi(t;\boldsymbol{\lambda}), \end{aligned} \tag{24.28}$$

and the amplitude vector $\mathcal{A}^\mu$, defined as

$$\begin{aligned} \mathcal{A}^1 &= \ A_+\cos\phi_0\cos 2\psi - A_\times\sin\phi_0\sin 2\psi, \\ \mathcal{A}^2 &= \ A_+\cos\phi_0\sin 2\psi + A_\times\sin\phi_0\cos 2\psi, \\ \mathcal{A}^3 &= -A_+\sin\phi_0\cos 2\psi - A_\times\cos\phi_0\sin 2\psi, \\ \mathcal{A}^4 &= -A_+\sin\phi_0\sin 2\psi + A_\times\cos\phi_0\cos 2\psi. \end{aligned} \tag{24.29}$$

Different emission mechanisms of continuous GWs result in different expressions for the amplitude parameters $\mathcal{A}$ in terms of the source parameters, and in different relations between the rotation frequency ν of the neutron star and the GW frequency f in (24.22). Some interesting special cases are triaxial neutron stars rotating around a principal axis, in which case $f = 2\nu$. Free precession emits additional power at a frequency $f \approx \nu$, and r-mode oscillations emit near $f \approx 4\nu/3$. In order to simplify the following discussion, it is convenient to express the amplitudes $A_{+,\times}$ in terms of the source parameters of a non-precessing triaxial neutron star (e.g., [49]), namely

$$A_+ = \frac{1}{2}h_0\left(1+\cos^2\iota\right), \qquad A_\times = h_0\cos\iota, \tag{24.30}$$

where h_0 is the overall amplitude (24.11), and ι is the angle between the spin-axis of the neutron star and the line-of-sight $\boldsymbol{n}$. This is conceptually the simplest source model, and it does not entail any loss of generality, as the mapping between $\{h_0, \cos\iota\}$ and $A_{+,\times}$ is one-to-one.

24.4.2 Signals in Noise

In practice, the strain $x(t)$ measured by a detector is mainly dominated by noise $n(t)$, such that even in the presence of a signal $h(t)$ we have

$$x(t) = n(t) + h(t; \mathcal{A}, \boldsymbol{\lambda}) \,. \tag{24.31}$$

The measured output is not a continuous function of time, but a discrete time series of data points $x_i = x(t_i)$ with $t_i = i\Delta t$, sampled at a finite rate $f_{\mathrm{samp}} = 1/\Delta t$, e.g., for LIGO and GEO600 $f_{\mathrm{samp}} = 16{,}384\,\mathrm{Hz}$ and $f_{\mathrm{samp}} = 20{,}000\,\mathrm{Hz}$ for Virgo. A continuous-time formulation is often used for convenience of notation, however. Let us make the idealized assumption of Gaussian stationary noise n_i with zero mean and covariance $\gamma_{jk} \equiv E[n_j n_k]$, where $E[\ldots]$ denotes the expectation-value of a random variable. If we define the scalar product $(x\|y)$ of two (real-valued) time series x_i and y_i as

$$(x\|y) \equiv \sum_{j,l} x_j \, \gamma^{-1}_{jl} \, y_k \,, \tag{24.32}$$

then the probability of a particular (pure-noise) time series $\{n_j\}_{j=0}^{M-1}$ is expressible as

$$P(\{n_j\}|\gamma) = (2\pi)^{-M/2} \, |\gamma|^{-1/2} \, e^{-\frac{1}{2}(n\|n)} \,. \tag{24.33}$$

In the continuum limit of $\Delta t \to 0$, the scalar product (24.32) can be shown (cf. [41]) to converge to the expression

$$(x\|y) \overset{\Delta t \to 0}{\to} 4\Re \int_0^\infty \frac{\widetilde{x}(f)\,\widetilde{y}^*(f)}{S_{\mathrm{n}}(f)} \, df \,, \tag{24.34}$$

which is the classical Wiener filter of matched-filtering theory [86]. Here $\widetilde{x}(f)$ is the Fourier transform of $x(t)$, and * denotes complex conjugation. $S_{\mathrm{n}}(f)$ is the single-sided power spectral density, which is defined as the Fourier transform of the auto-correlation function, i.e.

$$S_{\mathrm{n}}(f) = 2 \int_{-\infty}^{\infty} E[n(0)\, n(t)] \, e^{-i2\pi f t} \, dt \,. \tag{24.35}$$

In practice, this definition is not very useful for computing S_{n}, however, and a more practical estimate for S_{n} can be obtained from the finite discrete time series $\{n_j\}$ using the Wiener–Khintchine theorem, namely

$$S_{\mathrm{n}}(f) \approx \frac{2}{T_{\mathrm{obs}}} E\left[|\widetilde{n}(f)|^2\right] \,, \tag{24.36}$$

which holds exactly in the limit of infinite duration $T_{\rm obs}$ of the time-series, i.e. when $T_{\rm obs} \equiv M\,\Delta t \to \infty$. Here $\widetilde{n}(f)$ is the discrete Fourier transform of n_j, defined as

$$\widetilde{n}(f) = \Delta t \sum_{j=0}^{M-1} n_j\, e^{-i2\pi f\, j\Delta t}\,. \tag{24.37}$$

The quantity $\sqrt{S_{\rm n}(f)}$ (which has units of $\mathrm{Hz}^{-1/2}$) is the most commonly-used measure of the noise performance of GW detectors, e.g., see Fig. 24.2. Note that in the case of nearly-monochromatic signals $h(t)$, as considered here, only a very narrow frequency band around the signal frequency f_0 will contribute to the scalar product (24.34). In this case, $S_{\rm n}(f)$ can be approximated as constant in the neighborhood of f_0, and the scalar product therefore simplifies to

$$(x\|y) \approx \frac{2}{S_{\rm n}(f_0)} \int_0^{T_{\rm obs}} x(t)\, y(t)\, dt\,. \tag{24.38}$$

Using (24.31) and (24.33), the probability of measuring a strain $x(t)$ in the presence of Gaussian noise $n(t)$ and a signal $h(t;\mathcal{A},\boldsymbol{\lambda})$ can be expressed as

$$P(x|\mathcal{A},\boldsymbol{\lambda},S_{\rm n}) \propto e^{-\frac{1}{2}(x-h\|x-h)}\,. \tag{24.39}$$

The signal-to-noise ratio (SNR) of matched filtering is conventionally defined as $\rho \equiv \sqrt{(h\|h)}$, and for continuous GWs it is straightforward to show [37, 49, 65] that the SNR scales as

$$\rho = \sqrt{(h\|h)} \propto \frac{h_0}{\sqrt{S_{\rm n}}}\,\sqrt{T_{\rm obs}\,\mathcal{N}}\,, \tag{24.40}$$

with the observation time $T_{\rm obs}$ and the number of equal-sensitivity detectors $\mathcal{N}$. This illustrates why it is essential for continuous-wave searches to integrate the data over the longest possible observation time $T_{\rm obs}$ (and use as many sensitive detectors $\mathcal{N}$ as possible).

There are two different ways of proceeding from this point, depending on the paradigm of statistics used: Bayesian or frequentist. These approaches yield sometimes similar-looking answers (especially in Gaussian noise), but they require fundamentally different interpretations and provide different tools in practice. The conceptual difference between the two frameworks lies in the meaning of 'probability', while the axioms for *calculating* with probabilities are the same in both cases.

24.4.3 Frequentist Framework: Hypothesis Testing

The frequentist approach is based on the frequency-interpretation of probability: the probability $P(A)$ of an event A is defined as the limiting fraction of events A in an

infinite number of 'identical'[1] trials. The frequentist detection problem is formulated as one of hypothesis testing: let H_0 be the hypothesis that there is no signal in the data (i.e. $h = 0$), and H_1 stands for the hypothesis that there is a nonzero signal h. Now we need a criterion to decide in an optimal way between the two hypotheses given a measurement $x(t)$. This can be achieved by computing a scalar *detection statistic* $\Lambda(x)$, and setting a threshold Λ^* such that H_0 is accepted if $\Lambda(x) < \Lambda^*$, while H_1 is accepted otherwise. From the probability distribution (24.39) of $x(t)$, we can calculate $P(\Lambda|H_0)$ and $P(\Lambda|H_1)$ for the two hypothesis. This allows us to define the *false alarm* probability $f_{\mathrm{A}}(\Lambda^*)$, namely

$$f_{\mathrm{A}}(\Lambda^*) \equiv \int_{\Lambda^*}^{\infty} P(\Lambda|H_0)\, d\Lambda\,, \tag{24.41}$$

which is the probability of Λ crossing the threshold Λ^* despite H_0 being true. Similarly, we define the *false dismissal* probability $f_{\mathrm{D}}(\Lambda^*, h)$ of a signal h as

$$f_{\mathrm{D}}(\Lambda^*, h) \equiv \int_{-\infty}^{\Lambda^*} P(\Lambda|H_1)\, d\Lambda\,, \tag{24.42}$$

which is the probability that Λ does not cross the threshold Λ^*, even though H_1 is true. The detection probability $\eta \equiv \int_{\Lambda^*}^{\infty} \mathcal{P}(\Lambda|H_1)\, d\Lambda$ is then simply the complement to f_{D}, namely $\eta = 1 - f_{\mathrm{D}}$. A standard criterion for the optimality of a hypothesis test $\Lambda(x)$ is that the test should maximize the detection probability $\eta(\Lambda^*, h)$ at a given false-alarm rate $f_{\mathrm{A}}(\Lambda^*)$. According to the Neyman–Pearson lemma, the optimal test is given by the likelihood ratio, which is defined as

$$\Lambda(x;h) \equiv \frac{P(x|H_1)}{P(x|H_0)}\,. \tag{24.43}$$

Applying this to the Gaussian detection problem (24.39), we find

$$\ln\Lambda(x;h) = (x\|h) - \frac{1}{2}(h\|h)\,, \tag{24.44}$$

which is the well-known expression for the matched-filtering amplitude. If some of the parameters of the signal $h(t;\mathcal{A},\boldsymbol{\lambda})$ are unknown, one tries to find the *maximum* of $\ln\Lambda$ as a function of $\{\mathcal{A},\boldsymbol{\lambda}\}$, which yields the corresponding maximum-likelihood estimators (MLE) for these parameters.

The $\mathcal{F}$-Statistic

In targeted searches of GWs from known pulsars, the Doppler parameters $\boldsymbol{\lambda}$, i.e. sky-position $\boldsymbol{n}$ and spins $f^{(k)}$, are usually well known, but even in this case one has generally no information about the four amplitude parameters $\mathcal{A}$, for which we have to find the maximum-likelihood estimators. In wide-parameter searches

[1] The trials can obviously not be truly identical or they would yield the same result.

the Doppler-parameters $\boldsymbol{\lambda}$ of possible signals are also treated as unknown. However, as shown in [49], the maximization over $\mathcal{A}^\mu$ can be performed analytically, thereby reducing the number of remaining unknown parameters that need to be searched. Inserting the factored expression (24.27) for the filters $h(t;\mathcal{A},\boldsymbol{\lambda})$ into (24.44), we find

$$\ln\Lambda(x;\mathcal{A},\boldsymbol{\lambda}) = \mathcal{A}^\mu\, x_\mu - \frac{1}{2}\mathcal{A}^\mu\mathcal{A}^\nu\,\mathcal{M}_{\mu\nu}\,, \tag{24.45}$$

with implicit summation over $\mu,\nu = 1,2,3,4$, and where we defined

$$x_\mu(\boldsymbol{\lambda}) \equiv (x\|h_\mu)\,, \quad \text{and} \quad \mathcal{M}_{\mu\nu}(\boldsymbol{\lambda}) \equiv (h_\mu\|h_\nu)\,. \tag{24.46}$$

We can now maximize $\ln\Lambda$ over $\mathcal{A}^\mu$ in order to obtain their maximum-likelihood estimators $\mathcal{A}^\mu_{\mathrm{ML}}$ from the data $x(t)$, namely

$$\frac{\partial\ln\Lambda}{\partial\mathcal{A}^\mu} = 0 \implies \mathcal{A}^\mu_{\mathrm{ML}} = \mathcal{M}^{\mu\nu}\,x_\nu\,, \tag{24.47}$$

where $\mathcal{M}^{\mu\alpha}\mathcal{M}_{\alpha\nu} = \delta^\mu_\nu$. Substituting these $\mathcal{A}^\mu_{\mathrm{ML}}$ into (24.45), we obtain a new detection statistic, which only depends on the Doppler parameters $\boldsymbol{\lambda}$, namely

$$2\mathcal{F}(x;\boldsymbol{\lambda}) = x_\mu\,\mathcal{M}^{\mu\nu}\,x_\nu\,, \tag{24.48}$$

which is known as the "$\mathcal{F}$-statistic" in this context[2]. The coherent multi-detector generalization of the $\mathcal{F}$-statistic was derived recently by [37], but for simplicity we restrict the following discussion to the case of a single detector. In the presence of a signal $h(t;\mathcal{A}_{\mathrm{s}},\boldsymbol{\lambda}_{\mathrm{s}})$, the expectation value of the $\mathcal{F}$-statistic with perfectly matched Doppler parameters, $\boldsymbol{\lambda} = \boldsymbol{\lambda}_{\mathrm{s}}$, is found as

$$E[2\mathcal{F}] = 4 + \rho^2\,, \tag{24.49}$$

where ρ is the optimal SNR defined previously in (24.40). One can show (cf. [37, 49]) that $2\mathcal{F}$ is a random variable with a χ^2-distribution with 4 degrees of freedom and a non-centrality parameter ρ^2 (for the definition of the non-central χ^2-distribution, see for example [10]). In the absence of a signal, i.e. $\rho = 0$, this reduces to the central χ^2-distribution, namely

$$P(2\mathcal{F};0) = \frac{1}{2}\,\mathcal{F}\,e^{-\mathcal{F}}\,. \tag{24.50}$$

Using the known probability distribution of $2\mathcal{F}$, we can compute the false-alarm probability $f_{\mathrm{A}}(2\mathcal{F}^*)$ and the false-dismissal probability $f_{\mathrm{D}}(2\mathcal{F}^*;\rho^2)$ for a threshold $2\mathcal{F}^*$ and SNR ρ. The false-alarm probability (24.41) is easily integrated and yields

$$f_{\mathrm{A}}(2\mathcal{F}^*) = (1+\mathcal{F}^*)\,e^{-\mathcal{F}^*}\,, \tag{24.51}$$

[2] Not to be confused with the F-statistic or the F-test in the statistics literature

while the false-dismissal probability (24.42) generally needs to be integrated numerically. If we choose a false-alarm rate of $f_{\mathrm{A}}(2\mathcal{F}^*) = 1\%$, say, then (24.51) determines a detection threshold of $2\mathcal{F}^* \approx 13.3$. With this threshold, the required SNR for a false-dismissal rate of 10%, say, is given by the solution of $f_{\mathrm{D}}(2\mathcal{F}^*; \rho^2) = 10\%$, which results in $\rho \approx 4.5$. Using (93) of [49] relating the *average* SNR $\langle\rho\rangle$ (over sky-location $\boldsymbol{n}$, orientation $\cos\iota$ and polarization ψ), to the amplitude h_0, we can express the smallest average amplitude $\langle h_0\rangle$ that would be detectable with a 1% false-alarm and 10% false-dismissal rate as

$$\langle h_0\rangle^{f_{\mathrm{D}}=10\%}_{f_{\mathrm{A}}=1\%} \approx 11.4\sqrt{\frac{S_{\mathrm{n}}}{T_{\mathrm{obs}}}}\,, \tag{24.52}$$

where T_{obs} is the coherently-integrated observation time. This is a useful measure of the sensitivity of a search. Note, however, that the false-alarm rate (24.51) refers to a *single* trial, and therefore this sensitivity-estimate only applies to targeted, single-template searches. When using a coherent network of detectors with respective noise floors S_{X}, the combined noise-floor to use in (24.52) is given by $S_{\mathrm{n}}^{-1} = \sum S_{\mathrm{X}}^{-1}$. Therefore, the combined sensitivity of $\mathcal{N}$ equal-noise detectors is improved by a factor of $\sqrt{\mathcal{N}}$. In the case of LIGO I, the combined design-sensitivity of H1, L1 and H2 (cf. Sec. 24.3) would be roughly a factor $\sqrt{2.25}$ better, as H2 has half the arm length and is only about half as sensitive as H1 and L1. Advanced LIGO will consists of three 4 km interferometers, and the combined H1+H2+L1 detector will therefore be a factor $\sqrt{3}$ more sensitive than any single one.

Another important quantity is the *upper limit* on the amplitude of gravitational waves that we can obtain from an observation that did not detect a signal. The standard frequentist upper limit of confidence C is defined as the amplitude h_0^C of signals that would result in values $2\mathcal{F}$ exceeding the loudest candidate $2\mathcal{F}_0$ that was actually measured in a fraction C of trials, i.e.

$$C = \int_{2\mathcal{F}_0}^{\infty} P(2\mathcal{F}|h_0^C)\, d2\mathcal{F}\,, \tag{24.53}$$

which will often be computed using Monte-Carlo integration. Note that, contrary to the Bayesian approach described below, this is not a statement about the confidence that the true value of h_0 is contained in the interval $[0, h_0^C]$, but about the frequency with which the so-constructed interval would contain the true value in repeated experiments. For a more detailed discussion and an elegant method of constructing frequentist confidence intervals, see [40].

24.4.4 Bayesian Analysis: Parameter Estimation

Bayesian statistics is built on a different concept of probability, quantifying the degree of certainty (or "degree of belief") of a statement being true (see [53, 71] for general introduction and references). Freed from the narrow frequentist definition

of probability, one can now assign probabilities $P(A|I) \in [0,1]$ to any statement A within some model I, quantifying one's (possibly incomplete) knowledge about the truth of A. The probabilities $P(A|I) = 1$ and $P(A|I) = 0$ reflect the extreme cases of certainty about A being true or false, respectively. The axioms of probability provide a natural framework to calculate with such quantified partial knowledge. A central tool in this approach is Bayes' theorem (an elementary consequence of the axioms of probability), namely

$$P(A|x,I) = P(x|A,I)\,\frac{P(A|I)}{P(x|I)}\,. \tag{24.54}$$

Using this together with (24.39), we can express the 'posterior probability' of a signal $h(t;\mathcal{A},\boldsymbol{\lambda})$ being present, *given* the measurement $x(t)$, as

$$P(\mathcal{A},\boldsymbol{\lambda}|x,I) = k\,P(x|\mathcal{A},\boldsymbol{\lambda},I)\,P(\mathcal{A},\boldsymbol{\lambda}|I)\,, \tag{24.55}$$

where k is a normalization constant. The term $P(\mathcal{A},\boldsymbol{\lambda}|I)$ is the "prior probability", which expresses our previous knowledge about the signal, either from other measurements or from theoretical considerations. Equation (24.55) quantifies how our state of knowledge is transformed from the prior $P(\mathcal{A},\boldsymbol{\lambda}|I)$ to the posterior $P(\mathcal{A},\boldsymbol{\lambda}|x,I)$ in the light of new information $x(t)$. One of the somewhat controversial aspects of Bayesian statistics is the assignment of prior probabilities. One often tries to use a prior reflecting 'ignorance' or minimal bias (a common choice is a flat prior, i.e. $P(\mathcal{A},\boldsymbol{\lambda}|I) = \text{const.}$), but this is not unproblematic and there is no unique choice of such a zero-information prior. Substituting the likelihood (24.39) in (24.55), we find the posterior probability

$$P(\mathcal{A},\boldsymbol{\lambda}|x,I) = k'\,P(\mathcal{A},\boldsymbol{\lambda}|I)\,\Lambda(x;\mathcal{A},\boldsymbol{\lambda})\,, \tag{24.56}$$

where k' is another normalization constant. We see that are naturally lead back to an expression resembling the likelihood ratio (24.44). However, the statistical interpretation in this case is very different from the frequentist framework, as the posterior (24.56) determines the probability of a signal with certain parameters being present, while we cannot assign meaningful frequentist probabilities to such statements. Equation (24.56) formulates the detection problem in terms of *parameter estimation* of the signal, while the frequentist approach is typically based on *hypothesis testing*.

A powerful tool of the Bayesian framework is *marginalization* over 'nuisance parameters'. Let us assume for simplicity that we have performed a targeted search with known Doppler parameters $\boldsymbol{\lambda}$. If we want to express the posterior for only a subset of the four unknown amplitude parameters $\mathcal{A}$, e.g., we might be most interested in $P(h_0|x,I)$, say, then we can compute this by simply summing the posterior over all the possible values of the 'uninteresting' parameters $\cos\iota$, ψ and ϕ_0, i.e.

$$P(h_0|x,I) \propto \int P(\mathcal{A}|x,I)\,d\phi_0\,d\psi\,d\cos\iota\,. \tag{24.57}$$

The Bayesian way of determining an upper limit $h_0^{\mathbf{C}}$ of confidence $\mathbf{C}$ consists simply of solving the equation

$$\mathbf{C} = \int_0^{h_0^{\mathbf{C}}} P(h_0|x,I)\, dh_0\,, \tag{24.58}$$

i.e. the true amplitude h_0 lies within $[0, h_0^{\mathbf{C}}]$ with probability $\mathbf{C}$. Note that this 'confidence' $\mathbf{C}$ has an entirely different meaning from the frequentist confidence in (24.53). A more detailed discussion of the application of Bayesian statistics to the problem of detecting continuous GWs is found in [39] and [32].

24.4.5 Parameter Space of Coherent Wide-Parameter Searches

The sensitivity of wide-parameter (as opposed to targeted) searches is severely limited by the large number of required templates, which is a rapidly growing function of the coherent observation time T_{obs}. The measure for how densely templates need to be placed in the Doppler-parameter space is determined by the relative loss m of detection statistic $\mathcal{F}$ caused by an offset $d\boldsymbol{\lambda} = \boldsymbol{\lambda} - \boldsymbol{\lambda}_{\mathrm{s}}$ from a putative signal position $\boldsymbol{\lambda}_{\mathrm{s}}$. This mismatch m induces a natural distance measure and a corresponding local *metric* g_{ij} on the parameter space, first introduced by [21] and [59], namely

$$m(\boldsymbol{\lambda}_{\mathrm{s}}, d\boldsymbol{\lambda}) = \frac{E[\mathcal{F}(\boldsymbol{\lambda}_{\mathrm{s}})] - E[\mathcal{F}(\boldsymbol{\lambda})]}{E[\mathcal{F}(\boldsymbol{\lambda}_{\mathrm{s}})]} = g_{ij}(\boldsymbol{\lambda}_{\mathrm{s}})\, d\boldsymbol{\lambda}^i\, d\boldsymbol{\lambda}^j + \mathcal{O}(d\boldsymbol{\lambda}^3)\,, \tag{24.59}$$

where we used the fact that $E[\mathcal{F}(\boldsymbol{\lambda}_{\mathrm{s}})]$ is a local maximum of $\mathcal{F}$ if there is a signal in $\boldsymbol{\lambda}_{\mathrm{s}}$. It can be shown (cf. [26, 65]) that this metric can be approximated as

$$g_{ij} \sim \big\langle \partial_i\phi\, \partial_j\phi \big\rangle - \big\langle \partial_i\phi \big\rangle \big\langle \partial_j\phi \big\rangle\,, \tag{24.60}$$

in terms of the signal phase $\phi(t)$, and where we defined $\partial_i = \partial/\partial\boldsymbol{\lambda}^i$ and where $\langle \ldots \rangle$ denotes the time-average over T_{obs}. Considering the explicit phase model (24.22), (24.24) for isolated neutron stars with one spin-down, i.e. $\boldsymbol{\lambda}^i \in \{\boldsymbol{n}, f, \dot{f}\}$, one can easily show (e.g., [65]) the following dominant scaling relations

$$g_{\theta\theta} \propto f^2\, T_{\mathrm{obs}}^2\, (V/c)^2\,, \qquad g_{ff} \propto T_{\mathrm{obs}}^2\,, \qquad g_{\dot{f}\dot{f}} \propto T_{\mathrm{obs}}^4\,, \tag{24.61}$$

where θ is the angular separation on the sky and $V/c \sim 10^{-4}$ is the maximal Doppler shift due to the orbital velocity V. The required number of templates dN_p per small parameter-space region $d^4\boldsymbol{\lambda} = d\Omega \times df \times d\dot{f}$ (with sky solid-angle $d\Omega$) is therefore

$$dN_p \propto \sqrt{|\det g_{ij}|}\; d^4\boldsymbol{\lambda} \propto T_{\mathrm{obs}}^5\, f^2\, d^4\boldsymbol{\lambda}\,. \tag{24.62}$$

As noted in [65], the $\mathcal{O}(T_{\mathrm{obs}}^2)$ growth of the number of sky templates should only be considered as a lower bound, and a more detailed analysis is required to determine the exact scaling with T_{obs}. In a wide-parameter search we need to integrate (24.38)

for each template, i.e. the computing cost c_p per template is $c_p \propto T_{\rm obs}$, and the total computing cost dC_p per parameter space $d^4\boldsymbol{\lambda}$ scales (at least) as

$$dC_p \propto T_{\rm obs}^6 f^2 d^4\boldsymbol{\lambda}\,. \tag{24.63}$$

On the other hand, recall that longer integration times are required in order to increase the SNR (24.40) of weak signals. This rapid growth of the computing cost $C_p(T_{\rm obs})$ severely limits the longest integration time $T_{\rm obs}$ that is affordable for all-sky, wide-frequency searches to about $T_{\rm obs}\sim 10\,{\rm h} - 30\,{\rm h}$ with currently realistic levels of computing power, e.g., ~ 50 Tflops with Einstein@Home (cf. Sect. 24.4.7). The second effect of the large number of templates N_p is to reduce the sensitivity compared to a targeted search with the *same* observation time and false-alarm probability: increasing the number of templates increases the number of expected false-alarm candidates at fixed detection threshold. Therefore the detection-threshold needs to be raised to maintain the same false-alarm rate, thereby decreasing the sensitivity.

Note that increasing the number of equal-sensitivity detectors $\mathcal{N}$ improves the SNR (24.40) in the same way as increasing the integration time $T_{\rm obs}$. However, the expression (24.60) for the metric and the scaling (24.61) are still approximately valid even for such a network of detectors, as shown in [65]. This implies that increasing the number of detectors $\mathcal{N}$ does *not* increase the required number of templates N_p, which makes this the computationally cheapest way to improve the SNR of coherent wide-parameter searches.

24.4.6 Semi-Coherent Methods

Coherent matched-filtering is the optimal method for targeted, single-template searches. However, the discussion in the previous section shows that wide-parameter searches will require techniques that trade off statistical 'optimality' for lower computing cost (i.e. a smaller number of templates). These 'semi-coherent' methods are less sensitive than matched filtering for the same observation time. However, as they require far fewer templates in parameter space, they allow one to over-compensate this apparent loss of sensitivity by using a *longer* observation time and *lower* thresholds, which typically results in more sensitive searches at substantially lower cost in computing power.

Here we focus on the simplest type of semi-coherent methods, which operate on successive short Fourier transforms (SFTs) of the measured strain data $x(t)$. There are three main variants of such SFT-based semi-coherent methods currently in use for GW searches, known respectively as "StackSlide" (also known as the "Radon transform"), the "Hough transform" and "PowerFlux" (see [8] for a more detailed description). The aim of these methods is to detect a statistical excess of power in the frequency-bins corresponding to the time-frequency 'path' of the signal of frequency $\hat{f}(t)$ at the detector, as illustrated in Fig. 24.3. The instantaneous frequency

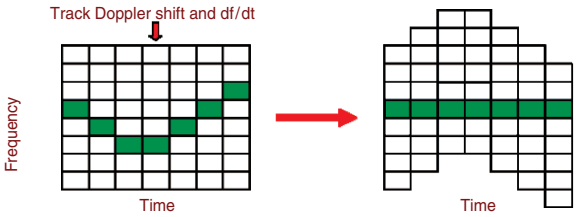

Fig. 24.3 An illustration of the principle used in semi-coherent methods to detect continuous GWs: The dark pixels represent a signal in the data. Its frequency changes with time due to Doppler shifts and intrinsic evolution of the source. By appropriately sliding the frequency bins of successive coherent 'stacks' (shown vertically), the power of the signal can be lined up and summed (from [8])

$\hat{f}(t)$ of a signal at the detector can be approximately (e.g., see [52]) related to the instantaneous intrinsic frequency $f(t)$ of a GW by

$$\hat{f}(t) = \left(1 + \frac{\mathbf{v}(t)\cdot\boldsymbol{n}}{c}\right) f(t)\,, \tag{24.64}$$

where $\mathbf{v}(t)$ is the detector velocity with respect to the SSB frame. In the semi-coherent methods, the total observation time T_{obs} is divided into N 'stacks' of duration $T_{\mathrm{coh}} = T_{\mathrm{obs}}/N$. The time series $x_j^{(l)}$ in stack l is Fourier-transformed, which gives the SFT $\tilde{x}_k^{(l)}$ for the stack l, with frequency bins $f_k = k/T_{\mathrm{coh}}$. The normalized power $\rho_k^{(l)}$ in frequency-bin k of stack l is defined as

$$\rho_k^{(l)} \equiv \frac{2|\tilde{x}_k^{(l)}|^2}{T_{\mathrm{coh}}\, S_{\mathrm{n}}}\,, \tag{24.65}$$

such that in the absence of a signal, the expectation value is $E[\rho_k^{(l)}] = 1$. The maximal length of SFT stacks is constrained by the requirement that the signal power should not be spread over more than one frequency bin by the Doppler shift. This typically limits SFT stacks to about $T_{\mathrm{coh}} \lesssim 60$ min.

The *StackSlide* method computes the total power $P = N^{-1}\sum_l \rho_{k(l)}^{(l)}$ along the path of frequency bins $k(l)$ corresponding to the signal frequency (24.64), as illustrated in Fig. 24.3. The *PowerFlux* method is a variant of StackSlide, summing *weighted* power in order to improve the sensitivity by taking account of non-stationarities of the noise and the direction-dependent antenna-patterns. The *Hough transform*, on the other hand, sums binary *number counts* $n_k^{(l)}$ instead of power. These number counts are obtained by setting a threshold ρ_{th} on the normalized power (24.65), namely $n_k^{(l)} = 1$ if $\rho_k^{(l)} \geq \rho_{\mathrm{th}}$, and $n_k^{(l)} = 0$ otherwise. The final Hough detection statistic is the total number count $n = \sum_l n_{k(l)}^{(l)}$ of threshold-crossings along the time-frequency path $k(l)$. Summing binary number counts instead of power slightly reduces the sensitivity of the Hough method compared to StackSlide and PowerFlux,

but it increases its robustness with respect to transient disturbances, as no single stack can contribute more than '1' to the final number count.

Semi-coherent methods combine 'power' from different stacks, while the phase information between stacks has been lost, which reduces the sensitivity compared to fully coherent matched filtering with the same observation time T_{obs} (by increasing the false-alarm probability). This effect can be seen, for example, in the expression for the average amplitude h_0 of the weakest signal detectable in a targeted Hough-search with a false-alarm rate of $f_{\mathrm{A}} = 1\%$ and a false-dismissal of $f_{\mathrm{D}} = 10\%$ [52], namely

$$\langle h_0 \rangle^{f_{\mathrm{D}}=10\%}_{f_{\mathrm{A}}=1\%} \approx 8.5 N^{1/4} \sqrt{\frac{S_{\mathrm{n}}}{T_{\mathrm{obs}}}} = 8.5 N^{-1/4} \sqrt{\frac{S_{\mathrm{n}}}{T_{\mathrm{coh}}}} \,. \tag{24.66}$$

Similar expressions hold for StackSlide and PowerFlux [8]. Comparing this to the analogous matched-filtering expression (24.52) shows that a coherent search over the full observation time T_{obs} would be more sensitive by about a factor of $N^{1/4}$. This comparative loss in sensitivity, however, is accompanied by an enormous advantage, namely a substantially lower parameter-space resolution compared to a coherent search with the same T_{obs}. We can estimate the frequency resolution of a semi-coherent search as $\delta f \sim 1/T_{\mathrm{coh}}$, which is the frequency-resolution of the SFT stacks. The resolution in spin-down $\delta \dot{f}$ and angular sky-position $\delta\theta$ can be estimated from the requirement that the frequency should not drift by more than one frequency-bin δf over the total observation time T_{obs} (cf. [8]), which results in

$$\delta \dot{f} \sim \frac{1}{T_{\mathrm{obs}}\, T_{\mathrm{coh}}} \,, \quad \delta\theta \sim \frac{1}{f\, T_{\mathrm{coh}}\, V/c} \,. \tag{24.67}$$

The number of required templates per parameter-space $d^4\boldsymbol{\lambda}$ in a search for isolated neutron stars with one spin-down therefore scales as

$$dN_p \propto T_{\mathrm{obs}}\, T_{\mathrm{coh}}^4\, f^2\, d^4\boldsymbol{\lambda} \,. \tag{24.68}$$

Each parameter-space point requires summing $N \propto T_{\mathrm{obs}}$ numbers, so the computing cost dC_p scales as

$$dC_p \propto T_{\mathrm{obs}}^2\, T_{\mathrm{coh}}^4\, f^2\, d^4\boldsymbol{\lambda} \,, \tag{24.69}$$

which shows that the increase in computing cost with T_{obs} is *substantially* weaker than for the fully coherent case (24.63). The search can therefore be extended over much longer total observation times T_{obs}, of the order of several months, thereby achieving a better sensitivity at lower computing cost than fully coherent matched-filtering. The semi-coherent methods are not restricted to using SFT stacks, but we can also use 'demodulated' stacks [52] such as the $\mathcal{F}$-statistic (24.48). This allows to increase the length of the coherent stacks T_{coh} beyond the short duration $T_{\mathrm{coh}} \lesssim$ 60 min of SFT stacks, which increases the sensitivity (24.66), but also the computing cost (24.69).

24.4.7 Hierarchical Searches and Einstein@Home

Neither the matched-filtering nor the semi-coherent methods described in the previous sections optimize by themselves the sensitivity of wide-parameter searches at given finite computing power: the sensitivity can be further improved by appropriately combining several stages of such coherent and semi-coherent steps, in what is generally known as 'hierarchical' schemes [25, 38, 42].

The general idea is to start with a wide-parameter search using a relatively short observation time and therefore low resolution in parameter space. In this first stage a low threshold is used in order to increase the chances of a weak signal crossing the threshold. This will result in a large number of random-chance candidates, however, which are followed up in a second stage search using a longer observation time and a higher threshold. This is computationally affordable due to the reduced number of templates required to follow up the first-stage candidates, as opposed to scanning the entire parameter space at high resolution. This step can be iterated several times with increasingly longer observation times and higher thresholds, successively gaining confidence in the surviving candidates. There are several free parameters in such a scheme, such as the number of stages, the length of respective stacks and their corresponding thresholds, all of which need to be optimized in order to obtain the best possible sensitivity per computing cost. A first study of this optimization problem was carried out by [38], and the results suggest that about three stages might be sufficient.

In addition to the (still ongoing) effort to develop such an optimal search algorithm, one also wants to maximize the available computing power in order to optimize the absolute sensitivity of the search. This second goal is accomplished by the Einstein@Home project,[3] a public distributed-computing project launched in Feb. 2005. Einstein@Home is based on the distributed-computing platform BOINC,[4] which was originally developed for Seti@Home, and which is now used by a growing number of distributed-computing projects. The search for continuous GWs is ideally suited for this kind of distributed approach, as it can be split into a large number of small, independent problems: each participating host analyzes only a small portion $\Delta\boldsymbol{\lambda}$ of the total Doppler parameter space. After completing this search, the host returns the results to a central project server and requests the next 'work-unit' to analyze. By Aug. 2006, Einstein@Home has attracted more than 100,000 participants, contributing more than 200,000 CPUs, and delivering more than 50 Tflops of continuous computing power. The hierarchical search scheme currently under development for Einstein@Home is ultimately expected to yield the most sensitive wide-parameter search available for continuous GWs from unknown spinning neutron stars.

[3] http://einstein.phys.uwm.edu/

[4] http://boinc.berkeley.edu/

24.5 Current Status of the Search for Continuous GWs

24.5.1 Overview of Continuous-Wave Searches

Figure 24.4 gives an overview of the current status of searches for continuous GWs from spinning neutron stars. This figure shows *approximate* levels of published upper limits, *estimated* sensitivities of current and future searches, and astrophysically motivated upper limits. The spin-down upper limits (24.18) for known pulsars shown in Fig. 24.4 are based on the pulsar parameters in the ATNF catalog [54], allowing for a distance uncertainty of $\pm 10\%$ and a moments of inertia in the range $I_{zz} = (1-3) \times 10^{38}\ \mathrm{kg\,m^2}$ (see [7] for discussion). The astrophysical limit for Sco X-1 is based on the Bildsten–Wagoner mechanism (24.20). The curves 'LIGO-I', 'Virgo', 'eLIGO' and 'AdvLIGO' in Fig. 24.4 are based on (24.52), describing a targeted coherent integration over 1 year of data at the respective design sensitivity. The AdvLIGO curve corresponds to a wideband tuning of the detectors (with anticipated fundamental noise sources), but Advanced LIGO can also be tuned in different ways in order to pinpoint an anticipated high-frequency source with narrow-banding, or increase the sensitivity at low frequencies (at the expense

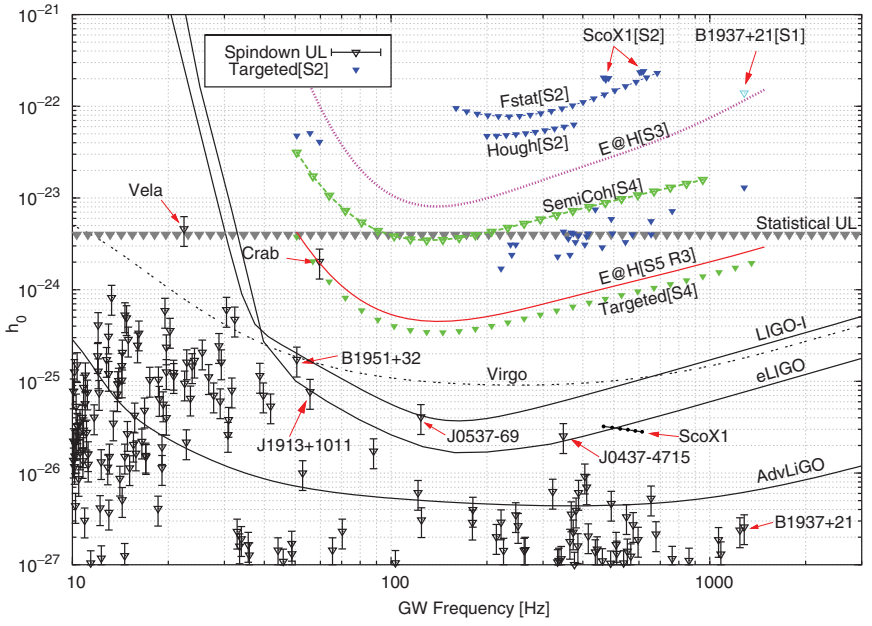

Fig. 24.4 Summary plot of approximate levels of published upper limits (cf. Sect. 24.5.2), estimated sensitivities of various current and future searches (cf. Sect. 24.5.3) and astrophysical upper limits (cf. Sect. 24.5.1). The 'Statistical UL' refers to the loudest expected signal from a population of unknown isolated neutron stars spinning down due to GWs (cf. Sect. 24.2.2, (24.14))

of higher frequencies). In the case of LIGO-I, eLIGO and AdvLIGO the sensitivities plotted in Fig. 24.4 refer to multi-detector searches using the network of three detectors (H1+H2+L1). These sensitivities can only be reached in targeted searches for known pulsars, assuming ideal conditions of well-constrained parameters (e.g., negligible timing-noise and no glitches). As discussed in Sect. 24.4.5, wide-parameter searches are inherently less sensitive due to the large number of templates required.

24.5.2 Results from Completed Searches

S1: Targeted Search for PSR B1937+21

The fully coherent methods described in Sects. 24.4.3 and 24.4.4 were used to perform a targeted search for the millisecond pulsar PSR B1937+21, using data from the first LIGO science run (S1) [2]. The Doppler parameters (sky-position + spin) of this pulsar are well known and are extremely stable, which allows a single-template search. From the spin-down upper limit for this pulsar (cf. Fig. 24.4), it is obvious that no detection was expected, the motivation for this search was mainly to illustrate the methods and set an upper limit on the GW emission at $f = 2\nu$. The resulting best upper limit obtained was $h_0^{95\%} \sim 1.4 \times 10^{-22}$.

S2: $\mathcal{F}$-Statistic Wide-Parameter Search for Sco X-1

A coherent wide-parameter $\mathcal{F}$-statistic search for Sco X-1 was performed [6] using data from the S2 science run. Sco X-1 is a neutron star in a 18.9 h orbit around a low-mass companion, at a distance of $d \sim 2.8$ kpc from Earth. The sky-position $\boldsymbol{n}$ and orbital period P of Sco X-1 are well determined from X-ray observations, but both the projected semi-major axis a_p and the orbital phase $\bar{T}$ have large uncertainties and need to be treated as unknown (Doppler) parameters. The rotation frequency ν of the neutron star is also highly uncertain. Assuming the (not uncontroversial) beat-frequency model for QPOs [83], and a triaxial neutron star emitting GWs at a frequency $f = 2\nu$, the frequency window of the search would span at least $f \in [460, 620]$ Hz. Due to the enormous computational cost of this search, however, the frequency band had to be reduced to two smaller bands $f \in [464, 484]$ Hz and $f \in [604, 624]$ Hz. The scaling of the number of templates N_p for this Doppler parameter space ($\boldsymbol{\lambda} = \{f, a_p, \bar{T}\}$) is $N_p \propto T_{\mathrm{obs}}^6$, which severely limited the maximum possible observation time T_{obs}. The analysis pipeline consisted of two $\mathcal{F}$-statistic searches over the most sensitive $T_{\mathrm{obs}} = 6$ h of data from L1 and H1 respectively, followed by a coincidence step to reduce the number of false-alarm candidates. Upper limits of the order $h_0^{95\%} \sim 2 \times 10^{-22}$ were obtained over the range of parameters analyzed (labeled 'ScoX1[S2]' in Fig. 24.4).

S2: $\mathcal{F}$-Statistic All-Sky Search for Unknown Isolated Neutron Stars

A similar wide-parameter search with the $\mathcal{F}$-statistic was performed for unknown isolated neutron stars over the whole sky and in the frequency range $f \in [160, 729]\,\mathrm{Hz}$, assuming a frequency-derivative of less than $|\dot{f}| < 4 \times 10^{-10}\,\mathrm{Hz/s}$. The scaling of the number of templates with observation time T_{obs} for this Doppler space $\boldsymbol{\lambda} = \{\alpha, \delta, f\}$ is $N_p \propto T_{\mathrm{obs}}^3$, see Sect. 24.4.5. The analysis consisted of a similar pipeline to the Sco X-1 search, using the most sensitive $T_{\mathrm{obs}} = 10\,\mathrm{h}$ of data from L1 and H1, respectively, and reducing the false-alarm rate by a coincidence step. The best all-sky (frequentist) upper limit achieved was of the order $h_0^{95\%} \sim 7 \times 10^{-23}$, as shown in Fig. 24.4 (label 'Fstat[S2]').

S2: Hough All-Sky Search for Unknown Isolated Neutron Stars

The Hough-transform method (cf. Sect. 24.4.6) was used in an all-sky search for unknown isolated neutron stars [3] in the frequency range $f \in [200, 400]\,\mathrm{Hz}$, including one spin-down parameter $\dot{f} \in [-10^{-9}, +10^{-10}]\,\mathrm{Hz/s}$. The data from all three LIGO detectors was analyzed over the *whole* duration of $T_{\mathrm{obs}} = 2$ months of S2. This required searching of the order $N_p \sim 10^{12}$ templates (many orders of magnitude less than a coherent search would require for the same T_{obs}), which took less than half a day to complete on a 200-CPU cluster. The best all-sky upper limit obtained in this frequency-range was $h_0^{95\%} \sim 4.4 \times 10^{-23}$, and the results are summarized in Fig. 24.4 (label 'Hough[S2]'). The sensitivity achieved by this semi-coherent search is about a factor of *two* better than the equivalent $\mathcal{F}$-statistic search ('Fstat[S2]'), which required similar computing power. This is a consequence of the lower parameter-space resolution of semi-coherent methods, which allowed to use the full 2 months of data as opposed to only 10 h (cf. Sect. 24.4.6).

S2: Targeted Search for 28 Known Pulsars

The results from a targeted, fully coherent search for 28 known isolated radio pulsars in the LIGO band ($f = 2\nu \gtrsim 50\,\mathrm{Hz}$) have been reported in [4]. The analysis was based on the Bayesian approach described in Sect. 24.4.4, but the actual implementation used a highly efficient complex-heterodyning method described in [39]. Data from the S2 science run was analyzed, combining H1, L1 and H2 coherently (GEO600 did not take part in S2). The resulting Bayesian 95% confidence upper limits are shown in Fig. 24.4 (label 'Targeted[S2]'). Most of these upper limits are still a few orders of magnitude above the corresponding spin-down limits (where available), but for the globular-cluster pulsars with apparent spin-up, these are the first direct constraints available. The best strain upper limit obtained was $h_0^{95\%} \sim 1.7 \times 10^{-24}$ (for PSR J1910-5959D), and the best upper limit on the quadrupolar deformation was $\varepsilon^{95\%} \sim 4.5 \times 10^{-6}$ (for PSR J2124-3358). The upper limit for the Crab pulsar (PSR B0531+21) was found as $h_0^{95\%} \sim 4 \times 10^{-23}$, which is

within a factor of 30 from the spin-down upper limit. As discussed in Sect. 24.4.5, fully coherent targeted searches provide the best possible sensitivity, which is illustrated by these results: at similar computing cost, the targeted S2 search is about 25 times more sensitive than the semi-coherent searches, and about 50 times more sensitive than the fully coherent wide-parameter searches.

S4: Coherent Targeted Searches for Known Pulsars

Using the data from all three LIGO interferometers and GEO600 taken during the S3 and S4 science runs, a fully coherent targeted search for known pulsars (at $f = 2\nu$) has recently been completed [7]. The detailed upper limits are found in this paper, here we restrict ourselves to estimating the average sensitivity of this search by (24.52), and this estimate is shown in Fig. 24.4 (label 'Targeted[S4]'). According to this rough estimate the search would already appear to beat the spin-down limit of the Crab pulsar, but unfortunately this is not the case: the noise is less stationary at lower frequencies and there are also some side-effects from the strong spectral disturbance at 60 Hz (visible in Fig. 24.2), which stems from the mains power-line frequency. As a result the upper limit for the Crab pulsar still lies about a factor of 2.2 above the spin-down limit in this search. Using several months of S5 data, however, the Crab spin-down limit will be beaten for the first time, setting the astrophysically most relevant upper limit on the GW emission of any pulsar so far.

S4: Semi-Coherent Searches

An all-sky search for unknown isolated neutron stars in the frequency range $f \in [50\,\text{and}\,1,000]$ Hz on data from the S4 run ($T_{\text{obs}} \sim 500$ h) was completed [8] using the semi-coherent methods described in Sect. 24.4.6, namely Hough, StackSlide and PowerFlux. The stacks consisted of SFTs of duration $T_{\text{coh}} = 30$ min, and data from all three LIGO interferometers were used. The expected sensitivity for these searches can be directly estimated using (24.66), which is shown in Fig. 24.4 (label 'SemiCoherent[S4]').

24.5.3 Ongoing and Future Searches

Einstein@Home: S3 and Beyond

Einstein@Home (cf. Sect. 24.4.7) has completed a search on $T_{\text{obs}} = 600$ h of LIGO S3 data, and the results have been posted online [5]. The analysis pipeline consisted of $N = 60$ stacks (of $T_{\text{coh}} = 10$ h each) of coherent all-sky, wide-frequency searches using the $\mathcal{F}$-statistic. This coherent step was performed on the participating hosts and the results were returned to the central server for post-processing, where they were combined using a stacking/coincidence scheme.

Einstein@Home is aiming for detection, and no upper limits have been set so far. In order to obtain a rough estimate of the *approximate* level of sensitivity of such searches, we assume (somewhat optimistically) that the post-processing step results in a $\propto N^{1/4}$ improvement in sensitivity, as is characteristic for semi-coherent methods, e.g., (24.66). However, the numerical pre-factor in (24.66) critically depends on the threshold $2\mathcal{F}^*$ used in the coherent $\mathcal{F}$-statistic stacks. For Einstein@Home we had to choose a relatively high threshold of $2\mathcal{F}^* = 25$, in order to limit the total amount of (false-alarm) data from the individual stacks sent back to the central server for post-processing. Furthermore, due to the large total number of templates searched, we use a low false-alarm probability of $f_A = 3 \times 10^{-13}$. Using (6.40) of [52] and applying an extra factor of $1/\sqrt{m} \sim 1.4$ in order to account for an average grid mismatch of $m = 0.5$, we find a numerical pre-factor of ~ 72 instead of 8.5 as used in (24.66). The corresponding sensitivity-estimate is plotted in Fig. 24.4 (label 'E@H[S3]'). A similar search was performed on S4 data, using a total of $T_{obs} = 510$ h of data divided in $N = 17$ stacks of $\mathcal{F}$-statistic integrations over $T_{coh} = 30$ h. The results from this run are currently in the post-processing stage. A search on S5 data using the same pipeline has been completed as well, using $N = 28$ stacks of $T_{coh} = 30$ h.

The sensitivity of all these searches suffered from the same problem mentioned above for the S3 search, namely the high $2\mathcal{F}^*$-threshold required. This limitation, however, will be overcome in the setup for the current Einstein@Home search (labeled 'S5 R3'), which includes a semi-coherent Hough step *on* the host, combining the $\mathcal{F}$-statistic searches from 84 stacks of $T_{coh} = 25$ h. This hierarchical approach substantially reduces the amount of (false-alarm) data that needs to be sent back, allowing to use the optimal threshold $2\mathcal{F}^* = 5.2$ [52]. We can estimate the corresponding 'optimal' sensitivity of such an Einstein@Home search, which yields a numerical pre-factor of ~ 20 in (24.66), and the corresponding sensitivity estimate is shown in Fig. 24.4, labeled 'E@H [S5 R3]'.

24.5.4 Previous Upper Limits from Other Detectors

Bar Detectors: an earlier attempt to specifically target the Crab pulsar (at $f = 2\nu \sim 60$ Hz) was made with a specially-designed bar detector [74], setting an upper limit of $h_0 \sim 2 \times 10^{-22}$. A search targeting the millisecond pulsar PSR B1937+21 (at $f = 2\nu \sim 1284$ Hz) was performed by [46] using a split bar detector, producing an upper limit of $h_0 \sim 10^{-20}$. A search for unknown isolated neutron stars in a small frequency-band $f = (921.35 \pm 0.03)$ Hz and a small sky-region in the galactic center was performed using 95 days of data from the EXPLORER bar detector, and an upper limit of $h_0 \sim 3 \times 10^{-24}$ was obtained [17]. An all-sky search with 2 days of EXPLORER data in the frequency-band $f = (921.38 \pm 0.38)$ Hz was carried out using the $\mathcal{F}$-statistic, setting an upper limit of $h_0^{99\%} \sim 2 \times 10^{-23}$, reported in [18]. This, was later revised to $h_0^{90\%} \sim 10^{-22}$ in [19] using different conventions to determine the upper-limit. Another directed search was presented in [55]: data from

the ALLEGRO bar detector was searched for periodic GWs from the Galactic center and from the globular cluster 47 Tuc in the two antenna bands (896.80 ± 0.50) and (920.26 ± 0.50) Hz, setting an upper limit of $h_0 \sim 8 \times 10^{-24}$.

Interferometers: the first search using a broadband interferometer was carried out with the prototype 40 m detector at Caltech by [45]. The search was targeting PSR B1937+21, and resulted in upper limits of the order $h_0 \sim 3 \times 10^{-17}$ at $f = \nu$, and $h_0 \sim 1.5 \times 10^{-17}$ at $f = 2\nu$. Data from the first science run of the TAMA detector was searched for continuous GWs from SN1987A using coherent matched filtering over $T_{\mathrm{obs}} = 1,200$ h of data in a 0.05 Hz band at ~ 934.9 Hz, and the reported upper limit [72] was about $h_0^{99\%} \sim 5 \times 10^{-23}$. An earlier upper-limit result on SN1987A was obtained from a directed search using $T_{\mathrm{obs}} = 100$ h of data from the Garching prototype interferometer, which determined an upper limit of $h_0^{95\%} \sim 9 \times 10^{-21}$ in 4 Hz bands around $f = \nu \sim 1,670$ Hz and $f = 2\nu$ [58].

24.6 Future Prospects

LIGO has made enormous progress over the past 4 years, as seen in Fig. 24.2, reaching its design sensitivity with the S5 science run. This progress in sensitivity is also reflected in improving sensitivities of successive continuous-wave searches shown in Fig. 24.4. A detection of a spinning neutron star with LIGO-I is still somewhat unlikely (albeit not implausible), but continuous-wave searches are already beginning to enter a regime of increasing astrophysical relevance:

(1) A targeted pulsar search with S5 will beat the spin-down upper limit for the Crab pulsar. This is the first time that direct GW observations set an astrophysical constraint on the contribution of GWs to the observed pulsar spin-down.
(2) With 1 year of data from S5, the spin-down limits of at least two more pulsars (J0537-6910 and B1951+32) should be (marginally) reachable (see Fig. 24.4).
(3) The upper limits on the non-axisymmetry ε of known pulsars are entering the regime $\varepsilon \lesssim 10^{-6}$, which is physically possible according to our current understanding of neutron-star physics (cf. Sect. 24.2.1).
(4) The statistical upper-limit level $h_0 \sim 4 \times 10^{-24}$ for unknown isolated neutron stars (cf. Sect. 24.2.2) has been marginally reached by the semi-coherent searches using S4 data, and will be substantially surpassed by semi-coherent searches using S5 (especially Einstein@Home). Passing this milestone suggests that the possibility of a detection of an unknown isolated neutron star is becoming increasingly plausible.

Furthermore, the Virgo detector is beginning to approach comparable sensitivities to LIGO. Once it has reached its design sensitivity, Virgo should be able to beat the spin-down limit of up to three more known pulsars (including Vela), as seen in Fig. 24.4. Combining Virgo with the LIGO detector network will result in a further increase of $\sim 20\%$ in average sensitivity with respect to LIGO-I.

The Enhanced LIGO (eLIGO) upgrade might allow to reach the spin-down limit of two more known pulsars, and to beat the spin-down limit of J0537-6910. Following this, Advanced LIGO will be by far the most exciting instrument in the near future for GW searches from neutron stars, as seen in Fig. 24.4. It will allow to surpass the spin-down limits of several tens of known pulsars with 1 year of data, and it will comfortably include the Bildsten–Wagoner emission-level (24.20) of Sco X-1 (assuming, however, that substantially better observational constraints on the Sco X-1 parameters are available for a directed search). Advanced LIGO will dig down nearly three orders of magnitude below the statistic upper limit (24.14), making a detection of neutron-star signals seem rather likely. Given the current pace of progress and the encouraging prospects about future developments, it seems reasonable to be optimistic that gravitational-wave astrophysics of neutron stars will finally become a reality within the next decade or two.

References

1. Abbott, B. et al. (LIGO Collaboration): 2004a, *Nucl. Instrum. Methods Phys. Res. A.* **517**, 154
2. Abbott, B. et al. (LIGO Collaboration): 2004b, *Phys. Rev. D.* **69**, 082004
3. Abbott, B. et al. (LIGO Collaboration): 2005a, *Phys. Rev. D.* **72**, 102004
4. Abbott, B. et al. (LIGO Collaboration): 2005b, *Phys. Rev. Lett.* **94**, 181103
5. Abbott, B. et al. (LIGO Collaboration): 2005c, *Report on Einstein@Home S3 analysis*, http://einstein.phys.uwm.edu/
6. Abbott, B. et al. (LIGO Collaboration): 2007, *Phys. Rev. D.* **76**, 082001
7. Abbott, B. (LIGO Collaboration), Kramer, M., Lyne, A. G., et al. : 2007, *Phys. Rev. D.* **76**, 042001
8. Abbott, B. et al. (LIGO Collaboration): 2008, *Phys. Rev. D.* **77**, 022001
9. Abramovici, A. et al.: 1992, *Science* **256**, 325
10. Abramowitz, M., Stegun, I. A.: 1964, *Handbook of Mathematical Functions*, National Bureau of Standards
11. Andersson, N.: 1998, *ApJ* **502**, 708
12. Andersson, N.: 2003, *Class. Quant. Grav.* **20**, 105
13. Andersson, N., Kokkotas, K. D.: 1998, *MNRAS* **299**, 1059
14. Andersson, N., Kokkotas, K. D.: 2001, *Int. J. Mod. Phys. D* **10**, 381
15. Andersson, N., Kokkotas, K. D., Stergioulas, N.: 1999, *ApJ* **516**, 307
16. Andersson, N., Jones, D. I., Kokkotas, K. D.: 2002, *MNRAS* **337**, 1224
17. Astone, P. et al.: 2002, *Phys. Rev. D.* **65**, 022001
18. Astone, P. et al.: 2003, *Class. Quant. Grav.* **20**, 665
19. Astone, P. et al.: 2005, *Class. Quant. Grav.* **22**, S1243
20. Baiotti, L. et al.: 2007, *Phys. Rev. D.* **75**, 044023
21. Balasubramanian, R., Sathyaprakash, B. S., Dhurandhar, S. V.: 1996, *Phys. Rev. D.* **53**, 3033
22. Bildsten, L.: 1998, *ApJ* **501**, L89
23. Bonazzola, S., Gourgoulhon, E.: 1996, *A&A* **312**, 675
24. Bonazzola, S., Gourgoulhon, E.: 1997, in J.-A. Marck, J.-P. Lasota (eds.), *Relativistic Gravitation and Gravitational Radiation*, Cambridge Contemporary Astrophysics, UK, p. 151
25. Brady, P. R., Creighton, T.: 2000, *Phys. Rev. D.* **61**, 082001
26. Brady, P. R., Creighton, T., Cutler, C., Schutz, B. F.: 1998, *Phys. Rev. D.* **57**, 2101
27. Caron, B., Dominjon, A., Drezen, C., Flaminio, R., et al.: 1997, *Nucl. Phys. B Proc. Suppl.* **54**, 167
28. Carter, B., Langlois, D., Sedrakian, D. M.: 2000, *A&A* **361**, 795

29. Centrella, J. M., New, K. C. B., Lowe, L. L., Brown, J. D.: 2001, *ApJL* **550**, L193
30. Chakrabarty, D. et al.: 2003, *Nature* **424**, 42
31. Chandrasekhar, S.: 1970, *Phys. Rev. Lett.* **24**, 611
32. Christensen, N., Dupuis, R. J., Woan, G., Meyer, R.: 2004, *Phys. Rev. D.* **70**, 022001
33. Clark, J., Heng, I. S., Pitkin, M., Woan, G.: 2007, *Phys. Rev. D.* **76**, 043003
34. Cook, G. B., Shapiro, S. L., Teukolsky, S. A.: 1994, *ApJ* **424**, 823
35. Cutler, C.: 2002, *Phys. Rev. D.* **66**, 084025
36. Cutler, C., Jones, D. I.: 2001, *Phys. Rev. D.* **63**, 024002
37. Cutler, C., Schutz, B. F.: 2005, *Phys. Rev. D.* **72**, 063006
38. Cutler, C., Gholami, I., Krishnan, B.: 2005, *Phys. Rev. D.* **72**, 042004
39. Dupuis, R. J., Woan, G.: 2005, *Phys. Rev. D.* **72**, 102002
40. Feldman, G. J., Cousins, R. D.: 1998, *Phys. Rev. D.* **57**, 3873
41. Finn, L. S.: 1992, *Phys. Rev. D.* **46**, 5236
42. Frasca, S., Astone, P., Palomba, C.: 2005, *Class. Quant. Grav.* **22**, 1013
43. Friedman, J. L., Morsink, S. M.: 1998, *ApJ* **502**, 714
44. Friedman, J. L., Schutz, B. F.: 1978, *ApJ* **222**, 281
45. Hereld, M.: 1984, *Ph.D. Thesis (Caltech)*
46. Hough, J. et al.: 1983, *Nature* **303**, 216
47. Jaranowski, P., Królak, A.: 1994, *Phys. Rev. D.* **49**, 1723
48. Jaranowski, P., Królak, A.: 2005, *Living Rev. Relativ.* **8**, 3, http://www.livingreviews.org/lrr-2005-3
49. Jaranowski, P., Królak, A., Schutz, B. F.: 1998, *Phys. Rev. D.* **58**, 063001
50. Jones, D. I., Andersson, N.: 2002, *MNRAS* **331**, 203
51. Kittel, C.: 2005, *Introduction to solid state physics*, 8th edition, Wiley, New York
52. Krishnan, B., Sintes, A. M., Papa, M. A., Schutz, B. F., Frasca, S., Palomba, C.: 2004, *Phys. Rev. D.* **70**, 082001
53. Loredo, J. T.: 1990, in P. F. Fougère (ed.), *Maximum Entropy and Bayesian Methods*, pp 81–142, Kluwer Academic Publishers, The Netherlands
54. Manchester, R. N. et al.: 2005, *Astron. J.* **129**, 1993, http://www.atnf.csiro.au/research/pulsar/psrcat/
55. Mauceli, E., McHugh, M. P., Hamilton, W. O., et al., 2000, eprint arXiv:gr-qc/0007023
56. Melatos, A., Payne, D. J. B.: 2005, *ApJ* **623**, 1044
57. Misner, C. W., Thorne, K. S., Wheeler, J. A.: 1973, *Gravitation*, W. H. Freeman and Company, New York)
58. Niebauer, T. M. et al.: 1993, *Phys. Rev. D.* **47**, 3106
59. Owen, B. J.: 1996, *Phys. Rev. D.* **53**, 6749
60. Owen, B. J.: 2005, *Phys. Rev. Lett.* **95**, 211101
61. Owen, B. J.: 2006, *Class. Quant. Grav.* **23**, 1
62. Owen, B. J. et al.: 1998, *Phys. Rev. D.* **58**, 084020
63. Papaloizou, J., Pringle, J. E.: 1978, *MNRAS* **184**, 501
64. Payne, D. J. B., Melatos, A.: 2006, *ApJ* **641**, 471
65. Prix, R.: 2007, *Phys. Rev. D.* **75**, 023004
66. Ruderman, M.: 1969, *Nature* **223**, 597
67. Ruderman, M.: 1976, *ApJ* **203**, 213
68. Saijo, M., Gourgoulhon, E.: 2006, *Phys. Rev. D.* **74**, 084006
69. Schutz, B. F., Tinto, M.: 1987, *MNRAS* **224**, 131
70. Shapiro, S. L., Zane, S.: 1998, *ApJS* **117**, 531
71. Sivia, D. S.: 1996, *Data Analysis. A Bayesian Tutorial*, Oxford Science Publications, Oxford, UK
72. Soida, K. et al. (TAMA Collaboration): 2003, *Class. Quant. Grav.* **20**, 645
73. Stergioulas, N.: 2003, *Living Rev. Relativ.* **6**, 3, http://relativity.livingreviews.org/Articles/lrr-2003-3/
74. Suzuki, T.: 1995, in E. Coccia, G. Pizzella, F. Ronga (eds.), *First Edoardo Amaldi Conference on Gravitational Wave Experiments*, p. 115
75. Taylor, J. H., Weisberg, J. M.: 1989, *ApJ* **345**, 434

76. Thorne, K. S.: 1980, *Rev. Mod. Phys.* **52**, 299
77. Thorne, K. S.: 1987, in S. W. Hawking, W. Israel (eds.), *300 Years of Gravitation*, Chapt. 9, p. 330, Cambridge University Press, Cambridge, UK
78. Tinto, M., Estabrook, F. B., Armstrong, J. W.: 2004, *Phys. Rev. D.* **69**, 082001
79. Tsubono, K.: 1995, in E. Coccia, G. Pizzella, F. Ronga (eds.), *First Edoardo Amaldi Conference on Gravitational Wave Experiments*, p. 112
80. Unno, W., Osaki, Y., Ando, H., Saio, H., Shibahashi, H.: 1989, *Nonradial Oscillations of Stars*, second edition, University of Tokyo Press, Tokyo, Japan
81. Ushomirsky, G., Cutler, C., Bildsten, L.: 2000, *MNRAS* **319**, 902
82. Van Den Broeck, C.: 2005, *Class. Quant. Grav.* **22**, 1825
83. van der Klis, M., Wijnands, R. A. D., Horne, K., Chen, W.: 1997, *ApJL* **481**, L97
84. Wagoner, R. V.: 1984, *ApJ* **278**, 345
85. Wagoner, R. V.: 2002, *ApJ* **578**, L63
86. Wainstein, L., Zubakov, V.: 1962, *Extraction of Signals from Noise*, Prentice-Hall, Englewood Cliffs
87. Watts, A. L., Strohmayer, T. E.: 2007, *Astrophys. Space Sci.*, **308**, 625
88. Weisberg, J. M., Taylor, J. H.: 1984, *Phys. Rev. Lett.* **52**, 1348
89. Willke, B., Aufmuth, P., Aulbert, C., Babak, S., et al.: 2002, *Class. Quant. Grav.* **19**, 1377
90. Zimmermann, M., Szedenits, Jr., E.: 1979, *Phys. Rev. D.* **20**, 351

Acknowledgments

J. Arons: I have benefitted from many discussions with A. Spitkovsky, P. Chang, N. Bucciantini, E. Amato, R. Blandford, F. Coroniti, D. Backer and E. Quataert. My research efforts on these topics have been supported by NSF grant AST-0507813 and NASA grant NNG06G108G, both to the University of California, Berkeley; by the Department of Energy contract to the Stanford Linear Accelerator Center no. DE-AC3-76SF00515; and by the taxpayers of California.

W. Becker: I'm grateful to the Heraeus-Foundation for financing the 363rd Heraeus-Seminar on Neutron Stars and Pulsars which took place in May 2006 at the Physikzentrum in Bad Honnef. A selection of papers presented at this meeting and at the IAU Joined Discussion JD02 in Prague in August 2006 became the groundwork to produce this book. I'm further thankful to Joachim Trümper and Harald Lesch for their help and support in organizing the Heraeus-Seminar and to Günther Hasinger as well as the MPE for additional financial support. Without the great organizational talent and help of Christa Ingram the meetings would not have been what they were. Thanks also for her help in producing this book. Christian Saedtler has spend many days in producing the index of this book. Sincere thanks to him for taking the time. All articles in this book were refereed. I am much obliged to all colleagues who helped in this process. Special thanks goes to Dr. Jaroslaw Dyks, Dr. Ulrich Geppert, Prof. Dr. Yashwant Gupta, Dr. John Kirk, Dr. Maura McLaughlin, Prof. Dr. Andreas Reisenegger and Prof. Dr. Bronislaw Rudak.

K.S. Cheng: We are benefited from the useful conversions and suggestions from H.K. Chang, J.J. Jia, K. Hirotani, J. Takata, M. Ruderman, Anisia Tang, and L. Zhang. This work is partially supported by a RGC grant of Hong Kong Government under HKU7015/05P.

U. Geppert: I gratefully acknowledge collaboration and discussions with W. Becker, F. Haberl, D. Page, J. Pons, K.-H. Rädler, M. Rheinhardt, and J. Trümper. I am especially grateful to J. Pons and M. Rheinhardt for carefully reading this manuscript.

J. Grindlay and S. Bogdanov: We thank our collaborators on our various MSP papers as cited here. This work was supported in part by various Chandra grants, currently GO7-8033A.

K. Hurley: This research has made use of data obtained from the High Energy Astrophysics Science Archive Research Center (HEASARC), provided by NASA's Goddard Space Flight Center.

O.C. de Jager and A. Djannati-Ataï: The first author acknowledges support from the South African Department of Science & Technology and National Research Foundation Research Chair: Astrophysics & Space Science. Support from the GDRI-GREAT French, German, South African & Namibian multinational funding source is also acknowledged. The authors would like to thank members of the Supernova Remnant, Pulsar and Plerion working group of the H.E.S.S. collaboration for useful discussions.

J.G. Kirk, Y. Lyubarsky, and J. Pétri: Our work was supported by a grant from the G.I.F. the German-Israeli Foundation for Scientific Research and Development.

M. Kramer: I am grateful to all my co-workers who contributed so significantly to this work. They are I.H. Stairs, R.N. Manchester, M.A. McLaughlin, A.G. Lyne, R.D. Ferdman, M. Burgay, D.R. Lorimer, A. Possenti, N. D'Amico, J.M. Sarkissian, G.B. Hobbs, J.E. Reynolds, P.C.C. Freire and F. Camilo. It is a pleasure to thank Thibault Damour and Norbert Wex for very useful discussions. The Parkes radio telescope is part of the Australia Telescope which is funded by the Commonwealth of Australia for operation as a National Facility managed by CSIRO. The National Radio Astronomy Observatory is a facility of the U.S. National Science Foundation operated under cooperative agreement by Associated Universities, Inc.

J.M.E Kuipers: I would like to thank my collaborators P.-K. Fung (Royal Netherlands Meteorological Institute, De Bilt, The Netherlands), and D. Khechinashvili (Abastumani Astrophysical Observatory, Georgia), and Dr. A. Jessner for their stimulating discussions.

D.R. Lorimer: While the text is a significant update of an earlier article and presents my personal views on this topic, many of my opinions have been formed from the investigations and results of others. In particular, I wish to acknowledge numerous stimulating discussions and debates on pulsar statistics over the years with M. Bailes, Ed van den Heuvel, S. Johnston, R.N. Manchester, A.G. Lyne and J. Cordes.

M. McLaughlin: Many thanks to J. Cordes, A.G. Lyne, N. Rea, D. Lorimer and M. Kramer for their contributions to the work described in my review. I am also grateful to WVU undergraduates D. Ludovici and G. Habib for their discoveries of new RRATs in the PMPS and PH survey and to WVU graduate student J. Boyles for his help processing new GBT data on the RRATs. I thank M. Burgay and J. Deneva for their assistance with new RRATs found in the PH and PALFA survey. None of this work would be possible without the observing assistance of the PMPS team. Many thanks also to all on the PH, DMB and PALFA survey teams.

D. Page: The results presented in my paper are strongly indebted to my recent collaborators, M. Küker, U. Geppert, J.M. Lattimer, M. Prakash, S. Reddy, and A.W. Steiner, but the content and its errors are only the fault of the author. I also warmly acknowledge many discussions with Dima Yakovlev, either directly or through e-mail, whose impact on my work could not be overstated. Jillian A. Henderson is also warmly acknowledged for careful reading of this manuscript. This work was partially supported by a grant from UNAM's DGAPA program PAPIIT, #IN-119306.

R. Prix (for the LIGO Scientific Collaboration): The authors gratefully acknowledge the support of the United States National Science Foundation for the construction and operation of the LIGO Laboratory and the Particle Physics and Astronomy Research Council of the United Kingdom, the Max-Planck-Society and the State of Niedersachsen/Germany for support of the construction and operation of the GEO600 detector. The authors also gratefully acknowledge the support of the research by these agencies and by the Australian Research Council, the Natural Sciences and Engineering Research Council of Canada, the Council of Scientific and Industrial Research of India, the Department of Science and Technology of India, the Spanish Ministerio de Educacion y Ciencia, The National Aeronautics and Space Administration, the John Simon Guggenheim Foundation, the Alexander von Humboldt Foundation, the Leverhulme Trust, the David and Lucile Packard Foundation, the Research Corporation, and the Alfred P. Sloan Foundation. This document has been assigned LIGO Laboratory document number LIGO-P060039-05-Z.

M. Ruderman: I am happy to thank A. Beloborodov, E.V. Gotthelf, J.P. Halpern, P. Jones, A. Lyne, J. Sauls, J. Trümper, and colleagues at the Institute of Astronomy (Cambridge) and the Center for Astrophysics and Space Sciences (UCSD) for helpful discussions and hospitality. I am especially grateful to U. Geppert for his excellent advice and criticism.

S. Tsuruta: I acknowledge with special thanks the contributions by and valuable discussions with W. Becker, T. Takatsuka, R. Tamagaki, J. Sadino, A. Liebmann, M.A. Teter, A. Kobelsky, J. Thiel, H. Umeda, K. Nomoto, T. Tatsumi, W. Candler, and K. Fukumura. Thanks are due to K. Nomoto and T. Tatsumi for their hospitality during our visits to Tokyo University and Kyoto University. Our work for this paper has been supported in part by NASA grants NAG5-12079, AR3-4004A, and G02-3097X.

F. Weber, R. Negreiros, and P. Rosenfield: The material used in this review paper is based upon work supported by the National Science Foundation under Grant No. 0457329, and by the Research Corporation.

V.E. Zavlin: I gratefully acknowledge the collaboration with George Pavlov and many other colleagues in studying neutron stars during the last 15 years. This work was supported in part by a NASA Associateship Award.

Index